Transactions of the ASME®

Journal of Applied Mechanics

Published Quarterly by The American Society of Mechanical Engineers

VOLUME 63 • NUMBER 2 • JUNE 1996

Technical Editor, **LEWIS T. WHEELER (1997)**

Department of Mechanical Engineering,
University of Houston,
Houston, TX 77204-4792

APPLIED MECHANICS DIVISION

Chairman, **T. A. CRUSE**
Secretary, **A. NEEDLEMAN**
Associate Technical Editors,
R. ABEYARATNE (1997)
T. R. AKYLAS (1997)
D. M. BARNETT (1996)
R. BECKER (1998)
S. A. BERGER (1997)
I. M. DANIEL (1996)
W. J. DRUGAN (1997)
J. T. JENKINS (1996)
J. W. JU (1998)
S. KYRIAKIDES (1997)
S. LICHTER (1998)
W. K. LIU (1996)
X. MARKENSCOFF (1997)
M. ORTIZ (1998)
J. N. REDDY (1998)
W. N. SHARPE, JR. (1996)
S. W. SHAW (1997)
M. SHINOZUKA (1997)
M. TAYA (1996)

BOARD ON COMMUNICATIONS

Chairman and Vice-President
R. MATES

Members-at-Large
T. BARLOW, N. H. CHAO, A. ERDMAN, G. JOHNSON, L. KEER, E. M. PATTON, S. PATULSKI, S. ROHDE, R. SHAH, F. WHITE, J. WHITEHEAD, K. T. YANG

OFFICERS OF THE ASME
President, **D. T. KOENIG**
Executive Director, **D. L. BELDEN**
Treasurer, **R. A. BENNETT**

PUBLISHING STAFF
Managing Director, Engineering
CHARLES W. BEARDSLEY
Director, Technical Publishing
PHILIP DI VIETRO
Managing Editor, Technical Publishing
CYNTHIA B. CLARK
Managing Editor, Transactions
CORNELIA MONAHAN
Production Coordinator
JUDITH SIERANT
Production Assistant
MARISOL ANDINO

Transactions of the ASME, Journal of Applied Mechanics (ISSN 0021-8936) is published quarterly (Mar., June, Sept., Dec.) for $210.00 per year by The American Society of Mechanical Engineers, 345 East 47th Street, New York, NY 10017.

Second class postage paid at New York, NY and additional mailing office. POSTMASTER: Send address changes to Transactions of the ASME, Journal of Applied Mechanics, c/o THE AMERICAN SOCIETY OF MECHANICAL ENGINEERS, 22 Law Drive, Box 2300, Fairfield, NJ 07007-2300.

CHANGES OF ADDRESS must be received at Society headquarters seven weeks before they are to be effective. Please send old label and new address. **PRICES:** To members, $40.00, annually: to nonmembers, $210.00. Add $30.00 for postage to countries outside the United States and Canada.

STATEMENT from By-Laws. The Society shall not be responsible for statements or opinions advanced in papers or . . . printed in its publications (B7.1, Para. 3). **COPYRIGHT © 1996** by The American Society of Mechanical Engineers. Authorization to photocopy material for internal or personal use under circumstances not falling within the fair use provisions of the Copyright Act is granted by ASME to libraries and other users registered with the Copyright Clearance Center (CCC). Transactional Reporting Service provided that the base fee of $3.00 per article is paid directly to CCC, Inc., 222 Rosewood Drive, Danvers, MA 01923. Request for special permission or bulk copying should be addressed to Reprints/Permission Department.

INDEXED by Applied Mechanics Reviews and Engineering Information, Inc.
Canadian Goods & Services Tax Registration #126148048.

TECHNICAL PAPERS

245 **Surface Displacements due to a Steadily Moving Point Force**
J. R. Barber

252 **Stress Singularity in Three-Phase Bonded Structure**
Hideo Koguchi, Tadanobu Inoue, and Toshio Yada

259 **The Rebound of an Elastic Sphere Against a Rigid Wall**
P. Villaggio

264 **Singularities at the Tip of a Crack Terminating Normally at an Interface Between Two Orthotropic Media**
J. C. Sung and J. Y. Liou

271 **Interface Cracks in a Layered Solid Subjected to Contact Stresses**
C. H. Liu and I-Feng Chen

278 **The Boundary Contour Method for Three-Dimensional Linear Elasticity**
A. Nagarajan, S. Mukherjee, and E. Lutz

287 **Three-Dimensional Analysis of Surface Cracks in an Elastic Half-Space**
Quanxin Guo, Jian-Juei Wang, and R. J. Clifton

295 **Singularities at Grain Triple Junctions in Two-Dimensional Polycrystals With Cubic and Orthotropic Grains**
R. C. Picu and V. Gupta

301 **Stress Distributions During Fiber Pull-Out**
R. Krishna Kumar and J. N. Reddy

307 **A Critical Study of the Applicability of Rigid-Body Collision Theory**
D. Stoianovici and Y. Hurmuzlu

317 **Bifurcation of Orthotropic Solids**
G. deBotton and K. Schulgasser

321 **Localization due to Damage in Two-Direction Fiber-Reinforced Composites**
F. Hild, P.-L. Larsson, and F. A. Leckie

327 **A Method to Determine the Plane-Strain Yield Locus for Ductile Crystals**
R. R. Nikolic

331 **Conservation Laws for Thermo or Poroelasticity**
N. Chien and G. Herrmann

337 **Transient Elastic Waves in a Transversely Isotropic Plate**
R. L. Weaver, W. Sachse, and Kwang Yul Kim

347 **An Efficient Calculation of the Load and Coefficient of Restitution of Impact Between Two Elastic Bodies With a Liquid Lubricant**
L. Chang

353 **A Split Hopkinson Bar Technique to Evaluate the Performance of Accelerometers**
T. C. Togami, W. E. Baker, and M. J. Forrestal

357 **The Effective Dilatational Response of Fiber-Reinforced Composites With Nonlinear Interface**
A. J. Levy

365 **Three-Dimensional Finite Element Analysis of Surface Deformation and Stresses in an Elastic-Plastic Layered Medium Subjected to Indentation and Sliding Contact Loading**
E. R. Kral and K. Komvopoulos

376 **A General Orthotropic von Mises Plasticity Material Model With Mixed Hardening: Model Definition and Implicit Stress Integration Procedure**
M. Kojić, N. Grujović, R. Slavković, and M. Živković

383 **Dynamics and Control of Electrostatic Structures**
L. Silverberg and L. Weaver, Jr.

392 **Dynamics of Plane Motion of an Elastic Rod**
T. M. Atanackovic and L. J. Cveticanin

399 **Nonstandard Models for Thin-Walled Beams With a View to Applications**
N. Rizzi and A. Tatone

404 **Instability of Laminar Natural Convection Boundary Layer Flow on a Vertical Porous Flat Plate**
T. Watanabe, H. Taniguchi, and I. Pop

411 **Dynamics of a Gas Permeable Contact Lens During Blinking**
P. E. Raad and A. S. Sabau

(Contents continued on Outside Back Cover)

Downloaded 04 May 2010 to 171.66.16.52. Redistribution subject to ASME license or copyright; see http://www.asme.org/terms/Terms_Use.cfm

CONTENTS (CONTINUED)

419 **The Strain Energy Density of Compressible, Rubber-Like Shells of Revolution**
R. F. Yükseler

424 **On the Definition of the Deformed Reference Surface of Rubber-Like Shells of Revolution**
R. F. Yükseler

429 **Melnikov Process for Stochastically Perturbed, Slowly Varying Oscillators: Application to a Model of Wind-Driven Coastal Currents**
E. Simiu

436 **The Flow Near a Rotating Disk: An Approximate Solution**
P. D. Ariel

439 **Vibration and Stability of a Spinning Disk Under Stationary Distributed Edge Loads**
Jen-San Chen

445 **Transition From Soliton to Chaotic Motion Following Sudden Excitation of a Nonlinear Structure**
M. A. Davies and F. C. Moon

450 **Stress and Strain Analysis in Molecular Dynamics Simulation of Solids**
P. A. Scagnetti, R. J. Nagem, G. V. H. Sandri, and T. G. Bifano

453 **Prediction of Mode Parameters and Moment-Rotation Curves for Crushed Thin-Walled Trapezoidal Tubes in Bending**
M. S. Park and B. C. Lee

460 **On the Growth-of-Waviness in Fiber-Reinforced Polymer Composites: Viscoelastic Bifurcation and Imperfection Sensitivity**
M. S. Bhalerao and T. J. Moon

467 **Derivation of a Thin Film Equation by a Direct Approach**
F. Y. Huang and C. D. Mote, Jr.

474 **Dynamic Analysis of Nonuniform Beams With Time-Dependent Elastic Boundary Conditions**
Sen Yung Lee and Shueei Muh Lin

479 **An Analysis of Cracking in a Layered Medium With a Functionally Graded Nonhomogeneous Interface**
Hyung Jip Choi

487 **Chaotic Vibration in Fluid-Stiffness-Controlled Instability of a Tube Row in Crossflow**
S. H. Chen and S. S. Chen

493 **Exact Stationary Solutions of Stochastically Excited and Dissipated Integrable Hamiltonian Systems**
W. Q. Zhu and Y. Q. Yang

501 **Chaos in a Spacecraft Attitude Maneuver Due to Time-Periodic Perturbations**
G. L. Gray, I. Dobson, and D. C. Kammer

509 **Analysis of a Nonlinear System Exhibiting Chaotic, Noisy Chaotic, and Random Behaviors**
H. Lin and S. C. S. Yim

517 **A Simple Model of a Stiffened Shell-Type Structure for an Investigation Into the Vibration-Buckling Correlation**
V. M. Ryaboy and T. Weller

523 **Transient Solutions of the Ring-Spinning Balloon Equations**
D. M. Stump and W. B. Fraser

529 **Modeling of Interfacial Shear for Gas Liquid Flows in Annular Film Condensation**
A. Narain

539 **A Simplified Displacement-Rotation Form for the Equations of Motion of Nonlinearly Elastic Shells of Revolution Undergoing Combined Bending and Torsion**
J. G. Simmonds

543 **Flow Past a Flat Plate With a Vortex/Sink Combination**
N. J. Mourtos and M. Brooks

BRIEF NOTES

Viscoelastic Minimum Principles Revisited 551
S. Hazanov

Some Faults in the Stress Analysis of Power-Hardening Materials With Pseudo-Stress Function Method 554
Peng Yafei, Shen Yapeng, and Chen Yiheng

555 Application of Normal Mode Expansion to Accoustic Emission Waves in Finite Plates
M. R. Gorman and W. H. Prosser

(Contents continued on page 492)

Downloaded 04 May 2010 to 171.66.16.52. Redistribution subject to ASME license or copyright; see http://www.asme.org/terms/Terms_Use.cfm

CONTENTS (CONTINUED)

DISCUSSION

558 **Three-Dimensional Elasticity Solution for the Buckling of Transversely Isotropic Rods: The Euler Load Revisited, by G. A. Kardomateas—Discussions by K. T. Chau and C. W. Bert**

560 **Initial Post-buckling Behavior of Thick Rings Under Uniform External Hydrostatic Pressure, by Lei Fu and A. M. Waas—Discussion by R. Schmidt**

BOOK REVIEW

561 **Micromechanics: Overall Properties of Heterogeneous Materials, by S. Nemat-Nasser and M. Lori—Reviewed by S. K. Datta**

ERRATA

418 **A Nonlinear Wound Roll Model Allowing for Large Deformation, by R. C. Benson and published in the Dec. 1995 issue of the *Journal of Applied Mechanics***

ANNOUNCEMENTS AND SPECIAL NOTES

251	68th Annual Meeting of The Society of Rheology—Announcement
277	3rd EUROMECH Solid Mechanics Conference—Announcement
326	Change of Address form
444	Thermal Stresses '97—Announcement
562	Worldwide Mechanics Meetings Conference Listing
inside back cover	Information for Authors

Downloaded 04 May 2010 to 171.66.16.52. Redistribution subject to ASME license or copyright; see http://www.asme.org/terms/Terms_Use.cfm

J. R. Barber
Department of Mechanical Engineering
and Applied Mechanics,
University of Michigan,
Ann Arbor, MI 48109-2125

Surface Displacements due to a Steadily Moving Point Force

Closed-form expressions are obtained for the normal surface displacements due to a normal point force moving at constant speed over the surface of an elastic half-space. The Smirnov-Sobolev technique is used to reduce the problem to a linear superposition of two-dimensional stress and displacement fields.

1 Introduction

In this paper we shall investigate the normal surface displacement of the isotropic elastic half-space $z > 0$, due to a normal point force, F, which moves with constant speed, V, in the x-direction over the surface $z = 0$. This problem defines the Green's function for a class of elastodynamic contact problems for the half-space in which a frictionless rigid indenter moves at constant speed over the surface.

We assume that the force has been moving for a long time, so that the stress and displacement fields have achieved a steady state when viewed in a frame of reference that moves with the force. The more challenging transient problem in which the half-space is initially quiescent and the force moves for a finite time was investigated by Payton (1964), who gave results for the special case where Poisson's ratio $\nu = \frac{1}{4}$. A more convenient solution to the steady-state problem for general Poisson's ratio was given by Churilov (1977), who also extended the argument to give simple solutions to some elastodynamic contact problems (Churilov, 1978).

The steady-state problem is self-similar and we can therefore use equilibrium and dimensional arguments to demonstrate that the stresses must decay with R^{-2} and the displacements with R^{-1}, where R is the distance from the moving force (see, for example, Willis, 1967; Barber and Sturla, 1992). The problem therefore reduces to the determination of the ϕ-dependence of the normal surface displacements in a cylindrical polar coordinate system (r, ϕ, z) moving with the force.

Churilov's solution is based on his observation that the governing elastodynamic equations in the moving frame of reference have the same form as the elastostatic equations for a fictitious anisotropic material. The problem is thereby reduced to that of the point force acting on a half-space of this fictitious material, for which Churilov uses the method of Sveklo (1964), which is in turn based on a technique due to Smirnov and Sobolev (see for example Eringen and Suhubi, 1975, Section 8.8). However, it can be shown that Churilov's fictitious anisotropic material has physically reasonable (i.e., positive definite) elastic constants if and only if the speed V in the real problem is less than the shear wave speed c_2.

In the present paper, we shall demonstrate that the Smirnov-Sobolev technique can be applied directly to the elastodynamic problem, without invoking the analogy to anisotropic elastostatics. This will permit us to obtain simple closed-form expressions for the normal surface displacements over the entire speed range and also points up some interesting relationships between the present three-dimensional problem and the two-dimensional problem of a line load moving on the surface of a half-plane solved by Cole and Huth (1958).

2 Solution of the Problem

2.1 The Smirnov-Sobolev Technique. The basis of the Smirnov-Sobolev technique is to represent a fairly general three-dimensional field by the superposition of two-dimensional fields of differing orientation. We define a fixed Cartesian coordinate system x, y, z in which the plane $z = 0$ is the surface of the half-space $z > 0$. We then define a second system x_1, y_1, z rotated through angle θ about the z-axis, through the relations

$$x_1 = x \cos \theta + y \sin \theta; \tag{1}$$

$$y_1 = y \cos \theta - x \sin \theta. \tag{2}$$

We can envisage a two-dimensional solution in the rotated system in which a scalar field quantity $f(x_1, z)$ is independent of y_1. A more general three-dimensional solution can then be obtained by superposing such functions with different values of θ. The most general such function can be written

$$g(x, y, z) = \int_{-\pi/2}^{\pi/2} f(x_1, z, \theta) d\theta, \tag{3}$$

where we remark that θ appears in the function $f(x_1, z, \theta)$ only as a parameter. In other words, f is any two-dimensional solution of the field equations expressed in the rotated system (x_1, y_1, z). Notice that it is not necessary to include a full 2π range in θ, since a rotation of π maps the coordinate system into itself except for a sign change.

We emphasise the superpositional nature of this representation because it is then clear that the method can be applied to any linear system. In particular, it is not necessary to resort to Churilov's device of reducing the elastodynamic problem to an equivalent anisotropic elastostatic problem. Instead, we shall develop the solution by direct superposition of relatively simple two-dimensional elastodynamic results.

Equation (3) can also be written in terms of polar coordinates (r, ϕ, z), where $x = r \cos \phi$, $y = r \sin \phi$. Using (1), we then have

$$g(r, \phi, z) = \int_{-\pi/2}^{\pi/2} f(r \cos (\theta - \phi), z, \theta) d\theta. \tag{4}$$

The special case where f is independent of the parameter θ and even in x_1 leads to an axisymmetric function g. To prove this, note that Eq. (4) then reduces to

$$g(r, \phi, z) = \int_{-\pi/2}^{\pi/2} f(r \cos (\theta - \phi), z) d\theta. \tag{5}$$

A change of variable $\psi = \theta - \phi$ and the evenness of the function f then require that this integral be the same as

Contributed by the Applied Mechanics Division of THE AMERICAN SOCIETY OF MECHANICAL ENGINEERS for publication in the ASME JOURNAL OF APPLIED MECHANICS.

Discussion on this paper should be addressed to the Technical Editor, Professor Lewis T. Wheeler, Department of Mechanical Engineering, University of Houston, Houston, TX 77204-4792, and will be accepted until four months after final publication of the paper itself in the ASME JOURNAL OF APPLIED MECHANICS.

Manuscript received by the ASME Applied Mechanics Division, Jan. 19, 1995; final revision, Apr. 11, 1995. Associate Technical Editor: D. M. Barnett.

Copyright © 1996 by ASME

Downloaded 04 May 2010 to 171.66.16.33. Redistribution subject to ASME license or copyright; see http://www.asme.org/terms/Terms_Use.cfm

$$g(r, \phi, z) = \int_{-\pi/2}^{\pi/2} f(r \cos \psi, z) d\psi, \quad (6)$$

which is clearly independent of ϕ.

2.2 The Sveklo Transformation. The function $f(x_1, z, \theta)$ can be regarded as a transform of $g(r, \phi, z)$. For it to be useful, it is desirable that we be able to invert the transform—i.e., to determine the two-dimensional function f that will generate a given three-dimensional function g. Sveklo (1964) has shown that this inversion can be reduced to the solution of an Abel integral equation when the function g is axisymmetric. Consider the equation

$$g(r) = \int_{-\pi/2}^{\pi/2} f(r \cos \theta) d\theta. \quad (7)$$

Writing $s = r \cos \theta$, we then have

$$g(r) = 2 \int_0^r \frac{f(s) ds}{\sqrt{r^2 - s^2}}, \quad (8)$$

which is an Abel integral equation for f with solution

$$f(s) = \frac{1}{\pi} \frac{d}{ds} \int_0^s \frac{r g(r) dr}{\sqrt{s^2 - r^2}}. \quad (9)$$

The technique will generally be applied to boundary-value problems in which some quantity $g(r, \phi, 0) \equiv g(r)$ is defined to be axisymmetric on the surface $z = 0$. We note however that z appears only as a parameter in Eq. (5) and hence the same inversion would permit us to determine the two-dimensional function $f(x_1, z)$ from the axisymmetric function $g(r, z)$.

2.3 Uniform Loading Over the Circle. To avoid the singularity associated with the concentrated normal force, it is convenient to consider the case where the half-space is loaded by a uniform pressure

$$p(r) = \frac{F}{\pi a^2}; \quad 0 < r < a, \quad (10)$$

the rest of the surface, $r > a$, being traction-free. We can later recover the point force result by allowing the radius a of the loaded region to tend to zero. Replacing g in (9) by p and evaluating the integral, we find

$$f(x_1) = \frac{F}{\pi^2 a^2}; \quad |x_1| < a \quad (11)$$

$$= \frac{F}{\partial^2 a^2} \left(1 - \frac{|x_1|}{\sqrt{x_1^2 - a^2}} \right); \quad |x_1| > a. \quad (12)$$

The function $f(x_1)$ describes a two-dimensional distribution of pressure on the surface that is uniform in the strip $-a < x_1 < a$ and negative outside this strip. Readers preferring a physical interpretation of Sveklo's transformation might note that, if such a distribution of pressure is superposed under rotation about the z-axis, the resulting axisymmetric pressure distribution is that defined by Eq. (10). Thus, if we can find the surface displacement due to the two-dimensional pressure distribution (11), (12), a similar superposition will enable us to find the same quantity for the axisymmetric pressure distribution (10).

Notice that the final displacement field will only exhibit the same axisymmetry as the load if the displacement associated with the two-dimensional problem in the transformed domain is the same for all θ. This will clearly not be the case if the material is generally anisotropic, since the elastic constants will depend on orientation.

When the load (10) moves at constant speed V in the x-direction over the surface, the corresponding transformed problem involves a two-dimensional field defined by (11), (12) also moving at speed V in the x-direction. Denoting the velocity vector $\mathbf{V} = V\mathbf{i}$, where $\mathbf{i}$ is the unit vector in the x-direction, we note that the component of $\mathbf{V}$ in the y_1-direction causes no change in the pressure distribution with time, so the transformed problem is the same as if the distribution (11), (12) were to move at speed $V \cos \phi$ in the direction x_1. We now proceed to the solution of this problem.

2.4 Solution of the Two-Dimensional Problem. The surface displacement due to the distribution (11), (12) moving at constant speed $V \cos \phi$ in direction x_1 could be obtained by convolution on the two-dimensional elastodynamic Green's function due to Cole and Huth (1958) and corrected by Rahman (1990) and Georgiadis and Barber (1993a,b). These authors showed that the normal surface displacement due to a line load P moving at constant speed V is

$$u_z(x, 0) = \frac{P}{\mu} [F_1(V) \log (r) + F_2(V) H(-x)] \quad (13)$$

(omitting an arbitrary rigid-body displacement), where $r = |x|$ is the distance from the moving load and

$$F_1(V) = \frac{M_2^2 \sqrt{1 - M_1^2}}{\pi R(V)}; \quad V < c_2$$

$$= \frac{M_2^2 (2 - M_2^2)^2 \sqrt{1 - M_1^2}}{\pi [(2 - M_2^2)^4 + 16(1 - M_1^2)(M_2^2 - 1)]}; \quad c_2 < V < c_1$$

$$= 0; \quad V > c_1 \quad (14)$$

$$F_2(V) = 0; \quad V < c_2$$

$$= \frac{4 M_2^2 (1 - M_1^2) \sqrt{M_2^2 - 1}}{(2 - M_2^2)^4 + 16(1 - M_1^2)(M_2^2 - 1)}; \quad c_2 < V < c_1$$

$$= \frac{M_2^2 \sqrt{M_1^2 - 1}}{(2 - M_2^2)^2 + 4\sqrt{(M_1^2 - 1)(M_2^2 - 1)}}; \quad V > c_1. \quad (15)$$

In these equations,

$$M_i = \frac{V}{c_i}; \quad i = 1, 2, \quad (16)$$

$c_1 = \sqrt{(\lambda + 2\mu)/\rho}$, $c_2 = \sqrt{\mu/\rho}$ are the dilatational and shear wave speeds, respectively, λ, μ are Lamé's constants, ρ is the density, and

$$R(V) \equiv (2 - M_2^2)^2 - 4\sqrt{(1 - M_1^2)(1 - M_2^2)} \quad (17)$$

is the Rayleigh function, which passes through zero at the Rayleigh wave speed c_R.

Readers familiar with the fracture mechanics literature will immediately recognize Eq. (11), (12) as defining the traction distribution on the crack plane for a Griffith crack $-a < x_1 < a$ opened by a uniform pressure $F/(\pi^2 a^2)$—see, for example, Barber (1992), Eq. (13.37). Thus, for the static case ($V = 0$), the normal displacement on the plane $z = 0$ is given by Eq. (13.41) of Barber (1992) as

$$u_z(x_1, 0) = \frac{F(1 - \nu)}{\pi^2 a^2 \mu} \sqrt{a^2 - x_1^2} \quad -a < x_1 < a \quad (18)$$

$$= 0 \quad |x_1| > a. \quad (19)$$

Furthermore, we notice from (13)–(15), that for $V < c_2$ the Green's function reduces to $u_z(x, 0) = [PF_1(V)/\mu] \log (r)$, which is identical with the static Green's function for a material with a reduced elastic modulus

$$\mu^* = \frac{\mu F_1(0)}{F_1(V)} = -\frac{\mu(1 - \nu)}{\pi F_1(V)}. \quad (20)$$

Notice that $F_1(V) < 0$ for $0 < V < c_R$ and also that $\mu^* \to 0$

Downloaded 04 May 2010 to 171.66.16.33. Redistribution subject to ASME license or copyright; see http://www.asme.org/terms/Terms_Use.cfm

as $V \to c_R$ because of the factor $R(V)$ in the denominator of $F_1(V)$.

The normal surface displacement due to the distribution (11), (12) moving at speed $V \cos\theta < c_2$ can therefore be obtained immediately from (18), (19), by replacing μ with the effective modulus corresponding to the speed $V \cos\theta$, with the result

$$u_z(x_1, 0) = -\frac{FF_1(V\cos\theta)}{\pi a^2 \mu}\sqrt{a^2 - x_1^2} \quad -a < x_1 < a \tag{21}$$

$$= 0 \quad |x_1| > a. \tag{22}$$

It is convenient at this stage to proceed to the limit in which the radius a of the loaded circle tends to zero, while the total force F remains constant. In this limit, it can be shown by evaluating the integral $\int_{-\infty}^{\infty} u_z(x_1, 0)dx_1$ that Eqs. (21), (22) define the delta function

$$u_z(x_1, 0) = -\frac{FF_1(V\cos\theta)}{2\mu}\delta(x_1). \tag{23}$$

Transonic and Supersonic Cases. When $V \cos\theta > c_2$, the above argument still applies to the logarithmic term in Eq. (13), but additional displacements are obtained from the second step-function term. These are conveniently found by convolution. We obtain

$$u_z(x_1, 0) = \frac{F_2(V\cos\theta)}{\mu}\int_{-\infty}^{\infty} f(s)H(s - x_1)ds. \tag{24}$$

In the range $x_1 > a$, this reduces to

$$u_z(x_1, 0) = \frac{F_2(V\cos\theta)}{\mu}\int_{x_1}^{\infty} f(s)ds$$

$$= -\frac{FF_2(V\cos\theta)}{\pi^2 a^2 \mu}[x_1 - \sqrt{x_1^2 - a^2}], \tag{25}$$

after substituting for $f(s)$ from (11), (12) and performing the integrations.

Proceeding to the limit as $a \to 0$, we obtain

$$u_z(x_1, 0) = -\frac{FF_2(V\cos\theta)}{2\pi^2 \mu x_1}. \tag{26}$$

A similar procedure applied in the range $x_1 < -a$ yields the same result. Thus, the complete solution for the surface displacements in the two-dimensional problem is

$$u_z(x_1, 0) = -\frac{F}{2\mu}\left[F_1(V\cos\theta)\delta(x_1) + \frac{F_2(V\cos\theta)}{\pi^2 x_1}\right]. \tag{27}$$

2.5 Inversion of the Surface Displacement. The normal surface displacement due to the moving point load can now be found by substituting (27) into the integral superposition (3) or (4) and evaluating the resulting integrals.

The contribution from the first (delta function) term in Eq. (27) is easily evaluated as

$$u_z(r, \phi, 0) = -\frac{F}{2\mu}\int_{-\pi/2}^{\pi/2} F_1(V\cos\theta)\delta(r\cos(\theta - \phi))d\theta$$

$$= -\frac{FF_1(V\sin\phi)}{2\mu r}. \tag{28}$$

The inversion of the second term in Eq. (27) leads to a more complicated integral, which is evaluated in the Appendix.

3 Results

3.1 Subsonic Speeds, $0 < V < c_R$. Equation (28) defines the complete solution to the problem for $0 < V < c_2$, since in this range $F_2(V \cos\theta) = 0$ for all θ. It agrees with the results of Churilov (1977), when recast in his notation. However, Eq. (28) draws out an interesting relation between the three-dimensional point force solution and the corresponding two-dimensional problem for the moving line load, summarized in Eq. (13)–(15). The same method could also be used to establish a similar relation between the point and line load problems for the elastostatic problem for a generally anisotropic material. This was proved by a different (and less straightforward) method by Barber and Sturla (1992). Notice that the surface displacement is proportional to r^{-1}, as we deduced from self-similarity considerations in the Introduction.

The function $F_1(V \sin\phi)$ increases with ϕ to a maximum at $\phi = \pi/2$, indicating that, for a given distance r from the load, the maximum normal surface displacement occurs on the line orthogonal to the direction of motion. As $V \to c_R$, the displacement along this line increases without limit, causing the half-space to mimic the elastostatic behavior of a very flexible material with stiffeners orthogonal to the direction of motion. We would therefore anticipate that the Hertzian contact area for all quadratic indenters would tend to an ellipse elongated in the direction of motion as the speed approaches the Rayleigh wave speed.

3.2 Speeds in the Range $c_R < V < c_2$. In this speed range, $F_2(V \cos\theta)$ remains zero for all θ, so the solution is still given by Eq. (28). However, there will now be two lines defined by

$$\phi = \pm\frac{\pi}{2} \pm \gamma; \quad \gamma = \cos^{-1}(c_R/V) \tag{29}$$

along which the normal surface displacement will be singular and two sectors $\pi/2 - \gamma < |\phi| < \pi/2 + \gamma$ in which it is negative—i.e., opposite in direction to the applied force.

For $V > c_R$, the solution is not unique, since the homogeneous problem of the unloaded half-space has nontrivial Rayleigh wave solutions that can be superposed to yield a fairly general standing wave disturbance.

As discussed in Section 2.3, a two-dimensional disturbance $f(x_1)$ moving at speed V in direction x is indistinguishable from the same disturbance moving at speed $V \cos\theta$ in direction x_1, since the y_1 component of V involves no change in the field. Such a disturbance will be a solution of the homogeneous problem—i.e., it will correspond to a moving displacement field with no associated surface tractions—if we choose θ such that $V \cos\theta = c_R$. This in turn implies that $\theta = \pm\gamma$. It follows that the most general surface displacement that is invariant in the moving frame of reference in the speed range $c_R < V < c_2$ is

$$u_z(r, \phi, 0) = -\frac{FF_1(V\sin\phi)}{2\mu r}$$

$$+ h_1(r\cos(\phi - \gamma)) + h_2(r\cos(\phi + \gamma)), \tag{30}$$

where h_1, h_2 are arbitrary functions.

For the steady-state problem, there is no reason for preferring any particular form (including zero) for the two arbitrary functions. However, if we conceive of the steady-state problem as the limit at large time of a transient problem in which an initially quiescent half-space is loaded by a point load that moves at constant speed V, we would expect to see Rayleigh wave disturbances in the sector behind the lines $\phi = \pm(\pi/2 + \gamma)$ but not ahead of the load. In order to achieve such a solution, the functions h_1, h_2 must be chosen to cancel the Rayleigh singularities along the forward facing lines lines $\phi = \pm(\pi/2 - \gamma)$, which in turn requires that $h_1(x) = h_2(x) \sim x^{-1}$ and hence that

$$h_1(r\cos(\phi - \gamma)) + h_2(r\cos(\phi + \gamma))$$

$$= \frac{C\cos\phi}{r(m_1 - M_2^2\sin^2\phi)}, \tag{31}$$

where C is a constant to be chosen to ensure boundedness at $\phi = \pm(\pi/2 - \gamma)$.

Downloaded 04 May 2010 to 171.66.16.33. Redistribution subject to ASME license or copyright; see http://www.asme.org/terms/Terms_Use.cfm

The singular term in $F_1(V \sin \phi)$ can be extracted using (A2) and the factorizations (A15), (A17) from the Appendix. Choosing C to cancel this singularity in (30), we obtain

$$C = \frac{FM_2\sqrt{1 - \Lambda m_1}[(2 - m_1)^2 + 4\sqrt{(1 - m_1)(1 - \Lambda m_1)}]}{2\pi\mu(m_3 - m_1)(m_1 - m_2)\sqrt{M_2^2 - m_1}}, \tag{32}$$

leaving the solution

$$u_z(r, \phi, 0) = -\frac{F}{2\mu r}\left[F_1(V \sin \phi) - \frac{M_2 \cos \phi\sqrt{1 - \Lambda m_1}[(2 - m_1)^2 + 4\sqrt{(1 - m_1)(1 - \Lambda m_1)}]}{\pi(m_3 - m_1)(m_1 - m_2)(m_1 - M_2^2 \sin^2 \phi)\sqrt{M_2^2 - m_1}}\right] \tag{33}$$

for the moving load problem in the range $c_R < V < c_2$.

In this solution, the normal surface displacement is positive in the trailing Rayleigh sector, $(\pi/2) + \gamma < |\phi| < \pi$, but negative elsewhere including all points ahead of the moving load.

3.3 Transonic Speeds, $c_2 < V < c_1$. In this range, the surface displacement contains an additional contribution from F_2, through the integral I_1 of the Appendix, since $M_2 > 1$ and hence (A14) defines a real angle α. We obtain

$$\begin{aligned} u_z(r, \phi, 0) = -\frac{F}{2\pi\mu r}\Bigg\{ & G_1(V \sin \phi)F_3(V \sin \phi) \\ & + G_2(V \sin \phi)F_4(V \sin \phi) \\ & + \left[\sum_{i=1}^{3} \frac{A_i M_2 \cos \phi}{(M_2^2 \sin^2 \phi - m_i)}\sqrt{\frac{m_i - 1}{m_i - M_2^2}}\right] \\ & - G_1(V \sin \phi)F_3(V \sin \phi) \operatorname{sgn}(\cos \phi)\Bigg\} \\ & + \frac{C \cos \phi}{r(m_1 - M_2^2 \sin^2 \phi)} \end{aligned} \tag{34}$$

from (A1), (A12), (A22), where we have expanded the function F_1 using (A2) and also included the standing Rayleigh wave solution from (31). The identity $\operatorname{sgn}(x) \equiv 1 - 2H(-x)$ permits the two terms involving G_1F_3 to be combined. As in the previous section, we choose C to cancel the singularity at $\phi = \pm(\pi/2 - \gamma)$, with the result

$$\begin{aligned} u_z(r, \phi, 0) = & -\frac{F}{2\pi\mu r}\Bigg\{2G_1(V \sin \phi)F_3(V \sin \phi)H(-\cos \phi) \\ & + G_2(V \sin \phi)F_4(V \sin \phi) \\ & + \left[\sum_{i=2}^{3} \frac{A_i M_2 \cos \phi}{(M_2^2 \sin^2 \phi - m_i)}\sqrt{\frac{m_i - 1}{m_i - M_2^2}}\right] \\ & - \frac{M_2 \cos \phi\sqrt{1 - \Lambda m_1}(2 - m_1)^2}{(m_3 - m_1)(m_1 - m_2)(m_1 - M_2^2 \sin^2 \phi)\sqrt{M_2^2 - m_1}}\Bigg\}. \end{aligned} \tag{35}$$

Notice that the term involving A_1 is of the same form as the standing Rayleigh wave and is therefore cancelled by the assignment of C. The resulting expression is continuous in the sector $0 < |\phi| < (\pi/2) + \alpha$. There is a slope discontinuity along the trailing shear wave fronts $\phi = \pm((\pi/2) + \alpha)$ and a Cauchy singularity, with a change of sign in the displacements at the Rayleigh wave fronts $\phi = \pm((\pi/2) + \gamma)$. The displacement is positive behind the Rayleigh wave front and usually negative in front. However, for certain transonic values of M_2 there is also a small range of positive displacements ahead of the Rayleigh wave front.

3.4 Supersonic Speeds, $V > c_1$. In this case, contributions are obtained from both I_1, I_2 of (A12), giving

$$\begin{aligned} u_z(r, \phi, 0) = -\frac{F}{2\pi\mu r}\Bigg\{ & G_1(V \sin \phi)F_3(V \sin \phi) \\ & + G_2(V \sin \phi)F_4(V \sin \phi) \\ & + \left[\sum_{i=1}^{3} \frac{A_i M_2 \cos \phi}{(M_2^2 \sin^2 \phi - m_i)}\sqrt{\frac{m_i - 1}{m_i - M_2^2}}\right] \\ & - G_1(V \sin \phi)F_3(V \sin \phi) \operatorname{sgn}(\cos \phi) \\ & + \left[\sum_{i=1}^{3} \frac{B_i M_2 \cos \phi}{(M_2^2 \sin^2 \phi - m_i)}\sqrt{\frac{\Lambda m_i - 1}{m_i - M_2^2}}\right] \\ & - G_2(V \sin \phi)F_4(V \sin \phi) \operatorname{sgn}(\cos \phi)\Bigg\} \\ & + \frac{C \cos \phi}{r(m_1 - M_2^2 \sin^2 \phi)}. \end{aligned} \tag{36}$$

The two series terms can be added to give

$$\sum_{i=1}^{3} \frac{M_2 \cos \phi}{(M_2^2 \sin^2 \phi - m_i)}\left[A_i\sqrt{\frac{m_i - 1}{m_i - M_2^2}} + B_i\sqrt{\frac{\Lambda m_i - 1}{m_i - M_2^2}}\right].$$

For $i = 2$, $m_2 > 1$ and we can substitute for A_2, B_2 from (A16), (A18) to obtain

$$\begin{aligned} & A_2\sqrt{\frac{m_2 - 1}{m_2 - M_2^2}} + B_2\sqrt{\frac{\Lambda m_2 - 1}{m_2 - M_2^2}} \\ & = \frac{\sqrt{\Lambda m_2 - 1}[(2 - m_2)^2 - 4\sqrt{(\Lambda m_2 - 1)(m_2 - 1)}]}{(m_1 - m_2)(m_2 - m_3)\sqrt{m_2 - M_2^2}}. \end{aligned} \tag{37}$$

By definition, we have that $D = 0$ when $M_2^2 = m_2$ and it follows on comparing (A9) and (37) that the factor $[(2 - m_2)^2 - 4\sqrt{(\Lambda m_2 - 1)(m_2 - 1)}]$ in (37) must be zero. Thus, there is no contribution to (36) from the terms with $i = 2$. A similar argument can be made for the terms with $i = 3$.

For $i = 1$, a nonzero result is obtained because the arguments of the square roots change sign, but the resulting term has the

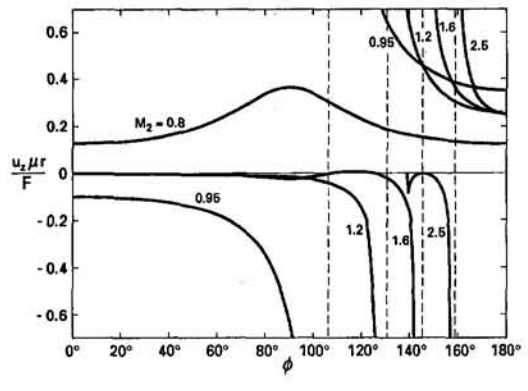


Fig. 1 Displacement as a function of polar angle ϕ for $\nu = 0.2$, ($c_R = 0.911c_2$, $c_1 = 1.633c_2$), and various speeds. The dotted lines are asymptotes to the unbounded displacements at the Rayleigh wave front $\phi = \gamma + 90$ deg, which occurs at 106.5 deg, 130.6 deg, 145.3 deg, 158.6 deg for $M_2 = 0.95$, 1.2, 1.6, 2.5, respectively.

Downloaded 04 May 2010 to 171.66.16.33. Redistribution subject to ASME license or copyright; see http://www.asme.org/terms/Terms_Use.cfm

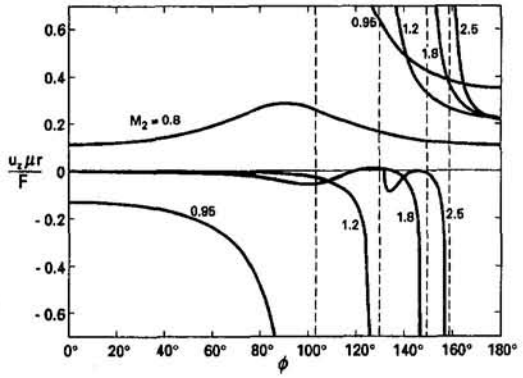


Fig. 2 Displacement as a function of polar angle ϕ for $\nu = 0.3$, ($c_R = 0.927c_2$, $c_1 = 1.871c_2$), and various speeds. The dotted lines are asymptotes to the unbounded displacements at the Rayleigh wave front $\phi = \gamma + 90$ deg, which occurs at 102.6 deg, 129.4 deg, 149.0 deg, 158.2 deg for $M_2 = 0.95, 1.2, 1.8, 2.5$, respectively.

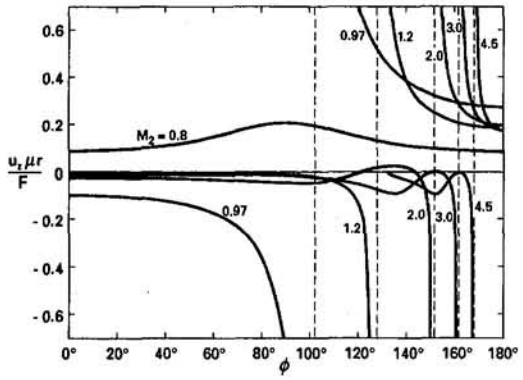


Fig. 3 Displacement as a function of polar angle ϕ for $\nu = 0.45$, ($c_R = 0.949c_2$, $c_1 = 3.317\, c_2$), and various speeds. The dotted lines are asymptotes to the unbounded displacements at the Rayleigh wave front $\phi = \gamma + 90$ deg, which occurs at 101.9 deg, 127.7 deg, 151.7 deg, 161.6 deg, 167.8 deg for $M_2 = 0.97, 1.2, 2.0, 3.0, 4.5$, respectively.

same form as the standing Rayleigh wave and is eliminated when C is chosen so as to cancel the leading Rayleigh singularity.

The final solution therefore contains only the two step-function terms—i.e.,

$$u_z(r, \phi, 0) = -\frac{F}{\pi\mu r}[G_1(V\sin\phi)F_3(V\sin\phi)H(-\cos\phi) + G_2(V\sin\phi)F_4(V\sin\phi)H(-\cos\phi)] = -\frac{FF_1(V\sin\phi)H(-\cos\phi)}{\mu r} \quad (38)$$

using Eq. (A2).

As we should expect, when the force moves at supersonic speed, the surface displacement is zero in front of the trailing dilatational wave fronts $\phi = \pm((\pi/2) + \beta)$, where $\cos\beta = M_1^{-1}$. A slope discontinuity occurs at the shear wave fronts and a Cauchy singularity with a sign change at the Rayleigh wave fronts.

It is interesting to note that this result can be predicted without performing the integrations on F_2 explicitly. Since we know that the total expression must be zero for $|\phi| < (\pi/2)$, it follows that the contribution in this sector from F_2 must be equal and opposite to that from F_1 and given by (28). However, the integral from F_1 is symmetrical about the line $\phi = \pm(\pi/2)$, whereas that from F_2 is antisymmetrical, so it follows that the contributions must add in the trailing sector, giving just twice that due to F_1 alone, as is confirmed by (38).

4 Conclusions

The above results define in closed form the normal surface displacements due to the steadily moving normal point force throughout the range of speeds. Collecting results for convenience we have

These expressions are easily evaluated, making use of the results of Rahman and Barber (1995) for m_1, m_2, m_3 as required. Sample results for various speeds are given in Figs. 1 to 3, for $\nu = 0.2, 0.3, 0.45$, respectively. In each case, the displacement is positive (i.e., in the same direction as the load) in any region accessible to Rayleigh waves emanating from the moving load. Displacements in regions not so accessible are usually negative, except for a small region in certain transonic examples. Of course, the displacement is zero in the supersonic case for all points that are not accessible to dilatational waves emanating from the source.

The displacements are continuous functions of speed through the values $V = c_2, c_1$—e.g., Eqs. (41) with $V = c_1 - \epsilon$ and (42) with $V = c_1 + \epsilon$ converge on the same limit as $\epsilon \to 0$. However, a more dramatic change occurs as the speed passes through the Rayleigh wave speed c_R. The displacement at $\phi = \pm(\pi/2)$ increases without limit as $V \to 0$ from below, but above $V = c_R$ a Cauchy singularity occurs at the trailing Rayleigh lines $\phi = \pm((\pi/2) + \gamma)$.

The results can be used as Green's functions to formulate three-dimensional elastodynamic contact problems for a frictionless indenter moving at constant speed over the half-space.

Acknowledgments

The author is pleased to acknowledge support from the National Science Foundation under contract number MSS-9200762. He also wishes to thank Dr. Mujibur Rahman for discussions and contributions to the solution and the preparation of the figures.

$$u_z(r, \phi, 0) = -\frac{FF_1(V\sin\phi)}{2\mu r}; \quad 0 < V < c_R \quad (39)$$

$$= -\frac{F}{2\mu r}\left[F_1(V\sin\phi) - \frac{M_2\cos\phi\sqrt{1-\Lambda m_1}[(2-m_1)^2 + 4\sqrt{(1-m_1)(1-\Lambda m_1)}]}{\pi(m_3-m_1)(m_1-m_2)(m_1-M_2^2\sin^2\phi)\sqrt{M_2^2-m_1}}\right]; \quad c_R < V < c_2 \quad (40)$$

$$= -\frac{F}{2\pi\mu r}\left\{2G_1(V\sin\phi)F_3(V\sin\phi)H(-\cos\phi) + G_2(V\sin\phi)F_4(V\sin\phi) \quad (41)\right.$$

$$\left. + \left[\sum_{i=2}^{3}\frac{A_i M_2\cos\phi}{(M_2^2\sin^2\phi - m_i)}\sqrt{\frac{m_i-1}{m_i-M_2^2}}\right] - \frac{M_2\cos\phi\sqrt{1-\Lambda m_1}(2-m_1)^2}{(m_3-m_1)(m_1-m_2)(m_1-M_2^2\sin^2\phi)\sqrt{M_2^2-m_1}}\right\}; \quad c_2 < V < c_1$$

$$= -\frac{FF_1(V\sin\phi)H(-\cos\phi)}{\mu r}; \quad V > c_1. \quad (42)$$

Downloaded 04 May 2010 to 171.66.16.33. Redistribution subject to ASME license or copyright; see http://www.asme.org/terms/Terms_Use.cfm

References

Barber, J. R., 1992, *Elasticity,* Kluwer, Dordrecht.

Barber, J. R., and Sturla, F. A., 1992, "Application of the reciprocal theorem to some problems for the elastic half-space," *Journal of the Mechanics and Physics of Solids,* Vol. 40, pp. 17–25.

Churilov, V. A., 1977, "On the effect of a normal load moving at constant velocity along the boundary of an elastic half-space," *Journal of Applied Mathematics and Mechanics,* Vol. 41, pp. 125–132.

Churilov, V. A., 1978, "Action of an elliptic stamp moving at a constant speed on an elastic half-space," *Journal of Applied Mathematics and Mechanics,* Vol. 42, pp. 1176–1182.

Cole, J. D., and Huth, J. H., 1958, "Stresses Produced in a Half-Plane by Moving Loads," ASME JOURNAL OF APPLIED MECHANICS, Vol. 25, pp. 433–436.

Eringen, A. C., and Suhubi, E. S., 1975, *Elastodynamics,* Vol. II, Academic Press, New York.

Georgiadis, H. G., and Barber, J. R., 1993a, "On the super-Rayleigh/subseismic elastodynamic indentation problem," *Journal of Elasticity,* Vol. 31, pp. 141–161.

Georgiadis, H. G., and Barber, J. R., 1993b, "Steady-State Transonic Motion of a Line Load Over an Elastic Half-Space (The Corrected Cole/Huth Solution)," ASME JOURNAL OF APPLIED MECHANICS, Vol. 60, pp. 772–774.

Gradshteyn, I. S., and Ryzhik, I. M., 1980, *Tables of Integrals, Series and Products,* Academic Press, New York.

Payton, R. G., 1964, "An application of the dynamic Betti-Rayleigh reciprocal theorem to moving point loads in elastic media," *Quarterly of Applied Mathematics,* Vol. 21, pp. 299–313.

Rahman, Mujibur, 1990, private communication.

Rahman, Mujibur, and Barber, J. R., 1995, "Exact Expressions for the Roots of the Secular Equation for Rayleigh Waves," ASME JOURNAL OF APPLIED MECHANICS, Vol. 62, pp. 250–252.

Sveklo, V. A., 1964, "Boussinesq type problems for the anisotropic half-space," *Journal of Applied Mathematics and Mechanics,* Vol. 28, pp. 1099–1105.

Willis, J. R., 1967, "Boussinesq problems for an anisotropic half-space," *Journal of the Mechanics and Physics of Solids,* Vol. 15, pp. 331–339.

APPENDIX

Substituting the second term in (27) into (4), we obtain the expression

$$u_z(x, y, 0) = -\frac{F}{2\pi^2 \mu r}\int_{-\pi/2}^{\pi/2} \frac{F_2(V\cos\theta)d\theta}{\cos(\theta-\phi)}. \quad \text{(A1)}$$

In this Appendix, we shall evaluate this integral for the two cases $c_2 < V < c_1$ and $V > c_1$.

It is convenient to rationalize the expressions $F_1(V)$, $F_2(V)$ of Eqs. (14), (15). We find

$$F_1 = (G_1F_3 + G_2F_4)/\pi; \quad F_2 = (G_3F_3 + G_4F_4), \quad \text{(A2)}$$

where

$$G_1(V) = H(c_2 - V)\sqrt{1 - M_2^2} \quad \text{(A3)}$$

$$G_2(V) = H(c_1 - V)\sqrt{1 - M_1^2} \quad \text{(A4)}$$

$$G_3(V) = H(V - c_2)\sqrt{M_2^2 - 1} \quad \text{(A5)}$$

$$G_4(V) = H(V - c_1)\sqrt{M_1^2 - 1}. \quad \text{(A6)}$$

$H(.)$ is the Heaviside step function,

$$F_3(V) = \frac{4M_2^2(1 - M_1^2)}{D} \quad \text{(A7)}$$

$$F_4(V) = \frac{M_2^2(2 - M_2^2)^2}{D} \quad \text{(A8)}$$

and

$$D = (2 - M_2^2)^4 - 16(1 - M_1^2)(1 - M_2^2). \quad \text{(A9)}$$

Note that D can be expanded as a polynomial in M_2^2, giving

$$D = M_2^2[M_2^6 - 8M_2^4 + 8(3 - 2\Lambda)M_2^2 - 16(1 - \Lambda)]$$
$$= M_2^2(M_2^2 - m_1)(M_2^2 - m_2)(M_2^2 - m_3), \quad \text{(A10)}$$

where

$$\Lambda = \frac{M_1^2}{M_2^2} = \frac{c_2^2}{c_1^2} = \frac{(1 - 2\nu)}{2(1 - \nu)} \quad \text{(A11)}$$

and m_1, m_2, m_3 are the roots of the Rayleigh polynomial—i.e., the values of M_2^2 at which $D(M_2) = 0$—and are given explicitly in closed form by Rahman and Barber (1995). Note that one of these roots (taken here to be m_1) is always real and equal to $(c_R/c_2)^2$, but the other two may be real or a pair of complex conjugates depending on the value of ν. We shall argue below for the case where the roots are all real, but the complex conjugate case can be treated by the same method and yields the same final result.

With this notation, the evaluation of Eq. (A1) reduces to that of the two integrals

$$I_1 = \int_{-\pi/2}^{\pi/2} \frac{G_3(V\cos\theta)F_3(V\cos\theta)d\theta}{\cos(\theta-\phi)};$$

$$I_2 = \int_{-\pi/2}^{\pi/2} \frac{G_4(V\cos\theta)F_4(V\cos\theta)d\theta}{\cos(\theta-\phi)}. \quad \text{(A12)}$$

The derivations are tedious but routine and will only be briefly outlined here.

We first note that $G_3(V)$ is nonzero only in the range $V > c_2$ and hence I_1 can be rewritten

$$I_1 = \int_{-\alpha}^{\alpha} \frac{G_3(V\cos\theta)F_3(V\cos\theta)d\theta}{\cos(\theta-\phi)}, \quad \text{(A13)}$$

where

$$\cos\alpha = M_2^{-1}. \quad \text{(A14)}$$

Substituting (A9) into (A7), we can write $F_3(V)$ in the form

$$F_3(V) = \frac{4(1 - M_1^2)}{(M_2^2 - m_1)(M_2^2 - m_2)(M_2^2 - m_3)}$$
$$= \sum_{i=1}^{3} \frac{A_i}{(M_2^2 - m_i)}, \quad \text{(A15)}$$

where the constants A_i are given by

$$A_1 = -\frac{4(1 - \Lambda m_1)}{(m_3 - m_1)(m_1 - m_2)};$$

$$A_2 = -\frac{4(1 - \Lambda m_2)}{(m_1 - m_2)(m_2 - m_3)};$$

$$A_3 = -\frac{4(1 - \Lambda m_3)}{(m_2 - m_3)(m_3 - m_1)}. \quad \text{(A16)}$$

The corresponding expansion of $F_4(V)$ is

$$F_4(V) = \frac{(2 - M_2^2)^2}{(M_2^2 - m_1)(M_2^2 - m_2)(M_2^2 - m_3)}$$
$$= \sum_{i=1}^{3} \frac{B_i}{(M_2^2 - m_i)}, \quad \text{(A17)}$$

where

$$B_1 = -\frac{(2 - m_1)^2}{(m_3 - m_1)(m_1 - m_2)};$$

$$B_2 = -\frac{(2 - m_2)^2}{(m_1 - m_2)(m_2 - m_3)};$$

$$B_3 = -\frac{(2 - m_3)^2}{(m_2 - m_3)(m_3 - m_1)}. \quad \text{(A18)}$$

Downloaded 04 May 2010 to 171.66.16.33. Redistribution subject to ASME license or copyright; see http://www.asme.org/terms/Terms_Use.cfm

Using (A15), (A5) in (A13), we have

$$I_1 = \sum_{i=1}^{3} A_i \int_{-\alpha}^{\alpha} \frac{\sqrt{M_2^2 \cos^2 \theta - 1}\, d\theta}{(M_2^2 \cos^2 \theta - m_i) \cos (\theta - \phi)}. \quad \text{(A19)}$$

We now make the monotonic change of variable $\sin \theta = x$ and rationalize the resulting integrals, with the result

$$I_1 = \sum_{i=1}^{3} A_i \int_{-\sqrt{1-1/M_2^2}}^{\sqrt{1-1/M_2^2}} \times \frac{\sqrt{M_2^2 - 1 - M_2^2 x^2}\left[\cos \phi - \frac{x}{\sqrt{1-x^2}} \sin \phi\right] dx}{(M_2^2 - m_i - M_2^2 x^2)(\cos^2 \phi - x^2)}. \quad \text{(A20)}$$

The term multiplying $\sin \phi$ in the integrand is odd in x and hence makes no contribution to the integral. The remaining $\cos \phi$ term can be decomposed further into two partial fractions and evaluated using 3.613 of Gradshteyn and Ryzhik (1980).

We obtain

$$I_1 = \sum_{i=1}^{3} \frac{A_i \pi}{(M_2^2 \sin^2 \phi - m_i)} \times \left[M_2 \cos \phi \sqrt{\frac{m_i - 1}{m_i - M_2^2}} - \text{sgn} (\cos \phi) \sqrt{1 - M_2^2 \sin^2 \phi}\right], \quad \text{(A21)}$$

where the square roots are to be taken as zero when their arguments are negative.

Some simplification in this expression can be made by noting that the second term does not contain m_i. The summation on this term can therefore be performed, using (A15), with the result

$$I_1 = \left[\sum_{i=1}^{3} \frac{A_i \pi M_2 \cos \phi}{(M_2^2 \sin^2 \phi - m_i)} \sqrt{\frac{m_i - 1}{m_i - M_2^2}}\right] - \pi G_1(V \sin \phi) F_3(V \sin \phi) \text{ sgn } (\cos \phi). \quad \text{(A22)}$$

An essentially similar procedure for the integral I_2 yields the result

$$I_2 = \left[\sum_{i=1}^{3} \frac{B_i \pi M_2 \cos \phi}{(M_2^2 \sin^2 \phi - m_i)} \sqrt{\frac{\Lambda m_i - 1}{m_i - M_2^2}}\right] - \pi G_2(V \sin \phi) F_4(V \sin \phi) \text{ sgn } (\cos \phi). \quad \text{(A23)}$$

Downloaded 04 May 2010 to 171.66.16.33. Redistribution subject to ASME license or copyright; see http://www.asme.org/terms/Terms_Use.cfm

Hideo Koguchi
Associate Professor.

Tadanobu Inoue
Graduate Student.

Toshio Yada
Professor.

Department of Mechanical Engineering,
Nagaoka University of Technology,
1603-1 Kamitomioka,
Nagaoka, Niigata, 940-21, Japan

Stress Singularity in Three-Phase Bonded Structure

The plane problem of three-phase materials consisting of three isotropic homogeneous wedges with arbitrary angles, which are with two interfaces and two free surfaces, is analyzed under arbitrary normal and shearing tractions by the theory of elasticity. An eigenequation to examine the order of stress singularity at the apex in the three-phase bonded structure is analytically derived. In particular, this paper emphasizes to investigate the order of singularity in the stress field at the apex when materials of both side regions against intermediate region in three regions are identical. For several bonded wedge geometries, it is demonstrated how the order of stress singularity varies with material pairs. Finally, it is shown that the bonding order of materials also influences on the order of stress singularity in the three-phase bonded structure.

1 Introduction

Characteristic on the singularity of stress field in bonded structure have so far been studied in detail by many investigators: Williams (1952), Bogy (1968, 1970, 1971a), Theocaris (1989), and Blanchard and Ghoniem (1989). Bogy (1971a) deduced an eigenequation to obtain the order of stress singularity at the apex for the two-phase bonded structure, and then expressed it using two Dundurs composite parameters α and β (Dundurs, 1969). Theocaris (1989) discussed on the stress singularity for bonded structure formed from n-wedges coalescing at a vertex, and derived eigenequations for single and two-phase bonded structure by the eigenfunction expansion method.

In the present paper, the stress singularity at the apex in the three-phase bonded structure is precisely discussed for several pairs of materials. The bonded structure studied here can be seen in welded structures or parts of electronic package such as Si chip-die pad-resin in the ICs and LSIs. Many investigations have been carried out on the two-phase bonded structure, but studies on the three-phase one have been rarely performed. In this paper, the eigenequation for the three-phase bonded structure is newly derived to investigate the order of singularity for the stress field at the apex. At this time, four Dundurs composite parameters—α_{12}, β_{12} for materials 1 and 2 and α_{23}, β_{23} for materials 2 and 3 composed of three pairs of shear modulus and Poisson's ratio—are introduced and the order of stress singularity is compared with the results of the two-phase materials deduced by identifying properties for two materials in the three-phase structure. The emphasis here is placed for investigating the order of stress singularity at the apex when materials of both side regions against intermediate region are identical.

The eigenequation is first derived using the parameters α_{12}, β_{12}, α_{23}, and β_{23} and is compared with the equations on the single wedge derived by Williams (1952) for various boundary conditions. After that, in cases where the bonded wedge forms in (A) half-planes, (B) three-quarters planes, and (C) full planes, it is investigated on the α-β plane how the order of stress singularity varies with several pairs of materials. A relationship between the order of stress singularity and the bonding order of materials is also examined.

Contributed by the Applied Mechanics Division of THE AMERICAN SOCIETY OF MECHANICAL ENGINEERS for publication in the ASME JOURNAL OF APPLIED MECHANICS.

Discussion on this paper should be addressed to the Technical Editor, Professor Lewis T. Wheeler, Department of Mechanical Engineering, University of Houston, Houston, TX 77204-4792, and will be accepted until four months after final publication of the paper itself in the ASME JOURNAL OF APPLIED MECHANICS.

Manuscript received by the ASME Applied Mechanics Division, Sept. 13, 1993; final revision, Feb. 24, 1995. Associate Technical Editor: M. Taya.

2 Eigenequation for Three-Phase Bonded Structure

2.1 Model for Analysis and Boundary Conditions. A model for the analysis of three-phase bonded structure, where two-dimensional regions Ω_1, Ω_2, and Ω_3 occupied by three isotropic homogeneous wedges of angles φ_1, φ_2, and φ_3 ($\varphi_1 + \varphi_2 + \varphi_3 \leqq 2\pi$) are bonded on each straight segment B_{12} and B_{23}, is illustrated in Fig. 1. The straight segments F_1 and F_3 denote free surfaces. Polar coordinates (r, θ) and Cartesian coordinates (x, y) having origin at the vertex are defined as shown in Fig. 1. Three regions for the structure are assumed to be isotropic homogeneous elastic materials and to have no body forces. In Fig. 1, G (G_1 on Ω_1, G_2 on Ω_2, G_3 on Ω_3) is constant shear modulus and ν (ν_1 on Ω_1, ν_2 on Ω_2, ν_3 on Ω_3) is constant Poisson's ratio. Moreover, n and t (n_1, t_1 on F_1 and n_3, t_3 on F_3) are the normal and the shearing tractions.

Thus, we consider the problem in the plane theory (plane strain or plane stress) of isotropic, homogeneous, and linear elastostatics. We first represent the stress and displacement fields with plane polar components by the Airy stress function ϕ, which is satisfied the bi-harmonic equation denoted by

$$\nabla^4 \phi = 0. \tag{1}$$

The stress components (σ_{rr}, $\sigma_{r\theta}$, $\sigma_{\theta\theta}$) and the displacement ones (u_r, u_θ) are defined by using the stress function ϕ as follows:

$$\sigma_{rr} = \frac{1}{r}\frac{\partial \phi}{\partial r} + \frac{1}{r^2}\frac{\partial^2 \phi}{\partial \theta^2}, \quad \sigma_{\theta\theta} = \frac{\partial^2 \phi}{\partial r^2}$$

$$\sigma_{r\theta} = -\frac{1}{r}\frac{\partial^2 \phi}{\partial r \partial \theta} + \frac{1}{r^2}\frac{\partial \phi}{\partial \theta} \tag{2}$$

$$\frac{\partial u_r}{\partial r} = \frac{1}{2G}\left\{\frac{1}{r}\frac{\partial \phi}{\partial r} + \frac{1}{r^2}\frac{\partial^2 \phi}{\partial \theta^2} - \left(1 - \frac{m}{4}\right)\nabla^2 \phi\right\}$$

$$\frac{\partial u_\theta}{\partial r} - \frac{u_\theta}{r} + \frac{1}{r}\frac{\partial u_r}{\partial \theta} = \frac{1}{G}\left(-\frac{1}{r}\frac{\partial^2 \phi}{\partial r \partial \theta} + \frac{1}{r^2}\frac{\partial \phi}{\partial \theta}\right). \tag{3}$$

Constant m (m_1 on Ω_1, m_2 on Ω_2, m_3 on Ω_3) in (3) is denoted by Poisson's ratio as follows:

$$m_\delta = \begin{cases} 4(1 - \nu_\delta) & \text{for plane strain} \\ \dfrac{4}{1 + \nu_\delta} & \text{for plane stress} \end{cases} \quad (\delta = 1, 2, 3), \tag{4}$$

where δ denotes the region number.

The following conditions must be satisfied on the free surfaces (F_1 and F_3) and the bonded interfaces (B_{12} and B_{23}) illustrated in Fig. 1.

Copyright © 1996 by ASME

Downloaded 04 May 2010 to 171.66.16.33. Redistribution subject to ASME license or copyright; see http://www.asme.org/terms/Terms_Use.cfm

Free surfaces: F_1 and F_3

$$\sigma_{\theta\theta}|_1(r, -\varphi_1) = n_1(r), \quad \sigma_{r\theta}|_1(r, -\varphi_1) = t_1(r)$$
$$\sigma_{\theta\theta}|_3(r, \varphi_2 + \varphi_3) = n_3(r), \quad \sigma_{r\theta}|_3(r, \varphi_2 + \varphi_3) = t_3(r). \quad (5)$$

Bonded interface $(1 - 2)$: B_{12}

$$\sigma_{\theta\theta}|_1(r, 0) = \sigma_{\theta\theta}|_2(r, 0), \quad \sigma_{r\theta}|_1(r, 0) = \sigma_{r\theta}|_2(r, 0)$$
$$u_r|_1(r, 0) = u_r|_2(r, 0), \quad u_\theta|_1(r, 0) = u_\theta|_2(r, 0). \quad (6)$$

Bonded interface $(2 - 3)$: B_{23}

$$\sigma_{\theta\theta}|_2(r, \varphi_2) = \sigma_{\theta\theta}|_3(r, \varphi_2), \quad \sigma_{r\theta}|_2(r, \varphi_2) = \sigma_{r\theta}|_3(r, \varphi_2)$$
$$u_r|_2(r, \varphi_2) = u_r|_3(r, \varphi_2), \quad u_\theta|_2(r, \varphi_2) = u_\theta|_3(r, \varphi_2) \quad (7)$$

2.2 Application of Mellin Transform. The boundary value problem represented by (1)–(7) can be solved by using the Mellin transform (Sneddon, 1951; Davis, 1984). Mellin transform of a function $f(r)$ is defined by

$$f^*(s) = \mathfrak{M}[f(r); s] = \int_0^\infty f(r) r^{s-1} dr, \quad (8)$$

where s is a complex transform parameter. The Mellin transform is applied to (1) and then the transformed stress function ϕ^* is represented by

$$\phi^*(s, \theta) = \int_0^\infty \phi(r, \theta) r^{s-1} dr. \quad (9)$$

Consequently, $\phi^*(s, \theta)$ is described by

$$\phi^*(s, \theta) = a(s) \sin(s\theta) + b(s) \cos(s\theta) + c(s) \sin[(s + 2)\theta] + d(s) \cos[(s + 2)\theta]. \quad (10)$$

Equation (10) is substituted into the equations of stress and displacement through the Mellin transform of (2) and (3). Then, the functions $a(s) \sim d(s)$ ($a_1(s) \sim d_1(s)$ of ϕ_1^* for Ω_1, $a_2(s) \sim d_2(s)$ of ϕ_2^* for Ω_2, $a_3(s) \sim d_3(s)$ of ϕ_3^* for Ω_3) are unknown functions involving the parameter s established from the Mellin transform of the boundary conditions (5)–(7). Simultaneous equations concerning the 12 unknown functions $a_1(s) \sim d_1(s)$, $a_2(s) \sim d_2(s)$, $a_3(s) \sim d_3(s)$ can be obtained from the boundary conditions of the transformed stresses and displacements.

$$-a_1 \sin(s\varphi_1) + b_1 \cos(s\varphi_1) - c_1 \sin[(s + 2)\varphi_1] + d_1 \cos[(s + 2)\varphi_1] = L_1(s)$$
$$a_1 s \cos(s\varphi_1) + b_1 s \sin(s\varphi_1) + c_1(s + 2) \cos[(s + 2)\varphi_1] + d_1(s + 2) \sin[(s + 2)\varphi_1] = L_2(s)$$
$$b_1 + d_1 - b_2 - d_2 = 0$$
$$a_1 s + c_1(s + 2) - a_2 s - c_2(s + 2) = 0$$
$$b_1 s + d_1(s + m_1) - b_2 k_{12} s - d_2 k_{12}(s + m_2) = 0$$
$$a_1 s + c_1(s + 2 - m_1) - a_2 k_{12} s - c_2 k_{12}(s + 2 - m_2) = 0$$
$$a_3 \sin[s(\varphi_2 + \varphi_3)] + b_3 \cos[s(\varphi_2 + \varphi_3)] + c_3 \sin[(s + 2)(\varphi_2 + \varphi_3)] + d_3 \cos[(s + 2)(\varphi_2 + \varphi_3)] = L_3(s)$$
$$a_3 s \cos[s(\varphi_2 + \varphi_3)] - b_3 s \sin[s(\varphi_2 + \varphi_3)] + c_3(s + 2) \cos[(s + 2)(\varphi_2 + \varphi_3)] - d_3(s + 2) \sin[(s + 2)(\varphi_2 + \varphi_3)] = L_4(s)$$
$$a_2 \sin(s\varphi_2) + b_2 \cos(s\varphi_2) + c_2 \sin[(s + 2)\varphi_2] + d_2 \cos[(s + 2)\varphi_2] - a_3 \sin(s\varphi_2) - b_3 \cos(s\varphi_2) - c_3 \sin[(s + 2)\varphi_2] - d_3 \cos[(s + 2)\varphi_2] = 0$$
$$a_2 s \cos(s\varphi_2) - b_2 s \sin(s\varphi_2) + c_2(s + 2) \cos[(s + 2)\varphi_2] - d_2(s + 2) \sin[(s + 2)\varphi_2] - a_3 s \cos(s\varphi_2) + b_3 s \sin(s\varphi_2) - c_3(s + 2) \cos[(s + 2)\varphi_2] + d_3(s + 2) \sin[(s + 2)\varphi_2] = 0$$
$$a_2 s \sin(s\varphi_2) + b_2 s \cos(s\varphi_2) + c_2(s + m_2) \sin[(s + 2)\varphi_2] + d_2(s + m_2) \cos[(s + 2)\varphi_2] - a_3 k_{23} s \sin(s\varphi_2) - b_3 k_{23} s \cos(s\varphi_2) - c_3 k_{23}(s + m_3) \sin[(s + 2)\varphi_2] - d_3 k_{23}(s + m_3) \cos[(s + 2)\varphi_2] = 0$$
$$-a_2 s \cos(s\varphi_2) + b_2 s \sin(s\varphi_2) - c_2(s + 2 - m_2) \times \cos[(s + 2)\varphi_2] + d_2(s + 2 - m_2) \sin[(s + 2)\varphi_2] + a_3 k_{23} s \cos(s\varphi_2) - b_3 k_{23} s \sin(s\varphi_2) + c_3 k_{23}(s + 2 - m_3) \cos[(s + 2)\varphi_2] - d_3 k_{23}(s + 2 - m_3) \sin[(s + 2)\varphi_2] = 0, \quad (11)$$

where

$$\begin{cases} L_1 = \dfrac{n_1^*(s)}{s(s + 1)}, & L_2 = \dfrac{t_1^*(s)}{s + 1} \\ L_3 = \dfrac{n_3^*(s)}{s(s + 1)}, & L_4 = \dfrac{t_3^*(s)}{s + 1} \end{cases} \quad (12)$$

$$k_{12} = \frac{G_1}{G_2}, \quad k_{23} = \frac{G_2}{G_3} \quad (13)$$

in which the transformed functions $n^*(s)$ and $t^*(s)$ ($n_1^*(s)$, $t_1^*(s)$ on F_1 and $n_3^*(s)$, $t_3^*(s)$ on F_3) denote tractions applied the Mellin transform with respect to r of $r^2 n(r)$ and $r^2 t(r)$.

2.3 Derivation of Eigenequation. Equation (11) reduces to a homogeneous equation when the right side is all the zeros ($n_1^*(s) = t_1^*(s) = n_3^*(s) = 0$). The full prerequisite yielding nontrivial solutions in (11) is that the determinant (12×12) of the coefficients becomes zero. The eigenequation for the three-phase bonded structure can be explicitly expressed by expanding and arranging the determinant. Also, six elasticity constants in the homogeneous equations are represented by four Dundurs composite parameters α_{12}, β_{12}, α_{23} and β_{23}.

$$\alpha_{12} = \frac{k_{12} m_2 - m_1}{k_{12} m_2 + m_1}, \quad \beta_{12} = \frac{k_{12}(m_2 - 2) - (m_1 - 2)}{k_{12} m_2 + m_1}$$
$$\alpha_{23} = \frac{k_{23} m_3 - m_2}{k_{23} m_3 + m_2}, \quad \beta_{23} = \frac{k_{23}(m_3 - 2) - (m_2 - 2)}{k_{23} m_3 + m_2}. \quad (14)$$

The complex variable p is defined by

$$p = -s - 1 = \xi + i\eta, \quad (15)$$

where ξ and η are the real and imaginary parts of p.

Consequently, the determinant of the coefficients in (11) can be arranged as follows.

$$\boldsymbol{S}(\varphi_1, \varphi_2, \varphi_3, \alpha_{12}, \beta_{12}, \alpha_{23}, \beta_{23}; p) = \boldsymbol{A}(\varphi_1, \varphi_2, \varphi_3, \alpha_{12}, \beta_{12}, \alpha_{23}, \beta_{23}; p) + \boldsymbol{B}(\varphi_1, \varphi_2, \varphi_3, \alpha_{12}, \beta_{12}, \alpha_{23}, \beta_{23}; p) + \boldsymbol{C}(\varphi_1, \varphi_2, \varphi_3, \alpha_{12}, \beta_{12}, \alpha_{23}, \beta_{23}; p) + \boldsymbol{D}(\varphi_1, \varphi_2, \varphi_3; p), \quad (16)$$

where

$$\boldsymbol{A}(\varphi_1, \varphi_2, \varphi_3, \alpha_{12}, \beta_{12}, \alpha_{23}, \beta_{23}; p) = A_1(\varphi_1, \varphi_2, \varphi_3; p)\beta_{12}^2\beta_{23}^2 + A_2(\varphi_1, \varphi_2, \varphi_3; p)\beta_{12}\beta_{23} + A_3(\varphi_1, \varphi_2, \varphi_3; p)\alpha_{12}\alpha_{23}\beta_{12}\beta_{23} + A_4(\varphi_1, \varphi_2, \varphi_3; p)\alpha_{12}^2\alpha_{23}^2 + A_5(\varphi_1, \varphi_2, \varphi_3; p)\alpha_{12}\alpha_{23}$$

Downloaded 04 May 2010 to 171.66.16.33. Redistribution subject to ASME license or copyright; see http://www.asme.org/terms/Terms_Use.cfm

$$
\begin{aligned}
&\boldsymbol{B}(\varphi_1, \varphi_2, \varphi_3, \alpha_{12}, \beta_{12}, \alpha_{23}, \beta_{23}; p)\\
&\quad = \sum_{i=1}^{2} \{B_1(\varphi_1, \varphi_2, \varphi_3; p)\alpha_{2,n}\beta_{2,m}^2\beta_{2,n}\\
&\qquad + B_2(\varphi_1, \varphi_2, \varphi_3; p)\beta_{2,m}^2 + B_3(\varphi_1, \varphi_2, \varphi_3; p)\alpha_{2,m}^2\beta_{2,n}^2\\
&\qquad + B_4(\varphi_1, \varphi_2, \varphi_3; p)\alpha_{2,m}\beta_{2,m} + B_5(\varphi_1, \varphi_2, \varphi_3; p)\alpha_{2,m}\beta_{2,n}\\
&\qquad + B_6(\varphi_1, \varphi_2, \varphi_3; p)\alpha_{2,m}^2\alpha_{2,n}\beta_{2,n}\\
&\qquad\qquad + B_7(\varphi_1, \varphi_2, \varphi_3; p)\alpha_{2,m}^2\}\\
&\boldsymbol{C}(\varphi_1, \varphi_2, \varphi_3, \alpha_{12}, \beta_{12}, \alpha_{23}, \beta_{23}; p)\\
&\quad = 2\sum_{i=1}^{2} (-1)^{i-1}\{C_1(\varphi_1, \varphi_2, \varphi_3; p)\beta_{2,m}\beta_{2,n}^2\\
&\qquad + C_2(\varphi_1, \varphi_2, \varphi_3; p)\alpha_{2,m}\beta_{2,n}^2\\
&\qquad + C_3(\varphi_1, \varphi_2, \varphi_3; p)\alpha_{2,n}\beta_{2,m}\beta_{2,n}\\
&\qquad + C_4(\varphi_1, \varphi_2, \varphi_3; p)\beta_{2,m} + C_5(\varphi_1, \varphi_2, \varphi_3; p)\alpha_{2,n}^2\beta_{2,m}\\
&\qquad + C_6(\varphi_1, \varphi_2, \varphi_3; p)\alpha_{2,m}\alpha_{2,n}\beta_{2,n}\\
&\qquad + C_7(\varphi_1, \varphi_2, \varphi_3; p)\alpha_{2,m}\alpha_{2,n}^2 + C_8(\varphi_1, \varphi_2, \varphi_3; p)\alpha_{2,m}\}\\
&\qquad \boldsymbol{D}(\varphi_1, \varphi_2, \varphi_3; p) = K[p, (\varphi_1 + \varphi_2 + \varphi_3)] \qquad (17)
\end{aligned}
$$

with

where the auxiliary functions $K(p, a)$, $Q(p, a, b, c)$, $R_1(p, a, b)$, $R_2(p, a, b)$, $T(p, a, b)$, and $U(p, a, b, c)$, and parameters m, n, $\alpha_{2,1}$, $\beta_{2,1}$, $\alpha_{2,3}$, and $\beta_{2,3}$ are defined by

$$
\begin{aligned}
K(p, a) &= \sin^2(pa) - p^2\sin^2(a)\\
Q(p, a, b, c) &= \sin^2(pa)\sin^2(b)\sin^2(pc)\\
&\quad - p^2\sin^2(a)\sin^2(pb)\sin^2(c)\\
R_1(p, a, b) &= \sin^2(a)K(p, b) + \sin^2(b)K(p, a)\\
R_2(p, a, b) &= \sin^2(a)K(p, b) - \sin^2(b)K(p, a)\\
T(p, a, b) &= \sin^2(pa)\sin^2(b) - \sin^2(a)\sin^2(pb)\\
U(p, a, b, c) &= 4p^2(p^2 - 1)\sin^2(a)\sin^2(b)\sin^2(c) \qquad (19)\\
m &= 2i - 1, \quad n = -2i + 5\\
\alpha_{12} &= \alpha_{2,1}, \quad \beta_{12} = \beta_{2,1}, \quad \alpha_{23} = \alpha_{2,3}, \quad \beta_{23} = \beta_{2,3}. \qquad (20)
\end{aligned}
$$

We can prove that (16) generally satisfies the following relation.

$$
\begin{cases}
A_1(\varphi_1, \varphi_2, \varphi_3; p) = 16K(p, \varphi_1)K(p, \varphi_2)K(p, \varphi_3)\\
A_2(\varphi_1, \varphi_2, \varphi_3; p) = 8\{K(p, \varphi_1)K(p, \varphi_3) + 2p^2Q(p, \varphi_1, \varphi_2, \varphi_3)\}\\
A_3(\varphi_1, \varphi_2, \varphi_3; p) = -A_2 + 32p^4R_1(p, \varphi_1, \varphi_3)\sin^2\varphi_2\\
A_4(\varphi_1, \varphi_2, \varphi_3; p) = K[p, (\varphi_1 - \varphi_2 + \varphi_3)] - 4p^2[U(p, \varphi_1, \varphi_2, \varphi_3) + (p^2 - 1)\\
\qquad\qquad \times \{\sin\varphi_1 \sin 2\varphi_2 \sin\varphi_3 \sin(\varphi_1 + \varphi_3) - \sin^2\varphi_2(\sin^2\varphi_1 + \sin^2\varphi_3)\}]\\
A_5(\varphi_1, \varphi_2, \varphi_3; p) = 4\{K(p, \varphi_1) - K(p, \varphi_2) + K(p, \varphi_3)\} - 8[K(p, \varphi_1)\{\sin^2(p\varphi_2) + p^2\sin^2\varphi_3\}\\
\qquad - K(p, \varphi_2)\{\sin^2(p\varphi_1) + \sin^2(p\varphi_3)\} + K(p, \varphi_3)\{\sin^2(p\varphi_1) + \sin^2(p\varphi_2)\}] + 16p^2Q(p, \varphi_1, \varphi_2, \varphi_3)\\
B_1(\varphi_1, \varphi_2, \varphi_3; p) = 16p^2K(p, \varphi_m)R_1(p, \varphi_2, \varphi_n)\\
B_2(\varphi_1, \varphi_2, \varphi_3; p) = 4K(p, \varphi_m)K[p, (\varphi_2 + \varphi_n)]\\
B_3(\varphi_1, \varphi_2, \varphi_3; p) = 4K(p, \varphi_n)\left\{U\left(p, \varphi_m, \varphi_2, \frac{\pi}{2}\right) + K[p, (\varphi_m - \varphi_2)]\right\}\\
B_4(\varphi_1, \varphi_2, \varphi_3; p) = 4p^2R_1[p, \varphi_m, (\varphi_2 + \varphi_n)]\\
B_5(\varphi_1, \varphi_2, \varphi_3; p)\\
\qquad = 8p^2\{K(p, \varphi_m)\sin^2\varphi_n + R_2(p, \varphi_2, \varphi_n) - 2Q(p, \varphi_m, \varphi_2, \varphi_n)\} \qquad (18)\\
B_6(\varphi_1, \varphi_2, \varphi_3; p) = 4p^2\{U(p, \varphi_m, \varphi_2, \varphi_n)\\
\qquad\qquad - 2K(p, \varphi_n)\sin^2\varphi_m + R_1[p, (\varphi_m - \varphi_2), \varphi_n)]\} - 4U\left(p, \varphi_m, \varphi_2, \frac{\pi}{2}\right)K(p, \varphi_n)\\
B_7(\varphi_1, \varphi_2, \varphi_3; p) = U\left[p, \varphi_m, (\varphi_2 + \varphi_n), \frac{\pi}{2}\right] + K[p, (\varphi_m - \varphi_2 - \varphi_n)]
\end{cases}
$$

$$
\begin{cases}
C_1(\varphi_1, \varphi_2, \varphi_3; p) = 8p^2K(p, \varphi_n)T(p, \varphi_m, \varphi_2)\\
C_2(\varphi_1, \varphi_2, \varphi_3; p) = 4K(p, \varphi_n)\{K(p, \varphi_m) - K(p, \varphi_2)\} - C_1\\
C_3(\varphi_1, \varphi_2, \varphi_3; p) = -4K(p, \varphi_n)\{K(p, \varphi_m) + 2p^2\sin^2(p\varphi_m)\sin^2\varphi_2\} - 8p^4R_2(p, \varphi_m, \varphi_2)\sin^2\varphi_n\\
C_4(\varphi_1, \varphi_2, \varphi_3; p) = -2p^2R_2[p, \varphi_m, (\varphi_2 + \varphi_n)]\\
C_5(\varphi_1, \varphi_2, \varphi_3; p) = -2p^2\{2K(p, \varphi_m)\sin^2\varphi_n + R_2[p, \varphi_m, (\varphi_2 - \varphi_n)]\} - 2U(p, p\varphi_m, \varphi_2, \varphi_n)\\
C_6(\varphi_1, \varphi_2, \varphi_3; p) = 4p^2\sin^2\varphi_n\{K(p, \varphi_m) + 2p^2R_2(p, \varphi_m, \varphi_2)\}\\
\qquad\qquad + 4p^2\{2\sin^2\varphi_2\sin^2(p\varphi_m)K(p, \varphi_n) - R_1(p, \varphi_2, \varphi_n)\}\\
C_7(\varphi_1, \varphi_2, \varphi_3; p) = K(p, \varphi_m)\cos 2[p(\varphi_2 - \varphi_n)] - \cos 2(p\varphi_m)\left\{U\left(p, \varphi_2, \varphi_n, \frac{\pi}{2}\right) + K[p, (\varphi_2 - \varphi_n)]\right\}\\
C_8(\varphi_1, \varphi_2, \varphi_3; p) = K(p, \varphi_m) - K[p, (\varphi_2 + \varphi_n)] - C_4,
\end{cases}
$$

Downloaded 04 May 2010 to 171.66.16.33. Redistribution subject to ASME license or copyright; see http://www.asme.org/terms/Terms_Use.cfm

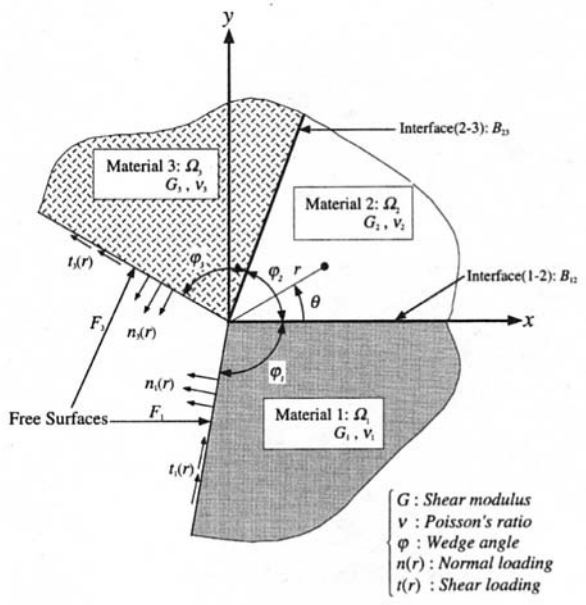


Fig. 1 Model for analysis of three-phase bonded structure under surface tractions

$$S(\varphi_1, \varphi_2, \varphi_3, \alpha_{12}, \beta_{12}, \alpha_{23}, \beta_{23}; p) = S(\varphi_3, \varphi_2, \varphi_1, -\alpha_{23}, -\beta_{23}, -\alpha_{12}, -\beta_{12}; p) \quad (21)$$

3 Eigenequation in the Case of Region $1(G_1, \nu_1) = 3(G_3, \nu_3)$

When materials of regions 1 and 3 are identical, the following relation holds good between α_{12}, β_{12}, α_{23} and β_{23}:

$$\begin{cases} \alpha = \alpha_{12} = -\alpha_{23} \\ \beta = \beta_{12} = -\beta_{23}. \end{cases} \quad (22)$$

Then, (16) can be expressed as

$$\begin{aligned} S(\varphi_1, \varphi_2, \varphi_3, \alpha, \beta, -\alpha, -\beta; p) &= A(\varphi_1, \varphi_2, \varphi_3, \alpha, \beta, -\alpha, -\beta; p) \\ &+ B(\varphi_1, \varphi_2, \varphi_3, \alpha, \beta, -\alpha, -\beta; p) \\ &+ C(\varphi_1, \varphi_2, \varphi_3, \alpha, \beta, -\alpha, -\beta; p) \\ &+ D(\varphi_1, \varphi_2, \varphi_3; p) = 0. \end{aligned} \quad (23)$$

The order of stress singularity is given by the real part of root of $S = 0$ existing in $0 < \mathrm{Re}(p) < 1$ (stress σ and the root p is related by $\sigma \propto r^{p-1}$). Here, the root p satisfying the following relations is examined.

$$S(\varphi_1, \varphi_2, \varphi_3, \alpha, \beta, -\alpha, -\beta; p_1) = 0$$

$$\frac{d}{dp} S(\varphi_1, \varphi_2, \varphi_3, \alpha, \beta, -\alpha, -\beta; p_1)|_{p_1 \to 1} = 0 \quad (24)$$

The second equation is the condition for which the stress field possesses logarithmic singularity (Bogy, 1970, 1971a). The root will be represented as p_1. Furthermore, when the eigenequation has multiple roots in $0 < \mathrm{Re}(p) < 1$, the root having the smallest real part will be chosen as p_1.

Elastic constants for each material are within the following ranges:

$$0 < G_1, G_2, G_3 < \infty, \quad 0 \leqq \nu_1, \nu_2, \nu_3 \leqq 0.5. \quad (25)$$

Using the relations of Dundurs parameters expressed by (22), the values of α_{12}, β_{12}, α_{23}, and β_{23} fall within a parallelogram (Bogy, 1970) defined on the α-β plane for all the pairs of materials as shown in Fig. 2. Since the values corresponding to plane stress are included within the domain of the values for plane strain, the results of plane stress are not shown here.

Next, we will demonstrate that the eigen equation for a single wedge derived by Williams (1952) is deduced by rearranging the eigen equation presented in this paper. When α approaches to 1, i.e., $k_{12} \to \infty$, (23) can be arranged to

$$\begin{aligned} S\left(\varphi_1, \varphi_2, \varphi_3, 1, \frac{m_2 - 2}{m_2}, -1, \frac{-(m_2 - 2)}{m_2}; p\right) &= \{\sin^2(p\varphi_1) - p^2 \sin^2 \varphi_1\} \\ &\times \{(m_2 - 1)^2 \sin^2(p\varphi_2) - p^2 \sin^2 \varphi_2\} \\ &\times \{\sin^2(p\varphi_3) - p^2 \sin^2 \varphi_3\} = 0 \end{aligned} \quad (26)$$

which corresponds to Eqs. (15) and (16) in Williams (1952) for the free-free single wedge (reported in Williams, 1952) of angles φ_1 and φ_3, and for the fixed-fixed one of angle φ_2, respectively. Also, when α approaches to -1, i.e., $k_{12} \to 0$, (23) becomes

$$\begin{aligned} S\left(\varphi_1, \varphi_2, \varphi_3, -1, \frac{-(m_1 - 2)}{m_1}, 1, \frac{m_1 - 2}{m_1}; p\right) &= \{4(m_1 - 1)\sin^2(p\varphi_1) + 4p^2 \sin^2 \varphi_1 - m_1^2\} \\ &\times \{\sin^2(p\varphi_2) - p^2 \sin^2 \varphi_2\}\{4(m_1 - 1)\sin^2(p\varphi_3) \\ &+ 4p^2 \sin^2 \varphi_3 - m_1^2\} = 0 \end{aligned} \quad (27)$$

which corresponds to Eqs. (15) and (17) in Williams (1952) for the free-free single wedge of angle φ_2 and for the fixed-free one of angles φ_1 and φ_3, respectively.

4 Numerical Results and Discussion

4.1 Loci for Roots on the α-β Plane. The loci for root p_1 for the bonded wedges in the following cases are plotted on the α-β plane.

(A) half-planes $\begin{cases} \pi/3 - \pi/3 - \pi/3 \\ \pi/6 - 2\pi/3 - \pi/6 \end{cases}$

(B) three-quarters planes $\begin{cases} \pi/2 - \pi/2 - \pi/2 \\ \pi/3 - 5\pi/6 - \pi/3 \end{cases}$

(C) full planes $\begin{cases} 2\pi/3 - 2\pi/3 - 2\pi/3 \\ \pi/2 - \pi - \pi/2 \end{cases}$

Figures 3, 4, and 5 show the loci for p_1 for (A) half-planes, (B) three-quarters planes and (C) full planes, respectively. Roots for full planes correspond to ones for a straight crack that meets the bonded plane at an arbitrary angle. Furthermore, $p_1 \to 1.00$ noted on the α-β plane represents the loci for roots exhibiting logarithmic singularity.

In Figs. 3–5, all the materials are identical under the condition of $(\alpha, \beta) = (0, 0)$ in the α-β plane. Then, (23) is represented by the following equation:

$$S(\varphi_1, \varphi_2, \varphi_3, 0, 0, 0, 0; p) = \sin^2[p(\varphi_1 + \varphi_2 + \varphi_3)] - p^2 \sin^2(\varphi_1 + \varphi_2 + \varphi_3) = 0 \quad (28)$$

which agrees with the equation for the free-free single wedge derived by Williams (1952). Hence, the roots agree with ones for the free-free wedge. Roots at $\alpha = -1$ ($k_{12} \to 0$) correspond to ones for the fixed-free single wedge with the angles φ_1 and

Downloaded 04 May 2010 to 171.66.16.33. Redistribution subject to ASME license or copyright; see http://www.asme.org/terms/Terms_Use.cfm

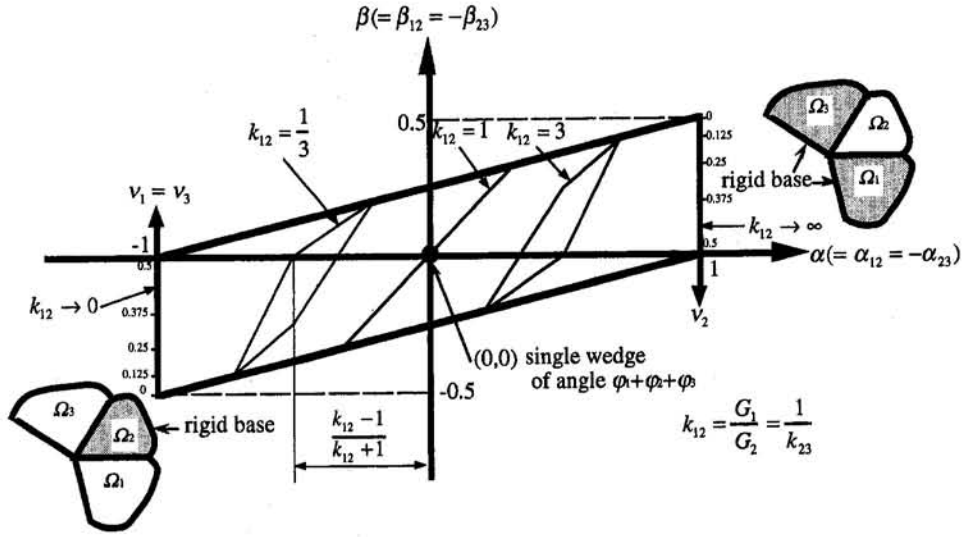


Fig. 2 Parallelogram on the α-β plane for pairs of materials in case where materials of both sides are identical

φ_3, and then (27) yields a double root because of $\varphi_1 = \varphi_3$. Incidentally, roots occur also in the free-free single wedge with the angle φ_2, but these roots are not plotted in Figs. 3–5, because the roots is larger than ones for the fixed free. Furthermore, the roots for the fixed-free single wedge approach to zero as $\alpha \to 1$ ($k_{12} \to$). The loci for the roots p_1 become to be parallel with the β-axis as the wedge angle φ_2 increases (Figs. 3–5 (a) → Figs. 3–5(b)). Moreover, when the wedge angle φ_2 more increases, i.e., $\varphi_1 = \varphi_3 \to 0$, the loci for p_1 come together at a point of $(\alpha, \beta) = (0, 0)$ on the α-β plane.

When $\varphi_1 = \varphi_3 = \pi/2$ and $\varphi_2 = \pi$, logarithmic singularity occurs over a whole α-β plane (see Fig. 5), then the eigenequation can be expressed as

$$S\left(\frac{\pi}{2}, \pi, \frac{\pi}{2}, \alpha, \beta, -\alpha, -\beta; p\right) = \sin^2(p\pi)\{2p^2(\alpha-\beta)(\beta+1) + \beta^2 - \alpha + (1-\beta^2)\cos(p\pi)\}^2 = 0. \quad (29)$$

The first factor, in the right side, that is independent of pairs of materials induces logarithmic singularity. The loci for roots plotted in Fig. 5 are calculated from the second factor, where all the roots are then double root. Equation (29) agrees with the equation derived by Bogy (1971b), Lin and Mar (1976), who analyzed a half-crack exists in either bonded half-planes. It also can be seen that the roots p_1 become smaller as $\alpha \to 1$

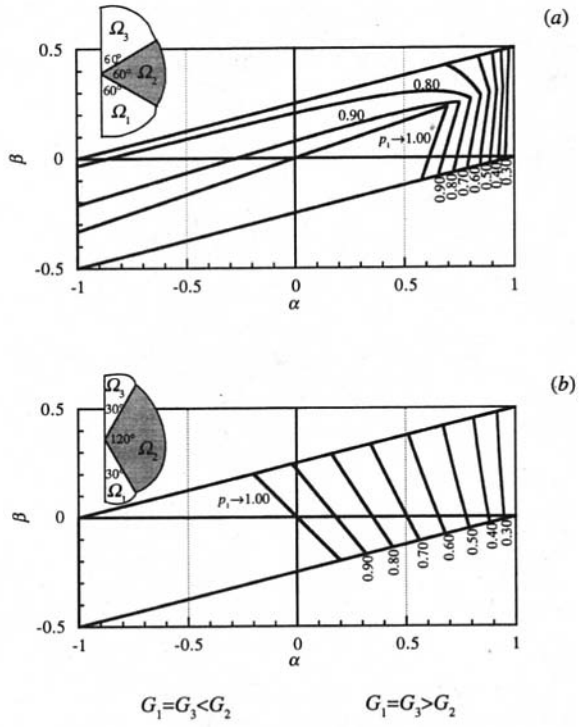


Fig. 3 Loci for roots $p = p_1$ of $S(\varphi_1, \varphi_2, \varphi_3, \alpha, \beta, -\alpha, -\beta; p_1) = 0$ for (a) $\varphi_1 = \varphi_2 = \varphi_3 = \pi/3$, ($b$) $\varphi_1 = \varphi_3 = \pi/6$, $\varphi_2 = 2\pi/3$

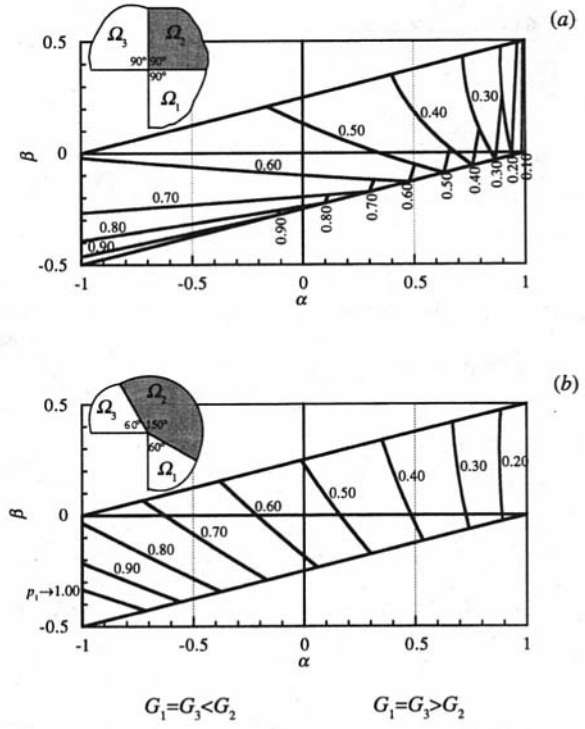


Fig. 4 Loci for roots $p = p_1$ of $S(\varphi_1, \varphi_2, \varphi_3, \alpha, \beta, -\alpha, -\beta; p_1) = 0$ for (a) $\varphi_1 = \varphi_2 = \varphi_3 = \pi/2$, ($b$) $\varphi_1 = \varphi_3 = \pi/3$, $\varphi_2 = 5\pi/6$

Downloaded 04 May 2010 to 171.66.16.33. Redistribution subject to ASME license or copyright; see http://www.asme.org/terms/Terms_Use.cfm

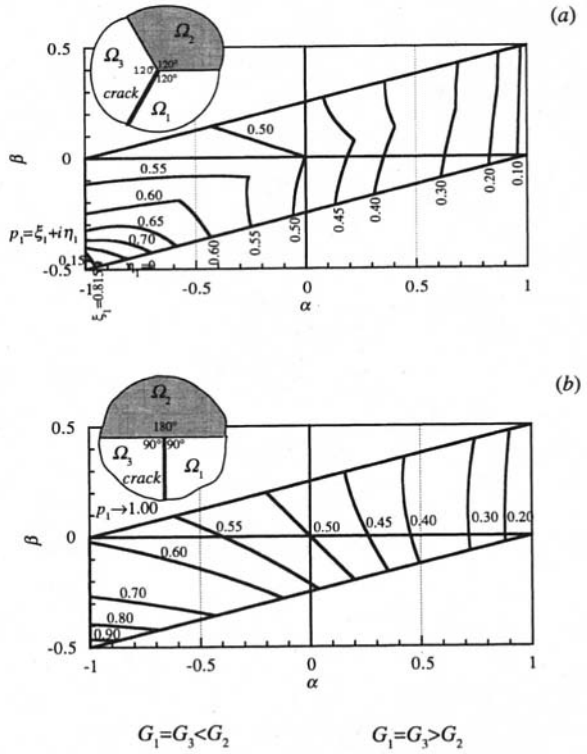


Fig. 5 Loci for roots $p = p_1$ of $S(\varphi_1, \varphi_2, \varphi_3, \alpha, \beta, -\alpha, -\beta; p_1) = 0$ for (a) $\varphi_1 = \varphi_2 = \varphi_3 = 2\pi/3$, (b) $\varphi_1 = \varphi_3 = \pi/2$, $\varphi_2 = \pi$

and larger as $\alpha \to -1$ on the α-β plane. That is, the order $O(r^{p-1})$ of stress singularity tends to increase when $G_1 = G_3 > G_2$, and to decrease when $G_1 = G_3 < G_2$. Moreover, it is found from Fig. 5 that the order $O(r^{p-1})$ of singularity at the tip of a crack existing in the stiff side of the two-phase material becomes large in comparison with that of the soft side. This result agrees with the one obtained by Bogy (1971b), Fenner (1976), and Lin and Mar (1976).

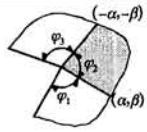
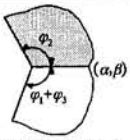
4.2 Variations of Roots for Bonding Order of Materials. The order $O(r^{p-1})$ of stress singularity for the two-phase bonded structure depends on pairs of wedge angles of regions and their mechanical properties. Let us prove here that the bonding order of materials also influences on the order $O(r^{p-1})$ of stress singularity in the case of the three-phase bonded structure. All the roots p in $0 < \mathrm{Re}(p) < 1$ are listed in Table 1 for the three-phase materials with the relations of $\varphi_2 = \varphi_1 + \varphi_3$ and $\varphi_2 \gg \varphi_1 + \varphi_3$, for the two-phase ones combined regions 1 and 3 with holding the relation of each angle and for a single wedge of $\varphi_1 + \varphi_2 + \varphi_3$.

As seen from Table 1, the order $O(r^{p-1})$ of stress singularity for the three-phase bonded structure in the case of $G_1 = G_3 \gg G_2$ is larger than that in the case of $G_1 = G_3 \ll G_2$. When $\varphi_2 = \varphi_1 + \varphi_3$, the order $O(r^{p-1})$ for the two-phase bonded structure obtained by changing the bonding order of materials in the three-phase structure is smaller than that for the three-phase one when $G_1 = G_3 \gg G_2$, and is large when $G_1 = G_3 \ll G_2$. Therefore, it is found that the order $O(r^{p-1})$ of singularity can be reduced by suitably changing the bonding order of materials. Similarly, the order $O(r^{p-1})$ for the single wedge material is smaller than that for the three-phase structure when $G_1 = G_3 \gg G_2$, and is large when $G_1 = G_3 \ll G_2$. When $\varphi_2 \gg \varphi_1 + \varphi_3$ and $G_1 = G_3 \ll G_2$, since a whole region of bonded structure is occupied with more rigid region Ω_2 than regions Ω_1 and Ω_3, all the roots p approach to those for a single wedge. Hence, even if the bonding order of materials is altered, the order $O(r^{p-1})$ of singularity varies little in such a case.

5 Conclusions

The eigenequation for three-phase bonded structure with arbitrary angles was theoretically derived by expanding and arranging the determinant (12×12) of the coefficients in the simultaneous equations obtained from the boundary conditions of stress and displacement through the Mellin transform. Then, four Dundurs composite parameters, α_{12}, β_{12} for materials 1 and 2 and α_{23}, β_{23} for materials 2 and 3, were introduced for representing six elastic constants of three materials. The derived eigenequation is also applicable for two-phase bonded structure under the free-free and the fixed-free boundary conditions, for two-phase one existing a crack in either material and for single wedge under several different boundary conditions; free-free, fixed-free, and fixed-fixed. Under the condition that mechanical properties of materials 1 and 3 are identical, the loci of the fixed order $O(r^{p-1})$ of stress singularity were shown on the α-β plane for the dissimilar materials of half-planes, three-quarters planes, and full planes. Variations of roots with the bonding order of materials were also investigated. The order $O(r^{p-1})$ of singularity becomes larger as the intermediate material in the three-phase bonded structure becomes softer than both side materials, and vice versa. When $\varphi_1 = \varphi_3 = \pi/2$, $\varphi_2 = \pi$ and materials 1 and 3 are identical, it was proved that logarithmic singularity occurs regardless of different pairs of materials. Furthermore, the order $O(r^{p-1})$ of stress singularity can be reduced by suitably changing the bonding order of materials and by replacing the material at intermediate region with material that is stiffer than the both side materials. For instance, when $\varphi_1 + \varphi_3 \approx \varphi_2$ and $G_1 < G_2$, the order $O(r^{p-1})$ of singularity for the two-phase bonded structure composed of materials 1 and 2 with the wedge angles $\varphi_1 + \varphi_3$ and φ_2 can be reduced by changing the two-phase structure into the three-phase one with the bonded wedge angle $\varphi_1 - \varphi_2 - \varphi_3$.

Table 1 Roots p in $0 < \mathrm{Re}(p) < 1$ for the cases of $\varphi_2 = \varphi_1 + \varphi_3$, $\varphi_2 \gg \varphi_1 + \varphi_3$ (three-phase bonded), $\varphi_1 + \varphi_3 - \varphi_2$ (two-phase bonded) and a single wedge of angle $\varphi_1 + \varphi_2 + \varphi_3$

	 Three-phase bonded $\varphi_1-\varphi_2-\varphi_3$		 Two-phase bonded $\varphi_1+\varphi_3-\varphi_2$		 single wedge $\varphi_1+\varphi_2+\varphi_3$
(α,β)	(0.85,0.30) $G_1=G_3\gg G_2$	(-0.85,-0.30) $G_1=G_3\ll G_2$	(0.85,0.30) $G_{13}\gg G_2$	(-0.85,-0.30) $G_{13}\ll G_2$	
wedge angle	$\pi/4-\pi/2-\pi/4$		$\pi/2-\pi/2$		half-plane
Root p	0.4928 0.9551	NON	0.8301		$p\to1.00$
wedge angle	3—174—3 deg		6—174 deg		
Root p	0.6122	NON	0.7006	NON	
wedge angle	67.5—135—67.5 deg		135—135 deg		three quarter-plane
Root p	0.2116 0.4699	0.8662 0.9387	0.6338 0.7750		0.5445 0.9085
wedge angle	5—260—5 deg		10—260 deg		
Root p	0.4376 0.5923	0.5613 0.9741	0.4287 0.7364	0.5613 0.9738	
wedge angle	$\pi/2-\pi-\pi/2$		$\pi-\pi$		full-plane
Root p	0.2291 0.2304 $p\to1.00$	0.7082 $p\to1.00$	0.50+i0.099 $p\to1.00$		0.5000 $p\to1.00$
wedge angle	6—348—6 deg		12—348 deg		
Root p	0.3065 0.4990 0.7011	0.5001 0.5325	0.3505 0.4990 0.8317	0.5001 0.5325	

Downloaded 04 May 2010 to 171.66.16.33. Redistribution subject to ASME license or copyright; see http://www.asme.org/terms/Terms_Use.cfm

References

Blanchard, J. P., and Ghoniem, N. M., 1989, "An Eigenfunction Approach to Singular Thermal Stresses in Bonded Strips," *Journal of Thermal Stresses,* Vol. 12, pp. 501–527.

Bogy, D. B., 1968, "Edge-Bonded Dissimilar Orthogonal Elastic Wedges Under Normal and Shear Loading," ASME JOURNAL OF APPLIED MECHANICS, Vol. 35, pp. 460–466.

Bogy, D. B., 1970, "On the Problem of Edge-Bonded Elastic Quarter-planes Loaded at the Boundary," *International Journal of Solids and Structures,* Vol. 6, pp. 1287–1313.

Bogy, D. B., 1971a, "Two-Edge Bonded Elastic Wedges of Different Materials and Wedge Angles Under Surface Tractions," ASME JOURNAL OF APPLIED MECHANICS, Vol. 38, pp. 377–386.

Bogy, D. B., 1971b, "On the Plane Elastostatic Problem of a Loaded Crack Terminating at a Material Interface," ASME JOURNAL OF APPLIED MECHANICS, Vol. 38, pp. 911–918.

Davis, B., 1984, *Integral Transforms and Their Applications,* Springer-Verlag, New York, pp. 195–224.

Dundurs, J., 1969, "Discussion of Edge-Bonded Dissimilar Orthogonal Elastic Wedges Under Normal and Shear Loading," ASME JOURNAL OF APPLIED MECHANICS, Vol. 36, pp. 650–652.

Fenner, D. N., 1976, "Stress Singularities in Composite Materials with an Arbitrarily Oriented Crack Meeting an Interface," *International Journal of Fracture,* Vol. 12, No. 5, pp. 705–721.

Lin, K. Y., and Mar, J. W., 1976, "Finite Element Analysis of Stress Intensity Factors for Cracks at a Bi-Material Interface," *International Journal of Fracture,* Vol. 12, No. 4, pp. 521–531.

Sneddon, I. N., 1974, *The Use of Integral Transforms,* McGraw-Hill, New York, pp. 262–297.

Theocaris, P. S., 1989, "The Order of Singularity at a Multi-Wedge Corner of a Composite Plate," *International Journal of Engineering Science,* Vol. 12, pp. 107–120.

Williams, M. L., 1952, "Stress Singularities Resulting From Various Boundary Conditions in Angular Corners of Plates in Extension," ASME JOURNAL OF APPLIED MECHANICS, Vol. 19, pp. 526–528.

Downloaded 04 May 2010 to 171.66.16.33. Redistribution subject to ASME license or copyright; see http://www.asme.org/terms/Terms_Use.cfm

The Rebound of an Elastic Sphere Against a Rigid Wall

P. Villaggio
Istituto di Scienza Delle Costruzioni,
Via Diotisalvi, 2,
I-56126 Pisa, Italy

The normal impact of an elastic sphere against a rigid plane is described using an elastic solution for a heavy sphere on a rigid plane found by Bondareva (1970). The solution is valid only in the case of equilibrium, but may be extended also to the dynamical case, provided that the time of duration of the impact is much larger that the time employed by the elastic waves in traversing the whole sphere after the first impact. The fundamental result is that, according to the new solution, the time of adherence between the first contact and the detachment is slightly higher than the same time evaluated according to the classical Hertz's theory.

1 Introduction

The simplest case of impact between elastic bodies is that of an elastic sphere which moves normally to a rigid plane, impinges against it, and, after a certain time during which the sphere remains in contact with the plane, the sphere rebounds in the opposite direction with opposite velocity. The explanation of the phenomenon and its mathematical description was given by Hertz (1881), as an extension of his theory of the frictionless contact between elastic bodies. Hertz's theory is based upon two fundamental assumptions. The first is that the deformation is completely localized in the vicinity of the contact area, which is a small circle around the point of the surface of the sphere where the contact occurs for the first time. The second is that all other points of the sphere, outside the region where elastic deformations are concentrated, have the same velocity at each time. In a pictorial form, the impact of the elastic sphere may be visualized as the collision of a rigid railway truck equipped with two light spring buffers: the deformation are concentrated in the springs, whose inertia is neglected, and the truck moves as a rigid body (Johnson, 1985). Hertz's theory is quasi-static because it neglects the influence of propagation of elastic waves in the interior of the sphere and their reflection at the boundary. In addition, in order to evaluate the relationship between the instantaneous deformation of the sphere, measured by the distance of its center from the wall, and the instantaneous resultant pressure over the compressed area, Hertz regarded the sphere as an elastic half-plane loaded over a small circular region of its surface.

Hertz' solution, despite its elegance, rests on such drastic assumptions that it is natural to ask how the solution may be modified when they are removed. More precisely, is it really true that, still maintaining the quasi-static approach, the influence of the elastic deformation of the sphere is negligible, so that it may be regarded as a rigid body? Again, is it also legitimate to disregard the local curvature of the spherical surface in the evaluation of the resulting contact force?

A precise evaluation of these effects is possible in principle, but useless in practice because it would require the solution of a complicated system of integral equations which are difficult to treat, even by a purely numerical procedure (Goodman and Keer, 1965). An alternative way for partially answering to the perplexities arising from Hertz's approximations is offered by a solution relative to the elastic sphere, found by Bondareva (1969), as a generalization of a previous solution of Lur'e (1955). The author found the explicit form of the Green's function for a sphere under normal loads and solved, as an example, the problem of a heavy sphere kept in equilibrium by a vertical force P concentrated at its lower pole A (Fig. 1). She did not simply write the formal expansion of the solution in the form of two series of spherical harmonics, but could sum up these series obtaining a closed solution.

Subsequently Bondareva (1970) utilized her solution to solve the contact problem of a heavy sphere on a rigid plane. Due to the local flattening of the sphere, the area of contact is a plane circle, whose radius is not know in advance. In this case, however, it is no longer possible to find a finite solution, but only an approximation of it by an asymptotic method.

An alternative procedure to solve approximately this problem is that of pre-assigning the contact pressure at the interface and of solving the integral equations only in the mean. If this latter approximate solution is accepted, it is possible to treat the problem of the impact of the sphere in an analogous way as did Hertz, but employing a statical solution that accounts for the curvature of the sphere and its global deformability. The results may be compared to those predicted by Hertz's theory and the conclusion is the following. The analytical relation between the reaction P_0 and the vertical displacement δ_0 of the lower pole A (Fig. 1), is different in the two theories, but the structure of the function $P_0(\delta_0)$ remains almost the same. The duration of the impact, measured by the time during which the sphere remains in contact with the wall, is slightly higher if the new solution is adopted.

2 Bondareva's Equation

Let a sphere of radius R_0 referred to a system of spherical coordinates (r, ϑ, φ) be such that its origin 0 is placed at the centre and, therefore, the region occupied by the sphere is $0 \leq r \leq R_0$. The sphere is made of an elastic, homogeneous, isotropic material characterized by a tangential modulus G and Poisson's ratio $\sigma(-1 < \sigma < (1/2))$. The Young's modulus E is equal to $E = 2G(1 + \sigma)$. Let ρ_0 be the density so that $\gamma_0 = \rho_0 g$ represents the specific weight of the material.

The sphere is subject to body forces directed along the vertical z-axis oriented dawnwards. The resultant of these forces is

$$P_0 = \tfrac{4}{3}\pi\gamma_0 R_0^3. \tag{2.1}$$

At equilibrium, the body forces are balanced by a distribution of contact pressures acting on the domain of contact, which is a small horizontal circle with centre on the vertical axis. The radius of this circle depends on the flattening of the sphere around its lower pole.

Contributed by the Applied Mechanics Division of THE AMERICAN SOCIETY OF MECHANICAL ENGINEERS for publication in the ASME JOURNAL OF APPLIED MECHANICS.

Discussion on this paper should be addressed to the Technical Editor, Professor Lewis T. Wheeler, Department of Mechanical Engineering, University of Houston, Houston, TX 77204-4792, and will be accepted until four months after final publication of the paper itself in the ASME JOURNAL OF APPLIED MECHANICS.

Manuscript received by the ASME Applied Mechanics Division, June 9, 1994; final revision, Mar. 28, 1995. Associate Technical Editor: X. Markenscoff.

Copyright © 1996 by ASME

Downloaded 04 May 2010 to 171.66.16.33. Redistribution subject to ASME license or copyright; see http://www.asme.org/terms/Terms_Use.cfm

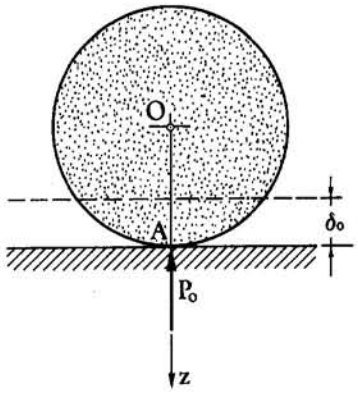


Fig. 1

In order to formulate the contact problem for the heavy sphere it is convenient to consider for the moment the case in which the body forces are absent and the sphere is simply loaded at its surface by purely normal axisymmetric tractions $N(\vartheta)$. Thus the boundary conditions of the problem are

$$\sigma_r = N(\vartheta),\ \tau_{r\vartheta} = \tau_{r\varphi} = 0 \text{ for } r = R_0,\ 0 < \vartheta < \pi, \quad (2.2)$$

where $\sigma_r, \tau_{r\vartheta}, \tau_{r\theta}$ denote, respectively, the radial and tangential stress components on the surface. Bondareva (1970) proved that the radial displacement $u_r(R_0, \vartheta)$ at the surface of the sphere produced by the normal tractions $N(\vartheta)$ can be represented in the following form:

$$u_r(R_0, \vartheta) = \frac{R_0}{2\pi G}\int_0^\pi N(\alpha)H(\vartheta, \alpha)\sin\alpha d\alpha, \quad (2.3)$$

where $H(\vartheta, \alpha)$ is expressed by the finite formula

$$H(\vartheta, \alpha) = \frac{\pi}{2}\frac{1-2\sigma}{1+\sigma} + 4(1-\sigma)U(1) + \mathrm{Re}\int_0^1 \left(\frac{A}{y^\lambda} + \frac{1}{y^2}\right)U(y)dy, \quad (2.4)$$

with

$$U(y) = U(y, \vartheta, \alpha) = \frac{K(k)}{h} - \frac{\pi}{2}(1 + y\cos\vartheta\cos\alpha), \quad (2.5)$$

$$h^2 = (1-y)^2 + 4y\sin^2\frac{\vartheta+\alpha}{2},$$

$$k^2h^2 = 4y\sin\vartheta\sin\alpha, \quad (2.6)$$

$$A = 8\sigma^2 - 8\sigma + 1 + i\frac{16\sigma^3 - 16\sigma^2 - 4\sigma + 5}{\sqrt{3-4\sigma^2}} = \text{const.}, \quad (2.7)$$

$$\lambda = \frac{1-2\sigma}{2} + i\frac{\sqrt{3-4\sigma^2}}{2}, \quad (2.8)$$

and $K(k)$ is the complete elliptic integral of the first kind. The function $H(\vartheta, \alpha)$ is the Green's function of the boundary value problem under boundary conditions of the type (2.2). It enjoys the properties of symmetry

$$H(\vartheta, \alpha) = H(\alpha, \vartheta), \quad H(\vartheta, \alpha) = H(\pi - \vartheta, \pi - \alpha). \quad (2.9)$$

The function $H(\vartheta, \alpha)$ is continuous everywhere except for $\vartheta = \alpha$, and the nature of the singularity at $\vartheta = \alpha$ is determined by the relationship

$$H(\vartheta, 0)\frac{1}{\pi} = (1-\sigma)\left(\frac{1}{\sin\frac{\vartheta}{2}} - 4\cos^2\frac{\vartheta}{2}\right) + \frac{1-2\sigma}{2(1+\sigma)} - (1-2\sigma)^2\left[\cos\vartheta\ln\sin\frac{\vartheta}{2}\left(1+\sin\frac{\vartheta}{2}\right) + 2\sin\frac{\vartheta}{2}\left(1-\sin\frac{\vartheta}{2}\right)\right] + \mathrm{Re}\frac{P+Q}{2}\int_0^1 \frac{y^{1-n_1}-1}{y^2} \times \left[\frac{1}{(y^2 - 2y\cos\vartheta - 1)^{1/2}} - 1 - y\cos\vartheta\right]dy, \quad (2.10)$$

where P and Q are constants given by

$$P = 4\sigma^2 - 6\sigma + 2 + i\frac{8\sigma^3 - 12\sigma^2 + \sigma + 3}{\sqrt{3-4\sigma^2}},$$

$$Q = 4\sigma^2 - 2\sigma - 1 + i\frac{8\sigma^3 - 4\sigma^2 - 5\sigma + 2}{\sqrt{3-4\sigma^2}};$$

and n_1 is

$$n_1 = -\frac{1+2\sigma}{2} + \frac{i}{2}\sqrt{3-4\sigma^2}.$$

If the sphere, subject to purely normal loads $N(\vartheta)$, is pressed against the rigid plane, its load may be represented as

$$N(\vartheta) = \begin{cases} Q(\vartheta) & \text{for } \gamma < \vartheta < \pi, \\ \sigma(\vartheta) & \text{for } 0 < \vartheta < \gamma, \end{cases} \quad (2.11)$$

where the circle $\vartheta = \gamma$, $r = R_0$ bounds the domain of contact (Fig. 2), $Q(\vartheta)$ is prescribed, and $\sigma(\vartheta)$ is the pressure of contact. It is clear that $Q(\vartheta)$ and $\sigma(\vartheta)$ are related by the equilibrium condition

$$\int_0^\gamma \sigma(\alpha)\sin\alpha\cos\alpha d\alpha + \int_\gamma^\pi Q(\alpha)\sin\alpha\cos\alpha d\alpha = 0. \quad (2.12)$$

On the contact region $0 \le \vartheta < \gamma$ the pressure $\sigma(\vartheta)$ is unknown, but the radial displacement is known and given by the equation (Fig. 2)

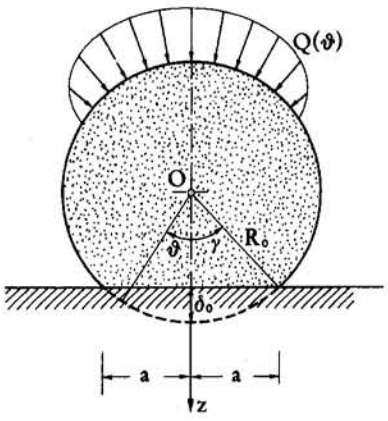


Fig. 2

Downloaded 04 May 2010 to 171.66.16.33. Redistribution subject to ASME license or copyright; see http://www.asme.org/terms/Terms_Use.cfm

$$u_r(R_0, \vartheta) = -R_0 + \frac{R_0 - \delta_0}{\cos \vartheta} = v(\vartheta), \qquad (2.13)$$

where, according to the customary convention, radial displacements directed inwards are negative. The substitution of the boundary conditions (2.11) and (2.13) into (2.3) yields an integral equation for the contact pressure:

$$\frac{R_0}{2\pi G} \int_0^\gamma \sigma(\alpha) H(\vartheta, \alpha) \sin \alpha d\alpha = v(\vartheta)$$

$$- \frac{R_0}{2\pi G} \int_\gamma^\pi Q(\vartheta) H(\vartheta, \alpha) \sin \alpha d\alpha \quad (0 < \vartheta < \gamma). \quad (2.14)$$

Bondareva converted this equation into a Fredholm integral equation of the second kind and suggested a method of solution in the form of a uniformly convergent power series of the parameter $\epsilon = tg(\gamma/2)$. If, however, the contact region is a small portion of the surface, the solution of (2.14) can be approximated with a simpler procedure.

3 Solution of (2.14)

The rigorous solution of (2.14), in which $\sigma(\vartheta)$ and γ are unknown, is very complicated. But the difficulty may be avoided by observing that, by analogy with Hertz's case, $\sigma(\vartheta)$ has a maximum at $\vartheta = 0$ and vanishes at $\vartheta = \gamma$. This suggests taking

$$\sigma(\vartheta) = \sigma_0 \sqrt{1 - \frac{\vartheta^2}{\gamma^2}}, \qquad (3.1)$$

where σ_0 is a constant whose value is determined by condition (2.12). Since

$$\int_\gamma^\pi Q(\alpha) \sin \alpha \cos \alpha d\alpha = \frac{P_0}{2\pi R_0^2},$$

is known, Eq. (2.12) yields

$$\sigma_0 \int_0^\gamma \sqrt{1 - \frac{\alpha^2}{\gamma^2}} \sin \alpha \cos \alpha d\alpha = - \frac{P_0}{2\pi R_0^2}. \qquad (3.2)$$

If γ is small the integral on the left-hand side of (3.2) can be simplified by putting $\sin \alpha \simeq \alpha$ and $\cos \alpha \simeq 1$, so that (3.2) becomes

$$\sigma_0 \int_0^\gamma \sqrt{1 - \frac{\alpha^2}{\gamma^2}} \alpha d\alpha = - \frac{P_0}{2\pi R_0^2}. \qquad (3.3)$$

The evaluation of the integral in (3.3) is elementary and hence (3.3) gives

$$\sigma_0 = - \frac{3}{2} \frac{P_0}{\pi R_0^2 \gamma^2}. \qquad (3.4)$$

For small values of γ, $R_0\gamma$ can be identified with a, the radius of the circle of contact (Fig. 2). Thus the value of σ_0 is the same as that calculated according to Hertz's theory (Szabó, 1964).

The integral Eq. (2.14) has been written in the case in which a normal pressure $Q(\vartheta)$ is prescribed on the part $\gamma < \vartheta < \pi$ of the surface of the sphere. The third term in (2.14) represents the radial displacement, due to the pressure $Q(\vartheta)$, arising in the part $0 < \vartheta < \gamma$ of the surface. If, conversely, the surface of the sphere outside the contact region is free from surface tractions, and the external loads are body forces of magnitude $\gamma_0 = \rho_0 g$ acting in the positive direction of the z-axis, then a particular solution of the equations of elasticity corresponding to these forces is

$$\sigma_r = \sigma_\vartheta = \sigma_\varphi = -r \cos \vartheta \gamma_0, \quad \tau_{r\vartheta} = 0,$$

and the associated displacements are

$$u_r = -r^2 \cos \vartheta \frac{1 - 2\sigma}{1 + \sigma} \frac{\gamma_0}{4G},$$

$$u_\vartheta = -r^2 \sin \vartheta \frac{1 - 2\sigma}{1 + \sigma} \frac{\gamma_0}{4G}. \qquad (3.5)$$

In this case Eq. (2.14) may be replaced by the simpler equation

$$\frac{R_0}{2\pi G} \int_0^\gamma \sigma(\alpha) H(\vartheta, \alpha) \sin \alpha d\alpha$$

$$= v(\vartheta) + R_0^2 \cos \vartheta \frac{1 - 2\sigma}{1 + \sigma} \frac{\gamma_0}{4G} \quad (0 < \vartheta < \gamma). \quad (3.6)$$

The solution of (3.6) cannot be obtained in an elementary way. But a simple, though approximate, solution is obtainable through the following considerations. First, instead of satisfying (3.6) for each $0 < \vartheta < \gamma$, the equation must be verified only for $\vartheta = 0$. Second, only the dominant terms in the kernel $H(\vartheta, \alpha)$ are taken into account, so that (2.10) may be written in the approximate form

$$H(\vartheta, 0) \frac{1}{\pi} \simeq (1 - \sigma) \frac{1}{\sin \frac{\vartheta}{2}}$$

$$- (1 - 2\sigma)^2 \cos \vartheta \ln \sin \frac{\vartheta}{2}, \quad (3.7)$$

in which only the singular terms are retained. Both these approximations are legitimate if γ is small. Since, at this level of approximation, $\sigma(\alpha)$ may be given the form (3.1), Eq. (3.6) becomes

$$\frac{R_0 \sigma_0}{2\pi G} \int_0^\gamma \sqrt{1 - \frac{\alpha^2}{\gamma^2}} H(0, \alpha) \sin \alpha d\alpha$$

$$= v(0) + R_0^2 \frac{1 - 2\sigma}{1 + \sigma} \frac{\gamma_0}{4G}. \quad (3.8)$$

This equation leads to the determination of γ.

The calculation of the integral in (3.8) may be further simplified by putting

$$H(0, \alpha) \sin \alpha$$

$$\simeq \pi \left[(1 - \sigma) \frac{1}{\sin \frac{\alpha}{2}} - (1 - 2\sigma)^2 \cos \alpha \ln \sin \frac{\alpha}{2} \right] \sin \alpha$$

$$\simeq \pi[2(1 - \sigma) - (1 - 2\sigma)^2 \alpha \ln \alpha]. \qquad (3.9)$$

Recalling that $\sigma_0 = -(3/2)(P_0/\pi R_0^2 \gamma^2)$ and that $(4/3)\pi R_0^3 \gamma_0 = P_0$, Eq. (3.8) may be written in the form

$$- \frac{R_0}{2G} \frac{3}{2} \frac{P_0}{\pi R_0^2 \gamma^2} \int_0^\gamma \sqrt{1 - \frac{\alpha^2}{\gamma^2}} [2(1 - \sigma)$$

$$- (1 - 2\sigma)^2 \alpha \ln \alpha] d\alpha = -\delta_0 + \frac{1 - 2\sigma}{1 + \sigma} \frac{3}{4} \frac{P_0}{\pi R_0} \frac{1}{4G}. \quad (3.10)$$

Since, by direct integration or by using the table of integrals (Gradshteyn and Ryzhik, 1964), it is known that

$$\int_0^\gamma \sqrt{1 - \frac{\alpha^2}{\gamma^2}} d\alpha = \frac{\pi}{4} \gamma,$$

$$\int_0^\gamma \alpha \sqrt{1 - \frac{\alpha^2}{\gamma^2}} \ln \alpha d\alpha = \gamma^2 \left(\frac{1}{3} \ln 2 - \frac{4}{9} + \frac{1}{3} \ln \gamma \right),$$

Downloaded 04 May 2010 to 171.66.16.33. Redistribution subject to ASME license or copyright; see http://www.asme.org/terms/Terms_Use.cfm

Eq. (3.10) becomes

$$\frac{3}{4}\frac{P_0}{G}\frac{1}{\pi R_0\gamma^2}\left[\frac{\pi}{2}\gamma(1-\sigma)-(1-2\sigma)^2\gamma^2 \times\left(\frac{1}{3}\ln 2-\frac{4}{9}+\frac{1}{3}\ln\gamma\right)\right]=\delta_0 - \frac{3}{4}\frac{P_0}{\pi G}\frac{1}{4R_0}\frac{1-2\sigma}{1+\sigma}. \quad (3.11)$$

In this equation γ may be written as a function of δ_0 by using the (approximate) relation

$$R_0\gamma^2=\delta_0. \quad (3.12)$$

It follows that, after a rearrangement of the terms, Eq. (3.11) may be written as

$$\frac{(1-\sigma)}{2G}\frac{3}{4}\frac{P_0}{R_0^{1/2}\delta_0^{1/2}}\left[1-2\frac{(1-2\sigma)}{(1-\sigma)}\frac{1}{\pi}\left(\frac{\delta_0}{R_0}\right)^{1/2} \times\left(\frac{1}{3}\ln 2-\frac{4}{9}+\frac{1}{3}\ln\left(\frac{\delta_0}{R_0}\right)^{1/2}\right) + \frac{(1-2\sigma)}{(1-\sigma^2)}\frac{1}{2\pi}\left(\frac{\delta_0}{R_0}\right)^{1/2}\right]=\delta_0. \quad (3.13)$$

Introducing the "reduced" Young's modulus $E^* = E/(1-\sigma^2) = 2G(1+\sigma)/(1-\sigma^2)$ (Johnson, 1985), Eq. (3.13) delivers the relationship between P_0 and δ_0.

$$P_0=\frac{4}{3}E^*\delta^{3/2}R_0^{1/2}\left[1-\frac{2}{3}\frac{(1-2\sigma)}{(1-\sigma)}\frac{1}{\pi}\left(\frac{\delta_0}{R_0}\right)^{1/2}\left(\ln 2-\frac{2}{3} + \ln\left(\frac{\delta_0}{R_0}\right)^{1/2}\right)+\frac{1}{2}\frac{(1-2\sigma)}{(1-\sigma^2)}\frac{1}{\pi}\left(\frac{\delta_0}{R_0}\right)^{1/2}\right]^{-1}. \quad (3.14)$$

Formula (3.14) gives the sought dependence $P_0 = P_0(\delta_0)$ and deserves some comments. For small values of the ratio $(\delta/R_0)^{1/2}$ the sum of the terms within the bracket does not differ appreciably from unity and therefore (3.14) may be replaced by Hertz's formula

$$P_0=\tfrac{4}{3}E^*\delta_0^{3/2}R_0^{1/2}. \quad (3.15)$$

If, conversely, $(\delta/R_0)^{1/2}$ is not negligible, as happens for $\gamma = (\delta/R_0)^{1/2} \geq \pi/6$, the second and third term within the bracket in (3.14) may produce a considerable deviation from Hertz's result. For instance, if $\gamma = \pi/6$ and $\sigma = 0$, relation (3.14) becomes

$$P_0=\tfrac{4}{3}E^*\delta^{3/2}R_0^{1/2}(0.8678\cdots). \quad (3.16)$$

A surprising property of (3.14) is that the corrective terms vanish for $\sigma = \frac{1}{2}$, that is when the material is incompressible.

4 The Equation of Motion

Formula (3.14) may be applied to the problem of the impact of a heavy sphere against a rigid wall. Let the sphere impinge normally on the wall with velocity v_1. After the first contact in correspondence of the lower pole, the distance of the centre of the sphere from the wall continues to decrease, but the motion is gradually arrested by the elastic reaction produced on the place of contact. At a certain instant the approach of the sphere to the wall reaches a maximum. Then the motion is reversed and the center of the sphere gradually departs from the wall until when it detaches from it rebounding with opposite velocity to that of arrival. The interval of time elapsed from the first contact and the complete detachment is called the "period of duration" of the impact. In order to apply formula (3.14) it is necessary that the duration of the impact should be much larger that the time required by the elastic waves, generated at the point of first impact, to propagate through the whole body. If this condition is satisfied, then the local compressive force P_0 may be regarded as a statical effect.

In this case the equation of motion during the time of contact assumes the form

$$M\ddot{\delta}_0(t)+P_0(t)=0 \quad t>0, \quad (4.1)$$

where $M = \rho_0(4/3)\pi R_0^3$ is the mass, $\delta_0(t)$ is the instantaneous distance of the center of the sphere from the wall, $P_0(t)$ is instantaneous elastic reaction. Under the assumption that the statical theory applies, the relationships between $P_0(t)$ and $\delta_0(t)$ is just like (3.14) the only difference being that both $P_0(t)$ and $\delta_0(t)$ depend on the time. Equation (4.1) is accompanied by the initial condition

$$\delta_0(0)=0, \quad \dot{\delta}_0(0)=v_1, \quad (4.2)$$

which states that at the initial instant the relative displacement of the center of the sphere from the wall is zero, and the velocity of approach of the sphere before the impact is v_1.

After substitution of (3.14) in (4.1) and introduction of the quantity $\kappa(\delta_0)$ such that

$$\kappa(\delta_0)=\frac{4}{3}E^*R_0^{1/2}\left[1-\frac{2}{3}\frac{(1-2\sigma)^2}{(1-\sigma)}\frac{1}{\pi}\left(\frac{\delta_0}{R_0}\right)^{1/2}\left(\ln 2-\frac{2}{3} + \ln\left(\frac{\delta_0}{R_0}\right)^{1/2}\right)+\frac{1}{2}\frac{(1-2\sigma)}{(1-\sigma)^2}\frac{1}{\pi}\left(\frac{\delta_0}{R_0}\right)^{1/2}\right]^{-1}, \quad (4.3)$$

Eq. (4.1) becomes

$$\ddot{\delta}_0=-\frac{\kappa(\delta_0)}{M}\delta_0^{3/2}. \quad (4.4)$$

The term $\kappa(\delta_0)$, sometimes called the "rigidity" of the elastic sphere, is a constant in Hertz's theory, but is instead a nonlinear function of the ratio δ_0/R_0 when Hertz's assumptions are partially removed.

The integration of (4.4) with the initial conditions (5.2) presents some difficulties because the right-hand side is not Lipschitz-continuous in δ_0/R_0 for any value of δ_0/R_0 and therefore it is not obvious if the initial value problem admits a solution. The difficulty is, however, overcome by reducing (4.4) to a first-order equation after multiplication of the equation by $\dot{\delta}_0$ and use of the identities

$$\dot{\delta}_0\ddot{\delta}_0=\frac{d}{dt}\left(\frac{\dot{\delta}_0^2}{2}\right), \quad \kappa(\delta_0)\delta_0^{3/2}\dot{\delta}_0=\frac{d}{dt}\int_0^{\delta_0}\kappa(\xi)\xi^{3/2}d\xi,$$

so that (4.4) may be written in the form

$$\frac{d}{dt}\left[\frac{\dot{\delta}_0^2}{2}+\frac{1}{M}\int_0^{\delta_0}\kappa(\xi)\xi^{3/2}d\xi\right]=0, \quad (4.5)$$

from which, by integrating with respect to the time, the equation

$$\frac{\dot{\delta}_0^2}{2}+\frac{1}{M}\int_0^{\delta_0}\kappa(\xi)\xi^{3/2}d\xi=\frac{v_1^2}{2} \quad (4.6)$$

is derived. Let T the duration of the impact. The solutions of interest are those for $0 \leq t \leq T/2$, in which $\dot{\delta}_0 \geq 0$, and such that δ_0 is sufficiently small, say $0 \leq \delta_0 \leq R_0$. In this region Eq. (4.6) may be put in the normal form

Downloaded 04 May 2010 to 171.66.16.33. Redistribution subject to ASME license or copyright; see http://www.asme.org/terms/Terms_Use.cfm

$$\dot{\delta}_0 = \sqrt{v_1^2 - \frac{2}{M}\int_0^{\delta_0} \kappa(\xi)\xi^{3/2} d\xi}\,. \tag{4.7}$$

Here the right-hand side is Lipschitz-continuous in the rectangle $0 \le t \le T/2$, $0 \le \delta_0 \le R_0$ and therefore the Cauchy's theorem applies. On the other hand, it is not possible to find an explicit solution to (4.7) because the integral under the square root cannot be evaluated by elementary means. But the solution may be bounded from above and from below by observing that, for $-1 < \sigma < \frac{1}{2}$, the ratios $(1-2\sigma)^2/(1-\sigma)$ and $(1-2\sigma)/(1-\sigma)^2$ are both positive. Therefore, for $\delta_0/R_0 \le 1$, $\kappa(\delta_0)$ satisfies the inequalities

$$\kappa_1 \ge \kappa(\delta_0) \ge \kappa_1 \left[1 + \frac{2}{3}\frac{(1-2\sigma)^2}{(1-\sigma)}\frac{1}{\pi}\left(\frac{2}{3} - \ln 2 + \frac{1}{e}\right) \times \frac{1}{2}\frac{(1-2\sigma)}{(1-\sigma)^2}\frac{1}{\pi}\right]^{-1} = \kappa_1(1+\beta(\sigma))^{-1}, \tag{4.8}$$

where $\kappa_1 = (4/3)E^* R_0^{1/2}$ = constant and $\beta(\sigma)$ is the non-negative factor

$$\beta(\sigma) = (0.07244\cdots)\frac{(1-2\sigma)^2}{(1-\sigma)} + (0.15915\cdots)\frac{(1-2\sigma)}{(1-\sigma)^2}\,.$$

Having obtained an upper and lower bound for $\kappa(\delta_0)$, it is possible to apply the comparison theorem for differential equations (Stampacchia et al., 1978), which states that $\delta_0(t)$ solution to (4.7) may be bounded from above and from below in the form

$$\delta_0^-(t) \le \delta_0(t) \le \delta_0^+(t), \tag{4.9}$$

where δ_0^- and δ_0^+ are solutions of the equations

$$\dot{\delta}_0^- = \sqrt{v_1^2 - \frac{4\kappa_1}{5M}(\delta_0^-)^{5/2}}\,, \quad \delta_0^-(0) = 0, \tag{4.10}$$

$$\dot{\delta}_0^+ = \sqrt{v_1^2 - \frac{4\kappa_1}{5(1+\beta)M}(\delta_0^+)^{5/2}}\,, \quad \delta_0^+(0) = 0. \tag{4.11}$$

Now Eqs. (4.10) and (4.11) are directly integrable by separation of variables, just as happens for Hertz's equation. In particular, Eq. (4.10) is exactly Hertz's differential equation, whereas Eq. (4.11) has the same form as Hertz's equation but with the difference that the constant κ_1 is replaced by $[\kappa_1/(1+\beta)]$ $(\beta \ge 0)$. Thus the solution of (4.10) and (4.11) are contained in all textbooks of three-dimensional elasticity (Love, 1927) and may be expressed as follows. The value of $\delta_0^-(t)$ at the instant of greatest compression is

$$(\delta_0^-)_{\max} = \left(\frac{5}{4}\frac{M}{\kappa_1}\right)^{2/5} v_1^{1/5}, \tag{4.12}$$

and the duration of the impact is

$$T^- = 2\int_0^{(\delta_0^-)_{\max}} \frac{d\delta_0^-}{\left[v_1^2 - \frac{4}{5}\frac{\kappa_1}{M}(\delta_0^-)^{5/2}\right]^{1/2}},$$

or, after calculation of the integral,

$$T^- = (2.9432\cdots)\frac{(\delta_0^-)_{\max}}{v_1}\,. \tag{4.13}$$

Considering instead Eq. (4.11), the greatest compression $(\delta_0^+)_{\max}$ is given by the formula

$$(\delta_0^+)_{\max} = \left(\frac{5}{4}\frac{(1+\beta(\sigma))M}{\kappa_1}\right)^{2/5} v_1^{1/5} \tag{4.14}$$

and the duration of the impact by

$$T^+ = (2.9432\cdots)\frac{(\delta_0^+)_{\max}}{v_1}\,. \tag{4.15}$$

As a consequence of the theorem of inclusion for the solution of the differential Eq. (4.7), the greatest compression $(\delta_0)_{\max}$ is bounded by

$$(\delta_0^-)_{\min} \le (\delta_0)_{\max} \le (\delta_0^+)_{\max}, \tag{4.16}$$

and also the time of duration of the impact obeys the inequality

$$T^- \le T \le T^+, \tag{4.17}$$

where the lower and upper bound in each of (4.16) and (4.17) are explicitly computable.

5 Two Numerical Examples

Let the impinging sphere have diameter $D = 2R_0 = 3$ cm, and initial velocity $v_1 = 1$ m/sec. The sphere is made of iron having density $\rho_0 = 8.00 \times 10^{-6}$ kp sec^2/cm^4, elastic modulus $G = 0.8 \times 10^6$ kp/cm^2 and Poisson's ratio $\sigma = \frac{1}{3}$ (Szabó, 1964). The mass M is equal to $(4/3)\pi R_0^3 \rho_0$, and the coefficient κ_1, expressed in terms of G, is equal to $(4/3)[2G/(1-\sigma)]$, so that T^- and T^+ can be written as

$$T^- = (2.9432\cdots)\left(\frac{25}{32}\pi^2\frac{\rho^2(1-\sigma)^2}{v_1 G^2}\right)^{1/5} R_0,$$

$$T^+ = (2.9432\cdots)\left(\frac{25}{32}\pi^2(1+\beta(\sigma))^2\frac{\rho^2(1-\sigma)^2}{v_1 G^2}\right)^{1/5} R_0,$$

and their numerical values are

$$T^- = (8.9513\cdots)10^{-5} \text{ sec}, \quad T^+ = (9.1751\cdots)10^{-5} \text{ sec}.$$

Considering instead the impact of a sphere having radius $R_0 = 6370$ km (the radius of the Earth) and velocity $v_1 = 1$ cm/sec against a rigid wall and assuming that material is again steel with the same density and moduli as before, the lower and upper time of duration have the values

$$T^- = 95485.8 \text{ sec} = 26.52 \text{ h}, \quad T^- = 97873.5 \text{ sec} = 27.18 \text{ h}.$$

Both the examples show that the correction of the duration of the impact due to the curvature of the striking sphere and to its overall deformability is not very important. This may be an explanation of the success of Hertz's formulae among engineers.

References

Bondareva, V. F., 1969, "The Effect of an Axisymmetric Normal Loading on an Elastic Sphere," *P.M.M.*, Vol. 33, pp. 1001–1005.

Bondareva, V. F., 1970, "Contact Problem for an Elastic Sphere," *P.M.M.*, Vol. 35, pp. 37–45.

Goodman, L. E., and Keer, L. M., 1965, "The Contact Stress Problem for an Elastic Sphere Indenting an Elastic Cavity," *Int. J. Solids Struct.*, Vol. 1, pp. 407–415.

Gradshteyn, I. S., and Ryzhik, I. M., 1965, *Tables of Integrals, Series, and Products*, Academic Press, New York.

Hertz, J., 1882, "Über die Berührung fester elastischer Körper," *J. reine und angew. Math.*, Vol. 92.

Johnson, K. L., 1985, *Contact Mechanics*, Cambridge University Press, Cambridge, U.K.

Love, A. H. E., 1927, *A Treatise on the Mathematical Theory of Elasticity*, Cambridge University Press, Cambridge, U.K.

Lur'e, A. I., 1955, *Three-dimensional Problems in Elasticity Theory*, Gostekhizdat, Moscow.

Szabó, I., 1964, *Höhere Technische Mechanik*, Springer, Berlin.

Stampacchia, G., Piccinini, L., Vidossich, G., 1978, *Equazioni Differenziali Ordinarie in R^n*, Liguori, Naples.

Downloaded 04 May 2010 to 171.66.16.33. Redistribution subject to ASME license or copyright; see http://www.asme.org/terms/Terms_Use.cfm

Singularities at the Tip of a Crack Terminating Normally at an Interface Between Two Orthotropic Media

J. C. Sung
Professor.

J. Y. Liou
Graduate Student.

Department of Civil Engineering,
National Cheng Kung University,
Tainan, Taiwan 70101, R.O.C.

The order of stress singularities at the tip of a crack terminating normally at an interface between two orthotropic media is analyzed. Characteristic equation in complex form for the power of singularity s, *where* $0 < Re\{s\} < 1$, *is first set up for two general anisotropic materials. Attention is then focused on the problem that is composed by two orthotropic media where one of them (say, material #2) the material principal axes are aligned while the other one (say, material #1) the principal axes can have an angle* γ *relative to the interface. For such a problem, a real form of the characteristic equation is obtained. The roots are functions of* γ *in general. Two real roots exist for most values of* γ; *however, there are possible ranges of* γ *that the complex roots will occur. The roots* s *are found to be independent of* γ *when material #1 has the property that* $\delta^{(1)} = 1$. *When* $\gamma = 0$, *two roots are always real. Furthermore, each of these two roots is associated with symmetric or antisymmetric mode and they become equal when* $\Delta = 1$. *Many other features of the effects of the material parameters on the behaviors of the roots* s *are further investigated in the present work, where the six generalized Dundurs' constants, expressed in terms of Krenk's parameters, play an important role in the analysis.*

1 Introduction

The order of stress singularities at the tip of a crack terminating normally at an interface between two isotropic materials was investigated very early by Zak and Williams (1963). Bogy (1971) extends that investigation by considering a crack terminating at the interface at an angle relative to the interface. Other related works include, for example, Cook and Erdogan (1972), Gupta (1973), Erdogan and Biricikoglu (1973), and Erdogan and Bakioglu (1976), etc. The corresponding problem for two aligned orthotropic materials has been studied by Delale and Erdogan (1979), and Gupta et al. (1992). Since only the deformation for the symmetric mode is considered, hence, only one real root is found for the power of singularities s for most of the material combinations in their investigations. Ting and Hoang (1984) have studied the problem of materials being generally anisotropic. They employ essentially the common approach that assumes the stress singularities to be of the form r^{-s}, where $0 < \mathrm{Re}\{s\} < 1$, to obtain the characteristic equation for the power of singularities s. The characteristic equation is set up in terms of a determinant of a matrix whose size is 18×18. No explicit expressions are given due to the complexity of that matrix. From numerical results, they demonstrated that three distinct real roots have, in general, existed. The materials employed in their analysis are orthotropic and the material axes are oriented in such a manner that the antiplane deformation is coupled with the in-plane deformation, which accounts for the existence of three distinct roots. In this paper we found through numerical examples that even for in-plane deformation only, there exist complex roots.

The problem that we will investigate is similar to that which has been treated by Ting and Hoang (1984). We first derive from a different way the characteristic equation for the power of singularities s for materials on both sides of the interface being general anisotropic. The obtained equation is expressed in terms of a determinant of a 3×3 matrix which is, in general, in complex form. This equation is then specialized to the problem that is composed by two orthotropic materials. One of the orthotropic materials the material principal axes are aligned, while the other material's axes can have an angle γ relative to the interface (Fig. 1). Two orthotropic materials are connected in a manner that the antiplane deformation is decoupled from the inplane deformation. For such a problem, the characteristic equation can be expressed in real form where the dependence of the roots s on the material parameters is shown explicitly, and some features of the roots can be investigated analytically. The roots are in general functions of γ. Two real roots $s_{1,2}$ exist for most values of γ. However, for some ranges of γ complex roots may occur. These two roots are invariant under the rotation of both material principal axes by 90 deg. The roots s are found to be independent of γ when material #1 has the property that $\delta^{(1)} = 1$, a peculiar behavior that has also been observed in the analysis of similar problem but for a subinterface crack (Sung and Liou, 1994b). When $\gamma = 0$, two roots are always real, each one is associated with the symmetric (denoted as s_s) or antisymmetric (denoted as s_a) mode and the root for the symmetric mode (s_s) is switched to that for the antisymmetric mode (s_a) when Δ is replaced by Δ^{-1}. Furthermore, they become equal when $\Delta = 1$. For degenerate materials, e.g., for isotropic materials on both sides of the interface, the present characteristic equation is reduced to that developed by Erdogan and Biricikoglu (1973). Many other features are further discussed in the present work, where the defined generalized Dundurs' constants, expressed in terms of Krenk's parameters, are found to play an important role in the analysis.

2 Stroh Formalism

The general expressions for the displacement $\mathbf{u}$ and stress function $\boldsymbol{\phi}$ for a two-dimensional deformation of a linear elastic

Contributed by the Applied Mechanics Division of THE AMERICAN SOCIETY OF MECHANICAL ENGINEERS for publication in the ASME JOURNAL OF APPLIED MECHANICS.

Discussion on this paper should be addressed to the Technical Editor, Professor Lewis T. Wheeler, Department of Mechanical Engineering, University of Houston, Houston, TX 77204-4792, and will be accepted until four months after final publication of the paper itself in the ASME JOURNAL OF APPLIED MECHANICS.

Manuscript received by the ASME Applied Mechanics Division, May 26, 1994; final revision, Mar. 15, 1995. Associate Technical Editor: C. F. Shih.

Copyright © 1996 by ASME

Downloaded 04 May 2010 to 171.66.16.33. Redistribution subject to ASME license or copyright; see http://www.asme.org/terms/Terms_Use.cfm

solid whose field quantities are functions of x_1 and x_2 are (Eshelby et al., 1953; Stroh, 1958)

$$\mathbf{u} = 2\,\mathrm{Re}\{\mathbf{A}\,\mathbf{f}(\mathbf{z})\}, \quad \boldsymbol{\phi} = 2\,\mathrm{Re}\{\mathbf{B}\,\mathbf{f}(\mathbf{z})\} \tag{1}$$

where Re{ } denotes the real part, $\mathbf{f}(\mathbf{z}) = (f_1(z_1), f_2(z_2), f_3(z_3))^T$ with $z_k = x_1 + p_k x_2$, $(k = 1, 2, 3)$. Superscript T represents the transpose. Matrix $\mathbf{A}$, with components denoted by a_{kj} and constants p_k, are determined from the following eigenvalue problem:

$$\{c_{i1k1} + p_j(c_{i1k2} + c_{i2k1}) + p_j^2 c_{i2k2}\}a_{kj} = 0 \quad \text{(no sum on } j\text{)} \tag{2}$$

where c_{ijkl} are the elastic constants. Without loss of generality, one may take the imaginary part of p_k to be positive. Matrix $\mathbf{B}$ in Eq. (1) is defined by $\mathbf{B} = \mathbf{R}^T\mathbf{A} + \mathbf{TAP}$ where $R_{ik} = c_{i1k2}$, $T_{ik} = c_{i2k2}$ and $\mathbf{P} = \mathrm{diag}\,\langle p_1, p_2, p_3\rangle$. Stress function $\boldsymbol{\phi}$ are related to the stress components by

$$(\sigma_{11}, \sigma_{12}, \sigma_{13})^T = -\boldsymbol{\phi}_{,2} = -2\,\mathrm{Re}\{\mathbf{BP}\,\mathbf{f}'(\mathbf{z})\} \tag{3}$$

$$(\sigma_{21}, \sigma_{22}, \sigma_{23})^T = \boldsymbol{\phi}_{,1} = 2\,\mathrm{Re}\{\mathbf{B}\,\mathbf{f}'(\mathbf{z})\} \tag{4}$$

where

$$\mathbf{f}'(\mathbf{z}) = \frac{d\mathbf{f}(\mathbf{z})}{d\mathbf{z}} = \left(\frac{df_1(z_1)}{dz_1}, \frac{df_2(z_2)}{dz_2}, \frac{df_3(z_3)}{dz_3}\right)^T. \tag{5}$$

The matrices $\mathbf{A}$ and $\mathbf{B}$ satisfy the following orthogonality relations (Stroh, 1958; Chadwick and Smith, 1977):

$$\begin{bmatrix}\mathbf{A} & \bar{\mathbf{A}}\\ \mathbf{B} & \bar{\mathbf{B}}\end{bmatrix}\begin{bmatrix}\mathbf{B} & \bar{\mathbf{B}}\\ \mathbf{A} & \bar{\mathbf{A}}\end{bmatrix}^T = \begin{bmatrix}\mathbf{I} & \mathbf{0}\\ \mathbf{0} & \mathbf{I}\end{bmatrix} \tag{6}$$

where $\mathbf{I}$ is a 3×3 unit matrix and a bar over a quantity represents the conjugate of that quantity.

3 Characteristic Equation

The order of singularities of a crack that is normal to and ends at an interface between two anisotropic materials has been studied by Ting and Hoang (1984) (Fig. 1). A characteristic equation written in terms of a determinant of an 18×18 square matrix is developed basically by the common approach of eigenfunction expansion technique. Due to complexity, no explicit form of the 18×18 matrix is given. In the following, we will develop the explicit characteristic equation from a different approach. Employing the basic solution due to a point dislocation acting in a solid that is composed by two half-plane anisotropic media joined perfectly along the interface, the problem of a crack embedded in one of the materials, say material #2, and oriented normally relative to the interface as sketched in Fig. 1, can be formulated in terms of the following singular integral equations (Sung and Liou, 1994b):

$$\frac{-1}{2\pi}\left\{\int_h^l \frac{\mathbf{b}(t)}{t-\xi}\,dt + \int_h^l \mathbf{K}(\xi, t)\mathbf{b}(t)dt\right\} = \mathbf{t}_\eta(\xi), \quad h < \xi < l \tag{7}$$

where $\mathbf{b}(t)$ is related to the physical dislocation densities $\mathbf{b}^*(t)$ by

$$\mathbf{b}(t) = 2i\mathbf{B}^{(2)}\mathbf{B}^{(2)^T}\mathbf{b}^*(t), \quad h < t < l \tag{8}$$

and $\mathbf{t}_\eta$ is the traction applied on the crack faces. The kernel function $\mathbf{K}(\xi, t)$ is expressed as

$$\mathbf{K}(\xi, t) = -\sum_{k=1}^{3}\sum_{j=1}^{3}\mathrm{Re}\{Z_{kj}(\xi, t)\mathbf{E}_k^{(2)}\mathbf{M}\overline{\mathbf{E}_j^{(2)}}\} \tag{9}$$

where

$$Z_{kj}(\xi, t) = \frac{p_k^{(2)}}{\xi p_k^{(2)} - t\bar{p}_j^{(2)}} = \frac{-p_k^{(2)}}{\bar{p}_j^{(2)}}\left[t + \left(\frac{-p_k^{(2)}}{\bar{p}_j^{(2)}}\right)\xi\right]^{-1}, \quad h < \xi < l,\ h < t < l \tag{10}$$

$$\mathbf{E}_k^{(2)} = \mathbf{B}^{(2)}\mathbf{I}_k\mathbf{B}^{(2)^{-1}}, \quad \mathbf{M} = -\overline{\mathbf{F}^{-1}\mathbf{G}} \tag{11}$$

where matrices $\mathbf{F}$ and $\mathbf{G}$ are defined by

$$\mathbf{F} = (i\mathbf{A}^{(1)}\mathbf{B}^{(1)^{-1}}) + \overline{(i\mathbf{A}^{(2)}\mathbf{B}^{(2)^{-1}})},$$
$$\mathbf{G} = (i\mathbf{A}^{(1)}\mathbf{B}^{(1)^{-1}}) - (i\mathbf{A}^{(2)}\mathbf{B}^{(2)^{-1}}). \tag{12}$$

Matrices $\mathbf{I}_k$ $(k = 1, 2, 3)$ appearing in Eq. (11) are defined as

$$\mathbf{I}_1 = \mathrm{diag}\,\langle 1, 0, 0\rangle, \quad \mathbf{I}_2 = \mathrm{diag}\,\langle 0, 1, 0\rangle,$$
$$\mathbf{I}_3 = \mathrm{diag}\,\langle 0, 0, 1\rangle. \tag{13}$$

Note that the upper indices 1 or 2 with parenthesis appearing in all quantities represent the quantities that are associated with upper (#1) or lower (#2) materials. The singular behaviors of stresses at points h and l are well-known square root singularities when h and l are both not zero. To investigate the order of the singularities for stresses when point h terminates at the interface, we follow the method developed by Muskhelishvili (1945) by assuming that the unknown function $\mathbf{b}(t)$ may be expressed as

$$\mathbf{b}(t) = \mathrm{Re}\left\{\frac{\hat{\mathbf{b}}(t)}{t^s(l-t)^{1/2}}\right\}, \quad 0 < \mathrm{Re}\{s\} < 1 \tag{14}$$

where the square root singularity at point l is assumed while s represents the power of singularity at the point $h = 0$ that is to be determined, $\hat{\mathbf{b}}(t)$ is a regular function defined on the interval $0 \le t \le l$. Note first that the term associated with Cauchy singularity has the property that (Muskhelishvili, 1945)

$$\frac{1}{\pi}\int_0^l \frac{\hat{\mathbf{b}}(t)}{t^s(l-t)^{1/2}}\frac{dt}{t-\xi} \approx \frac{\hat{\mathbf{b}}(0)}{\sqrt{l}}\cot(\pi s)\xi^{-s}, \quad \xi \to 0, \tag{15}$$

and note also that the term related to the kernel function behaves as

$$\frac{1}{\pi}\int_0^l \frac{\hat{\mathbf{b}}(t)}{t^s(l-t)^{1/2}}\left(\frac{-p_k^{(2)}}{\bar{p}_j^{(2)}}\right)\left[t + \left(\frac{-p_k^{(2)}}{\bar{p}_j^{(2)}}\right)\xi\right]^{-1}dt \approx \frac{\hat{\mathbf{b}}(0)}{\sqrt{l}}\left(\frac{-p_k^{(2)}}{\bar{p}_j^{(2)}}\right)^{1-s}\frac{\xi^{-s}}{\sin(\pi s)}, \quad \xi \to 0. \tag{16}$$

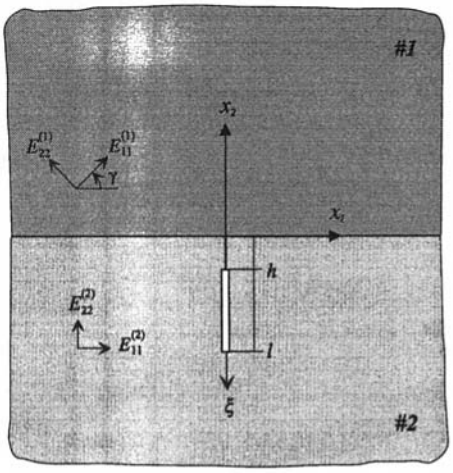


Fig. 1 A crack impinges normally on an interface

Downloaded 04 May 2010 to 171.66.16.33. Redistribution subject to ASME license or copyright; see http://www.asme.org/terms/Terms_Use.cfm

By substituting (14) into Eq. (7), using the results of Eqs. (15) and (16), and then collecting all the singular terms that are related to the power s one can obtain

$$[\cos(\pi s)\mathbf{I} + \mathbf{Q}(s)]\hat{\mathbf{b}}(0)\frac{\xi^{-s}}{\sin(\pi s)} + [\cos(\pi\bar{s})\mathbf{I} + \mathbf{Q}(\bar{s})]\overline{\hat{\mathbf{b}}(0)}\frac{\xi^{-\bar{s}}}{\sin(\pi\bar{s})} = \mathbf{0}, \quad \xi \to 0 \quad (17)$$

where

$$\mathbf{Q}(s) = -\frac{1}{2}\sum_{k=1}^{3}\sum_{j=1}^{3}\left\{\left(\frac{-p_k^{(2)}}{\bar{p}_j^{(2)}}\right)^{1-s}\mathbf{E}_k^{(2)}\mathbf{M}\overline{\mathbf{E}_j^{(2)}} + \left(\frac{-\bar{p}_k^{(2)}}{p_j^{(2)}}\right)^{1-s}\overline{\mathbf{E}_k^{(2)}\mathbf{M}}\mathbf{E}_j^{(2)}\right\}. \quad (18)$$

Equation (17) implies that

$$[\cos(\pi s)\mathbf{I} + \mathbf{Q}(s)]\hat{\mathbf{b}}(0) = \mathbf{0}, \quad 0 < \mathrm{Re}\{s\} < 1. \quad (19)$$

For nontrivial solutions of $\hat{\mathbf{b}}(0)$, we obtain

$$\det[\cos(\pi s)\mathbf{I} + \mathbf{Q}(s)] = 0, \quad 0 < \mathrm{Re}\{s\} < 1, \quad (20)$$

which is the characteristic equation for the power of singularity s. It is apparent that when s is the root of above equation, then $\bar{s}$ is also a root of that equation since $\overline{\mathbf{Q}(s)} = \mathbf{Q}(\bar{s})$. Elements of matrix $\mathbf{Q}(s)$ defined in (18) are generally complex-valued if both materials considered are general anisotropic. Hence, the characteristic Eq. (20) is usually complicated and difficult to investigate. Instead of discussing the general behaviors of the roots of Eq. (20) for general anisotropic materials, we will in the following investigate the special problem that is composed by two orthotropic materials. For such a problem, the characteristic equation can be expressed explicitly in real form from which some features of the roots s can be studied.

The problem considered is sketched in Fig. 1 where the principal axes of material #2 are aligned along the coordinate axes while those of material #1 can have an arbitrary angle γ relative to the interface boundary. Since both materials' principal axes in the out-of-plane direction are assumed to be parallel with the x_3-axis, the antiplane deformation will be decoupled from the in-plane deformation. Hence, we will ignore the antiplane deformation in the following. Due to this fact, the size of all matrices and vectors previously defined and appearing in what follows will be 2×2 and 2×1, respectively. As has been discussed in previous papers (Sung and Liou, 1994a, b), the matrix $\mathbf{E}_k^{(2)}$ and quantity $p_k^{(2)}$ appearing in (18) can be expressed in terms of two Krenk's parameters, $\delta^{(2)}$ and $\kappa^{(2)}$ (Krenk, 1979; Sung and Liou, 1995) as follows:

$$\mathbf{E}_{1,2}^{(2)} = \begin{cases} \dfrac{1}{2\omega_-^{(2)}}\begin{bmatrix} \omega_-^{(2)} \pm \omega_+^{(2)} & \pm i\delta^{(2)} \\ \pm i\delta^{(2)^{-1}} & \omega_-^{(2)} \mp \omega_+^{(2)} \end{bmatrix}, & \kappa^{(2)} > 1 \\ \dfrac{1}{2\omega_-^{(2)}}\begin{bmatrix} \omega_-^{(2)} \mp i\omega_+^{(2)} & \pm\delta^{(2)} \\ \pm\delta^{(2)^{-1}} & \omega_-^{(2)} \pm i\omega_+^{(2)} \end{bmatrix}, & |\kappa^{(2)}| < 1 \end{cases} \quad (21)$$

$$p_{1,2}^{(2)} = \begin{cases} i\delta^{(2)}(\omega_+^{(2)} \pm \omega_-^{(2)}), & \kappa^{(2)} > 1 \\ \delta^{(2)}(i\omega_+^{(2)} \mp \omega_-^{(2)}), & |\kappa^{(2)}| < 1, \end{cases} \quad (22)$$

where

$$\omega_+^{(\alpha)} = \sqrt{(1 + \kappa^{(\alpha)})/2}, \quad \omega_-^{(\alpha)} = \sqrt{|1 - \kappa^{(\alpha)}|/2}, \quad \alpha = 1, 2. \quad (23)$$

Matrix $\mathbf{M}$ in (18) can also be expressed in terms of six generalized Dundurs' constants as (Sung and Liou, 1994b, c)

$$\mathbf{M} = \begin{bmatrix} \alpha_1 + \beta_1\beta_2 + \lambda_1\lambda_2 & (\lambda_1 - i\beta_1)(1 + \alpha_2) \\ (\lambda_2 + i\beta_2)(1 + \alpha_1) & \alpha_2 + \beta_1\beta_2 + \lambda_1\lambda_2 \end{bmatrix} \Big/ (1 - \beta_1\beta_2 - \lambda_1\lambda_2) \quad (24)$$

where the six generalized Dundurs' constants are defined as

$$\begin{pmatrix} \alpha_1 \\ \beta_1 \\ \lambda_1 \end{pmatrix} = \begin{pmatrix} (1 + \alpha_o) - d\Delta^{-1} \\ \delta^{(2)}2\beta_o \\ \delta^{(2)}d^{**} \end{pmatrix} / ((1 + \alpha_o) + d\Delta^{-1}),$$

$$\begin{pmatrix} \alpha_2 \\ \beta_2 \\ \lambda_2 \end{pmatrix} = \begin{pmatrix} (1 + \alpha_o) - d^*\Delta \\ \delta^{(2)^{-1}}2\beta_o \\ \delta^{(2)^{-1}}d^{**} \end{pmatrix} / ((1 + \alpha_o) + d^*\Delta) \quad (25)$$

where

$$\alpha_o = \left(\frac{\omega_+^{(2)}}{E^{(2)}} - \frac{\omega_+^{(1)}}{E^{(1)}}\right) \Big/ \left(\frac{\omega_+^{(2)}}{E^{(2)}} + \frac{\omega_+^{(1)}}{E^{(1)}}\right),$$

$$\beta_o = \left(\frac{1 - \nu^{(2)}}{E^{(2)}} - \frac{1 - \nu^{(1)}}{E^{(1)}}\right) \Big/ \left(2\left(\frac{\omega_+^{(2)}}{E^{(2)}} + \frac{\omega_+^{(1)}}{E^{(1)}}\right)\right) \quad (26a)$$

and

$$d = (1 - \alpha_o)\Delta^{-1}(1 + \sin^2(\gamma)(\delta^{(1)^2} - 1)),$$
$$d^* = (1 - \alpha_o)\Delta(1 + \sin^2(\gamma)(\delta^{(1)^{-2}} - 1)),$$
$$d^{**} = (1 - \alpha_o)\sin(\gamma)\cos(\gamma)(\delta^{(1)} - \delta^{(1)^{-1}}),$$
$$\Delta = \delta^{(1)}/\delta^{(2)}. \quad (26b)$$

Material parameters $E^{(\alpha)}$ and $\nu^{(\alpha)}$ appearing above are the other two Krenk's parameters. These four Krenk's parameters $E^{(\alpha)}$, $\nu^{(\alpha)}$, $\delta^{(\alpha)}$, and $\kappa^{(\alpha)}$ are related to engineering elastic constants. For details please refer to the paper by Krenk (1979). It is noted that when isotropic materials are considered, two of the Krenk's parameters i.e., $\kappa^{(\alpha)}$ and $\delta^{(\alpha)}$, will both take values of unity while the other two become (for plane strain case) $E^{(\alpha)} = E_i^{(\alpha)}/(1 - \nu_i^{(\alpha)^2})$ and $\nu^{(\alpha)} = \nu_i^{(\alpha)}/(1 - \nu_i^{(\alpha)})$, respectively, where $E_i^{(\alpha)}$ is the Young's modulus and $\nu_i^{(\alpha)}$ is the Poisson ratio for isotropic material (subscript i is not a free index here). As to the generalized Dundurs' constants, they become $\alpha_1 = \alpha_2 = \alpha_o$, $\beta_1 = \beta_2 = \beta_o$ and $\lambda_1 = \lambda_2 = 0$, where α_o and β_o are reduced, respectively, to the Dundurs' constants α and β (1968). Substituting results of (21), (22), and (24) into (18), one finds that the characteristic Eq. (20) for the present two orthotropic materials becomes

$$D(\alpha_o, \beta_o, \gamma, \delta^{(1)}, \delta^{(2)}, \kappa^{(2)}; s) = \cos^2(\pi s) + [Q_{11}(s) + Q_{22}(s)]\cos(\pi s) + [Q_{11}(s)Q_{22}(s) - Q_{12}(s)Q_{21}(s)] = 0 \quad (27)$$

where

$$\begin{pmatrix} Q_{11}(s) \\ Q_{22}(s) \end{pmatrix} = 2(2\omega_-^{(2)})^{-2}\Big\{[(N_{11} + N_{22}) \times (1 - \cos(2(s - 1)\varphi)) + (N_{12} - N_{21})\omega_-^{(2)} \times \sin(2(s - 1)\varphi)) + (N_{12} + N_{21})\omega_+^{(2)} \times (\cos(2(s - 1)\varphi) - 1)]\begin{pmatrix} 1 \\ 1 \end{pmatrix} - 2\omega_-^{(2)^2}\begin{pmatrix} N_{11} \\ N_{22} \end{pmatrix}\Big\}$$

Downloaded 04 May 2010 to 171.66.16.33. Redistribution subject to ASME license or copyright; see http://www.asme.org/terms/Terms_Use.cfm

$$\begin{pmatrix} Q_{12}(s) \\ Q_{21}(s) \end{pmatrix} = 2(2\omega_-^{(2)})^{-2}\Big\{[(1-2\omega_-^{(2)^2})\cos(2(s-1)\varphi)-1] \times \begin{pmatrix} \delta^{(2)}\hat{N}_{12} \\ \delta^{(2)^{-1}}\hat{N}_{21} \end{pmatrix} + 2\omega_+^{(2)}\omega_-^{(2)}\sin(2(s-1)\varphi) \times \begin{pmatrix} \delta^{(2)}\hat{N}_{12} \\ -\delta^{(2)^{-1}}\hat{N}_{21} \end{pmatrix} + [1-\cos(2(s-1)\varphi)] \times \begin{pmatrix} \delta^{(2)}\hat{N}_{21} \\ \delta^{(2)^{-1}}\hat{N}_{12} \end{pmatrix}\Big\} \quad (28)$$

when $|\kappa^{(2)}| < 1$ and

$$\begin{pmatrix} Q_{11}(s) \\ Q_{22}(s) \end{pmatrix} = (2\omega_-^{(2)})^{-2}\Big\{[(N_{11}+N_{22})(q_+^{(2)^{2s-2}} + q_-^{(2)^{2s-2}}) - N_{12}(q_+^{(2)^{2s-3}} + q_-^{(2)^{2s-3}}) - N_{21}(q_+^{(2)^{2s-1}} + q_-^{(2)^{2s-1}}) + (N_{12}+N_{21})(q_+^{(2)} + q_-^{(2)})]\begin{pmatrix} 1 \\ 1 \end{pmatrix} - (q_+^{(2)^2} + q_-^{(2)^2})]\begin{pmatrix} N_{11} \\ N_{22} \end{pmatrix} - 2\begin{pmatrix} N_{22} \\ N_{11} \end{pmatrix}\Big\}$$

$$\begin{pmatrix} Q_{12}(s) \\ Q_{21}(s) \end{pmatrix} = (2\omega_-^{(2)})^{-2}\Big\{[q_+^{(2)^{2s-2}} + q_-^{(2)^{2s-2}} - 2]\begin{pmatrix} \delta^{(2)}\hat{N}_{21} \\ \delta^{(2)^{-1}}\hat{N}_{12} \end{pmatrix} - [q_+^{(2)^{2s-4}} + q_-^{(2)^{2s-4}} - 2]\begin{pmatrix} \hat{N}_{12} \\ 0 \end{pmatrix} - [q_+^{(2)^{2s}} + q_-^{(2)^{2s}} - 2]\begin{pmatrix} \hat{N}_{12} \\ 0 \end{pmatrix}\Big\} \quad (29)$$

when $\kappa^{(2)} > 1$. The quantities $\hat{N}_{12}$, $\hat{N}_{21}$, $N_{\alpha\beta}$ ($\alpha, \beta = 1, 2$) appearing in Eqs. (28) and (29) are

$$\begin{pmatrix} N_{11} \\ N_{22} \end{pmatrix} = \begin{pmatrix} \alpha_1 + r \\ \alpha_2 + r \end{pmatrix} \Big/ (1-r)$$

$$\begin{pmatrix} N_{12} \\ N_{21} \end{pmatrix} = \begin{pmatrix} (1+\alpha_2)\beta_1\delta^{(2)^{-1}} \\ (1+\alpha_1)\beta_2\delta^{(2)} \end{pmatrix} \Big/ (1-r)$$

$$\begin{pmatrix} \hat{N}_{12} \\ \hat{N}_{21} \end{pmatrix} = \begin{pmatrix} (1+\alpha_2)\lambda_1\delta^{(2)^{-1}} \\ (1+\alpha_1)\lambda_2\delta^{(2)} \end{pmatrix} \Big/ (1-r)$$

$$r = \beta_1\beta_2 + \alpha_1\alpha_2 \quad (30)$$

which are all functions of γ since the generalized Dundurs' constants defined in (25) are in general functions of γ. The parameters φ and $q_+^{(2)}$, $q_-^{(2)}$ are defined as $\varphi = \tan^{-1}(\omega_-^{(2)}/\omega_+^{(2)})$, $q_+^{(2)} = \omega_+^{(2)} + \omega_-^{(2)}$, $q_-^{(2)} = \omega_+^{(2)} - \omega_-^{(2)}$. Since the six generalized Dundurs' constants are completely determined by α_o, β_o, γ, $\delta^{(1)}$ and $\delta^{(2)}$ as shown in (25), hence, it is not difficult to see that the quantities $Q_{\alpha\beta}(s)$ defined in (28) or (29) will depend explicitly on the following parameters: $Q_{\alpha\beta} = Q_{\alpha\beta}(s, \alpha_o, \beta_o, \gamma, \delta^{(1)}, \delta^{(2)}, \kappa^{(2)})$. Therefore, the roots s determined by the characteristic Eq. (27) will also depend on these parameters, i.e., $D = D(\alpha_o, \beta_o, \gamma, \delta^{(1)}, \delta^{(2)}, \kappa^{(2)}; s) = 0$. Since the explicit dependence of the roots on the parameters is completely known, it is then not difficult to investigate the effects of these parameters on the behaviors of the roots. In the following, some features of the roots are first observed and then numerical results are presented in the next section.

(A) $\boldsymbol{\delta^{(1)} \to \delta^{(1)^{-1}}, \delta^{(2)} \to \delta^{(2)^{-1}}}$. Suppose that $\delta^{(1)}$ and $\delta^{(2)}$ are replaced by $\delta^{(1)^{-1}}$ and $\delta^{(2)^{-1}}$, respectively. Replacing these two parameters in this way is equivalent to rotating 90 deg of both materials' principal axes. Observing that under such replacements the generalized Dundurs' constants will be changed according to $\alpha_1(\boldsymbol{\delta}) = \alpha_2(\boldsymbol{\delta}^*)$, $\alpha_2(\boldsymbol{\delta}) = \alpha_1(\boldsymbol{\delta}^*)$, $\beta_1(\boldsymbol{\delta}) = \beta_2(\boldsymbol{\delta}^*)$, $\beta_2(\boldsymbol{\delta}) = \beta_1(\boldsymbol{\delta}^*)$, $\lambda_1(\boldsymbol{\delta}) = -\lambda_2(\boldsymbol{\delta}^*)$, and $\lambda_2(\boldsymbol{\delta}) = -\lambda_1(\boldsymbol{\delta}^*)$, where $\boldsymbol{\delta} = (\delta^{(1)}, \delta^{(2)})$, $\boldsymbol{\delta}^* = (\delta^{(1)^{-1}}, \delta^{(2)^{-1}})$, hence, it is not difficult to verify that $Q_{11}(s, \boldsymbol{\delta}) = Q_{22}(s, \boldsymbol{\delta}^*)$, $Q_{22}(s, \boldsymbol{\delta}) = Q_{11}(s, \boldsymbol{\delta}^*)$ and $Q_{12}(s, \boldsymbol{\delta})Q_{21}(s, \boldsymbol{\delta}) = Q_{12}(s, \boldsymbol{\delta}^*)Q_{21}(s, \boldsymbol{\delta}^*)$. Therefore, one can confirm that the expression for D will have the following property:

$$D(\alpha_o, \beta_o, \gamma, \delta^{(1)}, \delta^{(2)}, \kappa^{(2)}; s) = D(\alpha_o, \beta_o, \gamma, \delta^{(1)^{-1}}, \delta^{(2)^{-1}}, \kappa^{(2)}; s) \quad (31)$$

which implies that the roots will remain the same when $\delta^{(1)}$ and $\delta^{(2)}$ are replaced by $\delta^{(1)^{-1}}$ and $\delta^{(2)^{-1}}$, respectively. This is an invariant property of the roots s.

(B) $\boldsymbol{\gamma = 0}$. The dependence of D on the parameters can be simplified when $\gamma = 0$. The result is $D = D(\alpha_o, \beta_o, \Delta, \kappa^{(2)}; s)$ where the dependence of D on the parameters $\delta^{(1)}$ and $\delta^{(2)}$ is now only through their ratio, i.e., $\Delta = \delta^{(1)}/\delta^{(2)}$. This is simply because the six generalized Dundurs' constants will take the following values when $\gamma = 0$:

$$\begin{pmatrix} \alpha_1 \\ \beta_1 \end{pmatrix} = \begin{pmatrix} (1+\alpha_o) - (1-\alpha_o)\Delta^{-1} \\ \delta^{(2)}2\beta_o \end{pmatrix} \Big/ ((1+\alpha_o) + (1-\alpha_o)\Delta^{-1})$$

$$\begin{pmatrix} \alpha_2 \\ \beta_2 \end{pmatrix} = \begin{pmatrix} (1+\alpha_o) - (1-\alpha_o)\Delta \\ \delta^{(2)^{-1}}2\beta_o \end{pmatrix} \Big/ ((1+\alpha_o) + (1-\alpha_o)\Delta) \quad \lambda_1 = \lambda_2 = 0. \quad (32)$$

Hence, from (30), quantities $\hat{N}_{12}$ and $\hat{N}_{21}$ will both vanish and $N_{\alpha\beta}$ are found to depend on the parameters $\delta^{(1)}$ and $\delta^{(2)}$ through their ratio, i.e., $\Delta = \delta^{(1)}/\delta^{(2)}$. Besides the property just discussed above, the characteristic equation has further properties when $\gamma = 0$. It is easy to see that $Q_{12}(s) = Q_{21}(s) = 0$ when $\gamma = 0$. Therefore, characteristic Eq. (27) becomes

$$D(\alpha_o, \beta_o, \Delta, \kappa^{(2)}; s) = [\cos(\pi s) + Q_{11}(s)][\cos(\pi s) + Q_{22}(s)] = 0 \quad (33)$$

which implies that the two modes (symmetric and antisymmetric) can be investigated separately. The first bracket gives rise to the root for symmetric mode (denoted by s_s) while the second produces the root for antisymmetric mode (denoted by s_a). These two roots are usually distinct and are real. However, only one real root will exist when $\Delta = 1$, since $Q_{11}(s) = Q_{22}(s)$ when the value of parameter Δ is equal to one. The symmetric and antisymmetric roots obtained from Eq. (33) are related to each other if one replaces Δ by Δ^{-1}. The relation can be set up by noting that when Δ is replaced by Δ^{-1} the four generalized Dundurs' constants will be transformed according to $\alpha_1(\Delta) = \alpha_2(\Delta^{-1})$, $\alpha_2(\Delta) = \alpha_1(\Delta^{-1})$, $\delta^{(2)^{-1}}\beta_1(\Delta) = \delta^{(2)}\beta_2(\Delta^{-1})$ and $\delta^{(2)}\beta_2(\Delta) = \delta^{(2)^{-1}}\beta_1(\Delta^{-1})$. Therefore, $Q_{11}(s, \Delta) = Q_{22}(s, \Delta^{-1})$ and the root for symmetric mode s_s is found to be related to that for antisymmetric mode s_a as

$$s_s(\alpha_o, \beta_o, \Delta, \kappa^{(2)}) = s_a(\alpha_o, \beta_o, \Delta^{-1}, \kappa^{(2)}) \quad (34)$$

or replacing Δ by Δ^{-1}, one has

$$s_a(\alpha_o, \beta_o, \Delta, \kappa^{(2)}) = s_s(\alpha_o, \beta_o, \Delta^{-1}, \kappa^{(2)}) \quad (35)$$

Downloaded 04 May 2010 to 171.66.16.33. Redistribution subject to ASME license or copyright; see http://www.asme.org/terms/Terms_Use.cfm

which reflects that the root for symmetric mode (antisymmetric mode) is switched to that for antisymmetric mode (symmetric mode) when Δ is replaced by Δ^{-1}. Note that the replacement of Δ by Δ^{-1} is equivalent to rotating both materials' principal axes by 90 deg. Although the characteristic equation for two aligned orthotropic materials ($\gamma = 0$) has been studied by Delale and Erdogan (1979) and Gupta et al. (1992), their results are restricted to symmetric mode and the behaviors of the roots on the material parameters are not further pursued.

(C) $\delta^{(1)} = 1$. When material #1 has the special property that $\delta^{(1)} = 1$, the roots are found to be independent of γ. This is because λ_1 and λ_2 will both vanish and α_1, α_2, β_1 and β_2 are all independent of angle γ when $\delta^{(1)} = 1$. Hence, the quantities $Q_{\alpha\beta}$ will be independent of γ too. The explicit dependence of $Q_{\alpha\beta}$ on the parameters is now $Q_{\alpha\beta} = Q_{\alpha\beta}(s, \alpha_o, \beta_o, \delta^{(2)}, \kappa^{(2)})$, which implies that the roots s found in Eq. (27) will be functions of α_o, β_o, $\delta^{(2)}$ and $\kappa^{(2)}$ only and independent of γ.

(D) Degenerate Materials. Let's consider the case of material #2 being degenerate, i.e., $\kappa^{(2)} = 1$ ($\omega_-^{(2)} = 0$). For such case, the quantities $Q_{\alpha\beta}$ will take the following form:

$$\begin{pmatrix} Q_{11}(s) \\ Q_{22}(s) \end{pmatrix} = s(s-2)\begin{pmatrix} N_{11} \\ N_{22} \end{pmatrix} + (1-s)^2\begin{pmatrix} N_{22} \\ N_{11} \end{pmatrix} + [N_{12}(s-2)(1-s) + N_{21}s(1-s)]\begin{pmatrix} 1 \\ 1 \end{pmatrix}$$

$$\begin{pmatrix} Q_{12}(s) \\ Q_{21}(s) \end{pmatrix} = (1-s)^2\begin{pmatrix} \delta^{(2)}\hat{N}_{21} \\ \delta^{(2)^{-1}}\hat{N}_{12} \end{pmatrix} - \begin{pmatrix} \delta^{(2)}\hat{N}_{12}(2-s)^2 \\ \delta^{(2)^{-1}}\hat{N}_{21}s^2 \end{pmatrix} \quad (36)$$

which can be obtained either from Eq. (28) or Eq. (29) by employing the limiting process of L'Hospital rule. These $Q_{\alpha\beta}$ are functions of γ. The symmetric and antisymmetric mode can also be identified individually for $\gamma = 0$, since $Q_{12}(s) = Q_{21}(s) = 0$ when $\gamma = 0$. When materials considered are both isotropic, the quantities $Q_{\alpha\beta}$ in (36) can be further simplified. For such degenerate materials, the characteristic equation is found to be identical to that obtained early by Erdogan and Biricikoglu (1973) and the roots in this case will depend on two Dundurs' constants only, i.e., $s = s(\alpha, \beta)$.

4 Numerical Results and Discussions

In this section, we will investigate numerically the behaviors of the roots s for two cases. First case is $\gamma = 0$, i.e., when both materials are aligned along the coordinate axes and next consider $\gamma \neq 0$. Before doing these, we recall that the possible physical values of Krenk's parameters are $-1 < \nu^{(\alpha)} < 1$, $\kappa^{(\alpha)} > -1$, $E^{(\alpha)} > 0$, $\delta^{(\alpha)} > 0$ when the strain energy is positive definite. However, in our discussions we will restrict the values of $\nu^{(\alpha)}$ to be non-negative. Under this restriction, it is easily seen that the value of parameter α_o defined in Eq. (26) is $-1 < \alpha_o < 1$ and the parameter β_o is related to α_o by $\beta_o = (\omega_+^{(1)}(1-\nu^{(2)})(\alpha_o+1) + \omega_+^{(2)}(1-\nu^{(1)})(\alpha_o-1))/(4\omega_+^{(1)}\omega_+^{(2)})$. Hence, when $\alpha_o = 1$, the value of β_o is $\beta_o = (1-\nu^{(2)})/(2\omega_+^{(2)})$ which is between zero and $(2\omega_+^{(2)})^{-1}$ since $0 \le \nu^{(2)} < 1$. This corresponds to the line segment AB in Fig. 2 (point A corresponds to $\nu^{(2)} = 0$ and point B corresponds to $\nu^{(2)} = 1$). Similarly, when $\alpha_o = -1$, the value of β_o is $\beta_o = -(1-\nu^{(1)})/(2\omega_+^{(1)})$ which is between zero and $-(2\omega_+^{(1)})^{-1}$ due to $0 \le \nu^{(1)} < 1$. This corresponds to the line segment CD in Fig. 2 (point C corresponds to $\nu^{(1)} = 0$ and point D corresponds to $\nu^{(1)} = 1$). The line segment AD corresponds to $\nu^{(2)} = 0$ and $\nu^{(1)} = 1$ while line segment BC corresponds to $\nu^{(2)} = 1$ and $\nu^{(1)} = 0$. The region enclosed by these four line segments is the possible values of α_o and β_o. For the special

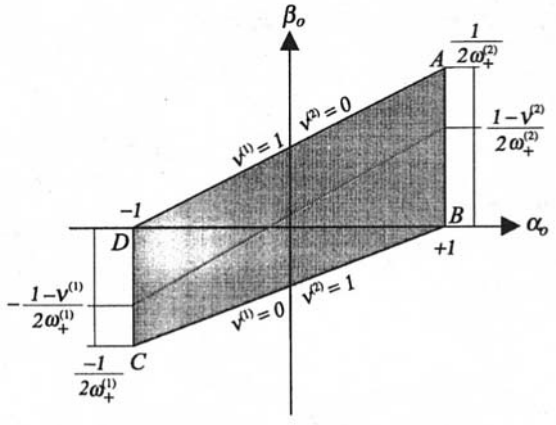


Fig. 2 Regions of physically relevant material combinations

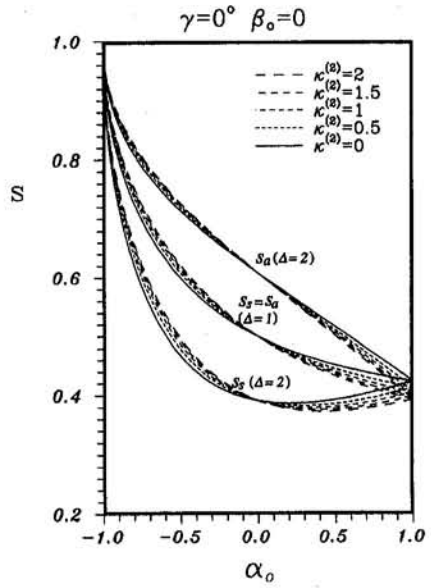


Fig. 3(a) $\beta_o = 0$

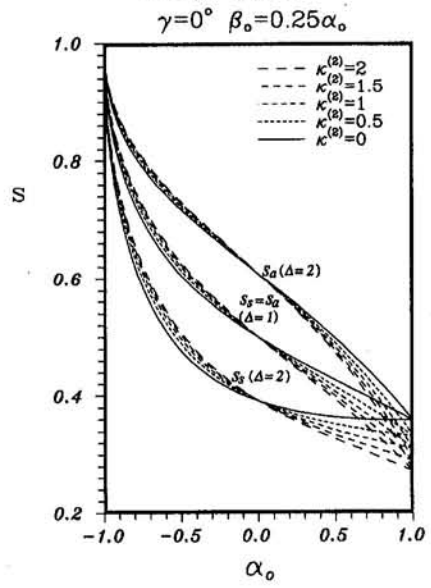


Fig. 3(b) $\beta_o = 0.25\alpha_o$

Fig. 3 Roots of s_s and s_a versus α_o for various values of $\kappa^{(2)}$ and for $\gamma = 0$

Downloaded 04 May 2010 to 171.66.16.33. Redistribution subject to ASME license or copyright; see http://www.asme.org/terms/Terms_Use.cfm

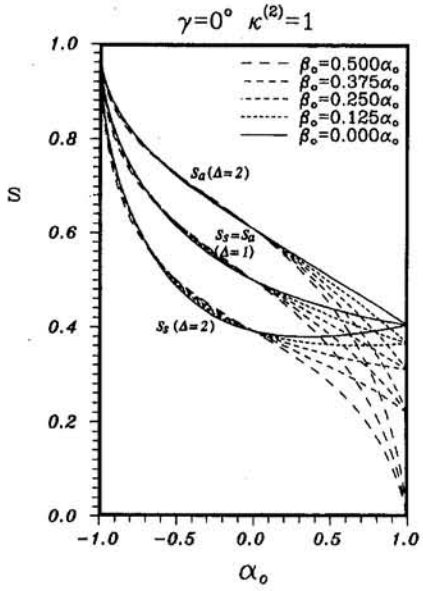


Fig. 4 Roots of s_s and s_a versus α_o for various values of β_o and for $\gamma = 0$ and $\kappa^{(2)} = 1$

case when $\omega_+^{(2)} = \omega_+^{(1)} = \omega_+$ (or letting $\kappa^{(1)} = \kappa^{(2)}$), the parameters α_o and β_o take simpler form, i.e., $\alpha_o = (E^{(1)} - E^{(2)})/(E^{(1)} + E^{(2)})$, $\beta_o = ((2 - \nu^{(1)} - \nu^{(2)})\alpha_o + (\nu^{(1)} - \nu^{(2)}))/(4\omega_+)$. If the condition $\nu^{(1)} = \nu^{(2)} = \nu$ is further enforced, β_o can be simplified further to $\beta_o = \alpha_o(1 - \nu)/(2\omega_+)$ which is a straight line passing through the origin with slop $m = (1 - \nu)/(2\omega_+)$.

(I) $\gamma = 0$. We have shown in the previous section that when both orthotropic materials are aligned along the coordinate axes, i.e., $\gamma = 0$, then the roots s are functions of $s = s(\alpha_o, \beta_o, \Delta, \kappa^{(2)})$ and they are reduced to $s = s(\alpha, \beta)$ for both materials being isotropic. For general orthotropic materials, there are many possible combinations of α_o and β_o. In order to see the effects of the anisotropy of the parameters Δ and $\kappa^{(2)}$ on the roots s, we select only the values of α_o and β_o in such a manner that $\alpha_o = m\beta_o$ where m is a constant. This is equivalent to assuming that $\nu^{(1)} = \nu^{(2)}$ and $\kappa^{(1)} = \kappa^{(2)}$ are both satisfied for the selected orthotropic materials. For the case of $\gamma = 0$, we select $m = 0$ and 0.25 for the numerical calculations. Let's first investigate the effect of $\kappa^{(2)}$ on s for some fixed values of Δ. Fig. 3(*a*) ~ Fig. 3(*b*) are the results of s versus α_o for $m = 0, 0.25$, respectively. In these figures, we first note that only one real root s is obtained for $\Delta = 1$ since the root for the symmetric mode (denoted as s_s) is the same as that for the antisymmetric mode (denoted as s_a). Note also that those curves corresponding to $\kappa^{(2)} = 1$ and $\Delta = 1$ are results for isotropic bimaterials. When $\Delta \neq 1$, we will obtain in general two distinct real roots, i.e., $s_s \neq s_a$. In each figure we select two values of Δ, i.e., $\Delta = 1$ and $\Delta = 2$, for presentation. As mentioned in Eqs. (34) or (35), the roots s for symmetrical and antisymmetric modes are related to each other when Δ is replaced by Δ^{-1}. Hence, the results of s_s ($\Delta = 2$) are valid for s_a ($\Delta = \frac{1}{2}$), and

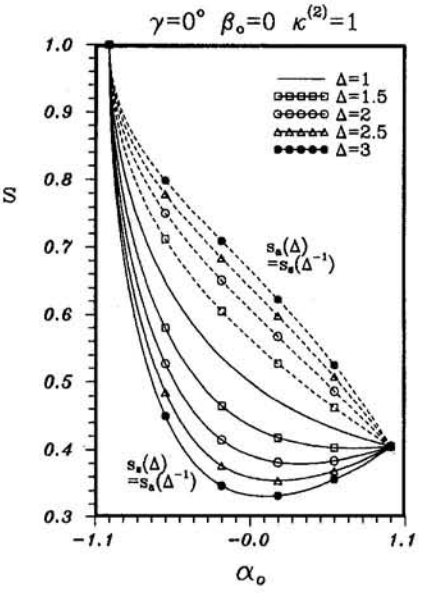


Fig. 5 Roots of s_s and s_a versus α_o for various values of Δ and for $\gamma = 0$, $\beta_o = 0$ and $\kappa^{(2)} = 1$

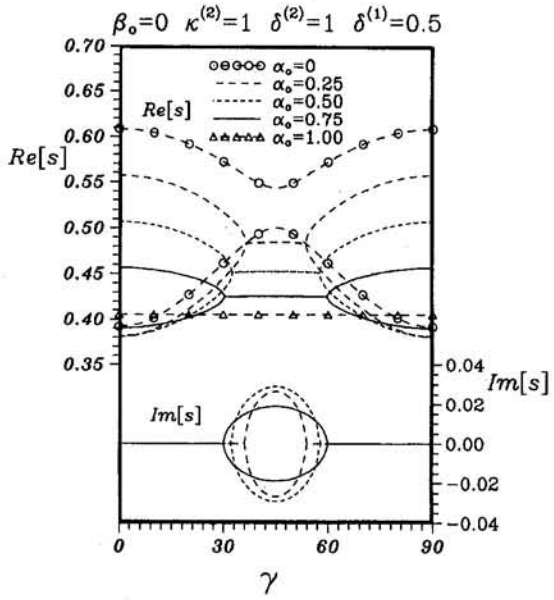


Fig. 6(*a*) $\delta^{(2)} = 1$ and $\delta^{(1)} = 0.5$

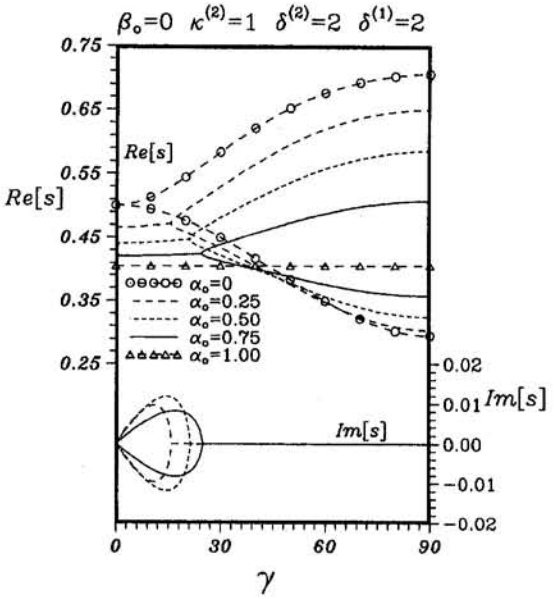


Fig. 6(*b*) $\delta^{(2)} = 2$ and $\delta^{(1)} = 2$

Fig. 6 Roots of s versus γ for various values of α_o and for $\beta_o = 0$, $\kappa^{(2)} = 1$

Downloaded 04 May 2010 to 171.66.16.33. Redistribution subject to ASME license or copyright; see http://www.asme.org/terms/Terms_Use.cfm

similarly results of s_a ($\Delta = 2$) can be applied for s_s ($\Delta = \frac{1}{2}$). It is also worthy to mention that for some special values of α_o and (or) β_o the roots of s_s and s_a have certain special properties. For example, when $(\alpha_o, \beta_o) = (0, 0)$, we found that the roots s are independent of the parameter $\kappa^{(2)}$. This is clear because $\alpha_1 = -\alpha_2 = (\Delta - 1)/(\Delta + 1)$, $\beta_1 = \beta_2 = 0$ when $\alpha_o = \beta_o = 0$, hence, $Q_{11}(s) = -Q_{22}(s) = (1 - \Delta)/(1 + \Delta)$, which are independent of $\kappa^{(2)}$. Actually, for $(\alpha_o, \beta_o) = (0, 0)$, the two roots can be found explicitly to be $s_s = \cos^{-1}((\Delta - 1)/(\Delta + 1))/\pi$ and $s_a = \cos^{-1}((1 - \Delta)/(1 + \Delta))/\pi$ and furthermore these two roots are related by the equation $s_s(\Delta) + s_a(\Delta) = 1$. By letting $\Delta = 1$, the roots become $s_s = s_a = 0.5$, a fact that is also observed in these two figures. Another special value of α_o considered is $\alpha_o = 1$. In this case, the roots are independent of Δ. This is because $\alpha_1 = \alpha_2 = 1$, $\delta^{(2)^{-1}}\beta_1 = \delta^{(2)}\beta_2 = \beta_o$ when $\alpha_o = 1$, which are all independent of Δ. Therefore, $Q_{11}(s)$ and $Q_{22}(s)$ will be also independent of Δ. The obtained quantities $Q_{11}(s)$ and Q_{22} for $\alpha_o = 1$ are actually the same, i.e., $Q_{11}(s, \beta_o, \kappa^{(2)}) = Q_{22}(s, \beta_o, \kappa^{(2)})$. Therefore, the roots corresponding to $\alpha_o = 1$ will be not only independent of Δ but also the same. Finally, let's consider the case when $\alpha_o \to -1$. In this case, we observe that all roots s approach $+1$ for all values of $\kappa^{(2)}$. As to the effect of $\kappa^{(2)}$ on the roots s, we observed from these two figures that the roots are insensitive to the magnitude of $\kappa^{(2)}$ when α_o is approximately less than 0.5. Only when α_o is near 1, i.e., when material #1 is quite stiff, will the significance of the magnitude of $\kappa^{(2)}$ on the roots become more important. Hence, in the rest of the following discussions of the effects of other parameters, we will present only the results of $\kappa^{(2)} = 1$ for simplicity.

Next, let's consider the effect of $\beta_o = m\alpha_o$ on the power of singularity s. Figure 4 presents s versus α_o for several values of m, i.e., $m = 0, \frac{1}{8}, \frac{1}{4}, \frac{3}{8}$ and $\frac{1}{2}$. It is clearly seen that the effect of the magnitude of β_o is small when $\alpha_o < 0$. The effect of the parameter Δ is presented in Fig. 5. In this case we select $\beta_o = 0$ and $\kappa^{(2)} = 1$ for presentation. It is seen from Fig. 5 that the effect of Δ on s is more pronounced than previous parameters that have been discussed. Due to the selection of the values of the parameter Δ in the presentation of Fig. 5, i.e., $\Delta > 1$, the order of singularity for the antisymmetric mode is seen to be higher than that for the symmetric mode. Suppose one takes $\Delta < 1$, then the above phenomenon will be reversed.

(II) $\gamma \neq 0$. As mentioned in Section 3, the roots s will be independent of γ if the material #1 has the property that $\delta^{(1)} = 1$. Hence, to see the effect of γ on s, we choose $\delta^{(1)} \neq 1$. Fig. 6(a), (b) are results for the cases where $\delta^{(1)} = \frac{1}{2}$, $\delta^{(2)} = 1$ ($\Delta = \frac{1}{2}$) and $\delta^{(1)} = 2$, $\delta^{(2)} = 2$ ($\Delta = 1$), respectively. For both cases the values of parameters β_o and $\kappa^{(2)}$ are chosen as $\beta_o = 0$, $\kappa^{(2)} = 1$. It is seen from Fig. 6(a), (b) that for all γ ($0 \text{ deg} \leq \gamma \leq 90 \text{ deg}$) two distinct real roots s exist when $\alpha_o = 0$ (line with circular symbol) (except in Fig. 6(b) where only one real root exists for $\gamma = 0$) and these two real roots become the same and are independent of γ when $\alpha_o = 1$ (line with triangular symbol). For other values of α_o plotting in Fig. 6(a), (b), we found that for some ranges of γ there exist complex roots for s. For example, for the case of $\alpha_o = 0.75$ as shown in Fig. 6(a), two real different roots s_1 and s_2 are observed for $0 \text{ deg} \leq \gamma < 30 \text{ deg}$ or $60 \text{ deg} < \gamma \leq 90 \text{ deg}$. However, for $30 \text{ deg} < \gamma < 60 \text{ deg}$, these two roots become complex and they are complex conjugate. For instance, two complex roots $s_{1,2} = 0.4259 \pm i\,0.01883$ occur at $\gamma = 45$ deg, as shown in Fig. 6(a) for $\alpha_o = 0.75$. One may notice that the imaginary part of s is a small number comparing to the magnitude of the real part of that root. In the paper of Ting and Hoang (1984), they obtain in general three distinct real roots for s. No complex roots are found. In our numerical examples we do find that there exist complex roots even for the inplane deformation only. It is noted that the results of Fig. 6(a) are applicable for the case of $\delta^{(1)} = 2$ while those shown in Fig. 6(b) are applicable for the case of $\delta^{(1)} = \delta^{(2)} = \frac{1}{2}$. Also note that $s_{1,2}(\gamma) = s_{1,2}(\pi/2 - \gamma)$ as long as $\delta^{(2)} = 1$, a fact that can be verified without any difficulty.

References

Bogy, D. B., 1971, "On the Plane Elastostatic Problem of a Loaded Crack Terminating at a Material Interface," ASME JOURNAL OF APPLIED MECHANICS, Vol. 38, pp. 911–918.

Chadwick, P., and Smith, G. D., 1977, "Foundations of the Theory of Surface Waves in Anisotropic Elastic Materials," *Advances in Applied Mechanics,* Vol. 17, pp. 303–376.

Cook, T. S., and Erdogan, F., 1972, "Stresses in Bonded Materials with a Crack Perpendicular to the Interface," *Int. J. Engng Sci.,* Vol. 10, pp. 677–697.

Delale, F., and Erdogan, F., 1979, "Bonded Orthotropic Strips with Cracks," *Int. J. Fracture,* Vol. 15, pp. 343–364.

Dundurs, J., 1968, *Elastic Interaction of Dislocations with Inhomogeneities: Mathematic Theory of Dislocation,* ASME, New York, pp. 70–115.

Erdogan, F., and Biricikoglu, V., 1973, "Two Bonded Half Planes with a Crack Going Through the Interface," *Int. J. Engng Sci.,* Vol. 11, pp. 745–766.

Erdogan, F., and Bakioglu, M., 1976, "Two Bonded Half Planes with a Crack Going Through the Interface," *Int. J. Fracture,* Vol. 12, No. 1, pp. 71–84.

Eshelby, J. D., Read, W. T., and Shockley, W., 1953, "Anisotropic Elasticity with Applications to Dislocation Theory," *Acta Metallurgica,* Vol. 1, pp. 251–259.

Gapta, G. D., 1973, "A Layered Composite with a Broken Laminate," *International Journal of Solids and Structures,* Vol. 9, pp. 1141–1154.

Gupta, V., Argon, A. S., and Suo, Z., 1992, "Crack Deflection at an Interface Between Two Orthotropic Media," ASME JOURNAL OF APPLIED MECHANICS, Vol. 59, pp. 79–87.

Krenk, S., 1979, "On the Elastic Constants of Plane Orthotropic Elasticity," *Journal of Composite Materials,* Vol. 13, pp. 108–116.

Muskhelishvili, N. I., 1945, *Singular Integral Equations,* Noordhoff.

Stroh, A. N., 1958, "Dislocations and Cracks in Anisotropic Elasticity," *Philos. Mag.,* Vol. 7, pp. 625–646.

Sung, J. C., and Liou, J. Y., 1994a, "Some Phenomena of Cracks Perpendicular to an Interface Between Dissimilar Orthotropic Materials," ASME JOURNAL OF APPLIED MECHANICS, accepted for publication.

Sung, J. C., and Liou, J. Y., 1994b, "Subinterface Crack in Dissimilar Orthotropic Materials," *International Journal of Solids and Structures,* to appear.

Sung, J. C., and Liou, J. Y., 1995, "Analysis of a Crack Embedded in a Linear Elastic Half-Plane Solid," ASME JOURNAL OF APPLIED MECHANICS, Vol. 62, pp. 62–86.

Ting, T. C. T., and Hoang, P. H., 1984, "Singularities at the Tip of a Crack Normal to the Interface of an Anisotropic Layered Composite," *International Journal of Solids and Structures,* Vol. 20, pp. 439–454.

Zak, A. K., and Williams, M. L., 1963, "Crack Point Stress Singularities at a Bi-material Interface," ASME JOURNAL OF APPLIED MECHANICS, Vol. 30, pp. 142–143.

Downloaded 04 May 2010 to 171.66.16.33. Redistribution subject to ASME license or copyright; see http://www.asme.org/terms/Terms_Use.cfm

Interface Cracks in a Layered Solid Subjected to Contact Stresses

C. H. Liu
Department of Mechanical Engineering,
Tamkang University,
Tamsui, Taipei,
Taiwan 250, R.O.C.

I-Feng Chen
Materials Research Laboratories,
Industrial Technology Research Institute,
Hsinchu, Taiwan, R.O.C.

A boundary element technique has been developed to analyze interface cracks in a layered solid. The loading applied on the solid may be tension, compression, shear, or an arbitrary combination of these. Crack surfaces may be open, closed, or partially open and partially closed. In all these cases, energy release rates can always be determined by using this technique. Crack-tip conditions are determined by an iterative procedure so that they themselves are parts of the solutions of a problem. The numerical technique is utilized to analyze subsurface interface cracks in a layered solid. Results are shown for various materials and under various loading conditions.

Introduction

Many engineering failures are caused by interface cracks in layered solids. In a layered composite, for example, cracks may grow along a weak interface, leading to debonding or delamination failures. In a case hardened rolling or sliding component, a subsurface crack may grow along the case and core interface for a distance before it grows in the transverse direction, ultimately leading to case crushing of this component. While the knowledge of interface crack growth is crucial for structural analysis and machine design, to the knowledge of the investigators, the analysis method for such cracks has not yet been fully developed. The purpose of this paper is therefore to develop a boundary element technique to analyze arbitrarily loaded interface cracks. This technique is then utilized to analyze subsurface cracks in rolling or sliding components.

So far all analyses for interface cracks are performed either under the condition of open crack tips, or the condition of closed crack tips, in which cases they are called *the open model* and *the closed model,* respectively. It is known that the open model gives rise to physically unreasonable oscillatory crack-tip stresses and displacements (Williams, 1959; Erdogan, 1963; England, 1965; Rice and Sih, 1965). The closed model is based on the assumption that there always exists crack-tip contact zones. Comninou (1977a, 1977b) showed that crack-tip fields were not oscillatory under this assumption. She also formulated integral equations for a crack along an infinite interface. By using numerical techniques, she solved these integral equations and found stress intensity factors K_2 under various loading conditions. Exact solutions of these integral equations were obtained later by Gautesen and Dundurs (1987 and 1988).

The existing numerical techniques for interface cracks are either finite element methods or boundary element methods. Clech, Lewis, and Keer (1986) developed a comparative finite element technique. They showed that this method may be used to determine stress intensity factors of *no-slip* bimaterial cracks. van der Zande and Grootenboer (1986) developed a hybrid displacement finite element technique to calculate mode II stress intensity factors for interface cracks with crack-tip contact zones. Their results agreed with Comninou's solutions for tension cracks. For central cracks under both tension and shear, their K_2 values for the left tip and right tip are either both positive or both negative. Comninou (1990) pointed out that this *cannot* be correct. Reynolds, Kokini, and Chen (1990) modeled closed crack tips with the gap elements originally developed by Oden and Carey (1984) for contact problems. They calculated fracture parameters by using the crack flank displacement methods developed by Smelser (1979). Even when the smallest mesh size is used, their results still differ with Comninou's solutions by 11 percent. Lee and Choi (1988) derived a formula with which stress intensity factors K_1 and K_2 of an open crack tip may be determined from displacements along the interface. However, Raveendra and Banerjee (1991) pointed out that stress intensity factors K_1 and K_2 for bimaterial interface cracks should be coupled, and that Lee and Choi erroneously used uncoupled mode I and mode II stress intensity factors. In the same paper Raveendra and Banerjee derived correct formulas, and they utilized the boundary element technique to find interface displacements so that K_1 and K_2 may be determined. Tan and Gao (1990) also utilized the boundary element technique to analyze interface cracks under the open model assumption.

Most of the numerical techniques mentioned above are for open tips only. It is known that there always exists a large crack-tip contact zone when the interface crack is subjected to shear stresses (i.e., $S \neq 0$ in Fig. 1) (see Comninou and Schmueser, 1979; Gautesen and Dundurs, 1988). For problems with shear stresses, so far we have only the work of van der Zande and Grootenboer (1986). However, as it is mentioned in the last paragraph, their results did not agree with Comninou's solutions. Our desire is to develop a numerical technique to study the subsurface interface cracks under the application of contact stresses $p(x)$ and $fp(x)$ on the surface (see Fig. 2).

The Boundary Element Method

The boundary integral equations defined along the boundary C of a two-dimensional linear elastic solid Ω are

$$k_x(P)u_x(P) = \int_C [\mathbf{U}_{xx}(P, Q)t_x(Q) + \mathbf{U}_{xy}(P, Q)t_y(Q)]ds(Q) - \int_C [\mathbf{T}_{xx}(P, Q)u_x(Q) + \mathbf{T}_{xy}(P, Q)u_y(Q)]ds(Q) \quad (1a)$$

$$k_y(P)u_y(P) = \int_C [\mathbf{U}_{yx}(P, Q)t_x(Q) + \mathbf{U}_{yy}(P, Q)t_y(Q)]ds(Q) - \int_C [\mathbf{T}_{yx}(P, Q)u_x(Q) + \mathbf{T}_{yy}(P, Q)u_y(Q)]ds(Q) \quad (1b)$$

Contributed by the Applied Mechanics Division of THE AMERICAN SOCIETY OF MECHANICAL ENGINEERS for publication in the ASME JOURNAL OF APPLIED MECHANICS.

Discussion on this paper should be addressed to the Technical Editor, Prof. Lewis T. Wheeler, Department of Mechanical Engineering, University of Houston, Houston, TX 77204-4792, and will be accepted until four months after final publication of the paper itself in the ASME JOURNAL OF APPLIED MECHANICS.

Manuscript received by the ASME Applied Mechanics Division, May 28, 1993; final revision, July 14, 1994. Associate Technical Editor: C. F. Shih.

Copyright © 1996 by ASME

Downloaded 04 May 2010 to 171.66.16.33. Redistribution subject to ASME license or copyright; see http://www.asme.org/terms/Terms_Use.cfm

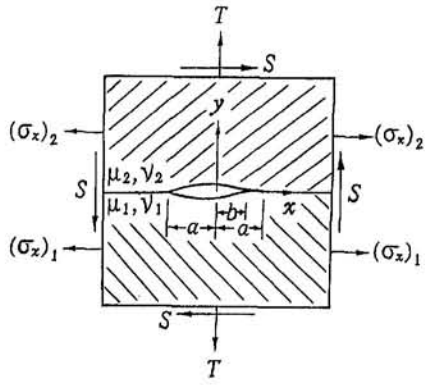


Fig. 1 A bimaterial interface crack

where $u_x(P)$ and $u_y(P)$ are displacements of a point P on the boundary, $u_x(Q)$, $u_y(Q)$, $t_x(Q)$, and $t_y(Q)$ are displacements and tractions of the integration point Q, $\mathbf{U}_{ij}(P, Q)$ and $\mathbf{T}_{ij}(P, Q)$ are fundamental solutions of an infinite elastic solid and are due to Kelvin. If a unit point load in the direction of x_i is applied at a point in an infinite elastic media, then $\mathbf{U}_{ij}$ and $\mathbf{T}_{ij}$ denote corresponding displacements and tractions in the direction of x_j at an arbitrary point in the solid. Explicit expressions for $\mathbf{U}_{ij}$ and $\mathbf{T}_{ij}$ may be found in many textbooks, hence they are not shown in this paper. Coefficients $k_x(P)$ and $k_y(P)$ shown in Eqs. (1*a*) and (1*b*) depend on the shape of the curve C at P. If C is smooth at P, then $k_x = k_y = \frac{1}{2}$.

There are four variables (t_x, t_y, u_x, and u_y) associated with an arbitrary point on the boundary. For a well-posed boundary value problem, two of these four variables are specified. Then Eqs. (1*a*) and (1*b*) are boundary integral equations to be solved for the remaining two variables. To solve these equations numerically, the boundary C is first divided into a series of segments, called boundary elements. Each element contains a certain number of nodes. Since a curved boundary may be well approximated by a series of quadratic curves, quadratic boundary elements are thus very widely used. Displacements and tractions at a point in a quadratic element are given by

$$(u_x, u_y) = \sum_{k=1}^{3} N_k(u_x, u_y)_k \tag{2a}$$

$$(t_x, t_y) = \sum_{k=1}^{3} N_k(t_x, t_y)_k \tag{2b}$$

where $(u_x, u_y)_k$ and $(t_x, t_y)_k$ are nodal displacements and nodal tractions of the kth node in this element, N_k are interpolation functions given by

$$(N_1, N_2, N_3) = (-\alpha(1-\alpha)/2, (1+\alpha)(1-\alpha), \alpha(1+\alpha)/2) \tag{3}$$

in which α is the dimensionless coordinate varying from -1 to $+1$ (see Fig. 3).

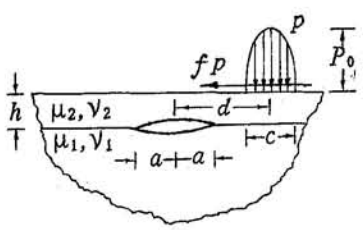


Fig. 2 An interface crack in a layered solid

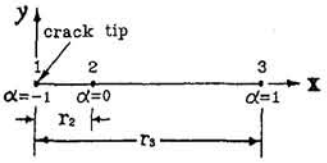


Fig. 3 A quarter-point element

Special Elements

A quadratic element is called a *quarter-point element* if all the three nodes are collinear, and the middle node is at the quarter-point position. Blandford, Ingraffea, and Liggett (1981) have shown that displacements in such an element behave according to $r^{1/2}$.

A quarter-point element is called a *traction singular quarter-point element* if, instead of using nodal tractions $(t_x, t_y)_k$, we use normalized nodal tractions $(p_x, p_y)_k$ defined by

$$(p_x, p_y)_k = (r_k/l)^{1/2}(t_x, t_y)_k \tag{4}$$

where r_k are distances from the crack tip to the kth node (see Fig. 3), and l is the length of the crack-tip element. Note that normalized crack-tip tractions $(p_x, p_y)_1$ are finite. With this definition, one may write tractions at a point in this element in the following form

$$(t_x, t_y) = \sum_{k=1}^{3} M_k(p_x, p_y)_k \tag{5}$$

where the modified shape functions M_k are defined by

$$M_k = (l/r_k)^{1/2}N_k. \tag{6}$$

Blandford, Ingraffea, and Liggett (1981) have shown that tractions in such an element behave according to $r^{-1/2}$.

Formulation of Bimaterial Cracks

A bimaterial interface crack may be formulated by using the method of subregions, which has already been widely used in problems of homogeneous cracks. Two subregions shown in Fig. 4 are bonded together along the surface S_b by imposing the compatibility conditions, i.e., $(u_{x1}, u_{y1}) = (u_{x2}, u_{y2})$ and $(t_{x1}, t_{y1}) = -(t_{x2}, t_{y2})$. Note that indexes 1 and 2 have been used to denote the variables are associated with the lower and upper bodies, respectively. For a point on the crack surface but *not at the crack tip,* we may impose traction free conditions, i.e., $(t_{x1}, t_{y1}) = (t_{x2}, t_{y2}) = 0$ if at this point crack surfaces are open, and impose frictionless contact conditions, i.e.,

$$t_{y1} = -t_{y2} \tag{7a}$$

$$t_{x1} = t_{x2} = 0 \tag{7b}$$

$$u_{y1} = u_{y2} \tag{7c}$$

if at this point crack surfaces are in contact. In the case of monotonically increasing tension loading, and tension starts from zero, Comninou (1977b) concluded that friction made the

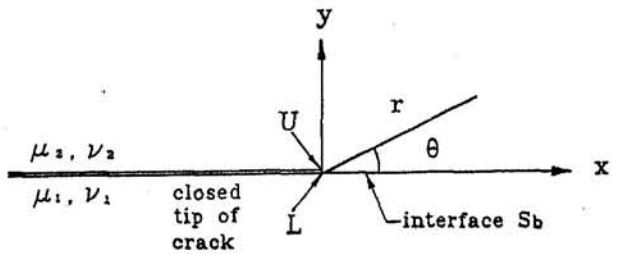


Fig. 4 A closed crack tip

Downloaded 04 May 2010 to 171.66.16.33. Redistribution subject to ASME license or copyright; see http://www.asme.org/terms/Terms_Use.cfm

crack-tip singularity weaker. In this paper the contact is assumed to be frictionless.

We now consider conditions to be imposed at crack tips. We use the right tip ($x = a$, $y = 0$) for illustration. There are six unknowns associated with the right tip on the upper surface (i.e., node U in Fig. 4), namely, two tractions $(t_{x2}, t_{y2})^-$ just before (i.e., $x < a$) the node, two tractions $(t_{x2}, t_{y2})^+$ just after (i.e., $x > a$) the node, and two nodal displacements (u_{x2}, u_{y2}). There are also six unknowns for node L on the lower surface. We have two integral equations (i.e., Eqs. (1a) and (1b)) for node U and two equations for node L. Also we have four compatibility conditions implied in the following equations:

$$(t_{x1}, t_{y1})^+ = -(t_{x2}, t_{y2})^+ \tag{8a}$$

$$(u_{x1}, u_{y1}) = (u_{x2}, u_{y2}). \tag{8b}$$

If the crack tip is open, then we have four more conditions

$$(t_{x1})^- = (t_{y1})^- = (t_{x2})^- = (t_{y2})^- = 0. \tag{9}$$

If the crack tip is closed, we know

$$(t_{x1})^- = (t_{x2})^- = 0 \tag{10a}$$

$$(p_{y1})^- = -(p_{y2})^-. \tag{10b}$$

We still need one more equation if the crack tip is closed. The singular behavior around a closed tip has been studied by Comninou (1977a), but her results have never been utilized in numerical calculations. She showed that $(t_{y2})^+$ is finite, but both $(t_{y2})^-$ and $(t_{x2})^+$ are infinite. In terms of normalized tractions her result is

$$(p_{y2})^- = -\beta(p_{x2})^+ \tag{11}$$

where β is one of the Dundurs parameters given by

$$\beta = \frac{\mu_2(\kappa_1 - 1) - \mu_1(\kappa_2 - 1)}{\mu_2(\kappa_1 + 1) + \mu_1(\kappa_2 + 1)}. \tag{12}$$

In the last equation, μ_i are shear moduli of elasticity, $\kappa_i = 3 - 4\nu_i$ for plane-strain problems. Thus there are always 12 equations for the 12 unknowns associated with node U and node L.

The left tip can be treated in the same way as the right tip. The only difference is that Eq. (11) should be replaced by the expression

$$(p_{y2})^+ = \beta(p_{x2})^- \tag{13}$$

where $(p_{x2})^-$ and $(p_{y2})^+$ are normalized tractions at the point just before (i.e., $x < -a$) and the point just after (i.e., $x > -a$) the left tip ($x = -a$, $y = 0$) respectively.

When both of the two crack tips are closed, from the previous discussions we know that both of Eq. (11) and Eq. (13) have to be included so that there are enough equations to solve for unknowns. Since Eqs. (11) and (13) correctly show K_2 for the right tip and K_2 for the left tip have opposite signs, thus van der Zande and Grootenboer's error may be removed. This is so if one uses the boundary element method. Solutions based upon the traditional assumed-displacement finite element formulation only satisfy displacement boundary conditions. Constraints conditions are also for displacements only. Therefore the stress conditions shown in Eqs. (11) or (13) can not be easily imposed upon solutions. There are special elements developed for finite element analysis of contact problems. The authors are not certain if the stress conditions shown in Eqs. (11) and (13) may be imposed on, and if the crack-tip stress and displacement fields may be generated within such elements.

Fracture Parameters

The stress intensity factor K_2 for a closed crack tip is

$$K_2 = \lim_{r\to 0} (2\pi r)^{1/2}\tau_{xy}|_{\theta=0} = \lim_{r\to 0} (2\pi r)^{1/2} t_x|_{\theta=0}. \tag{14}$$

Crack-tip elements are placed along the x-axis (i.e., $\theta = 0$). Hence by making use of Eq. (4), one may write

$$K_2 = (\pi l)^{1/2}(p_x)_1. \tag{15}$$

Making use of the known relation between K_2 and the energy release rate G, we may write

$$G^c = (K_2)^2/(4D) = \pi l[(p_x)_1]^2/(2D) \tag{16}$$

where the superscript c denotes that the variable is for a closed crack tip and D is a material constant defined by the relation

$$D = \frac{2(1+\alpha)\mu_1}{(\kappa_1+1)(1-\beta^2)} = \frac{2(1+\alpha)\mu_2}{(\kappa_2+1)(1-\beta^2)} \tag{17}$$

in which α and β are Dundurs parameters defined by Eq. (12) and by the following equation:

$$\alpha = \frac{\mu_2(\kappa_1+1) - \mu_1(\kappa_2+1)}{\mu_2(\kappa_1+1) + \mu_1(\kappa_2+1)}. \tag{18}$$

It may be shown that the energy release rate for an open tip is

$$G^o = K\bar{K}(C_1 + C_2)/(16\cosh^2\pi\epsilon) \tag{19}$$

where K is the complex stress intensity factor defined by Hutchinson, Mear, and Rice (1987) and is given by

$$K = \lim_{r\to 0} (2\pi r)^{1/2}[(\sigma_y + i\tau_{xy})r^{-i\epsilon}]_{\theta=0}$$
$$= \lim_{r\to 0} (2\pi r)^{1/2}(t_y + it_x)r^{-i\epsilon}. \tag{20}$$

$\bar{K}$ is the complex conjugate of K, C_1, C_2, and ϵ are material constants defined by the following equations:

$$C_i = (1+\kappa_i)/\mu_i, \quad i = 1 \text{ or } 2 \tag{21a}$$

$$\epsilon = \frac{1}{2\pi}\log[(\mu_1 + \kappa_1\mu_2)/(\mu_2 + \kappa_2\mu_1)]. \tag{21b}$$

We defined $K_o = (K\bar{K})^{1/2}$ then it may be seen from Eq. (19) that the parameter K_o is proportional to G^o. Hence Tan and Gao (1990) used K_o as the fracture parameter. By using Eq. (20) and then Eq. (4), we may show

$$K_o = \lim_{r\to 0}[2\pi r(t_y)^2 + 2\pi r(t_x)^2]^{1/2}$$
$$= (2\pi l)^{1/2}\{[(p_y)_1]^2 + [(p_x)_1]^2\}^{1/2} \tag{22}$$

Therefore the energy release rate G^o for an open tip may be obtained from $(p_y)_1$ and $(p_x)_1$ by using Eq. (22) and then Eq. (19). The energy release rate G^o for a closed tip may be obtained from $(p_x)_1$ by using Eq. (16).

Numerical Techniques

We have mentioned that there exists two models for problems of interface cracks, namely, the open model and the closed model. Among these two models, the closed model is much more complicated since it usually requires a lot of effort to simulate crack-tip contact zones. This is because at least one of the two crack-tip contact zones is extremely small. For tension cracks both crack-tip contact zones are extremely small. For cases with shear stresses, one of the crack-tip contact zones is fairly large compare to crack length, but the other contact zone is extremely small (Comninou and Schmueser, 1979; Gautesen and Dundurs, 1988). The open model is not suitable for cases with shear stresses because there always exist fairly large crack-tip contact zones. Therefore in this paper these two models are combined into a model we call *the mixed model.* The closed model is adopted whenever it is possible. The open model is utilized only for extremely small crack-tip contact zones, so that numerical difficulties may be avoided. By doing this we may take a crack tip with very small contact zone to be open. It is known that either the open or the closed model

Downloaded 04 May 2010 to 171.66.16.33. Redistribution subject to ASME license or copyright; see http://www.asme.org/terms/Terms_Use.cfm

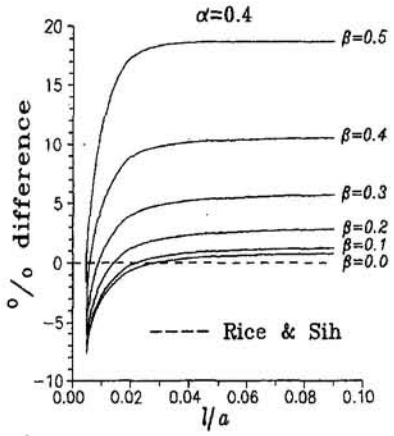


Fig. 5 Percentage difference in K_0 for the crack shown in Fig. 1 with $T > 0$ and $S = 0$

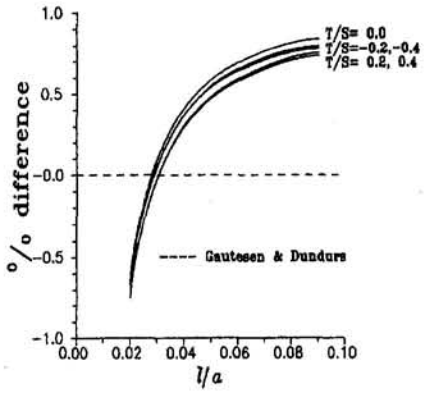


Fig. 6 Percentage difference in K_2 for various T/S values

would give the same value of energy release rate, therefore we use the energy release rate G as the fracture parameter.

The size of the contact region are determined by an iterative procedure. In the initial analysis the whole crack surface is assumed to be open. If displacements along crack surfaces imply interpenetration, then, in the next iteration, the region of interpenetration is taken to be the contact zone. The size of this contact region is further modified if, after the analysis, interpenetration still exists or if there exists tension in the contact zone. The process continues until there is no interpenetration and no tension in the contact region.

By using either the open or the closed model, crack-tip conditions (i.e., open or closed) must be determined *prior to* analyses. What is special about the mixed model is that crack-tip conditions are themselves parts of the solutions of a problem. The size of a crack-tip contact zone may be large enough to be detected by the numerical technique, in which case the closed model will be used. The crack-tip contact zone may also be extremely small, if it even exists, then the open model will be used.

It can be seen from Eqs. (16) and (22) that numerical values of G depend upon l, the length of the crack-tip element. The suitable length of the crack-tip element may be determined by comparing the numerical results to known analytic solutions. In Fig. 5 we show comparisons to Rice and Sih (1965) for open tips under pure tension. Stresses $(\sigma_x)_1$ and $(\sigma_x)_2$ (see Fig. 1) are applied to ensure $(\epsilon_{xx})_1 = (\epsilon_{xx})_2$ along the interface (Rice and Sih, 1965, p. 423). Crack-tip contact zones are too small (if they exist) to be found in these cases, therefore the open model is used. So far all the existing numerical analyses for open tips are performed with fixed sizes of crack-tip elements. Figure 5 shows, however, that correct sizes (i.e., sizes which give rise to zero errors) of the crack-tip element decrease with increasing β. Also, these curves are very steep in the neighborhood of correct l/a values. This implies that numerical results are very sensitive to l/a, thus it is extremely important to use correct l/a values. According to our numerical experiences, correct l/a values do not depend on the Dundurs' parameter α. In all the subsequent analyses for open tips, these correct l/a values are used.

Comparisons to Gautesen and Dundurs (1988) for cases with both tension (T) and shear (S) are shown in Fig. 6. Each case shown in this figure was analyzed by the iterative procedure mentioned above. These results are all for the right tip of the interface crack shown in Fig. 1. It can be seen from Fig. 6 that closed-tip solutions are insensitive to sizes of crack-tip elements. We have also found that correct l/a values are independent of α and β, thus results shown in Fig. 6 are valid for all values of α or β. All the subsequent analyses for closed tips are performed with the fixed element size $l = 0.03a$.

All the previous discussions about l/a values are for interface cracks subjected to remote mechanical loadings. The authors have not tried problems with crack surface loadings, thermal loadings, hygrothermal effects, etc.

Results and Discussions

We once again compare our numerical results to Gautesen and Dundurs (1988). Comparisons are shown in Figs. 7(*a*) and 7(*b*). Closed-tip and open-tip solutions are represented by dark

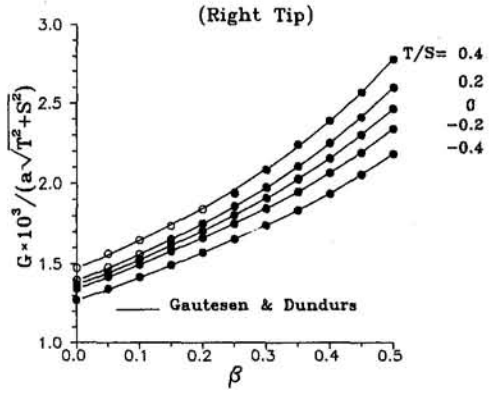


Fig. 7(*a*)

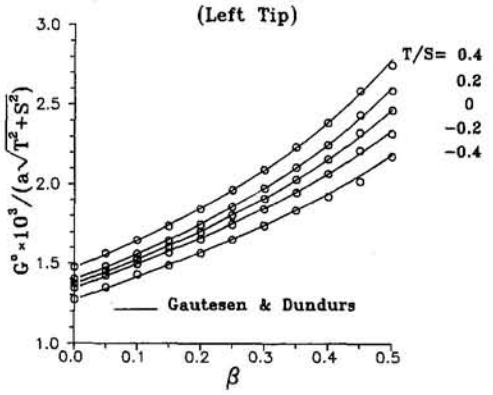


Fig. 7(*b*)

Fig. 7 Energy release rate G for crack shown in Fig. 1; (*a*) right tip, (*b*) left tip

Downloaded 04 May 2010 to 171.66.16.33. Redistribution subject to ASME license or copyright; see http://www.asme.org/terms/Terms_Use.cfm

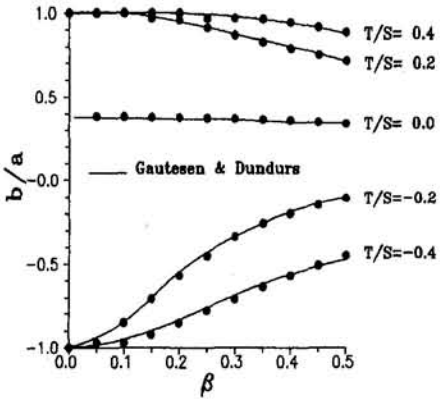


Fig. 8 Sizes of crack-tip contact zones; b is length of the region shown in Fig. 1

circles and bright circles, respectively. Also, positive and negative T/S values represent applied normal stresses which are tension and compression, respectively. It is not surprising to find numerical solutions agree very well with Gautesen and Dundurs because we have adjusted the size of the crack-tip element to match analytical solutions. What these figures show is that it is more difficult to close the left tip by compression (Fig. 7(b)) than to open the right tip by tension (Fig. 7(a)). As a matter of fact, for all the cases we have studied, the left tip is always open. Therefore, we never had a chance to simultaneously impose Eq. (11) to the right tip and Eq. (13) to the left tip. In Fig. 8 we compare sizes of contact regions under various loading conditions. They agree well with Gautesen and Dundurs. The crack-opening displacements g ($=u_{y2} - u_{y1}$) for the extreme case $\beta = 0.5$ are shown in Fig. 9. Comninou and Schmueser (1979) have analyzed the same case with the closed model. In their results, the maximum value of crack-opening displacement *increases* with the compressive load. Figure 9 shows this phenomenon may be removed if the mixed model is used.

Subsurface Interface Cracks

Composite materials have been widely used in rolling or sliding mechanical components such as gears, cams, wheels, and bearings. Also, rolling or sliding components are often covered with surface coatings or hardened cases to increase wear resistance. It is known that interface cracks in these components may grow in the direction parallel to the outer surface. So far all existing studies for subsurface cracks are for homogeneous materials only (see, for example, Keer, Bryant, and Haritos, 1982; Keer and Bryant, 1983; Sheppard, Barber, Comninou, 1985, 1987). The numerical technique developed in this paper is now utilized to find energy release rates of the subsurface interface crack in the semi-infinite solid shown in Fig. 2. When there is no tangential load (i.e., when $f = 0$), energy release rates for various locations of the normal load p are shown in Figs. 10(a) and 10(b). Open and closed-tip results are represented by dotted lines and solid lines, respectively. Results for cases with $\alpha = 0$, $f = 0.1$ are shown in Figs. 11(a) and 11(b). It is interesting to notice that, while the far tip is always closed, the near tip, however, may be opened by the compressive load when $d > a$. Also, it seems that the larger the mismatch constant β is, the easier the near tip may be opened by the load.

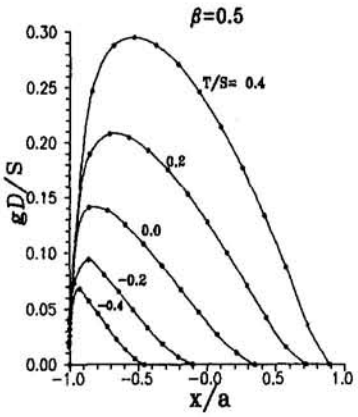


Fig. 9 Crack-opening displacements; $g = u_{y2} - u_{y1}$, d is defined by Eq. (17)

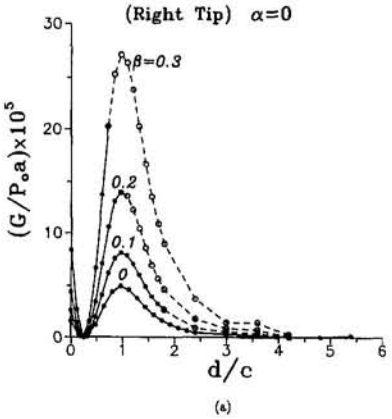


Fig. 10(a)

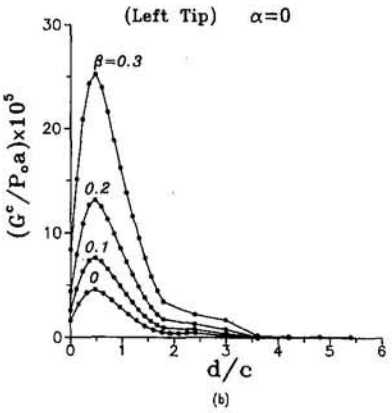


Fig. 10(b)

Fig. 10 Variations of G with d for the case $f = 0$, $h = c = 2a$; (a) right tip, (b) left tip

To give a possible explanation, we first notice that when a horizontal unit load is applied on the surface of a plane-strain semi-infinite solid, the surface ahead of the load is depressed by the amount $(1 - 2\nu)/(4\mu)$ and the surface behind the load is raised by the same amount (see, e.g., Johnson, 1985, p. 18). Now we consider the directions of interfacial shear stresses at *the right tip* (i.e., *the near tip*). It is expected that when $f > 0$ interfacial shear stresses on the lower body are in the same direction as fp shown in Fig. 2, and on the upper body they are in the direction opposite to fp. These arguments lead us to conclude that interfacial crack-tip shear stresses cause both the upper and the lower crack surfaces to have downward displacements. Magnitudes of these displacements may be characteristically denoted by $(1 - 2\nu_2)/(4\mu_2)$ for the upper body and $(1 - 2\nu_1)/(4\mu_1)$ for the lower body. Since $\beta > 0$ generally implies $\mu_2 > \mu_1$ and $\nu_2 > \nu_1$, the lower crack surface moves further

Downloaded 04 May 2010 to 171.66.16.33. Redistribution subject to ASME license or copyright; see http://www.asme.org/terms/Terms_Use.cfm

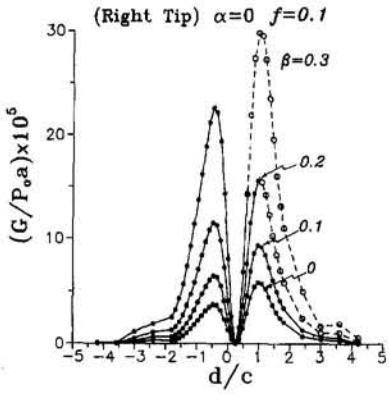


Fig. 11(a)

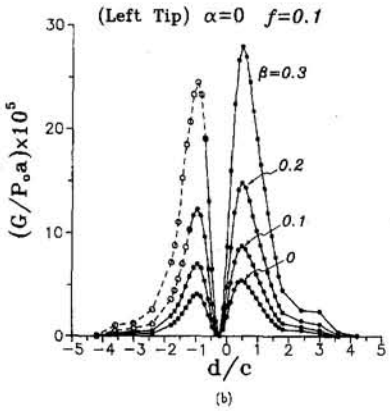


Fig. 11(b)

Fig. 11 Variations of G with *d* for the case $F = 0.1$, $h = c = 2a$; (*a*) right tip, (*b*) left tip

down than the upper crack surface and the right tip is thus open when $\beta > 0$. By using similar arguments we may show that the left tip is closed when $\beta > 0$. When $f = 0$ these arguments are still valid because there are interfacial shear stresses due to bending and these stresses are in the same directions as we discussed above.

For a given value of β, the range of the energy release rate is defined by

$$\Delta G = G_{\max} - G_{\min} \tag{23}$$

where $G_{\max}$ and $G_{\min}$ are, respectively, the maximum and minimum values of G for this β. It may be seen from Figs. 10–11 that the range ΔG increases with β. This means that fatigue resistance is weaker for a crack in an interface with a higher value of β. Therefore, as one may improve wear resistance by using composite materials, surface coatings, or case hardening techniques, these techniques, however, produce a weak interface for fatigue crack growth. Notice that 0.3 is approximately the highest value β can reach when $\alpha = 0$. Hence, it is possible to estimate the degree by which the fatigue resistance may be weakened, because, in all these figures, the value of ΔG in the case $\alpha = 0$ and $\beta = 0.3$ is roughly five times the value of ΔG in homogeneous case (i.e., the case $\alpha = \beta = 0$).

Conclusions

A boundary element technique has been developed to analyze interface cracks in a layered solid. Crack-tip conditions (open or closed) are determined by an iterative procedure so that they are parts of the solutions themselves. Energy release rate is used as the fracture parameter since its value is the same for both open and closed tips. Whenever a crack tip is closed, appropriate boundary conditions for tractions (i.e., Eqs. (11) and (13)) have been imposed on the solutions so that, if both tips are closed, K_2 for the right tip and K_2 for the left tip may correctly have opposite signs. Crack tips with extremely small contact zones may be treated as open tips to avoid numerical difficulties. The correct size of a crack-tip element depends upon β when a crack tip is open. Its value must be determined by comparing the numerical results to known analytical solutions. Results may be seriously erroneous if the correct size is not used.

Energy release rates of an interface crack in a semi-infinite solid are calculated by using the numerical technique developed in this paper. In all the cases we have studied, the near tips are easier to open by the compressive load. A possible explanation is given in this paper. We also find fatigue resistance decreasing with increasing values of β. The value of the energy release rate range ΔG in the case $\alpha = 0$ and $\beta = 0.3$ is approximately five times the value of ΔG in the homogeneous case.

Acknowledgment

We gratefully acknowledge National Science Council of R.O.C., the supporter of this research, under the Grant No. NSC 81-0401-E-032-03. We are also grateful to one reviewer of this paper, who has made many valuable suggestions.

References

Blandford, G. E., Ingraffea, A. R., and Liggett, J. A., 1981, "Two-Dimensional Stress Intensity Factor Computations Using the Boundary Element Method," *International Journal for Numerical Methods in Engineering,* Vol. 17, pp. 387–404.

Clech, J. P., Lewis, J. L., and Keer, L. M., 1986, "A Finite Element Technique for Determining Mode I Stress Intensity Factors: Application to No-Slip Bimaterial Crack Problems," *Computers and Structures,* Vol. 23, No. 6, pp. 715–724.

Comninou, M., 1977a, "The Interface Crack," ASME JOURNAL OF APPLIED MECHANICS, Vol. 44, pp. 631–638.

Comninou, M., 1977b, "Interface Crack with Friction in the Contact Zone," ASME JOURNAL OF APPLIED MECHANICS, Vol. 44, pp. 780–781.

Comninou, M., 1978, "The Interface Crack In a Shear Field," ASME JOURNAL OF APPLIED MECHANICS, Vol. 45, pp. 287–290.

Comninou, M., 1990, "An Overview of Interface Cracks," *Engineering Fracture Mechanics,* Vol. 37, No. 1, pp. 197–208.

Comninou, M., and Schmueser, D., 1979, The Interface Crack in a Combined Tension-Compression and Shear Field, ASME JOURNAL OF APPLIED MECHANICS, Vol. 46, pp. 345–348.

England, A. H., 1965, "A Crack Between Dissimilar Media," ASME JOURNAL OF APPLIED MECHANICS, Vol. 32, pp. 400–402.

Erdogan, F., 1965, "Stress Distributions in Bonded Dissimilar Materials with Cracks," ASME JOURNAL OF APPLIED MECHANICS, Vol. 32, pp. 403–410.

Gautesen, A. K., and Dundurs, J., 1987, "The Interface Crack in a Tension Field," ASME JOURNAL OF APPLIED MECHANICS, Vol. 54, pp. 93–98.

Gautesen, A. K., and Dundurs, J., 1988, "The Interface Crack under Combined Loading," ASME JOURNAL OF APPLIED MECHANICS, Vol. 55, pp. 580–586.

Hutchinson, J. W., Mear, M., and Rice, J. R., 1987, Crack Paralleling the Interface Between Dissimilar Materials, ASME JOURNAL OF APPLIED MECHANICS, Vol. 54, pp. 828–832.

Johnson, K. L., 1985, *Contact Mechanics,* Cambridge University Press, Cambridge, UK.

Keer, L. M., and Bryant, M. D., 1983, "A Pitting Model for Rolling Contact Fatigue," ASME *Journal of Lubrication Technology,* Vol. 105, pp. 198–205.

Keer, L. M., Bryant, M. D., and Haritos, G. K., 1982, Subsurface and Surface Cracking due to Hertzian Contact, ASME *Journal of Lubrication Technology,* Vol. 104, pp. 347–351.

Lee, K. Y., and Choi, H. J., 1988, "Boundary Element Analysis of Stress Intensity Factors for Bimaterial Interface Cracks," *Engineering Fracture Mechanics,* Vol. 29, No. 4, pp. 461–472.

Oden, J. T., and Carey, G. F., 1984, *Finite Elements: Special Problems in Solid Mechanics,* Vol. 5, Prentice-Hall, Englewood Cliffs, N.J.

Raveendra, S. T., and Banerjee, P. K., 1991, "Computation of Stress Intensity Factors for Interface Cracks," *Engineering Fracture Mechanics,* Vol. 40, No. 1, pp. 89–103.

Reynolds, R. R., Kokini, K., and Chen, G., 1990, "The Mechanics of the Interface Crack Using the Finite Element Method," ASME *Journal of Engineering Materials and Technology,* Vol. 112, pp. 38–43.

Rice, J. R., 1988, "Elastic Fracture Mechanics Concepts for Interfacial Cracks," ASME JOURNAL OF APPLIED MECHANICS, Vol. 55, pp. 98–103.

Rice, J. R., and Sih, G. C., 1965, "Plane Problems of Cracks in Dissimilar Media," ASME JOURNAL OF APPLIED MECHANICS, Vol. 32, pp. 418–423.

Downloaded 04 May 2010 to 171.66.16.33. Redistribution subject to ASME license or copyright; see http://www.asme.org/terms/Terms_Use.cfm

Sheppard, S., Barber, J. R., and Comninou, M., 1985, "Short Subsurface Cracks under Conditions of Slip and Stick Caused by a Moving Compressive Load," ASME JOURNAL OF APPLIED MECHANICS, Vol. 52, pp. 811–817.

Sheppard, S., Barber, J. R., and Comninou, M., 1987, "Subsurface Cracks under Conditions of Slip, Stick, and Separation Caused by a Moving Compressive Load," ASME JOURNAL OF APPLIED MECHANICS, Vol. 54, pp. 393–398.

Smelser, 1979, "Evaluation of Stress Intensity Factors for Bi-Material Bodies Using Numerical Flank Displacement Data," *International Journal of Fracture*, Vol. 15, No. 2, pp. 135–143.

Tan, C. L., and Gao, Y. L., 1990, "Treatment of Bimaterial Interface Crack Problems Using the Boundary Element Method," *Engineering Fracture Mechanics*, Vol. 36, No. 6, pp. 919–932.

van der Zande, H. D., and Grootenboer, H. J., 1986, "A Finite Element Approach to Interface Crack," ASME JOURNAL OF APPLIED MECHANICS, Vol. 53, pp. 573–578.

Williams, M. L., 1959, "The Stresses Around a Fault or Crack in Dissimilar Media," *Bulletin of the Seismological Society of America*, Vol. 49, pp. 199–204.

Downloaded 04 May 2010 to 171.66.16.33. Redistribution subject to ASME license or copyright; see http://www.asme.org/terms/Terms_Use.cfm

A. Nagarajan[1]
Research Staff Member,
IBM, Almaden Research Center,
650 Hawy Road,
San Jose, CA

S. Mukherjee
Professor,
Department of Theoretical
and Applied Mechanics,
Cornell University,
Ithaca, NY 14853
Fellow ASME

E. Lutz
1335 Jackson Lane,
West Chester, PA 19380

The Boundary Contour Method for Three-Dimensional Linear Elasticity

This paper presents a novel variant of the boundary element method, here called the boundary contour method, applied to three-dimensional problems of linear elasticity. In this work, the surface integrals on boundary elements of the usual boundary element method are transformed, through an application of Stokes' theorem, into line integrals on the bounding contours of these elements. Thus, in this formulation, only line integrals have to be numerically evaluated for three-dimensional elasticity problems—even for curved surface elements of arbitrary shape. Numerical results are presented for some three-dimensional problems, and these are compared against analytical solutions.

Introduction

The conventional boundary element method, for linear elasticity, requires numerical evaluation of surface integrals for three-dimensional problems (see, for example, Mukherjee, 1982). Nagarajan et al. (1994) in a recent paper have proposed a novel approach, called the boundary contour method, that achieves a further reduction in dimension. The boundary contour method, for three-dimensional linear elasticity problems, only requires numerical evaluation of line integrals over closed contours that lie on the surface of a body. These contours bound the usual surface boundary elements that can be curved, and of arbitrary shape.

Two-dimensional elasticity problems were the focus of Nagarajan et al. (1994). A mathematical formulation for two-dimensional problems, together with numerical results for some examples, was presented there. This formulation converts line integrals from the usual two-dimensional boundary element method to function evaluations at the ends of an interval, thus completely avoiding numerical integration. The more difficult three-dimensional elasticity problem is the focus of the present paper. Here, it is shown how surface integrals from the usual three-dimensional boundary element method can be systematically converted to line integrals.

The main idea in this work is the exploitation of the divergence-free property of the usual boundary element method integrand and a very useful application of Stokes' Theorem, to convert surface integrals on boundary elements to line integrals on closed contours that bound these elements. This idea was originally proposed and applied to the Laplace equation by Lutz (1991) and Lutz et al. (1992). Generalization to linear elasticity has been carried out by Nagarajan et al. (1994) and Lutz (1994). In fact, Nagarajan et al. (1994) have presented a general mathematical proof that demonstrates that linear problems that admit boundary element method formulations have divergence free integrands! This property is intrinsically linked to the way the boundary integral equation is derived for linear problems. Thus, in principle, conversion of surface integrals to line integrals, through application of Stokes' Theorem, is possible for a wide class of linear problems. To date, however, details have only been worked out for problems of potential theory and linear elasticity.

Recent work by Zienkiewicz and his co-workers, on applications of the Trefftz method in boundary elements, should be mentioned here. Jin, Cheung, and Zienkiewicz (1990) have applied the method to planar elasticity problems based on the stress function approach while Cheung, Jin, and Zienkiewicz (1989, 1991) have solved the harmonic and Helmholtz equations, respectively.

In the work on linear elasticity (Jin, Cheung, and Zienkiewicz, 1990), the authors set up a boundary element system of equations in which the weighting and/or trial functions are derived from complete solutions for the stress function in the domain of the body (hence the Trefftz method). This avoids the use of singular kernels in the boundary element method equations. The rest of the treatment follows the usual boundary element method approach in that interpolation functions must be chosen for the boundary element geometries and the physical variables on the boundary, and integrations must be carried out over boundary elements. This work of Zienkiewicz's group is analogous to the present work to the extent that global solutions in the domain of the body are also used in their work. The present work, however, is quite different from Zienkiewicz's group in the sense that the boundary contour method requires no numerical integration at all for two-dimensional problems and only requires numerical evaluation of line integrals for three-dimensional problems.

Other related work for two-dimensional problems, this time using complex variables, is due to Piltner and Taylor (1990) and Lee (1992). In the both cases, the starting point is the use of complex stress and displacement potentials based on the classical work of Muskhelishvili (1963). The complex potentials are represented in terms of basis functions by the Cauchy integral formula. These unknown complex basis functions are discretized on boundary elements and nodal unknowns are solved for by using standard collocation methods. Piltner and Taylor (1990) carry out closed-form integrals of the basis shape functions on straight boundary elements. Lee (1992) realizes that these complex integrals on boundary elements are, in fact, path independent (provided suitable branch cuts are used). Lee's work, however, is based on complex variables theory and is restricted to two-dimensional problems. It should also be mentioned that Watson (1986) has used path independence for

[1] Formerly Graduate Student, Department of Theoretical and Applied Mechanics, Cornell University, Ithaca, NY.

Contributed by the Applied Mechanics Division of THE AMERICAN SOCIETY OF MECHANICAL ENGINEERS for publication in the ASME JOURNAL OF APPLIED MECHANICS.

Discussion on this paper should be addressed to the Technical Editor, Professor Lewis T. Wheeler, Department of Mechanical Engineering, University of Houston, Houston, TX 77204-4792, and will be accepted until four months after final publication of the paper itself in the ASME JOURNAL OF APPLIED MECHANICS.

Manuscript received by the ASME Applied Mechanics Division, May 9, 1994; final revision, Feb. 7, 1995. Associate Technical Editor: W. K. Liu.

Copyright © 1996 by ASME

Downloaded 04 May 2010 to 171.66.16.33. Redistribution subject to ASME license or copyright; see http://www.asme.org/terms/Terms_Use.cfm

singular real integrals in two-dimensional fracture problems. The present paper uses real variables for three-dimensional problems.

The outline of this paper is as follows. First, the basic theory is presented to show that three-dimensional boundary element method surface integrals can be converted to contour integrals through the use of Stokes' theorem. This requires the determination of certain potential functions corresponding to the usual boundary element method integrand which contains the unknown displacements ($\mathbf{u}$) and tractions (τ). Thus, shape functions for $\mathbf{u}$ and $\boldsymbol{\tau}$ must be chosen in global coordinates and potential functions derived for each linearly independent shape function. Discussion of these shape functions and formulation of suitable boundary elements constitutes the next two sections of the paper. This is followed by the actual derivation of the potential functions. Once these functions are derived, it is possible to replace the boundary element method equations with boundary contour method equations involving only contour integrals. The unknowns at this stage, called artificial variables, can be related to primary physical variables through a transformation matrix T. This step, discussed in the section entitled "Numerical Implementation," results in significant condensation of the resulting linear algebraic system. This condensed system is solved in order to obtain the unspecified primary physical variables on the surface of the body. Secondary physical variables are then obtained as a post-processing step. The next section presents a method for determination of stresses throughout the body. This is followed by a presentation of numerical results for some example problems involving cubes and rectangular slabs with elliptical cutouts. Finally, some conclusions are drawn.

The Basic Theory

The starting point is the standard boundary element method formulation due to Rizzo (1967), which can be written as (with range of indices 1, 2, 3)

$$c_{ik}(P)u_i(P) = \int_{\partial B} [U_{ik}(P, Q)\sigma_{ij}(Q) - \Sigma_{ijk}(P, Q)u_i(Q)]\mathbf{e}_j \cdot d\mathbf{S}. \quad (1)$$

Rewriting the vector in the integrand of Eq. (1) as $\mathbf{F}_k$, one gets

$$c_{ik}(P)u_i(P) = \int_{\partial B} \mathbf{F}_k \cdot d\mathbf{S}. \quad (2)$$

Here, ∂B is the bounding surface of a body B with the infinitesimal surface area $d\mathbf{S} = dS\mathbf{n}$, where $\mathbf{n}$ is the unit outward normal to ∂B at a point on it. The stress tensor is $\boldsymbol{\sigma}$ and $\mathbf{e}_j$ ($j = 1, 2, 3$) are global Cartesian unit vectors. The corner tensor is denoted by $\mathbf{c}$. The boundary element method Kelvin kernels are written in terms of (boundary) source points P and field points Q. These are

$$-\Sigma_{ijk} = \frac{1}{8\pi(1-\nu)r^2}[(1-2\nu)(r_{,i}\delta_{jk} + r_{,j}\delta_{ik} - r_{,k}\delta_{ij}) + 3r_{,i}r_{,j}r_{,k}] \quad (3)$$

$$U_{ik} = \frac{1}{16\pi\mu(1-\nu)r}[(3-4\nu)\delta_{ik} + r_{,i}r_{,k}], \quad (4)$$

in terms of r, the Euclidean distance between P and Q, and the shear modulus μ and Poisson's ratio ν of the isotropic elastic solid. Also, $\boldsymbol{\delta}$ is the Kronecker delta and ($_{,i} = \partial/(\partial x_i(Q))$).

The first task is to show that $\mathbf{F}_k$, in Eq (2), is divergence-free. Writing in component form,

$$\mathbf{F}_k = F_{jk}\mathbf{e}_j = (\sigma_{ij}U_{ik} - \Sigma_{ijk}u_i)\mathbf{e}_j.$$

Taking the divergence of the above at a field point Q,

$$(\nabla_Q \cdot \mathbf{F}_k) = F_{jk,j} = (\sigma_{ij}E_{ijk} - \Sigma_{ijk}\epsilon_{ij}) + (\sigma_{ij,j}U_{ik} - \Sigma_{ijk,j}u_i) \quad (5)$$

where the Kelvin strain tensor $\mathbf{E}$ and the strain field $\boldsymbol{\epsilon}$ are

$$E_{ijk} = \tfrac{1}{2}(U_{ik,j} + U_{jk,i})$$

and

$$\epsilon_{ij} = \tfrac{1}{2}(u_{i,j} + u_{j,i}). \quad (6)$$

Let $(\mathbf{u}, \boldsymbol{\sigma})$ correspond to a body force free elastostatic state with the same elastic constants as the Kelvin solution. The stress and strain tensors σ_{ij} and ϵ_{ij}, respectively, are related to each other by the usual Hooke's law. The corresponding Kelvin stress and strain tensors Σ_{ijk} and E_{ijk}, respectively, are related by Hooke's law in exactly the same manner (see, for example, Mukherjee, 1982). As a consequence, the first expression on the right-hand side of Eq. (5) vanishes. Also, equilibrium, in the absence of body forces, demands that σ_{ij} be divergence-free. The corresponding Kelvin stress tensor Σ_{ijk} is also divergence-free, except at the point of singularity. Therefore, the second expression on the right-hand side of Eq. (5) also vanishes everywhere, except at the point of singularity. Thus, $\mathbf{F}_k$ in Eq. (5) is divergence-free.

The above property demonstrates the existence of vector potential functions $\mathbf{V}_k$ (Kaplan, 1984) such that

$$\mathbf{F}_k = \nabla \times \mathbf{V}_k. \quad (7)$$

As a consequence of Eq. (7), the surface integral in Eq. (2), over any open surface patch $S \in \partial B$, can be converted into a contour integral around the bounding curve C of S, by applying Stokes' theorem, i.e.,

$$\int_S \mathbf{F}_k \cdot d\mathbf{S} = \oint_C \mathbf{V}_k \cdot d\mathbf{r}. \quad (8)$$

In subsequent sections, S will be chosen to be a boundary element. Note that $\mathbf{F}_k$ contains the unknown fields $\mathbf{u}$ and $\boldsymbol{\sigma}$. Thus, shape functions must first be chosen for these variables and potential functions determined for each linearly independent shape function. This is done in the next few sections of this paper.

Shape Functions

The shape functions for $\mathbf{u}$ and $\boldsymbol{\tau}$, in this work, are somewhat unusual. As mentioned above (see Eq. (8)), $\mathbf{F}_k$ contains the unknown fields $\mathbf{u}$ and $\boldsymbol{\tau}$, and the potentials $\mathbf{V}_k$ must be found for each $\mathbf{F}_k$ in global coordinates. Thus, one must start with shape functions in global coordinates. In order for the surface to contour integral conversion (Eq. (8)) to be valid in general, the shape functions for $\mathbf{u}$ must satisfy, a priori, the Cauchy-Navier equations:

$$\nabla^2\mathbf{u} + \frac{1}{1-2\nu}\nabla(\nabla \cdot \mathbf{u}) = \mathbf{0} \quad (9)$$

and the shape functions for $\boldsymbol{\tau}$ must be derived from those of $\mathbf{u}$ using the kinematic equations, Hooke's law and the equation $\boldsymbol{\tau} = \boldsymbol{\sigma} \cdot \mathbf{n}$, i.e.,

$$\tau_i = [\lambda u_{k,k}\delta_{ij} + \mu(u_{i,j} + u_{j,i})]n_j \quad (10)$$

where λ and $G = \mu$ are Lamé constants for the material. Finally, piecewise functions are employed in the sense that $\mathbf{u}$ and $\boldsymbol{\tau}$ are written as linear combinations of the above shape functions, with constants that are particular to each boundary element.

A linear shape function of the form

$$\mathbf{u} = (a_i + b_i x + c_i y + d_i z)\mathbf{e}_i \quad (11)$$

Downloaded 04 May 2010 to 171.66.16.33. Redistribution subject to ASME license or copyright; see http://www.asme.org/terms/Terms_Use.cfm

in which a_i, b_i, c_i, and d_i are constants, x, y, and z are global Cartesian coordinates, trivially satisfies Eq. (9). In this paper, a shape function consisting of constant and first-degree terms will be referred to as a linear shape function. A shape function consisting of a linear term and second degree terms will be called a quadratic shape function.

All second-degree functions, of course, do not satisfy Eq. (9). When a function of the form

$$\mathbf{u} = (l_i x^2 + m_i y^2 + p_i z^2 + q_i xy + r_i yz + s_i xz)\mathbf{e}_i \quad (12)$$

with 18 constants, is substituted into Eq. (10), three scalar equations relating the various constants result. These equations can be used to eliminate three constants leaving $(18 - 3) = 15$ independent constants. Thus, there are 15 linearly independent second-degree shape functions that satisfy Eq. (9). A linear combination of these, together with the linear shape functions given by Eq. (11), make up the quadratic shape function for $\mathbf{u}$. This has a total of 27 independent constants.

Constructing second-degree shape functions by direct elimination can be cumbersome for three-dimensional problems. Fortunately, most of the second-degree shape functions for three-dimensional problems can be constructed from two-dimensional plane-strain shape functions (Nagarajan, 1994). Using this approach, one gets four shape functions for $\mathbf{u} = (u_1, u_2, u_3)$ as

$$(1)\quad (x^2, -4(1-\nu)xy, 0), \quad (2)\quad (y^2, -2(1-2\nu)xy, 0)$$

$$(3)\quad (-2(1-2\nu)xy, x^2, 0), \quad (4)\quad (-4(1-\nu)xy, y^2, 0).$$

By cyclically permuting x, y, and z and the three (global) Cartesian basis vectors, two more sets of four second-degree shape functions are obtained. This accounts for 12 out of 15 second-degree shape functions. The remaining three can be got by inspection by choosing functions that satisfy both $\nabla^2\mathbf{u} = \mathbf{0}$ and $\nabla \cdot \mathbf{u} = 0$. These functions are $(yz, 0, 0)$, $(0, xz, 0)$ and $(0, 0, xy)$. The complete list of shape functions is given in the Appendix. The important issue of linear independence of these shape functions will be addressed later in this paper.

The quadratic shape function is a linear combination of 27 shape functions. The constants of a linear combination are denoted by β_l, $l = 1, \ldots, 27$. The shape functions are numbered in the order they are mentioned: $(l = 1, 2, 3)$ correspond to the constant shape functions, $(l = 4, \ldots, 12)$ correspond to the first-degree shape functions and $(l = 13, \ldots, 27)$ correspond to the second-degree shape functions (see the Appendix). The ith component of the lth shape function is denoted by u_{li}, $l = 1, \ldots, 27$. σ_{lij} will have a similar meaning (Hooke's Law is used to obtain σ_{lij} from u_{li}). This notation leads to the following compact representation for the quadratic shape function for $\mathbf{u}$:

$$\mathbf{u} = \beta_l u_{li}\mathbf{e}_i \quad l = 1, \ldots, 27. \quad (13)$$

Derivation of higher order shape functions by direct elimination can be algebraically complicated. A simpler approach might be to start from polynomial solutions to the three-dimensional Laplace equation which are readily available (e.g., Kellogg, 1929). The Papkovitch-Neuber potentials relate solutions of the three-dimensional Cauchy-Navier equations of elasticity (Eq. (9)) to those of the three-dimensional Laplace equation. Hence, Papkovitch-Neuber potentials can be used to derive polynomial solutions of the elasticity equations from those of Laplace's equation.

Another interesting observation is the following. Let $u(x, y, z)$ be a function which is locally smooth in the neighborhood of the point (x_0, y_0, z_0) and satisfies the Cauchy-Navier equations. Now, a Taylor expansion of $u(x, y, z)$ about (x_0, y_0, z_0) will be a linear combination of the boundary contour method shape functions. As a direct consequence, a second-order shape function in the boundary contour method (which is a linear combination of all solutions of degree ≤ 2) is equivalent to considering the first three terms of the Taylor expansion of $u(x, y, z)$ about (x_0, y_0, z_0). As a simple illustration of the above, consider Laplace's equation in two dimensions. The second-degree terms of a Taylor expansion of $u(x, y)$ about $(0, 0)$ is of the form

$$u_{xx}(0, 0)\frac{x^2}{2!} + u_{yy}(0, 0)\frac{y^2}{2!} + u_{xy}(0, 0)xy.$$

In view of the fact that $u(x, y)$ is harmonic, $u_{xx}(0, 0) = -u_{yy}(0, 0)$, so that one gets the linearly independent boundary contour method second-degree shape functions

$$x^2 - y^2 \quad \text{and} \quad xy.$$

Boundary Elements

Primary and Secondary Physical Variables. In the usual boundary element method, the displacements and tractions at each boundary node are primary boundary variables. The boundary contour method, described in this paper, can also be used to solve any well-posed problem in linear elasticity, with traction and displacement components given as boundary conditions in the usual way. However, a departure from the usual boundary element method is that a set of primary physical variables are first chosen at appropriate points on a boundary element. Some of these would be specified as boundary conditions and the rest would be unknown in a given problem. The first step in the boundary contour method solution procedure is to determine the values of appropriate variables that are not specified as boundary conditions. Once all the primary physical variables are known, the rest of the physical variables (the secondary ones), are obtained as a postprocessing step.

Three Boundary Elements. Three possible choices of boundary elements (in general, they can be curved) appear in Fig. 1. The first one (Fig. 1(*a*)), called CI4, has displacements as primary variables at the corner nodes C_1, C_2, and C_3, while the traction is the primary physical variable at an interior node I. Quadratic elements for $\mathbf{u}$, called CI6 and CIM9, are shown in Figs. 1(*b*) and 1(*c*), respectively.

The CI6 element has been used in the numerical implementation of the boundary contour method in this work. This element is described first. Here, the displacement $\mathbf{u}$ is the primary physical variable at all the six nodes, the corner nodes C_i and the interior nodes I_i $(i = 1, 2, 3)$. The traction τ is a primary physical variable at the interior nodes I_i. Thus, there are a total of 27 scalar components of primary physical variables that matches β_l, $l = 1, \ldots, 27$ (called artificial variables) in Eq.

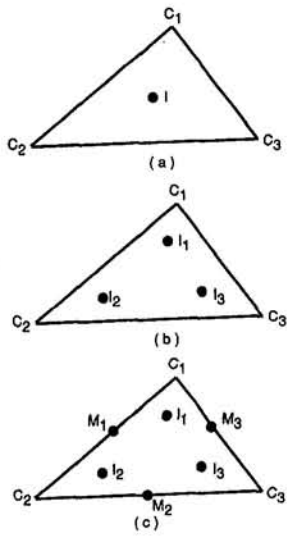


Fig. 1 Boundary elements: (*a*) CI4, (*b*) CI6, (*c*) CIM9

Downloaded 04 May 2010 to 171.66.16.33. Redistribution subject to ASME license or copyright; see http://www.asme.org/terms/Terms_Use.cfm

(13). This equality is crucial for invertibility of a certain transformation matrix, as will be seen later.

The interior nodes capture the geometry of the surface. This is important, since the boundary integral is evaluated only around the bounding contour of the boundary element. The CI6 element enforces inter-element continuity of **u** at the corner nodes only. A significant advantage of this element is that physical corners on the surface of a body can be modeled easily since only displacements appear as primary variables on the boundary of the element. Thus, one does not have to explicitly model traction jumps across elements.

In the CIM9 element shown in Fig. 1(*c*), **u** is again a primary physical variable at six nodes, the three corner nodes C_i and the three midside nodes M_i; while tractions are primary physical variables at the internal nodes I_i. Again, there are 27 scalar primary physical variables. This element has the advantage of enforcing continuity of **u** across the midside nodes also.

In general, the number of primary physical variables that can be assigned on an element is decided by the order of the shape function. This issue is discussed rigorously in Chapter 4 of Nagarajan (1994) (see, also, the Section "Invertibility of the T matrix . . ." later in the present paper).

As mentioned before, the number of primary physical variables on an element matches the number of artificial variables. These are related through a transformation matrix T as follows:

$$\{p\} = [T]\{\beta\} \tag{14}$$

where, for the CI6 element, **p** is a column vector consisting of the 18 displacement components and 9 traction components and β is a column vector consisting of the 27 constants (β_is) of the linear combination of shape functions. Clearly, T is a square matrix. The invertibility of this matrix on planar elements is discussed in a subsequent section.

Equations and Unknowns. The boundary element method equations are enforced at all the nodes on a CI6 element. It is discussed next how, at the element level, such a situation generally leads to an overdetermined system of linear equations for this element, with a sufficient number of equations always guaranteed.

Let the vertices C_1, C_2, and C_3 of the CI6 element be shared by p, q, and r elements each, respectively. Now, in an "average" sense per element, one has

number of primary physical variables/element = $3 \times 6 + 3/p + 3/q + 3/r$,
number of boundary element method equations/element = $3 \times 3 + 3/p + 3/q + 3/r$,
number of boundary conditions = b, where
for a displacement specified problem, $b = 9 + 3/p + 3/q + 3/r$, and
for a traction specified problem, $b = 9$.

It should be noted here that a problem with only tractions prescribed on the boundary of a body is not well posed, since rigid-body motion would not be eliminated in this case. Of course, one could have certain elements with only tractions prescribed on them.

In general, $9 \leq b \leq 9 + 3/p + 3/q + 3/r$ so that one has a sufficient number of equations. Generally, for a boundary contour method formulation with this element, the number of equations exceeds the number of unknowns.

This completes a discussion of a count of equations and unknowns at the element level. A count at a global level, for an example problem of a cube, appears in a later section on numerical implementation.

Invertibility of the T Matrix on Planar Elements. In this section, the invertibility of the transformation matrix T in Eq. (14) is examined for planar elements. Using this, it is shown indirectly that the solutions which make up the quadratic shape function are linearly independent.

For this purpose, one considers a planar element which lies on the xy-plane and whose normal is in the positive z-direction. On this element, **u** is a function of x and y only. For the sake of clarity, the idea behind the proof will be explained using the second-degree part of the shape function. On this element, since $z = 0$, the second-degree parts of the three displacement components are (see the Appendix),

$$\begin{aligned} u_1 &= (\beta_{13} + \beta_{24})x^2 + \beta_{14}y^2 + (\beta_{15}k_2 + \beta_{16}k_1)xy \\ u_2 &= (k_1\beta_{13} + k_2\beta_{14})xy + \beta_{15}x^2 + (\beta_{16} + \beta_{17})y^2 \\ u_3 &= \beta_{22}x^2 + \beta_{19}y^2 + \beta_{27}xy \end{aligned} \tag{15}$$

where the constants k_1 and k_2 are $-4(1 - \nu)$ and $-2(1 - 2\nu)$, respectively. It is evident that the three functions in Eq. (15) are linearly independent since the constants multiplying the x^2, y^2, and xy terms are independent (k_1 and k_2 should be nonzero; this is true if ν is less than 0.5). It should be noted that only 9 of the 15 constants appear in these expressions. The remaining six should be captured by tractions for the matrix T to be invertible. This is, in fact, the case as shown below.

The tractions can be derived as usual (see Eq. (10)) from the second-degree shape functions for **u**. These are

$$\begin{aligned} \tau_1 &= \beta_{23}k_1\mu x + 4\beta_{18}k_1\mu y + \ldots \quad \tau_2 = \beta_{14}\mu x + 4\beta_{20}\mu y + \ldots \\ \tau_3 &= \beta_{23}k_1\mu x + 4\beta_{18}k_1\mu y + \ldots \end{aligned} \tag{16}$$

where the terms multiplying the constants already present in Eq. (15) have been dropped. Clearly, the six constants not present in Eq. (15) are captured by the tractions. It is easy to see that a second-degree shape function for **u** reduces to a locally second-order approximation for **u** and a first-order approximation for $\boldsymbol{\tau}$ on a planar element. This result does not hold for curved elements, since x and y then become dependent on each other. However, many elements in practice are planar or nearly planar and results derived for planar elements can be useful pointers to the robustness of shape functions and elements. Proceeding along similar lines, it can be shown that a linear shape function for **u** is equivalent to a locally linear approximation for **u** and constant approximation for $\boldsymbol{\tau}$ on planar elements.

To ensure invertibility of the matrix T, when a quadratic shape function is used for **u**, tractions should be specified on three noncollinear points and displacements on six points not lying on an ellipse, parabola, hyperbola, or a pair of straight lines. This is normally ensured for the CI6 element by choosing three points to be the vertices of a triangle and the remaining three to be three noncollinear interior points. For the CIM9 element, one chooses three vertices of a triangle, three midside nodes, and three noncollinear interior points (see Fig. (1)). Also, the number of tractions or displacements that can be chosen on an element is fixed since, for example, specifying traction at a fourth point on the element would lead to a singular transformation matrix T on a planar element.

Since displacements and tractions uncouple on a planar element, certain terms can be dropped if necessary from the original set of shape functions. This enables one to use the well-developed theory of Vandermonde matrices and Lagrangian interpolation functions that are widely used in the finite element method.

Considering a planar element is also useful in checking the linear independence of the shape functions. This can be easily verified by substituting $x = 0$ and $y = 0$ in the shape functions (in Eq. (15)), in turn, and by observing that the resulting **u**s are linearly independent. This cyclic substitution ensures that all shape functions are covered while checking for linear independence.

Downloaded 04 May 2010 to 171.66.16.33. Redistribution subject to ASME license or copyright; see http://www.asme.org/terms/Terms_Use.cfm

Potential Functions

A local coordinate system (x_1, x_2, x_3), centered at a source point, is first introduced. The global base vectors $\mathbf{e}_i$, $i = 1, 2, 3$, remain as the base vectors for the local system.

The shape functions in the Appendix, expressed in the global coordinate system, can be converted into the local coordinates by the substitution $x = x_0 + x_1$; $y = y_0 + x_2$; $z = z_0 + x_3$ where (x_0, y_0, z_0) are the coordinates of the source point with respect to global coordinates. Translation merely changes the constants of the linear combination; it leaves the form of the shape functions intact. For example, $u_1 = yz$ becomes $u_1 = x_2x_3 + x_2z_0 + y_0x_3 + y_0z_0$. The resulting first-degree functions can be combined with the linear part of the shape function. The new constants of the linear combination are related to the original ones through x_0, y_0, and z_0.

Potentials for Nonsingular Functions. The homogeneous nature of the Kelvin kernels are exploited in deriving the potential functions. From Eqs. (3) and (4), it is clear that both $\mathbf{\Sigma}_{ijk}$ and U_{ik} are ratios of homogeneous polynomials and are therefore homogeneous. Here, $\mathbf{\Sigma}$ is of degree -2 and $\mathbf{U}$ is of degree -1. If a shape function is of degree α, then the resulting vector $\mathbf{F}_{lk}$ is of degree $(\alpha - 2)$. In this work, shape functions with $\alpha = 0$, 1 and 2 are used (see the Appendix). Here, the vector $\mathbf{F}_{lk}$ denotes the vector in Eq. (2), $\mathbf{F}_k$, corresponding to the lth shape function ($l = 1, \ldots, 27$).

The above fact regarding Kelvin kernels facilitates the use of an inversion integral to calculate the inverse curl of a given vector field of zero divergence (Kaplan, 1982). Thus, if $\mathbf{F}_{lk} = \nabla \times \mathbf{V}_{lk}$,

$$\mathbf{V}_{lk} = \left[\int_0^1 t\mathbf{F}_{lk}(tx_1, tx_2, tx_3)dt \right] \times \mathbf{r} \tag{17}$$

where $\mathbf{V}_{lk}$ is the potential corresponding to $\mathbf{F}_{lk}$. Because of the homogeneous nature of $\mathbf{F}_{lk}$,

$$\mathbf{F}_{lk}(tx_1, tx_2, tx_3) = t^{\alpha-2}\mathbf{F}_{lk}(x_1, x_2, x_3). \tag{18}$$

This makes the evaluation of integrals in Eq. (17), for the case $\alpha \neq 0$, straightforward. For $\alpha \neq 0$,

$$\mathbf{V}_{lk} = \frac{1}{\alpha}\mathbf{F}_{lk}(x_1, x_2, x_3) \times \mathbf{r}. \tag{19}$$

This means that, for every shape function, once the vector $\mathbf{F}_{lk}$ is constructed, it is easy to derive the vector potential $\mathbf{V}_{lk}$ as long as α is not equal to zero!

The case $\alpha = 0$, predictably, corresponds to the constant displacement shape functions. This is the singular case and has to be treated in a different manner.

Potentials for the Singular Case. This case is dealt with in detail in Ghosh and Mukherjee (1987). The discussion below summarizes and expands upon the results given in the above paper. Now $u_{li} = \delta_{li}$ for the singular case ($l = 1, 2, 3$) since $\mathbf{u} = (1, 0, 0)$ for $l = 1$, $\mathbf{u} = (0, 1, 0)$ for $l = 2$ and $\mathbf{u} = (0, 0, 1)$ for $l = 3$. Now, in general, from Eqs. (1), (2):

$$\mathbf{F}_{lk} = [U_{ik}(P, Q)\sigma_{lij}(Q) - \mathbf{\Sigma}_{ijk}(P, Q)u_{li}(Q)]\mathbf{e}_j \tag{20}$$

where the additional subscript l, as stated before, denotes the lth shape function.

Substituting $u_{li} = \delta_{li}$ and $\sigma_{lij} = 0$ into Eq. (20), one gets

$$\mathbf{S}_{lk} = -\mathbf{\Sigma}_{ijk}\delta_{li}\mathbf{e}_j = -\mathbf{\Sigma}_{ljk}\mathbf{e}_j \tag{21}$$

where $\mathbf{S}_{lk}$, $l = 1, 2, 3$, are vectors corresponding to the singular states. The right-hand side of Eq. (21) can be expanded using Eqs. (3), (4) to give

$$\mathbf{S}_{lk} = \frac{1}{8\pi(1-\nu)r^2}[(1-2\nu)(r_{,l}\delta_{jk} + r_{,j}\delta_{lk} - r_{,k}\delta_{lj}) + 3r_{,l}r_{,j}r_{,k}]\mathbf{e}_j. \tag{22}$$

Rearranging terms,

$$\mathbf{S}_{lk} = f(r)[2(1-\nu)r_{,j}\delta_{lk} + (3r_{,l}r_{,j}r_{,k} - r_{,j}\delta_{lk}) + (1-2\nu)(r_{,l}\delta_{jk} - r_{,k}\delta_{lj})]\mathbf{e}_j, \tag{23}$$

where $f(r) = 1/(8\pi(1-\nu)r^2)$. In the above equation, it can be easily shown that each of the three terms, $f(r)(r_{,j}\delta_{lk})\mathbf{e}_j$, $f(r)(3r_{,l}r_{,j}r_{,k} - r_{,j}\delta_{lk})\mathbf{e}_j$ and $f(r)(r_{,l}\delta_{jk} - r_{,k}\delta_{lj})\mathbf{e}_j$ have zero divergence. Therefore, each term can be written as the curl of a vector.

It can be shown by index manipulation that

$$8\pi(1-\nu)f(r)(3r_{,l}r_{,j}r_{,k} - r_{,j}\delta_{lk})\mathbf{e}_j = \nabla \times \epsilon_{kmj}\frac{r_{,l}r_{,m}}{r}\mathbf{e}_j$$

$$8\pi(1-\nu)f(r)(r_{,l}\delta_{jk} - r_{,k}\delta_{lj})\mathbf{e}_j = \nabla \times \epsilon_{lkm}\frac{\mathbf{e}_m}{r} \tag{24}$$

where the ϵ_{ijk} are the components of the alternating tensor. The remaining term, i.e., $(r_{,j}/4\pi r^2)\delta_{lk}\mathbf{e}_j$ has to be handled carefully. It is a well-known fact in solid geometry (Kellogg, 1929) that

$$\int_S \frac{r_{,j}}{r^2}\mathbf{e}_j \cdot d\mathbf{S} = \Theta \tag{25}$$

where Θ is the solid angle subtended at the source point by the open surface S. This solid angle term accounts for the left-hand side of the Eq. (1) (in two dimensions, one gets a corresponding planar angle term). If integration is carried out over the whole surface, this solid angle term yields 2π or 4π depending on whether the source point is on or inside the domain (defined by the whole surface), respectively.

It should be noted that the solid angle term does not depend on the values of l and k when $l = k$ and is zero when $l \neq k$. The solid angle Θ, subtended by a surface patch S at a source point, can be written as a contour integral on its bounding contour C as (Lutz, 1994):

$$\Theta = \oint_C \frac{x_3}{r}\left[\frac{x_2}{x_1^2 + x_2^2}\mathbf{e}_1 - \frac{x_1}{x_1^2 + x_2^2}\mathbf{e}_2\right] \cdot d\mathbf{r}. \tag{26}$$

This formula holds only for surface elements through which the x_3-axis does not pass (see Lutz, 1994). This problem, if it occurs, can be circumvented in numerical implementation by considering cyclic permutations of the above equation, i.e.,

$$\Theta = \oint_C \frac{x_1}{r}\left[\frac{x_3}{x_2^2 + x_3^2}\mathbf{e}_2 - \frac{x_2}{x_2^2 + x_3^2}\mathbf{e}_3\right] \cdot d\mathbf{r}$$

$$\Theta = \oint_C \frac{x_2}{r}\left[\frac{-x_3}{x_1^2 + x_3^2}\mathbf{e}_1 + \frac{x_1}{x_1^2 + x_3^2}\mathbf{e}_3\right] \cdot d\mathbf{r}. \tag{27}$$

Finally, putting all of the above together and choosing an appropriate expression for Θ from the three above, the discretized form of the Eq. (1), which will be used in numerical implementation, can be written as

$$\sum_{m=1}^{N} \oint_{C_m} \sum_{l=1}^{27} \beta_l^m \mathbf{V}_{lk} \cdot d\mathbf{r} = c_{ik}u_i \tag{28}$$

where N is the total number of elements on the discretized surface of the three-dimensional body and C_m is the bounding contour of each surface element. The constant β_l^i is the value of β_l on the ith (surface) boundary element.

For $l = 4, \ldots, 27$, the line integrals are evaluated numerically over all element sides and contour integrals over elements are

Downloaded 04 May 2010 to 171.66.16.33. Redistribution subject to ASME license or copyright; see http://www.asme.org/terms/Terms_Use.cfm

obtained by adding the appropriate line integrals. For $l = 1, 2, 3$ (the singular case), contour integrals for each element have to be evaluated separately, since different vector potentials might have to be used for different elements.

Numerical Implementation

Primary Physical Variables on ∂B. For the sake of illustration, consider a displacement boundary value problem on a cubic body as shown in Fig. (2*a*). The discretized cubic faces are shown in Fig. (2*b*). The cube is discretized into 12 CI6 elements, two per face. There are eight corner nodes and 36 internal nodes (three per element).

The discretized form given by Eq. (28) is enforced at all nodes and this leads to a system of linear algebraic equations. The β_m^l are the unknowns at this stage. The resulting linear system consists of a rectangular matrix which is made up of the integrals of shape functions over each element. This rectangular matrix multiplies an unknown column vector $\{\beta\}$ consisting of all the β_l of each element. The right-hand side will consist of the contributions due to the $c_{ik}u_i$ of Eq. (28). Denoting the matrix by A, and the column vectors by $\{\beta\}$ and $\{b\}$, respectively, the final system can be written as

$$[A]\{\beta\} = \{b\}. \tag{29}$$

In this particular example, A has 132 rows and 324 columns (number of rows = number of nodes × 3; number of columns = number of elements × 27). Now, the artificial variables in $\{\beta\}$ are converted into primary physical variables using the transformation matrix T in Eq. (14). The resulting system is condensed to reflect the continuity of displacement across corner nodes. At this stage, the boundary conditions are enforced. These two operations greatly reduce the size of the matrix (specifically, the number of columns). In this particular example,

total number of displacement components = (8 × 3 + 36 × 3) = 132,
(8 corner nodes and 36 internal nodes),
total number of traction components = 36 × 3 = 108,
total number of primary physical variables = 132 + 108 = 240,
total number of boundary conditions = 132 (all displacement components), and
total number of boundary element method equations = (8 × 3 + 36 × 3) = 132.

Referring back to the section "Boundary Elements," please note that in the cube example, $p = 6$, $q = 4$, and $r = 4$ for an element. Thus, there are 20 primary physical variables per CI6 element, giving a total of 240. The number of boundary conditions in this displacement prescribed boundary value problem is 11 per element giving a total of 132. The total number of boundary element method equations is also 11 per element, giving a total of 132. Thus, there are 24 more equations than unknowns. This difference decreases if, instead of displacements, tractions are specified on parts of the boundary. For a traction boundary value problem, the resulting system is square! (Of course, a traction boundary value problem is singular because of unrestricted rigid-body displacements.)

The condensed system of (usually overdetermined but consistent) linear equations is solved in order to obtain the unspecified primary physical variables. At this stage, together with the boundary conditions, all the primary physical variables on the surface of the body are determined.

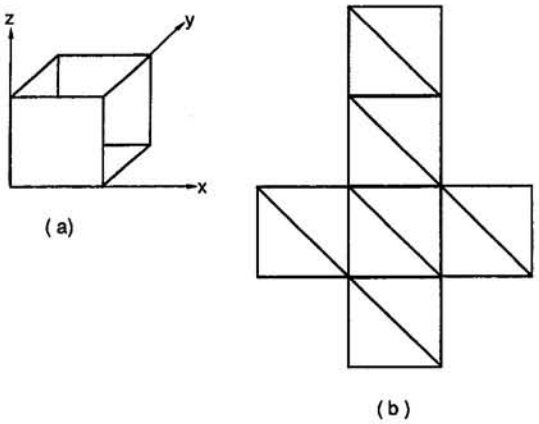


Fig. 2 Discretization of a cube

Secondary Physical Variables on ∂B. There are secondary physical variables, for example the tractions at the corner nodes of a CI6 element, that have not figured in the calculations so far. These quantities, however, are easily calculated at a postprocessing step. One first uses Eq. (14) to obtain the artificial variables β_l (at the element level) from the primary physical variables p_l. Once the β_l are known, the unknown tractions are easily obtained, for each element, through the shape functions (Eq. (13)) and Eq. (10).

Determination of Stresses

Boundary Stresses. In this formulation, boundary stresses can be obtained directly from the displacement shape functions using Hooke's law

$$\sigma_{ij} = \lambda u_{k,k}\delta_{ij} + \mu(u_{i,j} + u_{j,i}) \tag{30}$$

where λ and $G = \mu$ are the usual Lame's constants. This is justified since the shape function for **u** are valid not just on an element, but in its neighborhood as well. Also, tractions have been derived based on this assumption (Eq. (10)). However, the numerical accuracy of stresses near the bounding contour of an element may deteriorate, since **u** is only continuous across the corner nodes of contiguous elements. This difficulty can possibly be overcome by employing Eq. (30) only at the internal nodes I_i of the CI6 element (Fig. 1) and extrapolating to other points on the elements if necessary.

Internal Stresses. If the components of the displacement gradient tensor are known, stresses can be determined easily by using Eq. (30). The boundary element method equation for the derivatives of displacement components is the differentiated form of Eq. (1). The differentiation is carried out with respect to the source point. Writing

$$\frac{\partial u_i(P)}{\partial x_m(P)} = u_{i,M},$$

the differentiated form of the Equation (1) can be written as

$$u_{k,M}(p) = \int_{\partial B} [U_{ik,M}(p, Q)\sigma_{ij}(Q) - \Sigma_{ijk,M}(p, Q)u_i(Q)]\mathbf{e}_j \cdot d\mathbf{S} \tag{31}$$

(where p is a source point inside the body B) since, at an internal point, $c_{ik} = \delta_{ik}$. Using the identity $r_{,M} = -r_{,m}$, the differentiated kernels in Eq. (30) can be converted into field point derivatives, i.e.,

$$U_{ik,M} = -U_{ik,m} \quad \Sigma_{ijk,M} = -\Sigma_{ijk,m}. \tag{32}$$

These differentiated kernels can be found, for example, in Mukherjee (1982). Introducing, again, the index l ($l = 1, \ldots, 27$), which, as before, denotes the shape function number, the vector $\mathbf{F}_{lkm}$ can be directly obtained from Eq. (31) as

Downloaded 04 May 2010 to 171.66.16.33. Redistribution subject to ASME license or copyright; see http://www.asme.org/terms/Terms_Use.cfm

$$\mathbf{F}_{lkm}(p, Q) = [-U_{ik,m}(p, Q)\sigma_{lij}(Q) + \Sigma_{ijk,m}(p, Q)u_{li}(Q)]\mathbf{e}_j. \quad (33)$$

It is easy to verify that $\mathbf{F}$ is divergence-free.

As in the regular problem, the inverse curl of $\mathbf{F}_{lkm}$ has to be found. Fortunately, the differentiated Kelvin kernels are also homogeneous in nature and differentiation reduces their degree by one. Equation (19) can be used again, but, in this case, $\mathbf{F}_{lkm}$ is of degree $\alpha - 3$ if a shape function is of degree α. Since

$$\int_0^1 t^{(\alpha-2)}dt = \frac{1}{\alpha - 1},$$

the singular case $\alpha = 1$ has to be handled separately. This corresponds to the first-degree shape functions (linear displacements and constant stresses), i.e., $l = 4, 12$ (see the Appendix). This is not surprising since the derivative of u_i appears in the stress equation.

To handle the singular case, Eq. (33) has to be rewritten using the product rule as

$$\mathbf{F}_{lkm}(p, Q) = [-U_{ik}(p, Q)\sigma_{lij}(Q) + \Sigma_{ijk}(p, Q)u_{li}(Q)]_{,m}\mathbf{e}_j - \Sigma_{ijk}(p, Q))u_{li,m}(Q)\mathbf{e}_j. \quad (34)$$

This makes use of the fact that $\sigma_{lij,m} = 0$ for the singular case. $\mathbf{F}_{lkm}$ given by Eq. (34) is made up of two parts. The first part (inside the square bracket) can be handled easily by using the following identity, (which is valid if $\nabla \cdot \mathbf{v} = 0$)

$$\mathbf{v}_{,m} = \nabla \times (\mathbf{v} \times \mathbf{e}_m). \quad (35)$$

The second part (with linear displacement) is almost identical to the right-hand side of Eq. (21). As before, this term includes the solid angle term. Here again, it is this solid angle term that accounts for the nonzero left-hand side of Eq. (31).

Using these inverse curls in numerical implementation is easy since the constants β_l of the linear combination of the shape functions for $\mathbf{u}$ (or, in other words, the artificial variables) are already known. Calculation of internal stresses, therefore, only involves computation of integrals over the bounding contours of surface elements. As in Eq. (28), the final form of the differentiated boundary element method Eq. (30), used in numerical implementation, can be written as

$$\sum_{n=1}^{N} \oint_{C_n} \sum_{l=1}^{27} \beta_l^n \mathbf{V}_{lkm} \cdot d\mathbf{r} = u_{k,m}. \quad (36)$$

The difference compared to Eq. (28) is that the β_l^n are known this time.

A second method of obtaining the vectors $\mathbf{V}_{lkm}$ may be found in Lutz (1994), where they are obtained by differentiating the contour vectors of the primary boundary integral element. This avoids any explicit formation of gradient boundary integral element surface integrands.

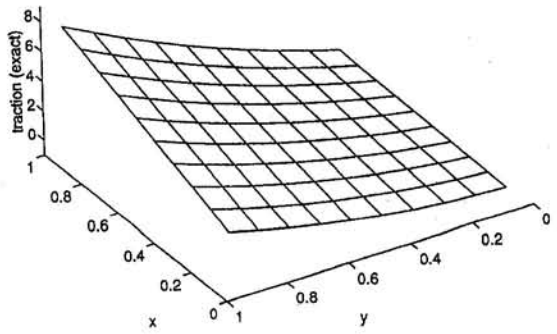


Fig. 3 The x-component of traction (analytical) on the face $z = 0$ (see Fig. 2)

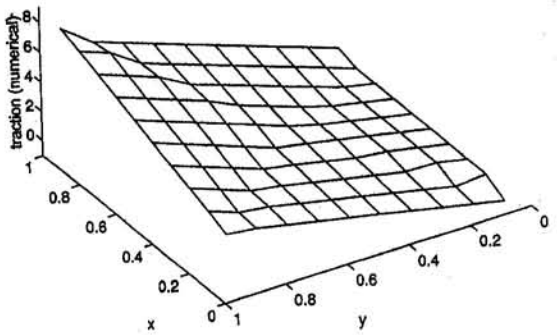


Fig. 4 The x-component of traction (four elements per face) on $z = 0$ (see Fig. 2)

Numerical Results for Boundary Variables

A computer program, based on the boundary contour method formulation described above, has been developed. It has been tested on two kinds of three-dimensional linear elasticity problems—one kind involving a cube and the other a slab with an elliptical cutout. The material constants are $E = 2.5$ (in appropriate units) and Poisson's ratio $\nu = 0.3$. Only CI6 elements are used in these calculations.

A Cube Problem. In this test problem, a known displacement field

$$\mathbf{u} = (y^3 - 3yz^2)\mathbf{e}_1 + (z^3 - 3zx^2)\mathbf{e}_2 + (x^3 - 3xy^2)\mathbf{e}_3$$

is imposed on a cube shown in Fig. 2(a) and tractions are obtained numerically. The chosen displacement field is cubic and the idea is to test the accuracy of the computer program with quadratic displacement shape functions. The numerical values of the surface tractions, for two different meshes, are compared against analytical ones. The first mesh consists of four triangular elements per face and the second has eight triangular elements per face (Note that Fig. 2(b) shows two elements per face.) The analytical results for τ_x on the face $z = 0$ are shown in Fig. 3 and the numerical values, for two meshes, in Figs. 4 and 5, respectively. While both the numerical results are of acceptable accuracy, results are seen to be better for the finer mesh.

Rectangular Slab With Elliptical Cutout. A rectangular slab with an elliptical cutout is loaded by a remote uniaxial tensile traction $\tau_y = 1$ (see Fig. 6). This is a three-dimensional problem that is modeled by the boundary contour method. In order to compare the numerical results with analytical ones, plane-strain boundary conditions ($u_z = 0$, $\tau_x = \tau_y = 0$) are imposed on the two side faces that are parallel to the x-y plane. Ellipse aspect ratios a/b of 2 and 1 are considered here.

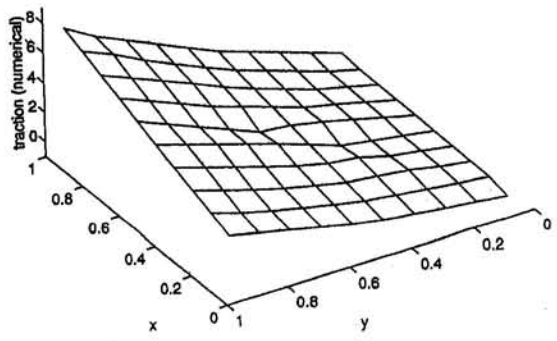
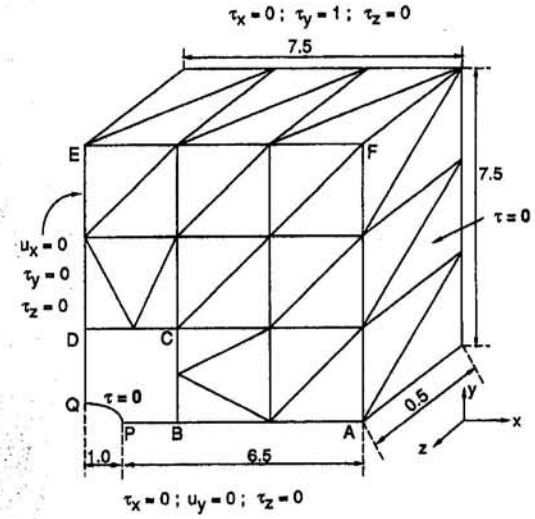


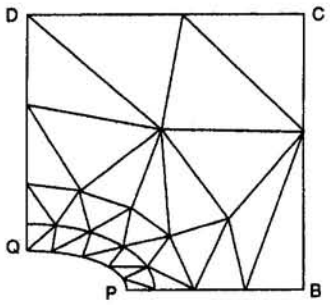
Fig. 5 The x-component of traction (eight elements per face) on $z = 0$ (see Fig. 2)

Downloaded 04 May 2010 to 171.66.16.33. Redistribution subject to ASME license or copyright; see http://www.asme.org/terms/Terms_Use.cfm



(a)

Fig. 6(*a*)



(b)

Fig. 6(*b*)

Fig. 6 Slab with elliptical cutout—(*a*) quarter slab with mesh and boundary conditions; (*b*) details of mesh on BCDQP

A quarter of the slab, with the boundary contour method mesh (for $a/b = 2$) is shown in Fig. 6. The mesh for the circular hole is a small modification of this mesh. The boundary conditions on the faces parallel to the z-axis are also shown on this figure. The two side faces are meshed in identical fashion (the face AFEDQPB is shown in Fig. 6). The surfaces of the slab, parallel to the z-axis, are first divided into rectangles and each rectangle is further subdivided into two triangular elements.

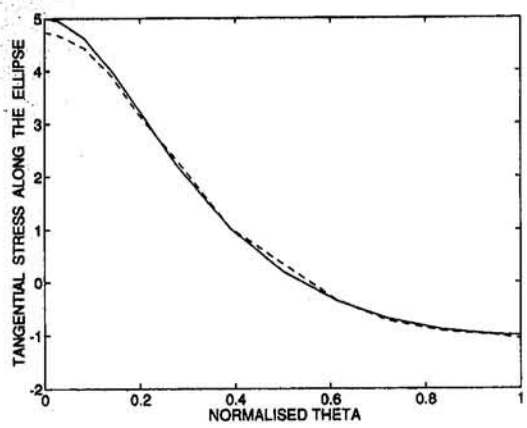


Fig. 7 Tangential stress around the quarter ellipse (see Fig. 6)—Ellipse aspect ratio = 2. —— Exact solution; ----- boundary contour method solution.

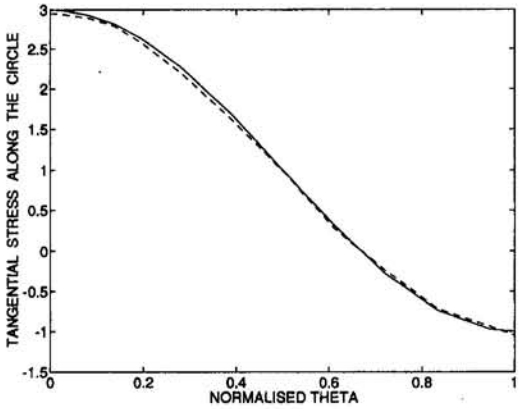


Fig. 8 Tangential stress around the quarter circle (see Fig. 6). —— Exact solution; ----- boundary contour method solution.

Numerical results for the tangential stress around the ellipse, for an ellipse with axis ratio equal to 2, are shown in Fig. 7. The analytical result for an elliptical cutout in an infinite plate (Timoshenko and Goodier, 1970; see also Nagarajan et al., 1994) also appears in Fig. 7. The results are seen to be in good agreement with each other.

The same quantities, this time for a circular cutout, are shown in Fig. 8. The mesh used here is a minor modification of that shown in Fig. 6. Again, the agreement between the analytical and boundary contour method solutions are satisfactory.

It should be mentioned here that similar results with the two-dimensional boundary contour method have been reported in Nagarajan et al. (1994). There, also, the agreement between the boundary contour method and analytical results are very good.

Conclusions

This paper demonstrates that the boundary contour method makes it possible to solve general problems in three-dimensional linear elasticity by only carrying out numerical evaluation of line integrals! Numerical results from the boundary contour method, for the examples considered here, are sufficiently accurate.

A major advantage of the boundary contour method, for practical computations, is that it preserves the seamless geometry interface requirement of a truly integrated Computer Aided Design (CAD) system, because the line integrals need to be evaluated over the same contours that are usually defined in a CAD geometry model. Another advantage is the relative ease of numerical evaluation of line integrals (as opposed to surface or volume integrals). Finally, the method has potential advantages for automatic adaptive meshing algorithms (see Paulino (1995) for use of sensitivities in error estimation and adaptive meshing).

It should also be noted here that modeling of corners with conforming elements in the boundary contour method is quite straightforward if elements such as CI6 or CIM9 (see Fig. 1) are used. This is because, in this formulation, only displacement components (not tractions) are used as primary variables. The final matrices in the resultant algebraic system are, as in the usual boundary element method, nonsymmetric and dense.

Overall, the boundary contour method appears to be an extremely promising approach for obtaining numerical solutions of practical large-scale linear problems in science and engineering.

Downloaded 04 May 2010 to 171.66.16.33. Redistribution subject to ASME license or copyright; see http://www.asme.org/terms/Terms_Use.cfm

Acknowledgments

The authors of this paper gratefully acknowledge the help of Dr. Glaucio H. Paulino at every stage of this research and in the preparation of this manuscript.

References

Cheung, Y. K., Jin, W. G., and Zienkiewicz, O. C., 1989, "Direct Solution Procedure for Solution of Harmonic Problems using Complete, Non-Singular, Trefftz Functions," *Communications in Applied Numerical Methods,* Vol. 5, pp. 159–169.

Cheung, Y. K., Jin, W. G., and Zienkiewicz, O. C., 1991, "Solution of Helmholtz Equation by Trefftz Method," *International Journal for Numerical Methods in Engineering,* Vol. 32, pp. 63–78.

Ghosh, N., and Mukherjee, S., 1987, "A New Boundary Element Method Formulation for Three-dimensional Problems in Linear Elasticity," *Acta Mechanica,* Vol. 67, pp. 107–119.

Jin, W. G., Cheung, Y. K., and Zienkiewicz, O. C., 1990, "Application of the Trefftz Method in Plane Problems," *International Journal for Numerical Methods in Engineering,* Vol. 30, pp. 1147–1161.

Kaplan, W., 1984, *Advanced Calculus,* 3rd ed., Addison-Wesley.

Kellogg, O. D., 1929, *Foundations of Potential Theory,* Verlag Von Julius Springer, Berlin.

Lee, K. J., 1993, "A Boundary Element Technique for Plane Isotropic Elastic Media using Complex Variable Techniques," *Computational Mechanics,* Vol. 11, pp. 83–91.

Lutz, E. D., 1991, "Numerical Methods for Hypersingular and Near-Singular Boundary Integrals in Fracture Mechanics," Ph.D. Dissertation, Cornell University, Ithaca, NY.

Lutz, E. D., Back, A., Gray, L., and Ingraffea, A., 1992, "Systematic Conversion of Boundary Integral Surface Integrals to Contour Integrals," Technical Report, 92-6, Apr., Structural Engineering, School of Civil and Environmental Engineering, Cornell University, Ithaca, NY.

Lutz, E. D., 1994, "Systematic Derivation of Contour Integration Formulae for Laplace and Elastostatic Gradient BIE's," *Computational Mechanics,* Vol. 14, pp. 339–353.

Mukherjee, S., 1982, *Boundary Element Methods in Creep and Fracture,* Elsevier Applied Science, London.

Muskhelishvili, N. I., 1963, *Some Basic Problems of the Mathematical Theory of Elasticity,* Noordhoff Ltd., Groningen.

Nagarajan, A., 1994, "A Novel Boundary Element Method for Linear Elasticity," Ph.D. Dissertation, Cornell University, Ithaca, NY.

Nagarajan, A., Lutz, E., and Mukherjee, S., 1994, "A Novel Boundary Element Method for Linear Elasticity with No Numerical Integration for Two-Dimensional and Line Integrals for Three-Dimensional Problems," ASME JOURNAL OF APPLIED MECHANICS, Vol. 61, pp. 264–269.

Paulino, G. H., 1995, "Novel Formulations of the Boundary Element Method for Fracture Mechanics and Error Estimation," Ph.D. Dissertation, Cornell University, Ithaca, NY.

Piltner, R., and Taylor, R. L., 1990, "A Boundary Element Algorithm using Compatible Boundary Displacements and Tractions," *International Journal for Numerical Methods in Engineering,* Vol. 29, pp. 1323–1341.

Rizzo, F. J., 1967, "An Integral Equation Approach to Boundary Value Problems of Classical Elastostatics," *Quarterly of Applied Mathematics,* Vol. 25, pp. 83–95.

Timoshenko, S. P., and Goodier, J. N., 1970, *Theory of Elasticity,* 3rd ed., McGraw Hill, NY.

Watson, J. O., 1986, "Hermitian Cubic and Singular Elements for Plane Strain," *Developments in Boundary Elements,* Vol. 4, P. K. Banerjee and J. O. Watson, eds., Elsevier, New York, pp. 1–28.

APPENDIX

Shape Functions u_{li}, $l = 1, \ldots, 27$, $i = 1, 2, 3$

For a given value of l, the quantities below, within parentheses, are (u_{l1}, u_{l2}, u_{l3}). For example, for $l = 1$, $u_{11} = 1$, $u_{12} = 0$, $u_{13} = 0$ is written as $(1, 0, 0)$.

Constant: 3 shape functions $l = 1, 2, 3$.

$$(1, 0, 0), \quad (0, 1, 0), \quad (0, 0, 1)$$

First degree: 9 shape functions $l = 4, \ldots, 12$.

$$(x, 0, 0), \quad (0, x, 0), \quad (0, 0, x)$$

$$(y, 0, 0), \quad (0, y, 0), \quad (0, 0, y)$$

$$(z, 0, 0), \quad (0, z, 0), \quad (0, 0, z)$$

Second degree: 15 shape functions $l = 13, \ldots, 27$.

$$(x^2, -4(1-\nu)xy, 0), \quad (y^2, -2(1-2\nu)xy, 0)$$

$$(-2(1-2\nu)xy, x^2, 0), \quad (-4(1-\nu)xy, y^2, 0)$$

$$(0, y^2, -4(1-\nu)yz), \quad (0, z^2, -2(1-2\nu)yz)$$

$$(0, -2(1-2\nu)yz, y^2), \quad (0, -4(1-\nu)yz, z^2)$$

$$(-4(1-\nu)zx, 0, z^2), \quad (-2(1-2\nu)zx, 0, x^2)$$

$$(z^2, 0, -2(1-2\nu)zx), (x^2, 0, -4(1-\nu)zx)$$

$$(yz, 0, 0), \quad (0, xz, 0), \quad (0, 0, xy)$$

Downloaded 04 May 2010 to 171.66.16.33. Redistribution subject to ASME license or copyright; see http://www.asme.org/terms/Terms_Use.cfm

Three-Dimensional Analysis of Surface Cracks in an Elastic Half-Space

Quanxin Guo

Jian-Juei Wang
Mem. ASME.

TerraTek, Inc.
420 Wakara Way
Salt Lake City, UT 84108

R. J. Clifton
Division of Engineering,
Brown University,
Providence, RI 02912
Mem. ASME

A numerical method is presented for analyzing arbitrary planar cracks in a half-space. The method is based on the fundamental solution for a dislocation loop in a half-space, which is derived from the Mindlin solution (Mindlin, Physics, *Vol. 7, 1936) for a point force in a half-space. By appropriate replacement of the Burgers vectors of the dislocation by the differential crack-opening displacement, a singular integral equation is obtained in terms of the gradient of the crack opening. A numerical method is developed by covering the crack with triangular elements and by minimizing the total potential energy. The singularity of the kernel, when the integral equation is expressed in terms of the gradient of the crack opening, is sufficiently weak that all integrals exist in the regular sense and no special numerical procedures are required to evaluate the contributions to the stiffness matrix. The integrals over the source elements are converted into line integrals along the perimeter of the element and evaluated analytically. Numerical results are presented and compared with known results for both surface breaking cracks and near surface cracks.*

1 Introduction

Surface or near-surface defects often exist in engineering materials and structural components. These defects are three-dimensional in nature and are often the sites of failure initiation. In fracture mechanics applications, three-dimensional elasticity solutions are often called for, but not considered in most cases because of the much greater difficulty involved. In critical applications, three-dimensional analysis is essential for obtaining reliable solutions. Murakami and Nemat-Nasser (1982, 1983), Murakami (1985), Keer, Farris, and Lee (1986), and Dai, Nowell and Hills (1993), among many others, used a body-force method developed from Mura's eigenstrain approach (see for example, Mura, 1982), to reduce the problem for a planar crack in a half-space to singular integral equations for the crack-opening displacement over the crack surface. Lee and Keer (1987), Lee, Farris, and Keer (1987), and Hanson, Lin, and Keer (1989) extended the method to analyze planar cracks in a two-phase material. For an edge-crack normal to a free surface, Bueckner (1977) obtained an integral equation relating crack pressure and crack opening using Boussinesq-Papkovich potentials. All these formulations lead to singular surface integral equations with singularity of $1/r^3$, where r is the distance between the field point and the integration point or source point. Since the singular integrals exist only in Hadamard's finite part sense (Hadamard, 1952), the main difficulty in solving the strongly singular integral equation is the evaluation of the singular integrals. Special numerical techniques are required to evaluate the matrix coefficients of the linear algebraic equations of the discretized version of the equations. One approach to evaluating these integrals is to use a combination of a closed-form integral and numerical integration, as developed by Murakami and Nemat-Nasser (1983). Another approach is to reduce the two-dimensional singular integrals to one-dimensional integrals along the boundary of the domain by carrying out the radial integration analytically, as proposed by Dai, Nowell, and Hills (1993). After carrying out the radial integration analytically the one-dimensional integrals along the boundary exist in the regular sense as long as the field point is not on the boundary.

Bui (1977), Weaver (1977), Clifton and Abou-Sayed (1981), Sladek and Sladek (1986), Guo et al. (1994), and Xu and Ortiz (1993) presented a different method for solving three-dimensional cracks in an unbounded body. Instead of starting directly from the integral equations with strong singularity, they derived singular integral equations in terms of the gradients of the crack-opening displacement. The singularity of the kernel is reduced to $1/r^2$. Because all the integrals exist in the regular sense, numerical difficulties in evaluating matrix elements are reduced greatly. Clifton and Abou-Sayed (1981), and Guo et al. (1994) went further to evaluate most of the integrals analytically to minimize the computational time so that the method can be used for numerical simulation of computationally intensive processes such as hydraulic fracturing in oil/gas recovery and fatigue.

Herein, a numerical method is presented for three-dimensional analysis of cracks in a half-space. The method is based on the fundamental solution for a dislocation segment in a half-space. This solution is derived from the fundamental solution for a point force in a half-space (Mindlin, 1936) by means of the reciprocal theorem, following the approach used by Kurashige and Clifton (1992) for an unbounded, fluid-filled, poroelastic solid. The fundamental solution is the half-space counterpart of the Mura formula (Mura, 1963) for stresses due to a dislocation loop in an unbounded space. By appropriate replacement of the Burgers vectors of the dislocations by the gradients of the jumps in displacements across the crack surface one obtains the singular integral equation for the crack-opening displacement. The derived integral equation is the counterpart, expressed in terms of crack-opening gradients, of the equation derived by Weaver (1973) in terms of crack openings. The method can be regarded as the three-dimensional form of the well-established dislocation method in two-dimensional crack problems (Bilby and Eshelby, 1968). Lee, Advani, and Lee (1988) obtained similar singular integral equations by ex-

Contributed by the Applied Mechanics Division of THE AMERICAN SOCIETY OF MECHANICAL ENGINEERS for publication in the ASME JOURNAL OF APPLIED MECHANICS.

Discussion on this paper should be addressed to the Technical Editor, Professor Lewis T. Wheeler, Department of Mechanical Engineering, University of Houston, Houston, TX 77204-4792, and will be accepted until four months after final publication of the paper itself in the ASME JOURNAL OF APPLIED MECHANICS.

Manuscript received by the ASME Applied Mechanics Division, June 23, 1994; final revision, May 5, 1995. Associate Technical Editor: X. Markenscoff.

Copyright © 1996 by ASME

Downloaded 04 May 2010 to 171.66.16.33. Redistribution subject to ASME license or copyright; see http://www.asme.org/terms/Terms_Use.cfm

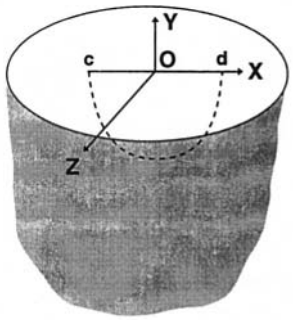


Fig. 1 A planar crack in a half-space

tending the method used by Lee and Keer (1986) based on the concept of eigen or transformation strains. However, their results differ from those of Lee and Keer (1986) and Weaver (1973). The exact derivation used here allows for direct assessment of the applicability of related integral equations obtained using the eigenstrain approach of Mura (1987) and assumed distributions of eigenstrains within an inclusion that represents the crack volume (Lee and Keer, 1986; Lee, Advani, and Lee, 1988).

The integral equation over the crack surface is solved by means of the variational approach of minimizing the total potential energy, as used by Clifton and Abou-Sayed (1981) for planar cracks in an unbounded body. The crack surface is covered by triangular elements and the crack-opening displacements are assumed to vary linearly over each element. Near the crack front the crack-opening displacement is assumed to vary as the square root of the distance from the tip. The method is tested by comparing the numerical results for long, rectangular surface-breaking and subsurface cracks with the corresponding two-dimensional results; comparisons are also made for other crack problems with known results.

2 Method of Analysis

In this section, the boundary integral equation will be derived. The method for a crack in a half-space is similar to the one used for a crack in an unbounded body by Guo et al. (1994). Consider a planar crack of arbitrary shape in an isotropic, linearly elastic half-space. The Cartesian coordinate (x, y, z) or x_i $(i = 1, 2, 3)$ is oriented such that the crack lies on the x-y plane, as shown in Fig. 1.

By means of the reciprocal theorem, the displacement $\mathbf{u}(\mathbf{x})$ at the point $\mathbf{x}$ due to a dislocation loop that bounds a surface A can be expressed as (see, e.g., Kurashige and Clifton, 1992; Guo et al., 1994)

$$\mathbf{P}\cdot\mathbf{u}(\mathbf{x}) = -\iint_A \{\boldsymbol{\sigma}(\mathbf{x}';\mathbf{x})\mathbf{b}(\mathbf{x}')\}\cdot\mathbf{n}(\mathbf{x}')dS', \quad (1)$$

where $\boldsymbol{\sigma}(\mathbf{x}';\mathbf{x})$ is the stress tensor at point $\mathbf{x}'$ due to a point load $\mathbf{P}\delta(\mathbf{x}'-\mathbf{x})$ at the point $\mathbf{x}$ in a half-space (Mindlin, 1936), $\mathbf{b} = \mathbf{u}_+ - \mathbf{u}_-$ is the jump in displacement across the surface, $\mathbf{n} = \mathbf{n}_+ = -\mathbf{n}_-$ is the unit normal to the lower surface of A; subscripts "+" and "−" denote evaluation on the lower and upper surface of A and the dot "·" denotes the inner product of two vectors. From Eq. (1) one obtains the displacement component in the x_m-direction as

$$\mathbf{u}_m(\mathbf{x}) = -\iint_A \sigma_{(m)ij}(\mathbf{x}';\mathbf{x})b_i(\mathbf{x}')n_j(\mathbf{x}')dS', \quad (2)$$

where $\sigma_{(m)ij}(\mathbf{x}';\mathbf{x})$ is the stress σ_{ij} at $\mathbf{x}'$ due to a unit force in the x_m-direction at $\mathbf{x}$; the convention of summation over repeated indices is used here and throughout the paper.

For a half-space, with the y-axis perpendicular to the free surface we have

$$\frac{\partial}{\partial x_s}\sigma_{(m)ij}(x'-x, z'-z, y', y) = -\frac{\partial}{\partial x'_s}\sigma_{(m)ij}(x'-x, z'-z, y', y). \quad (s = 1, 3) \quad (3)$$

Differentiating Eq. (2) with respect to x_s and using Eq. (3) one obtains

$$\frac{\partial u_m(\mathbf{x})}{\partial x_s} = b_i\iint_A n_j\frac{\partial}{\partial x'_s}\sigma_{(m)ij}(\mathbf{x}';\mathbf{x})dS' - \delta_{2s}b_i\iint_A n_i\left(\frac{\partial}{\partial y}+\frac{\partial}{\partial y'}\right)\sigma_{(m)ij}dS', \quad (4)$$

where δ_{ij} is the Kronecker delta. Using the equilibrium equations on $\sigma_{(m)ij}(\mathbf{x}';\mathbf{x})$ and applying the Stoke's theorem to the first area integral in Eq. (4) one obtains

$$\frac{\partial u_m(\mathbf{x})}{\partial x_s} = \epsilon_{jsn}b_i\oint\sigma_{(m)ij}(\mathbf{x}';\mathbf{x})dx'_n - \delta_{2s}b_i\iint_A n_j\left(\frac{\partial}{\partial y}+\frac{\partial}{\partial y'}\right)r_{(m)ij}(\mathbf{x}';\mathbf{x})dS', \quad (5)$$

where the permutation symbols ϵ_{ijk} are zero, except $\epsilon_{123} = \epsilon_{312} = \epsilon_{231} = 1$, $\epsilon_{132} = \epsilon_{321} = \epsilon_{213} = -1$, and

$$r_{(m)ij}(\mathbf{x}';\mathbf{x}) = \sigma_{(m)ij}(\mathbf{x}';\mathbf{x}) - s_{(m)ij}(\mathbf{x}'-\mathbf{x}), \quad (6)$$

is the regular part with

$$s_{(m)ij}(\mathbf{x}';\mathbf{x}) = \frac{1}{8\pi(1-\nu)}\left\{-(1-2\nu)\times\frac{\delta_{im}(x'_j-x_j)+\delta_{jm}(x'_i-x_i)-\delta_{ij}(x'_m-x_m)}{|\mathbf{x}'-\mathbf{x}|^3} - 3\frac{(x'_m-x_m)(x'_i-x_i)(x'_j-x_j)}{|\mathbf{x}'-\mathbf{x}|^5}\right\}, \quad (7)$$

as the singular part or the Kelvin solution (Kelvin, 1882) for a unit force in an unbounded space; Poisson's ratio is denoted by ν. For a dislocation loop in an unbounded space, $r_{(m)ij}(\mathbf{x}';\mathbf{x}) = 0$ and Eq. (5) becomes the Mura formula (Mura, 1963; Mura, 1982). For a dislocation loop in a half-space, the line integral in Eq. (5) has the form of the Mura formula except that the $\sigma_{(m)ij}(\mathbf{x}';\mathbf{x})$ are the stress components due to a unit concentrated force in a half-space rather than in an unbounded space as in the Mura formula. The area integral in Eq. (5) is required to satisfy the free-surface condition.

Consider a planar dislocation loop, say on the plane $z = 0$, with $b_1 = b_2 = 0$. For this case, application of Hooke's law to the displacement gradients of Eq. (5) gives the following expression for the dislocation-induced traction $\sigma_{33}(x, y)$ on the plane $z = 0$:

$$\sigma_{33} = L_{33ms}\epsilon_{jsn}b_l\oint\sigma_{(m)ij}(\mathbf{x}';\mathbf{x})dx'_n - L_{3322}b_3\iint_A\left(\frac{\partial}{\partial y}+\frac{\partial}{\partial y'}\right)r_{(2)33}(\mathbf{x}';\mathbf{x})dS', \quad (8)$$

Downloaded 04 May 2010 to 171.66.16.33. Redistribution subject to ASME license or copyright; see http://www.asme.org/terms/Terms_Use.cfm

where

$$L_{pqms} = G\left[\delta_{pm}\delta_{qs} + \delta_{ps}\delta_{qm} + \frac{2\nu}{1-2\nu}\delta_{pq}\delta_{ms}\right], \quad (9)$$

in which G is the elastic modulus and, from Mindlin's solution (Mindlin, 1936),

$$r_{(2)33} = -\frac{1}{8\pi(1-\nu)}\left\{(1-2\nu)\frac{3(y'-y)+4\nu(y+y')}{R_2^3} - \frac{6y(y+y')[(1-2\nu)y'-2\nu y]}{R_2^5} - \frac{4(1-\nu)(1-2\nu)}{R_2(R_2-y-y')}\right\}, \quad (10)$$

$$R_2^2 = (x'-x)^2 + (y'+y)^2. \quad (11)$$

Using

$$\frac{\partial r_{(2)33}}{\partial y} = \frac{\partial r_{(2)33}}{\partial y'} - \frac{1}{8\pi(1-\nu)}\frac{\partial}{\partial y'}\frac{2(1-2\nu)(y+y')-4y}{R_2^3} + \frac{4(1-2\nu)}{8\pi(1-\nu)}\left(\frac{\partial}{\partial x'}\frac{x'-x}{R_2^3} + \frac{\partial}{\partial y'}\frac{y'+y}{R_2^3}\right), \quad (12)$$

one can rewrite the area integral in Eq. (8) as a line integral, from which the stress increment caused by a dislocation segment with Burgers vector b_3 and line segment dx_n' can be written as

$$d\sigma_{33}(x,y) = L_{33ms}\epsilon_{jsn}b_3\sigma_{(m)3j}(\mathbf{x};\mathbf{x}')dx_n' + L_{3322}b_3\left\{\left(2r_{(2)33} + \frac{1}{8\pi(1-\nu)}\frac{2(1-2\nu)(y+y')+4y}{R_2^3}\right)dx_1' - \frac{1-2\nu}{2\pi(1-\nu)}\frac{x'-x}{R_2^3}dx_2'\right\}. \quad (13)$$

This may be regarded as the half-space counterpart of the Mura formula in stress form.

For a dislocation segment with components dx in the x-direction and dy in the y-direction, the products of Burgers vector $\mathbf{b}$ and the dislocation segment can be expressed in terms of the crack opening $w_i(x', y') = u_i(x', y', 0^+) - u_i(x', y', 0^-)$ as

$$b_i dx' = -\langle w_i\rangle dx' - \frac{\partial w_i}{\partial y'}dx'dy', \quad (14)$$

$$b_i dy' = \frac{\partial w_i}{\partial x'}dx'dy', \quad (15)$$

where

$$\langle w_i(x', y')\rangle = \begin{cases} w_i, & \text{if } y' = 0 \\ 0, & \text{if } y' \neq 0 \end{cases} \quad (16)$$

for a free surface at $y' = 0$. Substitution of Eqs. (14) and (15) into Eq. (13) allows the line integral to be replaced by an area integral. The result is the following surface integral equation that relates the traction on the crack surface to the derivatives of the crack opening over the crack surface:

$$-\sigma_{33}(x,y) = \sigma_0\iint (S_{33}^{3\beta} - R_{33}^{3\beta})\frac{\partial w_3}{\partial x_\beta'}dx'dy' - \sigma_0\int_c^d L_3^3(x,y,x')w_3(x')dx', \quad (17)$$

where $c < x' < d$ is the intersection of the crack with the free surface and

$$\sigma_0 = \frac{G}{4\pi(1-\nu)}, \quad (18)$$

$$S_{33}^{3\beta} = (x_\beta - x_\beta')/R^3, \quad (\beta = 1, 2) \quad (19)$$

$$R_{33}^{31} = -\frac{1-\nu}{1-2\nu}R_{(3)31} + \frac{\nu}{1-2\nu}R_{(1)33} - 4\nu\frac{x'-x}{R_2^3}, \quad (20)$$

$$R_{33}^{32} = -\frac{1-\nu}{1-2\nu}R_{(3)32} + \frac{\nu}{1-2\nu} \times \left\{-R_{(2)33} - \frac{2(1-2\nu)(y+y')+4y}{R_2^3}\right\}, \quad (21)$$

$$L_3^3 = -\left\{4\nu\frac{1-\nu(1-2\nu)}{1-2\nu}\frac{y}{R_2^3} - \frac{12\nu^2}{1-2\nu}\frac{y^3}{R_2^5} + 4\nu(1-\nu)\frac{1}{R_2(R_2-y)}\right\}, \quad (22)$$

in which

$$R^2 = (x'-x)^2 + (y'-y)^2. \quad (23)$$

The quantities $R_{(m)ij} = 8\pi(1-\nu)r_{(m)ij}$ in Eqs. (21) and (22) can be obtained from Mindlin's solution (Mindlin, 1936) (see Appendix A). The line integral in Eq. (17) vanishes for buried cracks.

3 Comparison of the Present Formulation With Others

Weaver (1973) derived integral equations for cracks in a half-space using a different method. In his integral equations the singular part is expressed in terms of the gradient of the crack opening while the regular part is expressed in terms of the crack opening itself. Integrating Eq. (17) by parts for the regular part results in integral equations having the form of Weaver (1973). One can prove that the final results from the two formulations are the same, noting that $(\partial R_{(3)31}/\partial x' + \partial R_{(3)32}/\partial y')$, $\partial R_{(1)33}/\partial x'$, $-\partial R_{(2)33}/\partial y'$ correspond, respectively, to the terms $\partial T_{33}^+/\partial X_3$, $\partial T_{23}^+/\partial X_2$, $\partial T_{13}^+/\partial X_1$ in Weaver (1973).

Integrating Eq. (17) by parts one obtains an integral equation of the form

$$\sigma_{33}(x,y) = \sigma_0\iint\left\{\frac{1}{R^3} + K_0(x,y;x'y')\right\}w_3(x',y')dx'dy', \quad (24)$$

which has the form derived by Lee and Keer (1986) for a crack in a body consisting of two half-spaces of different materials. The regular kernel K_0 in Eq. (24) can be obtained from Eq. (17) and the derivatives of $R_{(m)ij}$. For a crack in a half-space, and for Poisson's ratio $\nu = 0$ or 0.5, one can prove directly that the kernel K_0 obtained from Eq. (17), Eq. (21) and Eq. (22) is exactly the same as Eq. (17) in Lee and Keer (1986). For arbitrary ν, a direct proof would be lengthy and cumbersome. Instead, we evaluated numerically the kernels corresponding to the present formulation and the formulation of Lee

Downloaded 04 May 2010 to 171.66.16.33. Redistribution subject to ASME license or copyright; see http://www.asme.org/terms/Terms_Use.cfm

and Keer (1986). Numerical results show that the values obtained by the two approaches agree to the accuracy of the computer.

Although the above approves that Eq. (17) can be derived from the known integral Eq. (24) through an integration by parts, the exact derivation presented here based on the reciprocal theorem allows for direct assessment of the applicability of assumed distributions of eigenstrain within an inclusion that represents the crack volume (Murakami and Nemat-Nasser, 1982; Lee and Keer, 1986; Lee, Advani, and Lee, 1988). The present derivation, which also gives the half-space counterpart of the Mura formula (Mura, 1963) for stresses due to a dislocation loop in an unbounded space, is direct and attractive for its power in generalizing the method to other classes of problems such as nonplanar cracks in an unbounded space (Xu and Ortiz, 1993) and planar cracks in a poroelastic body filled with fluid (Kurashige and Clifton, 1992).

Lee, Advani, and Lee (1988) also derived an integral equation for a planar crack perpendicular to the interface of two half-spaces by extending the method of Lee and Keer (1986) and by writing the eigen-strains in terms of "eigen-displacements" using compatibility equations. Their integral equation, expressed in terms of the gradient of the crack opening, is similar to the one given by Eq. (17). For a subsurface crack in a half-space, they have

$$-\sigma_{33}(x, y) = \sigma_0 \iint (S_{33}^{3\beta} - G^{\beta}) \frac{\partial w_3}{\partial x'_\beta} dx'dy', \quad (25)$$

where the regular kernels (G^{β}, $\beta = 1, 2$) are listed in the Appendix B from Eq. (20) of Lee, Advani, and Lee (1988). The regular kernels of Lee, Advani, and Lee (1988) differ from those given in Eqs. (20) and (21). The existence of a discrepancy between their results and the mutually consistent results of Lee and Keer (1986), Weaver (1976) and the present paper can be readily demonstrated by taking Poisson's ratio equal to 0.5. Then, putting Eq. (25) into the form of Eq. (24) by integration by parts, one finds that the regular kernel corresponding to K_0 in Eq. (24), has the asymptotic form of $6y'(y' - 2y)/\{(1 - 2\nu)R_2^5\}$. Thus, as Poisson's ratio ν goes to 0.5, the regular term is unbounded, which is not the case in our formulation. The error in the formulation of Lee, Advani, and Lee (1988) appears to be in the use of compatibility equations for the eigenstrains which are fictitious strains used to introduce body forces and need not be compatible with any displacement field (Mura, 1982).

4 Numerical Implementation

The integral equations can be solved numerically using a variational approach similar to the one introduced by Clifton and Abou-Sayed (1981) for a pressurized crack in an unbounded space. The crack surface "A" is divided into a meshed region "A_0," which is subdivided into triangles, and a crack-tip region "∂A." Figure 2 shows the meshed region for a surface-breaking rectangular crack. The narrow crack-tip region "∂A" outside the meshed region is not shown in Fig. 2. Over each triangle, the crack opening $w_3(x, y)$ and the traction $\sigma_{33}(x, y)$ are expressed in terms of the local trial functions $f_i(x, y)$ and nodal values w_3^i and σ_{33}^i ($i = 1, 2, \ldots, N$), according to

$$w_3(x, y) = \sum_{i=1}^{i=N} w_3^i f_i(x, y), \quad (26)$$

$$\sigma_{33}(x, y) = \sum_{i=1}^{i=N} \sigma_{33}^i f_i(x, y), \quad (27)$$

where N is the total number of nodes and the trial function $f_i(x, y)$ has (i) the value of unity at the ith node, (ii) varies linearly over adjacent triangles, and (iii) vanishes along the opposite side of these triangles and outside the adjacent triangles. In the near-tip region, the crack opening $w_3(x, y)$ varies as the square root of the distance from the crack tip, i.e.,

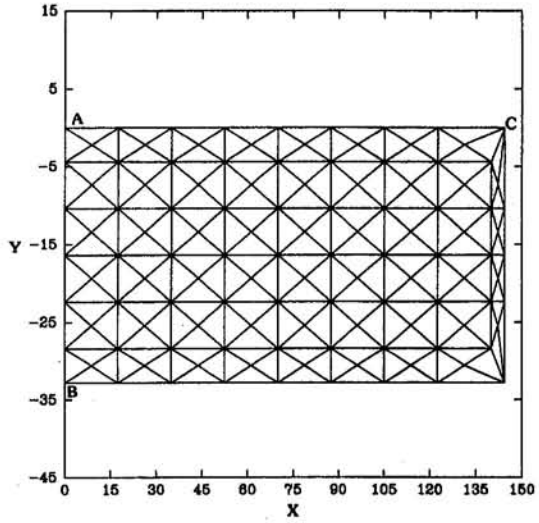


Fig. 2 One half of the meshed region for a rectangular crack

$$w_3(x, y) = w_3(s)\left(\frac{\eta}{\epsilon}\right)^{1/2} \quad (28)$$

where ϵ is the width of the crack-tip region "∂A" and η is the distance from the crack tip to the point (x, y). The function $w_3(s)$ is taken to vary linearly over the straight line segments which represent the inner boundary of "∂A". Since ϵ is very small and the traction $\sigma_{33}(x, y)$ does not vary much across this narrow region, we assume that the traction is constant over each near-tip element.

From the principle of the minimum of the total potential energy, the crack opening $w_3(x, y)$ that vanishes along the crack front and satisfies Eq. (17) is the function that minimizes the total potential energy $U + V$, where

$$U = \frac{\sigma_0}{2} \iint_A w_3(x, y) \left\{ \iint_A (S_{33}^{3\beta} - R_{33}^{3\beta}) \frac{\partial w_3}{\partial x'_\beta} dx'dy' - \int_c^d L_3^3(x, y, x') w_3(x') dx' \right\} dxdy, \quad (29)$$

$$V = -\iint_A w_3(x, y)\sigma_{33}(x, y)dxdy. \quad (30)$$

Minimizing the total potential energy one obtains a system of algebraic equations for the nodal crack-opening displacements w_3^i. These equations can be written in matrix form as

$$\frac{\sigma_0}{2} \mathbf{Kw} = \mathbf{p}, \quad (31)$$

where $\mathbf{w}$ is an N-dimensional column vector of the nodal crack openings and $\mathbf{p}$ is an N-dimensional column vector of nodal forces

$$p_i = \iint \sigma_{33}(x, y) f_i(x, y) dxdy. \quad (32)$$

The stiffness matrix

$$K_{ij} = \iint dxdy \iint \left((S_{33}^{3\beta} - R_{33}^{3\beta}) f_i \frac{\partial f_j}{\partial x'_\beta} + (S_{33}^{3\beta} - R_{33}^{3\beta}) f_j \frac{\partial f_i}{\partial x'_\beta} \right) dx'dy'$$

Downloaded 04 May 2010 to 171.66.16.33. Redistribution subject to ASME license or copyright; see http://www.asme.org/terms/Terms_Use.cfm

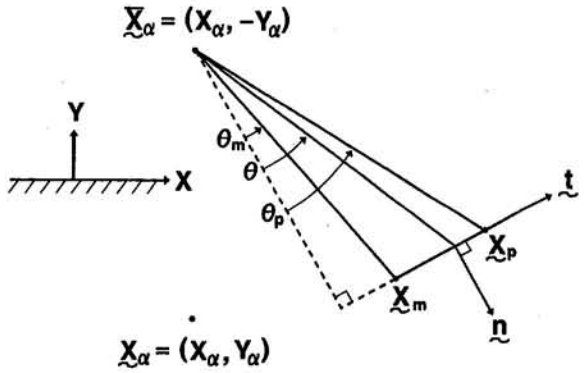


Fig. 3 Definition of the parameters in the evaluation of line integrals along a side of a triangle

$$- \iint dxdy \int L_3^3 f_i(x, y) f_j(x', 0) dx' - \int dx \iint L_3^3 f_j(x, 0) f_i(x', y') dx' dy', \quad (33)$$

is a full, symmetric matrix; the one-dimensional integral is over the line of intersection of the crack with the free surface $y' = 0$.

Contributions to the stiffness matrix from the singular kernels have been evaluated by Clifton and Abou-Sayed (1981). One needs to consider only the contributions from the regular kernels. Consider first the regular contributions from the area integrals in Eq. (33),

$$(\Delta K)_{ij} = \iint_{A_p} f_i dxdy \iint_{A_q} \frac{\partial f_j}{\partial x'_\beta} R_{33}^{3\beta}(x', y'; x, y) dx' dy'. \quad (34)$$

For convenience in describing the evaluation of the above integrals it is helpful to distinguish two cases: (a) triangular elements where both the field element A_p and the source element A_q are triangular elements; and (b) near-tip elements where either A_p or A_q is in the near-tip region.

4.1 Triangular Elements. From the linearity of the trial function over the source element A_q, and three-point Gaussian numerical integration over the field element A_p, Eq. (34) can be written as

$$(\Delta K)_{ij} = \sum_{\alpha=1}^{\alpha=3} \frac{A_p}{3} f_i(x_\alpha, y_\alpha) \frac{\partial f_j}{\partial x'_\beta} \times \iint_{A_q} R_{33}^{3\beta}(x', y'; x_\alpha, y_\alpha) dx' dy', \quad (35)$$

where A_p is the area of the field element, (x_α, y_α) are the quadrature points, and the integrands are given in Eqs. (21) and (22). The area integral in Eq. (35) can be converted into line integrals along the perimeter of the triangular element. Since the procedures are the same, let us consider the first term $R_{(3)31}$ in Eq. (21) as an illustration. Using integration by parts one obtains

$$\iint_{A_q} R_{(3)31}(x', y'; x_\alpha, y_\alpha) dx' dy' = \oint_{S_q} \left(- \frac{1 - 2\nu}{R_2} + \frac{4(1 - \nu)(1 - 2\nu)}{R_2 - y_\alpha - y} + \frac{2y_\alpha y'}{R_2^3} \right) n_x ds', \quad (36)$$

where $\mathbf{n} = (n_x, n_y)$ is the unit exterior normal of the perimeter s_q of the element A_q.

All the line integrals can be evaluated analytically along each side of the triangle. For example, integrating along a side with starting point $\mathbf{x}_m$ and end point $\mathbf{x}_p$ of the triangular element A_q (Fig. 3), one obtains

$$\int \frac{1}{R_2} ds' = \frac{1}{2} \left(\ln \frac{1 + \sin\theta}{1 - \sin\theta} \right)_{\theta_m}^{\theta_p}. \quad (37)$$

For the special case $|\sin\theta| = 1$, one obtains instead

$$\int \frac{1}{R_2} ds' = \ln \left(\frac{r^+}{r^-} \right), \quad (38)$$

where r^- and r^+ $(r^- < r^+)$ are the distances from the point $(x_\alpha, -y_\alpha)$ to the two ends of the side.

4.2 Near-Tip Elements. For a near-crack-tip element, the trial function has the form

$$f_i(x, y) = \phi_i(s) \left(\frac{\eta}{\epsilon} \right)^{1/2}, \quad (39)$$

where $\phi_i(s)$ is a linear function of "s" over the rectangular element with width ϵ and length l. If the element A_p is in the near-crack-tip region ∂A, but A_q is not, then integration of Eq. (34) with respect to η over the element A_p and use of Eq. (39) yields

$$(\Delta K)_{ij} = \frac{\partial f_j}{\partial x'_\beta} \frac{2\epsilon}{3} \int_0^l \phi_j(s) ds \iint_{A_q} R_{33}^{3\beta}(x', y'; s, \eta_q) dx' dy', \quad (40)$$

where $\eta_q = 4\epsilon/9$ locates the quadrature point of the parabolic trial function of Eq. (39). The integrals over a triangular element A_q have been evaluated analytically according to the method outlined from Eqs. (35) to (38).

If the element A_q is in the near-crack-tip region ∂A, but A_p is not, then integration of Eq. (34) over η' for A_q and use of three-point Gaussian integration over A_p results in

$$(\Delta K)_{ij} = \sum_{\alpha=1}^{\alpha=3} \frac{A_p}{3} f_i(x_\alpha, y_\alpha) \int_0^l \left\{ R_{33}^{3\eta}(s'; x_\alpha, y_\alpha) \phi_j(s') + \frac{2\epsilon}{3} R_{33}^{3\xi}(s', x_\alpha, y_\alpha) \phi'_j(s') \right\} ds', \quad (41)$$

where

$$R_{33}^{3\eta} = (R_{33}^{31}, R_{33}^{32}) \cdot \mathbf{n}, \quad R_{33}^{3\xi} = (R_{33}^{31}, R_{33}^{32}) \cdot \mathbf{t}, \quad (42)$$

and $(\mathbf{n}, \mathbf{t})$ are the unit vectors associated with η and s, respectively.

To simplify the evaluation of the integrals in Eq. (41) the trial function $\phi_j(s')$ is taken to be constant (i.e., $\phi_j(s') = 1/2$). The integrals to be evaluated then have the form

$$I_\alpha^\eta = 0.5 \int_0^l R_{33}^{3\eta}(s'; x_\alpha, y_\alpha) ds', \quad (43)$$

where the integrands have terms of the types

$$\frac{1}{R_2^3}, \ \frac{1}{R_2^5}, \ \frac{x' - x}{R_2^3}, \ \frac{x' - x}{R_2^5}, \ \frac{y' + y}{R_2^3}, \ \frac{y' + y}{R_2^5}, \ \frac{(y + y')^2}{R_2^5}, \ \frac{1}{R_2(R_2 - y - y')}, \ \frac{x' - x}{R_2(R_2 - y - y')^2} \quad (44)$$

in which the subscript "α" on x and y has been dropped for convenience. For the line segment from (x'_2, y_2) to (x'_3, y'_3), the integrals in Eqs. (43) and (44) have been evaluated analytically except the last two terms in Eq. (44). Although the last two terms could also be evaluated analytically, the final expressions for some cases would be cumbersome. Numerical integration is used for these cases.

Downloaded 04 May 2010 to 171.66.16.33. Redistribution subject to ASME license or copyright; see http://www.asme.org/terms/Terms_Use.cfm

If both A_p and A_q are in the near-crack-tip region, trial functions of Eq. (39) should be used for both f_i and f_j in Eq. (34). The contributions from this case are evaluated by using, respectively, the method in Eq. (40) for integration over the field element A_p and the method in Eqs. (41)–(44) for integration over the source element A_q.

4.3 Contributions from the line integral. Contributions to the stiffness matrix from the line integrals in Eq. (33) have the form

$$(\Delta K)_{ij} = \iint_{A_p} f_i(x, y)dxdy \int_{x_2}^{x_3'} f_j(x', 0)L_3^3(x'; x, y)dx', \quad (45)$$

for a line segment (x_2', x_3') on the free surface. The area integral in Eq. (45) over A_p is evaluated using Gaussian quadrature as used in obtaining Eq. (35) or Eq. (40), while the line integrals in Eq. (45) have been evaluated analytically, taking advantage of linearity of the trial function $f_j(x', 0)$.

5 Numerical Results and Discussion

In the implementation of the above analysis in a computer code the symmetry of the stiffness matrix has been used to minimize storage requirements and computational time—both in evaluation of the elements of the stiffness matrix and in its numerical inversion by means of the Cholesky scheme. Numerical results provide the crack-opening displacement w_3 over the crack. The stress intensity factor along the crack front is extracted from the crack surface displacements by means of (see, for example, Eq. (3.1)–(16) in Kanninen and Popelar, 1985)

$$K_I = \sigma_0 \pi w_3 \sqrt{2\pi/\epsilon}, \quad (46)$$

where w_3 is the crack-opening displacement evaluated at a small distance "ϵ" from the crack front.

To validate the code by comparison with known solutions, numerical results have been obtained for a rectangular crack of width "$2a$" and length "$2b$," where "b" is 6.1 times "a." The mesh is generated by a robust mesh generator (see Clifton and Wang, 1991; Guo et al., 1994) and is shown in Fig. 2. For $b \gg a$, the effects from the two ends $x = a$ and $x = -a$ on the solutions at $x = 0$ are small and the two-dimensional solution (i.e., for $b = \infty$) for a crack of depth "$2a$" should be a good approximation. Figure 4 shows the calculated stress intensity factor at points A and B for the subsurface rectangular crack of Fig. 2, subjected to a uniform pressure p. The results compare favorably with the corresponding two-dimensional results of Isida (1967).

For a surface-breaking crack, the stresses near the intersection of the crack front with the free surface have the form (Benthem, 1977; Bazant and Estenssoro, 1979; Ghahremani and Shih, 1992)

$$\sigma_{ij} = K_A r^{-t} + K_S r^{-s} + \ldots, \quad (47)$$

where $t \geq 0.5 \geq s$ and r is the distance from the intersecting point. The leading term in the series corresponds to the antisymmetric mode with amplitude K_A (field producing in-plane and out-of-plane shears), while the second term corresponds to the opening mode with amplitude K_S. For a crack perpendicular to the free surface and subjected to pure pressure on the crack face, the stress intensity factor K_A is zero. Thus, for this case the stress singularity can not be greater than $1/r^{1/2}$. Bazant and Estenssoro (1979), Ghahremani and Shih (1992) show that $s = 0.5$ results only for Poisson's ratio $\nu = 0$; otherwise $s < 0.5$ for $\nu > 0$. It is interesting to note from Eq. (23) that the line integral in Eq. (17) vanishes for $\nu = 0$.

For a two-dimensional surface-breaking crack of depth "a" under a uniform pressure p, the stress intensity factor at point B (Fig. 2), normalized by the stress intensity factor of the crack with half crack width "a" in an infinite body, is 1.12. Numerical results for rectangular surface-breaking cracks under a uniform pressure have been obtained for both $\nu = 0$ and $\nu = 0.3$. The length of the crack is 8.6 times the crack depth "a." The calculated values of the normalized stress intensity factor at the point B (Fig. 2) are 1.09 and 1.12 for $\nu = 0$ and 0.3, respectively.

Numerical results have also been obtained for a surface breaking semi-circular crack of radius "a" under a uniform pressure p for $\nu = 0$ and $\nu = 0.3$. One half of the mesh is shown in Fig. 5. The stress intensity factor at the deepest point, normalized by $p(\pi a)^{1/2}$, is 0.631 and 0.655 for $\nu = 0$ and 0.3, respectively. These values agree reasonably well with values of 0.636, 0.640 which were reported for $\nu = 0$ by Nasitani and Murakami (1974) and by Murakami (1985), and with values of 0.666, 0.666, and 0.662 for $\nu = 0.3$ which were obtained by Murakami (1985), Lee, Farris, and Keer (1987) and Dai, Nowell, and Hills (1993), respectively.

The order of stress singularity changes where the crack breaks the surface. Since the stress singularity at the surface is less than $r^{-0.5}$ (e.g., $r^{-0.45}$ for $\nu = 0.3$), and a square root singularity in the stress is explicitly enforced here, as well as in other researcher's work, the computed value of stress intensity factor at the surface should be zero. For a semi-circular crack of radius "a" under a uniform pressure p, our numerical value of stress intensity factor for $\nu = 0.3$, normalized by $p(\pi a)^{1/2}$, is 0.399. This value is much closer to the theoretical value of 0 than are the values 0.744, 0.748, and 0.732 obtained by Murakami (1985), Lee, Farris, and Keer (1987), and Dai, Nowell, and Hills (1993), respectively. This comparison suggests that the present numerical procedure allows a better resolution at the locations where the crack front intersects the free surface.

As further indication of the numerical attractiveness of the current approach, the condition number of the stiffness matrix $\mathbf{K}$ is found to be acceptably small. The condition number, defined as $\|\mathbf{K}\|\|\mathbf{K}^{-1}\|$ where the norm of a matrix can be defined as

$$\|\mathbf{K}\| = \max_i \left(\max_j \left(|\mathbf{K}_{ij}|\right)\right), \quad (48)$$

is a measure of the error in the solution due to errors in the right-hand side of Eq. (31). For the formulation presented here the condition number of the stiffness matrix varies from 50 to 100 for surface cracks and from 15 to 25 for buried cracks. These values indicate that the stiffness matrix is well conditioned.

6 Concluding Remarks

A numerical method has been developed for three-dimensional analysis of surface-breaking or subsurface cracks in a half-space. The method is based on the fundamental solution for a dislocation segment in a half-space. A singular integral equation with the gradient of the crack opening as the unknown is obtained by replacing the Burgers vectors of the dislocation by the gradient of the crack opening. The singular integral equation derived here is one order less singular than that of the singular integral equations that are derived from the eigenstrain method. As a result, numerical difficulties are greatly reduced. Comparison of the integral equation derived here with those presented by others shows agreement with those of Lee and Keer (1986), Weaver (1973), but disagreement with Lee, Advani, and Lee (1988). The latter formulation appears to be incorrect due to the error introduced by imposing compatibility conditions on the eigenstrains.

The surface integral equations are solved by means of the variational approach of minimizing the total potential energy. The crack surface is covered by triangular elements and the crack displacements are assumed to vary linearly over each

Downloaded 04 May 2010 to 171.66.16.33. Redistribution subject to ASME license or copyright; see http://www.asme.org/terms/Terms_Use.cfm

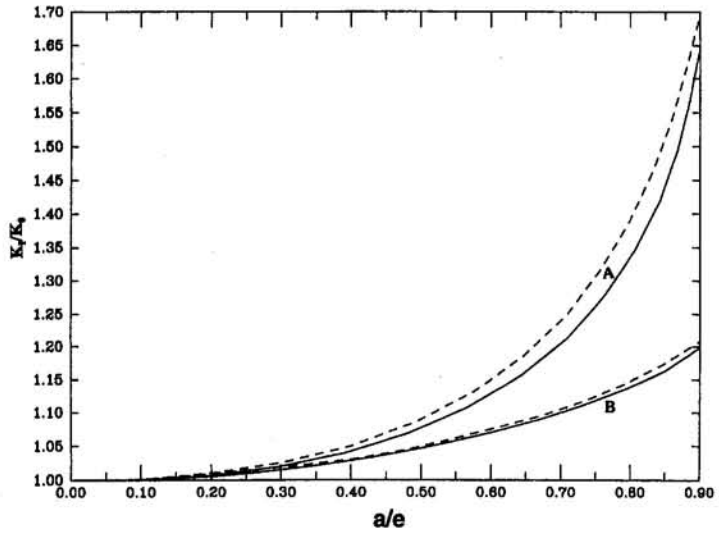


Fig. 4 Normalized stress intensity factors for a sub-surface rectangular crack under uniform pressure, where "a" is one half of the crack height and "e" is the distance of the crack center to the free surface. The crack length is 6.1 times the crack height. The Poisson's ratio $\nu = 0.3$.

element. Near the crack front the crack-opening displacements are assumed to vary as the square root of the distance from the tip. The variational formulation results in a full, symmetric stiffness matrix.

The regular kernel becomes singular for surface-breaking cracks when the field point is on the free surface. Because the singularity in the present formulation is one order less than in the previous formulations (e.g., Weaver, 1973; Murakami, 1985; Lee and Keer, 1986), special numerical techniques are not required to evaluate the integrals when the field point is near the free surface. In fact, the partial integrations over source elements have been evaluated analytically. Thus, the computational advantages obtained previously for the singular terms (Guo et al., 1994) extend to the singularity which arises from the "regular" terms when the field point approaches the free surface. These advantages in the numerical evaluation of the stiffness elements are believed to improve computational efficiency substantially. When combined with the symmetry of the stiffness matrix obtained from the variational formulation, the accurate representation of the near-tip field, and the use of continuous displacement fields the method appears to be capable of providing quite accurate results with a relatively course mesh.

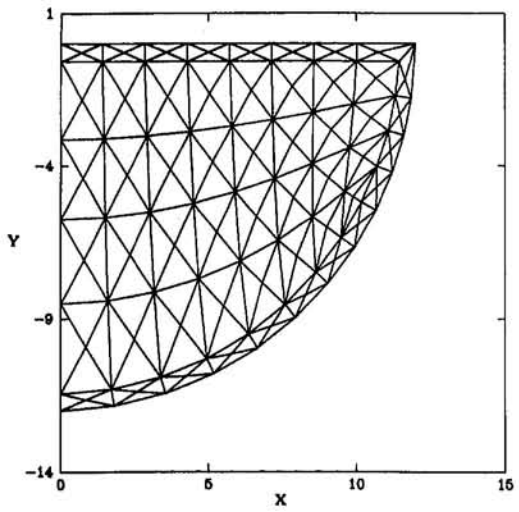


Fig. 5 One half of the meshed region for a semi-circular crack

Acknowledgment

This work was carried out in the course of a project sponsored by the Naval Air Warfare Center through the Small Business Innovation Research (SBIR) program under Contract No. N00421-91-C-0119. Dr. L. J. Mertaugh is the project monitor.

References

Bazant, Z. P., and Estenssoro, L. F., 1979, "Surface singularity and crack propagation," *International Journal of Solids and Structures,* Vol. 15, pp. 405–426 (see also erratum Vol. 19, p. 661, 1983).

Benthem, J. P., 1977, "State of stress at the vertex of a quarter-infinite crack in a half-space," *International Journal of Solids and Structures,* Vol. 13, pp. 479–492.

Bilby, B. A., and Eshelby, J. D., 1968, "Dislocations and the Theory of Fracture," *Fracture,* H. Liebowitz, ed., Vol. 1, Academic Press, New York, pp. 99–182.

Bueckner, H. F., 1977, "The Edge Crack in a Half Space," Proceedings of *International Conference on Fracture Mechanics and Technology,* G. C. Sih and C. L. Chow, eds., Sijthoff and Noordhoff, The Netherlands, pp. 1091–1107.

Bui, H. D., 1977, "An integral equations method for solving the problem of a plane crack of arbitrary shape," *Journal of the Mechanics and Physics of Solids,* Vol. 25, pp. 29–39.

Clifton, R. J., and Abou-Sayed, A. S., 1981, "A variational approach to the prediction of the three-dimensional geometry of hydraulic fractures," SPE/DOE Paper No. 9879, *Proceedings of Low Permeability Symposium,* Denver, Co., pp. 457–463.

Clifton, R. J., and Wang, J. J., 1991, "Adaptive optimal mesh generator for hydraulic fracturing modeling," *Rock Mechanics as a Multidisciplinary Science,* pp. 607–616.

Dai, D. N., Nowell, D., and Hills, D. A., 1993, "Eigenstrain methods in three-dimensional crack problems: An alternative integration procedure," *Journal of the Mechanics and Physics of Solids,* Vol. 41, pp. 1003–1017.

Ghahremani, F., and Shih, C. F., 1992, "Corner Singularities of Three-Dimensional Planar Interface Cracks," ASME JOURNAL OF APPLIED MECHANICS, Vol. 59, pp. 62–68.

Guo, Q., Wang, J. J., Clifton, R. J., and Mertaugh, L. J., 1995, "Elastic Analyses of Planar Cracks of Arbitrary Shape," ASME JOURNAL OF APPLIED MECHANICS, Vol. 62, pp. 108–115.

Hanson, M. T., Lin, W., and Keer, L. M., 1989, "Three-Dimensional Analysis of Cracking Through the Boundary of a Two-Phase Material," ASME JOURNAL OF APPLIED MECHANICS, Vol. 56, pp. 850–857.

Hirth, J. P., and Lothe, J., 1982, *Theory of Dislocations,* 2nd ed., pp. 98–101.

Isida, M., 1966, "Stress Intensity Factors for the Tension of an Eccentrically Cracked Strip," ASME JOURNAL OF APPLIED MECHANICS, Vol. 33, pp. 674–675.

Kanninen, M. F., and Popelar, C. H., 1985, *Advanced fracture mechanics,* Cambridge University Press, Cambridge, U.K., pp. 142–145.

Lord Kelvin, 1882, "Note on the integration of the equations of equilibrium of an elastic solid," *Mathematical and Physical Papers,* Vol. 1, Cambridge University Press, Cambridge, U.K., pp. 97–98.

Keer, L. M., Farris, T. N., and Lee, J. C., 1986, "Knoop and Vickers indentation of ceramics analyzed as a three-dimensional fracture," *Journal of the American Ceramic Society,* Vol. 69, pp. 393–396.

Downloaded 04 May 2010 to 171.66.16.33. Redistribution subject to ASME license or copyright; see http://www.asme.org/terms/Terms_Use.cfm

Kurashige, M., and Clifton, R. J., 1992, "Integral equations for the problem of a 3D crack in an infinite, fluid-filled, poroelastic solid," *SPE Production Engineering,* Feb., pp. 34–38.

Lee, J. C., Farris, T. N., and Keer, L. M., 1987, "Stress intensity factors for cracks of arbitrary shape near an interfacial boundary," *Engineering Fracture Mechanics,* Vol. 27, pp. 27–41.

Lee, J. C., and Keer, L. M., 1986, "Study of a Three-Dimensional Crack Terminating at an Interface," ASME JOURNAL OF APPLIED MECHANICS, Vol. 53, pp. 311–316.

Lee, T. S., Advani, S. H., and Lee, J. K., 1987, "Three-Dimensional Analysis of an Arbitrary Shaped Pressurized Crack Traversing a Bi-Material Interface," *Engineering Fracture Mechanics,* Vol. 30, pp. 191–209.

Lin, W., and Keer, L. M., 1989, "Analysis of a Vertical Crack in a Multilayered Medium," ASME JOURNAL OF APPLIED MECHANICS, Vol. 56, pp. 63–69.

Mindlin, R. D., 1936, "Force at a point in the interior of a semi-infinite solid," *Physics,* Vol. 7, pp. 195–202.

Mura, T., 1963, "Continuous Distribution of Moving Dislocations," *Philosophical Magazine,* Vol. 8, pp. 843–857.

Mura, T., 1982, *Micromechanics of Defects in Solids,* Martinus Nijhoff Publishers.

Murakami, Y., 1985, "Analysis of stress intensity factors of modes I, II and III for inclined surface cracks of arbitrary shape," *Engineering Fracture Mechanics,* Vol. 22, pp. 101–114.

Murakami, Y., and Nemat-Nasser, S., 1982, "Interacting dissimilar semi-elliptical surface flaws under tension and bending," *Engineering Fracture Mechanics,* Vol. 16, pp. 373–386.

Murakami, Y., and Nemat-Nasser, S., 1983, "Growth and stability of interacting surface flaws of arbitrary shape," *Engineering Fracture Mechanics,* Vol. 17, pp. 193–210.

Nisitani, H., and Murakami, Y., 1974, "Stress intensity factors of an elliptical crack or a semi-elliptical crack subject to tension," *International Journal of Fracture,* Vol. 10, pp. 353–368.

Sladek, J., and Sladek, V., 1986, "Dynamic stress intensity factors studied by boundary integro-differential equations," *International Journal for Numerical Methods in Engineering,* Vol. 23, pp. 919–928.

Weaver, J., 1973, "A Simple Earthquake Control Model," Ph.D. thesis, Harvard University.

Weaver, J., 1977, "Three-dimensional crack analysis," *International Journal of Solids and Structures,* Vol. 13, pp. 321–330.

Xu, G., and Ortiz, M., 1993, "A Variational Boundary Integral Method for the Analysis of 3D Cracks of Arbitrary Geometry Modeled as Continuous Distributions of Dislocation Loops," *International Journal for Numerical Method in Engineering,* Vol. 36, pp. 3675–3701.

Appendix A

The $R_{(m)ij}$ terms in Eq. (21) and Eq. (22) are listed here.

$$R_{(3)31} = (x' - x)\left\{\frac{1 - 2\nu}{R_2^3} - \frac{4(1 - \nu)(1 - 2\nu)}{R_2(R_2 - y' - y)^2} - \frac{6y'y}{R_2^5}\right\}, \quad \text{(A1)}$$

$$R_{(1)33} = (x' - x)\left\{\frac{(1 - 2\nu)(3 - 4\nu)}{R_2^3} - \frac{4(1 - \nu)(1 - 2\nu)}{R_2(R_2 - y' - y)^2} - \frac{6y[y - (1 - 2\nu)(y + y')]}{R_2^5}\right\}, \quad \text{(A2)}$$

$$R_{(3)32} = -\left\{\frac{(1 - 2\nu)(y - y')}{R_2^3} + \frac{6y'y(y + y')}{R_2^5}\right\}, \quad \text{(A3)}$$

$$R_{(2)33} = -\left\{\frac{(1 - 2\nu)[3(y - y') + 4\nu(y + y')]}{R_2^3} - \frac{4(1 - \nu)(1 - 2\nu)}{R_2(R_2 - y' - y)} - \frac{6y(y + y')[(1 - 2\nu)y' - 2\nu y]}{R_2^5}\right\}. \quad \text{(A4)}$$

Appendix B

The regular kernels G^β ($\beta = 1, 2$) in Eq. (25) for a subsurface crack in a half-space have been given in Lee, Advani, and Lee (1988) as follows:

$$G^1 = (x' - x)\left\{\frac{1 - 4\nu}{R_2^3} + \frac{2(1 - 2\nu)}{R_2(R_2 - y - y')^2} - 2\frac{(y' + y)(2R_2 - y - y')}{R_2^3(R_2 - y - y')^2} - \frac{6}{1 - 2\nu}\frac{y'[2\nu(y + y') - y]}{R_2^5}\right\}, \quad \text{(B1)}$$

$$G^2 = -\frac{(3 - 4\nu)[y - y' - 2\nu(y + y')] + 4\nu y'}{(1 - 2\nu)R_2^3} - \frac{4(1 - \nu)}{R_2(R_2 - y' - y)} + \frac{6}{1 - 2\nu}\frac{y'(y + y')[2\nu(y + y') - y]}{R_2^5}. \quad \text{(B2)}$$

Downloaded 04 May 2010 to 171.66.16.33. Redistribution subject to ASME license or copyright; see http://www.asme.org/terms/Terms_Use.cfm

Singularities at Grain Triple Junctions in Two-Dimensional Polycrystals With Cubic and Orthotropic Grains

R. C. Picu
Division of Engineering,
Brown University,
Providence, RI 02912

V. Gupta
Department of Mechanical
and Aerospace Engineering,
University of California,
Los Angeles, CA 90095
Mem. ASME

Stress singularities at grain triple junctions are evaluated for various asymmetric grain boundary configurations and random orientations of cubic and orthotropic grains. The analysis is limited to elastic plane-strain deformation and carried out using the Eshelby-Stroh formalism for anisotropic elasticity. For both the cubic and orthotropic grains, the most singular configuration corresponds to the fully symmetric case with grain boundaries 120 deg apart, and with symmetric orientations of the material axes. The magnitude of the singularities are obtained for several engineering polycrystals.

1 Introduction

The stress concentration at grain-triple junctions due to elastic anisotropy of grains is the primary source of crack nucleation in brittle solids. In addition to elastic anisotropy, the thermal expansion anisotropy of the grains can also result in stress concentrations. Considering a group of hexagonal grains with different orientations of the principal axes of thermal anisotropy, Evans (1978) and Fu and Evans (1985) showed that the stress at the triple junction exhibits a weak logarithmic singularity. The combined case with consideration to elastic anisotropy was analyzed by Tvergaard and Hutchinson (1988). They limited their study to planar triple-junction geometries with symmetrically oriented grain boundaries 120 deg apart, and with one symmetric orientation of the material axes of the grains. The resulting stress field was found to be of power-law type, with singularity exponent ranging only from -0.1 to -0.2 for typical engineering ceramics with cubic and orthotropic grains.

The aim of our study is to establish if more severe stress singularities will result for realistic triple junction geometries with random orientations of the material axes. The analysis was carried out using Eshelby-Stroh formalism and limited to two-dimensional polycrystals with cubic and orthotropic grains. The motivation for these calculations came from the need to understand the mechanism of crack nucleation in two-dimensional columnar freshwater ice polycrystals where the microstructure normal to the column axis (normal to the c-axis) shows nonsymmetric triple junction configurations. The results presented here are, however, general, and applicable to other brittle materials like rocks and ceramics.

Although most studies including the current one are limited to two-dimensional geometries, some attempts have been made to study the stress concentrations in three-dimensional configurations. Bazant and Keer (1974) and Keer and Parihar (1978) analyzed the elastic stress singularities at conical inclusions considering both materials to be isotropic. Somaratna and Ting (1986) studied the general problem related with the three-dimensional stress singularities at the vertex of anisotropic conical wedges. They extended the numerical technique of Bazant and Estenssoro (1979) to determine the power of the singularity for any shape of the lateral surface of the conical wedge. Ghahremani et al. (1990) determined stress concentration at vertices of a conical isotropic inclusion in an isotropic matrix with differing moduli and found singularities steeper than -0.5 (super singularities) when the shear modulus of the inclusion was about five times that of the matrix. Similarly, when the inclusion and the matrix material were considered to be same but with different orientations of the transversely isotropic axes, super singularities were obtained for moderate levels of anisotropy. However, the singularities at the vertex formed by four cubic grains were weaker than -0.5 for typical levels of anisotropy found in real polycrystals. In general they found that the vertices concentrate much higher stress than the two-dimensional junctions. Such super singularities were also unearthed in the current work at junctions of orthotropic grains, albeit for very high degree of elastic anisotropy. The presence of super singularities suggest spontaneous nucleation of a crack from a precursor of arbitrarily small size.

2 Eshelby-Stroh Formalism for Anisotropic Elasticity

The constitutive law for a hyperelastic material within the small strain and rotation idealization can be written as

$$\sigma_{ij} = c_{ijks} u_{k,s}, \tag{1}$$

where c_{ijks} is the elasticity tensor relating the stresses σ_{ij} to the gradients of the displacement components u_k. For plane deformations with displacement field only a function of x_1 and x_2, the displacement components u_k can be expressed in terms of an analytical function $f(Z)$ as (Eshelby et al., 1953; Lekhnitskii, 1963)

$$u_k = a_k f(Z), \quad k = 1, 2, 3 \tag{2}$$

with

$$Z = x_1 + p x_2.$$

Substituting Eq. (2) in Eq. (1) and using the equilibrium equation $\sigma_{ij,j} = 0$ leads to the following eigenvalue problem with eigenvalues p and eigenvector $\mathbf{a}$:

$$\{c_{i1k1} + p(c_{i1k2} + c_{i2k1}) + p^2 c_{i2k2}\} a_k = 0. \tag{3}$$

Equation (3) can be expressed in matrix notation (Ting, 1986) by defining matrices $\mathbf{Q}$, $\mathbf{R}$ and $\mathbf{T}$ with components

Contributed by the Applied Mechanics Division of THE AMERICAN SOCIETY OF MECHANICAL ENGINEERS for publication in the ASME JOURNAL OF APPLIED MECHANICS.

Discussion on this paper should be addressed to the Technical Editor, Professor Lewis T. Wheeler, Department of Mechanical Engineering, University of Houston, Houston, TX 77204-4792, and will be accepted until four months after final publication of the paper itself in the ASME JOURNAL OF APPLIED MECHANICS.

Manuscript received by the ASME Applied Mechanics Division, July 1, 1994; final revision, Mar. 20, 1995. Associate Technical Editor: J. T. Jenkins.

Copyright © 1996 by ASME

Downloaded 04 May 2010 to 171.66.16.33. Redistribution subject to ASME license or copyright; see http://www.asme.org/terms/Terms_Use.cfm

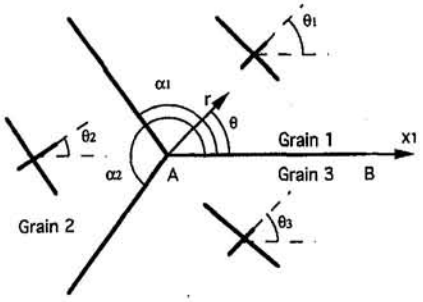


Fig. 1 Geometry of a grain-triple junction defining the orientations of the grain boundaries and material axes of the grains

$$Q_{ik} = c_{i1k1}$$
$$R_{ik} = c_{i1k2}$$
$$T_{ik} = c_{i2k2} \tag{4a}$$

as

$$\{\mathbf{Q} + p(\mathbf{R} + \mathbf{R}^T) + p^2\mathbf{T}\}\mathbf{a} = \mathbf{0}. \tag{4b}$$

The six eigenvalues p_α appear only in complex conjugate pairs as $p_{\alpha+3} = \bar{p}_\alpha$ with $\alpha = 1, 2, 3$ (Eshelby et al., 1953). Here and in the following, an overbar denotes the complex conjugates. The displacement $\mathbf{u}$ and traction vector $\mathbf{t}$ on a radial line making an angle θ to the x_1-axis can be expressed as a linear combination of eigenvectors $\mathbf{a}_\alpha$ as

$$\mathbf{u} = \sum_{\alpha=1}^{3} [m_\alpha \mathbf{a}_\alpha f(Z_\alpha) + n_\alpha \bar{\mathbf{a}}_\alpha f(\bar{Z}_\alpha)]$$

$$\mathbf{t}(\theta) = \frac{1}{r}\sum_{\alpha=1}^{3}\left[m_\alpha \mathbf{b}_\alpha Z_\alpha \frac{d}{dZ_\alpha} f(Z_\alpha) + n_\alpha \bar{\mathbf{b}}_\alpha \bar{Z}_\alpha \frac{d}{d\bar{Z}_\alpha} f(\bar{Z}_\alpha)\right] \tag{5}$$

where $\mathbf{b}_\alpha$ is an associate vector directly related to the eigenvector $\mathbf{a}_\alpha$ and the matrices $\mathbf{Q}$, $\mathbf{R}$ and $\mathbf{T}$ as

$$\mathbf{b}_\alpha = (\mathbf{R}^T + p_\alpha \mathbf{T})\mathbf{a}_\alpha = -\frac{1}{p_\alpha}(\mathbf{Q} + p_\alpha \mathbf{R})\mathbf{a}_\alpha, \tag{6}$$

and m_α, n_α ($\alpha = 1, 2, 3$) are arbitrary constants which depend upon the specific boundary value problem at hand.

3 Problem Statement and Solution Strategy

Figure 1 defines a typical triple junction geometry between three grains with different orientations of the principal material axes. With x_1-axis aligned with the grain boundary AB, the orientation of the other two boundaries is defined by the angles α_1 and α_2 with respect to the polar coordinate system centered at the triple point. The orientation of the three grains are specified, respectively, by the angles θ_1, θ_2, and θ_3 of the most compliant direction (shown by a shorter line in Fig. 1) with respect to the global x_1-axis for orthotropic grains. For cubic grains these angles define orientations of one of the material axes. The stress singularities at the triple junction were determined for different combinations of α_1, α_2, θ_1, θ_2, and θ_3. Since the material in all grains is identical, the elastic deformation within each grain will be governed by the eigenvalue problem in Eq. (3), with eigenvectors $\mathbf{a}_\alpha$ and the associates $\mathbf{b}_\alpha$ (Eq. (6)). Let us further define matrices $\mathbf{A}$ and $\mathbf{B}$ as the collection of these eigenvectors as

$$\mathbf{A} = [\mathbf{a}_1, \mathbf{a}_2, \mathbf{a}_3]$$
$$\mathbf{B} = [\mathbf{b}_1, \mathbf{b}_2, \mathbf{b}_3]. \tag{7}$$

Since the stress field is of separable form near the triple junction, the complex function $f(Z)$ in Eq. (5) can be taken as

$$f(Z) = \frac{1}{\gamma + 1} Z^{\gamma+1}, \tag{8}$$

where γ is a complex number. The displacements and the tractions on a radial plane can be expressed in the local coordinate system of the grain "i" (denoted by the superscript) using Eqs. (5) and (8) as

$$\mathbf{u}^i = \frac{1}{\gamma + 1}[\mathbf{A}\mathbf{Z}^i\mathbf{m}^i + \bar{\mathbf{A}}\bar{\mathbf{Z}}^i\mathbf{n}^i]$$

$$\mathbf{t}^i(\theta) = \frac{1}{r}[\mathbf{B}\mathbf{Z}^i\mathbf{m}^i + \bar{\mathbf{B}}\bar{\mathbf{Z}}^i\mathbf{n}^i] \tag{9}$$

where

$$\mathbf{Z}^i = \begin{pmatrix} Z_1^i & 0 & 0 \\ 0 & Z_2^i & 0 \\ 0 & 0 & Z_3^i \end{pmatrix}^{\gamma+1}$$

$$Z_\alpha^i = x_1^i + p_\alpha x_2^i = r(\cos\theta^i + p_\alpha \sin\theta^i) \quad i = 1, 2, 3 \tag{10}$$

and $\mathbf{m}^i$ and $\mathbf{n}^i$ are two 3×1 vectors with unknown components m_α^i and n_α^i, which in turn are to be determined for each grain from the boundary conditions.

The boundary value problem associated with the configuration in Fig. 1 is defined by the continuity of displacements $\mathbf{u}$ and tractions $\mathbf{t}$ at the three grain boundaries. This leads to a system of 18×18 equations in terms of the unknown components m_α^i and n_α^i. This can be reduced to a set of 6×6 equations by using the identities (Ting, 1986)

$$\mathbf{A}^T\mathbf{B} + \mathbf{B}^T\mathbf{A} = I$$
$$\mathbf{A}^T\bar{\mathbf{B}} + \mathbf{B}^T\bar{\mathbf{A}} = \mathbf{0}$$
$$\bar{\mathbf{A}}^T\bar{\mathbf{B}} + \bar{\mathbf{B}}^T\bar{\mathbf{A}} = I$$
$$\bar{\mathbf{B}}^T\mathbf{A} + \bar{\mathbf{A}}^T\mathbf{B} = \mathbf{0} \tag{11}$$

For a nontrivial solution, the determinant of the coefficients should be zero leading to a eigenvalue problem with eigenvalues γ and eigenvectors $[\mathbf{m}^1, \mathbf{n}^1, \mathbf{m}^2, \mathbf{n}^2, \mathbf{m}^3, \mathbf{n}^3]^T$. The determinant of the reduced set of equations can be written in a simplified form by defining two new matrices Ω^{ij} and $\mathbf{M}^i$ as

$$\det(\mathbf{D}) = 0 \tag{12a}$$

$$\mathbf{D} = \mathbf{M}^1\Omega^{31} - \Omega^{21}\mathbf{M}^2\Omega^{32}\mathbf{M}^3. \tag{12b}$$

The matrix Ω^{ij} is defined in terms of the rotational matrix ω^{ij} relating the local coordinate systems in grains i and j. In terms of a 3×3 null matrix $\mathbf{0}$, Ω^{ij} takes the following form:

$$\Omega^{ij} = \begin{pmatrix} \omega^{ij} & \mathbf{0} \\ \mathbf{0} & \omega^{ij} \end{pmatrix}, \tag{13}$$

where

$$\omega^{ij} = \begin{pmatrix} \cos(\theta_i - \theta_j) & \sin(\theta_i - \theta_j) & 0 \\ -\sin(\theta_i - \theta_j) & \cos(\theta_i - \theta_j) & 0 \\ 0 & 0 & 1 \end{pmatrix}, \tag{14}$$

and θ_i, θ_j are measured in the global coordinate system shown in Fig. 1. Further, the matrix $\mathbf{M}^i$ for grain i is defined as

$$\mathbf{M}^i = \mathbf{U}\mathbf{X}^i\mathbf{U}^{-1} = \mathbf{U}\mathbf{X}^i\mathbf{U}^T\mathbf{J} \tag{15}$$

with $\mathbf{U}$ being a 6×6 matrix containing the eigenvectors $\mathbf{a}_\alpha$ and $\mathbf{b}_\alpha$

Downloaded 04 May 2010 to 171.66.16.33. Redistribution subject to ASME license or copyright; see http://www.asme.org/terms/Terms_Use.cfm

Table 1 Q and R values for several cubic materials along with the largest values of the singularity exponent. The elastic constants used to compute Q and R were taken from Simmons and Wang (1985).

Material	Q	R	γ
magnetite	0.91	1.07	-0.015
pyrite	2.15	8.11	-0.126
CaO	0.54	1.25	-0.07
ZrC	3.57	0.78	NS
TiC	1.54	0.92	NS
Ge	1.39	1.41	-0.065
Si	1.27	1.39	-0.058

$$\mathbf{U} = \begin{pmatrix} \mathbf{A} & \bar{\mathbf{A}} \\ \mathbf{B} & \bar{\mathbf{B}} \end{pmatrix}, \tag{16}$$

and $\mathbf{J}$ defined in terms of a 3×3 null and an identity matrix $\mathbf{I}$ as

$$\mathbf{J} = \begin{pmatrix} \mathbf{0} & \mathbf{I} \\ \mathbf{I} & \mathbf{0} \end{pmatrix}. \tag{17}$$

Finally, the matrix $\mathbf{X}^i$ in Eq. (15) is a 6×6 diagonal matrix with elements

$$X^i_{\alpha\alpha} = \left[\frac{\cos \theta^{ij} + p_\alpha \sin \theta^{ij}}{\cos \theta^{ik} + p_\alpha \sin \theta^{ik}} \right]^{\gamma+1}, \tag{18}$$

where θ^{ij} and θ^{ik} refers to the position of the grain boundaries that grain i makes with grains j and k, respectively. Further, both angles are measured in the local coordinate system of grain i with grains j and k located counterclockwise and clockwise to grain i, respectively. Here, $\alpha = 1, 2, \ldots 6$, and for $\alpha > 3$, $p_\alpha = \bar{p}_{\alpha-3}$.

The matrix $\mathbf{D}$ in Eq. (12b) is a function of γ through the matrices $\mathbf{M}^i$ and $\mathbf{X}^i$, such that Eq. (12a) defines an eigenvalue problem. The roots of Eq. (12a) were found numerically. An important help in this task comes from the theorem presented by Ting (1984) which allows the determination of the number of roots in a given region of the complex γ plane.

In general the γ values were found to be complex. The real values of γ in the interval $(-1, 0)$ imply singular stress field ($\sigma_{ij} \propto r^\gamma$) at the triple junction, while the complex values lead to nonphysical oscillations, similar to those known for interface cracks. Next, we determine the singularity γ for several polycrystals with cubic and orthotropic grains.

4 Results and Discussions

When the x_1-x_2 coordinate system is aligned with the material axes of an orthotropic grain, the elastic constitutive relations under a plane deformation are prescribed in terms of four independent elastic constants c_{11}, c_{22}, c_{12}, and c_{44} as

$$\begin{aligned} \sigma_{11} &= c_{11}\epsilon_{11} + c_{12}\epsilon_{22} \\ \sigma_{22} &= c_{12}\epsilon_{11} + c_{22}\epsilon_{22} \\ \sigma_{12} &= 2c_{44}\epsilon_{12}. \end{aligned} \tag{19}$$

The constitutive relations for the cubic materials can be prescribed by setting $c_{11} = c_{22}$ in Eqs. (19).

Let us consider first the case of transversely cubic grains with their 1-2 axes aligned with the x_1 and x_2-axes, respectively. For traction-prescribed boundary conditions, the plane deformation is characterized by two nondimensional parameters Q and R defined as

$$Q = \frac{c_{44}}{c_{12}}, \quad R = \frac{c_{12} + 2c_{44}}{c_{11}}. \tag{20}$$

For isotropic materials, R assumes a value of unity while increasing values of Q and R represent higher degrees of elastic anisotropy. Table 1 gives values for these parameters for some representative ceramics and minerals. Several configurations were investigated and only those that yield the most singular stress field are presented here. Unless stated, all calculations discussed below correspond to $Q = 0.49$ and $R = 1.45$.

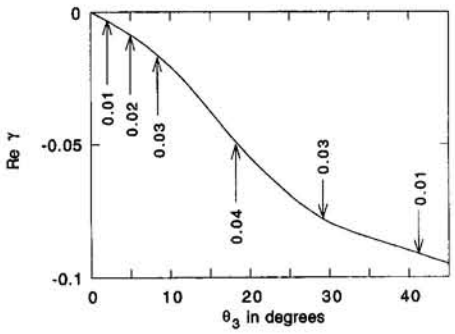


Fig. 2 Variation of the singularity exponent with θ_3 for a junction of cubic grains defined by $\alpha_1 = 120$ deg, $\alpha_2 = 240$ deg, $\theta_1 = \theta_3$, and $\theta_2 = 0$ deg

A polycrystal of cubic grains when subjected to a macroscopic hydrostatic stress reproduces at the local scale the same uniform stress. Thus there always exists an eigenvalue $\gamma = 1$ such that $\sigma_{ij} \propto \delta_{ij}$. Singularities under nonhydrostatic loading are given below. Figure 2 shows the variation of the singularity γ with θ_3 ($=\theta_1$) when the three grain boundaries are 120 deg apart, and $\theta_2 = 0$ deg. A peak value of $\gamma = -0.095$ is obtained for $\theta_3 = 45$ deg. The imaginary parts of the roots are shown through arrows in Fig. 2.

Next, by keeping the grain boundaries at 120 deg, configurations with random grain orientations were explored. Figure 3 shows the real part of the singularity for the case when θ_1 was fixed at 30 deg while varying θ_3 arbitrarily and keeping $\theta_2 = 0$ deg throughout. The singularities are generally low, with the largest values of $\gamma = -0.139$ corresponding to the fully symmetric case.

Figure 4 provides a singularity map in the $\theta_3 - \alpha_1$ space for the case when $\theta_2 = 0$ deg, $\theta_3 = -\theta_1$ and $\alpha_2 = 360$ deg $- \alpha_1$. This calculation to some extent explores the interaction of randomness in grain boundary configuration and that of the grain axes. The singularity contours construct a hill with a peak of -0.139 corresponding to the fully symmetric case with $\alpha_1 = 120$ deg and $\theta_3 = 30$ deg. This is the same configuration considered by Tvergaard and Hutchinson (1988) with identical γ value. Notably, the upper half of the singularity map corresponds to configurations with no singularity in the stress field; with the diagonal separating the singular and nonsingular zones.

Finally, Fig. 5 shows the singularity contours in the Q-R space for the most singular symmetric configuration found above. All values in this chart represent the real part of γ. The imaginary part of the exponent is very small, ranging from 10^{-7} for R

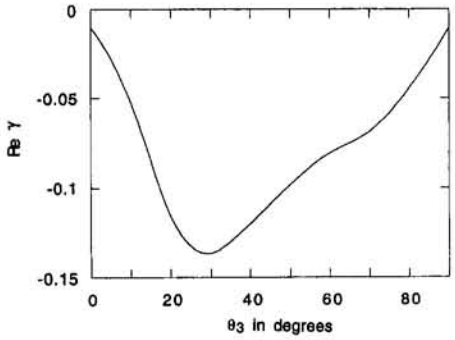


Fig. 3 Variation of the real part of the singularity γ with θ_3 for a junction of cubic grains defined by $\alpha_1 = 120$ deg, $\alpha_2 = 240$ deg, $\theta_1 = 30$ deg, and $\theta_2 = 0$ deg

Downloaded 04 May 2010 to 171.66.16.33. Redistribution subject to ASME license or copyright; see http://www.asme.org/terms/Terms_Use.cfm

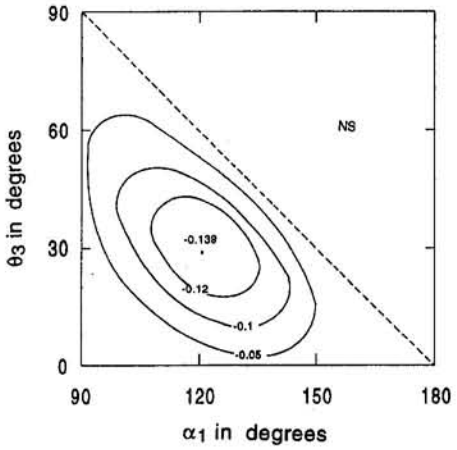


Fig. 4 Contours of the singularity exponent γ in the α_1-θ_3 plane for a symmetric cubic grain junction defined by $\alpha_2 = 360$ deg $- \alpha_1$, $\theta_1 = -\theta_3$ and $\theta_2 = 0$ deg

close to 1 to 10^{-4} for $R = 2$ and $Q = 0.5$. The bold line in Fig. 5 represents the border below which real materials cannot exist since the condition of the positive definiteness of the strain energy density is not satisfied. As one approaches this border the singularity exponent γ is close to -0.3 for $1.2 < R < 1.4$, and -0.4 for $1.4 < R < 2$. For all materials listed in Table 1, the singularities are smaller than -0.13. Next we consider the triple junctions between orthotropic grains.

For a simply connected domain with traction-prescribed boundary conditions, the stresses σ_{ij} and hence the singularity exponent depend only on two nondimensional combinations of the elastic moduli λ and ρ defined as (Suo, 1991)

$$\lambda = \frac{c_{22}}{c_{11}}$$

$$\rho = \frac{1}{c_{44}} \frac{c_{11}c_{22} - c_{12}^2 - 2c_{12}c_{44}}{2\sqrt{c_{11}c_{22}}}. \qquad (21)$$

A value of $\lambda = 1$ corresponds to the transversely cubic case, whereas for $\lambda = \rho = 1$ the material degenerates to a transversely isotropic case. This is consistent with a recent general result provided by Ting (1995), where he shows that the order of the stress singularity at a triple junction formed by wedges of the same material with differing orientations but all having the x_1-x_2 plane as the plane of material symmetry (as is the case here), depends only on the two eigenvalues p_1 and p_2 of the eigenvalue problem (3).

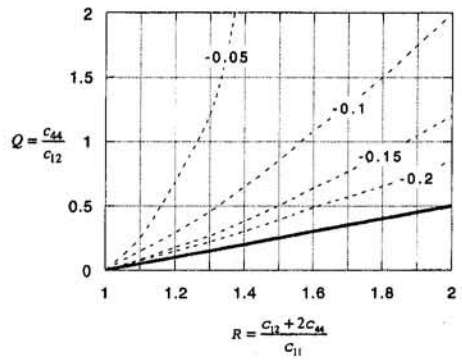


Fig. 5 Variation of the singularity exponent γ with the two nondimensional material parameters Q and R for the fully symmetric junction of cubic grains ($\alpha_1 = 120$ deg, $\alpha_2 = 240$ deg, $\theta_1 = -30$ deg, $\theta_3 = 30$ deg and $\theta_2 = 0$ deg)

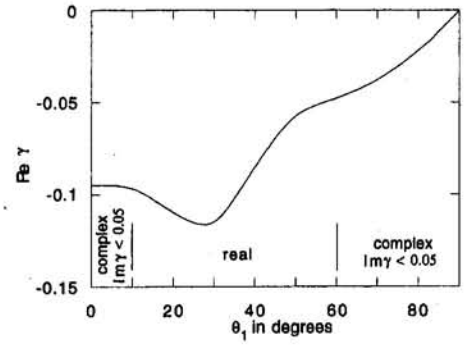


Fig. 6 A plot of γ versus θ_1 for a junction of orthotropic grains defined by $\alpha_1 = 120$ deg, $\alpha_2 = 240$ deg, $\theta_1 = \theta_3$ and $\theta_2 = 90$ deg

Most engineering materials take ρ values between -1 and 5, and λ values between 1 and 10. First by using $\lambda = 2$ and $\rho = 0.52$, we searched the junction configuration yielding the most singular behavior. Figure 6 shows the variation of the real part of the singularity γ with the angle θ_1 for the case where the grain boundaries were placed 120 deg apart and with $\theta_1 = \theta_3$ throughout and $\theta_2 = 90$ deg. The largest $\mathrm{Re}(\gamma)$ value of only -0.12 results for $\theta_1 = 25$ deg. In addition to the real roots, two domains with complex singularities were also obtained. However, the imaginary part of such singularities was quite weak, Fig. 6.

Beside the above configurations, all possible orientations of the principal axes of the grains were investigated albeit by keeping the grain boundaries in the symmetric 120 deg configuration. The results are presented in Figs. 7(*a*)-(*d*) in the θ_1-θ_3 plane while keeping the θ_2 angle constant and equal to 0 deg, 30 deg, 60 deg, and 90 deg in Figs. 7(*a*), (*b*), (*c*), and (*d*), respectively. Several common features can be observed in all the four plots. All plots show complex roots which mainly border the nonsingular zone, which in turn, are shown by dotted lines with the engulfed non-singular zone designated by NS. The regions with complex roots is designated by "*complex*" in Fig. 7. The most singular values ranging only from -0.15 to -0.05 lie in the range: -60 deg $< \theta_1 < 0$ deg and 0 deg $< \theta_3 < 60$ deg, with the largest value of -0.149 corresponding to the fully symmetric case with $\alpha_1 = 120$ deg, $\alpha_2 = 240$ deg, $\theta_1 = -30$ deg, $\theta_2 = 90$ deg and $\theta_3 = 30$ deg. Interestingly, this was also the case analyzed by Tvergaard and Hutchinson (1988). We recovered their results for material constants assumed in their calculations.

Singularities were also obtained for other symmetric grain boundary configurations varying α_1 arbitrary while $\alpha_2 = 360$ deg $- \alpha_1$, and choosing $\theta_1 = -\theta_3$ and $\theta_2 = 90$ deg. The results are shown as contours of $\mathrm{Re}(\gamma)$ in the α_1-θ_3 plane in Fig. 8 only for the quadrant with 90 deg $< \alpha_1 < 180$ deg. The values of $\mathrm{Re}(\gamma)$ in the region: 0 deg $< \alpha_1 < 90$ deg and 0 deg $< \theta_3 < 90$ deg are smaller than the ones in the above quadrant with the largest value of only -0.124 for $\alpha_1 = 90$ deg and $\theta_3 = 40$ deg. All configurations falling in the remaining quadrant with 0 deg $< \alpha_1 < 90$ deg and -90 deg $< \theta_3 < 0$ deg were found to be nonsingular. The largest value of $\mathrm{Re}(\gamma) = -0.149$ in the entire α_1-θ_3 space corresponded to the fully symmetric case with $\alpha_1 = 120$ deg, $\alpha_2 = 240$ deg, $\theta_1 = -30$ deg, $\theta_2 = 90$ deg and $\theta_3 = 30$ deg.

Figure 9 shows the stress singularities for various orthotropic crystals for the most singular configuration obtained above. In general, the real part of the singularity γ increases with λ, and this effect was more pronounced at low values of ρ. When λ becomes bigger than 10 one even obtains super-singularities, i.e., $\gamma < -0.5$. For example a singularity exponent of -0.502 results for $\rho = 0$ and $\lambda = 10$. For $\lambda = 1$ the material becomes transversely cubic and the singularities can be found only when

Downloaded 04 May 2010 to 171.66.16.33. Redistribution subject to ASME license or copyright; see http://www.asme.org/terms/Terms_Use.cfm

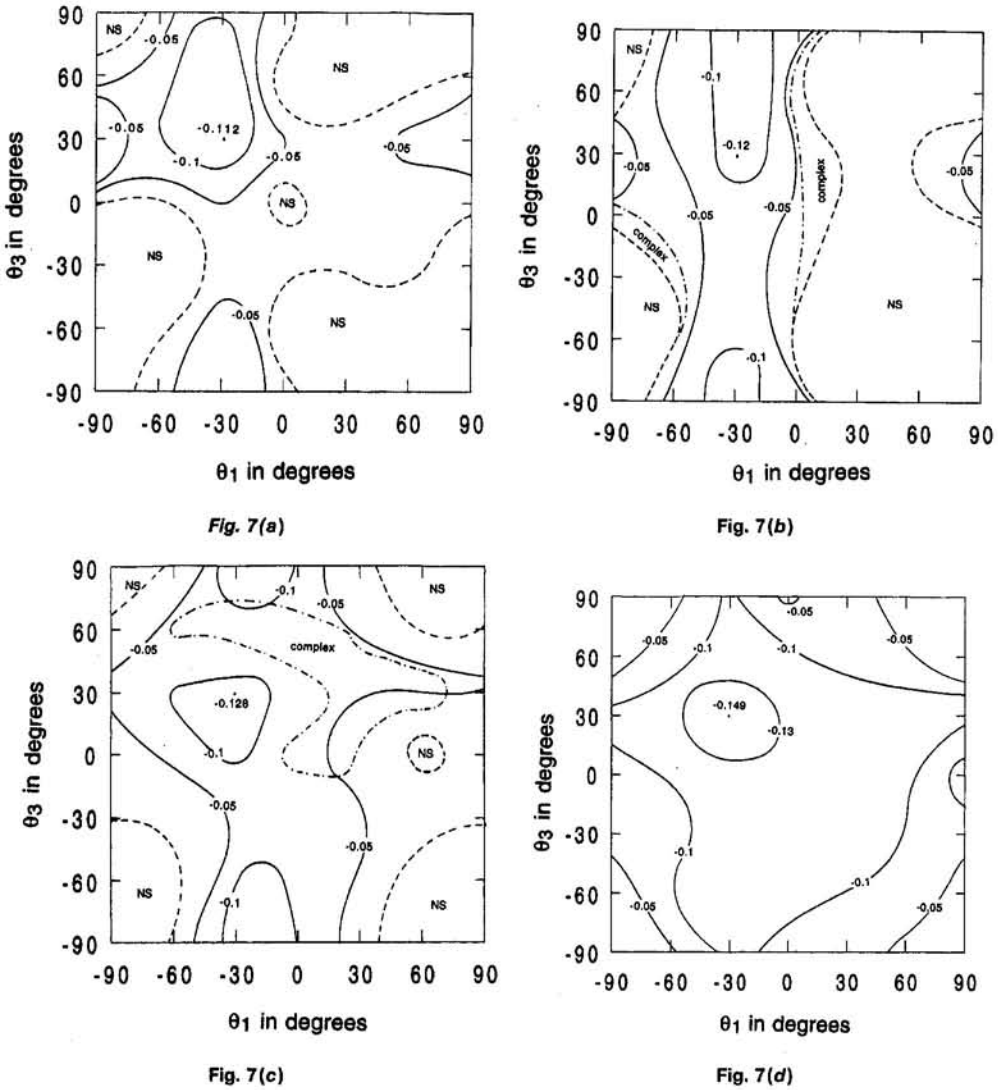


Fig. 7 Contours of γ in the θ_1-θ_3 plane for a junction of orthotropic grains defined by $\alpha_1 = 120$ deg, $\alpha_2 = 240$ deg while keeping θ_2 to be constant and equal to 0 deg in (*a*), 30 deg in (*b*), 60 deg in (*c*), and 90 deg in (*d*)

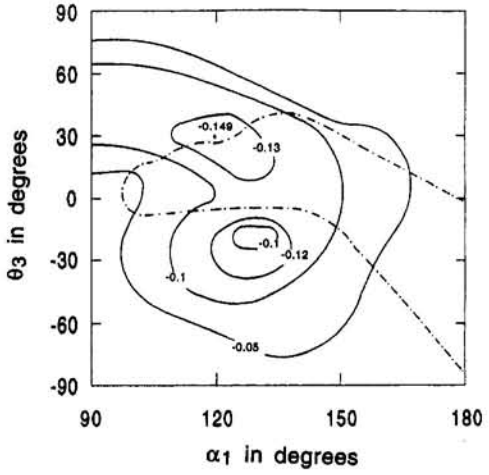


Fig. 8 Contours of the singularity exponent γ in the α_1-θ_1 plane for a symmetric junction of orthotropic grains defined by $\alpha_2 = 360$ deg $- \alpha_1$, $\theta_3 = -\theta_1$ and $\theta_2 = 90$ deg

$\rho < 1$. Table 2 gives the real part of the singularity for some ceramics and rock minerals.

Finally, consider the case of freshwater columnar ice polycrystal with two-dimensional columnar grains since the present calculations were performed to understand the mechanism of crack nucleation in this material. Interestingly, the fully sym-

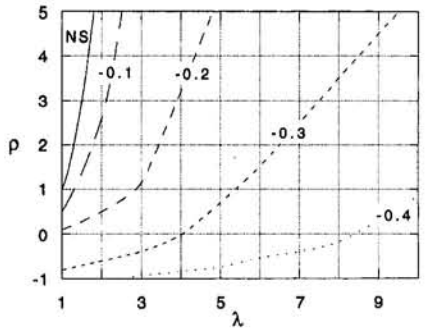


Fig. 9 Values of the singularity exponent γ for various polycrystals with orthotropic grains characterized by the two materials parameters λ and ρ. The calculations were performed for the fully symmetric configuration defined by $\alpha_1 = 120$ deg, $\alpha_2 = 240$ deg, $\theta_1 = -30$ deg, $\theta_3 = 30$ deg and $\theta_2 = 0$ deg.

Downloaded 04 May 2010 to 171.66.16.33. Redistribution subject to ASME license or copyright; see http://www.asme.org/terms/Terms_Use.cfm

Table 2 λ and ρ values for several orthotropic materials along with the largest values of the singularity exponent. The elastic constants used to compute λ and ρ were taken from Simmons and Wang (1985).

Material	λ	ρ	γ
apatite	1.19	0.5	-0.133
calcite	1.72	0.65	-0.19
sapphire	1.08	1.36	NS
TiB_2	1.57	0.28	-0.22
$BaTiO_3$	1.05	0.95	-0.038

metric case turns out to be nonsingular since $\lambda = 1.09$ and $\rho = 1.53$ for ice at -10°C (Gammon et al., 1983). Since the elastic anisotropy in ice is quite weak, the largest value for all probed orientations, including that of the grains, was obtained to be only -0.035. This corresponded to the triple junction configuration with $\alpha_1 = 80$ deg, $\alpha_2 = 280$ deg, $\theta_1 = -\theta_3 = -30$ deg and $\theta_2 = 90$ deg. The specific singularity map for ice in the α_1-θ_3 plane and the associated details related to crack nucleation are discussed in Picu and Gupta (1994).

6 Conclusions

The stress singularities at grain triple junctions were obtained for several orientations of the grain boundaries and the material axes of the grains. Both cubic and orthotropic grains were considered. For most materials the largest singularity corresponded to the fully symmetric case with grain boundaries 120 deg apart, and $\theta_1 = -\theta_3 = -30$ deg, $\theta_2 = 90$ deg, with the exception (possibly more) of ice where such a configuration yielded no singularity. Since the key motivation for this work was to understand how cracks nucleate in ice under high strain loading, where ductile stress concentrating mechanisms like the dislocation pile-ups at the grain boundaries are inhibited, the question remains regarding the sources of such cracks. In fact, through a combined experimental and numerical study (Picu and Gupta, 1995a, b) we have confirmed that it is the local grain boundary sliding in these materials even at high strain rates that is responsible for nucleating cracks from the grain triple junctions. Nevertheless, the results provided here should be of interest to other brittle solids like ceramics and rocks.

Complex singularities were obtained in some cases suggesting a nonphysical oscillatory behavior for the stress and displacements, similar to those uncovered for the interface cracks. Finally, super singularities remain a possibility at junctions of orthotropic grains with small ρ and $\lambda > 10$. Interestingly, super singularities were also obtained in cases where the grain boundaries were allowed to slide freely (Picu and Gupta, 1995c), in contrast to the study here where all boundaries were perfectly bonded. In such cases the precursor of arbitrarily small size can grow from the triple junction as the corresponding energy release rate becomes unbounded.

Acknowledgments

This work is being supported by the ONR Grant No. N00014-92-J-1247 for which we are grateful to Drs. Y. D. S. Rajapakse, Steve Ramberg, and Tom Curtin of that agency.

We are also grateful to Dr. Russell Harmon of ARO for additional support through Grant No. DAAL03-92-G-0250.

References

Bazant, Z. P., and Estenssoro, L. F., 1979, "Surface Singularity and Crack Propagation," *International Journal of Solids and Structures,* Vol. 15, pp. 405–426.

Bazant, Z. P., and Keer, L. M., 1974, "Singularities of Elastic Stresses and of Harmonic Functions at Conical Notches or Inclusions," *International Journal of Solids and Structures,* Vol. 10, pp. 957–964.

Eshelby, J. D., Read, W. T., and Shockley, W., 1953, "Anisotropic Elasticity with Applications to Dislocations Theory," *Acta Metallurgica,* Vol. 1, pp. 251–259.

Evans, A. G., 1978, "Microfracture from Thermal Expansion Anisotropy-I. Single Phase Systems," *Acta Metallurgica,* Vol. 26, pp. 1845–1853.

Fu, Y., and Evans, A. G., 1985, "Some Effects of Microcracks on the Mechanical Properties of Brittle Solids—I. Stress-Strain Relations," *Acta Metallurgica,* Vol. 33, pp. 1515–1523.

Gammon, P. H., Kiefte, H., Clouter, M. J., and Denner, W. W., 1983, "Elastic Constants of Artificial and Natural Ice Samples by Brillouin Spectroscopy," *Journal of Glaciology,* Vol. 29, pp. 433–459.

Ghahremani, F., Hutchinson, J. W., and Tvergaard, V., 1990, "Three-Dimensional Effects in Microcrack Nucleation in Brittle Polycrystals," *Journal of the American Ceramic Society,* Vol. 73, pp. 1548–1554.

Keer, L. M., and Parihar, K. S., 1978, "Elastic Stress Singularity at Conical Inclusions," *International Journal of Solids and Structures,* Vol. 14, pp. 261–263.

Lekhnitskii, S. G., 1963, *Theory of Elasticity of an Anisotropic Body,* Holden-Day, San Francisco.

Picu, R. C., and Gupta, V., 1994, "Crack Nucleation in Polycrystalline Columnar Ice Due to Anisotropic Grains," *Proceedings of the 12th International Symposium on Ice at the IAHR 94 Conference,* Trondheim, Norway, Aug. 23-26, pp. 464–473.

Picu, R. C., and Gupta, V., 1995a, "Observations of Crack Nucleation in Columnar Ice due to Grain Boundary Sliding," *Acta Metallurgica et Materialia,* Vol. 43, No. 10, pp. 3791–3797.

Picu, R. C., and Gupta, V., 1995b, "Crack Nucleation in Columnar Ice due to Elastic Anisotropy and Grain Boundary Sliding," *Acta Metallurgica et Materialia,* Vol. 43, No. 10, pp. 3783–3790.

Picu, R. C., and Gupta, V., 1995c, "Stress Singularities at Triple Junctions with Freely Sliding Grains," *International Journal of Solids and Structures,* in press.

Simmons, G., and Wang, H., 1985, *Single Crystal Elastic Constants and Calculated Aggregate Properties: a Handbook,* MIT Press, Cambridge, MA.

Somaratna, N., and Ting, T. C. T., 1986, "Three-Dimensional Stress Singularities in Anisotropic Materials and Composites," *International Journal of Engineering Sciences,* Vol. 24, pp. 1115–1134.

Suo, Z., 1990, "Delamination Specimens for Orthotropic Materials," ASME JOURNAL OF APPLIED MECHANICS, Vol. 57, pp. 627–634.

Ting, T. C. T., and Hoang, P. H., 1984, "Singularities at the Tip of a Crack Normal to the Interface of an Anisotropic Layered Composite," *International Journal of Solids and Structures,* Vol. 20, pp. 439–454.

Ting, T. C. T., 1986, "Explicit Solutions and Invariance of the Singularities at an Interface Crack in Anisotropic Composites," *International Journal of Solids and Structures,* Vol. 22, pp. 965–983.

Ting, T. C. T., 1995, "Generalized Dundurs Constants for Anisotropic Bimaterials," *International Journal of Solids and Structures,* Vol. 32, pp. 483–500.

Tvergaard, V., and Hutchinson, J. W., 1988, "Microcracking in Ceramics Induced by Thermal Expansion or Elastic Anisotropy," *Journal of the American Ceramic Society,* Vol. 71, pp. 157–166.

Downloaded 04 May 2010 to 171.66.16.33. Redistribution subject to ASME license or copyright; see http://www.asme.org/terms/Terms_Use.cfm

Stress Distributions During Fiber Pull-Out

R. Krishna Kumar[1]
Associate Professor,
Department of Mechanical Engineering,
Indian Institute of Technology,
Madras 600036, India

J. N. Reddy
Oscar S. Wyatt Chair,
Department of Mechanical Engineering,
Texas A&M University,
College Station, TX 77843-3123
Fellow ASME

Fiber pull-out resistance is an important mechanism of energy absorption during the failure of fiber-reinforced composite materials. This paper deals with axial stress distribution in the fiber during a pull-out. The frictional constraint between the fiber and the matrix is modeled with a perturbed Lagrangian approach and Coulomb's law of friction. Stress distribution has been determined for three cases, using the finite element method. The first case deals with the pull out of a fully embedded fiber. The second determines the stress distribution during fiber pull-out in the presence of a broken-embedded fiber. The third model attempts to solve the pull out of a coated fiber. The results for the first case compares favorably with those in existing literature. A local "pinching" effect, due to the matrix collapse behind the pulled fiber, is brought out clearly by this model. The second study indicates that the "plug" effect may not be significant in affecting the stress distribution. Lastly, the effects of coating stiffness and thickness are investigated.

1 Introduction

The energy consumed during the failure of a composite material is due to various competing failure mechanisms that operate during a fracture. These can be classified as matrix fracture, fiber-matrix interface debonding, fiber pull-out, and fiber fracture (Kim and Mai, 1991). It has been recognized that in brittle matrix composites post-debonding friction and fiber pull-out may be important mechanisms of energy consumption during failure (Kim and Mai, 1991; Suzuki et al., 1992; Budiansky et al., 1986). According to Suzuki et al. (1992), the fiber pull-out resistance may be a thousand times more than that of monolithic ceramics. A number of experimental and theoretical studies have been carried out in recent times, some of which are reviewed by Desarmot and Favre (1991).

Though a single fiber pull-out is an impossibility in realistic fracture situations, it has been used to study the fiber pull-out mechanism. Khanna (1992) has successfully used single fiber pull-out tests to explain certain observations made on the overall failure of composite materials. Also, single fiber pull-out tests have been used traditionally to understand the fiber matrix interface strength in composite materials (Atkinson et al., 1982; Bowling and Groves, 1979; Favre and Menenne, 1981).

Fiber pull-out has been theoretically studied by a number of investigators (Hutchinson and Jensen, 1990; Aboudi, 1989; Gao et al., 1988; Dollar and Steif, 1988). Hutchinson and Jensen (1990) considered debonding and frictional sliding, and constructed approximate closed-form solutions based on the solutions of the Lamé problem. They also constructed a numerical solution and considered two cases, one with a constant friction, and the other with Coulomb friction along the interface. Aboudi (1989) carried out a micromechanical analysis of the problem, incorporating debonding by a critical shear stress model. Friction was accounted through a Coulomb friction law. Alternatively, Gao et al. (1988) used the fracture mechanics approach to study debonding and determined the role of friction following debonding. They used the plane-strain Lamé solutions to study the fiber/matrix interaction. Dollar and Steif (1988) used a continuous distribution of dislocations to model Coulomb friction. This technique results in a singular integral equation which is solved to determine the load transfer. Their major conclusion was that the constant shear stress approximation results in substantially inaccurate results. Freund (1992) studied the problem of a circular fiber slipping through an unbounded elastic material. This study brings out the effect of the stiffness ratio of the fiber and the matrix on the stress distribution. Again, an integral equation was solved numerically to obtain the results.

The finite element analysis of the problem, however, has surprisingly been extremely limited. Povirk and Needleman (1993) simulated the fiber pull-out problem using a rate-dependent internal variable friction constitutive equation. The fiber was considered to be rigid and the analysis was essentially concerned with the effect of the friction law in explaining the stick-slip instability during a pull-out. Ballarani and Ahmed (1989) modeled the frictional slip, with the assumption that both the fiber and the matrix are made of the same material. Marotzke (1994) studied the pull-out using finite element analysis without considering the frictional slip. Faber et al. (1986) conducted preliminary finite element analysis of push-out problems for a stiff fiber in a soft matrix.

A survey of the literature shows that no detailed finite element analysis, especially of the fiber axial stress which determines the axial force, has been carried out. The more important problem of stress distribution in the presence of a broken fiber has not attracted the attention of researchers in the field. As observed by Khanna (1992), most fiber fractures take place not exactly at the crack plane, but away from it. Hence, as the fiber is pulled out, its broken parts remain in the matrix. This broken fiber may have a "plug" effect and alter the axial and radial stresses near the free end of the pulled fiber. Another problem of interest is determining the effect of an interfacial coating on the shear and axial stress distributions in the pulled fiber. The stress transfer during a pull-out with an elastic interface has been analyzed only to a limited extent (Hsueh, 1993). An understanding of this phenomenon is important in designing proper interfacial coatings.

The present study was undertaken in light of the technical issues described above. The three fiber pull-out problems were analyzed for stress distributions. The finite element model, based on the perturbed Lagrangian approach and Coulomb's friction law, was used. A linear elastic model with contact algorithm was used to simulate the pull-out.

[1] The research was carried out while the author visited Texas A&M University on a fellowship from the U.S. Agency for International Development.

Contributed by the Applied Mechanics Division of THE AMERICAN SOCIETY OF MECHANICAL ENGINEERS for publication in the ASME JOURNAL OF APPLIED MECHANICS.

Discussion on this paper should be addressed to the Technical Editor, Professor Lewis T. Wheeler, Department of Mechanical Engineering, University of Houston, Houston, TX 77204-4792, and will be accepted until four months after final publication of the paper itself in the ASME JOURNAL OF APPLIED MECHANICS.

Manuscript received by the ASME Applied Mechanics Division, Aug. 1, 1994; final revision, May 30, 1995. Associate Technical Editor: L. T. Wheeler.

Copyright © 1996 by ASME

Downloaded 04 May 2010 to 171.66.16.33. Redistribution subject to ASME license or copyright; see http://www.asme.org/terms/Terms_Use.cfm

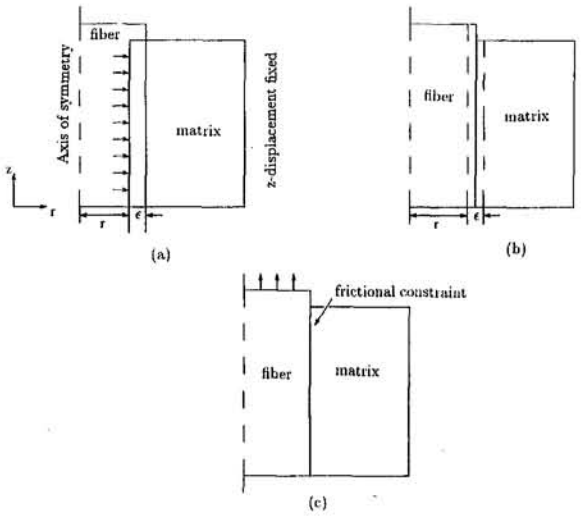


Fig. 1 Fiber pull-out model of a fully embedded fiber. (*a*) The matrix is compressed by displacing it by ϵ. (*b*) The matrix/fiber interface is allowed to come to equilibrium. (*c*) The fiber is pulled against the frictional constraint.

2 Description of the Problems

It is well known that compressive residual stresses which develop in many composite material systems during manufacturing (Majumdar et al., 1988), are primarily responsible for the frictional resistance during a pull-out. As the residual stresses depend on the fiber-matrix interaction, a technique followed by Freund (1992) is used in this study.

A fiber of diameter $d + 2\epsilon$ is assumed to remain in a matrix hole of diameter d before the pull-out. This produces a residual compressive stress on the fiber and induces a frictional resistance against the pull-out. To simulate this situation, the radius of the hole in the matrix is increased by ϵ so that the hole in the matrix just accommodates the fiber of diameter $d + 2\epsilon$ (Fig. 1). At this stage the fiber develops no stresses and the matrix is compressed. Next, the compressed matrix is brought into contact with the fiber. The contact algorithm is invoked and the two bodies are allowed to interact without penetration until an equilibrium is established. This forms the basis of the numerical simulation of the pull-out process. The results are normalized by ϵ, as suggested by Freund (1992). Therefore, the actual value of ϵ, which is necessarily small compared to the diameter, has no significance in the conclusions drawn from this study. The outer dimensions of the matrix are taken to be nearly ten times the diameter of the fiber. Thus the geometry is one of two concentric cylinders with friction between them. The outer boundary of the larger cylinder is fixed, and the axisymmetric model is solved using the algorithm described in Section 3.

The focus of the second problem is to determine the effect of a broken fiber embedded in the matrix on fiber pull out. The two parts of the broken fiber (Fig. 2(*a*)) are in equilibrium with the matrix, achieved essentially in the same fashion as described for single fiber. As one part of the broken fiber is pulled out, the other is made to remain in the matrix (Fig. 2(*b*)). Two different ratios of the moduli E_m/E_f, where E_m is the modulus of the matrix and E_f is the modulus of the fiber, have been used in this study. It should be noted that the stresses presented here are the result of fiber pull-out alone, and it is assumed in both these studies that the entire fiber matrix surface has been debonded.

The third and last problem deals with the pull out of a coated fiber with elastic properties from an elastic matrix. The essential purpose of this study is to compare the stresses obtained from this study to those with an uncoated fiber. The friction coefficient for the coated fiber is assumed to be 0.5. Again two values of E_m/E_f, namely, 0.25 and 4.0, are used. It is also assumed that a complete debonding of the coated layer from the matrix has taken place. For the composite with a stiffer fiber, two types of coatings, one with $E_c/E_f = 0.1$ and the other with a $E_c/E_f = 0.4$, are used. Poisson's ratio for all the materials is assumed to be 0.3.

3 The Finite Element Model

The contact model including friction is based on the perturbed Lagrangian approach (Ju and Taylor, 1988). The formulation uses a master-slave slide line contact approach, originally proposed by Hallquist (1985). The perturbed Lagrangian functional can be expressed as

$$\Pi_{per}(\mathbf{u}, \mathbf{T}_n, \mathbf{T}_t) = \Pi(\mathbf{u}) + \mathbf{T}_n^T\mathbf{G}_n - \frac{1}{2c_n}\mathbf{T}_n^T\mathbf{T}_n + \mathbf{T}_t^T\mathbf{G}_t - \frac{1}{2c_t}\mathbf{T}_t^T\mathbf{T}_t \quad (1)$$

where $\mathbf{u}$ denotes the displacement vector, $\mathbf{T}_n$ and $\mathbf{T}_t$ are the normal and the tangential nodal contact force vectors, $\mathbf{G}_n$ and $\mathbf{G}_t$ the normal and tangential nodal gap vectors, and c_n and c_t are the penalty parameters. The contribution from Π_{per} to the stiffness matrix can be easily derived. This contribution is combined with the usual stiffness matrix associated with axisymmetric finite element. The additional force terms coming from Π_{per} are also summed up with the usual force terms. The contact tangent stiffness matrix and the contact residual force vector are given by (Ju and Taylor, 1988)

$$\mathbf{K}_c = c\Bigg\{[\mathbf{N}_s\mathbf{N}_s^T - \mu \text{ sign } (g_t)\mathbf{N}_t\mathbf{N}_s^T] - \frac{g_n}{\|\mathbf{x}_2 - \mathbf{x}_1\|}\left[\mathbf{N}\mathbf{T}_s^T + \mathbf{T}_s\mathbf{N}^T + \frac{g_n}{\|\mathbf{x}_2 - \mathbf{x}_1\|}\mathbf{N}\mathbf{N}^T\right] - \frac{\mu \text{ sign } (g_t)g_n}{\|\mathbf{x}_2 - \mathbf{x}_1\|}\left[\mathbf{N}_s^0\mathbf{N}^T + \mathbf{N}\mathbf{N}_s^T - \frac{g_n}{\|\mathbf{x}_2 - \mathbf{x}_1\|}(\mathbf{N}\mathbf{T}^T + \mathbf{T}\mathbf{N}^T)\right]\Bigg\} \quad (2)$$

where $c = c_n = c_t$, $\mathbf{x}_1$, and $\mathbf{x}_2$ are the current nodal coordinates of the master nodes, and g_n and g_t are the magnitudes of vectors $\mathbf{G}_n$ and $\mathbf{G}_t$, respectively. The remaining vectors are given below:

$$\mathbf{N}_s^0 = \{\mathbf{n}, -(1 - \alpha^0)\mathbf{n}, -\alpha^0\mathbf{n}\}^T$$

$$\mathbf{N}_s = \{\mathbf{n}, -(1 - \alpha)\mathbf{n}, -\alpha\mathbf{n}\}^T$$

$$\mathbf{T}_s = \{\mathbf{t}, -(1 - \alpha)\mathbf{t}, -\alpha\mathbf{t}\}^T$$

$$\mathbf{T} = \{0, -\mathbf{t}, \mathbf{t}\}^T$$

$$\mathbf{N} = \{0, -\mathbf{n}, \mathbf{n}\}^T$$

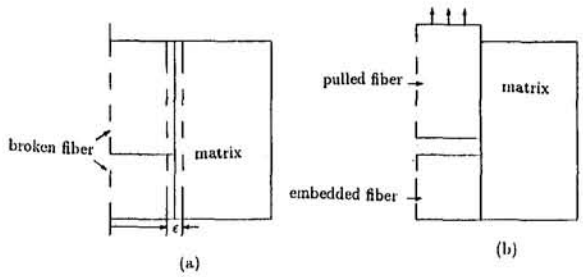


Fig. 2 Fiber pull-out model of a broken fiber. (*a*) Broken fiber in equilibrium with the matrix. (*b*) Fiber pull-out with an embedded fiber.

Downloaded 04 May 2010 to 171.66.16.33. Redistribution subject to ASME license or copyright; see http://www.asme.org/terms/Terms_Use.cfm

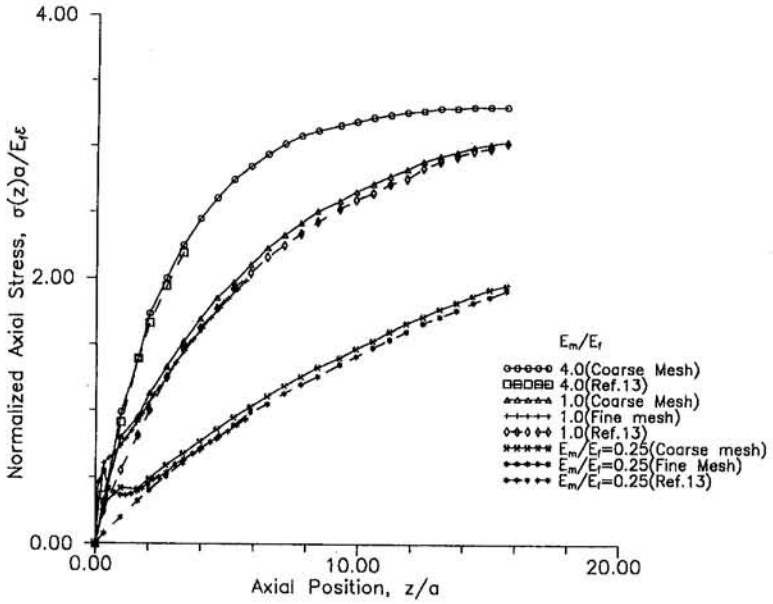


Fig. 3 Normalized axial stress along the length of the fiber; present finite element results (solid lines) are compared with the solutions of Freund (1992) (dashed lines)

$$\Delta \mathbf{u} = \{\Delta \mathbf{u}_s, \Delta \mathbf{u}_1, \Delta \mathbf{u}_2\}^T$$

$$\mathbf{N}_t = \left\{ \mathbf{t}, -(1-\alpha^0)\mathbf{t} - \frac{g_n}{\|\mathbf{x}_2 - \mathbf{x}_1\|}\mathbf{n}, -\alpha^0 \mathbf{t} + \frac{g_n}{\|\mathbf{x}_2 - \mathbf{x}_1\|}\mathbf{n} \right\}^T. \quad (3)$$

Here $\mathbf{n}$ and $\mathbf{t}$ denote the normal and tangent vectors of the master nodes, α is the normalized current surface coordinate, α^0 is the surface coordinates at the beginning of the time step, and μ denotes the friction coefficient.

The stiffness matrix thus obtained is not symmetric. The resulting nonlinear finite element model is solved using an iterative approach with an error norm of 10^{-5} in the residual force vector to signal convergence. A detailed flow chart of the computational procedure is given in Ref. 19. Couple of remarks on the computational model are in order.

Remark 1: The selection of the penalty parameters, c_n and c_t, is critical to the accuracy of the solution obtained. The selection of very small values of the penalty parameters does not satisfy the constraint equation and hence leads to inaccurate displacements. The magnitude of the penalty parameters should be such that the contribution from the constraint terms to the stiffness matrix should be larger than other contributions in order to satisfy the constraints. Thus, the minimum values of c_n and c_t are dictated by the values of Young's modulus of the mating surfaces and the size of the finite element. However, too large a value for c_n or c_t may result in ill-conditioning of the stiffness matrix, which in turn results in inaccurate or wrong solutions. Thus, the upper limit on the values of the penalty

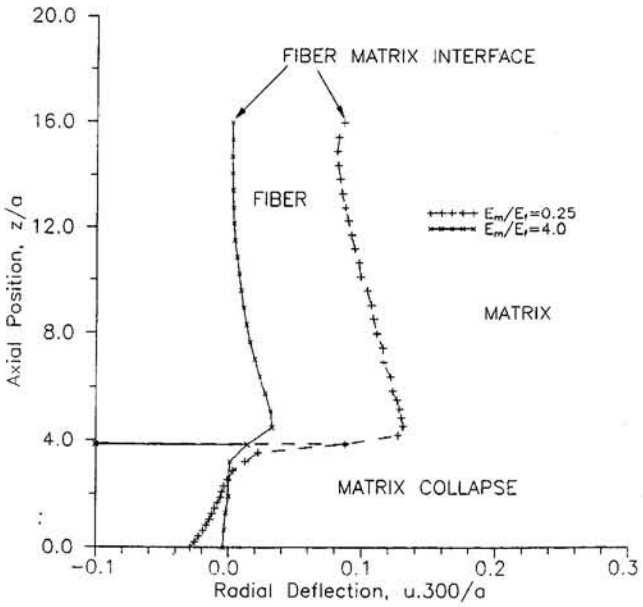


Fig. 4 Matrix collapse during fiber pull-out of a fully embedded fiber

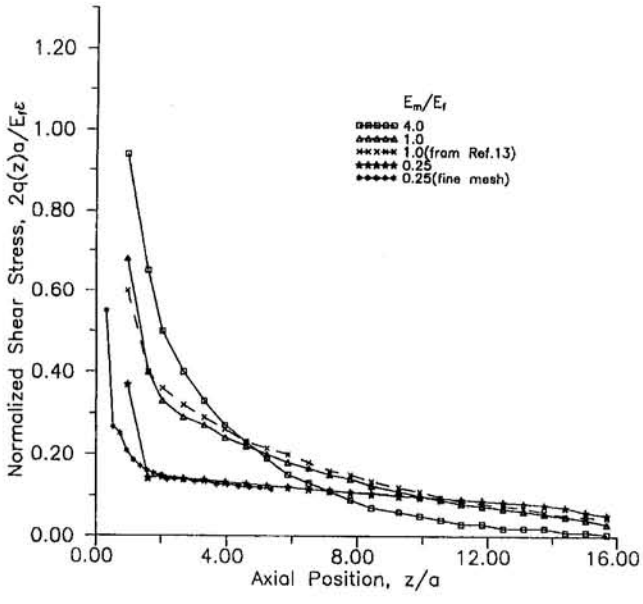


Fig. 5 Normalized shear stress distribution along the length of the fiber. Dashed line indicates the solution of Freund (1992).

Downloaded 04 May 2010 to 171.66.16.33. Redistribution subject to ASME license or copyright; see http://www.asme.org/terms/Terms_Use.cfm

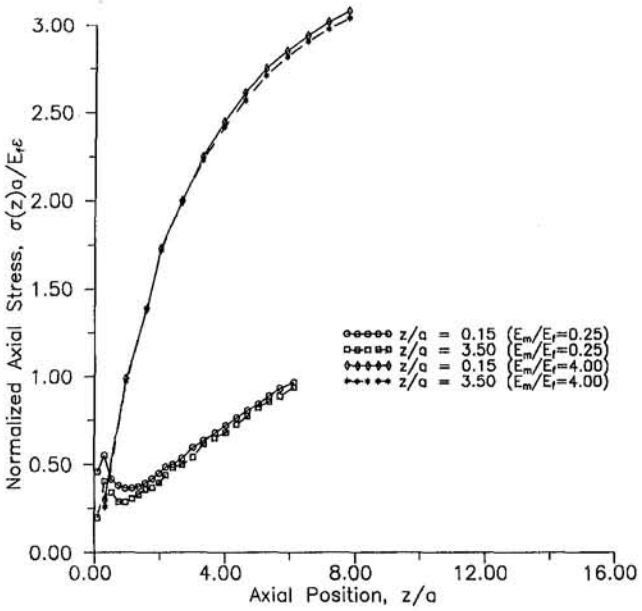


Fig. 6 Axial stress distribution as the fiber is pulled out of the matrix, expressed in terms of the pulled out length z'/a, for various values of E_m/E_f

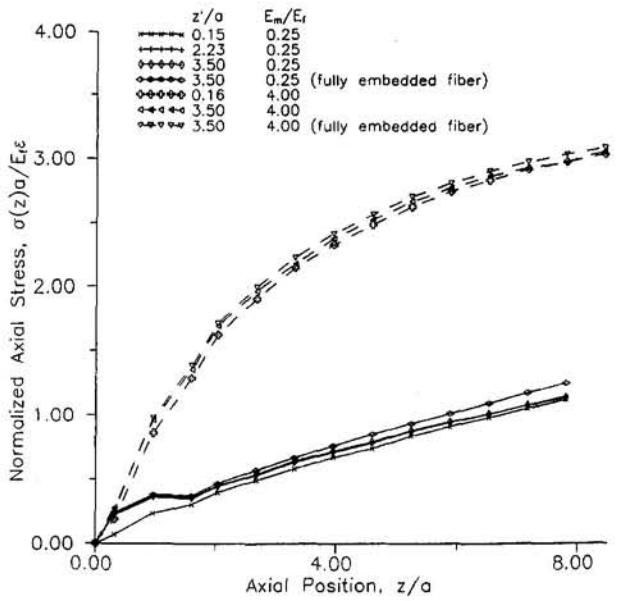


Fig. 7 Normalized axial stress distribution with an embedded broken fiber, as the fiber is pulled out, expressed in terms of the pulled-out length z'/a

parameters is dictated by the computer round-off and machine accuracy. In the present study, the parameters c_n and c_t are selected such that the error in the constraints is less than 0.2 percent.

Remark 2: The element aspect ratio (i.e., the ratio of the largest side to the smallest side of an element) for contact (or constrained) problems is less than what is allowable in noncontact (or unconstrained) problems. Even the aspect ratio of elements away from the contact zone seems to have an effect on the convergence of the solution.

The finite element analysis was performed using the axisymmetric geometry and the four-noded element with an isoparametric formulation. The total number of nodes and elements varied with the problem and a typical model consists of 672 nodes and 574 elements. The displacements are set to zero on the outer and bottom surfaces of the cylinder, and a specified displacement boundary condition is used at the top surface of the fiber. The top surface of the matrix is assumed to be stress-free.

4 Results and Discussion

4.1 Pull-Out of a Completely Embedded Fiber. Figure 3 shows the normalized axial stress distribution along the length of the fiber. Here $\sigma(z)$ denotes the axial stress and a the radius of the fiber. The present results are compared with those of Freund (1992). The plane-strain version of a similar problem with a large stiffness of the fiber has been reported by Takaku and Arridge (1973). It is seen from this figure that the general agreement between the two results is excellent. Nevertheless, there are certain points of departure. For a soft matrix, there is a marked difference between the two results near the free end of the fiber. The difference disappears as the stiffness of the matrix is increased. In order to investigate the accuracy of this departure, a very fine finite element mesh was used near the free edge. The mesh is refined in a small region—about two fiber diameters in size—near the free edge. The element size in the fine mesh is about half the size of the element in the coarse mesh. It is clear from the results presented in Fig. 4 that the difference between the two results persists.

To understand the above phenomena, the displacements of the fiber and the matrix are plotted in Fig. 4. The displacements are magnified 300 times to bring out the difference clearly. As can be seen from these figures, the "matrix collapse" and the internal radial movement of the matrix behind the pulled fiber are much higher for the softer matrix than for the stiffer matrix. This collapse has a "pinching" effect on the fiber, affecting the local stress distribution near the free surface. The Poisson effect can also be noted from these figures. Since the axial stress increases with the length of the fiber, there is a lateral contraction, which is more gradual for a soft matrix. The effect of the lateral contraction is to relax the radial compressive stresses, as depicted in Fig. 5, which contains a plot of the normalized shear stress distribution along the length of the fiber. The present results for $E_m/E_f = 1.0$ match closely with those of the integral equation solutions of Freund (1992). Shear stress values for other cases are not available from this reference. As seen from this result, the shear stresses are concentrated near

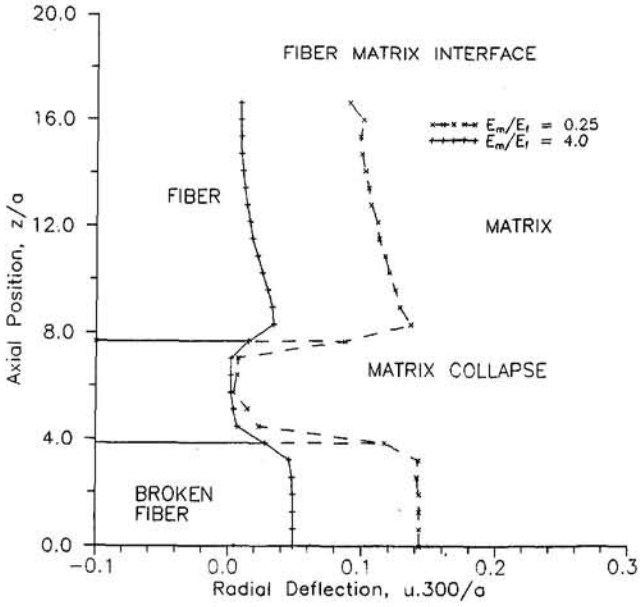


Fig. 8 Matrix deformation in the presence of a broken fiber

Downloaded 04 May 2010 to 171.66.16.33. Redistribution subject to ASME license or copyright; see http://www.asme.org/terms/Terms_Use.cfm

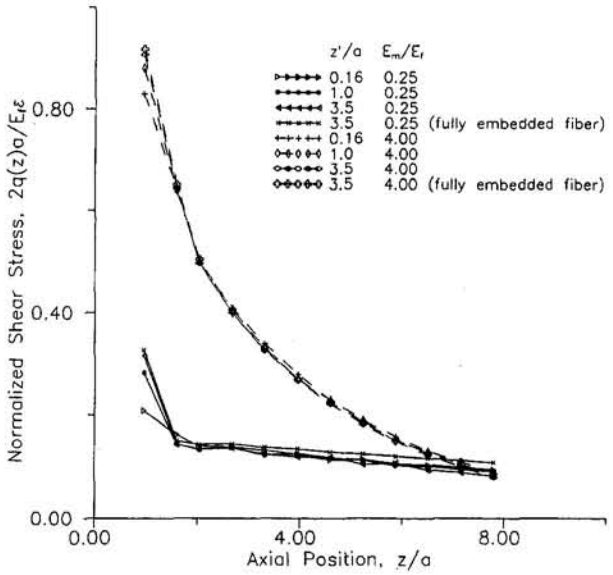


Fig. 9 Normalized shear stress distribution with an embedded broken fiber, as the fiber is pulled out, expressed in terms of the pulled-out length z'/a

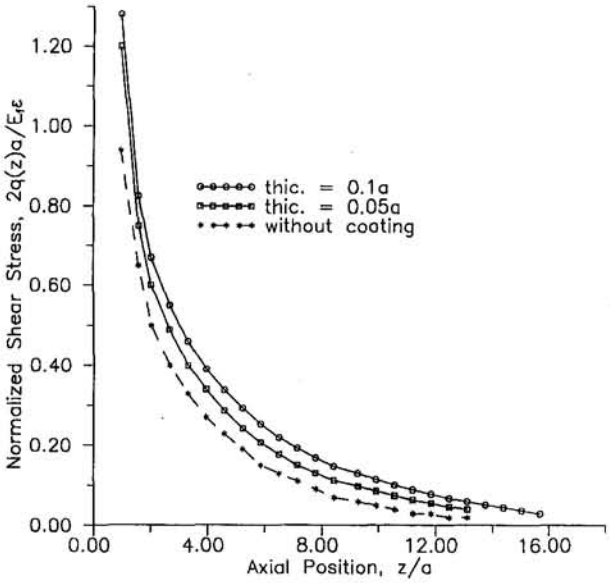


Fig. 11 Normalized shear stress distribution at the fiber/matrix interface along the length of the fiber for two values of coating thickness, $E_m/E_f = 4.0$ and $E_c/E_f = 4.0$

the free edge for a stiff matrix, and they are more uniform along the length of the fiber for a soft matrix. Similar observations were made by Freund (1992).

The question that arises from the above study is that whether the "pinching" effect depends on the pulled length of the fiber. This may be important when the complete pulled length is of the order of a few fiber diameters. Figure 6 shows that the pinching effect is an extremely local phenomena and is almost independent of the pull-out length. Axial stress distribution along the radial position of the fiber has been found to be almost uniform through the radius of the fiber, strengthening the assumption of a one-dimensional idealization of the fiber used by Freund (1992).

4.2 Stress Distribution in the Presence of an Embedded Broken Fiber. The results for this problem are presented in Figs. 7–9. Figure 7 contains the axial stress distribution for a $E_m/E_f = 0.25$. The axial stresses are marginally lower because of the plug effect, and the results are comparable with those of the pull out of a full length fiber. Though the pinching effect near the free edge is felt in this case as well, it takes almost one fiber diameter to be pulled out before it is fully realized. As the general pull out lengths during failure of composites are more than one fiber diameter, it may be concluded that the effect of pinching is almost the same in both the cases of fiber pull-out.

The normalized axial stress remains unaltered in the presence of a broken fiber when the matrix happens to be stiffer than the fiber. This can also be seen from Fig. 7, where the normalized axial stresses are plotted along the length of fiber. Matrix collapse for these two cases are brought out in Fig. 8. Comparison of these results with those in Fig. 4 show that the matrix collapse is unaffected near the free edge of the pulled fiber because of

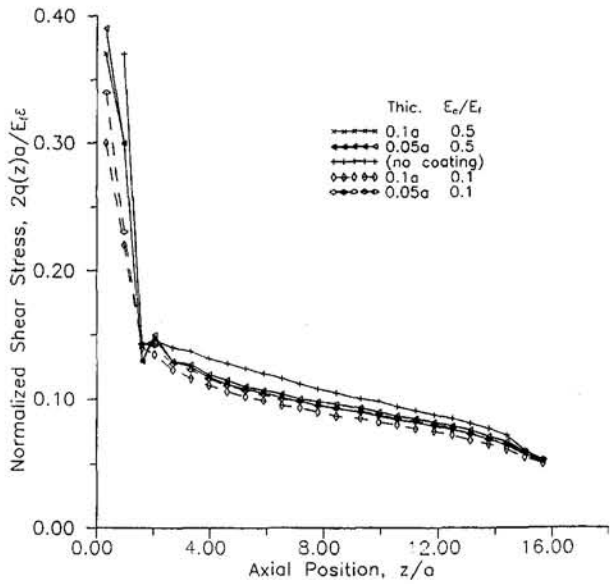


Fig. 10 Normalized shear stress distribution at the fiber/matrix interface along the length of the fiber

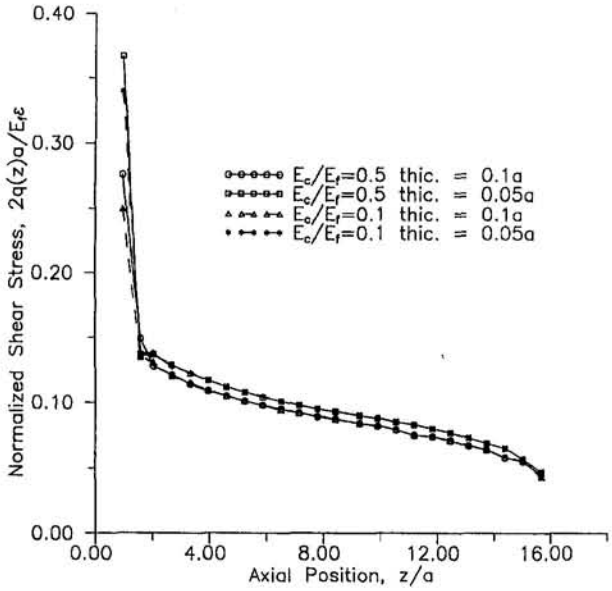


Fig. 12 Normalized shear stress distribution at the fiber/coating interface along the length of the fiber for two values of coating thickness

Downloaded 04 May 2010 to 171.66.16.33. Redistribution subject to ASME license or copyright; see http://www.asme.org/terms/Terms_Use.cfm

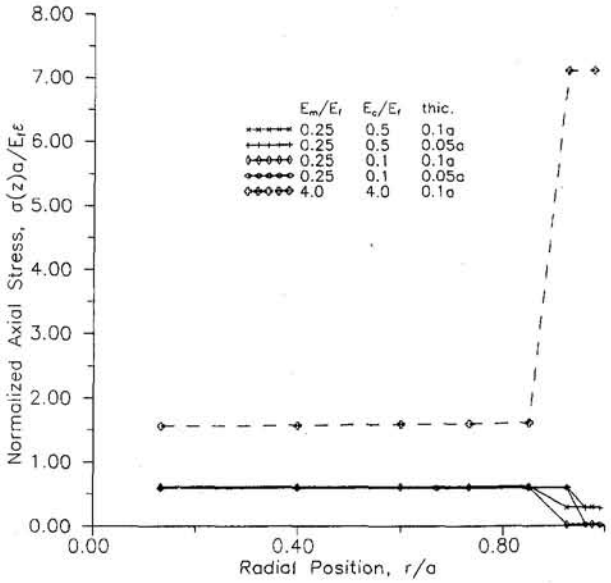


Fig. 13 Normalized axial stress distribution along the radial direction of the fiber for two values of coating thickness

the presence of a broken fiber. Hence, the pinching effect is not altered. Normalized shear stress distributions are shown in Fig. 9. The basic trends are similar to those seen for axial stresses.

4.3 Effect of Coatings on the Stress Distribution. The normalized shear stress distribution for two values of coating thickness with a E_m/E_f ratio of 0.25 and E_c/E_f of 0.5 are plotted in Fig. 10. The coated fiber shows a reduction of normalized shear stress. This is consistent with the fact that a coating of lower stiffness reduces the overall stiffness of the fiber/coating combination. This, in turn, produces an overall reduction in the axial stress for the same displacement and hence a reduction in shear stress. As can also be seen from Fig. 10, further reduction in the stiffness of the coating reduces the shear stress. Also, when the coating thickness is increased, the shear stresses decrease and are in tune with the observations on the reduction in coating stiffness.

Figure 11 contains a summary of the normalized shear stress distributions at the fiber/matrix interface along the length of the fiber for two values of coating thickness and for $E_m/E_f = 4.0$ and $E_c/E_f = 4.0$. In both cases, the friction is assumed to be 0.5. Again, the results are consistent with the above observations. Thicker and stiffer coatings increase the overall modulus and, hence, produce higher stresses for the same displacement. Normalized shear stress distributions at the fiber/coating interface are presented in Fig. 12. An interesting trend can be observed from Fig. 12. The coating thickness has a greater influence than the coating stiffness on the shear stress distribution. In fact, the shear stresses for the same coating thickness and two different stiffnesses are almost the same.

Figure 13 contains normalized axial stress distributions along the radial direction of the fiber. As expected, a softer coating takes a lower axial load and hence the axial stresses are lower.

5 Conclusions

A single fiber pull-out problem with friction has been modeled in this study. A fully embedded fiber, a broken fiber, and a coated fiber subjected to pull-out have been studied. The axial and shear stress distributions have been determined. The results indicate that a "pinching" effect near the free end of a fiber affects the local stresses, especially for small values of the stiffness of the matrix. Broken fiber (embedded in the matrix) does not seem to affect the overall stress distribution. The effect of coatings on the stress distribution depends on the ratios of the stiffness and the thickness of the coating. Thicker and stiffer coatings increase the overall modulus and hence produce higher stresses for the same displacement. The coating thickness has a greater influence than the coating stiffness on the shear stress distribution.

Acknowledgments

The first author wishes to acknowledge the support provided by U.S. AID during his stay at Texas A & M University. It is a pleasure to acknowledge discussions on fiber pull-out tests with Dr. Sanjeev Khanna. The second author acknowledges the support of his composites research by Sandia National Laboratories.

References

Aboudi, J., 1989, "Micromechanical analysis of fibrous composites with Coulomb frictional slippage between the phases," *Mechanics of Materials,* Vol. 8, pp. 103–115.

Atkinson, C., et al., 1982, "The rod pull out problem, theory and experiment," *Journal of Mechanics and Physics of Solids,* Vol. 30, No. 3, pp. 97–120.

Ballarami, R., and Ahmed, S., 1989, "Finite element modeling of frictionally restrained composite interfaces," NASA Contract report 182281.

Bowling, J., and Groves, G. W., 1979, "The debonding and pull-out of ductile wires from a brittle matrix," *Journal of Material Science,* Vol. 14, pp. 431–442.

Budiansky, B., et al., 1986, "Matrix Fracture in fiber-reinforced ceramics," *Journal of Mechanics and Physics of Solids,* Vol. 34, pp. 167–189.

Desarmot, G., and Favre, J. P., 1991, "Advances in pull-out testing and data analysis," *Composite Science & Technology,* Vol. 42, pp. 151–187.

Dollar, A., and Steif, P. S., 1988, "Load transfer in composites with a Coulomb friction interface," *International Journal of Solids & Structures,* Vol. 24, No. 8, pp. 789–803.

Faber, K. T., et al., 1986, "Frictional stress evaluation along the fiber-matrix interface in CMC's," *Journal of American Ceramic Society,* Vol. 69, No. 9, pp. C208–C209.

Favre, J. P., and Menenne, M. C., 1981, "Characterization of fiber/resin bonding in composites using a pull-out test," *International Journal of Adhesion and Adhesives,* Vol. 1, pp. 311–316.

Freund, L. B., 1992, "The axial force needed to slide a circular fiber along a hole in an elastic material and implications for fiber pull-out," *European Journal of Mechanics of Solids,* Vol. 11, pp. 1–19.

Gao, Y. C., et al., 1988, "Fracture of fiber reinforced materials," *Journal of Applied Mathematics and Physics (ZAMP),* Vol. 39, pp. 550–572.

Hallquist, J. O., et al., 1985, "Sliding interfaces with contact–impact in large-scale Lagrangian computations," *Computer Methods in Applied Mechanics & Engineering,* Vol. 51, pp. 107–137.

Hsueh, C. H., 1993, "Interfacial debonding and fiber pull-out stresses of fiber reinforced composites, X: With an elastic interfacial coating," *Material Science & Engng.,* Vol. A105, pp. 189–195.

Hutchinson, J. W., and Jensen, H. M., 1990, "Models of fiber debonding and pull out in brittle composites with friction," *Mechanics of Materials,* Vol. 9, pp. 139–163.

Ju, J. W., and Taylor, R. L., 1988, "A perturbed Lagrangian formulation for the finite element solution of nonlinear frictional contact problem," *Journal of Theoretical & Applied Mechanics,* Vol. 7, No. 1, pp. 1–14.

Khanna, S. K., 1992, "Effect of reinforcement and fiber-matrix interface on dynamic fracturing of fiber reinforced composite materials," Ph.D. Thesis, University of Rhode Island, Kingston, RI.

Kim, J. K., and Mai, Y. W., 1991, "High Strength, high fracture toughness fiber composites with interface control—A review," *Composite Science & Technology,* Vol. 41, pp. 333–378.

Majumdar, S., et al., 1988, "Determination of residual thermal stresses in Sic–Al_2O_3 composite using neutron diffraction," *Journal of American Ceramic Society,* Vol. 71, pp. 858–863.

Marotzke, 1994, "The elastic stress field arising in the single fiber pull-out test," *Composite Science & Technology,* Vol. 50, pp. 393–403.

Povirk, G. L., and Needleman, A., 1993, "Finite Element Simulations of Fiber Pull-Out," ASME *Journal of Engineering Materials and Technology,* Vol. 115, pp. 286–291.

Suzuki, T., et al., 1992, "Fiber pullout processes and mechanisms of carbon fiber reinforced silicon nitride ceramic composite," *Journal of Materials Research,* Vol. 7, No. 10, pp. 2809–2875.

Takaku, A., and Arridge, R. G. C., 1973, "The effect of interfacial radial and shear stress on fiber pull-out in composite materials," *Journal of Physics, D: Applied Physics,* Vol. 16, pp. 2038–2047.

Downloaded 04 May 2010 to 171.66.16.33. Redistribution subject to ASME license or copyright; see http://www.asme.org/terms/Terms_Use.cfm

A Critical Study of the Applicability of Rigid-Body Collision Theory

D. Stoianovici
Graduate Assistant

Y. Hurmuzlu
Associate Professor

Mechanical Engineering Department,
Southern Methodist University,
Dallas, TX 75275

This article deals with the collision of steel bars with external surfaces. The central issue of the article is the investigation of the fundamental concepts that are used to solve collision problems by using rigid-body theory. We particularly focus on low-velocity impacts of relatively rigid steel bars to test the applicability of these concepts. An experimental analysis was conducted to study the rebound velocities of freely dropped bars on a large external surface. A high-speed video system was used to capture the kinematic data. The number of contacts and the contact time were determined by using an electrical circuit and an oscilloscope. Tests were performed by using six bar lengths and varying the pre-impact inclinations and the velocities of the bars. The experimental results were used to verify the applicability of Coulomb's law of friction and the invariance of the coefficient of restitution in the class of impacts considered in this study. Then, given the unusual variation the coefficient of restitution as a result of changing pre-impact inclinations, a theoretical model was developed to explain this variation. A discrete model of the bar was used to obtain the equations of motion during impact. Computed and experimental results were compared to establish the accuracy of numerical model. The internal vibrations of the bar and multi impacts between the bar and the surface were found to be two main factors that cause the variation of the coefficient of restitution. Furthermore, a slenderness factor was proposed to identify the subset of collision problems where the coefficient of restitution was invariant to the inclination angle.

1 Introduction

Collision problems play an important role in many engineering applications. There has been an impressive number of publications that focus on analytical and experimental analysis of impact problems. Two basic approaches, which differ in the treatment of the colliding bodies, have been developed. The first approach simplifies the mathematical formulation by considering rigid colliding bodies (with the exception of local deformations in the neighborhood of the collision point). The second approach is more sophisticated and the colliding bodies are allowed to undergo local and global deformations.

The rigid-body treatment of impact dates back to Newton (1686). There has been a continuing effort up to date, geared toward improving the solution methods and handling more complicated problems. The latest focus point in the area has been the energetic consistency of the solutions of rigid-body collision problems in the presence of friction. The developments in the area have led to three definitions of e: kinematic (Whitaker, 1904), kinetic (Keller, 1986), and energetic (Stronge, 1990). In addition, two methods of formulation (algebraic and differential), were used to develop the necessary equations to solve impact problems. A comprehensive analysis of the theoretical outcomes that are predicted by each method can be found in Hurmuzlu and Marghitu (1993) for planar problems and Marghitu and Hurmuzlu (1995) for three-dimensional problems. The conclusion of the authors was that analytical solutions alone were not sufficient to judge the accuracy nor the completeness of the solutions. They further pointed out that in the light of the recent developments in the area, experimental evidence was needed to assess the validity of the proposed methods.

The main goal at the onset of the present study was to experimentally evaluate the recent impact theories for rigid bodies. We should emphasize that our main focus in this study lies in the area of robotics. Therefore, we strictly focus on low-velocity collisions of slender members with external surfaces. The recent developments were originated from the application of the classical methods to systems that consist of members with distributed masses such as kinematic chains (Kane and Levinson, 1985). For this purpose we developed an experimental set-up to investigate the collision of freely dropped steel bars with a hardened tool steel surface (hardened steel was chosen to approximate, as much as possible, rigid-body collisions). As we will show, the experimental results suggested that there was a secondary mechanism, beside the one that was being captured by the restitution factor in the theory of rigid collisions. This mechanism is strongly coupled with the vibrational motion of the bars during the collision process. Previous researchers conducted several studies to investigate the effect of elastic vibrations on the post-impact rigid-body velocities of slender bars. Shabana and Gau (1993) conducted several theoretical studies focusing on the longitudinal waves induced by a concentrated mass longitudinally impacting a constrained beam. Yigit et al. (1990a), developed a theoretical model of the dynamics of a radially rotating beam transversally impacting an external surface. They verified their model by simulation and experiment (Yigit et al., 1990b). Yigit et al. (1990b) noted the existence of multiple collisions in certain experiments they have conducted. This phenomenon was previously noted by other investigators in the area. Mason (1935) showed that an impact which appeared single to the naked eye consisted in reality of several collisions in quick succession. Goldsmith (1960) remarked that multiple impacts were a peculiar characteristic of impacts involving flexible systems. A comprehensive study of this phenomenon

Contributed by the Applied Mechanics Division of THE AMERICAN SOCIETY OF MECHANICAL ENGINEERS for publication in the ASME JOURNAL OF APPLIED MECHANICS.

Discussion on this paper should be addressed to the Technical Editor, Professor Lewis T. Wheeler, Department of Mechanical Engineering, University of Houston, Houston, TX 77204-4792, and will be accepted until four months after final publication of the paper itself in the ASME JOURNAL OF APPLIED MECHANICS.

Manuscript received by the ASME Applied Mechanics Division, Oct. 17, 1994; final revision, Mar. 13, 1995. Associate Technical Editor: W. N. Sharpe, Jr.

Copyright © 1996 by ASME

Downloaded 04 May 2010 to 171.66.16.33. Redistribution subject to ASME license or copyright; see http://www.asme.org/terms/Terms_Use.cfm

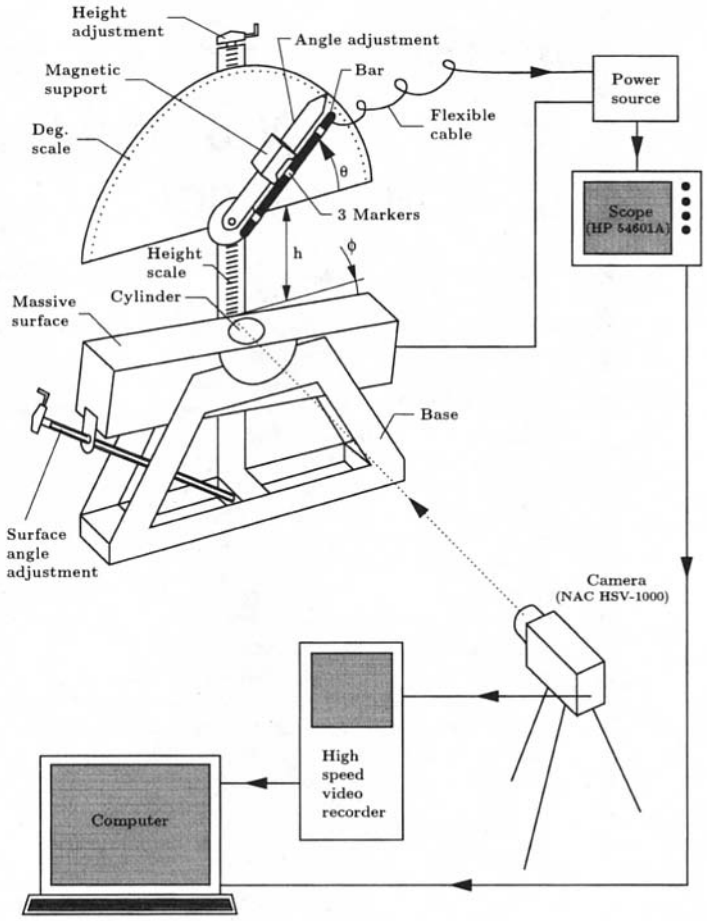


Fig. 1 Sketch of the experimental setup

and its effect on collision, however, was never conducted before.

In the present article we study the collisions of unconstrained slender rods with a massive external surface. The main difference of our experiments is that we consider the effect the eccentricity of collision on the post impact dynamics of the bar. We demonstrate that the orientation of the bar with respect to the external surface may become (depending on the length of the bar) by far the most dominant factor in the post-impulsive rigid-body motion. To the best of our knowledge, the drastic effect of the orientation on the coefficient of restitution was never analyzed nor explained before. In the succeeding part of the article we first present the experimental set-up. Then, the results of a set of experiments that exhibit the variation of the coefficient of restitution with the orientation of the bar are given. Next, we develop an analytical model based on the discretization of the bar. We verify our model by comparing theoretical outcomes with experimentally obtained results. Subsequently, using the model, we seek to capture two physical phenomena: internal vibrations and multiple collisions. We demonstrate that these factors lead to drastically different post-impact behavior than the one predicted by rigid-body analysis. We conclude the article by proposing a slenderness factor to identify the class of collision problems where the coefficient of restitution is invariant to the inclination angle.

2 The Experimental Design

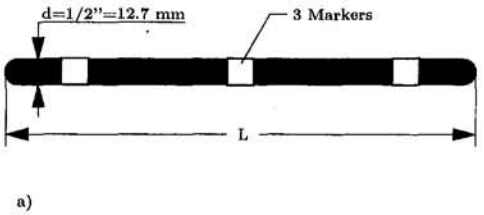
The main goal of the present investigation was to study the planar motion collisions of relatively rigid bars with massive external surfaces. For this purpose an experimental set-up was developed. The collision was created by dropping hardened steel bars from a vertical distance, on a massive cast iron block with an embedded tool steel cylinder at the impact point. We built a device to be able to vary the pre-impact orientation and velocity of the bar in a controlled and repeatable manner. A high-speed video system was used to capture the kinematic data. In addition, the contact time between the bar and the surface was measured by using an electrical circuit.

2.1 Instrumentation. The experimental set-up, shown schematically in Fig. (1), consists of the following main components:

1 The Bar: Six hardened steel bars (heat treated up to 55 HRC with circular cross sections and various lengths (Fig. 2(*a*)) were used. Each bar had semispherical ends to achieve relatively uniform contact conditions. The mass density of the bars was $\rho = 7876.74\ \text{Kg/m}^3$ and their Young's modulus of elasticity was $E = 2.1 * 10^{11}\ \text{N/m}^2$. The experiments were conducted with six different lengths ranging from 63.5 to 600 mm. The bars were painted flat black in order to obtain contrast during the video processing. Three reflective markers, one at the mass center and the other two located symmetrically at known distances from center, were used to capture the kinematic data.

2 The Dropping Device: The dropping device was designed to meet two requirements. First, the motion of the bar before and after the collision was to be remain as planar as possible. Second, the precollision velocities and orientations of the bar should be independently adjustable while maintaining the same impact point. As shown in Fig. 1, three adjustments were incorporated: (a) the dropping height, h (b) the orientation

Downloaded 04 May 2010 to 171.66.16.33. Redistribution subject to ASME license or copyright; see http://www.asme.org/terms/Terms_Use.cfm



Bar	L [mm]
1	63.5
2	100
3	200
4	300
5	400
6	600

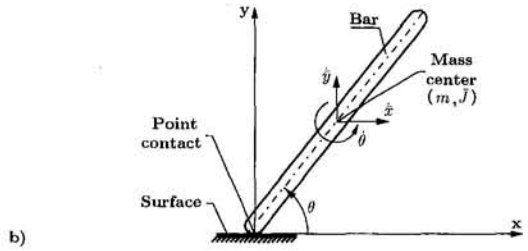


Fig. 2 The bar and the system of coordinates: (*a*) geometry of the bar and marker configuration, (*b*) system of coordinates

of the bar, θ, and (c) the orientation of the dropping surface, ϕ. The planar motion of the bar would be ensured if it was released in manner that prevents nonplanar motions. This was achieved by mounting the bar on electromagnets. The device includes a large cast iron block (130 × 130 × 590 mm) as the external impact surface. The impact point was further reinforced by embedding a tool steel cylinder at the point of collision (with a diameter of 40 mm).

3 The Data Acquisition System: A high-speed video system (NAC HSV-1000 with a capture rate of 1000 frames/sec) was used to acquire the kinematic data. Video images of each experiment were transferred to the computer and the center locations of the three markers on the bar were computed. The position data was then used to calculate the inclination angle of the bar at the instant of collision and the pre and post-impact velocities.

The contact between the bar and the surface was used as a switch in an electrical circuit in order to sense the duration of collision (Fig. 1). The contact events during the collision were detected by capturing the voltage generated in the circuit with a triggering oscilloscope.

2.2 Processing of the Kinematic Data. The high-speed video camera records the white markers on a black background. For each experiment, 30 frames before and after collision were used to estimate the kinematics of the bar. The images were transferred to the computer to be processed by a specialized program (developed for the present project) in order to digitize the position of the markers with respect to the global reference frame. Then, the data was divided into pre and post-collision parts. An algorithm based on the free motion of the bar in the gravitational field was used to interpolate both pre and post-position data. The angle of the bar at the contact instant (θ), the angular velocities of the bar immediately before and after collision ($\dot{\theta}^-, \dot{\theta}^+$), and the center of mass velocities ($\dot{x}^-, \dot{y}^-, \dot{x}^+, \dot{y}^+$) were estimated from the interpolated data (Fig. 2(b)).

We should note that, during the collision the position of the bar changes while the bar deforms. These deformations were on the order of micrometers, such that they could not be detected on the video images. Therefore, the experimentally obtained kinematic data only reflects the general rigid-body motion of the bar.

3 Testing Rigid Impact Hypotheses

Lately, there has been much discussion regarding the hypotheses used in solving rigid-body collisions. As we stated earlier the primary goal of the present research was to test these hypotheses. Generally, formulation of rigid-body collision problems are based on two physical laws, Coulomb's law of dry friction and balance of momentum. Also, an additional relation is obtained by using the coefficient of restitution. The most controversial aspect of the conventional methods has been the proper definition of this coefficient. Yet, theoretically speaking, it is well known that all definitions yield identical results when the slip direction at the contact point remains unchanged during the collision period. Accordingly, we tested the validity of Coulomb's law and the invariance of the coefficient of restitution for collisions where the slip direction remains unchanged.

3.1 Coulomb's Law of Dry Friction. The validity of the Coulomb's law for rigid impact problems was tested experimentally. For this purpose, the bar was dropped with zero tangential and angular velocities (Fig. 2(b)), $\dot{x}^- = 0$ and $\dot{\theta}^- = 0$. Four sets of experiments were performed with the normal pre-impact velocity $\dot{y}^-$ taken as 1, 2, 3, and 4 m/s, respectively. Meanwhile, during each set the inclination angle of the bar, θ, was varied between 0 deg and 90 deg.

Figure 3(a) depicts the experimentally computed tangential velocities of the tip of the bar before and after the impact. The initial tangential velocity was practically zero (slip reversal is impossible for a rigid bar with zero tangential velocity (Brach, 1989), while its value after the collision was negative. In each experiment the impulse ratio, μ, was computed as the ratio of the tangential and normal impulses over the collision:

$$\mu = \frac{\dot{x}^+ - \dot{x}^-}{\dot{y}^+ - \dot{y}^-}.$$

For large angles (Fig. 3(b)) the bar does not slip during the collision (approximately $\theta > 81$ deg). Accordingly, the impulse ratio is equal to the kinetic coefficient of friction, μ_k, in the unshaded region of the plot. We observed that the kinetic coefficient of friction was reasonably constant for the dynamic range (i.e., the bar slips during the collision). The kinetic coefficient of friction for the present study was estimated from the mean of the computed values in the dynamic range as $\mu_k \approx 0.075$.

Furthermore, one clearly observes the linear variation in the static range (the shaded region of the plot) as expected for the

Downloaded 04 May 2010 to 171.66.16.33. Redistribution subject to ASME license or copyright; see http://www.asme.org/terms/Terms_Use.cfm

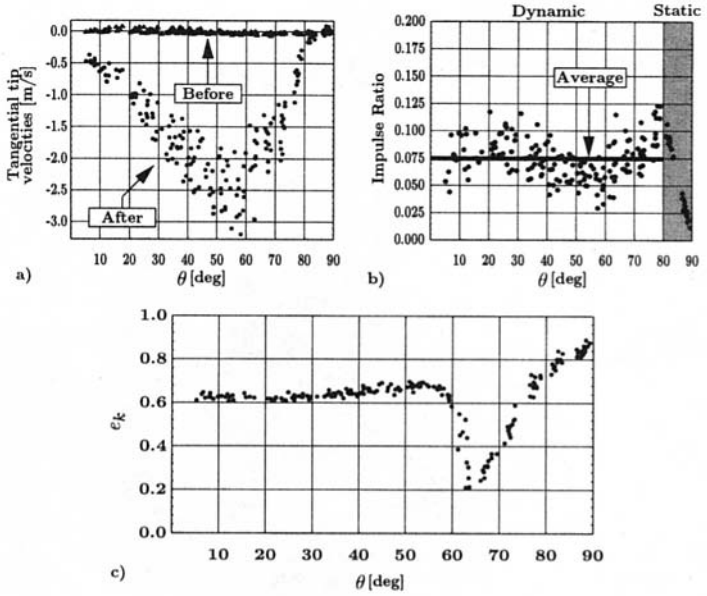


Fig. 3 Experimental results for the 200 mm bar: (*a*) tangential tip velocities, (*b*) impulse ratios, (c) kinematic coefficients of restitution

no slip case. The impulse ratio is equal to the static coefficient of friction, μ_s, when the slip is impending at $\theta \approx 81$ deg. Accordingly, μ_s was estimated as $\mu_s \approx 0.1$. From these observations, we may also conclude that the Coulomb's law remains generally valid in the class of collisions that are considered in this article.

3.2 Coefficient of Restitution. Since we have conducted the experiments such that there were no slip reversals, the coefficient of restitution was estimated from the kinematic data. The kinematic coefficient of restitution was computed as the ratio between post and pre-impact normal velocities at the contact point (Fig. 3(*c*)). The experimental results revealed that the coefficient of restitution exhibits significant variation as the inclination angle of the bar varied. This variation spanned over 70 percent of the expected range of all possible values of the coefficient (0-1). The figure depicts the coefficients for the four sets of experiments. It was clear that the dependence of the coefficient of restitution on the normal pre-impact velocity was negligible for the range of velocities used in our study. One important aspect of the experimental results is the lack of rebound for certain configurations during the impact, which will be addressed later in the article. It became clear to us that the restitution coefficient alone used with the rigid-body model was not sufficient to account for all the mechanisms involved in the energy loss.

These results prompted us to question the applicability of the concept of restitution for slender bars that are often used in example problems of rigid-body collision. The main objective was to determine geometrical factors that could be used to identify the class of problems where the rigid theory can be used without significant errors. We also opted to follow more complex methods that can be used to explain the causes of the variation in the kinematic coefficient of restitution. We particularly focused on incorporating additional mechanisms of energy loss to our formulation, such as transfer of energy from the rigid-body motion to internal elastic motion of the bar.

4 Theoretical Modeling

We used a discrete model to represent the dynamics of the bar during the collision process. Our main goal here was to capture the underlying physical behavior of the bar during impact. The ultimate test of the validity of the methods that were used was going to be the ability of the model to duplicate the physical behavior as it was captured by the video system. We remind the reader that the sampling time of the video system falls well short of the speed (micro-second time scale) and resolution (micrometers) requirements that were necessary to capture the micro-behavior.

4.1 Equations of Motion We sectioned the bar into n equal rigid segments of length $l = L/n$. The segments were connected to one another by a pair of viscoelastic links placed symmetrically at a transverse distance of $a/2$ from the neutral axis (see Fig. 4(*a*)). Each link consisted of a linear spring (assigned a uniform stiffness, k) and a viscous damper (assigned a uniform damping coefficient, b). The reason of using two links mounted as described was to establish coupling between the longitudinal and bending stresses developed in the bar. The longitudinal elasticity of the bar was set by choosing the constant k and the bending stiffness was set by choosing the distance a. The viscous dampers were used in order to take into account the internal dissipation of the bar.

Using n elements, the bar is replaced by a $2n + 1$ degree-of-freedom system with a generalized coordinate vector $\mathbf{x}$ given by

$$\mathbf{x} = \{x, y, u_0, q_1, u_1, q_2, u_2, \ldots, q_{n-1}, u_{n-1}\}^T.$$

The components of $\mathbf{x}$ were chosen as shown in Fig. 4(*a*). Equations of motion for the bar now can be written in the following general form:

$$\mathbf{M}(\mathbf{x})\ddot{\mathbf{x}} = [\mathbf{\Lambda}_1(\mathbf{x}) + \dot{\mathbf{x}}^T\mathbf{\Lambda}_2(\mathbf{x})]\dot{\mathbf{x}} + \mathbf{\Lambda}_3(\mathbf{x}, Q_n, Q_t) \quad (1)$$

where, $\mathbf{M}(\mathbf{x})$ is the $(2n + 1) \times (2n + 1)$ mass matrix, $\mathbf{\Lambda}_1$ and $\mathbf{\Lambda}_2$ are $(2n + 1) \times n$, $\mathbf{x}$ dependent matrices, and $\mathbf{\Lambda}_3$ is a $(2n + 1 \times 1)$ vector depending on $\mathbf{x}$, the normal force at the contact point, Q_n, and the tangential force at the contact point, Q_t. The equations of motion were generated by computer using *Mathematica,* and are rather complex and long. Therefore, their specific forms will not be presented here.

The normal force exerted by the surface at the contact point was modeled as

$$Q_n = (K - B\dot{y})|y| \quad (2)$$

where K is the surface stiffness (different than the one taken

Downloaded 04 May 2010 to 171.66.16.33. Redistribution subject to ASME license or copyright; see http://www.asme.org/terms/Terms_Use.cfm

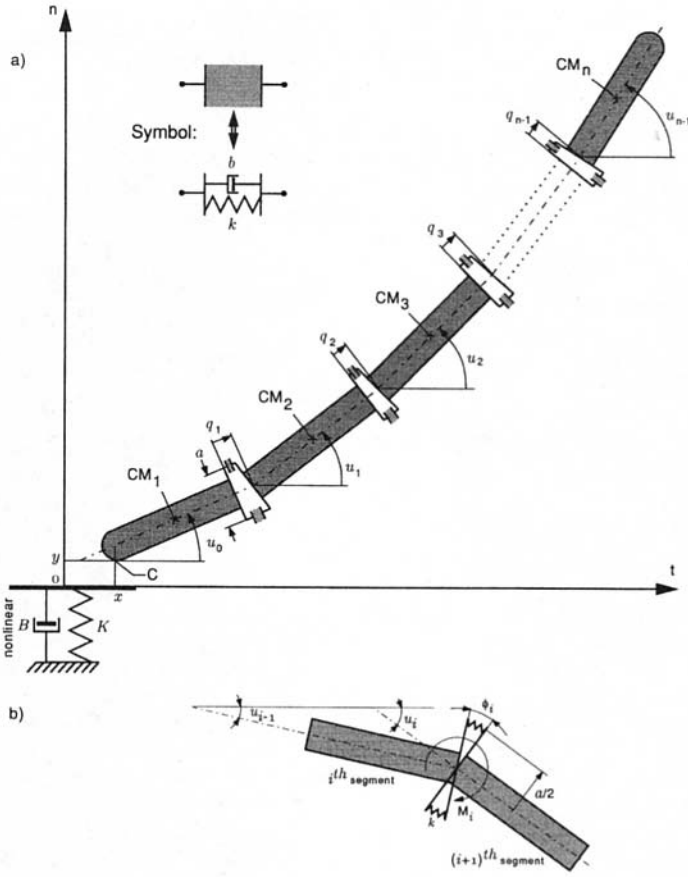


Fig. 4 Discretized model of the bar: (*a*) the model and the coordinate system, (*b*) rotation between two contiguous segments

for the bar), B is the ground damping coefficient (also different than the one taken for the bar). This form corresponds to a linear spring and a nonlinear viscous damper chosen in a form that was proposed in Lee and Wang (1983) (see also Yigit et al., 1990c).

The tangential component of the contact force was chosen using Coulomb's friction model with the static and kinetic coefficients of friction selected as $\mu_s = 0.100$ and $\mu_k = 0.075$, respectively (estimated from Fig. 3(*b*)).

4.2 The Rigid-Body Motion. Solution of the system of equations given in Eq. (1) yields the generalized coordinates and velocities that represent the motion of the elastic model of the bar. Further steps were required in order to contrast this data against the experimentally acquired kinematic data. We should recall that the experimentally acquired kinematic data reflected the general rigid-body motion of the bar. Kinematics of center of mass of the elastic bar could be directly compared to the rigid-body motion of the mass center. The rigid-body angular acceleration of the elastic bar was computed from

$$\ddot{\theta} = \frac{m}{2J}\{\ddot{x}[(L-d)\sin\theta + d/2] - \ddot{y}(L-d)\cos\theta)\}$$

where $\ddot{x}$ and $\ddot{y}$ are the central accelerations and J is the centroidal moment of inertia. The rigid-body angular velocity and displacement were obtained by numerically integrating the angular acceleration.

4.3 Estimation of the Bar and Surface Parameters. The elastic model involves five parameters k, b, a, K, B that have to be determined. The approach that was taken in this study to evaluate the parameters was kept as simple as possible. Again, the validity of the approach will be tested by comparing the simulated macro-behavior of the bar and the actual experimental data. The constants k and a were evaluated by using Hooke's law and Euler's equation. We consider two simple static problems:

1 Longitudinal Calibration of the Discrete Model: The axial static displacement at the center of a vertically hanged bar due to its weight can be expressed as

$$\delta_c = \frac{3\rho g L^2}{8EA} \tag{3}$$

where ρ (Kg/m) is the linear density, g (m/s^2) is the gravitational acceleration, L (m) is the total length of the bar, E (N/m^2) is the Young's modulus, and A (m^2) is the cross-sectional area of the bar.

The displacement of the central element of the discrete model in the same configuration can be written as

$$\delta_d = \sum_{i=1}^{(n-1)/2} \frac{F_i}{2k} \quad (n \text{ is odd}). \tag{4}$$

where, F_i is the cumulative gravitational force acting on the spring pair at the ith connection. Here, the number of elements n is odd, such that one element is exactly situated at the middle of the bar and its center coincides with the bar's center. Given that the weight of each element is $\rho L/n$ we obtain

$$\delta_d = \frac{\rho g L(n-1)(3n-1)}{16kn}. \tag{5}$$

Downloaded 04 May 2010 to 171.66.16.33. Redistribution subject to ASME license or copyright; see http://www.asme.org/terms/Terms_Use.cfm

Equating $\delta_c = \delta_d$ and solving for k we get

$$k = \frac{EA(n-1)(3n-1)}{6Ln}. \quad (6)$$

2 *Transversal Calibration of the Discrete Model:* The rotation of the transversal section at the center of a horizontal cantilever bar acted upon by its weight can be expressed as

$$u_c = \frac{7\rho g L^3}{48 E I_z} \quad (7)$$

where I_z is the cross-sectional moment of inertia ($I_z = \pi d^4/64$ for bar with circular cross section).

To proceed with the discrete model we consider the static equilibrium of a section of the discrete bar that starts from the ith connection and ends at the nth segment. For small deflections, the moment equation at the ith connection can be written as

$$\frac{\rho g L^2}{2}\frac{(n-i)^2}{n^2} - \frac{ka^2}{2}\phi_i = 0 \quad (i = 1, \ldots, n-1) \quad (8)$$

where, ϕ_i is the relative rotation (see Fig. 4(b)). Here, the first term is due to the weights of the segments in the section and the second term is the moment of the spring pair at the ith connection. In addition, the absolute rotation of the $(i+1)$th segment u_i can be written as

$$u_0 = 0 \quad \text{and} \quad u_i = \sum_{j=1}^{i} \phi_j \quad (i = 1, \ldots, n-1) \quad (9)$$

where ϕ_i is the relative angular deflection between segment $i-1$ and segment i. Using Eqs. (8) and (9), the rotation of the center segment is

$$u_d = \frac{\rho g L^2 (n-1)(7n-5)}{24 a^2 k n} \quad (n \text{ is odd}). \quad (10)$$

Setting $u_c = u_d$ and solving for a and replacing k by Eq. (6) we obtain

$$a = \sqrt{\frac{12 I_z (7n-5)}{7A(3n-1)}} \quad (11)$$

where we observe that a depends just on the number of elements n for bars with identical cross sections.

The effect of internal damping in the bar was neglected by choosing $b = 0$. This was done because it took several seconds (acoustically estimated) for the vibrations induced in the bar by collision to diminish, while the impact occurred in a span of several hundred microseconds (depending on the length of the bar).

The stiffness and the damping coefficients (K and B) at the contact point were estimated from central collisions of the bars (i.e., vertical drop angle). We discovered that the simulated collision time was mainly affected by the stiffness coefficient K and the number of elements n (the effect of the damping coefficient B was insignificant). In addition, the damping coefficient B could be used to adjust the simulated rebound velocity for central impact. It should be pointed out that the experimentally estimated energy loss for a central collision can only be achieved by properly setting the value of B.

Accordingly, the value of the stiffness was determined by simulating a central collision with a particular bar. Then the values of K and B were tuned such that the numerically computed contact time and the kinematic coefficient of restitution matched the experimental values. In the present study, we estimated these two parameters from the central collision of the 200 mm bar as $K = 5.5 \times 10^7$ N/m and $B = 2.0 \times 10^7$ N s/m^2. The number of segments n, was adjusted such that the results computed by the chosen coefficients exhibited acceptable agreement with experimental values for all bars and at all angles. We found out that nine segments ($n = 9$) were sufficiently many to satisfy this requirement.

5 Analysis of the Results

In the present analysis, first we demonstrate that the discrete model approximates the overall physical behavior of the bar. Once we verify the validity of the model, we use the discrete system to investigate the micro behavior during collision. One fundamental observation that was made in this study was the effect of internal vibrations and multiple "micro" collisions on the energetics of impact. We show that the internal vibrations may be the most dominant factor in causing the bars to lose energy (i.e., significantly higher that the one predicted by any restitution theory). Finally, we present a geometric factor that can be used as a guideline for the applicability of the rigid body theory in solving the collision problems of slender bars.

5.1 Experimental Verification of the Discrete Model. Five sets of experiments were performed using five bar lengths varying between 100-600 mm (see Fig. 2(a)), we will discuss the bar with $L = 63.5$ mm later in the article). Kinematic data and contact time measurement from the vertical drop experiment of the 200 mm bar were used to compute the five structural parameters. Having obtained the numerical values of the parameters, the results of the simulation were compared to the experimental outcomes for all bars dropped at angles ranging from 0 deg to 90 deg. All experiments were conducted with zero precontact tangential and rotational velocities (i.e., $\dot{x}^- = 0$ and $\dot{\theta}^- = 0$). In the normal direction, however, the precollision velocity was set to four discrete values for each drop angle ($\dot{y}^- = -1, -2, -3$, and -4 m/s).

As mentioned previously, the numerical computation was conducted with nine elements. The accuracy increased with the number of elements n used. Yet complexity of the equations of motion significantly increased with the increasing number of elements. We determined that $n = 9$ yields acceptable results for the bars considered in this study at a reasonable computational time.

The computed and experimental results for the five bars are depicted in Fig. 5. We observed that the macro-behavior of the real system (kinematic coefficient of restitution) was captured reasonably well by the discrete model. The drop in the coefficient of restitution was captured almost perfectly. This outcome was particularly encouraging, since the parameters were obtained from a single experiment with the 200 mm bar.

5.2 Analysis of the Multicollision Phenomenon. The experimental and numerical results demonstrated that the coefficient of restitution varied significantly as a result of varying the angle of the bar, θ. The primary reason in the variation of the normal rebound velocity was the exchange of energy between the rigid body and elastic motions of the bar. This exchange was inherently tied to the motion of the tip of the bar with respect to the impact surface during the collision event.

As can be seen from the coefficient of restitution plots (Fig. 5), the normal rebound velocity was maximum for the central collisions. Then, for all bars, a steady drop of the rebound was observed until a critical angle θ_c is reached. In addition we observed that all bars had one collision for a drop angle range of $\theta_c \le \theta \le \pi/2$. When the drop angle was less that the critical value, we observed an increase in the coefficient of restitution and emergence of second or more micro-collisions. The critical angle, θ_c depends on the length of the bar as can be observed from the graphs shown in Fig. 5.

Let us consider the energy profiles during the central collision of the 200 mm bar (Fig. 6). We identify four compartments of the energy that play key roles during the collision process:

Downloaded 04 May 2010 to 171.66.16.33. Redistribution subject to ASME license or copyright; see http://www.asme.org/terms/Terms_Use.cfm

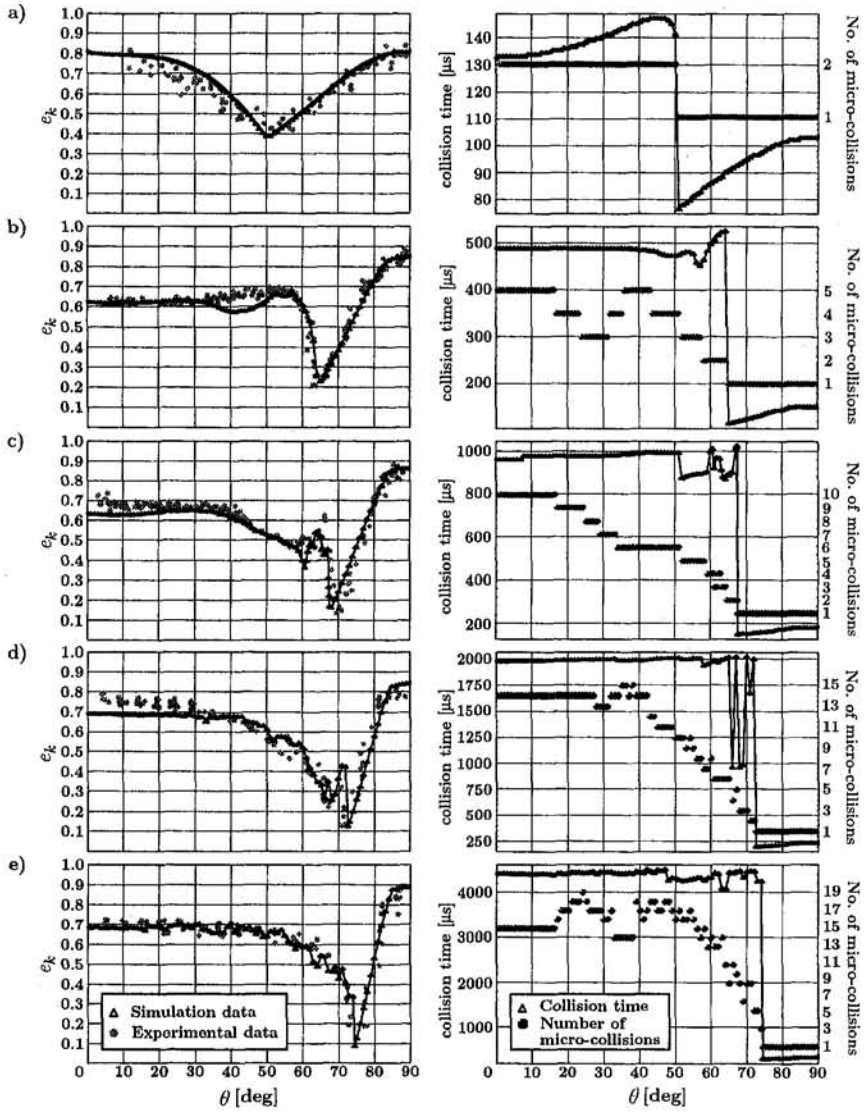


Fig. 5 Experimental and simulated kinematic coefficient of restitution, collision time, and number of micro-collisions for the: (*a*) 100 mm bar, (*b*) 200 mm bar, (*c*) 300 mm bar, (*d*) 400 mm bar, (*e*) 600 mm bar

1 The kinetic energy of the *rigid-bar*, E_r:

$$E_r = \tfrac{1}{2}\,[m(\dot{\bar{x}}^2 + \dot{\bar{y}}^2) + \bar{J}\dot{\theta}^2] \tag{12}$$

where m and $\bar{J}$ are the mass and the centroidal moment of inertia of the bar, respectively.

2 The elastic energy stored internally by the bar, E_i:

$$E_i = \sum_{j=1}^{n} K_j + \sum_{j=1}^{n-1} P_j - E_r \tag{13}$$

where K_j is the kinetic energy of the jth segment and P_j is the potential energy stored in the springs between the jth and $(j+1)$th segments.

3 The potential energy of the surface spring, E_s:

$$E_s = -\frac{K}{4}\,(y|y| - y^2). \tag{14}$$

This expression yields the surface spring energy (Ky^2) for $y < 0$, and is zero otherwise.

4 The energy dissipated by the surface friction and damping, E_f:

$$E_f = E_r^- - [E_r + E_i + E_s] \tag{15}$$

This term was evaluated as the difference between the total energy of the bar at the onset of the collision (E_r^-), and the remaining three energy components $(E_r + E_i + E_s)$.

Figure 6 depicts the numerically computed tip displacements and the energy components (as percentages of the total energy at the onset of impact). At $\theta = 90$ deg (Fig. 6(a)) the collision is central and we have a single collision. The total energy at the onset of the impact is solely composed of the kinetic energy of the bar due to the rigid-body motion (E_r^-). When the contact takes place, we observe a steady drop in E_r as a result of energy transfer to the three other compartments. Then, slightly before the instant of maximum compression at the tip (y is minimum), a reverse process takes place, during which energy is transferred back to the rigid-body compartment. The energy exchange between the internal and rigid compartments continues while the tip of the bar remains in contact with the collision surface. At the end of collision three percent of the initial energy (E_r^-) remains inside the bar as longitudinal vibrations (E_i^+) and 25 percent is dissipated through the surface damping and friction (E_f^+). When the bar loses contact with the surface the energy transfer between E_r and E_i does not take place. The vibrational

Downloaded 04 May 2010 to 171.66.16.33. Redistribution subject to ASME license or copyright; see http://www.asme.org/terms/Terms_Use.cfm

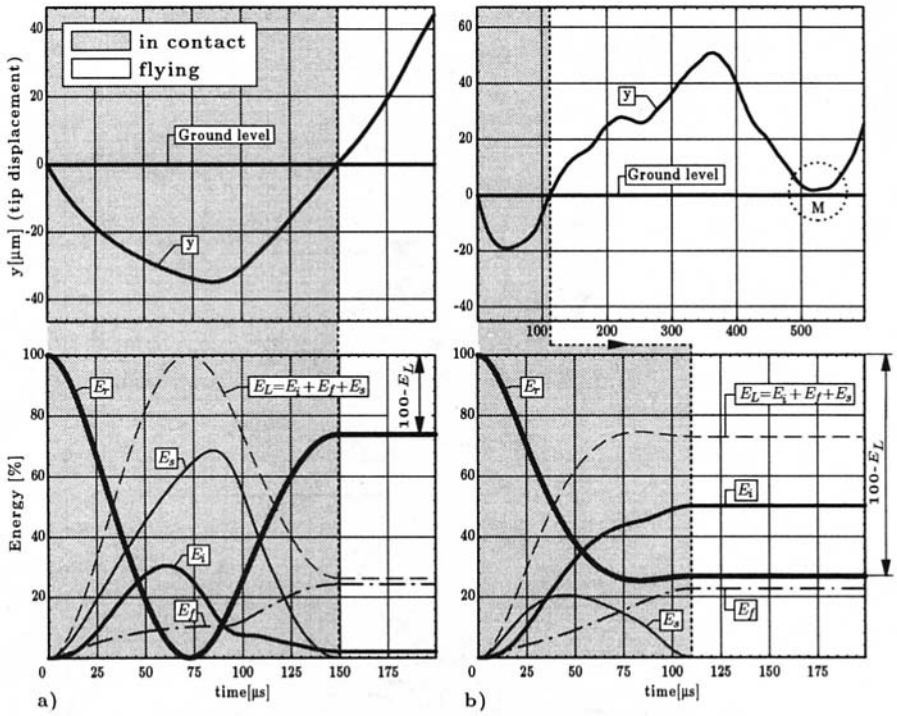


Fig. 6 Tip displacement and energy components for the 200 mm bar: (*a*) θ = 90 deg, (*b*) θ = 64.3 deg

energy of the bar at the end of the impact (E_i^+) will be eventually damped out internally and lost (i.e., will never be recovered by the rigid motion).

When the bar is dropped at the critical angle, $\theta = \theta_c = 64.3$ deg, we still have a single collision, yet the collision is not central. For this case, we also observe that the rigid-body energy of the bar decreases steadily during the initial phase of the collision. The profile of the E_f component of energy remains very similar to the central collision case. The difference, however, is due to the rate of transfer of energy from the internal compartment, E_i to E_r in the later stages of the collision. As a matter of fact, we observe a steady increase in E_i throughout the collision process, resulting in $E_i^+ = 50$ percent. *Thus, we conclude that the mechanism that leads to the significant variations in the coefficient of restitution is mainly due to the residual energy that remains internally in the bar when the contact is lost.* In addition, once the collision is over, one can see that the tip of the bar approaches the surface (due to the internal vibrations) and almost establishes contact once again (marked by M on Fig. 6(b)). The increase in the rebound velocities when the drop angle is decreased beyond the critical angle is inherently tied to the additional collisions that will arise for $\theta < \theta_c$ (see Fig. 5(b)). When a second collision takes place, the internal energy that was present in the bar at the end of the first collision, once again will be partially transferred to the rigid compartment due to the renewed contact. As more collisions appear a complex chain of events that depend on the phase of the elastic motion of the tip of the bar with respect to the contact surface leads to the behavior that was seen on Fig. 5. The same effect can be better highlighted by comparing the simulated internal energy that remains in the bar obtained by allowing the bar to have a single collision (other collisions suppressed numerically) to the full simulation results with multicollisions (Fig. 7). We observe that significant portions of elastic energy are transferred to the rigid-body energy compartment of the bar as a result of additional collisions. For example, for $\theta = 57$ deg we observe that approximately 30 percent of the energy that remained in the bar after the first collision is recovered when the second collision is complete.

5.3 Applicability of the Classical Restitution Hypothesis. Rigid-body models used in collision problems assume that a negligible fraction of the initial kinetic energy of the system is transformed into vibrations of the colliding bodies (Goldsmith, 1960). Therefore, rigid-body models produce acceptable results when the above assumption is valid but will be in error when a significant percentage of the initial energy is converted into vibrations. Hence, the main determinant in the applicability of the rigid theory to the problem at hand (i.e., collision of slender bars with external surfaces) hinges on two variables: the critical angle θ_c and the kinematic coefficient of restitution at this angle e_c.

To study this aspect of the problem, we considered the bars with a diameter of $\bar{d} = 12.7$ mm that we have used in the experiments. Then we have numerically obtained the values of $\bar{\theta}_c$ and $\bar{e}_c$ at the bar length that yields an e_c which is five percent less that of the central coefficient of restitution (i.e., the coefficient of restitution at $\theta = 90$ deg). Subsequently, we varied the diameter incrementally, and computed the corresponding bar length values that produced identical $\bar{e}_c$ values. Having obtained

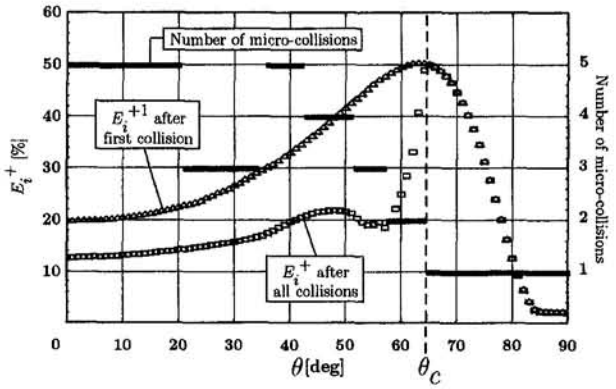


Fig. 7 Internal energy at the end of first and all micro-collisions (200 mm bar)

Downloaded 04 May 2010 to 171.66.16.33. Redistribution subject to ASME license or copyright; see http://www.asme.org/terms/Terms_Use.cfm

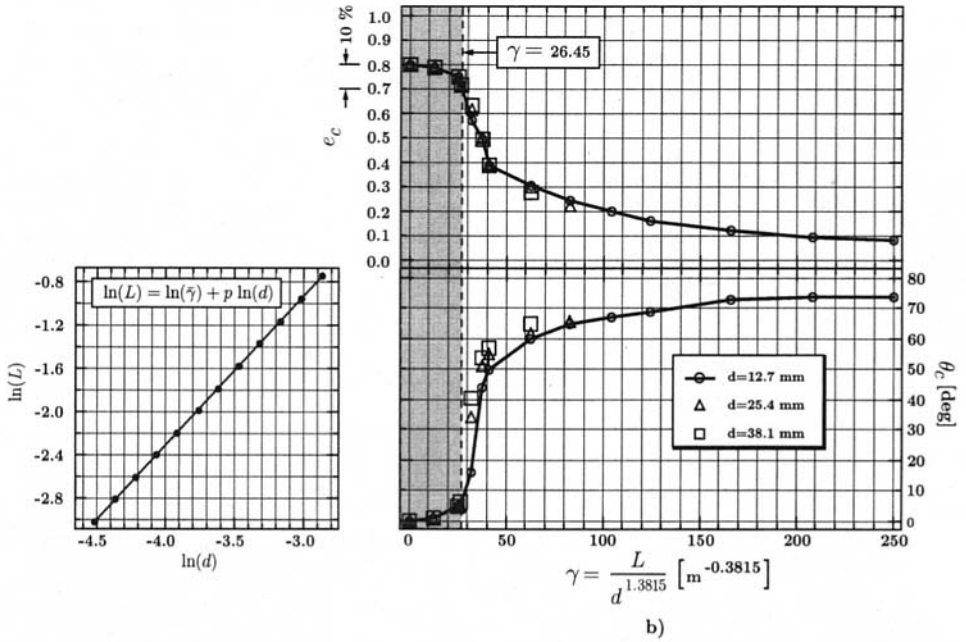


Fig. 8 Slenderness coefficient: (*a*) logarithmic plot of *L* and *d*, (*b*) θ_c and e_c versus the slenderness coefficient γ

sufficiently many pairs of values (12 points were used in the actual computation), we plotted the length versus diameter values in a log-log scale (Fig. 8(a)). In Fig. 8(a), the dimensions for d and L were chosen in meters. We varied the diameter d between 0.011–0.057 m and the corresponding length variation was computed as 0.049–0.476 m.

Noting the linearity of the relation we defined an empirical slenderness factor γ as

$$\gamma = \frac{L}{d^p} \tag{16}$$

where the exponent was computed as $p = 1.3815$ for the steel bars considered in this study. Next, we plotted the variables θ_c and e_c by varying γ for three diameter values and bar lengths up to 600 mm (Fig. 8(b)). The most striking observation from this figure was that the e_c values computed for a fixed value of γ were almost invariant. The same invariance was also observed, perhaps to a lesser extend for larger values of γ, in θ_c values.

Now, we assume that the rigid-body theory is only applicable when a ten percent variation of the coefficient of restitution due to the changing eccentricity can be tolerated. This assumption leads to the identification of the range of slenderness coefficient that can be used as a guideline to use the rigid-body theory (shaded gray in Fig. 8(b)):

$$\gamma = \frac{L}{d^{1.3815}} \leq 26.45\ \text{m}^{-0.3815} \tag{17}$$

One final experiment with a bar length, $L = 63.5$ mm and a diameter, $d = 12.7$ mm ($\gamma = 26.45$) was conducted to verify variation of the coefficient of restitution for a bar with a slenderness factor that was in the border of the shaded region of Fig. 8(b). Figure 9 depicts the simulated and experimental e_k values of the bar. As can be seen from the figure, the variation in e_k was substantially less for this case. We note that the excessive scatter in the experimental data for smaller angles was mainly due to the difficulties we have encountered in acquiring the kinematic data for the shortest bar.

6 Conclusions and Recommendations

In the present article we studied the collision of slender bars with external surfaces. We have made an attempt to approximate rigid collisions by selecting hardened steel bars and surfaces. As result of the study we can provide an answer to the following questions:

1 Is the coefficient of restitution relatively constant for highly rigid material and low-impact speeds? The most important outcome is that the rigid-body theory (the invariance of the coefficient of restitution) has a very limited applicability even for highly rigid material and low-impact speeds.

2 Is Coulomb's theory of dry friction valid for collisions? We have observed that Coulomb's theory of dry friction remains generally valid for the surface contact friction during the collision.

3 Is the coefficient of restitution a material constant that strictly depends on local contact properties? The coefficient of restitution, which is inherently tied to the internal vibrations evoked in the bar as result of collision, does not strictly depend on local contact properties. Indeed, we have observed that when the bar has a sufficiently low slenderness ratio, the coefficient of restitution remains relatively unchanged by the orientation of the bar. Then, it may seem that the coefficient of restitution depends on the local deformations at the contact point. Yet, in

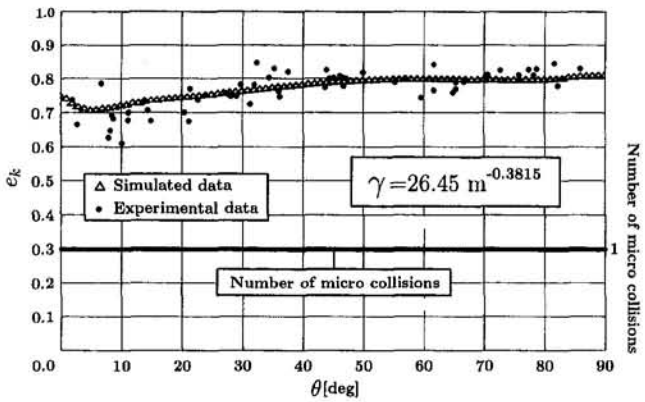


Fig. 9 Experimental and simulated kinematic coefficient of restitution for a bar with $L = 63.5$ mm and $d = 12.7$ mm

Downloaded 04 May 2010 to 171.66.16.33. Redistribution subject to ASME license or copyright; see http://www.asme.org/terms/Terms_Use.cfm

general, the coefficient is strongly tied to the global properties of the bars, and the outcome of the impact greatly depends on the overall material properties and the dynamic conditions during impact.

4 What are the physical phenomena that cause energy loss in collision? The first mechanism that caused energy loss was the local deformations in the neighborhood of the contact point and the dissipation of energy to the external surface. We have discovered, however, that a second, and an important factor was the internal vibrations of the bar induced by the impact. For certain configurations, the effect of the latter significantly superseded the effect of the former mechanism. Given that the rigid-body theory does not take into account the internal vibrations, it should be used with great caution and under very specific circumstances.

5 Is the impact event a single collision as generally perceived by the mechanics community? We observed that impact is generally a multicollision event. In noncentral impacts the flexural vibrations lead to lateral displacements at the contacting end that were significantly larger than the axial displacements. This increased the possibility of occurrence of the multiple collisions. The surprising finding, however, was that multiple collisions lead to energy recovery and an increase in the coefficient of restitution. Intuitively one may hypothesize that a second collision would lead to further energy loss as a result of local deformations. Although this is true to a certain extent, the recovery of internal energy has a more dominant effect. Consequently, the overall effect of additional contacts is often the elevation in the magnitude of the coefficient of restitution.

Because of the questions raised by the present study regarding the limited applicability of the rigid-body impact theory, it is natural to seek alternative methods to be used in place of the coefficient of restitution. One alternative method would be the approach taken in this paper, that is using discretized models. We have demonstrated that (at least for rigid slender bars) estimating the stiffness and damping coefficients produces acceptable results in terms of predicting the outcome of the collision. Continuous models based on modal analysis and finite element models may also be considered for this purpose.

Finally, we should emphasize that the study was conducted with slender rods and low-impact velocities. The natural applicability of these results should be in the area of robotics. Furthermore, additional tests with other materials and different geometries are needed in order to further generalize the results reported in the present article.

Acknowledgment

This material is based upon work supported by the National Science Foundation Grant No. MSS-9203097. Any opinions, findings, and conclusions or recommendations expressed in this material are those of the authors and do not necessarily reflect the views of the National Science Foundation. The authors would also like to express their gratitude to Dr. Dan Marghitu for his helpful suggestions that helped them to refine the theoretical model.

References

Brach, R. M., 1989, "Rigid Body Collisions," ASME JOURNAL OF APPLIED MECHANICS, Vol. 56, pp. 133–138.

Goldsmith, W., 1960, *Impact,* Edward Arnold Publishers Ltd., London, U.K.

Hurmuzlu, Y., and Chang, T., 1992, "Rigid Body Collisions of a Special Class of Planar Kinematic Chains," *IEEE Transactions on Systems, Man, and Cybernetics,* Vol. 22, No. 5, pp. 964–971.

Hurmuzlu, Y., and Marghitu, D. B., 1994, "Rigid Body Collisions of Planar Kinematic Chains with Multiple Contact Points," *The International Journal of Robotics Research,* Vol. 13, No. 1, pp. 82–92.

Kane, T. R., and Levinson, D. A., 1985, *Dynamics: Theory and Applications,* McGraw-Hill, New York.

Keller, J. B., 1986, "Impact with Friction," ASME JOURNAL OF APPLIED MECHANICS, Vol. 53, pp. 1–4.

Lee, T. W., and Wang, A. C., 1983, "On the Dynamics of Intermittent-Motion Mechanisms, Part 1: Dynamic Model and Response," ASME *Journal of Mechanisms, Transmissions, and Automation in Design,* Vol. 105, pp. 534–540.

Marghitu, D. B., and Hurmuzlu, Y., 1995, "Three-Dimensional Rigid-Body Collisions With Multiple Contact Points," ASME JOURNAL OF APPLIED MECHANICS, Vol. 62, pp. 725–732.

Mason, H. L., 1935, *Impact of Beams,* ASME, New York, Vol. 58, pp. A55–A61.

Stronge, W. J., 1990, "Rigid Body Collisions with Friction," *Proceedings of Royal Society, London,* Vol. A431, pp. 169–181.

Shabana, A. A., and Gau, W. H., 1993, "Propagation of Impact—Induced Longitudinal Waves in Mechanical Systems with Variable Kinematic Structure," *Journal of Sound and Vibration,* Vol. 115, pp. 1–8.

Whittaker, E. T., 1904, *A Treatise on the Analytical Dynamics of Particles and Rigid Bodies,* Cambridge, U.K.

Yigit, A. S., Ulsoy, A. G., and Scott, R. A., 1990a, "Dynamics of Radially Rotating Beam with Impact, Part 1: Theoretical and Computational Model," *Journal of Vibration and Acoustics,* Vol. 112, pp. 65–70.

Downloaded 04 May 2010 to 171.66.16.33. Redistribution subject to ASME license or copyright; see http://www.asme.org/terms/Terms_Use.cfm

G. deBotton

K. Schulgasser
Mem. ASME.

The Pearlstone Center for Aeronautical Engineering Studies,
Department of Mechanical Engineering,
Ben-Gurion University of the Negev,
Beer-Sheva 84105, Israel

Bifurcation of Orthotropic Solids

We consider a large deformation plane-strain problem involving a compressible orthotropic solid subjected to uniaxial compressive loading along one of the principle directions which is aligned with the boundary of a half-space. An exact solution for the displacement field is obtained and a condition for the smallest compressive load corresponding to the onset of a surface instability is determined. It is shown that when the compression occurs along the stiffest direction this condition is expressible in terms of a cubic polynomial, and that the corresponding critical load is lower than the well-known estimate which determines the critical load to be equal to the inplane shear modulus.

Introduction

Solids of orthotropic symmetry have become common in various engineering applications, and accordingly, the problem of predicting their stability limited compressive strength is of practical importance. Among the first works dealing with this subject we may cite the work of Biot (1965) and earlier references to his work therein; he developed a theory for dealing with prestressed solids and applied his approach to the study of the behavior of nonlinear rubber-like materials. Hill and Hutchinson (1975) carried out a general discussion concerning the bifurcation phenomena and obtained estimates for the critical tensile stresses of orthotropic solids.

With the growing usage of fiber-reinforced and other composites, the concept of bifurcation and loss of stability at the micro level was introduced. Rosen (1965) obtained, by making use of beam theory, the well-known estimate that the compressive strength is equal to the effective in-plane shear modulus of the composite. This result has been rederived by different methods in other works dealing with fiber and laminated composites. Among these works we mention the article by Ben-chin and Pipkin (1972) dealing with a class of inextensible fiber-reinforced incompressible matrices, the article by Steif (1987) demonstrating that beam theory is applicable only when the fiber diameter is very small compared with the variation of the deformation, and the article by Christensen (1994) providing an asymptotic solution for linear elastic composites in the limit of large ratios between the longitudinal Young's modulus and the other elastic moduli. Methods which take into account imperfections of reinforced composites, such as initial waviness or partial debonding of the fibers are also available, but this is outside the scope of the present study. (See, for example, the work by Budiansky (1983) and the comprehensive study by Kyriakides et al. (1995) for the former, and Steif (1988) for the later.)

An extensive and rigorous study concerning the microscopic and macroscopic instability mechanisms of nonlinear heterogeneous solids was carried out by Geymonat et al. (1993), generalizing previous work of Triantafyllidis and Maker (1985). These investigators obtained, within the general framework of finite deformations, rigorous results for the complete boundary value problem of elasticity in the long and short wave limits. Among other topics, they also demonstrated that under appropriate convexity assumptions homogenization and linearization procedures commute. Finally, a procedure for estimating the compressive strength of linearly elastic fiber-reinforced composites can be deduced from the work of Shield et al. (1994), who obtained rigorous results for the critical compressive strain of a thin layer bonded to an infinite matrix.

The present study deals with an orthotropic, linearly elastic macroscopically homogeneous solid subjected to uniaxial compression perpendicular to one of the symmetry planes. Beginning from the equilibrium equations we determine the general expression for the displacement field. Next, from the boundary conditions we find an exact condition for the lowest compressive stress which is compatible with a displacement field other than the homogeneous one. We stress that while Geymonat et al. (1993) solved an analogous problem for a class of materials more general than the one we consider here, the advantage of the present approach is centered on the simplicity of the resulting expressions. Thus, we obtain a simple *analytical* solution for the boundary value problem which leads to predictions for the critical compressive strength in a straightforward manner. The solution may also be used as a *benchmark* for more advanced, numerically based models for the prediction of compressive failures.

We specialize the general result to the practically important situation involving compression along the stiffest direction, and compare the resulting predictions for the critical loading with the well-known, beam theory based estimate of Rosen (1965). As was noticed by Christensen (1994), in the limit of highly anisotropic materials the exact result tends towards the beam theory estimate. However, we demonstrate that for more realistic materials the sharpness of this estimate strongly depends on some of the other elastic moduli characterizing the orthotropic solid. We also demonstrate the ability of the results obtained in this work to provide predictions for the critical compressive load of slightly anisotropic solids, circumstances where the beam theory estimate would apparently be of no practical usefulness.

Governing Equations for the Plane-Strain Problem

We consider a half-space, $x_2 \le 0$, of an orthotropic solid whose principle axes are aligned with the Cartesian axes. Initially, the solid is in a state of homogeneous strain corresponding to compressive uniform stress p parallel to the free boundary along the x_1-direction. In terms of the second Piola-Kirchhoff stress, which measures the tractions per unit undeformed area, the equilibrium equations are (see, for example, Malvern (1969))

$$\nabla \cdot [(\boldsymbol{\sigma} + \boldsymbol{\Sigma}) \cdot \nabla(\mathbf{x} + \mathbf{u})] = \mathbf{0}, \tag{1}$$

where we have neglected body forces. In the above relation, $\mathbf{x}$ and $\mathbf{u}$ are the position and displacement vectors, respectively, and $\boldsymbol{\sigma}$ is a small stress increment beyond the initially applied stress $\boldsymbol{\Sigma}$. We assume that the product terms $\boldsymbol{\sigma} \cdot \nabla \mathbf{u}$ and their

Contributed by the Applied Mechanics Division of THE AMERICAN SOCIETY OF MECHANICAL ENGINEERS for publication in the ASME JOURNAL OF APPLIED MECHANICS.

Discussion on this paper should be addressed to the Technical Editor, Professor Lewis T. Wheeler, Department of Mechanical Engineering, University of Houston, Houston, TX 77204-4792, and will be accepted until four months after final publication of the paper itself in the ASME JOURNAL OF APPLIED MECHANICS.

Manuscript received by the ASME Applied Mechanics Division, Mar. 21, 1995; final revision, Sept. 5, 1995. Associate Technical Editor: S. Kyriakides.

Copyright © 1996 by ASME

Downloaded 04 May 2010 to 171.66.16.33. Redistribution subject to ASME license or copyright; see http://www.asme.org/terms/Terms_Use.cfm

derivatives are small and ignore them in the subsequent analysis. Consequently, for plane-strain conditions, where $\Sigma_{11} = -p$ is the only nonvanishing component of the initial stress, the remaining two equilibrium equations may be expressed in the form

$$\frac{\partial \sigma_{11}}{\partial x_1} + \frac{\partial \sigma_{12}}{\partial x_2} - p\frac{\partial^2 u_1}{\partial x_1^2} = 0,$$

$$\frac{\partial \sigma_{12}}{\partial x_1} + \frac{\partial \sigma_{22}}{\partial x_2} - p\frac{\partial^2 u_2}{\partial x_1^2} = 0. \quad (2)$$

We note that, alternatively, we could obtain these equations by following the variational procedure outlined by Biot (1965) (chapter 2, Section 5), with the only difference being that instead of using his expressions for the strains in terms of the displacements, we should have used the more common definition of the Lagrangian strain tensor

$$\mathbf{e} = \tfrac{1}{2}[\nabla \mathbf{u} + (\nabla \mathbf{u})^T + \nabla \mathbf{u} \cdot (\nabla \mathbf{u})^T], \quad (3)$$

which is the appropriate conjugate variable to the second Piola-Kirchhoff stress in the undeformed configuration.

Following Biot (1965) (Chapter 2, Section 3), we assume a linear relationship between the stress increment and the *infinitesimal* strain increment. Accordingly, for an orthotropic solid in plane-strain condition we may write

$$\sigma_{11} = C_{11}\frac{\partial u_1}{\partial x_1} + C_{12}\frac{\partial u_2}{\partial x_2},$$

$$\sigma_{22} = C_{12}\frac{\partial u_1}{\partial x_1} + C_{22}\frac{\partial u_2}{\partial x_2},$$

$$\sigma_{12} = C_{66}\left(\frac{\partial u_1}{\partial x_2} + \frac{\partial u_2}{\partial x_1}\right), \quad (4)$$

where C_{11}, C_{12}, C_{22}, and C_{66} are the instantaneous elastic moduli of the solid in the vicinity of the prestressed configuration. Substituting these relations into the equilibrium Eqs. (2) we obtain the following expressions for the equilibrium equations in terms of the displacements, namely,

$$(C_{11} - p)\frac{\partial^2 u_1}{\partial x_1^2} + C_{66}\frac{\partial^2 u_1}{\partial x_2^2} + (C_{12} + C_{66})\frac{\partial^2 u_2}{\partial x_1 \partial x_2} = 0,$$

$$(C_{66} - p)\frac{\partial^2 u_2}{\partial x_1^2} + C_{22}\frac{\partial^2 u_2}{\partial x_2^2} + (C_{12} + C_{66})\frac{\partial^2 u_1}{\partial x_1 \partial x_2} = 0. \quad (5)$$

We recall that similar relations were previously obtained by Shield et al. (1994) for solids of isotropic symmetry and by Christensen (1994) for the same class of orthotropic solids considered above.

Generalizing the solution proposed by Shield et al. (1994) for the isotropic case, we find that the following choice for the displacement field components, namely

$$u_1 = [AH_a e^{ax_2} + Be^{bx_2}] \sin(x_1),$$

$$u_2 = [Ae^{ax_2} + BH_b e^{bx_2}] \cos(x_1), \quad (6)$$

satisfies the equilibrium Eqs. (5), where

$$H_a = -\frac{a[C_{22}(C_{11} - E) + a^2 C_{22}C_{66} + C_{66}(2C_{12} + p)]}{(C_{12} + C_{66})(C_{66} - p)},$$

$$H_b = -\frac{b[C_{22}(E - p) - b^2 C_{22}C_{66} - C_{66}(2C_{12} + C_{66})]}{(C_{12} + C_{66})(C_{66} - p)}, \quad (7)$$

a and b are the positive roots of the bi-quadratic

$$z^4 - 2H_2 z^2 + H_0 = 0, \quad (8)$$

where

$$H_2 = \frac{C_{22}(E - p) - C_{66}(2C_{12} + p)}{2C_{22}C_{66}},$$

$$H_0 = \frac{(C_{11} - p)(C_{66} - p)}{C_{22}C_{66}}, \quad (9)$$

and A and B are arbitrary constants. In the above relations

$$E = \frac{C_{11}C_{22} - C_{12}^2}{C_{22}} \quad (10)$$

is a Young's modulus such that, for a linear solid in *plane strain*, $\epsilon = p/E$ is the uniform compressive strain associated with the initial loading. It can be verified that the above displacements u_1 and u_2 decay as x_2 tend to negative infinity, and reduce to the appropriate expressions obtained by Shield et al. (1994) in the isotropic limit. We note that due to the lack of a characteristic length scale for this problem, the wavelength of the displacement field is undetermined. Accordingly, the displacement field components in Eqs. (6) may be expressed in terms of dimensionless axes $\xi_i = x_i/\lambda$, $i = 1, 2$, where λ is an arbitrary wave length.

The expressions for the stress components are determined by making use of relation (6) in the stress-displacement relations (4). These must satisfy the boundary conditions $\sigma_{12} = 0$ and $\sigma_{22} = 0$ at the free boundary $x_2 = 0$, providing a set of two homogeneous linear equations for the constants A and B. To obtain a nontrivial solution for these equations the determinant of the coefficients must vanish, and it can be shown that the roots of the determinant must satisfy the relation

$$(C_{11} - p)(C_{66} - p)(H_2^2 - H_0)(Y(p))^2 = 0, \quad (11)$$

where we note that the third term is a quadratic polynomial in p, and

$$Y(p) = C_{22}(C_{66} - p)(E - p)^2 - C_{66}(C_{11} - p)p^2 \quad (12)$$

is a cubic polynomial in p. Equation (11) is a condition for the onset of a surface instability, stating that a nontrivial solution to the problem can exists only when $p \geq p_{cr}$, where p_{cr} is the smallest real positive root.

Applications to Orthotropic Solids

We apply the results of the previous section to determine the critical compressive loading for which a solid of orthotropic symmetry becomes unstable. From a practical point of view, the interesting configuration is the one that involves compression along the stiff direction, e.g., along the fibers or the layers of fiber-reinforced or laminated composites, respectively. In this section, we restrict ourselves to this common loading situation.

For convenience, we express the elastic properties of the solid in terms of the engineering constants, E_i the Young's moduli along the x_i axes, ν_{ij} the Poisson ratios measuring the lateral contraction along the x_j axis due to uniaxial tension along the x_i-axis, and G_{12} the shear modulus in the (x_1, x_2)-plane. In terms of these engineering constants, the four independent components of the *plane-strain* compliance matrix $\mathbf{S}$ are

$$S_{11} \equiv \frac{1}{E} = \frac{1}{E_1}\left(1 - \frac{E_3}{E_1}\nu_{13}^2\right),$$

$$S_{12} = -\frac{1}{E_1}\left(\nu_{12} + \frac{E_3}{E_2}\nu_{13}\nu_{23}\right),$$

$$S_{22} = \frac{1}{E_2}\left(1 - \frac{E_3}{E_2}\nu_{23}^2\right), \quad (13)$$

Downloaded 04 May 2010 to 171.66.16.33. Redistribution subject to ASME license or copyright; see http://www.asme.org/terms/Terms_Use.cfm

and

$$S_{66} = \frac{1}{G_{12}},$$

and where the moduli C_{11}, C_{12}, C_{22}, and C_{66} are the appropriate components of $\mathbf{S}^{-1}$.

The predictions for the critical loading p_{cr} can be easily obtained from the solutions of the four polynomials composing relation (11). However, due to our assumption that the compression occurs along the stiff direction, we have that $G_{12} = C_{66} < C_{11}$ and we can rule out the root $p = C_{11}$. Furthermore, it can be shown that if

$$\frac{E_1}{E_2} > \frac{E_1 - G_{12}}{E_2 - G_{12}}, \tag{14}$$

where $E_1 = 2G_{12}(1 + \nu_{12})$, the roots of the quadratic term in (11) are complex, and since this inequality is satisfied for many orthotropic solids with $E_1 > E_2$, we may exclude the quadratic term as well. Thus, practically, the only possible roots of interest are the smallest root of the cubic polynomial $Y(p)$ and the root $p = G_{12}$. However, we also note that if $G_{12} < C_{11}$ the first and the second terms of Y are positive as long as $p < G_{12}$. This suggests that at least one real root of Y must lie in the interval $p < G_{12}$, and since $Y(G_{12}) < 0$ and $Y(0) > 0$ this root must also be positive. We conclude then, that p_{cr} is the smallest root of the cubic polynomial $Y(p)$, and it is always lower than the well-known estimate $p_R = G_{12}$ which was first proposed by Rosen (1965).

Estimates for the critical loading normalized by the in-plane shear modulus plotted versus the ratio of the longitudinal to transverse Young's moduli are shown in Fig. 1, for the choice of the elastic constants $E_3 = E_2$, $\nu_{12} = \nu_{13} = 0.3$ and $\nu_{23} = 0.4$. Results for two different values of the ratio between the in-plane shear modulus and the transverse Young's modulus (0.5 and 0.8) are shown. The continuous curves correspond to the exact results which were obtained from the solution of $Y = 0$ and the long dashed curve to the estimate $p_R = G_{12}$. We note that in this figure, and the subsequent ones, a circle at the point where a curve stops marks that the limit of the validity of inequality (14) has been reached. We observe that, as expected, in the limit $E_1 \gg E_2$ the exact results approach the beam theory based estimate p_R. A less obvious observation is that when the ratio G_{12}/E_2 is small enough (which is the case for many reinforced composites), Rosen's estimate provides an excellent approximation even for relatively low values of E_1/E_2. This is not the case for larger values of the ratio between the shear modulus and the transverse Young modulus. Thus, for moderate values of E_1 and G_{12}/E_2 approaching unity, the relative error between the exact and the approximate predictions for the critical loading is approximately ten percent.

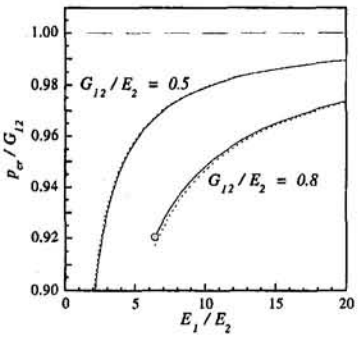


Fig. 1 Estimates for the critical compressive load normalized by the in-plane shear modulus versus the ratio between the longitudinal and transverse Young's moduli, for two different values of the ratio between the in-plane shear and the transverse Young's moduli and $E_3 = E_2$, $\nu_{12} = \nu_{13} = 0.3$, and $\nu_{23} = 0.4$. The continuous curves correspond to the exact estimate, the long dashed curve to the beam theory based estimate, and the short dashed curves to the first-order approximation (15). The circle at the point where the curve stops marks the limit of the validity of inequality (14).

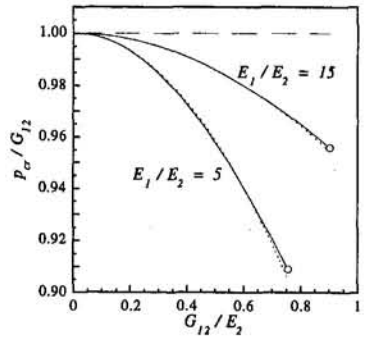


Fig. 2 Estimates for the critical compressive load normalized by the in-plane shear modulus versus the ratio between the in-plane shear and transverse Young's moduli, for two different values of the ratio between the longitudinal and the transverse Young's moduli and $E_3 = E_2$, $\nu_{12} = \nu_{13} = 0.3$, and $\nu_{23} = 0.4$. The continuous curves correspond to the exact estimate, the long dashed curve to the beam theory based estimate, and the short dashed curves to the first-order approximation (15). The circles at the points where the curves stop mark the limit of the validity of inequality (14).

The short dashed curves correspond to the first-order approximation for the smallest root of Y

$$p_e = G_{12}\left[1 - \left(1 - \frac{E_3}{E_2}\nu_{23}^2\right)\left(\frac{G_{12}}{E_2}\right)\left(\frac{G_{12}}{E}\right)\right], \tag{15}$$

in the limit when E_1 is larger than the other elastic moduli. Clearly, p_e provides an excellent estimate for p_{cr} throughout the entire range of possible ratios between the longitudinal and transverse Young's moduli. We note that the zero-order term in (15) is precisely the estimate p_R from beam theory, as well as the asymptotic result obtained by Christensen (1994) from relation (5) by an order of magnitude analysis. However, we stress that in spite of the fact that the solution proposed by Christensen (1994) for (5) delivers the zero-order approximation for the critical load, the associated displacement field does not decay as x_2 tends to negative infinity (as would happened for any *finite* E_1). In accordance with our earlier observations concerning Fig. 1, we note that the ratio G_{12}/E_2 appears already in the first order term and dominates the sharpness of the beam theory approximation.

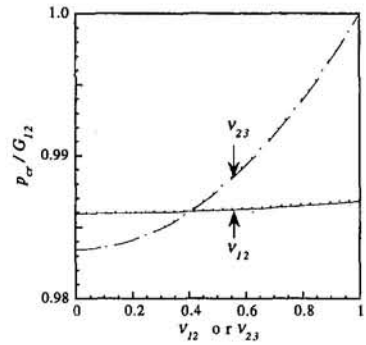


Fig. 3 Estimates for the critical compressive load normalized by the in-plane shear modulus versus the inplane and out-of-plane Poisson's ratios, where $E_1 = 15E_2$, $G_{12} = E_2/2$ and $E_3 = E_2$. The continuous curve corresponds to the in-plane Poisson's ratio with $\nu_{13} = \nu_{12}$ and $\nu_{23} = 0.4$, and the long dashed curve to the out-of-plane ratio ν_{23} with $\nu_{12} = \nu_{13} = 0.3$. The short dashed curves are the corresponding first-order approximations (15).

Downloaded 04 May 2010 to 171.66.16.33. Redistribution subject to ASME license or copyright; see http://www.asme.org/terms/Terms_Use.cfm

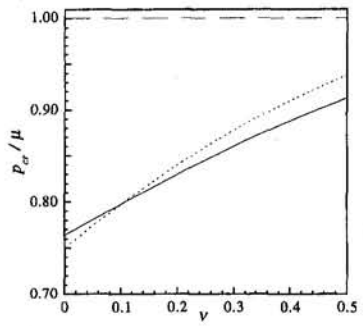


Fig. 4 Estimates for the critical compressive load of a slightly anisotropic solid normalized by the shear modulus versus the Poisson's ratio. The continuous curve corresponds to the exact estimate, the long dashed curve to the beam theory based estimate, and the short dashed curve to the first-order approximation (15).

Figure 2 shows values for the critical compressive load as functions of the ratio between the inplane shear and the transverse Young's moduli for the same choice of the elastic constants as in Fig. 1. The continuous curves correspond to the exact result and the long and short dashed curves to the zero and first-order approximations, respectively. Results for two different ratios of the longitudinal Young's modulus to the transverse Young's modulus are presented ((5) and (15)). We observe that, regardless of the value of E_2, in the limit of small in-plane shear modulus the critical compressive load is precisely G_{12}. We also observe the proximity of the first-order approximation p_e to the exact result, implying that this simple estimate captures the principal features of the solution.

The dependence of the critical load on the *in-plane* and *out-of-plane* Poisson's ratios (ν_{12} and ν_{23}, respectively) is shown in Fig. 3 for the choice of the elastic constants $E_1 = 15E_2$, $G_{12} = E_2/2$ and $E_3 = E_2$. The continuous curve depicts the dependence on the in-plane Poisson's ratio with $\nu_{13} = \nu_{12}$ and $\nu_{23} = 0.4$, and the long dashed curve the dependence on the out-of-plane ratio ν_{23} with $\nu_{12} = \nu_{13} = 0.3$. We note that the inplane Poisson's ratio has only negligible influence on the critical load, while the influence of the out-of-plane ratio is much more noticeable. Once again, we observe that the first-order approximation p_e is in near perfect agreement with the exact solution (note that the dependence on ν_{13} appears implicitly through the dependence on E).

An interesting limit is, of course, the isotropic limit. In this case relation (12) reduces to the form

$$Y(p) = (1-\nu)p^3 - 8(1-\nu)\mu p^2 + 8(2-\nu)\mu^2 p - 8\mu^3, \quad (16)$$

where μ and ν are the shear modulus and the Poisson's ratio of the isotropic solid, respectively. We emphasize that for isotropic solids equality holds in (14), and thus, the solution provided by (16) should be viewed as a limiting case for slightly anisotropic solids for which $E_1 \to E_2 = 2\mu(1+\nu)$. We note that the strains associated with p_{cr} in this limit are large (more than 20 percent) and it is unlikely that solids would undergo such strains while still in the linear regime. Results for the compressive strength normalized by the shear modulus of isotropic solids are shown in Fig. 4 as functions of the Poisson's ratio. We observe that, in a manner similar to that noted for orthotropic solids, for fixed μ the compressive strength is lower for solids with smaller Poisson's ratios. We also observe that the relative error between p_R (long dashed curve) and the exact result is more than ten percent, while the next order approximation p_e (short dashed curve) provides reasonable estimates even in this limit.

Concluding Remarks

A rigorous solution for a finite deformation plane-strain problem involving uniaxial compression along one of the principle axes of a linearly elastic orthotropic solid was determined. Based on this solution, an explicit condition for the smallest compressive stress which is compatible with a nonhomogeneous state of deformation was found. Special attention was given to the practically common situation of compression along the stiffest principle direction, and it was shown that in this case the stability condition can be expressed in terms of a cubic polynomial. It was further shown that the well-known beam theory estimate, which is commonly cited in applications for reinforced materials, overestimates the critical compressive strength.

Numerical predictions of the critical compressive loading of certain orthotropic solids were computed, demonstrating the domain of applicability of the beam theory estimate and highlighting the relative contribution of the various elastic coefficients. In particular, the high sensitivity of the critical loading to the ratio between the in-plane shear modulus and the transverse Young's modulus was detected. An explicit, higher order approximation for the compressive strength was determined, exhibiting excellent agreement with the exact result. Finally, it is stressed that the simple solution that was presented in this work can be incorporated into more sophisticated models that take into account initial imperfections of reinforced solids.

References

Ben-chin, K., and Pipkin, A. C., 1972, "Finite Buckling of Fiber-Reinforced Columns," *Acta Mechanica,* Vol. 13, pp. 265–280.

Biot, M. A., 1965, *Mechanics of Incremental Deformations,* John Wiley and Sons, New York.

Budiansky, B., 1983, "Micromechanics," *Computers and Structures,* Vol. 16, pp. 3–12.

Christensen, R. M., 1994, "Material Instability for Fiber Composites," ASME JOURNAL OF APPLIED MECHANICS, Vol. 61, pp. 476–477.

Geymonat, G., Müller, S., and Triantafyllidis, N., 1993, "Homogenization of nonlinearly elastic materials, microscopic bifurcation and macroscopic loss of rank-one convexity," *Arch. Rational Mech. Anal.,* Vol. 121, pp. 231–290.

Hill, R., and Hutchinson, J. W., 1975, "Bifurcation phenomena in the plane tension test," *J. Mech. Phys. Solids,* Vol. 23, pp. 239–264.

Kyriakides, S., Arseculeratne, R., Perry, E. J., and Liechti, K. M., 1995, "On the compressive failure of fiber reinforced composites," *Int. J. Solids Structures,* Vol. 32, pp. 689–738.

Malvern, L. E., 1969, *Introduction to the Mechanics of a Continuous Medium,* Prentice-Hall, Englewood Cliffs, NJ.

Rosen, B. W., 1965, "Mechanics of composite strengthening," *Fiber Composite Materials,* Am. Soc. Metals Seminar.

Shield, T. W., Kim, K. S., and Shield, R. T., 1994, "The Buckling of an Elastic Layer Bonded to an Elastic Substrate in Plane Strain," ASME JOURNAL OF APPLIED MECHANICS, Vol. 61, pp. 231–235.

Steif, P. S., 1987, "An exact two-dimensional approach to fiber micro-buckling," *Int. J. Solids Struct,* Vol. 23, pp. 1235–1246.

Steif, P. S., 1988, "A simple model for the compressive failure of weakly bonded, fiber reinforced composites," *J. Composite Materials,* Vol. 22, pp. 818–828.

Triantafyllidis, N., and Maker, B. N., 1985, "On the Comparison Between Microscopic and Macroscopic Instability Mechanisms in a Class of Fiber-Reinforced Composites," ASME JOURNAL OF APPLIED MECHANICS, Vol. 52, pp. 794–800.

Downloaded 04 May 2010 to 171.66.16.33. Redistribution subject to ASME license or copyright; see http://www.asme.org/terms/Terms_Use.cfm

F. Hild[1]
Department of Mechanical and Environmental Engineering, University of California, Santa Barbara, CA 93106-5070

P.-L. Larsson
Department of Solid Mechanics, Royal Institute of Technology, S-100 44 Stockholm, Sweden

F. A. Leckie
Department of Mechanical and Environmental Engineering, University of California, Santa Barbara, CA 93106-5070
Mem. ASME

Localization due to Damage in Two-Direction Fiber-Reinforced Composites

Fiber pull-out is one of the fracture features of fiber-reinforced ceramic matrix composites. The onset of this mechanism is predicted by using continuum damage mechanics, and corresponds to a localization of deformation. After deriving two damage models from a uniaxial bundle approach, different configurations are analyzed through numerical methods. For one model some very simple criteria can be derived, whereas for the second one none of these criteria can be derived and the general criterion of localization must be used.

1 Introduction

Ceramic matrix composites (CMCs) can either be reinforced by fibers in one direction or by fibers in two directions. The aim of this paper is to study composites reinforced with fibers in two perpendicular directions by extending a previous study on CMCs with fibers in one direction (Hild et al., 1992).

The rupture of most of the CMCs involves two separate failure mechanisms. The first mechanism is matrix cracking. The matrix cracks develop and their density saturates as the load level increases. The second mechanism is fiber breakage accompanied by fiber pull-out. Eventually, the final rupture will take place around one of the matrix cracks: it corresponds to *localized* fiber pull-out due to fiber breakage. The occurrence of this mechanism corresponds to the appearance of a macrocrack and will be described by a localization of deformation. The initiation of macrocracks in a structure during service often constitutes the early stage of the final failure of the structure. Starting from a material that is assumed free from any initial defect, the initiation of macrocracks can be predicted using continuum damage mechanics. The driving force is fiber breakage, which is accompanied by *distributed* pull-out. The approach using localization has successfully been used for ductile materials (Billardon and Doghri, 1989a, b; Doghri, 1989). The initiation stage is considered as the onset of a surface across which the velocity gradient is discontinuous. Under small deformation assumptions, this phenomenon is mainly driven by the damage mechanism that causes strain softening. For CMCs, the damage mechanism is related to fiber breakage, and the damage variable describes the percentage of broken fibers (Hild et al., 1992).

Although localization can be studied at the scale of fibers bonded to a matrix through an interface (Benallal et al., 1991a), i.e., at a micro level, localization also can be analyzed at a mesolevel, when the material is assumed to be homogeneous. Continuum damage mechanics, which represents a local approach to fracture (Benallal et al., 1991b), constitutes an efficient tool for this purpose. The progressive deterioration of the material is modeled by internal variables defined at the meso level. These variables are called *damage* variables. The damage state and the evolution of these variables is obtained through a uniaxial study based on fiber breakage (Coleman, 1958; Curtin, 1991). A two-dimensional plane-stress analysis is performed based on an extended model. The loss of uniqueness and the localization are studied for shear free states. A criterion referring to a critical value of the damage or to a maximum normal stress can describe the localization, which constitutes an objective criterion, from a design point of view.

2 Localization and Loss of Uniqueness

The failure at a meso level, with the initiation of a macrocrack, is defined as the bifurcation of the rate problem in certain modes, viz. the appearance of a surface across which the velocity gradient is discontinuous (Billardon and Doghri, 1989a). This phenomenon is referred to as *localization*, and corresponds to the failure of the ellipticity condition. The condition of localization can also be compared to the loss of uniqueness of the rate problem.

Stationary waves were studied by Hadamard (1903) in elasticity and by Hill (1962) and Mandel (1962) in elastoplasticity. Rice (1976) related the localization of plastic shear bands to jumps of the velocity gradient. Borré and Maier (1989) have given necessary and sufficient conditions for the onset of modes inside the body, and extended the results given by Rice (1976) and Rice and Rudnicki (1975, 1980).

Under small strain assumption and in elasticity coupled with damage, the behavior of a material is assumed to be described by the following piece-wise linear rate constitutive law:

$$\dot{\boldsymbol{\sigma}} = \begin{cases} \mathbf{E} : \dot{\boldsymbol{\epsilon}} & \text{if} \quad \dot{D} = 0 \\ \mathbf{H} : \dot{\boldsymbol{\epsilon}} & \text{if} \quad \dot{D} \neq 0 \end{cases} \tag{1}$$

where $\dot{\boldsymbol{\sigma}}$ and $\dot{\boldsymbol{\epsilon}}$, respectively, denote the stress and strain rates, $\mathbf{E}$ and $\mathbf{H}$ are fourth rank tensors, $\mathbf{E}$ is assumed to be positive definite, and D is either a single damage variable or a set of damage variables.

Localization occurs *inside* the body, *if and only if* (Rudnicki and Rice, 1975; Borré and Maier, 1989; Benallal et al., 1991a)

$$\text{Det}\,(\boldsymbol{n} \cdot \mathbf{H} \cdot \boldsymbol{n}) = 0 \quad \text{for a vector } \boldsymbol{n} \neq 0 \quad \text{and at a point inside a structure } \Omega. \tag{2}$$

[1] Visiting Postgraduate Researcher, also at the Laboratoire de Mécanique et Technologie, E.N.S. de Cachan/C.N.R.S./Universite Paris 6, 61 avenue du Président Wilson, F-94235 Cachan Cedex, France.

Contributed by the Applied Mechanics Division of THE AMERICAN SOCIETY OF MECHANICAL ENGINEERS for publication in the ASME JOURNAL OF APPLIED MECHANICS.

Discussion on this paper should be addressed to the Technical Editor, Professor Lewis T. Wheeler, Department of Mechanical Engineering, University of Houston, Houston, TX 77204-4792, and will be accepted until four months after final publication of the paper itself in the ASME JOURNAL OF APPLIED MECHANICS.

Manuscript received by the ASME Applied Mechanics Division, Feb. 25, 1992; final revision, Oct. 8, 1993. Associate Technical Editor: G. J. Dvorak.

Copyright © 1996 by ASME

Downloaded 04 May 2010 to 171.66.16.33. Redistribution subject to ASME license or copyright; see http://www.asme.org/terms/Terms_Use.cfm

This criterion corresponds to the failure of the ellipticity condition of the rate equilibrium equation; it also can be used as an indicator of the local failure of the material, at a meso scale (Billardon and Doghri, 1989a).

Furthermore, any loss of uniqueness, considered as bifurcation of the rate boundary value problem, is excluded provided

$$\dot{\boldsymbol{\sigma}} : \dot{\boldsymbol{\epsilon}} > 0. \tag{3}$$

In this study, the quantity that defines loss of uniqueness and localization is the linear tangent modulus $\mathbf{H}$. In the following, we analyze loss of uniqueness and loss of ellipticity (i.e., localization) for states when

$$\begin{cases} \epsilon_{11} = \alpha \epsilon_{22} \\ \epsilon_{12} = 0. \end{cases} \tag{4}$$

The parameter α is referred to as the strain ratio and its inverse is denoted by β. These particular states only are considered. When the hypothesis of Eq. (4) is satisfied, the nonvanishing components of the vector $\boldsymbol{n}$ are n_1 and n_2, and the matrix $\mathbf{A} = \boldsymbol{n} \cdot \mathbf{H} \cdot \boldsymbol{n}$ reduces to (Ortiz et al., 1987)

$$\mathbf{A} = \begin{bmatrix} n_1^2 H_{1111} + n_2^2 H_{1212} & n_1 n_2 (H_{1212} + H_{1122}) \\ n_1 n_2 (H_{1212} + H_{2211}) & n_1^2 H_{1212} + n_2^2 H_{2222} \end{bmatrix}. \tag{5}$$

If we rewrite $(n_1, n_2) = (\cos\theta, \sin\theta)$, $X = \tan^2\theta$, then the localization condition is equivalent to finding real positive roots of the following equation:

$$aX^2 + bX + c = 0 \tag{6}$$

with

$$\begin{aligned} a &= H_{1212} H_{2222} \\ b &= H_{1111} H_{2222} - H_{1122} H_{2211} - H_{1122} H_{1212} - H_{2211} H_{1212} \\ c &= H_{1212} H_{1111}. \end{aligned} \tag{7}$$

If real positive roots are found, then the localization direction is perpendicular to the vector $(n_1, n_2, 0) = (\cos\theta, \sin\theta, 0)$, characterized by the angle θ (Fig. 1). The values of H_{1111}, H_{2222}, H_{1122}, H_{2211} and H_{1212} are model dependent and specific models are now developed.

3 Constitutive Laws

This section is concerned with the development of two constitutive laws in the case of CMCs reinforced in two perpendicular directions. At constant temperature, the behavior of a CMC reinforced by unidirectional fibers in the x_2-direction (see Fig. 1) can be characterized by the Helmholtz free energy density ψ_2, which is a function of the state variables ϵ_{11}, ϵ_{22}, ϵ_{12}, and the damage variable D_2 in the x_2-direction

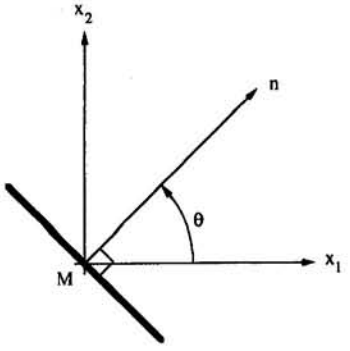


Fig. 1 Localization mode

$$\rho\psi_2 = \rho\psi(\epsilon_{11}, \epsilon_{22}, \epsilon_{12}, D_2, f_2, k_2), \tag{8}$$

where D_2 represents the fiber degradation in the x_2-direction, E_2 the Young's modulus in the x_2-direction, ν_{12} the Poisson's ratio, k_2 the ratio of the Young's modulus in the fiber direction (E_2) to the Young's modulus in the transverse direction (E_1), and G_{12} the shear modulus. It is worth noting that the elastic quantities depend on the volume fraction of fibers. The expression for the general Helmholtz free energy density ψ is given by

$$\begin{aligned} &\rho\psi(x, y, z, d, f, k) \\ &= \frac{E_2(f)}{2}\left[\frac{x^2 + 2\nu_{12}k(1-d)xy + ky^2}{k\{1 - \nu_{12}^2 k(1-d)\}}\right] + 2G_{12}z^2 \end{aligned} \tag{9}$$

where ρ is the material density, x, y, z are dummy variables representing strains, d damage, f volume fraction, and k Young's moduli ratio. The stresses and the thermodynamic force Y_2 associated to the damage variable D_2 are derived from the Helmholtz free energy density ψ_2 as follows:

$$\sigma_{11} = \rho\frac{\partial\psi_2}{\partial\epsilon_{11}} \quad \sigma_{22} = \rho\frac{\partial\psi_2}{\partial\epsilon_{22}} \quad 2\sigma_{12} = \rho\frac{\partial\psi_2}{\partial\epsilon_{12}}$$

$$Y_2 = \rho\frac{\partial\psi_2}{\partial D_2}. \tag{10}$$

The explicit expressions for the stresses related to the strains and the damage variable modeling the fiber degradation in the x_2-direction are given by

$$\begin{aligned} \sigma_{11} &= \frac{E_2}{k_2[1 - \nu_{12}^2(1-D_2)k_2]}[\epsilon_{11} + \nu_{12}(1-D_2)k_2\epsilon_{22}] \\ \sigma_{22} &= \frac{E_2(1-D_2)}{1 - \nu_{12}^2(1-D_2)k_2}(\epsilon_{22} + \nu_{12}\epsilon_{11}) \\ \sigma_{12} &= 2G_{12}\epsilon_{12}. \end{aligned} \tag{11}$$

The damage state of fibers in the x_2-direction, D_2 can be related to the stress (and is denoted by $D_2^{(1)}$) or strain state (and is denoted by $D_2^{(2)}$). The relationship is either implicit in terms of the normal stress in the x_2-direction (model #1)

$$D_2^{(1)} = 1 - \exp\left[-\left\{\frac{\sigma_{22}}{(1 - D_2^{(1)})f_2\sigma_c}\right\}^{m+1}\right]$$

$$\text{if} \quad \epsilon_{22} > 0 \quad \text{and} \quad \dot{\epsilon}_{22} > 0 \tag{12}$$

where m is the shape parameter of a Weibull law (Weibull, 1939), σ_c the characteristic strength (Henstenburg and Phoenix, 1989), and f_2 is the volume fraction of fibers in the x_2-direction; or explicit in terms of the normal strain in the x_2-direction (model #2)

$$D_2^{(2)} = 1 - \exp\left[-\left(\frac{\epsilon_{22}}{\epsilon_c}\right)^{m+1}\right]$$

$$\text{if} \quad \epsilon_{22} > 0 \quad \text{and} \quad \dot{\epsilon}_{22} > 0 \tag{13}$$

where ϵ_c is related to the characteristic strength σ_c by $\sigma_c = E_F\epsilon_c$ (E_F is the Young's modulus of the fibers). Both models describe the same material behavior when subjected to uniaxial tension. However, the models give different predictions for multiaxial loading states (Hild et al., 1992). It is worth noting that the damage evolution laws are a priori independent of the volume, since we assume that the local behavior of the fiber degradation is not dependent on the total length of the fiber (Curtin, 1991). This type of behavior is observed when *distributed* pull-out happens in conjunction with fiber breakage, and it can be shown that in most practical cases, the statistics driving the fiber breakage is independent of the total length of the composite. On the

Downloaded 04 May 2010 to 171.66.16.33. Redistribution subject to ASME license or copyright; see http://www.asme.org/terms/Terms_Use.cfm

other hand, if the composite length becomes very small, a length dependence is found again (Hild et al., 1994), and in this case the evolution of the damage variable is mainly given by a fiber-bundle-type of behavior, which leads to replacing $m + 1$ by m, the characteristic strength σ_c by $\sigma_0(L/L_0)^{-1/m}$, where σ_0 is the scale parameter of a Weibull law, and the scale strain ϵ_c by $\epsilon_0(L/L_0)^{-1/m}$, where L_0 is the gauge length at which the scale parameter has been identified, and $\sigma_0 = E_f\epsilon_0$. Since the results are the same for both damage evolution laws when the previous permutation is used, we will just express them in the case when the model is length independent, which is the most relevant in practice.

If the fibers are in the x_1-direction then the breakage can be modeled by a damage variable denoted by D_1. Using Eq. (9), the Helmholtz free energy density $\rho\psi_1$ is given by

$$\rho\psi_1 = \rho\psi(\epsilon_{22}, \epsilon_{11}, \epsilon_{12}, D_1, f_1, k_1). \tag{14}$$

If the fibers are in both x_1 and x_2-directions, then we assume as a first approximation that the total specific Helmholtz free energy $\rho\psi_{12}$ is given by a law of mixture of the Helmholtz free energy densities in the x_1 and in the x_2-directions

$$\rho\psi_{12} = (1 - f)\rho\psi_1 + f\rho\psi_2 \tag{15}$$

where f is the fraction of fibers in the x_2-direction ($f = f_2/(f_1 + f_2)$, and where f_1 and f_2 are the volume fraction of fibers in the x_1 and x_2-direction, respectively). This assumption also corresponds to a Lin-Taylor Hypothesis. The evolution of the stresses is given by

$$\sigma_{11} = \rho\frac{\partial\psi_{12}}{\partial\epsilon_{11}} = (1 - f)S_{11} + fS_{12}$$

$$\sigma_{22} = \rho\frac{\partial\psi_{12}}{\partial\epsilon_{22}} = (1 - f)S_{21} + fS_{22}$$

$$\sigma_{12} = \frac{1}{2}\rho\frac{\partial\psi_{12}}{\partial\epsilon_{12}} = 2G_{12}\epsilon_{12} \tag{16}$$

where the explicit expression for S_{ij} is given in Appendix A, and the corresponding thermodynamic forces associated to the two *independent* damage variables D_1 and D_2 are

$$Y_1 = \rho\frac{\partial\psi_{12}}{\partial D_1} = (1 - f)\rho\frac{\partial\psi_1}{\partial D_1}$$

$$Y_2 = \rho\frac{\partial\psi_{12}}{\partial D_2} = f\rho\frac{\partial\psi_2}{\partial D_2}. \tag{17}$$

Again, the evolution of the damage variables can either be implicit in terms of the respective normal stresses (model #1)

$$D_1^{(1)} = 1 - \exp\left[-\left\{\frac{\sigma_{11}}{(1 - D_1^{(1)})f_1\sigma_c}\right\}^{m+1}\right] \quad \text{if} \quad \epsilon_{11} > 0 \quad \text{and} \quad \dot{\epsilon}_{11} > 0$$

$$D_2^{(1)} = 1 - \exp\left[-\left\{\frac{\sigma_{22}}{(1 - D_2^{(1)})f_2\sigma_c}\right\}^{m+1}\right] \quad \text{if} \quad \epsilon_{22} > 0 \quad \text{and} \quad \dot{\epsilon}_{22} > 0 \tag{18}$$

or explicit in terms of the respective normal strains (model #2)

$$D_1^{(2)} = 1 - \exp\left[-\left(\frac{\epsilon_{11}}{\epsilon_c}\right)^{m+1}\right] \quad \text{if} \quad \epsilon_{11} > 0 \quad \text{and} \quad \dot{\epsilon}_{11} > 0$$

$$D_2^{(2)} = 1 - \exp\left[-\left(\frac{\epsilon_{22}}{\epsilon_c}\right)^{m+1}\right] \quad \text{if} \quad \epsilon_{22} > 0 \quad \text{and} \quad \dot{\epsilon}_{22} > 0. \tag{19}$$

It is worth noting that we assume that the statistical properties of the fibers are supposed to be identical in both directions. This hypothesis will be maintained throughout the paper since generalization would be straightforward. Both models are studied for shear free states when the strain ratio α (see Eq. (4)), and thus its inverse β are given.

3.1 Failure Criteria for Model #1. For model #1, the evolution of the damage variables is implicit in the sense that $D_1^{(1)}$ (respectively $D_2^{(1)}$) is a function of the normal stress σ_{11} (respectively σ_{22}) *and* the damage variable $D_2^{(1)}$ (respectively $D_2^{(1)}$) itself. The evolution is therefore computed by a numerical scheme based upon a Newton method. To study localization and loss of uniqueness, we need to compute the tangent operator, which takes the following form:

$$H_{1111} = \frac{[(1 - f)F_{11} + fF_{12}](1 + fF_{52}F_{72}) - fF_{22}F_{72}[(1 - f)F_{41} + fF_{42}]}{[1 + fF_{21}F_{72}](1 + fF_{52}F_{72}) - f(1 - f)F_{22}F_{72}F_{51}F_{71}}$$

$$H_{2222} = \frac{[(1 - f)F_{61} + fF_{62}][1 + (1 - f)F_{21}F_{71}] - (1 - f)F_{51}F_{71}[(1 - f)F_{41} + fF_{42}]}{[1 + fF_{21}F_{72}](1 + fF_{52}F_{72}) - f(1 - f)F_{22}F_{72}F_{51}F_{71}}$$

$$H_{1122} = \frac{[(1 - f)F_{41} + fF_{42}](1 + fF_{52}F_{72}) - fF_{22}F_{72}[(1 - f)F_{61} + fF_{62}]}{[1 + fF_{21}F_{72}](1 + fF_{52}F_{72}) - f(1 - f)F_{22}F_{72}F_{51}F_{71}}$$

$$H_{2211} = \frac{[(1 - f)F_{41} + fF_{42}][1 + (1 - f)F_{21}F_{71}] - (1 - f)F_{51}F_{71}[(1 - f)F_{11} + fF_{12}]}{[1 + fF_{21}F_{72}](1 + fF_{52}F_{72}) - f(1 - f)F_{22}F_{72}F_{51}F_{71}}$$

$$H_{1212} = 2G_{12} \tag{20}$$

where the explicit expressions for F_{ij} are given in Appendix B.

The loss of uniqueness and localization are investigated when the fiber fraction f and the strain ratio α vary. Although analytical results cannot be derived from criterion (2) in the general case, some simple results can be found when f is equal to 0 or 1. In these cases, the criteria derived by Hild et al. (1992) apply. If f is equal to 0 (fibers only in the x_1-direction), then localization and loss of uniqueness occur at the same load level when

$$D_1^{(1)} = D_c = 1 - \exp\left(\frac{-1}{m + 1}\right)$$

$$\sigma_{11} = \sigma_{u1} = f_1\sigma_c\left(\frac{1}{(m + 1)e}\right)^{1/(m+1)}$$

$$Y_1 = Y_c = \frac{\sigma_{u1}^2}{2E_1(1 - D_c)^2} \tag{21}$$

where the stress σ_{u1} corresponds to the ultimate tensile strength in the x_1-direction. It is worth noting that the three previous criteria are easier to compute than the general criterion (2). The direction of localization is $\theta = 0$ deg, i.e., a localization surface perpendicular to the fiber direction.

If f is equal to 1, the same kind of result apply and the direction of localization is $\theta = 90$ deg, i.e., a localization surface again perpendicular to the fiber direction. When $f \neq 0$ and $f \neq 1$, these results cannot be proved. However the computations show that loss of uniqueness and localization can be described very accurately by the two following criteria:

Downloaded 04 May 2010 to 171.66.16.33. Redistribution subject to ASME license or copyright; see http://www.asme.org/terms/Terms_Use.cfm

$$\text{Max}(D_1^{(1)}, D_2^{(1)}) = D_c = 1 - \exp\left(\frac{-1}{m+1}\right) \qquad (22)$$

$$\sigma_{11} = \sigma_{u1} \quad \text{or} \quad \sigma_{22} = \sigma_{u2} \qquad (23)$$

when the fiber properties are the same in the two directions. The maximum error is .5 percent in terms of criteria (22) and (23).

Criterion (22) shows that for model #1, maximum damage at localization depends only on the Weibull exponent of the fibers. Furthermore, criterion (23) shows that the maximum normal stress σ_{11} (respectively σ_{22}) depends only on the volume fraction of fibers in the x_1 (respectively x_2-) direction and on the fiber characteristics. This result is consistent with some experimental observations on woven carbon matrix composites reinforced with SiC (Nicalon) fibers (Heredia et al., 1992). On the other hand, the localization angle is dependent on the fiber percentage f (see Fig. 2). When the fiber percentage f and the sign of the strains ϵ_{11} and ϵ_{22} are constant, the variation of the localization angle is due to the fact that the maximum tensile stress is either reached in the x_1 or in the x_2-direction.

Moreover, if the strain ratio α is different from 0 and 1 then there is a complete symmetry of the results. If the strain ratio α is positive, the strains ϵ_{11} and ϵ_{22} are positive, changing α into β, f_2 into f_1, changes f into $1 - f$, and alters the absolute value of the localization angle $|\theta|$ into $\pi/2 - |\theta|$ and keeps the maximum stresses and damage levels constant. These two properties are referred to as *symmetry properties,* and are mainly due to the features of Eqs. (4), (8), (14), and (15).

When the strain ratio α is equal to 1 and the fiber percentage f is equal to .5, the localization angle is undetermined. This is due to the vanishing of the three constants a, b, and c in Eq. (6), for $H_{1111} = H_{1122} = H_{2211} = H_{2222} = 0$. Any value of the angle θ satisfies Eq. (6). This phenomenon can be observed when the fiber percentage f is different from 1: if $\sigma_{11} = \sigma_{u1}$ and $\sigma_{22} = \sigma_{u2}$ simultaneously, then $D_1^{(1)} = D_2^{(1)} = D_c$, and $H_{1111} = H_{1122} = H_{2211} = H_{2222} = 0$. This particular result shows that in terms of this model, for a given strain ratio α, it is possible to optimize locally a CMC reinforced by fibers in two perpendicular directions. Indeed, in terms of fiber breakage, a condition $\sigma_{11} = \sigma_{u1}$ and $\sigma_{22} = \sigma_{u2}$ leads to an optimum of the fiber behavior in both directions.

Model #1 constitutes a straightforward generalization of the fiber bundle models studied by Krajcinovic and Silva (1982), and Hult and Travnicek (1983). Finally, a shear stress has no influence on all the previous results since we assumed no coupling between the damage variables and the shear strain or stress for both model #1 and #2.

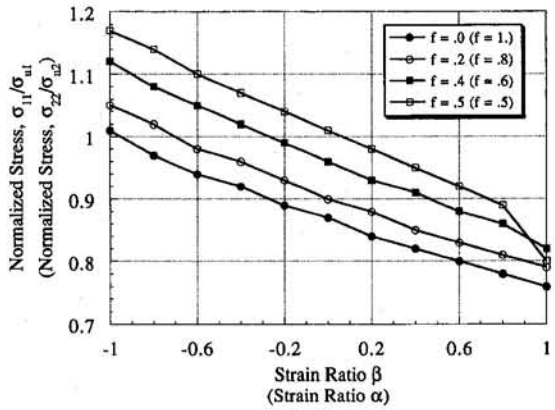


Fig. 3 Normalized maximum stress at localization for model #2, the main caption of the axes corresponds to the case where $f_2 = .5$, $f_1 = .0$, .125, .333, .5, and the captions in brackets correspond to the cases where $f_1 = .5$, $f_2 = .0$, .125, .333, .5

3.2 Study of Localization With Model #2. For model #2, the evolution of the damage variables is explicit and therefore is easier to compute. The tangent operator takes the form

$$H_{1111} = (1 - f)(F_{11} - F_{21}F_{31}) + fF_{12}$$
$$H_{2222} = (1 - f)F_{62} + f(F_{42} - F_{52}F_{32})$$
$$H_{1122} = (1 - f)F_{41} + f(F_{42} - F_{22}F_{32})$$
$$H_{2211} = (1 - f)(F_{41} - F_{21}F_{31}) + fF_{42}$$
$$H_{1212} = 2G_{12} \qquad (24)$$

where the explicit expressions for F_j are given in Appendix B. As shown in the case of fibers in only one direction (Hild et al., 1992), the localization criterion cannot be described by some simple criteria as those given by model #1. When fibers are in both directions the latter results are confirmed. A first consequence is that an optimization procedure can be performed since the maximum stress at localization, and the maximum damage at localization are dependent on both the strain ratio α and on the fiber percentage f.

Since the elastic law given in Eqs. (16) is identical for both models, the symmetry properties apply also for model #2 (see Figs. 3, 4, and 5). It can also be noticed that the maximum stress at localization varies with the fiber fraction f and with the strain ratio α.

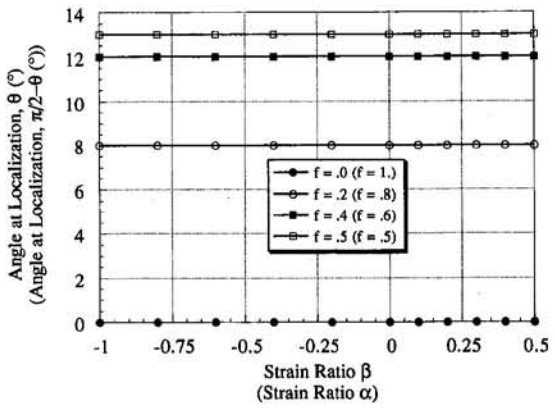


Fig. 2 Absolute value of the localization angle in degrees at localization for model #1, the main caption of the axes corresponds to the case where $f_2 = .5$, $f_1 = .0$, .125, .333, .5, and the captions in brackets correspond to the cases where $f_1 = .5$, $f_2 = .0$, .125, .333, .5

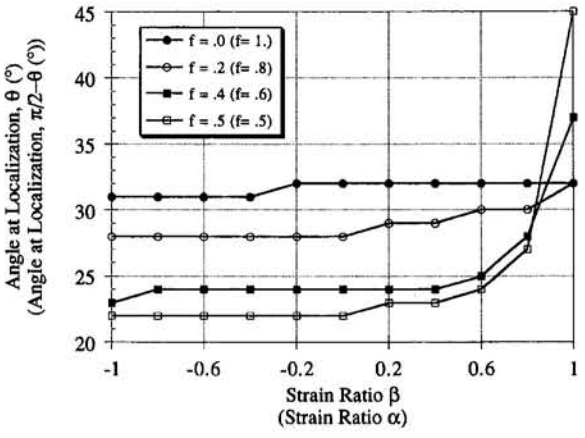


Fig. 4 Absolute value of the localization angle in degrees for model #2, the main caption of the axes corresponds to the case where $f_2 = .5$, $f_1 = .0$, .125, .333, .5, and the captions in brackets correspond to the cases where $f_1 = .5$, $f_2 = .0$, .125, .333, .5

Downloaded 04 May 2010 to 171.66.16.33. Redistribution subject to ASME license or copyright; see http://www.asme.org/terms/Terms_Use.cfm

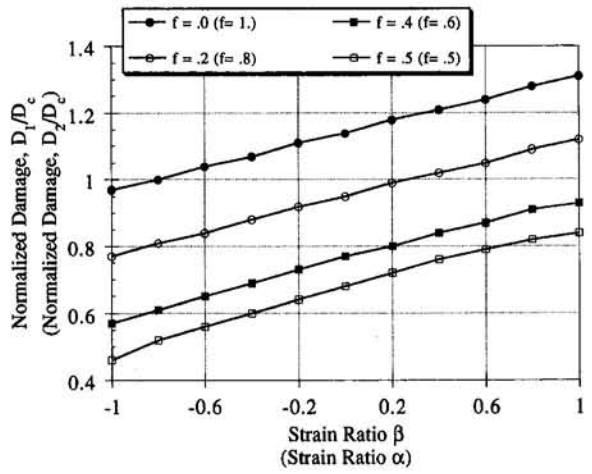


Fig. 5 Maximum normalized damage value at localization (m = 4.) for model #2, the main caption of the axes corresponds to the case where f_2 = .5, f_1 = .0, .125, .333, .5, and the captions in brackets correspond to the cases where f_1 = .5, f_2 = .0, .125, .333, .5

In the experiments reported by Heredia et al. (1992) the stress at localization was given by the ultimate tensile strength corresponding to the volume fraction of fibers in the same direction. This is not found by using model #2. Indeed, in a tensile test, when $f_1 = f_2 = .5$ the maximum stress σ_{22} normalized by the ultimate tensile strength σ_{u2} is given by .63, whereas the same tensile test when $f_1 = .0$ and $f_2 = .5$ would give a normalized tensile strength σ_{22}/σ_{u2} equal to 1. On the other hand, the damage at localization D_2 normalized by the critical damage D_c is equal to 1.04 when $f_1 = .5$ and $f_2 = .5$ and is equal to 1. when $f_1 = .0$ and $f_2 = .5$.

It is too early to draw a final conclusion, but it seems that the predictions of model #1 correspond more to reality than those of model #2. On the other hand, model #2 turned out to give results very close to model #1 when applied to structures with fibers in one direction (Hild et al., 1992). This will be addressed in the case of structures with fibers in two perpendicular directions such as spinning disks.

4 Conclusions

Using a one-dimensional study of fiber breakage modeled by a single damage variable, two models are derived. Both of them are then generalized to a two-dimensional plane stress analysis, with fibers in two perpendicular directions. Whereas model #1 constitutes a straightforward generalization of the elementary study, model #2 exhibits different features. Indeed, loss of uniqueness and localization can be described by some very simple criteria referring to Continuum Damage Mechanics for model #1. Conversely, these simple criteria do not apply for model #2. Physically, model #1 gives a better description of some experimental trends observed in the case of a carbon matrix reinforced with silicon carbide (Nicalon) fibers in two perpendicular directions. On the other hand, model #2 is easier to compute, and when applied to the study of spinning disc with fibers in one direction, it leads to load levels at localization of the same order of magnitude as model #1 (Hild et al., 1992).

Lastly, this study shows that the localization for model #1 can be described by using criterion (23) derived from the general criterion of localization (2). This criterion can also be used for a computation in elasticity and may turn out to be sufficient in first approximation to predict load levels at which a macrocrack initiates, instead of using a computation in elasticity coupled with damage.

5 Acknowledgments

The authors gratefully acknowledge the financial support of the U.S. Air Force through contract AFOSR-90-0132 with the Department of Mechanical and Environmental Engineering, University of California at Santa Barbara, and the DARPA University Research Initiative with the University of California at Santa Barbara (ONR contract N00014-86-K0753).

References

Benallal, A., Billardon, R., and Geymonat, G., 1991a, "Localization Phenomena at the Boundaries and Interfaces of Solids," *3rd Conference on Constitutive Laws for Engineering Materials: Theory and Applications,* C. S. Desai and G. Franlziskonis, eds., Tucson, AZ, Jan.

Benallal, A., Billardon, R., and Lemaitre, J., 1991b, "Continuum Damage Mechanics and Local Approach to Fracture: Numerical Procedures," *Comp. Meth. in Appl. Mech. and Eng.,* Vol. 92, pp. 141–155.

Billardon, R., and Doghri, I., 1989a, "Prévision de l'amorçage d'une macrofissure par la localisation de l'endommagement," *C. R. Acad. Sci. Paris,* Vol. 308, Serie II, pp. 347–352.

Billardon, R., and Doghri, I., 1989b, "Localization Bifurcation Analysis for Damage Softening Elasto-Plastic Materials," *Strain Localization and Size Effect due to Cracking and Damage,* J. Mazars and Z. P. Bazant eds., Elsevier, New York, pp. 295–307.

Borré, G., and Maier, G., 1989, "On Linear versus Nonlinear Flaw Rules in Strain Localization Analysis," *Meccanica,* Vol. 24, 36–41.

Coleman, B. D., 1958, "On the Strength of Classical Fibers and Fiber Bundles," *J. Mech. Phys. Solids,* Vol. 7, pp. 60–70.

Curtin, W. A., 1991, "Theory of Mechanical Properties of Ceramic-Matrix Composites," *J. Am. Ceram. Soc.,* Vol. 74, No. 11, pp. 2837–2845.

Doghri, I., 1989, "Etude de la localisation de l'endommagement," Thèse de l'Université Paris 6, May.

Hadamard, J., 1903, *Leçon sur la propagation des ondes et les équations de l'hydrodynamique,* Librairies scientifiques A, Hermann, Paris.

Heredia, F. E., Spearing, S. M., Evans, A. G., Mosher, P., and Curtin, W. A., 1992, "Mechanical Properties of Carbon Matrix Composites Reinforced with Nicalon Fibers." *J. Am. Ceram. Soc.,* Vol. 75, No. 11, pp. 3017–3025.

Henstenburg, R. B., and Phoenix, S. L., 1989, "Interfacial Shear Strength Studies Using the Single-Filament-Composite Test. Part II: A Probability Model and Monte-Carlo Simulations," *Polym. Comp.,* Vol. 10, No. 5, pp. 389–406.

Hild, F., Larsson, P.-L., and Leckie, F. A., 1992, "Localization Due to Damage in Fiber Reinforced Composites," *Int. J. Solids Struct.,* Vol. 29, No. 4, pp. 3221–3238.

Hild, F., Domergue, J.-M., Evans, A. G., and Leckie, F. A., 1994, "Tensile and Flexural Ultimate Strength of Fiber Reinforced Ceramic-Matrix Composites," *Int. J. Solids Struct.,* Vol. 31, No. 7, pp. 1035–1045.

Hill, R., 1962, "Acceleration Waves in Solids," *J. Mech. Phys. Solids,* Vol. 10, pp. 1–16.

Hult, J., and Travnicek, L., 1983, "Carrying Capacity of Fiber Bundles with Varying Strength and Stiffness," *Journal de Mécanique Théorique et Appliquée,* Vol. 2, No. 2, pp. 643–657.

Krajcinovic, D., and Silva, M. A. G., 1982, "Statistical Aspects of the Continuous Damage Theory," *Int. J. Solids Struct,* Vol. 18, No. 7, pp. 551–562.

Mandel, J., 1962, "Ondes Plastiques dans un Milieu Indéfini à Trois Dimensions," *J. de Mécanique* Vol. 1, No. 1, pp. 3–30.

Ortiz, M., Leroy, Y., and Needelman, A., 1987, "A Finite Element Method for Localized Failure Analysis," *Comput. Meths. Appl. Eng.,* Vol. 61, pp. 189–214.

Rice, J. R., 1976, "The Localization of Plastic Deformations," *Theoretical and Applied Mechanics,* W. T. Koiter, ed., Elsevier, New York, pp. 207–220.

Rice, J. R., and Rudnicki, J. W., 1980, "A Note on Some Features of the Theory of Localization of Deformation," *Int. J. Solids Struct.,* Vol. 16, pp. 597–605.

Rudnicki, J. W., and Rice, J. R., 1975, "Conditions for Localization of Deformation in Pressure-Sensitive Dilatant Materials," *J. Mech. Phys. Solids,* Vol. 23, pp. 371–394.

Weibull, W., 1939, "A Statistical Theory of the Strength of Materials," *Ingeniörsvetenskapakademiens,* Handlingar Nr 151.

Appendix A

$$k_1 = \frac{E_2(f_1)}{E_1}$$

$$k_2 = \frac{E_2(f_2)}{E_1}$$

$$S_{11} = \frac{E_2(f_1)(1 - D_1)}{1 - \nu_{12}^2(1 - D_1)k_1}(\epsilon_{11} + \nu_{12}\epsilon_{22})$$

$$S_{12} = \frac{E_2(f_2)}{k_2[1 - \nu_{12}^2(1 - D_2)k_2]}[\epsilon_{11} + \nu_{12}(1 - D_2)k_2\epsilon_{22}]$$

$$S_{21} = \frac{E_2(f_1)}{k_1[1 - \nu_{12}^2(1 - D_1)k_1]}[\epsilon_{22} + \nu_{12}(1 - D_1)k_1\epsilon_{11}]$$

Downloaded 04 May 2010 to 171.66.16.33. Redistribution subject to ASME license or copyright; see http://www.asme.org/terms/Terms_Use.cfm

$$S_{22} = \frac{E_2(f_2)(1 - D_2)}{1 - \nu_{12}^2(1 - D_2)k_2}(\epsilon_{22} + \nu_{12}\epsilon_{11})$$

Appendix B

$$F_{11} = \frac{E_2(f_1)(1 - D_1)}{1 - \nu_{12}^2(1 - D_1)k_1}$$

$$F_{12} = \frac{E_2(f_2)}{k_2(1 - \nu_{12}^2(1 - D_2)k_2)}$$

$$F_{21} = \frac{E_2(f_1)(\nu_{12}\epsilon_{11} + \epsilon_{22})}{(1 - \nu_{12}^2(1 - D_1)k_1)^2}$$

$$F_{22} = \frac{E_2(f_2)\nu_{12}(\nu_{12}\epsilon_{11} + \epsilon_{22})}{(1 - \nu_{12}^2(1 - D_2)k_2)^2}$$

$$F_{41} = \frac{E_2(f_1)\nu_{12}(1 - D_1)}{1 - \nu_{12}^2(1 - D_1)k_1}$$

$$F_{42} = \frac{E_2(f_2)\nu_{12}(1 - D_2)}{1 - \nu_{12}^2(1 - D_2)k_2}$$

$$F_{51} = \frac{E_2(f_1)\nu_{12}(\nu_{12}\epsilon_{11} + \epsilon_{22})}{(1 - \nu_{12}^2(1 - D_1)k_1)^2}$$

$$F_{52} = \frac{E_2(f_2)(\nu_{12}\epsilon_{11} + \epsilon_{22})}{(1 - \nu_{12}^2(1 - D_2)k_2)^2}$$

$$F_{61} = \frac{E_2(f_1)}{k_1(1 - \nu_{12}^2(1 - D_1)k_1)}$$

$$F_{62} = \frac{E_2(f_2)(1 - D_2)}{1 - \nu_{12}^2(1 - D_2)k_2}$$

$$F_{31} = \frac{m + 1}{\epsilon_c}\left(\frac{\epsilon_{11}}{\epsilon_c}\right)^m \exp\left[-\left(\frac{\epsilon_{11}}{\epsilon_c}\right)^{m+1}\right]$$

$$F_{32} = \frac{m + 1}{\epsilon_c}\left(\frac{\epsilon_{22}}{\epsilon_c}\right)^m \exp\left[-\left(\frac{\epsilon_{22}}{\epsilon_c}\right)^{m+1}\right]$$

$$F_{71} = \frac{\frac{m + 1}{f_1\sigma_c}\left[\frac{\sigma_{11}}{(1 - D_1)f_1\sigma_c}\right]^m}{1 - (m + 1)\left[\frac{\sigma_{11}}{(1 - D_1)f_1\sigma_c}\right]^{m+1}}$$

$$F_{72} = \frac{\frac{m + 1}{f_2\sigma_c}\left[\frac{\sigma_{22}}{(1 - D_2)f_2\sigma_c}\right]^m}{1 - (m + 1)\left[\frac{\sigma_{22}}{(1 - D_2)f_2\sigma_c}\right]^{m+1}}$$

Downloaded 04 May 2010 to 171.66.16.33. Redistribution subject to ASME license or copyright; see http://www.asme.org/terms/Terms_Use.cfm

A Method to Determine the Plane-Strain Yield Locus for Ductile Crystals

R. R. Nikolic
Assistant Professor,
Faculty of Mechanical Engineering,
University of Kragujevac,
Sestre Janjica 6
Yu-34000, Kragujevac, Yugoslavia

This paper presents a new method for determining the plane-strain yield surfaces based on the application of the lower bound limit theorem of the theory of plasticity. The method is very simple and by use of linear programming optimization routine the points of the yield surface in the stress space are generated automatically.

1. Introduction

When a single crystal is loaded so that it undergoes an arbitrary strain, the problem arises of finding the active slip systems. Assuming that slip is governed by Schmid's law, the active slip systems will be those for which the maximum resolved shear stress is the largest. For the case of a simple tension test of a single crystal, this is the same as to say that the active systems will be those for which the value $M = \sigma/\tau$ is minimum. Here M is the inverse of the Schmid's factor, σ is the tensile stress, and τ is the resolved shear stress. Taylor (1938) had analyzed the deformation of an f.c.c. crystal. Based on the principle of virtual work and assuming that the critical resolved shear stress is equal for all possible slip systems Taylor (1938) concluded that "out of 12 possible slip systems the one is operative for which the absolute value of glide shear is minimum." If the deformation imposed is such that more than one slip system needs to be activated to accommodate it, then that particular combination of slip systems will be activated for which the sum of absolute values of glide shears is minimum. In the case of general deformation, the largest number of necessary slip systems to accommodate deformation is 5. Bishop and Hill (1951) showed that this hypothesis of least shear of Taylor is equivalent to a maximum work principle. They did not calculate the yield surface in detail, but they concluded that it has to be a cylindrical surface in the stress space, since the hydrostatic part of stress has no influence on yielding. They also defined the lower and upper limit of the yield surface, i.e., two cylindrical surfaces between which the actual yield surface has to lie. The limits are defined based on the application of maximum work and minimum shear principles. Chin and Mammel (1967) later provided computer solutions for Taylor analysis for both f.c.c. and b.c.c. crystals, for the case of axisymmetric flow. They obtained the contours of constant minimum M for different orientations of single crystal that lie within the standard stereographic triangle. Kocks and Chandra (1982) calculated the yield surfaces for two special cases of boundary conditions that deviate from the ideal plane-strain conditions, i.e., for deformation of metal in channel die and sheet rolling. Tome and Kocks (1985) calculated the yield surfaces of h.c.p. crystals, based on Schmid's law and the maximum work principle.

Contributed by the Applied Mechanics Division of THE AMERICAN SOCIETY OF MECHANICAL ENGINEERS for publication in the ASME JOURNAL OF APPLIED MECHANICS.

Discussion on this paper should be addressed to the Technical Editor, Professor Lewis T. Wheeler, Department of Mechanical Engineering, University of Houston, Houston, TX 77204-4792, and will be accepted until four months after final publication of the paper itself in the ASME JOURNAL OF APPLIED MECHANICS.

Manuscript received by the ASME Applied Mechanics Division, June 9, 1992; final revision, Aug. 10, 1994. Associate Technical Editor: R. M. McMeeking.

2. The Method for Determining the Plane-Strain Yield Surfaces

The method for determining the plane-strain yield surfaces presented here is based on application of the lower bound limit theorem of the theory of plasticity. Consider an element of material loaded by pure shear stress σ'_{12} and constrained to deform in plane strain, Fig. 1. Assume that symmetry is such that only a single reaction stress σ_{33} can develop (i.e., no antiplane stress of type σ_{31} or σ_{32} is induced). From the lower bound theorem of limit analysis, since an appropriate solution of the equilibrium equation is provided by any homogeneous stress state $\sigma'_{12}, \sigma_{33}$, the value of σ'_{12} at yield is the largest possible value consistent with the yield condition

$$|\tau| = |n_i \sigma_{ij} s_j| \leq \tau_{\text{yield}} \tag{1}$$

for each slip system. Here the notation is such that $n = \{n_1, n_2, n_3\}$ denotes the slip plane normal and $s = \{s_1, s_2, s_3\}$ the slip plane direction for the kth slip system, and σ denotes the applied stress.

Stress σ'_{12} corresponds to

$$\frac{\sigma_{22} - \sigma_{11}}{2} + i\sigma_{12} = ie^{-2i\theta}\sigma'_{12} \tag{2}$$

with $(\sigma_{22} + \sigma_{11})/2 = 0$. From that we get

$$\sigma_{12} = \sigma'_{12} \cos 2\theta \tag{3}$$

$$\sigma_{22} = -\sigma_{11} = \sigma'_{12} \sin 2\theta. \tag{4}$$

Developing (1) and comparing with (3) and (4) we get

$$\begin{aligned}\tau &\equiv n_1 s_1 \sigma_{11} + (n_1 s_2 + n_2 s_1)\sigma_{12} + n_2 s_2 \sigma_{22} + n_3 s_3 \sigma_{33} \\ &\equiv n_1 s_1 (-\sigma'_{12} \sin 2\theta) + (n_1 s_2 + n_2 s_1)\sigma'_{12} \cos 2\theta \\ &\quad + n_2 s_2 \sigma'_{12} \sin 2\theta + n_3 s_3 \sigma_{33} \\ &\equiv [(n_1 s_2 + n_2 s_1) \cos 2\theta\end{aligned}$$

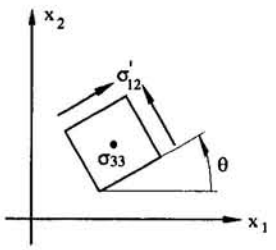


Fig. 1 Sketch of element of material loaded in pure shear

Copyright © 1996 by ASME

Downloaded 04 May 2010 to 171.66.16.33. Redistribution subject to ASME license or copyright; see http://www.asme.org/terms/Terms_Use.cfm

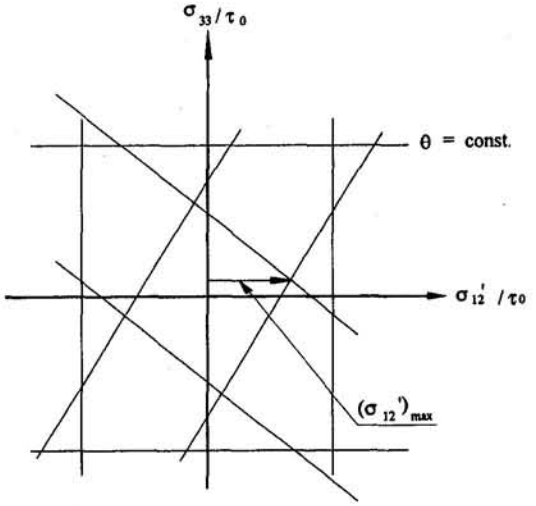


Fig. 2 Set of lines corresponding to slip systems needed for determination of the maximum value of σ'_{12} that does not violate yield

$$+ (n_2s_2 - n_1s_1) \sin 2\theta]\sigma'_{12} + n_3s_3\sigma_{33}$$

$$\equiv \alpha^k(\theta)\sigma'_{12} + \beta^k\sigma_{33} \tag{5}$$

where

$$\alpha^k = (n_1s_2 + n_2s_1) \cos 2\theta + (n_2s_2 - n_1s_1) \sin 2\theta \tag{6}$$

$$\beta^k = n_3s_3. \tag{7}$$

3. Yield Surfaces Calculations

The procedure for obtaining the yield surface is the following. For any fixed angle θ we evaluate the coefficients $\alpha^k(\theta)$ and β^k for each slip system. Then we draw the set of lines corresponding to the equation (see Fig. 2),

$$1 = \alpha^k(\theta)\left(\frac{\sigma'_{12}}{\tau_0}\right) + \beta^k\left(\frac{\sigma_{33}}{\tau_0}\right) \tag{8}$$

where τ_0 is the yield stress. From this diagram we then measure the maximum value of σ'_{12}/τ_0 not violating yield. The finding of the maximum value of σ'_{12}/τ_0 has been done by use of linear programming routine, LP88, Version 7.03 (an IMSL routine). The next step is to plot the point whose coordinates are σ'_{12} and 2θ on the yield surface, 2θ being measured from the σ'_{12}/τ_0 axis, see Fig. 3. Then the whole procedure is repeated for the next value of θ. The increment used in these calculations was 5 in the range for θ of 0 to 90 deg, which gives the points for constructing the left hand side of the yield surface, and then by symmetry the whole yield surface can be constructed. For the procedure described a computer program was written that, as input data, uses the Miller indices of the coordinate system x_1, x_2, x_3, expressed in the unit cube reference frame. The second part of the input file contains the data about the slip planes normals and the slip vectors directions, again expressed in the x, y, z, coordinate system. The output of the program are the coefficients $\alpha^k(\theta)$ and β^k. These are then used as input data for the linear programming routine that maximizes the value of σ'_{12}/τ_0. The yield surfaces constructed based on these calculations are given in Figs. 4 to 7 for the orientations shown in Table 1. The upper figures, (a), show the yield surfaces with the coordinates of the intersecting points on the coordinate axes in the $(\sigma_{11} - \sigma_{22})/2\tau_0$, σ_{12}/τ_0 space, (τ_0 is the critical resolved shear stress for yielding), and the lower figures, (b), show the slip systems that can be activated along each flat segment of the yield surface. At a stress state corresponding to a vertex we expect that slip systems corresponding to both adjacent flat segments can be activated. The 24 slip systems of the f.c.c. crystals of type $\{111\}\langle 1\bar{1}0\rangle$, and the 24 slip systems of type $\{101\}\langle 11\bar{1}\rangle$ and the 48 slip systems of type $\{121\}\langle 1\bar{1}1\rangle$ of the b.c.c. crystals were searched in this optimization procedure.

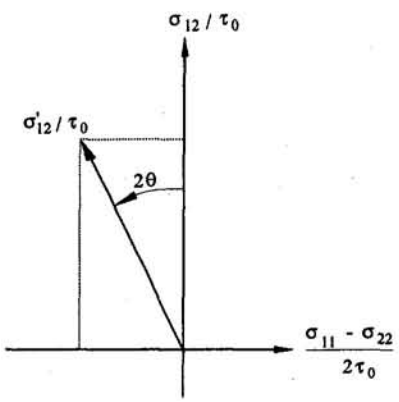
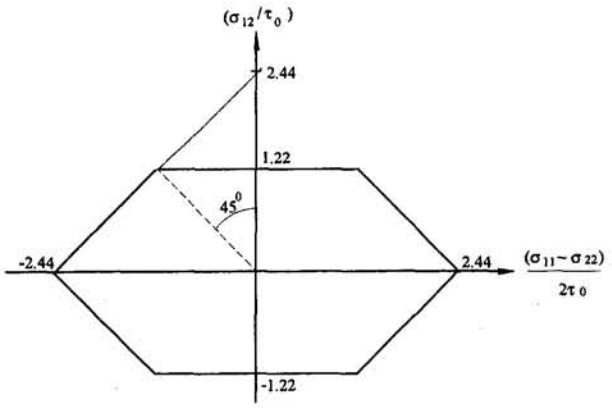


Fig. 3 Construction of the yield surface



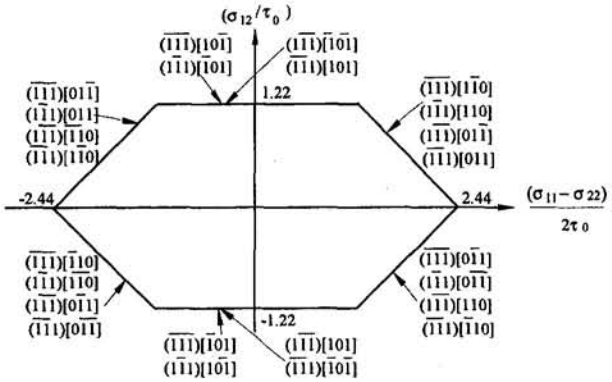


Fig. 4 Plane-strain yield surface for the FCC crystal for orientations: $x_1 \equiv [\bar{1}01]$, $x_2 \equiv [101]$, $x_3 \equiv [010]$ and $x_1 \equiv [010]$, $x_2 \equiv [101]$, $x_3 \equiv [10\bar{1}]$

4. Discussion of Results

Figure 4 shows the yield surface for two orientations of the f.c.c. crystals, i.e., $x_1 \equiv [\bar{1}01]$, $x_2 \equiv [101]$, $x_3 \equiv [010]$ and $x_1 \equiv [010]$, $x_2 \equiv [101]$, $x_3 \equiv [10\bar{1}]$. Slip systems that are active along a flat segment of the yield surface in the second orientation are "switched" from the left-hand side segments to the

Downloaded 04 May 2010 to 171.66.16.33. Redistribution subject to ASME license or copyright; see http://www.asme.org/terms/Terms_Use.cfm

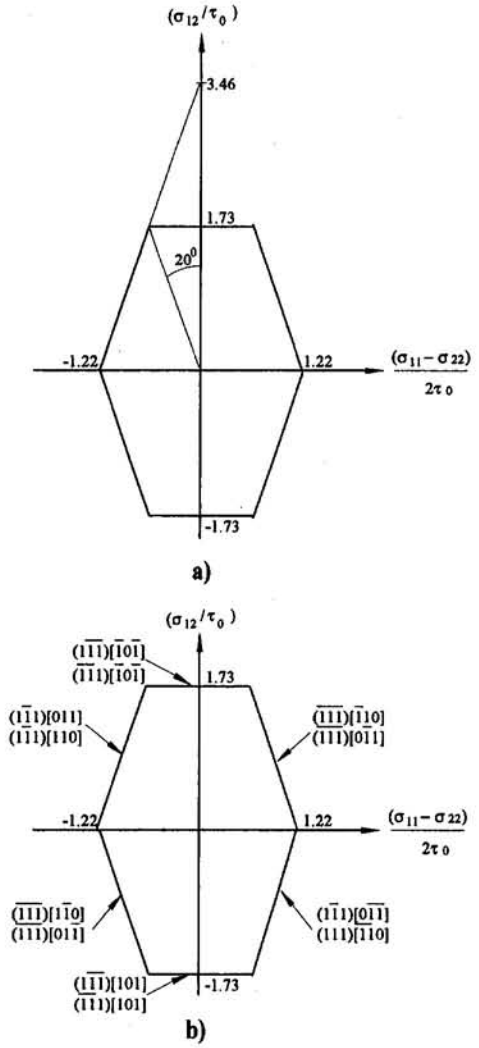


Fig. 5 Plane-strain yield surface for the FCC crystal for the orientation: $x_1 \equiv [101]$, $x_2 \equiv [010]$, $x_3 \equiv [\bar{1}01]$

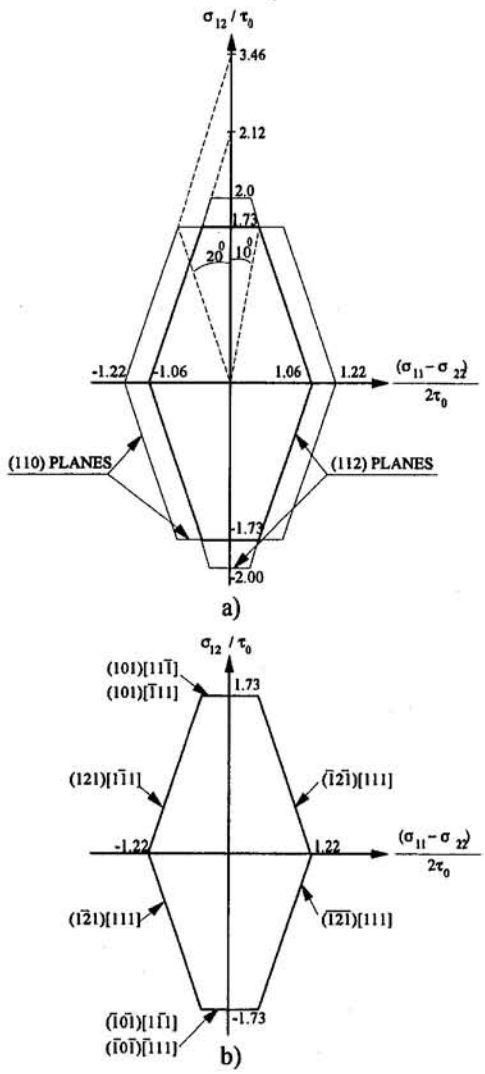


Fig. 6 Plane-strain yield surface for the BCC crystal for orientations: $x_1 \equiv [101]$, $x_2 \equiv [0\bar{1}0]$, $x_3 \equiv [10\bar{1}]$, and $x_1 \equiv [010]$, $x_2 \equiv [101]$, $x_3 \equiv [10\bar{1}]$

right-hand side segments and from the upper horizontal segment to the lower horizontal segment with respect to the first orientation. Another case of the f.c.c. crystals orientation, whose yield surface is not shown here, $x_1 \equiv [010]$, $x_2 \equiv [100]$, $x_3 \equiv [00\bar{1}]$, is actually a rotated version of case a) shown in Table 1. The hexagon that represents the yield surface is identical to that of Fig. 4, only rotated for 90 deg.

In Fig. 6 is shown the yield surface obtained for the two orientation of the b.c.c. crystals, i.e., $x_1 \equiv [101]$, $x_2 \equiv [0\bar{1}0]$, $x_3 \equiv [10\bar{1}]$ and $x_1 \equiv [010]$, $x_2 \equiv [101]$, $x_3 \equiv [10\bar{1}]$. Slip systems that are active along a flat segment of the yield surface in the second orientation are "moved" to the flat segments rotated by 180 deg with respect to the same segments in the first orientation. This yield surface is interesting because both families of the slip systems, $\{101\}\langle 11\bar{1}\rangle$ and $\{121\}\langle 1\bar{1}1\rangle$ are activated simultaneously (Fig. 6(a)). Final form of the yield surface, Fig. 6(b), consists of six flat segments, the horizontal ones corresponding to the $\{101\}$ planes, and others to the $\{121\}$ planes. On the other hand, for the second case of orientation of the b.c.c. crystals, $x_1 \equiv [112]$, $x_2 \equiv [\bar{1}10]$, $x_3 \equiv [111]$, the yield surface shown in Fig. 7 is a regular hexagon. The flat segments correspond only to the $\{101\}$ planes, since the yield stress needed for activation of the $\{121\}$ planes is larger. For another orientation of the b.c.c. crystal, $x_1 \equiv [010]$, $x_2 \equiv [100]$, $x_3 \equiv [00\bar{1}]$, whose yield surface is not shown, again both types of slip systems are activated simultaneously. The yield surface is a polygon with 12 flat segments which correspond alternatively to one or the other family of slip systems.

5. Conclusion

This work presents a new method for determining the plane-strain yield surfaces which is a very simple one. The method is based on the application of the lower bound limit theorem of the theory of plasticity, and by use of a linear programming optimization routine, points of the yield surface as a curve in the stress space are generated automatically. The appropriate computer program was written that as input data uses the Miller indices of the coordinate system x_1, x_2, x_3, expressed in the unit cube reference frame, and as output it gives directly the yield surface points coordinates in the $(\sigma_{11} - \sigma_{22})/2\tau_0, \sigma_{12}/\tau_0$ space. These data are then used for drawing the yield surface.

The application of this method enables us to obtain the plane strain yield surfaces very easily. One of the applications, where the analysis of yield surfaces is a very important part of understanding the problem, is the analysis of the deformation and stress fields around the crack tip in ductile single crystals. The yield surfaces are different for different orientations of the crack plane and crack front in the crystal and so are the stress and deformation fields. For complete understanding of the influence of different orientations on stress and deformation fields many possible cases ought to be analyzed and that demands drawing

Downloaded 04 May 2010 to 171.66.16.33. Redistribution subject to ASME license or copyright; see http://www.asme.org/terms/Terms_Use.cfm

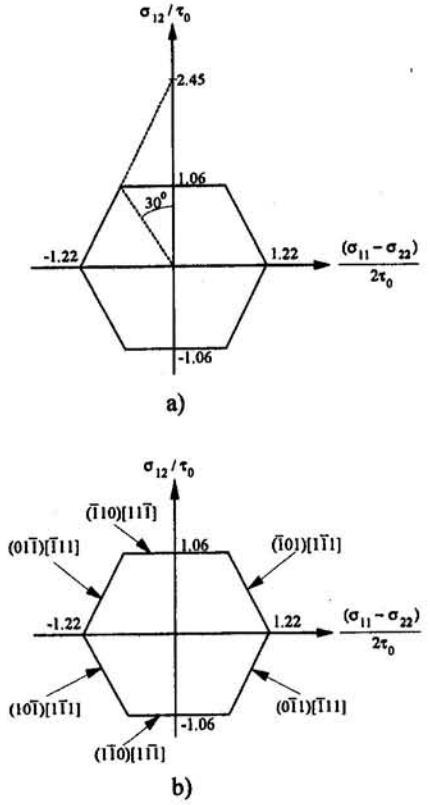


Fig. 7 Plane-strain yield surface for the BCC crystal for the orientation: $x_1 = [112]$, $x_2 = [\bar{1}10]$, $x_3 = [111]$

of many different yield surfaces. Thus having a method for easy determination of yield surfaces is very important. This is one example where the application of this method is very useful, but there are also others.

Acknowledgment

This work was done while the author was a Ph.D. student at Harvard University, Cambridge, MA, and was partially financially supported by the U.S. National Science Foundation Materials Research Laboratory at Harvard and by the Mechanics Division of the Office of Naval Research. I wish to express my deepest gratitude to my advisor, Prof. James R. Rice, for his support and help, and for his useful suggestions and advice concerning this work.

Table 1 Sketches of the orientations analyzed: (a), (b) FCC crystals; (c), (d) BCC crystals

	a)	b)
x_1 axis	$[\bar{1}01]$	[101]
x_2 axis	[101]	[010]
x_3 axis	[010]	$[\bar{1}01]$
	c)	d)
x_1 axis	[101]	$[11\bar{2}]$
x_2 axis	$[0\bar{1}0]$	$[\bar{1}10]$
x_3 axis	$[10\bar{1}]$	[111]

References

Bishop, J. F. W., and Hill, R., 1951, "A Theory of the Plastic Distortion of a Polycrystalline Aggregate under Combined Stresses," *The Philosophical Magazine,* Vol. 42, pp. 414–427.

Chin, G. Y., and Mammel, W. L., 1967, "Computer Solution of the Taylor Analysis for Axisymmetric Flow," *Transactions of the AIME,* Vol. 239, pp. 1400–1405.

Kocks, U. F., and Chandra, H., 1982, "Slip Geometry in Partially Constrained Deformation," *Acta Metallurgica,* Vol. 30, pp. 695–709.

Taylor, G. I., 1938, "Analysis of Plastic Strain in Cubic Crystal," *Stephen Timoshenko 60th Anniversary Volume,* McMillan, New York, pp. 218–233.

Tome, C., and Kocks, U. F., 1985, "The Yield Surface of the H.C.P. Crystals," *Acta Metallurgica,* Vol. 33, pp. 603–621.

Downloaded 04 May 2010 to 171.66.16.33. Redistribution subject to ASME license or copyright; see http://www.asme.org/terms/Terms_Use.cfm

N. Chien
Postdoctoral Scholar.

G. Herrmann
Professor of Applied Mechanics, Emeritus, Honorary Mem. ASME.

Division of Applied Mechanics, Stanford University, Stanford, CA 94305-4040

Conservation Laws for Thermo or Poroelasticity

It is the purpose of the present paper to establish conservation laws for time-independent and time-dependent thermoelasticity in two dimensions via the NA method. Due to the analogy between the mechanics of a thermoelastic and a poroelastic medium, the results obtained can be applied to studies of poroelasticity. The conservation laws derived here should prove useful in studies of fracture and defects in a linear elastic body under the influence of nonuniform temperature fields and in a porous elastic solid whose pores are filled with a compressible viscous fluid. In particular, a path-independent integral was derived which represents the energy release rate accompanying crack growth.

1 Introduction

In this paper, the conservation laws of interest are relations expressible in a divergence-free form. Mathematically, a conservation law of a physical system with four independent variables x, y, z, and t, for example, is an equation of the form

$$\text{Div } \mathbf{P} = D_x P^x + D_y P^y + D_z P^z + D_t P^t = 0, \qquad (1)$$

where $\mathbf{P} = (P^x, P^y, P^z, P^t)$ is a vector function that can depend on the independent variables, the dependent variables and derivatives of the dependent variables of the system; and D_x, D_y, D_z, D_t are operators indicating total differentiation with respect to x, y, z, and t, respectively. Physically, a conservation law states that the rate of change of P^t inside any domain is equal to the net flux of the "currents" (P^x, P^y, P^z) through the surface of the domain. In the special case of systems with only one independent variable, conservation laws will lead to quantities which are constant.

The importance of conservation laws is widely recognized in many fields of physics and mechanics. Conserved quantities such as mass, energy, momentum, and angular momentum are fundamental in classical mechanics and they provide insights into the behavior of various systems, from dynamics of rigid bodies to continuum mechanics. In continuum mechanics, conservation laws represented as path-independent integrals ($\mathbf{J}$, $\mathbf{L}$, and M) have captured the interests of many researchers such as Eshelby (1956), Fletcher (1976), Günther (1962), Gurtin (1979), and Knowles and Sternberg (1972), and these integrals contribute significantly to the study of fracture and defects.

Classically, conservation laws are obtainable through Noether's first theorem (1918) and through its extension by Bessel-Hagen (1921). These methodologies are based on variational principles, and can be applied only to Lagrangian systems with Lagrangian functionals whose variations would yield the Euler-Lagrange equations governing the systems. As systems with damping and various other dissipative mechanisms do not possess Lagrangian functionals explicitly, to obtain conserved quantities for these systems via Noether's approach, one must solve the inverse problem in calculus of variations. That is, one must seek a Lagrangian functional whose variations will lead to the governing equations for the dissipative system of interest. Since solving the inverse problem is often a difficult, if not impossible task, an alternate procedure for constructing conservation laws which is applicable to nondissipative as well as to dissipative systems was established by Honein et al. (1991). Given any system governed by a set of differential equations, this procedure, termed the "Neutral Action (NA)" method in (Chien 1992), allows one to systematically construct divergence-free quantities applicable to the system considered.

It is the purpose of this contribution to formally derive conservation laws valid for time-independent and time-dependent thermoelasticity in two dimensions using the NA method. We also attempt to provide physical interpretations of the results obtained. By identifying familiar quantities appearing in the conservation laws (such as elastic energy, strain rate, heat absorbed, etc.), and by observing the parallel in form of the conservation laws with well-known results (such as the $\mathbf{J}$-integrals), we can interpret most of the balance laws presented here in physical terms.

Some of the results obtained here, however, bear no resemblances to known concepts or form. It is therefore difficult to provide meaning to these conservation laws. At most, these balance laws can offer insight into the existence of other fundamental quantities of the system; and at least, these laws, lacking a physical interpretation, can still be valulable in their potential use in numerical analysis.

It was shown by M. A. Biot (1956) that the equations governing thermoelasticity and mechanics of a porous medium are identical in form. Therefore, all the results derived here can also be applied to the mechanics of a porous medium.

The conservation laws presented here are not exhaustive, but as a limited set, they serve as examples to demonstrate the power and efficiency of the NA method. These laws should prove useful in the analysis of defects and fracture in linear elastic bodies under the influence of nonuniform temperature fields and in elastic porous solids whose pores are filled with a compressible viscous fluid.

It is also worth noting that the conservation laws derived here differ substantially from those obtained by Francfort and Golebiewska Herrmann (1982) on the same subject. The results presented here are local conservation laws which depend on a point in space (x, y) and time (t). By contrast, the conservation laws obtained by Francfort and Golebiewska Herrmann (1982) are nonlocal in time; i.e., their results depend on a time interval rather than on an instant of time.

Other contributors on conservation laws for thermoelasticity include Ainsworth et al. (1978), Eischen and Herrmann (1987), Gurtin (1979), Herrmann (1980), Kishimoto et al. (1980), Kuo et al. (1987), Wilson and Yu (1979), Xu Li (1991), and Yeh et al. (1993). The results presented by Herrmann (1980) are generalizations of the Eshelby's tensor for

Contributed by the Applied Mechanics Division of THE AMERICAN SOCIETY OF MECHANICAL ENGINEERS for publication in the ASME JOURNAL OF APPLIED MECHANICS.

Discussion on this paper should be addressed to the Technical Editor, Professor Lewis T. Wheeler, Department of Mechanical Engineering, University of Houston, Houston, TX 77204-4792, and will be accepted until four months after final publication of the paper itself in the ASME JOURNAL OF APPLIED MECHANICS.

Manuscript received by the ASME Applied Mechanics Division, June 21, 1993; final revision, Nov. 10, 1993. Associate Technical Editor: F. Y. M. Chen.

Copyright © 1996 by ASME

Downloaded 04 May 2010 to 171.66.16.33. Redistribution subject to ASME license or copyright; see http://www.asme.org/terms/Terms_Use.cfm

thermoelasticity. However, as pointed out by Francfort and A. G. Herrmann (1982), great difficulties arise in handling the time dependence in this contribution. The balance laws presented for thermoelasticity by Eischen and Herrmann (1987) are also different from our contribution in that they are applicable only to systems of uncoupled thermoelasticity with free thermal expansion. By introducing a conjugate temperature field, Kuo et al. (1987) and Yeh et al. (1993) also obtained conservation laws for thermoelasticity. The different J-integrals obtained for thermoelasticity by Ainsworth et al. (1978), Kishimoto et al. (1980), Wilson and Yu (1979), and Xu Li (1991) consist of a surface integral and a volume integral. Due to the presence of volume integrals, these results cannot be expressed in a divergence-free form, and thus are not within the class of conservation laws under investigation here. In our list of references, except those of Kuo et al. (1987) and Yeh et al. (1993) which require an additional solution for the conjugate temperature field, only the J-integral presented by Gurtin (1979) fits into our definition of a conservation law, and this result will be reproduced here as a special case of our derivations.

2 The Neutral Action (NA) Method

Given a system with m independent variables x^i ($i = 1, 2, \ldots, m$) and n dependent variables u^k ($k = 1, 2, \ldots, n$), the governing set of q differential equations can be represented by

$$\Delta^\alpha(x^i, u^k, u^k_J) = 0, \quad \alpha = (1, 2, \ldots, q). \tag{2}$$

Using the multi-index notation introduced by Olver (1986), u^k_J in (2) represents all possible pth order partial derivatives of u^k,

$$u^k_J \equiv \frac{\partial^p u^k}{\partial x^{j_1} \partial x^{j_2} \ldots \partial x^{j_p}},$$

with $J = (j_1, j_2, \ldots, j_p)$ as an unordered p-tuple of integers, $1 \le j_\alpha \le m$ indicating which derivatives are being taken, and $\#J = p$ indicating how many derivatives are being taken.

For any system governed by a set of differential equations as in (2), the "Neutral Action (NA)" method proposed by Honein et al. (1991) states that it is possible to construct conservation laws valid for the system in the form of

$$f^\alpha \Delta^\alpha = D_i P^i = 0, \tag{3}$$

if

$$E^k(f^\alpha \Delta^\alpha) \equiv 0, \tag{4}$$

for all dependent variables u^k. Here, $f^\alpha = f^\alpha(x^i, u^k, u^k_J)$ are called the characteristics of conservation laws, $P^i = P^i(x^i, u^k, u^k_J)$ are the currents of the conservation law $D_i P^i = 0$, and E^k is the Euler operator defined as

$$E^k(L) = (-D)_J \frac{\partial L}{\partial u^k_J}, \quad 0 \le \#J \le p, \tag{5}$$

$$(-D)_J = (-1)^{\#J} D_J, \tag{6}$$

with

$$D_J \equiv D_{j_1} D_{j_2} \ldots D_{j_p}$$

representing all possible p^{th} order total derivatives.

Since our objective is to construct some divergence-free expressions from $f^\alpha \Delta^\alpha$, and since the Euler operator E^k acting on any total divergence always yields a null result by calculus of variations, it follows that (4) is a requirement for the existence of conservation laws. Equation (4) also implies that $f^\alpha \Delta^\alpha$ is a null Lagrangian functional whose action integral,

$$A = \int_\Omega f^\alpha \Delta^\alpha dV, \tag{7}$$

has vanishing variation for any dependent variable u^k, i.e., $\delta A = 0$. In other words, in order to construct conservation laws for any system (dissipative or Lagrangian) governed by a set of differential equations, $\Delta^\alpha = 0$, by the NA method, we try to construct a product of $f^\alpha \Delta^\alpha$ whose action integral does not change variationally. Hence the name "Neutral Action" method given to this procedure.

In practice, given any set of differential equations, $\Delta^\alpha = 0$, one must first decide on the arguments of the characteristics f^α, which may be functions of the independent variables, the dependent variables and all derivatives of the dependent variables. Subsequently, one would use (4) to solve for these characteristics. Having solved for f^α, one can then proceed to construct the conserved currents P^i valid for the system governed by this set of differential equations from the product $f^\alpha \Delta^\alpha$.

As noted in Honein et al. (1991), the tools necessary to establish the NA method are well known. They can be found, for example, in (Olver 1986). However, to the authors' knowledge, these tools have not been presented for systematical determination of conservation laws for dissipative systems.

3 Thermoelasticity

Using a linearized theory and assuming a source-free temperature field, the equation of equilibrium for thermoelasticity is given as

$$\mu u^i_{kk} + (\lambda + \mu) e_i - \beta \theta_i = 0, \tag{8}$$

and the equation for heat conduction as

$$k\theta_{kk} - c\theta_t - T\beta e_t = 0. \tag{9}$$

These equations are the governing equations for thermoelasticity (Biot, 1956) and they describe the time history of the deformation and thermal fields of the system. Here, i and k are indices ranging over the spatial variables (x and y for a 2-D problem), t is the time coordinate, subscripts indicate partial differentiation, and repeated indices imply summation.

In the above equations, u^x, $u^y = u(x, y, t)$, $v(x, y, t)$ are displacements in the x and y direction, $\theta = \theta(x, y, t)$ represents an increment of temperature from a reference state T, $e = u^i_i$ is the dilatation, λ and μ are the Lamè constants, β is defined as $\beta = (\lambda + (2\mu/3))\alpha_t$ with α_t being the coefficient of thermal expansion, k is the coefficient of heat conduction, and c is the specific heat per unit volume.

The stress components of the system are given as

$$\sigma^{xx} = 2\mu u_x + \lambda e - \beta\theta,$$
$$\sigma^{yy} = 2\mu v_y + \lambda e - \beta\theta,$$
$$\sigma^{xy} = \mu(u_y + v_x), \tag{10}$$

and the heat absorbed per unit volume as

$$h = c\theta + T\beta e. \tag{11}$$

3.1 Time-Independent Thermoelasticity. The governing equations for a two-dimensional elastic body under the influence of a time-independent temperature field are given by (8) and (9) as

$$\Delta^1: \quad (\lambda + 2\mu)u_{xx} + \mu u_{yy} + (\lambda + \mu)v_{xy} - \beta\theta_x = 0, \tag{12}$$

$$\Delta^2: \quad (\lambda + 2\mu)v_{yy} + \mu v_{xx} + (\lambda + \mu)u_{xy} - \beta\theta_y = 0, \tag{13}$$

$$\Delta^3: \quad \theta_{xx} + \theta_{yy} = 0. \tag{14}$$

To construct conservation laws for this system by the NA method, we require that

Downloaded 04 May 2010 to 171.66.16.33. Redistribution subject to ASME license or copyright; see http://www.asme.org/terms/Terms_Use.cfm

$$E^k(f^1\Delta^1 + f^2\Delta^2 + f^3\Delta^3) \equiv 0. \quad (15)$$

Assuming the characteristics f^α's to be linear functions of u, u_x, u_y, v, v_x, v_y θ, θ_x, and θ_y, the solution to the above equation is found to be

$$f^1 = A_0\left[(\lambda+3\mu)u_x + (\lambda+2\mu)v_y - \beta\frac{\lambda+2\mu}{\lambda+\mu}\theta\right] + A_1\mu v_x + A_2[(\lambda+3\mu)u_y - \mu v_x] + A_3\left[-(\lambda+2\mu)v_y - \frac{\beta\mu}{\lambda+\mu}\theta\right] + A_4\theta_x - A_5\theta_y,$$

$$f^2 = A_0\mu u_y + A_1\left[(\lambda+3\mu)v_y + (\lambda+2\mu)u_x - \beta\frac{\lambda+2\mu}{\lambda+\mu}\theta\right] + A_2\left[-(\lambda+2\mu)u_x - \frac{\beta\mu}{\lambda+\mu}\theta\right] + A_3[(\lambda+3\mu)v_x - \mu u_y] + A_4\theta_y + A_5\theta_x,$$

$$f^3 = A_0\frac{\beta\mu^2}{\lambda+\mu}u + A_1\frac{\beta\mu^2}{\lambda+\mu}v + A_2\beta\mu\frac{\lambda+2\mu}{\lambda+\mu}v + A_3\beta\mu\frac{\lambda+2\mu}{\lambda+\mu}u + A_4[(\lambda+2\mu)(u_x+v_y) - \beta\theta] + A_5(\mu v_x - \mu u_y) + A_6\theta_x + A_7\theta_y, \quad (16)$$

where all A_i's are arbitrary constants.

The corresponding conservation laws, $D_xP^x + D_yP^y = 0$, constructed out of the product $f^\alpha\Delta^\alpha$ are as follows.

For only $A_0 \neq 0$,

$$P^x = (\lambda+3\mu)\left[u_x\sigma^{xx} - \frac{\lambda+2\mu}{2}u_x^2 - \lambda u_xv_y - \frac{\mu}{2}u_y^2\right] + (\lambda+2\mu)\left[v_y\sigma^{xx} + \frac{1}{2}(\mu-\lambda)v_y^2\right] + \mu\left[u_y\sigma^{xy} + \frac{1}{2}(\lambda-\mu)u_y^2\right] + \frac{\beta}{\lambda+\mu}\left[\frac{1}{2}\beta(\lambda+2\mu)\theta^2 + \mu^2(u\theta_x - \theta u_x)\right],$$

$$P^y = (\lambda+3\mu)[u_x\sigma^{xy} + \lambda u_xv_x] - (\lambda+2\mu)^2u_xv_x + \mu[u_y\sigma^{yy} - \lambda u_xu_y] + \frac{\beta\mu^2}{\lambda+\mu}[u\theta_y - \theta u_y]. \quad (17)$$

For only $A_1 \neq 0$,

$$P^x = (\lambda+3\mu)[v_y\sigma^{xy} + \lambda v_yu_y] - (\lambda+2\mu)^2v_yu_y + \mu[v_x\sigma^{xx} - \lambda v_xv_y] + \frac{\beta\mu^2}{\lambda+\mu}[v\theta_x - \theta v_x],$$

$$P^y = (\lambda+3\mu)\left[v_y\sigma^{yy} - \frac{\lambda+2\mu}{2}v_y^2 - \lambda u_xv_y - \frac{\mu}{2}v_x^2\right] + (\lambda+2\mu)\left[u_x\sigma^{yy} + \frac{1}{2}(\mu-\lambda)u_x^2\right] + \mu\left[v_x\sigma^{xy} + \frac{1}{2}(\lambda-\mu)v_x^2\right] + \frac{\beta}{\lambda+\mu}\left[\frac{1}{2}\beta(\lambda+2\mu)\theta^2 + \mu^2(v\theta_y - \theta v_y)\right]. \quad (18)$$

For only $A_2 \neq 0$,

$$P^x = (\lambda+3\mu)[u_y\sigma^{xx} - \lambda u_yv_y] + (\lambda+2\mu)^2u_yv_y - \mu[v_x\sigma^{xx} - \lambda v_xv_y] + \beta\mu\frac{\lambda+2\mu}{\lambda+\mu}[v\theta_x - \theta v_x],$$

$$P^y = (\lambda+3\mu)\left[u_y\sigma^{xy} - \frac{\lambda+2\mu}{2}u_x^2 - \mu u_yv_x - \frac{\mu}{2}u_y^2\right] - (\lambda+2\mu)\left[u_x\sigma^{yy} + \frac{1}{2}(\mu-\lambda)u_x^2\right] - \mu\left[v_x\sigma^{xy} + \frac{1}{2}(\lambda-\mu)v_x^2\right] + \frac{\beta}{\lambda+\mu}\left[\frac{\beta\mu}{2}\theta^2 + \mu(\lambda+2\mu)(v\theta_y - \theta v_y)\right]. \quad (19)$$

For only $A_3 \neq 0$,

$$P^x = (\lambda+3\mu)\left[v_x\sigma^{xy} - \frac{\lambda+2\mu}{2}v_y^2 - \mu u_yv_x - \frac{\mu}{2}v_x^2\right] - (\lambda+2\mu)\left[v_y\sigma^{xx} + \frac{1}{2}(\mu-\lambda)v_y^2\right] - \mu\left[u_y\sigma^{xy} + \frac{1}{2}(\lambda-\mu)u_y^2\right] + \frac{\beta}{\lambda+\mu}\left[\frac{\beta\mu}{2}\theta^2 + \mu(\lambda+2\mu)(u\theta_x - \theta u_x)\right],$$

$$P^y = (\lambda+3\mu)[v_x\sigma^{yy} - \lambda u_xv_x] + (\lambda+2\mu)^2u_xv_x - \mu[u_y\sigma^{yy} - \lambda u_xu_y] + \beta\mu\frac{\lambda+2\mu}{\lambda+\mu}[u\theta_y - \theta u_y]. \quad (20)$$

For only $A_4 \neq 0$,

$$P^x = \theta_x\sigma^{xx} + \theta_y\sigma^{xy} + 2\mu(v_y\theta_x - \theta_yu_y),$$
$$P^y = \theta_y\sigma^{yy} + \theta_x\sigma^{xy} + 2\mu(u_x\theta_y - \theta_xv_x). \quad (21)$$

For only $A_5 \neq 0$,

$$P^x = -\theta_y\sigma^{xx} + \theta_x\sigma^{xy} - 2\mu(v_y\theta_y + \theta_xu_y),$$
$$P^y = -\theta_y\sigma^{xy} + \theta_x\sigma^{yy} + 2\mu(u_x\theta_x + \theta_yv_x). \quad (22)$$

For only $A_6 \neq 0$,

$$P^x = \tfrac{1}{2}\theta_x^2 - \tfrac{1}{2}\theta_y^2,$$
$$P^y = \theta_x\theta_y. \quad (23)$$

For only $A_7 \neq 0$,

$$P^x = \theta_x\theta_y,$$
$$P^y = \tfrac{1}{2}\theta_y^2 - \tfrac{1}{2}\theta_x^2. \quad (24)$$

Conservation laws listed above are valid independently or in combination with each other. For $A_6, A_7 \neq 0$, the corresponding conservation laws relate to balances of the temperature gradients which arise from the harmonic nature of the temperature field. Note also that since the constants A_6 and A_7 do not appear in the characteristics f^1 and f^2, these balance laws can hold for systems where Δ^1 and $\Delta^2 \neq 0$.

For $A_4, A_5 \neq 0$, the conservation laws express balances of stresses, displacement gradients, and temperature gradients whose physical meaning is not readily apparent.

The laws corresponding to A_0, A_1, A_2, and $A_3 \neq 0$, which express various balances of stresses, displacements, displacement gradients, temperature and temperature gradients, can be combined in a special way that will yield balance laws leading to modified J-integrals for this thermoelasticity problem. In the

Downloaded 04 May 2010 to 171.66.16.33. Redistribution subject to ASME license or copyright; see http://www.asme.org/terms/Terms_Use.cfm

absence of thermal effects, these modified J-integrals will reduce to the J-integrals for elasticity.

Denoting the elastic strain energy as

$$W^e = \mu\epsilon^{ij}\epsilon^{ij} + \frac{\lambda}{2}(\epsilon^{kk})^2,$$

$$\epsilon^{ij} = \tfrac{1}{2}(u^i_j + u^j_i), \tag{25}$$

and setting $A_0 = A_3 = 1/(\lambda + 3\mu)$, the corresponding conservation law becomes

$$P^x = -W^e + u_x\sigma^{xx} + v_x\sigma^{xy} + \frac{1}{2}\frac{\beta^2}{\lambda+\mu}\theta^2 + \frac{\beta\mu}{\lambda+\mu}(u\theta_x - \theta u_x),$$

$$P^y = u_x\sigma^{xy} + v_x\sigma^{yy} + \frac{\beta\mu}{\lambda+\mu}(u\theta_y - \theta u_y); \tag{26}$$

also, by setting $A_1 = A_2 = 1/(\lambda + 3\mu)$, the corresponding conservation law will read

$$P^x = v_y\sigma^{xy} + u_y\sigma^{xx} + \frac{\beta\mu}{\lambda+\mu}(v\theta_x - \theta v_x),$$

$$P^y = -W^e + v_y\sigma^{yy} + u_y\sigma^{xy} + \frac{1}{2}\frac{\beta^2}{\lambda+\mu}\theta^2 + \frac{\beta\mu}{\lambda+\mu}(v\theta_y - \theta v_y). \tag{27}$$

Since we have Div $\mathbf{P} = D_xP^x + D_yP^y = 0$, and by divergence theorem,

$$\int_\Omega \text{Div } \mathbf{P}\,dA = \int_{\partial\Omega} P^i n^i dl, \tag{28}$$

where dA is an area element in the space Ω, and dl is a line element on the boundary $\partial\Omega$ of Ω with outward normal n^i, we can rewrite (26) and (27) into path-independent integrals of the form

$$\int_{\partial\Omega}\left[u^k_i\sigma^{kj}n^j - W^e n^i + \frac{1}{2}\frac{\beta^2}{\lambda+\mu}\theta^2 n^i - \frac{\mu\beta}{\lambda+\mu}(\theta u^i_j n^j - u^i\theta_j n^j)\right]dl = 0, \tag{29}$$

with $i = 1$ corresponds to (26) and $i = 2$ corresponds to (27).

In the absence of a thermal field, setting $\theta = 0$, it can be readily verified that (29) is identical to the J-integrals for linear elasticity (except for sign). It is also of interest to note that (29) is identical to that obtained by Gurtin (1979), which he presented, however, without showing how it was obtained. Gurtin also did not discuss the physical meaning of this integral, e.g., as an energy release rate.

The usefulness of the J-integral in linear elasticity lies in its path-independence and in its representation of the energy released accompanying crack extension. Similarly, an identical connection can be made between the path-independent integral presented in Eq. (29) and the energy released during crack growth in a thermoelastic medium. The simplest way to illustrate this is by rewriting Eq. (29) as follows:

$$-J^i = \int_{\partial\Omega}(W^e n^i - \sigma^{kj^e}n^j u^k_i)dl + \int_\Omega \beta\theta_k u^k_i dA, \tag{30}$$

and by considering the thermoelastic problem as an elastic problem with body forces such that

thermoelastic medium	elastic medium with body forces
$\sigma^{ij} = \sigma^{ij^e} - \beta\delta_{ij}\theta$	$\sigma^{ij} = \sigma^{ij^e}$
$\sigma^{ij}_j = 0$	$\sigma^{ij}_j = f^i;$ $\quad f^i = \beta\theta_i.$ (31)

Since the energy release rate (G) accompanying crack extension in an elastic medium with body forces can be easily derived as

$$G = \int_{\partial\Omega}(W^e n^i - \sigma^{kj^e}n^j u^k_i)dl + \int_\Omega f^k u^k_i dA, \tag{32}$$

the connection between (29) and energy release rate is immediately apparent through (30) (31) and (32). Therefore, the J-integral for thermoelasticity, (29), with its path independence and it being the energy release rate, is truly an extension of the J-integral for linear elasticity.

3.2 Time-Dependent Thermoelasticity. The governing equations for two-dimensional thermoelasticity with a time-dependent temperature field are given by (8) and (9) as

$$\begin{aligned}
&\Delta^1\text{:}\quad (\lambda+2\mu)u_{xx} + \mu u_{yy} + (\lambda+\mu)v_{xy} - \beta\theta_x = 0,\\
&\Delta^2\text{:}\quad (\lambda+2\mu)v_{yy} + \mu v_{xx} + (\lambda+\mu)u_{xy} - \beta\theta_y = 0,\\
&\Delta^3\text{:}\quad k(\theta_{xx} + \theta_{yy}) - c\theta_t - T\beta(u_{xt} + v_{yt}) = 0.
\end{aligned} \tag{33}$$

To obtain conservation laws for this system, the NA method requires that

$$E^k(f^1\Delta^1 + f^2\Delta^2 + f^3\Delta^3) \equiv 0. \tag{34}$$

Assuming the characteristics f^1, f^2, and f^3 to be functions of $x, y, t, u, u_x, u_y, u_t, v, v_x, v_y, v_t, \theta, \theta_x, \theta_y$, and θ_t; with f^1 and f^2 depending only linearly and quadratically on $u_x, u_y, v_x, v_y, \theta$, the solution to the above equation is found to be

$$\begin{aligned}
f^1 &= g^1(x,y,t)\left[-\frac{\lambda+2\mu}{\mu}(u_x+v_y)^2 + \frac{\mu}{\lambda+2\mu}(u_y-v_x)^2 + 2\frac{\beta}{\mu}(u_x+v_y)\theta - \frac{\beta^2}{\mu(\lambda+2\mu)}\theta^2\right]\\
&\quad + 2g^2(x,y,t)\left[u_x + v_y - \frac{\beta}{\lambda+2\mu}\theta\right][v_x - u_y]\\
&\quad + g^3(t)[(\lambda+2\mu)(u_x+v_y) + \mu(v_x-u_y) - \beta\theta]\\
&\quad + A\left[\frac{k}{\lambda+2\mu}\theta_x - \left(\frac{T\beta}{\lambda+2\mu} + \frac{c}{\beta}\right)u_t\right] + g^4(x,y,t),\\
f^2 &= g^2(x,y,t)\left[\frac{\lambda+2\mu}{\mu}(u_x+v_y)^2 - \frac{\mu}{\lambda+2\mu}(u_y-v_x)^2 - 2\frac{\beta}{\mu}(u_x+v_y)\theta + \frac{\beta^2}{\mu(\lambda+2\mu)}\theta^2\right]\\
&\quad + 2g^1(x,y,t)\left[u_x + v_y - \frac{\beta}{\lambda+2\mu}\theta\right][v_x - u_y]\\
&\quad + g^3(t)[(\lambda+2\mu)(u_x+v_y) + \mu(u_y-v_x) - \beta\theta]\\
&\quad + A\left[\frac{k}{\lambda+2\mu}\theta_y - \left(\frac{T\beta}{\lambda+2\mu} + \frac{c}{\beta}\right)v_t\right] + g^5(x,y,t),\\
f^3 &= A\left[u_x + v_y - \frac{\beta}{\lambda+2\mu}\theta\right] + g^6(x,y,t),
\end{aligned} \tag{35}$$

where g^1, g^2, g^4, g^5, and g^6 are functions of x, y, and t satisfying

$$\begin{aligned}
g^1_x &= g^2_y,\\
g^1_y &= -g^2_x,
\end{aligned} \tag{36}$$

Downloaded 04 May 2010 to 171.66.16.33. Redistribution subject to ASME license or copyright; see http://www.asme.org/terms/Terms_Use.cfm

$$(\lambda + 2\mu)g^4_{xx} + (\lambda + \mu)g^5_{xy} + \mu g^4_{yy} - T\beta g^6_{xt} = 0,$$

$$(\lambda + 2\mu)g^5_{yy} + (\lambda + \mu)g^4_{xy} + \mu g^5_{xx} - T\beta g^6_{yt} = 0,$$

$$\beta(g^4_x + g^5_y) + k(g^6_{xx} + g^6_{yy}) + cg^6_t = 0, \quad (37)$$

g^3 is any arbitrary function of t, and A is an arbitrary constant.

Having solved for the characteristics, the corresponding conservation laws can be constructed from the product of $f^\alpha \Delta^\alpha$, and the results are as follows.

For only $g^1, g^2 \neq 0$,

$$\begin{aligned} P^x = {} & g^1(x, y, t)\{-\tfrac{1}{3}[(\lambda + 2\mu)(u_x + v_y) - \beta\theta]^3 \\ & + \mu^2(v_x - u_y)^2[(\lambda + 2\mu)(u_x + v_y) - \beta\theta]\} \\ & + g^2(x, y, t)\{\mu(\lambda + 2\mu)^2(u_x + v_y)^2(v_x - u_y) \\ & + \tfrac{1}{3}\mu^3(u_y - v_x)^3 + \beta\mu(u_y - v_x) \\ & \times \theta[2(\lambda + 2\mu)(u_x + v_y) - \beta\theta]\}, \end{aligned}$$

$$\begin{aligned} P^y = {} & g^2(x, y, t)\{\tfrac{1}{3}[(\lambda + 2\mu)(u_x + v_y) - \beta\theta]^3 \\ & - \mu^2(v_x - u_y)^2[(\lambda + 2\mu)(u_x + v_y) - \beta\theta]\} \\ & + g^1(x, y, t)\{\mu(\lambda + 2\mu)^2(u_x + v_y)^2(v_x - u_y) \\ & + \tfrac{1}{3}\mu^3(u_y - v_x)^3 + \beta\mu(u_y - v_x) \\ & \times \theta[2(\lambda + 2\mu)(u_x + v_y) - \beta\theta]\}. \quad (38) \end{aligned}$$

For only $g^3 \neq 0$,

$$\begin{aligned} P^x = {} & \tfrac{1}{2}(\sigma^{xx})^2 + \tfrac{1}{2}(\sigma^{xy})^2 + \sigma^{xx}[2\mu v_y + \mu v_x - \mu u_y] \\ & + \sigma^{xy}[2\mu u_x + \mu u_y - \mu v_x] - 2\mu^2[u_y(u_x + v_y) \\ & + v_x(u_x - v_y) + u_y^2 - v_y^2], \end{aligned}$$

$$\begin{aligned} P^y = {} & \tfrac{1}{2}(\sigma^{yy})^2 + \tfrac{1}{2}(\sigma^{xy})^2 + \sigma^{xy}[2\mu v_y + \mu v_x - \mu u_y] \\ & + \sigma^{yy}[2\mu u_x + \mu u_y - \mu v_x] - 2\mu^2[v_x(u_x + v_y) \\ & + u_y(v_y - u_x) + v_x^2 - u_x^2]. \quad (39) \end{aligned}$$

As g^1, g^2, and g^3 do not appear in the characteristic f^3, these conservation laws will be valid for a system with displacements and a temperature field that do not satisfy equation $\Delta^3 = 0$. In this sense, these laws do not represent the full system of interest. However, given any elastic body under the influence of a time-dependent temperature field, these conservation laws must hold along the solution of the system. Thus, despite the deficiency of the above laws, they might still be useful in the analysis of the present system. Nonetheless, the physical significance of these laws is not readily apparent.

For only $A \neq 0$,

$$\begin{aligned} P^x = {} & [k\beta\theta_x - (T\beta^2 + c(\lambda + 2\mu))u_t]\sigma^{xx} + [k\beta\theta_y - (T\beta^2 \\ & + c(\lambda + 2\mu))v_t]\sigma^{xy} + 2k\beta\mu(\theta_x v_y - \theta_y u_y), \end{aligned}$$

$$\begin{aligned} P^y = {} & [k\beta\theta_y - (T\beta^2 + c(\lambda + 2\mu))v_t]\sigma^{yy} + [k\beta\theta_x - (T\beta^2 \\ & + c(\lambda + 2\mu))u_t]\sigma^{xy} + 2k\beta\mu(\theta_y u_x - \theta_x v_x), \end{aligned}$$

$$\begin{aligned} P^t = {} & c(\lambda + 2\mu)\left[\frac{\lambda + 2\mu}{2}(u_x^2 + v_y^2) + \lambda u_x v_y \right. \\ & \left. + \frac{\mu}{2}(u_y^2 + 2u_y v_x + v_x^2) - \beta\theta(u_x + v_y)\right] \\ & + T\beta^2\mu\left[\frac{1}{2}(u_y + v_x)^2 - 2u_x v_y\right] + \frac{1}{2}\beta^2 c\theta^2. \quad (40) \end{aligned}$$

This conservation law can be rewritten as

$$\frac{D}{Dt}U = \epsilon^{ij}_t \sigma^{ij} + h^c_t, \quad (41)$$

where U is the total energy (elastic strain energy W^e plus the heat absorbed h) and h^c is the heat absorbed at the current temperature $T^c = T + \theta$. By the second law of thermodynamics, h^c is given by the product of T^c and the entropy $[C(\theta/(T + \theta)) + \beta\epsilon^{ij}]$ of the system. This conservation law is related to the first law of thermodynamics where the rate of change of internal energy $(D/Dt)U$ is equal to the rate of work done by tractions $(\epsilon^{ij}_t \sigma^{ij})$ plus the rate of heat absorbed (h^c_t) at $T = T^c$. This conservation law can also be expressed in the form of a line integral being equal to the time rate of change of a volume integral as

$$\begin{aligned} & \int_{\partial\Omega}\{\sigma^{ij}[k\beta\theta_j - (T\beta^2 + c(\lambda + 2\mu)u^j_t)]n_i \\ & + \theta_i u^j_t n_i - \theta_i u^j_t n_j\} dl = -D_t \int_\Omega \{c(\lambda + 2\mu) \\ & \times [W^e - \beta\theta(u_x + v_y)] + T\beta^2\mu[\tfrac{1}{2}(u_y + v_x)^2 \\ & - 2u_x v_y] + \tfrac{1}{2}\beta^2 c\theta^2\} dV. \quad (42) \end{aligned}$$

For only $g^4, g^5, g^6 \neq 0$,

$$\begin{aligned} P^x = {} & g^4\sigma^{xx} + g^5\sigma^{xy} + g^6 k\theta_x - u[(\lambda + 2\mu)g^4_x + \lambda g^5_y] \\ & - v[\mu(g^4_y + g^5_x)] + T\beta g^6_t u - g^6_x k\theta, \\ P^y = {} & g^5\sigma^{yy} + g^4\sigma^{xy} + g^6 k\theta_y - v[(\lambda + 2\mu)g^5_y + \lambda g^4_x] \\ & - u[\mu(g^4_y + g^5_x)] + T\beta g^6_t v - g^6_y k\theta, \\ P^t = {} & -g^6 h. \quad (43) \end{aligned}$$

If g^4, g^5, and g^6 are taken to be constants, the above law will reduce to the governing equations of the system in conserved form.

4 Mechanics of a Porous Medium

In 1956, M. A. Biot has shown that mechanics of a porous medium and thermoelastic continua are isomorphic, i.e., the governing equations of an elastic porous solid whose pores are filled with a compressible viscous fluid are analogous to that of thermoelasticity and may be obtained from each other by a change of notation.

The constitutive relation between fluid pressure (p), solid dilatation (e) and fluid dilatation (ϵ) for a porous medium is given by Biot (1956) as

$$p = -\frac{1}{f}(Qe + R\epsilon), \quad (44)$$

where Q and R are material constants, and f is the porosity of the solid. The solid and fluid dilatation are related to the displacement components of the solid (u^i) and of the fluid (U^i) by

$$\begin{aligned} e &= u^i_i, \\ \epsilon &= U^i_i. \quad (45) \end{aligned}$$

Renaming constants $N = \lambda$, $S = \lambda - (Q^2/R)$, $\alpha = (Q + R)(f/R)$, $1/M = f^2/R$, and with k_1 being the permeability coefficient of the material, the governing equations for the mechanics of a porous medium are given by Biot (1956) as

$$\begin{aligned} & Nu^i_{kk} + (N + S)e_i - \alpha p_i = 0, \\ & k_1 p_{kk} - \frac{1}{M}p_t - \alpha e_t = 0. \quad (46) \end{aligned}$$

Downloaded 04 May 2010 to 171.66.16.33. Redistribution subject to ASME license or copyright; see http://www.asme.org/terms/Terms_Use.cfm

The porous media governing Eqs. (46) are identical in form to the thermoelastic governing Eqs. (8) and (9). With the fluid pressure p playing the role of the temperature increment θ, and with the following change of notation for the constant coefficients, $N \to \mu$, $S \to \lambda$, $\alpha \to \beta$, $k_1 \to k/T$, $1/M \to c/T$; it is apparent that (46) will be transformed into the governing equations of thermoelasticity, (8) and (9). Thus, conservation laws obtained for all cases of thermoelasticity in Section 3 apply immediately to mechanics of a porous medium with the same change of notation. Interpretations of the conservation laws for thermoelasticity, if any, can also be analogously applied to that for mechanics of a porous medium.

5 Conclusions

In the present contribution, conservation laws are presented for time-independent and time-dependent thermoelasticity in two dimensions. The results obtained can also be applied to mechanics of a porous medium. These divergence-free expressions are obtained using the Neutral Action (NA) method applicable for constructing conservation laws for dissipative systems (Honein et al., 1991).

For time-independent (steady-state) thermoelasticity, eight conservation laws were obtained. Some of these laws express balances that are obvious from the governing equations of the system, and they offer no new insight into the behavior of the systems considered. Of the results presented, the conservation laws that contain the elastic strain energy term are perhaps the most significant. These balance laws constitute path-independent integrals that are counterparts to the well-known J-integrals in linear elasticity, and they are shown to represent the energy release rate accompanying crack extension in a thermoelastic or poroelastic medium. Therefore, these results should prove useful in the analysis of fracture and defects in thermo and poroelasticity.

For time-dependent problems, seven groups of conservation laws were derived. These are "groups" of conservation laws because each of them involves one unknown function of space and time (with the exception of that correspond to $A \neq 0$). By assuming different forms, these functions will generate an array of conservation laws. If some of these functions are set equal to constants, the corresponding balance laws will be the governing equations of the system in conserved form; again, these laws will not contribute to a better understanding of the systems considered. Conservation laws involving the dissipation of the total energy could be the most important among the different groups of balance laws obtained. These divergence-free expressions relate to the first and second law of thermodynamics and they depict the balances for dissipation of total energy of the system considered.

The conservation laws derived here are not exhaustive. If one allows the characteristics of conservation laws to be general functions of higher derivatives of the dependent variables, additional conservation laws can be obtained. But this would require rather extensive symbolic manipulation. As a limited set, however, these laws represent nontrivial results for thermo and poroelasticity and they serve as examples of the application of the Neutral Action method.

Acknowledgments

This work was performed with the support of the U.S. Department of Energy and the Air Force Office of Scientific Research. This support is gratefully acknowledged.

References

Ainsworth, R. A., Neale, B. K., and Price, R. H., 1978, "Fracture Behavior in the Presence of Thermal Strains," *Proceedings of the Institute of Mechanical Engineers Conference on Tolerance of Flaws in Pressurized Components*, London, U.K., pp. 171–178.

Bessel-Hagen, E., 1921, "Über die Erhaltungssätze der Electrodynamik," *Math. Ann.*, Vol. 84, pp. 258–276.

Biot, M. A., 1956, "Thermoelasticity and Irreversible Thermodynamics," *Journal of Applied Physics*, Vol. 27, pp. 240–253.

Chien, N., 1992, "Conservation Laws in Non-Homogeneous and Dissipative Mechanical Systems," Ph.D. Dissertation, Stanford University, Stanford, CA.

Eischen, J. W., and Herrmann, G., 1987, "Energy Release Rates and Related Balance Laws in Linear Elastic Defect Mechanics," ASME JOURNAL OF APPLIED MECHANICS, Vol. 54, pp. 388–392.

Eshelby, J. D., 1956, "The Continuum Theory of Lattice Defects," *Solid State Physics*, Vol. 3, F. Seitz and D. Turnbull, eds., Academic Press, New York, pp. 79–144.

Fletcher, D. C., 1976, "Conservation Laws in Linear Elastodynamics," *Archive for Rational Mechanics and Analysis*, Vol. 60, pp. 329–353.

Francfort, G., and Golebiewska Herrmann, A., 1982, "Conservation Laws and Material Momentum in Thermoelasticity," ASME JOURNAL OF APPLIED MECHANICS, Vol. 49, pp. 710–714.

Günther, W., 1962, "Uber Einige Randintegrale der Elastomechanik," *Abhandlungen der Braunschweigischen Wissenschaftlichen Gesellschaft*, Vol. XIV, Verlag Friedr. Vieweg, Branschweig, pp. 53–72.

Gurtin, M. E., 1979, "On a Path-Independent Integral for Thermoelasticity," *International Journal of Fracture*, Vol. 15, pp. R169–R170.

Herrmann, G., 1980, "Some Applications of Invariant Variational Principles in Mechanics of Solids," *Variational Methods in the Mechanics of Solids*, S. Nemat-Nasser, ed., Pergamon Press, New York, pp. 145–150.

Honein, T., Chien, N., and Herrmann, G., 1991, "On Conservation Laws for Dissipative Systems," *Physics Letters A*, Vol. 155, pp. 223–224.

Kishimoto, K., Aoki, S., and Sakata, M., 1980, "On the Path Independent Integral-$\hat{J}$" *Engineering Fracture Mechanics*, Vol. 13, pp. 841–850.

Knowles, J. K., and Sternberg, E., 1972, "On a Class of Conservation Laws in Linearized and Finite Elastostatics," *Archive for Rational Mechanics and Analysis*, Vol. 44, pp. 187–211.

Kuo, A.-Y., and Riccardella, P. C., 1987, "Path-independent Line Integrals for Steady-state, Two-dimensional Thermoelasticity," *International Journal of Fracture*, Vol. 35, pp. 71–79.

Noether, E., 1918, "Invariante Variationsprobleme," *Nachr. K. Ges. Wiss. Göttingen, Math.-Phys. Kl.*, pp. 235–257 (see Transport Theory and Statistical Physics, Vol. 1, 1971, pp. 186–207 for an English translation).

Olver, P. J., 1986, *Applications of Lie Groups to Differential Equations*, Springer-Verlag, New York.

Wilson, W. K., and Yu, I. W., 1979, "The Use of the J-integral in Thermal Stress Crack Problems," *International Journal of Fracture*, Vol. 15, pp. 377–387.

Xu Li, 1991, "J^*-Integral for Thermoelasticity," *Engineering Fracture Mechanics*, Vol. 38, pp. 23–26.

Yeh, C.-S., Shu, Y.-C., and Wu. K.-C., 1993, "Conservation Laws in Anisotropic Elasticity (II)—Extension and Application to Thermoelasticity," *Proceedings of the Royal Society of London, Series A*, in press.

Downloaded 04 May 2010 to 171.66.16.33. Redistribution subject to ASME license or copyright; see http://www.asme.org/terms/Terms_Use.cfm

R. L. Weaver
Department of Theoretical and Applied Mechanics,
University of Illinois at Urbana-Champaign,
Urbana, IL 61801
Mem. ASME

W. Sachse

Kwang Yul Kim
Mem. ASME

Department of Theoretical and Applied Mechanics,
Cornell University,
Ithaca, NY 14853-1503

Transient Elastic Waves in a Transversely Isotropic Plate

The elastodynamic response of a thick plate, with the axis of transverse isotropy normal to the plate surface, is calculated by double numerical inverse transforms, a method particularly well-suited for calculations of responses in the near field of layered structures. Applications of these calculations include point-source/point-receiver *ultrasonics, quantitative acoustic emission measurements, and seismology. The singularities of the integrand are eliminated by the introduction of a small, but nonzero, imaginary part to the frequency. We discuss issues of numerical efficiency and accuracy in the evaluation of the resulting integrals. The method can be generalized to calculate the responses in materials of more general symmetry, in viscoelastic materials and to include the effects of finite aperture sources and receivers. The calculated responses are compared to those measured in a single crystal specimen of zinc.*

1 Introduction

Ultrasonic measurements which rely on elastic waves propagating through a material can provide an ideal means for determining the macroscopic properties of the material or for detecting flaws and inhomogeneities. The focus of much research over the past decade has been on the development of quantitative active ultrasonic and passive acoustic emission (AE) techniques. The use of ultrasound for nondestructive materials evaluation is especially appealing because of the direct connection between the characteristics of the wave propagation and the mechanical properties of a material. In contrast, passive AE techniques are attractive because they are able to monitor in situ the integrity of a large structure and to provide a means of investigating details of dynamic failure processes in materials.

The theory of quantitative acoustic emission represents AE signals as spatial and temporal convolutions between the unknown source functions and the elastic wave Green's functions of the specimen. Recovery of the source function, which characterizes a source of emission, is possible only if the appropriate components of a specimen's elastic wave Green's function are known. The theory of transient wave propagation in bounded isotropic materials is now well established and has been used for the characterization of AE sources in such materials (Scruby, 1985; Kim et al., 1989). This approach has formed the basis of quantitative AE analysis in which the waveforms detected by well-characterized receivers are processed to recover the characteristics of the source, that is, its type, orientation, and time-dependence. Similar applications in anisotropic materials have not yet been demonstrated, owing in part to the less well-developed theory for such materials. While the theory of harmonic wave propagation in unbounded elastic anisotropic media in well understood, cf. Synge (1957), Buchwald (1959), and Musgrave (1970), this is not the case for transient signals.

A recent advance for obtaining ultrasonic waveform data in materials has been the development of the point-source/point-receiver (PS/PR) technique (Sachse and Kim, 1986, 1987a, 1987b; Sachse et al., 1990). The technique employs small-aperture sources and receivers and uses knowledge of the wave propagation to interpret the detected ultrasonic signals. The method exhibits a number of distinct advantages over conventional, plane-wave ultrasonic measurements. Specimen preparation requirements are reduced and broadband excitations are easily realizable. Except in special cases, a point source generates both longitudinal and shear waves in a specimen, therefore information about each of these wave modes can be extracted from a waveform. Further, since PS/PR signals are simultaneously propagated in a wide range of directions in a specimen, one can easily determine the direction dependence of the propagation speeds and attenuations of various wave modes. Recent application of such measurements to characterize anisotropic materials has focused on inverting ultrasonic group velocities, obtained from pulse arrival time data in signals that have propagated in nonprincipal directions in an uncut specimen, to obtain the matrix of elastic stiffness of the specimen material (Castagnede et al., 1991; Every et al., 1991; Every et al., 1990; Niu, 1992).

A more detailed analysis of the waveforms, and, in particular, their evolving amplitudes and shapes, however, requires that the signals be detected by a sensor of known transfer characteristics and interpreted with an understanding of the propagation of transient elastic waves in a bounded specimen. Such measurements and signal analysis can form the basis of an absolute, *quantitative* materials characterization technique in specimens of isotropic materials (Weaver et al., 1989). The same procedures should in principle also be applicable for waves in bounded, anisotropic materials, but this has not yet been demonstrated.

Essential to the development of active and passive quantitative techniques in anisotropic materials is the development of an understanding of the propagation of transient elastic waves in bounded media. This would provide a rational basis for processing and interpreting ultrasonic signals to recover the characteristics of a source of emission or to determine the propagation characteristics of the material. Preliminary work has shown that the measured dynamic Green's functions in a plate-like specimen of an anisotropic material differ significantly from those in isotropic materials (Kim et al., 1993a). A theoretical basis for calculating the transient elastic waves in a bounded anisotropic material is of great fundamental as well as practical importance. Here we take the first step, that is, the development of a method for the calculation of such waveforms in transversely isotropic plates. The method promises to be readily extendable to plates of more arbitrary anisotropy and viscous properties.

Contributed by the Applied Mechanics Division of THE AMERICAN SOCIETY OF MECHANICAL ENGINEERS for publication in the ASME JOURNAL OF APPLIED MECHANICS.

Discussion on this paper should be addressed to the Technical Editor, Professor Lewis T. Wheeler, Department of Mechanical Engineering, University of Houston, Houston, TX 77204-4792, and will be accepted until four months after final publication of the paper itself in the ASME JOURNAL OF APPLIED MECHANICS.

Manuscript received by the ASME Applied Mechanics Division, Dec. 8, 1993; final revision, Apr. 29, 1994. Associate Technical Editor: D. M. Barnett.

Copyright © 1996 by ASME

Downloaded 04 May 2010 to 171.66.16.33. Redistribution subject to ASME license or copyright; see http://www.asme.org/terms/Terms_Use.cfm

2 Elastodynamics of Thick Plates

The calculation of elastodynamic responses in thick plates is a generalization of "Lamb's" problem, in which the response of an isotropic half-space or plate to a concentrated transient surface load may be represented as a problem of solving the quiescent initial condition partial differential equation

$$\sigma_{ij,j} = \rho \frac{\partial^2 u_i}{\partial t^2}, \tag{1}$$

where the stress tensor field is

$$\sigma_{ij} = \lambda \delta_{ij} u_{k,k} + \mu(u_{i,j} + u_{j,i}) \tag{2}$$

and traction boundary conditions are applied at the free and loaded surfaces, and traction on the other surfaces equal to the applied loads. For the case of a load $\mathbf{F}(t)$ concentrated at a point $x = y = 0$, the traction on the loaded surface at $z = h$ is

$$t_i = \sigma_{ij} n_j = F_i(t)\delta(x)\delta(y) \quad \text{at} \quad z = h. \tag{3}$$

These equations may be treated by finite difference algorithms (see, for example, Chang and Sun (1988) or Wu and Kuo (1990)) in which all derivatives with respect to time and space are replaced with finite difference equivalents and the resulting difference equations iterated in time. The method, in essence, numerically solves differential equations in all spatial coordinates and in time. For systems which lack translation invariance in x and y this may be the most efficient procedure.

For plates with translation invariance, however, it may be expected that the integral transform method, with attendant analytical solution of the differential equation in z, is more efficient. This is the approach taken by most researchers. The invariance of the plate under translations in time and in the coordinates x and y make it convenient to proceed by means of a Fourier, or Laplace, transform in time and a double Fourier transform in space. The result is a set of coupled, ordinary differential equations in z for the transformed fields u_i or their associated displacement potentials. In homogeneous materials, the ODE's are constant coefficient and therefore solvable in terms of linear combinations of exponentials in z. The coefficients in the linear combinations are determinable from the transformed boundary conditions. The solution is the triply transformed response of the plate.

Ben-Mehahem and Sena (1990) have obtained, by a variant of the above procedure, the transformed response of a transversely isotropic half-space to an arbitrary point source. Their interest is primarily in the frequency domain response and so they needed to perform only a single inverse transform. They did this analytically, at asymptotically high frequencies.

Because we are concerned with arbitrary frequencies, and with the time domain, we are faced with the need for exact inversion of all transforms. At least three different methods for that inversion exist. One is Generalized Ray Theory (Pao and Gajewski, 1977) in which the response is written as a superposition of expressions corresponding to rays from the source to the receiver, each associated with a definite arrival time. Another method expresses the response as a sum of inverse integral transforms associated with individual branches of the dispersive guided waves (Weaver and Pao, 1982a; Vasudevan and Mal, 1985). Felsen (1985) has suggested a hybrid method in which the response is written as a sum of a finite number of rays and a remainder which is approximated as a truncated sum of normal modes. A third method attempts a completely numerical multiple inverse integral transform (Bouchon and Aki, 1977; Weaver et al., 1989; Lih and Mal, 1992).

Generalized ray theory in which the double transform is inverted by the Cagniard method has been successfully applied to the calculation of the transient responses of isotropic half-spaces (Pekeris, 1955; Knopoff, 1958), and transversely isotropic half-spaces (Payton, 1983). Ray theory has also been successfully applied to the calculation of near-field responses in isotropic plates (Ceranoglu and Pao, 1981; Hsu, 1985) with numerous applications to acoustic emission source characterization and to point-source/point-receiver ultrasonics measurements, e.g., Scruby (1985) and Sachse and Kim (1986). Generalized ray theory (Pao and Gajewski, 1977) expresses responses as superpositions of integrals associated with rays traveling from the source to the receiver, either directly or after one or more surface reflections, each with a well-defined arrival time. At finite time there are a finite number of rays that contribute. In practice, however, the number of rays that contribute may be very large. The calculations are therefore cumbersome unless interest is confined to the very earliest times. Ray theory is generally not applicable to viscoelastic media (Weaver et al., 1989).

As Payton (1983) has demonstrated, responses in anisotropic media are, in principle, also decomposable into a sum of generalized rays. The calculations, however, can become very difficult to carry out because of the complexity of the folded group velocity surfaces. No one to our knowledge has attempted to carry out such calculations except for the simplest of anisotropic media: that of a transversely isotropic half-space for which the symmetry axis is normal to the surface (Payton, 1983) and that of an unbounded medium of more arbitrary symmetry (Every and Kim, 1993). The response of an unbounded medium and a half-space to a transient line load has been calculated by Nayfeh and Kim (1993). Van der Hijden (1987) has discussed the necessary procedures for a ray calculation in the general case of an arbitrarily layered anisotropic medium. Bedding and Willis (1980) have discussed and calculated high-frequency wavefront approximations which are valid near ray arrival times.

Owing to the multitude of rays needed, ray theory is not amenable to calculation of plate responses in the far field. Nevertheless, responses in an anisotropic plate at receiver positions far from a source have been calculated by means of one analytical inverse transform done with the aid of the Cauchy residue theorem followed by a numerical inverse transform of the remaining integral (Weaver and Pao, 1982a, 1982b; Vasudevan and Mal, 1985; Santosa and Pao, 1989). The use of the Cauchy residue theorem requires the location of the poles corresponding to the Rayleigh-Lamb-like waves of the plate and this can be conceptually complicated, especially in media with arbitrary layering, viscous properties and/or elastic symmetries (Nayfeh and Chimenti, 1989). Furthermore, a large number of pole locations are required for the calculation of responses with fine time resolution. This suggests that the method is not appropriate for high-frequency or large bandwidth applications.

A number of researchers (Weaver et al., 1990; Xu and Mal, 1985; Lih and Mal, 1992; Kundu and Mal, 1985; Bouchon and Aki, 1977; Duprey, 1993) have discussed and implemented schemes in which the location of the Rayleigh-Lamb poles is unnecessary. In these studies, all the inversions are carried out numerically. These integrations confront one with a need to write algorithms in which the contributions from the singularities at the poles corresponding to the Rayleigh-Lamb waves are correctly evaluated. As Kundu and Mal (1985) discuss, there are a variety of techniques which have been employed to negotiate these poles. One may write an algorithm which recognizes the pole and evaluates the contribution from its vicinity by taking a numerical Cauchy principal value and supplementing it with an analytic expression for a half residue. This could be cumbersome. Mal and co-workers (Xu and Mal, 1985; Kundu and Mal, 1985; Lih and Mal, 1992) have proceeded by introducing dissipation into their materials. Except for the strong pole at low wave number and frequency, this moves the poles off the line of numerical integration. It also disperses the sharp ray arrivals. Weaver et al. (1989) and Duprey (1993) have followed the method suggested by, amongst others, Bouchon and Aki (1977), of letting their frequency gain a small constant imagi-

Downloaded 04 May 2010 to 171.66.16.33. Redistribution subject to ASME license or copyright; see http://www.asme.org/terms/Terms_Use.cfm

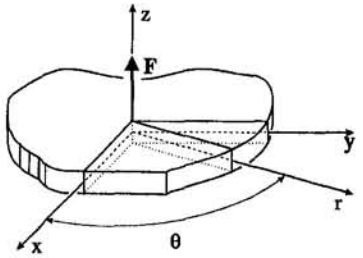


Fig. 1 The geometry of the problem

nary part, hence $\omega = \omega_r = \iota\delta$ where δ is small and positive. After the calculation is completed, the effect of δ is removed by multiplying responses by $\exp\{\delta t\}$. This method has the presumed disadvantage of amplifying numerical noise at late times. On the other hand it does preserve the sharp wave arrivals characteristic of nondissipative materials. It has been demonstrated (Weaver et al., 1989; Duprey, 1993) that this approach may readily be extended to the viscoelastic case and to the use of finite aperture receivers (Duprey, 1993). Because of the presumed poor accuracy at late times the method is probably most appropriate for calculation of the responses at early times and consequently for short source/receiver separations. It promises also to be extendable to the case of arbitrary anisotropy with some additional computational effort. Thus it is ideally suited for calculation of the waveforms expected in ultrasonic point-source/point-receiver measurements and in near-field acoustic emission signals. It is this procedure which will be followed here.

In the following section we derive analytic expressions for the transformed displacement response to a step point load acting on the surface of a transversely isotropic plate and discuss the extensions necessary for the treatment of other sources. The numerical inversion of the transform by the method outlined above is discussed in Section 3. In Section 4 we present comparisons of the numerically calculated responses with calculations by means of Generalized Rays (assuming isotropic symmetry), and with experimentally determined responses in a single crystal plate specimen of zinc. We conclude with a discussion of the prospects for extending this method to materials of more arbitrary anisotropy.

3 Double Transform of Plate Response

Consider the slab of thickness $2h = H$ pictured in Fig. 1. We imagine an excitation consisting of a point unit vertical step force $\mathbf{F}(t) = H(t)\hat{\mathbf{e}}_z$ acting on an initially quiescent system, though generalization to other time dependencies, loading positions, directions and distributions is not difficult. The formal elastodynamic boundary value, initial value problem seeks the solution $\mathbf{u}(\mathbf{r}, t)$ of the following partial differential equation:

$$c_{ijkl}u_{k,lj} = \rho\frac{\partial^2 u_i}{\partial t^2} \tag{4}$$

with quiescent initial conditions and with boundary conditions given by

$$c_{3jkl}u_{k,l} = F_j\delta(x)\delta(y) \quad \text{at} \quad z = +h \tag{5}$$

and

$$c_{3jkl}u_{k,l} = 0 \quad \text{at} \quad z = -h.$$

Upon performing a single temporal and a double spatial, Fourier transform on u

$$U_i(k_x, k_y, \omega, z) = \iiint u_i(x, y, z, t)\exp\{\iota(k_x x + k_y y - \omega t)\}\,dxdydt, \tag{6}$$

we find that the PDE reduces to a set of coupled ordinary differential equations. When the material is transversely isotropic with its axis of symmetry oriented normal to the plate surface, we may, without loss of generality, assume that k_y vanishes, and construct the following ODE's, where a prime signifies a derivative with respect to the z-coordinate

$$-c_{1111}k^2U_1 + c_{1313}U_1'' - \iota k[c_{1133} + c_{1331}]U_3' = -\rho\omega^2U_1$$

$$-c_{3131}k^2U_3 + c_{3333}U_3'' - \iota k[c_{3131} + c_{3311}]U_1' = -\rho\omega^2U_3, \tag{7}$$

in which U_2 decouples. General symmetry constraints amongst the elastic moduli tell us further that $c_{1313} = c_{3131} = c_{3113} = c_{1331}$ and $c_{1133} = c_{3311}$.

If one seeks solutions of the form $U_i\exp(\iota\alpha z)$, one recovers an algebraic problem:

$$[\mathbf{Q}]\{\mathbf{U}\} = \{\mathbf{0}\} \quad \text{or,}$$

$$\begin{bmatrix} \rho\omega^2 - c_{1111}k^2 - c_{1313}\alpha^2 & k\alpha(c_{1133} + c_{1331}) \\ k\alpha(c_{1133} + c_{1331}) & \rho\omega^2 - c_{3131}k^2 - c_{3333}\alpha^2 \end{bmatrix}\begin{Bmatrix} U_1 \\ U_3 \end{Bmatrix} = \begin{Bmatrix} 0 \\ 0 \end{Bmatrix}, \tag{8}$$

for which the characteristic equation $\det[\mathbf{Q}] = 0$ is, at fixed ω and k, a quadratic for α^2. We label the two distinct solutions of this quadratic by the subscript a which takes on the values of 1 or 2. Each value of a is associated with two related solutions, $\pm\alpha_a$, each of which is associated with an eigenvector, labeled as $\{U_\pm^a\}$. Rather than labeling the related solutions by the sign of α_a, it is convenient instead to characterize the solutions as *symmetric* (even) and *antisymmetric* (odd). One therefore takes linear combinations of the solutions associated with $\pm\alpha_a$ and forms the solutions

$$\{U^{a,e}(z)\} = \tfrac{1}{2}[\{U_+^a\}\exp(\iota\alpha_a z) + \{U_-^a\}\exp(-\iota\alpha_a z)] = \begin{Bmatrix} -\iota k\alpha_a(c_{1133} + c_{1331})\sin\alpha_a z \\ (\rho\omega^2 - c_{1111}k^2 - c_{1313}\alpha_a^2)\cos\alpha_a z \end{Bmatrix} \tag{9}$$

and

$$\{U^{a,o}(z)\} = \frac{1}{2i}[\{U_+^a\}\exp(\iota\alpha_a z) - \{U_-^a\}\exp(-\iota\alpha_a z)] = \begin{Bmatrix} \iota k\alpha_a(c_{1133} + c_{1331})\cos\alpha_a z \\ (\rho\omega^2 - c_{1111}k^2 - c_{1313}\alpha_a^2)\sin\alpha_a z \end{Bmatrix}. \tag{10}$$

The general solution of the ordinary differential equation (Eq. (7)) is an arbitrary linear combination of $\{U^{1,o}(z)\}$, $\{U^{1,e}(z)\}$, $\{U^{2,o}(z)\}$, and $\{U^{2,e}(z)\}$. That is

$$\{U\} = \sum\sum A^{a,o}\{U^{a,\sigma}\}, \tag{11}$$

where the sums are over $a = 1, 2$ and $\sigma = e, o$. Invocation of the boundary conditions allows one to determine the coefficients A of the linear combination. The transformed boundary conditions are, at the upper surface,

$$c_{3311}(-\iota k)U_1 + c_{3333}U_3'|_{z=+h} = \frac{F}{\iota\omega}$$

and

$$c_{1313}U_1' - \iota k c_{1313}U_3|_{z=+h} = 0. \tag{12}$$

At the lower surface of the plate ($z = -h$) both these expressions vanish.

In principle, the resulting system of equations for the A's is 4×4, however the use of even and odd solutions rather than

Downloaded 04 May 2010 to 171.66.16.33. Redistribution subject to ASME license or copyright; see http://www.asme.org/terms/Terms_Use.cfm

upgoing and downgoing solutions uncouples this 4×4 system to give two distinct 2×2 systems.

For the even modes one finds

$$\sum A^{ae}[c_{3311}(-k^2\alpha_a)(c_{1133} + c_{1331}) \sin \alpha_a h - \alpha_a c_{3333}(\rho\omega^2 - c_{1111}k^2 - c_{1313}\alpha_a^2) \sin \alpha h] = \frac{F}{2\iota\omega} \quad (13)$$

and

$$\iota k \sum A^{ae}[c_{1313}\alpha_a^2(c_{1133} + c_{1331}) \cos \alpha_a h - c_{1331}(\rho\omega^2 - c_{1111}k^2 - c_{1313}\alpha_a^2) \cos \alpha h] = 0, \quad (14)$$

where the sums are over $a = 1, 2$. For the odd modes one finds

$$\sum A^{ao}[c_{3311}(k^2\alpha_a)(c_{1133} + c_{1331}) \cos \alpha_a h + \alpha_a c_{3333}(\rho\omega^2 - c_{1111}k^2 - c_{1313}\alpha_a^2) \cos \alpha h] = \frac{F}{2\iota\omega} \quad (15)$$

and

$$\iota k \sum A^{ao}[c_{1313}\alpha_a^2(c_{1133} + c_{1331}) \sin \alpha_a h + c_{1331}(\rho\omega^2 - c_{1111}k^2 - c_{1313}\alpha_a^2) \sin \alpha h] = 0. \quad (16)$$

For a fixed value of ω and k one may determine the two thickness direction wave numbers α_a by solving the quadratic $\det [\mathbf{Q}] = 0$, determine the associated transformed displacement fields from Eqs. (9)–(11), and determine the coefficients A from the 2×2 systems of Eqs. (13)–(16). This completes the determination of the transformed displacement field responses. At $z = -h$, the transformed normal response is

$$U_3|_{z=-h} = \sum A^{ae}(\rho\omega^2 - c_{1111}k^2 - c_{1313}\alpha_a^2) \cos \alpha_a h - \sum A^{ao}(\rho\omega^2 - c_{1111}k^2 - c_{1313}\alpha_a^2) \sin \alpha_a h. \quad (17)$$

At $z = +h$, the transformed response is

$$U_3|_{z=+h} = \sum A^{ae}(\rho\omega^2 - c_{1111}k^2 - c_{1313}\alpha_a^2) \cos \alpha_a h + \sum A^{ao}(\rho\omega^2 - c_{1111}k^2 - c_{1313}\alpha_a^2) \sin \alpha_a h. \quad (18)$$

The response at a receiver location (x, y), located at a distance $r = \sqrt{(x^2 + y^2)}$ from the point of application of the force is then given by the inverse triple transform:

$$u_3(x, y, z = \pm h, t) = (2\pi)^{-3} \iiint U_3(k_x, k_y, \omega, z = \pm h) \times \exp\{-\iota(k_x x + k_y y - \omega t)\} dk_x dk_y d\omega. \quad (19)$$

Using the assumed transverse isotropy, one may recognize that U_3 is a function only of the magnitude of k and hence one can perform the integration over the direction of k analytically. One is left with the following inverse double Fourier-Hankel transform,

$$u_3(r, z = \pm h, t) = (2\pi)^{-2} \int_{-\infty}^{+\infty} \int_0^{\infty} U_3(k, \omega, z = \pm h) \times J_0(kr) \exp(\iota\omega t) k dk d\omega, \quad (20)$$

where J_0 is the Bessel function of first kind, zeroth order. Except for the relatively greater complexity of the expressions for U, this double inverse transform is identical to that obtained for the response of an isotropic slab (Vasudevan and Mal, 1985; Weaver and Sachse, 1988; Weaver et al., 1989).

The above analysis has described the method for the generation of doubly transformed displacement responses to normal surface loads. The method is, however, of greater generality and may be used to calculate responses to more arbitrary loadings. The right side of Eqs. (13)–(16) are essentially the transformed applied surface tractions, which could be generalized to loads other than normal loads. Buried sources would be slightly more complicated, the ODE (Eq. (7)) acquiring inhomogeneous forces, functions of z. Their solution would not, however, be difficult. Nayfeh and Kim (1993) have discussed doubly transformed responses to line loads in anisotropic media. Van der Hijden (1987) has formulated the procedures for the calculations of the transformed responses to point loads in arbitrarily layered anisotropic media.

The response to some of these other loadings is implicit in the present calculation. For example, the displacement response to a pair of horizontal double forces may be obtained as described in the following paragraph.

The displacement response in the radial direction to a vertical impulse may be shown to be

$$u_r(r, z = \pm h, t) = -\iota(2\pi)^{-2} \iint U_1(k, \omega, z = \pm h) \times J_1(kr) \exp(\iota\omega t) k dk d\omega, \quad (21)$$

where U_1 is obtained from Eqs. (9)–(16) as was U_3. Symmetry arguments may be used to show that the response in the θ direction vanishes. The in-plane (two-dimensional) divergence of the in-plane displacement field may then be formally constructed from

$$\nabla_{2d} \cdot (u_r \mathbf{e}_r) = -\iota(2\pi)^{-2} \iint U_1(k, \omega, z = \pm h) \times (1/r) d[rJ_1(kr)]/dr \exp(\iota\omega t) k dk d\omega \quad (22)$$

$$= -\iota(2\pi)^{-2} \iint U_1(k, \omega, z = \pm h) \times J_0(kr) \exp(\iota\omega t) k^2 dk d\omega. \quad (23)$$

While measurements of in-plane divergence responses to normal surface loads are rarely, if ever, made, the reciprocal measurement of a normal surface displacement response to an in-plane dilation precisely corresponds to a common case in which laser generated thermoelastic sources generate ultrasound which is detected by sensors of normal surface motion. Thus, by reciprocity, Eq. (23) corresponds to an important PS/PR testing configuration.

The effect of a finite aperture receiver may be incorporated into Eqs. (20) or (23) by the insertion of a factor corresponding to the Hankel transform of the receiver sensitivity into the integrand. This has been demonstrated for the isotropic case (Duprey, 1993).

The principal interest of the present communication is in a proposed method for the evaluation of integrals such as those appearing in Eqs. (20), (21), or (23). We therefore do not concern ourselves further with the calculation of the integrand in the general case, but only with the integral. We choose to address Eq. (20).

Evaluation of one of the two integrals appearing in Eqs. (20), (21), or (23) may, as discussed in the Introduction, be effected by contour integration and the Cauchy residue theorem. That procedure requires the location of the poles, the roots of the dispersion relations for the guided waves of the plate. Alternatively one might attempt an algebraically cumbersome semi-analytical evaluation of the response by writing it as a ray sum. See, for example, the work of Knopoff (1958) or Ceranoglu and Pao (1981) for discussions of this approach in an isotropic plate and Van der Hjiden (1987) for an anisotropic plate. If $u_3(r, z = \pm h, t)$ were expanded in powers of $\exp(\iota\alpha h)$ and each term in the series identified with a multiply reflected wave in the standard fashion (Knopoff, 1958; Ceranoglu and Pao, 1981), one could then truncate the series (which would correspond to the inclusion of a finite number of rays) and integrate the result. The resulting integrand would lack poles but would

Downloaded 04 May 2010 to 171.66.16.33. Redistribution subject to ASME license or copyright; see http://www.asme.org/terms/Terms_Use.cfm

include branch points. It is not clear whether this procedure would be more computationally efficient than the one followed here. It would most certainly be more complicated analytically.

Here we follow the algebraically less cumbersome, but computationally more demanding numerical evaluation of the double integral expressed by Eq. (20). We judge it expedient to carry out the integration in ω by means of an FFT algorithm. The numerical integration may be done in a variety of ways. It is most important to recognize that the k-integration along the real k-axis passes arbitrarily close to a finite number of discrete poles at the real roots $k(\omega)$ of the guided mode dispersion relation for the plate. A reliable numerical algorithm for the navigation of these poles is, in principle, possible. However, in the spirit of constructing an algebraically simple, albeit computationally intensive method, it is arguably more appropriate to avoid the need for such programming. Mal and co-workers (Xu and Mal, 1985; Kundu and Mal, 1985; Lih and Mal, 1992) have treated the difficulty by including dissipation in their constitutive relations $c_{ijkl}(\omega)$. For real, nonzero ω this moves the poles off the real k-axis. The consequent high attenuations at high frequencies have also limited the high frequencies in their responses, thereby allowing truncation of the inverse Fourier transform at moderately low frequencies. By also limiting the low-frequency content of their excitations, the pole at $\omega = 0$ is eliminated.

In this paper we follow an alternative scheme in which the Fourier transform is generalized by $\omega \to \omega_r - \iota\delta$ where δ is small and positive. While δ may, if desired, be allowed to have a dependence upon ω_r as one would if one were to make one's excursions into the complex plane only in the vicinity of the poles, the choice of a constant δ preserves the applicability of the FFT algorithm for the final ω inversion. With a constant, positive δ, it is a simple matter to show that Eq. (20) is exactly equivalent to

$$u_3(r, z = \pm h, t) = \exp(\delta t)(2\pi)^{-2} \times \int_{-\infty}^{+\infty} \int_0^{\infty} U_3(k, \omega_r - \iota\delta, z = \pm h) \times J_0(kr) \exp(\iota\omega_r t) k dk d\omega_r. \quad (24)$$

The integrand is a nonsingular function of the real variables ω_r and k. It may now be integrated numerically without ambiguity.

In the absence of the factor $\exp(\delta t)$, Eq. (24) gives the response of a dissipative material with an arbitrary and physically unlikely form of damping. If one wished to apply Eq. (24) to the case of a dissipative and dispersive material, one should employ complex frequency-dependent wavespeeds in the evaluation of u_3, as has been discussed by Weaver et al. (1989) for isotropic materials.

4 Double Numerical Inverse Transform

The computational burden associated with the performance of the double integral appearing in Eq. (24) is not prohibitive. Issues of efficiency are therefore not critical. Inasmuch, however, as we imagine ultimate extension of the technique to the triple integrals required for responses in slabs of arbitrary elastic symmetry, we do expect issues of efficiency to be ultimately relevant. We therefore consider them here.

The integration of Eq. (24) is performed first with respect to k at fixed ω_r, and then with respect to ω_r by an FFT algorithm. Upon choosing a temporal resolution Δt, and a range in time T, one concludes that the frequency resolution $\Delta\omega$ can be no more coarse than $\Delta\omega = 2\pi/T$. We choose $\Delta\omega = 2\pi/\nu T$ with $\nu \geq 1$ chosen to be an integer power of 2. The maximum unaliased frequency is $\omega_{\max} = \pi/\Delta t$. Thus the number of independent frequencies for which the inverse Hankel transform must be evaluated and summed for the inverse Fourier transform is $\nu N/2$. For ease in implementing the FFT, we choose the number of points in the time record, $N = T/\Delta t$, to be a power of 2.

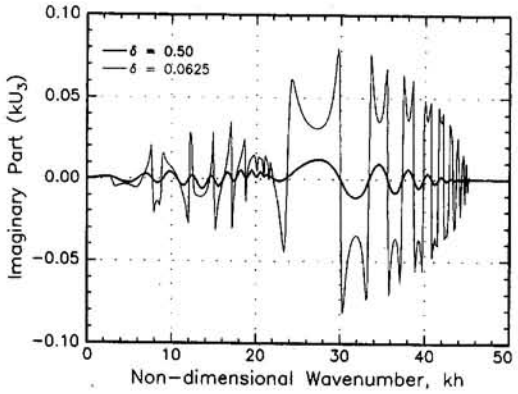


Fig. 2 The behavior of $\Im\{kU_3\}$ versus k at $\omega = 35.54$, $z = -h$ for a small (0.0625, light line) and large (0.5, heavy line) values of δ. The units are those described at the end of Section 4.

It is important when evaluating the integration with respect to k to anticipate the rate at which the integrand is likely to vary and the consequent requirements on the spacing Δk in the k-integration. The integrand of Eq. (21) has variation with k due to more than one cause. At moderate distances, when r is less than a few times the thickness $2h$, the oscillation resulting from the factor J_0 is fairly slow so that the variations in U are dominated by other causes. For large r, it is evident that the required spacings in k will be constrained due to the factor J_0 by an inequality such as $\Delta k < 1/r$.

The poles in U at the roots of the dispersion relation also contribute to rapid variations in the integrand. For a small imaginary frequency shift δ, the poles in U are very sharp, leading to the requirement that the spacing Δk in the k-integration be small. Thus there is an advantage to choosing large δ. On the other hand, a large δ will lead to large numerical noise at late times. Hence, there is some optimal choice for δ. The pole for branch "b" is located at $k_b(\omega) \approx k_b(w_r) - k_b'(\omega_r)\iota\delta$ which lies a distance $\delta|k_b'(w_r)| = \delta/|v_g|$ from the real k-axis. Here v_g is the group velocity of the branch at frequency w_r. Thus, one may anticipate that the requirement on Δk for a correct evaluation of the integral in the vicinity of the pole is something like $\Delta k < \delta/v$ where v is the group velocity of a typical guided wave mode.

One also anticipates oscillatory variations in $U(k)$ at fixed ω_r related to the presence of factors such as $\exp\{\iota\alpha_a(k, \omega)/h\}$ in the expressions for U. At most points in k this factor varies with k on a scale of $1/h$. The exponent is, however, especially sensitive to variations in k near the cutoff values of k where $d\alpha_a/dk$ diverges with a square root singularity. After some algebra, one concludes with a constraint of the form $\Delta k < (h)^{-1}(\delta/\omega_r)^{1/2}$ which is important only in the vicinity of those few points for which $d\alpha_a/dk$ diverges. In isotropic materials, these are the points where α_a vanishes. In an arbitrary material, these are points with group velocity in the $(x\text{-}y)$-plane; one would therefore anticipate that they are important only in the case that source and receiver are on the same side of the plate.

In Fig. 2 is a plot of $\Im(kU_3)$ versus k for different values of δ. Note the existence of some of the anticipated scales of variation with k. The sharp behavior near the poles is evident in the limit of small δ. At larger δ there remains a smooth variation on the scale of $1/h$, comparable to the spacing between the poles. As Fig. 3 illustrates, the rapid variations versus k, anticipated to occur at the points where $d\alpha_a/dk$ diverges, are observed at $kh \approx 22$ and ≈ 45.

In order to estimate an optimal value for the imaginary frequency shift δ we need to determine the value of δ for which a large Δk is tolerable because maximal Δk will correspond to

Downloaded 04 May 2010 to 171.66.16.33. Redistribution subject to ASME license or copyright; see http://www.asme.org/terms/Terms_Use.cfm

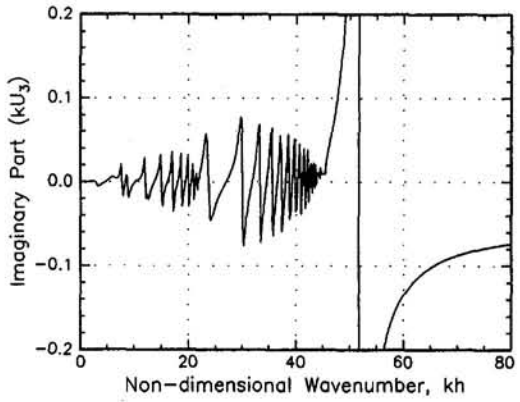


Fig. 3 The behavior of $\Im\{kU_3\}$ versus k at $\omega = 35.54$, $\delta = 0.0025$ and for $z = +h$. Note the surface acoustic wave pole at $kh \simeq 52$ and the slow convergence as $k \to \infty$.

a minimal computation time. As described above, we expect Δk to be chiefly constrained by δ/v. This reasoning would lead one to choose large values of δ. Such large values will lead, however, to severe constraints on integration accuracy, because errors will be multiplied by $\exp\{\delta T\}$. If we seek an absolute error in the computed displacements u which is less than ϵ, then the absolute error in the double integral appearing in Eq. (24) at time T must be less than $\epsilon(2\pi)^2 \exp(-\delta T)$. This corresponds to an absolute error in each point ω of the inverse Hankel transform

$$v(\omega) = \int_0^\infty U_3(k, \omega_r - \iota\delta, z = \pm h) J_0(kr) k dk, \quad (25)$$

which must be less than $\epsilon(2\pi)^2 \exp(-\delta T)/\omega_{\max}$. If the integral appearing in Eq. (25) is evaluated using Simpson's rule (Press, et al., 1989), it has a discretization error which scales with the fourth power of (Δk), $A(\Delta k/[\delta/v])^4$ where A is an unimportant scaling factor. Assuming that the discretization error dominates the error in evaluations of Eq. (25), one concludes that Δk required for the specified accuracy is determined from

$$A\left\{\frac{\Delta k}{[\delta/v]}\right\}^4 < \frac{\epsilon(2\pi)^2 \exp(-\delta T)}{\omega_{\max}}. \quad (26)$$

By solving Eq. (26) for Δk and differentiating with respect to δ, the maximal value for Δk is then found at $\delta = 4/T$.

As this argument depends upon the assumption that δ is small, the conclusion follows only for sufficiently large T. For moderate r and T, Δk is chiefly constrained by $1/h$. Thus the optimal value for δ is merely whatever δ makes the constraints equal, that is, $1/h \approx \delta/v$. Unfortunately this argument is not quantitatively precise and in practice we find the optimal value of δ operationally. We find optimal values of δ of the order of $2/T$. Complete theoretical understanding of these issues awaits further work.

The integral appearing in Eq. (25) is evaluated by a succession of calls to a double precision complex Simpson's rule integrator adapted from the routine QSIMP in *Numerical Recipes* (Press et al., 1986) with an relative error bound of one part in 10^6. A more sophisticated Romberg integration scheme was not found to increase efficiency.

Mal and co-workers (Xu and Mal, 1985; Lih and Mal, 1992) have developed an integration method for integrals such as that appearing in Eq. (25) in which Δk varies with k adaptively and in which the need for the constraint $\Delta k < 1/r$ is not present because the integrand without the factor J_0 is fit locally to a polynomial in k and the local integration of the oscillatory factor times the polynomial can be done exactly. This procedure is well suited for large distances r for which the chief constraint on Δk would be $1/r$, but it is less indicated in the present case in which r is small. The adaptive variation method is not pursued here, but it is arguably more efficient than the use of uniform spacings even at small r. As Fig. 2 illustrates, the scale over which U varies does vary with k, most notably in the vicinity of the points where $\partial\alpha/\partial k$ diverges.

The integral appearing in Eq. (25) runs to infinite k. Evaluation of this improper integral is, therefore, problematic. As seen from Fig. 2, however, the integrand for the case that the receiver is on the side opposite from the source converges rapidly for k greater than some characteristic value of the order of ω_r/c_{saw}, where c_{saw} is the speed of the surface wave. A numerical evaluation of this integral may then safely be truncated at a value of k equal to $k_{\max}$ somewhat larger than ω_r/c_{saw}.

It is clear from Fig. 3, that on the top surface, when k is equal to ω_r/c_{saw}, there is a large peak, corresponding to the surface wave pole. For k larger than ω_r/c_{saw} the integrand asymptotes to a constant value. Therefore a truncation is not appropriate in this case. The integration converges only by virtue of the gently diminishing oscillations in the Bessel function J_0. At $r = 0$ the integral does not converge at all, corresponding to the $1/r$ singularity at a point force on a half space. In order to compute this integral numerically we have chosen to evaluate the integral from the point $k_{\max}$ to ∞ by means of an asymptotic expression.

Consider the integral $I = \int_{k_{\max}}^\infty A(k) J_0(kr) dk$ where $A(k) = kU_3(k)$ is close to its asymptotic value for all $k \geq k_{\max}$. We expand the Bessel function asymptotically to obtain

$$(2/\pi r)^{1/2} \int A(k)(k)^{-1/2}[\cos(kr - \pi/4) + \sin(kr - \pi/4)/ 8kr - 9\cos(kr - \pi/4)/128k^2r^2] dk. \quad (27)$$

By defining the quantities

$$\zeta \equiv \frac{k}{k_{\max}}, \quad a(\zeta) \equiv \frac{A(k)}{\sqrt{\zeta}}, \quad b(\zeta) \equiv \frac{a(\zeta)}{\zeta},$$

$$c(\zeta) \equiv \frac{a(\zeta)}{\zeta^2} \quad \text{and} \quad x \equiv k_{\max} r \gg 1, \quad (28)$$

Eq. (24) can be rewritten to obtain

$$k_{\max}\left(\frac{2}{2\pi x}\right)^{1/2} \int_1^\infty a(\zeta)\cos(\zeta x - \pi/4) + b(\zeta)\sin(\zeta x - \pi/4)/ 8x - 9c(\zeta)\cos(\zeta x - \pi/4)/128x^2] d\zeta. \quad (29)$$

This integral can now be evaluated for asymptotically large values of x. We find

$$I \sim k_{\max}\left(\frac{2}{\pi x}\right)^{1/2} [-a(1)\sin(x - \pi/4)/x - a'(1)\cos(x - \pi/4)/x^2 + a''(1)\sin(x - \pi/4)/x^3 + \left(\frac{1}{8}\right)\{b(1)\cos(x - \pi/4)/x^2 - b'(1)\sin(x - \pi/4)/x^3\} + \left(\frac{9}{128}\right)c(1)\sin(x - \pi/4)/x^3], \quad (30)$$

where the primes indicate derivatives with respect to ζ. This expression is added to the Simpson's rule evaluation of the integral from zero to $k_{\max}$. Its accuracy is checked by investigating the invariance of the final result under changes of $k_{\max}$.

Downloaded 04 May 2010 to 171.66.16.33. Redistribution subject to ASME license or copyright; see http://www.asme.org/terms/Terms_Use.cfm

The response $u(t)$ is given by an inverse Fourier transform on v. That is

$$u(t) = \frac{\exp(\delta t)}{4\pi^2}\int_{-\infty}^{+\infty} v(w_r - \iota\delta)\exp\{\iota\omega t\}d\omega$$

$$= 2\Re\left[\frac{\exp(\delta t)}{4\pi^2}\int_0^{\infty} v(\omega_r - \iota\delta)\exp\{\iota\omega t\}d\omega\right], \quad (31)$$

where $\Re$ indicates the real part of the expression. We evaluate the integral, however, by means of a discrete sum on v_n, where v_n is defined by

$$v_n = v((n + 1/2)\Delta\omega - \iota\delta) \quad \text{for}$$

$$n = 0, 1, 2, \ldots \left(\frac{\nu N}{2} - 1\right). \quad (32)$$

The final determination of u is found in the form

$$u(t)|_{t=m\Delta t} = 2\Re\left[\exp\{\delta t + \iota\Delta\omega t/2\}\frac{\Delta\omega}{4\pi^2}\right.$$

$$\left.\times \sum v_n \exp\left\{\frac{2\iota\pi nm}{\nu N}\right\} f(\omega_r)\Big|_{\omega_r=(n+1/2)\Delta\omega}\right], \quad (33)$$

where f is a low-pass filter function that brings the summand smoothly to zero at ω_{max} in order to avoid Gibbs oscillations at the ray arrival times. The sum over n is from zero to $\nu N/2 - 1$. By padding the array v with an additional $\nu N/2$ zeros, however, and extending the sum to νN terms, the sum becomes identical in form to that of a discrete Fourier Transform. It may be computed efficiently by an FFT algorithm.

The sum is a good approximation to the integral appearing Eq. (31) only if the points of the integrand are sufficiently closely sampled in the sum. If we insist that there be at least ν points per cycle of the kernel $\exp\{\iota\omega t\}$ of the integrand, we conclude that $\Delta\omega$ must be smaller than $2\pi/\nu t$ for all t of interest, i.e., $\Delta\omega = 2\pi/\nu T$. This provides an alternative meaning for the computation parameter ν, as the number of points summed in the inverse Fourier Transform per cycle of its kernel. Only the first N elements of the resulting νN element array u_m are reported, corresponding to times from zero to T.

The parameter $\nu \geq 1$ permits trading accuracy and computational burden. Large values for ν corresponding to a fine resolution in ω imply a better approximation between the sum ap-

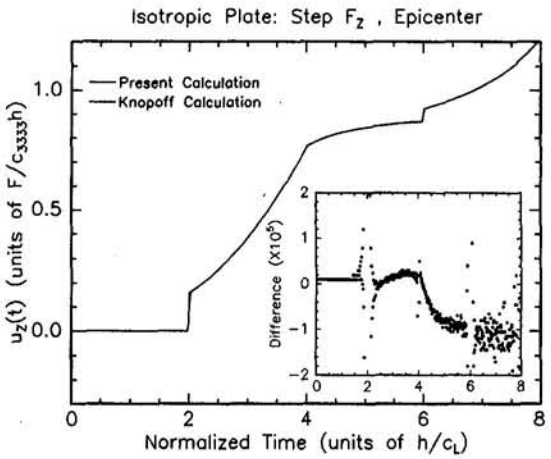


Fig. 4 The displacement response at epicenter in an isotropic plate as calculated by the present method is indistinguishable from the explicit formula given by Knopoff (1958). The insert shows the difference between these two approaches on an expanded scale.

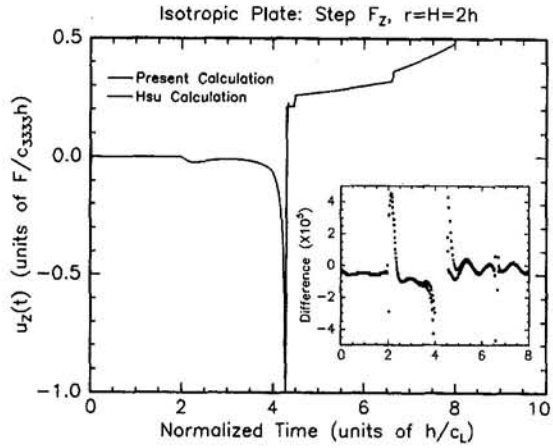


Fig. 5 The response at a distance $r = 2h$ from the source on the same side as the detector in an isotropic slab is calculated by the present method and by generalized rays. The difference is shown in the insert. Note in particular the significant Rayleigh wave arrival.

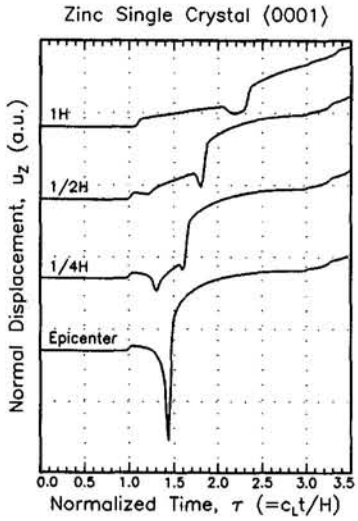


Fig. 6(*a*)

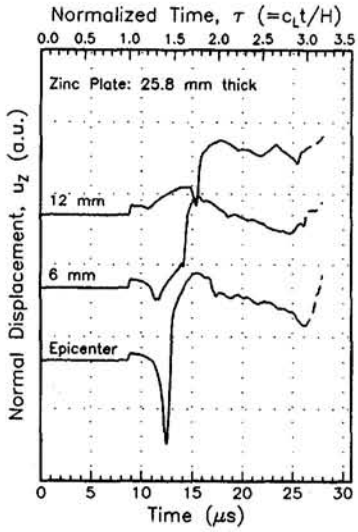


Fig. 6(*b*)

Fig. 6 Responses at several positions on the side of the plate opposite from the source. (*a*) Calculated responses. (*b*) Measured results.

Downloaded 04 May 2010 to 171.66.16.33. Redistribution subject to ASME license or copyright; see http://www.asme.org/terms/Terms_Use.cfm

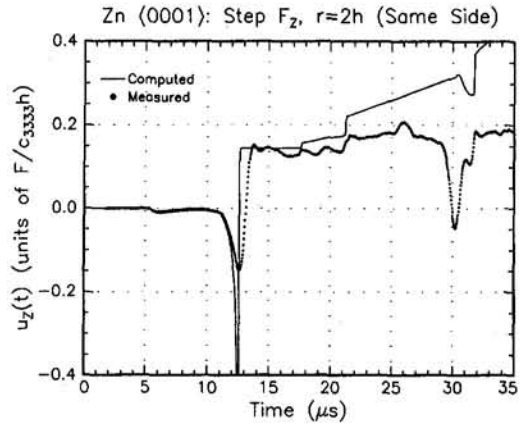


Fig. 7 Computed and measured responses in zinc at $r = H = 2h$ on the same side of the plate as the source. The measured waveform has been shifted horizontally by a constant (corresponding to the pre-trigger time) to bring the first arrival signals into coincidence and scaled vertically by a constant (corresponding to the source strength and charge amplifier gain) to bring the amplitude after the surface wave arrival into agreement.

pearing in Eq. (30) and the integral appearing in Eq. (29). The total computational effort very nearly scales with ν, however, and computations at large ν can therefore be prohibitively slow. In the results we present below, ν has been taken to equal 4. Larger values lead only to slight changes which are indistinguishable on the plots presented here. On the other hand, $\nu = 1$ leads to obvious errors, of the order of a couple of percent.

The evaluation of U and the integration of U with respect to k was conducted with 16-byte complex arithmetic. The FFT was summed with 8-byte complex arithmetic. A unit step force (i.e., $F = 1$) was used and units such that $h = \rho = c_{3333} = 1$ were used. Thus the resulting displacements are in units of $F/c_{3333}h$ and are given as a function of time in normalized time units of h/c_L where c_L is defined as the speed $\sqrt{c_{3333}/\rho}$ of a longitudinal wave along the axis of symmetry through the plate thickness. Computational times varied with the desired accuracy and desired time resolution; typical calculations required a few minutes on a workstation.

5 Results and Comparison With Experiment

To investigate the accuracy of the present method we have calculated the response of an isotropic slab and numerically compared it to the response obtained by generalized ray theory. We have considered the case $c_{ijkl} = \lambda\delta_{ij}\delta_{kl} + \mu(\delta_{ik}\delta_{jl} + \delta_{il}\delta_{jk})$ with $\lambda = 2\mu$ corresponding to a Poisson's ratio of $\frac{1}{3}$ and a ratio of longitudinal to shear wave speeds of 2. Figure 4 shows the response at epicenter ($z = -h$, $r = 0$) calculated by the present scheme using parameters $T = 8(h/c_L)$, $\delta = 2/T$, and $\nu = 4$. The results of a generalized ray calculation at epicenter (cf. Knopoff, 1958) in which the response is given by an explicit algebraic expression are superposed. As in our previous work (Weaver and Sachse, 1988; Weaver et al., 1989), the slight differences cannot be discerned on the scale of the plot. The difference between the calculations is shown in the inset in which it can be seen that, except near the ray arrival times at which the very high frequency limitations of the present technique are most evident, typical errors are less than 10^{-5}. As anticipated, they increase at later times.

Results from the present calculation for a receiver on the same side ($z = +h$) as the source and at a distance of $r = 2h = H$ are shown in Fig. 5, superposed upon the results of a generalized ray calculation calculated using the code developed by Hsu (1985). The maximum discrepancy is less than 10^{-5} except in the vicinity of the arrival times. Much of the error has a characteristic time scale and appears nonstochastic, indicating that the discrepancies are not the result of round-off error or finite precision in the integrations, but rather the result of some small systematic error in the code. They are not removed by increasing the parameter ν, nor by demanding that the k-integrations be carried out to an accuracy of one part in 10^7, nor do they change upon adjusting the nominally arbitrary parameter $k_{\max}$.

We also apply the present algorithm to the case of a zinc single crystal plate whose elastic symmetry axis is aligned normal to the surface. We choose the following values for the ratios of the elastic moduli: $c_{1111}/c_{3333} = 2.6021$, $c_{1313}/c_{3333} = 0.6147$, and $c_{1133}/c_{3333} = 0.8339$. In Fig. 6 we show a set of responses at $z = -h$, calculated for a series of different source/receiver separations. Results from measurements in zinc, reported elsewhere (Kim and Sachse, 1993), are also shown. The agreement is good, the differences at late times being ascribable to side wall reflections in the experiment and to low frequency rolloff in the ultrasonic receiver electronics. In particular one should note the strong (ideally infinite) response at the arrival of the focused conical point rays. The behavior of these curves has been discussed at length elsewhere (Kim and Sachse, 1993).

The computed and measured responses on the same side as the source (at $z = +h$) at a distance $r = 2h$ are shown in Fig. 7. Note in particular, the strong surface wave arrival in the computed waveform, at $t = r/c_{saw} = 2.91$ in units of h/c_L or 12.54 μs and also the conical point wave reflected off the bottom of the plate specimen, arriving at $t = 30.5$ μs. The first signal is at $t = 1.24$ in units of h/c_L or 5.45 μs, corresponding to the propagation of the very fast longitudinal wave in the direction normal to the symmetry axis. The arrival of the surface wave in the measured normal displacement waveform is in excellent agreement with that computed. The surface wave amplitude is significantly smaller than that of the computed signal and there is noticeable spreading of the trailing edge of this signal. The measured signal exhibits other differences from the ideal computed case after ~20 μs. The differences are likely the result of material damping (not included in the calculation), the arrivals of reflected signals from the boundaries of the specimen, and the low-frequency rolloff in the receiver electronics.

In previous work we have shown that by stacking a large number of signals measured or calculated at adjacent source/receiver configurations, one obtains a *scan image* which represents the detailed spatial and temporal characteristics of the elastic wave field in a material that can be directly related to the material's anisotropy and macrostructure (Every and Sachse, 1991). Figure 8 shows a synthetic scan image consisting of a stack of 101 waveforms similar to those of Fig. 6, corresponding to a range of receiver positions between epicenter and 20 mm off-epicenter in a 25.8-mm-thick single crystal plate of zinc whose c-axis was aligned with the normal to the plate. This image clearly shows the wave arrivals of the various bulk wave modes and, in particular, their amplitude evolution. Of particular recent interest has been the extraordinarily high amplitude of the epicentral conical ray, which is the result of the focusing of the quasi-transverse wave modes toward the symmetry direction. This is related to the phenomenon of *external conical refraction* (Kim et al., 1993b, c).

6 Discussion and Conclusions

We have shown the applicability of a conceptually simple, albeit computationally demanding, procedure for the calculation for wave responses in a transversely isotropic thick plate by means of double numerical inverse transforms. This method is particularly well-suited for calculations of responses in the near field of layered structures, and is easily generalized for calculation of responses in viscoelastic media, and to include the effects of finite aperture sources and receivers. The singularities of the integrand are eliminated by the introduction of a small, but

Downloaded 04 May 2010 to 171.66.16.33. Redistribution subject to ASME license or copyright; see http://www.asme.org/terms/Terms_Use.cfm

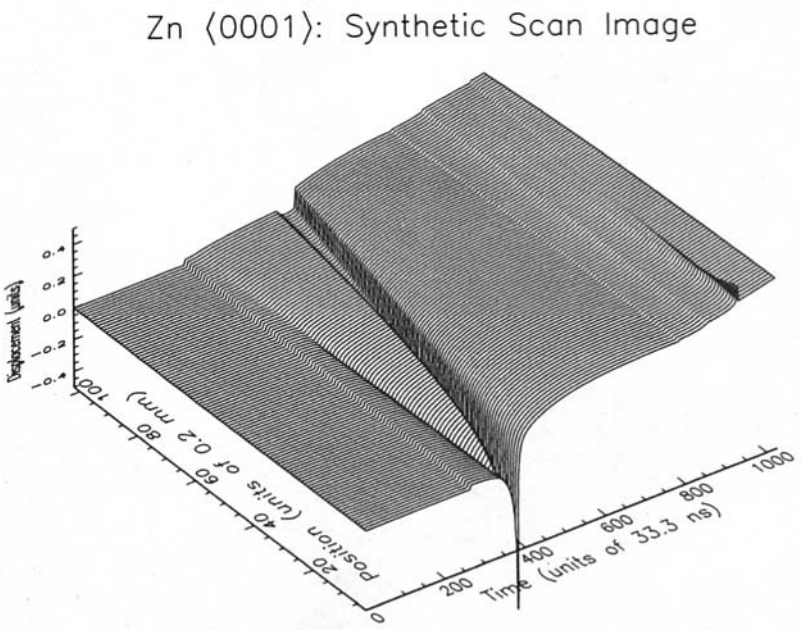


Fig. 8 Synthetic *scan image* of a single crystal plate specimen of zinc. The receiver position ranges from epicenter to 20 mm off-epicenter on the opposite side of the plate as the source.

nonzero, imaginary part to the frequency. Except for issues of numerical accuracy, the procedure is, in principle, exact. By including another numerical transform, the method can be generalized to calculate the responses in materials of more general symmetry.

Generalization to materials of more arbitrary anisotropy is of particular importance for future work. The consequent additional numerical inverse transform can be expected to significantly increase the computational burden. If the accuracies and time resolution achieved here were to be retained in the nonaxisymmetric case, one estimates the computational burden in the generalization to be greater by a factor of about 10^4. For such applications, it may therefore prove worthwhile to seek additional methods for the k-integration which are more efficient than the simple Simpson's rule used here.

As an illustration, we have used this approach to calculate synthetic plate responses which could be compared to those measured in a single crystal specimen of zinc. Expected application of these calculations include point-source/point-receiver ultrasonics, quantitative acoustic emission measurements, and seismology.

Acknowledgments

This work has been supported in part by the MRL Program of the National Science Foundation under Award No. DMR-9121654. R. L. W. was also supported, in part, by NSF grant MSS91-14360. W. S. and K. Y. K. were also supported in part by the Office of Naval Research (Physical Acoustics Program).

References

Bedding, R. J., and Willis, J. R., 1980, "The elastodynamics Green's tensor for a half space with an embedding anisotropic layer," *Wave Motion,* Vol. 2, No. 1, pp. 51–62.

Ben-Menahem, A., and Sena, A. G., 1990, "The elastodynamic Green's tensor in an anisotropic half-space," *Geophys. J. Int.,* Vol. 102, pp. 421–443.

Bouchon, M., and Aki, K., 1977, "Discrete wavenumber representation of seismic-source wave fields," *Bull. Seism. Soc. of Am.,* Vol. 67, pp. 259–277.

Buchwald, V. T., 1959, "Elastic waves in anisotropic media," *Proc. R. Soc. London,* Vol. A253, pp. 563–580.

Castagnede, B., Kim, K. Y., Sachse, W., and Thompson, M. O., 1991, "Determination of the elastic constants of anisotropic materials using laser-generated ultrasonic signals," *J. Appl. Phys.,* Vol. 70, No. 1, pp. 150–157.

Ceranoglu, A. N., and Pao, Y. H., 1981, "Propagation of Elastic Pulses and Acoustic Emission in a Plate," ASME JOURNAL OF APPLIED MECHANICS, Vol. 48, pp. 125–147.

Chang, C., and Sun, C. T., 1988, "Acoustic emissions and transient elastic waves in an orthotropic laminate plate," *Composite Sci. Tech.,* Vol. 33, pp. 213–236.

Duprey, K., 1993, "Attenuation Recovery in Viscoelastic Plates including the Effects of Finite Aperture Transducers," M.S. Dissertation, Cornell University, Ithaca, NY.

Every, A. G., and Sachse, W., 1990, "Determination of the elastic constants of anisotropic solids from acoustic wave group velocity measurements," *Physical Review B,* Vol. 42, No. 13, pp. 8196–8205.

Every, A. G., and Sachse, W., 1991, "Imaging of laser-generated ultrasonic waves in silicon," *Physical Review B,* Vol. 44, No. 13, pp. 6689–6699.

Every, A. G., Sachse, W., Kim, K. Y., and Niu, L., 1991, "Determination of elastic constants of anisotropic solids from group velocity data," *Review of Progress in Quantitative Nondestructive Evaluation,* Vol. 10B, D. O. Thompson and D. E. Chimenti, eds., Plenum Press, New York, pp. 1663–1668.

Every, A. G., and Kim, K. Y., 1994, "Time domain dynamic response functions of elastically anisotropic solids," *J. Acoust. Soc. Am.,* Vol. 95, No. 5, pp. 2505–2516.

Hsu, N. N., 1985, "Dynamic Green's Functions of an Infinite Plate—A Computer Program," NBSIR 85-3234, National Bureau of Standards, Gaithersburg, MD.

Kim, K. Y., and Sachse, W., 1994, "Direct determination of group velocity surfaces in a cuspidal region in zinc," *J. Appl. Phys.,* Vol. 75, No. 3, pp. 1435–1441.

Kim, K. Y., Sachse, W., and Hsieh, P., 1989, "Quantitative study of fracture by acoustic emission from cracks," *Advances in Fracture Research,* Vol. 5, K. Salama, K. Ravichandar, D. M. R. Taplin, and P. R. Rao, eds., Pergamon Press, New York, pp. 3185–3196.

Kim, K. Y., Sachse, W., and Every, A. G., 1993a, "On the determination of sound speeds in cubic crystals and isotropic media using a broadband ultrasonic point-source/point-receiver method," *J. Acoust. Soc. Am.,* Vol. 93, No. 3, pp. 1393–1406.

Kim, K. Y., Every, A. G., and Sachse, W., 1993b, "Focusing of acoustic energy at the conical point in zinc," *Phys. Rev. Letters,* Vol. 70, pp. 3443–3446.

Kim, K. Y., Every, A. G., and Sachse, W., 1994, "Focusing of Quasi-Transverse Modes in Zinc at Ultrasonic Frequencies," *Int. J. Mod. Phys. B,* Vol. 8, No. 17, pp. 2327–2352.

Knopoff, L., 1958, "Surface Motions of a Thick Plate," *J. Appl. Phys.,* Vol. 24, pp. 661–670.

Kundu, T., and Mal, A. K., 1985, "Elastic waves in a multilayered solid due to a dislocation source," *Wave Motion,* Vol. 7, pp. 459–471.

Lih, S. S., and Mal, A. K., 1992, "Elastodynamic response of unidirectional composite laminates to concentrated loads," ASME JOURNAL OF APPLIED MECHANICS, Vol. 59, pp. 878–886; 887–894.

Lu, I. T., and Felsen, L. B., 1985, "Ray, mode, and hybrid options for source excited propagation in an elastic plate," *J. Acoust. Soc. Am.,* Vol. 78, No. 2, pp. 701–714.

Downloaded 04 May 2010 to 171.66.16.33. Redistribution subject to ASME license or copyright; see http://www.asme.org/terms/Terms_Use.cfm

Musgrave, M. J. P., 1970, *Crystal Acoustics,* Holden-Day, San Francisco. Chapters 7 and 8.

Nayfeh, A., and Chimenti, D., 1989, "Free wave propagation in plates of general anisotropic media," ASME JOURNAL OF APPLIED MECHANICS, Vol. 56, pp. 881–888.

Nayfeh, A., and Kim, Y.-Y., 1993, "Wave propagation in anisotropic media due to internal transient line loads," paper read at the ASME-AMD Summer Meeting, Charlottesville, VA, June, 1993; in *Meet'N'93, Abstracts,* p. 504.

Niu, L., 1992, "The Determination of the Elastic Constants of Composite Materials from Ultrasonic Group Velocity Data," Ph.D. Dissertation, Cornell University, Ithaca, NY.

Pao, Y. H., and Gajewski, R., 1977, "The Generalized Ray Theory and Transient Responses of Layered Elastic Solids," *Physical Acoustics,* Vol. XIII, W. P. Mason and R. N. Thurston, eds., Academic Press, New York, pp. 183–265.

Payton, R. G., 1983, *Elastic Wave Propagation in Transversely Isotropic Media,* Martinus Nijhoff, Hague.

Pekeris, C. L., 1955, "The seismic surface pulse," *Proc. Natl. Acad. Sci.,* Vol. 41, pp. 469–480; 629–638.

Press, W. H., Flannery, B. P., Teukolsky, S. A., and Vetterling, W. T., 1986, *Numerical Recipes,* Cambridge University Press, Cambridge, UK.

Sachse, W., and Kim, K. Y., 1986, "Point-source/point-receiver materials testing," *Review of Quantitative Nondestructive Evaluation,* Vol. 6A, D. O. Thompson and D. E. Chimenti, eds., Plenum Press, New York, pp. 311–320; also: 1987a, *Ultrasonic Materials Characterization II,* J. Boussière, J. P. Monchalin, C. O. Ruud, and R. E. Green, eds., Plenum Press, New York, pp. 707–715.

Sachse, W., and Kim, K. Y., 1987b, "Quantitative acoustic emission and failure mechanics of composite materials," *Ultrasonics,* Vol. 25, pp. 195–203.

Sachse, W., Castagnede, B., Grabec, I., Kim, K. Y., and Weaver, R. L., 1990a, "Recent developments in quantitative ultrasonic NDE of composites," *Ultrasonics,* Vol. 28, pp. 97–104.

Sachse, W., Every, A. G., and Weaver, R. L., 1991, "Interpretation of ultrasonic PS/PR amplitude data," *Review of Progress in Quantitative Nondestructive Evaluation,* Vol. 10A, D. O. Thompson and D. E. Chimenti, eds., Plenum Press, New York, pp. 129–136.

Santosa, F., and Pao, Y. H., 1989, "Transient axially asymmetric response of an elastic plate," *Wave Motion,* Vol. 11, pp. 271–295.

Scruby, C. B., 1985, "Quantitative acoustic emission techniques," *Research Techniques in Nondestructive Testing,* Vol. VIII, R. S. Sharpe, ed., Academic Press, London, pp. 141–210.

Synge, J. L., 1957, "Elastic waves in anisotropic media," *J. Math. Phys.,* Vol. 35, pp. 323–334.

Van der Hijden, J. H. M. T., 1987, *Propagation of Transient Elastic Waves in Stratified Anisotropic Media, Applied Mathematics and Mechanics,* Vol. 32, North-Holland, Amsterdam.

Vasudevan, N., and Mal, A. K., 1985, "Response of an elastic plate to localized transient sources," ASME JOURNAL OF APPLIED MECHANICS, Vol. 52, pp. 356–362.

Weaver, R. L., and Pao, Y. H., 1982a, "Axisymmetric waves excited by a point source in a plate," ASME JOURNAL OF APPLIED MECHANICS, Vol. 49, pp. 821–836.

Weaver, R. L., and Pao, Y. H., 1982b, "Spectra of transient elastic waves in elastic plates," *J. Acoust. Soc. Am.,* Vol. 72, pp. 1933–1941.

Weaver, R. L., and Sachse, W., 1994, "Asymptotic viscoelastic rays in a thick plate," ASME JOURNAL OF APPLIED MECHANICS, Vol. 61, pp. 429–432.

Weaver, R. L., Sachse, W., and Niu, L., 1989, "Transient ultrasonic waves in a viscoelastic plate, Part I: Theory; Part II: Applications to materials characterization," *J. Acoust. Soc. Am.,* Vol. 85, No. 6, pp. 2255–2261; 2262–2267.

Wu, T. T., and Kuo, C.-L., 1990, "A study of acoustic emission waves in double layer composite plates," *Progress in Acoustic Emission V,* Japanese Society for NDI, Tokyo, pp. 217–221.

Xu, P. C., and Mal, A. K., 1985, "An adaptive integration scheme for irregularly oscillating functions," *Wave Motion,* Vol. 7, pp. 235–243.

Downloaded 04 May 2010 to 171.66.16.33. Redistribution subject to ASME license or copyright; see http://www.asme.org/terms/Terms_Use.cfm

An Efficient Calculation of the Load and Coefficient of Restitution of Impact Between Two Elastic Bodies With a Liquid Lubricant

L. Chang
Department of Mechanical Engineering,
The Pennsylvania State University,
University Park, PA 16802
Mem. ASME

This paper complements several previous papers on modeling of the impact between two elastic bodies with a liquid lubricant. The main feature of the work is the efficient incorporation of various engineering aspects of the impact process making use of approximations consistent with the physical insights of the problem. The model can very efficiently calculate the impact load and the coefficient of restitution with reasonable accuracy for a wide range of the problem domain. The modeling concepts and methodology may be useful in future research on interdisciplinary analyses of the dynamics of mechanical systems in which the interactions are strong between vibrations of the components and impacts in the lubricated kinematic pairs.

Introduction

A mechanical system consists of links and lubricated kinematic pairs with clearances. Impacts often occur between the kinematic pair as the machine operates. The impact generates noise and increases contact stresses and wear. Furthermore, the impulsive forces excite component vibration. The impact, vibration, noise and contact wear are among the major topics of interest in applied mechanics research.

Researchers in the area of mechanical design have studied the impact-induced vibration of flexible mechanisms. The impact is modeled as an impulse which generates kinematic discontinuity of the machine elements. The velocity of the element immediately after the impact is determined by the value of the coefficient of restitution which is often assumed. Khulief and Shabana (1986) used this method to study the effects of impacts in flexible mechanical systems generated by intermittent motion. Changizi and Shabana (1986) devised an active pulse control strategy to reduce the impact-induced vibration in multibody systems. Yigit et al. (1990) presented a model for the dynamics of a radially rotating beam when impacting on a stationary, rigid object.

The dynamic behavior of vibroimpacts and noise emission have been the topics of interest in contact mechanics research. The study focuses on the modeling of local stiffness and damping characteristics of the impacting bodies and their effects on impact forces and noise generation. In these studies, the global dynamics of the impacting members are modeled as rigid-body motions and the effect of the lubricant in the impact conjunction is neglected. Among the major contributors in this area of research are Hunt and Crossley (1975), Hayashi et al. (1975), and Herbert and MaWhannell (1977) who studied the multiple impact processes of an elastic body between two elastic plates.

Researchers in the area of tribology focus their attention on tribological variables such as the film thicknesses and pressure distributions during impact of two elastic bodies with a liquid lubricant. The solution requires simultaneously solving a set of field integral and differential equations in time, which is computationally intensive and difficult. Consequently, the solution is often obtained for a very short duration of the impact process (Christensen, 1962; Lee and Cheng, 1971), or the approach half of the process (Young and Wen, 1991), or, most recently, one complete impact (Larsson and Hoglund, 1994). The latest report by Larsson and Hoglund (1994) shows that the presence of the lubricant can significantly affect the impact process and system variables such as the impact load and the coefficient of restitution.

Modeling of machine dynamics with impacts between lubricated kinematic pairs is a challenging, interdisciplinary task. Much work has been done in the past by focusing attention on one area or the other. This has been and will always be a good engineering practice if the coupling between global and local variables such as component vibration and impact intensity is not strong. However, there are mechanisms in which this coupling needs to be modeled to obtain meaningful results. An example is the chain-sprocket mechanism in which the vibration of the chain and the impact between the roller of the chain and the tooth of the sprocket, thus the noise emission, are strongly related as shown in Wang et al. (1992). In addition, the continued demand of high performance of modern machinery will make the interdisciplinary modeling and analysis more unavoidable for improved design of the machines.

This paper attempts to devise an efficient modeling strategy for lubricated impacts that can be incorporated into the global dynamics model of a mechanical system. The impact of an elastic ball on a rigid surface with a lubricant layer is modeled to demonstrate the modeling concepts and methodology.

Formulation of the Model

Governing Equations. Neglecting wave propagation in the solid and assuming isothermal conditions, the impact process is governed by three equations: (1) equation of motion of the ball, (2) Reynolds equation which models the generation of hydrodynamic pressure in the conjunction, and (3) the elasticity

Contributed by the Applied Mechanics Division of THE AMERICAN SOCIETY OF MECHANICAL ENGINEERS for publication in the ASME JOURNAL OF APPLIED MECHANICS.

Discussion on this paper should be addressed to the Technical Editor, Professor Lewis T. Wheeler, Department of Mechanical Engineering, University of Houston, Houston, TX 77204-4792, and will be accepted until four months after final publication of the paper itself in the ASME JOURNAL OF APPLIED MECHANICS.

Manuscript received by the ASME Applied Mechanics Division, Aug. 8, 1994; final revision, Mar. 3, 1995. Associate Technical Editor: J. T. Jenkins.

Copyright © 1996 by ASME

Downloaded 04 May 2010 to 171.66.16.33. Redistribution subject to ASME license or copyright; see http://www.asme.org/terms/Terms_Use.cfm

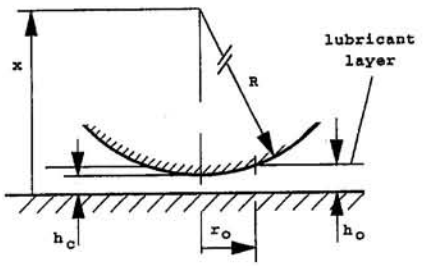


Fig. 1 The impact conjunction at an early stage of the process

equation which relates the lubricant film gap to the surface deformation of the ball due to the pressure. An impact model incorporating these equations was first formulated and numerically solved by Davis et al. (1986) and Barnocky and Davis (1989) to study the behavior of small particles in a viscous fluid during filtration or coagulation. For clarity, the governing equations are given below. The equation of motion of the ball is given by

$$m\ddot{x}(t) = F \tag{1}$$

where m and x are the mass and displacement of the ball, t is time, and F the impact force; a dot over a variable denotes its time derivative. The impact force is obtained by integrating the hydrodynamic pressure distribution generated by the squeeze action of the lubricant in the conjunction

$$F(t) = 2\pi \int_0^{r_0} p(r, t) r dr \tag{2}$$

The initial conditions of Eq. (1) are $x = R + h_0$ and $\dot{x} = \dot{x}_0 < 0$ (Fig. 1), which correspond to the state when the ball just penetrates the lubricant layer with an initial velocity of $\dot{x}_0$. Neglecting compressibility of the lubricant, the Reynolds equation in polar coordinates is given by

$$\frac{\partial}{\partial r}\left(\frac{h^3}{\mu} r \frac{\partial p}{\partial r}\right) = 12r \frac{\partial h}{\partial t} \tag{3}$$

where h is the film thickness and μ, viscosity of the lubricant. The boundary conditions of Eq. (3) are $p = 0$ at $r = r_0$ and $\partial p/\partial r = 0$ at $r = 0$. The elasticity equation for a point impact (contact) conjunction is given by (Dowson and Higginson, 1977)

$$h(r, t) = h_c(t) + \frac{r^2}{2R} + d(r, t). \tag{4}$$

For an axisymmetric problem, the deformation is given by (Timoshenko and Goodier, 1972)

$$d(r, t) = \frac{2}{\pi E'} \int_0^{2\pi} \int_0^{r_0} \frac{p(r', t)}{(r^2 + r'^2 - 2rr' \cos\theta)^{1/2}} r' dr' d\theta \tag{5}$$

where the equivalent Young's modulus, E', is related to the Young's modulus, E, and Poisson's ratio, ν, of the ball by $E' = E/(1 - \nu^2)$. The viscosity and density of the lubricant both increase with pressure. Barnocky and Davis (1989) showed that the effect of density change on the impact process is relatively small but the effect of viscosity change is more pronounced. A popular viscosity-pressure relation used in the research of elastohydrodynamic lubrication is the Roelands law which may be written as (Wang et al., 1991):

$$\mu = \mu_0 \exp\left\{\frac{p_r \alpha}{Z}\left[(1 + p/p_r)^Z - 1\right]\right\}. \tag{6}$$

The Roelands exponent, Z, may be expressed in terms of the ambient viscosity, μ_0, and pressure-viscosity coefficient of the lubricant, α, by

$$Z = p_r \alpha / \ln(\mu_0/\mu_r) \tag{7}$$

where p_r and μ_r may be defined as the Roelands reference pressure and reference viscosity, respectively. The Roelands law will be used to model the change of viscosity due to pressure as the lubricant in the conjunction experiences similar transient loading in both lubricated impact and elastohydrodynamic lubrication processes.

The impact process may be simulated by simultaneously solving Eqs. (1), (3), and (4) in conjunction with Eqs. (2), (5), and (6) at successive time increments. Numerical methods need to be used to obtain the solution. In particular, the Reynolds equation (Eq. (3)) needs to be converted into a set of algebraic equations by numerical discretization and the pressure distribution needs to be numerically integrated to obtain the impact force of Eq. (1) and the deformation of Eq. (5). Iterations are required to arrive at a converged solution at every time increment. This method of solution is not only computationally intensive but also subjected to numerical instability problems when simulating relatively severe impact processes. While a number of researchers have analyzed this type of problems such as Christensen (1962), Lee and Cheng (1971), and Young and Wen (1991), the full numerical solutions of the above governing equations (or their equivalence) were only reported in Barnocky and Davis (1989) and more recently in Larsson and Hoglund (1994). A simplified model of the impact problem was developed in Wells (1993). By assuming that the deformation profile of the impact conjunction is similar to that of a Hertzian contact and that the fluid is isoviscous, a fourth-order system of ordinary differential equations was obtained to govern the impact process.

The work reported in this paper complements the full numerical models and the simplified model cited above. Approximations are made consistent with the physical insights of the impact process to derive closed-form model equations. The model includes all major engineering aspects of the impact process. It can efficiently calculate the impact load and coefficient of restitution with reasonable accuracy for a wide range of the problem domain.

Modeling. The coefficient of restitution and impact load are system quantities of the impact process. Since these quantities are obtained through time and spatial integration, they may be obtainable without computing the time history of the exact pressure distributions and film shapes in the impact conjunction. Accordingly, a simple physical model with a thin, rigid disk attached to the lowest surface point of the ball will be used as shown in Fig. 2. The use of this equivalent-disk model eliminates the spatial variations of the impact conjunction (i.e., $h_e = h_e(t)$) and, thus, allows closed-form model equations to be developed based on the theories of hydrodynamics (Eq. (3)) and contact mechanics (Eq. (5)).

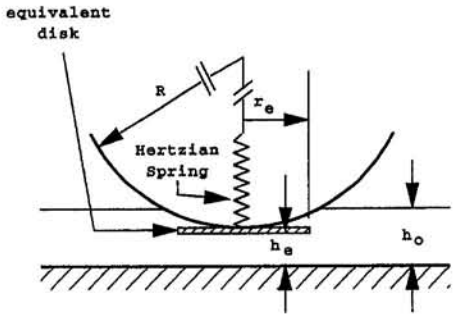


Fig. 2 Schematic of the equivalent-disk impact model

Downloaded 04 May 2010 to 171.66.16.33. Redistribution subject to ASME license or copyright; see http://www.asme.org/terms/Terms_Use.cfm

First, the equation for the pressure force, F. Integrating Eq. (3) with respect to r yields

$$\frac{h_e^3}{\mu} r \frac{\partial p}{\partial r} = 6r^2 \dot{h}_e + c_1 \quad \dot{h}_e < 0 \tag{8}$$

where $\dot{h}_e = dh_e/dt$. To generate squeeze action in the impact conjunction, the film gap, h_e, must keep reducing or the pressure vanishes; this is implied in the equations that follow. Application of boundary condition, $\partial p/\partial r = 0$ at $r = 0$, gives $c_1 = 0$. Thus, upon rearrangement and further integration, Eq. (8) becomes

$$p(r, t) = \frac{6\dot{h}_e}{h_e^3} \int \mu r dr + c_2. \tag{9}$$

Since the viscosity of lubricant, μ, varies with pressure, the integral in Eq. (9) cannot be analytically carried out. An approximation is then made in which an effective viscosity, μ_{eff}, is used over the impact conjunction. The use of an effective viscosity is consistent with the use of the equivalent-disk model described earlier. While these approximations can result in significant errors in the spatial distributions of the variables, the errors in the system variables such as total pressure force are likely to be averaged out by the integration over the impact conjunction. Due to high nonlinearities of the problem and the use of equivalent-disk approximation, the best pressure with which to calculate the effective viscosity may not be analytically obtainable. In this work, the average pressure over the conjunction is chosen to calculate the effective viscosity and is found to be acceptable by comparing the results with those from the full numerical solutions of Larsson and Hoglund (1994). Thus, the effective viscosity, according to Eq. (6), is given by

$$\mu_{eff} = \mu_0 \exp\left\{ \frac{p_r \alpha}{Z} [(1 + p_{ave}/p_r)^Z - 1] \right\}. \tag{10}$$

Substituting μ by μ_{eff} in Eq. (9) and integrating, with the boundary condition of $p = 0$ at $r = r_e$, yields

$$p(r, t) = \frac{3\dot{h}_e}{h_e^3} \mu_{eff}(r^2 - r_e^2). \tag{11}$$

Substituting the above expression for pressure distribution into Eq. (2), the pressure force over the impact conjunction is given by

$$F(t) = \begin{cases} -1.5\pi r_e^4 \mu_{eff} \dot{h}_e / h_e^3 & \dot{h}_e < 0 \\ 0 & \text{otherwise.} \end{cases} \tag{12}$$

The use of the equivalent-disk model and the associated equations developed above requires a meaningful choice of the disk radius, r_e. This radius should vary during the impact as, in the early stage of the process, the pressure distribution is relatively flat over the entire conjunction and, later on, it becomes more and more concentrated around the center of the impact. Formulation of r_e and its variation are presented next.

In the early stage of the impact, the deformation of the ball is negligible and the process is viscous. It may be modeled as the normal approach of two rigid bodies with an isoviscous fluid as used in Barnocky and Davis (1989) and Larsson and Hoglund (1994). The pressure distribution and the resulting pressure force are given by (Larsson and Hoglund, 1994)

$$p(r, t) = 12\mu_0 \dot{x} R^3 \left[\frac{1}{4R^2 h_0^2} - \frac{1}{(2Rh_0 + r^2)^2} \right] \tag{13}$$

and

$$F(t) = -6\pi\mu_0 \dot{x} R^2 \frac{(h_0 - h_c)^2}{h_0^2 h_c} \quad \dot{x} < 0 \tag{14}$$

where h_c may be expressed as (Fig. 1)

$$h_c(t) = x - R. \tag{15}$$

When the surface deflection becomes large as the impact proceeds, the process transitions from viscous to viscoelastic and the model equations based on the equivalent-disk model are then used. The radius of the equivalent disk, r_e, at the time of this transition, t_{ve}, is determined by equating the impact forces calculated by Eqs. (12) and (14). At this instant, $h_e = h_c$, $\dot{h}_e = \dot{x}$ and $\mu_{eff} = \mu_0$, giving

$$r_e(t_{ve}) = [4R^2(h_0 - h_c)^2 h_c^2 / h_0^2]^{1/4}. \tag{16}$$

Equation (5) is used to determine the surface deflection induced by the hydrodynamic pressure given by Eq. (13). Since, at the center location of the impact conjunction, the deflection is the largest and the film thickness smallest, it suffices to only calculate the deflection at this location to determine the instant at which to switch the model equations. Evaluating the integral of Eq. (5) at $r = 0$, with $r_0 = \sqrt{2R(h_0 - h_c)}$ from Eq. (4) (assuming $d(r_0, t)$ to be negligibly small), yields

$$d(0, t) = \frac{12\mu_0 R^2 \dot{x}}{E'} \left(\frac{1}{h_0^2} \sqrt{\frac{h_0 - h_c}{2R}} - \frac{1}{h_c^2} \sqrt{\frac{h_c}{2R}} \tan^{-1} \sqrt{\frac{h_0}{h_c} - 1} \right). \tag{17}$$

The viscoelastic stage of the impact process is assumed to commence when $d(0, t)$ reaches 1.0 percent of $h_c(t)$. This value of the deformation is chosen for the transition as, for most practical problems (say $h_0 \geq 2h_c$, $h_c \leq 10$ μm, $R \geq 1.0$ mm and $E' \leq 230$ GPa), the maximum pressure evaluated using Eqs. (13) and (17) would not appreciably increase the viscosity so that the assumption of isoviscous fluid is valid for the entire viscous stage of the impact process. As the impact furthers on in the viscoelastic stage, the pressure distribution becomes more and more concentrated around the central region of the conjunction. This change of the pressure distribution is modeled by reducing the radius of the equivalent disk as the film gap reduces. Owing to the complexity of the problem and various modeling approximations, the expression that best determines the reduction of the radius may not be analytically obtainable. Furthermore, any expression used needs to be evaluated by numerical analyses. In this work, the following expression is used:

$$r_e(t) = r_{eo}(h_e/h_{eo})^{0.5} \tag{18}$$

where r_{eo} and h_{eo} are the radius of the equivalent disk and the film gap at the onset of the viscoelastic stage of the impact process. The radius reduces more gradually at beginning and the rate of reduction increases as the film gap decreases. This pattern of the reduction of the equivalent disk appears to be consistent with the rate of pressure localization around the central region of the conjunction as the impact progresses in the viscoelastic stage. It is found to be acceptable by comparing the results with those from the full numerical solutions of Larsson and Hoglund (1994). The film gap in this stage is related to the location of the center of the ball through surface deformation. The relation is given by

$$h_e(t) = x(t) - R + d(0, t). \tag{19}$$

The deformation is due to the pressure distribution of Eq. (11). Substituting Eq. (11) into Eq. (5) and evaluating the integral at $r = 0$ yields

$$d(0, t) = -\frac{8\dot{h}_e}{E' h_e^3} \mu_{eff} r_e^3. \tag{20}$$

As the impact progresses in the viscoelastic stage, the defor-

Downloaded 04 May 2010 to 171.66.16.33. Redistribution subject to ASME license or copyright; see http://www.asme.org/terms/Terms_Use.cfm

mation of the ball increases. Furthermore, the lubricant in the conjunction becomes more and more viscous due to pressure-viscosity enhancement (Eq. (6)). This increase of viscosity makes squeeze of the lubricant out of the conjunction difficult. Eventually, the squeeze diminishes and the impact process transitions to the elastic stage. The transition from the viscoelastic stage to the elastic stage of the impact is modeled by considering the condition in a dry, elastic impact (contact) process. In such a process, the surface deflection of the ball at the center of the conjunction is related to the impact (contact) force by (Johnson, 1985):

$$d(0, t) = \left(\frac{3F}{2E'R^{1/2}}\right)^{2/3}. \tag{21}$$

Therefore, the transition is assumed to take place when the deformation calculated by Eq. (20) increases to that calculated by Eq. (21). Eliminating $\mu_{eff}\dot{h}_e/h_e^3$ in Eq. (20) using Eq. (12) yields the force-deformation relation of the equivalent-disk model

$$d(0, t) = \frac{8F}{1.5\pi E' r_e}. \tag{22}$$

Equating Eqs. (21) and (22) gives an equation to calculate the radius of the equivalent disk in the elastic stage of the impact process

$$r_e(t) = 1.296(RF/E')^{1/3}. \tag{23}$$

In summary, as the impact progresses in the viscoelastic stage, the radius of the equivalent disk determined by Eq. (18) will eventually reduce to a value below that calculated by Eq. (23). At this point in time, the impact transitions to the elastic stage and, thereafter, r_e is determined by Eq. (23), increasing as the impact further intensifies and decreasing as the ball begins rebounding back. This variation of r_e is consistent with the time-sequence results from the full numerical solutions of Larsson and Hoglund (1994).

The governing equations of the impact model developed in this paper are Eqs. (1), (14), and (15) in the viscous stage, Eqs. (1), (12), and (18) to (20) in the viscoelastic stage, and Eqs. (1), (12), (19), (20), and (23) in the elastic stage. The impact problem is fully defined by the following nine dimensional parameters: m, R, E', $\dot{x}_0$, h_0, μ_0, α, p_r, and μ_r; the last two are associated with the use of Roelands pressure-viscosity relation of Eqs. (6) and (7). Nondimensionalization of the governing equations will reduce the parameters required to six. Dimensionless parameters and variables defined in Young and Wen (1991) are used. The six parameters that fully define the impact problem are $M = mE'/R\mu_0^2$, $V_0 = \mu_0\dot{x}_0/E'R$, $H_0 = h_0/R$, $G = E'\alpha$, $P_r = p_r/E'$ and $\bar{\mu}_0 = \mu_0/\mu_r$; the last two are associated with the Roelands viscosity law. The variables are $T = (E'/\mu_0)t$, $W = F/E'R^2$, $V = \mu_0\dot{x}/E'R$, $X = x/R$, $H = h/R$, $P = p/E'$ and $D = d/R$. Furthermore, the dimensionless radius of the equivalent disk and effective viscosity associated with the current model are defined by $\bar{r}_e = r_e/R$ and $\bar{\mu}_{eff} = \mu_{eff}/\mu_0$. Making use of the above definitions, relevant model equations can be converted into dimensionless forms by straightforward substitutions and rearrangements. The dimensionless model equations are given as follows and each is labeled as Eq. (#D) corresponding to its dimensional counterpart of Eq. (#):

$$M\ddot{X}(T) = W \tag{1D}$$

$$Z = P_r G/\ln \bar{\mu}_0 \tag{7D}$$

$$\bar{\mu}_{eff}(T) = \exp\left\{\frac{P_r G}{Z}\left[(1 + P_{ave}/P_r)^Z - 1\right]\right\} \tag{10D}$$

$$W(T) = -1.5\pi\bar{r}_e^4\bar{\mu}_{eff}\dot{H}_e/H_e^3 \tag{12D}$$

$$W(T) = -6\pi\dot{X}\frac{(H_0 - H_c)^2}{H_0^2 H_c} \tag{14D}$$

$$H_c(T) = X - 1 \tag{15D}$$

$$\bar{r}_e(T_{ve}) = [4(H_0 - H_c)^2 H_c^2/H_0^2]^{1/4} \tag{16D}$$

$$D(0, T) = 12\dot{X}\left(\frac{1}{H_0^2}\sqrt{\frac{H_0 - H_c}{2}} - \frac{1}{H_c^2}\sqrt{\frac{H_c}{2}}\tan^{-1}\sqrt{\frac{H_0}{H_c} - 1}\right) \tag{17D}$$

$$\bar{r}_e(T) = \bar{r}_{eo}(H_e/H_{eo})^{0.5} \tag{18D}$$

$$H_e(T) = X(T) - 1 + D(0, T) \tag{19D}$$

$$D(0, T) = -8\dot{H}_e\bar{\mu}_{eff}\bar{r}_e^3/H_e^3 \tag{20D}$$

$$\bar{r}_e(T) = 1.296W^{1/3}. \tag{23D}$$

Method of Solution. The impact process governed by the above twelve dimensionless equations is an initial value problem. The following procedure outlines the method of solution:

(1) Specify the six parameters: M, V_0, G, H_0, P_r and $\bar{\mu}_0$ and calculate Z using Eq. (7D).

(2) Set the initial conditions of Eq. (1D) to $X(0) = 1 + H_0$ and $\dot{X}(0) = V_0$.

(3) For the viscous stage of the impact, numerically integrate Eq. (1D) in conjunction with Eqs. (14D) and (15D) to obtain $H_c(T)$, $W(T)$, $X(T)$ and its time derivatives. A fifth-order GEAR predictor-corrector integration algorithm is used (Gear, 1971).

(4) Calculate $D(0, T)$. When it reaches one percent of $H_c(T)$, calculate $\bar{r}_e(T_{ve})$ using Eq. (16D). At this point in time, the impact transitions to the viscoelastic stage in which Eq. (1D) is integrated in conjunction with Eqs. (10D), (12D), and (18D) to (20D) to determine $\bar{r}_e(T)$, $W(T)$, $X(T)$, and its time derivatives. At the time of this transition, H_e and $\dot{H}_e$ in Eq. (12D) are equal to H_c and $\dot{X}$, respectively. Thereafter, $\dot{H}_e$ is approximated by a backward finite difference formula: $\dot{H}_e(T) \approx (H_e(T) - H_e(T - \Delta T))/\Delta T$. The average pressure, P_{ave}, at the previous time-step is used to calculate the effective viscosity. A bisection-iterative procedure is used to determine the value of $H_e(T)$ so that all the equations are satisfied at time T.

(5) When $\bar{r}_e$ calculated by Eq. (18D) becomes smaller than that calculated by Eq. (23D), the impact transitions to the elastic stage in which $\bar{r}_e$ is determined by Eq. (23D).

(6) When $\dot{H}_e$ in Eq. (12D) becomes positive, the impact process is completed. Calculate the coefficient of restitution by $e = |\dot{X}_f/\dot{X}_0|$ and output results.

Evaluation of the Model

The impact model developed in this paper has been evaluated by physically interpreting the simulation results and by comparing the results with experimental data. The calculated impact load and the coefficient of restitution decrease as the viscosity of the lubricant and the thickness of the lubricant layer on the impacting surface increase, which is physically intuitive. A larger mass of the ball or a higher impact velocity yields a higher value of the coefficient of restitution. This result is expected as a larger proportion of the kinetic energy associated with the impact is converted to strain energy in the ball through larger elastic deformation; this energy is restored upon rebounding of

Downloaded 04 May 2010 to 171.66.16.33. Redistribution subject to ASME license or copyright; see http://www.asme.org/terms/Terms_Use.cfm

Table 1 Simulated and measured minimum drop heights of the balls

a	h_0 = 36 μm		h_0 = 66 μm	
(mm)	d_s (cm)	d_m (cm)	d_s (cm)	d_m (cm)
0.8	26	38	50	60
1.2	12	18	22	29
1.6	7	10	12	16
2.0	5	7	8	10

a = radius of the ball
h_0 = thickness of fluid layer
d_s = simulated minimum drop height
d_m = measured minimum drop height

the ball. Furthermore, the predicted coefficient of restitution of the impact process generally increases along with the pressure-viscosity coefficient of the lubricant. This prediction is sensible as a higher value of α results in more rapid increase in viscosity upon loading, thus reducing the viscous loss of the impact. However, the effect of the pressure-viscosity coefficient is far less than that of the viscosity itself, which is in agreement with the experimental results of Imado (1994). Their experiments also showed that the material with a higher Young's modulus yields a higher coefficient of restitution, which once again supports the model's prediction.

The model is quantitatively evaluated using the experimental data reported in Barnocky and Davis (1988). The experiments were conducted to delineate the conditions under which small spheres rebound, as opposed to stick, when dropped on a smooth quartz surface overlaid with a thin layer of a viscous fluid. The minimum drop heights that allowed the ball to rebound out of the fluid were determined for a number of ball sizes and fluid layer thicknesses, among other parameters. Using the parameters given in the experiments, the model calculates the corresponding minimum drop heights. A calculated rebound height of 1.0 mm above the fluid layer is made equivalent to the experimental rebound out of the fluid which was determined by simple eye detection. Table 1 shows the calculated results and the experimental data taken from Fig. 2 of Barnocky and Davis (1988). Comparison indicates that the calculated minimum drop heights underestimate their experimental counterparts or the simulated impacts are not as viscous as in the actual events. Nevertheless, the errors are relatively uniform for all four sizes of the balls, being about 30 percent when the thickness of the fluid layer is 36 μm and 20 percent when it is 66 μm. The average scattering in the experimental data was seen to be about ten percent and the values shown in Table 1 were taken from the curves fitting the data. That the simulated impacts underestimate the viscous effects of the actual events may be attributed to the very small sizes of the balls used in the experiments. With a small radius of curvature of the impact body, the viscous force generated by the fluid outside the Hertzian circle may be significant *throughout* the entire impact process.

The model is also quantitatively evaluated by comparing the results with the full numerical solutions reported in Larsson and Hoglund (1994). The difference in these two sets of results provides a measure of the error resulting from the approximations used in the equivalent-disk model. Larsson and Hoglund (1994) reported the maximum forces and the coefficients of restitution for 16 cases of the impact processes ranging from near pure viscous impact to elastically dominant impact. The sixteen cases were defined by the values of the following four dimensionless parameters: M, V_0, G, and H_0. The values of the other two parameters, P_r and $\bar{\mu}_0$, that are associated with the Roelands pressure-viscosity relation were not given. Since p_r and μ_r in the Roelands model are often chosen as 1.96×10^8 Pa and 6.33×10^{-5} Pa-s, respectively (Wang et al., 1991), $P_r = 8.71 \times 10^{-4}$ and $\bar{\mu}_0 = 948$ are used in this study, which corresponds to impact between two steel members with typical industrial lubricants. Nevertheless, the values of P_r and $\bar{\mu}_0$ are found, through numerical parametric studies, not to sensitively affect the calculated impact load and coefficient of restitution. Table 2 defines the 16 cases of the impact processes and compares the impact loads and the coefficients of restitution with those calculated by Larsson and Hoglund (1994). The comparison is reasonably good; the differences in these two sets of results are generally under ten percent for all 16 cases that span viscously to elastically dominant impact processes. Figure 3 compares the simulated time histories of the impact loads and ball velocities for Case 3. For reference, results for dry impact are also shown in the figure. The results of the equivalent-disk model are seen to have a similar pattern to the full numerical solutions. The differences in the results are seen to be comparable to the differences between the approximate results of Wells (1993) and the full numerical solutions of Davis et al. (1986) for isoviscous fluids.

The simulation using the equivalent-disk model takes a couple of seconds to complete each case on a median-grade workstation (SGI Indigo R4000). On the other hand, the simulation, not to mention numerical instability problems, would normally take two to three orders of magnitude longer by numerically solving all the field equations in time. The computational efficiency and robustness of the equivalent-disk model can lead to tractable interdisciplinary analyses of machine dynamics with impact in the lubricated kinematic pairs.

Conclusion

This paper models the impact processes between two elastic bodies with the presence of a liquid lubricant. The model is formulated making use of the concept of an equivalent disk in the impact conjunction. This use allows closed-form model equations to be derived incorporating all major engineering aspects of the problem. The effect of the lubricant on the impact load and the coefficient of restitution can be very efficiently

Table 2 Parameters and results of 16 cases of the impact processes

Case number	$M \times 10^{-13}$	$V_0 \times 10^{12}$	G	$H_0 \times 10^2$	Equivalent-disk model		Larsson et al. (1994)	
					$W_{max} \times 10^5$	e	$W_{max} \times 10^5$	e
1	7.475	1.30	3500	0.500	0.0245	0.145	0.0231	0.148
2	7.475	4.35	3500	0.500	0.3360	0.715	0.3140	0.708
3	7.475	8.70	3500	0.500	0.9460	0.872	0.8640	0.844
4	7.475	21.70	3500	0.500	3.1300	0.960	2.9000	0.933
5	7.475	43.50	3500	0.500	7.3800	0.981	6.9600	0.966
6	14.950	8.70	3500	0.500	1.5500	0.941	1.4300	0.910
7	1.490	8.70	3500	0.500	0.2170	0.486	0.1870	0.451
8	2.990	8.70	3500	0.500	0.4320	0.753	0.4010	0.680
9	0.750	8.70	3500	0.500	0.0584	0.063	0.0509	0.080
10	0.750	43.50	3500	0.500	1.4780	0.801	1.4000	0.784
11	7.475	8.70	4600	0.500	0.9180	0.859	0.8600	0.849
12	7.475	8.70	1800	0.500	0.9370	0.854	0.8690	0.825
13	7.475	8.70	3500	1.000	0.9020	0.837	0.8340	0.821
14	7.475	8.70	3500	2.500	0.8550	0.798	0.8040	0.794
15	7.475	8.70	3500	0.250	0.9960	0.913	0.8990	0.875
16	7.475	8.70	3500	0.125	1.0500	0.953	0.9490	0.931

W_{max} = dimensionless impact load
e = coefficient of restitution

Downloaded 04 May 2010 to 171.66.16.33. Redistribution subject to ASME license or copyright; see http://www.asme.org/terms/Terms_Use.cfm

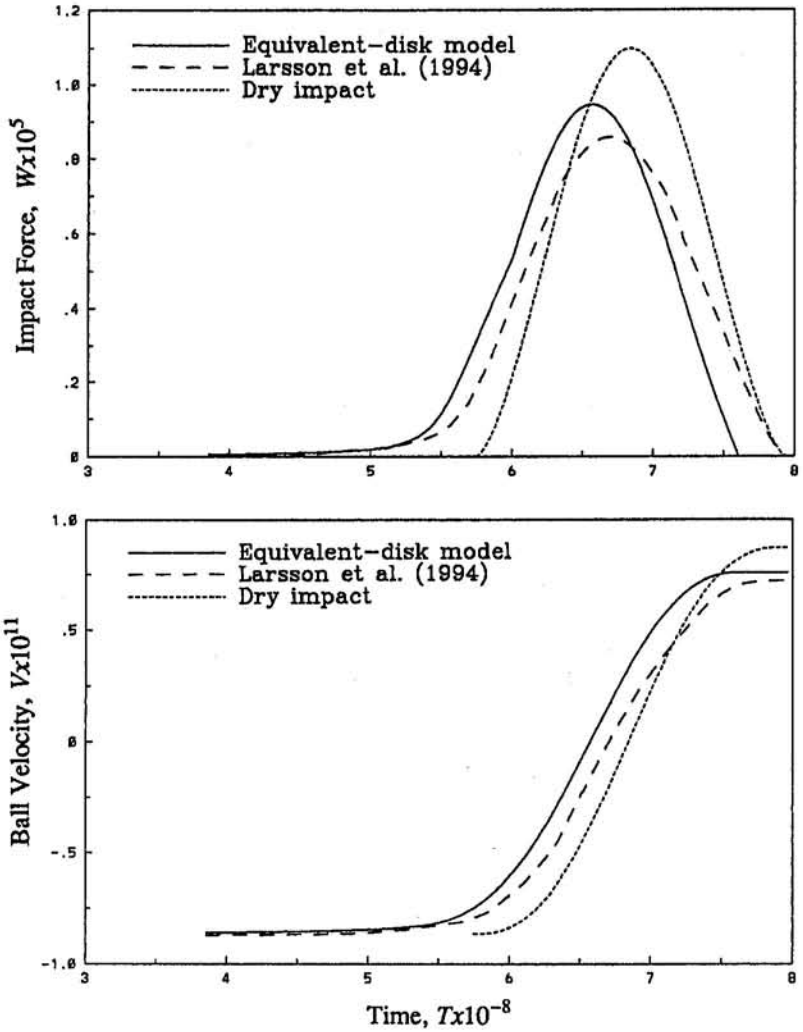


Fig. 3 Comparison of the simulated time histories of the impact process for Case 3

determined with reasonable accuracy. The modeling concepts and methodology presented in this paper may be useful in future research on interdisciplinary analyses of the dynamics of mechanical systems. Such analyses will become important and may lead to improved design of the machines when the interactions are strong between vibrations of the components and impacts in the lubricated kinematic pairs.

References

Barnocky, G., and Davis, R. H., 1988, "Elastohydrodynamic Collision and Rebound of Spheres: Experimental Verification," *Phys. Fluids,* Vol. 31, No. 6, pp. 1324–1329.

Barnocky, G., and Davis, R. H., 1989, "The Influence of Pressure-Dependent Density and Viscosity on the Elastohydrodynamic Collision and Rebound of Two Spheres," *Journal of Fluid Mechanics,* Vol. 209, pp. 501–519.

Changizi, K., and Shabana, A. A., 1986, "Pulse Control of Flexible Multibody Systems," *Computers & Structures,* Vol. 24, No. 6, pp. 875–884.

Christensen, H., 1962, "The Oil Film in a Closing Gap," *Proc. Royal Soc., London,* Vol. A226, pp. 312–328.

Davis, R. H., Serayssol, J. M., and Hinch, E. J., 1986, "The Elastohydrodynamic Collision of Two Spheres," *Journal of Fluid Mechanics,* Vol. 163, pp. 479–492.

Dowson, D., and Higginson, G. R., 1977, *Elastohydrodynamic Lubrication,* 2nd ed. Pergamon Press, New York.

Gear, C. W., 1971, *Numerical Initial Value Problems in Ordinary Differential Equations,* Prentice-Hall, New York.

Herbert, R. G., and McWhannell, D. C., 1977, "Shape and Frequency Composition of Pulses from an Impact Pair," ASME *Journal of Engineering for Industry,* Vol. 99, pp. 513–518.

Hunt, K. H., and Crossley, F. R. E., 1975, "Coefficient of Restitution Interpreted as Damping in Vibroimpact," ASME JOURNAL OF APPLIED MECHANICS, Vol. 93, pp. 440–445.

Imado, K., Miyagawa, H., Miura, A., Ueyama, N., and Hirano, F., 1994, "Behavior of Traction Oils under Impact Loads," *STLE Tribology Transactions,* Vol. 37, No. 2, pp. 378–386.

Johnson, K. L., 1985, *Contact Mechanics,* Cambridge University Press, Cambridge, U.K.

Khulief, Y. A., and Shabana, A. A., 1986, "Impact Responses of Multi-Body Systems with Consistent and Lumped Masses," *Journal of Sound and Vibration,* Vol. 104, No. 2, pp. 187–207.

Larsson, R., and Hoglund, E., 1994, "Elastohydrodynamic Lubrication at Impact Loading," ASME *Journal of Tribology,* Vol. 116, pp. 770–776.

Lee, K., and Cheng, H. S., 1971, "The Pressure and Deformation Profile between Two Colliding Lubricated Cylinders," NASA CR-1944, Washington, D.C.

Timoshenko, S., and Goodier, J. N., 1972, *Theory of Elasticity,* 3rd ed. McGraw-Hill, New York.

Veluswami, M. A., Crossley, F. R. E., and Horvay, G., 1975, "Multiple Impacts of a Ball Between Two Places, Part 2: Mathematical Modelling," ASME *Journal of Engineering for Industry,* Vol. 97B, pp. 828–835.

Wang, K. W., Liu, S. P., Hayek, S. I., and Chen, F. H. K., 1992, "On the Impact Intensity of Vibrating Axially Moving Roller Chains," ASME *Journal of Vibration and Acoustics,* Vol. 114, No. 3, pp. 397–403.

Wang, S., Cusano, C., and Conry, T. F., 1991, "Thermal Analysis of Elastohydrodynamic Lubrication of Line Contacts Using the Ree-Eyring Fluid Model," ASME *Journal of Tribology,* Vol. 113, No. 2, pp. 232–244.

Wells, J. C., 1993, "Mathematical Modeling of Normal Collision of Smooth Elastic Spheres," *Powders and Grains 93,* Proc. 2nd International Conference on Micromechanics of Granular Media, Birmingham, UK, pp. 45–50.

Yigit, A. S., Ulsoy, A. G., and Scott, R. A., 1990, "Dynamics of a Rotating Beam with Impact, Part 1: Theoretical and Computational Model," ASME *Journal of Vibration and Acoustics,* Vol. 112, pp. 65–70.

Young, P., and Wen, S., 1991, "Pure Squeeze Action in an Isothermal Elastohydrodynamically Lubricated Spherical Conjunction. Part I. Theory and Dynamic Load Results," *Wear,* Vol. 142, No. 1, pp. 1–16.

Downloaded 04 May 2010 to 171.66.16.33. Redistribution subject to ASME license or copyright; see http://www.asme.org/terms/Terms_Use.cfm

A Split Hopkinson Bar Technique to Evaluate the Performance of Accelerometers

T. C. Togami

W. E. Baker
Mem. ASME.

Department of Mechanical Engineering,
University of New Mexico,
Albuquerque, NM 87131

M. J. Forrestal
Sandia National Laboratories,
Albuquerque, NM 87185-0312
Fellow ASME

We developed a split Hopkinson bar technique to evaluate the performance of accelerometers that measure large amplitude pulses. A nondispersive stress pulse propagates in an aluminum bar and interacts with a tungsten or steel disk at the end of the bar. We measure stress at the aluminum bar-disk interface with a quartz gage and measure acceleration at the free end of the disk with an accelerometer. The rise time of the incident stress pulse in the aluminum bar is long enough and the disk length is short enough that the response of the disk can be approximated closely as rigid-body motion; an experimentally verified analytical model supports this assumption. Since the cross-sectional area and mass of the disk are known, we calculate acceleration of the rigid disk from the stress measurement and Newton's Second Law. Comparisons of accelerations calculated from the quartz gage data and measured acceleration data show excellent agreement for acceleration pulses with the peak amplitudes between 20,000 and 120,000 G (1 G = 9.81m/s^2), rise times as short as 20 μs, and pulse durations between 40 and 70 μs.

Introduction

We begin this section with the problem motivation and then discuss work related to accelerometer calibration and performance evaluation.

A goal of our current penetration technology program is to obtain a better understanding of the penetration process for geological and concrete targets. Analytical and computational models that attempt to predict the response of projectiles require material and penetration data for model verification. Most experimental studies report depth of penetration versus striking velocity data (Forrestal, Altman, Cargile, and Hanchak, 1994). However, the development of penetration models start with force on the projectile nose, so rigid-body projectile deceleration data provides more definitive information. Penetration studies that include deceleration data (Forrestal, 1986; Forrestal and Luk, 1992) use onboard recording packages that are structurally mounted within the projectiles. Current and future penetration tests include more resistive targets and projectiles with smaller masses, so projectile decelerations are expected to increase to the performance limits of available accelerometers. While current accelerometers[1] can record up to 200,000 G (1 G = 9.81m/s^2) for some transient loading conditions, we plan to use the laboratory-scale technique described in this paper to evaluate the performance of accelerometers and onboard digital recorders prior to much more expensive field tests.

In this paper, we use the terms calibration and performance evaluation. Calibration refers to an experimental procedure that determines a transducer sensitivity with an internationally accepted input calibration standard. Currently, a shaker table and interferometer arrangement (Robinson, Serbyn, and Payne, 1987) can calibrate accelerometers to 10 G (9.81m/s^2 = 1 G) with a frequency range to 10 kHz. For larger acceleration amplitudes, investigators are limited to performance evaluation experiments that compare measured accelerations with other experimental methods (Togami, 1994). Sill (1983) presents a performance evaluation technique for piezoresistive accelerometer with an amplitude range beyond 100,000 G (1 G = 9.81m/s^2). In that technique, an accelerometer mounted at the end of a Hopkinson bar responds to a nondispersive stress pulse that propagates in a 16-mm-diameter titanium bar. Because the incident stress pulse in the bar is nondispersive, Sill (1983) uses elementary bar theory to show that an integration of the accelerometer output is proportional to strain measured on the bar surface. Thus, the performance evaluation technique reported by Sill (1983) requires an integration of the accelerometer output. Bateman, Leisher, Brown, and Davie (1993) report additional results with the method first published by Sill (1983).

In this study, we present a split Hopkinson bar technique to evaluate the performance of accelerometers that does not require an integration of the accelerometer output. A nondispersive stress pulse propagates in an aluminum bar and interacts with a tungsten or steel disk at the end of the bar. We measure stress at the aluminum bar-disk interface with a quartz gage and measure acceleration at the free end of the disk with an accelerometer. The rise time of the incident stress pulse in the aluminum bar is long enough and the disk length is short enough that the response of the disk can be approximated closely as rigid-body motion; an experimentally verified analytical model supports this assumption. Since the cross-sectional area and mass of the disk are known, we calculate acceleration of the disk from the stress measurement and Newton's Second Law. Comparisons of accelerations calculated from the quartz gage data and measured acceleration data show excellent agreement for peak acceleration amplitudes between 20,000 and 120,000 G (1 G = 9.81m/s^2) using the tungsten and steel disks.

For excellent agreement between acceleration and stress measurements, one essential feature is that the impedance of the disc material must be larger than the impedance of the incident bar material. Therefore, we used an aluminum incident bar and tungsten or steel disks for our experiments. To demonstrate this requirement, we also conducted experiments with an aluminum incident bar and an aluminum disk. Results of the experiments with an aluminum disk show reasonable agreement, but not excellent agreement.

Contributed by the Applied Mechanics Division of THE AMERICAN SOCIETY OF MECHANICAL ENGINEERS for publication in the ASME JOURNAL OF APPLIED MECHANICS.

Discussion on this paper should be addressed to the Technical Editor, Professor Lewis T. Wheeler, Department of Mechanical Engineering, University of Houston, Houston, TX 77204-4792, and will be accepted until four months after final publication of the paper itself in the ASME JOURNAL OF APPLIED MECHANICS.

Manuscript received by the ASME Applied Mechanics Division, Nov. 30, 1994; final revision, Mar. 24, 1995. Associate Technical Editor: W. N. Sharpe, Jr.

[1] Endevco 7270A-200K; Endevco Corp. 30700 Rancho Viejo Road, San Juan Capistrano, CA 92675.

Copyright © 1996 by ASME

Downloaded 04 May 2010 to 171.66.16.33. Redistribution subject to ASME license or copyright; see http://www.asme.org/terms/Terms_Use.cfm

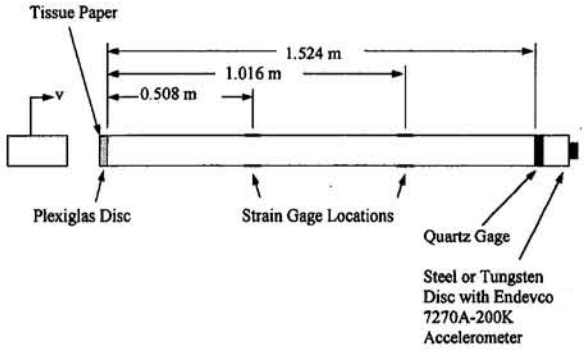


Fig. 1 Experimental apparatus

Experiment Description and Procedure

Figure 1 shows a schematic of the split Hopkinson bar apparatus. The 1.52-m-long, 19.0-mm-diameter, 7075-T651 aluminum incident bar has strain gages (Baldwin-Lima-Hamilton FAB-06N-1256) mounted diametrically opposed at 0.51 m and 1.02 m from the impact end. A 17.8-mm-long disk of tungsten or steel has a 2.54-mm-thick quartz stress gage (Valpey-Fisher) bonded to one end with conductive epoxy,[2] the diameter of the disk and the stress gage is the same diameter as the incident bar. An accelerometer (Endevco Model 7270A-200K Shock Accelerometer) is attached to the free end of the disk with screws following the manufacturer specifications.[3] Table 1 gives material properties and the mass m of the disk and mounted accelerometer. The accelerometer and mounting screws have masses 1.61×10^{-3} kg and 1.32×10^{-3} kg, respectively. We call the stress gage, disk, and accelerometer assembly the fly-away. A vacuum collar holds the fly-away in contact with the incident bar.

A 2.84-mm-thick Plexiglas disk is attached to the impact end of the incident bar with a thin layer of vacuum grease. Also, one or two layers of tissue paper are placed on the impact surface with a thin layer of vacuum grease. This combination of materials placed on the impact surface of the incident bar is called the pulse shaper.[4] A 7075-T651 aluminum, 19.0-mm-diameter projectile with length $L = 76.2$ or 152 mm is launched from a gas gun to velocity V. After the projectile strikes the pulse shaper, a nondispersive, sine-squared strain pulse that rises to a flat plateau propagates along the incident bar. The pairs of strain gages at two locations measure the incident strain pulses and check for dispersion and attenuation. Next, the strain pulse interacts with the fly-away. For tungsten and steel disks, a compression wave reflects back along the incident bar and the quartz gage measures the sum of the incident and reflected stress pulses. As shown in Table 1, quartz has nearly the same impedance as aluminum, so there are negligible reflections at the interface of the incident bar and the quartz gage. Eventually the stress at the interface between the incident bar and the fly-away becomes tensile, and the fly-away separates from the incident bar and vacuum collar. We later present data that shows the fly-away separates after the time duration of interest for the experiments. Finally, the fly-away is caught in a foam-lined catcher after about 50 mm of travel.

The rise time of the stress pulse in the incident bar is long enough and the length of the disk is short enough that the response of the disk and accelerometer with mass m can be closely approximated as rigid-body motion. Data and an analytical model support this assumption. Since the cross-sectional area and mass of the disk and mounted accelerometer are known, we calculate acceleration from the stress measurement and Newton's Second Law. Thus, acceleration calculated from the stress gage is

$$a(t) = \frac{\sigma(t)A}{m} \tag{1}$$

where $\sigma(t)$ is from the stress gage, A is the bar cross-sectional area, and m is the mass of the disc and mounted accelerometer. For our procedure, we compare accelerations calculated from the quartz stress gage with measured accelerations.

The authors point out that other wave propagation experiments that use strain gages and quartz stress gages have previously been published. Readers are referred to the works of Kenner and Goldsmith (1968), Kenner, Goldsmith, and Sackman (1969), and Kenner and Goldsmith (1969).

Model

A nondispersive stress wave propagates along the incident bar and interacts with the disk modeled as a rigid mass. A compressive wave reflects back from the bar-mass interface and the mass moves with displacement $y(t)$. For a nondispersive wave the elementary theory for rods is applicable, and from Newton's Second Law, motion of the rigid mass is given by

$$A(\sigma_i + \sigma_r) = m\frac{d^2y(t)}{dt^2}, \tag{2}$$

where A is cross-sectional area; σ_i and σ_r are the incident and reflected stresses at the bar-mass interface, taken positive in compression; m is the mass of the disk and mounted accelerometer; and t is time starting from when the incident wave strikes the bar-mass interface. For continuity, particle velocity in the bar at the interface is equal to the rigid-body velocity of the mass. Thus,

$$v_i - v_r = \frac{\sigma_i}{\rho c} - \frac{\sigma_r}{\rho c} = \frac{dy(t)}{dt}, \tag{3}$$

where v_i and v_r are the incident and reflected particle velocities, and ρ and c are the density and propagation velocity of the bar. Eliminating σ_r from (2) and (3), we obtain the equation of motion for the rigid mass:

$$\frac{d^2y}{dt^2} + \lambda\frac{dy}{dt} = \frac{2A}{m}\sigma_i, \quad \lambda = \frac{A\rho c}{m}. \tag{4}$$

For our experiments,

$$\sigma_i(t) = \sigma_m \sin^2\left(\frac{\pi t}{2\tau}\right), \quad \text{for} \quad t < \tau, \tag{5a}$$

$$\sigma_i(t) = \sigma_m, \quad \text{for} \quad t > \tau, \tag{5b}$$

where (5a, b) approximates closely results from strain measurements, τ is the rise time, and σ_m is the plateau stress. For a rigid mass originally at rest, the acceleration of the rigid mass is

Table 1 Fly-Away Descriptions

Material	ρ (kg/m^3)	c (m/s)	ρc (kg/m^{2}s)	m (kg)
Tungsten	17,200	4,610	79.3×10^6	0.0993
Steel	7,830	5,140	40.2×10^6	0.0416
Aluminum	2,710	5,040	13.7×10^6	0.0163
Quartz	2,650	5,490	14.5×10^6	0.0015

[2] Valpey-Fisher Corporation, 1994, *The User's Guide to Ultrasound Products*, 75 South Street, Hopkinton, MA 01748.

[3] Endevco General Catalog, 1991, 30700 Rancho Viejo Road, San Capistrano, CA 92675.

[4] Another pulse-shaping technique is reported by Nemat-Nasser, Isaacs, and Starrett, 1991.

Downloaded 04 May 2010 to 171.66.16.33. Redistribution subject to ASME license or copyright; see http://www.asme.org/terms/Terms_Use.cfm

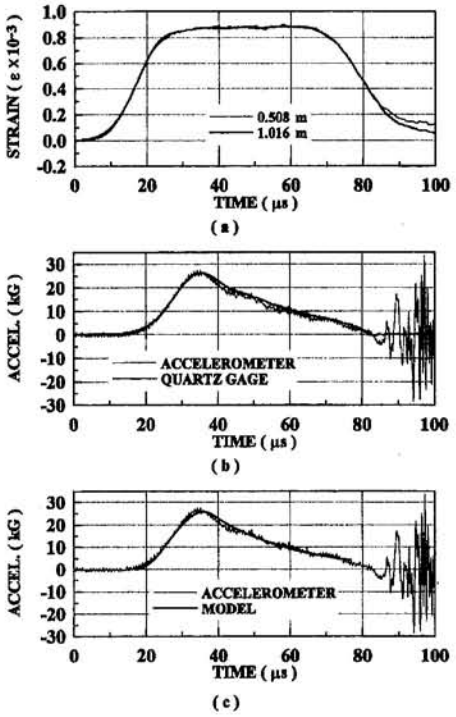


Fig. 2 Data and prediction for L = 152 mm, V = 9.36 m/s; tungsten disk and mounted accelerometer with mass 99.3 grams

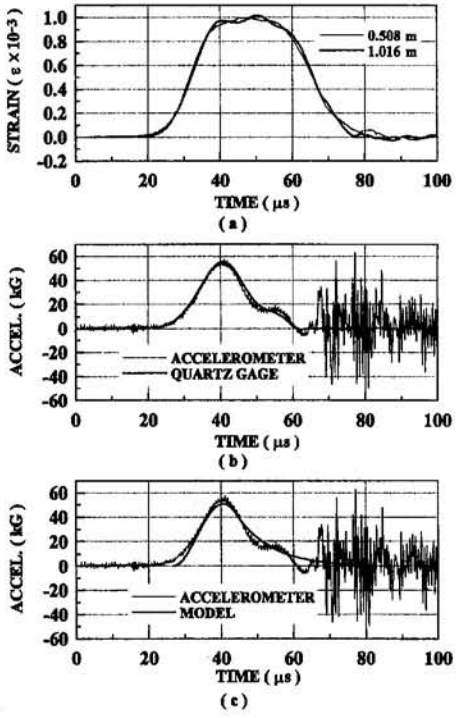


Fig. 3 Data and prediction for L = 76.2 mm, V = 13.9 m/s; steel disk and mounted accelerometer with mass 41.6 grams

$$\frac{d^2y(t)}{dt^2} = \frac{A\pi^2\sigma_m}{m(\pi^2 + \lambda^2\tau^2)} e^{-\lambda\tau} - \frac{A\pi^2\sigma_m \cos\left(\frac{\pi t}{\tau}\right)}{m(\pi^2 + \lambda^2\tau^2)} + \frac{A\lambda\pi\tau\sigma_m \sin\left(\frac{\pi t}{\tau}\right)}{m(\pi^2 + \lambda^2\tau^2)}, \quad \text{for} \quad t < \tau \quad (6a)$$

$$\frac{d^2y(t)}{dt^2} = \lambda e^{-\lambda t} e^{\lambda\tau} \left(\frac{2\sigma_m}{\rho c} - \frac{A\pi^2\sigma_m}{\lambda m(\pi^2 + \lambda^2\tau^2)} - \frac{2A\lambda\tau^2\sigma_m}{m(\pi^2 + \lambda^2\tau^2)} + \frac{A\pi^2\sigma_m}{\lambda m(\pi^2 + \lambda^2\tau^2)} e^{-\lambda\tau} \right), \quad \text{for} \quad t > \tau, \quad (6b)$$

where λ is given in (4).

Results and Discussion

Figures 2-5 show the results of our study.[5] In these figures, we present strain-time data that show the nondispersive incident strain pulses, comparisons between the accelerometer and stress gage data, and comparisons between model predictions and acceleration data. Each data channel was triggered independently from an internal trigger mode, so the time correlation among the channels of data presented in Figs. 2-5 is not known. Plots of the data were superimposed based on the first bit deviation above the noise level. Thus, zero time in Figs. 2-5 corresponds to the first bit deviation.

The strain histories in Figs. 2(*a*)-5(*a*) show that our pulse-shaping technique produces a nearly sine-squared strain pulse that rises to a flat plateau, which is the functional form used in our model (5*a*,*b*). By measuring strain time at two locations, we show that the strain pulses are nondispersive. These data justify the use of the elementary theory of wave propagation in rods for our model. The strain pulses eventually drop from the nearly flat plateaus, but by that time we acquire the information needed for the accelerometer performance evaluation. We point out that the strain measurements are only used for input to our model, which is used for estimating acceleration-time profiles

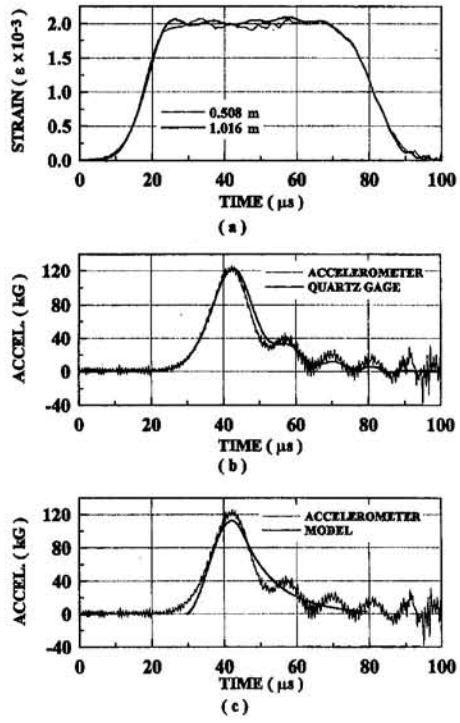


Fig. 4 Data and prediction for L = 152 mm, V = 26.2 m/s; steel disk and mounted accelerometer with mass 41.6 grams

[5] For additional results, the readers are referred to the report by Togami (1994).

Downloaded 04 May 2010 to 171.66.16.33. Redistribution subject to ASME license or copyright; see http://www.asme.org/terms/Terms_Use.cfm

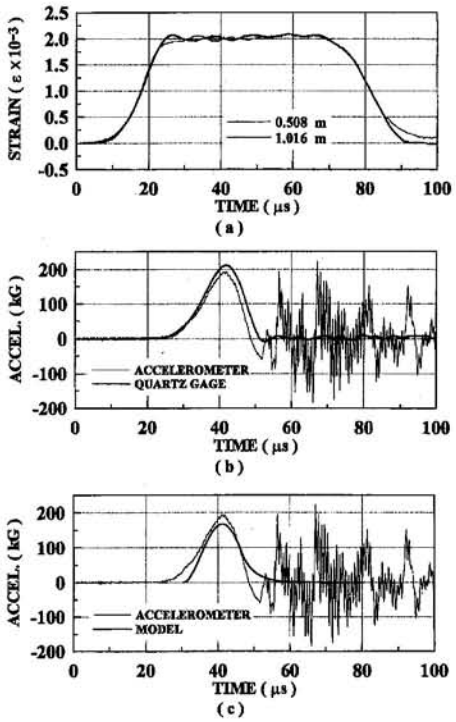


Fig. 5 Data and prediction for L = 152 mm, V = 25.9 m/s; aluminum disk and mounted accelerometer with mass 16.3 grams

prior to experimentation. In addition, the measured strain pulses were fitted with the analytical form given by (5*a, b*) for the model predictions given in Figures 2(*c*)-5(*c*).

Figures 2(*b*)-5(*b*) show comparisons of accelerometer data and acceleration-time calculated from (1) that use input from the stress gage. For the data in Fig. 2, we used a tungsten disk, and recorded a peak acceleration of about 28,000 G (1 G = 9.81 m/s^2) and a pulse width of about 70 μs. The high-frequency oscillations superimposed on the main acceleration-time profile correspond to the mounted resonant frequency stated by the manufacturer for the accelerometer (1.2 MHz).[6] The acceleration-time response after about 85 μs in Fig. 2(*b*) corresponds to the fly-away breaking away from the vacuum collar. Figure 2(*b*) shows excellent agreement between measurements from the accelerometer and the stress gage. For the data in Figs. 3 and 4 we used a steel disk. Figures 3(*b*) and 4(*b*) show peak accelerations of about 58,000 and 120,000 G (1 G = 9.81 m/s^2) and pulse widths of about 40 and 60 μs, respectively. Again, comparisons between accelerometer and stress gage measurements are in excellent agreement.

As discussed previously, we selected an aluminum incident bar and tungsten or steel disks, so the impedance of each disk was larger than the impedance of the incident bar (see Table 1). With this experimental design, a compressive stress pulse reflects back along the incident bar after the incident stress pulse strikes the higher impedance disk. Thus, the stresses acting on the disk consist of the incident and reflected stresses. This combination of stress components lengthens the loading time at the incident bar-disk interface and allows time for the particle velocities in the disk to ring up or nearly equilibrate. For this combination of materials and disk length, the disk response closely approximates that of a rigid body. To demonstrate this effect, we also conducted several experiments with an aluminum disk (Togami, 1994). For an aluminum disk there is no reflected wave at the incident bar-disk interface, so there is not enough time for the particle velocity in the aluminum disk to equilibrate. Figure 5(*b*) shows a comparison between the accelerometer and stress gage data for an aluminum disk. While the agreement in Fig. 5(*b*) is reasonable, agreement with the data in Figs. 2(*b*), 3(*b*), and 4(*b*) for tungsten or steel disks is excellent.

Figures 2(*c*)-5(*c*) show comparisons between our mathematical model and acceleration data. For input to our model, we fit the measured incident strain data with a sine-squared pulse that rises to a flat plateau (5*a,b*). While this procedure is subject to curve fitting estimates, scoping calculations with the model helped design the experiments and avoided trial experiments outside our range of interest. Comparisons of model predictions and acceleration data (Figs. 2(*c*)-5(*c*)) show our model to be a valuable experimental design tool.

Summary

We present a split Hopkinson bar technique to evaluate the performance of accelerometers that measure large amplitude pulses. A direct comparison of accelerometer data and stress gage data shows excellent agreement. Previously published techniques required an integration of the acceleration-time data for performance evaluation (Sill, 1983). We plan to use this laboratory-scale technique to evaluate the performance of accelerometers and onboard recorders prior to much more expensive penetration tests.

Acknowledgments

This work was supported by Sandia National Laboratories, Joint DoD/DOE Safe Arm & Fire and Penetration Technology Projects. The authors thank Dr. D. E. Grady for recommending Plexiglas disks for pulse shaping.

References

Bateman, V. I., Leisher, W. B., Brown, F. A., and Davie, N. T., 1993, "Calibration of a Hopkinson Bar with a Transfer Standard," *Shock and Vibration,* Vol. 1, No. 2, pp. 145–152.

Endevco General Catalog, 1991, 30700 Rancho Viejo Road, San Juan Capistrano, CA 92675.

Forrestal, M. J., 1986, "Penetration into Dry Porous Rock," *International Journal of Solids and Structures,* Vol. 22, No. 12, pp. 1485–1500.

Forrestal, M. J., and Luk, V. K., 1992, "Penetration into Soil Targets," *International Journal of Impact Engineering,* Vol. 12, No. 3, pp. 427–444.

Forrestal, M. J., Altman, B. S., Cargile, J. D., and Hanchak, S. J., 1994, "An Empirical Equation for Penetration Depth of Ogive-Nose Projectiles into Concrete Targets," *International Journal of Impact Engineering,* Vol. 15, No. 4, pp. 395–405.

Kenner, V. H., and Goldsmith, W., 1968, "Elastic Waves in Truncated Cones," *Experimental Mechanics,* Vol. 8, pp. 442–449.

Kenner, V. H., Goldsmith, W., Sackman, J. L., 1969, "Longitudinal Impact on a Hollow Cone," ASME JOURNAL OF APPLIED MECHANICS, Vol. 36, pp. 445–450.

Kenner, V. H., and Goldsmith, W., 1969, "One-Dimensional Wave Propagation Through a Short Discontinuity," *The Journal of the Acoustical Society of America,* Vol. 45, No. 1, pp. 115–118.

Nemat-Nasser, S., Isaacs, J. B., and Starrett, J. E., 1991, "Hopkinson Techniques for Dynamic Recovery Experiments," *Proc R Soc Lond,* Vol. A435, pp. 371–391.

Robinson, D. C., Serbyn, M. R., and Payne, B. F., 1987, "A Description of NBS Calibration Services in Mechanical Vibration and Shock," NBS Tech. Note 1232, National Bureau of Standards, Gaithersburg, MD.

Sill, R. D., 1983, "Shock Calibration of Accelerometers at Amplitudes to 100,000 G Using Compression Waves," Endevco Tech. Paper, TP 283, San Juan Capistrano, CA.

Sill, R. D., 1983, "Testing Techniques Involved with the Development of High Shock Acceleration Sensors," Endevco Tech. Paper, TP 284, San Juan Capistrano, CA.

Togami, T. C., 1994, "Hopkinson Bar Method for Direct Evaluation of High G Accelerometers," Thesis submitted in partial fulfillment for the Degree of Master of Science in Mechanical Engineering, University of New Mexico, Albuquerque, NM.

Valpey-Fisher Corporation, 1994, *The User's Guide to Ultrasound Products,* 75 South Street, Hopkinton, MA 01748.

[6] Endevco General Catalog, 1991.

Downloaded 04 May 2010 to 171.66.16.33. Redistribution subject to ASME license or copyright; see http://www.asme.org/terms/Terms_Use.cfm

The Effective Dilatational Response of Fiber-Reinforced Composites With Nonlinear Interface

A. J. Levy
Department of Mechanical, Aerospace and Manufacturing Engineering, Syracuse University, Syracuse, NY 13244
Mem. ASME

This paper presents a model of the dilatational response of fiber-reinforced composites for situations where the fibers interact with the matrix through a nonlinear interfacial separation mechanism. The solution to a planar solitary fiber-interface-matrix problem is employed together with the geometrically consistent composite cylinders model to obtain an exact solution for the bulk response of an elastic matrix reinforced with unidirectional elastic fibers. In the solitary fiber problem interface characterization assumes the form of a nonlinear force-separation law which couples the normal component of displacement jump to the normal component of interface traction and which requires a characteristic length for its prescription. Under decreasing values of characteristic length to inclusion radius ratio ductile or brittle decohesion or closure can occur provided the applied load, interface strength and elastic moduli of fiber and matrix are within the required bounds. Interaction effects due to finite fiber volume concentration, along with the phenomenon of brittle decohesion arising in the solitary fiber problem from the bifurcation of equilibrium separation at the fiber matrix interface, are shown to precipitate instability in the composite. An inequality relating the elastic moduli and interface properties is provided which governs the smooth or abrupt transition in composite response from rigid interface behavior to void behavior. The results are shown to apply equally well for composite geometry based on the three-phase model.

1 Introduction

In composite materials containing fiber or particulate reinforcement the interface separating matrix from inclusion is widely believed to be a dominant influence affecting the overall stiffness and damage tolerance characteristics of the composite. The improvement in a materials stiffness properties with the introduction of stiffer reinforcement can only be realized to the extent that the interface mediates effectively between matrix and inclusion. Likewise damage accumulation in a composite often depends on the character of the mechanical response of the interface that, in the case of a weak interface, may precipitate such separation phenomena as brittle or ductile decohesion. Separation phenomena at strong interfaces are often defect dominated so that interface and/or inclusion cracking governs damage accumulation. In many fiber-reinforced composite systems weak interfaces are desirable since they generally raise the toughness of the composite by keeping the reinforcement intact and therefore capable of supporting load. Improvements in toughness, however, are often at the expense of composite stiffness. This is especially true for (low) stiffness properties transverse to the fiber direction which, unlike the (high) axial stiffness which is governed by the fiber, are governed by the matrix. Accurate assessment of overall stiffness characteristics of a composite containing fibers weakly bonded to the matrix is therefore extremely important in the attempt to obtain improved composite performance.

Numerous models currently exist to obtain the effective moduli of spherical and cylindrical composite systems which, for linear elastic constituent behavior and coherently bonded interfaces, are reviewed in Christensen (1979), Hashin (1983), Aboudi (1991), and Nemat-Nasser and Hori (1993). Recently attempts have been made to extend these models to situations where the interface can separate. Achenbach and Zhu (1989, 1990) and Moran et al. (1991) have employed the finite element method and boundary element method, respectively, to study the effects of debonding on the effective moduli of fiber-reinforced systems while Pagano and Tandon (1990) have utilized the generalized self-consistent or three-phase model (Smith, 1974, 1975; Christensen and Lo, 1979) to obtain the effective properties of unidirectional composites containing fibers which can debond from the matrix. Employing the method of cells (Aboudi, 1991), Beneviste and Aboudi (1984) obtained effective properties of fiber-reinforced materials which allow for only shear interface discontinuities while Aboudi (1987) utilizes the same method and allows for linear shear and normal interface force-separation behavior. For particulate reinforced material, Hashin (1991a, 1991b) has utilized the composite spheres model (Hashin, 1962) and the generalized self-consistent model to obtain effective properties of composites with interfaces which can separate. Benveniste (1985) has used the generalized self-consistent model as well to obtain the effective properties of particulate reinforced composites containing particle interfaces which suffer only shear discontinuities. More recently Qu (1993) has employed the Mori-Tanaka method (Mori and Tanaka, 1973; Benveniste, 1987) to obtain the effective moduli of a composite containing ellipsoidal inclusions which can separate from the matrix. Because the standard material models require for their implementation the solution to a solitary inclusion-interface-matrix system the problem of obtaining effective material properties for a composite is, to a large extent, dependent

Contributed by the Applied Mechanics Division of THE AMERICAN SOCIETY OF MECHANICAL ENGINEERS for publication in the ASME JOURNAL OF APPLIED MECHANICS.

Discussion on this paper should be addressed to the Technical Editor, Professor Lewis T. Wheeler, Department of Mechanical Engineering, University of Houston, Houston, TX 77204-4792, and will be accepted until four months after final publication of the paper itself in the ASME JOURNAL OF APPLIED MECHANICS.

Manuscript received by the ASME Applied Mechanics Division, Dec. 19, 1994; final revision, June 22, 1995. Associate Technical Editor: J. N. Reddy.

Copyright © 1996 by ASME

Downloaded 04 May 2010 to 171.66.16.33. Redistribution subject to ASME license or copyright; see http://www.asme.org/terms/Terms_Use.cfm

on the availability of the elastic field solutions to the solitary problem. For the case of a unidirectional fiber-reinforced composite which can reasonably be regarded as having effective transverse isotropic and homogeneous material properties this amounts to the solution of the solitary problem under a variety of loading conditions.

In all of the work just cited, the interface was characterized by a linear relation between interfacial traction and interfacial displacement jump (or, if the interface has finite thickness, a linear interphase constitutive law) so that the phenomenon of cavity formation by interfacial decohesion was not accounted for. (The linear interface force law has the additional drawback of predicting material interpenetration at the fiber-matrix interface when the composite is subjected to complex loading.) This paper represents a natural extension of existing models in that a more realistic nonlinear interface separation mechanism is considered in the problem of effective transverse bulk response of a composite containing random distributions of unidirectional linear elastic fibers embedded in a linear elastic matrix in dilute and nondilute concentration. The following section of the paper is concerned with solutions of the rotationally symmetric solitary inclusion problem in different geometrical configurations consistent with the dilute approximation, the composite cylinders model, and the three-phase model. The interface is assumed to be characterized by the uniform, physically based interface force law of Ferrante, Smith, and Rose (1982). Rotationally symmetric equilibrium interface separations and elastic field solutions are sought as functions of remote load, interface parameters, and matrix and inclusion elastic moduli. An analysis of the problem of bifurcation of equilibrium separation at the inclusion-matrix interface under decreasing values of characteristic length to inclusion radius ratio is carried out as well revealing three types of separation behavior (ductile decohesion, brittle decohesion, closure). The third section of the paper is concerned primarily with the implementation of the solitary fiber-interface-matrix solution in the composite cylinders model and an exact solution, consistent with this geometry, is obtained for the effective bulk response of the composite. Results for the dilute approximation are presented there as well. In the concluding section a composite geometry based on the three-phase model is shown to yield identical results obtained for the composite cylinders model. An appendix collects some material not included in the main text.

2 The Solitary Inclusion-Interface-Matrix Problem

Consider three concentric circular regions composed of an inner circle Ω_1 (the fiber cross section) bounded by the interface $\partial\Omega_{12}$, an inner circular annulus $\Omega_2 - \Omega_1$ bounded by interfaces $\partial\Omega_{12}$, $\partial\Omega_{2\mathcal{B}}$, and an outer circular annulus $\mathcal{B} - \Omega_2$ bounded by interface $\partial\Omega_{2\mathcal{B}}$ and surface $\partial\mathcal{B}$ (Fig. 1). This geometrical configuration is sufficiently general to describe geometries applicable to the dilute approximation model ($\mathcal{B} = \Omega_2$ unbounded), the composite cylinders model ($\mathcal{B} = \Omega_2$), and the three-phase model ($\mathcal{B}$ unbounded). Assume that Ω_1 has elastic bulk and shear moduli κ_1, μ_1, $\Omega_2 - \Omega_1$ has elastic moduli κ_2, μ_2 while $\mathcal{B} - \Omega_2$ has elastic moduli κ^*, μ^*. Given a cartesian coordinate system[1] with origin at the inclusion center, point (x_1, x_2) and base vectors $\mathbf{e}_1$, $\mathbf{e}_2$, introduce a polar coordinate system with coordinates (r, θ) and base vectors $\mathbf{e}_r$, $\mathbf{e}_\theta$. The simplest problem of uniform separation at a circular interface $\partial\Omega_{12}$ (characterized by radius r_1) arises when the displacement vector applied to the outer surface $\partial\mathcal{B}$ (characterized by radius R) is uniform and equibiaxial, i.e., $\mathbf{u} = \epsilon R\mathbf{e}_r$ where 2ϵ is the plane-strain dilatation given by the two-dimensional trace of the strain tensor (tr $\mathbf{E}$). In what is to follow the interface $\partial\Omega_{12}$ is assumed to be characterized by a nonlinear uniform (coordinate independent) constitutive equation relating the components of interface traction to components of interface displacement jump. If only normal interfacial traction develops from the normal component of displacement jump then, owing to rotational symmetry, the force law assumes the form

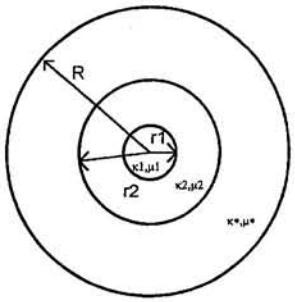


Fig. 1 Fiber-matrix composite geometry

$$\mathbf{s}_I(\mathbf{n}) = f([u_r])\mathbf{n}, \tag{1}$$

where $\mathbf{s}_I(\mathbf{n})$ is the interface traction vector acting on the interface $\partial\Omega_{12}$ and f is a scalar function of radial interface displacement jump $[u_r]$. Then provided that the interfacial separation is constrained to remain rotationally symmetric for all parameter values the equation governing the equilibrium interface displacement jump can be obtained from elementary rotationally symmetric stress and displacement fields. Thus, in each of the regions Ω_1, $\Omega_2 - \Omega_1$, $\mathcal{B} - \Omega_2$ assume that the stress and displacement fields are of the form

$$\begin{aligned} S_{rr} &= 2\kappa C - 2\mu C' r^{-2}, \\ S_{\theta\theta} &= 2\kappa C + 2\mu C' r^{-2}, \\ u_r &= Cr + C' r^{-1}, \end{aligned} \tag{2}$$

where μ is the shear modulus and κ is the plane-strain bulk modulus given by the sum of the two Lame constants $(\lambda + \mu)$. Furthermore, the moduli will take on different values in each of the three regions so that there are six constants (two in each of the three regions Ω_1, $\Omega_2 - \Omega_1$, $\mathcal{B} - \Omega_2$). The constants are obtained from boundary conditions of traction, continuity, and regularity and are given by

$$\begin{aligned} &\text{Lim } u_r \text{ bounded}, \ r \downarrow 0, \\ &S_{rr}(r \uparrow r_1) = f, \\ &S_{rr}(r \downarrow r_1) = f, \\ &S_{rr}(r \uparrow r_2) = S_{rr}(r \downarrow r_2) \\ &u_r(r \uparrow r_2) = u_r(r \downarrow r_2) \\ &u_r(r = R) = \epsilon R, \end{aligned} \tag{3}$$

where r_2 is the radius of the circle Ω_2. The application of the boundary conditions (3) to elastic fields of the form (2) yields a sixth-degree matrix equation $\mathbf{Ac} = \mathbf{b}$ where

$$\mathbf{A} = \begin{bmatrix} 0 & 1 & 0 & 0 & 0 & 0 \\ 2\kappa_1 & -2\mu_1 r_1^{-2} & 0 & 0 & 0 & 0 \\ 0 & 0 & 2\kappa_2 & -2\mu_2 r_1^{-2} & 0 & 0 \\ 0 & 0 & 2\kappa_2 & -2\mu_2 r_2^{-2} & -2\kappa^* & 2\mu^* r_2^{-2} \\ 0 & 0 & r_2 & r_2^{-1} & -r_2 & -r_2^{-1} \\ 0 & 0 & 0 & 0 & R & R^{-1} \end{bmatrix}$$

$$\mathbf{b} = [0 \quad f \quad f \quad 0 \quad 0 \quad \epsilon R]^T, \tag{4}$$

and $\mathbf{c}$ is the vector of constants (C_1, C_2 associated with Ω_1, C_3, C_4 associated with $\Omega_2 - \Omega_1$ and C_5, C_6 associated with $\mathcal{B} - \Omega_2$). The solution is straightforward and, for the case where $\mathcal{B}$ is unbounded, i.e., $R \to \infty$, is given by

[1] Tensor notation used in this paper is consistent with Gurtin (1984).

Downloaded 04 May 2010 to 171.66.16.33. Redistribution subject to ASME license or copyright; see http://www.asme.org/terms/Terms_Use.cfm

$$C_1 = \frac{f}{2\kappa_1},\ C_2 = 0,\ C_3 = \frac{1}{2}\frac{2(\kappa^* + \mu^*)\epsilon - f(1 - \mu^*/\mu_2)c}{\kappa_2 + \mu^* - \kappa_2(1 - \mu^*/\mu_2)c},$$

$$C_4 = \frac{r_1^2}{2}\frac{2\kappa^*\epsilon(\kappa_2/\mu_2 + (\kappa_2/\kappa^*)(\mu^*/\mu_2)) - f(\kappa_2/\mu_2 + \mu^*/\mu_2)}{\kappa_2 + \mu^* - \kappa_2(1 - \mu^*/\mu_2)c},$$

$$C_5 = \epsilon,$$

$$C_6 = \frac{r_2^2}{2}\frac{2\kappa^*\epsilon(1 + (\kappa_2/\mu_2)c + (\kappa_2/\kappa^*)c - \kappa_2/\kappa^*) - r_2^3 cf(1 + \kappa_2/\mu_2)}{\kappa_2 + \mu^* - \kappa_2(1 - \mu^*/\mu_2)c}, \tag{5}$$

where the last row in matrix **A** of (4) has been modified to account for the boundary condition $E_{rr} = E_{\theta\theta} = \epsilon$, $r \to \infty$ which now replaces the last condition in (3). Note that in (5) c is the fiber volume concentration defined to be r_1^2/r_2^2. Expressions for the stress and displacement fields in Ω_1, $\Omega_2 - \Omega_1$, and $\mathcal{B} - \Omega_2$ follow directly from (2) and (5). An equation governing the equilibrium displacement jump at the interface $\partial\Omega_{12}$ can be obtained from (2) and (5) and the relation $[u_r] = \text{Lim } u_r(r \downarrow r_1) - \text{Lim } u_r(r \uparrow r_1)$. Thus,

$$u = h\kappa^*\epsilon - \alpha f(u), \tag{6}$$

where u is the nondimensionalized displacement jump $[u_r]/r_1$, and the parameters h, α are given by

$$h = \frac{1 + \mu^*/\kappa^* + (\kappa_2/\kappa^*)(\mu^*/\mu_2) + \kappa_2/\mu_2}{\kappa_2 + \mu^* - (\kappa_2 - \mu^*\kappa_2/\mu_2)c},$$

$$\alpha = \frac{1}{2}\frac{(1 - \mu^*/\mu_2)c + \frac{3}{4}\kappa_2/\mu_2 + \mu^*/\mu_2}{\kappa_2 + \mu^* - (\kappa_2 - \mu^*\kappa_2/\mu_2)c} + \frac{1}{2\kappa_1}. \tag{7}$$

For the case where $\mathcal{B} = \Omega_2$, i.e., $r_2 \uparrow R$, the constants can be obtained by obvious modifications of (3) and (4) and are given by

$$C_1 = \frac{f}{2\kappa_1},\quad C_2 = 0,\quad C_3 = \frac{1}{2}\frac{2\mu_2\epsilon + fc}{\mu_2 + \kappa_2 c},$$

$$C_4 = \frac{r_1^2}{2}\frac{(2\kappa_2\epsilon - f)}{\mu_2 + \kappa_2 c}. \tag{8}$$

As in the previous case expressions for stresses and displacements in the regions Ω_1 and $\mathcal{B} - \Omega_1$ follow directly from (2) together with the constants C_i. The interface equation for this geometrical configuration is of the form (6) with constants h and α given by

$$h = \frac{1 + \mu_2/\kappa_2}{\mu_2 + \kappa_2 c},$$

$$\alpha = \frac{1}{2}\frac{(1 + \mu_2/\kappa_1) - (1 - \kappa_2/\kappa_1)c}{\mu_2 + \kappa_2 c}. \tag{9}$$

Finally when $\mathcal{B} = \Omega_2$ unbounded, i.e., $r_2 \uparrow R \uparrow \infty$, the constants assume the form

$$C_1 = \frac{f}{2\kappa_1},\quad C_2 = 0,\quad C_3 = \epsilon,\quad C_4 = \frac{r_1^2}{2}\frac{2\kappa_2\epsilon - f}{\mu_2}, \tag{10}$$

so that the interface equation, for this case, has the form (6) with constants h and α given by

$$h = \frac{1}{\kappa_2} + \frac{1}{\mu_2},\quad \alpha = \frac{1}{2\kappa_1} + \frac{1}{2\mu_2}. \tag{11}$$

With the prescription of the constitutive equation for the interface $f(u)$ the analysis of (6) can proceed for a particular geometry as characterized by (7), (9), or (11). In this work the interface force will be taken in the form

$$f(u) = e\sigma_{\text{MAX}}\beta(r_1/\delta)u\exp(-\beta r_1 u/\delta), \tag{12}$$

where $\delta(>0)$ is the characteristic interface force length, $\sigma_{\text{MAX}}(>0)$ is the interface strength, e is exp(1), and β is a fit parameter, which can be arbitrarily chosen to be five provided δ is regarded as a phenomenological parameter. This value of β is approximately the value for which the work of separation of (12) is equal to the work of separation for the third-degree polynomial approximation of $f(u)$. Note that the maximum value of f is σ_{MAX}, which occurs at $u = \beta^{-1}\delta/r_1$, and the interface traction f vanishes asymptotically with increasing u (Fig. 2). The interface constitutive law (12) was developed by Ferrante, Smith, and Rose (1982) from first principles and governs the adhesive properties of bimetallic interfaces. It is universal in the sense that it is derived from a single binding energy relation which describes adhesion and cohesion in metals. The functional form (12), however, is much more general in that it can describe the adhesive and cohesive properties of a wide variety of material interfaces (Ferrante et al., 1982; Cherepanov, 1979; Smith and Horn, 1990). Now substitute f given by (12) into (6), the equation governing the interface displacement jump, to get

$$F_\rho(\omega) = h\kappa^*\epsilon - \rho\omega - (\alpha e\sigma_{\text{MAX}})\beta\omega e^{-\beta\omega} = 0, \tag{13}$$

where the nondimensional length parameter $\rho\ (=\delta/r_1)$ has been introduced and $\omega\ (=ur_1/\delta)$ is the normalized (with respect to characteristic force length) interface displacement jump.

The behavior of solutions of (13) have been completely described in Levy (1994) for the case where $\mathcal{B} = \Omega_2$ unbounded. There it was demonstrated that, under decreasing values of length parameter, three regimes of rotationally symmetric separation behavior (ductile decohesion, brittle decohesion, closure) can occur provided the remote load, interface strength, and elastic moduli are within certain bounds. The same behavior applies to the other two geometries considered provided the correct constants are chosen, i.e., (7) or (9). In particular, for values of the ratio $\sigma_{\max}(\kappa^*\epsilon)^{-1}$ which are greater than a nondimensional function h/α of elastic moduli, the interfacial separation monotonically decreases to zero with decreasing length parameter (closure). It can be shown as well that for the ratio $\sigma_{\max}(\kappa^*\epsilon)^{-1}$ contained within the interval $(0.6806\ h/\alpha,\ h/\alpha)$ the interfacial separation eventually jumps discontinuously under decreasing length parameter (brittle decohesion) while for $\sigma_{\max}(\kappa^*\epsilon)^{-1}$ less than $0.6806h/$

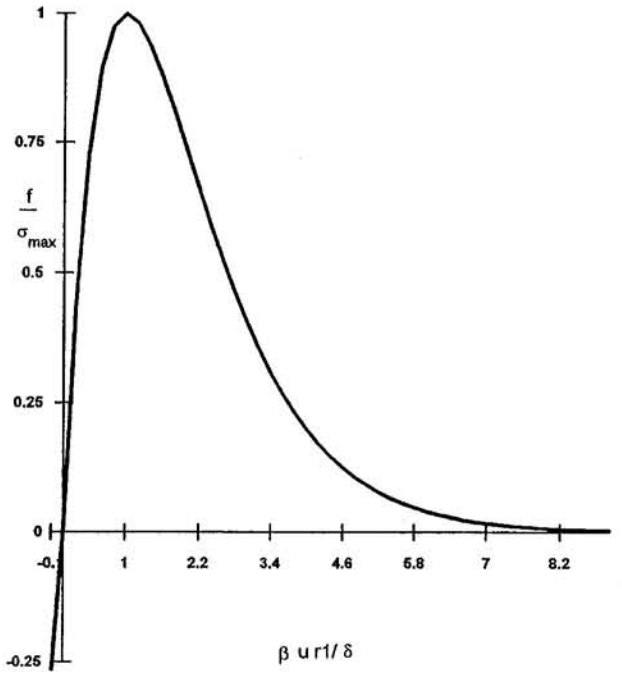


Fig. 2 The interface force law

Downloaded 04 May 2010 to 171.66.16.33. Redistribution subject to ASME license or copyright; see http://www.asme.org/terms/Terms_Use.cfm

α the interfacial separation increases gradually under decreasing length parameter (ductile decohesion).

3 The Effective Transverse Bulk Modulus

The idea of obtaining effective properties of composites that have constituent interfaces that can separate as initial debonding through complete decohesion is particularly attractive since the effective properties so obtained would provide a physically based model for damage accumulation. Based on the results of the solitary fiber-interface-matrix problems described in the previous section, this idea is developed here for the simplest case of composite aggregate response, i.e., transverse bulk behavior of a unidirectional fiber composite system.

3.1 Formulation. It is well known that a composite consisting of randomly distributed isotropic and unidirectional elastic fibers embedded in an elastic matrix may be modeled, through a representative volume element, as effectively homogeneous and transversely isotropic. This is true provided that three length scales exist such that a characteristic dimension at the fiber-reinforcement level is much smaller than the size of the representative volume element (with effective properties of the composite), which in turn is much smaller than a characteristic dimension of the composite body. For such a material the aggregate response is completely characterized by five moduli. In this paper our sole concern is the transverse (or plane-strain) bulk modulus (κ^*) which relates equibiaxial, transversely plane stresses and strains through the relation

$$\sigma = 2\kappa^*\epsilon, \tag{14}$$

where the base vectors $\mathbf{e}_1$, $\mathbf{e}_2$ lie in the plane perpendicular to the fiber length and the quantity 2σ is defined as the two-dimensional trace of the stress tensor (tr $\mathbf{S}$). A principal result of composite materials theory relates the effective moduli of the composite to the moduli and phase volume averages of its constituents provided the mean strain (or stress) in an inclusion (fiber) phase (Ω_1) is known as a function of prescribed (uniform) boundary condition. This relationship, for the case of the transverse bulk modulus, is presented here without derivation (see Benveniste, 1985; Aboudi, 1991) and is given by

$$\kappa^* = \kappa_2 + c(\kappa_1 - \kappa_2)\frac{\overline{\epsilon}_1}{\epsilon_H} - \kappa_2\frac{a}{\epsilon_H}, \tag{15}$$

where κ^* is the effective transverse bulk modulus of the composite, $\kappa_1(\kappa_2)$ is the modulus of the fiber (matrix), c (=vol(Ω_1)/vol($\mathcal{B}$)) is the phase volume average of the fiber, and $\overline{\epsilon}_1$, ϵ_H are, respectively, the (plane) dilatational mean strain in the fiber phase and the uniform dilatational strain applied on the boundary $\partial\mathcal{B}$, i.e.,

$$\mathbf{u} = \epsilon_H R\mathbf{e}_r \text{ on } r = R. \tag{16}$$

The quantity a represents the effects of interface separation and is defined, for uniform separation by

$$a = \frac{1}{2 \text{ vol } (\mathcal{B})}\int_{\partial\Omega_1}[\mathbf{u}]\cdot\mathbf{n}dA = uc, \tag{17}$$

where u is the normalized (with respect to inclusion radius r_1) radial interfacial separation introduced in the previous section. (Analogous results may be written for the traction problem.) Expressions (15) and (17) can be used along with the solution to a solitary fiber-interface-matrix problem to obtain the effective modulus κ^* provided a geometrically consistent composite materials model is employed. Although other models may be considered as well, in this paper we concentrate primarily on the composite cylinders model first introduced by Hashin and Rosen (1964).

The geometry associated with the composite cylinders model consists of an infinitely long cylindrical fiber (radius r_1) surrounded by a cylindrical cage of matrix material (radius r_2), i.e., $\mathcal{B} = \Omega_2$ in Fig. 1. In order to obtain a volume filling configuration composite cylinders are assumed to vary in diameter down to the vanishingly small provided the ratio r_1/r_2 is fixed. For the composite cylinder cross section of Fig. 1 the mean strain in the fiber $\overline{\epsilon}_1$ under boundary condition ϵ_H, follows from (2) and (8) and is $f/2\kappa_1$. Then (15) and (17) yield the modulus (κ_c^*) for an equivalent homogeneous cylinder

$$\kappa_c^* = \kappa_2 + c(\kappa_1 - \kappa_2)\frac{f(u)}{2\kappa_1\epsilon_H} - \kappa_2 c\frac{u}{\epsilon_H}, \tag{18}$$

where it is understood that the applicability of (18) to the entire composite will need further consideration (see Section 3.2). Analogous results for the case where an equibiaxial traction is prescribed to the outer composite cylinder boundary are given in the Appendix. Note that κ_c^* depends on the interface displacement jump (u) which plays the role of damage variable in the model. Thus, in order to complete the description, (6) and (12) (with h and α given by (9)) must be coupled to (18). Also note that relation (18) can be obtained in an alternative manner by applying the displacement boundary condition to the composite cylinder and an equivalent homogeneous cylinder with effective property κ_c^*. By requiring the tractions at the outer boundaries of the two cylinders to be equal relation (18) is recovered. The equivalent modulus κ_c^*, under the limiting conditions of coherent interface behavior ($u = 0$, $f = h\kappa_2\epsilon/\alpha$) and behavior in which the interface supports no traction ($\sigma_{MAX} = 0$), is given by

$$\kappa_c^* = \kappa_2 + \frac{c(\kappa_1 - \kappa_2)(\kappa_2 + \mu_2)}{\kappa_1 + \mu_2 - c(\kappa_1 - \kappa_2)},$$

$$\kappa_v^* = \kappa_2 - \frac{c\kappa_2(\kappa_2 + \mu_2)}{\mu_2 + c\kappa_2}, \tag{19}$$

where κ_c^* is the equivalent modulus for a composite cylinder containing a rigidly bonded fiber, κ_v^* is the equivalent modulus for a composite cylinder containing a cylindrical void, and μ_2 is the shear modulus of the matrix. The forms given in (19) are consistent with Hashin and Rosen (1964) who proved that κ_c^* and κ_v^* are applicable to a representative volume element of a composite consisting of a volume filling configuration of composite cylinders of varying diameters ranging in size down to the vanishingly small provided the ratio r_1/r_2 remains constant. Note that when fiber and matrix interact through the nonlinear force law (1) in order to maintain geometrically similar composite cylinders f (and u) in (18), (6) and (12) must be the same for all cylinders which form the volume filling configuration. This can be true if the ratios r_1/r_2, ρ (=δ/r_1) are constant for all cylinders. In order to see this write (14), (18), (6), and (12) in the form

$$\sigma = 2\kappa_2\epsilon\frac{(1-c)\mu_2}{\mu_2 + c\kappa_2} + \frac{c(\kappa_2 + \mu_2)}{\mu_2 + c\kappa_2}e\sigma_{MAX}\beta\omega e^{-\beta\omega},$$

$$0 = -\rho\omega + \frac{\kappa_2 + \mu_2}{\mu_2 + c\kappa_2}\epsilon - \frac{1}{2}\left[\frac{1-c}{\mu_2 + c\kappa_2} + \frac{1}{\kappa_1}\right]e\sigma_{MAX}\beta\omega e^{-\beta\omega}, \tag{20}$$

where ω (=ur_1/δ) is independent of r_1. (Recall that u is the interface displacement jump normalized with respect to fiber radius r_1.) Clearly a constant phase volume average c and force length parameter ρ imply geometrical similarity of the cylinders. The fact that ρ (=δ/r_1) is required to be constant for all cylinders is somewhat unsatisfying physically for it would imply that the characteristic force length of an interface changes in constant proportion to the fiber radius. This fact has been ex-

Downloaded 04 May 2010 to 171.66.16.33. Redistribution subject to ASME license or copyright; see http://www.asme.org/terms/Terms_Use.cfm

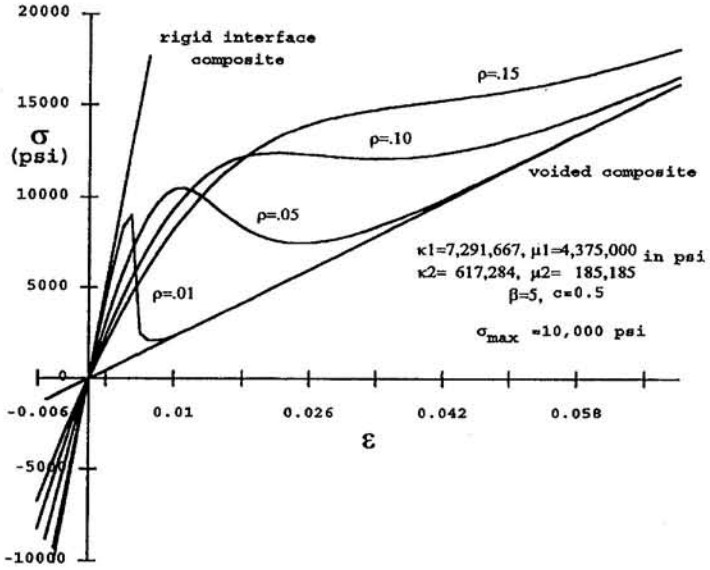


Fig. 3 Composite response for various force length to fiber radius ratios

pressed by Hashin (1991b) in the context of effective properties of particulate reinforced composites whose interfaces separate linearly.

Figure 3 illustrates the behavior of the model ((14), (18), (6), (12), (9)) utilizing mechanical properties for a glass fiber-reinforced epoxy matrix and assuming that the interface can be modeled by the force law (12). The interface strength σ_{MAX} is chosen to be $\frac{1}{50}$ of the matrix elastic modulus. Figure 3 depicts stress (σ) versus strain (ϵ) curves for varying characteristic length to inclusion radius ratios ρ at a fiber phase volume average of 0.5. Also included are the lines depicting the limiting behavior of the rigid interface composite and the voided composite (19). As anticipated a transition occurs between the two limiting cases with increasing stress and, depending on the range of action of the interface force law $\delta\ (=\rho r_1)$, the transition can be gradual or abrupt.

3.2 Variational Bounding. In order to prove that the modulus in (18) applies to an entire representative volume element of the composite we employ energetic arguments along the lines of Hashin and Rosen (1964). Thus we show that upper and lower bounds to the true strain energy of the composite, based on fields obtained from the composite cylinder displacement and traction problems, coincide. First, assume that the displacement field in a composite cylinder with displacement vector (16) prescribed on its outer boundary forms a kinematically admissible displacement field[2] for the displacements in the entire representative volume element of the composite. That this is true follows from the fact that a rigid-body displacement superimposed on the boundary displacement of a composite cylinder, while leaving the strain energy unaffected, renders homogeneous boundary displacements for the representative volume element. Now the potential energy $\Phi\{\epsilon\}$ stored in a single composite cylinder subject to displacement condition (16) can be calculated from (2), (6), (8), and (9) and is given by

$$\Phi\{\epsilon\} = \left[\frac{2\kappa_2\mu_2(1-c)}{\mu_2 + c\kappa_2}\epsilon^2 + \left(\frac{c(1-c)}{2(\mu_2 + c\kappa_2)} + \frac{c}{2\kappa_1}\right)f^2 + 2c\int^u f\,d\tau\right]v(\mathcal{B}), \quad (21)$$

where $v(\mathcal{B})$ is the volume of the composite cylinder. (Note that the vanishing of the derivative $D_u\Phi$ implies relation (6) while $D_\epsilon[v^{-1}(\mathcal{B})\Phi] = 4\kappa_c^*\epsilon$.) Then an upper bound to the potential energy for the representative volume element of the composite, based on the admissible displacement field, is $\Phi\{\epsilon\}v/v(\mathcal{B})$ where v is the volume of the representative volume element. Next, assume that the homogeneous stress field, produced by the traction boundary condition (A1) applied to the composite cylinder boundary, is a statically admissible stress field[3] for the entire representative volume element. Then the complementary energy for a single composite cylinder is given by

$$\Psi\{\sigma\} = \left[\frac{\mu_2 + c\kappa_2}{2(1-c)\kappa_2\mu_2}\sigma^2 - \left(\frac{c\mu_2 + \kappa_2}{2(1-c)\kappa_2\mu_2} + \frac{1}{2\kappa_1}\right)cf^2 - 2c\int^u f\,d\tau\right]v(\mathcal{B}), \quad (22)$$

where use has been made of (2), (A2), (A3). (The vanishing of the derivative $D_f\Psi$ implies relation (A3) while $D_\sigma[v^{-1}(\mathcal{B})\Psi] = (\kappa_\sigma^*)^{-1}\sigma$ where κ_σ^* is given by (A4).) An upper bound to the complementary energy for the representative volume element of the composite, based on the statically admissible stress field, is then given by $\Psi\{\sigma\}v/v(\mathcal{B})$. The potential (complementary) energy given in (21) ((22)) may be regarded as the strain (stress) energy for an equivalent homogeneous cylinder owing to the displacement (traction) condition applied on its surface. Now upper and lower bounds on the true strain energy (U) of the displacement problem follow from the bounding theorem (Gurtin, 1984)

$$\int_{\partial\mathcal{B}} \bar{\mathbf{s}}\cdot\hat{\mathbf{u}}\,da - U_k\{\bar{\mathbf{S}}\} \le U \le U_c\{\tilde{\mathbf{E}}\}, \quad (23)$$

where $\tilde{\mathbf{E}}$ is a kinematically admissible strain field, $\bar{\mathbf{S}}$ is a statically admissible stress field with $\bar{\mathbf{s}}$ the corresponding surface traction, and $U_k\{\bar{\mathbf{S}}\}$ ($U_c\{\tilde{\mathbf{E}}\}$) the stress (strain) energy. Alternatively, for the traction problem with zero body force the bounding theorem takes the form

$$\int_{\partial\mathcal{B}} \hat{\mathbf{s}}\cdot\tilde{\mathbf{u}}\,da - U_c\{\tilde{\mathbf{E}}\} \le U \le U_k\{\bar{\mathbf{S}}\}, \quad (24)$$

where $\tilde{\mathbf{u}}$ is a kinematically admissible displacement field, $\tilde{\mathbf{E}}$ the

[2] That is, one that satisfies the displacement boundary condition and is twice continuously differentiable.

[3] One that satisfies the equilibrium equation and traction boundary condition.

Downloaded 04 May 2010 to 171.66.16.33. Redistribution subject to ASME license or copyright; see http://www.asme.org/terms/Terms_Use.cfm

corresponding strain field, and $\bar{\mathbf{S}}$ a statically admissible stress field. For the present problem (23) may be written as

$$2v\sigma\epsilon - \Psi\{\sigma\}v/v(\mathcal{B}) \leq U \leq \Phi\{\epsilon\}v/v(\mathcal{B}), \quad (25)$$

where Φ, Ψ are given by (21), (22). In order to show that the left and right sides of the inequality (25) coincide first, note that for the (composite cylinder) displacement problem

$$\sigma = 2\kappa_\epsilon^*(\epsilon)\epsilon \quad (26)$$

(with κ_ϵ^* given by (18)) while for the (composite cylinder) traction problem

$$\epsilon = (2\kappa_\sigma^*(\sigma))^{-1}\sigma \quad (27)$$

(with κ_σ^* given by (A4)). By solving (27) for σ, (26) is recovered so that $\kappa_\epsilon^*(\epsilon) = \kappa_\sigma^*(\sigma(\epsilon))$. To show equality of upper and lower bounds to the strain energy simply substitute (26) and (22) into the left side of (25) taking into account (21). Thus, the strain energy of a representative volume element of the composite is given by $U = \Phi\{\epsilon\}$ and the stress-strain relation follows from

$$\sigma = D_\epsilon(v^{-1}U) = 2\kappa^*\epsilon, \quad (28)$$

where κ^* is the strain dependent bulk modulus of the entire composite which is given by (18).

3.3 Bifurcation of Composite Response. In order to analyze bifurcation in the effective composite response consider the constitutive relation (14), (18), (6), and (12) to be represented symbolically in the continuum damage form

$$\sigma = \hat{\sigma}(\epsilon, \omega), \quad g(\epsilon, \omega) = 0, \quad (29)$$

where $\hat{\sigma}$ and g are defined in (20). In (29) the first equation characterizes the stress-strain response while the second characterizes the state of internal damage in the composite at strain ϵ arising from interfacial decohesion. Here, the "damage" variable ω physically represents the average and normalized separation of the fiber-matrix interface. If the first equation in (29) is written as $H(\sigma, \epsilon, \hat{\omega}(\epsilon)) = 0$ then in order for a C^1 function $\hat{\epsilon}$ to exist near an equilibrium (σ_0, ϵ_0) satisfying $H = 0$ it is required that $D_\epsilon H(\sigma_0, \sigma_0)$ be C^1 and nonvanishing. A necessary condition for bifurcation is therefore the vanishing of the derivative (zero slope of the $\sigma - \epsilon$ curve) or the loss of its continuity (infinite slope of the $\sigma - \epsilon$ curve). Using the expressions in (20) it is a straightforward calculation to arrive at the derivative

$$D_\epsilon H = -\frac{d\hat{\sigma}}{d\epsilon} = -\frac{\partial\hat{\sigma}}{\partial\epsilon} - \frac{\partial\hat{\sigma}}{\partial\omega}\frac{h\kappa_2}{\rho + \alpha D_\omega f}, \quad (30)$$

where f is the interface force (12) and the derivatives occuring on the right-hand side of (30) are bounded. The vanishing of (30) yields the following necessary condition for bifurcation:

$$\rho + \left[\frac{\kappa_2 + c\mu_2}{2(1-c)\kappa_2\mu_2} + \frac{1}{2\kappa_1}\right] e\sigma_{MAX}\,\beta(1-\beta\omega)e^{-\beta\omega} = 0, \quad (31)$$

while the unboundedness of (30), i.e., $\rho + \alpha D_\omega f = 0$, yields the condition

$$\rho + \left[\frac{(1-c)}{2(\mu_2 + c\kappa_2)} + \frac{1}{2\kappa_1}\right] e\sigma_{MAX}\,\beta(1-\beta\omega)e^{-\beta\omega} = 0. \quad (32)$$

Expression (32) is nothing more then the bifurcation condition for an isolated fiber-interface-matrix system, i.e., from (13) and $D_\omega F_\rho = 0$, so that brittle decohesion in the solitary fiber-interface-matrix system corresponds to an infinite slope of the $\sigma - \epsilon$ curve. It is obvious from Fig. 3 that, under increasing stress, condition (31) (corresponding to a vanishing slope) will be reached prior to condition (32) (corresponding to an infinite slope) so that the abrupt transition in strain is in effect due to the interaction mechanism inherent in the composite cylinder model. (For a single composite cylinder, increasing the concentration c $(=r_1^2/r_2^2)$ increases r_1 at fixed r_2 and decreases the force length parameter ρ $(=\delta/r_1)$.) Critical values of parameters required for the abrupt transition in strain under increasing stress follows from (31). Roots to

$$\gamma(\beta\omega - 1) = e^{\beta\omega},$$
$$\gamma = \frac{\kappa_2 + c\mu_2 + (1-c)\kappa_2\mu_2/\kappa_1}{2(1-c)\kappa_2\mu_2}\frac{e\sigma_{MAX}\beta}{\rho} \quad (33)$$

indicate values of γ and $\beta\omega$ for vanishing slope of the $\sigma - \epsilon$ curve. It is not hard to show that two roots $(\beta\omega > 0)$ to (33) will exist if and only if $\gamma > 7.39$. The requirement $\gamma = 7.39$, is the minimum γ (or the largest ρ) to insure that the slope of the $\sigma - \epsilon$ curve vanishes at a value of ϵ obtained from $g = 0$. Thus, for vanishing slope,

$$\gamma = \left[\frac{1}{(1-c)}\frac{\sigma_{MAX}}{\mu_2} + \frac{c}{(1-c)}\frac{\sigma_{MAX}}{\kappa_2} + \frac{\sigma_{MAX}}{\kappa_1}\right]\frac{e\beta}{2\rho} \geq 7.39, \quad (34)$$

revealing the fact that bifurcation is favored by large interface strengths, small force length-fiber radius ratios, and large fiber volume concentrations. Equation (34) can therefore be used to obtain the critical value of concentration required for bifurcation (or two distinct strain states at a single value of stress) given the mechanical properties of the interface and the constituent elastic moduli by simply solving the equality (34) for c_{cr}, the critical concentration,

$$c_{cr} = \frac{5.44\mu_2\rho - \beta\sigma_{MAX}\,(1 + \mu_2/\kappa_1)}{5.44\mu_2\rho + \beta\mu_2\sigma_{MAX}\,(1/\kappa_2 - 1/\kappa_1)}. \quad (35)$$

The effect of concentration on the response is shown in Fig. 4 for the fixed values of interface properties and constituent elastic moduli given previously (Fig. 3). Clearly increasing the concentration reduces the stiffness at a given stress level and bifurcation of composite response occurs consistent with (35).

3.4 The Dilute Approximation. When the volume fraction of embedded fibers is so small each fiber can be assumed to be essentially isolated and the geometry of Section 2 with $\mathcal{B} = \Omega_2$ (unbounded) is appropriate, i.e., $r_2 \uparrow R \to \infty$ (Fig. 1). Then (2) and (10) imply that the strain within the fiber $(\bar{\epsilon}_1)$ is $f/2\kappa_1$ so that by (14), (15), and (17)

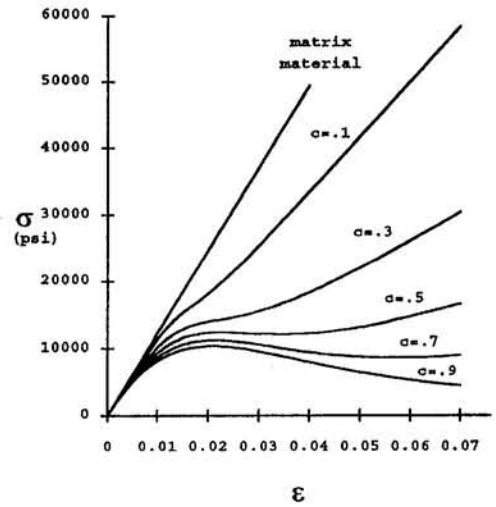


Fig. 4 The effect of concentration on composite response

Downloaded 04 May 2010 to 171.66.16.33. Redistribution subject to ASME license or copyright; see http://www.asme.org/terms/Terms_Use.cfm

$$\sigma = 2\kappa_2\left[1 - c\left(1 + \frac{\kappa_2}{\mu_2}\right)\right]\epsilon + c\left[1 + \frac{\kappa_2}{\mu_2}\right]f(u), \quad (36)$$

where use has been made of the interface Eq. (6), (11),

$$u = \left[1 + \frac{\kappa_2}{\mu_2}\right]\epsilon - \left[\frac{1}{2\mu_2} + \frac{1}{2\kappa_1}\right]f(u). \quad (37)$$

Equations (36) and (37) are consistent with the composite cylinder model provided that in (20) we expand nonlinear terms (in c) in power series about $c = 0$, keeping only the first term in each of the expansions. By noting (12) we recover (36) and (37) which can now be regarded as the limiting response of the composite cylinders model as $c \downarrow 0$. When the volume concentration vanishes (36) indicates that the composite response is simply that of the matrix material which is consistent with Fig. 4.

The limiting behavior of the composite cylinder model (20) as the fiber volume concentration approaches unity is given by

$$\sigma = \frac{2\kappa_2\mu_2}{\mu_2 + \kappa_2}(1 - c)\epsilon + f(u), \quad c \uparrow 1,$$

$$u = \epsilon - \left[\frac{1 - c}{2(\mu_2 + \kappa_2)} + \frac{1}{2\kappa_1}\right]f(u), \quad c \uparrow 1, \quad (38)$$

which indicates that the stress (σ) applied to the composite is essentially transmitted directly to the interfaces. Thus, for fiber volume concentrations of unity the model predicts an asymptotically vanishing stress with increasing strain (recall Fig. 2). This behavior is indicated in Fig. 4. For the situation where the interfaces are coherent the composite response is essentially that of a fiber, i.e., $u \to 0$, $c \uparrow 1$ in (38). Note that the limit $c \uparrow 1$ is meaningful for the composite cylinder model since the composite geometry consists of a volume filling configuration of composite cylinders of varying diameters down to the vanishingly small.

4 Concluding Remarks

This paper has treated aspects of the effective nonlinear response of unidirectional fiber-reinforced composite materials through the analysis of a simple rotationally symmetric elasticity problem. Because the fiber-matrix interfaces are characterized by a nonlinear force-separation relation which allows for initial debonding through complete decohesion, the interaction of finite fiber volume concentration and nonlinear interfacial separation are captured in the effective composite response. Indeed the analysis presented leads to a simple constitutive framework in which one expression relates the equibiaxial tension to the plane dilatation and average separation (damage) variable, and another expression governs the average separation or, state of internal "damage" at a given state of strain. A nice feature of the model is that the local interface constitutive parameters (interface strength, force-length ratio) occur explicitly in the equations governing aggregate behavior. This allows for the rational determination of the effects of interface properties on stress-strain response (Fig. 3).

It can be shown (Levy, 1995) that under an equibiaxial load rotationally symmetric interface separations must give way to nonsymmetric separations when the interface force has attained its maximum value. This aspect of behavior, however, is not included in the development of the transverse bulk modulus where only rotationally symmetric separations are allowed to occur. The incorporation of nonsymmetric separation phenomena in the effective modulus calculation would require a complete knowledge of the nonuniform equilibrium separation and fiber strain. Thus the application of equibiaxial boundary conditions to a composite cylinder would produce nonrotationally symmetric stress and deformation fields so it is unlikely that plane bulk and shear moduli will be uncoupled.

While the solution for the effective bulk response presented in this paper is exact for the composite geometry considered, its utility in modeling real fiber composites is limited owing to the geometry of the composite cylinders model, i.e., a volume filling configuration of cylinders of varying dimensions down to the vanishingly small. It has been pointed out by Hashin and Rosen (1964) that the geometry is best suited to composite materials containing fibers with varying cross sections. Another composite geometry that has been used to obtain effective properties is the three-phase model (Smith, 1974, 1975; Christensen and Lo, 1979). This geometry is shown in Fig. 1 and is such that $\mathcal{B}$ is unbounded, i.e., $R \uparrow \infty$, with an exterior boundary condition which is a remote strain ϵ_∞. Equations (15) and (17) still apply and, from (2) and (5), the mean strain in the fiber is $f/2\kappa_1$. Thus, the effective bulk modulus is of the form

$$\kappa^* = \kappa_2 + c(\kappa_1 - \kappa_2)\frac{f(u)}{2\kappa_1\epsilon_\infty} - \kappa_2 c\frac{u}{\epsilon_\infty}, \quad (39)$$

which is identical in form to (18) obtained for the composite cylinders model. The interface equation for the three-phase model is given by (6) and (7). While not obvious it can be shown that the effective moduli for the limiting conditions of coherent interface behavior ($u = 0$, $f = h\kappa^*\epsilon_\infty/\alpha$) and behavior in which the interface supports no traction ($\sigma_{MAX} = 0$) are of the form (19). This result is consistent with the well-known result that the composite cylinders model and the three-phase model yield the same effective transverse bulk modulus under coherent interface or void conditions. For situations in which the interface responds according to a linear force-separation law it has been shown (Hashin, 1991b) that the composite spheres model and the three-phase model yield the same bulk modulus as well. In order to show that this feature of composite behavior is preserved when the interface responds according to a nonlinear interface separation mechanism, solve (6) for κ^* using (7) for the three-phase model. By substituting the result into (39) and collecting terms the interface Eqs. (6) and (9) for the composite cylinders model is recovered.

An analysis of transverse effective shear response is complicated by the fact that the solution to the solitary fiber-matrix-interface problem subjected to applied shear on its outer boundary is not straightforward. Nevertheless future work will address this problem along with the related issue of effective composite response.

Acknowledgment

The author is grateful to the NASA Center for Hypersonics at Syracuse University for partial support of this project.

References

Aboudi, J., 1987, "Damage in Composites-Modeling of Imperfect Bonding," *Composites Science and Technology,* Vol. 28, pp. 103–128.

Aboudi, J., 1991, *Mechanics of Composite Materials,* Elsevier, Amsterdam.

Achenbach, J. D., and Zhu, H., 1989, "Effect of Interfacial Zone on Mechanical Behavior and Failure of Fiber-Reinforced Composites," *Journal of the Mechanics and Physics of Solids,* Vol. 37, pp. 381–393.

Achenbach, J. D., and Zhu, H., 1990, "Effect of Interphases on Macromechanical Behavior of Hexagonal-Array Fiber Composites," ASME JOURNAL OF APPLIED MECHANICS, Vol. 57, pp. 956–963.

Benveniste, Y., and J. Aboudi, 1984, "A Continuum Model for Fiber Reinforced Materials with Debonding," *International Journal of Solids and Structures,* Vol. 20, pp. 935–951.

Benveniste, Y., 1985, "The Effective Mechanical Behavior of Composite Materials with Imperfect Contact Between the Constituents," *Mechanics of Materials,* Vol. 4, pp. 197–208.

Benveniste, Y., 1987, "A New Approach to the Application of Mori-Tanaka's Theory in Composite Materials," *Mechanics of Materials,* Vol. 6, pp. 147–157.

Buck, R. C., 1965, *Advanced Calculus,* McGraw-Hill, New York.

Cherepanov, G. P., 1979, *Mechanics of Brittle Fracture,* McGraw-Hill, New York.

Downloaded 04 May 2010 to 171.66.16.33. Redistribution subject to ASME license or copyright; see http://www.asme.org/terms/Terms_Use.cfm

Christensen, R. M., 1979, *Mechanics of Composite Materials,* John Wiley and Sons, New York.

Christensen, R. M., and Lo, K. H., 1979, "Solutions for the Effective Shear Properties in Three Phase Sphere and Cylinder Models," *Journal of the Mechanics and Physics of Solids,* Vol. 27, pp. 315–330.

Ferrante, J., Smith, J. R., and Rose, J. H., 1982, "Universal Binding Energy Relations in Metallic Adhesion," *Microscopic Aspects of Adhesion and Lubrication,* Elsevier, Amsterdam, pp. 19–30.

Gurtin, M. E., 1984, "The Linear Theory of Elasticity," *Mechanics of Solids,* Vol. 2, Springer-Verlag, Heidelberg, pp. 1–273.

Hashin, Z., 1962, "The Elastic Moduli of Heterogeneous Materials," ASME JOURNAL OF APPLIED MECHANICS, Vol. 29, pp. 143–150.

Hashin, Z., and Rosen, B. W., 1964, "The Elastic Moduli of Fiber Reinforced Materials," ASME JOURNAL OF APPLIED MECHANICS, Vol. 31, pp. 223–232.

Hashin, Z., 1983, "Analysis of Composite Materials," ASME JOURNAL OF APPLIED MECHANICS, Vol. 50, pp. 481–505.

Hashin, Z., 1991a, "The Spherical Inclusion with Imperfect Interface," ASME JOURNAL OF APPLIED MECHANICS, Vol. 58, pp. 444–449.

Hashin, Z., 1991b, "Thermoelastic Properties of Particulate Composites with Imperfect Interface," *Journal of the Mechanics and Physics of Solids,* Vol. 39, pp. 745–762.

Levy, A. J., 1994, "Separation at a Circular Interface under Biaxial Load," *Journal of the Mechanics and Physics of Solids,* Vol. 42, pp. 1087–1104.

Levy, A. J., 1995, "Nonsymmetric Cavity Formation at a Circular Inclusion under Remote Equibiaxial Load," *Journal of the Mechanics and Physics of Solids,* Vol. 43, pp. 1003–1024.

Mori, T., and Tanaka, K., 1973, "Average Stress in Matrix and Average Elastic Energy of Materials with Misfitting Inclusions," *Acta Metallurgica,* Vol. 21, pp. 571–574.

Moran, B., Gosz, M., and Achenbach, J. D., 1991, "Effect of Viscoelastic Interfacial Zone on the Mechanical Behavior and Failure of Fiber-Reinforced Composites," *Inelastic Deformation of Composite Materials,* Springer-Verlag, New York, pp. 35–49.

Nemat-Nasser, S., and Hori, M., 1993, *Micromechanics: Overall Properties of Heterogeneous Materials,* North-Holland, Amsterdam.

Pagano, N. J., and Tandon, G. P., 1990, "Modelling of Imperfect Bonding in Fiber Reinforced Brittle Matrix Composites," *Mechanics of Materials,* Vol. 9, pp. 49–64.

Qu, J., 1993, "The Effect of Slightly Weakened Interfaces on the Overall Elastic Properties of Composite Materials," *Mechanics of Materials,* Vol. 14, pp. 269–281.

Smith, D. T., and Horn, R. G., 1990, "Surfaces Forces and Adhesion Between Dissimilar Materials Measured in Various Environments," *Materials Research Society Proceedings,* Vol. 170, pp. 3–9.

Smith, J. C., 1974, "Correction and Extension of van der Poel's Method for Calculating the Shear Modulus of a Particulate Composite," *Journal of Research of the National Bureau of Standards,* Vol. 78A, pp. 355–361.

Smith, J. C., 1975, "Simplification of van der Poel's Formula for the Shear Modulus of a Particulate Composite," *Journal of Research of the National Bureau of Standards,* Vol. 79A, pp. 419–423.

APPENDIX

Consider the composite cylinder composite geometry of Fig. 1 ($r_2 = R$) with prescribed traction on its boundary $r = r_2$, i.e.,

$$\mathbf{s}(\mathbf{n}) = \sigma\mathbf{n} \text{ on } r = r_2. \tag{A1}$$

Then provided that the displacement is bounded at the origin and the interface traction (f) is continuous at r_1 the stress and displacement fields are of the form (2) with constants

$$C_1 = \frac{f}{2\kappa_1}, \quad C_2 = 0, \quad C_3 = \frac{\sigma - cf}{2\kappa_2(1-c)},$$

$$C_4 = \frac{\sigma - f}{2\mu_2(1-c)} r_1^2. \tag{A2}$$

The interface equation, analogous to (6), is of the form

$$u = \frac{\mu_2 + \kappa_2}{2\mu_2\kappa_2(1-c)}\sigma - \left[\frac{c\mu_2 + \kappa_2}{2\mu_2\kappa_2(1-c)} + \frac{1}{2\kappa_1}\right] f \tag{A3}$$

and has been obtained by evaluating the jump in radial displacement on the interface $r = r_1$. In order to obtain an equivalent modulus for a homogeneous cylinder with the same traction boundary condition ((A1)) require the displacements on the boundary $r = r_2$ of the homogeneous cylinder and the composite cylinder to be equal. Then

$$\kappa_\sigma^* = \frac{(1-c)\kappa_2\mu_2}{\mu_2 + c\kappa_2 - \dfrac{cf}{\sigma}(\mu_2 + \kappa_2)}. \tag{A4}$$

Downloaded 04 May 2010 to 171.66.16.33. Redistribution subject to ASME license or copyright; see http://www.asme.org/terms/Terms_Use.cfm

Three-Dimensional Finite Element Analysis of Surface Deformation and Stresses in an Elastic-Plastic Layered Medium Subjected to Indentation and Sliding Contact Loading

E. R. Kral[1]
Graduate Research Assistant,
Assoc. Mem. ASME.

K. Komvopoulos
Associate Professor,
Mem. ASME.

Department of Mechanical Engineering,
University of California,
Berkeley, CA 94720

Three-dimensional finite element simulations of the indentation and sliding of a rigid sphere on a half-space with a harder and stiffer layer are presented. The sphere is modeled by contact elements, thereby avoiding a priori assumptions for the pressure profile. Indentations are performed to normal loads of 100 and 200 times the initial yield load of the substrate material and subsequent sliding is performed at a constant normal load to distances of approximately twice the indentation contact radius. Two complete load cycles are performed in selected cases to assess the effect of repeated sliding on the surface displacements and contact stresses. The effects of layer material properties, interface friction, and normal load on the sliding and residual contact stresses and forward plastic flow are examined. Emphasis is given to the sliding and residual tensile stresses at the surface in order to assess the consequences for crack initiation and subsequent failure as a function of the layer material properties, the coefficient of friction, and normal load. The finite element results are shown to be in good agreement with the results of analytical and experimental studies.

1 Introduction

The use of layers to enhance surface contact fatigue and sliding wear resistance of interacting solids requires detailed knowledge of the stresses and deformations arising in layered media subjected to normal and tangential surface tractions. Sliding contact occurs in almost all contacting interfaces, either with large relative displacements as in magnetic storage devices during startup and shutdown, or with very small relative displacements as in thermally induced fretting in electrical contacts. Previous elastic analyses have yielded important information about the deformation characteristics of sliding contact on both layered and homogeneous media. Hamilton and Goodman (1966) performed both plane-strain and three-dimensional analyses of rigid circular sliders contacting an elastic homogeneous half-space. It was found that the maximum von Mises stress, and hence the point of first yield, occurred in the subsurface directly below the slider for a sufficiently low friction coefficient, moving toward the surface with increasing friction. King and O'Sullivan (1987) examined the stresses in a layered elastic half-space in contact with a rigid cylinder sliding in both the in-plane and antiplane (along the cylinder axis) directions. They considered the complete plane-strain formulation and also a membrane approximation for the layer, which is reasonable for layer thicknesses significantly less than the contact dimension. This analysis demonstrated that the point of maximum von Mises stress occurred at the surface near the front of the contact area for sufficiently high friction and that a high tensile stress arose at the surface in the rear of the contact region. Similar results have been reported by Komvopoulos et al. (1987) and O'Sullivan and King (1988) for sliding of a rigid cylinder and a rigid sphere, respectively, on an elastic layered half-space.

Several studies have examined elastic-plastic sliding contact. However, analytical solutions of elastic-plastic sliding contact require many simplifying assumptions in order to obtain a tractable problem. One of the earliest analytical studies is that of Merwin and Johnson (1963), who approached the problem by assuming a Hertzian contact pressure and by approximating the total strain cycle (elastic and plastic) by an equivalent elastic strain cycle. The latter assumption implies that equilibrium is not necessarily satisfied during the strain cycle. In spite of these simplifications, this analysis explained many aspects of the plastic flow observed in contacting rotating cylinders, particularly the accumulation of residual stresses in a layer beneath the surface and the cumulative displacement of the surface in the forward direction, or "forward flow." In addition, it was shown that rolling at a peak pressure less than four times the shear yield stress results in shakedown to an elastic state under repeated loading. Other researchers have also proposed variations on the Merwin and Johnson method for analyzing elastic-plastic stress fields arising in rolling contact. Jiang and Sehitoglu (1994) introduced a method in which the stress cycle during elastic-plastic contact is assumed to be the same as that occurring in elastic contact, the contact pressure is assumed Hertzian, and the residual stress and strain conditions are met by an appropriate relaxation procedure after each passage of the load.

As a result of the complexity associated with analytical approaches to elastic-plastic problems, the analysis of elastic-plas-

[1] Currently at the IBM Almaden Research Center, 650 Harry Road, PHP/802, San Jose, CA 95120.

Contributed by the Applied Mechanics Division of THE AMERICAN SOCIETY OF MECHANICAL ENGINEERS for publication in the ASME JOURNAL OF APPLIED MECHANICS.

Discussion on this paper should be addressed to the Technical Editor, Professor Lewis T. Wheeler, Department of Mechanical Engineering, University of Houston, Houston, TX 77204-4792, and will be accepted until four months after final publication of the paper itself in the ASME JOURNAL OF APPLIED MECHANICS.

Manuscript received by the ASME Applied Mechanics Division, Dec. 6, 1994; final revision, June 19, 1995. Associate Technical Editor: W. K. Liu.

Copyright © 1996 by ASME

Downloaded 04 May 2010 to 171.66.16.33. Redistribution subject to ASME license or copyright; see http://www.asme.org/terms/Terms_Use.cfm

tic sliding contact has remained mostly within the domain of finite element methods. Tian and Saka (1991a, 1991b) performed a plane-strain finite element analysis of indentation and sliding contact on a two-layer half-space consisting of a gold top layer, a nickel interlayer, and a copper substrate. Frictional sliding was simulated by applying a surface shear traction proportional to the pressure produced under normal contact, which was found to differ from the classical Hertz profile. Under combined normal and tangential loading, the maximum shear stress approached the surface, and a surface tensile normal stress was produced in the wake. The interfacial shear stresses were found to depend significantly on the friction coefficient, and sufficiently large friction coefficients also produced a pile-up region in front of the slider. Bhargava et al. (1985a, 1985b) simulated repeated plane-strain frictionless sliding contact on a homogeneous half-space by translating a modified Hertzian pressure distribution over the finite element mesh for several passes, and observed a significantly greater amount of residual shear strain and forward flow per cycle than that predicted by the model of Merwin and Johnson. Kulkarni et al. (1990, 1991a, 1991b) analyzed the problem of repeated frictionless rolling contact of a sphere on a homogeneous half-space by translating a Hertzian pressure distribution over the finite element mesh using loads both at and above the shakedown limit.

Although these studies have yielded valuable insight into the mechanics of sliding contact on elastic-plastic media, they have not given detailed information about the surface stress fields for three-dimensional contact on layered media or have been based on the assumption of a Hertzian or modified Hertzian pressure profile. The objective of this study, therefore, is to provide a comprehensive analysis of the effects of friction, layer material properties, and normal load on the displacements and surface stresses in three-dimensional sliding contact on an elastic-plastic layered half-space without resorting to such assumptions. In the present study, the sphere was modeled by contact elements, thus eliminating the simplification of an assumed pressure profile. A single layer thickness was investigated, and the effect of layer material properties was assessed by modeling layers two and four times stiffer and harder than the substrate. Both the friction coefficient and the normal load were varied to examine the effects of these factors on the contact stresses and deformations observed during sliding. Results examining the effects of layer material properties, surface friction, and normal load on the evolution of the deformation and contact stresses will be presented for repeated sliding contact. In addition, the significance of material properties, friction, and normal load on the residual surface stresses will also be discussed.

2 Modeling Procedures

2.1 Finite Element Mesh. The analysis was performed with the multipurpose finite element code ABAQUS. The three-dimensional finite element mesh used for simulating indentation and sliding of a rigid sphere over a layered medium is shown in Fig. 1. The figure shows only half of the mesh corresponding to the region $x \geq 0$. The mesh consists of 8146 eight-node linear interpolation reduced integration elements comprising a total of 10,347 nodes. The reduced integration elements use a Gaussian integration scheme one order less than the usual 2×2 linear integration, resulting in one integration point per element. For analyses of nonlinear material behavior, this often proves to be a better approximation than full integration when the isoparametric coordinate lines remain orthogonal in the physical space (Barlow, 1976). This will be the case with parallelepiped elements undergoing small strains, as in the present case. The mesh extends from -1120 to 1120 nm in the x direction, from zero to 960 nm in the y direction, and from zero to 1070 nm in the z direction. A rigid spherical indenter with a radius, R, of 1500 nm was modeled, giving normalized mesh dimensions of $-0.747 \leq x/R \leq 0.747$, $0 \leq y/R \leq 0.64$, and

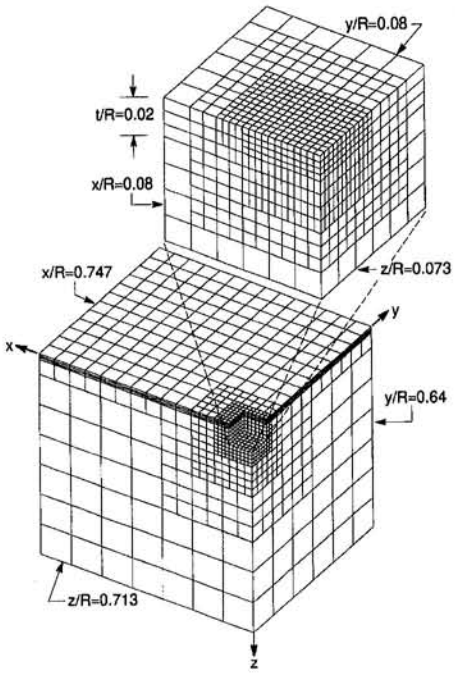


Fig. 1 Three-dimensional finite element discretization of the layered half-space

$0 \leq z/R \leq 0.713$. The plane $y = 0$ is a plane of symmetry, and sliding proceeds in the positive x direction. The plane of symmetry and the bounding plane $y/R = 0.64$ are constrained against displacement in the y direction, the bounding planes $x/R = -0.747$ and 0.747 are constrained against displacement in the x direction, and the plane $z/R = 0.713$ is constrained against displacement in the z direction. Favorable results with similar or smaller mesh dimensions in the axisymmetric indentation studies confirmed that the mesh boundaries were sufficiently remote to properly model a half-space.

In the interest of computational efficiency, the mesh was designed to model only a single layer with thickness, t, equal to 30 nm, yielding a normalized thickness $t/R = 0.02$. The layer is shown in the inset of Fig. 1, which shows the mesh region $0 \leq x/R \leq 0.08$, $0 \leq y/R \leq 0.08$, and $0 \leq z/R \leq 0.073$. The inset also shows the finer mesh in the sliding contact region. The smallest elements are 5 nm square, which is equivalent to the contact radius at initial yielding of the substrate material, a_y. Finer surface meshes were considered, but were too computationally expensive. The given mesh gave good results for elastic indentations and compared favorably with elastic-plastic indentation results of axisymmetric simulations (Kral et al., 1995a, 1995b). Mesh refinement was accomplished by means of linear constraints, either linear for corner nodes of two elements lying on the edge of a larger element, or bilinear for corner nodes lying at the face center of a larger element.

The indenting and sliding sphere was modeled by 429 two-node rigid surface contact elements. One node of each contact element corresponded to a common master node through which loads and displacements were applied to the sphere. Indentation was modeled by incrementally applying normal loads to the master node. Normal traction was applied only when the clearance between the surface nodes of the layered medium and the indenter surface reached zero (''hard'' contact). The contact elements define S^α with $\alpha = 1, 2$ as locally orthogonal surface coordinates on the rigid surface. The first and second variations of the equation for the surface overclosure may then be decomposed into normal and tangential components, yielding equations for the first and second variations in the overclosure, δh and $d(\delta h)$, respectively, and the rate of slip along the contacting

Downloaded 04 May 2010 to 171.66.16.33. Redistribution subject to ASME license or copyright; see http://www.asme.org/terms/Terms_Use.cfm

interface in the surface tangential directions S^α, $\delta\gamma_\alpha$ (ABAQUS Theory Manual, 1989).

The surface contact kinematic rates δh and $\delta\gamma_\alpha$ are integrated over an iteration to obtain measures of the overclosure and relative displacement, h and γ_α, respectively. Elastic behavior is assumed for the normal pressure, $p = p(h)$. The stiffness, dp/dh, may be infinite at $h = 0$ for "hard" contact. In the surface tangential directions, the following decomposition is assumed:

$$d\gamma_\alpha = d\gamma_\alpha^{el} + d\gamma_\alpha^{sl}, \tag{1}$$

where $d\gamma_\alpha^{el}$ is the "elastic" part of the relative displacement and $d\gamma_\alpha^{sl}$ is the rate of frictional slip. The decomposition of Eq. (1) is integrated over an increment to yield

$$\Delta\gamma_\alpha = \Delta\gamma_\alpha^{el} + \Delta\gamma_\alpha^{sl}.$$

The rate of elastic relative displacement is used to aid convergence by allowing some relative motion at the interface without requiring the satisfaction of a slip condition. Thus, the friction model is not strictly a Coulomb model, with stick occurring prior to slip. This facilitates convergence at the expense of losing some physical significance. The stiffness of the elastic part must be chosen to achieve an adequate rate of convergence while maintaining a reasonably small amount of elastic relative displacement. The elastic part of the relative displacement is assumed linear

$$\tau_\alpha = G\gamma_\alpha^{el},\ \gamma_\alpha^{el} = \sum \Delta\gamma_\alpha^{el}, \tag{2}$$

where τ_α are the components of the surface traction τ in the surface orthogonal directions S^α and the summation is taken over all increments since the initial contact of the surfaces. The stiffness G is known as the stiffness in stick and controls the amount of relative displacement allowed between the surfaces when there is no slip. The stiffness serves as a penalty to simulate the fact that there should be only a limited amount of relative displacement at the interface (ideally none) prior to slip. Typically, G is chosen as the expected friction stress, defined as the product of the coefficient of friction, μ, and the local normal stress, p, divided by the amount of elastic displacement that is considered reasonable on physical grounds.

The presence of frictional slip is assessed on the basis of a slip condition

$$f(p, \tau_\alpha) = (\tau_\alpha\tau_\alpha)^{1/2} - \bar{\tau}^{sl}, \tag{3}$$

where $\bar{\tau}^{sl} = \min(\mu p, \tau^o)$, in which τ^o is a shear stress limit used in cases of high friction where the friction stress μp may exceed the shear yield stress. If $f \le 0$ while assuming $\Delta\gamma_\alpha^{sl} = 0$, then no slip occurs; however, if $f > 0$, then slip must occur. For $\mu p < \tau^o$, this is the standard Coulomb friction model in which slip occurs when the interfacial shear force exceeds that which may be supported by the friction. When slip occurs, the yield condition $f = 0$ is imposed. Slip occurs in the direction of τ and is governed by the relation

$$d\gamma_\alpha^{sl} = d\bar{\gamma}^{sl}\frac{\tau_\alpha}{\bar{\tau}^{sl}}, \tag{4}$$

where $d\bar{\gamma}^{sl}$ is the equivalent slip rate given by

$$d\bar{\gamma}^{sl} = \frac{1}{G}[(\tau_\alpha^{el}\tau_\alpha^{el})^{1/2} - \bar{\tau}^{sl}],$$

in which τ_α^{el} is the value of τ_α that would result at the end of the increment if slip did not occur. Equations (1)–(4) for the slip condition, along with the condition $f = 0$, are analogous to a nonassociated flow plasticity model.

2.2 Material Properties and Plasticity Models. According to the von Mises yield criterion adopted in this study, the yield condition is

$$f = J_2 - k^2 = 0,$$

where k is a material constant and J_2 is the second invariant of the deviatoric stress tensor, given by

$$J_2 = \tfrac{1}{2}S_{ij}S_{ij}, \quad \text{where} \quad S_{ij} = \sigma_{ij} - \tfrac{1}{3}\delta_{ij}\sigma_{kk}.$$

In terms of the uniaxial yield stress, the yield criterion reduces to

$$\sigma_M = [\tfrac{3}{2}S_{ij}S_{ij}]^{1/2} = \sigma^o, \tag{5}$$

where σ_M is the von Mises equivalent stress and σ^o is the yield stress. The material model used for plastic deformation is based on the flow rule

$$d\epsilon_{ij}^p = d\lambda S_{ij},$$

where $d\epsilon_{ij}^p$ are the components of plastic strain increment and $d\lambda$ is a function of the flow stress and the plastic strain rate. The usual assumption of negligible plastic volume change was maintained. To account for boundary nonlinearities arising from the use of contact elements, an updated Lagrangian formulation was used. The equivalent plastic strain, ϵ_{eq}, is defined as

$$\epsilon_{eq} = \int_S [\tfrac{2}{3}d\epsilon_{ij}^p\, d\epsilon_{ij}^p]^{1/2}, \tag{6}$$

where S is the strain path. The flow rule applies only to yielding material for which $\sigma_M = \sigma^o$. When $\sigma_M < \sigma^o$, the usual elastic constitutive equations apply. Elastic-perfectly plastic material properties are used throughout in order to provide a basis for comparison with other studies (Merwin and Johnson, 1963; Bhargava et al., 1985a, 1985b) and to provide a foundation of data for full three-dimensional sliding contact simulations. Results for the contact behavior of isotropic hardening layered media under normal loading have been presented in previous publications (Kral et al., 1995a, 1995b). Continuum models may be used to model thin layers provided the ratio of the typical grain size to the layer thickness and/or the contact dimension is small. For a layer thickness of 30 nm, a reasonable correspondence between a continuum model and the physical layer is expected for layer grain sizes less than about 10 nm.

Elastic moduli, stresses, and pressures were normalized by the yield stress of the substrate, σ_y. Loads and distances were normalized, respectively, by the load, P_y, and contact radius, a_y, corresponding to the initial yield condition of a homogeneous substrate with an elastic modulus equal to $684.6\sigma_y$. Results are presented in terms of the parameter β, which is the ratio of both the layer-to-substrate normalized elastic moduli and the layer-to-substrate yield stresses.

2.3 Simulation of Indentation and Sliding. Only a limited number of material cases were investigated due to the computational cost of the three-dimensional analysis. The assumed layer thickness, $t/R = 0.02$, is fairly typical of carbon overcoats applied on thin-film magnetic recording disks. Simulations were performed for layers both two times stiffer and stronger than the substrate ($\beta = 2$) and four times stiffer and stronger than the substrate ($\beta = 4$). In all cases, both the layer and the substrate were modeled as elastic-perfectly plastic materials. Each simulation was performed by incrementally loading the sphere to a normal load, P, equal to 100 or 200 times that required for initial yield of the substrate material with no intervening layer (i.e., $P/P_y = 100$ and 200, respectively), followed by sliding at a constant normal load and friction coefficient in 2 nm increments to a total distance, Δx, of 60 nm (i.e., $\Delta x/a_y = 12$), which was approximately twice the initial contact radius. The simulations were then completed by incrementally unloading the sphere in the same steps as the loading. Simulations were performed at normal loads $P/P_y = 100$ for cases with $\beta = 2$ and $\mu = 0.1$, $\beta = 4$ and $\mu = 0.1$, $\beta = 4$ and $\mu =$

Downloaded 04 May 2010 to 171.66.16.33. Redistribution subject to ASME license or copyright; see http://www.asme.org/terms/Terms_Use.cfm

Table 1 Summary of three-dimensional simulations

	β=2	β=4		
	μ=0.1	μ=0.1		μ=0.25
P/P_y	100	100	200	100
$\Delta x/a_y$	12	12	12	12
$(x/a_y)_i$	-8	-8	-8	-8
$(x/a_y)_f$	4	4	4	4
# load cycles	2	2	2	1

$(x/a_y)_i$ = initial x coordinate of sphere center
$(x/a_y)_f$ = final x coordinate of sphere center

0.25, and at $P/P_y = 200$ for $\beta = 4$ and $\mu = 0.1$. The low-friction cases ($\beta = 2$, $\mu = 0.1$, and $\beta = 4$, $\mu = 0.1$ at normal loads $P/P_y = 100$ and 200) were subjected to an identical second load pass performed by reloading the sphere at the original location, sliding to a distance $\Delta x/a_y = 12$, and then unloading. These simulations are summarized in Table 1. Typical CPU times for a 2 nm sliding increment were approximately 36 to 44 hours on an IBM RS6000 Model 540 workstation and 16 to 18 hours on an IBM RS6000 Model 580 workstation. The convergence tolerance for most runs was equal to $10^{-5}\sigma_y$, although a smaller tolerance was used for some runs. The stiffness in stick for the cases with $\mu = 0.1$ was equal to 10 nm^{-1}, yielding a maximum elastic relative displacement at the contact interface of 0.11 nm (2 percent of the surface element dimension) before slip was allowed, based on the maximum observed contact pressure. For the simulation with $\mu = 0.25$, the stiffness was 12.5 nm^{-1}, giving a maximum elastic relative displacement of 0.16 nm. This was necessary in order to improve the convergence for the higher friction coefficient. In both cases, the allowable elastic slip was very small compared to the total sliding distance.

2.4 Verification of the Three-Dimensional Finite Element Model. Elastic frictionless indentations were performed on the three-dimensional mesh without a layer, and the data were compared with analytical results (Hamilton and Goodman, 1966). The normalized modulus for the comparison was $E/\sigma_y = 103.25$ and the contact radius was 30 nm, i.e., $a/R = 0.02$. Stresses and coordinates were normalized by the yield stress, σ_y, and the contact radius, a, respectively.

Figure 2 shows the surface and near-surface stresses obtained from the finite element simulation and the analysis of Hamilton and Goodman (1966) on the plane $x = y$. Since the reduced integration elements have only one integration point per element, at the element center, both the corner nodes and the integration points of the elements bisected by the plane $x = y$ lie in the plane $x = y$. Figures 2(*a*) and 2(*b*) show stresses extrapolated to the surface nodes ($z/a = 0$) as a function of radial distance along the line $x = y$. Figures 2(*c*) and 2(*d*) show stresses at the first subsurface integration points, at a depth $z/a = 0.0625$, as a function of radial distance along $x = y$. For an axisymmetric indentation, on the plane $x = y$, $\sigma_{xx} = \sigma_{yy}$ and $\sigma_{xz} = \sigma_{yz}$. Along the surface nodes, shown in Figs. 2(*a*) and 2(*b*), the agreement between the finite element and analytical results is relatively good. The errors may be attributed primarily to the averaging of the stress data from the integration points to the surface nodes, as was the case with indentation simulations presented previously (Kral et al., 1993). Figures 2(*c*) and 2(*d*) indicate excellent agreement between the finite element and analytical results. In view of the favorable comparisons with analytical results, it may be concluded that the finite element mesh and contact elements provide a suitable model for simulating the three-dimensional contact of a rigid sphere on a layered half-space.

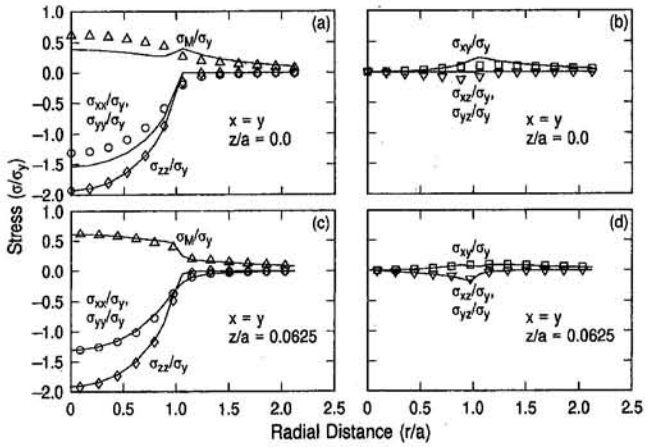


Fig. 2 Comparison of finite element (discrete points) and analytical (continuous lines) stress results for an elastic indentation: (*a*) and (*b*) stresses at the surface; (*c*) and (*d*) stresses near the surface

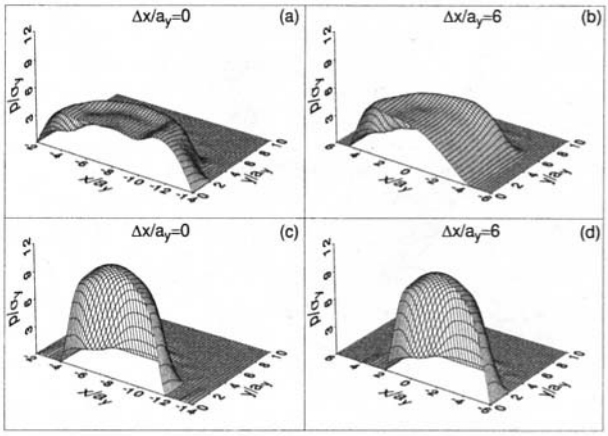


Fig. 3 Contact pressure profiles for $\beta = 2$ and $\mu = 0.1$ at $P/P_y = 100$ as a function of sliding distance: (*a*) and (*b*) finite element results; (*c*) and (*d*) equivalent Hertzian profiles

3 Results and Discussion

Elastic-plastic finite element solutions for surface stress and deformation fields associated with the indentation and sliding of a rigid sphere over a layered half-space are presented and discussed in this section. The material properties, normal loads, sliding distances, and friction coefficients used in the three-dimensional simulations are summarized in Table 1. All simulations with a friction coefficient of 0.1 consisted of two load cycles comprising an indentation to the prescribed load and subsequent incremental sliding to the specified distance shown in Table 1, followed by unloading to zero load and a repeat of the previous load cycle. Only one load cycle was performed for the higher friction case. The effect of an increase in the stiffness and yield strength of the layer will be shown by comparison of the $\beta = 2$ and $\beta = 4$ cases with otherwise identical loading conditions ($P/P_y = 100$ and $\mu = 0.1$), while the effects of normal load and friction coefficient will be shown by comparisons among cases with $\beta = 4$. In the subsequent discussion, it will be understood that either "stiffer" or "harder" refers to the layer with the larger elastic modulus and yield strength (or hardness) ratio (i.e., $\beta = 4$), while "softer" or "more compliant" refers to the layer with the smaller elastic modulus and yield strength ratio (i.e., $\beta = 2$).

3.1 Contact Pressure Distribution and Surface Displacements. Figure 3 shows the development of the contact pressure for low-friction sliding ($\mu = 0.1$) with $\beta = 2$ and $P/P_y =$

Downloaded 04 May 2010 to 171.66.16.33. Redistribution subject to ASME license or copyright; see http://www.asme.org/terms/Terms_Use.cfm

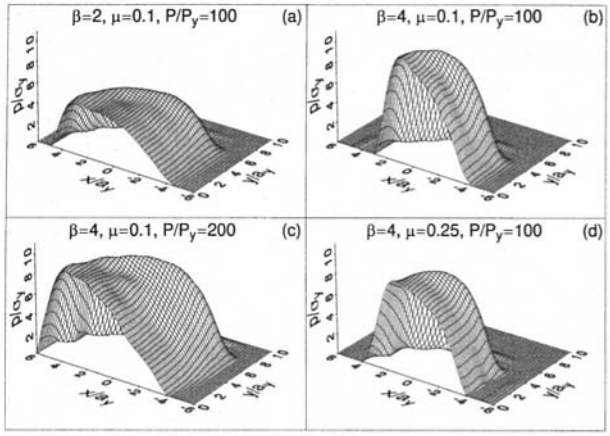


Fig. 4 Contact pressure profiles at a sliding distance $\Delta x/a_y = 6$

100, and the equivalent Hertz pressure profile for the same normal load. Shown in Fig. 3(*a*) is the contact pressure under indentation. There is no relative displacement of the rigid surface, i.e., the interface friction stress is less than the friction coefficient times the normal contact pressure. The indentation pressure profile exhibits higher pressure at the contact edge, which was also observed in the axisymmetric simulations of the indentation of a layered half-space (Kral et al., 1995a). Figure 3(*b*) shows the steady-state pressure profile at a sliding distance $\Delta x/a_y = 6$. At steady state, the mean contact pressure is slightly higher and occurs over a smaller contact area than in the indentation pressure profile, with a higher peak pressure arising at the front and side (transverse) edges of the contact region since the bulk of the sphere load is supported by the frontal area of contact. The pressure toward the rear of the indenter decreases rapidly. In all sliding cases, the steady-state sliding profile is achieved fairly quickly, typically by a sliding distance $\Delta x/a_y = 2$ to 4. Under sliding conditions, all interfacial nodes are slipping, producing a shear stress that is scaled by the friction coefficient. Slipping commences with the onset of sliding, and there is no observed stick-slip behavior. Comparison of both the indentation and sliding profiles with the equivalent Hertz profiles shown in Figs. 3(*c*) and 3(*d*) indicates that the actual pressure profile exhibits a significantly larger contact area and smaller maximum pressure. Previous three-dimensional finite element analyses of sliding or rolling contact (Kulkarni et al., 1990, 1991a, 1991b) have modeled the sliding sphere by a translating Hertzian profile, which may yield significantly different results.

The steady-state contact pressure profiles for all the simulation cases at a sliding distance $\Delta x/a_y = 6$ during the first load cycle are compared in Fig. 4. Figure 4(*a*) shows the steady-state profile for $\beta = 2$ and $\mu = 0.1$ at a normal load $P/P_y = 100$, previously shown in Fig. 3(*b*). The pressure profiles for the layer with $\beta = 4$ are shown in Fig. 4(*b*) for $\mu = 0.1$ and $P/P_y = 100$, in Fig. 4(*c*) for $\mu = 0.1$ and $P/P_y = 200$, and in Fig. 4(*d*) for $\mu = 0.25$ and $P/P_y = 100$. All the pressure profiles exhibit similar qualitative characteristics, with a higher pressure at the front and transverse contact edges and the pressure decreasing rapidly near the rear of the contact area. Comparison of Figs. 4(*a*) and 4(*b*) indicates that the harder and stiffer layer produces a much higher maximum pressure and a smaller contact area, which is consistent with the results for indentation of layered media (Kral et al., 1995a). Comparison of the profiles shown in Figs. 4(*b*) and 4(*c*) demonstrates the effect of normal load on the contact pressure under otherwise identical conditions. The higher load does not produce a higher contact pressure, as might be expected, but rather a slightly lower mean pressure over a larger area. This is due to the increased plastic deformation, primarily in the substrate, which will be presented in a forthcoming publication. A similar phenomenon was observed for the indentation of layered media (Kral et al., 1995a, 1995b), in which the peak pressure was attained at a relatively early stage of the indentation, while increasing the load produced a much larger contact area and a lower mean pressure. The effect of surface friction on the contact pressure may be seen by comparing Figs. 4(*b*) and 4(*d*). The pressure under the higher friction coefficient exhibits a slightly lower maximum value and a slightly larger contact area, while also exhibiting a less pronounced maximum pressure at the contact edge. Otherwise, the characteristics of the contact pressure profiles for the two friction coefficients are very similar.

The surface displacements under indentation, sliding, and residual conditions are shown in more detail in Fig. 5 for $\beta = 2$, $\mu = 0.1$, and $P/P_y = 100$. Figure 5(*a*) shows the surface displacements on the axis of symmetry, with the initial indentation occurring at $x/a_y = -8$. Under sliding conditions, the indentation depth increases slightly as a greater portion of the normal load is supported near the front of the contact area. This agrees with the results for the contact pressure shown in the previous figures. After a sliding distance $\Delta x/a_y = 2$, the indentation depth remains relatively constant, and the material in front of the indenter begins to form a pile-up region which grows slightly by the end of the sliding simulation at $\Delta x/a_y = 12$. After unloading, the permanent residual groove exhibits a relatively constant depth, with a pronounced pile-up region in front of the indenter. A similar residual pile-up region at the contact edge was also observed for repeated indentations of a homogeneous elastic-perfectly plastic half-space (Kral et al., 1993). The pile-up region in the sliding cases corresponds to a subsurface region of tensile residual normal stress in the direction normal to the surface, σ_{zz}; subsurface stresses will be discussed in detail in a future publication. Figure 5(*b*) shows the surface displacements on transverse planes at the sphere center as a function of sliding distance. Again, an initial increase in indentation depth and contact width is observed as sliding commences; after a sliding distance $\Delta x/a_y = 2$, the indentation depth and contact width remain relatively constant. In addition, a pile-up region also begins to form at the transverse contact edge by a sliding distance $\Delta x/a_y = 8$. The height of the transverse pile-up region increases slightly with sliding distance as a steady-state condition is approached, and is expected to remain constant during

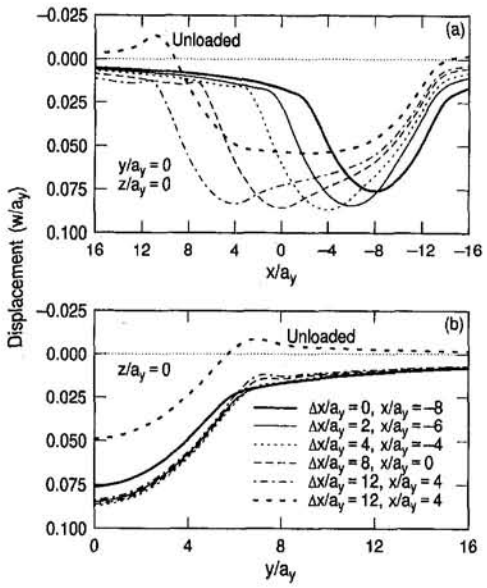


Fig. 5 Comparison of surface displacements at different sliding distances $\Delta x/a_y$ with the unloaded (residual) surface profile: (*a*) on the plane of symmetry and (*b*) on transverse planes at the sphere center for $\beta = 2$ and $\mu = 0.1$ at $P/P_y = 100$

Downloaded 04 May 2010 to 171.66.16.33. Redistribution subject to ASME license or copyright; see http://www.asme.org/terms/Terms_Use.cfm

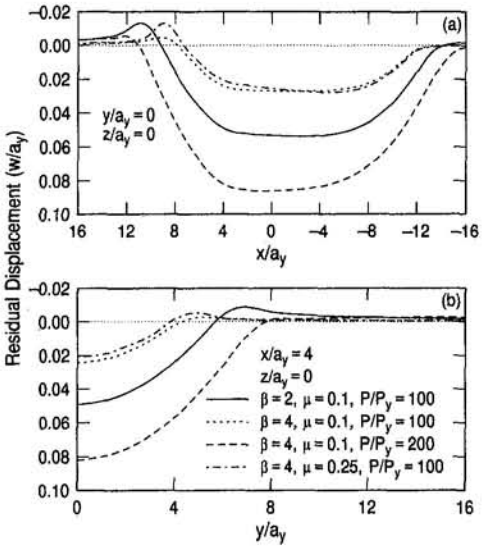


Fig. 6 Residual surface displacements after sliding to a distance $\Delta x/a_y = 12$ under the indicated load and unloading to $P/P_y = 0$: (a) along the plane of symmetry and (b) along a transverse plane at the sphere center

steady-state sliding. Finally, when the sphere is unloaded, a significant residual pile-up region forms at the transverse edge of the indentation, which increases in height toward the front of the contact region. The formation of a wave at the edge of the contact groove is consistent with predictions for blunt contact with low friction based on a slip-line analysis of sliding cones with various contact angles (Childs, 1992). This study includes micrographs clearly showing pile-up regions in silver scratched with a relatively blunt diamond cone.

Figure 6 shows the residual surface displacements for all the material cases after completing the first load cycle. The residual profiles on the axis of symmetry are shown in Fig. 6(a). The surface displacement profiles under sliding conditions are qualitatively similar, with the major difference being the groove depth. Comparison of results indicates that increasing the layer stiffness and hardness from $\beta = 2$ to 4 decreases the depth of the residual indentation by approximately half. Results for the in situ indentation depth during sliding also indicated roughly half the indentation depth for the harder and stiffer layer. In addition, the front and transverse pile-up regions are smaller for the harder and stiffer layer. Increasing the normal load from $P/P_y = 100$ to 200 increases the residual groove depth by almost a factor of 4, but does not significantly affect the height of the pile-up region in front of the contact groove. Increasing the friction coefficient from $\mu = 0.1$ to 0.25 has little effect on the residual groove depth, with the exception of a slight decrease in the groove depth with sliding distance. The higher friction case exhibits larger front and transverse pile-up regions, indicating that increasing the coefficient of friction produces more deformation of the surface material in the sliding direction. The larger frontal pile-up region may be responsible for the decrease in groove depth with sliding distance, since a larger prow supports a larger fraction of the normal load, resulting in a slightly shallower groove. The residual displacements along the transverse plane at the sphere center, shown in Fig. 6(b), exhibit trends similar to those shown in Fig. 6(a), with the exception that there is almost no remaining transverse pile-up region for the simulation at $P/P_y = 200$, which is consistent with the smaller amount of pile-up observed in front of the contact groove for this case. The smaller amount of residual pile-up after sliding at the higher normal load may be due to a relatively small amount of elastic recovery after unloading, as compared to the significantly larger amount of plastic deformation. Regions of residual pile-up at the contact edges are commonly observed under normal contact of elastic-perfectly plastic or fully work hardened materials (Kral et al., 1993). These pile-up regions may also be associated with near-surface tensile residual σ_{zz} stresses (normal to the surface) arising around the edge of the residual contact groove. This residual stress field will be discussed in more detail in another publication.

Results for the total tangential (friction) force as a function of the sliding distance, not shown here for the sake of brevity, indicated that the tangential force increased rapidly from zero during indentation to a constant steady-state value after a sliding distance $\Delta x/a_y \approx 1$ for all the cases considered. As expected, the high friction case ($\mu = 0.25$) exhibited the largest tangential force, followed by the case with $P/P_y = 200$ and $\mu = 0.1$. The two cases having $P/P_y = 100$, $\mu = 0.1$, and $\beta = 2$ and 4, showed rather similar values throughout. In addition, the total tangential force is very close to the product of the coefficient of friction and the normal force, indicating that the tangential force is dominated by the shearing component, with very little effect of the plowing (tangential) component of the normal force. This indicates that the contact geometry is extremely shallow, even for the contact at the higher normal load.

3.2 Surface Stresses. The next several figures show the surface in-plane normal stresses under both sliding and residual conditions for the first load cycle. Emphasis will be placed on the tensile stresses, which indicate the susceptibility to cracking and the strength necessary for the layer to maintain its integrity.

The in situ σ_{xx} and σ_{yy} surface stresses at the maximum sliding distance for all the cases considered are shown in Fig. 7. Figure 7(a) shows the surface σ_{xx} stress on the plane of symmetry ($y/a_y = 0$), and Fig. 7(b) shows the surface σ_{yy} stress in the same region. Figure 7(a) shows a significant tensile surface stress in the wake of the indenter, exhibiting a considerably larger maximum for the harder and stiffer layer. The maximum tensile σ_{xx} stress also increases with the normal load and friction coefficient, but these effects are secondary compared to the effect of the layer properties. It may be noted that the maximum surface tensile stress may show greater sensitivity to the normal load and coefficient of friction for a strain-hardening material, since both the higher load and higher friction cases exhibit greater magnitudes of plastic strain on the surface. A comprehensive analysis of the plastic strain fields will be presented in a future publication. However, for the elastic-perfectly plastic materials investigated in the present study, the maximum tensile stress is relatively insensitive to these factors. The σ_{xx} surface

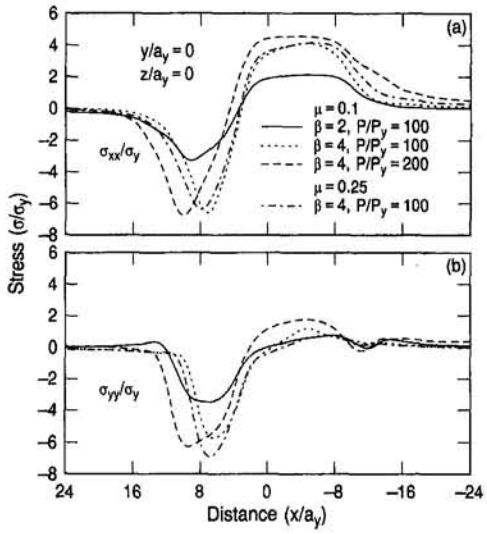


Fig. 7 Surface stresses along the plane of symmetry for a sliding distance $\Delta x/a_y = 12$: (a) σ_{xx} stress and (b) σ_{yy} stress

Downloaded 04 May 2010 to 171.66.16.33. Redistribution subject to ASME license or copyright; see http://www.asme.org/terms/Terms_Use.cfm

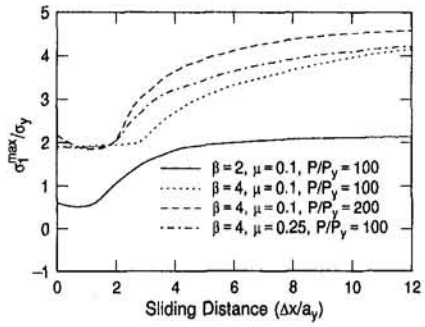


Fig. 8 Maximum value of the maximum principal stress σ_1 versus sliding distance $\Delta x/a_y$

tensile stress is the maximum principal stress in the layer and is responsible for the initiation of transverse (or ring) cracks in the wake of sliding indenters, which has been frequently observed experimentally. Wake ring cracks in brittle materials may be seen in micrographs of a groove produced by a sliding cone on glass (Lawn, 1992) and in sliding contact experiments conducted on carbon-coated magnetic storage rigid disks (Wu, 1991).

A similar situation may be seen for the normal stress perpendicular to the sliding direction, σ_{yy}, shown in Fig. 7(*b*). Again, a region of tensile surface stress develops in the wake of the sphere, though the magnitude of this tensile stress is considerably less than that of the tensile σ_{xx} stress in the same region shown in Fig. 7(*a*). Thus, cracks parallel to the sliding direction may also be initiated, but this would be expected to occur only if surface flaws were oriented so as to make that direction preferred, as in the case of sliding parallel to texture marks on the surface of a magnetic data storage disk. The low-friction cases with $\beta = 4$ exhibit a slightly higher maximum tensile σ_{yy} stress than the $\beta = 2$ case in the wake region. This tensile stress decreases with increasing contact friction and/or decreasing normal load. Thus, the higher normal load increases the tendency for crack initiation parallel to the sliding direction, although again the propensity for such cracks to form is much less than for transverse cracks due to the lower tensile stress; thus, the latter will be more commonly observed unless some surface feature such as texturing increases the susceptibility to parallel cracks. In addition, the softer and more compliant layer ($\beta = 2$) exhibits a region of tensile σ_{yy} stress in front of the contact region, which may be associated with a subsurface hoop stress surrounding the plastic zone. A similar subsurface hoop stress was observed during indentation of layered media (Kral et al., 1995a, 1995b). Although the harder and stiffer layers also exhibit a tensile hoop stress in the same region, it does not extend to the surface for those cases.

Some of the features discussed in the previous sections regarding the effect of layer material properties, normal load, and contact interface characteristics may be interpreted in terms of the maximum tensile principal stress in the layer, σ_1, which is a surface σ_{xx} stress in the sliding wake, shown in Fig. 8 as a function of sliding distance. The maximum tensile stress continues to increase at a sliding distance $\Delta x/a_y = 12$ in all cases, though the rate of increase for $\beta = 2$ is very small. This indicates that a true steady-state sliding condition has not quite been reached. However, the curves exhibit a continuously decreasing slope, indicating that the maximum tensile stress is approaching a constant value. As previously noted, the harder and stiffer layer is subjected to much greater tensile stresses than the softer and more compliant layer. The maximum tensile stress in the harder and stiffer layer increases slightly with friction and more significantly with the normal load. In all cases, a relatively uniform maximum tensile stress exists in the early sliding stages ($\Delta x/a_y \approx 1$ to 3) and then begins to increase. The transition from uniform to increasing maximum tensile stress may be related to the development of the steady-state pressure profile, which typically occurs at $\Delta x/a_y \approx 2$.

Tensile principal stresses also occur in the substrate during sliding (not shown here), but the magnitude of these tensile stresses is much less than that of the surface contact stresses shown in Fig. 8. Therefore, the layer protects the substrate from high tensile surface stresses that would otherwise occur under direct sliding contact, and thus decreases the likelihood of crack initiation and damage in the substrate. However, since increasing the hardness and stiffness of the layer also increases the tensile stresses to which the layer is subjected (Fig. 7), it will be necessary to assess the degree to which a harder and stiffer layer provides better protection for the substrate. In summary, both the tensile σ_{xx} and σ_{yy} surface stresses in the sliding wake are greater in the stiffer and harder layer, increasing the probability of initiating cracks from surface defects. Increasing the normal load increases the surface tensile stresses in the sliding wake slightly and results in a larger contact area and lower mean contact pressure, as was the case for layered media subjected to purely normal contact loads (Kral et al., 1995a, 1995b). The effect of increasing the friction coefficient from 0.1 to 0.25 on the surface normal stresses is marginal.

3.3 Residual Surface Stresses. Unloading of the sphere after sliding was simulated by restraining the x and y displacements of the sphere and removing the normal load in 10 steps or 14 steps for sliding performed at $P/P_y = 100$ or 200, respectively, in the reverse order of the loading steps during the initial indentation. Thus, the position of the sphere during unloading is the same as that at the last sliding step, shown in Table 1. Again, emphasis will be placed on the tensile residual normal stresses.

Figure 9 shows the surface residual σ_{xx} and σ_{yy} stresses for all the cases simulated. The surface residual σ_{xx} stress, shown in Fig. 9(*a*), is tensile over the entire surface contact area. The qualitative pattern of the stresses is very similar to that for the same stresses under sliding conditions, shown in Fig. 7, with a tensile residual stress occurring over the contact region, followed by a compressive stress in front of the contact which asymptotically approaches zero. However, the surface area subjected to the tensile stress is much greater in the residual state than during sliding contact. The maximum tensile residual σ_{xx} stress increases with the stiffness (and hardness) of the layer and with the normal load during sliding, and decreases margin-

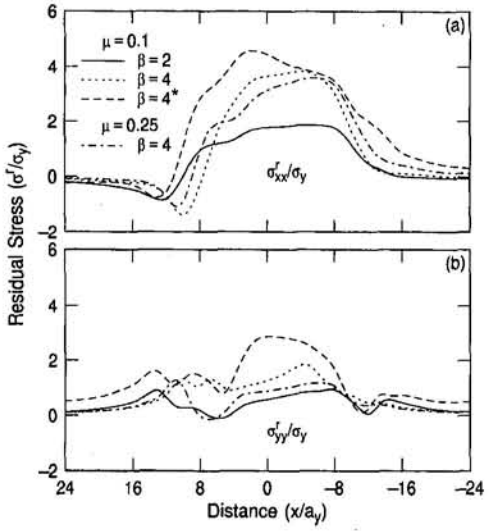


Fig. 9 Residual surface stresses along the plane of symmetry after unloading from $P/P_y = 100$ ($P/P_y = 200$ for (*) case) at a sliding distance $\Delta x/a_y = 12$: (*a*) σ_{xx} stress and (*b*) σ_{yy} stress

Downloaded 04 May 2010 to 171.66.16.33. Redistribution subject to ASME license or copyright; see http://www.asme.org/terms/Terms_Use.cfm

ally with higher friction. In addition, the area subjected to a tensile residual stress increases with the normal load and decreases with the layer stiffness. Contours of the residual σ_{xx} stress, not shown here, also indicate that the tensile residual stress extends deeper into the layer for the higher load. Thus, the higher load increases the likelihood of crack initiation not only by inducing higher residual stresses, but also by subjecting a larger volume of the layer to a tensile stress. Comparison of the results shown in Figs. 7 and 9 indicates that the maximum tensile residual stress is less than that under sliding conditions for the lower load cases ($P/P_y = 100$), but comparable to the maximum sliding stress for the higher load case ($P/P_y = 200$). However, in all cases, the tensile residual stress occurs over a larger region than the tensile stress under sliding, due to a tensile residual stress arising in front of the sphere center, approximately from $x/a_y = 4$ to 12, where only compressive stresses occurred during contact. Thus, the susceptibility to cracking increases during unloading in the frontal contact region, indicating a higher propensity for transverse crack initiation during unloading. In most cases, the tendency for initiation of cracks behind the sphere center will be greatest during sliding due to a higher maximum tensile stress, but this will be sensitive to the normal load, as the higher load produces a residual tensile stress in the wake comparable to that occurring during sliding.

Figure 9(b) shows that the residual σ_{yy} stress at the surface is predominantly tensile, approaching zero asymptotically from the positive side in both the front and the rear of the contact region. Contour plots, not shown here, demonstrate that the tensile residual σ_{yy} stress in front of the contact region extends to the layer interface. The maximum residual stress increases with the layer stiffness and hardness and also with the normal load during sliding, while it decreases with increasing friction. These results may be compared with those for surface stresses under sliding, shown in Fig. 7(b), which are tensile behind the sphere center, compressive at the prow, and slightly tensile again in front of the contact region, whereas the residual stresses are tensile throughout. In addition, the maximum residual tensile stresses are greater than the contact stresses shown in Fig. 7(b) for all the cases studied. Thus, not only are the maximum tensile residual stresses greater than those under sliding, but tensile stresses arise over a larger volume. Therefore, the appearance of cracks parallel to the sliding direction at the layer surface is much more likely during unloading.

In summary, the residual σ_{xx} stress generally exhibits lower maximum tensile magnitudes after unloading than during sliding. The exception occurs for the case of sliding at $P/P_y = 200$, in which the maximum surface residual σ_{xx} stress is comparable to that arising during contact. The surface residual σ_{yy} stress exhibits larger maximum values after unloading in all cases. In addition, both tensile residual stress components occur over larger volumes than under sliding conditions and extend into regions that were subject to only compressive stresses during sliding. Thus, there exists a significant possibility of inducing damage during unloading in previously undamaged material, particularly in front of the contact groove.

3.4 Repeated Load Cycles. All the low friction cases were subjected to a second load cycle in order to assess the effect of the residual groove geometry and residual stresses on the contact stresses and displacements for repeated loading. In each case the first load cycle was simply repeated, i.e., the sphere was replaced at the initial indentation location and was reloaded to the same normal load with the same load history. The sphere was then translated a total distance $\Delta x/a_y = 12$ at a constant normal load as before and then unloaded following the same load history. In the following figures, the contact pressures, displacements, and surface stresses for the second load cycle are presented and compared with the corresponding results for the first load cycle.

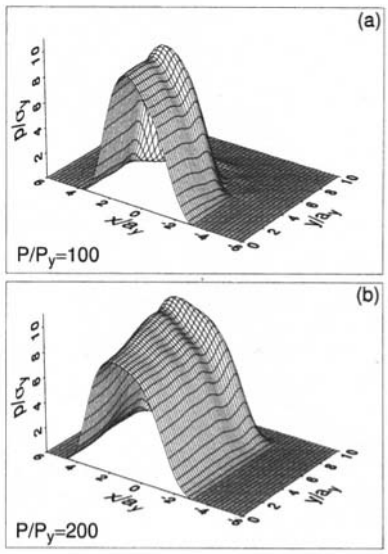


Fig. 10 Contact pressure profiles for the second load cycle at a sliding distance $\Delta x/a_y = 8$ for $\beta = 4$ and $\mu = 0.1$: (*a*) $P/P_y = 100$ and (*b*) $P/P_y = 200$

The steady-state contact pressure profiles during the second load cycle for the $\beta = 4$ cases are shown in Fig. 10. Both are shown at a sliding distance $\Delta x/a_y = 8$, which is sufficient to establish the steady-state profiles but not far enough to encounter an influence from the residual pile-up region left by the previous load cycle; these are the expected pressure profiles for steady-state sliding in the residual groove. Figure 10(a) shows results for $P/P_y = 100$, and Fig. 10(b) shows results for $P/P_y = 200$. In both cases, the high normal pressure at the front of the sphere associated with the formation of a prow is absent due to the presence of the residual groove, yielding a symmetric profile along the axis of symmetry. The higher normal pressure at the transverse edge of the contact is still present. As with the first load cycle, the higher load case does not exhibit a significantly higher maximum contact stress, but rather supports the additional load over a much larger contact area. The contact pressure distributions during the second load cycle are characterized by a decrease in the contact length along the axis of symmetry (from about 14 percent to about 25 percent) and a corresponding increase in the contact width (approximately 20 to 25 percent). The maximum pressure during the second load cycle is comparable to that arising during the first load cycle for the lower load case, but is approximately 15 percent greater for the case with $P/P_y = 200$. Thus, the conformity of the residual groove does not produce a lower contact pressure in all cases.

The maximum forward flow of the material at the contact surface per load cycle is given in Table 2. In order to provide a basis of comparison for forward flow for different layer thick-

Table 2 Maximum forward flow at the contact surface as a function of load cycle

	β=2	β=4		
	μ=0.1	μ=0.1		μ=0.25
P/Py	100	100	200	100
p_o/k_{eff}	6.55	6.02	6.22	5.32
$\bar{\delta}_{max}$, 1st cycle	0.421	0.120	0.166	0.489
$\bar{\delta}_{max}$, 2nd cycle	0.605	0.148	0.211	--
$\Delta\bar{\delta}$	0.184	0.028	0.045	--

Downloaded 04 May 2010 to 171.66.16.33. Redistribution subject to ASME license or copyright; see http://www.asme.org/terms/Terms_Use.cfm

nesses and material properties, the forward flow in Table 2 is normalized as

$$\overline{\delta} = \frac{\delta(G/\sigma_y)_{\text{eff}}}{(p_o/\sigma_y)a}, \tag{7}$$

where δ is the forward displacement, $(G/\sigma_y)_{\text{eff}}$ is the normalized effective shear modulus, p_o/σ_y is the normalized maximum pressure, and a is the steady-state contact half-width. To further aid the comparison, the ratio of the peak pressure to the effective shear yield stress, p_o/k_{eff}, is also given in Table 2. For nonlayered media, these are the same expressions used by Merwin and Johnson (1963). The effective shear modulus and shear yield stress will depend on the layer thickness, the layer and substrate material properties, and the ratio of the contact width to the layer thickness. Suitable relationships may be adapted from those used for the investigation of repeated indentation of a layered half-space (Kral et al., 1995a). The normalized effective shear modulus may be obtained from the effective elastic modulus, based on an analysis of indentation of elastic layered media (King, 1987), by replacing the material property terms with the shear moduli of the layer and substrate materials. The normalized effective shear modulus may thus be expressed as

$$\left(\frac{G}{\sigma_y}\right)_{\text{eff}} = \left(\frac{E/\sigma_y}{2(1+\nu)}\right)_{\text{eff}} = \left[\frac{2(1+\nu_l)}{E_l/\sigma_y}(1 - e^{-\alpha t/a\sqrt{\pi}}) + \frac{2(1+\nu_s)}{E_s/\sigma_y} e^{-\alpha t/a\sqrt{\pi}}\right]^{-1}, \tag{8}$$

where E and ν are the elastic modulus and Poisson's ratio, respectively (the subscripts s and l refer to substrate and layer properties, respectively), t is the layer thickness, and α is a numerical factor for the indentation of a circular flat-ended rigid punch calculated by a sixth-order polynomial fit to selected data points obtained from King (1987). The ratio of the peak pressure to the effective shear yield stress is given by

$$\frac{p_o}{k_{\text{eff}}} = \sqrt{3}\frac{p_o}{(\sigma_y)_{\text{eff}}} = \sqrt{3}\frac{p_o}{\sigma_y}\frac{\sigma_y}{(\sigma_y)_{\text{eff}}}. \tag{9}$$

A suitable expression for the ratio of the effective normal yield stress to the substrate normal yield stress is given by (Kral et al., 1995a)

$$\frac{(\sigma_y)_{\text{eff}}}{\sigma_y} = \frac{\sigma_s}{\sigma_y}\left\{1 + \left(\frac{\sigma_l}{\sigma_s} - 1\right)\exp\left[-\left(\frac{a}{t}\right)\Big/\left(\frac{E_l}{E_s}\right)^{1/2}\right]\right\},$$

where σ_s and σ_l are the representative flow stresses for the substrate and layer, respectively. Since the materials in this study are elastic-perfectly plastic, the representative flow stresses remain constant and equal to the yield stresses throughout the deformation. Hence, the above expression may be simplified to

$$\frac{(\sigma_y)_{\text{eff}}}{\sigma_y} = 1 + (\beta - 1)\exp\left(-\frac{a}{t\sqrt{\beta}}\right), \tag{10}$$

where β is the ratio of the layer-to-substrate yield stress and the layer-to-substrate elastic modulus. The normalized forward flow can be obtained by substituting Eqs. (8)–(10) into Eq. (7). The values in Table 2 were obtained by substituting the maximum forward displacement of the surface nodes into Eq. (7).

The maximum displacement on the surface, $\overline{\delta}_{\max}$, given in Table 2 is obtained after unloading at the completion of the respective load cycle. The maximum always occurs on the plane of symmetry, as would be expected. In all cases, the effective applied contact pressure exceeds the shakedown limit of $p_o/k = 4.7$ for point contact on a homogeneous elastic-perfectly plastic half-space (Johnson, 1985); since the comparison is based on effective values that account for the layer material properties and the contact geometry, it is expected that the shakedown limit will be similar for the effective applied pressure. However, since this shakedown limit is calculated assuming a Hertzian contact pressure, the limit in this case may also differ due to the difference in the applied pressure profile. Table 2 shows that the surface forward flow is primarily affected by the friction coefficient and the layer stiffness. For the first load cycle, the maximum forward flow increases by a factor of about 4 as the friction coefficient increases from 0.1 to 0.25, and by a factor of 3.5 as the layer stiffness and hardness decrease by a factor of 2. The maximum forward flow increases secondarily with normal load, exhibiting an increase of approximately 38 percent as the normal load increases from $P/P_y = 100$ to 200. Similar trends also occur after the second load cycle. The increment in maximum forward flow between the first and second load cycles, $\Delta\overline{\delta}$, for the more compliant layer ($\beta = 2$) is relatively close to that predicted by an extrapolation of the results of Merwin and Johnson (1963), but well below that predicted by Bhargava et al. (1985). For the harder layers ($\beta = 4$), the increment in maximum forward flow is well below that predicted by either of the above analyses. However, the forward flow in three-dimensional contact would be expected to be less than that in a plane-strain line-contact analysis due to the constraint of the material outside the contact groove and the existence of a more complicated residual stress field. In addition, as mentioned before, the value of the peak contact pressure used in the present analysis is that taken directly from the contact pressure calculations and differs considerably from an equivalent Hertzian pressure rendering the same normal load. Furthermore, the particular methods used to calculate the effective material properties may give slightly too much weight to the substrate properties, particularly when the shear strain, γ_{xz}, that is primarily responsible for the forward flow reaches a maximum entirely within the layer. Nevertheless, the presence of a significant increment in the maximum forward flow between the two load cycles confirms that the structure is not yet approaching an elastic cycle.

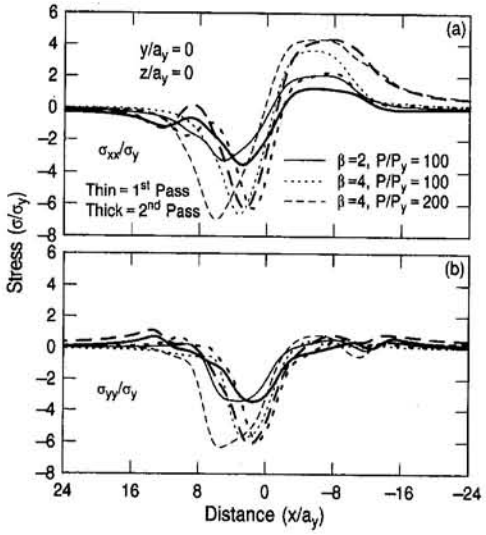


Fig. 11 Comparison of surface stresses for repeated sliding on the plane of symmetry for a sliding distance $\Delta x/a_y = 8$: (a) σ_{xx} stress and (b) σ_{yy} stress

The surface stresses generated during sliding as a function of the load cycle are shown in Fig. 11. The results are shown at a sliding distance $\Delta x/a_y = 8$ rather than 12 (i.e., the sphere center is at $x/a_y = 0$ instead of 4) in order to avoid any influence of the residual pile-up region on the results for the second load

Downloaded 04 May 2010 to 171.66.16.33. Redistribution subject to ASME license or copyright; see http://www.asme.org/terms/Terms_Use.cfm

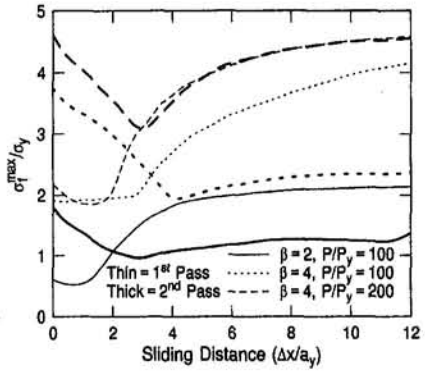


Fig. 12 Maximum value of the maximum principal stress σ_1 versus sliding distance $\Delta x/a_y$ and load pass

cycle. In these figures, the linetypes correspond to the material and load case, and the line thickness indicates the load cycle for which the results are given, with the thin and thick lines indicating results from the first and second load pass (load cycle), respectively. In all cases, the surface σ_{xx} stress, shown in Fig. 11(a), is tensile in the wake of the sphere. However, in the lower load cases ($P/P_y = 100$) the tensile stress exhibits a much smaller magnitude, while the second load cycle for $P/P_y = 200$ exhibits a comparable magnitude of the tensile stress in the wake with the first load cycle. In addition, the higher load case also exhibits a slightly tensile σ_{xx} stress in front of the sphere on the second cycle, whereas the stress in the same region was entirely compressive on the first pass. The surface σ_{yy} stress, shown in Fig. 11(b), exhibits comparable magnitudes of tensile stress in the wake for the two load cycles. However, for the $\beta = 4$ cases, a region of tensile stress appears in front of the contact region during the second load cycle, whereas the σ_{yy} stress was entirely compressive in this region during the first load cycle. For the more compliant layer, the magnitude of the tensile surface stress in front of the contact increases during the second cycle. The magnitude of the tensile σ_{yy} stresses in front and in the wake are comparable for the second load cycle.

Figure 12 shows the maximum principal stress in the layer as a function of sliding distance and load cycle. During the second load cycle, the maximum principal stress in the layer again occurs on the surface, and may be identified with a surface tensile σ_{xx} stress in the wake of the sphere. The initially high tensile stress during the second load cycle is the tensile residual stress remaining after the first load cycle (see Fig. 9(a)). The lower load cases exhibit a marked decrease in the maximum tensile stress during the second load cycle as compared to the first, whereas the higher load case exhibits almost identical results after a sliding distance $\Delta x/a_y \approx 3$. This is an indication that the residual stresses in the lower load cases are sufficient to protect the surface from high tensile stresses during additional load passes, whereas the higher load case must undergo further plastic deformation in order to generate sufficiently protective residual stresses to compensate for the applied load. Obviously, the greatest likelihood of initiation of ring cracks in the wake occurs during the first load cycle for the lighter loads, whereas the heavier load produces an almost identical driving stress for these cracks on the second load cycle as well. Further load cycles may also induce a more protective residual stress field for the heavier load case; however, additional load cycles to verify this were not performed due to the high computational cost.

Figure 13 shows a comparison between the residual stresses arising after the completion of the second load cycle with those from the first load cycle shown in Fig. 9. The σ_{xx} residual stress on the axis of symmetry, shown in Fig. 13(a), decreases after the second load cycle for all the cases. The greatest relative decrease occurs for the lower load cases, with a 30 percent decrease for $\beta = 2$ and a 48 percent decrease for $\beta = 4$. The higher load case exhibits a much smaller decrease of only about 14 percent. The stresses are qualitatively similar, with a large region of tensile residual stress occurring over the entire contact area. Figure 13(b) shows that the maximum tensile σ_{yy} residual stress after the second load cycle also decreases for all cases. For this stress component, the maximum magnitude on the axis of symmetry for both $\beta = 4$ cases decreases by about 25 percent, while the $\beta = 2$ case exhibits a decrease of only about six percent after the second load cycle. Thus, the lower load cases develop beneficial residual stresses after the first load cycle that decrease the tensile stresses occurring during subsequent cycles, thereby decreasing the maximum tensile stresses under both sliding and residual conditions. The residual stresses for the higher load case, however, are as yet insufficient to incur any benefit in reducing tensile surface stresses during sliding, although the residual tensile stresses are somewhat reduced after the second load cycle.

In separate experimental work, the finite element simulation results were compared with data obtained from a series of scratch tests performed on magnetic storage disks coated with approximately 30 nm of sputtered, primarily amorphous, i–carbon (Kral et al., 1996). The stress and plastic strain fields obtained from the finite element analysis were used to successfully validate material hardness models applied to the experimental data and to aid the interpretation of the experimental results.

4 Conclusions

The surface deformation characteristics resulting from indentation and sliding contact on a layered half-space were examined by performing three-dimensional finite element simulations. A rigid sphere was modeled by contact elements, precluding the necessity of using an assumed pressure profile. A 30-nm-thick layer was modeled, with stiffness and yield stress both two and four times that of the substrate. Elastic-perfectly plastic material behavior was assumed throughout the analysis. Sliding was performed at two normal loads, both 100 and 200 times the yield load of the substrate material, and friction coefficients of 0.1 and 0.25 in order to determine the effect of the normal load and friction on the surface stresses and deformation of the layered half-space.

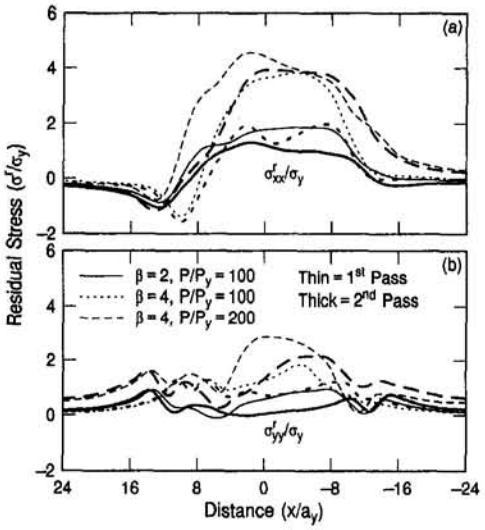


Fig. 13 Residual surface stresses on the plane of symmetry for repeated sliding after unloading from the indicated load for $\beta = 4$ and $\mu = 0.1$: (a) σ_{xx} stress and (b) σ_{yy} stress

Downloaded 04 May 2010 to 171.66.16.33. Redistribution subject to ASME license or copyright; see http://www.asme.org/terms/Terms_Use.cfm

The contact pressure profiles under low friction conditions ($\mu = 0.1$) exhibited a higher pressure at the front and transverse edges of the contact area in the steady state. As sliding commenced, the contact pressure developed a higher peak stress and slightly smaller contact area than that occurring under purely normal contact. Sliding on the harder and stiffer layer produced a much higher contact pressure and a smaller contact area. Sliding at the higher normal load $P/P_y = 200$ did not produce a significant increase in the peak contact pressure, but rather a much larger contact area and a lower mean pressure. The contact pressure profiles for higher friction exhibited slightly lower peak pressures and slightly larger contact areas. Surface displacements showed a pile-up region in front and around the transverse edges of the contact region. The amount of pile-up decreased slightly with increasing stiffness and hardness of the layer and increased with the friction coefficient. A very pronounced residual pile-up occurred upon unloading.

Surface tensile normal stresses occurred in the sliding direction (σ_{xx}) and normal to the sliding direction (σ_{yy}) in the wake of the sphere. The tensile σ_{xx} stress was the larger of the two tensile stress components, indicating a tendency toward the formation of transverse (ring) cracks on the surface in the wake of the indenter. The magnitudes of these tensile stresses increased with the stiffness and hardness of the layer, the normal load, and slightly with the coefficient of friction.

The residual σ_{xx} stresses exhibited lower or comparable magnitudes than the sliding stresses for all load cases, while the opposite was true for the residual σ_{yy} stress. However, the residual stresses were tensile over a larger area than the sliding stresses, particularly in front of the contact region. Thus, material that had been subjected to only compressive stresses under sliding conditions could be subjected to tensile stresses in the residual state, indicating that cracking may occur during both sliding and unloading.

A second load cycle was performed for all the low friction cases. The contact pressures exhibited symmetric profiles along the axis of symmetry and a slightly higher pressure at the transverse edge. The lower load cases showed considerably lower tensile stresses during the second load cycle and lower tensile residual stresses for both relatively compliant (soft) and stiff (hard) layers. In the higher load case, there was little change in the tensile stresses during the second load cycle. Therefore, the first load cycle will be most likely to produce cracks in the lower load cases, while there is expected to be little dependence of crack initiation on load cycle for the higher load case, at least over the two cycles investigated in the present study. The maximum forward flow at the contact surface increased primarily with friction and decreasing stiffness and hardness of the layer, and secondarily with normal load during the first load cycle. The positive increment of forward flow during the second load cycle indicated continued plastic deformation in the layer.

Acknowledgments

This work was partially supported by the Surface Engineering and Tribology Program of the National Science Foundation under Grant No. MSS-8996309 and the Computer Mechanics Laboratory at the University of California at Berkeley.

References

ABAQUS Theory Manual, 1989, Hibbitt, Karlsson, and Sorensen, Inc., Providence, RI.

Barlow, J., 1976, "Optimal Stress Location in Finite Element Models," *International Journal of Numerical Methods in Engineering,* Vol. 10, pp. 243–251.

Bhargava, V., Hahn, G. T., and Rubin, C. A., 1985a, "An Elastic-Plastic Finite Element Model of Rolling Contact, Part 1: Analysis of Single Contacts," ASME JOURNAL OF APPLIED MECHANICS, Vol. 52, pp. 67–74.

Bhargava, V., Hahn, G. T., and Rubin, C. A., 1985b, "An Elastic-Plastic Finite Element Model of Rolling Contact, Part 2: Analysis of Repeated Contacts," ASME JOURNAL OF APPLIED MECHANICS, Vol. 52, pp. 75–82.

Childs, T. H. C., 1992, "Deformation and Flow of Metals in Sliding Friction," *Fundamentals of Friction: Macroscopic and Microscopic Processes,* Singer, I. L., and Pollock, H. M., eds., NATO ASI Series E: Applied Sciences, Vol. 220, pp. 209–225.

Hamilton, G. M., and Goodman, L. E., 1966, "The Stress Field Created by a Circular Sliding Contact," ASME JOURNAL OF APPLIED MECHANICS, Vol. 33, pp. 371–376.

Jiang, Y., and Sehitoglu, H., 1994, "An Analytical Approach to Elastic-Plastic Stress Analysis of Rolling Contact," ASME *Journal of Tribology,* Vol. 116, pp. 577–587.

Johnson, K. L., 1985, *Contact Mechanics,* Cambridge University Press, Cambridge, U.K., pp. 159–184.

King, R. B., 1987, "Elastic Analysis of Some Punch Problems for a Layered Medium," *International Journal of Solids and Structures,* Vol. 23, pp. 1657–1664.

King, R. B., and O'Sullivan, T. C., 1987, "Sliding Contact Stresses in a Two-Dimensional Layered Elastic Half-Space," *International Journal of Solids and Structures,* Vol. 23, pp. 581–597.

Komvopoulos, K., Saka, N., and Suh, N. P., 1987, "The Role of Hard Layers in Lubricated and Dry Sliding," ASME *Journal of Tribology,* Vol. 109, pp. 223–231.

Kral, E. R., Komvopoulos, K., and Bogy, D. B., 1995, "Elastic-Plastic Finite Element Analysis of Repeated Indentation of a Half-Space by a Rigid Sphere," ASME JOURNAL OF APPLIED MECHANICS, Vol. 60, pp. 829–841.

Kral, E. R., Komvopoulos, K., and Bogy, D. B., 1995a, "Finite Element Analysis of Repeated Indentation of an Elastic-Plastic Layered Medium by a Rigid Sphere, Part I: Surface Results," ASME JOURNAL OF APPLIED MECHANICS, Vol. 62, pp. 20–28.

Kral, E. R., Komvopoulos, K., and Bogy, D. B., 1995b, "Finite Element Analysis of Repeated Indentation of an Elastic-Plastic Layered Medium by a Rigid Sphere, Part II: Subsurface Results," ASME JOURNAL OF APPLIED MECHANICS, Vol. 62, pp. 29–42.

Kral, E. R., Komvopoulos, K., and Bogy, D. B., 1996, "Hardness of Thin-Film Media: Scratch Experiments and Finite Element Simulations," ASME *Journal of Tribology,* Vol. 118, pp. 1–11.

Kulkarni, S. M., Hahn, G. T., Rubin, C. A., and Bhargava, V., 1990, "Elastoplastic Finite Element Analysis of Three-Dimensional, Pure Rolling Contact at the Shakedown Limit," ASME JOURNAL OF APPLIED MECHANICS, Vol. 57, pp. 57–65.

Kulkarni, S. M., Hahn, G. T., Rubin, C. A., and Bhargava, V., 1991a, "Elasto-Plastic Finite Element Analysis of Three-Dimensional Pure Rolling Contact Above the Shakedown Limit," ASME JOURNAL OF APPLIED MECHANICS, Vol. 58, pp. 347–353.

Kulkarni, S. M., Hahn, G. T., Rubin, C. A., and Bhargava, V., 1991b, "Elasto-Plastic Finite Element Analysis of Repeated Three-Dimensional, Elliptical Rolling Contact With Rail Wheel Properties," ASME *Journal of Tribology,* Vol. 113, pp. 434–441.

Lawn, B., 1992, "Friction Processes in Brittle Fracture," *Fundamentals of Friction: Macroscopic and Microscopic Processes,* Singer, I. L., and Pollock, H. M., eds., NATO ASI Series E: Applied Sciences, Vol. 220, pp. 137–165.

Merwin, J. E., and Johnson, K. L., 1963, "An Analysis of Plastic Deformation in Rolling Contact," *Proceedings of the Institution of Mechanical Engineers,* Vol. 177, pp. 676–690.

O'Sullivan, T. C., and King, R. B., 1988, "Sliding Contact Stress Field Due to a Spherical Indenter on a Layered Elastic Half-Space," ASME *Journal of Tribology,* Vol. 110, pp. 235–240.

Tian, H., and Saka, N., 1991a, "Finite Element Analysis of an Elastic-Plastic Two-Layer Half-Space: Normal Contact," *Wear,* Vol. 148, pp. 47–68.

Tian, H., and Saka, N., 1991b, "Finite Element Analysis of an Elastic-Plastic Two-Layer Half-Space: Sliding Contact," *Wear,* Vol. 148, pp. 261–285.

Wu, T. W., 1991, "Microscratch and Load Relaxation Tests for Ultra-thin Films," *Journal of Materials Research,* Vol. 6, pp. 407–426.

Downloaded 04 May 2010 to 171.66.16.33. Redistribution subject to ASME license or copyright; see http://www.asme.org/terms/Terms_Use.cfm

A General Orthotropic von Mises Plasticity Material Model With Mixed Hardening: Model Definition and Implicit Stress Integration Procedure

M. Kojić
Professor.

N. Grujović
Assistant Professor.

R. Slavković
Professor.

M. Živković
Assistant Professor.

Faculty of Mechanical Engineering,
University of Kragujevac,
Ul. S. Janjic 6
34000 Kragujevac, Serbia
Yugoslavia

A general orthotropic von Mises plasticity model, with an extension of the Hill's yield criterion to include mixed hardening, is introduced in the paper. Material constants and equivalent stress-equivalent plastic strain curves are defined in a way to suggest their experimental determination. The model represents a special case of a general anisotropic metal plasticity model proposed by the authors. An implicit stress integration procedure, representing an application of the governing parameter method (GPM) introduced by the first author, is presented. The GPM is briefly described, and the computational procedure, together with calculation of the consistent tangent moduli, are given in some detail for a general three-dimensional deformation, with direction of application to plane stress/shell conditions. Numerical examples illustrate applicability of the model and effectiveness of the computational algorithm.

1 Introduction

An important class of metal plasticity models used in practice are anisotropic models. We here mention some of the relevant references in this field. One of the first and commonly employed models is due to Hill (1950). A selection of engineering plasticity material models, with the implicit stress integration procedures, is given by Kojic (1993), and a general anisotropic metal plasticity behavior is described by Szczepinski (1992). The failure criteria of anisotropic materials are introduced and discussed in numerous papers (ex. Theocaris, 1991, 1992) and they may be employed as yield criteria in plasticity. Also, the anisotropic plasticity yield criteria may be used as creep potential for modeling of anisotropic thermoplasticity and/or creep metal behavior (Rees, 1983).

Besides the efforts to adequately describe the real material behavior in the inelastic domain, a very important actual task is to develop numerical algorithms for calculation of the material response under general loading and deformation conditions, especially within the finite element method. Significant research have been directed to this area of problems and a number of computational procedures have been proposed (Kojic et al., 1993, 1994a, 1987a, b, 1992a, b; Simo et al., 1985, 1988; Ortiz et al., 1983). One of the general concepts, the governing parameter method (GPM), proposed by Kojic (1993), leads to an efficient, stable, and generally applicable numerical procedure, which also is applied to the model here and is implemented into a general-purpose finite element code PAK (Kojic et al., 1994b).

The paper is organized as follows: In Section 2 we describe the material model, in Section 3 we outline the GPM, and in Section 4 we present the implicit stress integration procedure. Some illustrative numerical examples are solved in Section 5, and in the final section we give some concluding remarks.

2 Material Model Description

Anisotropic metal behavior in the plastic domain can be due to technological treatment, as in case of sheet metals, or it may be the deformation-induced anisotropy. A general anisotropic metal plasticity model can be described by the yield condition of the form

$$f_y = \tfrac{1}{2}\hat{\mathbf{S}}^T\mathbf{N}\hat{\mathbf{S}}' - \tfrac{1}{3}\hat{\sigma}_y^2 = 0 \tag{2.1}$$

where $\hat{\mathbf{S}}$ is the vector of the yield surface radius with tensorial components $(\hat{S}_{11}, \ldots, \hat{S}_{13})$, $\hat{\mathbf{S}}'$ is $\hat{\mathbf{S}}$ with doubled shear terms, $\hat{\sigma}_y$ is yield stress, and $\mathbf{N}$ is a matrix of material coefficients. Here we specify the yield condition (2.1) to correspond to orthotropic plasticity.

Following the Hill's yield condition (Hill, 1950), which is proposed for the orthotropic perfect plasticity, we can extend it to include change of the yield surface size and its position in the deviatoric stress space, by writing (2.1) in the form

$$2f_y = F(\hat{S}_{yy} - \hat{S}_{zz})^2 + G(\hat{S}_{zz} - \hat{S}_{xx})^2 + H(\hat{S}_{xx} - \hat{S}_{yy})^2 + 2L\hat{S}_{xy}^2 + 2I\hat{S}_{yz}^2 + 2K\hat{S}_{xz}^2 - 1 = 0 \tag{2.2}$$

where $F, G, \ldots, I, K$ are material constants which change during plastic deformation, and x, y, z are material orthotropy axes. We further can introduce a yield stress $\hat{\sigma}_y$ as a measure of the yield surface size, and transform (2.2) into a form

$$f_y = \tfrac{1}{2}[N_1(\hat{S}_{xx} - \hat{S}_{yy})^2 + N_2(\hat{S}_{xx} - \hat{S}_{zz})^2 + N_3(\hat{S}_{yy} - \hat{S}_{zz})^2 + 2(N_{xy}\hat{S}_{xy}^2 + N_{yz}\hat{S}_{yz}^2 + N_{xz}\hat{S}_{xz}^2)] - \tfrac{1}{3}\hat{\sigma}_y^2 = 0 \tag{2.3}$$

where

$$N_1 = \tfrac{2}{3}H\hat{\sigma}_y^2, \ldots, N_{xz} = \tfrac{2}{3}K\hat{\sigma}_y^2. \tag{2.4}$$

Contributed by the Applied Mechanics Division of THE AMERICAN SOCIETY OF MECHANICAL ENGINEERS for publication in the ASME JOURNAL OF APPLIED MECHANICS.

Discussion on this paper should be addressed to the Technical Editor, Professor Lewis T. Wheeler, Department of Mechanical Engineering, University of Houston, Houston, TX 77204-4792, and will be accepted until four months after final publication of the paper itself in the ASME JOURNAL OF APPLIED MECHANICS.

Manuscript received by the ASME Applied Mechanics Division, Aug. 8, 1994; final revision, Apr. 19, 1995. Associate Technical Editor: C. F. Shih.

Copyright © 1996 by ASME

Downloaded 04 May 2010 to 171.66.16.33. Redistribution subject to ASME license or copyright; see http://www.asme.org/terms/Terms_Use.cfm

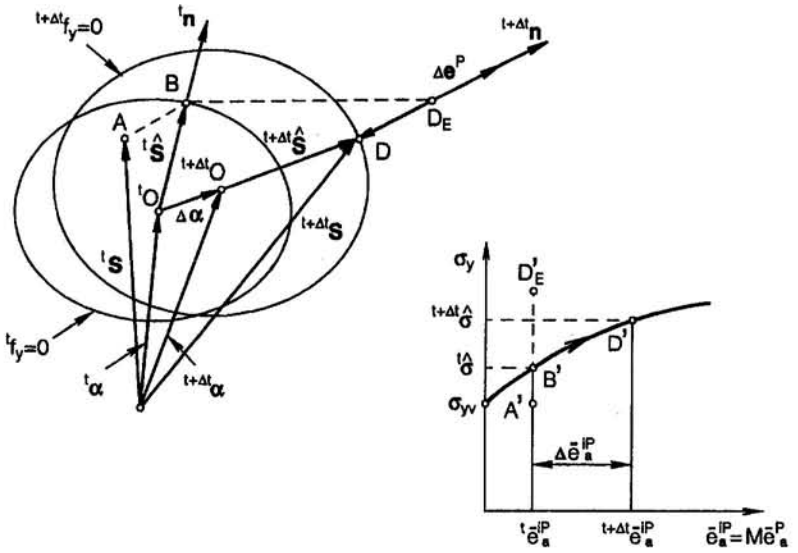


Fig. 1 Stress states at time t and at time $t + \Delta t$ in deviatoric plane and on the yield curve

Equation (2.3) can be written in the matrix form (2.1), with matrix $\mathbf{N}$ (with the nonzero terms) as

$$\mathbf{N} = \begin{bmatrix} N_1+N_2 & -N_1 & -N_2 & & & \\ & N_1+N_3 & -N_3 & & & \\ & & N_2+N_3 & & & \\ & & & N_{xy} & & \\ & \text{symmetric} & & & N_{yz} & \\ & & & & & N_{xz} \end{bmatrix}. \quad (2.5)$$

One form of $\hat{\sigma}_y$, which takes into account yield stresses X, Y, Z in uniaxial tension or compression in the material axes, and Y_{xy}, Y_{yz}, Y_{xz}—yield shear stresses in the material orthotropy planes, can be

$$\hat{\sigma}_y = \{\tfrac{1}{2}[\tfrac{1}{3}(X^2 + Y^2 + Z^2) + Y_{xy}^2 + Y_{yz}^2 + Y_{xz}^2]\}^{1/2}. \quad (2.6)$$

A schematic representation of the yield surface (2.3) is shown in Fig. 1.

Constitutive relations in plasticity can be obtained from the flow rule (Hill, 1950) so that from (2.1) and (2.5) follows

$$d\mathbf{e}^P = d\lambda \frac{\partial f_y}{\partial \boldsymbol{\sigma}} = d\lambda \mathbf{N}\hat{\mathbf{S}} \quad (2.7)$$

where $d\mathbf{e}^P$ is increment of plastic strain tensor $\mathbf{e}^P$ and $d\lambda$ is a positive scalar. As it is common in metal plasticity, we introduce equivalent stress (or modified effective stress) $\hat{\sigma}_a$ as

$$\hat{\sigma}_a = (\tfrac{3}{2}\hat{\mathbf{S}}^T\mathbf{N}\hat{\mathbf{S}}')^{1/2} \quad (2.8)$$

so that the yield condition (2.1) or (2.3) can be written in the form

$$f_y = \hat{\sigma}_a - \hat{\sigma}_y = 0. \quad (2.9)$$

From the condition of equality of plastic work dW^{iP} corresponding to isotropic hardening at a material point and on the yield curve $(\hat{\sigma}_a, \bar{e}_a^{iP})$,

$$dW^{iP} = \hat{\mathbf{S}}^T d\hat{\mathbf{e}}^{iP} = \hat{\sigma}_a d\bar{e}_a^{iP} \quad (2.10)$$

where $d\hat{\mathbf{e}}^{iP}$ contains double shear terms, and

$$d\mathbf{e}^{iP} = M d\mathbf{e}^P \quad (2.11)$$

we obtain, for $\mathbf{N}$ given by (2.5),

$$d\bar{e}_a^P = (\tfrac{2}{3}(d\mathbf{e}^P)^T\mathbf{N}^{-1}d\hat{\mathbf{e}}^P)^{1/2}. \quad (2.12)$$

Of course, $\mathbf{e}^{iP}$ and $\bar{e}_a^{iP}$ are the current plastic and equivalent plastic strains, as integrals of $d\mathbf{e}^{iP}$ and $d\bar{e}_a^P$, corresponding to isotropic part of hardening, and $d\hat{\mathbf{e}}^P$ is $d\mathbf{e}^P$ with double shear terms.

Since plastic deformation is incompressible, one of the normal plastic strains can be expressed in terms of the other two, and in practical calculation of $d\bar{e}_a^P$ we use the 5×5 $\mathbf{N}$ matrix which can be inverted (the original 6×6 matrix $\mathbf{N}$ is singular).

Another form of the above expression for $d\bar{e}_a^P$ is given in Kojic (1993) and Chen et al. (1988). In (2.11) M is the mixed hardening parameter, $0 \le M \le 1$, with $M = 1$ and $M = 0$ corresponding to isotropic and kinematic hardening, respectively. It is useful for numerical procedures presented in Section 4, to write the relation

$$d\lambda = \frac{3}{2}\frac{d\bar{e}_a^P}{\hat{\sigma}_y} \quad (2.13)$$

which follows from (2.7)–(2.9) and (2.12), with $\hat{\sigma}_y = \hat{\sigma}_y(M\bar{e}_a^P)$.

According to the above description of the model, a series of simple experiments can be performed, leading to the yield curve

$$\sigma_y = \sigma_y(\bar{e}_a^P) \quad (2.14)$$

as schematically shown in Fig. 2. From these experiments we calculate coefficients $F, G, \ldots, K$, to satisfy (2.2), values of $\hat{\sigma}_y$ according to (2.6) and $N_1, \ldots, N_{xz}$ from (2.4), for various stages of plastic deformation (expressed in terms of, for exam-

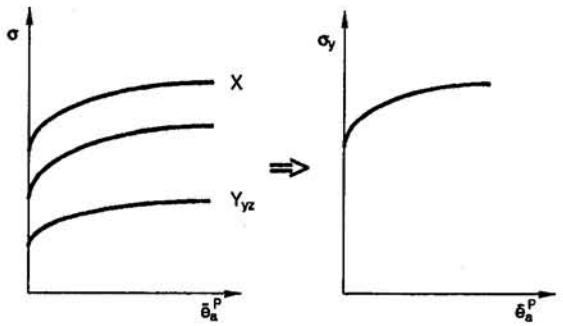


Fig. 2 Yield curves corresponding to simple experiments and the yield curve $\sigma_y(\bar{e}_a^P)$

Downloaded 04 May 2010 to 171.66.16.33. Redistribution subject to ASME license or copyright; see http://www.asme.org/terms/Terms_Use.cfm

ple, effective plastic strain $\bar{\varepsilon}^P = \int (\frac{2}{3} d\mathbf{e}^P_{ij} d\mathbf{e}^P_{ij})^{1/2}$ as a measure). Then, using (2.12) we determine yield curves shown in Fig. 2 and the equivalent yield curve $\sigma_y(\bar{\varepsilon}^P_a)$.

In order to complete the material model description, we need constitutive relations for the back stress $\boldsymbol{\alpha}$. An approach, analogous to isotropic plasticity, leads to the expression

$$d\boldsymbol{\alpha} = (1 - M)\mathbf{C}^P d\mathbf{e}^P \tag{2.15}$$

where $\mathbf{C}^P$ is the matrix of plastic moduli. A simple form of $\mathbf{C}^P$ based on diagrams in Fig. 2, which provides the deviatoric character of $\boldsymbol{\alpha}$, is

$$C^P_{ij} = \tfrac{2}{3}(1 - M)N_{ij}E_{Pj} \quad \text{no sun in } j \tag{2.16}$$

where E_{Pi} are plastic moduli of the yield curves in Fig. 2. We will use these expressions for C^P_{ij} further in the paper. A special case of (2.15) is

$$C^P_{ij} = c\delta_{ij} \tag{2.17}$$

which corresponds to assumption adopted in Baltov and Sawczuk (1965).

In order to reduce the above orthotropic model to the isotropic von Mises material, we should have, according to (2.4), (2.6), and (2.16),

$$X = Y = Z = Y_{xy}/\sqrt{3} = Y_{yz}/\sqrt{3} = Y_{xz}/\sqrt{3} = \sigma_y$$

$$N_1 = N_2 = N_3 = \tfrac{1}{3}N_{xy} = \tfrac{1}{3}N_{yz} = \tfrac{1}{3}N_{xz} = \tfrac{1}{3}$$

$$E_{P1} = E_{P2} = E_{P3} = E_P$$

$$E_{P4} = E_{P5} = E_{P6} = E_P\sqrt{3}. \tag{2.18}$$

3 The Governing Parameter Method

In this section we briefly present the main idea of the governing parameter method (GPM) (Kojic, 1993) developed for implicit integration of inelastic constitutive relations within incremental solution procedure of the strain-driven problems. The GPM has been implemented to various material models in plasticity, thermoplasticity, and/or creep of isotropic and anisotropic metals; to soil plasticity, and to viscoplasticity of metals and soils; and to two-dimensional, three-dimensional shell and beam conditions, for small and large strains (Kojic 1992a, 1993; Kojic et al., 1992b, 1994a, b). According to the GPM, the problem of stress integration is reduced to solution of one nonlinear equation, providing an efficient computational procedure, applicable to large strain increments in time (load) step. Also, the tangent moduli can be calculated by a straightforward differentiations.

We suppose that at the start of the time-step the known quantities are

$${}^t\boldsymbol{\sigma},\ {}^t\mathbf{e},\ {}^t\mathbf{e}^{IN},\ {}^t\boldsymbol{\beta},\ {}^{t+\Delta t}\mathbf{e} \tag{3.1}$$

where ${}^t\boldsymbol{\sigma}$, ${}^t\mathbf{e}^{IN}$ and ${}^t\boldsymbol{\beta}$ are stresses, inelastic strains, and internal variables; and ${}^t\mathbf{e}$ and ${}^{t+\Delta t}\mathbf{e}$ are strains at the start and end of the time-step. The unknowns are the following quantities at the end of the time-step

$${}^{t+\Delta t}\boldsymbol{\sigma},\ {}^{t+\Delta t}\mathbf{e}^{IN},\ {}^{t+\Delta t}\boldsymbol{\beta}. \tag{3.2}$$

Next, we suppose that the unknowns can be expressed in terms of one (governing) parameter p, i.e., we can write

$$\begin{aligned}
{}^{t+\Delta t}\boldsymbol{\sigma} &= \boldsymbol{\sigma}({}^t\boldsymbol{\sigma},\ {}^t\mathbf{e},\ {}^t\mathbf{e}^{IN},\ {}^t\boldsymbol{\beta},\ {}^{t+\Delta t}\mathbf{e},\ p)\\
{}^{t+\Delta t}\mathbf{e}^{IN} &= \mathbf{e}^{IN}({}^t\boldsymbol{\sigma},\ {}^t\mathbf{e},\ {}^t\mathbf{e}^{IN},\ {}^t\boldsymbol{\beta},\ {}^{t+\Delta t}\mathbf{e},\ p)\\
{}^{t+\Delta t}\boldsymbol{\beta} &= \boldsymbol{\beta}({}^t\boldsymbol{\sigma},\ {}^t\mathbf{e},\ {}^t\mathbf{e}^{IN},\ {}^t\boldsymbol{\beta},\ {}^{t+\Delta t}\mathbf{e},\ p).
\end{aligned} \tag{3.3}$$

The governing parameter method consists in the following steps:

1 Express the unknowns according to (3.3).
2 Form the governing equation $f(p) = 0$.
3 Solve $f(p) = 0$ for the governing parameter ${}^{t+\Delta t}p$.
4 Substitute ${}^{t+\Delta t}p$ into (3.3) to determine the unknowns.

Finally, the tangent moduli $\mathbf{C}^{IN}$ can be obtained as

$${}^{t+\Delta t}\mathbf{C}^{IN} = \frac{\partial {}^{t+\Delta t}\boldsymbol{\sigma}}{\partial {}^{t+\Delta t}\mathbf{e}} = \frac{\partial {}^{t+\Delta t}\boldsymbol{\sigma}}{\partial {}^{t+\Delta t}p}\frac{\partial {}^{t+\Delta t}p}{\partial {}^{t+\Delta t}\mathbf{e}} \tag{3.4}$$

where derivatives $\partial {}^{t+\Delta t}p/\partial {}^{t+\Delta t}\mathbf{e}$ can be calculated by differentiation of the governing equation,

$$\frac{\partial f}{\partial {}^{t+\Delta t}\mathbf{e}} = \left(\frac{\partial f}{\partial {}^{t+\Delta t}\boldsymbol{\sigma}}\frac{\partial {}^{t+\Delta t}\boldsymbol{\sigma}}{\partial {}^{t+\Delta t}p} + \frac{\partial f}{\partial {}^{t+\Delta t}\mathbf{e}^{IN}}\frac{\partial {}^{t+\Delta t}\mathbf{e}^{IN}}{\partial {}^{t+\Delta t}p} + \frac{\partial \mathrm{f}}{\partial {}^{t+\Delta t}\boldsymbol{\beta}}\frac{\partial {}^{t+\Delta t}\boldsymbol{\beta}}{\partial {}^{t+\Delta t}p}\right)\frac{\partial {}^{t+\Delta t}p}{\partial {}^{t+\Delta t}\mathbf{e}} + \frac{\partial f}{\partial {}^{t+\Delta t}\mathbf{e}} = 0. \tag{3.5}$$

4 Implicit Stress Integration Procedure

Here we implement the above presented governing parameter method (GPM) to stress integration for the material model described in Section 2.

Elastic constitutive relations for deviatoric stresses ${}^{t+\Delta t}\mathbf{S}$ at the end of the time (load) step are

$${}^{t+\Delta t}\mathbf{S} = \mathbf{C}'^E {}^{t+\Delta t}\mathbf{e}^E = \mathbf{C}'^E({}^{t+\Delta t}\mathbf{e}'' - \Delta\lambda\ {}^{t+\Delta t}\mathbf{N}^{t+\Delta t}\hat{\mathbf{S}}) \tag{4.1}$$

where ${}^{t+\Delta t}\mathbf{e}^E$ is elastic strain, $\mathbf{C}'^E$—elastic matrix corresponding to deviatoric stress, $\Delta\lambda$—positive scalar, and

$${}^{t+\Delta t}\mathbf{e}'' = {}^{t+\Delta t}\mathbf{e} - {}^t\mathbf{e}^P. \tag{4.2}$$

Here ${}^{t+\Delta t}\mathbf{e}$ is the strain at the end of time step, and ${}^t\mathbf{e}^P$—plastic strain at start of the time-step. In writing (4.1) we have employed plasticity constitutive relations (2.7), now for the time-step Δt, and under the implicit integration assumption

$$\Delta\mathbf{e}^P = \Delta\lambda\ {}^{t+\Delta t}\mathbf{N}^{t+\Delta t}\hat{\mathbf{S}} \tag{4.3}$$

as indicated in Fig. 1. Also, we use the matrix ${}^{t+\Delta t}\mathbf{N}$ evaluated for equivalent plastic strain ${}^{t+\Delta t}\bar{\varepsilon}^P_a = {}^t\bar{\varepsilon}^P_a + \Delta\bar{\varepsilon}^P_a$. The elastic matrix $\mathbf{C}'^E$ corresponds to orthotropic elasticity, and the nonzero coefficients relating normal stresses to strains are expressible in terms of the Young's moduli E_i and the Poisson's ratios ν_{ij} (Jones, 1975), while the part of $\mathbf{C}'^E$ attributed to shear terms is diagonal and only contains the shear moduli G_{ij}. The mean stress ${}^{t+\Delta t}\sigma_m$ can be expressed in the form

$${}^{t+\Delta t}\sigma_m = C^{mE}_{11}\,{}^{t+\Delta t}e^E_{xx} + C^{mE}_{22}\,{}^{t+\Delta t}e^E_{yy} + C^{mE}_{33}\,{}^{t+\Delta t}e^E_{zz} \tag{4.4}$$

where C^{mE}_{ii} are elastic constants which can directly be written in terms of elastic matrix coefficients C^E_{ij}.

We note that the relations (4.1) and (4.3) correspond to a general three-dimensional deformation. However, they can easily be transformed into the relations for plane stress (or shell) conditions. Namely, by imposing the zero-stress condition for stress ${}^{t+\Delta t}\sigma_{zz}$, we practically modify the elastic coefficients C'^E_{ij} into $\bar{C}'^E_{ij}$ and instead of (4.1) write the modified first two relations as

$${}^{t+\Delta t}S_i = \bar{C}'^E_{i1}\,{}^{t+\Delta t}e^E_{xx} + \bar{C}'^E_{i2}\,{}^{t+\Delta t}e^E_{yy} \quad i = 1, 2. \tag{4.5}$$

In further analysis we assume the three-dimensional deformation, but we will refer to plane stress/shell conditions in the sense of the above presentation.

The increment of the back stress $\Delta\boldsymbol{\alpha}$ can be expressed by using (2.15), (2.16), and (4.3) as

$$\Delta\boldsymbol{\alpha} = \bar{\mathbf{C}}^P\Delta\mathbf{e}^P = \Delta\lambda\bar{\mathbf{C}}^P\,{}^{t+\Delta t}\mathbf{N}\,{}^{t+\Delta t}\hat{\mathbf{S}} \tag{4.6}$$

Downloaded 04 May 2010 to 171.66.16.33. Redistribution subject to ASME license or copyright; see http://www.asme.org/terms/Terms_Use.cfm

Table 1 Computational steps for stress integration

1. Suppose Δe_a^{-P}
2. Determine ${}^{t+\Delta t}\hat{\sigma}_y$ from the yield curve ${}^{t+\Delta t}\hat{\sigma}_y = \sigma_y[M({}^t e_a^{-P} + \Delta e_a^{-P})]$
3. Calculate $\Delta\lambda$ from (4.10)
4. Calculate ${}^{t+\Delta t}\hat{\mathbf{S}}$ from (4.8)
5. Check for $|{}^{t+\Delta t}f_y| \le \varepsilon$ according to (4.11) If the condition is not satisifed, go to Step 1 with a new trial value Δe_a^{-P}.
6. Calculate final quantities for the time-step, ${}^{t+\Delta t}\mathbf{S}$, ${}^{t+\Delta t}\boldsymbol{\alpha}$, ${}^{t+\Delta t}\mathbf{e}^P$, ${}^{t+\Delta t}\boldsymbol{\sigma}$

where $\bar{C}_{ij}^P$ are calculated according to (2.16) with use of weighted moduli E_{Pi} in the time-step. According to Fig. 1 and relation (4.6), we can express the yield condition in the form

$$ {}^{t+\Delta t}\mathbf{S} = {}^t\boldsymbol{\alpha} + (\mathbf{I} + \Delta\lambda\bar{\mathbf{C}}^P\,{}^{t+\Delta t}\mathbf{N})\,{}^{t+\Delta t}\hat{\mathbf{S}}. \tag{4.7}$$

Now, from (4.1) and (4.7) we solve for ${}^{t+\Delta t}\hat{\mathbf{S}}$ as

$$ {}^{t+\Delta t}\hat{\mathbf{S}} = [\Delta\lambda(\mathbf{C}'^E + \bar{\mathbf{C}}^P)^{t+\Delta t}\mathbf{N} + \mathbf{I}]^{-1}\,{}^{t+\Delta t}\hat{\mathbf{S}}^E \tag{4.8}$$

where

$$ {}^{t+\Delta t}\hat{\mathbf{S}}^E = \mathbf{C}'^E\,{}^{t+\Delta t}\mathbf{e}'' - {}^t\boldsymbol{\alpha} \tag{4.9}$$

is the elastic solution for the radius ${}^{t+\Delta t}\hat{\mathbf{S}}$. The necessary relation follows from (2.13):

$$ \Delta\lambda = \frac{3}{2}\frac{\Delta\bar{e}_u^P}{{}^{t+\Delta t}\hat{\sigma}_y}. \tag{4.10}$$

Recapitulating the above relations we can state that all unknowns are functions of one parameter $\Delta\bar{e}_a^P$. Namely, for a given value $\Delta\bar{e}_a^P$ and the yield curve we determine ${}^{t+\Delta t}\hat{\sigma}_y$ corresponding to $M({}^t\bar{e}_a^P + \Delta\bar{e}_a^P)$, then calculate $\Delta\lambda$ from (4.10), use ${}^{t+\Delta t}N_{ij}$ and $\bar{C}^P$ from the material description, and find $\Delta\mathbf{e}^P$—from (4.3), $\Delta\boldsymbol{\alpha}$—from (4.6), ${}^{t+\Delta t}\mathbf{S}$—from (4.1) or (4.7), and ${}^{t+\Delta t}\sigma_m$—from (4.4). Then, according to the GPM, we form the governing equation by employing the yield condition of the form (2.1) (or (2.3)),

$$ {}^{t+\Delta t}f_y = \tfrac{1}{2}{}^{t+\Delta t}\hat{\mathbf{S}}^T\,{}^{t+\Delta t}\mathbf{N}\,{}^{t+\Delta t}\hat{\mathbf{S}}' - \tfrac{1}{3}{}^{t+\Delta t}\hat{\sigma}_y^2 = 0 \tag{4.11}$$

which we solve for the governing parameter $\Delta\bar{e}_a^P$. With the solution for $\Delta\bar{e}_a^P$ we calculate also the final stresses

$$ {}^{t+\Delta t}\boldsymbol{\sigma} = {}^{t+\Delta t}\mathbf{S} + {}^{t+\Delta t}\boldsymbol{\sigma}_m. \tag{4.12}$$

The computational steps according to the described procedure is summarized in Table 1. In solving for $\Delta\bar{e}_a^P$, a stable bisection procedure with possible acceleration schemes (Kojic et al., 1994b) may be employed. A maximum $\Delta\bar{e}_a^P$ can be obtained from elastic solution for time step and equivalent yield curve. We use $0.1*(\Delta\bar{e}_a^P)_{\max}$ as initial value and increase it by a scale factor until we obtain ${}^{t+\Delta t}f_y < 0$. In practical application of the algorithm we have around ten trials until the relative increment between two trials and $|{}^{t+\Delta t}f_y|$ become smaller than 1.E-10.

We mention here that it is computationally more efficient to solve explicitly for ${}^{t+\Delta t}\hat{\mathbf{S}}$ instead to invert the matrix as indicated in (4.8). Then, we transform (4.8) into

$$ {}^{t+\Delta t}\hat{S}_{xx} = ({}^{t+\Delta t}\hat{S}_{xx}^E + \Delta\lambda D_{xx})/D_\lambda$$

$$ {}^{t+\Delta t}\hat{S}_{yy} = ({}^{t+\Delta t}\hat{S}_{yy}^E + \Delta\lambda D_{yy})/D_\lambda$$

$$ {}^{t+\Delta t}\hat{S}_{zz} = -{}^{t+\Delta t}\hat{S}_{xx} - {}^{t+\Delta t}\hat{S}_{yy}$$

$$ {}^{t+\Delta t}\hat{S}_i = {}^{t+\Delta t}\hat{S}_i^E/[1 + \Delta\lambda(2G_{ii} + \bar{C}_{ii}^P){}^{t+\Delta t}N_{ii}]$$

$$ i = 4, 5, 6 \quad \text{no sum on } i \tag{4.13}$$

where

$$ D_{xx} = C_{yy}\,{}^{t+\Delta t}\hat{S}_{xx}^E + C_{xy}\,{}^{t+\Delta t}\hat{S}_{yy}^E$$

$$ D_{yy} = C_{yx}\,{}^{t+\Delta t}\hat{S}_{xx}^E + C_{xx}\,{}^{t+\Delta t}\hat{S}_{yy}^E$$

$$ D_\lambda = 1 + \Delta\lambda(C_{xx} + C_{yy}) + (\Delta\lambda)^2(C_{xx}C_{yy} - C_{xy}C_{yx}) \tag{4.14}$$

and

$$ C_{xx} = (C_{1k}'^E + \bar{C}_{1k}^P)({}^{t+\Delta t}N_{k1} - {}^{t+\Delta t}N_{k3})$$

$$ C_{xy} = -(C_{1k}'^E + \bar{C}_{1k}^P)({}^{t+\Delta t}N_{k2} - {}^{t+\Delta t}N_{k3})$$

$$ C_{yx} = -(C_{2k}'^E + \bar{C}_{2k}^P)({}^{t+\Delta t}N_{k1} - {}^{t+\Delta t}N_{k3})$$

$$ C_{yy} = (C_{2k}'^E + \bar{C}_{2k}^P)({}^{t+\Delta t}N_{k2} - {}^{t+\Delta t}N_{k3}) \tag{4.15}$$

Here we have taken into account deviatoric character of the radius ${}^{t+\Delta t}\hat{\mathbf{S}}$. The above relations are directly applicable to plane stress/shell conditions, with the corresponding corrections of elastic constants, as previously mentioned (Eq. (4.5)).

Finally, we present a concept of calculation of elastic-plastic matrix ${}^{t+\Delta t}\mathbf{C}^{EP}$, according to the GPM. By definition, we have

$$ {}^{t+\Delta t}\mathbf{C}^{EP} = \frac{\partial\,{}^{t+\Delta t}\boldsymbol{\sigma}}{\partial\,{}^{t+\Delta t}\mathbf{e}} = {}^{t+\Delta t}\mathbf{C}' + {}^{t+\Delta t}\mathbf{C}^m \tag{4.16}$$

where the components of ${}^{t+\Delta t}\mathbf{C}'$ and ${}^{t+\Delta t}\mathbf{C}^m$ are

$$ {}^{t+\Delta t}C_{ij}' = \frac{\partial\,{}^{t+\Delta t}S_i}{\partial\,{}^{t+\Delta t}e_j} \quad i, j = 1, 2, \ldots, 6 \tag{4.17}$$

$$ {}^{t+\Delta t}C_{ij}^m = \frac{\partial\,{}^{t+\Delta t}\sigma_m}{\partial\,{}^{t+\Delta t}e_j} \quad i = 1, 2, 3; \quad j = 1, 2, \ldots, 6$$

$$ {}^{t+\Delta t}C_{ij}^m = 0 \quad i = 4, 5, 6; \quad j = 1, 2, \ldots, 6 \tag{4.18}$$

We note that in the above expressions it is common to use

$$ e_4 = \gamma_{xy}, \quad e_5 = \gamma_{yz}, \quad e_6 = \gamma_{xz} \tag{4.19}$$

In calculation of coefficients of ${}^{t+\Delta t}\mathbf{C}^{EP}$ according to (4.17) and (4.18) we use expressions (4.7) and (4.4) for ${}^{t+\Delta t}\mathbf{S}$ and ${}^{t+\Delta t}\sigma_m$. To simplify calculation we neglect derivatives of material coefficients ${}^{t\Delta t}N_{ij}$. Since ${}^{t+\Delta t}\mathbf{S}$ and ${}^{t+\Delta t}\sigma_m$ are functions of ${}^{t+\Delta t}\mathbf{e}''$, and ${}^{t+\Delta t}\mathbf{e}''$ are defined in terms of ${}^{t+\Delta t}\mathbf{e}$ by relations (4.2), the problem of calculation of ${}^{t+\Delta t}\mathbf{C}^{EP}$ is reduced to computation of derivatives of ${}^{t+\Delta t}\mathbf{S}$ and ${}^{t+\Delta t}\sigma_m$ with respect to ${}^{t+\Delta t}\mathbf{e}''$; those derivatives can be obtained as follows.

From (4.7) we have

$$ {}^{t+\Delta t}\bar{C}_{ij}' = {}^{t+\Delta t}S_{i,j} = (l_P\bar{C}_{is}^P + \Delta\lambda\hat{E}_{is}')^{t+\Delta t}N_{sk}\,{}^{t+\Delta t}\hat{S}_k(\Delta\bar{e}^P)_{,j}$$

$$ + (\delta_{ik} + \Delta\lambda\bar{C}_{is}^P{}^{t+\Delta t}N_{sk})^{t+\Delta t}\hat{S}_{k,j} \tag{4.20}$$

where $_{,j} = \partial/\partial\,{}^{t+\Delta t}e_j''$, and

$$ l_P = \frac{1}{{}^{t+\Delta t}\hat{\sigma}_y}\left(\frac{3}{2} - M\,{}^{t+\Delta t}\hat{E}_P\Delta\lambda\right) \tag{4.21}$$

$$ \hat{E}_{is}' = \frac{2}{3}(1 - M)^{t+\Delta t}N_{is}\frac{\partial\bar{E}_{Ps}}{\partial(\Delta\bar{e}_a^P)} \quad \text{no sum on } s. \tag{4.22}$$

In (4.21) ${}^{t+\Delta t}\hat{E}_P = \partial\,{}^{t+\Delta t}\hat{\sigma}_y/\partial(\Delta\bar{e}_a^P)$ is a plastic modulus evaluated on the equivalent yield curve for $\bar{e}_a^P = M\,{}^{t+\Delta t}\bar{e}_a^P$. In writing (4.20) we have used (4.10) and (2.16). Next, from (4.13) we can express derivatives ${}^{t+\Delta t}\hat{S}_{k,j}$ in the form

$$ {}^{t+\Delta t}\hat{S}_{k,j} = P_{kj} + Q_k(\Delta\bar{e}_a^P)_{,j} \tag{4.23}$$

where P_{kj} and Q_k are coefficients obtained by the corresponding differentiations. For example,

$$ P_{1j} = [(1 + \Delta\lambda C_{yy})C_{1j}'^E + \Delta\lambda C_{xy}C_{2j}'^E]/D_\lambda$$

$$ Q_1 = [l_P D_{xx} + \Delta\lambda D_{xx}' - {}^{t+\Delta t}\hat{S}_{xx}(l_P D_{\lambda,\lambda} + D_\lambda')]/D_\lambda \tag{4.24}$$

Downloaded 04 May 2010 to 171.66.16.33. Redistribution subject to ASME license or copyright; see http://www.asme.org/terms/Terms_Use.cfm

$$P_{ij} = \frac{C'^{E}_{ii}}{1 + \Delta\lambda(2G_{ii} + \bar{C}^{P}_{ii})^{t+\Delta t}N_{ii}}\,\delta_{ij} \quad i = 4, 5, 6 \text{ no sum on } i$$

$$Q_i = \frac{-{}^{t+\Delta t}\hat{S}_i\ {}^{t+\Delta t}N_{ii}}{1 + \Delta\lambda(2G_{ii} + \bar{C}^{P}_{ii})\ {}^{t+\Delta t}N_{ii}} \times [l_P(2G_{ii} + \bar{C}^{P}_{ii}) + \Delta\lambda\hat{E}'_{ii})] \quad (4.25)$$

where $D'_{xx} = \partial D_{xx}/\partial(\Delta\bar{\varepsilon}^{P}_{a})$ which follows directly from (4.14) and (4.15), $D'_{\lambda} = \partial D_{\lambda}/\partial(\Delta\bar{\varepsilon}^{P}_{a})$ with $\Delta\lambda$ = const., and $D_{\lambda,\lambda} = \partial D_{\lambda}/\partial(\Delta\lambda)$. We note that from the third relation of (4.13) follows

$$P_{3j} = -(P_{1j} + P_{2j}), \quad Q_3 = -Q_1 - Q_2. \quad (4.26)$$

Further, to calculate derivatives $(\Delta\bar{\varepsilon}^{P}_{a})_{,j}$ we, according to the GPM, Equation (3.5), differentiate (4.11) and obtain

$$(\Delta\bar{\varepsilon}^{P}_{a})_{,j} = -W_j/W_0 \quad (4.27)$$

where

$$W_j = {}^{t+\Delta t}N_{ik}\ {}^{t+\Delta t}\hat{S}_i\hat{P}_{kj}$$

$$W_0 = {}^{t+\Delta t}N_{ik}\ {}^{t+\Delta t}\hat{S}_i\hat{Q}_k - \tfrac{2}{3}M\ {}^{t+\Delta t}\hat{\sigma}_y\ {}^{t+\Delta t}\hat{E}_P. \quad (4.28)$$

Here $\hat{P}_{kj}$ and $\hat{Q}_k$ are P_{kj} and Q_k with double terms corresponding to shear components. With derivatives $(\Delta\bar{\varepsilon}^{P}_{a})_{,j}$ from (4.27) we can compute ${}^{t+\Delta t}\hat{S}_{k,j}$ from (4.23) and ${}^{t+\Delta t}\hat{C}'_{ij}$ from (4.20).

Finally, derivatives ${}^{t+\Delta t}\bar{C}^{m}_{j} = \partial\,{}^{t+\Delta t}\sigma_m/\partial\,{}^{t+\Delta t}e''_j$, from which ${}^{t+\Delta t}C^{m}_{ij}$ in (4.18) can be determined, may be obtained from (4.3), (4.4), and (4.23) as

$$\bar{C}^{m}_{j} = C^{mE}_{jj} - \Delta\lambda P^{m}_{j} + Q^{m}_{j} \quad j = 1, 2, 3 \quad \text{no sum on } j$$

$$\bar{C}^{m}_{j} = Q^{m}_{j} \quad j = 4, 5, 6 \quad (4.29)$$

where

$$P^{m}_{j} = C^{mE}_{ii}\ {}^{t+\Delta t}N_{ik}P_{kj}$$

$$Q^{m}_{j} = C^{mE}_{ii}\ {}^{t+\Delta t}N_{ik}(l_P\ {}^{t+\Delta t}\hat{S}_k + \Delta\lambda Q_k)\,\frac{W_j}{W_0}. \quad (4.30)$$

With all coefficients ${}^{t+\Delta t}\bar{C}'_{ij}$ from (4.20) and $\bar{C}^{m}_{j}$ from (4.29), we determine ${}^{t+\Delta t}\mathbf{C}^{EP}$ by (4.16). The elastic-plastic matrix ${}^{t+\Delta t}\mathbf{C}^{EP}$ is the tangent constitutive matrix since it corresponds to the stress/strain state at the end of the load step. In the case of plane stress/shell, beam, or pipe conditions, the above concept of differentiation of the governing relations can be followed, or the corresponding static condensations can be performed on the ${}^{t+\Delta t}\mathbf{C}^{P}$ given by (4.16) for a three-dimensional deformation.

5 Numerical Examples

We give solutions for two examples.

Example 1: Plate Loaded by In-Plane Loads. A plate, modeled by one linear finite element (two-dimensional plane stress, or shell, or three-dimensional), which gives a uniform stress/strain state, is loaded as shown in Fig. 3. Material data corresponding to orthotropic elastic and plastic material behavior are given in the same figure.

This example serves to demonstrate applicability of the developed material model and the numerical algorithm regarding accuracy and convergence rate characteristics.

In Fig. 3(*b*) are given solutions for displacements obtained by using two steps only for various values of the hardening parameter M. Since the loading in step 2 has the reverse character, there is plastic flow in step 2 for $M < 1$, while for $M = 1$ the stress point remains on the yield surface of step 1, but on the opposite position. We have employed the full Newton iteration procedure within the program PAK (Kojic, et al., 1994b) and the convergence rate is illustrated through unbalanced energies $E^{(i)}$ calculated for iteration "i" as

$$E^{(i)} = ({}^{t+\Delta t}\mathbf{F}^{\text{ext}} - {}^{t+\Delta t}\mathbf{F}^{(i-1)})^{T}\Delta\mathbf{U}^{(i)}$$

where ${}^{t+\Delta t}\mathbf{F}^{\text{ext}}$ and ${}^{t+\Delta t}\mathbf{F}^{(i-1)}$ are external and internal (corresponding to calculated stresses ${}^{t+\Delta t}\boldsymbol{\sigma}^{(i-1)}$) nodal forces, and $\Delta\mathbf{U}^{(i)}$ are increments of nodal displacements. From the table in Fig. 3(*c*) we see a high convergence rate which is in accordance with the derivation of ${}^{t+\Delta t}\mathbf{C}^{EP}$ in Section 4. Namely, the convergence rate is not the true quadratic, since in the derivation of ${}^{t+\Delta t}\mathbf{C}^{EP}$ we have neglected derivatives of ${}^{t+\Delta t}N_{ij}$. We mention here that the convergence rate can be improved by the addition of, for example, a line search in the iterative scheme.

Finally, we illustrate accuracy characteristics of the developed algorithm by an error analysis. We solve this example with various numbers of steps in the plastic domain and compare the final solution for effective plastic strain $\bar{\varepsilon}^{P}_{a}$ with respect to the solution corresponding to 150 steps. From the diagram in Fig. 3(*d*) we see that the solution approaches very fast to the 150 step solution.

Example 2: Multilayered Hinged Cylindrical Shell Loaded by Concentrated Force. A cylindrical shell, used by Bathe and Bolourchi (1980), with dimensions given in Fig. 4(*a*), is loaded by a central force. Due to symmetry, one quarter of the structure is modeled by an 8 × 8 mesh of four-node shell elements with incompatible displacements for membrane behavior (Slavkovic et al., 1994) and mixed interpolations for transversal strains (Dvorkin and Bathe, 1984).

This example serves to demonstrate applicability of the developed numerical procedure to a more realistic, complex engineering problem.

The problem is solved by the FE program PAK, using the arc-length method, with automatic load incrementation and eight steps, since the structure has the snap-through behavior.

We have solved four cases, as shown in Fig. 4, using two layers and with the angle between the first material axis and the longitudinal direction of the structure ±45 deg.

The solution for an isotropic elastic material is shown for comparison with results from the literature; the present solution is obtained with an anisotropic material model and isotropic material constants $E = 3102.75$ MPa $\nu = 0.3$. The second curve from the top corresponds to an anisotropic elastic material with material constants (moduli in MPa)

$$E_1 = 3102.75; \quad E_2 = E_3 = 1000.$$

$$Y_{12} = 0.3; \quad Y_{23} = Y_{31} = 0.25$$

$$G_{12} = 1193.36; \quad G_{23} = G_{31} = 800.$$

The solution for isotropic elasto-plastic material is obtained with the orthotropic model of Section 2 and with elastic constants as for the curve (*a*). The yield curves are of the Rambert-Osgood type given in Fig. 3(*a*), with the following constants:

$$(\sigma^0_y)_1 = (\sigma^0_y)_2 = (\sigma^0_y)_3 = 5 \text{ MPa}$$

$$(\sigma^0_y)_{12} = (\sigma^0_y)_{23} = (\sigma^0_y)_{31} = 5/\sqrt{3} \text{ MPa}$$

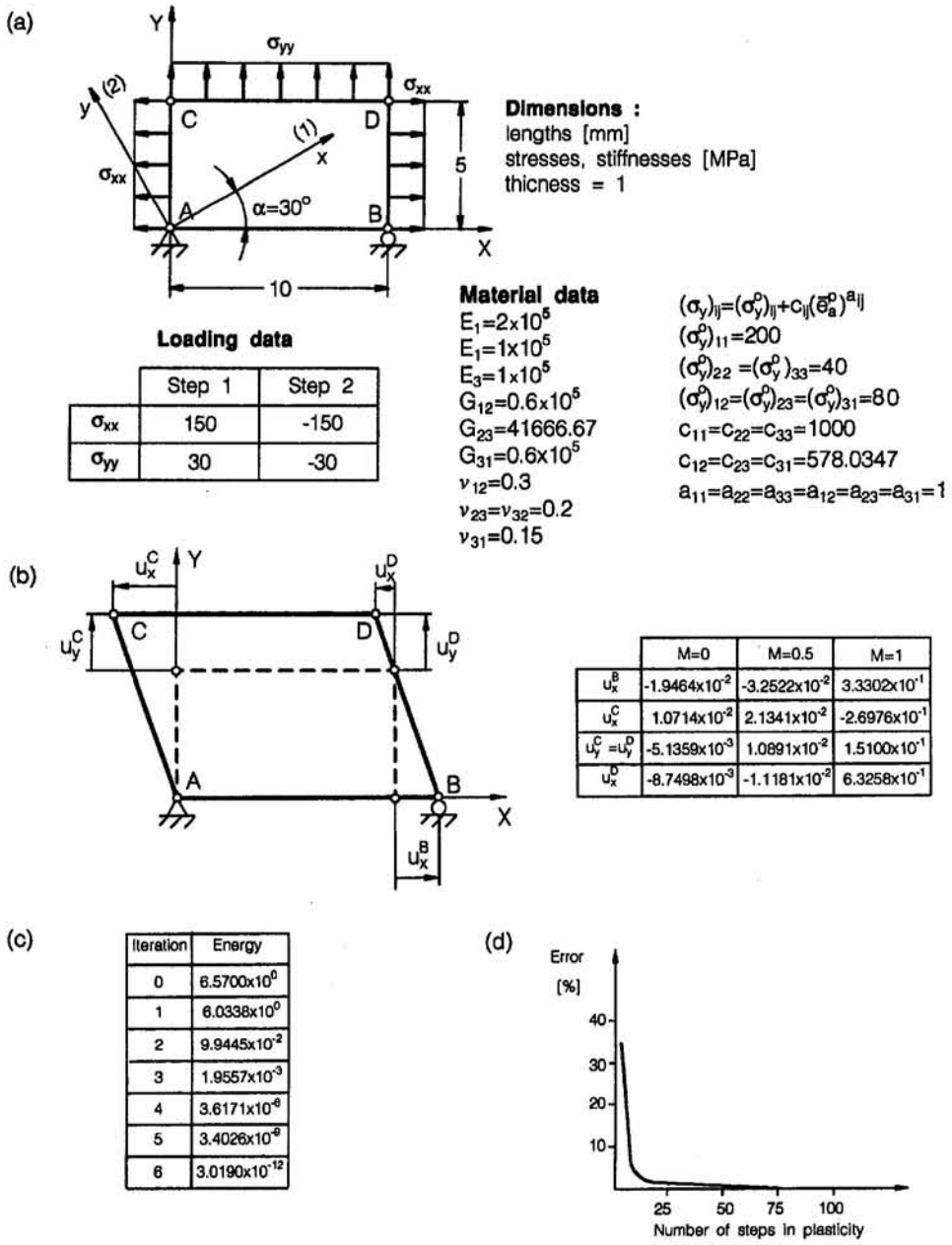
$$c_1 = c_2 = c_3 = 25 \text{ MPa}$$

$$c_{12} = c_{23} = c_{31} = 25/\sqrt{3} \text{ MPa}$$

$$a_1 = a_2 = \ldots = a_{31} = 1$$

and the mixed hardening parameter $M = 0.5$. The force-displacement dependence is shown as curve (*c*). The solution given by curve (*d*) is obtained with elastic material constants as for the problem (*b*), and the yield curves are defined by constants (moduli in MPa)

Downloaded 04 May 2010 to 171.66.16.33. Redistribution subject to ASME license or copyright; see http://www.asme.org/terms/Terms_Use.cfm



	Step 1	Step 2
σ_{xx}	150	-150
σ_{yy}	30	-30

	M=0	M=0.5	M=1
u_x^B	$-1.9464x10^{-2}$	$-3.2522x10^{-2}$	$3.3302x10^{-1}$
u_x^C	$1.0714x10^{-2}$	$2.1341x10^{-2}$	$-2.6976x10^{-1}$
$u_y^C=u_y^D$	$-5.1359x10^{-3}$	$1.0891x10^{-2}$	$1.5100x10^{-1}$
u_x^D	$-8.7498x10^{-3}$	$-1.1181x10^{-2}$	$6.3258x10^{-1}$

Iteration	Energy
0	$6.5700x10^{0}$
1	$6.0338x10^{0}$
2	$9.9445x10^{-2}$
3	$1.9557x10^{-3}$
4	$3.6171x10^{-6}$
5	$3.4026x10^{-9}$
6	$3.0190x10^{-12}$

Fig. 3 Plastic deformation of an orthotropic plate; (*a*) geometry, boundary conditions, material and loading data, (*b*) displacements corresponding to step 2, (*c*) unbalanced energy in iterations in step 1 ($M = 0.5$), (*d*) error analysis for final solution of $\bar{\varepsilon}_a^p$

$$(\sigma_y^0)_1 = 5;\ (\sigma_y^0)_2 = (\sigma_y^0)_3 = 1$$

$$(\sigma_y^0)_{12} = (\sigma_y^0)_{23} = (\sigma_y^0)_{31} = 2$$

$$c_1 = c_2 = c_3 = 25$$

$$c_{12} = c_{23} = c_{31} = 15$$

$$a_1 = a_2 = \ldots = a_{31} = 1$$

and $M = 0.5$.

The solutions given by curves (*b*), (*c*), and (*d*) are not compared with other solutions, since the authors did not find the corresponding solutions in the literature. We note here that the maximum number of iterations in one step was four for any of the problems (*a*) to (*d*).

6 Concluding Remarks

We have proposed a general form of the yield condition for the orthotropic metal plasticity, with change of the size and position of the yield surface during plastic deformation of the material. The definition of the plasticity material constants are given in a form which suggests their experimental determination.

The computational procedure for stress integration of the strain-driven problems is implicit and represents an application of the governing parameter method, briefly described in this paper. The algorithm provides high accuracy of the implicit schemes, it is numerically efficient—since the problem is reduced to a solution of one nonlinear governing equation, and it is robust because it is applicable to large strain increments within the time-step (there is one zero of the corresponding monotonic governing function (Kojic, 1993)). The derived expressions for a three-dimensional stress/strain state can be simply modified for special conditions, as shell, beam, or pipe deformation. The consistent differentiation, according to the GPM, presented in Section 4, leads to determination of the true tangent moduli, which is very important for convergence rate in the equilibrium iterations on the structural level.

Downloaded 04 May 2010 to 171.66.16.33. Redistribution subject to ASME license or copyright; see http://www.asme.org/terms/Terms_Use.cfm

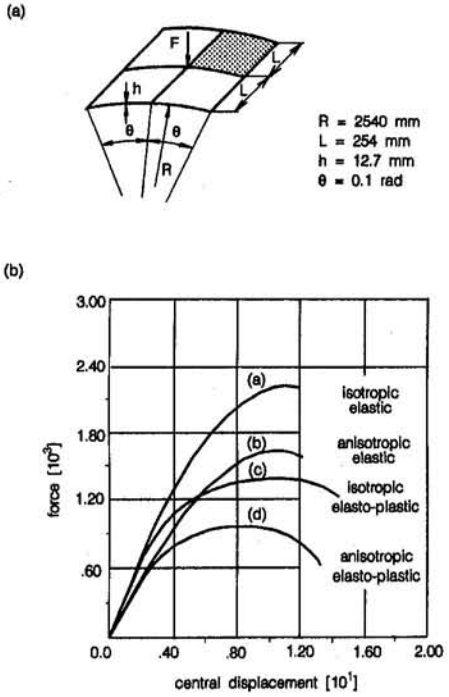


Fig. 4 Multilayered hinged cylindrical shell loaded by concentrated force, (*a*) geometrical data, (*b*) force displacement curves

The solved examples demonstrate applicability of the proposed material model to engineering problems and emphasize the main characteristics of the developed numerical procedure.

References

Baltov, A. and Sawczuk, A., 1965, "A Rule of Anisotropic Hardening," *Acta Mechanica,* No. 1-2, pp. 81–92.

Bathe, K. J., Bolourchi, S., 1980, "A Geometric and Material Nonlinear Plate and Shell Element," *Computers & Structures,* Vol. 11, pp. 23–48.

Chen, F., and Han, D. J., 1988, *Plasticity for Structural Engineers,* Springer-Verlag, New York.

Dvorkin, E., Bathe, K. J., 1984, "A Continuum Mechanics Based Four-Node Shell Element for General Nonlinear Analysis," *Engineering Computations,* Vol. 1, pp. 77–88.

Hill, R., 1950, *The Mathematical Theory of Plasticity,* Oxford University Press, London.

Jones, R. M., 1975, *Mechanics of Composite Materials,* McGraw-Hill, New York.

Kojic, M., and Bathe, K. J., 1987a, "The 'Effective Stress-Function' Algorithm for Thermo-Elasto-Plasticity and Creep," *International Journal for Numerical Methods in Engineering,* Vol. 24, pp. 1509–1532.

Kojic, M., and Bathe, K. J., 1987b, "Thermo-Elastic-Plastic and Creep Analysis of Shell Structures," *Computers & Structures,* Vol. 26, No. 1-2, pp. 135–143.

Kojic, M., 1992a, "An Implicit Procedure for Stress Integration of a General Anisotropic von Mises Material," *Proceedings of the Third International Conference on Computational Plasticity (Complas III),* Barcelona, pp. 263–269.

Kojic, M., Vukicevic, M., and Slavkovic, R., 1992b, "An Implicit Procedure for Stress Integration in Elastic-Plastic Deformation of the Modified Cam-clay Material," *Proceedings of the Third International Conference on Computational Plasticity (Complas III),* Barcelona, pp. 929–934.

Kojic, M., 1993, *A General Concept of Implicit Integration of Constitutive Relations for Inelastic Material Deformation,* (in Serbian), Center for Scientistic Research, Serbian Academy of Sciences and Arts and University of Kragujevac, Kragujevac, Yugoslavia.

Kojic, M., Slavkovic, R., Grujovic, N., and Vukicevic, M., 1994b, "Implicit Stress Integration Algorithm for the Modified Cam-Clay Material," *Theoretical and Applied Mechanics,* Vol. 20, pp. 95–118.

Kojic, M., Slavkovic, R., Zivkovic, M., and Grujovic, N., 1994a, *PAK Finite Element Program for Linear and Nonlinear Structural Analysis and Heat Transfer,* Kragujevac.

Ortiz, M. P., Pinsky, M., and Taylor, R. L., 1983, "Operator Split Methods for the Numerical Solution of the Elastoplastic Dynamic Problem," *Computer Methods in Applied Mechanics and Engineering,* Vol. 39, pp. 137–159.

Rees, D. W. A., 1983, "The Potential Theory of Creep," *Engineering Approaches to High Temperature Design,* B. Wilshire and D. R. J. Owen, eds., Vol. 2, Pineridge Press, pp. 57–84.

Simo, J. C., and Taylor, R. L., 1985, "Consistent Tangent Operators for Rate Independent Elasto-Plasticity," *Computer Methods in Applied Mechanics and Engineering,* Vol. 48, pp. 101–113.

Simo, J. C., and Hughes, T. J. R., 1988, *Elastoplasticity and Viscoplasticity—Computational Aspects,* Department of Applied Mechanics, Stanford University, Stanford, CA.

Szczepinski, W., 1992, "On Deformation-Induced Plasticity of Sheet Metals," *Archive of Mechanics,* Vol. 44, pp. 663–698.

Slavkovic, R., Zivkovic, M., and Kojic, M., 1994, "Enchanced 8-Node Three-Dimensional Solid and 4-Node Shell Elements with Incompatibile Generalized Displacements," *Communications in Numerical Methods in Engineering,* Vol. 10, pp. 699–709.

Theocaris, P. S., 1991, "Differences in Shear Strengths of Orthotropic Bodies," *Acta Mechanica,* Vol. 87, pp. 59–72.

Theocaris, P. S., 1992, "Tensor Failure Criteria for Composites: Properties and Comparison of the Ellipsoid Failure Surfaces with Experiments," *Advanced Polymer Technology,* Vol. 11, No. 1, pp. 27–40.

Downloaded 04 May 2010 to 171.66.16.33. Redistribution subject to ASME license or copyright; see http://www.asme.org/terms/Terms_Use.cfm

Dynamics and Control of Electrostatic Structures

L. Silverberg
Mem. ASME.

L. Weaver, Jr.

Mars Mission Research Center,
North Carolina State University,
Raleigh, NC 27695-7921

This paper formulates the equations governing the dynamics and control of electrostatic structures. Using a Lagrangian mechanics approach, a potential energy function composed of a strain component, an electric component, and a gravitational component is defined. The resulting system of nonlinear ordinary differential equations are linearized about the electrostatic equilibrium leading to a linear system of ordinary differential equations characterized by mass, stiffness, damping, gyroscopic, and circulatory effects. In the absence of feedback control, the damping, gyroscopic, and circulatory effects vanish resulting in a symmetric system that admits normal mode vibration. Voltages applied over the charged subsurfaces (control points) of the electrostatic structure can control its shape. In the presence of feedback controls, control gains can be tailored to produce desirable levels of stiffness and damping.

Two different control approaches are studied, one using control points that are attached to the electrostatic structure and one where the control points are fixed in space. Example problems illustrate the dynamics and control; specifically, circumstances that lead to instabilities, shape control using attached control surfaces, shape control using fixed control surfaces, and electrostatic damping.

1 Introduction

Over the last 100 years the fields of classical mechanics and electrostatics have been set on a firm physical and mathematical foundation. Problems that couple the two fields are of more recent vintage, having arose in several of today's engineering technologies. Examples of engineering technologies that couple classical structural dynamics and electrostatics are electrostatic speakers (Streng, 1989, 1990), scientific instruments (Rhim, Collender, Hyson, Simms, and Elleman, 1985; Rhim, Chung, Hyson, Trinh, and Elleman, 1987), and space-based reflector antennas (Yam, Lang, Staelin, and Johnson, 1988; Mihora and Redmond, 1979; Silverberg, 1994). We have observed that the mathematical foundation upon which the sited technologies rest is comparatively weak, and it can be claimed that these and other technologies would benefit from a stronger mathematical foundation particularly in problems that demand a more intricate degree of coupling between structural dynamics and electrostatics. We characterize the dynamics and control of electrostatic structures in this spirit.

The next section formulates the electrostatic structures problem, bringing together expressions for potential energy from the fields of mechanics and electrostatics. The kinetic energy and potential energy are then discretized, leading to energy expressions in terms of a set of generalized coordinates. Then we use Lagrangian mechanics to obtain the nonlinear system of ordinary differential equations that governs the motion of the electrostatic structure. The equilibrium position and the equilibrium charge are determined along with the linearized system of ordinary differential equations that govern small motions of the electrostatic structure about its equilibrium. The linearized behavior is characterized by stiffness, damping, gyroscopic, and circulatory effects.

The third section examines the stability and control of an electrostatic string employing fixed (in space) control points.

The fourth section introduces a different approach to controlling electrostatic structures, using attached (to the electrostatic structure) control points. The parameters of an electrostatic bar are varied in order to observe their effects on the bar's equilibrium shapes. Feedback control of the bar is also demonstrated.

The fifth section deals with general shape control strategies for electrostatic systems. Applied voltages over the charged subsurfaces are varied according to a Newton's method and a steepest descent method to achieve the desired shape. Fixed control points were used for the shape control. Feedback control is also employed for the purposes of electrostatic damping.

Finally, section six gives some closing remarks.

2 Formulation of the Governing Equations

We now develop expressions for the potential energy and the kinetic energy of an electrostatic structure. Denoting the position vector by $\mathbf{r}$, the electric potential at $\mathbf{r}$ is (Jackson, 1975)

$$V(\mathbf{r}) = k \int_Q \frac{dQ(\mathbf{r}')}{|\mathbf{r} - \mathbf{r}'|} \tag{1}$$

where $\kappa = (4\pi\epsilon_0)^{-1}$, $\epsilon_0 = 8.854 \times 10^{-12}$ farad/meter is the permittivity of free space, $dQ(\mathbf{r}')$ is the differential charge at $\mathbf{r}'$ and where the integration is carried out over the charged surface Q. The kinetic energy of the structure is (Meirovitch, 1980)

$$T = \tfrac{1}{2} \int_v m(\mathbf{r}) \dot{\mathbf{r}} \cdot \dot{\mathbf{r}} dv \tag{2}$$

where $m(\mathbf{r})$ is the mass density at $\mathbf{r}$, dv is the differential volume, $\dot{\mathbf{r}}$ is the velocity and where the integration is carried out over the volume v. The potential energy is (Jackson, 1975; Meirovitch, 1980)

$$U = \tfrac{1}{2} \int_v \mathbf{r}_S \cdot K \mathbf{r}_S dv - \int_v m(\mathbf{r}) \mathbf{r} dv \cdot \mathbf{g} + \tfrac{1}{2} \int_Q V(\mathbf{r}) dQ(\mathbf{r}) \tag{3}$$

where the left integral is the strain component, the middle integral is the gravitational component and the right integral is the electric component. The strain component of the position vector is denoted by $\mathbf{r}_S$, K denotes a linear self-adjoint, positive (semi) definite stiffness operator, and $\mathbf{g}$ is a constant gravity vector.

Contributed by the Applied Mechanics Division of THE AMERICAN SOCIETY OF MECHANICAL ENGINEERS for publication in the ASME JOURNAL OF APPLIED MECHANICS.

Discussion on this paper should be addressed to the Technical Editor, Professor Lewis T. Wheeler, Department of Mechanical Engineering, University of Houston, Houston, TX 77204-4792, and will be accepted until four months after final publication of the paper itself in the ASME JOURNAL OF APPLIED MECHANICS.

Manuscript received by the ASME Applied Mechanics Division, Sept. 20, 1993; final revision, Mar. 4, 1995. Associate Technical Editor: M. Taya.

Copyright © 1996 by ASME

Downloaded 04 May 2010 to 171.66.16.33. Redistribution subject to ASME license or copyright; see http://www.asme.org/terms/Terms_Use.cfm

The charged surface Q is discretized into subsurfaces over which the charge is assumed to be constant. The center positions of the subsurfaces are denoted by $\mathbf{r}_1, \mathbf{r}_2, \ldots, \mathbf{r}_N$. By evaluating Eq. (1) at the center positions, we get the discretized electric potential

$$V(\mathbf{r}_i) = k\left[\sum_{\substack{j=1\\ j\neq i}}^{N} \frac{Q_j}{|\mathbf{r}_j - \mathbf{r}_i|} + \frac{Q_i}{S_i}\int_{S_i} \frac{dS'}{|\mathbf{r}' - \mathbf{r}_i|}\right] \tag{4}$$

where Q_i is the charge on the ith subsurface, and S_i is its surface area. Equation (4) is rewritten in the form

$$V_i = \sum_{j=1}^{N} P_{ij}Q_j, \quad i = 1, N \tag{5a}$$

in which $V_i = V(\mathbf{r}_i)$ and the coefficients of potential are

$$P_{ij} = \begin{cases} \dfrac{\kappa}{|\mathbf{r}_j - \mathbf{r}_i|}, & i \neq j \\ \dfrac{\kappa}{S_i}\displaystyle\int_{S_i} \frac{dS'}{|\mathbf{r}' - \mathbf{r}_i|}, & i = j. \end{cases} \tag{5b}$$

Substituting Eqs. (4) or (5) into the electric component of Eq. (3), we obtain the discretized electric component of the potential energy

$$U_E = \tfrac{1}{2}\sum_{i=1}^{N} V(\mathbf{r}_i)Q_i = \tfrac{1}{2}\sum_{i=1}^{N}\sum_{j=1}^{N} P_{ij}Q_iQ_j. \tag{6}$$

The position vectors $\mathbf{r}_1, \mathbf{r}_2, \ldots, \mathbf{r}_N$ make up a set which can be dependent or, if independent, may be unsuitable for use as independent coordinates of the system. Instead, we can express the position vectors in terms of an independent set of coordinates, $\theta_1, \theta_2, \ldots, \theta_M$, called generalized coordinates, and express the position vectors and their time derivatives in the functional form

$$\mathbf{r}_i = \mathbf{r}_i(\theta_1, \theta_2, \ldots, \theta_M), \quad \dot{\mathbf{r}}_i = \sum_{j=1}^{M} \frac{\partial \mathbf{r}_i}{\partial \theta_j}\dot{\theta}_j, \quad i = 1, N. \tag{7a, b}$$

The volume v is divided into subvolumes in which the mass density is assumed to be constant. Substituting Eq. (7b) into Eq. (3), yields the discretized kinetic energy

$$T = \frac{1}{2}\sum_{i=1}^{N} m_i\dot{\mathbf{r}}_i\cdot\dot{\mathbf{r}}_i = \frac{1}{2}\sum_{i=1}^{N}\sum_{j=1}^{M}\sum_{k=1}^{M} m_i \frac{\partial \mathbf{r}_i}{\partial\theta_j}\cdot\frac{\partial \mathbf{r}_i}{\partial\theta_k}\dot{\theta}_j\dot{\theta}_k \tag{8}$$

where m_i denotes the mass of the ith subvolume. Similarly, substituting Eq. (7a) into Eq. (3), we obtain the discretized gravitational component of the potential energy

$$U_G = -\sum_{i=1}^{N} m_i\mathbf{r}_i\cdot\mathbf{g}. \tag{9}$$

In this section we will focus our attention on an electrostatic beam. The beam is a one-dimensional hinged-free structure undergoing bending displacements. The strain component of the position vector is denoted by $\mathbf{r}_S = u(x, t)\hat{n}$ where $\hat{n}$ is a unit vector, $u(x, t)$ denotes the bending displacement at x and time t, and the stiffness operator is given by $K = (\partial^2/\partial x^2)(EI(\partial^2/\partial x^2))$. Substituting these expressions for $\mathbf{r}_S$ and K into Eq. (3), and twice integrating the result by parts, we obtain the symmetric form of the strain component of the potential energy

$$U_S = \frac{1}{2}\int_0^L EI(x)\left(\frac{\partial^2 u(x, t)}{\partial x^2}\right)^2 dx \tag{10}$$

where dv has been replaced by dx so the integration is now carried out over the interval from 0 to L (Meirovitch, 1980; Park, 1992). Dividing the interval into subintervals of length h, and assuming in Eq. (10) that $\theta_i = (\partial u(x, t))/(\partial x)$ is constant over the ith subinterval, we obtain

$$U_S = \tfrac{1}{2}\sum_{i=1}^{M}\sum_{j=1}^{M} K_{Sij}\theta_i\theta_j,$$

$$K_S = \frac{EI}{h}\begin{bmatrix} 1 & -1 & 0 & \cdots & & 0 \\ -1 & 2 & -1 & 0 & \cdots & 0 \\ 0 & -1 & 2 & -1 & 0 & 0 \\ \vdots & & & \ddots & & \vdots \\ \cdots & & 0 & -1 & 2 & -1 \\ 0 & \cdots & \cdots & 0 & -1 & 1 \end{bmatrix} \tag{11a, b}$$

where K_{Sij} are elements of the positive semi-definite symmetric stiffness matrix K_S in Eq. (11b).

The motion of the electrostatic structure and its charge distribution can be controlled by the voltages V_i, $(i = 1, N)$. If so, we could prescribe the voltages as functions of the generalized coordinates and their time derivatives in an algorithm, expressed in the functional form

$$V_i = V_i(\theta_1, \theta_2, \ldots, \theta_M, \dot{\theta}_1, \dot{\theta}_2, \ldots, \dot{\theta}_M), \quad i = 1, N. \tag{12}$$

Sections 3 and 4 will discuss Eq. (12) in more detail.

The equations governing the motion of the electrostatic structure are now derived from Lagranges' equations (Meirovitch, 1980),

$$\frac{d}{dt}\left(\frac{\partial L}{\partial \dot{\theta}_l}\right) - \frac{\partial L}{\partial \theta_l} = 0, \quad l = 1, M \tag{13}$$

where from Eqs. (6), (8), (9), and (11a), we define the Lagrangian

$$L = T - U = \frac{1}{2}\sum_{i=1}^{N}\sum_{j=1}^{M}\sum_{k=1}^{M} m_i \frac{\partial \mathbf{r}_i}{\partial\theta_j}\cdot\frac{\partial \mathbf{r}_i}{\partial\theta_k}\dot{\theta}_j\dot{\theta}_k - \frac{1}{2}\sum_{i=1}^{M}\sum_{j=1}^{M} K_{Sij}\theta_i\theta_j + \sum_{i=1}^{N} m_i\mathbf{r}_i\cdot\mathbf{g} - \frac{1}{2}\sum_{i=1}^{N}\sum_{j=1}^{N} P_{ij}Q_iQ_j. \tag{14}$$

From Eq. (14), the derivatives needed in Eq. (13) are

$$\frac{\partial L}{\partial\theta_l} = \sum_{i=1}^{N}\sum_{j=1}^{M}\sum_{k=1}^{M} m_i \frac{\partial \mathbf{r}_i}{\partial\theta_j}\cdot\frac{\partial^2 \mathbf{r}_i}{\partial\theta_k\partial\theta_l}\dot{\theta}_j\dot{\theta}_k - \sum_{i=1}^{M} K_{Sli}\theta_i + \sum_{i=1}^{N} m_i \frac{\partial \mathbf{r}_i}{\partial\theta_l}\cdot\mathbf{g} - \sum_{i=1}^{N}\sum_{j=1}^{N}\frac{1}{2}\frac{\partial P_{ij}}{\partial\theta_l}Q_iQ_j \tag{15a}$$

$$\frac{\partial L}{\partial\dot{\theta}_l} = \sum_{i=1}^{N}\sum_{j=1}^{M} m_i \frac{\partial \mathbf{r}_i}{\partial\theta_j}\cdot\frac{\partial \mathbf{r}_i}{\partial\theta_l}\dot{\theta}_j \tag{15b}$$

$$\frac{d}{dt}\left[\frac{\partial L}{\partial\dot{\theta}_l}\right] = \sum_{i=1}^{N}\sum_{j=1}^{M} m_i\left[\frac{\partial \mathbf{r}_i}{\partial\theta_j}\cdot\frac{\partial \mathbf{r}_i}{\partial\theta_l}\ddot{\theta}_j + \sum_{k=1}^{M}\left(\frac{\partial \mathbf{r}_i}{\partial\theta_j}\cdot\frac{\partial^2 \mathbf{r}_i}{\partial\theta_k\partial\theta_l} + \frac{\partial^2 \mathbf{r}_i}{\partial\theta_j\partial\theta_k}\cdot\frac{\partial \mathbf{r}_i}{\partial\theta_l}\right)\dot{\theta}_j\dot{\theta}_k\right]. \tag{15c}$$

Substituting Eqs. (15) into Eq. (13), we obtain a nonlinear system of M ordinary differential equations describing the motion of the electrostatic structure[1]

$$\sum_{i=1}^{N}\sum_{j=1}^{M} m_i\left[\frac{\partial \mathbf{r}_i}{\partial\theta_j}\cdot\frac{\partial \mathbf{r}_i}{\partial\theta_l}\ddot{\theta}_j + \sum_{k=1}^{M}\frac{\partial^2 \mathbf{r}_i}{\partial\theta_j\partial\theta_k}\cdot\frac{\partial \mathbf{r}_i}{\partial\theta_l}\dot{\theta}_j\dot{\theta}_k\right] + \sum_{i=1}^{M} K_{Sli}\theta_i - \sum_{i=1}^{N} m_i\frac{\partial \mathbf{r}_i}{\partial\theta_l}\cdot\mathbf{g} + \sum_{i=1}^{N}\sum_{j=1}^{N}\frac{1}{2}\frac{\partial P_{ij}}{\partial\theta_l}Q_iQ_j = 0, \quad l = 1, M. \tag{16}$$

[1] The steps leading to Eq. (16) held the charges constant and allowed the voltages to vary. The same equation is obtained when the charges are allowed to vary and the voltages are held constant.

Downloaded 04 May 2010 to 171.66.16.33. Redistribution subject to ASME license or copyright; see http://www.asme.org/terms/Terms_Use.cfm

The equilibrium positions of the electrostatic structure are found by letting $\dot{\theta}_k = 0$ and $\ddot{\theta}_k = 0$ $(k = 1, M)$ in Eq. (16). We obtain the system of M coupled nonlinear algebraic equations governing the equilibrium positions

$$\sum_{i=1}^{M} K_{sli}\theta_{i0} - \sum_{i=1}^{N} m_i\left(\frac{\partial \mathbf{r}_i}{\partial \theta_l}\right)_0 \cdot \mathbf{g} + \frac{1}{2}\sum_{i=1}^{N}\sum_{j=1}^{N}\left(\frac{\partial P_{ij}}{\partial \theta_l}\right)_0 Q_{i0}Q_{j0} = 0,$$

$$l = 1, M \quad (17)$$

in which the 0 subscript refers to the evaluation of a quantity at the equilibrium position.

Next, the equations describing the motion of the electrostatic structure are linearized about the equilibrium position. We first introduce the generalized coordinates

$$\eta_i(t) = \theta_i(t) - \theta_{i0}, \quad i = 1, M \quad (18)$$

and expand Eq. (16) about the equilibrium position in a Taylor series. Having retained only the linear terms, we get

$$\sum_{j=1}^{M} m_{ij}\ddot{\eta}_j + a_{ij}\dot{\eta}_j + b_{ij}\eta_j = 0, \quad i = 1, M \quad (19)$$

in which

$$m_{ji} = m_{ij} = \left(\frac{\partial f_i}{\partial \ddot{\eta}_j}\right)_0 = \sum_{k=1}^{N} m_k\left(\frac{\partial \mathbf{r}_k}{\partial \theta_i}\right)_0 \cdot \left(\frac{\partial \mathbf{r}_k}{\partial \theta_j}\right)_0 \quad (20)$$

$$a_{ij} = \left(\frac{\partial f_i}{\partial \dot{\eta}_j}\right)_0 = \sum_{k=1}^{N}\sum_{l=1}^{N}\left(\frac{\partial P_{kl}}{\partial \theta_i}\right)_0\left(\frac{\partial Q_k}{\partial \dot{\theta}_j}\right)_0 Q_{l0} \quad (21)$$

$$b_{ij} = \left(\frac{\partial f_i}{\partial \eta_j}\right)_0 = K_{sij} - \sum_{k=1}^{N} m_k\left(\frac{\partial^2 \mathbf{r}_k}{\partial \theta_i \partial \theta_j}\right)_0 \cdot \mathbf{g} + \sum_{k=1}^{N}\sum_{l=1}^{N}\left[\frac{\partial P_{kl}}{\partial \theta_i}\frac{\partial Q_k}{\partial \theta_j}Q_l + \frac{1}{2}\frac{\partial^2 P_{kl}}{\partial \theta_i \partial \theta_j}Q_kQ_l\right]_0 \quad (22)$$

From Eqs. (5) we obtain expressions for the following terms in Eq. (21):

$$\frac{\partial P_{kl}}{\partial \theta_j} = \begin{cases} \dfrac{-\kappa}{|\mathbf{r}_k - \mathbf{r}_l|^3}(\mathbf{r}_k - \mathbf{r}_l)\cdot\dfrac{\partial(\mathbf{r}_k - \mathbf{r}_l)}{\partial \theta_j} & k \neq l \\ 0 & k = l \end{cases} \quad (23a)$$

and

$$\frac{\partial Q_k}{\partial \dot{\theta}_j} = \sum_{r=1}^{N} C_{kr}\frac{\partial V_r}{\partial \dot{\theta}_j} \quad (23b)$$

where C_{kr} are coefficients of capacitance obtained by a matrix inverse of the coefficients of potential. From Eqs. (5) we obtain expressions for the following terms in Eq. (22):

$$\frac{\partial^2 P_{kl}}{\partial \theta_j \partial \theta_i} = \begin{cases} \dfrac{\kappa}{|\mathbf{r}_k - \mathbf{r}_l|^5}\left\{\begin{array}{l} 3(\mathbf{r}_k - \mathbf{r}_l)\cdot\dfrac{\partial}{\partial \theta_i}(\mathbf{r}_k - \mathbf{r}_l)(\mathbf{r}_k - \mathbf{r}_l)\cdot\dfrac{\partial}{\partial \theta_j}(\mathbf{r}_k - \mathbf{r}_l) - |\mathbf{r}_k - \mathbf{r}_l|^2 \times \\ \left[\dfrac{\partial}{\partial \theta_i}(\mathbf{r}_k - \mathbf{r}_l)\cdot\dfrac{\partial}{\partial \theta_j}(\mathbf{r}_k - \mathbf{r}_l) + (\mathbf{r}_k - \mathbf{r}_l)\cdot\dfrac{\partial^2}{\partial \theta_i \partial \theta_j}(\mathbf{r}_k - \mathbf{r}_l)\right] \end{array}\right\} & k \neq l \\ 0 & k = l \end{cases} \quad (24a)$$

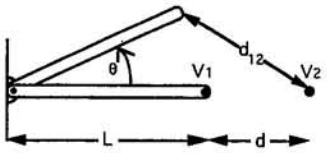


Fig. 1 Electrostatic string ($M = 1$)

and

$$\frac{\partial Q_k}{\partial \theta_j} = -\sum_{r=1}^{N}\sum_{s=1}^{N} C_{kr}\frac{\partial P_{rs}}{\partial \theta_j}Q_s + \sum_{r=1}^{N} C_{kr}\frac{\partial V_r}{\partial \theta_j}. \quad (24b)$$

Referring to Eq. (19), the coefficients m_{ij} make up a positive definite and symmetric *mass matrix*. The symmetric part of a_{ij} is denoted by $c_{ij} = (1/2)(a_{ij} + a_{ji})$. The matrix made from the entries of c_{ij} is referred to as the *damping matrix*. The matrix made from the skew-symmetric part of a_{ij}, denoted by $g_{ij} = (1/2)(a_{ij} - a_{ji})$, is referred to as the *gyroscopic matrix*. The symmetric part of b_{ij} is denoted by $k_{ij} = (1/2)(b_{ij} + b_{ji})$. The matrix made from the entries of k_{ij} is referred to as the *stiffness matrix*. The matrix made from the skew-symmetric entries of b_{ij}, denoted by $h_{ij} = (1/2)(b_{ij} - b_{ji})$, is referred to as the *circulatory matrix*. The stability properties of the electrostatic structure depend on the definiteness properties of the stiffness matrix and the damping matrix and on the presence of the circulatory matrix. The gyroscopic matrix has no effect on stability. The circulatory matrix is unpredictable so a control algorithm in Eq. (12) that would cause the circulatory matrix to vanish would be very attractive. In the absence of the circulatory matrix, the electrostatic structure is guaranteed to be stable when the mass matrix is positive definite, the stiffness matrix is positive (semi)-definite and the damping matrix is positive (semi)-definite (Meirovitch, 1980).

3 Stability and Control

The second section formulated the dynamics of electrostatic structures. This section explores charged subsurfaces governed by algorithms for the control of electrostatic structures, as was suggested in Eq. (12). These charged subsurfaces will be referred to as control points.

We begin by recognizing that prescribing the voltage of a control point in the neighborhood of an electrostatic structure alters its charge distribution which in turn can alter the structure's equilibrium position as well as its dynamic properties. When the interest lies in prescribing voltages at control points in order to alter the structure's dynamic properties but not its equilibrium position, the question arises how not to alter the structure's equilibrium position.

We first consider the rigid pinned-free bar shown in Fig. 1. The bar is a one-degree-of-freedom system that has an equilibrium position at $\theta = 0$. A light torsional spring and damper are placed at the pinned connection, causing the equilibrium position to be stable.

We attempt to increase the natural frequency of the bar by electrostatic control. Toward this end we attempt to appropri-

Downloaded 04 May 2010 to 171.66.16.33. Redistribution subject to ASME license or copyright; see http://www.asme.org/terms/Terms_Use.cfm

ately prescribe the voltages of the moving control point (i.e., the bar) and the fixed control point. The interest lies in leaving the bar's equilibrium position unaltered by the fixed control point. To do this, it becomes apparent that the steady-state voltage V_2 of the fixed control point must be set equal to the free-space voltage of that point which corresponds to the case when its charge is identically zero. Furthermore, as the following will show, holding the voltage of the fixed control point constant at the free-space voltage has the unfortunate distinction of causing the equilibrium position to become unstable.

The system is now displaced from equilibrium (see Fig. 1). The voltages V_1 and V_2 are constants, the charge Q represents the charge on the moving point at equilibrium while Q_1 and Q_2 represent the charges at the displaced position. Equating the voltages at $\theta = 0$ to the voltages at an arbitrary angle leads to

$$\begin{pmatrix} V_1 \\ V_2 \end{pmatrix} = \kappa \begin{bmatrix} \frac{1}{r} & \frac{1}{d_{12}} \\ \frac{1}{d_{12}} & \frac{1}{r} \end{bmatrix} \begin{pmatrix} Q_1 \\ Q_2 \end{pmatrix} = \kappa Q_0 \begin{pmatrix} \frac{1}{r} \\ \frac{1}{d} \end{pmatrix} \tag{25}$$

in which r denotes the effective radius of the bar and the control point and d_{12} denotes the distance between the control point and the bar. In Eq. (25) we let V_2 lie on the x-axis ($e = 0$) and then invert the result to obtain Q_1 and Q_2.

$$\frac{1}{Q_0}\begin{pmatrix} Q_1 \\ Q_2 \end{pmatrix} = \frac{d_{12}}{d(d_{12}^2 - r^2)}\begin{pmatrix} d_{12}d - r^2 \\ r(d_{12} - d) \end{pmatrix}. \tag{26}$$

It is clear that the two displaced charges have the same sign, (since $d_{12} \geq d$ and $d \gg r$). Thus the electrostatic force between the fixed control point and the moving control point, given by

$$\frac{F}{\kappa Q_0^2} = \frac{\kappa Q_1 Q_2}{\kappa Q_0^2 d_{12}^2} = \frac{r(d_{12}d - r^2)(d_{12} - d)}{d^2(d_{12}^2 - r^2)^2}, \tag{27}$$

is repulsive instead of restoring the system to equilibrium. For a sufficiently small torsional spring constant the zero equilibrium point becomes unstable by introducing the fixed control point regardless of the system parameters.

In this problem we placed the fixed control point on the x-axis. When placed off the x-axis, we again found that the fixed control point, when set to the free-space voltage so as not to disturb the bar's equilibrium position, had the unfortunate consequence of destabilizing the bar. This problem illustrates a property that holds for many electrostatic structures; that stable fixed control points change the equilibrium position of the electrostatic structure unless certain accommodations are made.

The next approach to electrostatic control is shown in Fig. 2. Voltages of two symmetrically placed control points (points 10 and 11 when $M = 9$) are chosen as the negative of the voltage of the electrostatic string. Based on symmetry arguments, it is clear that the equilibrium position is not affected by the two fixed control points. Furthermore, by letting the voltages of the fixed control points be opposite the voltage of the electrostatic string, our intention is to cause the fixed control points to attract the electrostatic string, hopefully avoiding the destabilizing effects found previously. As it will be shown, the stability of the current system depends on d/L.

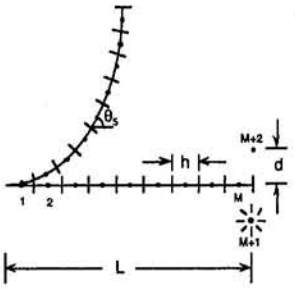


Fig. 2 Electrostatic beam

As shown in Fig. 2 the string is modeled by M segments. Let us now consider the case $M = 1$ followed by higher order cases, which are explored numerically.

The voltages of the simple electrostatic string ($M = 1$) are related to their corresponding charges by

$$\mathbf{V} = P\mathbf{Q} = \kappa \begin{bmatrix} \frac{1}{r} & \frac{1}{d_{12}} & \frac{1}{d_{13}} \\ \frac{1}{d_{12}} & \frac{1}{r} & \frac{1}{d_{23}} \\ \frac{1}{d_{13}} & \frac{1}{d_{23}} & \frac{1}{r} \end{bmatrix} \mathbf{Q} \tag{28}$$

where r denotes the effective radius of the control points. Inverting Eq. (28) and evaluating the result at equilibrium yields the charges

$$\mathbf{Q}_0 = P_0^{-1}\mathbf{V}_0 = C_0\mathbf{V}_0 \tag{29}$$

where

$$C_0 = \frac{r}{\kappa d_0}\begin{bmatrix} \left(d^2 + \frac{L^2}{4}\right)^2(4d^2 - r^2) & 2rd\left(d^2 + \frac{L^2}{4}\right)^{3/2}(r - 2d) & 2rd\left(d^2 + \frac{L^2}{4}\right)^{3/2}(r - 2d) \\ 2rd\left(d^2 + \frac{L^2}{4}\right)^{3/2}(r - 2d) & 4d^2\left(d^2 + \frac{L^2}{4}\right)\left(d^2 + \frac{L^2}{4} - r^2\right) & 2rd\left(d^2 + \frac{L^2}{4}\right)\left(2rd - \left[d^2 + \frac{L^2}{4}\right]\right) \\ 2rd\left(d^2 + \frac{L^2}{4}\right)^{3/2}(r - 2d) & 2rd\left(d^2 + \frac{L^2}{4}\right)\left(2rd - \left[d^2 + \frac{L^2}{4}\right]\right) & 4d^2\left(d^2 + \frac{L^2}{4}\right)\left(d^2 + \frac{L^2}{4} - r^2\right) \end{bmatrix}$$

and

$$d_0 = \left(d^2 + \frac{L^2}{4}\right)\left(\left[d^2 + \frac{L^2}{4}\right][4d^2 - r^2] - 8r^2d^2 + 4r^3d\right).$$

The simple electrostatic string is a single-degree-of-freedom system. Therefore its linearized motion is governed by Eq. (19) in which its stability characteristics are dictated by the stiffness B and the damping A both reduced to scalars. The gyroscopic matrix and the circulatory matrix are reduced to zero. It follows, as discussed below Eq. (24), that the motion of the simple electrostatic string is stable only if B and A are positive. The evaluation of B and A require the following terms that appeared in Eqs. (23a) and (24a):

Downloaded 04 May 2010 to 171.66.16.33. Redistribution subject to ASME license or copyright; see http://www.asme.org/terms/Terms_Use.cfm

$$\left(\frac{\partial P}{\partial \theta}\right)_0 = \kappa \begin{bmatrix} 0 & \frac{-1}{d_{12}^2}\frac{\partial d_{12}}{\partial \theta} & \frac{-1}{d_{13}^2}\frac{\partial d_{13}}{\partial \theta} \\ \frac{-1}{d_{12}^2}\frac{\partial d_{12}}{\partial \theta} & 0 & 0 \\ \frac{-1}{d_{13}^2}\frac{\partial d_{13}}{\partial \theta} & 0 & 0 \end{bmatrix}$$

$$= \frac{\kappa DL}{2\left(d^2 + \frac{L^2}{4}\right)^{3/2}} \begin{bmatrix} 0 & -1 & 1 \\ -1 & 0 & 0 \\ 1 & 0 & 0 \end{bmatrix} \tag{30}$$

The sign of A depends on the sign of the control gain g_2. In fact, both A and B can be prescribed by g_1 and g_2 yielding any desired dynamic control properties. Note, however, that the term in { } that multiplies both g_1 and g_2 in Eqs. (33) and (34) is typically much smaller in magnitude than B_{unc}. Thus, B_{unc} is the important parameter to study when investigating stability.

By numerically computing B_{unc} for cases in which M varies from 1 to 5, the value of d/L critical is obtained, as shown in Fig. 3. As shown, the value of d/L critical decreases as M increases. Therefore, with higher discretization (and thus more modes participating in the system), the control points must be located closer to the axis of the electrostatic string. When d/L is greater than the critical value for any particular M, the system becomes unstable. When this occurs, there exists another stable equilibrium that the electrostatic string tends to approach. It is

$$\left(\frac{\partial^2 P}{\partial \theta^2}\right)_0 = \kappa \begin{bmatrix} 0 & \frac{-1}{d_{12}^2}\frac{\partial^2 d_{12}}{\partial \theta^2} + \frac{2}{d_{12}^3}\left(\frac{\partial d_{12}}{\partial \theta}\right)^2 & \frac{-1}{d_{13}^2}\frac{\partial^2 d_{13}}{\partial \theta^2} + \frac{2}{d_{13}^3}\left(\frac{\partial d_{13}}{\partial \theta}\right)^2 \\ \frac{-1}{d_{12}^2}\frac{\partial^2 d_{12}}{\partial \theta^2} + \frac{2}{d_{12}^3}\left(\frac{\partial d_{12}}{\partial \theta}\right)^2 & 0 & 0 \\ \frac{-1}{d_{13}^2}\frac{\partial^2 d_{13}}{\partial \theta^2} + \frac{2}{d_{13}^3}\left(\frac{\partial d_{13}}{\partial \theta}\right)^2 & 0 & 0 \end{bmatrix}$$

$$= \frac{\kappa L^2\left(d^2 - \frac{L^2}{2}\right)}{4\left(d^2 + \frac{L^2}{4}\right)^{5/2}} \begin{bmatrix} 0 & 1 & 1 \\ 1 & 0 & 0 \\ 1 & 0 & 0 \end{bmatrix}. \tag{31}$$

We next distinguish between the uncontrolled system in which $V_2 = (V_2)_0$ and the controlled system in which $V_2 = (V_2)_0 + g_1\theta + g_2\dot{\theta}$, in which V_2 represents the voltage of the lower control point. Considering first the uncontrolled system, we obtain

$$B_{unc} = -\mathbf{V}^T\left(C_0\left(\frac{\partial P}{\partial \theta}\right)_0\right)^2 C_0\mathbf{V}_0 + \frac{1}{2}\mathbf{V}_0^T C_0\left(\frac{\partial^2 P}{\partial \theta^2}\right)_0 C_0\mathbf{V}_0 = -\frac{dL^2V^2r^2\left(4rd + [r+2d]\left[d^2 + \frac{L^2}{4}\right]^{1/2}\right)}{\kappa\left(d^2 + \frac{L^2}{4}\right)^2(2d-r)\left(\left[d^2 + \frac{L^2}{4}\right][2d+r] - 4r^2d\right)^2}$$

$$\times\left[d^2r\left(4rd + [2d+r]\left[d^2 + \frac{L^2}{4}\right]^{1/2}\right) + \left(d^2 - \frac{L^2}{2}\right)(2d-r)\left(d^2 + \frac{L^2}{4}\right)^{1/2}\left(r + \left[d^2 + \frac{L^2}{4}\right]^{1/2}\right)\right]. \tag{32}$$

Clearly this term can be positive or negative depending on the magnitude of d/L. There exists a critical value of d/L for which $B = 0$ at which point the system switches from stable to unstable. Next, in the presence of the feedback terms g_1 and g_2, we get

$$B_c = B_{unc} + \mathbf{V}_0^T C_0\left(\frac{\partial P}{\partial \theta}\right)_0 C_0\left(\frac{\partial \mathbf{V}}{\partial \theta}\right)_0 = B_{unc} - g_1\left\{\frac{VLd^2r^2\left[\left(d^2 + \frac{L^2}{4}\right)^{1/2}(2d+r) + 4rd\right]}{\kappa\left(d^2 + \frac{L^2}{4}\right)(2d-r)\left[\left(d^2 + \frac{L^2}{4}\right)(2d+r) - 4r^2d\right]}\right\}. \tag{33}$$

The damping term A is

$$A = \mathbf{V}_0^T C_0\left(\frac{\partial P}{\partial \theta}\right)_0 C_0\left(\frac{\partial \mathbf{V}}{\partial \dot{\theta}}\right)_0 = -g_2\left\{\frac{VLd^2r^2\left[\left(d^2 + \frac{L^2}{4}\right)^{1/2}(2d+r) + 4rd\right]}{\kappa\left(d^2 + \frac{L^2}{4}\right)(2d-r)\left[\left(d^2 + \frac{L^2}{4}\right)(2d+r) - 4r^2d\right]}\right\}. \tag{34}$$

Downloaded 04 May 2010 to 171.66.16.33. Redistribution subject to ASME license or copyright; see http://www.asme.org/terms/Terms_Use.cfm

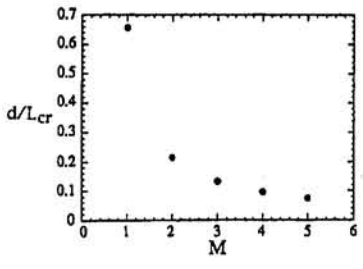


Fig. 3 Instability study

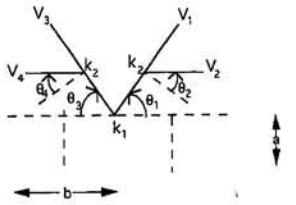


Fig. 4 Attached control surfaces

interesting to note that in each of the cases considered, (M = 1, 2, 3, 4, 5), the instability occurred in the highest mode of vibration.

We next examine a control algorithm for the case $M = 9$. The control point was placed within the stable region determined earlier. The algorithm governs the voltage at the control point located below the tip of the beam while holding the other voltages constant. We write

$$V_{N-1} = -V_0 - (g_1 \mathbf{r}_{N-2} + g_2 \dot{\mathbf{r}}_{N-2}) \cdot \hat{n} \qquad (35)$$

in which g_1 and g_2 are constant control gains and $\hat{\mathbf{n}}$ is a unit vector in the transverse direction. We let $g_1 = 10^4$, and $g_2 = 3 \times 10^4$, $d = 0.05$, $L = 1$ (so $h = 1/9$), and the equilibrium voltages are set to 20 kV. The frequencies and decay rates associated with the controlled system are obtained from the eigenvalue problem associated with Eq. (19). They are given in Table 1. From Table 1, the control algorithm achieves a significant level of electrostatic damping in the second and third modes and the other modes become lightly damped in comparison.

4 Attached Control Surfaces

The previous electrostatic control problem used fixed control points which suffer from the disadvantage that their effective range of influence is small in the sense that the force they exert on the structure becomes very small as the electrostatic structure's displacements increase (a direct consequence of Coulomb's inverse square law). An alternative consists of replacing the fixed control points with control points that are attached to the electrostatic structure. These attached control points "follow" the structure so that the effective range of their influence increases. We consider now a system of two rigid bars joined by a torsional spring k_1. Control surfaces, which are also rigid, are attached to the bars by the torsional springs k_2 (see Fig. 4). We eliminate the rotational rigid-body motion by selecting the torsional spring k_3 to be of significantly higher magnitude than k_1 and k_2. Letting $k_3 \gg k_1$ and $k_3 \gg k_2$, the equilibrium angle θ_1 is zero. The system stiffness matrix becomes (see Eq. (11b))

$$K_S = \begin{bmatrix} k_1 + k_3 & 0 & k_1 & 0 \\ 0 & k_2 & 0 & 0 \\ k_1 & 0 & k_1 & 0 \\ 0 & 0 & 0 & k_2 \end{bmatrix}. \qquad (36)$$

As a further simplification we apply the voltages symmetrically, that is we let V_1 and V_3 be equal, as well as V_2 and V_4. This symmetry of voltages ensures that θ_2 and θ_4 will be equal. The main design goal is now to arbitrarily select the opening angle $\theta_0 = \pi - \theta_1 - \theta_3$ between the two main pieces.

We first conduct a parametric study; varying three sets of parameters to determine their effect on the opening angle. The three sets of parameters to be varied are the voltages V_1 and V_2, the spring constants k_1 and k_2, and the lengths a and b. The parameters are varied from the nominal set of values $V_1 = V_2 = 20$ kV, $k_1 = 2E - 6$, $k_2 = 2E - 4$, $a = b = 1$. The equilibrium positions are determined iteratively by first approaching the neighborhood of the solution in the steepest descent direction and then by determining the solution using a Newton/Rhapson method. The results are shown in Fig. 5.

As shown, the opening angle decreases as the control surface area ab increases. Conversely, as b decreases the areas of the open surfaces decrease causing the opening angle to increase. As the voltages on the control surfaces increase (and conversely as the voltage on the opening surface decreases) the opening angle increases. Finally, as the spring constant k_1 increases, the opening angle increases and as the spring constant k_2 increases, the opening angle decreases. These results are rather expected, indicating that the attached subsurfaces can be used with relative ease to generate desired opening angles.

Next, we examine feedback control of the simple electrostatic bar using the attached control surfaces. We introduce the following control law:

$$\mathbf{V} = \mathbf{V}_0 + \begin{bmatrix} 0 & 0 & 0 & 0 \\ 1 & 1 & 0 & 0 \\ 0 & 0 & 0 & 0 \\ 0 & 0 & 1 & 1 \end{bmatrix} [g_1(\boldsymbol{\theta} - \boldsymbol{\theta}_0) + g_2 \dot{\boldsymbol{\theta}}] \qquad (37)$$

where $\boldsymbol{\theta} = (\theta_1 \quad \theta_2 \quad \theta_3 \quad \theta_4)^T$ and $\mathbf{V} = (V_1 \quad V_2 \quad V_3 \quad V_4)^T$. Equation (37) is considered along with the parameters $g_1 = -10{,}000$, $g_2 = -1{,}000$, $a = b = 1$, $k_1 = 2 \times 10^{-6}$, $k_2 = 2 \times 10^{-4}$, $k_3 = 0.01$, and all four equilibrium voltages are set to 20 kV. The associated controlled frequencies of oscillation and damping rates are given in Table 2.

Table 1 Electrostatic frequencies and decay rates

Mode	Uncontrolled frequency (rad/sec)	Controlled frequency (rad/sec)	Controlled decay rate (rad/sec)
1	.792270598749833	.815521960922205	-2.656588629E-002
2	1.53378390182082	1.70400642052293	-.302038192419373
3	2.26475128600376	2.10612256060644	-.312862959798554
4	3.45543720738760	3.42336167837993	-6.95505993730E-002
5	5.23784348163390	5.23167900683778	-2.28250539533E-002
6	7.88941044560408	7.88818752304731	-7.47090257631E-003
7	12.3282280303338	12.3279797230859	-2.50275880360E-003
8	21.9911677754522	21.9911185893282	-5.71031291159E-004
9	67.7499620929191	67.7492896314889	-6.31022494614E-005

5 Shape Control

The final electrostatic structure to be examined is a representation of a flexible membrane controlled and shaped by discrete back charges. The membrane is modeled as two electrostatic strings, pinned in the middle as shown in Fig. 6. The position of the membrane is represented by the angles of the partitioned segments. In the cases to be considered, the length of the membrane is 1 and the control points are symmetrically placed at 0.2 and 0.4 from the origin, respectively, and d is 0.1.

Let us first determine a control algorithm that controls the membrane shape. Toward that end, a first attempt consisted of prescribing the algorithm used earlier to control the electrostatic string (see Eq. (35)). In that algorithm the voltage of a control point was proportional to the position of the string. The next attempt to control the membrane consisted of feeding back angles in the neighborhood of the control points. Both attempts failed to control the membrane. The membrane was successfully controlled by weighting the angles of the membrane in propor-

Downloaded 04 May 2010 to 171.66.16.33. Redistribution subject to ASME license or copyright; see http://www.asme.org/terms/Terms_Use.cfm

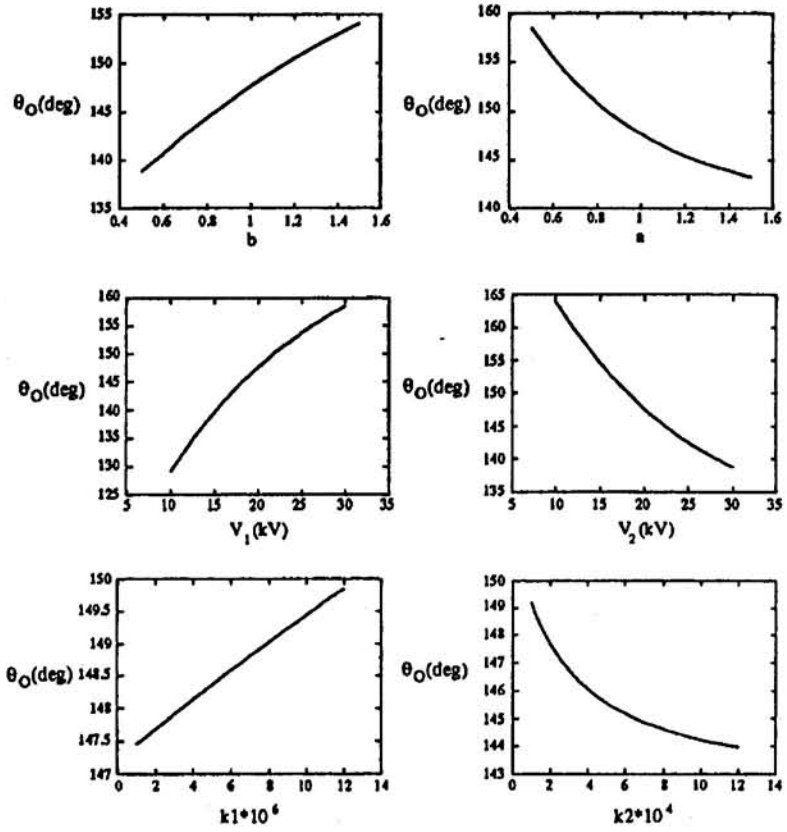


Fig. 5 The opening angle versus the varied parameter

tion to their distances from the center. We obtain the control algorithm

$$\mathbf{V} = \mathbf{V}_0 + \left[\begin{array}{cccc|cccc} & & \mathbf{0}_{M\times M} & & & & & \\ \hline & \mathbf{0}_{1\times(M/2)} & & & 1 & .1 & .1^2 \cdots & .1^{(M/2)-1} \\ & \mathbf{0}_{1\times(M/2)} & & & 1 & .1 & .1^2 \cdots & .1^{(M/2)-1} \\ 1 & .1 \quad .1^2 \cdots & .1^{(M/2)-1} & & & \mathbf{0}_{1\times(M/2)} & & \\ 1 & .1 \quad .1^2 \cdots & .1^{(M/2)-1} & & & \mathbf{0}_{1\times(M/2)} & & \end{array}\right] [g_1(\boldsymbol{\theta} - \boldsymbol{\theta}_0) + g_2\dot{\boldsymbol{\theta}}] \quad (38)$$

where $\boldsymbol{\theta} = (\theta_1 \quad \theta_2 \quad \cdots \quad \theta_M)^T$ and $\mathbf{V} = (V_1 \quad V_2 \quad \cdots \quad V_N)^T$.

Letting $M = 5$, $g_1 = -5000$, $g_2 = -15{,}000$ and all equilibrium voltages = 20 kV, we obtain Table 3. The linearized decay rates and controlled frequencies given in Table 3 indicate that the membrane was successfully controlled (asymptotically stable) using four control points in which up to ten modes participated in the controlled system response.

With the objective of controlling the membrane about equilibrium established, the next important step was to achieve a desired shape by appropriately varying the equilibrium voltages. Since there are five voltages to vary, (the membrane and the four control points), the equilibrium positions can be either overdetermined or underdetermined depending on the number

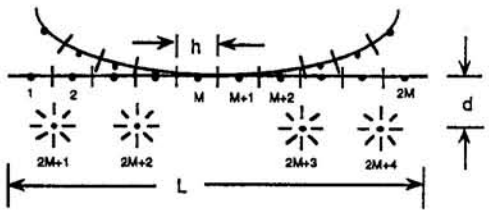


Fig. 6 Membrane

Table 2 Control with attached surfaces

Mode	Uncontrolled frequency(rad/sec)	Controlled frequency (rad/sec)	Controlled decay rate (rad/sec)
1	0.1311533466191533	0.1374873647872766	-7.907933804383225 8E-05
2	0.3967573950035937	0.4083173983156798	-4.523841609264115 1E-04
3	0.5295401272256329	0.5372373406522831	-4.279942896915295 1E-04
4	1.619640287300514	1.619825455843793	-3.009524813402088 3E-05

Table 3 Control of membrane

Mode	Uncontrolled frequency(rad/sec)	Controlled frequency (rad/sec)	Controlled decay rate (rad/sec)
1	0.42071975379996	0.4534231433495 7	-0.03931361312
2	0.58360879448638	0.59619270805069	-0.01874817878
3	1.53665443380549	1.56053518410222	-0.16078572223
4	1.70862708746123	1.73965325658873	-0.15606265253
5	3.64579634857746	3.63850815308131	-0.14056709661
6	3.79383526308544	3.78578695495111	-0.22296648082
7	8.15211683311237	8.14970359697421	-0.04358334380
8	8.23028958189212	8.21982540432809	-0.13298851959
9	27.2063239005999	27.2062128324056	-0.00663873439
10	27.2299252131194	27.2273343605098	-0.08421796502

Downloaded 04 May 2010 to 171.66.16.33. Redistribution subject to ASME license or copyright; see http://www.asme.org/terms/Terms_Use.cfm

Table 4 Underdetermined shape

V1	V2	V3	V4	V5	J(V)
20000	20000	20000	20000	20000	0.3971825
13492	7633	7633	13492	12085	0.2672423
12448	1829	1829	12448	10121	0.0409519
12528	1297	1297	12528	10181	0.0006641
12526	1306	1306	12526	10180	0.0000000

Table 5 Overdetermined shape

V1	V2	V3	V4	V5	J(V)
20000	20000	20000	20000	20000	0.5130988
20843	20418	20418	20843	17353	0.4224052
22088	19724	19724	22088	14133	0.3685340
24484	11370	11370	24484	11931	0.2973576
25180	6237	6237	2518 0	10133	0.2452399
25351	1595	1595	25351	8132	0.1869125
25332	193	193	25332	7363	0.1717889
26115	-2779	-2779	26115	4115	0.1504494

of membrane degrees-of-freedom. When each side is divided into two subsurfaces, the equilibrium equations are underdetermined and there exists an infinite set of voltages capable of achieving a given shape. This problem is resolved by an iteration scheme using first a steepest descent method, followed by a Newton/Rhapson approach.

The steepest descent formulation begins with defining the error functional

$$J(\mathbf{V}) = (\boldsymbol{\theta} - \boldsymbol{\theta}_d)^T(\boldsymbol{\theta} - \boldsymbol{\theta}_d) \tag{39}$$

in which $\boldsymbol{\theta}_d$ denotes a vector of desired angles. The derivatives of this functional are determined numerically to be

$$DJ_i(\mathbf{V}) = \frac{J(\mathbf{V} + \Delta\mathbf{V}_i) - J(\mathbf{V})}{\Delta V_i} \tag{40}$$

and the voltages are updated according to

$$\mathbf{V}(k+1) = \mathbf{V}(k) - \sigma\mathbf{D}J(\mathbf{V}) \tag{41}$$

where σ is a weighting factor chosen to go as far as possible in the steepest descent direction while still lowering the value of the functional J in Eq. (39). As the steepest descent method levels out, the switch is made to a Newton's method. Toward this end, we form the functions

$$f_i(\mathbf{V}_0) = \sum_{j=1}^{M} K_{Sij}\theta_{j,0} + \frac{1}{2}\mathbf{V}_0^T C_0\left(\frac{\partial P}{\partial \theta_i}\right)_0 C_0\mathbf{V}_0 \tag{42}$$

and their derivatives with respect to V_1 through V_5, given by

$$\frac{\partial f_i}{\partial \mathbf{V}_0} = 2C_0\left(\frac{\partial P}{\partial \theta_i}\right)_0 C_0\mathbf{V}_0. \tag{43}$$

Equation (43) is written compactly as

$$G = \left[\frac{\partial f_1}{\partial \mathbf{V}_0} \quad \frac{\partial f_2}{\partial \mathbf{V}_0} \quad \cdots \quad \frac{\partial f_M}{\partial \mathbf{V}_0}\right]^T \tag{44}$$

where G is a $M \times N$ matrix. The voltages are now varied according to

$$\mathbf{V}(k+1) = \mathbf{V}(k) - \sigma G^{**}\mathbf{f} \tag{45}$$

where the pseudo inverse of G, denoted by G^{**}, is a minimum norm solution in the underdetermined case.

The case $M = 2$ is shown in Table 4. The chosen equilibrium angles $\theta_1 = 0.566$ rad, and $\theta_2 = 0.866$ rad are achieved within a few iterations. The initial and final shapes are shown in Fig. 7.

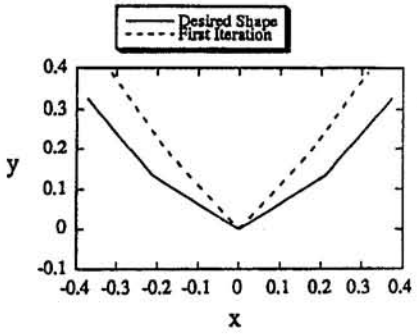


Fig. 7 Shapes for $M = 2$

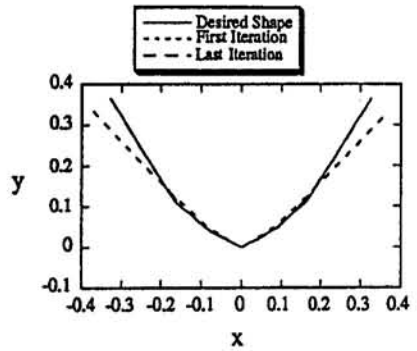


Fig. 8 Shapes for $M = 5$

In the over determined cases (i.e., $M > 2$), an arbitrarily chosen shape is not achievable. However, by using the steepest descent method, described above, the voltages can be found to give the "closest" approximation of the desired equilibrium. By closest it is meant that the functional J has achieved a minimum value. This generally requires more iterations than earlier. Table 5 shows the case $M = 5$, for which the chosen equilibrium angles were given by (.5, .7, 1, 1, 1 rad). The initial shape, the final shape, and the desired shape are shown in Fig. 8. As shown, the final iteration yields an error of $J = 0.1504494$.

6 Conclusions

This paper formulated the equations that govern the dynamics and control of electrostatic structures. The formulation adopted an energy approach resulting in nonlinear and linearized equations of motion. These equations were used to conduct a number of studies that illustrate the shaping and feedback control of electrostatic structures. The paper first considered the effect of externally applied control points on the stability of electrostatic structures. A simple feedback control algorithm then demonstrated electrostatic damping of an electrostatic string. Next our attention turned to electrostatic structures employing attached control points and the shape control of a bar system was conducted. Feedback control of the bar system was also demonstrated. Perhaps the most important results are drawn from the shape control studies of electrostatic structures. Two iterative methods demonstrated shape control of an electrostatic string. The studies suggest the feasibility of electrostatic shape control of systems, in general.

Downloaded 04 May 2010 to 171.66.16.33. Redistribution subject to ASME license or copyright; see http://www.asme.org/terms/Terms_Use.cfm

References

Jackson, J. D., 1975, *Classical Electrodynamics,* John Wiley and Sons, New York.

Meirovitch, L., 1980, *Computational Methods in Structural Dynamics,* Sijthoff and Noordhoff, Rockville, MD.

Mihora, D. H., and Redmond, P. J., 1979, "Electrostatically Formed Antennas," General Research Corporation, Santa Barbara, CA, Internal Memo 2222.

Park, K., 1992, "An Investigation of Planar Electrodynamic Structures," Ph.D. Dissertation, North Carolina State University, Raleigh, NC.

Rhim, W. K., Collender, M., Hyson, M. T., Simms, W. T., and Elleman, D. D., 1985, "Development of an Electrostatic Positioner for Space Material Processing," *Review of Scientific Instruments,* Vol. 56, No. 2, pp. 307–317.

Rhim, N. K., Chung, S. K., Hyson, M. T., Trinh, E. H., and Elleman, D. D., 1987, "Large Charged Drop Levitation Against Gravity," *IEEE Transactions on Industry Applications,* Vol. IA-23, No. 6, pp. 975–979.

Silverberg, L., 1994, "Electrostatically Shaped Membranes," U.S. Patent No. 5,307,082.

Streng, J. H., 1990, "Charge Movements on the Stretched Membrane in a Circular Electrostatic Push-Pull Loudspeaker," *Journal of the Audio Engineering Society,* Vol. 38, No. 5, pp. 331–338.

Streng, J. H., 1989, "Sound Radiation from Circular Stretched Membranes in Free Space," *Journal of the Audio Engineering Society,* Vol. 37, No. 3, pp. 107–118.

Yam, Y., Lang, J. H., Staelin, D. H., and Johnson, T. L., 1988, "The Experimental Computer Control of a Two-Dimensional Hyperbolic System," *IEEE Transactions on Automatic Control,* Vol. 33, No. 1, pp. 79–87.

Downloaded 04 May 2010 to 171.66.16.33. Redistribution subject to ASME license or copyright; see http://www.asme.org/terms/Terms_Use.cfm

Dynamics of Plane Motion of an Elastic Rod

T. M. Atanackovic

L. J. Cveticanin

Faculty of Technical Sciences,
University of Novi Sad,
Trg D. Obradovica 6,
21000 Novi Sad, Yugoslavia

Plane motion of an elastic rod, subjected to a compressive force is analyzed. Equations of motions are derived for the case when deformations are not small. It is assumed that the compressive force has a periodic component, so that parametric instability is possible. Stability boundary is estimated analytically and determined numerically. In the special case of static loading a new formula for the slenderness ratio, below which there is no buckling, is obtained. In deriving the differential equations of motion a generalized constitutive equations taking into account compressibility and shear stresses are used.

1 Introduction

The study of dynamics of an elastic rod experiencing large deformation is important for both theoretical and practical reasons. In structural engineering, mechanisms and robotics many elements are modeled as an elastic rod. They are often subjected to transverse and axial forces that could be constant, stochastic, and periodic. Under such loads the rod could vibrate in a complicated manner, with possibility of loosing stability. Thus, it becomes extremely important to predict properties of the motion, such as boundedness of solutions and periodicity. This is often an interesting mathematical problem. Generally speaking, equations of motion for an elastic rod undergoing *large strains, large displacements,* are formulated by two procedures, which differ according to the coordinate systems used. In the first procedure, called a shadow beam method, the equations of motion are formulated in a moving coordinate system that follows rigid-body motion of the rod (Laskin, Likins, and Longman, 1983). This procedure has a consequence that, in the of case large strains and large displacements, the equations of motion are highly nonlinear and coupled in the inertia terms. In the second procedure, formulated by Simo and Vu-Quoc (1986), for example, the fixed coordinate system is used, so that the resulting equations of motion are linear in the inertia terms. Our intention in this work is to formulate finite strain, finite displacements equations of motion of an elastic rod in the unmovable reference frame. We shall assume that the rod axis is extensible and we take into account the effect of shear stresses. As far as loading is concerned, we assume that the rod is loaded by a constant compressive force and that to this force a periodic perturbation is added. This leads to the possibility of parametric excitations (see Nayfeh and Mook, 1979).

As far as constitutive equations are concerned we shall use the generalized rod model, that takes shear effect into account in the form suggested by Engesser (see Gjelsvik, 1991). This model, in a nonlinear version, was formulated by Schmidt and DaDeppo (1971) and used by Atanackovic and Spasic (1991), for example. Our results will depend on this choice. For different possibilities in choosing models that take shear into account see Atanackovic and Spasic (1994).

The resulting nonlinear partial differential equations of motion are linearized, written in the integral (weak) form and then, using a Galerkin discretization in the spatial variable, reduced to a standard system of linear differential equations in time. This system is studied numerically and analytically (Floquet theory).

We determined stability boundary, numerically, for some values of parameters in the equations of motion. To check accuracy of numerical procedure we used two new first integrals for the reduced form of the differential equations of motion. This integrals are of the Lewis type (see Lewis, 1968) and were recently obtained by Vujanovic (1992).

2 Formulation

Consider a thin, heavy elastic rod, simply supported at both ends, with the support at the end B fixed. The rod is loaded at the end C by an axial force. We assume that the rod constrained to move in fixed plane Π (see Fig. 1) to which its axis belongs initially.

Let $\bar{x}$ and $\bar{y}$ be the Cartesian coordinate system with the origin at B. We assume that the axis of the rod is extensible in the unloaded state straight and has length L. An element of the axis that at the initial moment $t = 0$ (in which rod is undeformed) has length dS in the deformed state at time t has length ds. Then, the strain of the rod axis is

$$\epsilon = \frac{ds - dS}{dS}. \tag{1}$$

We use D'Alembert's principle and write equations of motion as equilibrium equation of active and inertia forces and couples. From Fig. 1(b) we obtain the equilibrium equations, for an element of length ds in the deformed state, as

$$dH = -q_x dS, \quad dV = -q_y dS,$$
$$dM = Vdx - Hdy + mdS \tag{2}$$

where H and V are $\bar{x}$ and $\bar{y}$-components of the contact force, respectively, M is the bending moment, and x and y are coordinates of an arbitrary point. Also in (2) q_x, q_y and m are the intensities of distributed forces (in the $\bar{x}$ and $\bar{y}$ direction) and couples, per unit length of the undeformed rod axis. We assume that the only distributed forces and couples come from the inertia so that

$$q_x = -\rho \frac{\partial^2 x}{\partial t^2}; \quad q_y = -\rho \frac{\partial^2 y}{\partial t^2}; \quad m = -\rho r^2 \frac{\partial^2 \vartheta}{\partial t^2}, \tag{3}$$

where ρ is the mass per unit length in the undeformed state, ϑ is the angle between the tangent to the rod axis and $\bar{x}$-axis, and r is the radius of gyration of a section of the rod about the axis through the center of gravity perpendicular to the plane of of

Contributed by the Applied Mechanics Division of THE AMERICAN SOCIETY OF MECHANICAL ENGINEERS for publication in the ASME JOURNAL OF APPLIED MECHANICS.

Discussion on this paper should be addressed to the Technical Editor, Professor Lewis T. Wheeler, Department of Mechanical Engineering, University of Houston, Houston, TX 77204-4792, and will be accepted until four months after final publication of the paper itself in the ASME JOURNAL OF APPLIED MECHANICS.

Manuscript received by the ASME Applied Mechanics Division, Mar. 11, 1994; final revision, Mar. 22, 1995. Associate Technical Editor: J. N. Reddy.

Copyright © 1996 by ASME

Downloaded 04 May 2010 to 171.66.16.33. Redistribution subject to ASME license or copyright; see http://www.asme.org/terms/Terms_Use.cfm

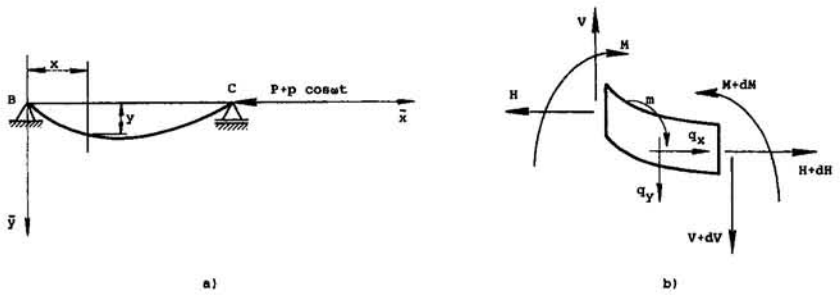


Fig. 1 Coordinate system and load configuration

motion (Π). To the equilibrium equations we adjoin the following geometrical relations

$$\frac{\partial x}{\partial S} = (1 + \epsilon)\cos\vartheta; \quad \frac{\partial y}{\partial S} = (1 + \epsilon)\sin\vartheta, \tag{4}$$

where we used (1). The constitutive equations we take in the form given by Schmidt and DaDeppo (1971), that is

$$\epsilon = \frac{N}{EA}; \quad \gamma = k\frac{Q}{GA}; \quad \frac{\partial\vartheta}{\partial S} - \frac{\partial\gamma}{\partial S} = -\frac{M}{EI\cos\gamma}. \tag{5}$$

In (5) γ is the shear angle, EI is the bending rigidity, GA is the shear rigidity, k is the shear correction number, N is the component of the contact force in the direction of the tangent to the rod axis and Q is the component of the contact force in the direction of the sheared planes (Q has angle $\frac{1}{2}\pi + \gamma$ with the tangent to the rod axis). The constitutive equations $(5)_{1,2}$ (first and second equations in the system (5)) correspond to the so called Engesser type of constitutive equations. Instead of (5) one could use, for example, Haringx's type of constitutive equations, as presented by Libai (1992).

We express Q and N in terms of H and V. From the definitions it follows that (see Atanackovic and Spasic, 1991)

$$Q = V\frac{\cos\vartheta}{\cos\gamma} - H\frac{\sin\vartheta}{\cos\gamma};$$

$$N = H\frac{\cos(\vartheta - \gamma)}{\cos\gamma} + V\frac{\sin(\vartheta - \gamma)}{\cos\gamma}. \tag{6}$$

We use now $(6)_1$ in $(5)_2$ and differentiate the resulting expression to eliminate $\partial\gamma/\partial S$ in $(5)_3$. Then, from (2), (3), (5), and (6) we obtain

$$\frac{\partial H}{\partial S} - \rho\frac{\partial^2 x}{\partial t^2} = 0; \quad \frac{\partial V}{\partial S} - \rho\frac{\partial^2 y}{\partial t^2} = 0;$$

$$\frac{\partial M}{\partial S} - V\frac{\partial x}{\partial S} + H\frac{\partial y}{\partial S} + \rho r^2\frac{\partial^2\vartheta}{\partial t^2} = 0;$$

$$\frac{\partial x}{\partial S} - \left(1 + \frac{1}{EA}\frac{H\cos(\vartheta - \gamma) + V\sin(\vartheta - \gamma)}{\cos\gamma}\right)\cos\vartheta = 0;$$

$$\frac{\partial y}{\partial S} - \left(1 + \frac{1}{EA}\frac{H\cos(\vartheta - \gamma) + V\sin(\vartheta - \gamma)}{\cos\gamma}\right)\sin\vartheta = 0;$$

$$\frac{\partial\vartheta}{\partial S} + \frac{\dfrac{M}{EI\cos\gamma} - \dfrac{k}{GA}\dfrac{\rho[(\partial^2 y/\partial t^2)\cos\vartheta - (\partial^2 x/\partial t^2)\sin\vartheta]}{(\cos\gamma - \gamma\sin\gamma)}}{1 + \dfrac{V\sin\vartheta + H\cos\vartheta}{(\cos\gamma - \gamma\sin\gamma)}\dfrac{k}{GA}} = 0;$$

$$\frac{\partial\gamma}{\partial S} + \frac{k}{GA}\frac{V\sin\vartheta - H\cos\vartheta}{\cos\gamma - \gamma\sin\gamma}\frac{\partial\vartheta}{\partial S}$$

$$- \frac{k}{GA}\frac{\rho[(\partial^2 y/\partial t^2)\cos\vartheta - (\partial^2 x/\partial t^2)\sin\vartheta]}{(\cos\gamma - \gamma\sin\gamma)} = 0, \tag{7}$$

describing large plane motions of an elastic rod with the constitutive equations (5). To the system (7) we adjoin the following boundary and initial conditions

$$x(0, t) = 0; \quad y(0, t) = 0; \quad M(0, t) = 0;$$

$$y(L, t) = 0; \quad H(L, t) = -P + p\cos\omega t; \quad M(L, t) = 0;$$

$$x(S, 0) = F_1(S); \quad \frac{\partial x}{\partial t}(S, 0) = v_1(S);$$

$$y(S, 0) = F_2(S); \quad \frac{\partial y}{\partial t}(S, 0) = v_2(S). \tag{8}$$

Note that, from $(7)_{4,5}$ we have

$$\frac{\partial y}{\partial S} = \frac{\partial x}{\partial S}tg\vartheta, \tag{9}$$

so that the initial conditions for $\vartheta(S, t)$ satisfy

$$\frac{dF_2}{dS} = \frac{dF_1}{dS}tg\vartheta(S, 0);$$

$$\frac{dv_2}{dS} = \frac{dv_1}{dS}\frac{1}{\cos^2\vartheta(S, 0)}\frac{\partial\vartheta(S, 0)}{\partial t}. \tag{10}$$

The system of equations (7), when solved, gives H, V, M, x, y, ϑ, and γ as functions of S and t.

We shall not be concerned with the general solution of the nonlinear system (7). However, we could find the trivial solution to (7), i.e., the solution in which the rod axis remains straight. Thus we take

$$V^0 = 0; \quad M^0 = 0; \quad y^0 = 0; \quad \vartheta^0 = 0; \quad \gamma^0 = 0, \tag{11}$$

and the remaining equilibrium equations become

$$\frac{\partial H^0}{\partial S} - \rho\frac{\partial^2 x^0}{\partial t^2} = 0; \quad \frac{\partial x^0}{\partial S} - \left(1 + \frac{H^0}{EA}\right) = 0. \tag{12}$$

From (4), $(5)_{1,2}$, and (6) we have

$$H = \left[EA\left(\frac{\dfrac{\partial x}{\partial S}}{\cos\vartheta} - 1\right)\cos\vartheta - \frac{GA}{k}\gamma\sin(\vartheta - \gamma)\right];$$

$$V = \left[EA\left(\frac{\dfrac{\partial x}{\partial S}}{\cos\vartheta} - 1\right)\sin\vartheta + \frac{GA}{k}\gamma\cos(\vartheta - \gamma)\right]. \tag{13}$$

Downloaded 04 May 2010 to 171.66.16.33. Redistribution subject to ASME license or copyright; see http://www.asme.org/terms/Terms_Use.cfm

The trivial solution of equation (13) is given by

$$H^0 = EA\left(\frac{\partial x^0}{\partial S} - 1\right). \tag{14}$$

With (14), the boundary conditions $(8)_{1,5}$ corresponding to (12) read

$$x^0(0, t) = 0;$$

$$EA\left(\frac{\partial x^0(L, t)}{\partial S} - 1\right) = -P + p\cos\omega t. \tag{15}$$

The solution to (12), (15) is

$$x^0 = S\left(1 - \frac{P}{EA}\right) + \frac{p\sin\nu S}{\nu EA\cos\nu L}\cos\omega t;$$

$$H^0 = -P + \frac{p\cos\nu S}{\cos\nu L}\cos\omega t, \tag{16}$$

where

$$\nu = \omega\sqrt{\frac{\rho}{EA}}. \tag{17}$$

Note that $\nu L = \pi/2$ corresponds to the resonance of axial vibrations. We take now the solution to (7) in the form

$$H = H^0 + \bar{H};\quad V = V^0 + \bar{V};\quad M = M^0 + \bar{M};\quad x = x^0 + \bar{u};$$
$$y = y^0 + \bar{v};\quad \vartheta = \vartheta^0 + \bar{\vartheta};\quad \gamma = \gamma^0 + \bar{\gamma}. \tag{18}$$

Introducing the nondimensional quantities

$$\mathcal{H} = \frac{\bar{H}L^2}{EI};\quad \mathcal{V} = \frac{\bar{V}L^2}{EI};\quad \mathcal{M} = \frac{\bar{M}L}{EI};\quad u = \frac{\bar{u}}{L};$$

$$v = \frac{v}{L};\quad \xi = \frac{S}{L};\quad \tau = \Omega_1 t;\quad \gamma_1 = \frac{r}{L};$$

$$\lambda = \frac{PL^2}{EI};\quad h = \frac{L^2 p}{EI};\quad \Omega_1 = \sqrt{\frac{EI}{\rho L^4}};\quad \Omega = \frac{\omega}{\Omega_1};$$

$$\mu = \sqrt{\frac{AL^2}{I}};\quad \beta = \frac{GAL^2}{kEI};\quad \eta = \nu L, \tag{19}$$

substituting (18) into (7) and neglecting the higher order terms in perturbed variables, we get

$$\frac{\partial\mathcal{H}}{\partial\xi} = \frac{\partial^2 u}{\partial\tau^2};\quad \frac{\partial\mathcal{V}}{\partial\xi} = \frac{\partial^2 v}{\partial\tau^2};$$

$$\frac{\partial\mathcal{M}}{\partial\xi} = -\gamma_1^2\frac{\partial^2\vartheta}{\partial\tau^2} + \mathcal{V}\left(1 - \frac{\lambda}{\mu^2} + \frac{h\cos\eta\xi}{\mu^2\cos\eta}\cos\Omega\tau\right)$$
$$-\left(-\lambda + \frac{h\cos\eta\xi}{\cos\eta}\cos\Omega\tau\right)\frac{\partial v}{\partial\xi};$$

$$\frac{\partial u}{\partial\xi} = \frac{\mathcal{H}}{\mu^2};\quad \frac{\partial v}{\partial\xi} = \left(1 - \frac{\lambda}{\mu^2} + \frac{h\cos\eta\xi}{\mu^2\cos\eta}\cos\Omega\tau\right)\vartheta;$$

$$\frac{\partial\vartheta}{\partial\xi} = -\frac{\mathcal{M} - \frac{1}{\beta}\frac{\partial^2 v}{\partial\tau^2} - \left[\frac{\Omega}{\beta\mu}\frac{h\sin\eta\xi}{\cos\eta}\cos\Omega\tau\right]\vartheta}{1 + \frac{1}{\beta}\left[-\lambda + \frac{h\cos\eta\xi}{\cos\eta}\cos\Omega\tau\right]};$$

$$\frac{\partial\gamma}{\partial S} = -\left[-\lambda + \frac{h\cos\eta\xi}{\cos\eta}\cos\Omega\tau\right]$$
$$\times\frac{\mathcal{M} - \frac{1}{\beta}\frac{\partial^2 v}{\partial\tau^2} - \left[\frac{\Omega}{\beta\mu}\frac{h\sin\eta\xi}{\cos\eta}\cos\Omega\tau\right]\vartheta}{1 + \frac{1}{\beta}\left[-\lambda + \frac{h\cos\eta\xi}{\cos\eta}\cos\Omega\tau\right]}$$
$$+\frac{1}{\beta}\frac{\partial^2 v}{\partial\tau^2} + \left[\frac{\Omega}{\beta\mu}\frac{h\sin\eta\xi}{\cos\eta}\cos\Omega\tau\right]\vartheta. \tag{20}$$

The boundary conditions for the perturbed system (20) are

$$u(0, \tau) = 0;\quad v(0, \tau) = 0;\quad \mathcal{M}(0, \tau) = 0;$$
$$\mathcal{H}(1, \tau) = 0;\quad v(1, \tau) = 0;\quad \mathcal{M}(1, \tau) = 0;$$
$$\beta\gamma(1, \tau) = \mathcal{V}(1, \tau) - (-\lambda + h\cos\Omega\tau)\vartheta(1, t). \tag{21}$$

From (20) it is seen that the equations determining $\mathcal{H}$, u, and γ could be solved after the solution to the following system is found:

$$G_1 = \frac{\partial\mathcal{V}}{\partial\xi} - \frac{\partial^2 v}{\partial\tau^2} = 0;$$

$$G_2 = \frac{\partial\mathcal{M}}{\partial\xi} + \gamma_1^2\frac{\partial^2\vartheta}{\partial\tau^2} - \mathcal{V}\left(1 - \frac{\lambda}{\mu^2} + \frac{h\cos\eta\xi}{\mu^2\cos\eta}\cos\Omega\tau\right)$$
$$+\left(-\lambda + \frac{h\cos\eta\xi}{\cos\eta}\cos\Omega\tau\right)\frac{\partial v}{\partial\xi} = 0;$$

$$G_3 = \frac{\partial v}{\partial\xi} - \left(1 - \frac{\lambda}{\mu^2} + \frac{h\cos\eta\xi}{\mu^2\cos\eta}\cos\Omega\tau\right)\vartheta = 0;$$

$$G_4 = \frac{\partial\vartheta}{\partial\xi}\left\{1 + \frac{1}{\beta}\left[-\lambda + \frac{h\cos\eta\xi}{\cos\eta}\cos\Omega\tau\right]\right\}$$
$$+\mathcal{M} - \frac{1}{\beta}\frac{\partial^2 v}{\partial\tau^2} - \left[\frac{\Omega h\cos\eta\xi}{\beta\mu\cos\eta}\cos\Omega\tau\right]\vartheta = 0, \tag{22}$$

In what follows we intend to analyze the system (22). The corresponding boundary conditions that follow from (21) are

$$v(0, \tau) = v(1, \tau) = 0;\quad \mathcal{M}(0, \tau) = \mathcal{M}(1, \tau) = 0. \tag{23}$$

We turn now to the solution of (22).

3 The Weak Form of Equations: Spatial Discretization

Defining the vector function $\mathbf{G}$ by $\mathbf{G} = (G_1, \ldots, G_4)$, taking the dot product of this vector with the vector of weighting function $\mathbf{g} = (g_1, \ldots, g_4)$ and integrating over the spatial domain (0, 1) we get

$$R(\mathbf{w}, \mathbf{g}) = \int_0^1 (G_1 g_1 + \ldots + G_4 g_4)d\xi = 0. \tag{24}$$

The solution vector $\mathbf{w} = (\mathcal{V}, \mathcal{M}, v, \vartheta)$, that through (22) generates $\mathbf{G}$, and the weighting function $\mathbf{g}$ belong to appropriately chosen Sobolev spaces V_1 and V_2 given below

$$V_1 = \{\mathbf{w} \in [H^1(0, 1)]^4 \times [C^\infty(0, \infty)]^4,$$
$$\mathcal{M}(0, \tau) = 0,\ \mathcal{M}(1, \tau) = 0,\ v(0, \tau) = 0,\ v(1, \tau) = 0\};$$

Downloaded 04 May 2010 to 171.66.16.33. Redistribution subject to ASME license or copyright; see http://www.asme.org/terms/Terms_Use.cfm

$$V_2 = \{\mathbf{g}: \mathbf{g} \in [H^1(0, 1)]^4 \times [C^\infty(0, \infty)]^4\ g_1(0, \tau) = 0,\ g_1(0, \tau) = 0,\ g_4(0, \tau) = 0,\ g_4(0, \tau) = 0\}. \quad (25)$$

In (25), $H^1(0, 1)$ denotes the space of square integrable functions having square integrable (distributional) derivative in the interval (0, 1). We note that from the Sobolev imbeding theorem, Adams (1975), it follows that $H^1(0, 1)$ is subspace of the space of continuous functions on (0, 1). The solution vector $\mathbf{w}$ and the weighting function $\mathbf{g}$ are interpolated in the spatial variable ξ as

$$\mathbf{w}(\xi, \tau) = \sum_{i=1}^{N} \mathbf{X}_i(\xi)\mathbf{f}_i(\tau); \quad \mathbf{g}(\xi) = \sum_{i=1}^{N} \mathbf{X}_i(\xi)\mathbf{C}_i, \quad (26)$$

where $\mathbf{X}_i$ are suitable chosen trial functions and $\mathbf{C}_i$ are constant vectors. For simplicity we take $N = 1$ in (26) and

$$\mathbf{w} = \begin{bmatrix} \mathcal{V} \\ \mathcal{M} \\ v \\ \vartheta \end{bmatrix} = \begin{bmatrix} (\cos \pi\xi) f_V(\tau) \\ (\sin \pi\xi) f_M(\tau) \\ (\sin \pi\xi) f_v(\tau) \\ (\cos \pi\xi) f_\vartheta(\tau) \end{bmatrix};$$

$$\mathbf{g}(\xi) = \begin{bmatrix} C_1 \cos \pi\xi \\ C_2 \sin \pi\xi \\ C_3 \sin \pi\xi \\ C_4 \cos \pi\xi \end{bmatrix}, \quad (27)$$

where C_i are arbitrary constants ($i = 1, \ldots, 4$). In general $\mathbf{X}_i(\xi)$ could be chosen from any complete (in $H^1(0, 1)$) set of functions. If one uses only few terms in $(26)_1$, those terms should be chosen in such a way that the boundary and initial conditions are satisfied. Since we use only one term in $(26)_1$ we selected $\mathbf{X}_1(\xi)$ from the solution of linear problem corresponding to (22). Our functions $\mathbf{w}$ and $\mathbf{g}$ satisfy the boundary conditions that follow from (26). Using (27) in (22) and (24) we get

$$\pi f_V = -\ddot{f}_v;$$

$$\pi f_M = -\gamma_1^2 \ddot{f}_\vartheta + f_v\left\{1 - \frac{\lambda}{\mu^2} + \frac{h}{\mu^2 \cos \eta} 2I_1 \cos \Omega\tau\right\} - \pi f_v\left\{-\lambda + \frac{h}{\cos \eta} 2I_1 \cos \Omega\tau\right\};$$

$$\pi f_v = \left\{1 - \frac{\lambda}{\mu^2} + \frac{h}{\mu^2 \cos \eta} 2I_1 \cos \Omega\tau\right\} f_\vartheta;$$

$$-\pi\left\{1 + \frac{1}{\beta}\left[-\lambda + \frac{h}{\cos \eta} 2I_2 \cos \Omega\tau\right]\right\} f_\vartheta = -f_M + \frac{1}{\beta}\ddot{f}_v + f_\vartheta\left[\frac{\Omega}{\beta\mu} \frac{h}{\cos \eta} 2I_3 \cos \Omega\tau\right], \quad (28)$$

where $(\ddot{\cdot}) = d^2(\cdot)/d\tau^2$ and

$$I_1 = \frac{2\pi^2 - \eta^2}{\eta(4\pi^2 - \eta^2)} \sin \eta; \quad I_2 = \frac{\pi}{\eta(4\pi^2 - \eta^2)} \sin \eta;$$

$$I_3 = -\frac{\pi}{4\pi^2 - \eta^2} \sin \eta. \quad (29)$$

Introducing new function $f(\tau)$ by

$$f = \left[\frac{1}{\beta}\left(1 - \frac{\lambda}{\mu^2} + \frac{h}{\mu^2 \cos \eta} 2I_1 \cos \Omega\tau\right) + \frac{1}{\pi^2}\left(1 - \frac{\lambda}{\mu^2} + \frac{h}{\mu^2 \cos \eta} 2I_1 \cos \Omega\tau\right)^2 + \gamma_1^2\right] f_\vartheta, \quad (30)$$

the system (28) could be reduced to a single second-order equation

$$\ddot{f} + p(\tau) f = 0, \quad (31)$$

where

$$p(\tau) = \pi^2 \frac{\pi^2\left(1 - \frac{P_2}{\beta}\right) - P_1\left(1 - \frac{P_1}{\mu^2}\right) + \pi \frac{\Omega P_3}{\beta\mu}}{\left[\frac{1}{\beta}\left(1 - \frac{P_1}{\mu^2}\right) + \gamma_1^2\right]\pi^2 + \left(1 - \frac{P_1}{\mu^2}\right)^2}, \quad (32)$$

and

$$P_1 = \lambda - \frac{2hI_1}{\cos \eta} \cos \Omega\tau; \quad P_2 = \lambda - \frac{2hI_2}{\cos \eta} \cos \Omega\tau; \quad P_3 = \frac{2hI_3}{\cos \eta} \cos \Omega\tau. \quad (33)$$

Equation (31) is the central equation of our analysis. It is Hill's equation since $p(\tau) = p(\tau + T)$, where $T = 2\pi/\Omega$, and represents a generalization of the earlier studied equations for the same problem, since it includes compressibility and shear stress effects. Namely for $\beta \to \infty$ and $\mu \to \infty$ (incompressible rod with infinite shear stiffness) we obtain from (31) the equations studied by Nayfeh and Mook (1979) and Bolotin (1964), for example. Since h models small perturbation of the compressive force, we assume that

$$\lambda - \frac{2hI_1}{\cos \eta} > 0. \quad (34)$$

Note that $f \equiv 0$ is the (trivial) solution to (31) for which the axis of the rod remains straight. Boundness of solutions of (31) guarantees boundness of f_v and thus stability of transverse vibrations. For Eq. (31) we have the following:

Theorem: Let δ and Δ be constants defined by

$$\delta = \pi^2\left[1 - \frac{1}{\beta}\left(\lambda + \frac{h}{\cos \eta} 2I_2\right)\right] + \pi \frac{\Omega}{\beta\mu} \frac{h}{\cos \eta} 2I_3 - \left(\lambda + \frac{h}{\cos \eta} 2I_1\right) + \frac{1}{\mu^2}\left(\lambda - \frac{h}{\cos \eta} 2I_1\right)^2 > 0;$$

$$\Delta = \gamma_1^2 + \frac{1}{\pi^2}\left(1 - \frac{\lambda}{\mu^2} - \frac{h}{\mu^2 \cos \eta} 2I_1\right)^2 + \frac{1}{\beta}\left(1 - \frac{\lambda}{\mu^2} - \frac{h}{\mu^2 \cos \eta} 2I_1\right). \quad (35)$$

Then, all solutions of (31) are bounded if

$$\delta > 0; \quad \frac{\delta}{\Delta} \le \frac{4}{\pi^2}. \quad (36)$$

Moreover, for small h the parameters of the system on boundary of stability region (separating bounded from unbounded solutions) satisfy

$$\frac{\left[\pi^2\left[1 - \frac{\lambda}{\beta}\right] - \lambda + \frac{\lambda^2}{\mu^2}\right]}{\gamma_1^2 + \frac{1}{\pi^2}\left(1 - \frac{\lambda}{\mu^2}\right)^2 + \frac{1}{\beta}\left(1 - \frac{\lambda}{\mu^2}\right)} = \left(\frac{\Omega}{2} K\right)^2, \quad K = 0, 1, \ldots. \quad (37)$$

Downloaded 04 May 2010 to 171.66.16.33. Redistribution subject to ASME license or copyright; see http://www.asme.org/terms/Terms_Use.cfm

Proof: To prove the Theorem we note that $p(\tau)$ in (31) is periodic with the period $T = 2\pi/\Omega$. Then, the solutions are bounded if the following conditions hold (see Demidovich, 1967)

$$p(\tau) \geq 0; \quad 0 < \frac{2\pi}{\Omega} \int_0^{2\pi/\Omega} p(\tau) d\tau \leq 4. \tag{38}$$

Using (34) in (32) and (38) and observing that $I_1 > 0$, $I_2 > 0$, $I_3 < 0$ we get (36). To prove the second part of the Theorem, we write (31) as

$$\dot{f}_1 = f_2; \dot{f}_2 = -p(\tau) f_1 \tag{39}$$

where $(\dot{\cdot}) = d(\cdot)/d\tau$.

Let $\mathbf{A}(\lambda, \beta, \mu, h): R^2 \to R^2$ be the matrix of the transformation at the period, defined as

$$\begin{bmatrix} f_1(0) \\ f_2(0) \end{bmatrix} = \begin{bmatrix} a_{11} & a_{12} \\ a_{21} & a_{22} \end{bmatrix} \begin{bmatrix} f_1(T) \\ f_2(T) \end{bmatrix}. \tag{40}$$

The system (39) is Hamiltonian. Then, stability of the trivial solution of (39) implies strong stability of trivial solution (see Arnold, 1980, p. 117). Therefore, the trivial solution of every system "close" to (39), is also stable under the conditions (38) (for definition of the distance between the systems, see Arnold, 1980, p. 117). To use the fact that (39) is strongly stable we replace $p(\tau)$ in (39) by p_0 obtained from $p(\tau)$ by setting $h = 0$. Then we consider the modified system

$$\ddot{f} + p_0 f = 0, \tag{41}$$

where $(\ddot{\cdot}) = d^2(\cdot)/d\tau^2$ and

$$p_0 = \frac{\left[\pi^2\left[1 - \frac{\lambda}{\beta}\right] - \lambda + \frac{\lambda^2}{\mu^2}\right]}{\gamma_1^2 + \frac{1}{\pi^2}\left(1 - \frac{\lambda}{\mu^2}\right)^2 + \frac{1}{\beta}\left(1 - \frac{\lambda}{\mu^2}\right)}. \tag{42}$$

For the system (41) the matrix of the mapping at the period $\mathbf{A}_0$ is obtained as

$$\mathbf{A}_0 = \begin{bmatrix} \cos\frac{2\pi}{\Omega}\sqrt{p_0} & \frac{1}{\sqrt{p_0}}\sin\frac{2\pi}{\Omega}\sqrt{p_0} \\ -\sqrt{p_0}\sin\frac{2\pi}{\Omega}\sqrt{p_0} & \cos\frac{2\pi}{\Omega}\sqrt{p_0} \end{bmatrix}. \tag{43}$$

The system (41) is stable if $|tr\,\mathbf{A}_0| < 2$ (see Nayfeh and Mook, 1979). Thus, stability boundary of (41) that follows from the condition $|tr\,\mathbf{A}_0| = 2$ is also stability boundary of (31) for small h. Using (43) and $|tr\,\mathbf{A}_0| = 2$ we get (37). That completes the proof of the Theorem.

Remark 1: The condition $(36)_1$ reduces, in the special case of static load, i.e., for $\Omega = 0$, to

$$\pi^2\left(1 - \frac{\lambda}{\beta}\right) - \lambda\left(1 - \frac{\lambda}{\mu^2}\right) > 0. \tag{44}$$

The critical load is obtained by setting the expression on the left-hand side of (44) equal to zero, so that

$$(\lambda_{cr})_{1,2} = \frac{\mu^2}{2}\left[\left(1 + \frac{\pi^2}{\beta}\right) \pm \sqrt{\left(1 + \frac{\pi^2}{\beta}\right)^2 - \frac{4\pi^2}{\mu^2}}\right]. \tag{45}$$

In (45) the smaller value should be chosen. This value for the static critical load of compressible column was obtained by Atanackovic (1989), for the special case when $\beta \to \infty$. An interesting conclusion follows from (45). Namely the compressible elastic rod, loaded statically ($\Omega = 0$), cannot lose stability (because (45) gives complex values) if

$$\mu\left(1 + \frac{\pi^2}{\beta}\right) < 2\pi. \tag{46}$$

The bound for μ given by (46) generalizes the known results of static stability analysis (see Atanackovic, 1989; Bret, 1990) since it takes into account shear stresses. When $\beta \to \infty$ inequality (44) becomes $\mu < 2\pi$. This value is in agreement with the results of Huddelston (1968) and Atanackovic (1989) for example. It was questioned recently by Bret (1990) where the bound $\mu < \pi$ was obtained. The dynamic stability analysis presented here confirms the bound $\mu < 2\pi$.

Remark 2: For the case when the frequency of the superimposed force p is small we can neglect the influence of the axial vibrations. Then in (17) we set $\nu = 0$. The case for which $\nu = \pi/2$, as noted earlier, corresponds to resonance in axial vibration of the rod.

4 Numerical Study of the Stability Properties of Eq. (31)

In this section we shall numerically determine the regions of instability for (31). Our procedure will be based on the Theorem (see Arnold, 1980, p. 116) that connects stability conditions of trivial solution to (31) with the matrix A defined by (40). Namely the stability boundary of the trivial solution to (31) is defined by

$$|tr\,\mathbf{A}| = |a_{11} + a_{22}| = 2. \tag{47}$$

The elements a_{11} and a_{22} could be determined from the fundamental set of solutions of (31). Since $p(\tau)$ is an even function of τ we have $a_{11} = a_{22}$ (see Kamke, 1959) so that (47) becomes

$$|a_{11}| = 1. \tag{48}$$

Let f be a fundamental solution of (31), i.e., a solution with the initial conditions

$$f(0) = 1; \quad \dot{f}(0) = 0. \tag{49}$$

Then we have $a_{11} = f(T)$. In numerical implementation of (48) we choose h and determined λ so that solution of (31) satisfies (49) and $f(T) = 1$ or $f(T) = -1$. The results are shown in Figs. 2 and 3 for $\Omega = 2$ and for two sets of parameters μ, β and γ_1.

In solving (31) with the initial conditions (49) we used the fourth-order Runge-Kutta procedure. Since the value of $f(T)$ (in our calculations $T = \pi$) was needed with high accuracy, we checked, indirectly, the accuracy of the integration by calculating, in each step of the integration, two first integrals for the system (31). Since $p(\tau)$ is a function of time we do not have an energy type of the first integral for (31). Recently, however, Vujanovic (1992) found two new first integrals of the Lewis type for the class of equations to which (31) belongs. Namely from Vujanovic (1992) we have that on each solution f of (31) the following quantity.

$$C_1 = (\dot{f}q - \dot{q}f)^2 + \left(\frac{f}{q}\right)^2 \tag{50}$$

is a constant, where q is *any* solution of the auxiliary equation

$$\ddot{q} + p(\tau)q - \frac{1}{q^3} = 0. \tag{51}$$

Downloaded 04 May 2010 to 171.66.16.33. Redistribution subject to ASME license or copyright; see http://www.asme.org/terms/Terms_Use.cfm

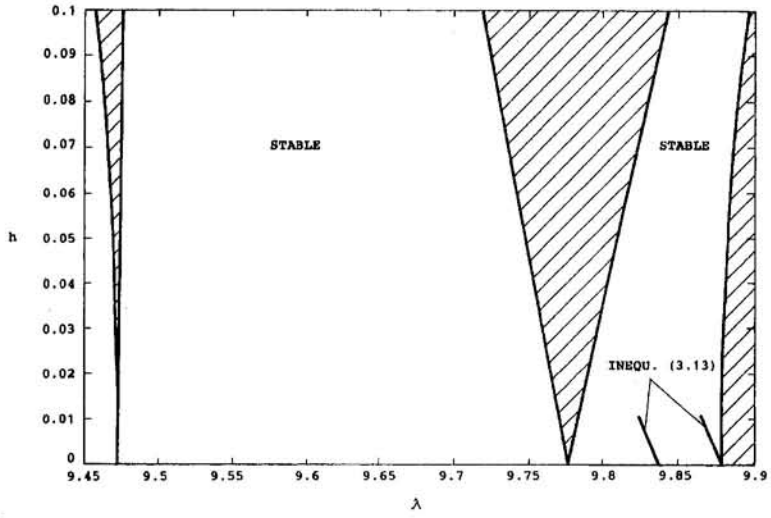


Fig. 2 Stability region for $\gamma_1 = 0$, $\mu = 105$, $\beta = 10^7$

Also we have that the quantity

$$C_2 = \left(\frac{\dot{f}}{B}\right)^2 + \left(Bf + \frac{\dot{B}}{p}\dot{f}\right)^2 \tag{52}$$

is constant on the solution f of (31), if $B(\tau)$ is *any* solution of

$$\frac{d}{d\tau}\left(\frac{\dot{B}}{p}\right) + B - \frac{p}{B^3} = 0. \tag{53}$$

In the calculations leading to the results shown in Figs. 2 and 3 we took

$$q(0) = 1; \quad \dot{q}(0) = 0; \quad B(0) = 1; \quad \dot{B}(0) = 0. \tag{54}$$

Then we solved, numerically, (31), (51), and (53) with the initial conditions (49), (54). From the initial conditions we get $C_1 = C_2 = 1$. The differences between the left and right-hand sides of (50) and (52) i.e.,

$$\Delta_1 = 1 - (\dot{f}q - \dot{q}f)^2 + \left(\frac{f}{q}\right)^2;$$

$$\Delta_2 = 1 - \left(\frac{\dot{f}}{B}\right)^2 + \left(Bf + \frac{\dot{B}}{p}\dot{f}\right)^2, \tag{55}$$

are used as the measures of the error of integration. In our calculations the differences Δ_1 and Δ_2 were of the order 10^{-12} on the numerical solutions of (31), (51), and (53). This indicates that the numerical integration had satisfactory accuracy.

In Fig. 4 we showed solutions $f(\tau)$ for three sets of parameters (points 1, 2 and 3 on Fig. 3). They correspond to stable, periodic (stability boundary), and unstable motions. The general form of the solutions is in agreement with the diagrams shown by Nayfeh and Mook (1979, p. 278).

6 Conclusions

In this work we analyzed the plane motion of an elastic rod. It is assumed that the rod is made of perfectly elastic material. Both extensibility of the rod axis and the influence of shear stresses (Engesser approach) are taken into account. It is assumed that the rod is loaded by an axial force that has constant and time-periodic component. We obtained the following results:

1 The system of nonlinear equations describing the motion of the rod is presented in Section 2. For this system the trivial solution (in which rod axis remains straight) is obtained. As

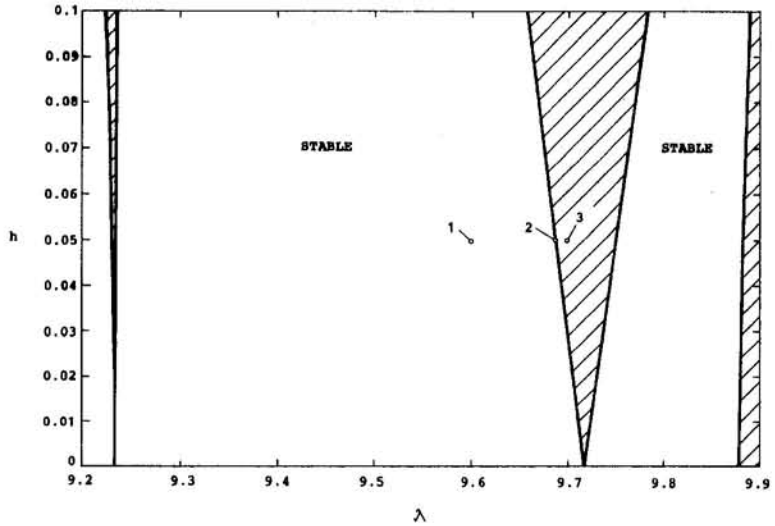


Fig. 3 Stability region for $\gamma_1 = 0.06$, $\mu = 105$, $\beta = 10^7$

Downloaded 04 May 2010 to 171.66.16.33. Redistribution subject to ASME license or copyright; see http://www.asme.org/terms/Terms_Use.cfm

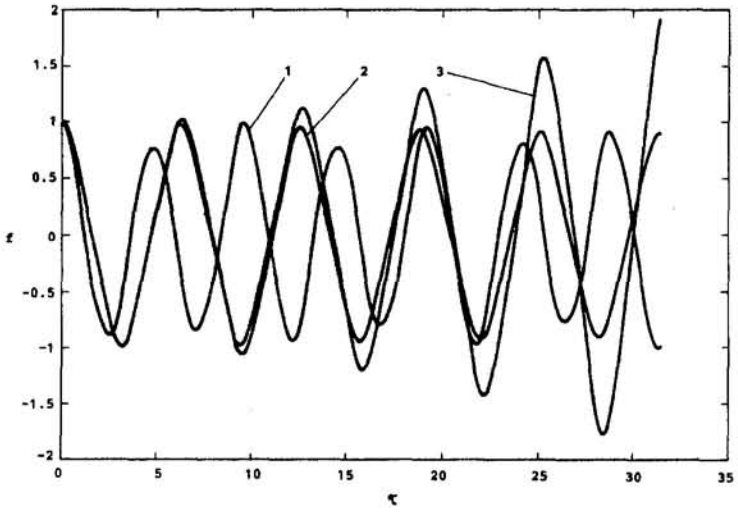


Fig. 4 Function $f(\tau)$ for different parameters

could be seen (see (16)) this solution can exhibit axial resonance.

2 Small plane deformations are superimposed on the trivial solution. The system of linear partial differential equations describing superimposed motion is presented (see (22)). This system is by spatial discretization reduced to the single second-order Eq. (31). This equation, that we believe is new, describes, qualitatively, the temporal evolution of all variables (see (29), (30)).

3 On the basis of the equation describing temporal evolution we obtained stability conditions for the rod. This conditions are stated in the Theorem of Section 3. Note that all the stability conditions depend on the parameter η, that is, transverse and axial vibrations are coupled. Our stability conditions reduce to known results, obtained by the static method, in the limit when the frequency of the time periodic component of the axial force tends to zero. In this respect we generalize the bound on the slenderness ratio μ, below which the rod is stable, no matter how large a static load is applied. This generalization is given by inequality (44), and it reduces to known expression when $\beta \to \infty$.

4 Using numerical integration we obtained a detailed stability chart for Eq. (31). The physically important parameters, i.e., the magnitudes of the constant and time-periodic component of the axial force are varied. In this respect our diagrams in Figs. 2 and 3 resemble the Ince-Strutt chard for the Mathieu equation. From Figs. 2 and 3 we conclude that the width of the instability regions depend on the rotary inertia term. The point in which the instability region touches the λ-axis are obtained analytically from (43).

5 The accuracy of the numerical integration was checked by evaluation of two first integrals of the Lewis type (50) and (52). For their evaluation it was necessary to solve two auxiliary problems (51), (53).

Acknowledgment

The financial support of the Science Foundation of Serbia and SANU is most gratefully acknowledged.

References

Adams, R., 1975, *Sobolev Spaces,* Academic Press, New York.

Arnold, V. I., 1980, *Mathematical Methods of Classical Mechanics,* Springer-Verlag, New York.

Atanackovic, T. M., 1989, "Stability of a Compressible Elastic Rod with Imperfections," *Acta Mechanica,* Vol. 76, pp. 203–222.

Atanackovic, T. M., and Spasic, D. T., 1991, "Effect of shear and compressibility on stability of a heavy column with an end load," *Q. Jl. Mech. Appl. Math.,* Vol. 44, pp. 601–617.

Atanackovic, T. M., and Spasic, D. T., 1994, "A model for plane elastica with simple shear deformation pattern," *Acta Mechanica,* Vol. 104, pp. 241–253.

Bret, C. W., 1990, "Effect of Axial Compressibility on Buckling of Columns," *ASCE Journal of Engineering Mechanics,* Vol. 116, pp. 728–732.

Bolotin, V. V., 1964, *The Dynamic Stability of Elastic Systems,* Holden-Day, San Francisco.

Demidovich, B. P., 1967, *Lectures on the Mathematical Theory of Stability,* Nauka, Moscow (in Russian).

Gjelsvik, A., 1991, "Stability of built-up columns," *ASCE Journal of Engineering Mechanics,* Vol. 117, pp. 1331–1345.

Huddelston, J. V., 1968, "Effect of axial strain on buckling and postbuckling behavior of elastic columns," *Developments in Theoretical and Applied Mechanics,* D. Frederick ed., Proc. 4th Southeastern Conf. Thor. Appl. Mech., New Orleans, LA, Pregamon, Oxford, U.K.

Kamke, E., 1959, *Differentialgleichungen, Lösungmethoden und Lösungen I,* Geest und Portig, Leipzig.

Laskin, R. A., Likins, P. W., and Longman, R. W., 1983, "Dynamical Equations of a Free-Free Beam Subject to Large Overall Motions," *The Journal of the Astronautical Sciences,* Vol. 31, pp. 507–528.

Leipholz, H., 1970, *Stability Theory,* Academic Press, New York.

Lewis, H. R., 1968, "Class of Exact Invariants for Classical and Quantum Time-Dependent Harmonic Oscillators," *Journal of Mathematical Physics,* Vol. 9, pp. 1976–1985.

Libai, A., 1992, "Equations for Nonlinear Planar Deformation of Beams," ASME JOURNAL OF APPLIED MECHANICS, Vol. 59, pp. 1028–1030.

Nayfeh, A. H., and Mook, D. T., 1979, *Nonlinear Oscillations,* John Wiley and Sons, New York.

Schmidt, R., and DaDeppo, D. A., 1971, "Nonlinear theory of arches with transverse shear deformation and rotary inertia," *Journal of the Industrial Mathematics Soc.,* Vol. 21, pp. 33–49.

Simo, J. C., and Vu-Quoc, L., 1983, "On the Dynamics of Flexible Beams Under Large Overall Motions The Plane Case: Part I and II," ASME JOURNAL OF APPLIED MECHANICS, Vol. 53, pp. 849, 854, and 855–863.

Vujanovic, B. D., 1992, "Application of the Hamilton-Jacobi Method to the Study of Rheo-Linear Oscillators," *Acta Mechanica,* Vol. 93, pp. 179–190.

Downloaded 04 May 2010 to 171.66.16.33. Redistribution subject to ASME license or copyright; see http://www.asme.org/terms/Terms_Use.cfm

Nonstandard Models for Thin-Walled Beams With a View to Applications

N. Rizzi
Terza Università di Roma,
Facoltà di Architettura,
via della Madonna de' Monti, 40,
00184 Roma, Italy

A. Tatone
Università de L'Aquila,
Facoltà di Ingegneria,
67040 Monteluco di Roio (Aq), Italy

A direct theory of a one-dimensional structured continuum is introduced in order to study the postbuckling behavior of thin-walled beams. A simply supported beam bent by end couples is analyzed showing that, in the case of nonsymmetric cross sections, lateral buckling gives rise to imperfection sensitivity. Then an axially loaded beam is studied taking also into account the interaction between torsional and flexural buckling. The results obtained prove that in this case imperfection sensitivity, though slighter than in the previous case, arises also for symmetric cross sections.

1 Introduction

In a previous work (Tatone and Rizzi, 1991) the writers have shown how some relevant aspects of the mechanical behavior of thin-walled beams can be described by means of a one-dimensional continuum. This continuum is endowed with a "minimal" local structure introduced *ab initio,* that is without any resort to other continuum theories. It can easily be seen that the classical (linear) theories of Wagner (1929), Kappus (1937) and Vlasov (1961), can be recovered by introducing suitable assumptions to the proposed theory and, in particular, by imposing an internal constraint.

The aim of this work is to analyze, making use of the cited theory, two cases of bifurcation of initially straight beams that can be considered exemplary in many aspects.

The first case regards a simply supported beam free to warp and loaded at the end sections by conservative bending couples. The buckling analysis performed will show that, while for the buckling load fair assumptions lead to the classical result of Timoshenko (1910), beams with nonsymmetric sections can be *imperfection sensitive,* as a consequence of the coupling between torsion, warping, and bending.

The second case consists of a cantilever beam, with warping restrained at the clamped end section, compressed by a force applied at the free end, showing both flexural and torsional buckling. By exploiting the exact kinematics of the model, the post-buckling analysis has been carried out within the framework of the asymptotic bifurcation theory. The results show that *also* beams with symmetric cross sections can show slight imperfection sensitivity, as a consequence of the interaction of the buckling modes.

It must be pointed out that all the results have been obtained in closed form, despite the complexity of the problems involved.

As an example a numerical computation is performed for the first case, just to show how to use the given general expressions to get their values corresponding to a particular cross section. Following this example one could compute those values for classes of cross sections of different shapes and get results useful from a technical point of view.

2 One-Dimensional Continuum Model

The body we call "beam" can be thought of as a continuous array of "sections" along a smooth curve (the beam axis). We will consider only motions of the body in which the beam axis remains a smooth curve while each section can undergo a rigid motion plus a warping. We will give an exact description of the motion, apart from the warping that will be taken into account by means of a single scalar parameter.

Let us consider a reference configuration for the beam, and denote by C_o the corresponding *beam axis.* Then we will call $X: s \mapsto X(s) \in \mathcal{E}$ a parametrization of C_o, where $s \in [0, l]$ is a curve length parameter and $\mathcal{E}$ is a three-dimensional Euclidean space[1].

Let the reference configuration be the one assumed by the beam in the given motion at time $t = 0$. The configuration at time t can be described by a parametrization $x(\cdot, t)$: $s \mapsto x(s, t) \in \mathcal{E}$ of the beam axis C_t, such that $x(s, t)$ is the place at time t corresponding to the place $X(s)$ at time $t = 0$, and for each s by the proper orthogonal tensor $\mathbf{R}(s, t)$ and a scalar $\alpha(s, t)$.

In our interpretation $\mathbf{R}(s, t)$ and $\alpha(s, t)$ describe the rotation and the warping, with respect to the reference configuration, of the beam cross section at $x(s, t)$. The functions x, $\mathbf{R}$, α will be assumed to be sufficiently smooth. The tensor $\mathbf{R}(s, t)$ is regarded as a linear transformation over the three-dimensional vector space V, defined as the translation space of $\mathcal{E}$[1].

The velocity is defined by

$$\mathbf{v} := \dot{\mathbf{x}}, \quad \mathbf{W} := \dot{\mathbf{R}}\mathbf{R}^T, \quad a := \dot{\alpha}, \tag{1}$$

where a dot denotes differentiation with respect to time, and $\mathbf{W}$ is a skew symmetric tensor. A suitable definition of strain measures, suggested by a similar definition in Capriz (1981), is given as follows:

$$\mathbf{e} := \mathbf{R}^T\mathbf{x}' - \mathbf{X}', \quad \mathbf{E} := \mathbf{R}^T\mathbf{R}', \quad \beta := \alpha', \tag{2}$$

where a prime denotes differentiation with respect to s and $\mathbf{E}$ is a skew symmetric tensor.

Note that $\mathbf{W}$ and $\mathbf{E}$ express a rate of change of $\mathbf{R}$ with respect to a scalar parameter (though such a parameter is not the same). Note, further, the different role played by $\mathbf{R}^T$ in the definitions of $\mathbf{W}$ and $\mathbf{E}$. A geometric interpretation of such a difference (which is helpful to motivate the above definitions) can be given looking at rotations as elements of a Lie group as in Simo and Vu Quoc (1986, 1988). From the mechanical point of view it is worth noting that the strain measures in (2) turn out to be constant in a change of frame.

Contributed by the Applied Mechanics Division of THE AMERICAN SOCIETY OF MECHANICAL ENGINEERS for publication in the ASME JOURNAL OF APPLIED MECHANICS.

Discussion on this paper should be addressed to the Technical Editor, Professor Lewis T. Wheeler, Department of Mechanical Engineering, University of Houston, Houston, TX 77204-4792, and will be accepted until four months after final publication of the paper itself in the ASME JOURNAL OF APPLIED MECHANICS.

Manuscript received by the ASME Applied Mechanics Division, May 2, 1994; final revision, Feb. 27, 1995. Associate Technical Editor: W. K. Liu.

[1] For a definition of Euclidean space and of the corresponding translation space see, e.g., Bowen and Wang (1976).

Copyright © 1996 by ASME

Downloaded 04 May 2010 to 171.66.16.33. Redistribution subject to ASME license or copyright; see http://www.asme.org/terms/Terms_Use.cfm

Corresponding to each point $\mathbf{x}(s, t)$, the contact actions are characterized by a vector $\mathbf{t}$, (the contact force) a skew-symmetric tensor $\mathbf{T}$ (the contact couple) and a scalar quantity ϖ, which in this context will be given the meaning of *bimoment,* while the body actions are characterized by a vector $\mathbf{b}$, a skew-symmetric tensor $\mathbf{B}$, and a scalar quantity η. Such a characterization of the actions results from the following expression of the mechanical power:

$$W := \int_0^l (\mathbf{b}\cdot\mathbf{v} + \mathbf{B}\cdot\mathbf{W} + \eta a)dS + [\mathbf{t}\cdot\mathbf{v} + \mathbf{T}\cdot\mathbf{W} + \varpi a]_0^l, \quad (3)$$

where the inner product of skew-symmetric tensors is defined as $\mathbf{B}\cdot\mathbf{W} = \frac{1}{2}\,tr(\mathbf{B}\mathbf{W}^T)$.

The conditions for the power to be objective are expressed by the following balance equations:

$$\mathbf{t}' + \mathbf{b} = \mathbf{0},$$
$$\mathbf{T}' + \mathbf{B} - \mathbf{x}' \wedge \mathbf{t} = \mathbf{0}. \quad (4)$$

Substituting these relations into the expression (3) we obtain the stress power formula

$$W = \int_0^l (\mathbf{s}\cdot\dot{\mathbf{e}} + \mathbf{S}\cdot\dot{\mathbf{E}} + \pi a + \varpi a')ds, \quad (5)$$

where $\mathbf{s} := \mathbf{R}^T\mathbf{t}$, $\mathbf{S} := \mathbf{R}^T\mathbf{T}\mathbf{R}$, $\dot{\mathbf{e}} = \mathbf{v}' - \mathbf{W}\mathbf{x}'$, $\dot{\mathbf{E}} = \mathbf{W}'$,

$$\text{and } \pi = \eta + \varpi'. \quad (6)$$

It is worth noting that this expression is a special case of (4.17) in (Green and Laws, 1966).

By choosing an orthonormal basis $(\mathbf{D}_1, \mathbf{D}_2, \mathbf{D}_3)$ of V, let us consider a beam reference configuration with a straight axis and orthogonal plane cross sections. If we assume $\mathbf{D}_1 = \mathbf{X}'$, we can define the components of $\mathbf{s}$, $\mathbf{S}$, $\mathbf{E}$, which will be used in the sequel, through the following relations

$$\mathbf{s} = Q_1\mathbf{D}_1 + Q_2\mathbf{D}_2 + Q_3\mathbf{D}_3,$$
$$\mathbf{S} = M_1\mathbf{D}_2 \wedge \mathbf{D}_3 + M_2\mathbf{D}_3 \wedge \mathbf{D}_1 + M_3\mathbf{D}_1 \wedge \mathbf{D}_2,$$
$$\mathbf{E} = \mu_1\mathbf{D}_2 \wedge \mathbf{D}_3 + \mu_2\mathbf{D}_3 \wedge \mathbf{D}_1 + \mu_3\mathbf{D}_1 \wedge \mathbf{D}_2. \quad (7)$$

The components introduced above can be easily recognized as those usually adopted in the engineering theory of beams. In particular Q_1 is the normal component of the stress while Q_2 and Q_3 are the shear components; M_1 is the twisting component of the stress couple and M_2 and M_3 are the bending ones; finally μ_1 is the torsional deformation measure and μ_2 and μ_3 the bending ones.

It also turns out to be useful to define the vector $\mathbf{u} := \mathbf{x} - \mathbf{X}$ and its components v_i with respect to the basis

$$\mathbf{d}_i := \mathbf{R}\mathbf{D}_i, \quad i = 1, 2, 3. \quad (8)$$

A parametrization of the rotation group is given by decomposing each rotation into the product of three rotations: the first one, of amplitude θ_1, about $\mathbf{D}_1$, the second one, of amplitude θ_2, about the vector obtained by applying the first rotation to $\mathbf{D}_2$, the third one, of amplitude θ_3, about the vector obtained by applying the previous rotations to $\mathbf{D}_3$.

Assuming that the material is elastic and homogeneous, it can be proved that because of the given definitions for the strain measures, the most general constitutive relations for the contact actions are of the form

$$S = \hat{S}(\mathbf{e}, \mathbf{E}, \alpha, \beta), \quad (9)$$

where S stands for one of the $\mathbf{s}$, $\mathbf{S}$, π, ϖ.

If we want to cast into our model the property that, as shown by experimental observations, the warping is an effect of the other strain measures, it seems reasonable to assume an internal constraint of the form

$$\alpha = \hat{\alpha}(\mathbf{e}, \mathbf{E}), \quad (10)$$

with $\hat{\alpha}(\mathbf{o}, \mathbf{O}) = 0$. This constraint, for any objective scalar function $\hat{\alpha}$, turns out to be objective, any change of frame leaving both $\mathbf{e}$ and $\mathbf{E}$ unchanged. By limiting ourselves to consider a linear constraint between warping and torsion, we put (10) in the form

$$\alpha = k\mu_1, \quad (k \in \mathbb{R}) \Rightarrow \beta = k\mu_1'. \quad (11)$$

Such a choice, despite its simplicity, proves to be effective for the cases we are interested in studying.

It can be useful to give some motivations about the assumptions on warping in (11). To this end the reference to theories in which one-dimensional beam models are derived from two or three-dimensional continua is the right tool to use.

In a recent work Simo and Vu Quoc (1991), dealing with the derivation of a one-dimensional beam model from a three-dimensional Cauchy continuum, assumed that for each cross section of the beam, the out-of-plane component of the displacement field (that we call w) was related to the warping deformation measure (α in this paper) by the following relationship

$$w = f\alpha, \quad (12)$$

f being the Saint-Venant warping function. Denoting by $\boldsymbol{D}$ the beam cross section, it follows immediately that $\alpha = \gamma \int_D w$, where $\gamma = (\int_D f)^{-1}$.

Such a result furnishes one of the possible kinematical meaning for the warping deformation measure α which results to be a weighted integral over the beam cross section of the out-of-plane displacement.

Coming then to the constraint (11) with the expression (12) in mind, one obtains $w = kf\mu_1$ that, in turn, can be seen as a generalization of the Saint-Venant solution to the uniform torsion problem.

Incidentally, it must be said that the constraint (11) is the one underlying the Vlasov's model.

Further, we will assume the material to be shear-indeformable and require

$$\mathbf{e} = \epsilon\,\mathbf{X}', \quad (13)$$

ϵ being the axial extensional deformation measure.

By the axiom of determinism for constrained materials—which states that the stress is determined by the motion only to within an arbitrary additive part which does no work in any motion compatible with the constraint—the indeterminate part of the stress corresponding to the above constraints, which will be denoted by a subscript v, must satisfy the following scalar relations

$$Q_{1v} = 0,\ M_{1v} = -k\pi_v,\ M_{2v} = 0,\ M_{3v} = 0,\ \varpi_v = 0, \quad (14)$$

while Q_{2v}, Q_{3v}, as well as π_v, can take any value.

The constitutive functions, consistent with all the material assumptions made till now, will be assumed to be

$$Q_1 = a\epsilon + \tfrac{1}{2}p\mu_1^2, \quad Q_2 = Q_{2v}, \quad Q_3 = Q_{3v},$$
$$M_1 = (c + q_2\mu_2 + q_3\mu_3 + p\epsilon + r\beta)\mu_1 + M_{1v},$$
$$M_2 = b_2\mu_2 + \tfrac{1}{2}q_2\mu_1^2, \quad M_3 = b_3\mu_3 + \tfrac{1}{2}q_3\mu_1^2,$$
$$\varpi = h\beta + \tfrac{1}{2}r\mu_1^2, \quad \pi = \pi_v. \quad (15)$$

If we also assume $\eta = 0$, from (6) and $(15)_8$ follows that

Downloaded 04 May 2010 to 171.66.16.33. Redistribution subject to ASME license or copyright; see http://www.asme.org/terms/Terms_Use.cfm

$\pi_v = \varpi'$. Then, by virtue of (11), the relations $(15)_4$, $(15)_7$, and $(15)_8$ finally become

$$M_1 = (c + q_2\mu_2 + q_3\mu_3 + p\epsilon)\mu_1 - k^2h\mu_1'',$$

$$\varpi = kh\mu_1' + \tfrac{1}{2}r\mu_1^2,$$

$$\pi = kh\mu_1'' + r\mu_1\mu_1'. \tag{16}$$

Although (15) and (16) are simple polinomial expressions, some comments must be done in order to better understand their mechanical meaning. It is clear that the coefficients a, b, c, stand for the axial, flexural, and torsional stiffnesses, while kh is the warping stiffness. The coefficient p accounts for the coupling between the torsion and the extension, and is responsible for the Poynting effect in the one-dimensional model. In fact it is a classical result in nonlinear elasticity that the axial force must depend nonlinearly on the torsion (see Truesdell and Noll, 1965). The same effect leads to the relationships between flexural couples and torsion which is accounted for by the coefficients q. Finally, the assumption that the bimoment depends nonlinearly on the torsion has been introduced here in view of the results shown by Møllmann (1986).

By transforming the strain-displacement relations (2) and the balance Eq. (4) into their scalar form, one obtains, by means of (15) and (16), a set of nonlinear field equations that, supplied with the boundary conditions, gives rise to a nonlinear boundary value problem.

3 Bifurcation Analysis

The nonlinear boundary value problems we are going to face are of the form

$$F(u, \lambda) = 0. \tag{17}$$

A solution (u, λ) consists of a set of functions describing a configuration, and a scalar parameter λ affecting the applied actions, such that the balance equations (4), together with the appropriate boundary conditions, are satisfied.

The graph of the solutions (u, λ) can be thought of as being made of regular branches. Usually a branch $(u^f(\tau), \lambda^f(\tau))$ crossing the point (0, 0), where $u = 0$ denotes the reference configuration, is easily computed and one is interested in finding a bifurcation point on it. Denoting by $(u^b(t), \lambda^b(t))$ an intersecting branch, assume the parametrization of the two branches be such that $u^b(0) = u^f(\tau_c)$, $\lambda^b(0) = \lambda^f(\tau_c) = \lambda_c$, and define the new set of functions

$$v := u^b - u^f, \tag{18}$$

made up with the differences of the corresponding functions in u^b and u^f.

As v inherits the parametrization from the intersecting branches, by assuming there exists a diffeomorphism relating the parameters t and τ, we can give the following series expansions near $t = 0$

$$v_t = \tilde{v}_c t + \tfrac{1}{2}\tilde{\tilde{v}}_c t^2 + o(t^2),$$

$$\lambda_t = \lambda_c + \tilde{\lambda}_c t + \tfrac{1}{2}\tilde{\tilde{\lambda}}_c t^2 + o(t^2), \tag{19}$$

where the subscript c denotes values at $t = 0$.

By using (18) and (19), the problem (17) can be recast in a sequence of linear systems of differential equations with corresponding boundary conditions. The first system results in an *eigenvalue problem* whose solution gives λ_c and $\tilde{v}_c$, while $\tilde{\lambda}_c$ is obtained by imposing a solvability condition to the second order system whose solution leads to $\tilde{\tilde{v}}_c$ and so on. As the aim of this section is just to introduce the symbols used in the next sections, the interested reader is referred to Budiansky (1974).

4 Simply Supported Beam Bent by Terminal Couples

In this section we will perform a bifurcation analysis of an initially straight beam of length l, simply supported at both ends, where the warping is free and the axial rotation is restrained, loaded by two opposite conservative bending couples.

Remembering that dead couples are not conservative, we will recover such a property if each couple is obtained by attaching two (opposite) dead forces to two (different) points of the same end section. Denoting by d the distance between the lines of action of the two forces and by f their intensity, we set

$$\mathbf{T}(l) = \lambda\mathbf{D}_1 \wedge \mathbf{d}_2, \quad \mathbf{T}(0) = -\mathbf{T}(l), \quad \text{with} \quad \lambda := fd. \tag{20}$$

In order to simplify the analysis, we assume the beam to be flexural indeformable in the plane spanned by the applied forces in the reference configuration, by adding the following internal constraint:

$$\mu_3 = 0. \tag{21}$$

The appropriate boundary conditions for the case at hand are

$$\mathbf{u} = \mathbf{0}, \quad M_1 = M_2 = \theta_1 = \varpi = 0, \quad \text{at} \quad s = 0,$$

$$v_2 = v_3 = Q_1 = M_1 = M_2 = \theta_1 = \varpi = 0, \quad \text{at} \quad s = l. \tag{22}$$

It can be easily seen that the stated boundary value problem, due to the assumed constitutive functions, has at least the following solution:

$$\mathbf{u} = \mathbf{0}, \quad \mathbf{R} = \mathbf{I}, \quad \alpha = 0,$$

$$\mathbf{s} = \mathbf{0}, \quad \varpi = 0, \quad \mathbf{S} = \lambda\mathbf{D}_1 \wedge \mathbf{D}_2, \tag{23}$$

which means that the reference configuration is balanced for any value of λ.

In order to investigate the possible bifurcations from the given solution, we linearize the field equations together with the boundary conditions near the above solution and arrive at the following equations:

$$b_2\tilde{v}_3''' - \lambda\tilde{\theta}_1'' = 0, \quad k^2h\tilde{\theta}_1''' - c\tilde{\theta}_1'' - \lambda\tilde{v}_3'' = 0, \tag{24}$$

with the boundary conditions

$$\tilde{v}_3 = \tilde{v}_3'' = 0 \quad \text{at} \quad s = 0, \quad \text{and} \quad s = l,$$

$$\tilde{\theta}_1 = \tilde{\theta}_1'' = 0 \quad \text{at} \quad s = 0, \quad \text{and} \quad s = l, \tag{25}$$

where $\tilde{}$ has the meaning introduced in Section 3.

By solving the eigenvalue problem (24), (25), one obtains the buckling load

$$\lambda_c = \frac{\pi}{l}\sqrt{b_2 c}\sqrt{1 + \frac{k^2h}{c}\left(\frac{\pi}{l}\right)^2}, \tag{26}$$

with the associate buckling mode

$$\tilde{v}_3 = -\frac{l}{\pi}\sqrt{\frac{c}{b_2}}\sqrt{1 + \frac{k^2h}{c}\left(\frac{\pi}{l}\right)^2}\sin\left(\frac{\pi s}{l}\right),$$

$$\tilde{\theta}_1 = \sin\left(\frac{\pi s}{l}\right) \tag{27}$$

normalized by setting $\tilde{\theta}_1\,(l/2) = 1$.

The increment of the load parameter corresponding to the solution of the eigenvalue problem is given by

Downloaded 04 May 2010 to 171.66.16.33. Redistribution subject to ASME license or copyright; see http://www.asme.org/terms/Terms_Use.cfm

$$\tilde{\lambda}_c = \frac{\pi}{l^2}\left(q_2 + \frac{\pi^2}{l}\frac{b_2 kr}{\lambda_c}\right), \tag{28}$$

showing that the beam considered can have an asymmetric bifurcation, that is, it *can be imperfection sensitive.*

Such a behavior originates from the fact that both the bending couple M_2 and the bimoment ϖ depend on the torsion μ_1, through the constants q_2 and r, respectively. It can be shown that if the beam cross section has at least one axis of symmetry, then $r = 0$ (Tatone, 1992), while q_2 vanishes only if the axis of symmetry is parallel to $\mathbf{D}_2$. Therefore one can have $\tilde{\lambda}_c \neq 0$ also if the beam section has one axis of symmetry, as shown in the following example.

It is interesting to examine Eqs. (V.1.10) obtained by Vlasov (1961) in its classical work, in order to evaluate the critical mode for "beams loaded at the ends by longitudinal forces and moments." Despite the approaches being completely different, in the balance Eq. $(V.1.10)_3$ can be recognized a constitutive function for the twisting couple M_1. By comparing that expression with $(16)_1$, and assuming a cartesian coordinate system with the origin at the centroid of the cross section and basis vectors $\mathbf{D}_1$, $\mathbf{D}_2$ collinear to the principal axes of inertia, the following identifications result:

$$a = EA, \quad q_2 = EI_{q_2}, \quad b_2 = EI_2, \quad q_3 = EI_{q_3},$$
$$b_3 = EI_3, \quad p = EI_p, \quad c = GI_c, \quad k^2 h = EI_\omega. \tag{29}$$

In (29), E and G are the Young and shear moduli, A is the area of the cross section, I_2 and I_3 the principal moments of inertia, I_c and I_p the moments of inertia with respect to the centroid and the shear center, I_ω is the sectorial warping rigidity, and $I_{q_2} = \int_D x_2 \rho^2 dA$, $I_{q_3} = -\int_D x_3 \rho^2 dA$ where x_2, x_3 are the coordinates of a point of the cross section and ρ its distance from the shear center. Note that as a consequence of the above identifications, the expression (26) becomes identical to the classical result of Timoshenko (1910).

Now, with the purpose of showing a numerical computation, let us consider a C-section beam with the end couples acting on a plane parallel to the web. By using the expressions for the constants in (29) taken from Vlasov's theory, we can first evaluate them and then compute the numerical values of λ_c and $\tilde{\lambda}/\lambda_c$.

Denoting by b the width of the flanges, h the height of the web, t the thickness, for the values $E = 2.1\ 10^4$ kg/mm^2, $G = 0.84\ 10^4$ kg/mm^2, $t = 3$ mm, $h = 100$ mm we get the following results:

b	l	$\lambda_c \times 10^6$	$\tilde{\lambda}/\lambda_c$
50	1000	1.520	0.794
100	1000	9.020	1.360
150	1000	26.700	1.990
50	2000	0.487	0.622
100	2000	2.440	1.250
150	2000	6.930	1.920

5 Axially Compressed Cantilever Beam

We consider next a straight beam of length l clamped at one end, where the warping is constrained to be zero, and compressed by an axial force λ applied at the free end. Thus the boundary conditions are

$$\mathbf{u} = \mathbf{0}, \quad \mathbf{R} = \mathbf{I}, \quad \alpha = 0, \quad \text{at} \quad s = 0,$$
$$\mathbf{s} = -\lambda \mathbf{D}_1, \quad \mathbf{S} = \mathbf{0}, \quad \varpi = 0, \quad \text{at} \quad s = l. \tag{30}$$

In the case of double symmetric cross sections ($q_2 = q_3 = r = 0$ in the (15), (16)), the resulting boundary value problem can easily be seen to have the following solution:

$$v_1 = -\lambda/a, \quad v_2 = 0, \quad v_3 = 0, \quad \alpha = 0, \quad \mathbf{R} = \mathbf{I},$$
$$Q_1 = -\lambda, \quad Q_2 = 0, \quad Q_3 = 0, \quad \mathbf{S} = \mathbf{0}, \quad \varpi = 0. \tag{31}$$

It can be shown that the previous solution has bifurcating branches that usually correspond to an axial-torsional behavior for the beam or to an axial-flexural behavior. By selecting from each of the two classes the branch corresponding to the smallest critical load, the following results are obtained.

The flexural mode is characterized by

$$\lambda_c = \frac{a}{2}\left(1 - \sqrt{1 - \frac{\pi^2}{l^2}\frac{b_3}{a}}\right), \quad \tilde{\lambda}_c = 0,$$
$$\frac{\tilde{\tilde{\lambda}}_c}{\lambda_c} = \frac{\pi^2 a^2}{16 l^2}\frac{a - 4\lambda_c}{(a - \lambda_c)^2 (a - 2\lambda_c)}. \tag{32}$$

There is nothing interesting about it but the fact that $0 \leq \lambda_c \leq a/2$. As a result, the ratio $\tilde{\lambda}_c/\lambda_c$ becomes negative whenever $\lambda_c > a/4$. The bifurcated branch, up to the second order, is given by

$$\tilde{v}_1 = 0, \quad \tilde{v}_2 = \cos\frac{\pi s}{2l} - 1,$$
$$\tilde{\tilde{v}}_2 = 0, \quad \tilde{\tilde{v}}_1 = \frac{\pi}{2l}\frac{a(a - 2\lambda_c)}{4(a - \lambda_c)^2}\left[\sin\left(\frac{\pi s}{l}\right) - \frac{\pi s}{l}\right], \tag{33}$$

being $v_3 = \theta_1 = 0$. Here the normalization condition $\tilde{v}_2(l) = -1$ has been assumed.

The torsional bifurcation mode is characterized by

$$\lambda_c = \frac{a}{p}\left(c + \frac{\pi^2}{4}\frac{k^2 h}{l^2}\right) = \frac{a(4cl^2 + \pi^2 k^2 h)}{4l^2 p}, \quad \tilde{\lambda}_c = 0,$$
$$\frac{\tilde{\tilde{\lambda}}_c}{\lambda_c} = -\frac{1}{\lambda_c}\frac{3\pi^2 p}{16 l^2} = -\frac{3\pi^2 p^2}{4a(4cl^2 + \pi^2 k^2 h)}, \tag{34}$$

and the associate bifurcated solution up to the second order is

$$\tilde{\tilde{v}}_1 = 0, \quad \tilde{\theta}_1 = \cos\left(\frac{\pi s}{2l}\right) - 1,$$
$$\tilde{\tilde{v}}_1 = \frac{\pi p}{8al}\left[\sin\left(\frac{\pi s}{l}\right) - \frac{\pi s}{l}\right], \quad \tilde{\tilde{\theta}}_1 = 0, \tag{35}$$

being $v_1 = v_3 = 0$. The normalization has been chosen so that $\tilde{\theta}_1(l) = -1$. Note that such a bifurcation can occur only if $p > c + \pi^2 k^2 h/4l^2$ and the value of $\tilde{\tilde{\lambda}}_c/\lambda_c$ is negative no matter the values of the constants of the constitutive functions are. This means that, despite what can be guessed by looking only at the results of the linearized analysis, torsional buckling due to an axial force is *imperfection sensitive.*

If the constitutive parameters and the length of the beam are such that the buckling loads in (32) and (34) take the same value, the two buckling modes occur simultaneously and the first-order part of the bifurcation branches can be put in the form

$$\tilde{u} = \nu_1 \tilde{u}_I + \nu_2 \tilde{u}_{II}, \tag{36}$$

where $\tilde{u}_I$ and $\tilde{u}_{II}$ stand for the torsional mode and the flexural mode, respectively.

The resulting mode interaction problem has been solved by following the procedure outlined by Pignataro and Rizzi (1982). It turns out that $\tilde{\lambda}_c = 0$ while, besides the torsional and flexural buckling modes occurring separately, two more solutions appear. Normalizing the coefficients ν_1, ν_2 by assuming that $\nu_1^2 + \nu_2^2 = 1$, the expressions for $\tilde{\tilde{\lambda}}_c$ and ν_1^2 can be easily obtained by solving the following two equations:

Downloaded 04 May 2010 to 171.66.16.33. Redistribution subject to ASME license or copyright; see http://www.asme.org/terms/Terms_Use.cfm

$$\frac{\tilde{\lambda}_c}{\lambda_c} = -\frac{3p\omega_1^2\nu_1^2}{4\lambda_c} - \left[\frac{16\tan(l\omega_3)\omega_1^2(\omega_1^2-\omega_3^2)^2}{lp(a-\lambda_c)\omega_3^3(4\omega_1^2-\omega_3^2)^2} + \frac{2(a-\lambda_c)(\omega_3^2-\omega_1^2)(\omega_3^2+8\omega_1^2)-3\omega_1^2\omega_3^2p(4\omega_1^2-\omega_3^2)}{4p(a-\lambda_c)^2(4\omega_1^2-\omega_3^2)\omega_3^2}\right]$$

$$\times a^2l^2(1-\nu_1^2)\frac{a^2l^2\omega_1^2(a-4\lambda_c)}{8p(a-\lambda_c)^3}(1-\nu_1^2)$$

$$+\left[\frac{8\tan(l\omega_3)\omega_1^2(\omega_1^2-\omega_3^2)^2}{lp\omega_3^3(4\omega_1^2-\omega_3^2)^2} + \frac{2(a-\lambda_c)(\omega_3^2-\omega_1^2)(\omega_3^2+8\omega_1^2)-3\omega_1^2\omega_3^2p(4\omega_1^2-\omega_3^2)}{8p(a-\lambda_c)(4\omega_1^2-\omega_3^2)\omega_3^2}\right]\times\nu_1^2$$

$$-\frac{(a-2\lambda_c)}{2p(a-\lambda_c)}\frac{\tilde{\lambda}_c}{\lambda_c} = 0 \quad (37)$$

where $\omega_1 = \pi/(2l)$ and $\omega_3 = |\sqrt{\lambda_c(a-\lambda_c)/(ab_2)}|$.

It must be noted that, depending on the values of ω_1 and ω_3, the value of $\tilde{\lambda}_c/\lambda_c$ given by the expression (37) can become negative and hence the beam can be imperfection sensitive.

6 Conclusions

The aim of this work was to describe a one-dimensional theory for thin-walled beams and to apply it to two simple problems. The given results show that, within the formal setting of the mechanical theory, a simple choice of the constitutive relations makes the model able to describe qualitatively some global behavior like flexural-torsional or axial-torsional bifurcations.

As an example of application of the theory some numerical results have been shown for the case of a beam bent by terminal couples. To this end the constitutive parameters have been identified with those underlying Vlasov's linear theory.

References

Bowen, R. M., and Wang, C.-C., 1976, *Introduction to Vectors and Tensors,* Plenum Press.

Budiansky, B., 1974, "Theory of Buckling and Postbuckling Behaviour of Elastic Structures," *Advances in Applied Mechanics,* Vol. 14, C. S. Yih, ed., Academic Press, New York.

Capriz, G., 1981, "A Contribution to the Theory of Rods," *Rivista Matematica dell'Università di Parma,* Vol. 7, No. 4.

Green, A. E., and Laws, N., 1966, "A General Theory of Rods," *Proceedings of the Royal Society, Mathematical and Physical Sciences,* Vol. A293, No. 1432.

Kappus, R., 1937, "Drillknicken zentrich gedrückter Stäbe mit offenem Profil im elastischen Bereich," *Luftfahrtforschung,* pp. 444–457, translated in 'Twisting Failure of Centrally Loaded Open-section Columns in the Elastic Range,' NACA TM n. 851, 1938.

Møllmann, H., 1986, "Theory of Thin-walled Elastic Beams with Finite displacements," *Finite Rotations in Structural Mechanics,* Proceedings of the EUROMECH Colloquium 197, Jablonna, Poland, W. Pietraszkiewicz, ed., Springer-Verlag, New York, pp. 195–209.

Pignataro, M., and Rizzi, N., 1982, "The Effect of Multiple Buckling Modes on the Postbuckling Behavior of Plane Elastic Frames. Part I. Symmetric Frames," *Journal of Structural Mechanics,* Vol. 10, No. 4, pp. 437–458.

Simo, J. C., and Vu Quoc, L., 1986, "A Three-Dimensional Finite-Strain Rod Model. Part II: Computational Aspects," *Computer Methods in Applied Mechanics and Engineering,* Vol. 58, pp. 79–116.

Simo, J. C., and Vu Quoc, L., 1988, "On the Dynamics in Space of Rods Undergoing Large Motions—A Geometrically Exact Approach," *Computer Methods in Applied Mechanics and Engineering,* Vol. 66, pp. 125–161.

Simo, J. C., and Vu Quoc, L., 1991, "A Geometrically-exact Rod Model Incorporating Shear and Torsion-Warping Deformation," *Int. J. Solids Structures,* Vol. 27, No. 3, pp. 371–393.

Tatone, A., and Rizzi, N., 1991, "A One-Dimensional Model for Thin-walled Beams," *Trends in Applications of Mathematics to Mechanics,* W. Schnider, H. Troger, F. Ziegler, eds., Longman, Avon, U.K., pp. 312–320.

Tatone, A., 1992, "Analisi della biforcazione per travi a sezione aperta e spessore sottile," *Proceedings, 11th AIMETA National Congress,* Trento, Italy, pp. 509–515.

Timoschenko, S. P., 1910, "Einige Stabilitätsprobleme der Elastizitätstheorie," *Zeitschrift für Mathematik und Physik,* Vol. 58, pp. 337–385, in *The Collected Papers of Stephen P. Timoschenko,* McGraw-Hill, Amsterdam, pp. 1–50 (1953).

Truesdell, C., and Noll, W., 1965, "The Non-linear Field Theories of Mechanics," *Encyclopedia of Physics,* Vol. III/3, Springer-Verlag, New York.

Vlasov, V. Z., 1961, *Thin-walled Elastic Beams,* Israel Program for Scientific Translations, Monson, Jerusalem.

Wagner, H., 1929, "Verdrehung und Knickung von offenen Profilen," Festschrift 25-Jahre T. H. Danzig, translated 'Torsion and Buckling of Open Sections,' NACA TM n.807 (1936).

Downloaded 04 May 2010 to 171.66.16.33. Redistribution subject to ASME license or copyright; see http://www.asme.org/terms/Terms_Use.cfm

T. Watanabe
Professor,
Department of Mechanical Engineering,
Faculty of Engineering,
Iwate University,
Morioka 020, Japan

H. Taniguchi
Graduate Student,
Department of Machine Intelligence
and System Engineering,
Faculty of Engineering,
Tohoku University,
Sendai 980, Japan

I. Pop
Professor,
Faculty of Mathematics,
University of Cluj,
R-3400 Cluj, CP253, Romania

Instability of Laminar Natural Convection Boundary Layer Flow on a Vertical Porous Flat Plate

The effects of uniform suction and injection on the linear stability theory of laminar natural convection boundary layer flow along a vertical porous flat plate which is maintained at a constant temperature are studied. The nonsimilar boundary layer equations for the basic steady flow have been solved numerically employing a very efficient finite difference scheme in combination with an iterative method for solving the resulting ordinary differential equations. The temporal neutral stability theory for wavelike disturbances of Tollmien-Schlichting type are then presented for the velocity and temperature functions. The corresponding eigenvalue problem for the disturbance amplitude functions is also solved numerically using a very accurate method. Results are presented graphically for both the basic and disturbance velocity and temperature profiles for some values of the modified local Grashof number G and suction or injection parameter X. The Prandtl number Pr is taken to be 0.73 (air) throughout this paper. The results show clearly the important role that suction or injection parameter X may have on the basic and disturbance flow characteristics in this problem.

1 Introduction

In recent years the topic of stability of vertical or horizontal natural convection boundary layer flow has become a major issue which attracted much attention. For a review of the fundamental work in this area, see Gebhart (1973a, b) and Gebhart et al. (1988). Indeed, such a concern has steadily been on the rise in the past few decades in an attempt to predict the transition from laminar to turbulent flow and also to gain a better understanding of the mechanism of turbulence. Some of the earliest theoretical and experimental studies on stability of vertical natural convection boundary layer are due to Plapp (1957), Szewczyk (1962), Kurtz and Crandall (1962), Knowles and Gebhart (1968), Hieber and Gebhart (1971a, b), and Gotoh et al. (1977). There is also a considerable body of work concerned with the nature of the stability flow in natural convective flows in a vertical enclosure filled with a porous medium carried out by Bejan (1979), Bejan and Anderson (1983), and Beckermann et al. (1988).

To the authors' knowledge similar papers dealing with the stability characteristics of natural convection boundary layer flow over a vertical porous flat plate do not exist. The purpose of this paper is to consider the effects which suction or injection have on the temporal stability of natural convection boundary layer arising from an isothermal vertical flat plate. We consider the case of uniform suction and injection with the porous plate held at a constant temperature. First, the boundary layer equations for the basic flow are solved numerically using a very efficient difference-differential method proposed by Hartree and Womersley (1937), and improved by Katagiri (1969). This method has been also successfully used in some recent papers by Pop and Watanabe (1992) and Watanabe and Pop (1993, 1994, 1995). Then, a linear stability analysis of the boundary layer flow for wavelike disturbances of Tollmien-Schlichting type is performed, where the basic flow is assumed to be steady laminar boundary layer flow. As in the papers by Hieber and Gebhart (1971a, b), the two-dimensional disturbance equations are simplified based on a scaling argument. The eigenvalue problem for the disturbance amplitudes of the stream function and temperature are solved numerically for a wide range of values of the Grashof number and suction or injection parameter. Thus, the temporal stability behavior of the flow and temperature characteristics are obtained. As a summary of what is presented below, the problem is formulated and solved in Section 2 with a discussion in Section 3 of the results obtained. The evolution of the flow and temperature fields is demonstrated by plotting the velocity and temperature fields of the basic flow along with the wave propagation velocity, temporal exponential amplification factor, and disturbance amplitudes of the velocity and temperature fields. Finally, in Section 4 we conclude the study with a review of the results obtained.

Mass transfer, produced via fluid suction or injection through surfaces, has often been investigated because of its dominant influence on flow characteristics. This phenomenon is important in relation with the surface cooling and boundary layer control problems. The effects of injection has been advocated as a method to protect the external surfaces of a hypersonic vehicle (missile or spacecraft) exposed to serve aerodynamic heating during entry in the earth's atmosphere. Turbine blades and rocket nozzles cooling may also be achieved by the injection of a foreign gas.

2 Basic Equations

Consider the steady-state laminar free convection flow over a semi-infinite vertical flat plate with uniform suction or injection as shown in Fig. 1. The plate is held at a constant temperature T_w greater than the ambient temperature T_∞. Neglecting viscous dissipation in the energy equation, the laminar, two-dimensional, incompressible conservative equations that describe the flow and temperature adjacent to the vertical surface can be written in nondimensional form as (see Gebhart et al., 1988)

Contributed by the Applied Mechanics Division of THE AMERICAN SOCIETY OF MECHANICAL ENGINEERS for publication in the ASME JOURNAL OF APPLIED MECHANICS.

Discussion on this paper should be addressed to the Technical Editor, Professor Lewis T. Wheeler, Department of Mechanical Engineering, University of Houston, Houston, TX 77204-4792, and will be accepted until four months after final publication of the paper itself in the ASME JOURNAL OF APPLIED MECHANICS.

Manuscript received by the ASME Applied Mechanics Division, Feb. 7, 1994; final revision, May 19, 1995. Associate Technical Editor: S. Lichter.

Copyright © 1996 by ASME

Downloaded 04 May 2010 to 171.66.16.33. Redistribution subject to ASME license or copyright; see http://www.asme.org/terms/Terms_Use.cfm

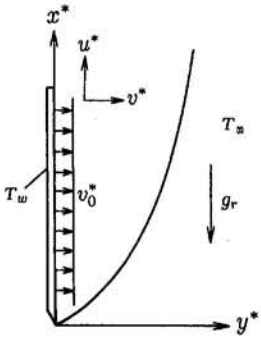


Fig. 1 Physical model and coordinate system

$$\frac{\partial}{\partial t}(\nabla^2\psi) + \frac{\partial\psi}{\partial y}\frac{\partial}{\partial x}(\nabla^2\psi) - \frac{\partial\psi}{\partial x}\frac{\partial}{\partial y}(\nabla^2\psi) = \mathrm{Gr}^{-1/2}\nabla^4\psi + \frac{\partial\theta}{\partial y} \quad (1)$$

$$\frac{\partial\theta}{\partial t} + \frac{\partial\psi}{\partial y}\frac{\partial\theta}{\partial x} - \frac{\partial\psi}{\partial x}\frac{\partial\theta}{\partial y} = \frac{1}{\mathrm{Pr}}\mathrm{Gr}^{-1/2}\nabla^2\theta \quad (2)$$

where ∇^2 is the Laplacian in Cartesian coordinates, Gr is the Grashof number, and Pr is the Prandtl number. The boundary conditions of the problem are

$$y = 0: \quad \frac{\partial\psi}{\partial x} = -v_0, \quad \frac{\partial\psi}{\partial y} = 0, \quad \theta = 1$$

$$y \to \infty: \quad \frac{\partial\psi}{\partial x} = 0, \quad \frac{\partial\psi}{\partial y} = 0, \quad \theta = 0 \quad (3)$$

where v_0 is the velocity of suction or injection, depending on whether $v_0 < 0$ or $v_0 > 0$, respectively. The nondimensional variables are defined as

$$(x, y) = (x^*, y^*)/l, \quad t = t^*U_0/l, \quad (u, v) = (u^*, v^*)/U_0,$$
$$v_0 = v_0^*/U_0, \quad \psi = \psi^*/U_0 l$$
$$\theta = (T - T_\infty)/\Delta T, \quad \mathrm{Gr} = g_r\tau\Delta T l^3/\nu^2,$$
$$U_0 = (g_r\tau\Delta T l)^{1/2}, \quad \Delta T = T_w - T_\infty \quad (4)$$

where (x^*, y^*) are Cartesian coordinates along and normal to the plate, respectively; t^* is the time; (u^*, v^*) are the velocity components along (x^*, y^*)-axes; T is the temperature; g_r is the gravitational acceleration; l is the characteristic length of the plate; τ is the thermal expansion coefficient; ν is the kinematic viscosity of the fluid; ψ^* is the stream function which is defined in the usual way $(u^*, v^*) = (\partial\psi^*/\partial y^*, -\partial\psi^*/\partial x^*)$.

2.1 Laminar Boundary Layer Flow With Uniform Suction or Injection. Undisturbed laminar boundary layer flow (basic flow) is first determined for use in linear stability analysis. To do this, we introduce the boundary layer variables

$$\bar{\psi}(x, y) = 4\mathrm{Gr}^{-1/4}(x^3/4)^{1/4}f(x, \eta), \quad \bar{\theta}(x, y) = g(x, \eta)$$
$$\eta = \mathrm{Gr}^{1/4}(x^3/4)^{1/4}\frac{y}{x}. \quad (5)$$

Then, the following partial differential equations are obtained (see Watanabe and Kawakami, 1989):

$$\frac{\partial^3 f}{\partial\eta^3} + 3f\frac{\partial^2 f}{\partial\eta^2} - 2\left(\frac{\partial f}{\partial\eta}\right)^2 + g = 4x\left(\frac{\partial^2 f}{\partial x\partial\eta}\frac{\partial f}{\partial\eta} - \frac{\partial f}{\partial x}\frac{\partial^2 f}{\partial\eta^2}\right) \quad (6)$$

$$\frac{1}{\mathrm{Pr}}\frac{\partial^2 g}{\partial\eta^2} + 3f\frac{\partial g}{\partial\eta} = 4x\left(\frac{\partial g}{\partial x}\frac{\partial f}{\partial\eta} - \frac{\partial f}{\partial x}\frac{\partial g}{\partial\eta}\right) \quad (7)$$

subject to the boundary conditions

$$\eta = 0: \quad \frac{\partial f}{\partial\eta} = 0, \quad \frac{3}{4}f + x\frac{\partial f}{\partial x} = X, \quad g = 1$$

$$\eta \to \infty: \quad \frac{\partial f}{\partial\eta} = 0, \quad g = 0 \quad (8)$$

where X is the parameter of suction ($X > 0$) or injection ($X < 0$), which is defined by

$$X = -\frac{v_0^* x^*}{4\nu}\left(\frac{\mathrm{Gr}_x}{4}\right)^{-1/4} \quad (9)$$

with $\mathrm{Gr}_x = g_r\tau\Delta T x^{*3}/\nu^2$ being the local Grashof number. Substitution of (9) into (6) and (7) gives

$$\frac{\partial^3 f}{\partial\eta^3} + \left(3f + X\frac{\partial f}{\partial X}\right)\frac{\partial^2 f}{\partial\eta^2} - X\frac{\partial^2 f}{\partial X\partial\eta}\frac{\partial f}{\partial\eta} - 2\left(\frac{\partial f}{\partial\eta}\right)^2 + g = 0 \quad (10)$$

$$\frac{1}{\mathrm{Pr}}\frac{\partial^2 g}{\partial\eta^2} + \left(3f + X\frac{\partial f}{\partial X}\right)\frac{\partial g}{\partial\eta} - X\frac{\partial g}{\partial X}\frac{\partial f}{\partial\eta} = 0 \quad (11)$$

with the boundary conditions

$$\eta = 0: \quad \frac{\partial f}{\partial\eta} = 0, \quad 3f + X\frac{\partial f}{\partial X} = 4X, \quad g = 1$$

$$\eta \to \infty: \quad \frac{\partial f}{\partial\eta} = 0, \quad g = 0. \quad (12)$$

Equations (10) and (11) subject to (12) are solved by employing the difference-differential method proposed by Hartree and Womersley (1937). To do this, we shall approximate these equations by a system of ordinary differential equations by replacing the partial derivatives with respect to X at $X = X_j = jh (j = 0, 1, \ldots)$ by finite differences using, for example, a four-point backward difference formula of Gregory-Newton (see Katagiri, 1969). Equations (10) and (11) can then be replaced by the following ordinary differential equations

$$\frac{d^3 f_j}{d\eta^3} + \left\{3f_j + \frac{j}{6}(11f_j - 18f_{j-1} + 9f_{j-2} - 2f_{j-3})\right\}\frac{d^2 f_j}{d\eta^2} - \frac{j}{6}\left(11\frac{df_j}{d\eta} - 18\frac{df_{j-1}}{d\eta} + 9\frac{df_{j-2}}{d\eta} - 2\frac{df_{j-3}}{d\eta}\right)\frac{df_j}{d\eta} - 2\left(\frac{df_j}{d\eta}\right)^2 + g_j = 0 \quad (13)$$

$$\frac{1}{\mathrm{Pr}}\frac{d^2 g_j}{d\eta^2} + \left\{3f_j + \frac{j}{6}(11f_j - 18f_{j-1} + 9f_{j-2} - 2f_{j-3})\right\}\frac{dg_j}{d\eta} - \frac{j}{6}(11g_j - 18g_{j-1} + 9g_{j-2} - 2g_{j-3})\frac{df_j}{d\eta} = 0 \quad (14)$$

subject to the boundary conditions

$$\eta = 0: \quad f_j = \pm jh, \quad \frac{df_j}{d\eta} = 0, \quad g_j = 1$$

$$\eta \to \infty: \quad \frac{df_j}{d\eta} = 0, \quad g_j = 0 \quad (15)$$

Downloaded 04 May 2010 to 171.66.16.33. Redistribution subject to ASME license or copyright; see http://www.asme.org/terms/Terms_Use.cfm

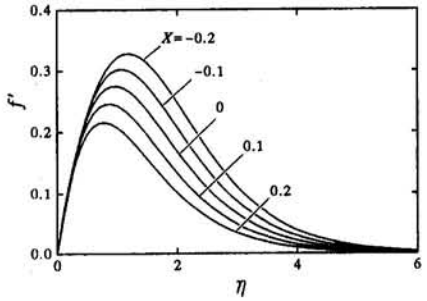


Fig. 2 Velocity profiles of the base flow for Pr = 0.73 and different values of X

where plus or minus signs denote suction or injection, respectively.

The solution of Eqs. (13) and (14) subject to (15) can be expressed at the jth station in the following form of integral equations

$$\frac{df_j}{d\eta} = \int_0^\eta H(\eta) \int_0^\eta \frac{I(\eta)}{H(\eta)}\, d\eta d\eta - \left\{ \int_0^\infty H(\eta) \int_0^\eta \frac{I(\eta)}{H(\eta)}\, d\eta d\eta \right\} \frac{J(\eta)}{J(\infty)} \quad (16)$$

$$f_j = \pm jh + \int_0^\eta \frac{df_j}{d\eta}\, d\eta \quad (17)$$

$$g_j = 1 - \left\{ 1 + \int_0^\infty K(\eta) \int_0^\eta \frac{L(\eta)}{K(\eta)}\, d\eta d\eta \right\} \frac{M(\eta)}{M(\infty)} + \int_0^\eta K(\eta) \int_0^\eta \frac{L(\eta)}{K(\eta)}\, d\eta d\eta \quad (18)$$

where

$$H(\eta) = \exp\left[-\int_0^\eta \left\{ 3f_j - \frac{j}{6}(11f_j - 18f_{j-1} + 9f_{j-2} - 2f_{j-3}) \right\} d\eta \right] \quad (19)$$

$$I(\eta) = \frac{j}{6}\left(11\frac{df_j}{d\eta} - 18\frac{df_{j-1}}{d\eta} + 9\frac{df_{j-2}}{d\eta} - 2\frac{df_{j-3}}{d\eta} \right)\frac{df_j}{d\eta} - g_j + 2\left(\frac{df_j}{d\eta}\right)^2 \quad (20)$$

$$J(\eta) = \int_0^\eta H(\eta)\, d\eta \quad (21)$$

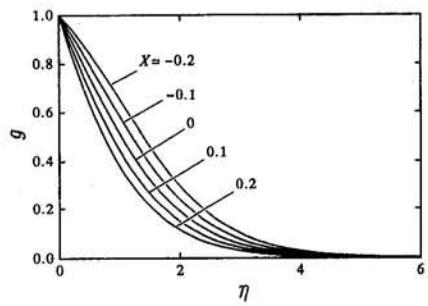


Fig. 3 Temperature profiles of the base flow for Pr = 0.73 and different values of X

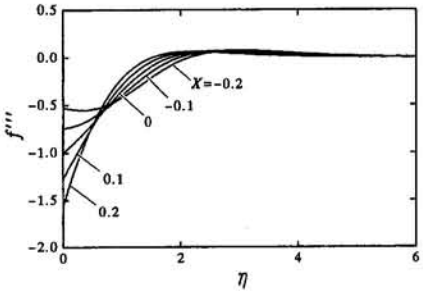


Fig. 4 Second-order derivative of the velocity profiles of the base flow for Pr = 0.73 and different values of X

$$K(\eta) = \exp\left[-\int_0^\eta \left\{ 3\mathrm{Pr} f_j - \frac{j\mathrm{Pr}}{6}(11f_j - 18f_{j-1} + 9f_{j-2} - 2f_{j-3}) \right\} d\eta \right] \quad (22)$$

$$L(\eta) = \frac{j\,\mathrm{Pr}}{6}(11g_j - 18g_{j-1} + 9g_{j-2} - 2g_{j-3})\frac{df_j}{d\eta} \quad (23)$$

$$M(\eta) = \int_0^\eta K(\eta)\, d\eta. \quad (24)$$

Iterative numerical quadrature of integral Eqs. (16), (17), and (18) are carried out using a Simpson's numerical integration scheme. The solutions at the station $X = X_j$ can be determined when the solutions at the three back steps $X = X_{j-1}$, X_{j-2} and X_{j-3} are known. The initial solutions at $X = X_0$ are the values of $X = 0$ ($x \neq 0$), which means the suction velocity $v_0 = 0$. The solution at $X = X_1$ and $X = X_2$ can be obtained by using a two-point and a three-point formula instead of a four-point formula. The criteria of convergence in the iteration was kept within 5×10^{-7} for $d^2f/d\eta^2$ and $dg/d\eta$.

Nondimensional velocity profiles $f'(=df/d\eta)$ and temperature distribution g are presented in Figs. 2 and 3 for Pr = 0.73 and several values of the parameter X. The distribution of the second-order derivative $f'''(=d^3f/d\eta^3)$ of the velocity and the first-order derivative $g'(=dg/d\eta)$ of the temperature are also shown in Figs. 4 and 5, respectively. These values are important for calculating the stability curves of the boundary layer.

2.2 Stability of Natural Convection Boundary Layer Flow. Linear stability theory is used to derive equations govering behaviour of small disturbance. The stream function and temperature are expressed in terms of the basic flow and disturbance quantities as

$$\psi(x, y, t) = \bar{\psi}(x, y) + \tilde{\psi}(x, y, t),$$
$$\theta(x, y, t) = \bar{\theta}(x, y) + \tilde{\theta}(x, y, t). \quad (25)$$

Small disturbance stream function $\tilde{\psi}$ and temperature distur-

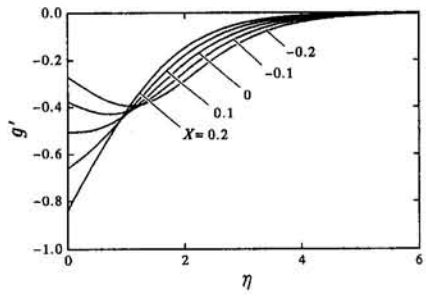


Fig. 5 First-order derivative of the temperature profiles of the base flow for Pr = 0.73 and different values of X

Downloaded 04 May 2010 to 171.66.16.33. Redistribution subject to ASME license or copyright; see http://www.asme.org/terms/Terms_Use.cfm

bance $\tilde{\theta}$ of the Tollmien-Schlichting type are assumed to be of the form

$$\tilde{\psi}(x, y, t) = \tilde{\phi}(y) \exp[i(\hat{\alpha}x - \hat{\beta}t)] \quad (26)$$

$$\tilde{\theta}(x, y, t) = \tilde{s}(y) \exp[i(\hat{\alpha}x - \hat{\beta}t)] \quad (27)$$

where $\hat{\alpha}$ is the real wave number, $\hat{\beta}$ is the complex frequency, and $i = \sqrt{-1}$ is the complex unity. The nondimensional disturbance amplitude functions, $\tilde{\phi}$ and $\tilde{s}$, are in general complex and the physical quantites correspond to the real part of complex functions. It should be mentioned that functions of wavelike disturbances of the Tollmien-Schlichting type (26) and (27) were previously used by Kobayashi (1972) and Watanabe (1978, 1986) to study the stability of magnetohydrodynamic boundary layer flows along a flat plate.

When (25) – (27) are substituted into Eqs. (1) and (2), we obtain the following standard ordinary differential equations for the functions ϕ and s

$$\left(f' - \frac{\beta}{\alpha}\right)(\phi'' - \alpha^2\phi) - f'''\phi$$

$$= \frac{1}{i\alpha G}(\phi'''' - 2\alpha^2\phi'' + \alpha^4\phi + s') \quad (28)$$

$$\left(f' - \frac{\beta}{\alpha}\right)s - g'\phi = \frac{1}{i\alpha\,\mathrm{Pr}G}(s'' - \alpha^2 s) \quad (29)$$

subject to the homogeneous boundary conditions

$$\eta = 0: \phi = \phi' = s = 0$$

$$\eta \to \infty: \quad \phi \to 0, \quad \phi' \to 0, s \to 0 \quad (30)$$

where $G = 4(\mathrm{Gr}_x/4)^{1/4}$ is the modified local Grashof number and primes denote differentiation with respect to η. The nondimensional quantities used in the above equations are defined as

$$\phi(\eta) = \frac{\tilde{\phi}(y)}{U\delta}, \quad s(\eta) = \tilde{s}(y), \quad f'(\eta) = \frac{\bar{u}}{U}$$

$$\alpha = \hat{\alpha}\delta = \frac{2\pi}{\lambda}\delta,$$

$$\beta = \frac{\hat{\beta}\delta}{U} = \frac{\hat{\beta}_r\delta}{U} + \frac{i\hat{\beta}_i\delta}{U} = \frac{2\pi}{\lambda}\frac{\delta}{U} + \frac{i\hat{\beta}_i\delta}{U} = \beta_r + i\beta_i$$

$$\delta = x(4/\mathrm{Gr}_x)^{1/4}, \quad U = 2x^{1/2} \quad (31)$$

where δ is the boundary layer thickness, β_r is the wave propagation velocity in the x-direction, β_i is the temporal exponential amplification factor, and λ is the wavelength of the disturbanced flow. The subscripts r and i denote the real and imaginary parts of the complex functions. Note that neutral stability corresponds to $\beta_i = 0$ and downstream amplification (unstable flow) occurs for $\beta_i > 0$.

The problem of stability flow has been reduced to an eigenvalue problem to find ϕ, s and β_r, β_i from Eqs. (28) and (29) with the boundary conditions (30) for given values of Pr, G, α, X and known velocity f' and temperature g. The eigenvalues and eigenfunctions are determined by integrating Eqs. (28) and (29) inward from $\eta = \eta_e$ to $\eta = 0$. Above the shear layer, the coefficients of these equations are constant at the outer edge of the boundary layer, and we can obtain the following equations:

$$\phi'''' - (a_1^2 + a_2^2)\phi'' + a_1^2a_2^2\phi + s' = 0 \quad (32)$$

$$s'' - a_3^2 s = 0 \quad (33)$$

where a_1, a_2, and a_3 are constants which are given by

$$a_1 = \alpha, \quad a_2 = (\alpha^2 - i\beta G)^{1/2}, \quad a_3 = (\alpha^2 - i\beta\mathrm{Pr}G)^{1/2}. \quad (34)$$

Equations (32) and (33) subject to the boundary conditions (30) is a Sturm-Liouville problem (see Bender and Orszag, 1978, p. 29). This problem has an infinite number of eigenvalues, which are all real and positive. We shall next determine the eigenfunction ϕ and s for this problem. These eigenfunctions may be expressed at the outer edge of the boundary layer ($\eta = \eta_e$) in terms of six pairs of linearly independent solutions of the form

$$\phi = C_1 \exp(-a_1\eta_e) + C_2 \exp(-a_2\eta_e) + C_3 \exp(-a_3\eta_e) + C_4 \exp(a_1\eta_e) + C_5 \exp(a_2\eta_e) + C_6 \exp(a_3\eta_e) \quad (35)$$

$$s = C_3\frac{(a_3^2 - a_1^2)(a_3^2 - a_2^2)}{a_3}\exp(-a_3\eta_e) - C_6\frac{(a_3^2 - a_1^2)(a_3^2 - a_2^2)}{a_3}\exp(a_3\eta_e) \quad (36)$$

where $C_1, C_2, \ldots, C_6$ are arbitrary constants. Several terms in Eqs. (35) and (36) may be shown to be exponentially large as $\eta_e \to \infty$ and they cannot satisfy the boundary conditions (30) at the outer edge of the disturbance boundary region. Therefore, we take $C_4 = C_5 = C_6 = 0$ and then the eigenfunctions $\phi(\eta)$ and $s(\eta)$ at the outer edge of the boundary layer are of the form

$$\phi = C_1 \exp(-a_1\eta_e) + C_2 \exp(-a_2\eta_e) + C_3 \exp(-a_3\eta_e) \quad (37)$$

$$s = C_3\frac{(a_3^2 - a_1^2)(a_3^2 - a_2^2)}{a_3}\exp(-a_3\eta_e) \quad (38)$$

The problem has now been reduced to the determination of the arbitrary constants C_1, C_2, and C_3. To do this, we shall integrate numerically Eqs. (32) and (33). The integration is performed inward from the outer edge of the boundary layer ($\eta = \eta_e$) to the surface ($\eta = 0$) using the Adams-Moulton method. We must then extend the solution of the outer edge of boundary layer through the shear layer and examine the condition that permits a perfect match with the surface solution. The solution contains three arbitrary constants, this requires three computing steps. Because the stability equation is linear, the solution can be obtained by superposing the solution of three integrations. We start the first step with the choice $C_2 = 0$ and $C_3 = 0$, and the solutions are expressed as ϕ_1, ϕ_1', and s_1. In the same way, the second step and the third step begins with $C_1 = 0$, $C_3 = 0$ and $C_1 = 0$, $C_2 = 0$, respectively, and the second and third solutions are expressed as ϕ_2, ϕ_2', s_2 and ϕ_3, ϕ_3', s_3, respectively. Using these solutions, the eigenfunctions ϕ, ϕ', and s become

$$\phi = C_1\phi_1 + C_2\phi_2 + C_3\phi_3$$

$$\phi' = C_1\phi_1' + C_2\phi_2' + C_3\phi_3'$$

$$s = C_1s_1 + C_2s_2 + C_3s_3. \quad (39)$$

The following relations are obtained from the boundary conditions (30):

$$\phi_1(0) + B_2\phi_2(0) + B_3\phi_3(0) = 0$$

$$\phi_1'(0) + B_2\phi_2'(0) + B_3\phi_3'(0) = 0$$

$$s_1(0) + B_2s_2(0) + B_3s_3(0) = 0 \quad (40)$$

where B_2 and B_3 are constants. Finally, we obtain for $\phi'(0)$ the following relation:

$$\phi'(0) = \phi_1'(0) + B_2\phi_2'(0) + B_3\phi_3'(0) \equiv k(\text{constant}). \quad (41)$$

The condition $k \to 0$ was satisfied only if the guessed eigenvalues β_r and β_i were correct. A Newton-Raphson technique was

Downloaded 04 May 2010 to 171.66.16.33. Redistribution subject to ASME license or copyright; see http://www.asme.org/terms/Terms_Use.cfm

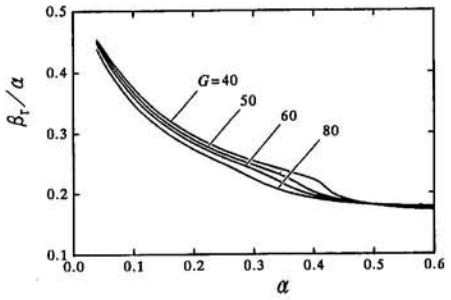


Fig. 6 Variation of the wave propagation velocity with the wave number for Pr = 0.73 and $X = -0.2$

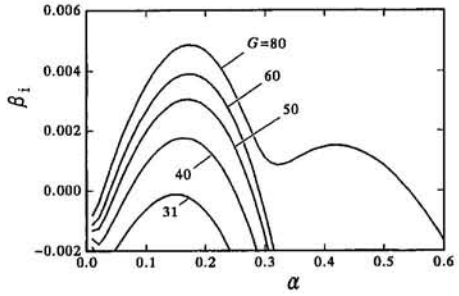


Fig. 8 Variation of the temporal exponential amplification factor with the wave number for Pr = 0.73 and $X = -0.2$

used to provide improved eigenvalues β_r and β_i. Iteration continued until k is less than some specified number, say 10^{-5}.

2.3 Disturbance Velocity and Temperature Distributions. The neutral disturbance velocity components $(\tilde{u}, \tilde{v})$ and temperature function $\tilde{\theta}$ of wavelike disturbances are obtained from the eigenfunctions (26) and (27) and can be expressed in the form

$$\tilde{u} = U(\phi_r'^2 + \phi_i'^2)^{1/2} \cos\left(\frac{\alpha}{\delta}x - \frac{\beta_r U}{\delta}t + \Theta_u\right) \quad (42)$$

$$\tilde{v} = \alpha U(\phi_r^2 + \phi_i^2)^{1/2} \sin\left(\frac{\alpha}{\delta}x - \frac{\beta_r U}{\delta}t + \Theta_v\right) \quad (43)$$

$$\tilde{\theta} = (s_r^2 + s_i^2)^{1/2} \cos\left(\frac{\alpha}{\delta}x - \frac{\beta_r U}{\delta}t + \Theta_T\right) \quad (44)$$

where Θ_u, Θ_v, and Θ_T are the phase angles. Since the magnitude of the disturbances cannot be obtained, we present here only the disturbance amplitude functions which are normalized by their maximum values, so that

$$\frac{\tilde{u}}{\tilde{u}_{\max}} = \frac{(\phi_r'^2 + \phi_i'^2)^{1/2}}{(\phi_r'^2 + \phi_i'^2)^{1/2}_{\max}} = \frac{|\phi'|}{|\phi'|_{\max}} \quad (45)$$

$$\frac{\tilde{v}}{\tilde{v}_{\max}} = \frac{(\phi_r^2 + \phi_i^2)^{1/2}}{(\phi_r^2 + \phi_i^2)^{1/2}_{\max}} = \frac{|\phi|}{|\phi|_{\max}} \quad (46)$$

$$\frac{\tilde{\theta}}{\tilde{\theta}_{\max}} = \frac{(s_r^2 + s_i^2)^{1/2}}{(s_r^2 + s_i^2)^{1/2}_{\max}} = \frac{|s|}{|s|_{\max}} \quad (47)$$

where the subscript max denotes maximum value.

3 Results and Discussion

A large number of numerical computation have been carried out to investigate the temporal linear stability behavior of the problem under consideration. However, since the effects of the Grashof and Prandtl numbers for an impermeable plate have been discussed before, see, for example, Gebhart (1973a, b), only the effects of the modified local Grashof number G and suction or injection parameter X will be illustrated for the present problem. The Prandtl number Pr is kept at the value of 0.73 (air) throughout this paper.

The variation of the wave propagation velocity in the x-direction β_r, temporal exponential amplification factor β_i, disturbance amplitudes of the velocity components along and normal to the plate $|\phi'|/|\phi'|_{\max}$ and $|\phi|/|\phi|_{\max}$, and disturbance amplitude of the temperature $|s|/|s|_{\max}$ is shown in Figs. 6 to 16 for some values of the parameters G and X. The effects of G and X on β_r and β_i can be clearly observed in Figs. 6 to 9. It is seen that G and suction $(X > 0)$ or injection $(X < 0)$ have a pronounced effect on β_r and β_i. Thus, β_r decreases with the increase of G and is smaller for suction than for injection. On the other hand, β_i becomes larger when G is increased, while it gets smaller when the suction parameter $(X > 0)$ increases and becomes higher for larger values of the injection parameter $(X < 0)$. Further, we see from Fig. 9 that the free convection flow along a porous plate is completely stable $(\beta_i < 0)$ for the case of suction and it can be stable or unstable $(\beta_i > 0)$ for the case of injection depending on the values of the wave number α. The instability becomes higher for $\alpha \cong 0.15$ when $X = -0.5$.

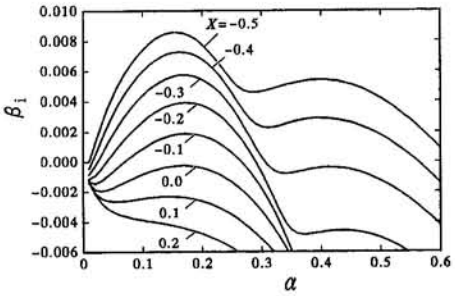


Fig. 9 Variation of the temporal exponential amplification factor with the wave number for Pr = 0.73 and $G = 60$

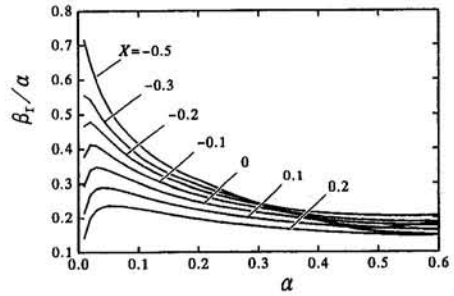


Fig. 7 Variation of the wave propagation velocity with the wave number for Pr = 0.73 and $G = 60$

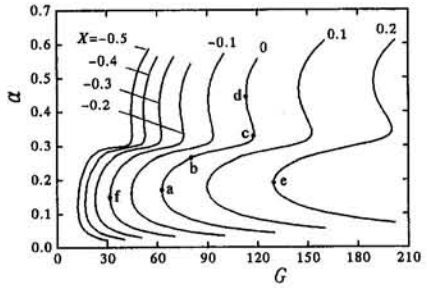


Fig. 10 Neutral stability curves for Pr = 0.73

Downloaded 04 May 2010 to 171.66.16.33. Redistribution subject to ASME license or copyright; see http://www.asme.org/terms/Terms_Use.cfm

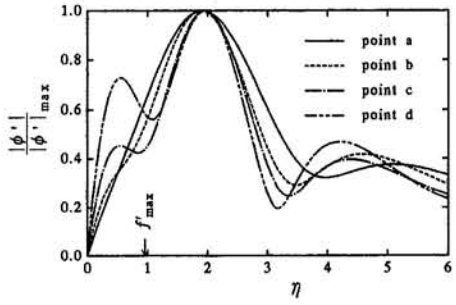


Fig. 11 Disturbance amplitude of the velocity component along the plate for Pr = 0.73 and $X = 0$ (impermeable plate); curves *a*, *b*, *c*, *d* correspond to Fig. 10

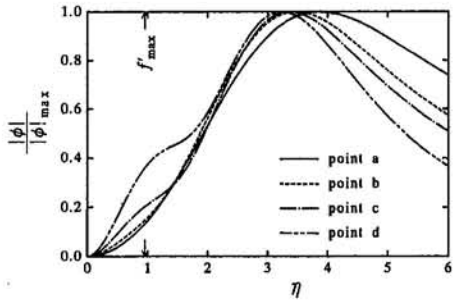


Fig. 12 Disturbance amplitude of the velocity component normal to the plate for Pr = 0.73 and $X = 0$ (impermeable plate); curves *a*, *b*, *c*, *d* correspond to Fig. 10

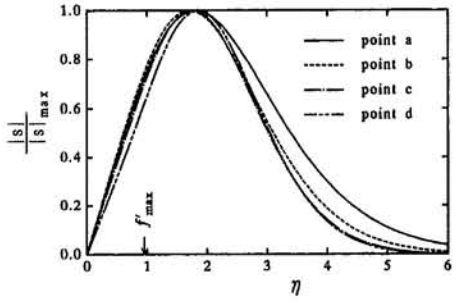


Fig. 13 Disturbance amplitude of the temperature for Pr = 0.73 and $X = 0$ (impermeable plate); curves *a*, *b*, *c*, *d* correspond to Fig. 10

Figure 10 shows the curves dividing the (α, G) plane into regions in which a particular disturbance will be either stable or unstable. The results again predict that the suction and injection will have a pronounced effects on the stability characteristics in this problem.

The distribution of the neutrally stable disturbance velocity components and temperature is depicted in Figs. 11 to 16 for both an impermeable ($X = 0$) and a porous ($X \neq 0$) plate. The points a, b, c, d, e, f are those indicated in Fig. 10. It is observed that these disturbances remain larger near the plate for the case of suction than for injection (see Figs. 14 to 16). At relatively large distances from the plate, the effect of injection is stronger than that of suction. The disturbance $\tilde{u}$-component of the velocity shows a single inner peak for the point a and another peak occuring at the edge of the boundary layer for lower values of G. The maximum in the disturbance velocity component $\tilde{u}$ occurs at the same location as for the disturbance temperature $\tilde{\theta}$. However, for an impermeable plate ($X = 0$) and higher values of G, a third local maximum occurs in the $\tilde{u}$-disturbance velocity component (see Figs. 11 and 13).

4 Conclusion

The effects of the modified local Grashof number and suction or injection parameter on the temporal stability flow characteristics for the problem of free convection along a vertical porous flat plate are investigated on the basis of a linear stability theory. Following the standard procedure in linear stability theory, a superimposing of arbitrarily small disturbance upon the primary (basic) flow, the governing equations for the basic flow and disturbance field, as expressed in terms of the linearized vorticity and energy equations, are derived. The boundary layer equations for the basic flow are solved numerically using a difference-differential method along with Simpson's rule while the eigenvalue problem for the disturbance flow is solved numerically employing Adams-Moulton method in combination with the Newton-Raphson technique. The main results are summarized as follows:

(1) The velocity and temperature profiles in the boundary layer (basic flow) were calculated with high accuracy, from which we can calculate the curves of neutral stability in the wide range of the modified local Grashof number and suction or injection parameter. It is shown that as the suction is in-

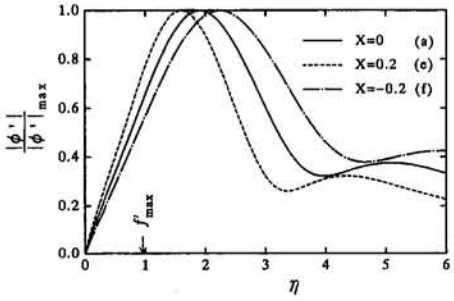


Fig. 14 Effect of suction and injection on the disturbance amplitude of the velocity component along the plate for Pr = 0.73; curves *a*, *e*, *f* correspond to Fig. 10

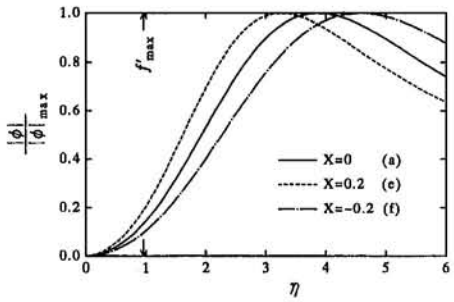


Fig. 15 Effect of suction and injection on the disturbance amplitude of the velocity component normal to the plate for Pr = 0.73; curves *a*, *e*, *f* correspond to Fig. 10

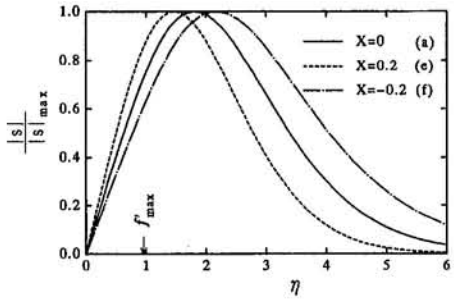


Fig. 16 Effect of suction and injection on the disturbance amplitude of the temperature for Pr = 0.73; curves *a*, *e*, *f* correspond to Fig. 10

Downloaded 04 May 2010 to 171.66.16.33. Redistribution subject to ASME license or copyright; see http://www.asme.org/terms/Terms_Use.cfm

creased the velocity and temperature fields decrease, while they increase with increasing the injection parameter (see Figs. 2 and 3).

(2) The neutral stability curves show that the natural convection flow is completely stable ($\beta_i < 0$) for the case of suction and could be stable or unstable ($\beta_i > 0$) for a porous plate subjected to injection. This is as expected since the boundary conditions at the surface play a significant role in the determination of the shape of the neutral curves.

Acknowledgments

The first author (T. Watanabe) is pleased to express his hearty thanks to Professor R. Kobayashi, Tohoku University, for his continuous support and encouragement. The authors greatly appreciate the constructive suggestions made by the reviewers of the original manuscript.

References

Beckermann, C., Viskanta, R., and Ramadhyani, S., 1988, "Natural Convection in Vertical Enclosures Containing Simultaneously Fluid and Porous Layers," *Journal of Fluid Mechanics,* Vol. 186, pp. 257–284.

Bejan, A., 1979, "On the Boundary Layer Regime in a Vertical Enclosure Filled with a Porous Medium," *Letter in Heat and Mass Transfer,* Vol. 6, pp. 93–102.

Bejan, A., and Anderson, R., 1983, "Natural Convection at the Interface Between a Vertical Porous Layer and an Open Space," ASME *Journal of Heat Transfer,* Vol. 105, pp. 124–129.

Bender, C. M., and Orszag, S. A., 1978, *Advanced Mathematical Methods for Scientists and Engineers,* McGraw-Hill, Singapore.

Gebhart, B., 1973a, "Instability Transition and Turbulence in Buoyancy-Induced Flow," *Annual Review of Fluid Mechanics,* Vol. 5, pp. 213–246.

Gebhart, B., 1973b, "Natural Convection Flow and Stability," *Advances in Heat Transfer,* Vol. 9, pp. 273–348.

Gebhart, B., Jaluria, Y., Mahajan, R. L., and Sammakia, B., 1988, *Buoyancy-Induced Flows and Transport,* Hemisphere, New York.

Gotoh, K., Yanase, S., and Mizushima, J., 1977, "The Instability of Natural Convection in a Vertical Fluid Layer in the Presence of an Adverse Temperature Gradient," *Journal of The Physical Society of Japan,* Vol. 43, pp. 1773–1782.

Hartree, D. R., and Womersley, J. R., 1937, "A Method of the Numerical or Mechanical Solution of Certain Types of Partical Differential Equations," *Proceeding of The Royal Society, London,* Vol. A161, pp. 353–366.

Hieber, C. A., and Gebhart, B., 1971a, "Stability of Vertical Natural Convection Boundary Layers: Some Numerical Solutions," *Journal of Fluid Mechanics,* Vol. 48, pp. 625–646.

Hieber, C. A., and Gebhart, B., 1971b, "Stability of Vertical Natural Convection Boundary Layers: Expansions at Large Prandtl Numbers," *Journal of Fluid Mechanics,* Vol. 49, pp. 577–591.

Katagiri, M., 1969, "The Effect of Hall Currents on the Magnetohydrodynamic Boundary Layer Flow Past a Semi-Infinite Flat Plate," *Journal of The Physical Society of Japan,* Vol. 27, pp. 1051–1059.

Knowles, C. P., and Gebhart, B., 1968, "The Stability of the Laminar Natural Convection Boundary Layer," *Journal of Fluid Mechanics,* Vol. 34, pp. 657–686.

Kobayashi, R., 1972, "Hydromagnetic Stability of Laminar Boundary Layer Along a Flat Plate," *Zeitschrift für Angewandte Mathematik und Physik,* Vol. 23, pp. 341–352 (in German).

Kurtz, E. F., and Crandall, S. H., 1962, "Computer Aided Analysis of Hydrodynamic Stability," *Journal of Mathematical Physics,* Vol. 41, pp. 264–279.

Mahajan, R. L., and Gebhart, B., 1979, "An Experimental of Transition Limits in a Vertical Natural Convection Flow Adjacent to a Surface," *Journal of Fluid Mechanics,* Vol. 91, pp. 131–154.

Plapp, J. E., 1957, "The Analytic Study of Laminar Boundary-Layer Stability in Free Convection," *Journal of Aeronautical Science,* Vol. 24, pp. 318–319.

Pop, I., and Watanabe, T., 1992, "Free Convection with Uniform Suction or Injection from a Vertical Cone for Constant Wall Heat Flux," *International Communications in Heat and Mass Transfer,* Vol. 19, pp. 275–283.

Pop, I., and Watanabe, T., 1994, "Hall Effects on Magnetohydrodynamic Free Convection about a Semi-Infinite Vertical Flat Plate," *International Journal of Engineering Science,* Vol. 32, pp. 1903–1911.

Szewczyk, A. A., 1962, "Stability and Transition of the Free-Convection Boundary Layer along a Vertical Flat Plate," *International Journal of Heat and Mass Transfer,* Vol. 5, pp. 903–914.

Watanabe, T., 1978, "Magnetohydrodynamic Stability of Boundary Layers along a Flat Plate in the Presence of a Transverse Magnetic Field," *Zeitschrift für Angewandte Mathematik und Mechanik,* Vol. 58, pp. 555–560.

Watanabe, T., 1986, "Magnetohydrodynamic Stability of Boundary Layers along a Flat Plate with Pressure Gradient," *Acta Mechanics,* Vol. 65, pp. 41–50.

Watanabe, T., and Kawakami, H., 1989, "Effect of Uniform Suction or Injection on Free Convection Boundary Layers," *Transactions of The Japan Society of Mechanical Engineers,* Vol. 55-B, pp. 3365–3369 (in Japanese).

Watanabe, T., and Pop, I., 1993, "Magnetohydrodynamic Free Convection Flow over a Wedge in the Presence of a Transverse Magnetic Field," *International Communications in Heat and Mass Transfer,* Vol. 20, pp. 871–881.

Watanabe, T., and Pop, I., 1995, "Hall Effects on Magnetohydrodynamic Boundary Layer Flow over a Continuous Moving Flat Plate," *Acta Mechanica,* Vol. 108, pp. 35–47.

Downloaded 04 May 2010 to 171.66.16.33. Redistribution subject to ASME license or copyright; see http://www.asme.org/terms/Terms_Use.cfm

Dynamics of a Gas Permeable Contact Lens During Blinking

P. E. Raad
Associate Professor,
Mem. ASME.

A. S. Sabau
Graduate Assistant.

Mechanical Engineering Department,
Southern Methodist University,
Dallas, TX 75275-0337

The dynamics of a gas permeable contact lens during blinking are analyzed. The contact lens is considered to be a planar, circular, porous disk of specified permeability. On one side, the lens is in solid contact with the eyelids, while on the other, it is separated from the corneal surface by a thin tear film. The rigid-body dynamics of the lens are coupled with the fluid dynamics of the tear film, and a velocity slip condition is imposed at their interface. The coupled system of ordinary and partial differential equations is solved by a combination of analytical and numerical techniques subject to boundary conditions and physical constraints limiting the duration and extent of the motion of the lens. In addition to the contact lens aspect ratio, this work investigates the effects of those variables that characterize the porous nature of the lens such as the Darcy number and the effective slip coefficient. The motion of a permeable contact lens can be controlled by a proper choice of the lens material microstructure. In fact, analysis of the results indicates that the motion of the lens is enhanced by lower values of the slip coefficient and higher values of the Darcy number, independent of the lens thickness. In addition, it is found that thicker lenses as well as thicker tear films cause the lens to move faster.

1 Introduction

In this paper, a method of analysis is presented that enables the study of the coupled dynamics of a permeable contact lens and a thin tear film. The aim of such a study is to determine the influence of the characteristic parameters of a permeable contact lens on its motion during the closing phase of a blink. The motion of a contact lens is critical to the delivery of oxygen to the covered corneal surface. When the cornea is uncovered, the flowing tear film delivers oxygen continually to its surface. When, on the other hand, the cornea is covered by a contact lens, oxygen delivery to the cornea is severely restricted. However, during the blinking process, the lens moves, and as a result, the corneal surface is temporarily exposed and fresh oxygenated tear fluid is supplied to the normally covered cornea. Unfortunately, the relatively large size of the lens and the short duration of normal blinks are such that only part of the corneal surface is exposed. This issue is further aggravated by the fact that most of the involuntary, unforced blinks are incomplete (Doane, 1980). Hence, it is important to ascertain and attempt to enhance the motion of the lens since it is the amount of tangential motion that primarily determines the extent of oxygen delivery to the cornea. The lens motion, however, should not be excessive in order to minimize the possibility of abrasive contact and the chance of injury to the sulcus located at the edge of the eye socket (Mandell, 1974).

As the upper eyelid descends during blinking, it pushes down and squeezes the lens forcing it to undergo a combined sliding and squeezing motion. The lens motion as well as the velocity and the pressure fields in the tear film are of interest in predicting the oxygen tension under the lens (Allaire et al., 1977) and in the elimination of debris for extended-wear contact lenses. Low oxygen tension is an indication of low amounts of oxygen in the corneal epithelium, which is harmful to the health of the cornea. Allaire et al. (1977) state that the diffusion of the oxygen toward the eye is small compared to the transport of oxygenated tear fluid achieved by the pumping action that occurs during a blink. They studied the oxygen tension during a blink for the case of an impermeable lens undergoing a sliding and squeezing motion. The lens motion in their study was limited, however, to a constant velocity in each direction.

It was conjectured by Conway (1982) and later explained by Knoll and Conway (1987) that the extent of lens movement is determined largely by the geometry of the lens. In fact, given a rigid lens of a specified diameter, the lens will come to rest as soon as its edge reaches the corneo-scleral junction (sulcus). Indeed, neither the viscous drag of the tear film, nor the buildup of negative pressure in the postlens tear film could account for the abrupt stopping of the lens. The stopping of the lens before the end of the blink phase poses a constraint on the lens motion, which is considered in this work.

Conway and Knoll (1986) presented a study of the dynamics of an impermeable contact lens, but their study assumed that the postlens tear film thickness varies linearly in time. Jenkins and Shimbo (1984) considered a stationary, axisymmetric soft lens and sought to determine the postlens pressure distribution necessary to hold the lens in conformity to the corneal surface which has a slightly different shape than the lens. Although some experimental studies on the blinking-induced motion of the lens have been performed, e.g., Hayashi (1977), there is a lack of precise data on important aspects such as the transient force exerted by the upper lid on the lens and the time history of the thickness of the tear film.

An accurate analysis of the dynamics of a gas permeable contact lens must take into consideration the lens' permeability and porosity which in practice can vary over a wide range (e.g., $0.3 \leq \phi \leq 0.7$). This work considers the hard lens to be a porous, flat disk of specified diameter. A thorough study is performed to determine the influence of design parameters that characterize the system consisting of the tear film and the porous lens on the motion of permeable contact lenses. The parameters considered include the Darcy number Da, the effective slip coefficient γ, the lens aspect ratio ϵ, and the ratio of the thicknesses of the tear film and the lens h_{f0}.

The dynamics of the tear film both within the porous lens and between it and the cornea are analyzed in Section 2. The contact lens is bounded by the tear film on one side and by the

Contributed by the Applied Mechanics Division of THE AMERICAN SOCIETY OF MECHANICAL ENGINEERS for publication in the ASME JOURNAL OF APPLIED MECHANICS.

Discussion on this paper should be addressed to the Technical Editor, Professor Lewis T. Wheeler, Department of Mechanical Engineering, University of Houston, Houston, TX 77204-4792, and will be accepted until four months after final publication of the paper itself in the ASME JOURNAL OF APPLIED MECHANICS.

Manuscript received by the ASME Applied Mechanics Division, May 12, 1994; final revision, Mar. 13, 1995. Associate Technical Editor: J. T. Jenkins.

Copyright © 1996 by ASME

Downloaded 04 May 2010 to 171.66.16.33. Redistribution subject to ASME license or copyright; see http://www.asme.org/terms/Terms_Use.cfm

eyelids on the other. The lens is considered to be permeable on the tear interface, and since it is assumed that during blinking the eyelids are in solid contact with the lens, the prelens tear film is neglected. The tear fluid flow within the porous lens is described by Darcy's equation. To better model the interface between the permeable contact lens and the tear film, a velocity slip condition at the interface is taken into account as suggested by Beavers and Joseph (1967). Expressions for the dimensionless pressure and velocities in the tear film are derived analytically by means of the Hankel transformation (Nowacki, 1963).

In Section 3, the dimensionless equations governing the rigid-body motion of the lens are derived. The squeezing force exerted by the eyelid on the lens is considered to vary inversely proportionally to the cube power of the tear film thickness (Acheson, 1990). This type of behavior is well supported by the theory and experience of hydrodynamic lubrication (Gross et al., 1980; Raad and Karageorghis, 1993). The sliding force exerted by the upper lid, on the other hand, is considered to be independent of time since it is applied by means of friction due to the relative motion between the lens and the eyelids. The sliding force is applied until the closing phase of the blinking process is completed since the eyelid itself will continue to slide over the lens after the lens has come to rest against the sulcus (Hayashi, 1977). The coupled equations of solid and fluid dynamics governing the saturated porous lens and the clear tear fluid are solved subject to the aforementioned conditions. The computational procedure including an iterative technique used to couple the governing equations is described in Section 4. Finally, the results and conclusions are presented in Section 5.

2 Tear Film Dynamics During Blinking

In this work, the contact lens is considered to be a flat porous disk parallel to the corneal plane. The geometry of the lens and the forces acting on it are shown in Fig. 1. The sliding and squeezing motions must be coupled since the tear film velocity which results from the sliding motion is of the same order of magnitude as the velocity caused by the squeezing motion (Allaire et al., 1977). For typical lens parameters, the tear fluid flow within the lens is governed by Darcy's equation, and the Brinkman and Forchheimer terms can be neglected (see scaling in the Appendix). By assuming that during blinking the eyelids are in full contact with the lens, only the lens surface in contact with the postlens tear film is considered to be permeable and the prelens tear film is thus neglected. The tear film motion is described with respect to a system of coordinates (S_{cl}) attached to the lens as shown in Fig. 1. With respect to S_{cl}, the cornea is moving past a stationary contact lens. The laws governing the dynamics of the tear fluid both within and behind the contact lens are presented next.

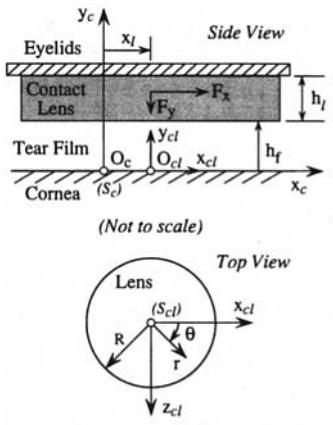


Fig. 1 Model geometry and coordinate systems

2.1 Tear Flow Within the Contact Lens. Darcy's law, which represents a balance between the pressure gradient and the microscopic viscous drag, appears as

$$\mathbf{u}_{PM} = -\frac{K}{\mu}\nabla P, \tag{1}$$

where $\mathbf{u}_{PM} = (u_{PM}, v_{PM}, w_{PM})$ is the three-dimensional velocity of the tear fluid within the lens measured relative to the lens, K is the permeability of the lens, μ is the viscosity of the tear fluid, and P is the fluid pressure within the lens. The continuity equation for the incompressible tear fluid appears as

$$\nabla \mathbf{u}_{PM} = 0. \tag{2}$$

Some of the appropriate boundary and symmetry conditions associated with the system of Eqs. (1) and (2) are

$$\left.\begin{aligned} P(r = R, \theta, y, t) &= p_0, \\ v_{PM}(x, y = h_f + h_l, z, t) &= 0, \\ \frac{\partial P}{\partial z}(x, y, z = 0, t) &= 0, \end{aligned}\right\} \tag{3}$$

where p_0 is the atmospheric pressure, t is time, and all other independent variables are defined in Fig. 1. The subscript cl on the independent variables (x, y, z) is omitted in this section for brevity. Substituting Darcy's law (1) into the continuity Eq. (2) results in a single scalar equation for the fluid pressure P inside the contact lens:

$$\nabla^2 P = 0, \tag{4}$$

subject to the following boundary and symmetry conditions:

$$\left.\begin{aligned} P(r = R, \theta, y, t) &= p_0, \\ \frac{\partial P}{\partial y}(r, \theta, y = h_f + h_l, t) &= 0, \\ \frac{\partial P}{\partial \theta}(r, \theta = 0, y, t) &= 0, \\ \frac{\partial P}{\partial \theta}(r, \theta = \pi, y, t) &= 0. \end{aligned}\right\} \tag{5}$$

2.2 Tear Film Flow Behind the Contact Lens. As shown in Berger (1974), the inertia forces in the thin tear film may be neglected and the Reynolds equation of lubrication applies. For the thin tear film separating a porous medium (contact lens) and an impermeable moving wall (cornea), the Reynolds equation (Gross et al., 1980), modified to account for the effects of permeability (Bhat and Patel, 1981) and the effects of the slip velocity at the interface of the contact lens and the tear film (Prakash and Vij, 1974), is

$$\frac{\partial}{\partial x}\left[h_f^3(1 + \zeta_1)\frac{\partial p}{\partial x}\right] + \frac{\partial}{\partial z}\left[h_f^3(1 + \zeta_1)\frac{\partial p}{\partial z}\right] = 6\mu\left[-U\frac{\partial}{\partial x}[h_f(1 + \zeta_0)] + 2V\right] - 12K\left.\frac{\partial P}{\partial y}\right|_{y=h_f}, \tag{6}$$

where

p = pressure in the tear film, Pa
U = sliding lens velocity, dx_l/dt, m/s
V = squeezing lens velocity, dh_f/dt, m/s
γ = effective slip coefficient (Prakash and Vij, 1974)
ζ_0 = first slip coefficient, $\sqrt{K}/(\sqrt{K} + h_f\gamma)$
ζ_1 = second slip coefficient, $3\,[2K\gamma + h_f\sqrt{K}]/[h_f(\sqrt{K} + h_f\gamma)]$.

Downloaded 04 May 2010 to 171.66.16.33. Redistribution subject to ASME license or copyright; see http://www.asme.org/terms/Terms_Use.cfm

Since the lens is considered to be parallel to the corneal surface, it follows that the tear film thickness is uniform in the x and z-directions. As a result, Eq. (6) reduces to the following tear film pressure equation:

$$\frac{1}{r}\frac{\partial}{\partial r}\left(r\frac{\partial p}{\partial r}\right)+\frac{1}{r^2}\frac{\partial^2 p}{\partial \theta^2} = \frac{12\mu}{h_f^3(1+\zeta_1)}\left(V-\frac{K}{\mu}\frac{\partial P}{\partial y}\bigg|_{y=h_f}\right). \quad (7)$$

The boundary conditions for the pressure and velocity components (u, v, w) in the tear film region are

$$p(r=R,\theta,t)=p_0,\quad u(r,\theta,y=0,t)=-U,\quad w(r,\theta,y=0,t)=0, \quad (8)$$

and the matching conditions at the tear-lens interface for the pressure and the slip velocity boundary conditions (Beavers and Joseph, 1967) are

$$\left.\begin{aligned}\frac{\gamma}{\sqrt{K}}[u(r,\theta,h_f,t)-u_{PM}(r,\theta,h_f,t)] &= -\frac{\partial u}{\partial y}\bigg|_{y=h_f},\\ v(r,\theta,h_f,t) &= v_{PM}(r,\theta,h_f,t)+V,\\ \frac{\gamma}{\sqrt{K}}[w(r,\theta,h_f,t)-w_{PM}(r,\theta,h_f,t)] &= -\frac{\partial w}{\partial y}\bigg|_{y=h_f},\\ P(r,\theta,h_f,t) &= p(r,\theta,t).\end{aligned}\right\} \quad (9)$$

2.3 Tear Film Dynamics. The mathematical model of the physical problem under consideration is represented by Eqs. (4) and (7), subject to the boundary, symmetry, and matching conditions (5), (8), and (9). The problem requires the solution of the three-dimensional Darcy equation in the porous lens coupled with the two-dimensional Reynolds equation in the tear film region between the lens and the cornea. The solution of this type of problem can be obtained by discretizing the complete domains of the lens and clear fluid, and approximating the system of partial differential equations by finite differences or finite elements (Eidelberg and Booker, 1976). In this work, however, the assumption that the lens is parallel to the cornea enables a more efficient analytical approach where numerical computations are postponed until the ordinary differential equations governing the rigid body dynamics of the lens are obtained. In effect, the Reynolds equation can be thought of as a boundary condition for the Darcy equation. Making use of the Hankel transformation (Nowacki, 1963) in Eq. (4), the fluid pressure within the contact lens is solved for analytically and written in the following form:

$$P(r,\theta,y,t) = p_0+\sum_{n=1}^{\infty}A_n(t)\cosh[\beta_n(y-h_f-h_l)/R]J_0(\beta_n r/R). \quad (10)$$

The β_ns are the roots of the zeroth-order Bessel function of the first kind J_0 (Nowacki, 1963). The coefficients $A_n(t)$ are determined by introducing the pressure $p(r,\theta,t)=P(r,\theta,h_f,t)$ into the Reynolds Eq. (7) to yield:

$$A_n(t)=\frac{-24\mu VR^2}{\beta_n^2 J_1(\beta_n)[\beta_n h_f^3(1+\zeta_1)\cosh(\beta_n h_l/R)+12KR\sinh(\beta_n h_l/R)]}, \quad (11)$$

where J_1 is the first-order Bessel function of the first kind (Nowacki, 1963). Next, the fluid velocities within the contact lens, given by the radial (u_r) and circumferential (u_θ) components, are calculated by the use of Darcy's law (1) and the computed pressure field $P(r,\theta,y,t)$. The tear film velocity field, referenced to the lens system of coordinates (S_{cl}) defined in Fig. 1, is given by the thin film lubrication velocity components:

$$u_r(r,\theta,y,t)=\frac{1}{2\mu}\frac{\partial p}{\partial r}y\left[y-h_f\left(1+\frac{\zeta_1}{3}\right)\right]+\frac{U}{h_f}[y(1-\zeta_0)-h_f]\cos\theta, \quad (12)$$

and

$$u_\theta(r,\theta,y,t)=-\frac{U}{h_f}[y(1-\zeta_0)-h_f]\sin\theta. \quad (13)$$

Using the following characteristic and nondimensional parameters,

Da = Darcy number, K/h_l^2
h_{f0} = initial tear film thickness, m
$\bar{h}_{f0}$ = initial tear film to lens thickness ratio, h_{f0}/h_l
$\bar{h}_f(\bar{t})$ = dimensionless tear film thickness, $h_f(t)/h_{f0}$
p_c = characteristic pressure, $\mu R^2/(t_0 h_{f0}^2)$, Pa
$\bar{p}$ = dimensionless pressure, $(p-p_0)/p_c$
$\bar{r}$ = dimensionless radial coordinate, r/R
t_0 = reference time, 0.08 s (Doane, 1980)
$\bar{t}$ = dimensionless time, t/t_0
$\bar{u}_r, \bar{u}_\theta$ = dimensionless radial and circumferential velocities in tear film, $u_r t_0/R$, $u_\theta t_0/R$
$\bar{x}_l$ = dimensionless lens displacement, x_l/R
$\bar{y}$ = dimensionless Cartesian coordinate, y/h_{f0}
ϵ = lens aspect ratio, h_l/R,

the dimensionless pressure and velocities in the tear film become

$$\bar{p}(\bar{r},\theta,\bar{t})=\frac{\partial \bar{h}_f}{\partial \bar{t}}\sum_{n=1}^{\infty}\frac{-24J_0(\bar{r}\beta_n)}{J_1(\beta_n)\beta_n^2 B_n}, \quad (14)$$

$$\bar{u}_r(\bar{r},\theta,\bar{y},\bar{t})=\frac{1}{2}\frac{\partial \bar{p}}{\partial \bar{r}}\bar{y}\left[\bar{y}-\bar{h}_f\left(1+\frac{\zeta_1}{3}\right)\right]+\frac{d\bar{x}_l}{d\bar{t}}\left[\frac{\bar{y}}{\bar{h}_f}(1-\zeta_0)-1\right]\cos\theta, \quad (15)$$

and

$$\bar{u}_\theta(\bar{r},\theta,\bar{y},\bar{t})=-\frac{d\bar{x}_l}{dt}\left[\frac{\bar{y}}{\bar{h}_f}(1-\zeta_0)-1\right]\sin\theta, \quad (16)$$

where

$$B_n=\beta_n\bar{h}_f^3(1+\zeta_1)+12Da\tanh(\beta_n\epsilon)/(\epsilon\bar{h}_{f0}^3). \quad (17)$$

3 Dynamics of the Lens

The equations governing the horizontal and vertical rigid-body motion of the contact lens with respect to the corneal coordinate system (S_c) are

$$\left.\begin{aligned}M\frac{dU}{dt} &= F_x(t)-F_{\text{drag}},\\ M\frac{dV}{dt} &= -F_y(t)+F_{\text{lift}}\end{aligned}\right\} \quad (18)$$

where M is the mass of the lens, and $F_x(t)$ and $F_y(t)$ are the sliding and squeezing forces exerted by the lid on the lens, respectively. The lift and drag forces F_{lift} and F_{drag} are calculated as follows:

Downloaded 04 May 2010 to 171.66.16.33. Redistribution subject to ASME license or copyright; see http://www.asme.org/terms/Terms_Use.cfm

$$\left.\begin{aligned} F_{\text{lift}} &= \int_A (p - p_0)\,dA, \\ F_{\text{drag}} &= \int_A \tau\,dA, \\ \tau &= \mu \frac{\partial u}{\partial y}, \text{ and} \\ u &= u_r \cos\theta - u_\theta \sin\theta. \end{aligned}\right\} \tag{19}$$

Introducing the pressure and velocity relations given by Eqs. (14), (15), and (16) into Eqs. (18) and (19), yields the following motion equations:

$$C_\eta \frac{d^2\bar{h}_f}{d\bar{t}^2} = -\frac{\bar{F}_y(\bar{t})}{\epsilon^2 \bar{h}_{f0}} - \frac{C_{LD}}{\epsilon^4 \bar{h}_{f0}^3} \sum_{n=1}^{\infty} \frac{48}{\beta_n^3 B_n} \frac{d\bar{h}_f}{d\bar{t}}, \tag{20}$$

$$C_\eta \frac{d^2\bar{x}_l}{d\bar{t}^2} = \frac{\bar{F}_x(\bar{t})}{\epsilon} - \frac{C_{LD}}{\epsilon^2 \bar{h}_{f0} \bar{h}_f} (1 - \zeta_0) \frac{d\bar{x}_l}{d\bar{t}}, \tag{21}$$

where

C_η = inertia constant, $\pi\rho R^4/(t_0^2 F_{ye})$
C_{LD} = load and drag constant, $\mu\pi R^2/(t_0 F_{ye})$
F_{ye} = characteristic (maximum) squeezing force, 0.25 N (Hayashi, 1977)
$\bar{F}_y$ = dimensionless squeezing force, $F_y(t)/F_{ye}$
$\bar{F}_x$ = dimensionless sliding force exerted by the lid, F_x/F_{ye}
ρ = lens material density, 530 kg/m^3 (Hayashi, 1977).

Initially, the lens is at rest and the following initial conditions for $\bar{h}_f(\bar{t})$ and $\bar{x}_l(\bar{t})$ apply:

$$\bar{h}_f(0) = 1; \quad \frac{d\bar{h}_f}{d\bar{t}}(0) = 0; \quad \bar{x}_l(0) = 0; \quad \frac{d\bar{x}_l}{d\bar{t}}(0) = 0. \tag{22}$$

The initial tear film thickness h_{f0}, used to nondimensionalize $\bar{h}_f$, is the steady-state film thickness that is given by the static equilibrium of the lens existing in between blinks.

As mentioned in the Introduction, Conway and Knoll (1986) presented a dynamical analysis in which the tear film thickness was assumed to vary linearly in time, and the effect of lens inertia on the squeezing motion was neglected. In the current work, these limitations are removed. The forces applied by the upper eyelid on the lens are considered to also be time dependent. The upper lid squeezing force is taken to have the same time variation as the viscous forces that resist the normal motion of the lens toward the surface of the eye, i.e., inversely proportionally to the cube power of the tear film thickness. Further, the tangential force applied by the eyelid onto the contact lens is considered to be constant since it is applied by means of friction which is due to the relative motion between the lens and the upper eyelid; a motion that continues until the closing phase of the blink is completed (Hayashi, 1977).

Before proceeding to describe the iterative solution methodology for the rigid-body dynamics, it is important to emphasize the lack of precise experimental data for such quantities as the tear film thickness and the dynamic forces applied by the upper eyelid on the lens. However, the *magnitude* of the sliding force during the closing phase of blinking was determined experimentally by (Hayashi, 1977) to be $F_x = 5 \times 10^{-4}$ N. The squeezing force is variable with its maximum $F_{ye} = 0.25$ N occurring at the end of the lens movement at a time t_e which itself must be determined. During a blink, the duration of the downward motion of the lens cannot exceed the duration of the closing phase of the upper eyelid, which for a normal blink is $t_0 = 0.08$ s (Doane, 1980). In addition, it is noted that a rigid lens of a 10 mm-diameter cannot slide over the cornea for a distance that is larger than 2 mm (Knoll and Conway, 1987). Therefore, the lens is considered to come to rest either at a time of $t = 0.08$ s or after it slides 2 mm, whichever comes first. Consequently, in this work, the analysis is performed until one of the following constraints is satisfied:

$$\left.\begin{aligned} t_e = 0.08 \text{ s} \quad &\text{and} \quad x(t_e) \le 2 \text{ mm, or} \\ x_l(t_e) = 2 \text{ mm} \quad &\text{and} \quad t_e \le 0.08 \text{ s.} \end{aligned}\right\} \tag{23}$$

In dimensionless form, Eq. (23) becomes

$$\left.\begin{aligned} \bar{t}_e = 1.0 \quad &\text{and} \quad \bar{x}_l(\bar{t}_e) \le 0.4, \text{ or} \\ \bar{x}_l(\bar{t}_e) = 0.4 \quad &\text{and} \quad \bar{t}_e \le 1.0. \end{aligned}\right\} \tag{24}$$

The time constraint will be especially important for cases involving partial blinks which are not being considered here. Referring to relations (20) and (21), the dimensionless forces become

$$\left.\begin{aligned} \bar{F}_y(\bar{t}) &= \left[\frac{\bar{h}_f(\bar{t}_e)}{\bar{h}_f(\bar{t})}\right]^3, \\ \bar{F}_x(\bar{t}) &= 0.002, \end{aligned}\right\} \tag{25}$$

where $\bar{t}_e$ is the dimensionless time at which the lens comes to rest.

4 Methodology

The motion Eqs. (20), (21), and (25) with initial conditions (22) and constraints (24) are solved by the use of the following iterative technique:

1 Choose $\bar{t}_e = 1.0$ (i.e., $t_e = 0.08$ s).
2 Prescribe an initial value $\bar{h}_f(\bar{t}_e)$ between 0 and 1.
3 Solve the motion equations with the prescribed $\bar{h}_f(\bar{t}_e)$ and compute a tentative thickness $\bar{h}_f^*$.
4 Calculate the magnitude of the error between the prescribed and calculated final tear film thicknesses, $|\bar{h}_f(\bar{t}_e) - \bar{h}_f^*|$.
5 If $|\bar{h}_f(\bar{t}_e) - \bar{h}_f^*| > \delta$, a corrected $\bar{h}_f$, required for a new iteration beginning at step 3, is defined as follows:

$$\bar{h}_f(\bar{t}_e) \leftarrow [\bar{h}_f(\bar{t}_e) - \Delta h * Sign(\bar{h}_f(\bar{t}_e) - \bar{h}_f^*)]. \tag{26}$$

6 If $|\bar{h}_f(\bar{t}_e) - \bar{h}_f^*| \le \delta$, where δ is a small error criterion, then calculate $\bar{x}_l(\bar{t}_e)$ as follows:
   (a) If $\bar{x}_l(\bar{t}_e) \le 0.4$, then the correct and final solution has been reached.
   (b) Otherwise, a corrected $\bar{t}_e$, required for a new time iteration beginning at step 2, is calculated as the solution of the equation:

$$\bar{x}_l(\bar{t}_e) = 0.4. \tag{27}$$

In this work, δ is set at 10^{-4}, and during each iteration, Δh is set equal to half of the calculated error $|\bar{h}_f(\bar{t}_e) - \bar{h}_f^*|$ in order to achieve rapid convergence.

5 Results, Discussion, and Conclusions

In this paper, a methodology is presented for the study of the coupled dynamics of a permeable contact lens and the tear film behind it. The methodology takes into account slip velocity at the lens-tear film interface as well as boundary conditions and physical constraints which limit the duration and extent of the motion of the lens. The aim of this work is to determine the influence of key design variables of a gas permeable contact lens on its dynamics. The motivation is to ascertain the lens motion during a blink since it is by moving that the lens uncovers the cornea, allowing the washing tear film to supply oxygen to the otherwise covered corneal surface. Hence, a certain amount of motion is crucial to the health of the cornea, but excessive motion can be harmful to the sulcus. Given the large number of variables that could be considered, the emphasis is

Downloaded 04 May 2010 to 171.66.16.33. Redistribution subject to ASME license or copyright; see http://www.asme.org/terms/Terms_Use.cfm

placed on the aspect ratio of the lens as well as those variables that characterize its porous nature. In the model considered, which couples the lens and tear dynamics, the porosity ϕ does not influence the lens movement directly, but through its effect on the permeability described by the Carman-Kozeny relation (Nield and Bejan, 1992). In this work, a typical permeability range of $O(10^{-13})$ to $O(10^{-11})$ is considered for the porous matrix of the lens and its diameter is fixed at 10 mm. If desired, other lens diameters and permeability values may be considered by a simple change in data input. Typical contact lens thicknesses vary between 100 μm and 400 μm (Hayashi, 1977). A value of 300 μm is used in this work except when the effects of lens aspect ratio are investigated. Over the ranges of permeability and lens thickness considered, the Darcy number is thus varied from $Da = 0$ for the impermeable case to $Da = 4 \times 10^{-5}$.

Consideration of a slip boundary condition at the interface between the lens and the tear film gives rise to an additional dimensionless parameter γ. The parameter γ is the effective slip coefficient that depends on material parameters (except permeability) and characterizes the lens structure within the boundary region, but is independent of the type of fluid passing through the porous matrix (Beavers and Joseph, 1967). The theoretical upper limit on the effective slip coefficient γ is ∞, which corresponds to the no-slip condition; the actual value of γ is much smaller and depends on the lens material. The experimental results of Beavers and Joseph (1967) showed variations in the value of γ between different materials and even within the same family of materials depending on the surface structure. Trial numerical calculations show no significant influence on the motion of the lens when γ is varied from ∞ to 10. Therefore, two values of γ, namely 0.3 and 10, are considered in this work in order to cover a range of surface structures that different categories of contact lenses might possess. The significance of the effective slip coefficient as it relates to this work is that a thin layer of porous structure at the interface allows fluid flow at higher velocities than the Darcy velocity present in the remainder of the porous lens. Hence, lower shear stresses exist at the interface for smaller values of γ.

The coupled equations of motion (20), (21), and (25) with initial conditions (22) and constraints (24) are solved by the use of a code written in Mathematica (Wolfram, 1991). Trial calculations show that less than one percent difference exists between the results obtained with the first 50 terms in the infinite series of Eq. (20) and those results obtained with the first 60 terms. Consequently, the infinite series in Eq. (20) is truncated to the first 50 terms in all cases presented here.

In order to test the methodology, the case of an impermeable lens (i.e., $Da = 0$) considered by Conway and Knoll (1986) is simulated first. The lens aspect ratio ϵ and the initial tear film to lens thickness ratio $\bar{h}_{f0}$, are set equal to 0.053 and 0.03, respectively. The resulting final displacements, $\bar{h}_f = 0.861$ and $x_l = 1.846$ mm, are found to be identical to those calculated by Conway and Knoll (1986).

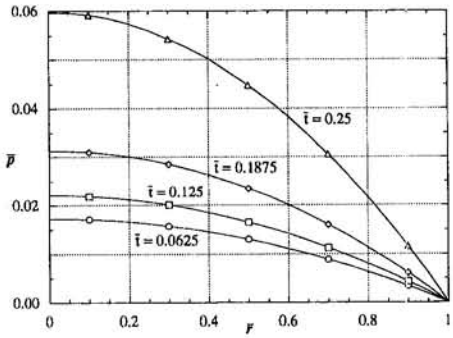


Fig. 2 Time history of pressure profile for a lens with $Da = 4 \times 10^{-6}$, $\gamma = 0.3$, $\bar{h}_{f0} = 0.033$ and $\epsilon = 0.06$

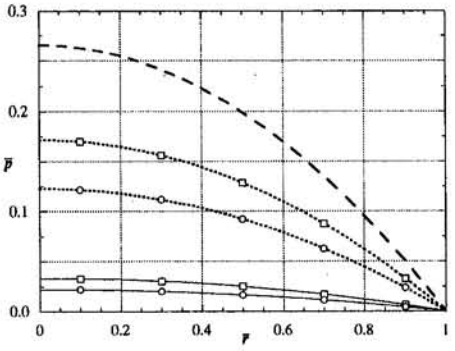


Fig. 3 Effects of the Darcy number and the slip coefficient on the pressure profile at $\bar{t} = 0.125$ for a lens with $\bar{h}_{f0} = 0.033$ and $\epsilon = 0.06$ (- - -, $Da = 0$; . . . . . , $Da = 4 \times 10^{-6}$; —, $Da = 4 \times 10^{-5}$; □, $\gamma = 10$; and ○, $\gamma = 0.3$)

In the remainder of this section, the combined effects of the lens aspect ratio, effective slip coefficient, Darcy number, and initial tear film thickness on the squeezing and sliding motions of the lens are assessed. In order to preserve their generality, results are presented in nondimensional form.

The coupling of the rigid-body dynamics of the lens with the fluid dynamics of the tear film is physically maintained through the pressure field generated within the tear film. Variations in the pressure field give rise to dynamic lift and drag forces which affect the position and motion of the lens. Some physical insight can be gained by examining the sensitivity of the tear film pressure field to the controlling lens parameters. Figure 2 shows the history of the tear fluid pressure as a highly permeable lens approaches the corneal surface. The drastic increase in the pressure of the tear fluid as the eyelids squeeze the lens is responsible for the deceleration of the lens. While the mounting fluid pressure decelerates the squeezing motion of the lens, the

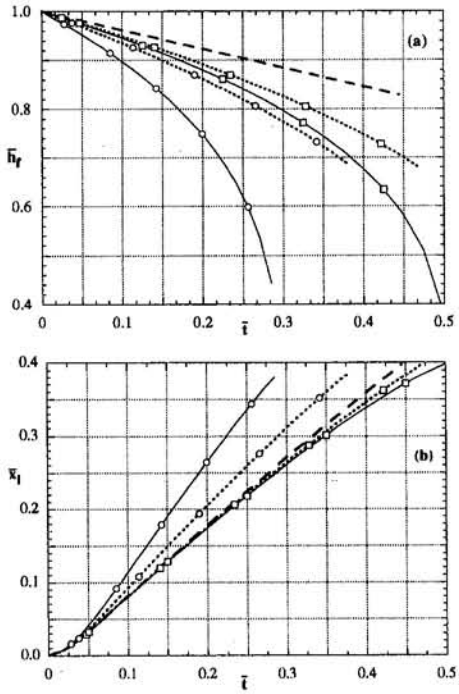


Fig. 4 Effects of the Darcy number and the slip coefficient on the (*a*) tear film thickness and (*b*) sliding displacement for $\bar{h}_{f0} = 0.033$ and $\epsilon = 0.06$ (- - -, $Da = 0$; . . . . . , $Da = 4 \times 10^{-6}$; —, $Da = 4 \times 10^{-5}$; □, $\gamma = 10$; and ○, $\gamma = 0.3$)

Downloaded 04 May 2010 to 171.66.16.33. Redistribution subject to ASME license or copyright; see http://www.asme.org/terms/Terms_Use.cfm

lens continues to slide over the corneal surface until it reaches the sulcus due to the tangential force applied on it by the eyelids.

Much higher pressures, however, are possible in the case of a less permeable lens since the squeezed fluid cannot easily escape through the lens. Figure 3 shows the tear fluid pressure profile at $\bar{t} = 0.125$ for different values of lens permeability and interface slip coefficient. As expected, the impermeable lens case gives rise to the highest tear fluid pressures, and for the permeable lens case, lower values of the effective slip coefficient give rise to lower pressures. This behavior may be understood by recalling that, for a given value of permeability, lower values of γ imply higher penetrations of the clear fluid velocity profile into the permeable lens. The resulting higher average velocities within the lens at its interface with the tear fluid facilitate the transport of the tear fluid radially as it is squeezed by the lens.

The first combination of parameters to be studied involves the Darcy number Da and the effective slip coefficient γ. The lens aspect ratio ϵ and the initial tear film thickness $\bar{h}_{f0}$ are set equal to 0.06 and 0.033, respectively. The solutions of Eqs. (20) and (21) for the nondimensional squeezing and tangential displacements are plotted in Fig. 4, where the dashed line refers to $Da = 0$, dotted lines to $Da = 4 \times 10^{-6}$, and solid lines to $Da = 4 \times 10^{-5}$; the square and circle symbols refer to $\gamma = 10$ and 0.3, respectively. As previously mentioned, the oxygenation of the cornea depends on the flow of fresh tear fluid over portions of the corneal surface that are normally covered by the contact lens. Hence, the delivery of oxygen to the cornea during a blink is proportional to both the tangential and the squeezing displacements of the lens. The enhancement in the squeezing motion as a result of an increasing Darcy number (Fig. 4(*a*)) is to be expected since the lift force (last term of Eq. (20)) decreases with Da. Interestingly though, the squeezing motion is also enhanced by lower values of the slip coefficient γ, an enhancement that becomes even more significant at higher values of the Da number. Described by the $\bar{x}_l$ curves of Fig. 4(*b*), the sliding motion exhibits different behaviors for higher and lower values of the slip coefficient. Higher values of γ, implying higher levels of shear at the lens-tear film interface, result in a deceleration of lens motion as the Da number is increased, while for lower values of γ the trend is reversed.

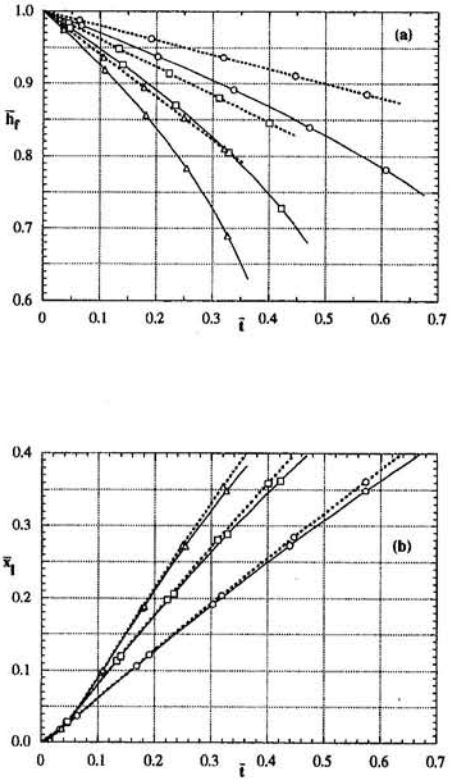


Fig. 5 Effects of the Darcy number and the lens aspect ratio on the (*a*) tear film thickness and (*b*) lens sliding displacement for $\gamma = 10$ and $\bar{h}_{f0} = 0.033$ (○, $\epsilon = 0.04$; □, $\epsilon = 0.06$; △, $\epsilon = 0.08$; . . . . . , $Da = 0$; and —, $Da = 4 \times 10^{-6}$)

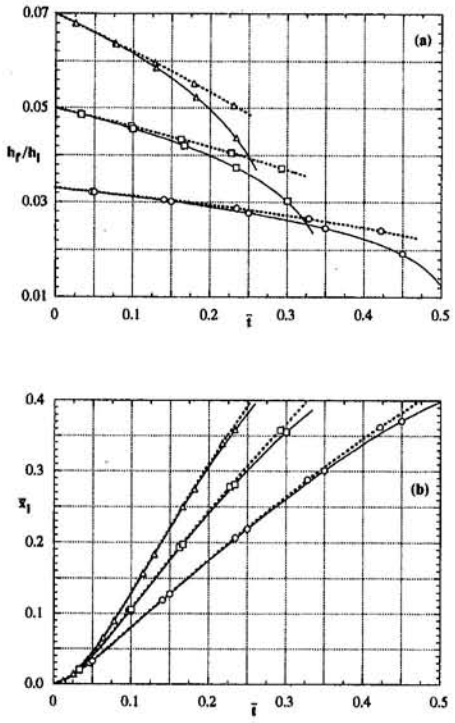


Fig. 6 Effects of the Darcy number and the initial tear film thickness on the (*a*) tear film thickness $h_f(t)/h_l$ and (*b*) sliding displacement for $\epsilon = 0.06$ and $\gamma = 10$ (○, $\bar{h}_{f0} = 0.033$; □, $\bar{h}_{f0} = 0.05$; △, $\bar{h}_{f0} = 0.07$; . . . . . , $Da = 4 \times 10^{-6}$; and —, $Da = 4 \times 10^{-5}$)

Next, the combined effects of the Darcy number Da and the lens aspect ratio ϵ are presented with the slip coefficient γ and the initial tear film thickness $\bar{h}_{f0}$ set equal to 10 and 0.033, respectively. With a lens radius fixed at 10 mm in this work, larger values of ϵ are associated with larger lens thicknesses. Solutions of Eqs. (20) and (21) for the squeezing ($\bar{h}_{f0}$) and tangential ($\bar{x}_l$) displacements are plotted in Fig. 5 where dotted lines refer to $Da = 0$ and solid lines to $Da = 4 \times 10^{-6}$; the circle, square, and triangle symbols refer to $\epsilon = 0.04$, 0.06, and 0.08, respectively. Examination of the results of both types of displacement indicates that thicker lenses move closer and faster toward the corneal surface, irrespective of lens permeability. However, when the lens permeability is taken into account, i.e., when $Da = 4 \times 10^{-6}$, increases in lens thickness result in higher squeezing displacements (Fig. 5(*a*)), but slightly lower tangential displacements (Fig. 5(*b*)). The result that thicker lenses move more than thinner ones is consistent with the observation made in Lowther and Tomlinson (1981). Also, the observed decrease in tangential motion for increasing Da values is consistent with the results of Fig. 4(*b*) where larger Da values yielded a deceleration in the tangential motion, albeit a slight one. The slow movement of the thinner lens ($\epsilon = 0.04$) is demonstrated by the longer travel time spent before the lens reaches the sulcus at $\bar{t} = 0.625$ s, a time longer than those calculated for the other cases considered in this work.

In another combination, variations in permeability (Da number) are combined with those of the initial tear film thickness $\bar{h}_{f0}$, while the lens aspect ratio ϵ and slip coefficient γ are fixed at 0.06 and 10, respectively. The solutions of Eqs. (20) and (21) for the tear film thickness and the lens sliding displacement

Downloaded 04 May 2010 to 171.66.16.33. Redistribution subject to ASME license or copyright; see http://www.asme.org/terms/Terms_Use.cfm

are shown in Fig. 6. Since the initial tear film thickness is being varied here, it is not an appropriate nondimensionalization parameter. Instead, the actual tear film thickness h_f is nondimensionalized with respect to the lens thickness h_l which is held fixed at 300 μm by setting $\epsilon = 0.06$. In Fig. 6, dotted lines refer to $Da = 4 \times 10^{-6}$ and solid lines to $Da = 4 \times 10^{-5}$, while the circle, square, and triangle symbols refer to $\bar{h}_{f0} = 0.033$, 0.05, and 0.07, respectively. As observed in previous cases, the squeezing motion is enhanced by increased lens permeability (Fig. 6(a)). As the lens travels toward the corneal surface, increased lens permeability reduces resistance to the motion by facilitating the flow of the squeezed tear film through the porous lens. As time progresses, the differences in squeezing displacements between the two Da number cases widen for all three values of the initial tear film thickness considered. However, on a percentage basis the differences are larger for lower values of the initial tear film thickness $\bar{h}_{f0}$. It is noted that when the lens starts out farther away from the cornea, the lens travels faster toward the cornea and covers a longer normal distance in a shorter period of time than when it starts out closer to the cornea. As pointed out in the Methodology, the duration of the lens motion is restricted to $\bar{t} = 1$ or to the time it takes the lens to reach the sulcus, whichever comes first. Even though in the case of $\bar{h}_{f0} = 0.07$, the lens travels faster and farther toward the cornea, the lens' tangential motion pushes it quickly against the sulcus where it is forced to stop after only $\bar{t} = 0.25$ (Fig. 6(b)). For smaller values of the initial tear film thickness, e.g., $\bar{h}_{f0} = 0.033$, the lens travels much slower, and has enough time to squeeze closer to the cornea before reaching the sulcus at $\bar{t} = 0.5$.

Finally, the effects of varying the initial tear film thickness $\bar{h}_{f0}$ and the slip coefficient γ are investigated, while the Darcy number and the lens thickness are set equal to 4×10^{-6} and 0.06, respectively. Here again, the squeezing motion results, shown in Fig. 7(a), are expressed in terms of the nondimensional ratio h_f/h_l where h_l is fixed at 300 μm. In Fig. 7, the dotted lines refer to $\gamma = 10$ and the solid lines to $\gamma = 0.3$, while the circle, square, and triangle symbols refer to $\bar{h}_{f0} = 0.033$, 0.05, and 0.07, respectively. The results plotted in Fig. 7(a) indicate that the squeezing motion is enhanced by a decrease in γ, which are consistent with the results of Fig. 4(a). The observed enhancement is apparent for all three values of $\bar{h}_{f0}$ considered. However, at a given value of time, say $\bar{t} = 0.2$, the difference between h_f/h_l for $\gamma = 10$ and $\gamma = 0.3$ decreases as $\bar{h}_{f0}$ increases. Similarly to the previous case, it is seen that the smaller the initial clearance is between the lens and the corneal surface, the slower is the lens motion toward the cornea and the greater is the duration of sliding motion before the lens reaches the sulcus (Fig. 7(b)). An increase in the value of γ further decelerates the sliding motion due to the increase in the shearing force between the sliding lens and the tear film. Physically, the increase in the shear force at the interface between the lens and the film is explained by noting that larger values of γ indicate less slip, and a no-slip condition gives rise to the maximum shear force.

A methodology for studying the coupled dynamics of a permeable lens and the tear fluid behind it has been presented and used to analyze the squeezing and sliding motions of the lens during blinking. To date, proposed improvements in lens motion have been based mainly on geometrical considerations (Conway and Knoll, 1986). However, the lens motion can also be controlled by a proper choice of structural lens material. The variables that characterize the porous nature of the lens material have been considered and their combined effects on the motion of the lens have been shown. Analysis of the results of this study indicates that the motion of the lens is enhanced by lower values of the interface slip coefficient and higher values of the Darcy number, independent of the lens thickness. It has further been shown that faster lens motion is achieved both with thicker lenses and with thicker initial tear films. The methodology presented in this work can be applied to help select the proper structural lens material so that an adequate oxygen delivery to the corneal surface is attained without excessive lens motion.

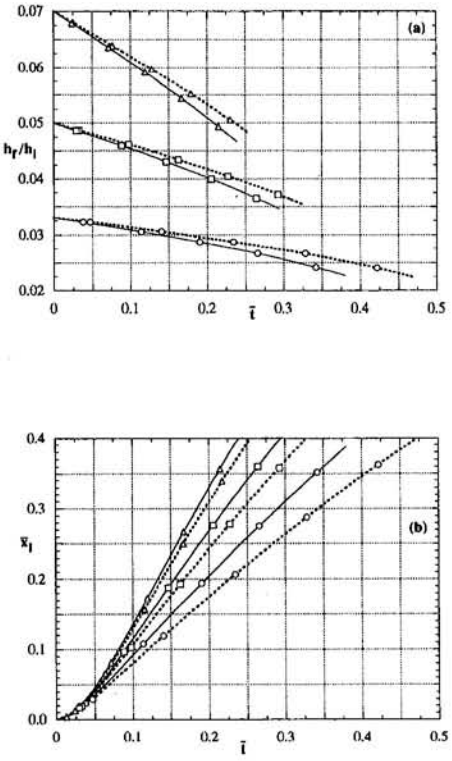


Fig. 7 Effects of the initial tear film thickness and the slip coefficient on the (a) tear film thickness $h_f(t)/h_l$ and (b) sliding displacement for $Da = 4 \times 10^{-6}$ and $\epsilon = 0.06$ (○, $\bar{h}_{f0} = 0.033$; □, $\bar{h}_{f0} = 0.05$; △, $\bar{h}_{f0} = 0.07$; ....., $\gamma = 10$; and —, $\gamma = 0.3$)

References

Acheson, D. J., 1990, *Elementary Fluid Dynamics,* Clarendon Press, Oxford, UK p. 243.

Allaire, P. E., Allison, S. W., and Gooray, A. M., 1977, "Tear-Film Dynamics and Oxygen Tension Under a Circular Contact Lens," *American Journal of Optometry and Physiological Optics,* Vol. 54, No. 9, pp. 617–626.

Beavers, G. S., and Joseph, D. D., 1967, "Boundary Conditions at a Naturally Permeable Wall," ASME *Journal of Fluid Mechanics,* Vol. 30, No. 1, pp. 197–207.

Berger, R. E., 1974, "Effect of Contact Lens Motion on the Oxygen Tension Distribution Under the Lens," *American Journal of Optometry and Physiological Optics,* Vol. 51, No. 7, pp. 441–456.

Bhat, M. V., and Patel, C. M., 1981, "The Squeeze Film in an Inclined Porous Slider Bearing," *Wear,* Vol. 66, pp. 189–193.

Conway, H. D., 1982, "The Motion of a Contact Lens Over the Eye During Blinking," *American Journal of Optometry and Physiological Optics,* Vol. 59, No. 10, pp. 770–773.

Conway, H. D., and Knoll, H. A., 1986, "Further Studies of Contact Lens Motion During Blinking," *American Journal of Optometry and Physiological Optics,* Vol. 63, No. 10, pp. 824–829.

Doane, M. G., 1980, "Interaction of Eyelids and Tears in Corneal Wetting and the Dynamics of the Normal Human Eyeblink," *American Journal of Ophthalmology,* Vol. 89, pp. 507–516.

Eidelberg, B. E., and Booker, J. F., 1976, "Application of Finite Element Methods to Lubrication: Squeeze Films Between Porous Surfaces," *Journal of Lubrication Technology,* Vol. 98, No. 1, pp. 175–180.

Gross, W. A., Matsch, L. A., Castelli, V., Eshel, A., Vohr, J. H., and Wildmann, M., 1980, *Fluid Film Lubrication,* John Wiley and Sons, New York.

Hayashi, T. T., 1977, "Mechanics of Contact Lens Motion," Ph.D. Dissertation, University of California, Berkeley, CA.

Jenkins, J. T., and Shimbo, M., 1984, "The Distribution of Pressure Behind a Soft Contact Lens," ASME JOURNAL OF BIOMECHANICAL ENGINEERING, Vol. 109, pp. 62–65.

Knoll, H. A., and Conway, H. D., 1987, "Analysis of Blink-Induced Vertical Motion of Contact Lenses," *American Journal of Optometry and Physiological Optics,* Vol. 64, No. 2, pp. 153–155.

Downloaded 04 May 2010 to 171.66.16.33. Redistribution subject to ASME license or copyright; see http://www.asme.org/terms/Terms_Use.cfm

Lowther, G. E., and Tomlinson, A., 1981, "Critical Base Curve and Diameter Interval in the Fitting of Spherical Soft Contact Lenses," *American Journal of Optometry and Physiological Optics,* Vol. 58, No. 5, pp. 355–360.

Mandell, R. B., 1974, *Contact Lens Practice,* 2nd ed., Springfield.

Martin, D. K., Boulos, J., Gan, J., Gavriel, K., and Harvey, P., 1989, "A Unifying Parameter to Describe the Clinical Mechanics of Hydrogel Contact Lenses," *Optometry and Vision Science,* Vol. 66, No. 2, pp. 87–91.

Mirejovsky, D., Patel, A. S., and Young, G., 1993, "Water properties of hydrogel contact lens materials: A possible predictive model for corneal desiccation staining," *Biomaterials,* Vol. 14, No. 14, pp. 1080–1088.

Nield, D. A., and Bejan, A., 1992, *Convection in Porous Media,* Springer-Verlag, New York.

Nowacki, W., 1963, *Dynamics of Elastic Systems,* John Wiley and Sons, New York.

Prakash, J., and Vij, S. K., 1974, "Analysis of Narrow Porous Journal Bearing Using Beavers-Joseph Criterion of Velocity Slip," ASME JOURNAL OF APPLIED MECHANICS, Vol. 96, pp. 348–354.

Wolfram, S., 1991, *Mathematica: A System for Doing Mathematics by Computer,* Addison-Wesley.

APPENDIX

Darcy's Model

The momentum equation for a saturated porous medium (Nield and Bejan, 1992) is

$$\underbrace{\rho_f\left[\frac{\partial \mathbf{u}}{\partial t}+(\mathbf{u}\cdot\nabla)\mathbf{u}\right]}_{\text{inertia term}} = -\nabla P - \underbrace{\frac{\mu\phi}{K}\mathbf{u}}_{\text{Darcy's term}} + \underbrace{\mu\nabla^2\mathbf{u}}_{\text{Brinkman's term}} - \underbrace{\frac{C_F\rho_f\phi^2}{\sqrt{K}}|\mathbf{u}|\mathbf{u}}_{\text{Forchheimer's term}} \tag{28}$$

where $\mathbf{u} = \mathbf{u}_{PM}/\phi$ is the velocity of the fluid in the porous medium pores, ρ_f and C_F are constants given below, and the other quantities are defined in Section 2. A scaling analysis of the various terms in Eq. (28) relative to Darcy's term leads to the following nondimensional groupings:

$$\frac{|\text{inertia}|}{|\text{Darcy}|} = \frac{K\rho_f}{\phi\mu t_0}; \quad \frac{|\text{Brinkman}|}{|\text{Darcy}|} = \frac{K}{\phi h_l^2};$$

$$\frac{|\text{Forchheimer}|}{|\text{Darcy}|} = \frac{C_F\phi\rho_f\sqrt{KR}}{\mu t_0}. \tag{29}$$

For typical values of the geometric and flow parameters describing the lens and tear film ($\phi \sim .7$ (Martin et al., 1989), $C_F \sim .55$ (Nield and Bejan, 1992), $\rho_f = 1000$ kg/m^3, $\mu = 10^{-3}$ Pa.s, $h_l = 100 - 400$ μm, $R = 5$ mm, (Hayashi, 1977), $t_0 = 0.08$ s (Doane, 1980), $K = 10^{-13} - 10^{-11}$ m^2 (Mirejovsky et al., 1993)), the ratios in Eq. (29) become

$$\frac{|\text{inertia}|}{|\text{Darcy}|} \sim 10^{-6} - 10^{-4}; \quad \frac{|\text{Brinkman}|}{|\text{Darcy}|} \sim 10^{-6} - 10^{-4};$$

$$\frac{|\text{Forchheimer}|}{|\text{Darcy}|} \sim 10^{-3} - 10^{-2}. \tag{30}$$

Therefore, the use of the Darcy model, Eq. (1), to describe the tear film within the lens is appropriate.

Downloaded 04 May 2010 to 171.66.16.33. Redistribution subject to ASME license or copyright; see http://www.asme.org/terms/Terms_Use.cfm

ERRATA

The paper "A Nonlinear Wound Roll Model Allowing for Large Deformation," by R. C. Benson, appearing in the Dec. 1995 issue of the ASME JOURNAL OF APPLIED MECHANICS, contains two typographical errors. In Eq. (28), on page 856, the term to the immediate left of the equal sign should read $C_i\epsilon_i$ (not C_i). On the last line of page 858, the number appearing there should be 448 (not 443). The author apologizes for any confusion caused by these errors.

Copyright © 1996 by ASME

Downloaded 04 May 2010 to 171.66.16.33. Redistribution subject to ASME license or copyright; see http://www.asme.org/terms/Terms_Use.cfm

The Strain Energy Density of Compressible, Rubber-Like Shells of Revolution

R. F. Yükseler
Associate Professor,
Department of Civil Engineering,
Yildiz Technical University,
Besiktas, Istanbul,
Turkey

An approach for the derivation of two-dimensional strain energy density functions of compressible, rubber-like shells of revolution which undergo axisymmetric, arbitrarily large rotations and strains including transverse normal and transverse shear strains is proposed. The proposed method is applied to polyurethane rubber, circular plates and numerical results for the flexural buckling of polyurethane circular plates are obtained for an illustrative comparison with a method presented previously.

1 Introduction

It has been observed by Blatz and Ko (1962), as noted in Simmonds (1987), that some of the rubber-like materials cannot be assumed to be incompressible and should be considered as compressible. Simmonds (1987) has adapted the method proposed in Simmonds (1986) for deriving two-dimensional strain energy densities of incompressible, rubber-like shells of revolution undergoing axisymmetric, large membrane strains and large transverse normal strains (but small bending strains and small transverse shear strains) to the compressible, rubber-like shells of revolution[1]. Simmonds (1987) has assumed a plane stress condition instead of the incompressibility.

The present study aims to evolve the subject further by removing the restrictions which have been put on the magnitudes of strains previously (Simmonds, 1987). Assumptions made in this study are

(i) material fibers normal to undeformed reference surface remain straight (but not necessarily normal) to the deformed reference surface and

(ii) plane stress condition exists.

This study proposes a method for the derivation of two dimensional strain energy density functions of compressible, rubber-like shells of revolution which undergo axisymmetric rotations and strains of unrestricted magnitudes. The method accomodates two alternative definitions of the deformed reference surface of the shell, similar to Taber (1987):

Theory I: Dynamic (or static) consistency condition, proposed by Simmonds (1986) (Eq. (2.22) of the present paper). According to this definition, deformed reference surface of the shell does not necessarily consist of the same material particles which were located in the undeformed reference surface of the shell.

Theory II: The reference surface is made up of the same material points, regardless of the deformation (Eq. (2.23) of the present study), as has generally been accepted in the relevant literature (e.g., Stumpf and Makowski, 1986).

In Section 2, the proposed approach is explained in general terms. The application of the proposed method to polyurethane circular plates is presented in Section 3.1. In Section 3.2, the two-dimensional strain energy density functions obtained in Section 3.1 and in Simmonds (1987) are used in the problem of flexural buckling of polyurethane circular plates subjected to axisymmetric radial loads for an illustrative comparison.

2 Analysis

2.1 Geometry. The undeformed and deformed geometries of a shell element are shown in Fig. 1. Here and henceforth, the subscript $_0$ is used to denote the values in the undeformed configuration. ζ, ϕ, and s are the deformed transverse coordinate, angle between a normal to the deformed reference surface and the axis of revolution, and arc length along the deformed meridian, respectively. (r, θ, z) are circular cylindrical coordinates with associated orthonormal base vectors

$$\mathbf{e}_r = \cos\theta\mathbf{i} + \sin\theta\mathbf{j},$$

$$\mathbf{e}_\theta = -\sin\theta\mathbf{i} + \cos\theta\mathbf{j}, \quad \mathbf{e}_z = \mathbf{k} \tag{2.1}$$

where $\{\mathbf{i}, \mathbf{j}, \mathbf{k}\}$ denote the orthonormal base vectors of a fixed Cartesian reference frame.

$\mathbf{R}_0$ and $\mathbf{R}$ denote the undeformed and deformed position vectors of a particle in the shell respectively and can be expressed as follows:

$$\mathbf{R}_0(s_0, \theta, \zeta_0) = \mathbf{r}_0(s_0, \theta) + \zeta_0\mathbf{e}_3(s_0, \theta),$$

$$\mathbf{R}(s_0, \theta, \zeta_0) = \mathbf{r}(s_0, \theta) + \zeta(s_0, \zeta_0)\mathbf{A}_3 \tag{2.2}$$

where

$$\mathbf{r}_0(s_0, \theta) = r_0(s_0)\,\mathbf{e}_r(\theta) + z_0(s_0)\mathbf{e}_z,$$

$$\mathbf{r}(s_0, \theta) = r(s_0)\mathbf{e}_r(\theta) + z(s_0)\mathbf{e}_z, \tag{2.3}$$

are the position vectors of a point in the undeformed and deformed reference surfaces respectively; $\mathbf{e}_3$, in the undeformed transverse direction, is a member of the orthonormal triad $\{\mathbf{e}_i\}$, shown in Fig. 1 and defined in the undeformed configuration as

$$\mathbf{e}_1 = \cos\phi_0\mathbf{e}_r - \sin\phi_0\mathbf{e}_z, \ \mathbf{e}_2 = \mathbf{e}_\theta,$$

$$\mathbf{e}_3 = \sin\phi_0\mathbf{e}_r + \cos\phi_0\mathbf{e}_z; \tag{2.4}$$

and $\mathbf{A}_3$, in the direction of the straight line containing the particles which have been on the normal to the undeformed reference surface, is a member of the orthonormal triad $\{\mathbf{A}_i\}$, shown in Fig. 1 and defined in the deformed configuration as

Contributed by the Applied Mechanics Division of THE AMERICAN SOCIETY OF MECHANICAL ENGINEERS for publication in the ASME JOURNAL OF APPLIED MECHANICS.

Discussion on this paper should be addressed to the Technical Editor, Professor Lewis T. Wheeler, Department of Mechanical Engineering, University of Houston, Houston, TX 77204-4792, and will be accepted until four months after final publication of the paper itself in the ASME JOURNAL OF APPLIED MECHANICS.

Manuscript received by the ASME Applied Mechanics Division, July 13, 1994; final revision, July 7, 1995. Associate Technical Editor: R. Abeyaratne.

[1] Strain energy density function of Simmonds (1986) coincides with Eq. (47) of Schieck et al. (1992) for shells of revolution with axisymmetric deformations (Schieck et al., 1992). The use of Eq. (47) of Schieck et al. (1992) has been proposed by Schieck et al. (1992) because of its having needed relatively small computer time for the numerical solutions of various problems.

Copyright © 1996 by ASME

Downloaded 04 May 2010 to 171.66.16.33. Redistribution subject to ASME license or copyright; see http://www.asme.org/terms/Terms_Use.cfm

$$\mathbf{A}_1 = \cos\alpha\mathbf{e}_r - \sin\alpha\mathbf{e}_z, \quad \mathbf{A}_2 = \mathbf{e}_\theta,$$

$$\mathbf{A}_3 = \sin\alpha\mathbf{e}_r + \cos\alpha\mathbf{e}_z \tag{2.5}$$

where

$$\alpha = \phi + \gamma, \tag{2.6}$$

γ is the transverse shear angle.

The natural base vectors $\{\mathbf{g}_i\}$ and $\{\mathbf{c}_i\}$ of the undeformed shell and the deformed shell, respectively, can easily be obtained from Eqs. (2.1)–(2.6) and

$$\mathbf{g}_1 = \mathbf{R}_0', \quad \mathbf{g}_2 = \partial\mathbf{R}_0/\partial\theta, \quad \mathbf{g}_3 = \partial\mathbf{R}_0/\partial\zeta_0,$$

$$\mathbf{c}_1 = \mathbf{R}', \quad \mathbf{c}_2 = \partial\mathbf{R}/\partial\theta, \quad \mathbf{c}_3 = \partial\mathbf{R}/\partial\zeta_0 \tag{2.7}$$

where $(\ )'$ indicates partial derivative with respect to s_0. It is, then, a matter of simple algebra to determine the covariant and contravariant components of the metric tensor in the undeformed configuration, namely g_{km} and g^{ln}, respectively, and the covariant components of Green deformation tensor c_{kl} to be used in

$$c_{(l)}^{(m)} = c_{kl}g^{km}\sqrt{g_{mm}/g_{ll}} \tag{2.8}$$

where $c_{(l)}^{(m)}$ are the physical mixed components of Green deformation tensor. The dashes at the bottom of the indices denote that the summation convention is not applied to these indices.

2.2 Expression of the Deformed Transverse Coordinate. The physical mixed components of Green deformation tensor $c_{(l)}^{(m)}$ can, then, be expressed as[2]

$$c_{(l)}^{(m)} = \begin{bmatrix} (G_\phi + G_\Omega) & 0 & \sqrt{G_z G_\Omega} \\ 0 & G_\theta & 0 \\ \sqrt{G_z G_\Omega} & 0 & G_z \end{bmatrix} \tag{2.9}$$

where[3]

$$G_\phi = \frac{(\lambda_\phi + k_\phi\zeta)^2}{(1 + k_{\phi_0}\zeta_0)^2}, \quad G_\Omega = \frac{\eta^2}{(1 + k_{\phi_0}\zeta_0)^2}$$

$$G_\theta = \frac{(\lambda_\theta + k_\theta\zeta)^2}{(1 + k_{\theta_0}\zeta_0)^2}, \quad G_z = \left(\frac{\partial\zeta}{\partial\zeta_0}\right)^2 \tag{2.10}$$

and

$$\lambda_\phi = s'\cos\gamma, \quad \lambda_\theta = \frac{r}{r_0}, \quad \eta = s'\sin\gamma$$

$$k_{\phi_0} = \phi_0', \quad k_{\theta_0} = \frac{\sin\phi_0}{r_0}$$

$$k_\phi = \alpha', \quad k_\theta = \frac{\sin\alpha}{r}. \tag{2.11}$$

λ_ϕ and λ_θ are extensional stretches, η is a transverse shear strain measure, k_ϕ and k_θ are deformed curvatures, and k_{ϕ_0} and k_{θ_0} are undeformed curvatures. The invariants of $c_{(l)}^{(m)}$ can then be written in the form

[2] Equation (2.9) can easily be checked by Eq. (10) of Makowski and Stumpf (1989), disregarding the incompressibility condition and taking care of some notational differences.

[3] Equation $(2.10)_2$ is an approximation of $G_\Omega = \frac{(\eta + \zeta')^2}{(1 + k_{\phi_0}\zeta_0)^2}$, assuming that stresses depend only on the local strains (Taber, 1987; Makowski and Stumpf, 1989).

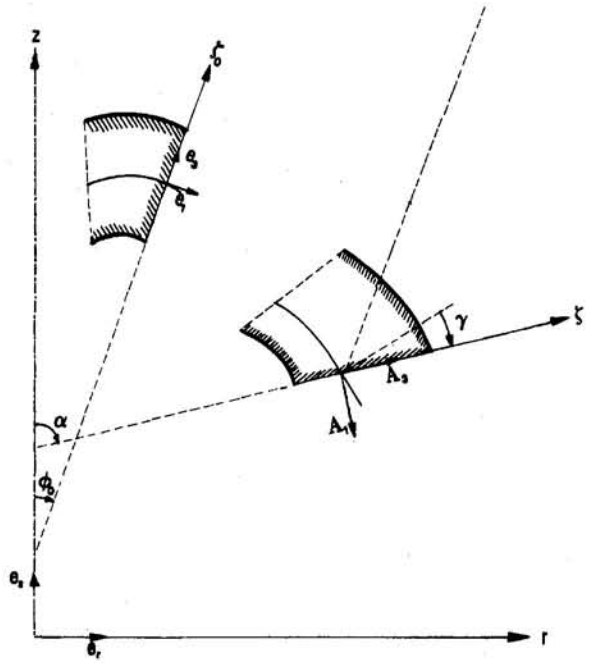


Fig. 1 Geometry of a shell element before and after deformation

$$I_1 = G_\phi + G_\theta + G_\Omega + G_z$$

$$I_2 = G_\theta G_z + G_\phi G_z + G_\theta G_\Omega + G_\theta G_\phi$$

$$I_3 = G_\theta G_\phi G_z. \tag{2.12}$$

The assumption of plane stress condition brings (Simmonds, 1987)[4]

$$\frac{\partial W}{\partial G_z} = 0 \tag{2.13}$$

where W is the three-dimensional strain energy (per unit undeformed volume). W is a function of the strain invariants (Treloar, 1975),

$$W = W(I_1, I_2, I_3), \tag{2.14}$$

and therefore equation (2.13) can be rewritten in the following form:

$$W_1 + (G_\theta + G_\phi)W_2 + G_\theta G_\phi W_3 = 0. \tag{2.15}$$

The subscript i ($i = 1, 2, 3$) stands for the derivative with respect to the ith invariant.

By virtue of Eqs. (2.15) and (2.12) and noting that expressions of $W_i = W_i(I_1, I_2, I_3)$ ($i = 1, 2, 3$) are known for a given compressible, rubber-like material,

$$G_z = G_z(G_\theta, G_\phi, G_\Omega) \tag{2.16}$$

can be obtained. With Eqs. (2.10), (2.16)

$$G_z = G_z(\lambda_\phi, \lambda_\theta, \eta, k_\phi, k_\theta, k_{\phi_0}, k_{\theta_0}; \zeta, \zeta_0) \tag{2.17}$$

can be obtained.

To get an asymptotic solution of ζ, the parameter

$$\epsilon = t/(2L) \tag{2.18}$$

[4] The proposed approach is applicable to incompressible, rubber-like shells of revolution as well if the incompressibility condition, $I_3 = 1$, is used instead of Eq. (2.13).

Downloaded 04 May 2010 to 171.66.16.33. Redistribution subject to ASME license or copyright; see http://www.asme.org/terms/Terms_Use.cfm

and the nondimensional quantities

$$(\zeta^*, \zeta_0^*) = (2/t)(\zeta, \zeta_0),$$

$$(k_\phi^*, k_\theta^*, k_{\phi_0}^*, k_{\theta_0}^*) = L(k_\phi, k_\theta, k_{\phi_0}, k_{\theta_0}) \qquad (2.19)$$

are defined as in Taber (1987). Here, t is undeformed shell thickness and L is deformation wavelength. Introducing Eqs. (2.18), (2.19), and $(2.10)_4$ into Eq. (2.17) gives

$$\dot{\zeta}^* = \dot{\zeta}^*(\lambda_\phi, \lambda_\theta, \eta, k_\phi^*, k_\theta^*, k_{\phi_0}^*, k_{\theta_0}^*; \zeta^*, \zeta_0^*, \epsilon), \qquad (2.20)$$

where $(\dot{})$ indicates partial derivative with respect to ζ_0^*.

We now assume a formal asymptotic expansion of the form

$$\zeta^* = \zeta^{(0)*} + \epsilon\zeta^{(1)*} + \epsilon^2\zeta^{(2)*} + \ldots. \qquad (2.21)$$

Introducing Eq. (2.21) into Eq. (2.20) and equating the like powers of ϵ; $\zeta^{(0)*}$, $\zeta^{(1)*}$, $\zeta^{(2)*}$, ..., etc. can be obtained through two alternative definitions of the deformed reference surface[5], mentioned in Section 1:

Theory I:

$$\int_{-1}^{1} \zeta^{(i)*} d\zeta_0^* = 0 \qquad (2.22)$$

for each i ($i = 0, 1, 2, \ldots$).

Theory II:

$$\zeta^{(i)*}|_{\zeta_0^* = 0} = 0 \qquad (2.23)$$

for each i ($i = 0, 1, 2, \ldots$). As Taber (1987) has done, a parameter q is chosen to be equal to 1 for Theory I and 0 for Theory II to accomodate both of the theories during the analysis. Substituting the expressions obtained for $\zeta^{(0)*}$, $\zeta^{(1)*}$, $\zeta^{(2)*}$, ... into Eq. (2.21) and dimensionalizing through Eqs. (2.18) and (2.19) leads to

$$\zeta = \zeta(\lambda_\phi, \lambda_\theta, \eta, k_\phi, k_\theta, k_{\phi_0}, k_{\theta_0}; \zeta_0, q). \qquad (2.24)$$

Via suitable curvature change measures K_ϕ and K_θ, deformed curvatures k_ϕ and k_θ can be replaced by K_ϕ and K_θ:

$$\zeta = \zeta(\lambda_\phi, \lambda_\theta, \eta, K_\phi, K_\theta, k_{\phi_0}, k_{\theta_0}; \zeta_0, q). \qquad (2.25)$$

2.3 Two-Dimensional Strain Energy Density Function. Via Eqs. (2.14), (2.12), (2.10), and (2.25), it is a matter of simple algebra to obtain a three-dimensional strain energy density function W in the following form:

$$W = W(\lambda_\phi, \lambda_\theta, \eta, K_\phi, K_\theta, k_{\phi_0}, k_{\theta_0}; \zeta_0, q). \qquad (2.26)$$

Two-dimensional strain energy function w per unit area of the undeformed reference surface[6] is defined as follows:

$$w = \int_{-t/2}^{t/2} W\beta d\zeta_0 \qquad (2.27)$$

where

$$\beta = 1 + (k_{\phi_0} + k_{\theta_0})\zeta_0 + k_{\phi_0}k_{\theta_0}\zeta_0^2, \qquad (2.28)$$

(Makowski and Stumpf, 1989; Schieck et al., 1992). By virtue of Eqs. (2.26), (2.27), and (2.28), two-dimensional strain energy density function w of a compressible, rubber-like shell of revolution which undergoes arbitrarily large rotations and strains, including transverse shear and transverse normal strains, can be obtained.

[5] Associated integration constants can be obtained accordingly.

[6] In the present study, the undeformed middle surface is taken as the undeformed reference surface.

3 Example

3.1 Two-Dimensional Strain Energy Density of Polyurethane Rubber Circular Plates. The three-dimensional strain energy density function W of polyurethane rubber is given as

$$W = \frac{\mu}{2}\left(I_1 + \frac{1-2\nu}{\nu} I_3^{-\nu/(1-2\nu)} - \frac{1+\nu}{\nu}\right) \qquad (3.1)$$

where μ is shear modulus and ν is Poisson's ratio (Blatz and Ko, 1962; Simmonds, 1987). As noted in Simmonds (1987), for $\nu = 0.5$ equation (3.1) becomes W of an incompressible neo-Hookean material.

Following the procedure outlined in Section 2,

$$\frac{\partial\zeta}{\partial\zeta_0} = \left[\frac{(\lambda_\phi + k_\phi\zeta)(\lambda_\theta + k_\theta\zeta)}{(1 + k_{\phi_0}\zeta_0)(1 + k_{\theta_0}\zeta_0)}\right]^p, \qquad (3.2)$$

and, furthermore,

$$\zeta = -\frac{t^2Bq}{24} + A\zeta_0 + \frac{B}{2}\zeta_0^2 + \frac{C}{3}\zeta_0^3 + \text{higher order terms}, \qquad (3.3)$$

where

$$p = \frac{\nu}{1-\nu}, \quad A = \lambda_\theta^p\lambda_\phi^p + \frac{t^2D}{4},$$

$$B = p\,\lambda_\theta^{2p}\lambda_\phi^{2p}\left(\frac{K_\phi}{\lambda_\phi} + \frac{K_\theta}{\lambda_\theta}\right),$$

$$C = \lambda_\theta^p\lambda_\phi^p p\left[\frac{1}{2}(1-p)(k_{\theta_0}^2 + k_{\phi_0}^2) - pk_{\phi_0}k_{\theta_0}\right.$$

$$+ \frac{1}{2}(p-1)(K_\theta^2\lambda_\theta^{2p-2}\lambda_\phi^{2p} + k_{\theta_0}^2 + 2K_\theta k_{\theta_0}\lambda_\theta^{p-1}\lambda_\phi^p$$

$$+ K_\phi^2\lambda_\phi^{2p-2}\lambda_\theta^{2p} + k_{\phi_0}^2 + 2K_\phi k_{\phi_0}\lambda_\phi^{p-1}\lambda_\theta^p)$$

$$+ p(K_\phi\lambda_\phi^{p-1}\lambda_\theta^p + k_{\phi_0})(K_\theta\lambda_\theta^{p-1}\lambda_\phi^p + k_{\theta_0})$$

$$\left. + \frac{B}{2}(K_\theta\lambda_\theta^{-1} + K_\phi\lambda_\phi^{-1})\right] - \frac{1}{2}Bp(k_{\phi_0} + k_{\theta_0}),$$

$$D = -\frac{pBq}{6}[k_{\theta_0} + k_{\phi_0} + \lambda_\theta^p\lambda_\phi^p(K_\theta\lambda_\theta^{-1} + K_\phi\lambda_\phi^{-1})], \qquad (3.4)$$

are obtained[7]. Here, as curvature change measures

$$K_\phi = k_\phi - \lambda_\theta^{-p}\lambda_\phi^{1-p}k_{\phi_0}, \quad K_\theta = k_\theta - \lambda_\phi^{-p}\lambda_\theta^{1-p}k_{\theta_0} \qquad (3.5)$$

are chosen. Equations (3.5) coincide with Eqs. (8) of Taber (1987) for neo-Hookean material ($\nu = 0.5$ or $p = -1$).

In view of Eqs. (3.1), (2.12), (2.10), (3.2), (3.3), $(3.4)_1$, and (3.5), two-dimensional strain energy density function of polyurethane rubber plates ($k_{\phi_0} = k_{\theta_0} = 0$, $\beta = 1$) can be expressed in the following form:

[7] During the determination of Eqs. (3.3) and (3.4), binomial series are used. For example,

$$(\lambda_\theta + \epsilon k_\theta^*\zeta^*)^p \cong \lambda_\theta^p\left[1 + p\frac{\epsilon k_\theta^*\zeta^*}{\lambda_\theta} + \frac{p(p-1)}{2}\frac{\epsilon^2k_\theta^{*2}\zeta^{*2}}{\lambda_\theta^2}\right].$$

Higher order terms of the binomial series are disregarded in this example.

Downloaded 04 May 2010 to 171.66.16.33. Redistribution subject to ASME license or copyright; see http://www.asme.org/terms/Terms_Use.cfm

$$w = \frac{t\mu}{2}\left[\lambda_\phi^2 + \lambda_\theta^2 + \eta^2 + A^2 - \frac{(1+\nu)}{\nu} + \frac{(1-2\nu)}{\nu}\lambda_\theta^{2p}\lambda_\phi^{2p} + \frac{t^2}{12}\left[B(1-q)(\lambda_\phi K_\phi + \lambda_\theta K_\theta) + A^2(K_\phi^2 + K_\theta^2) + B^2 + 2AC + \frac{(1-2\nu)}{\nu} \times \lambda_\phi^{2p}\lambda_\theta^{2p} p\left(B(1-q)\left(\frac{K_\phi}{\lambda_\phi} + \frac{K_\theta}{\lambda_\theta}\right) + A^2(2p-1) \times \left(\frac{K_\phi^2}{\lambda_\phi^2} + \frac{K_\theta^2}{\lambda_\theta^2}\right) + \frac{4A^2 p K_\phi K_\theta}{\lambda_\phi\lambda_\theta}\right)\right]\right] + 0(t^5). \quad (3.6)$$

3.2 Comparative Analysis on the Flexural Buckling of Polyurethane Circular Plates. In order to make a comparison of the two-dimensional strain energy density function obtained in this study, w^y, Eq. (3.6), with that obtained in Simmonds (1987) w^s,

$$w^s = \frac{t\mu}{2}\left[\left[\lambda_\phi^2 + \lambda_\theta^2 - p^{-1}(\lambda_\phi\lambda_\theta)^{2p} - \frac{1+\nu}{\nu}\right] + \frac{t^2}{12(\lambda_\phi\lambda_\theta)^{2(1+\nu)/(1-\nu)}}\left(\left[\frac{1+\nu}{1-\nu} + \lambda_\phi^{2(1-\nu)}\lambda_\theta^{-2p}\right]\lambda_\theta^2 K_\phi^2 - 4p\lambda_\phi\lambda_\theta K_\phi K_\theta + \left[\frac{1+\nu}{1-\nu} + \lambda_\phi^{-2p}\lambda_\theta^{2/(1-\nu)}\right]\lambda_\phi^2 K_\theta^2\right)\right], \quad (3.7)$$

the problem of flexural buckling of polyurethane circular plates is chosen.

The governing equation for the flexural buckling of a circular plate, the lateral boundary of which is constrained to remain parallel to the axis of symmetry of the plate under an axisymmetric radial compressive load, has been derived as

$$(3.8317)^2 = \frac{\chi_0^2 t^2}{4}\frac{w_{\lambda_\phi}|}{w_{K_\phi K_\phi}|}\left[\frac{w_{\lambda_\phi}|}{w_{\eta\eta}|} - \lambda\right] \quad (3.8)$$

in Makowski and Stumpf (1989)[8]. Subscripts of w denote partial differentiation with respect to the related subscripts (e.g., $w_{\eta\eta} = (\partial^2 w/\partial\eta^2)$). The symbol | denotes the value corresponding to the trivial solution according to which

$$\eta| = K_\phi| = K_\theta| = 0,\ \lambda_\phi| = \lambda_\theta| = \lambda = \frac{R}{R_0} \quad (3.9)$$

where R_0 and R are the undeformed and deformed radii of the plate, respectively. χ_0 is a thickness parameter

$$\chi_0 = \frac{2R_0}{t}. \quad (3.10)$$

The term $(w_{\lambda_\phi}|)/(w_{\eta\eta}|)$ in Eq. (3.8) should be taken to vanish when transverse shear strain is neglected, as in Simmonds (1987). The $w_{\lambda_\phi}|$ term can be checked to be the same for both approaches:

$$w^s_{\lambda_\phi}| = w^y_{\lambda_\phi}| = \mu t\,\lambda(1 - \lambda^{4p-2}). \quad (3.11)$$

[8] Equation (3.8) is taken from Makowski and Stumpf (1989) with some notational and presentation differences.

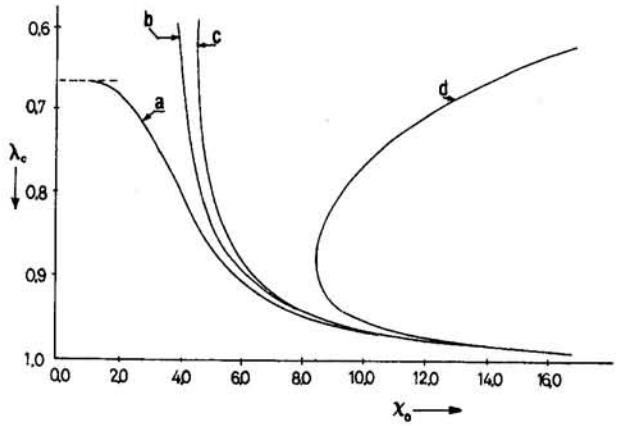


Fig. 2 λ_c versus χ_0 curves for $\nu = 0.5$ where (*a*) is a three-dimensional solution, (*b*) is a solution due to w^y with $q = 1$, (*c*) is a solution due to w^y with $q = 0$, and (*d*) is a solution due to w^s

Coefficients of λ^{8p-2} are the same for $w^s_{K\phi K\phi}|$ and $w^y_{K\phi K\phi}|$ (only for $q = 1$, Theory I):

$$w^s_{K\phi K\phi}| = \frac{\mu t^3}{12}[\lambda^{8p-2}(1-2p) + \lambda^{p(6p-8)/(p-1)}]$$

$$w^y_{K\phi K\phi}| = \frac{\mu t^3}{12}[\lambda^{8p-2}(1-3p+qp) + \lambda^{4p}(1+p-qp)]. \quad (3.12)$$

Additionally,

$$w^s_{\eta\eta}| = 0, \quad w^y_{\eta\eta}| = \mu t \quad (3.13)$$

with the note that $w^s_{\lambda\phi}|/w^s_{\eta\eta}|$ is taken to vanish, as mentioned above, according to the analysis made in Makowski and Stumpf (1989).

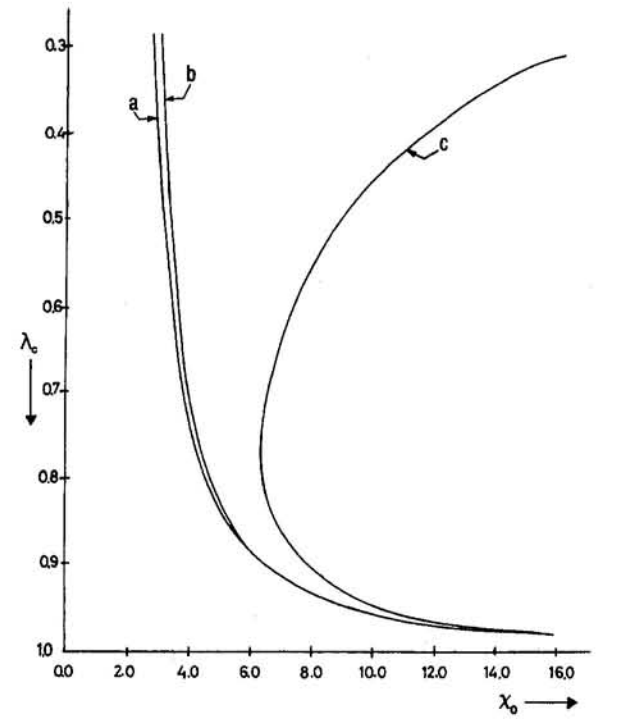


Fig. 3 λ_c versus χ_0 curves for $\nu = 0.2$ where (*a*) is a solution due to w^y with $q = 1$, (*b*) is a solution due to w^y with $q = 0$, and (*c*) is a solution due to w^s

Downloaded 04 May 2010 to 171.66.16.33. Redistribution subject to ASME license or copyright; see http://www.asme.org/terms/Terms_Use.cfm

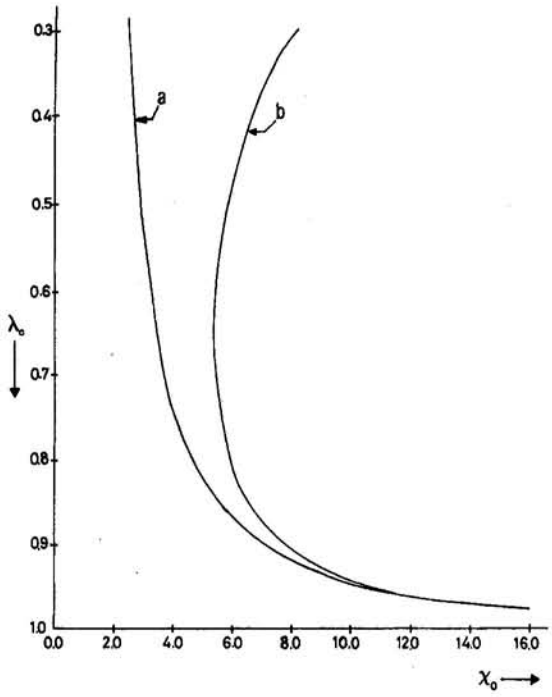


Fig. 4 λ_c versus χ_0 curves for $\upsilon = 0.0$ where (*a*) is a solution due to w^y with $q = 0$ and/or $q = 1$ and (*b*) is a solution due to w^s

Equation (3.8) is solved by a trial and error procedure using a very simple computer program for various values of υ and χ_0. λ_c (critical λ value) versus χ_0 curves corresponding to w^s and w^y (with $q = 0$ and $q = 1$ separately) for $\upsilon = 0.5$ are shown in Fig. 2. In Fig. 2, results of the three-dimensional solution of the problem for $\upsilon = 0.5$ (Guo, 1962; Makowski and Stumpf, 1989) are shown, too. Results due to w^y with $q = 0$ for $\upsilon = 0.5$ coincide with the two-dimensional solution obtained in Makowski and Stumpf (1989). As comparison with the three-dimensional solution, results due to w^y with $q = 1$ (Theory I) seem to be better than those due to w^y with $q = 0$ (Theory II) and those due to w^s. Within the error limit of one percent relative to the three-dimensional solution, the range of validity of w^y with $q = 1$ for this problem is approximately $\chi_0 > 5.9$ and that with $q = 0$ is approximately $\chi_0 > 7.5$. Both give quite good results for relatively thick plates. Results due to w^s seem to be valid only for very thin plates (approximately $\chi_0 > 10.4$ with the same error limit, specified above, considering only the smaller of the two λ_c values for each χ_0 value).

λ_c versus χ_0 curves for $\upsilon = 0.2$ and $\upsilon = 0.0$ are given in Fig. 3 and Fig. 4, respectively. They show the same characteristics of those for $\upsilon = 0.5$. Therefore, parallel critiques for these and other values of υ can reasonably be made.

Additional conclusions which can be deduced from Figs. 2, 3, and 4 are that as υ decreases

(i) results due to w^y with $q = 0$ approach those with $q = 1$. (They coincide for $\upsilon = 0.0$, Fig. 4.)
(ii) results due to w^s deviate less from those due to w^y.

Acknowledgment

This work was supported by Deutscher Akademischer Austauschdienst e.V. under grant No. 313 (IInd Program). I thank Professors Başar and Krätzig, Ruhr University (Bochum, Germany), for their help in getting this support and for their opening the facilities of Ruhr University. Professor Cinemre has my special thanks for offering many valuable suggestions. My thanks are also due to Associate Professor Güralp for his meticulous drawing of the figures of the paper.

References

Blatz, P. J., and Ko, W. L., 1962, "Application of Finite Elastic Theory to Deformation of Rubbery Materials," *Transactions of the Society of Rheology*, Vol. 6, pp. 233–251.

Guo, Z. H., 1962, "Vibration and Stability of a Cylinder Subject to Finite Deformation," *Archives of Mechanics*, Vol. 14, pp. 757–768.

Makowski, J., and Stumpf, H., 1989, "Finite Axisymmetric Deformation of Shells of Revolution with Application to Flexural Buckling of Circular Plates," *Ingenieur—Archiv*, Vol. 59, pp. 456–472.

Schieck, B., Pietraszkiewicz, W., and Stumpf, H., 1992, "Theory and Numerical Analysis of Shells Undergoing Large Elastic Strains," *International Journal of Solids and Structures*, Vol. 29, No. 6, pp. 689–709.

Simmonds, J. G., 1986, "The Strain-Energy Density of Rubber-Like Shells of Revolution Undergoing Torsionless, Axisymmetric Deformation (Axishells)," ASME JOURNAL OF APPLIED MECHANICS, Vol. 53, pp. 593–596.

Simmonds, J. G., 1987, "The Strain-Energy Density of Compressible, Rubber-Like Axishells," ASME JOURNAL OF APPLIED MECHANICS, Vol. 54, pp. 453–454.

Stumpf, H., and Makowski, J., 1986, "On Large Strain Deformations of Shells," *Acta Mechanica*, Vol. 65, pp. 153–168.

Taber, L. A., 1987, "Large Elastic Deformation of Shear Deformable Shells of Revolution: Theory and Analysis," ASME JOURNAL OF APPLIED MECHANICS, Vol. 54, pp. 578–584.

Treloar, L. R. G., 1975, *The Physics of Rubber Elasticity*, 3rd ed., Clarendon Press, Oxford, p. 215.

Downloaded 04 May 2010 to 171.66.16.33. Redistribution subject to ASME license or copyright; see http://www.asme.org/terms/Terms_Use.cfm

On the Definition of the Deformed Reference Surface of Rubber-Like Shells of Revolution

R. F. Yükseler
Associate Professor,
Department of Civil Engineering,
Yildiz Technical University,
Besiktas, Istanbul,
Turkey

A comparative analysis of rubber-like shells of revolution which undergo arbitrarily large rotations and strains is presented. The comparison is made between two alternative definitions of the deformed reference surface: (i) The deformed reference surface is composed of the same particles as the undeformed reference surface. (ii) The deformed reference is taken as the surface of mass of the shell (the dynamic consistency condition) according to which (i) is not necessarily valid. The results obtained from the buckling analysis of circular neo-Hookean plates under radial loads using various approaches strengthen the latter definition relative to the former one.

1 Introduction

A torsionless, axisymmetric displacement field accounting for large transverse normal strains, large membrane strains but small bending strains for rubber-like shells of revolution has been introduced in Simmonds (1986) who used the strain energy density introduced by Treloar (1975) for an incompressible, hyperelastic material, isotropic in the unstrained state. Simmonds (1986) has proposed a definition called the "dynamic consistency condition" (Eq. (23a) of the present paper) whereby the deformed reference surface of the shell is the "surface of mass" of the shell, analogous to the center of mass of a body, and does not necessarily consist of the same material particles composing the undeformed reference (middle) surface of the shell. Taber (1987) has achieved further steps on the theory proposed in Simmonds (1986) by including moderately large transverse shear deformations and moderately large bending strains. Taber (1987) has made two alternative definitions for the deformed reference surface:

Theory I: Dynamic (or static) consistency condition proposed by Simmonds (1986), mentioned above.

Theory II: The reference surface is made up of the same material points, regardless of the deformation (Eq. (24a) of the present paper).

Makowski and Stumpf (1989) have presented a very rigorous theory for shells of revolution undergoing "arbitrarily" large rotations and elastic strains, including transverse shear strains and transverse normal strains. Assuming that material fibers normal to undeformed reference surface remain straight but not necessarily normal to the deformed reference surface, as Taber (1987) has done, Makowski and Stumpf (1989) have used the assumption of Theory II of Taber (1987) to analyze the flexural buckling of circular plates under axisymmetric, radial loads. They have compared the results of (a) the three-dimensional solution of Guo (1962), (b) the solution obtained by Makowski and Stumpf (1989) accounting for transverse shear strains, (c) the solution obtained by Makowski and Stumpf (1989) disregarding transverse shear strains, and (d) the solution obtained using the two-dimensional strain energy density function due to Simmonds (1986).[1] Besides the importance of including the effects of transverse shear deformations for especially relatively thick shells, Makowski and Stumpf (1989) have concluded that the deformed reference surface defined in Simmonds (1986) is not a material surface but a weighted one.

The present study adapts the definition proposed by Simmonds (1986), Theory I of Taber (1987), to the shell theory of Makowski and Stumpf (1989) in Section 2 and repeats the comparative analysis made by Makowski and Stumpf (1989), mentioned in the previous paragraph, with the addition of the solutions obtained using the two-dimensional strain energy density function due to Taber (1987) for Theory I and Theory II in Section 3.

2 Analysis

The three-dimensional strain energy density per unit undeformed volume of a rubber-like material is a function of the strain invariants, (Green and Adkins, 1960):

$$W = W(I_1, I_2). \tag{1}$$

Here, I_1 and I_2 are the first and second invariants of the physical mixed components of Green deformation tensor, $c_{(l)}^{(m)}$,

$$c_{(l)}^{(m)} = c_{kl} g^{km} \sqrt{g_{\underline{mm}} / g_{\underline{ll}}} \tag{2}$$

where g^{km} and g_{ln} are the contravariant and covariant components of the metric tensor in the undeformed configuration respectively; c_{kl} are the covariant components of Green deformation tensor. The dashes at the bottom of the indices indicate that the summation convention is not applied to these indices. W does not depend on the third invariant I_3 ($I_3 = 1$) because the material is incompressible.

To make the comparative analysis in Section 3, the two-dimensional strain energy density function (per unit area of undeformed reference surface) Φ should be obtained from W through transverse integration (Makowski and Stumpf, 1989). To do so, W should be expressed in terms of the undeformed transverse coordinate ξ and strain measures defined on the reference surface. In Subsection 2.1, the strain invariants, of which W is a function, are determined in terms of strain measures defined on the reference surface, the undeformed transverse coordinate ξ, and the deformed transverse coordinate ζ on the foundations of the theory presented by Makowski and Stumpf

Contributed by the Applied Mechanics Division of THE AMERICAN SOCIETY OF MECHANICAL ENGINEERS for publication in the ASME JOURNAL OF APPLIED MECHANICS.

Discussion on this paper should be addressed to the Technical Editor, Professor Lewis T. Wheeler, Department of Mechanical Engineering, University of Houston, Houston, TX 77204-4792, and will be accepted until four months after final publication of the paper itself in the ASME JOURNAL OF APPLIED MECHANICS.

Manuscript received by the ASME Applied Mechanics Division, Aug. 4, 1994; final revision, July 7, 1995. Associate Technical Editor: R. Abeyaratne.

[1] The corresponding results are also shown in Fig. 2 and Fig. 3 of the present paper.

Copyright © 1996 by ASME

Downloaded 04 May 2010 to 171.66.16.33. Redistribution subject to ASME license or copyright; see http://www.asme.org/terms/Terms_Use.cfm

(1989). In Subsection 2.2, the deformed transverse coordinate ζ is expressed in terms of strain measures defined on the reference surface, the undeformed transverse coordinate ξ, and a parameter q allowing us to accomodate both Theory I and Theory II, mentioned in Section 1, to be used during the comparative analysis. Subsections 2.1 and 2.2 together provide the necessary preliminary information required in Section 3.

2.1 Determination of the Strain Invariants. Let $\{\mathbf{i}, \mathbf{j}, \mathbf{k}\}$ be the orthonormal base vectors of a fixed Cartesian reference frame and let (r, θ, z) denote circular cylindrical coordinates with associated orthonormal base vectors $\{\mathbf{e}_r, \mathbf{e}_\theta, \mathbf{e}_z\}$, where

$$\mathbf{e}_r = \cos\theta\mathbf{i} + \sin\theta\mathbf{j},$$
$$\mathbf{e}_\theta = -\sin\theta\mathbf{i} + \cos\theta\mathbf{j}, \quad \mathbf{e}_z = \mathbf{k}. \tag{3}$$

Let S_0 be the undeformed reference (middle) surface with the associated orthonormal triad $\{\mathbf{e}_i\}$:

$$\mathbf{e}_1 = \dot{\mathbf{r}}_0, \quad \mathbf{e}_2 = \mathbf{r}_0', \quad \mathbf{e}_3 = \mathbf{e}_1 \times \mathbf{e}_2 \tag{4}$$

where $\mathbf{r}_0$ is the position vector of a point in S_0:

$$\mathbf{r}_0 = r_0(s_0)\mathbf{e}_r(\theta) + z_0(s_0)\mathbf{e}_z. \tag{5}$$

Here and henceforth, the subscript $_0$ is used to denote that the related parameter belongs to the undeformed configuration; $(\ )'$ and $(\ \dot{}\ )$ denote the partial derivatives with respect to θ and the arc length along the undeformed meridian s_0, respectively.

Let S be the deformed reference surface and let the orthonormal triad $\{\mathbf{A}_i\}$, defined in the deformed configuration, be obtained from $\{\mathbf{e}_r, \mathbf{e}_\theta, \mathbf{e}_z\}$ through an orthogonal transformation such that $\mathbf{A}_3$ coincides with the straight line accomodating the particles which have been on the normal to the undeformed reference surface:

$$\mathbf{A}_1 = \cos\alpha\mathbf{e}_r - \sin\alpha\mathbf{e}_z, \quad \mathbf{A}_2 = \mathbf{e}_\theta,$$
$$\mathbf{A}_3 = \sin\alpha\mathbf{e}_r + \cos\alpha\mathbf{e}_z \tag{6}$$

where

$$\alpha = \phi + \gamma \quad \text{or} \quad \alpha = \psi + \phi_0. \tag{7}$$

α, ϕ_0, γ (the transverse shear angle) and ψ (the rotation angle) are defined in Fig. 1.

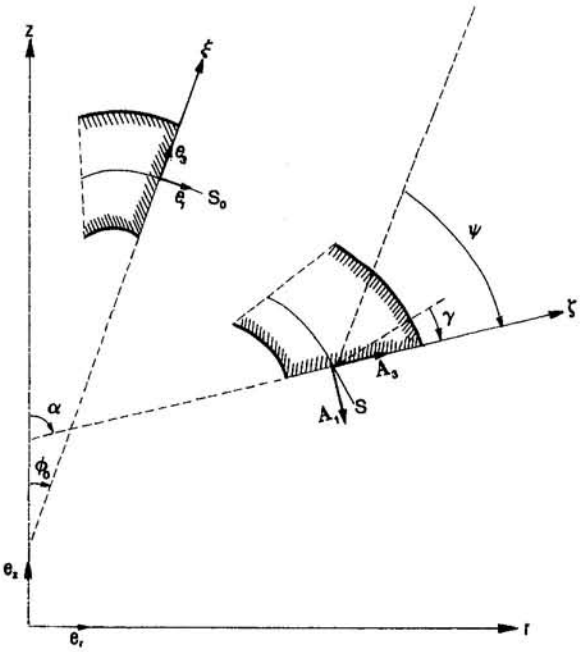


Fig. 1 Undeformed and deformed geometries of a shell element

The position vectors $\mathbf{R}_0$ and $\mathbf{R}$ of generic points in the undeformed and deformed shell spaces, respectively, can be expressed as follows:

$$\mathbf{R}_0(s_0, \theta, \xi) = \mathbf{r}_0(s_0, \theta) + \xi\mathbf{e}_3(s_0, \theta),$$
$$\mathbf{R}(s_0, \theta, \xi) = \mathbf{r}(s_0, \theta) + \zeta(s_0, \xi)\mathbf{A}_3 \tag{8}$$

where

$$\mathbf{r}(s_0, \theta) = r(s_0)\mathbf{e}_r(\theta) + z(s_0)\mathbf{e}_z \tag{9}$$

is the position vector of a point in S.

It is rather a simple procedure to determine the natural base vectors $\{\mathbf{g}_i\}$ and $\{\mathbf{c}_i\}$ of the undeformed and deformed shell spaces, respectively, from Eqs. (3)–(9):

$$\mathbf{g}_1 = \dot{\mathbf{R}}_0 = (1 + k_{\phi 0}\xi)\mathbf{e}_1,$$
$$\mathbf{g}_2 = \mathbf{R}_0' = r(1 + k_{\theta 0}\xi)\mathbf{e}_2,$$
$$\mathbf{g}_3 = \mathbf{R}_{0,\xi},$$
$$\mathbf{c}_1 = \dot{\mathbf{R}} = (\bar{\lambda}_\phi + \bar{k}_\phi\zeta)\mathbf{A}_1 + (\eta + \dot{\zeta})\mathbf{A}_3,$$
$$\mathbf{c}_2 = \mathbf{R}' = r(\lambda_\theta + \bar{k}_\theta\zeta)\mathbf{A}_2,$$
$$\mathbf{c}_3 = \mathbf{R}_{,\xi} = \zeta_{,\xi}\mathbf{A}_3 \tag{10}$$

where

$$\lambda_\phi = \dot{s}, \quad \lambda_\theta = r/r_0, \quad k_{\phi 0} = \dot{\phi}_0, \quad k_\phi = \dot{\phi},$$
$$k_{\theta 0} = \sin\phi_0/r_0, \quad k_\theta = \sin\phi/r_0,$$
$$\bar{k}_\phi = k_\phi + \gamma, \quad \bar{k}_\theta = \sin\alpha/r_0,$$
$$\bar{\lambda}_\phi = \lambda_\phi\cos\gamma, \quad \eta = \lambda_\phi\sin\gamma. \tag{11}$$

Here and henceforth, a comma accompanied with a subscript is used to denote partial derivative with respect to the subscript (e.g., $\mathbf{R}_{,\xi} = \partial\mathbf{R}/\partial\xi$).

It is a straightforward procedure to express $c_{(l)}^{(m)}$ via Eqs. (2), (10):

$$[c_{(l)}^{(m)}] = \begin{bmatrix} G_\phi + G_\Gamma & 0 & \sqrt{G_z G_\Gamma} \\ 0 & G_\theta & 0 \\ \sqrt{G_z G_\Gamma} & 0 & G_z \end{bmatrix} \tag{12}$$

where[2]

$$G_\phi = (\bar{\lambda}_\phi + \bar{k}_\phi\zeta)^2/(1 + k_{\phi 0}\xi)^2,$$
$$G_\Gamma = \eta^2/(1 + k_{\phi 0}\xi)^2, \quad G_z = (\zeta_{,\xi})^2$$
$$G_\theta = (\lambda_\theta + \bar{k}_\theta\zeta)^2/(1 + k_{\theta 0}\xi)^2. \tag{13}$$

Thus,

$$I_1 = G_\phi + G_\theta + G_\Gamma + G_z,$$
$$I_2 = G_\theta G_z + G_z G_\phi + G_\theta G_\Gamma + G_\theta G_\phi,$$
$$I_3 = G_\theta G_\phi G_z. \tag{14}$$

2.2 Expression of ζ. Incompressibility condition, together with Eqs. (13), $(14)_3$, yields

$$(\bar{\lambda}_\phi + \bar{k}_\phi\zeta)(\lambda_\theta + \bar{k}_\theta\zeta)\zeta_{,\xi} = (1 + k_{\phi 0}\xi)(1 + k_{\theta 0}\xi). \tag{15}$$

Introducing the nondimensional quantities, as has been done in Taber (1987),

$$(\xi^*, \zeta^*) = (2/t)(\xi, \zeta),$$
$$(\bar{k}_\phi^*, \bar{k}_\theta^*, k_{\phi 0}^*, k_{\theta 0}^*) = L(\bar{k}_\phi, \bar{k}_\theta, k_{\phi 0}, k_{\theta 0}) \tag{16}$$

[2] Equation $(13)_2$ is an approximation of $G_\Gamma = (\eta + \dot{\zeta})^2/(1 + k_{\phi 0}\xi)^2$, assuming that the deformation is sufficiently smooth (Taber, 1987; Makowski and Stumpf, 1989).

Downloaded 04 May 2010 to 171.66.16.33. Redistribution subject to ASME license or copyright; see http://www.asme.org/terms/Terms_Use.cfm

(where t is the initial thickness of the shell, L is the deformation wavelength). Defining a parameter ϵ as

$$\epsilon = t/2L, \tag{17}$$

we can rewrite Eq. (15) in the following nondimensional form:

$$(\bar{\lambda}_\phi + \epsilon \bar{k}^*_\phi \zeta^*)(\lambda_\theta + \epsilon \bar{k}^*_\theta \zeta^*)\zeta^*_{,\xi^*} = (1 + \epsilon k^*_{\phi 0}\xi^*)(1 + \epsilon k^*_{\theta 0}\xi^*). \tag{18}$$

As in Taber (1987), ζ is expanded asymptotically:

$$\zeta^* = \zeta^{(0)*} + \epsilon\zeta^{(1)*} + \epsilon^2\zeta^{(2)*} + \ldots. \tag{19}$$

Substituting Eq. (19) into Eq. (18), equating coefficients of like powers of ϵ (neglecting $O(\epsilon^3)$) and integrating gives

$$\begin{aligned} \zeta^{(0)*} &= \xi^*/(\lambda_\theta\bar{\lambda}_\phi), \\ \zeta^{(1)*} &= B^*(\xi^{*2} - q/3)/2, \\ \zeta^{(2)*} &= D^*\xi^* + C^*\xi^{*3}/3, \end{aligned} \tag{20}$$

where

$$B^* = -\bar{k}^*_\phi/(\lambda^2_\theta\bar{\lambda}^3_\phi) - \bar{k}^*_\theta/(\lambda^3_\theta\bar{\lambda}^2_\phi) + (k^*_{\phi 0} + k^*_{\theta 0})/(\lambda_\theta\bar{\lambda}_\phi),$$

$$C^* = -3B^*(\bar{k}^*_\phi\lambda_\theta + \bar{k}^*_\theta\bar{\lambda}_\phi)/[2(\lambda_\theta\bar{\lambda}_\phi)^2] - \bar{k}^*_\theta\bar{k}^*_\phi/(\lambda_\theta\bar{\lambda}_\phi)^4 + k^*_{\phi 0}k^*_{\theta 0}/(\bar{\lambda}_\phi\lambda_\theta),$$

$$D^* = qB^*(\bar{k}^*_\phi/\bar{\lambda}_\phi + \bar{k}^*_\theta/\lambda_\theta)/(6\bar{\lambda}_\phi\lambda_\theta), \tag{21}$$

and

$$q = \left\{ \begin{matrix} 1 \text{ for Theory I} \\ 0 \text{ for Theory II} \end{matrix} \right\}. \tag{22}$$

For the determination of the integration constants,

(i) Theory I:

$$\int_{-t/2}^{t/2} \zeta d\xi = 0 \tag{23a}$$

or, in nondimensional form,

$$\int_{-1}^{1} \zeta^{(i)*} d\xi^* = 0, \quad i = 0, 1, 2. \tag{23b}$$

(ii) Theory II:

$$\zeta(s_0, 0) = 0 \tag{24a}$$

or, in nondimensional form,

$$\zeta^{(i)*} = 0 \quad \text{at} \quad \xi^* = 0, \quad i = 0, 1, 2. \tag{24b}$$

Defining the curvature change measures as[3]

$$K_\phi = \bar{k}_\phi - \bar{\lambda}^2_\phi\lambda_\theta k_{\phi 0}, \quad K_\theta = \bar{k}_\theta - \bar{\lambda}_\phi\lambda^2_\theta k_{\theta 0}, \tag{25}$$

B^*, C^*, and D^* can be rewritten in terms of the strain measures in the following dimensional forms:

$$\begin{aligned} B &= B^*/L = -K_\phi/(\lambda^2_\theta\bar{\lambda}^3_\phi) - K_\theta/(\lambda^3_\theta\bar{\lambda}^2_\phi), \\ C &= C^*/L^2 = -3B[\lambda_\theta(K_\phi + \bar{\lambda}^2_\phi\lambda_\theta k_{\phi 0}) + \bar{\lambda}_\phi(K_\theta + \bar{\lambda}_\phi\lambda^2_\theta k_{\theta 0})]/[2(\lambda_\theta\bar{\lambda}_\phi)^2] - (K_\phi + \bar{\lambda}^2_\phi\lambda_\theta k_{\phi 0})(K_\theta + \bar{\lambda}_\phi\lambda^2_\theta k_{\theta 0})/(\lambda_\theta\bar{\lambda}_\phi)^4, \\ D &= D^*/L^2 = qB[K_\phi/(\bar{\lambda}^2_\phi\lambda_\theta) + K_\theta/(\bar{\lambda}_\phi\lambda^2_\theta) + k_{\phi 0} + k_{\theta 0}]/6. \end{aligned} \tag{26}$$

[3] If the transverse shear deformations had been neglected, curvature change measures defined in Eq. (25) would have coincided with those defined in Taber (1987).

Using Eqs. (16), (17), (19), (20), and (26),

$$\zeta = -qt^2B/24 + A\xi + B\xi^2/2 + C\xi^3/3, \tag{27}$$

where

$$A = 1/\bar{\lambda}_\phi\lambda_\theta + t^2D/4. \tag{28}$$

In view of Eqs. (26)–(28), the deformed transverse coordinate, ζ, has been expressed by the stretches $\bar{\lambda}_\phi$, λ_θ; curvature change measures K_ϕ, K_θ; initial curvatures $k_{\phi 0}$, $k_{\theta 0}$; transverse coordinate before deformation, ξ, and an additional parameter q, defined in Eq. (22), which allows us to include the results of Theory I or Theory II.

3 Comparative Analysis

Here is presented a comparative analysis of the buckling problem of neo-Hookean circular plates ($k_{\phi 0} = k_{\theta 0} = 0$), the edges of which cannot rotate under axisymmetric radial loads. The governing equation of the problem is taken from Makowski and Stumpf (1989):

$$(3.8317)^2 = t^2\chi_0^2\Phi_{,\lambda_\theta}|(\Phi_{,\lambda_\theta}|/\Phi_{,\eta\eta}| - \lambda)/(4\Phi_{,K_\phi K_\phi}|) \tag{29}$$

where χ_0 is an initial thickness parameter,

$$\chi_0 = 2R_0/t. \tag{30}$$

R_0 is the initial radius of the circular plate. The symbol $|$ denotes that the corresponding function is evaluated for the values obtained from the prebuckling (trivial) solution of the problem, which is

$$\begin{aligned} \bar{\lambda}_\phi| &= \lambda_\theta| = \lambda = R/R_0 \\ \eta| &= K_\phi| = K_\theta| = 0, \end{aligned} \tag{31}$$

where R is the radius of the deformed plate.

The two-dimensional strain energy density function of plates is defined as

$$\Phi = \int_{-t/2}^{t/2} W d\xi \tag{32}$$

(Makowski and Stumpf, 1989). The choice of the alternative definitions of the deformed reference surface (Theory I or Theory II) does not effect the form of Eq. (29) but does change Φ and, therefore, the solution of the problem.

For neo-Hookean material,

$$W = E(I_1 - 3), \tag{33}$$

where E is a material constant (Makowski and Stumpf, 1989).

Using Eq. $(14)_1$ together with Eqs. (13), (26), (27), and (28) in Eq. (33) and substituting the resulting equation into Eq. (32) and integrating, we obtain the two-dimensional strain energy density function of neo-Hookean circular plates accomodating both of the two foregoing definitions, Theory I ($q = 1$) and Theory II ($q = 0$):

$$\Phi^V = Et\{\bar{\lambda}^2_\phi + \lambda^2_\theta + \eta^2 + A^2 - 3 + t^2[A^2(K^2_\phi + K^2_\theta) + B(1 - q)(\bar{\lambda}_\phi K_\phi + \lambda_\theta K_\theta) + B^2 + 2AC]/12\} + \text{higher order terms}. \tag{34}$$

Consequently, in Eq. (29),

$$\begin{aligned} \Phi^V_{,\lambda_\theta}| &= 2Et(\lambda - \lambda^{-5}), \\ \Phi^V_{,K_\phi K_\phi}| &= Et^3(4\lambda^{-10} + q\lambda^{-4} - q\lambda^{-10})/6, \\ \Phi^V_{,\eta\eta}| &= 2Et. \end{aligned} \tag{35}$$

The results obtained from Eqs. (35) and (29) through a trial and error procedure are presented in Figs. 2 and 3 with the ones taken from Makowski and Stumpf (1989), which includes the

Downloaded 04 May 2010 to 171.66.16.33. Redistribution subject to ASME license or copyright; see http://www.asme.org/terms/Terms_Use.cfm

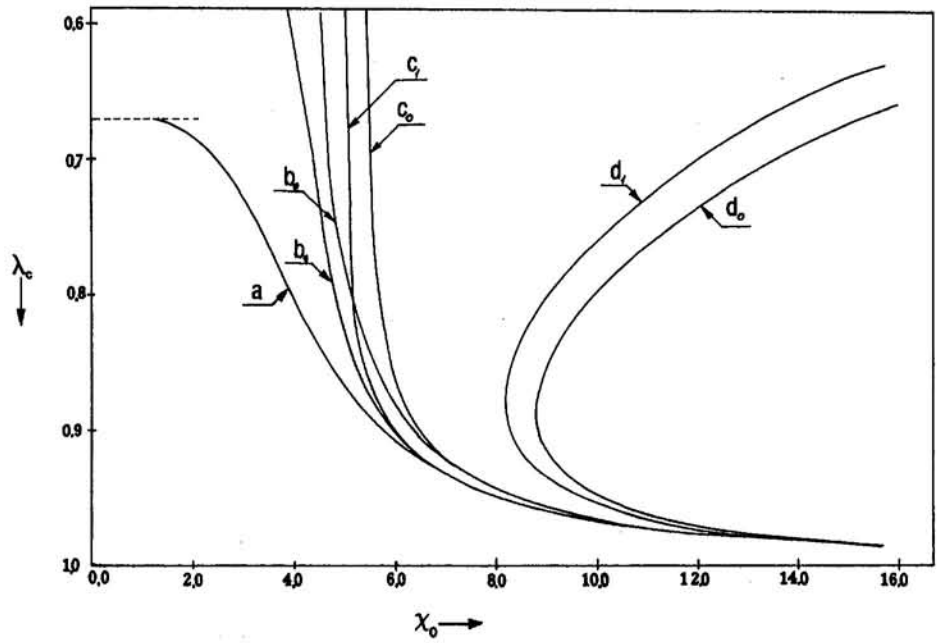


Fig. 2 Critical stretch versus initial thickness parameter χ_0 (a: Three-dimensional solution (Guo, 1962); b_1: solution due to Φ^Y with $q = 1$; b_0: solution due to Φ^Y with $q = 0$, coincides with shearable plate model of Makowski and Stumpf (1989); c_1: solution due to Φ^T with $q = 1$; c_0: solution due to Φ^T with $q = 0$; d_1: solution due to the two-dimensional strain energy density function of Simmonds (1986), $q = 1$; d_0: solution due to unshearable plate model of Makowski and Stumpf (1989), $q = 0$)

three-dimensional solution (Guo, 1962) and the results obtained through the two-dimensional strain energy density function due to Simmonds (1986) as well.

The results corresponding to $q = 1$ and $q = 0$ of Taber (1987) are added to Figs. 2 and 3. These results are obtained after a similar procedure followed above with the two-dimensional strain energy density function for neo-Hookean plates due to Taber (1987):

$$\Phi^T = Et[\lambda_\phi^2 + \lambda_\theta^2 + (\lambda_\phi\lambda_\theta)^{-2} - 3 + \eta^2/(1.2\lambda_\phi^2) + t^2\{K_\phi^2[\lambda_\phi^{-4}\lambda_\theta^{-2}(1 - q/4) + q/4] + K_\theta^2[\lambda_\phi^{-2}\lambda_\theta^{-4}(1 - q/4) + q/4] + K_\phi K_\theta[6(\lambda_\phi\lambda_\theta)^{-2} - \lambda_\phi^2 - \lambda_\theta^2 + q(\lambda_\phi^2 - 2\lambda_\phi^{-2}\lambda_\theta^{-2} + \lambda_\theta^2)]/(4\lambda_\phi\lambda_\theta)\}/3(\lambda_\phi\lambda_\theta)^2]. \quad (36)$$

From Figs. 2 and 3, the following statements can be deduced:

(i) Using the two-dimensional strain energy density function of the present study, Eq. (34), the results corresponding to $q = 1$ are better than those corresponding to $q = 0$, which

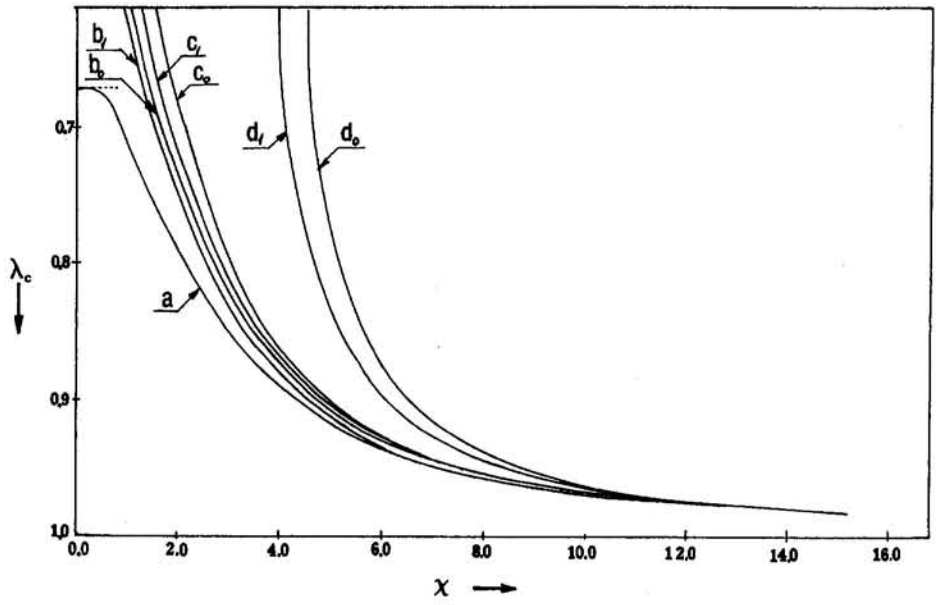


Fig. 3 Critical stretch versus current thickness parameter χ ($\chi = 2R/h = \lambda^3\chi_0$; h: current thickness) (a: Three-dimensional solution (Guo, 1962); b_1: solution due to Φ^Y with $q = 1$; b_0: solution due to Φ^Y with $q = 0$, coincides with shearable plate model of Makowski and Stumpf (1989); c_1: solution due to Φ^T with $q = 1$; c_0: solution due to Φ^T with $q = 0$; d_1: solution due to the two-dimensional strain energy density function of Simmonds (1986), $q = 1$; d_0: solution due to unshearable plate model of Makowski and Stumpf (1989), $q = 0$)

Downloaded 04 May 2010 to 171.66.16.33. Redistribution subject to ASME license or copyright; see http://www.asme.org/terms/Terms_Use.cfm

is what has been proposed in Makowski and Stumpf (1989) as shearable plate model.

(ii) Using Taber (1987), the results corresponding to $q = 1$ are better than those corresponding to $q = 0$.

(iii) For the relatively thin plates, the results corresponding to Simmonds (1986) in which transverse shearing strains are neglected and Theory I ($q = 1$) of Taber (1987) is used, are better than those corresponding to the unshearable plate model ($\eta = 0$) of Makowski and Stumpf (1989) in which Theory II ($q = 0$) of Taber (1987) is accepted.

4 Conclusions

According to the results obtained from the present study, the dynamic consistency condition of Simmonds (1986) produces a better approximation about the deformed reference surface of shells of revolution undergoing large strains and large rotations than the definition which assumes that the material composition of the reference surface does not change with deformation.

A by product of this study is an effective shell theory which is obtained by the modification of the theory presented by Makowski and Stumpf (1989). According to the results obtained, the resulting approach (with $q = 1$) seems to be the best of the ones mentioned in this paper and valid even for relatively thick rubber-like shells of revolution.

Acknowledgment

This work was supported by Deutscher Akademischer Austauschdienst e.V. under grant No. 313 (IInd Program). I thank Professors Başar and Krätzig, Ruhr University (Bochum, Germany), for their help in getting this support and for their opening the facilities of Ruhr University. Professor Cinemre has my special thanks for offering many valuable suggestions. My thanks are also due to Associate Professor Güralp for his meticulous drawing of the figures of the paper.

References

Green, A. E., and Adkins, J. E., 1960, *Large Elastic Deformations and Non-Linear Continuum Mechanics,* Clarendon Press, Oxford, U.K., p. 26.

Guo, Z. H., 1962, "Vibration and Stability of a Cylinder Subject to Finite Deformation," *Archives of Mechanics,* Vol. 14, pp. 757–768.

Makowski, J., and Stumpf, H., 1989, "Finite Axisymmetric Deformation of Shells of Revolution with Application to Flexural Buckling of Circular Plates," *Ingenieur—Archiv,* Vol. 59, pp. 456–472.

Simmonds, J. G., 1986, "The Strain-Energy Density of Rubber-Like Shells of Revolution Undergoing Torsionless, Axisymmetric Deformation (Axishells)," ASME JOURNAL OF APPLIED MECHANICS, Vol. 53, pp. 593–596.

Taber, L. A., 1987, "Large Elastic Deformation of Shear Deformable Shells of Revolution: Theory and Analysis," ASME JOURNAL OF APPLIED MECHANICS, Vol. 54, pp. 578–584.

Treloar, L. R. G., 1975, *The Physics of Rubber Elasticity,* 3rd ed., Clarendon Press, Oxford, U.K., pp. 214–218.

Downloaded 04 May 2010 to 171.66.16.33. Redistribution subject to ASME license or copyright; see http://www.asme.org/terms/Terms_Use.cfm

Melnikov Process for Stochastically Perturbed, Slowly Varying Oscillators: Application to a Model of Wind-Driven Coastal Currents

E. Simiu
NIST Fellow,
Building and Fire Research Laboratory,
National Institute of Standards
and Technology,
Gaithersburg, MD 20899

The stochastic Melnikov approach is extended to a class of slowly varying dynamical systems. It is found that (1) necessary conditions for chaos induced by stochastic perturbations depend on the excitation spectrum and the transfer function in the expression for the Melnikov transform; (2) the Melnikov approach allows the estimation of lower bounds for (a) the mean time of exit from preferred regions of phase space, and (b) the probability that exits from those regions cannot occur during a specified time interval. For a system modeling wind-induced currents, the deterministic Melnikov approach would indicate that chaotic transport cannot occur for certain parameter ranges. However, the more realistic stochastic Melnikov approach shows that, for those same parameter ranges, the necessary conditions for exits during a specified time interval are satisfied with probabilities that increase as the time interval increases.

Introduction

The Melnikov approach is a technique providing necessary conditions for the occurrence of chaos in a class of dynamical systems. Until recently it was considered to be applicable only to deterministic systems: deterministic chaos and stochastic motions were viewed as distinct and were analyzed from different, indeed contrasting points of view.

Beigie et al. (1991) extended Melnikov theory for a class of single-degree-of-freedom systems from the case of periodic to the case of quasi-periodic excitation. Their work allowed a further extension to the case of stochastic excitation (Frey and Simiu, 1993; Simiu and Frey, 1996). This extension used the representation of Gaussian excitations by Shinozuka processes (Shinozuka, 1971; Shinozuka and Deodatis, 1991), which have two properties needed for the application of Melnikov theory: uniform continuity and uniform boundedness. One result of this extension is that, under certain conditions, a motion can be both stochastic (i.e., induced by a realization of a stochastic process) *and* chaotic (i.e., sensitive to initial conditions).

Necessary conditions for chaos indicate the range of system parameters for which exits from preferred regions of phase space cannot occur. The Melnikov approach can thus help to study the exit problem for certain types of nonlinear stochastic systems to which no other analytical tools are applicable, e.g., multistable systems with dichotomous noise (Simiu and Hagwood, 1994). Examples of applications of the Melnikov approach include the rocking response of rigid objects to earthquakes (Yim and Lin, 1992) and the prediction of vessel capsizing in random beam seas (Hsieh, Troesch, and Shaw, 1994).

Necessary conditions for the occurrence of chaos in a class of slowly varying oscillators were obtained by Wiggins and Holmes (1987) and Wiggins and Shaw (1988) for the case of small periodic perturbations. This paper extends these authors' theory for perturbations that, rather than being periodic, are quasi-periodic or stochastic. Our results are based on arguments similar to those used by Beigie et al. (1991) and Frey and Simiu (1993) for single-degree-of-freedom systems, and on the application of the averaging theorem to systems with quasiperiodic perturbations (Verhulst, 1990).

We then consider a model of coastal currents over topography. We adopt the hydrodynamical model studied by Allen et al. (1991) for the ideal case of harmonic wind forcing, and apply our results to the more realistic case of forcing by randomly fluctuating wind.

Dynamical Systems

The systems we study are of the form

$$\dot{x} = \frac{\partial}{\partial y} H(x, y, z) + \epsilon g_1(x, y, z, t; \boldsymbol{\mu})$$

$$\dot{y} = -\frac{\partial}{\partial x} H(x, y, z) + \epsilon g_2(x, y, z, t; \boldsymbol{\mu})$$

$$\dot{z} = \epsilon g_3(x, y, z, t; \boldsymbol{\mu}) \tag{1.1}$$

where ϵ is small, the right-hand side is C^r differentiable ($r \geq 2$), $H(x, y, z)$ is a Hamiltonian with parameter z, $\boldsymbol{\mu}$ is a vector of parameters, and g_i ($i = 1, 2, 3$) are the perturbation functions. It is assumed that there exists an open interval $J \subset R$ such that, for every $z \in J$, the unperturbed system possesses a homoclinic orbit to a hyperbolic saddle point. In the full three-dimensional phase space the unperturbed system has a normally hyperbolic invariant one-dimensional manifold, $\gamma(z)$, assumed to be connected, and given by the union of saddle points of the one-parameter family of planar systems. $\gamma(z)$ has two-dimensional stable and unstable manifolds (denoted by $W^s(\gamma)$, $W^u(\gamma)$,

Contributed by the Applied Mechanics Division of THE AMERICAN SOCIETY OF MECHANICAL ENGINEERS for publication in the ASME JOURNAL OF APPLIED MECHANICS.

Discussion on this paper should be addressed to the Technical Editor, Professor Lewis T. Wheeler, Department of Mechanical Engineering, University of Houston, Houston, TX 77204-4792, and will be accepted until four months after final publication of the paper itself in the ASME JOURNAL OF APPLIED MECHANICS.

Manuscript received by the ASME Applied Mechanics Division, July 12, 1994; final revision, Jan. 23, 1995. Associate Technical Editor: M. Shinozuka.

Copyright © 1996 by ASME

Downloaded 04 May 2010 to 171.66.16.33. Redistribution subject to ASME license or copyright; see http://www.asme.org/terms/Terms_Use.cfm

respectively), such that their intersection $W^s(\gamma) \cap W^u(\gamma) \equiv \Gamma$ is the union of the homoclinic orbits of the planar systems.

Functions g_i ($i = 1, 2, 3$) With Common Period T

In this section we review pertinent material from Wiggins and Holmes (1987) and Wiggins and Shaw (1988). Let T^1 be the circle of unit length, and write Eq. (1) in the form

$$\dot{x} = \frac{\partial}{\partial y} H(x, y, z) + \epsilon g_1(x, y, z, \theta; \boldsymbol{\mu})$$

$$\dot{y} = -\frac{\partial}{\partial x} H(x, y, z) + \epsilon g_2(x, y, z, \theta; \boldsymbol{\mu})$$

$$\dot{z} = \epsilon g_3(x, y, z, \theta; \boldsymbol{\mu})$$

$$\dot{\theta} = \omega \tag{2.1}$$

where $\omega = 2\pi/T$. The normally invariant set at $\epsilon = 0$ is denoted by $M = (\gamma, \theta) = \gamma x T^1$, or

$$M = \left\{ (\gamma(z), \theta) \,|\, \gamma(z) = (x(z), y(z), z), \frac{\partial}{\partial y} H(x, y, z) \right.$$

$$\left. = -\frac{\partial}{\partial z} H(x, y, z) = 0, \left.\frac{\partial(\partial H/\partial y, -\partial H/\partial x)}{\partial(x, y)}\right|_{\gamma(z)} < 0, \theta \in T^1, z \in J \right\}. \tag{2.2}$$

Persistence Theorem. There exists ϵ_0 such that for $0 < \epsilon < \epsilon_0 \leq 1$ there exists a normally invariant manifold

$$M_\epsilon = \{(\gamma(z, \theta; \epsilon), \theta) = (\gamma(z) + O(\epsilon), \theta) | \theta \in T^1, z \in J\} \tag{2.3}$$

where $\gamma(z, \theta; \epsilon)$ is a C^r function of z and ϵ. M_ϵ has local stable and unstable manifolds $W^s_{\text{loc}}(M_\epsilon)$, $W^u_{\text{loc}}(M_\epsilon)$, which are C^r-close to the local stable and unstable manifolds of M, denoted $W^s_{\text{loc}}(M)$, $W^u_{\text{loc}}(M)$, respectively.

Flow on M_ϵ. For the perturbed vector field restricted to M_ϵ, Eqs. (2.1) and (2.3) yield

$$\dot{z} = \epsilon g_3(\gamma(z), \theta) + O(\epsilon^2). \tag{2.4}$$

($\boldsymbol{\mu}$ is omitted for simplicity). Consider the averaged system

$$\dot{z} = \epsilon \overline{g_3[\gamma(z)]}, \quad \overline{g_3[\gamma(z)]} = \frac{1}{T}\int_0^T g_3[\gamma(z), \theta] d\theta. \tag{2.5a, b}$$

If there exists $z_0 \in J$ such that

$$\overline{g_3(\gamma(z_0))} = 0, \quad \overline{d[g_3(\gamma(z_0))]}/dz \neq 0, \tag{2.6a, b}$$

then $(\gamma(z_0, \theta; \epsilon), \theta) = (\gamma(z_0) + O(\epsilon), \theta)$ is a hyperbolic periodic orbit on M_ϵ with period T. The orbit restricted to M_ϵ is stable or unstable for, respectively,

$$d\overline{[g_3(\gamma(z_0))]}/dz < 0 \quad \text{or} \quad d\overline{[g_3(\gamma(z_0))]}/dz > 0. \tag{2.7a, b}$$

Distance Between Stable and Unstable Manifolds and Necessary Condition for Chaos. We define the cross section through the unperturbed vector field $\Sigma = \{(x, y, z, \theta) | \theta = \theta_0 \in (0, 1)\}$ and the Poincaré map of Σ into itself, $P: \Sigma \to \Sigma$. If there exists $z_0 \in J$ satisfying Eqs. (2.6), the Poincaré section through the hyperbolic periodic orbit on M_ϵ is a hyperbolic fixed point $\gamma(z_0, \theta_0; \epsilon)$ having: a two-dimensional stable manifold and a one-dimensional unstable manifold if Eq. (2.7*a*) holds; or a one-dimensional stable manifold and a two-dimensional unstable manifold if Eq. (2.7*b*) holds. To first order, the distance between the stable and unstable manifolds of the perturbed system is proportional to the Melnikov function

$$m(s, \theta_0) = \int_0^\infty (\nabla H \cdot \mathbf{g})(q_0^{z_0}(t), \omega t + (\omega s + \theta_0)) dt - \frac{\partial H}{\partial z}(\gamma(z_0)) \int_0^\infty g_3(q_0^{z_0}(t), \omega t + (\omega s + \theta_0)) dt \tag{2.8}$$

where $\nabla H = (\partial H/\partial x, \partial H/\partial y, \partial H/\partial z)$, $\mathbf{g} = (g_1, g_2, g_3)$, z_0 satisfies Eqs. (2.6), $q_0^{z_0}(t)$ is the homoclinic orbit in the unperturbed system connecting the saddle point $\gamma(z_0)$ to itself, and (s, θ_0) specify a point on M and are therefore constant in the integral expression (Wiggins and Holmes, 1987). The Melnikov function can be interpreted as the sum of the outputs of three linear filters with inputs g_1, g_2, g_3, respectively.

If there exists an $\underline{s}$ such that, for fixed θ_0,

$$m(\underline{s}, \theta_0) = 0 \quad \text{and} \quad (\partial/\partial s)[m(\underline{s}, \theta_0)] \neq 0 \tag{2.9a, b}$$

then for sufficiently small ϵ near this point the stable and unstable manifolds of the fixed point $\gamma(z_0, \theta_0; \epsilon)$ intersect transversely. This implies the existence of transverse homoclinic points. The dynamics of the perturbed system can then give rise to a three-dimensional mapping with Smale horseshoes. This mapping has the same dynamics as a shift map acting on the space of bi-infinite sequences of 0's and 1's. The fact that the shift map has chaotic dynamics establishes that Eqs. (2.9) are a necessary condition for the perturbed system to be chaotic. This result is a special case of the Smale-Birkhoff theorem.

Quasi-Periodic Functions g_i ($i = 1, 2, 3$)

We now consider Eqs. (1.1), and assume that the perturbations are quasi-periodic in t, that is,

$$g_i(x, y, z, t) = g_{i0}(x, y, z) + \sum_{j=l_{(i-1)}+1}^{l_i} g_{ij}(x, y, z) \cos(\omega_j t + \theta_{j0})$$

$$(i = 1, 2, 3; l_0 = 0 < l_1 < l_2 < l_3 \equiv l \geq 2) \tag{3.1}$$

($\omega_j t + \theta_{j0} \equiv \theta_j$), where in general $\omega_1, \omega_2, \ldots, \omega_n$ are incommensurate. To study this system we follow the approach used by Beigie et al. (1991) for second-order systems with quasi-periodic vector fields. For Eq. (1.1) with quasi-periodic functions g_i the flow is no longer characterized by a Poincaré map, as is the case for periodic vector fields, but by a bi-infinite sequence of nonautonomous maps, where the maps are functions of time that change at each iteration.

Associated with the nonautonomous system involving l frequencies is the $(l + 3)$-dimensional autonomous system

$$\dot{x} = \frac{\partial}{\partial y} H(x, y, z) + \epsilon g_1(x, y, z, \theta_1, \theta_2, \ldots, \theta_{l1}; \boldsymbol{\mu})$$

$$\dot{y} = -\frac{\partial}{\partial x} H(x, y, z) + \epsilon g_2(x, y, z, \theta_{(l1+1)}, \theta_{(l1+2)}, \ldots, \theta_{l2}; \boldsymbol{\mu})$$

$$\dot{z} = \epsilon g_3(x, y, z, \theta_{(l2+1)}, \theta_{(l2+2)}, \ldots, \theta_l; \boldsymbol{\mu})$$

$$\dot{\theta}_1 = \omega_1$$

$$\vdots \tag{3.2}$$

$$\dot{\theta}_l = \omega_l.$$

The autonomous system's phase space for Eqs. (3.2) is $R^3 \times T^l$, where T^l is the l-torus. The expression

$$(x(t), y(t), z(t), \theta_1(t), \ldots, \theta_l(t)) = (\phi(t, t_0 = 0, x(0), y(0), z(0)), \omega_1 t + \theta_{10}, \ldots, \omega_l t + \theta_{l0}) \tag{3.3}$$

Downloaded 04 May 2010 to 171.66.16.33. Redistribution subject to ASME license or copyright; see http://www.asme.org/terms/Terms_Use.cfm

solves Eq. (3.2) and is referred to as the trajectory of Eq. (3.2) through $(x(0), y(0), z(0), \theta_{10}, \ldots, \theta_{l0})$ at time $t = 0$. For the unperturbed counterpart of Eqs. (3.2) the autonomous phase space contains for every $z \in J$ an l-dimensional normally hyperbolic invariant set $M^l = (\gamma, \theta_1, \ldots, \theta_l) = \gamma \times T^l$, or

$$M^l = \{(x, y, z, \theta_1, \ldots, \theta_l) | (x, y, z) = \gamma(z), z \in J\} \quad (3.4)$$

whose $(l + 1)$-dimensional stable and unstable manifolds, denoted $W^s(M^l)$ and $W^u(M^l)$, coincide along the $(l + 1)$-dimensional manifold given by

$$W^s(M^l) \cap W^u(M^l) = \{(x, y, z, \theta_1, \ldots, \theta_l) | (x, y, z) = q_0^z(t), t \in R\}. \quad (3.5)$$

Persistence Theorem. There exists ϵ_0 such that, for $0 < \epsilon < \epsilon_0 \leq 1$, there exists a normally invariant manifold

$$M_\epsilon^l = \{(\gamma(z, \theta_1, \theta_2, \ldots, \theta_l; \epsilon), \theta_1, \ldots, \theta_l) = (\gamma(z) + O(\epsilon), \theta_1, \ldots, \theta_l) | \times \theta_1, \ldots, \theta_l \in T^l, z \in J\} \quad (3.6)$$

where $\gamma(z, \theta_1, \theta_2, \ldots, \theta_l; \epsilon)$ is a C^r $(r \geq 2)$ function of z and ϵ. M_ϵ^l has local stable and unstable manifolds $W^s_{\text{loc}}(M_\epsilon^l)$ and $W^u_{\text{loc}}(M_\epsilon^l)$, which are C^r-close to the local stable and unstable manifolds of M^l, $W^s_{\text{loc}}(M^l)$ and $W^u_{\text{loc}}(M^l)$, respectively. The proof of the theorem is independent of whether g_i are periodic or quasi-periodic; it is the same as in Wiggins and Holmes (1987).

Flow on M_ϵ^l. For the perturbed vector field restricted to M_ϵ^l there follows from Eqs. (3.2) and (3.6)

$$\dot{z} = \epsilon g_3(\gamma(z), \theta_1, \ldots, \theta_l) + O(\epsilon^2). \quad (3.7)$$

We now consider the averaged system

$$\dot{z} = \epsilon \overline{g_3[\gamma(z)]}, \quad (3.8a)$$

$$\overline{g_3[\gamma(z)]} = \sum_{j=l_2+1}^{l} \frac{1}{T_j} \int_0^{T_j} g_3(\gamma(z), \theta_1, \ldots, \theta_l) d\theta_j \quad (3.8b)$$

$(T_j = 2\pi/\omega_j)$. If there exists $z_0 \in J$ such that

$$\overline{g_3(\gamma(z_0))} = 0, \quad d[\overline{g_3(\gamma(z_0))}]/dz \neq 0 \quad (3.9a, b)$$

then $(\gamma(z_0, \theta_1, \ldots, \theta_l; \epsilon), \theta_1, \ldots, \theta_l) = (\gamma(z_0) + O(\epsilon), \theta_1, \ldots, \theta_l)$ is a hyperbolic T^l-torus on M_ϵ^l, and the orbit restricted to M_ϵ^l is stable or unstable for, respectively,

$$d\overline{[g_3(\gamma(z_0))]}/dz < 0 \text{ or } d\overline{[g_3(\gamma(z_0))]}/dz > 0. \quad (3.10a, b)$$

The proof of this proposition follows exactly the same steps as its counterpart for periodic functions g_i, with one exception: instead of the classical averaging theorem, in which averaging is defined as in Eq. (2.5b), the proof uses the averaging theorem as applied to quasiperiodic perturbations, where averaging is defined as in Eq. (3.8a)—see, e.g. (Verhulst, 1990, p. 154).

Distance Between Stable and Unstable Manifolds and Necessary Condition for Chaos. A global cross section of the autonomous phase space is defined by

$$\Sigma^{\theta_{j0}}\{(x, y, z, \theta_1, \ldots, \theta_l) | \theta_j = \theta_{j0}\} \quad 1 \leq j \leq l. \quad (3.11)$$

The associated Poincaré map is

$$P_\epsilon: \Sigma^{\theta_{j0}} \to \Sigma^{\theta_{j0}} \quad (3.12)$$

$$(x, y, z, \boldsymbol{\theta}_0 + 2\pi n \boldsymbol{\omega}/\omega_j) \to \{\phi[(2\pi/\omega_j)(n + 1), (2\pi/\omega_j)n, x, y, z)], \boldsymbol{\theta}_0 + 2\pi n \boldsymbol{\omega}/\omega_j\} \quad (3.13)$$

where $\boldsymbol{\theta}_0 \equiv (\theta_{10}, \ldots, \theta_{(j-1)0}, \theta_{(j+1)0}, \ldots, \theta_{l0})$, $\boldsymbol{\omega} \equiv (\omega_1, \ldots, \omega_{j-1}, \omega_{j+1}, \ldots, \omega_l)$. Since this map is obtained from an autonomous system, it is independent of n. The Poincaré map is equivalent to sampling the trajectories of the system (3.2) at time intervals $2\pi/\omega_j$. For each z the Poincaré map of the unperturbed system has a normally hyperbolic $(l - 1)$-torus

$$\tau_0 = T_0 \cap \Sigma^{\theta_{j0}} = \{(x, y, z, \theta_1, \ldots, \theta_l) | (x, y, z) = \gamma(z), \theta_j = \theta_{j0}\} \quad (3.14)$$

with an l-dimensional homoclinic manifold

$$W^s(\tau_0) \cap W^u(\tau_0) = \{(x, y, z, \theta_1, \ldots, \theta_l) | (x, y, z) = q_0^z(t), \theta_j = \theta_{j0}, t \in R\}.$$

We now consider the generalized Melnikov function

$$m(s, \theta_1, \theta_2, \ldots, \theta_l) = \int_0^\infty (\nabla H \cdot \mathbf{g})(q_0^{z^0}(t), \omega_1 t + (\omega_1 s + \theta_1), \omega_2 t + (\omega_2 s + \theta_2), \ldots, \omega_l t + (\omega_l s + \theta_l)) dt - \frac{\partial H}{\partial z}(\gamma(z_0)) \int_0^\infty g_3(q_0^{z^0}(t)), \omega_1 t + (\omega_1 s + \theta_1), \omega_2 t + (\omega_2 s + \theta_2), \ldots, \omega_l t + (\omega_l s + \theta_l)) dt \quad (3.15)$$

where $\nabla H = (\partial H/\partial x, \partial H/\partial y, \partial H/\partial z)$, $\mathbf{g} = (g_1, g_2, g_3)$, z_0 satisfies Eqs. (3.9), $q_0^{z^0}(t)$ is the homoclinic orbit in the unperturbed system connecting $\gamma(z_0)$ to itself, and $(s, \theta_1, \theta_2, \ldots, \theta_{(l-1)}, \theta_l)$ specify a point on the manifold $W^s(M^l) \cap W^u(M^l)$ of the unperturbed system and are therefore constant in the integral expression. In the Poincaré section, the generalized Melnikov function has the same expression as in Eq. (3.15), except that θ_j takes on the fixed value θ_{j0}. Like the Melnikov function for periodic g_i's, the generalized Melnikov function may be interpreted as the sum of the outputs of three linear filters with inputs g_1, g_2, g_3, respectively.

For $\boldsymbol{\theta} \equiv (\theta_1, \theta_2, \ldots, \theta_{(j-1)}, \theta_{(j+1)}, \ldots, \theta_l) \in T^{l-1}$, we refer to the plane $\chi(x, y, z; \underline{\boldsymbol{\theta}}) \equiv \{x, y, z, \boldsymbol{\theta} | \boldsymbol{\theta} = \underline{\boldsymbol{\theta}}\}$ as a three-dimensional phase slice of the Poincaré section $\Sigma^{\theta_{j0}}$. If there exists a point $(\underline{s}, \underline{\theta}_1, \underline{\theta}_2, \ldots, \underline{\theta}_{(j-1)}, \underline{\theta}_{(j+1)}, \ldots, \underline{\theta}_l)$ such that

$$m(\underline{s}, \underline{\theta}_1, \underline{\theta}_2, \ldots, \underline{\theta}_{(j-1)}, \theta_{j0}, \underline{\theta}_{(j+1)}, \ldots, \underline{\theta}_l) = 0, \quad \text{and} \quad (3.16a)$$

$$(\partial/\partial s)[m(\underline{s}, \underline{\theta}_1, \underline{\theta}_2, \ldots, \underline{\theta}_{(j-1)}, \theta_{j0}, \underline{\theta}_{(j+1)}, \ldots, \underline{\theta}_l)] \neq 0 \quad (3.16b)$$

then, for sufficiently small ϵ, near this point the generalized Melnikov function in the Poincaré has simple zeros, that is, the stable and unstable manifolds of the Poincaré section of M_ϵ^l intersect transversely, i.e., there exist transverse homoclinic points. A phase slice in the quasiperiodic perturbation case differs from a Poincaré map for the periodic case in that the phase slice changes at each successive time $2\pi/\omega_{j0}$, whereas the Poincaré map repeats itself at successive times $2\pi/\omega$. This observation allows the extension of the Smale-Birkhoff theorem from the case of periodic perturbations to the case of quasiperiodic perturbations (Beigie et al., 1991). As is the case for the periodically perturbed system studied by Wiggins and Shaw (1988), the dynamics of the quasi-periodically perturbed system having a Melnikov function with simple zeros can give rise to a mapping with Smale horseshoes which is equivalent to a shift map acting on the space of bi-infinite sequences of 0's and 1's. This establishes that Eqs. (3.15) are a necessary condition for the system with quasi-periodic perturbation to be chaotic.

Necessary conditions for the occurrence of chaos follow immediately from Eqs. (3.15) for (a) perturbation functions g_1, g_2, g_3 with incommensurate periods T_1, T_2, T_3, respectively; (b) one quasi-periodic function and two periodic functions having

Downloaded 04 May 2010 to 171.66.16.33. Redistribution subject to ASME license or copyright; see http://www.asme.org/terms/Terms_Use.cfm

different or equal periods; (c) two quasi-periodic functions and one periodic function; (d) any set of perturbation functions that may be approximated by finite sums of harmonic terms.

Stochastic Perturbations

We now assume g_i $(i = 1, 2, 3)$ are additive Gaussian processes with specified spectral densities. Such processes may be modeled effectively by ensembles of harmonic sums. Since the proof of the persistence theorem—a prerequisite for Melnikov analysis—requires that the perturbations be bounded and uniformly continuous, we use the Shinozuka (1971) representation of Gaussian noise, which has the requisite properties

$$G_i(t) = (1/2\pi)^{1/2}(2/l)^{1/2} \sum_{n=1}^{l} \cos(\omega_{in}t + \theta_{in0}) \qquad (i = 1, 2, 3) \quad (4.1)$$

where l is a parameter of the model (the approximation of a Gaussian process by the model improves as l increases), $\{\omega_{in}, \theta_{in0}; n = 1, \ldots, l\}$ are independent random variables, $\{\theta_{in0}, n = 1, \ldots, l\}$ are identically uniformly distributed over the interval $[0, 2\pi]$, $\{\omega_{in}; n = 1, \ldots, l\}$ are non-negative with common distribution equal to the spectral density of the process, Ψ_{i0}, and

$$\frac{1}{2\pi}\int_0^\infty \Psi_{i0}(\omega)d\omega = 1. \qquad (4.2)$$

In this model all the harmonics have equal amplitude $(1/\pi l)^{1/2}$, and the number of harmonics with frequencies contained in a given interval is proportional to the area under the spectral curve within that interval. Equation (4.1) can approximate a Gaussian process as closely as desired provided that the finite value of l is sufficiently large. We assume

$$g_i(x, y, z, t) = g_{i0}(x, y, z) + \sigma_i G_i(t) \qquad (4.3)$$

$(i = 1, 2, 3)$. Each realization in Eq. (4.3) has a different set of random parameters $\{\omega_{in}, \theta_{in0}; n = 1, \ldots, l\}$. Since l is finite, the arguments presented in the previous section for quasiperiodic excitations apply without change for stochastic excitations approximated by the Shinozuka model as in Eq. (4.2) (Frey and Simiu, 1993). To each path there corresponds a Melnikov function similar to Eq. (3.15). We noted earlier that the Melnikov function is the sum of the outputs of three linear filters with inputs g_1, g_2, g_3. For sufficiently large l, each of the three sums approaches a Gaussian process, the mean and variance of which can easily be calculated since the filter properties are known. Therefore in the limit of large l the Melnikov process is Gaussian, and the probability that it has simple zeros is one—no matter how small the noise—provided that the time interval being considered is infinitely long (Frey and Simiu, 1993). However, the probability that a path of the Melnikov process has simple zeros during a finite time interval T is $p_T < 1$. Let the mean and standard deviation of the Melnikov process be $E[m]$ and σ_m. If the ratio $k = E[m]/\sigma_m$ is sufficiently large (say, $k > 2$), then p_T can be closely approximated by using: (a) the Kac-Rice formula (Rice, 1958) for the rate of upcrossing, $E(k)$, of a threshold k by a standardized Gaussian process with one-sided spectral density $\Psi_m(\omega)$, and (b) the assumption that the upcrossing is a rare event described by a Poisson process. Then

$$p_T = 1 - \exp[-E(k)T], \quad E(k) = \nu \exp(-k^2/2) \qquad (4.4a, b)$$

$$\nu = (1/2\pi)\left\{\left[\int_0^\infty \omega^2\Psi_m(\omega)d\omega\right] \Big/ \left[\int_0^\infty \Psi_m(\omega)d\omega\right]\right\}^{1/2}. \qquad (4.5)$$

Let t_{ex} be the mean time spent by the system in a region of phase space associated with a potential well before it exits from that region. In the limit of weak perturbations t_{ex} must be at least as large as $1/\nu$ (there can be no exit from that region as long as the stable and unstable manifolds do not intersect). Therefore $1/\nu$ is a lower bound for t_{ex}, and p_T is a lower bound for the probability that $t_{ex} > T$ (Simiu and Frey, 1996).

The case of multiplicative noise involves a simple modification of the Melnikov process filter (Frey and Simiu, 1995).

Necessary Conditions for Chaos in a Model of Wind-Induced Coastal Current

Allen et al. (1991) studied a model of ocean flow over a continental margin with variable bottom topography under wind forcing fluctuating harmonically. Our extension of the results by Wiggins and Holmes (1987) and Wiggins and Shaw (1988) to the case of stochastic forcing allows us to examine the model under the assumption that the wind fluctuations are random.

Fluctuating Wind and Surface Wind Stresses. We consider the horizontal wind speed fluctuations spectrum developed by Van der Hoven (1957). The spectrum has three main parts: one with a peak at a period of about four days, a second, known as the spectral gap, having negligible energy and extending over periods of about five hours to three minutes, and a third, with a peak at a period of about one minute, where fluctuations have relatively small spatial coherence and therefore a negligible overall effect at the scale of our problem (Simiu and Scanlan, 1986). The relevant part of the spectrum is, approximately,

$$S(\omega) = \begin{cases} 0.2823 \ln(\omega) + 1.300 & 0.01 \le \omega \le 0.10 \\ 0.4072 \ln(\omega) + 1.599 & 0.10 \le \omega \le 0.30 \\ -2.71[\ln(\omega)]^2 + 5 & 0.30 \le \omega \le 3.85 \end{cases} \qquad (5.1)$$

where $\omega = \Omega/\Omega_{pk}$, Ω is the dimensional frequency and $\Omega_{pk} \approx 2\pi/(\text{four days})$ is the dimensional frequency corresponding to the spectral peak, which occurs at $\omega = 1$. The units of $S(\omega)$ are m^2/s^2 (Fig. 1). For the spectrum of Eq. (5.1) the standard deviation of the wind speed fluctuations is $\sigma_w \approx 1.33$ m/s.

Surface wind stresses are proportional to the square of the wind speeds (Simiu and Scanlan, 1986). We assume that the effect of thermal stratification and of deviations from the prevailing wind direction is small. Mean wind speeds of about 6 m/s are consistent with the data used to obtain the Van der Hoven spectrum (NOAA, 1977), so that the coefficient of variation of the wind speed fluctuations is about 0.20. To a first approximation, one may therefore neglect the square of the wind speed fluctuations in the expansion of $[U + u(t)]^2$, where U and $u(t)$ are the mean and fluctuating wind speed (Simiu and Scanlan, 1986; Vaicaitis and Simiu, 1977). The normalized

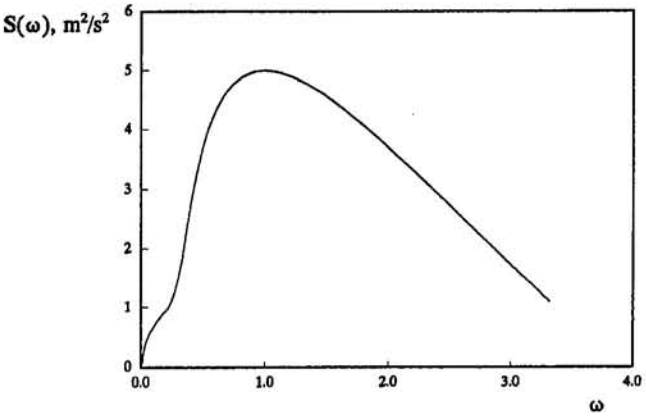


Fig. 1 Spectral density of wind speed fluctuations, $S(\omega)$

Downloaded 04 May 2010 to 171.66.16.33. Redistribution subject to ASME license or copyright; see http://www.asme.org/terms/Terms_Use.cfm

spectrum of the surface wind stresses is then $\Psi_0(\omega) \approx S(\omega)/\sigma_w^2$, and the wind stresses may be assumed to be Gaussian.

Offshore Flow Model. The nondimensional equations for the model flow are given by Eqs. (1.1), where x is a basic alongshore speed, y is proportional to the out-of-phase component of a stream function for motion due to the topography, and z is the energy-enstrophy:

$$g_1 = -rx + \tau_0 + \tau(t), \quad g_2 = -ry,$$

$$g_3 = -rz - \tfrac{1}{2}rx^2 + (x-1)[\tau_0 + \tau(t)] \qquad (5.2)$$

$$H(x, y, z) = \tfrac{1}{2}y^2 + zx + \tfrac{1}{2}(\omega_0^2 - z)x^2 - \tfrac{1}{2}x^3 + (\tfrac{1}{8})x^4,$$

$$\omega_0^2 = 1 + \delta^2. \qquad (5.3)$$

δ is the amplitude of the bottom topography corrugations, ϵr is a friction coefficient related to the eddy viscosity of the ocean flow, and $\epsilon\tau_0$ and $\epsilon\tau(t)$ are, respectively, the steady and fluctuating wind stress at the ocean surface (Allen et al., 1991).

We assume $\tau(t)$ is a Gaussian process with variance σ^2 and one-sided spectral density $\sigma^2\Psi_0(\omega)$, and approximate it as

$$\tau(t) = \sigma G(t) \qquad (5.4)$$

where $G(t)$ has an expression similar to that of $G_i(t)$ in Eq. (4.12). The stochastic excitation is multiplicative (Eq. (5.2c)).

The dynamics of the unperturbed system was studied by Allen et al. (1991), who showed that for $z > z_c = (\frac{3}{2})\delta^{4/3} + \delta^2 - \frac{1}{2}$ the phase plane diagram x-y (z = const) has a saddle point and two elliptic centers with coordinates satisfying the expressions

$$x^3 - 3x^2 + 2(\omega_0^2 - z)x + 2z = 0, \quad y = 0, \quad (5.5a, b)$$

and contains an asymmetrical eight-shaped homoclinic orbit which asymptotically approaches the saddle point in forward and backward time. The two lobes of the homoclinic orbit separate three distinct regions of phase space, corresponding to three oscillatory regimes: one inside each lobe of the separatrix and a third outside the separatrix. The saddle point corresponds to the intermediate root of Eq. (5.5a). The saddle point and the separatrix depend continuously on z and form, respectively, a one-dimensional manifold $\gamma(z)$ of (x, y, z) points and a two-dimensional manifold of (x, y, z) points.

The existence of an oscillatory solution—a hyperbolic T^l-torus—among the solutions of the invariant manifold M_ϵ of the perturbed system is established by solving Eqs. (3.9). Since the integrals of the harmonic terms vanish, Eqs. (3.9) yield exactly the same solution as in the harmonic perturbation case, that is,

$$z = -\tfrac{1}{2}x^2 + (x-1)\tau_0/r, \qquad (5.6)$$

$$d\overline{[g_3(\gamma(z_0))]}/dz < 0 \qquad (5.7)$$

(Allen et al., 1991). The coordinates (x_0, y_0, z_0) that define to first order the hyperbolic T^l-torus on the invariant manifold M_ϵ^l are obtained from Eqs. (5.5) and (5.6), and from Eq. (5.7) it follows that the orbit restricted to M_ϵ^l is linearly stable.

For harmonic excitation $\tau(t) = \tau_1 \cos(\omega t)$, Allen et al. (1991) obtained for the Melnikov function the expression

$$m(s, \theta_0) = rC_1 + \tau_1 C_2(\omega)\cos(\omega s + \theta_0) \qquad (5.8)$$

$$C_1 = C_1^{\pm} = (x_0 - \tau_0/r)[8d\tan^{-1}(V_{m\pm}/(2k_0)) - k_0 b] \qquad (5.9)$$

$$C_2(\omega) = C_2^{\pm}(\omega) = -4\pi d\,\frac{\sinh[\omega\cos^{-1}(\alpha_\pm)/k_0]}{\sinh(\omega\pi/k_0)} \qquad (5.10)$$

$$k_0 = (z_0 - \omega_0^2 + 3x_0 - (\tfrac{3}{2})x_0^2)^{1/2} > 0 \qquad (5.11)$$

$$d = k^2 + (x_0 - 1)^2, \quad \alpha_\pm = \frac{bV_{m\pm}}{8k_2 - bV_{m\pm}},$$

$$b = 4(x_0 - 1), \qquad (5.12a, b, c)$$

$$V_{m\pm} = \tfrac{1}{2}[-b \pm (b^2 + 16k^2)^{1/2}]. \qquad (5.12d)$$

$C_2(\omega)$ may be interpreted as a linear transfer function. It is also referred to as scaling actor (Beigie et al., 1991). From the linearity of Eq. (3.15) with respect to the perturbative terms it follows that, if the perturbation is given by Eqs. (5.2) and (5.4), the expression for the Melnikov process is

$$m(s, \theta_{10}, \theta_{20}, \ldots, \theta_{l0}) = rC_1 + [(1/2\pi)(2/l)]^{1/2}\sigma \sum_{n=1}^{l} C_2(\omega_n) \times \cos[\omega_n t + (\omega_n s + \theta_{n0})]. \qquad (5.13)$$

The expectation and variance are (Frey and Simiu, 1993):

$$E[m(s, \theta_{10}, \theta_{20}, \ldots, \theta_{l0})] = rC_1. \qquad (5.14)$$

$$\text{Var}[m(s, \theta_{10}, \theta_{20}, \ldots, \theta_{l0})] = \frac{\sigma^2}{2\pi}\int_0^\infty C_2^2(\omega)\Psi_0(\omega)d\omega. \qquad (5.15)$$

Example. We consider the case, also studied by Allen et al. (1991), $\delta = 0.3003$, $\tau_0/r = 3.236 \times 10^{-3}$. The unperturbed system has the fixed points $\{0, 0\}$, $\{1.236, 0\}$, and $\{1.764, 0\}$ (Eqs. (5.5)). From Eqs. (5.9) to (5.12), $C_1^+ = 2.524$, $C_1^- = -7.076$, and

$$C_2^+(\omega) = -4.8\sinh(2.064\omega)/\sinh(5.500\omega) \qquad (5.16)$$

$$C_2^-(\omega) = -4.8\sinh(3.436\omega)/\sinh(5.500\omega). \qquad (5.17)$$

For harmonic forcing (Eq. (5.7)) with $\omega = 1$ (a case examined by Allen et al., 1991), and assumed therein also to correspond to a dimensional time $T_{pk} \approx$ four days), $C_2^+ = -0.152$, $C_2^- = -0.609$, and the necessary condition for exits from the region corresponding to the interior of the left lobe is satisfied for $\sigma/r > 8.22$, where σ is the standard deviation of the harmonic forcing, i.e., $\sigma = \tau_1/(2)^{1/2}$. The inequality $\sigma/r > 11.74$ obtains for the right well. If $\sigma/r < 8.22$ there can be no exits from the left region and, a fortiori, from the right region as well. Note that, for $\omega = 1$, the excitation needed to satisfy the necessary condition for the occurrence of chaos is stronger for the right well (which is the smaller of the two wells) and weaker for the larger well.

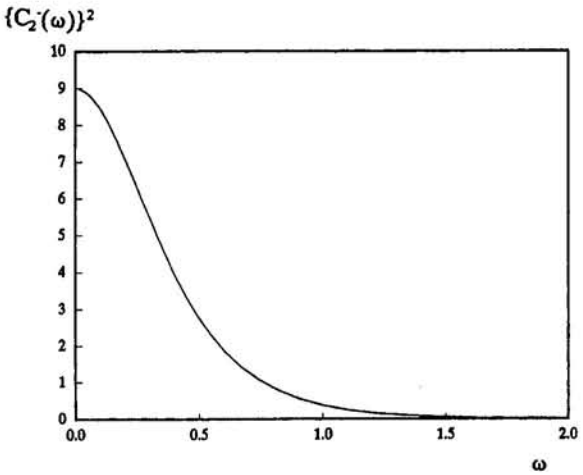


Fig. 2 Square of transfer function, $[C_2^-(\omega)]^2$

Downloaded 04 May 2010 to 171.66.16.33. Redistribution subject to ASME license or copyright; see http://www.asme.org/terms/Terms_Use.cfm

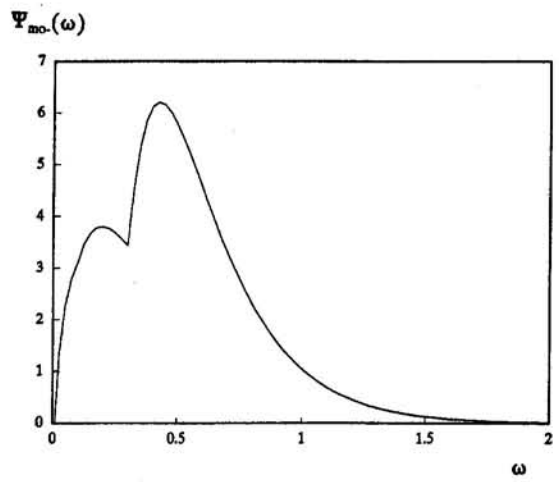


Fig. 3 Spectral density of Melnikov process $\Psi_{mo-}(\omega)$

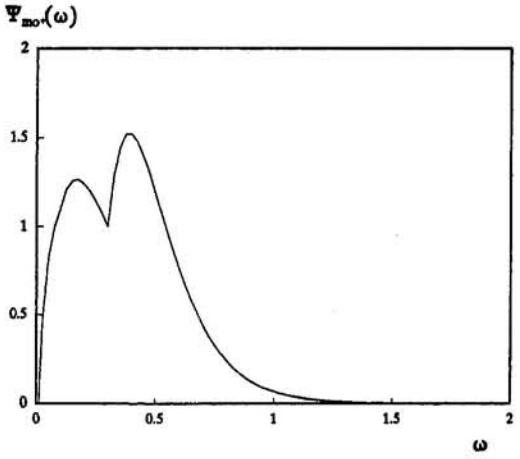


Fig. 5 Spectral density of Melnikov process $\Psi_{mo+}(\omega)$

We now consider the case of random forcing with spectrum $\sigma^2\Psi_0(\omega)$. Figures 2 and 3 show, respectively, the square of the transfer function, $[C_2^-(\omega)]^2$, and the spectral density of the Melnikov process for $\sigma = 1$, $\Psi_{mo-}(\omega) = [C_2^-(\omega)]^2\Psi_0(\omega)$. Figures 4 and 5 represent $[C_2^+(\omega)]^2$ and $\Psi_{mo+}(\omega) = [C_2^+(\omega)]^2\Psi_0(\omega)$, respectively. Equation (4.5) applied to $\Psi_{mo-}(\omega)$ and $\Psi_{mo+}(\omega)$ yields $\nu^- = 0.0702$ and $\nu^+ = 0.0534$, respectively. The transfer functions are seen to suppress or considerably reduce the spectral components of the wind stress with frequencies $\omega > 1$ or so, and to amplify lower frequency components. The standard deviations of the Melnikov process are $\sigma_{m+} = 0.359\sigma$ and $\sigma_{m-} = 0.778\sigma$, respectively, so $k_{-1} = |E[m_-]/\sigma_{m-}| = 9.1r/\sigma$ and $k_+ = |E[m_+]/\sigma_{m+}| = 7.03r/\sigma$. We assume $\sigma/r < 8.22$, say, $\sigma/r = 4$, so $k_- = 2.275$ and $k_+ = 1.76$. From Eq. (4.4b), $E(k_-) = 0.0053$ and $E(k_+) = 0.0113$. We have $1/E(k_-) = 188.6$ (i.e., $188.6 \times 4/(2\pi) = 119.7$ days) and $1/E(k_+) = 88.5$ (56.3 days), so $1/E(k_-) > 1/E(k_+)$, as one would intuitively expect (the left well is larger than the right well). For $T = 1$ month (i.e., 47.1 nondimensional time units), $p_{T-=1mo} = 0.22$ (Eq. (4.4a)); for one year $p_{T-=1yr} = 0.95$. Also, $p_{T+=1mo} = 0.41$, $p_{T+=1yr} = 0.998$.

Suppose a decision would hinge on whether, given the wind spectrum (5.1), the probability of nonoccurrence of chaotic jumps in the current would be at least 0.5 during one month. The lower bounds $1 - p_{T-=1mo} = 1 - 0.22 = 0.78$ and $1 - p_{T+=1mo} = 0.59$ would provide a conservative basis for such a decision.

To recapitulate, the possibility of chaos was assessed using the Melnikov approach for two cases for which the values of δ and τ_0/r were the same. In the first case the excitations induced by wind were harmonic with standard deviation $\sigma = 8.22r$ and frequency $\omega = 1$ (dimensional period $T =$ four days), that is, the entire energy of the wind stresses was concentrated at the frequency of the wind stress spectral peak. From the Melnikov approach it follows that no exits are possible in this case.

In the second case the wind stress fluctuations were random and were derived from the Van der Hoven wind spectrum whose peak is at $T_{pk} =$ four days. The standard deviation of the wind stresses was $\sigma = 4r$, that is, less than half as large as that of the largest harmonic forcing that precludes the occurrence of exits ($\sigma = 8.2r$). In this case the necessary conditions for the occurrence of chaos were satisfied with relatively high probability for an interval of one year, and with probability of the order of about 0.4 for an interval of one month. The probabilities would be considerably higher if the standard deviation of the wind stresses were assumed to be $\sigma = 8.2r$.

Illustrations of chaotic motions for $\delta = 0.3003$, $\epsilon = 0.001$, $\tau_0/r = 3.236$ and $r = 0.01$ are shown in Figs. 6(a) and 6(b). Figures 6 show time histories of $x(t)$ for (a) periodic forcing, $\sigma = 21.21$ ($\tau_1 = 30$), $\omega = 1$, $x(0) = 1.236$, $y(0) = z(0) = 0$, and (b) stochastic forcing (see Appendix), $\sigma = 8$, $x(0) = 10^{-5}$, $y(0) = z(0) = 0$. We note that while theoretical proofs require the use of uniformly bounded and uniformly continuous noise, the method used to generate a noise realization numerically need not conform to this requirement. The time histories were obtained by numerical integration with tolerances 10^{-6}. The sensitivity to initial conditions was verified numerically by following the evolutions in time of small separations introduced

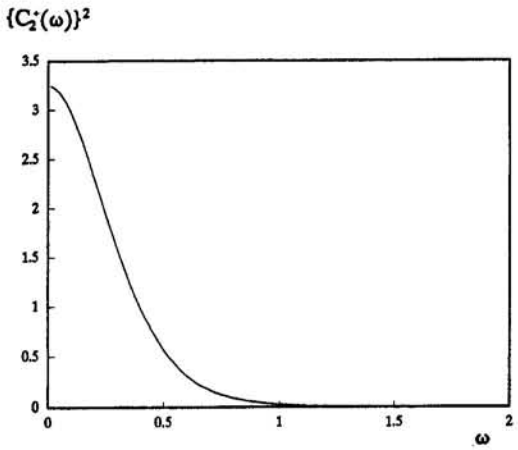


Fig. 4 Square of transfer function, $[C_2^+(\omega)]^2$

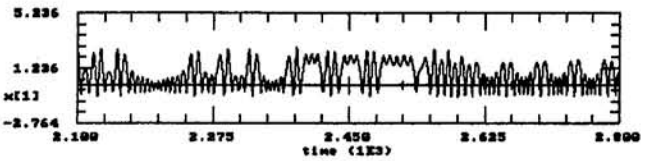


Fig. 6(a)

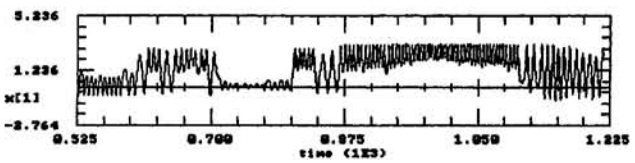


Fig. 6(b)

Fig. 6 Record of chaotic motion for (a) harmonic forcing; (b) realization of random forcing

Downloaded 04 May 2010 to 171.66.16.33. Redistribution subject to ASME license or copyright; see http://www.asme.org/terms/Terms_Use.cfm

in the initial values of the equations of motion—see, e.g., Bergé, Pomeau, and Vidal, 1984, p. 129.

Summary and Conclusions

For stochastically perturbed systems, the applicability of the Melnikov approach can be extended from a class of two-dimensional oscillators (Frey and Simiu, 1993) to a class of slowly varying oscillators studied by Wiggins and Holmes (1987) and Wiggins and Shaw (1988) for periodic perturbation. This extension was applied to a model of offshore currents driven by wind speed fluctuations, studied by Allen et al. (1991) for the periodic fluctuation case. The following results were obtained: (1) necessary conditions for chaos induced by stochastic perturbations depend on the shapes of both the spectra of the stochastic excitations *and* the transfer functions in the expression for the Melnikov transform; (2) the development of a stochastic Melnikov process allows the estimation of (a) a lower bound for the mean time of exit from each of the regions of phase space associated with a potential well; and (b) provided that the excitation is sufficiently small in relation to the damping, of an upper bound for the probability of occurrence of exits from each well during a specified time interval.

We then applied the Melnikov approach to a model of wind-driven coastal currents. If the wind fluctuations were assumed to be deterministic, the Melnikov approach led to the conclusion that for a certain range of parameters exits could not occur. For the same system, with the same parameters, but assumed to be excited by randomly fluctuating winds, the stochastic Melnikov approach led to the conclusion that the necessary conditions for the occurrence of exits during various specified time intervals were in fact satisfied with relatively high probabilities. Applying a deterministic Melnikov approach to a stochastic system may thus yield the result that exits cannot occur under conditions in which their occurrence is in fact possible.

Acknowledgments

Support by the Office of Naval Research, Ocean Eng. Div. (Contr. No. N00014-94-0028) is acknowledged with thanks. Doctor Tom Swean served as project monitor.

References

Allen, J. S., Samelson, R. M., and Newberger, P. A., 1991, "Chaos in a Model of Forced Quasi-Geostrophic Flow Over Topography: An Application of Melnikov's Method," *Journal of Fluid Mechanics,* Vol. 226, pp. 511–547.

Bergé, P., Pomeau, Y., and Vidal, C., 1984, *Order Within Chaos,* John Wiley and Sons, New York.

Beigie, D., Leonard, A., and Wiggins, S., 1991, "Chaotic Transport in the Homoclinic and Heteroclinic Tangle Regions of Quasiperiodically Forced Two-Dimensional Dynamical Systems," *Nonlinearity,* Vol. 4, pp. 775–819.

Frey, M., and Simiu, E., 1993, "Noise-Induced Chaos and Phase Space Flux," *Physica D,* pp. 321–340.

Frey, M., and Simiu, E., 1995, "Noise-Induced Transitions to Chaos," *Proceedings, NATO Advanced Workshop on Spatio-Temporal Patterns in Nonequilibrium Complex Systems,* P. Cladis and P. Pally-Muhoray, eds., Addison-Wesley, New York, pp. 529–544.

Hsieh, S. R., Troesch, A. W., and Shaw, S., 1994, "A Nonlinear Probabilistic Method for Predicting Vessel Capsizing in Random Beam Seas," *Proceedings, Royal Society of London,* Vol. A446, pp. 195–211.

NOAA, 1977, "Local Climatological Annual Summaries," National Oceanic and Atmospheric Administration, Environmental Data Service, Asheville, N.C.

Rice, S. O., 1954, "Mathematical Analysis of Random Noise," *Selected Papers in Noise and Stochastic Processes,* A. Wax, ed., Dover, New York.

Shinozuka, M., 1971, "Simulation of Multivariate and Multidimensional Random Processes," *Journal of the Acoustical Society of America,* Vol. 49, pp. 347–357.

Shinozuka, M., and Deodatis, G., 1991, "Simulation of Stochastic Processes by Spectral Representation," ASME *Applied Mechanics Reviews,* Vol. 44, pp. 191–204.

Simiu, E., and Scanlan, R. H., 1986, *Wind Effects on Structures, Second Edition,* John Wiley and Sons, New York.

Simiu, E., and Frey, M., 1996, "Noise-Induced Sensitivity to Initial Conditions," *Proceedings, Workshop on Fluctuations and Order,* M. Millonas, ed., Springer-Verlag, New York, pp. 81–90.

Simiu, E., and Hagwood, C., 1994, "Exits in Second-Order Nonlinear Systems Driven by Dichotomous Noise," *Proceedings, Conference on Computational Stochastic Mechanics,* P. Spanos and M. Shinozuka, eds., Athens, Sept. (in press).

Vaicaitis, R., and Simiu, E., 1977, "Nonlinear Pressure Terms and Along-Wind Response," *Journal of the Structural Division,* ASCE, Vol. 103, pp. 903–906.

Verhulst, F., 1990, *Nonlinear Differential Equations and Dynamical Systems,* Springer-Verlag, New York.

Van der Hoven, I., 1957, "Power Spectrum of Horizontal Wind Speed in the Frequency Range from 0.0007 to 900 Cycles per Hour," *Journal of Meteorology,* Vol. 14, pp. 160–163.

Wiggins, S., and Holmes, P., 1987, "Homoclinic Orbits in Slowly Varying Oscillators," *SIAM Journal for Mathematical Analysis,* Vol. 18, pp. 612–629; Errata: Vol. 19, pp. 1254–1255.

Wiggins, S., and Shaw, S. W., 1988, "Chaos and Three-Dimensional Horseshoes in Slowly Varying Oscillators," ASME JOURNAL OF APPLIED MECHANICS, Vol. 55, pp. 959–968.

Yim, S. C. S., and Lin, H., 1992, "Probabilistic Analysis of a Chaotic Dynamical System," *Applied Chaos,* J. H. Kim and J. Stinger, eds., John Wiley and Sons, New York.

APPENDIX

For the record of Fig. 6(*b*), $G(t) = \Sigma\, a_n \cos \omega_n t) + b_n \sin(\omega_n t)$, where $n = 1, 2, \ldots, 8$, $\omega_n = 0.2n$ and a_n, b_n were obtained by simulation (Rice, 1957). The values $\{a_1, b_1; a_2, b_2; \ldots; a_8, b_8\}$ were {.27, −.27; −.96, −.87; .84, .48; .33, −.68; .69, .58; .52, .34; .75, −.24; −.09, 1.31}.

Downloaded 04 May 2010 to 171.66.16.33. Redistribution subject to ASME license or copyright; see http://www.asme.org/terms/Terms_Use.cfm

The Flow Near a Rotating Disk: An Approximate Solution

P. D. Ariel[1]

Department of Mathematics
and Computer Science,
Moi University,
Eldoret, Kenya

An approximate solution to the problem of steady laminar flow near a rotating disk is presented. It is based upon the idea of stretching of the independent variable and the minimization of the residual in a differential equation using the least squares method. The solution is simple and gives results which compare favorably with those obtained by other approximate methods.

Introduction

The steady laminar flow of a viscous, incompressible fluid near a rotating disk is a classical problem in fluid dynamics. It is one of those few problems for which Navier-Stokes equations reduce to a boundary value problem (BVP) involving ordinary differential equations. Von Kármán (1921) was the first to examine this problem and he gave an approximate solution of the BVP using an integral approach in which the velocity components were approximated by low-degree polynomials. His analysis had a flaw and it was corrected by Cochran (1934) who, besides giving the approximate solution, also presented the exact numerical solution of the problem. Improved numerical results were later given by Stuart (1954), though probably the most accurate results so far have been reported by Ackroyd (1978), who used a series solution involving exponential functions.

The polynomial profiles are most commonly used in obtaining the approximate solutions in flow problems in fluid dynamics. However, profiles involving other functions have also been considered with some success, especially in the study of boundary layer flows (Loitsianski, 1967). Of late, the idea of stretching the independent variable and then using the least squares method to minimize the residual of the differential equation has gained considerable popularity. The results published so far are quite encouraging. The main advantage of the method is that the solution is often given in a very simple analytical form without putting any premium on the accuracy. Thus, for the Falkner-Skan equation, Dey (1989) gave a simple solution which is similar to the one for a convergent channel. The present author (Ariel 1994a, 1994b) obtained approximate solutions for the two-dimensional stagnation point flows in hydromagnetics and with suction at the boundary. He underscored an important aspect of the solution method, namely, that the boundary layers arising due to either magnetic field or suction, which usually wreak havoc with the approximate solutions involving polynomials, do not affect the accuracy of the solution when it is obtained by stretching the independent variable. In fact, because of the exponential form of the assumed solution, the results get better as the physical parameter characterizing the flow takes increasingly large values.

In the aforementioned investigations (Dey, 1989; Ariel 1994a, 1994b), the flow is governed by a single differential equation in f, the dimensionless stream function. However, for the flow due to a rotating disk one obtains a system of three coupled nonlinear differential equations which renders the task of obtaining an approximate solution much more difficult. This may explain why there have not been many attempts in this direction. Jain (1963) succeeded in obtaining an approximate solution of the above flow problem by making use of a version of the collocation point method, in which the collocation points are chosen optimally to minimize the maximum error. Choosing exponential functions and two parameters in his trial functions for the velocity components, Jain improved upon the approximate solutions given by von Kármán (1921) and Cochran (1934).

In the present work we present an approximate solution based on the idea of the stretching of variables of the flow problem of a viscous, incompressible fluid near a rotating disk. Only one parameter, the one which scales the independent variable, figures in the solution. The methodology for obtaining the solution of a system of equations is discussed in some detail. It is shown that the resulting solution is more accurate than all the previously published approximate solutions.

Equations of the Problem

We consider the steady laminar flow of a viscous, incompressible, fluid occupying the region $z > 0$. The flow takes place due to the rotation of an infinite disk in the x-y plane about the z-axis. It has been demonstrated by von Kármán (1921) that in this case the Navier-Stokes equations are reduced to the following BVP in F, G and H, the dimensionless velocity components in the radial, azimuthal, and axial directions, respectively:

$$F'' - HF' - F^2 + G^2 = 0, \tag{1}$$

$$G'' - HG' - 2FG = 0, \tag{2}$$

$$2F + H' = 0, \tag{3}$$

where a prime denotes the derivative with respect to ζ, the dimensionless independent variable in z-direction.

The boundary conditions on F, G, and H are

$$F(0) = 0, \quad G(0) = 1, \quad H(0) = 0, \tag{4}$$

$$F(\infty) = 0, \quad G(\infty) = 0. \tag{5}$$

Methodology of the Solution

Since there are three velocity components to be determined, for an approximate solution, it seems natural to assume *three* trial functions, one each for F, G, and H. This will result into a nonzero residual for each of the Eqs. (1), (2), and (3). One can form a weighted average of these residuals and attempt to minimize it. For a general system of equations this would probably be the only choice. However, intuitively at any rate, it appears a better idea to reduce to zero the residual of as many

[1] Present address: Department of Mathematics and Computer Science, Engineering College, Kota, India.

Contributed by the Applied Mechanics Division of THE AMERICAN SOCIETY OF MECHANICAL ENGINEERS for publication in the ASME JOURNAL OF APPLIED MECHANICS.

Discussion on this paper should be addressed to the Technical Editor, Professor Lewis T. Wheeler, Department of Mechanical Engineering, University of Houston, Houston, TX 77204-4792, and will be accepted until four months after final publication of the paper itself in the ASME JOURNAL OF APPLIED MECHANICS.

Manuscript received by the ASME Applied Mechanics Division, Aug. 25, 1993; final revision, Oct. 25, 1993. Associate Technical Editor: S. Lichter.

Copyright © 1996 by ASME

Downloaded 04 May 2010 to 171.66.16.33. Redistribution subject to ASME license or copyright; see http://www.asme.org/terms/Terms_Use.cfm

equations as possible. If the system of Eqs. (1)–(3) is expressed as a pair of equations in G and H using Eq. (3), evidently the residual of Eq. (3) becomes zero. Indeed this is how Jain (1963) obtained his solution using the collocation point method.

In the present work we go a step further and reduce the residual of Eq. (2) also to zero. This entails that Eq. (2) be solved for one of the two variables G or H. Since an analytical solution for G is not easy to obtain for a general form of $H(\zeta)$, we shall solve Eq. (2) for H in terms of G. Equation (2) can be rewritten as

$$G'' - HG' + H'G = 0. \tag{6}$$

It is a linear differential equation in H, and in view of the initial condition on H in (4), its solution is given by

$$H(\zeta) = -G \int_0^\zeta \frac{G''}{G^2}\, d\zeta. \tag{7}$$

$F(\zeta)$ can now be directly obtained from Eq. (3). Finally when the values of H and F are substituted from Eq. (7) in Eq. (1), it results into a single equation in G. Now assuming an approximate trial solution for G, involving the parameter of stretching, the residual of the above single equation in G is calculated. Its minimization using the least squares method determines the value of the stretching parameter. The solution for G is thus complete. Those for H and F can be obtained from Eqs. (7) and (3), respectively.

The Approximate Solution

Let us choose the stretched coordinate

$$\xi = \alpha\zeta, \tag{8}$$

where α is the stretching parameter that needs to be determined.

We shall be assuming the trial function for G in terms of the exponential functions $\exp(-n\xi)$, where n is a positive integer. The simplest choice for G satisfying the boundary conditions (4) and (5) is, of course, $\exp(-\xi)$. However, in order that the trial function may also satisfy the boundary condition on F in (4), it is necessary that the condition

$$G''(0) = 0 \tag{9}$$

is also satisfied, which can be easily verified from Eq. (2). The next trial function for G which satisfies (9) and involves the lowest values of n is

$$G(\xi) = \tfrac{1}{3}(4e^{-\xi} - e^{-2\xi}). \tag{10}$$

Substituting for G from Eq. (10) in Eq. (7) and performing the necessary integrations, one obtains

$$H(\xi) = \alpha\left[\frac{1}{8}(4e^{-\xi} - e^{-2\xi}) \ln\frac{4e^{\xi} - 1}{3} - \frac{1}{2}(2 - 3e^{-\xi} + e^{-2\xi})\right], \tag{11}$$

which when inserted into Eq. (3) leads to

$$F(\xi) = \alpha^2\left[\frac{1}{8}(2e^{-\xi} - e^{-2\xi}) \ln\frac{4e^{\xi} - 1}{3} + \frac{1}{2}(e^{-\xi} - e^{-2\xi})\right]. \tag{12}$$

Note that with the expressions (10), (11), and (12) for G, H, and F respectively, the residuals of Eqs. (2) and (3) have been reduced to zero. We next calculate the residual of Eq. (1) by substituting the values of F, G, and H into it. We obtain

$$R(\xi,\alpha) = \alpha^4 X_1(\xi) + X_2(\xi), \tag{13}$$

where

$$X_1 = \left[\frac{1}{4}(\eta - 2\eta^2) \ln\frac{4\eta^{-1} - 1}{3} + \frac{\eta^2(5 - \eta)}{(4 - \eta)^2} - 2\eta^2\right] - \left[\frac{1}{8}(4\eta - \eta^2) \ln\frac{4\eta^{-1} - 1}{3} - 1 + \frac{3}{2}\eta - \frac{1}{2}\eta^2\right] \times \left[\frac{1}{4}(-\eta + \eta^2) \ln\frac{4\eta^{-1} - 1}{3} - \frac{\eta}{4 - \eta} + \eta^2\right] - \left[\frac{1}{8}(2\eta - \eta^2) \ln\frac{4\eta^{-1} - 1}{3} + \frac{1}{2}\eta - \frac{1}{2}\eta^2\right]^2, \tag{14}$$

$$X_2 = \tfrac{1}{9}(4\eta - \eta^2)^2, \tag{15}$$

and

$$\eta = e^{-\xi}. \tag{16}$$

The residual R in Eq. (13) is minimized using the least squares method. Other schemes can also be used such as the collocation point method, Galerkin's method, integral method, etc. However, in practice, the least squares method seems to give the "best" results. Thus performing

$$\frac{\partial}{\partial\alpha}\int_0^\infty R^2(\xi, \alpha)\, d\xi = 0 \tag{17}$$

we obtain

$$\alpha^4 = -\int_0^1 \eta^{-1} X_1 X_2\, d\eta \Big/ \int_0^1 \eta^{-1} X_1^2\, d\eta, \tag{18}$$

from which α can be determined after performing the necessary integrations. Once α is known, F, G, and H can be obtained for any ζ from Eqs. (10), (11), and (12).

Results and Discussion

The integrals occurring in Eq. (18) can be calculated "by hand" and α can be expressed in the so-called closed form. However, the labor involved may be excessive and not justified. A better alternative seems to evaluate these integrals numerically using a suitable quadrature formula. The only source of trouble in the numerical evaluation can come from the logarithmic singularity in the second and higher derivatives at $\eta = 0$.

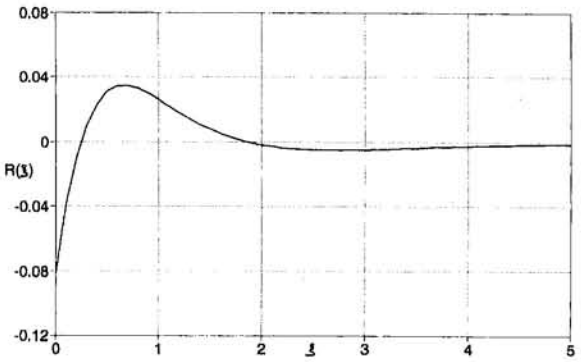


Fig. 1 Plot of error distribution $R(\xi)$ with ξ, the stretched independent variable

Downloaded 04 May 2010 to 171.66.16.33. Redistribution subject to ASME license or copyright; see http://www.asme.org/terms/Terms_Use.cfm

For this reason, the interval $0 \le \eta \le 1$ was divided into two parts: $0 \le \eta \le 0.02$ and $0.02 \le \eta \le 1$. In each of these intervals the integrals were computed to a sufficient degree of precision. The Gauss-Legendre 32-point formula was used for integration. The use of this formula yields the value of the integral $\int_0^1 \eta^2(\ln \eta)^2 d\eta = \frac{2}{27}$, correct to ten decimal places after the interval is split into two parts as indicated above. The value of α was found to be 0.91302 94741, which is believed to be accurate to the last digit.

It may be remarked here that, ideally speaking, one should not require the use of a computer for performing the calculations in an approximate method. The hallmark of an approximate method is its simplicity. A reasonable compromise is the use of a pocket computer. The above calculations were in fact first performed on the CASIO FX-720P computer using the Simpson's rule. It required only ten lines of BASIC code for Simpson's rule and another four for the integrands. The advantage of using pocket computers is, of course, their portability, but also the fact that the programming on them does not require the strict discipline demanded by the higher level languages such as PASCAL, FORTRAN, etc. One can therefore speedily obtain the desired results to a reasonable degree of accuracy. It was found that the value of α obtained on the pocket computer agreed with the exact result to five significant digits which, as we shall see below, is well within the accuracy provided by the approximate method.

The accuracy of an approximate method can be judged by several criteria. One of the rather obvious measures are the error distribution functions of the differential equations. For the present problem there is error only in Eq. (1) and it is given by Eq. (13). In Fig. 1, this is plotted against ξ for the calculated value of α. It can be seen that the error is well distributed and has the bounds

$$-0.080997 < R(\xi) < 0.034859, \quad 0 < \xi < \infty.$$

The error is of the same order of magnitude as reported by Jain (1963) who used a computationally expansive iterative scheme for locating the optimal collocation points. Jain also used four parameters in his velocity profiles: two each for F and G.

Another measure of accuracy is the root mean square error which is the value of square root of the integral of the square of the error. Its value is 0.035626 which is again reasonably small.

Probably the most useful indication of the accuracy is provided by the values of the quantities $F'(0)$, $G'(0)$, and $H(\infty)$ which also represent meaningful physical quantities; e.g., $G'(0)$ is a measure of the turning moment on the disk. From a computational point of view too, these quantities are of interest. For, if the values of $F'(0)$ and $G'(0)$ are known, the system of Eqs. (1)–(3) can be treated as an initial value problem and integrated by marching forward.

In Table 1, the values of $F'(0)$, $G'(0)$, and $H(\infty)$ are compared using the exact solution due to Ackroyd (1978) and various approximate solutions as given by Cochran (1934), Jain (1963), and the present method. It is clear that the approximate method given in the present paper provides the most accurate results.

Table 1 Comparison of the values of F' (0), G' (0), and H (∞) obtained by exact solution (Ackroyd, 1978) and various approximate methods

	Exact	Cochran	Jain	Present
F' (0)	0.510233	0.54	0.506711	0.507415
$-G'$ (0)	0.615722	0.54	0.626752	0.608686
$-H$ (∞)	0.884474	0.55	0.999596	0.913029

Finally, since the solution given by Ackroyd (1978) is also in a series form, it may be instructive to compare the expression of $G(\zeta)$ obtained by the present method with that given by Ackroyd. These are given as follows.

Exact:

$$G(\zeta) = 1.202212e^{-0.884474\zeta} - 0.376631e^{-2.653422\zeta} + 0.296847e^{-3.537896\zeta} - \ldots.$$

Approximate:

$$G(\zeta) = 1.333333e^{-0.913029\zeta} - 0.333333e^{-1.826059\zeta}.$$

Conclusion

In the present paper an approximate solution is presented for the steady laminar flow of a viscous, incompressible fluid near a rotating disk. The method of solution is based on the idea of stretching of the independent variable and then using the least squares method to minimize the error in the differential equations. For the problem at hand, even though the flow is governed by a system of three nonlinear coupled equations, the residual in two of the differential equations is reduced to zero. The minimization of the residual in the remaining equation yields the value of the stretching parameter. The values representing various physical quantities of interest are found to be in a very good agreement with the corresponding exact values.

References

Ackroyd, J. A. D., 1978, "On the Steady Flow Produced by a Rotating Disc with Either Surface Suction or Injection," *Journal of Engineering Mathematics*, Vol. 12, pp. 207–220.

Ariel, P. D., 1994a, "Hiemenz Flow in Hydromagnetics," *Acta Mechanica*, Vol. 103, pp. 31–43.

Ariel, P. D., 1994b, "Stagnation Point Flow with Suction—An Approximate Solution," ASME JOURNAL OF APPLIED MECHANICS, in press.

Cochran, W. G., 1934, "The Flow due to a Rotating Disc," *Proceedings of Cambridge Philosophical Society*, Vol. 30, pp. 365–375.

Dey, J., 1989, "A Simple Technique for Approximate Solution of the Falkner-Skan Equation," *Acta Mechanica*, Vol. 77, pp. 299–305.

Jain, M. K., 1963, "On Extremal Point Collocation Method for Fluid Flow Problems," *Applied Scientific Research*, Vol. 11, pp. 177–188.

Loitsianski, L. G., 1967, *Laminare Grenzschichten*, Akademie-Verlag, Berlin.

Stuart, J. T., 1954, "On the Effects of Uniform Suction on the Steady Flow due to a Rotating Disk," *Quarterly Journal of Mechanics and Applied Mechanics*, Vol. 7, pp. 446–457.

Von Kármán, Th., 1921, "Über Laminare und Turbulente Reibung," *Zeitschift für Angewandte Mathematik und Mechanik*, Vol. 1, pp. 233–252.

Downloaded 04 May 2010 to 171.66.16.33. Redistribution subject to ASME license or copyright; see http://www.asme.org/terms/Terms_Use.cfm

Vibration and Stability of a Spinning Disk Under Stationary Distributed Edge Loads

Jen-San Chen
Associate Professor,
Department of Mechanical Engineering,
National Taiwan University,
Taipei, Taiwan 107, R.O.C.

The vibration and stability of a spinning disk under conservative distributed edge tractions are studied both numerically and analytically. The edge traction is circumferentially stationary in the space. When the compressive traction is uniform, it is found that no modal interaction occurs and the natural frequencies of all nonreflected waves decrease, while the natural frequencies of the reflected waves increase. When the spinning disk is under distributed traction in the form of cos kθ*, where* k *is a nonzero integer, it is found that the eigenvalue only changes slightly under the edge traction if the natural frequency of interest is well separated from others. When two modes are almost degenerate, however, modal interaction may or may not occur. It is observed that when the difference between the number of nodal diameters of these two modes is equal to* $\pm$k*, frequency veering occurs when both modes are nonreflected, and merging occurs when one of these two modes is a reflected wave. In applying this rule, the number of nodal diameters of the forward and the reflected wave is considered as negative.*

Introduction

Transverse instability is a critical constraint in the optimal design and operation of computer disk drives and circular saws. In computer disk drives, excessive transverse vibrations degrade the signal from the read/write head and can destroy the disk by a "head crash." In analyzing the destabilizing mechanism, the disk drive is modeled as a spinning disk in contact with a stationary load system, which represents the read/write head and contains such elements as inertia, damping, and stiffness (Iwan and Moeller, 1976). On the other hand, the unique feature in circular saw application is the stationary in-plane load applied at the outer rim of the spinning disk during cutting operation (Mote and Szymani, 1978).

While the buckling analysis of a stationary circular disk subjected to general stationary in-plane loads is a classical problem and has been thoroughly investigated, the problem of a spinning disk under stationary in-plane edge loads attracts relatively few attentions. Srinivasan and Ramamurti (1980) considered the in-plane dynamic behavior of a stationary disk subjected to a spinning, concentrated, in-plane load on the outer boundary. They did not study the dynamic response associated with the bending of the disk. Carlin et al. (1975) first wrote the equation of motion for a nonrotating circular plate with asymmetric stresses due to a stationary concentrated normal edge load. In order to account for the effects of disk rotation, they then superposed the axisymmetric stresses due to the centrifugal force to the membrane stress field induced by the edge load. Radcliffe and Mote (1977) extended the work of Carlin et al. by considering a general concentrated edge load with both normal and tangential components. Since the equations of motion used in these two papers are nongyroscopic, they do not correspond to either a spinning disk-stationary edge load system, nor a stationary disk-spinning edge load system. On the contrary, their concentrated edge load appears to be spinning along with the spinning disk.

In order to account for the relative motion between the spinning disk and the stationary concentrated edge load, Chen (1994) formulated the problem with respect to the stationary coordinate system and studied various stability properties of the coupled system. He found that the concentrated edge load induces divergence instability before the critical speed and causes strong modal interactions whenever two modes are almost degenerate. While Chen can explain why instability occurs when two natural frequencies merge together with the concept of energy consumption, he was unable to explain why and when the natural frequency loci tend to merge together or veer away, partly due to the mathematical complexity associated with the concentrated force.

Since a general edge load, including the special case of a concentrated force, can be expressed as a Fourier series expansion, it is desirable to study the effects of each Fourier component of the edge load on the natural frequencies and stability of the spinning disk. The natural frequency variations and stability properties of the spinning disk under general edge loads may be considered as due to the combined effects of each Fourier component. In the present paper we consider a spinning flexible annular disk clamped at the inner radius and subjected to a stationary edge load in the form of cos $k\theta$ at the outer rim, where $k = 0, 1, 2, \ldots$. The equation of motion was first presented. Numerical results are obtained by a computation scheme based on Fourier series expansion and Galerkin's method. The effects of the number k on the eigenvalues and modal interactions are particularly of interest, and some rules are proposed based on the numerical results. In order to study analytically the first-order effects of the edge traction on the eigenvalues, we derive the derivative of the eigenvalue with respect to the magnitude of the in-plane traction. While this first-order derivative explains the behavior of eigenvalue changes when the natural frequency of interest is well separated from others, it can not account for the strong modal interactions when two modes are almost degenerate. In order to study the complex phenomena of modal interactions, we use a two-mode eigenfunction expansion theory to investigate the inherent mathematical structure and verify analytically the rules regarding the effects of the edge traction on various types of modal interactions.

Contributed by the Applied Mechanics Division of THE AMERICAN SOCIETY OF MECHANICAL ENGINEERS for publication in the ASME JOURNAL OF APPLIED MECHANICS.

Discussion on this paper should be addressed to the Technical Editor, Professor Lewis T. Wheeler, Department of Mechanical Engineering, University of Houston, Houston, TX 77204-4792, and will be accepted until four months after final publication of the paper itself in the ASME JOURNAL OF APPLIED MECHANICS.

Manuscript received by the ASME Applied Mechanics Division, Aug. 1, 1994; final revision, Dec. 24, 1994. Associate Technical Editor: S. W. Shaw.

Copyright © 1996 by ASME

Downloaded 04 May 2010 to 171.66.16.33. Redistribution subject to ASME license or copyright; see http://www.asme.org/terms/Terms_Use.cfm

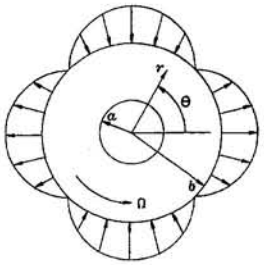


Fig. 1 A spinning disk subjected to stationary distributed edge load

Equation of Motion

Figure 1 shows a circular disk, which is clamped at the inner radius $r = a$ and subjected to a distributed normal traction at the outer radius $r = b$. The form of the traction is assumed to be $\epsilon \cos k\theta$. The disk is rotating with constant speed Ω, while the edge traction is circumferentially stationary in the space. The magnitude and direction of the edge traction remain the same when the disk vibrates laterally. In other words, the edge load is conservative. The equation of motion of the system, in terms of the transverse displacement w and with respect to the stationary coordinate system (r, θ), is

$$\rho h(w_{,tt} + 2\Omega w_{,t\theta} + \Omega^2 w_{,\theta\theta}) + D\nabla^4 w + \mathbf{L}w + \epsilon\hat{\mathbf{L}}w = 0 \quad (1)$$

where

$$D = \frac{Eh^3}{12(1 - \nu^2)}.$$

The standard subscript notation for partial derivative is used here. The parameters ρ, h, E, and ν are the mass density, thickness, Young's modulus, and Poisson ratio of the disk, respectively. $\mathbf{L}$ is the membrane operator associated with the axisymmetrical stress field due to the centrifugal force, and $\hat{\mathbf{L}}$ is the membrane operator associated with the stress field due to the normal edge traction $\epsilon \cos k\theta$ at $r = b$,

$$\mathbf{L} = -\frac{h}{r}\left[\frac{\partial}{\partial r}\left(r\sigma_r \frac{\partial}{\partial r}\right) + \frac{\partial}{\partial \theta}\left(\frac{1}{r}\sigma_\theta \frac{\partial}{\partial \theta}\right)\right]$$

$$\hat{\mathbf{L}} = -\frac{h}{r}\left[\frac{\partial}{\partial r}\left(r\hat{\sigma}_r \frac{\partial}{\partial r} + \hat{\sigma}_{r\theta}\frac{\partial}{\partial \theta}\right) + \frac{\partial}{\partial \theta}\left(\hat{\sigma}_{r\theta}\frac{\partial}{\partial r} + \frac{1}{r}\hat{\sigma}_\theta \frac{\partial}{\partial \theta}\right)\right].$$

σ_r and σ_θ are due to the centrifugal force and are proportional to Ω^2. On the other hand, $\hat{\sigma}_r$, $\hat{\sigma}_{r\theta}$, and $\hat{\sigma}_\theta$ are the stress fields induced by the edge traction and can be calculated as

$$\hat{\sigma}_r = \epsilon\sigma_r^*(r)\cos k\theta$$

$$\hat{\sigma}_\theta = \sigma_\theta^*(r)\cos k\theta \quad k = 0, 1, 2, \ldots.$$

$$\hat{\sigma}_{r\theta} = \epsilon\sigma_{r\theta}^*(r)\sin k\theta$$

σ_r^*, σ_θ^*, and $\sigma_{r\theta}^*$ are functions of radial coordinate r only, and can be found readily in Coker and Filon (1957). It is noted that $\hat{\sigma}_r$ and $\hat{\sigma}_\theta$ are odd functions of θ, and $\hat{\sigma}_{r\theta}$ is an even function of θ. Furthermore, $\sigma_r^*(b) = 1$ and $\sigma_{r\theta}^*(b) = 0$ due to the in-plane traction boundary conditions on the outer rim.

The associated boundary conditions for Eq. (1) are

$$w = w_{,r} = 0 \quad \text{at} \quad r = a \quad (2a)$$

$$\mathbf{B}_1 w + \epsilon\hat{\mathbf{B}}_1 w = \mathbf{B}_2 w = 0 \quad \text{at} \quad r = b \quad (2b)$$

where the boundary operators are defined as

$$\mathbf{B}_1 = \frac{\partial}{\partial r}\left(\frac{\partial^2}{\partial r^2} + \frac{\partial}{r\partial r} + \frac{\partial^2}{r^2\partial\theta^2}\right) + \frac{1-\nu}{r^2}\left(\frac{\partial^3}{\partial r\partial\theta^2} - \frac{\partial^2}{r\partial\theta^2}\right)$$

$$\hat{\mathbf{B}}_1 = \frac{h\cos(k\theta)}{D}\frac{\partial}{\partial r}$$

$$\mathbf{B}_2 = \frac{\partial^2}{\partial r^2} + \frac{\nu}{r}\left(\frac{\partial}{\partial r} + \frac{\partial^2}{r\partial\theta^2}\right).$$

The transverse component of the edge traction can also be included in Eq. (1), and excluded from boundary conditions (2b). The equivalent boundary value problem becomes

$$\rho h(w_{,tt} + 2\Omega w_{,t\theta} + \Omega^2 w_{,\theta\theta}) + D\nabla^4 w + \mathbf{L}w + \epsilon\left[\hat{\mathbf{L}} + h\delta(r-b)\cos k\theta\frac{\partial}{\partial r}\right]w = 0 \quad (3)$$

and

$$w = w_{,r} = 0 \quad \text{at} \quad r = a \quad (4a)$$

$$\mathbf{B}_1 w = \mathbf{B}_2 w = 0 \quad \text{at} \quad r = b. \quad (4b)$$

The equivalence between Eqs. (1), (2) and Eqs. (3), (4) can be easily seen by considering a spinning disk under conservative radial in-plane loads on circle $r = \xi$, where $a < \xi < b$. As the radius ξ approaches b, the response should approach that calculated for a spinning disk under in-plane edge loads at $r = b$.

For a freely spinning disk the eigenvalues λ_{mn} are purely imaginary and occur in complex conjugate pairs, i.e., $\lambda_{mn} = i\omega_{mn}$, where ω_{mn} is real. The eigenfunction corresponding to λ_{mn} is in general complex and assumes the form

$$w_{mn} = R_{mn}(r)e^{in\theta}. \quad (5)$$

R_{mn} is a real-valued function of r. The eigenfunction corresponding to $\bar{\lambda}_{mn}$ is $\bar{w}_{mn}$, where the overbar means complex conjugate. If we consider only the positive ω_{mn}, then w_{mn} in Eq. (5) with positive n is a backward traveling wave with n nodal diameters and m nodal circles, which is also denoted by $(m, n)_b$. Similarly, w_{mn} with negative n is a forward traveling wave $(m, -n)_f$. The critical speed Ω_c for the mode (m, n) is defined as the rotation speed at which ω_{mn} of the backward traveling wave $(m, n)_b$ becomes zero. For Ω greater than Ω_c, this mode is a forward traveling wave, and is termed a "reflected wave," denoted by $(m, -n)_r$.

Numerical Results

The nontrivial solution of Eq. (1) is assumed to be in the form of a Fourier sine and cosine series expansion. After substituting this expansion into Eq. (1), and by a finite element numerical analysis based on Galerkin's method with third order polynomial shape functions in the radial direction (Ono and Maeno, 1987), we can transform Eq. (1) into matrix algebraic equations and solve them with a generalized eigenvalue solver in EISPACK. From the viewpoints of both computing efficiency and accuracy, the number of elements in the radial direction and the maximum number of nodal diameters are chosen to be 6 and 4, respectively. The material properties of the disk used in the calculation are $\rho = 7.84 \times 10^3 \text{kg/m}^3$, $E = 203 \times 10^9$ N/m^2, $\nu = 0.27$, $h = 1.02$ mm (0.04 in.), $a = 101.6$ mm (4 in.), and $b = 203.2$ mm (8 in.).

For the case when the spinning disk is subjected to a concentrated conservative edge load, Chen (1994) reported that divergence instability occurs before the critical speed, and strong modal interactions are induced whenever two modes are almost

Downloaded 04 May 2010 to 171.66.16.33. Redistribution subject to ASME license or copyright; see http://www.asme.org/terms/Terms_Use.cfm

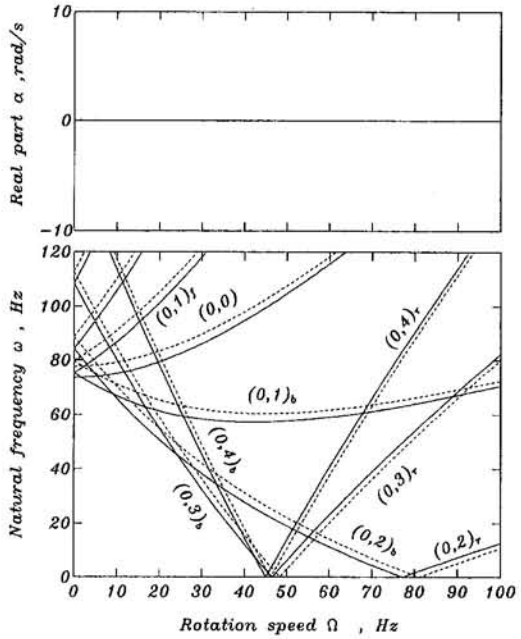


Fig. 2 Effects of uniform compressive edge traction on the eigenvalues of the spinning disk

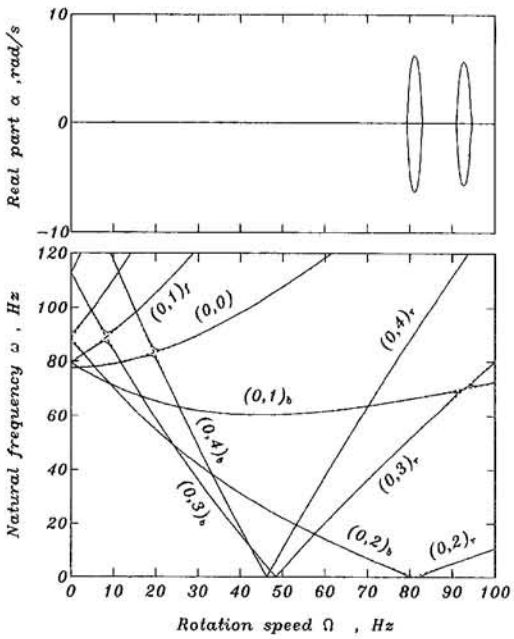


Fig. 4 Effects of edge traction $\epsilon \cos 4\theta$ on the eigenvalues of the spinning disk

degenerate. Figures 2, 3, 4, and 5 show the relations between the eigenvalues of the loaded spinning disk and the rotation speed. The ordinates are the natural frequency ω and the real part α of the eigenvalue ($\lambda = \alpha + i\omega$). The abscissa is the rotation speed Ω. The solid lines represent the case for $\epsilon = 4.5 \times 10^5 \text{N/m}^2$, and the dashed lines correspond to the case of a freely spinning disk (i.e., $\epsilon = 0$). Figure 2 shows the case when the spinning disk is under compressive uniform edge traction. It is found that compressive uniform edge traction tends to bring down the natural frequencies of all the forward and backward waves, but tends to raise the natural frequencies of the reflected waves. It is also noted that the uniform traction does not induce any modal interaction.

Figures 3 and 4 show the cases when the nonuniform edge traction is in the form of $\epsilon \cos k\theta$, where $k = 1$ and 4, respectively. When the natural frequency of interest is well separated from others, it is found that the eigenvalue only changes slightly under nonuniform edge tractions. On the other hand, when two modes are almost degenerate, modal interaction (frequency loci merging or veering) may or may not occur. Some rules regarding the behavior of modal interactions may be deduced by inspecting these figures carefully. In the case when the difference between the number of nodal diameters of these two modes is equal to $+k$ or $-k$, it is found that the frequency loci will merge together (when one of these two modes is a reflected wave) or veer away (when both modes are nonreflected). Otherwise, modal interaction will not occur and the frequency loci simply

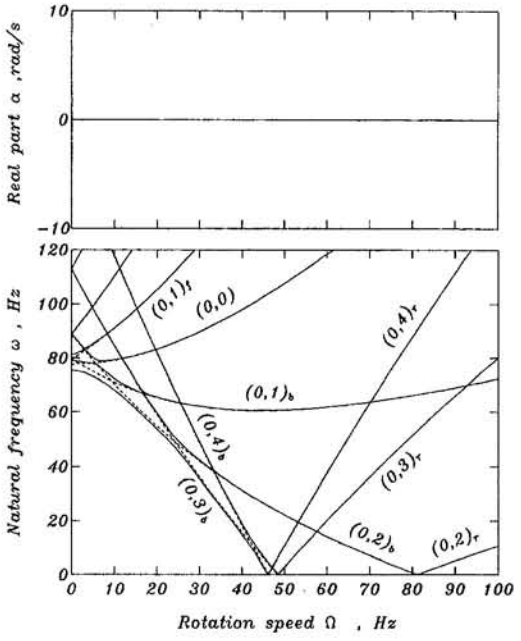


Fig. 3 Effects of edge traction $\epsilon \cos \theta$ on the eigenvalues of the spinning disk

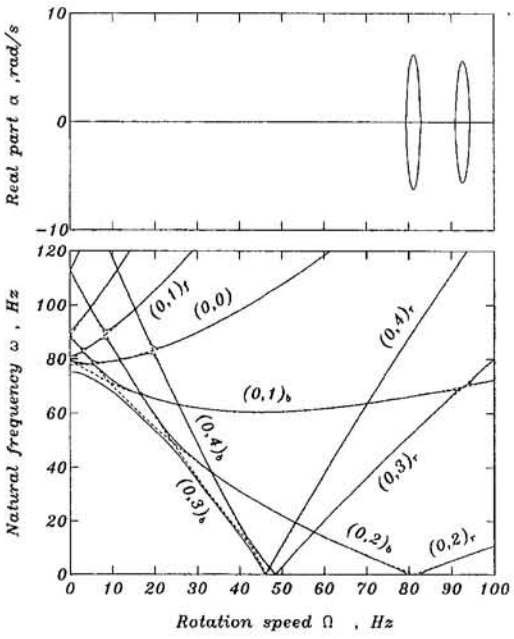


Fig. 5 Effects of edge traction $\epsilon(\cos \theta + \cos 4\theta)$ on the eigenvalues of the spinning disk

Downloaded 04 May 2010 to 171.66.16.33. Redistribution subject to ASME license or copyright; see http://www.asme.org/terms/Terms_Use.cfm

cross over. While veering does not change the stability properties of the system, frequency merging renders the spinning disk unstable. When merging occurs, it is noted that the degenerate frequency remains unchanged and merging occurs on both sides of the degenerate rotation speed in the natural frequency-rotation speed diagram. In applying these rules the number of nodal diameters of a forward or a reflected wave is considered as *negative*. For example, in Fig. 4 frequency loci merging occurs when $(0, 3)_r$ meets $(0, 1)_b$, crossing occurs when $(0, 3)_b$ meets $(0, 1)_b$, and veering occurs when $(0, 3)_b$ meets $(0, 1)_f$.

Figure 5 shows the case when the edge traction is in the form $\epsilon(\cos\theta + \cos 4\theta)$. By comparing Fig. 5 with Figs. 3 and 4, it can be seen that the effects of each Fourier component on the eigenvalues of the spinning disk are "additive." In other words, the eigenvalues of any two neighboring modes (m, n) and (p, q) will be affected only by a specific Fourier component $\cos k\theta$ with $k = \pm(n - q)$, but not others. Including or excluding the other harmonic components will not alter the behavior of modal interaction near the intersection of frequency loci of modes (m, n) and (p, q).

It is noted that these rules are deduced from observations on limited cases of finite element calculations. Furthermore, modal interaction is sometimes so weak that it may be ignored inadvertently in inspecting numerical results, unless an extremely large amount of calculation is performed. In order for these rules to stand on a firmer ground, it is desirable to investigate this problem by some other analytical approaches.

Derivative of Eigenvalue

The derivative of the eigenvalue λ_{mn} of the spinning disk with respect to the amplitude of the distributed edge traction ϵ can be derived either using Eqs. (3) and (4) and following a procedure described in Chen and Bogy (1992a), or using Eqs. (1) and (2) and following a procedure in Stakgold (1979) or Chen (1994). Both approaches give the same results. For the spinning disk under compressive uniform traction, it is found that

$$\frac{\partial\lambda_{mn}}{\partial\epsilon} = \frac{i\int_a^b \left[r\sigma_r^* \left(\frac{\partial R_{mn}}{\partial r}\right)^2 + \frac{n^2\sigma_\theta^*}{r} R_{mn}^2 \right] dr}{2\rho(\omega_{mn} \pm n\Omega)\int_a^b R_{mn}^2 r dr}. \quad (6)$$

Since this derivative is purely imaginary, the uniform traction affects the natural frequencies of the spinning disk, but not the real part of the eigenvalue. It is noted that the denominator is positive for a forward and a backward traveling wave, but is negative for a reflected wave (Chen and Bogy, 1992a). Furthermore, σ_r^* and σ_θ^* are negative because the edge traction is compressive. Therefore, the derivative is a negative imaginary number for a nonreflected wave, and is a positive imaginary number for a reflected wave. This verifies the observation that uniform compressive traction tends to bring down the natural frequencies of the forward and backward waves, but tends to raise the natural frequencies of the reflected waves. When the edge traction is tensile, on the other hand, the natural frequencies will change in the opposite way.

When the spinning disk is under distributed traction in the form $\epsilon \cos k\theta$ with $k \neq 0$, it is found that $(\partial\lambda_{mn}/\partial\epsilon) = 0$. This verifies the observation that nonuniform traction has no effect on the eigenvalues of the spinning disk, at least to the first order in the sense of Taylor series expansion. However, this conclusion is good only when the natural frequency of interest is well separated from others. When the natural frequencies of two modes are close together, strong modal interaction may occur, and first-order approximation fails to predict the complex behavior of eigenvalue changes.

Modal Interactions

When two modes are almost degenerate, as observed from the finite element solutions, modal interaction may or may not occur when nonuniform traction is applied. In this section we follow a procedure described in Chen and Bogy (1992b) based on a two-mode eigenfunction expansion theory to investigate the complex mathematical structure associated with various types of modal interactions.

Assume for the freely spinning disk that the two neighboring modes of interest are w_{mn} and w_{pq} with natural frequencies ω_{mn} and ω_{pq}, respectively. For the two-mode approximation, the eigenvalue λ of the spinning disk under distributed edge traction $\epsilon \cos k\theta$ can be obtained by solving the following quadratic equation,

$$\lambda^2(\alpha_0 + \alpha_2\epsilon^2) + \lambda(\beta_0 + \beta_2\epsilon^2) + \gamma_0 + \gamma_2\epsilon^2 = 0. \quad (7)$$

In the case when $n - q \neq \pm k$, α_2, β_2, and γ_2 are zero, and α_0, β_0, and γ_0 are

$$\alpha_0 = 16\pi^2\omega_{mn}\omega_{pq}(\omega_{mn} + n\Omega)(\omega_{pq} + q\Omega) \times \int_a^b R_{mn}^2 r dr \int_a^b R_{pq}^2 r dr$$

$$\beta_0 = -i(\omega_{mn} + \omega_{pq})\alpha_0$$

$$\gamma_0 = -\omega_{mn}\omega_{pq}\alpha_0.$$

The solution λ of Eq. (7) can then be solved as $i\omega_{mn}$ and $i\omega_{pq}$. Therefore, the eigenvalues of these two modes do not change when the edge traction $\epsilon \cos k\theta$ is applied, and no modal interaction is induced.

On the other hand, when $n - q = \pm k$ the coefficients α_0, β_0, and γ_0 remain the same, while α_2, β_2, and γ_2 become

$$\alpha_2 = -\left\{ \frac{\pi}{\rho}\int_a^b \left[r\sigma_r^* \frac{\partial R_{mn}}{\partial r}\frac{\partial R_{pq}}{\partial r} + q\left(n\frac{\sigma_\theta^*}{r} - \frac{\partial\sigma_{r\theta}^*}{\partial r}\right) R_{mn}R_{pq} - (n+q)\sigma_{r\theta}^* R_{mn}\frac{\partial R_{pq}}{\partial r} \right] dr \right\}^2$$

$$\beta_2 = -2i(\omega_{mn} + \omega_{pq})\alpha_2$$

$$\gamma_2 = -(\omega_{mn} + \omega_{pq})^2\alpha_2. \quad (8)$$

It is noted that the solution of Eq. (7) is independent of the sign of ϵ and can be written in terms of the parameter $\eta = \epsilon^2$ as

$$\lambda_\pm = \frac{-(\beta_0 + \beta_2\eta) \pm [4\omega_{mn}\omega_{pq}\alpha_0\alpha_2(\eta - \eta^*)]^{1/2}}{2(\alpha_0 + \alpha_2\eta)}$$

where

$$\eta^* = \frac{(\omega_{mn} - \omega_{pq})^2\alpha_0}{4\omega_{mn}\omega_{pq}\alpha_2}. \quad (9)$$

It is noted that α_0, α_2, γ_0, and γ_2 are real, while β_0 and β_2 are purely imaginary. Besides, α_2 is always negative. In the case when both modes are nonreflected, α_0 is positive (Chen and Bogy, 1992b) and η^* is therefore negative. Consequently, $\lambda_\pm$ become two different purely imaginary numbers, and veering occurs.

On the other hand, when one mode is a reflected wave and the other is nonreflected, α_0 is negative, and η^* is therefore positive. Consequently, $\lambda_\pm$ are two different purely imaginary numbers when $\eta < \eta^*$, and become two complex numbers with

Downloaded 04 May 2010 to 171.66.16.33. Redistribution subject to ASME license or copyright; see http://www.asme.org/terms/Terms_Use.cfm

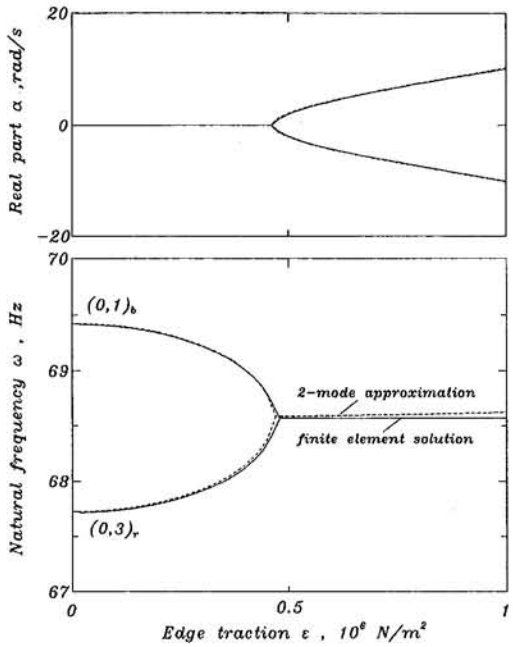


Fig. 6 Comparison between two-mode approximation (dashed lines) and finite element solution (solid lines) at Ω = 91*Hz*

the same imaginary parts when $\eta > \eta^*$. In Fig. 6 we fix the rotation speed Ω at 91 Hz, just a little lower than the degenerate rotation speed of modes $(0, 1)_b$ and $(0, 3)_r$, and change the edge traction amplitude ϵ from 0 to 10^6N/m^2. The dashed lines represent the eigenvalues obtained by solving the quadratic Eq. (7), while the solid lines represent the finite element solutions. It can be seen that the two-mode eigenfunction expansion is a very good approximation to the finite element solution in the neighborhood of the degenerate frequencies. Eigenfunction expansion with more than two modes can also be done as described in Chen and Bogy (1992b), if desired, and convergence of the expansion is ensured. η^* in Eq. (9) corresponds to the traction amplitude ϵ in Fig. 6 at which two dashed frequency loci merge. Since η^* in Eq. (9) is independent of the order of ω_{mn} and ω_{pq}, merging occurs on both sides of the degenerate rotation speed in the natural frequency-rotation speed diagram. This characteristic is different from the type of merging instability induced when a spinning disk is in contact with a stationary mass or spring, in which merging only occurs on one side of the degenerate rotation speed (Chen and Bogy, 1992b).

In the special case when the reflected wave and the nonreflected wave are degenerate, i.e., $\omega_{mn} = \omega_{pq}$, the solution of Eq. (7) becomes

$$\lambda_{\pm} = i\omega_{mn} \pm \frac{\omega_{mn}\sqrt{\alpha_0\alpha_2\eta}}{\alpha_0 + \alpha_2\eta}. \tag{10}$$

As a consequence, the degenerate natural frequency remains unchanged while the real parts of λ_+ and λ_- split into one positive and one negative numbers with the same absolute value. These analyses verify analytically those detailed observations on finite element calculations regarding the effects of edge tractions on modal interactions.

In the case when a backward wave $(m, n)_b$ meets its complex conjugate around the critical speed Ω_c, $w_{mn} = \bar{w}_{pq}$, and $n - q = 2n$. Equation (7) can then be reduced to

$$\lambda^2 = \frac{-\alpha_0\omega_{mn}^2}{\alpha_0 + \alpha_2\eta}.$$

In this case α_0 is positive on either side of the critical speed, i.e., for the rotation speed being higher or lower than Ω_c. Consequently, for fixed rotation speed close to Ω_c, $\lambda_{\pm}$ are purely imaginary until η exceeds $\sqrt{-(\alpha_0/\alpha_2)}$. For $\eta > \sqrt{-(\alpha_0/\alpha_2)}$, $\lambda_{\pm}$ become two real numbers with identical absolute value but different signs. Therefore, we can predict that divergence instability will be induced before and after the critical speed, as we have observed in the finite element solutions.

The above analyses can readily be extended to the case when the edge traction contains more than one Fourier component, for instance, $\epsilon(\cos k_1\theta + \cos k_2\theta)$, where $k_1 \neq k_2$. In doing so we can see that when $n - q = \pm k_1$, only the stress field induced by component $\cos k_1\theta$ affects the coefficients α_2, β_2, and γ_2 in Eqs. (8). In other words, the eigenvalues of the two-mode expansion are independent of the traction component $\cos k_2\theta$. This analysis verifies the observation in Fig. 5 that the effects of each Fourier component on the modal interactions are additive.

Conclusions and Discussions

Several rules regarding the behavior of eigenvalue changes when the spinning disk is under distributed traction in the form of $\cos k\theta$ are proposed after observing the finite element solutions and are verified analytically using first-order derivative of the eigenvalue and the two-mode eigenfunction expansion theory. When the spinning disk is under general edge traction in any form, we can always expand the general traction in a Fourier series. Since the effects of each Fourier component are additive, it is possible to predict the behavior of eigenvalue variations of the loaded spinning disk by considering the effect of the general traction as the combined effects of its individual components. It is noted that while the finite element solutions presented in this paper are only for a special radius ratio $a/b = 0.5$, the analytical verification is independent of the radius ratio. Therefore, the rules presented in this paper are independent of the radius ratio of the annular disk.

The cutting force on a circular saw could be modeled as a concentrated, conservative force acting in the plane of the disk. A Fourier decomposition of the force would include all the harmonics (Chen, 1994). The results presented in this paper imply that every intersection of frequency loci of two nonreflected waves would be a veering. Additionally, every intersection of frequency loci from a reflected wave and a nonreflected wave would be a merging. From a practical standpoint, this would mean that a circular saw could experience instability while cutting at speeds above the first critical speed even if it was not at a critical speed and it was isolated from aerodynamic forces that cause flutter. Depending on the size of the mergings and the divergence instabilities at critical speeds, this could effectively make impossible cutting at supercritical speed by an unguided circular saw.

Acknowledgments

The results presented here were obtained in the course of research supported by a grant from the National Science Council of the Republic of China.

References

Carlin, J. F., Appl, F. C., Bridwell, H. C., and Dubois, R. P., 1975, "Effects of Tensioning on Buckling and Vibration of Circular Saw Blades," ASME *Journal of Engineering for Industry*, Vol. 2, pp. 37–48.

Chen, J.-S., 1994, "Stability Analysis of a Spinning Elastic Disk Under a Stationary Concentrated Edge Load," ASME JOURNAL OF APPLIED MECHANICS, Vol. 61, pp. 788–792.

Chen, J.-S., and Bogy, D. B., 1992a, "Effects of Load Parameters on the Natural Frequencies and Stability of a Flexible Spinning Disk with a Stationary Load System," ASME JOURNAL OF APPLIED MECHANICS, Vol. 59, Part 2, pp. 230–235.

Chen, J.-S., and Bogy, D. B., 1992b, "Mathematical Structure of Modal Interactions in a Spinning Disk-Stationary Load System," ASME JOURNAL OF APPLIED MECHANICS, Vol. 59, Part 1, pp. 390–397.

Coker, E. G., and Filon, L. N. G., 1957, *A Treatise on Photo-Elasticity*, Cambridge University Press, London.

Downloaded 04 May 2010 to 171.66.16.33. Redistribution subject to ASME license or copyright; see http://www.asme.org/terms/Terms_Use.cfm

Mote, C. D., Jr., and Szymani, R., 1978, "Circular Saw Vibration Research," *The Shock and Vibration Digest,* Vol. 10, pp. 15–30.

Ono, K., and Maeno, T., 1987, "Theoretical and Experimental Investigation on Dynamic Characteristics of a 3.5-Inch Flexible Disk Due to a Point Contact Head," *Tribology and Mechanics of Magnetic Storage Systems,* Vol. 3, SP.21 (STLE), pp. 144–151.

Radcliffe, C. J., and Mote, C. D., Jr., 1977, "Stability of Stationary and Rotating Discs Under Edge Load," *International Journal of Mechanical Science,* Vol. 19, pp. 567–574.

Srinivasan, V., and Ramamurti, V., 1980, "Dynamic Response of an Annular Disk to a Moving Concentrated, In-Plane Edge Load," *Journal of Sound and Vibration,* Vol. 72, No. 2, pp. 251–262.

Stakgold, Ivar, 1979, *Green's Functions and Boundary Value Problems,* John Wiley and Sons, New York.

Downloaded 04 May 2010 to 171.66.16.33. Redistribution subject to ASME license or copyright; see http://www.asme.org/terms/Terms_Use.cfm

Transition From Soliton to Chaotic Motion Following Sudden Excitation of a Nonlinear Structure

M. A. Davies
Assoc. Mem. ASME.

F. C. Moon
Fellow ASME.

Sibley School of Mechanical and Aerospace Engineering, Cornell University, Ithaca, NY 14853

The existence of a transition from soliton-like motions to spatially and temporally disordered motions in a periodic structure with buckling nonlinearity is demonstrated. An experiment consisting of nine harmonic oscillators coupled with buckling sensitive elastica was constructed. This experiment is modeled using a modified Toda lattice. As has been shown in previous work, the experiment and the model show strong sensitivity to initial conditions. Here we show that this sensitivity may be related to a transition from relatively ordered solitary wave motion, immediately following the impact, to disordered motions at a later time. Some of the behavior of the observed wave structures is explained using Toda's analytical results; however, the reasons for the break-up of the waves and their role in the generation of spatio-temporal disorder is not fully understood. We speculate that some type of transient chaotic motion is responsible for the observed behavior. These findings are relevant to aircraft, ship, and space structures that are subjected to large dynamic loads.

1 Introduction

Periodically reinforced structures are used in the construction of spacecraft, aircraft, and ships to minimize weight while maintaining structural integrity. One of the common failure modes for such structures is the dynamic buckling of flexible structural elements. In this paper, we examine wave-like deformations that result from the nonlinear elastic buckling of a suddenly loaded periodic structure. Experiments and numerical simulation show that solitary waves in the system can evolve into complex spatial patterns with chaos-like dynamics. An understanding of these phenomena is necessary if the dynamics and ultimately the failure modes of periodic structures are to be predicted. These results may also be relevant to the interpretation of structural failure tests and large-scale numerical simulations, perhaps suggesting that an ensemble of tests might be necessary to determine the sensitivity of buckling behavior to small changes in loading and design parameters. Figure 1 illustrates the similarity of our experiment to more complex engineering structures.

Chaotic oscillations have been widely observed in structural systems. These oscillations arise from various nonlinearities. Impact and rattling nonlinearities were studied by Moon and Shaw (1983); dry friction by Feeny (1989); elastoplasticity by Pratap, Mukherjee, and Moon (1994); and geometric nonlinearities by Cusumano and Moon (1989) and Dowell (1982). Erratic oscillations in structural buckling were first documented by Tseng and Dugungi (1971) in their study of snap-through oscillations in a prebuckled arch. Holmes (1979) showed that these oscillations were actually chaotic, and that the prebuckled arch exhibits classic period-doubling bifurcations and fractal-like strange attractors. Shortly after, Moon and Holmes (1983) experimentally observed period doubling and chaotic strange attractors in a magnetically buckled beam. In addition to having temporally chaotic behavior, there is also strong evidence that nonlinear elastic structures exhibit highly complex, spatially chaotic deformation patterns (Davies, 1993; Mielke and Holmes, 1988; El Naschie, 1989; Thompson and Virgin, 1988). However, the work presented here is one of the first to experimentally and numerically examine the dynamics of a higher degree-of-freedom buckling structure in which spatially and temporally chaotic motions appear to coexist. Earlier publications by the authors (Davies and Moon, 1994) have demonstrated strong temporal sensitivity to initial conditions in this structure. In this paper and the dissertation work by Davies (1993), we extend this earlier work, investigating more quantitatively the behavior of the soliton-like disturbances responsible for the observed spatially and temporally complex motions.

2 Experiment

The experimental structure consisted of nine elastic oscillators, coupled through buckling sensitive elastica (Fig. 2). Each elastic oscillator was constructed by fastening a 157 gram aluminum block to the end of an 0.081 cm thick, 2.5 cm wide spring steel, cantilevered beam. The length of the oscillators (measured from the fixed end of the beam to the center of mass of the attached block) was approximately 17 cm, and the distance between centers of adjacent blocks was 19 cm. The elastic buckling elements clamped between blocks were made from 0.0127 cm (0.005 in.) thick steel feeler gage stock. Each was plastically deformed into a shallow arch to enhance its first-mode buckling response. One end of the structure was attached through a buckling element to an electromagnetic shaker and the other left free. In this paper, we discuss the response of this structure to the sudden release of compressive loads applied at the free end. Later papers will discuss forced nonlinear vibrations, but here the shaker is treated as a fixed end.

Bending measurements were taken from a strain gage pair at the base of each cantilevered beam. Strain measurements were correlated to mass displacement for first-mode deformations of the cantilevered beams. Higher-mode vibrations in the beams introduce mechanical signal noise; however, for the results dis-

Contributed by the Applied Mechanics Division of THE AMERICAN SOCIETY OF MECHANICAL ENGINEERS for publication in the ASME JOURNAL OF APPLIED MECHANICS.

Discussion on this paper should be addressed to the Technical Editor, Professor Lewis T. Wheeler, Department of Mechanical Engineering, University of Houston, Houston, TX 77204-4792, and will be accepted until four months after final publication of the paper itself in the ASME JOURNAL OF APPLIED MECHANICS.

Manuscript received by the ASME Applied Mechanics Division, Aug. 19, 1994; final revision, Apr. 25, 1995. Associate Technical Editor: S. W. Shaw.

Copyright © 1996 by ASME

Downloaded 04 May 2010 to 171.66.16.33. Redistribution subject to ASME license or copyright; see http://www.asme.org/terms/Terms_Use.cfm

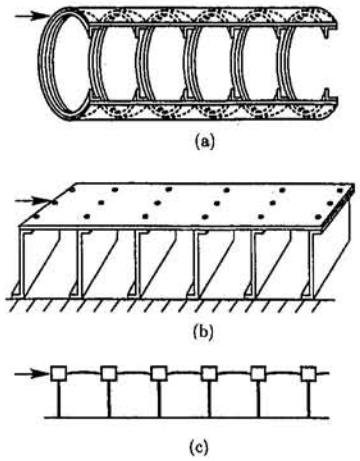


Fig. 1 Drawing showing the similarity between practical shell and plate-type structures (*a*) and (*b*) and our simplified experimental set-up (*c*)

cussed here the ratio of the first mode vibration amplitude to that of the higher modes was generally greater than 5:1. Data was taken by a Concurrent 5450 Data Acquisition System.

Small-amplitude vibration tests were used to characterize the linear behavior of the structural components. The first-mode vibration frequency of the elastic oscillators was approximately 4.3 Hz, corresponding to an effective spring constant of $k = 117$ N/m. The second mode of the elastic oscillators had a frequency of approximately 50 Hz; as noted above, in our experiments first mode cantilever deformations dominate and therefore the second and higher modes are ignored. For small motions, the behavior of the arched buckling elements was nearly linear with stiffness $\gamma = 362$ N/m. Due to differences in the elements, γ varied by as much as ± 6 percent from element to element. This nonuniformity in the buckling elements is the dominant source of parameter uncertainty in our characterization of the experiment.

Small motion tests were also used to characterize the vibration modes of the full nine-mass experimental set-up. Figure 3 shows the nine linear modal resonance frequencies of the structure plotted versus wave number. These data points trace out the dispersion relation for the structure. Analytical predictions indicate that for small motion the dispersion relation for this structure varies periodically with wave number, and thus the structure allows only a band of frequencies to propagate without attenuation (see next section, particularly Eq. (4)). The frequency response of the free-end mass to small-amplitude random excitation by the shaker table verifies this prediction, showing a sharp passband ranging from approximately 4.6 Hz to 16.2 Hz. This passband is known as a Brillouin zone (Brillouin,

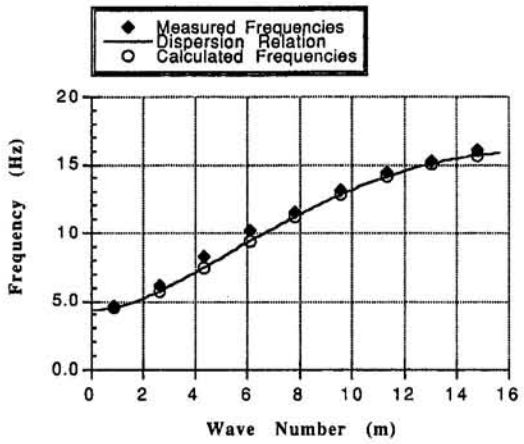


Fig. 3 Experimentally measured and analytically predicted dispersion relations for the small motion behavior of the structure and model. The plot shows a half-cycle of the dispersion relation which is a periodic function of the wave number, κ. Frequencies outside the band represented by the dispersion relation correspond to imaginary wave numbers and thus decay exponentially into the structure.

1946). The observed resonant frequencies and spatial shapes of the structural modes agree well with analytical calculations using linear lattice theory. Structural damping was found to be very low; logarithmic decay rates indicate that all modes are less than 0.1 percent critically damped.

To characterize the nonlinear behavior of the buckling elements, their static force-displacement behavior was measured. The measurement was done by rigidly clamping one end of the buckling element and attaching the other to an elastic oscillator. Known horizontal loads were applied to the mass, and its displacement was determined from the strain gages. The linear spring behavior of the cantilever beam was subtracted from the result, producing the solid curve in Fig. 4. The behavior of the elements was highly nonlinear, rapidly stiffening in tension (positive displacement) and softening rapidly in compression/buckling (negative displacement). Note also that the slope of the static force-displacement curve at the origin, γ, nearly matches the 362.0 N/m determined in vibration tests.

3 Numerical Model

The experiment was modeled as a one-dimensional lattice of point masses with nearest-neighbor nonlinear interactions (see Fig. 5). The accuracy of the model is based upon the following simplifying assumptions.

1 The aluminum blocks behave as point masses (mass m) moving along a horizontal line. Block rotations are ignored.

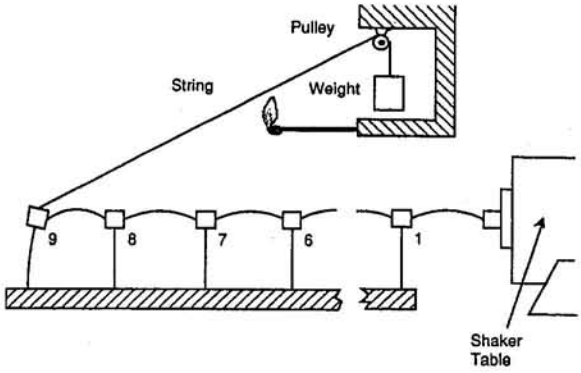


Fig. 2 Diagram of experiment consisting of nine elastic oscillators coupled through buckling sensitive elastica

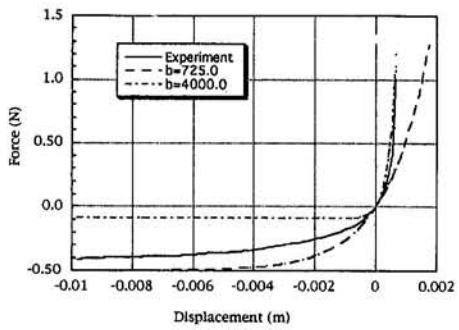


Fig. 4 Experimental measurement and mathematical approximation of the force-displacement behavior of the buckling elements. The mathematical approximation is shown for two values of *b*.

Downloaded 04 May 2010 to 171.66.16.33. Redistribution subject to ASME license or copyright; see http://www.asme.org/terms/Terms_Use.cfm

2 The elastic oscillators (cantilever-mass combinations) deform only in first mode, and can be treated as simple harmonic oscillators with stiffness k and mass m.

3 The buckling elements behave as simple nonlinear springs with the force-displacement behavior shown in Fig. 4. Higher buckling modes and moments in the elements are ignored.

4 Experimental components have uniform properties (all blocks have mass m, all cantilevers have stiffness k, etc.).

5 Damping is linear.

The equations of motion for the lattice model shown in Fig. 5 are

$$\ddot{x}_j = -\frac{c}{m}(3\dot{x}_j - \dot{x}_{j+1} - \dot{x}_{j-1}) - \frac{k}{m}x_j + \frac{1}{m}(F(x_{j+1} - x_j) - F(x_j - x_{j-1})), \quad j = 1, \ldots, N \quad (1)$$

with boundary conditions

$$x_0 = 0 \text{ (fixed-end/zero displacement)}$$
$$x_{N+1} = x_N \text{ (free-end/zero force).} \quad (2)$$

In Eq. (1), m is the block mass, k is the cantilevered beam stiffness, $F(\ )$ represents the nonlinear force-displacement relationship for the buckling elements, and the overdot represents differentiation with respect to time, t. The index j ranges from 1 to N, where N is the number of masses. The free and fixed boundary conditions (Eqs. (2)) are enforced by defining "dummy" masses 0 and $N + 1$.

To complete the model, it was necessary to find a functional expression for the force-displacement behavior of the buckling elements. Although planar elastica theory could have been used to derive this relationship (Frisch-Fay, 1962), evaluation of the results would require numerical solution of transcendental equations involving elliptic integrals. This approach was too computationally intensive to be practically used in numerical simulation. Instead, we chose to approximate buckling element force, $F(r)$, with an exponential

$$F(r_j) = \frac{\gamma}{b}(e^{br_j} - 1) \quad (3)$$

where $r_j = x_{j+1} - x_j$ is the relative displacement between two adjacent masses, γ the element's linearized stiffness $((dF(r)/dr)|_{r=0})$, and b determines the strength of the nonlinearity. Figure 4 shows a plot of the exponential force law for γ = 362.0 N/m and b = 725.0 m^{-1}. For this approximate value of b, the exponential force law and the experimentally measured behavior are qualitatively similar. Later in the paper, we discuss how to refine the value of b, based on experimental measurements, so that our analytical law more closely approximates the tensile behavior of the buckling elements.

The force law in Eq. (3) is the same as that used by Toda (1966, 1967, 1989) to model the interaction forces in an atomic lattice. If k and c are set to zero, Eqs. (1) and (3) reduce to those of a Toda lattice, which Toda showed to have exact nonlinear "soliton" solutions (see Eq. (5) for details). A "soliton" is defined as a localized nonlinear disturbance that *propagates without changing shape* and is left *unaltered by mutual interactions.* In a Toda lattice with γ and b both positive, a "soliton" would appear as a localized tensile wave with a nonlinear speed-amplitude dependence. We show in the next section that similar disturbances occur in our system.

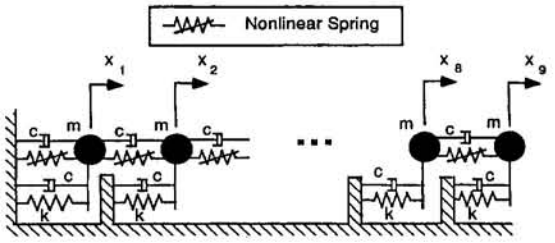


Fig. 5 Nonlinear lattice model of experimental structure

Substituting a periodic traveling wave solution into the linearized versions of Eqs. (1) and (3) and taking $c = 0$ produces the dispersion relation

$$\omega = \pm\sqrt{\frac{4\gamma}{m}\sin^2\left(\frac{\kappa a}{2}\right) + \frac{k}{m}} \quad (4)$$

where ω is the wave frequency, κ is the wave number, and a is the spacing between adjacent masses. The form of Eq. (4) indicates that the system allows only a band of frequencies to propagate without attenuation; this band is the Brillouin zone measured in the previous section. Substituting the measured values for γ and k into Eq. (4), we predict that the Brillouin zone for this structure should range from 4.3 to 15.9 Hz, in excellent agreement with the experiment. Figure 3 shows that the analytically calculated modal frequencies and dispersion relation agree well with experimental data. In the theory of atomic lattices, a branch of the dispersion relation which decreases to a nonzero frequency as the wave number goes to zero is known as an *optical branch,* Brillouin (1946). Thus, this structure has an *optical* but no *acoustic* branch in its dispersion relation.

The rate at which energy propagates in the linear system is governed by the slope of the dispersion relation or group velocity, $d\omega/d\kappa$. For the measured parameter values, the maximum possible group velocity for this system is approximately 6.9 m/s, which is the upper limit on the speed of energy propagation for the linearized system. However, as we see in the next section nonlinear wave speeds may greatly exceed this value.

Equations (1), (2), and (3) form a set of N coupled second-order nonlinear differential equations whose solution requires $2N$ initial conditions defining the positions and velocities of the N masses. These equations were integrated on a Micro-VAX computer, using a fifth-sixth order Runge-Kutta-Vernier routine from the International Math Subroutine Library (IMSL). Based upon previous discussion, the parameters used for the simulation were m = 157 g, γ = 362 N/m, b = 725 m^{-1}, k = 117 N/m and c = 0.01 N-s/m. Accuracy of the numerical integration was verified by checking conservation of energy for the zero-damping ($c = 0$) case.

4 Results

In this section the behavior of the experiment and model are compared. We began our examination of system dynamics by assessing the predictability of motions induced by sudden loading of the free end. Davies and Moon (1994) showed that in both the simulation and experiment, slight differences in the magnitude of the initial load produced large differences in the system state at later times, suggesting the possibility of transient chaos in this system.

To visualize the complex spatial and temporal dynamics that might lead to sensitive behavior in the system, we used contour plots of the compression/tension history of the buckling elements. Figure 6 shows a contour plot of the simulated impact dynamics of the model. Impact excitation was approximated by giving mass nine an initial velocity of −2.0 m/s and setting all other initial conditions to zero. The horizontal axis in the plot is the time and the vertical axis is the buckling element number. The strip of color to the right of each element label shows the relative level of compression (white) or tension (black) in that element over time. Figure 6 indicates that initially element nine enters an extreme state of buckling or compression. However, because the compressive force of the buckling elements is low,

Downloaded 04 May 2010 to 171.66.16.33. Redistribution subject to ASME license or copyright; see http://www.asme.org/terms/Terms_Use.cfm

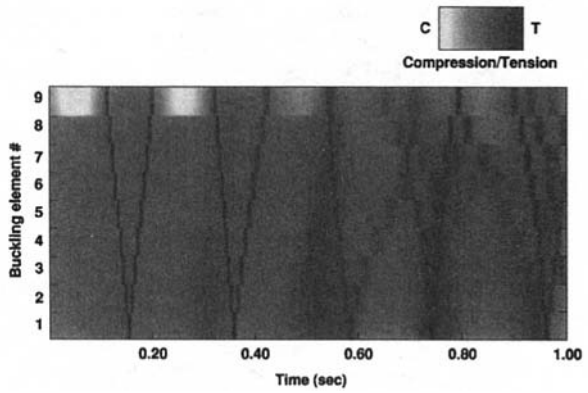


Fig. 6 Compression-tension contour of the impact dynamics of the model (one-second simulation)

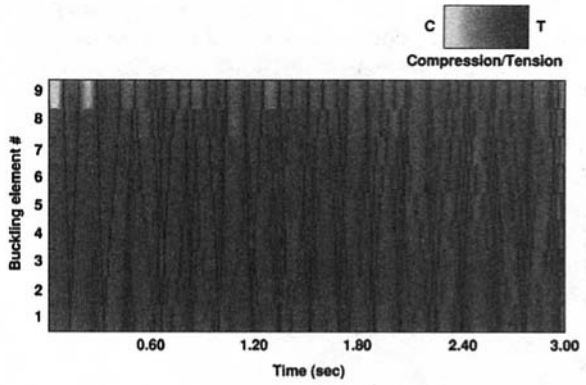


Fig. 8 Compression-tension contour of the impact dynamics of the model (three-second simulation)

this disturbance remains localized to element nine. After one-half of an oscillation cycle of the ninth mass-linear spring combination (approximately 0.1 sec), buckling element nine enters a state of tension. This initiates a high-force tensile disturbance that propagates rapidly through the structure. It reflects from the fixed-end and returns to the free-end, producing a second compression in buckling element nine at 0.2 seconds. The speed of this tensile wave is approximately 38 m/s, more than five times the maximum linear group velocity calculated in the previous section!

Figure 7 shows a compression/tension contour of experimental motions. In this case, mass 1 was rigidly fixed in place to ensure the fixed boundary condition, and the masses were renumbered 1 through 8 starting from the fixed end. The structure was excited by the sudden release of a compressive load applied to the free-end as shown in Fig. 2. For this case, the load was approximately 1 Newton; this load caused a deflection (from equilibrium) of -5 mm for mass 8, -1 mm for mass 7 and negligible amounts of the remaining masses. Release of the compressive load lead to a tensile wave like that seen in the simulation. The speed of this wave was approximately 22 m/s, more than three times the linear group velocity. For both the experiment and the simulation the fact that wave speeds greatly exceed the maximum group velocity is indicative of the strong nonlinearity of the observed motions.

Figures 6 and 7 show evidence of highly complex nonlinear wave dynamics. Particularly in the simulation, the wave breaks apart, splitting, fading, and re-emerging to produce complex interaction patterns in space and time. A contour plot of a three-second impact simulation (see Fig. 8) clearly illustrates the disordered dynamics which develop. The reason for the break-up of the initially ordered wave patterns is not clear. It may be that the observed tensile waves are perturbations of Toda "solitons" that break down into disordered patterns because the parameters k and c are nonzero. However, other evidence suggests that wave breakdown is most strongly linked to the boundary conditions. For example, we have found that releasing the fixed-end to produce a symmetric lattice greatly increases the longevity of the ordered wave patterns; in simulations for free-free boundary conditions, they have been found to persist for ten seconds or more. This data prompts complicated questions about links between soliton-like waves and sensitivity to initial conditions in nonlinear structural vibrations.

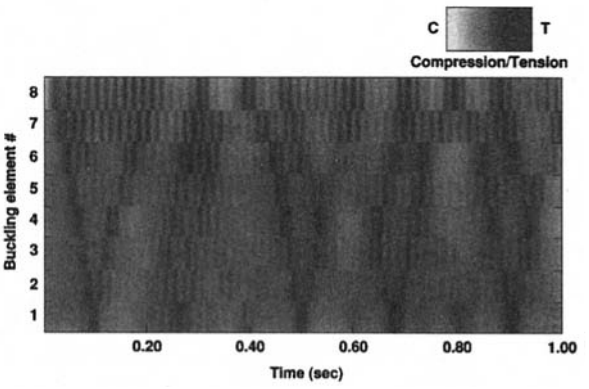


Fig. 7 Compression-tension contour of the experimental dynamics induced by a suddenly released compressive load of 1N

5 Discussion

Further understanding of the observed tensile waves is gained from a consideration of the forces associated with a wave. From the simulation data, we find that in the vicinity of a wave, the tensile forces in the nonlinear springs are 300 times higher than those exerted by the linear springs. In the experiment this ratio is lower, but the forces in the buckling elements still dominate in the vicinity of the wave. Thus, the effect of the linear springs on these waves is small, and for short periods of time they can be treated as Toda solitons.

The functional form of a Toda soliton is given below.

$$r_j = \frac{1}{b} \ln \left(\frac{m\beta^2}{\gamma} \operatorname{sech}^2 (\kappa j - \beta t) + 1 \right) \tag{5}$$

Substitution of Eq. (5) into Eqs. (1) and (3) with k and c set to zero, shows that it solves these equations if the following relation between β and κ is satisfied.

$$\beta = \sqrt{\frac{\gamma}{m}} \sinh \kappa \tag{6}$$

Equation 5 describes a localized wave that travels without changing shape. If $\gamma > 0$ and $b < 0$, $r_j(t) < 0$ for all values of j and t. This corresponds to the compressive atomic lattice waves studied by Toda. If, as in our case, $\gamma > 0$ and $b > 0$, then $r_j(t) > 0$ for all j and t and Eq. (5) represents a tensile wave. The speed of the wave in either case is

$$c = \frac{\beta a}{\kappa} \tag{7}$$

where a is the distance between masses. The speed of this nonlinear wave is dependent upon its amplitude. In general, larger narrower disturbances propagate faster than smaller broader ones.

Equation (7) should provide a reasonable estimate of the speed of the tensile waves observed in our system. As an example, we estimate the speed of the first tensile wave in Fig. 6.

Downloaded 04 May 2010 to 171.66.16.33. Redistribution subject to ASME license or copyright; see http://www.asme.org/terms/Terms_Use.cfm

From the data, we determined that the amplitude of this wave is approximately 0.0075 m. The expression for the amplitude of a Toda wave, denoted $\hat{r}$, is found by setting $\kappa j - \beta t = 0$ in Eq. (5).

$$\hat{r} = \frac{1}{b} \ln \left(\frac{m\beta^2}{\gamma} + 1 \right) \tag{8}$$

Substituting values of $\hat{r} = 0.0075$ m, $\gamma = 362.0$ N/m, $m = 0.157$ kg, and $b = 725.0\ \text{m}^{-1}$ allows us to determine an approximate value of $\beta = 727.3s^{-1}$ for our wave. Substituting this value into Eqs. (7) and (6) gives an approximate velocity for our tension wave of 40.6 m/s, which is only slightly greater than the observed velocity of 38 m/s. The difference is probably due to the fact that the linear springs do exert some small forces on the masses. As the wave passes, these forces work to reduce the acceleration of each mass and thus slightly delay the passage of the wave. The similarity of the tensile waves in the model and Toda solitons is illustrated in Fig. 9. The propagation and fixed-end reflection of the numerically simulated wave is shown in Fig. 10.

Using the experimental data, one can do a similar calculation to determine an improved value for b. From the experimental data shown in Fig. 7, approximate values of $c = 22.0$ m/s and $\hat{r} = 9.0 \times 10^{-4}$ m were determined. Using these values in an iterative solution to Eqs. (6), (7), and (8), we determined that b is approximately 4000 m^{-1} for the experimental system. A plot of the exponential force law for $b = 4000\ \text{m}^{-1}$ is shown in Fig. 4. This predicted value of b clearly brings the tensile portion of the analytical curve into excellent agreement with experimental data. The success of these wave speed calculations provide further evidence of the similarity between the waves observed in our system and Toda solitons.

6 Conclusions

In this paper, several new findings on the dynamics of nonlinear structures are reported. We have shown through experimental and numerical techniques that a nonlinear periodic structure subjected to a suddenly applied load exhibits complex transient dynamics that stems from the breakdown of ordered "soliton"-like waves into spatially and temporally disordered motions. These motions are characterized by the emergence of multiple wave-like structures with complex mutual interactions. Through calculations based upon Toda's analytical results, we were able to show a strong similarity between the waves observed in this system and Toda solitons. Previous work by the authors (Davies and Moon, 1994) provides evidence that the motions of this structure are an example of transient chaos with system states showing sensitivity to initial conditions during the early stages of a transient motion. However, further calculations possibly using Lyaponov exponents or entropy measures are necessary to determine the degree to which these motions are actually chaotic in time as well as the level of spatial disorder in the structural dynamics. The results of this paper are relevant to a broad array of nonlinear structures and prompt further inquiry into the role of nonlinear waves in generating spatio-temporal complexity.

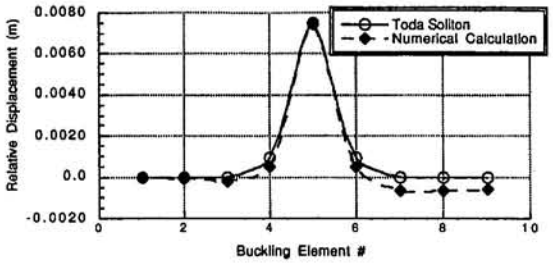


Fig. 9 Comparison of the tensile waves observed in the simulation data ($t = 0.134$ s) and a Toda soliton for $b = 725.0\ \text{m}^{-1}$, $\gamma = 362.0$ N/m, $m = 0.157$ kg, and $\beta = 727.3\ \text{s}^{-1}$

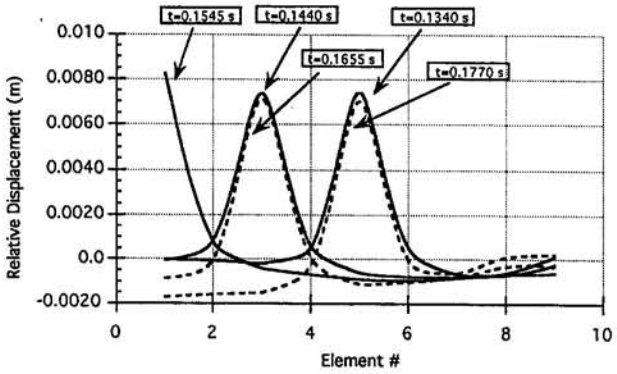


Fig. 10 Plot of the propagation of the simulated tensile wave and its reflection from the fixed end. Solid lines indicate the approaching (propagating left) and reflecting waves and dotted lines represent the reflected wave (propagating right). Parameter values are the same as discussed above.

Acknowledgments

This work was supported by the Air Force Office of Scientific Research, University Research Initiative, Grant No. AFOSR-90-0211, and by The Fannie and John Hertz Foundation.

References

Brillouin, L., 1946, *Wave Propagation in Periodic Structures,* McGraw-Hill, New York.

Cusumano, J., and Moon, F. C., 1989, "Low-Dimensional behavior in chaotic non-planar motion of a forced elastic rod: Experiment and Theory," *Proceedings of the IUTAM Symposium, Stuttgart Germany,* W. O. Schielen, ed., Springer-Verlag, New York.

Davies,.M. A., and Moon, F. C., 1993, "3-d spatial chaos in the elastica and the spinning top: Kirchhoff analogy," *Chaos,* Vol. 3, No. 1, pp. 93–99.

Davies, M. A., and Moon, F. C., 1994, "Transition from soliton to chaotic motion during the impact buckling of a nonlinear structure," *Journal of Chaos, Solitons and Fractals,* Vol. 3, No. 1, pp. 275–283.

Davies, M. A., 1993, "Spatio-Temporal Chaos and Solitons in Nonlinear Periodic Structures," Ph.D. Dissertation, Cornell University, Ithaca, NY.

Dowell, E. H., 1982, "Flutter of a buckled plate as an example of a chaotic motion of deterministic system," *Journal of Sound and Vibration,* Vol. 85, No. 3, pp. 333–344.

Feeny, B. F., 1989, "Autocorrelation and symbol dynamics for a chaotic dry friction oscillator," *Physics Letters A,* Vol. 141, Nos. 8 and 9, pp. 397–400.

Frisch-Fay, R., 1962, *Flexible Bars,* Butterworth and Co., London.

Holmes, P. J., 1979, "A nonlinear oscillator with a strange attractor," *Philosophical Transactions of the Royal Society of London,* Vol. 292, pp. 419–448.

Mielke, A., and Holmes, P. J., 1988, "Spatially complex equilibria of buckled rods," *Archive for Rational Mechanics and Analysis,* Vol. 101, pp. 319–348.

Moon, F. C., 1992, *Chaotic and Fractal Dynamics,* John Wiley and Sons, New York.

Moon, F. C., and Holmes, P. J., 1983, "A magnetoelastic strange attractor," *Journal of Sound and Vibration,* Vol. 18, pp. 465–477.

El Naschie, M. S., 1989, "On certain homoclinic solutions in elastic stability," *Journal of the Physical Society of Japan,* Vol. 58, pp. 4310–4321.

Pratap, R., Mukherjee, S., and Moon, F. C., 1994, "Dynamic behavior of a bilinear elastoplastic oscillator, Part I: Free oscillations," *Journal of Sound and Vibration,* Vol. 172, No. 3, pp. 321–337.

Thompson, J. M. T., and Virgin, L. N., 1988, "Spatial chaos and localization phenomena in nonlinear elasticity," *Physics Letters A,* Vol. 126, Nos. 8–9, pp. 491–496.

Toda, M., 1966, "Vibration of a chain with nonlinear interaction," *Journal of the Physical Society of Japan,* Vol. 22, No. 2, pp. 431–436.

Toda, M., 1967, "Wave propagation in anharmonic lattices," *Journal of the Physical Society of Japan,* Vol. 23, No. 3, pp. 501–506.

Toda, M., 1989, *Theory of Nonlinear Lattices,* Springer-Verlag, Berlin.

Tseng, W. Y., and Dugungi, J., 1971, "Nonlinear Vibrations of a Buckled Beam Under Harmonic Excitation," ASME JOURNAL OF APPLIED MECHANICS, Vol. 38, pp. 467–476.

Downloaded 04 May 2010 to 171.66.16.33. Redistribution subject to ASME license or copyright; see http://www.asme.org/terms/Terms_Use.cfm

P. A. Scagnetti
Department of Mechanical Engineering,
Massachusetts Institute of Technology,
Cambridge, MA

R. J. Nagem[1]
Assoc. Mem. ASME.

G. V. H. Sandri

T. G. Bifano
Assoc. Mem. ASME.

Department of Aerospace and
Mechanical Engineering,
Boston University,
Boston, MA

Stress and Strain Analysis in Molecular Dynamics Simulation of Solids

Molecular dynamics simulation of solid materials is applied to a two-dimensional indentation problem. Methods are presented for calculating the stress and strain tensors at interior points within the model. The stress calculations corresponding to the elastic deformation portion of the indentation process are compared with an analytical continuum solution. Stress calculations are also presented for the plastic deformation portion of the indentation process. The methods are derived independently so that future work can be directed at determining the constitutive relationship between stress and strain throughout the development of plastic flow and fracture in a solid material.

Introduction

Molecular dynamics modeling holds great potential as a means of simulating solid materials subjected to nanometer-scale deformation processes. The two most common mechanisms for permanent deformation in solids—plastic flow and fracture—are fundamentally atomistic in nature. It is possible to simulate small-scale processes using molecular dynamics, recapturing the essential atomic behavior of deformation and fracture. Molecular dynamics simulations have the potential to model elastic, plastic, and brittle behavior in a solid. Slip lines for plastic flow and parting lines for fracture are a result of the simulation, rather than an input to it.

In molecular dynamics simulation of solids, each atom (designated by the index i) is modeled as a Newtonian point mass m with position $\mathbf{r}_i$ subject to the equation of motion

$$m\frac{d^2\mathbf{r}_i}{dt^2} = \mathbf{F}_i^{\text{atomic}} + \mathbf{F}_i^{\text{external}} \tag{1}$$

where $\mathbf{F}_i^{\text{atomic}}$ is the interatomic force on the atom due to all other atoms and $\mathbf{F}_i^{\text{external}}$ is the externally applied force on the atom. A molecular dynamics model with N particles consists essentially of a set of N coupled ordinary differential equations of the form of Equation (1). A Verlet algorithm is typically used to integrate the system for a given set of initial conditions (Gould, and Tobochnik, 1988; Allen and Tildesley, 1987).

The results of a molecular dynamics simulation depend strongly upon the interatomic force model used. Molecular dynamics has been applied most often and most successfully to the study of gases and liquids. In such systems, interatomic forces are primarily due to the primary ionic and covalent bonds, while solid structures interact through the secondary van der Waals bonds (McClintock and Argon, 1966). In metals, there is also an interatomic force due to detachable valence electrons

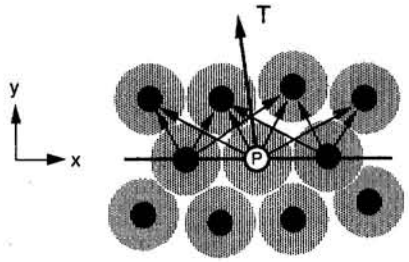


Fig. 1 Two-dimensional sketch of the interatomic forces used to compute the traction vector T at molecule P

which form a "free electron gas." This electron gas forms the metallic bond, which is a fundamentally quantum mechanical effect responsible for the close-packed crystalline structure of metals. Some aspects of metallic solids, such as macroscopic elastic constants, cannot be modeled accurately by a system of pairwise central forces between atoms (Holian et al., 1991). A noncentral model for interatomic forces in a crystalline lattice was developed by Gibson et al. (1960). A more recent non-pairwise model is the *embedded atom potential* used by Foiles et al. (1986) and Holian et al. (1991). These models attempt to describe the quantum mechanical free electron gas effects as part of the interatomic force in Eq. (1) (Hoover et al., 1990; Hoover et al., 1992; Belak and Stowers, 1990).

One of the current challenges in molecular dynamics is relating simulation results to the macroscopic notions of stress, strain, and the constitutive relation between stress and strain. Evaluation of stress, strain and their relationship is an important check of the quality of the molecular simulation. If the simulation accurately mirrors actual interatomic bonding in a metallic or covalent solid, then one would expect the molecular dynamics simulation of the solid material to exhibit both physically realistic behavior at the *atomic* scale and physically realistic macroscopic relationships between stress and strain. At the atomic scale, realistic material behavior should include stretching or contraction of intermolecular bonds, initiation and propagation of dislocations, and void formation. On a macroscopic scale, realistic material behavior should include elastic deformation, plastic deformation, and possibly fracture, along with naturally occurring transitions among these different stress-strain behaviors. In this paper, independent definitions of stress and strain are proposed by adapting continuum concepts to the dis-

[1] Address correspondence to Dr. Raymond Nagem, A/M Engineering, Boston University, 110 Cummington Street, Boston, MA 02215.

Contributed by the Applied Mechanics Division of THE AMERICAN SOCIETY OF MECHANICAL ENGINEERS for publication in the ASME JOURNAL OF APPLIED MECHANICS.

Discussion on this paper should be addressed to the Technical Editor, Professor Lewis T. Wheeler, Department of Mechanical Engineering, University of Houston, Houston, TX 77204-4792, and will be accepted until four months after final publication of the paper itself in the ASME JOURNAL OF APPLIED MECHANICS.

Manuscript received and accepted by the ASME Applied Mechanics Division, Oct. 26, 1994. Associate Technical Editor: J. T. Jenkins.

Copyright © 1996 by ASME

Downloaded 04 May 2010 to 171.66.16.33. Redistribution subject to ASME license or copyright; see http://www.asme.org/terms/Terms_Use.cfm

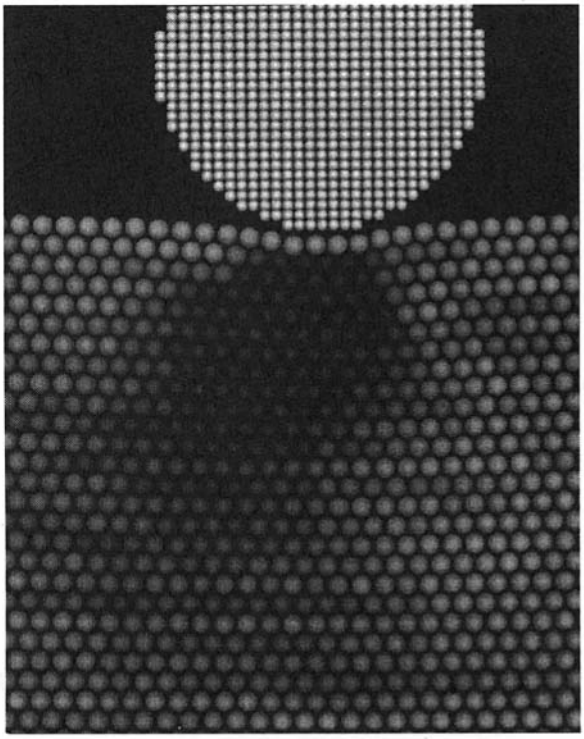


Fig. 2 Map of normalized stress invariant $(\sigma_{xx} + \sigma_{yy})(r^*)^3/\epsilon_o$ in the region beneath the indenter during the elastic phase of indentation. Normalizing constants r^* and ϵ_o are the equilibrium bond length and bond energy, respectively, for the potential function used in this simulation. Values of normalized stress invariant scale with the shade of the atom, with darker shades corresponding to larger compressive stresses.

crete nature of the molecular dynamics model. These definitions can be used in the interpretation and the development of atomic simulations that provide realistic models of solids.

Calculating Stress

Love (1944) has given a definition of stress in particulate systems which is directly applicable to molecular dynamics simulations. A finite segment of a plane is centered on a particular atom. The resultant of all the interatomic forces passing through the plane, divided by the area of the plane is defined as the traction vector, **T**, for the particular atom. Components of the stress tensor are calculated as projections of the traction vector in the coordinate directions. Figure 1 is a two-dimensional sketch of the traction vector **T** at the molecule P. The plane segment centered at P should be small enough to capture the local nature of the interatomic forces, but large enough to give a relatively smooth distribution of the traction vector throughout the body. We have found in the simulations described below that a plane with diameter equal to five times the undeformed interatomic spacing gives stresses that are both locally descriptive and relatively smooth.

Calculating Strain

The strain tensor can be computed using purely geometric information. In continuum mechanics, the strain tensor is defined as

$$\epsilon_{\alpha\beta} = \tfrac{1}{2}(u_{\alpha,\beta} + u_{\beta,\alpha} + u_{\gamma,\alpha}u_{\gamma,\beta}) \qquad (2)$$

where α, β, and γ are coordinate directions, u_α is the Cartesian component of the displacement vector in the α-direction, and a comma denotes differentiation with respect to the coordinate direction indicated by the subscript that follows.

In a molecular dynamics simulation, the displacement vector of each atom is available at each time step. The derivatives in Eq. (2), however, must be approximated using the spatially discrete atomic data. We propose to approximate the derivatives by fitting a linear function to each displacement component at each atom. The discrete displacement data in the neighborhood of a particular atom are used to compute a least squares fit and the slopes of the least squares fit are used to approximate the derivatives. The neighborhood used in the strain calculation should be of the same size as that used in the computation of the traction vector.

Indentation Simulation

We have simulated a two-dimensional indentation of a rectangular workpiece with a rigid, circular indenter. An 8192 processor parallel computer was used, with each processor responsible for one molecule in an initially perfect triangular lattice. The initial atomic velocities were randomly distributed. Interatomic forces were computed using a combination of pairwise central forces derived from a Lennard-Jones potential and noncentral forces derived from the embedded atom potential. A full description of the details of the simulation is given by Scagnetti (1992). The indenter was fixed above the rectangular workpiece for a period of time, allowing the workpiece to come to equilibrium. Next, the indenter moved into the workpiece with a con-

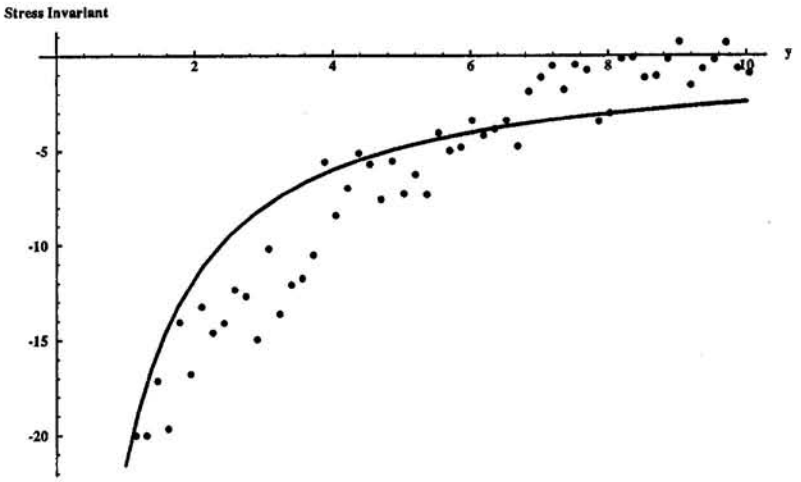


Fig. 3 Plot of normalized stress invariant $(\sigma_{xx} + \sigma_{yy})(r^*)^3/\epsilon_o$, as a function of depth directly beneath the indenter. Solid curve is a continuum Hertzian solution for the same geometry.

Downloaded 04 May 2010 to 171.66.16.33. Redistribution subject to ASME license or copyright; see http://www.asme.org/terms/Terms_Use.cfm

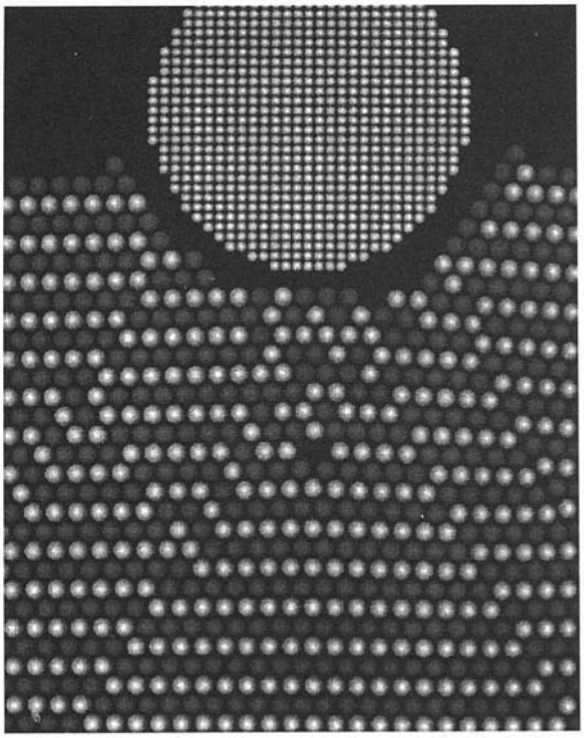


Fig. 4 Plot of molecule positions after indenting to a depth of 10r^*, then retracting the indenter. Atom shading is for visualization only.

stant downward velocity. Finally, the indenter returned to its original position with a constant upward velocity. In the initial phase of indentation, the geometry is very close to that of an elastic Hertzian contact between a cylinder and a semi-infinite half-plane, for which an exact solution exists (Timoshenko and Goodier, 1970).

Results

For the simulations performed, the following observations were made. First, plastic deformation starts to occur as the indenter reaches a depth of about $1.5r^*$, where r^* is the equilibrium spacing between two atoms. Second, the maximum stresses throughout the lattice do not increase after the deformation becomes plastic. Rather, slip lines form, and the stress remains at the maximum elastic value. In this sense, the slip acts to relieve any further stress by propagating dislocations.

At the simulation time shown in Fig. 2, the atomic lattice has deformed in the region beneath the indenter, but there are no discontinuities in the structure of the lattice. If the indenter were removed at this point in the simulation, the lattice would return to its original state. In Fig. 3, the two-dimensional stress invariant ($\sigma_{xx} + \sigma_{yy}$) is plotted as a function of depth directly beneath the indenter. The solid line is the stress invariant predicted by a Hertz analysis. The agreement is very good; better agreement is expected as the number of particles in the simulation is increased, as the speed with which the indenter is moved is reduced, and for initial lattices that more closely resemble a locally isotropic solid. This initial result shows that a molecular dynamics model is capable of producing realistic behavior in the elastic regime, and that our definition of stress can be used to interpret results of a molecular model in a quantitative manner.

Figure 4 shows a section of the lattice at a stage when the indenter has started to move away from the lattice. There is some tendency for the lattice to return to its original configuration ("elastic recovery"), and a stable vacancy or void remains in the lattice. Since voids are an important factor in the process of crack initiation, their natural occurrence in the simulation is a promising indication that atomic simulations can predict the microscopic phenomena that are the ultimate cause of macroscopic material behavior under realistic loading conditions.

References

Allen, M. P., and Tildesley, R., 1987, *Computer Simulations of Liquids*, Clarendon Press, Oxford, U.K.

Belak, J. F., and Stowers, I. F., 1990, "Molecular Dynamics Studies of Surface Indentation in Two Dimensions," *Materials Research Symposium: Atomic Scale Calculations of Structure in Materials*, Materials Research Society, Boston, Vol. 193, pp. 259–264.

Foiles, S. M., Baskes, M. I., and Daw, M. S., 1986, "Embedded-Atom-Method Functions for the FCC Metals CU, Ag, Au, Ni, Pd, Pt, and other Alloys," *Physical Review B*, Vol. 12, No. 33, pp. 7983–7991.

Gibson, J. B., Goland, A. M., Milgram, M., and Vineyard, G. H., 1960, "The Dynamics of Radiation Damage," *Physical Review Letters*, Vol. 120, pp. 1229–1253.

Gould, H., and Tobochnik, J., 1988, *An Introduction to Computer Simulation Methods—Applications to Physical Systems*—Part 1, Addison-Wesley, Reading, MA.

Holian, B. L., Voter, A. F., Wagner, N. J., Ravelo, R. J., Chen, S. P., Hoover, W. G., Hoover, C. G., Hamerberg, J. E., and Dontje, T. D., 1991, "Effects of Pairwise Versus Many Body Forces on High Stress Plastic Deformation," *Physical Review A*, Vol. 43, No. 6, pp. 2655–2661.

Hoover, W. G., DeGroot, A. J., Hoover, C. G., Stowers, I. F., Kawai, T., Holian, B. L., Boku, T., Ihara, S., and Belak, J. F., 1990, "Large-Scale Elastic-Plastic Indentation Simulation via Nonequilibrium Molecular Dynamics," *Physical Review A*, Vol. 42, No. 10, pp. 5844–5853.

Hoover, W. G., DeGroot, A. J., and Hoover, C. G., 1992, "Massively Parallel Computer Simulation Plane Strain Elastic-Plastic Flow via Nonequilibrium Molecular Dynamics and Lagrangian Continuum Mechanics," *Computers in Physics*, Vol. 6, No. 2, pp. 155–164.

Love, A. E. H., 1944, *A Treatise on the Mathematical Theory of Elasticity*, Dover, New York.

McClintock, F. A., and Argon, A. S., 1966, *Mechanical Behavior of Materials*, Addison-Wesley, Reading, MA.

Scagnetti, P. A., 1992, "Simulation of Microindentation Using Molecular Dynamics Simulation," M. S. Thesis, Boston University, Boston, MA.

Timoshenko, S. P., and Goodier, J. N., 1970, *Theory of Elasticity*, McGraw-Hill, New York.

Downloaded 04 May 2010 to 171.66.16.33. Redistribution subject to ASME license or copyright; see http://www.asme.org/terms/Terms_Use.cfm

Prediction of Mode Parameters and Moment-Rotation Curves for Crushed Thin-Walled Trapezoidal Tubes in Bending

M. S. Park
Ph.D. Student.

B. C. Lee[1]
Associate Professor.

Department of Mechanical Engineering,
Korea Advanced Institute of Science
and Technology,
373-1, Kusong-dong, Yusung-gu,
Taejon 305-701, Korea

In the context of kinematic models, a general procedure for the bending crush analysis of thin-walled members is proposed and applied to the trapezoidal and rectangular tubes in bending. The main emphasis of this study is given to the determination of collapse mode parameters and the prediction of post-collapse behaviors of the structural member. The mode shapes are determined by minimizing plastic energy rate of the members. Moment-rotation curves are obtained by differentiating the absorbed plastic energy with respect to the rotation angle. For small rotation angles the solution is modified by considering elastic buckling and plastic collapse moments. Through several examples a full range of post-collapse response of the thin-walled members is shown to be effectively calculated by the proposed method without making any recourse to experimental data.

1 Introduction

Thin-walled beams and columns are increasingly used for the members of vehicle, aircraft, and off-shore structures. Their post-buckling or post-collapse analyses are required for the design of such structures under crush conditions. As a simple and effective means of predicting post-collapse behavior, the crush analyses of thin-walled members using collapse mechanisms and the theory of rigid plasticity have been developed and widely used by many researchers. Load-displacement relationships after the point of collapse also can be useful as basic data for hybrid beam elements in nonlinear structural analysis.

It is not easy to predict post-buckling and post-collapse behavior of thin-walled members because of large displacement, large localized strains, possible thickness variation, and nonlinearities of materials. Usually, a rapid decrease in the resisting force of thin-walled members after the ultimate strength is reached is accompanied with crumpling or folding of hinged deformation elements. These characteristics of deformation have motivated to the development of the theoretical method of analysis based on kinematic models. Gerard (1957) and Pugsley (1960) suggested an empirical method to study axial collapse of thin-walled tubes.

Wierzbicki and Abramowicz (1983) and Meng et al. (1983) studied axial collapse of rectangular tubes. Johnson et al. (1977) and Abramowicz and Jones (1984) analyzed circular tubes under axial compression. Reid et al. (1986) analyzed rectangular sheet metal tubes filled with foam in axial compression. Most of authors calculated the mean crushing force rather than load-displacement relations under the assumption of constant folding lengths for the collapse mechanism.

Kecman (1983) and Kotelko and Krolak (1993) analyzed bending collapse of rectangular tubes and triangular girders, respectively. They calculated moment-rotation angle curves using the collapse mechanism. The folding lengths and the radius of traveling hinges were determined from experimental data. Murray and Khoo (1981) proposed some basic folding mechanisms for channel sections and analyzed axial-bending collapse. Cimpoeru and Murray (1993) studied empirical method for finding moment-deflection curves of rectangular bent tubes. Recently, the problems have been studied theoretically by Drazetic et al. (1993) and Wierzbicki et al. (1994).

Results of post-collapse analyses based on kinematic models also can be used in system-level analyses by means of a special hybrid finite element. Mahmood and Paluszny (1988) developed a hybrid method of simulating beam-type structures with locally buckled elements. Wierzbicki and Abramowicz (1988) also developed a special crush element based on their folding mechanism for axial deformation.

In general, theoretical method of predicting mode parameters and calculating load-displacement relations without supplement of any experimental data has been fairly well established. However, little applications exist to date to the class of problems involving bending collapse of rectangular tubes. In this paper, we will develop a solution procedure for bending collapse responses of prismatic thin-walled beams based on the kinematic method. We will apply the procedure to several trapezoidal sections to show its accuracy and usefulness. Since our main concern is given to practical aspects of estimating kinematic quantities, plastic energy, and mode parameters, we will adopt numerical techniques for the estimation rather than analytical derivation.

2 Bending Collapse Mechanism for the Trapezoidal Tube Section

We will select a trapezoidal tube section for the bending collapse analysis. Rectangular section can be considered as a special case of the trapezoidal section. Based on experimental observations, a bending collapse mechanism illustrated in Figs. 1 and 2 is assumed. This mechanism is similar to those of Kecman (1983) and Wierzbicki and Abramowicz (1983) for rectangular section. However, we make the dimensions of folding lengths (λ_1 and λ_2) and radius of traveling hinge (ρ) unknown. These unknown parameters of the collapse mechanism will be determined from an additional postulate.

[1] To whom all correspondence should be addressed.

Contributed by the Applied Mechanics Division of THE AMERICAN SOCIETY OF MECHANICAL ENGINEERS for publication in the ASME JOURNAL OF APPLIED MECHANICS.

Discussion on this paper should be addressed to the Technical Editor, Professor Lewis T. Wheeler, Department of Mechanical Engineering, University of Houston, Houston, TX 77204-4792, and will be accepted until four months after final publication of the paper itself in the ASME JOURNAL OF APPLIED MECHANICS.

Manuscript received by the ASME Applied Mechanics Division, Aug. 22, 1994; final revision, Feb. 25, 1995. Associate Technical Editor: S. Kyriadides.

Copyright © 1996 by ASME

Downloaded 04 May 2010 to 171.66.16.33. Redistribution subject to ASME license or copyright; see http://www.asme.org/terms/Terms_Use.cfm

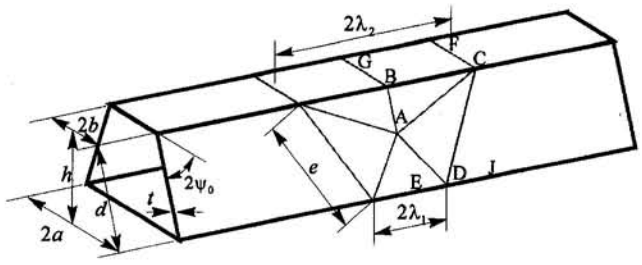


Fig. 1 Trapezoidal tube section beam

A quarter portion of the crushed tube will be considered because of the symmetric nature of deformation. In Fig. 1, widths of the bottom and top flanges are $2a$ and $2b$, respectively, height of the section is h, thickness of the plates is t and the external trapezoidal angle is $2\Psi_0$. When the locally buckled beam is bent as in Fig. 2, the compressed flange GBCF moves downward while the line segment GBA remains straight and horizontal. The point A begins to move from the point B and moves toward the point E when deformation progresses. According to the movement of the point A, the line segment AC leaves the line BC for the line EC. Plastic deformation is assumed to be localized and characterized by bending in stationary hinges and traveling hinges and extensional deformation surrounding the point A. This is a practical idealization in the study of local buckling behavior. A hinge is modeled as stationary when the traveled distance is small compared with the radius of bending. In stationary hinges deformation energy is mainly absorbed by plastic bending of the plate. Traveling hinges are introduced when the traveled distance is considerably large and the energy is mainly absorbed by rolling deformation of the plate. In our mechanism, the line segments BG, CF, DI, DE, DC, DA, and BA are considered as stationary bending hinges. The line segment AC is modeled as traveling hinge. Small area around point A is modeled as extensional deforming region similar to the basic folding mechanism of Wierzbicki and Abramowicz (1983).

The geometry of the crushed mechanism can be fully described by the position of the point A under the assumption of rigid plates and localized deformation. In Fig. 2, coordinates of point A are given as $(0, y_3, a + z_1)$, where

$$y_3 = y_1 - y_2 \tag{1a}$$

$$y_1 = c \sin(\gamma + \theta) \tag{1b}$$

$$y_2 = \sqrt{\lambda_2^2 - x_1^2}. \tag{1c}$$

The angle θ is the half of the rotation of the beam, which is a process control parameter of the bending collapse. The length x_1 is calculated from

$$x_1 = \lambda_1 + c \cos(\gamma + \theta). \tag{2}$$

The angles depicted in Fig. 2 are related with the basic lengths as follows:

$$\tan\gamma = \frac{h}{\lambda_2 - \lambda_1}; \quad \tan(\eta + \theta) = \frac{y_2}{x_1}; \quad \tan\epsilon = \frac{z_1}{y_3}. \tag{3}$$

Finally, the value of z_1 can be obtained from the following equation:

$$z_1 + (a - b) + \sqrt{z_1^2 + y_3^2} = d \tag{4}$$

which is an inextensibility condition of the line segments BA and AE. Solving Eq. (4), we obtain

$$z_1 = \frac{(d - a + b)^2 - y_3^2}{2(d - a + b)}. \tag{5}$$

Equations (1a) and (5) describe the position of point A. Locations of the other points such as the point F, C, G, and B can be easily determined from geometric relationships between vectors.

3 Formulation of Post-Collapse Analysis

A procedure will now be described for the estimation of plastic energy, mode parameters, and instantaneous bending moment. Material is assumed to be rigid plastic with linear strain hardening. The plastic energy rate equation for the deforming elements can be written as follows:

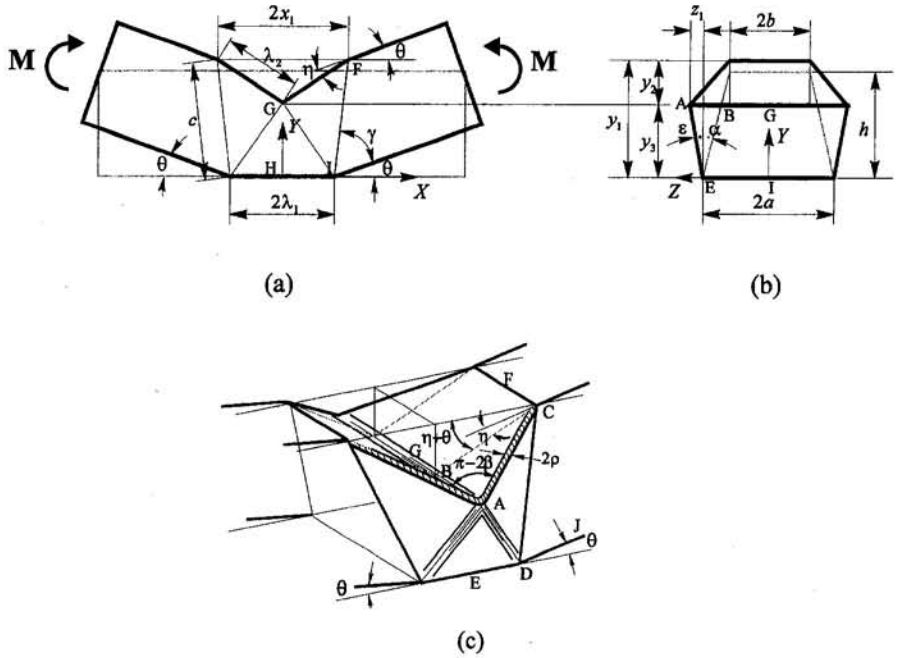


Fig. 2 Deformed shape of the collapsed beam; (*a*) front view, (*b*) side view, (*c*) perspective view

Downloaded 04 May 2010 to 171.66.16.33. Redistribution subject to ASME license or copyright; see http://www.asme.org/terms/Terms_Use.cfm

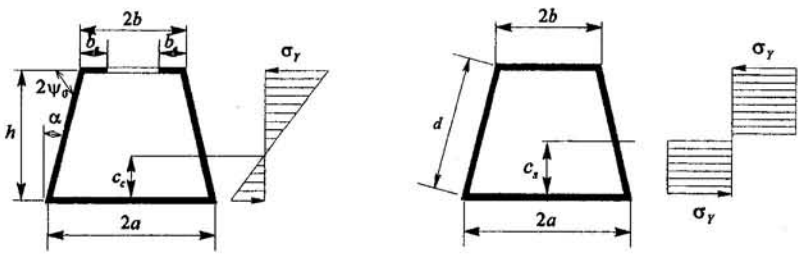


Fig. 3 Crippling and squashing of trapezoidal cross section beam; (*a*) crippling state, (*b*) squashing state

$$\dot{w} = \dot{w}(\mathbf{x}, \boldsymbol{\lambda}) = \int_V \sigma_{ij}\dot{\epsilon}_{ij}(\mathbf{x}, \boldsymbol{\lambda})dV. \tag{6}$$

Strain rate $\dot{\epsilon}_{ij}$ and stress σ_{ij} can be determined locally from the global kinematic data $\mathbf{x}$ that represent the motion of collapse mechanism. The kinematic data for the trapezoidal section consist of y_3, γ, η, ϵ, and z_1. In general, the kinematic quantities can be obtained from the solution of nonlinear kinematic compatibility equations. In Eq. (6), λ is a vector of mode parameters, that is, $\boldsymbol{\lambda} = (\lambda_1, \lambda_2, \rho)$ where ρ is the rolling radius.

For stationary hinge lines, Eq. (6) can be written as a function of the hinge length l and the bending angle φ:

$$\dot{w} = \int_0^l m(\varphi)\,\dot{\varphi}\,dS \tag{7}$$

where dS is the arc length parameter and

$$m(\varphi) = m_Y + H\varphi \tag{8}$$

where $m(\varphi)$ means the plastic bending moment of the hinge element. In Eq. (8), m_Y and H represent the yielding moment and the hardening modulus under bending, respectively. The moment and the modulus can be derived from the uniaxial stress-strain relation $\sigma = \sigma_Y + E_T\epsilon$ where σ_Y and E_T denote yield stress and tangent modulus, respectively. The moment, m_Y equals to $\sigma_Y t^2/4$ and H is given by $E_T t^2/8$. When the bending angle is constant along the hinge line, plastic energy can be written more simply as follows:

$$w = (m_Y\,\varphi + \tfrac{1}{2}H\varphi^2)l. \tag{9}$$

For the stationary bending hinges BG, CF, DI, DE, DC, DA, and BA, we can calculate associated plastic energies by Eqs. (7) or (9). For each bending hinge, the length and the bending angle for the calculation of plastic energy are obtained as follows:

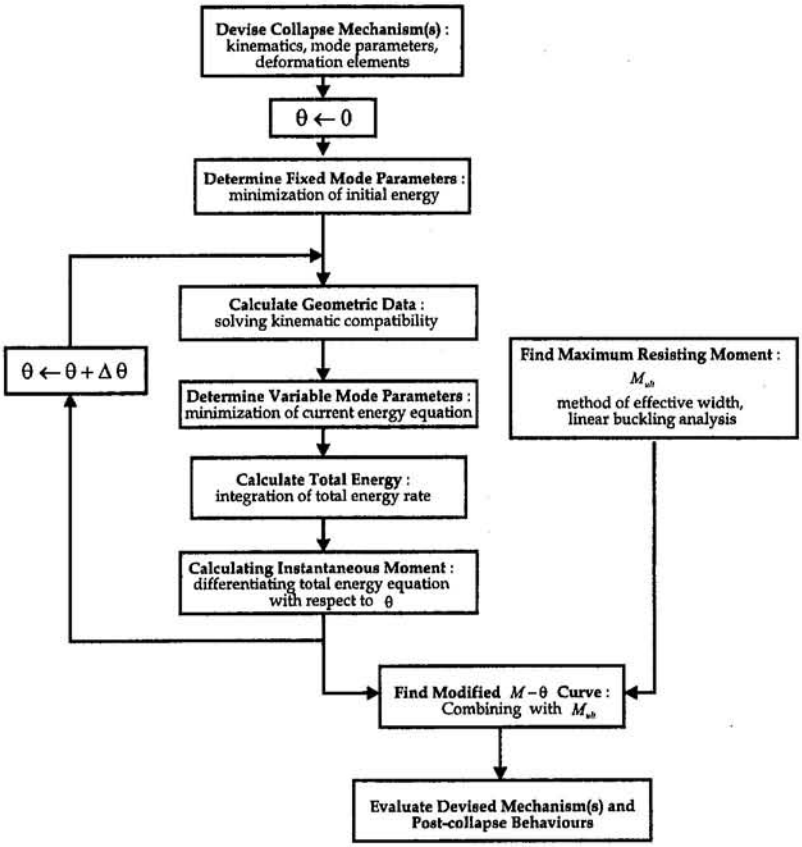


Fig. 4 Detailed flow chart of the post-collapse analysis

Downloaded 04 May 2010 to 171.66.16.33. Redistribution subject to ASME license or copyright; see http://www.asme.org/terms/Terms_Use.cfm

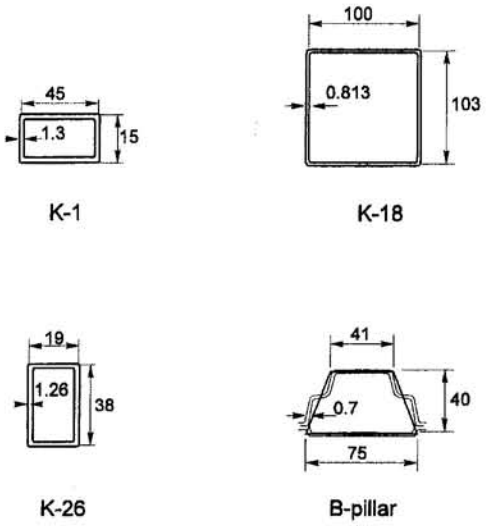


Fig. 5 Example sections

hinge	l	$\varphi(S)$	
BG	b	$2(\eta + \theta)$	(10a)
CF	b	η	(10b)
DI	a	θ	(10c)
DE	λ_1	$\alpha + \epsilon$	(10d)
DC	$\sqrt{d^2 + (\lambda_2 - \lambda_1)^2}$	$\cos^{-1}(\mathbf{n}_0 \cdot \mathbf{n}_1)$	(10e)
DA	$\sqrt{\lambda_1^2 + (d - z_1 - a + b)^2}$	$\cos^{-1}(\mathbf{n}_1 \cdot \mathbf{n}_2)$	(10f)
BA	$z_1 + a - b$	$2(1 - S/l)(\eta + \theta)$	(10g)

where α is the angle represented in Fig. 2(b) and S is the arc length measured from the point B to the point A. Vectors $\mathbf{n}_0$, $\mathbf{n}_1$, and $\mathbf{n}_2$ represent unit normal vectors of the plates CDJ, ADC and DAE, respectively:

$$\mathbf{n}_0 = (\sin\theta \sin\alpha, -\cos\theta \sin\alpha, \cos\alpha) \quad (11a)$$

$$\mathbf{n}_1 = \mathbf{r}_C \times \mathbf{r}_A / \|\mathbf{r}_C \times \mathbf{r}_A\| \quad (11b)$$

$$\mathbf{n}_2 = (0, -\sin\epsilon, \cos\epsilon). \quad (11c)$$

In Eq. (11b) $\mathbf{r}_C$ and $\mathbf{r}_A$ are position vectors of the point C and A relative to the point D, respectively:

$$\mathbf{r}_C = (c\cos(\gamma + \theta), c\sin(\gamma + \theta), b - a) \quad (12a)$$

$$\mathbf{r}_A = (-\lambda_1, y_3, z_1). \quad (12b)$$

For the traveling hinge AC and the small extensional deformation area around the point A, we utilize the results of Abramowicz and Wierzbicki (1989) for the corner deformation. The degree of deformation of the folding mechanism is represented by the angle η here (Fig. 2(c)). Following the results in the literature, the plastic energy rate for the traveling hinge can be written as follows:

$$\dot{w}_{AC} = mC_{AC}(\eta)\frac{\lambda_2^2}{\rho}\dot{\eta} \quad (13)$$

and the plastic energy rate for the extensional deformation region is

$$\dot{w}_A = nC_A(\eta)\rho\lambda_2\dot{\eta}. \quad (14)$$

In the above equation, $n = 4m/t$ represents the fully plastic membrane force and the coefficients used in Eqs. (13) and (14) are

Table 1 Material properties, collapse moments and folding lengths of the example sections

Section	σ_Y	E_T	M_{ult}	λ_1	λ_2
K-1	290	500	256	3.9	15
K-18	161	620	1301	12	45
K-26	290	500	502	5.4	21
B-pillar	300	500	399	5.3	21
(unit)	N/mm^2	N/mm^2	$N-m$	mm	mm

$(E = 200\times10^3\ N/mm^2,\ \nu = 0.3)$

$$C_{AC}(\eta) = 2\cos\eta\sqrt{1 + \frac{\sin^2\eta}{\tan^2\Psi_0}} \quad (15a)$$

$$C_A(\eta) = 2\cos\eta\int_0^{\beta(\eta)}\frac{d\Phi}{\sqrt{\tan^2\Psi_0 + \cos^2\Phi}} \quad (15b)$$

where $2\Psi_0$ represents the external angle and $\tan\beta = \tan\eta/\sin\Psi_0$. The total plastic energy rate is calculated by summing up energy rates of the local deformation elements.

$$\dot{W} = \dot{W}(\boldsymbol{\lambda}) = 2\dot{w}_{BG} + 2\dot{w}_{BA} + 4(\dot{w}_{CF} + \dot{w}_{DI} + \dot{w}_{DE} + \dot{w}_{DC} + \dot{w}_{DA} + \dot{w}_{AC} + \dot{w}_A) \quad (16)$$

Equation (16) contains three unknown mode parameters. We determine those values by applying minimum plastic energy postulate which can be stated by

$$\text{Minimize} \quad \dot{W} = \dot{W}(\boldsymbol{\lambda})$$
$$\text{subject to} \quad \lambda_1 \geq 0, \quad \lambda_2 \geq 0, \quad \rho \geq 0. \quad (17)$$

In general, the solution of problem (17) is a function of process variable θ but once the collapse mechanism has been set up, much smaller energy would be required for the deformation than for the development of new mechanism. So, we assume that the changes of the folding lengths λ_1 and λ_2 remain negligible during the deformation. From the necessary condition for

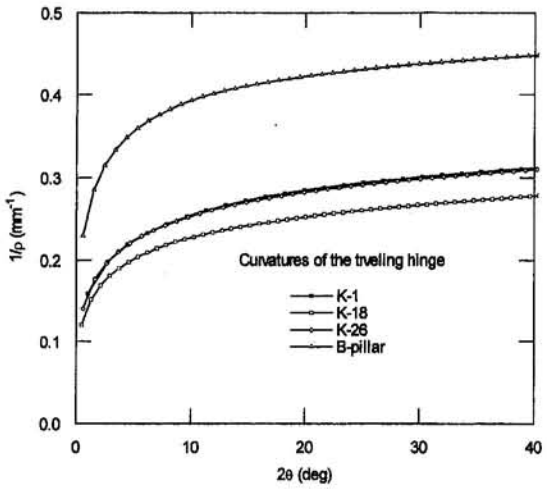


Fig. 6 Variation of a local curvature of the traveling hinge with rotation angle

Downloaded 04 May 2010 to 171.66.16.33. Redistribution subject to ASME license or copyright; see http://www.asme.org/terms/Terms_Use.cfm

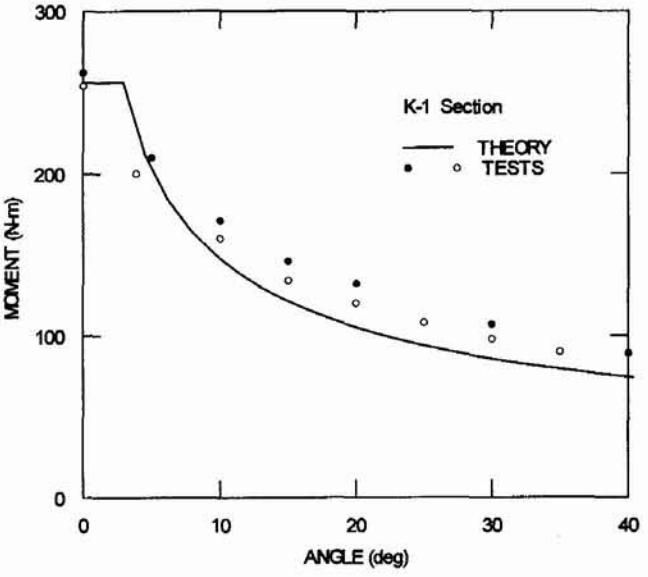


Fig. 7(a)

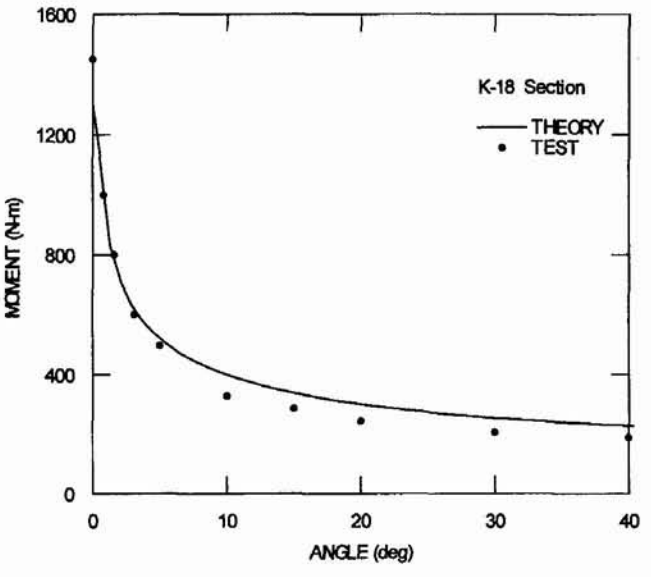


Fig. 7(b)

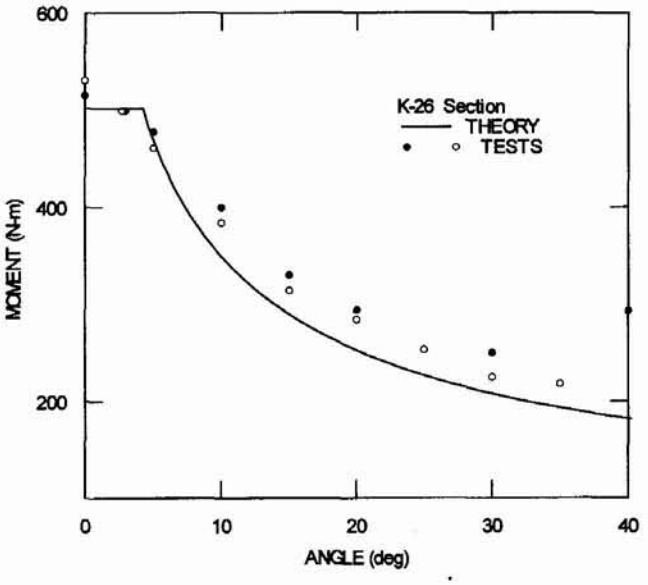


Fig. 7(c)

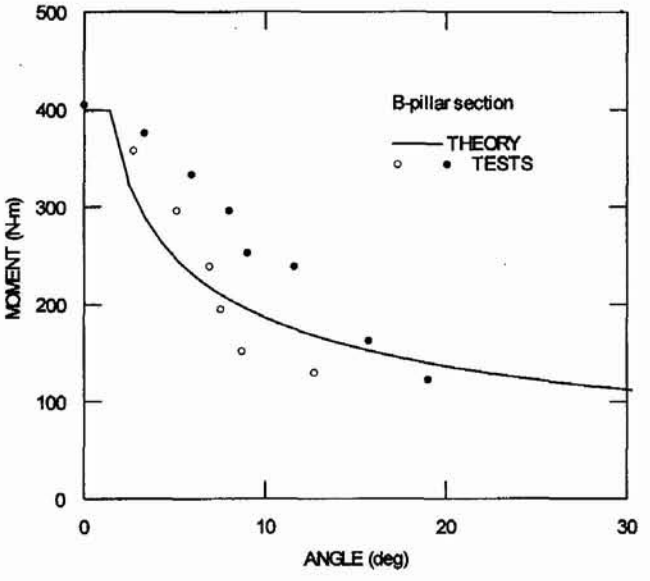


Fig. 7(d)

Fig. 7 Moment-angle curves; (*a*) K-1 section, (*b*) K-18 section, (*c*) K-26 section, (*d*) B-pillar section

the minimum of (17) with respect to the radius of traveling hinge, we arrive at

$$\frac{\partial \dot{W}}{\partial \rho} = 4(nC_A\lambda_2 - \frac{mC_{AC}}{\rho^2}\lambda_2^2)\dot{\eta} = 0. \tag{18}$$

Therefore, the values of ρ can be obtained as

$$\rho = \rho(\eta) = \frac{1}{2}\sqrt{\frac{C_{AC}(\eta)}{C_A(\eta)}}\, t\lambda_2. \tag{19}$$

Substituting this value into Eqs. (13) and (14), we obtain

$$\dot{w}_{AC} + \dot{w}_A = 2mt^{-1/2}\lambda_2^{3/2}\sqrt{C_{AC}C_A}\,\dot{\eta} \tag{20a}$$

$$w_{AC} + w_A = 2mt^{-1/2}\lambda_2^{3/2}\int_0^{\eta(\theta)}\sqrt{C_{AC}C_A}\,d\eta. \tag{20b}$$

It can be shown that the right-hand side of Eq. (20*a*) vanishes at the beginning of the collapse process ($\theta = 0$). Therefore, the effects of the rolling hinge would be negligible in determining the folding lengths at the initial stages of the plastic collapse.

Considering the assumption of constant folding lengths λ_1 and λ_2, it is clear that λ_1 and λ_2 are independent of process control parameter. Then, the necessary condition for the minimum of (17) can be expressed as

$$\frac{\partial}{\partial \lambda_i}\left(\frac{\partial W}{\partial t}\right) = \frac{\partial}{\partial t}\left(\frac{\partial W}{\partial \lambda_i}\right) = 0, \quad i = 1, 2. \tag{21}$$

The value of work rate in the first expression of Eq. (21) becomes very large at the beginning of collapse because of rigid-plastic assumption. So, we calculate the derivatives according to the second expression of Eq. (21) to determine the appropriate folding lengths. For the implementation of numerical method, it can be approximated as

$$\frac{\partial}{\partial t}\left(\frac{\partial W}{\partial \lambda_i}\right) \approx \frac{\left.\frac{\partial W}{\partial \lambda_i}\right|_{t=t_0} - \left.\frac{\partial W}{\partial \lambda_i}\right|_{t=0}}{t_0 - 0} = 0, \tag{22}$$

Downloaded 04 May 2010 to 171.66.16.33. Redistribution subject to ASME license or copyright; see http://www.asme.org/terms/Terms_Use.cfm

that can be rewritten as

$$\frac{\partial}{\partial \lambda_i}\{W(t_0, \lambda_1, \lambda_2) - W(0, \lambda_1, \lambda_2)\} = 0. \quad (23)$$

The second term in Eq. (23) vanishes. In rate form, mode parameters that satisfy the following equation are taken as a solution of (21):

$$\frac{\partial}{\partial \lambda_i}\int_0^{t_0} \dot{W}(t, \lambda_1, \lambda_2)dt = 0 \quad i = 1, 2. \quad (24)$$

In Eq. (24), t_0 is an initial control process parameter chosen to be sufficiently small and physically acceptable. Several iterations would be desirable in selecting t_0 so that the variations of λ_1 and λ_2 might be negligible.

The total plastic energy can be calculated by summing up plastic energies of Eqs. (9) and (20*b*) for each bending hinge and travelling hinge. Then, applying the virtual work principle, instantaneous moments can be obtained as follows:

$$M = M(\theta) = \frac{1}{2}\frac{\partial W(\theta)}{\partial \theta}. \quad (25)$$

We calculate the instantaneous moments by numerical differentiation.

4 Ultimate Strength Analysis

The values of moment calculated from Eq. (25) overestimate the initial collapse behavior in which the elastic deformation governs the structural response. So we will estimate the ultimate load considering the critical behavior at the initial stage and incorporate it into the moment-rotation relationship for deep collapse.

For relatively thin tubes, upper flange is compressed under bending and will be buckled locally. But a part of the flange remain effective in resisting the moment until it begins to yield. The critical behavior is designated as crippling. Stress distribution for the crippling state and the effective width of the flange are shown in Fig. 3(*a*). On the other hand, ultimate load carrying capacity of stocky tubes is associated with the plastic yielding or squashing as shown in Fig. 3(*b*).

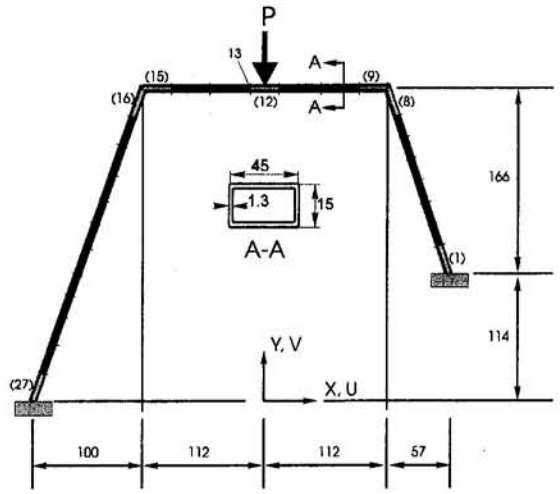
The collapse moment of the trapezoidal tube of Fig. 3 can be calculated by considering stress distribution for squashing state or crippling state. The local buckling stress of the compressed plate of the flange can be given approximately as (Kecman and Suthurst, 1984)

$$\sigma_{cr} = \left[5.23 + 0.16\left(\frac{2b}{h}\right)\right]\frac{\pi^2 E}{12(1-\nu^2)}\left(\frac{t}{2b}\right)^2. \quad (26)$$

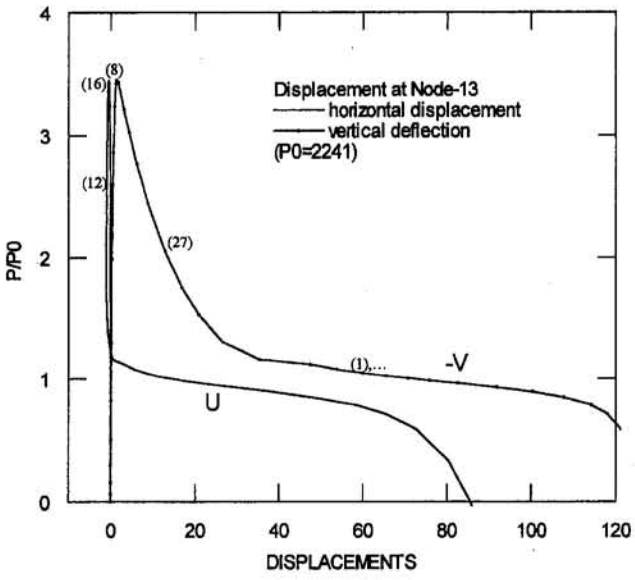
We can define the crippling stress, σ_c as the average stress of the compressed plate when the effective part of the plate begins to yield. The effective width can be obtained as follows (Johnston, 1976):

$$\frac{b_e}{b} = \frac{\sigma_c}{\sigma_Y} = \frac{1.0}{\mu} - \frac{0.22}{\mu^2} \quad (27)$$

where b_e is the effective width and $\mu = \sigma_{cr}/\sigma_Y$. Using Eq. (27), we can predict the stress distribution and the collapse moment, M_c for the crippling state. The beam will be collapsed by squashing when the local buckling of the compressed flange is more difficult to occur than plastic collapsing, that is, $\sigma_Y < \sigma_c$ or $\mu < 0.673$. The collapse moment by squashing, M_s can be obtained by simple integration of the stress distribution assumed in Fig. 3(*b*).



(a)



(b)

Fig. 8 A hybrid finite element analysis example; (*a*) thin-walled portal frame, (*b*) analysis result (numbers in parenthesis represent elements begin to collapse)

$$M_{ult} = M_c = 2t\sigma_Y\left[b_e(h - c_c) + \frac{ac_2^2}{(h - c_c)} + \frac{(h - c_c)^3 + c_c^3}{3(h - c_c)}\right], \quad \text{if} \quad \mu \geq 0.673 \quad (28a)$$

$$M_{ult} = M_s = 2t\sigma_Y\left[b(h - c_s) + ac_s + \frac{(h - c_s)^2 + c_s^2}{2}\right], \quad \text{if} \quad \mu < 0.673 \quad (28b)$$

In Eqs. (28), the parameters of c_c and c_s denote the distances from the bottom of the section to the neutral axes for crippling and squashing states, respectively.

Downloaded 04 May 2010 to 171.66.16.33. Redistribution subject to ASME license or copyright; see http://www.asme.org/terms/Terms_Use.cfm

$$c_c = \frac{2b_e + d}{a + b_e + d}\left(\frac{h}{2}\right) \tag{29a}$$

$$c_s = \frac{(b - a) + d}{d}\left(\frac{h}{2}\right) \tag{29b}$$

The moment-rotation angle curves can be fully determined by combining the collapse moment of Eq. (28) as an initial value of the post-collapse load and the moment obtained from Eq. (25) for the deep-collapse range. We will combine them by taking the smaller one for each θ. The general procedure of the post-collapse analysis described in this paper is summarized as a flow chart and given in Fig. 4.

5 Numerical Results and Discussions

We will show practicality and effectiveness of the present method through numerical examples. Four example sections considered are shown in Fig. 5 where K-sections are selected from Kecman (1983) and a B-pillar section is from Lee and Park (1990). We assume the actual B-pillar section to be an trapezoidal section as shown in Fig. 5. The material properties taken from the literature are listed in Table 1.

Folding lengths are predicted and listed in Table 1. In solving Eq. (24), we adopt the Newton method with numerical differentiation technique because of highly implicit and nonlinear nature of the deformation kinematics. To obtain folding lengths listed in Table 1, we take the initial small process parameter, θ_0 as 0.001 deg. Assumption of negligible variation of folding lengths to the process control parameter has been observed. In case of the K-1 section, for example, λ_2 is calculated as approximately 0.1 times smaller than that of listed in Table 1 when θ_0 is increased by ten times. In the table, ultimate bending collapse moments of the sections are given, too. The sections K-1 and K-26 begin to collapse by squashing while the sections K-18 and B-pillar begin to collapse by crippling and M_{ult} depends on the thickness to width ratio and material property. The radius of the traveling hinge as a function of θ is plotted in Fig. 6. The radius varies from 2 mm to 4 mm at the deep collapse range considered. These values are small compared with the folding lengths, so the assumption of localized deformations can be justified. Moment-rotation angle curves are obtained from (25) and (28) and shown in Fig. 7. Both the maximum moments and the deep-collapse moments are in reasonable agreement with those of the test results within fifteen percent deviations. A significant error in the case of the B-pillar seems to be mainly caused by the idealization the pillar.

As an illustration of the effectiveness of the present method, a typical large deformation elastoplastic analysis is performed using hybrid beam elements. We formulate the nonlinear hybrid beam element from constitutive moment-curvature relations based on the aforementioned method. A portal frame structure consists of K-1 sections is shown in Fig. 8(a). The post-collapse moment-curvature relation of Fig. 7(a) is utilized for the hybrid elements. The load-displacement curves of the structure are shown in Fig. 8(b). As a nonlinear solution technique, we adopt the numerical continuation method to trace equilibrium paths beyond the limit point (Rheinboldt, 1981). It seems to be clear that the methodology presented in this paper is effective and practical not only for the crush analyses of thin-walled members but also for system level structures.

6 Conclusions

A kinematic method of predicting mode parameters and post-collapse behavior of thin-walled members under bending is proposed and tested for several trapezoidal and rectangular tubes. Mode parameters are estimated consistently with the proposed collapse mechanisms from the condition of the minimum plastic energy rate at collapse.

Rectangular and trapezoidal prismatic tubes are modeled by three-DOF collapse mechanism. It includes two "fixed" mode parameters and one "variable" mode parameter. The deforming parts are modeled by stationary bending hinges and traveling hinges as localized plastic energy mechanisms. From the results of examples, it is clear that the proposed three-DOF model of kinematically admissible mechanism is an effective and practical tool for predicting the collapse behavior of prismatic beams.

Ultimate load-carrying capacities are determined by combining the collapse moment of crippling or squashing states and the instantaneous moment for deep collapse. Crippling loads are calculated from the linear buckling analysis with effective width. Both the maximum loads and the moment-rotation angle curves for deep collapse are in good agreement with the test results of references within fifteen percent error. Since computation times necessary to carry out kinematic analysis are much shorter than other numerical methods, member-level analyses by the method can be effectively utilized for the post-buckling analysis of beam-type structures.

References

Abramowicz, W., and Jones, N., 1984, "Dynamic axial crushing of circular tubes," *International Journal of Impact Engng.*, Vol. 2, No. 3, pp. 263–281.

Abramowicz, W., and Wierzbicki, T., 1989, "Axial Crushing of Multicorner Sheet Metal Columns," ASME JOURNAL OF APPLIED MECHANICS, Vol. 56, pp. 113–120.

Cimpoeru, S. J., and Murray, N. W., 1993, "The large-deflection pure bending properties of square thin-walled steel structures," *International Journal of Mechanical Science*, Vol. 35, No. 3-4, pp. 247–256.

Drazetic, P., Markiewicz, E., and Ravalard, Y., 1993, "Application of kinematic models to compression and bending in simplified crash calculations," *International Journal of Mechanical Science*, Vol. 34, No. 3-4, pp. 179–191.

Gerard, G., 1957, *Handbook of Structural Stability, Part V—Compressive strength of flat stiffened panels*, NACA Report TN3785.

Johnson, W., Soden, P. D., and Al-Hassani, S. T. S., 1977, "Inextensional collapse of thin-walled tubes under axial compression," *Journal of Strain Analysis*, Vol. 12, No. 4, pp. 317–330.

Johnston, B. G., 1976, *Guide to Stability Design Criteria for Metal Structures*, 3rd ed., John Wiley and Sons, New York, pp. 227–260.

Kecman, D., 1983, "Bending collapse of rectangular and square section tubes," *International Journal of Mechanical Science*, Vol. 25, No. 9-10, pp. 623–636.

Kecman, D., and Suthurst, G. D., 1984, "Theoretical determination of the maximum bending strength in the car body components," *IMechE paper* C181/84, pp. 53–61.

Kotelko, M., and Krolak, M., 1993, "Collapse behaviour of triangular cross-section girders subject to pure bending," *Thin-Walled Structures*, Vol. 15, pp. 127–141.

Lee, B. C., and Park, M. S., 1990, "A study on the nonlinear analysis of spatial frame structures with nonlinear rotational spring elements," *Journal of Korea Society of Automotive Engineers* (in Korean), Vol. 12, No. 2, pp. 29–42.

Mahmood, H. F., and Paluszny, A., and Tang, X., 1988, "Crash analysis of thin walled beam-type structures," *SAE* Paper No. 880894, pp. 4908–4917.

Meng, Q., Al-Hassani, S. T. S., and Soden, P. D., 1983, "Axial crushing of square tubes," *International Journal of Mechanical Science*, Vol. 25, No. 9-10, pp. 747–773.

Murray, N. W., and Khoo, P. S., 1981, "Some basic plastic mechanisms in the local buckling of thin-walled steel structures," *International Journal of Mechanical Science*, Vol. 23, No. 12, pp. 703–713.

Pugsley, Sir A., 1960, "The crumpling of tubular structures under impact conditions," *Proceedings of Symposium on The Use of Aluminum in Railway Rolling Stock*, Inst. Loco. Engineers, The Aluminum Development Assoc., London, p. 33.

Reid, S. R., Reddy, T. Y., and Gray, M. D., 1986, "Static and dynamic axial crushing of foam-filled sheet metal tubes," *International Journal of Mechanical Science*, Vol. 28, No. 5, pp. 295–332.

Rheinboldt, W. C., 1981, "Numerical analysis of continuation methods for nonlinear structural problems," *Comput. Struct.*, Vol. 13, pp. 103–113.

Wierzbicki, T., and Abramowicz, W., 1983, "On the Crushing Mechanics of Thin-Walled Structures," ASME JOURNAL OF APPLIED MECHANICS, Vol. 50, pp. 727–734.

Wierzbicki, T., and Abramowicz, W., 1988, "Development and implementation of special elements for crash analysis," *SAE* Paper No. 880895, pp. 103–109.

Wierzbicki, T., Recke, L., Abramowicz, W., and Gholami, T., 1994, "Stress profiles in thin-walled columns subjected to crush loading, Part I: Compression, Part II: Bending," *Computers and Structures*, Vol. 51, No. 6, pp. 611–641.

Downloaded 04 May 2010 to 171.66.16.33. Redistribution subject to ASME license or copyright; see http://www.asme.org/terms/Terms_Use.cfm

On the Growth-of-Waviness in Fiber-Reinforced Polymer Composites: Viscoelastic Bifurcation and Imperfection Sensitivity

M. S. Bhalerao
Graduate Research Assistant.

T. J. Moon[1]
Assoc. Mem. ASME.

Department of Mechanical Engineering,
ETC 5.146,
The University of Texas at Austin,
Austin, TX 78712-1603

The time-dependent, local microbuckling of fibers in polymer composites is modeled in the context of viscoelasticity. The instability or "growth-of-waviness"-type analysis is carried out for bifurcation (initially straight fibers), as well as for imperfection sensitivity (initially wavy fibers). The concept of dominant wavelength, previously defined for viscoelastic bifurcation by Biot, is generalized for viscoelastic imperfection sensitivity. A parametric study is presented to encompass a wide range of physically useful values to study the effects of matrix properties, fiber-matrix interfacial conditions, and time-dependent loads on dominant wavelengths. A marked difference is observed between the viscoelastic bifurcation and imperfection sensitivity dominant wavelength results. The bifurcation dominant wavelength is seen to depend negligibly on matrix properties, yet highly on the applied load and the interfacial conditions. On the other hand, the imperfection sensitive dominant wavelength is strongly dependent on matrix properties, while negligibly on load and interface conditions.

1 Introduction

In fiber-reinforced composites two types of fiber imperfections may be present, namely, fiber misalignment (Kyriakides et al., 1993) and fiber waviness (Daniel et al., 1993). Qualitatively, fiber misalignment is the deviation of fibers from their preferred straight orientation; while fiber waviness is a wavelike deformation of fibers about a nominally straight direction, growth of which is the focus of this research. Although no explicit reference is made to the manufacturing or in-service conditions, this work addresses the more basic mechanics question of identifying possible driving mechanisms for the fiber waviness. Therefore, the analysis is aimed at providing a comparison between viscoelastic bifurcation and viscoelastic imperfection sensitivity as a driving cause for fiber waviness during manufacturing. A generalization of this model for multilayered media is presented in Bhalerao and Moon (1995).

Prediction of the response of layered media under compressive load has received attention from various points of view, including such applications as the manufacturing and long-term behavior of fiber-reinforced composites, development of geological foldings. In the pioneering work of Biot (1965), an "incremental deformations" approach is adopted to explore the concept of "dominant wavelength" to describe the "growth-of-waviness" in viscoelastic media. Some of the research presented in this paper is motivated by the continuum stability work of Biot. In another study by Ting and Chen (1982), a comprehensive survey of several modeling schemes and solution approaches is presented for the problem of a beam supported by foundation. The effect of various material models, lateral load, and different boundary conditions (e.g., hinged-hinged, fixed-free, etc.) are investigated along with various solution procedures. From the structural perspective, Vinogradov (1987) presents theoretical studies for the creep buckling behavior of viscoelastic two-layered laminated columns under an eccentric axial compressive load. The solutions present a parametric study for long-term viscoelastic behavior considering viscoelastic material properties, layer thickness ratios, eccentricities, and equilibrium moduli. An experimental and theoretical failure analysis for notched specimens is presented by Guynn (1990) and Waas (1988). In these studies various geometries of plates and notches are considered and different failure mechanisms are analyzed. Lessard and Chang (1991) finds the the effect of nonuniform loading conditions and inter-fiber interactions are significant for fiber microbuckling in composites—especially for analyzing thick sectioned composites. Schapery (1991) presents a viscoelastic analysis for local buckling—shear and bending—in fiber-reinforced composites within the context of the classical beam theory. He presents closed-form solutions for constant and periodic load when the interfacial shear stress is absent. Comments on dominant wavelength are also presented. Slaughter and Fleck (1993) develop a model for the viscoelastic microbuckling of fiberous composites and predict the failure due to kinkbands and plastic microbuckling. For a more comprehensive review, the interested reader is referred to Guynn (1990), Schapery (1991), Shuart (1985), and Ting and Chen (1982).

2 Stability Equations for a Single Fiber in an Infinite Elastic Matrix

It is a common practice to model a laminated composite as a homogenized anisotropic continuum or as a multilayered medium (Biot, 1965). We adopt the later approach where we focus on the micromechanics of local growth of fiber waviness assuming the fiber is embedded in an infinite matrix medium. We assume that plain-strain conditions apply locally. The two

[1] To whom all correspondence should be addressed.

Contributed by the Applied Mechanics Division of THE AMERICAN SOCIETY OF MECHANICAL ENGINEERS for publication in the ASME JOURNAL OF APPLIED MECHANICS.

Discussion on this paper should be addressed to the Technical Editor, Professor Lewis T. Wheeler, Department of Mechanical Engineering, University of Houston, Houston, TX 77204-4792, and will be accepted until four months after final publication of the paper itself in the ASME JOURNAL OF APPLIED MECHANICS.

Manuscript received by the ASME Applied Mechanics Division, Aug. 19, 1994; final revision, June 16, 1995. Associate Technical Editor: I. M. Daniel.

Copyright © 1996 by ASME

Downloaded 04 May 2010 to 171.66.16.33. Redistribution subject to ASME license or copyright; see http://www.asme.org/terms/Terms_Use.cfm

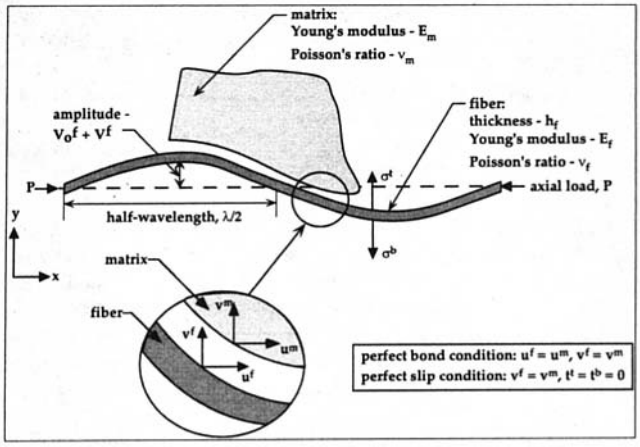


Fig. 1 Freebody diagram of a fiber in a matrix with a perfect interfacial slipping and bonding conditions

fiber-matrix interfacial conditions considered are perfect bond and perfect slip between fiber and matrix; real interface conditions lie within these two extreme limits. Analysis is developed within the context of Euler-Bernoulli beam theory, we assume that the plane cross-sections of fiber remain plane after deformation and any shear deformation of the beam is ignored. The local description of a wavy fiber, buckled or initially in a wavy state, is shown in Fig. 1.

The stability equations for a perfectly bonded unit-width-fiber in a matrix are (Minahen and Knauss, 1989; Waas, 1988)

$$E_f h \frac{d^2 u^f}{dx^2} + (\tau^b - \tau^t) = 0,$$

$$\frac{E_f h^3}{12(1-\nu_f^2)} \frac{d^4 v^f}{dx^4} + P\left(\frac{d^2 v^f}{dx^2} + \frac{d^2 v_0^f}{dx^2}\right) + (\sigma^b - \sigma^t) + \frac{h}{2}\left(\frac{d\tau^b}{dx} + \frac{d\tau^t}{dx}\right) = 0. \quad (1)$$

Various quantities in Eq. (1) are shown in Fig. 1. The axial load, P, is defined positive in compression and is expressed through the axial strain and displacement as $P = E_f h \epsilon_x = E_f h (du^f/dx)$. The governing equations are further simplified by assuming the fiber displacement to be of cosinusoidal and sinusoidal form, thus, the final form of the stability equations (Eq. (1)) is

$$-\alpha^2 E_f h U^f \cos \alpha x + (\tau^b - \tau^t) = 0,$$

$$\left[\alpha^4 \frac{E_f h^3}{12(1-\nu_f^2)} V^f - \alpha^2 P(V^f + V_0^f)\right] \sin \alpha x + (\sigma^b - \sigma^t) + \frac{h}{2}\left(\frac{d\tau^b}{dx} + \frac{d\tau^t}{dx}\right) = 0 \quad (2)$$

where U^f and V^f are the amplitudes in longitudinal and axial directions under the load P, V_0^f is the amplitude of initial imperfection, and $\alpha = 2\pi/\lambda$ is the wave number. The unknown reactions σ^b, τ^b, σ^t, τ^t imposed on the fiber by the matrix in Eq. (2) are evaluated by solving the equilibrium problem for the matrix medium above and below the fiber using linear elasticity (Timoshenko, 1934). Required displacement boundary conditions on the matrix are applied by the deformation of fiber. The interfacial stresses are obtained by evaluating the matrix stress field at the fiber-matrix interface. Moreover, we note that the normal and shear stresses in the stability equations appear in particular combinations in Eq. (2); thus we have

$$\sigma_- = \sigma^b - \sigma^t = 2\alpha\,[B_1 U^f E_m + B_2 V^f E_m] \sin \alpha x,$$
$$\tau_- = \tau^b - \tau^t = 2\alpha B_3 U^f E_m \cos \alpha x,$$
$$\tau_+ = \tau^b + \tau^t = -2\alpha B_4 V^f E_m \cos \alpha x \quad (3)$$

where B_i are defined as follows:

$$B_1 = [(1 - 2\nu_m)]/D, \quad B_3 = [2(1 - \nu_m)]/D,$$
$$B_2 = [2(1 - \nu_m) + \alpha h(1 - 2\nu_m)/2]/D,$$
$$B_4 = [(1 - 2\nu_m) + \alpha h(1 - \nu_m)]/D, \quad (4)$$

where $D = (1 + \nu_m)(3 - 4\nu_m)$. Substitution of Eq. (3) in the governing equations (Eq. (2)) yields elastic stability equations. Analysis of the elastic stability may be found in Minahen and Knauss (1989) which indicates that $U^f \equiv 0$ and that Eq. (2a) is identically satisfied. Therefore, only Eq. (2b) is considered in the subsequent analysis.

A simplified case of the perfectly bonded fiber is the perfectly slipping fiber which is obtained by setting the interfacial shear traction to be zero. Following the simplification outlined earlier, the governing equation is

$$\left[\alpha^4 \frac{E_f h^3}{12(1-\nu_f^2)} V^f - \alpha^2 P(V^f + V_0^f)\right] \sin \alpha x + (\sigma^b - \sigma^t) = 0 \quad \text{where} \quad \sigma_- = \frac{2\alpha E_m V^f}{2(1-\nu_m^2)} \sin \alpha x. \quad (5)$$

Simplification of the governing equation (Eq. (5)) yields elastic stability equation.

The next section uses Eqs. (2), (3), and (5), derived in this section for extending the analysis to viscoelastic stability.

3 Growth-of-Waviness in a Viscoelastic Matrix

We now extend the associated elastic fiber/elastic matrix stability problem to the viscoelastic matrix case invoking the viscoelastic Correspondence Principle (CP) (Biot, 1958; Morland and Lee, 1960; Schapery, 1975). In this context, we investigate the idea of dominant wavelength related to viscoelastic buckling and imperfection sensitivity (collectively referred to as "growth-of-waviness"). In this analysis any dynamic or damping effects are ignored for simplicity which may be a good approximation for the class of loads considered here.

3.1 Formulation of General Time-Dependent Response. Using the viscoelastic correspondence principle and Eq. (2b), and nondimensionalizing using characteristic length, h, (the fiber thickness) and initial imperfection amplitude, V_0^f, we express the stability equation for a perfectly bonded elastic fiber in a viscoelastic matrix as

$$\left[\frac{2B_2}{\bar{\eta}} + B_4\right] \int_{0^-}^{t} r_{ve}(t - \xi) \frac{d\bar{V}^f(\xi)}{d\xi}\, d\xi + \left[\frac{\bar{\eta}^2}{12(1-\nu_f^2)} - \bar{P}(t)\right] \bar{V}^f(t) = \bar{P}(t). \quad (6)$$

Equation (6) may also be interpreted to describe the time-dependent response of the fiber embedded in a viscoelastic matrix. The B_i defined in Eq. (4) are the same due to the negligible viscoelastic behavior of ν_m (see Appendix C). In Eq. (6) the nondimensionalization is wave number, $\bar{\eta} = 2\pi/\lambda = 2\pi h/\lambda$, amplitude, $\bar{V}^f = V^f/V_0^f$, load, $\bar{P} = P/(hE_f)$. The kernel, $r_{ve}(t) = E_m(t)/E_f$, of the integral equation is the nondimensional matrix relaxation modulus. It may be seen that $r_{ve}(t)$ is unbounded at zero-time implying the absence of any zero-time response, i.e., $d\bar{V}^f(t)/dt = 0$; hence, the integral vanishes. Moreover, $r_{ve}(t)$ has no other singularity for positive times. Thus, the

Downloaded 04 May 2010 to 171.66.16.33. Redistribution subject to ASME license or copyright; see http://www.asme.org/terms/Terms_Use.cfm

integrand is analytic. For other forms of property representations (Appendix C), the integrand can similarly be shown to be analytic. We notice that the interfacial stresses are obtained from the CP; for instance, the elastic σ_- in viscoelastic context is as follows:

$$\sigma_- = 2\alpha \left[B_1 \int_{0^-}^{t} E_m(t-\xi) \frac{dU^f(\xi)}{d\xi} d\xi + B_2 \int_{0^-}^{t} E_m(t-\xi) \frac{dV^f(\xi)}{d\xi} d\xi \right] \sin \alpha x \quad (7)$$

Similar expressions may also be written for τ_- and τ_+.

Similarly, using Eq. (5) with CP, the governing equation for viscoelastic stability and time-dependent response for a perfectly slipping fiber is

$$\frac{1}{\bar{\eta}(1-\nu_m^2)} \int_{0^-}^{t} r_{ve}(t-\xi) \frac{d\bar{V}^f(\xi)}{d\xi} d\xi + \left[\frac{\bar{\eta}^2}{12(1-\nu_f^2)} - \bar{P}(t) \right] \bar{V}^f(t) = \bar{P}(t). \quad (8)$$

It can be seen that the time-dependent response for a perfectly bonded fiber (Eq. (6)) and a perfectly slipping fiber (Eq. (8)) is formally identical; this observation is useful in setting up the solution procedure. If $\bar{P}(t)$ is independent of time t, Eq. (6) may be Laplace transformed and the transformed amplitude may be expressed as a function of material properties and the imperfection wavelength. However, for an arbitrary time-dependent applied load, use of Laplace transform (LT) is not practical. A numerical procedure may need to be adopted to evaluate the time-dependent response of the fiber or the growth/decay of the imperfection amplitude. Even under constant load conditions, the analytical inversion of Laplace transform into the time domain may be quite complex due to the very nature of the relaxation or creep functions; the direct inversion technique presented in Appendix B is conveniently employed in such cases.

3.2 Concept of Growth-of-Waviness. We note that the wave number, $\bar{\eta}$, is an arbitrary parameter in Eq. (6) and Eq. (8) and depending on the fiber and matrix materials and applied load, a relatively fast growing wavelength is observed to develop (Biot et al., 1961). In general, the deformation of a fiber at the viscoelastic bifurcation may be assumed to be composed of an infinite set of periodic functions in the form of a Fourier series. The spectral decomposition of an arbitrary waveform $v(x)$ is as $v(x) = \sum_{n=1}^{\infty} V_n^f \sin(2n\pi x/\lambda)$, where V_n^f is the amplitude corresponding to wavelength λ/n. Amongst the infinitely many possible wavelengths in a Fourier spectrum for a possible random deformation at buckling, the wavelength which admits the lowest buckling load is termed the "dominant wavelength." This is the wavelength that naturally develops in an initially straight fiber (or beam) during viscoelastic buckling. For the sake of clarity in future notations, the wavelength associated with the viscoelastic bifurcation is termed as the "bifurcation dominant wavelength" instead of simply dominant wavelength and is denoted as $\bar{\lambda}_{db}$. The corresponding wavenumber is denoted as $\bar{\eta}_{db}$. Because of the selective amplification of fiber amplitude due to the viscoelastic loading from the matrix onto the fiber, $\bar{\lambda}_{db}$ is the wavelength that is actually observed (Biot et al., 1961).

We postulate a similar phenomenon of development of a natural wavelength in an initially wavy fiber. The time-dependent change in amplitudes of various wavelengths in the Fourier spectrum of the initially imperfect fiber is evaluated and the wavelength associated with the fastest growing amplitude is identified as the dominant wavelength. In this way, we generalize the concept of the bifurcation dominant wavelength for an initially wavy fiber via the "viscoelastic imperfection sensitivity" approach. We introduce a new term for the dominant wavelength associated with the imperfection sensitivity as "imperfection-sensitive dominant wavelength." This wavelength and the associated wave number are denoted as $\bar{\lambda}_{di}$ and $\bar{\eta}_{di}$, respectively.

Equations (6) and (8) represent the dependence of fiber deformation amplitude, $\bar{V}^f$, on the applied load, P, and the material system, characterized by the ratio of fiber and matrix moduli, $r_{ve} = E_m/E_f$ for various wave numbers, $\bar{\eta}$. Also, both the equations involve, imperfection amplitude, V_0^f, through nondimensionalization. These equations, without the right-hand side, yield results for $\bar{\lambda}_{db}$, and with the right-hand side, yield $\bar{\lambda}_{di}$.

3.3 Evaluation of Bifurcation Dominant Wavelength, $\bar{\lambda}_{db}$. Without any imperfection in the fiber under a constant load, the Carson Transform, CT, (defined in Appendix A) of Eq. (6), yields the characteristic equation for stability as

$$f(\bar{\eta}, \bar{P}, s) = \frac{\bar{\eta}^2}{12(1-\nu_f^2)} + \left(\frac{2B_2}{\bar{\eta}} + B_4 \right) \bar{r}_{ve} - \bar{P} = 0. \quad (9)$$

The value of s (eventually the exponential growth rate) in $\bar{r}_{ve}$ goes through a maximum for a certain value of $\bar{\eta}$, namely $\bar{\eta}_{db}$, which yields the bifurcation dominant wavenumber (Biot, 1965). The dominant wave number is obtained by evaluating the extremum of f with respect to $\bar{\eta}$ as

$$\frac{\partial f}{\partial \bar{\eta}} + \frac{\partial f}{\partial s} \frac{\partial s}{\partial \bar{\eta}} = 0. \quad (10)$$

Differentiating Eq. (9) with respect to $\bar{\eta}$ with $\partial s/\partial \bar{\eta} = 0$ in Eq. (10), we get

$$\bar{r}_{ve} = \frac{\bar{\eta}_{db}^2}{6(1-\nu_f^2)} \frac{\bar{\eta}_{db}}{B_2 - \bar{\eta}_{db} B_4 + \bar{\eta}_{db}\zeta}, \quad \text{where} \quad \zeta = \frac{1-2\nu_m}{2(1+\nu_m)(3-4\nu_m)}. \quad (11)$$

Substituting the value of $\bar{r}_{ve}$ from Eq. (11) into the characteristic equation Eq. (9), we evaluate the interdependence between the applied load and $\bar{\eta}_{db}$. Using $\bar{\lambda}_{db} = \lambda/h = 2\pi/\bar{\eta}_{db} = k/\bar{\eta}_{db}$, we obtain

$$\bar{P} = \frac{k^2[(10\bar{\lambda}_{db}^2 + 3k^2)(1-\nu_m) + 6k\bar{\lambda}_{db}(1-2\nu_m)]}{12\bar{\lambda}_{db}^2(1-\nu_f^2)(1-\nu_m^2)(2\bar{\lambda}_{db}^2 - k^2)}. \quad (12)$$

For the simpler case of a perfectly slipping fiber in a viscoelastic matrix, we state the bifurcation dominant wavelength as (Biot, 1965; Schapery, 1991)

$$\bar{P} = \frac{k^2}{4(1-\nu_f^2)\bar{\lambda}_{db}^2}. \quad (13)$$

3.4 Analytical Observations on Bifurcation Dominant Wavelength. Equation (13) clearly shows that the critical load $\bar{P}$ is inversely proportional to the square of bifurcation dominant wavelength for the perfect slip case. In order to further investigate the variation of $\bar{P}$ with $\bar{\lambda}_{db}$ for perfect bond case (Eq. (12)), we note that (1) numerator and denominator are polynomials in $\bar{\lambda}_{db}$, (2) the coefficient of the highest power is largest and positive, and (3) the numerator and denominator are positive and monotonic in $\bar{\lambda}_{db}$ in the range of Euler-Bernoulli beam theory. As a result, $\bar{P} = f(k, \nu_f, \nu_m, \bar{\lambda}_{db})$ is monotonic in $\bar{\lambda}_{db}$ and there is a one-to-one correspondence between $\bar{P}$ and $\bar{\lambda}_{db}$ in the useful range of $\bar{\lambda}_{db}$. Most importantly, for a given load, the dominant wavelength is uniquely determined. Figure 2 is a plot of applied load against bifurcation dominant wavelength on a log-log scale for both the cases; perfect bond and

Downloaded 04 May 2010 to 171.66.16.33. Redistribution subject to ASME license or copyright; see http://www.asme.org/terms/Terms_Use.cfm

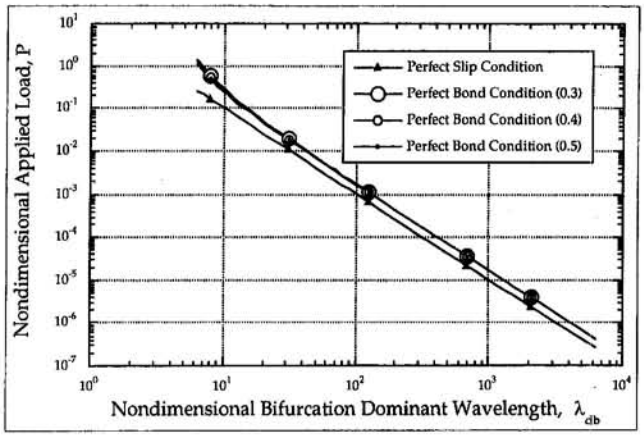


Fig. 2 Dependence of bifurcation dominant wavelength, $\bar{\lambda}_{db}$, on applied load $\bar{P}$ with matrix Poisson's ratios as a parameter

slip. The slope of all the four lines is −0.5 indicating the inverse square proportionality of $\bar{\lambda}_{db}$ with $\bar{P}$. As noted in Section 3.2, an experimental validation for this inverse square proportionality for the case of perfect interfacial slip condition is provided by Biot et al. (1961). Additionally, the loads in the case of a perfectly bonded fiber are higher than those of the perfectly slipping fiber for a particular wavelength; this observation is expected due the stronger constraints on buckling in the former case. The difference between the critical loads or dominant wavelengths is significant implying that the interfacial bonding plays an important role in viscoelastic bifurcation. A similar observation for elastic fiber and elastic matrix bifurcation is made by Minahen and Knauss (1989).

Equation (12) for a perfectly bonded fiber shows the matrix Poisson's ratio as a parameter in the $\bar{\lambda}_{db}$ versus $\bar{P}$ dependence; while based on a similar relationship for a perfectly slipping fiber, Eq. (13), the buckling load is independent of ν_m. Moreover, Fig. 2 shows that for all practical purposes in the range of interest, the ν_m-dependence in the perfect bond case is negligible. We also note that at higher loads, the bifurcation dominant wavelength is small and comparable to fiber thickness. In such a case the underlying Euler-Bernoulli beam theory is insufficient to describe the beam deformation and hence we discard any data in this "short wavelength" range.

In the elastic fiber/elastic matrix buckling analysis, the material stiffness terms appear in the form $r_e = E_m/E_f$ (Minahen and Knauss, 1989). Moreover, under constant load, the stability equations for an elastic fiber and viscoelastic matrix are analogous to those of an elastic fiber and an elastic matrix except that r_e is replaced by $\bar{r}_{ve}$ by the viscoelastic CP. Clearly, the $\bar{\lambda}_{db}$ expression in the case of viscoelastic matrix would remain the same, except for a change of notation, i.e., r_e to $\bar{r}_{ve}$. Therefore, we conclude that the elastic microbuckling treatment extends directly to viscoelastic buckling provided the load on fiber is independent of time.

3.5 Evaluation of Imperfection-Sensitive Dominant Wavelength, $\bar{\lambda}_{di}$. It can be shown that the growth of the imperfection amplitude under constant load may be obtained by the CT of Eq. (6) and yields

$$\frac{\tilde{V}^f(s)}{V^f_0} = \frac{\bar{P}}{\dfrac{\bar{\eta}^2}{12(1-\nu_f^2)} + \left(\dfrac{2B_2}{\bar{\eta}} + B_4\right)\tilde{\bar{r}}_{ve}(s) - \bar{P}}. \quad (14)$$

Since the analytical CT inversion of Eq. (14) to obtain the time-dependent response is quite involved and impractical, we apply the direct inversion technique (see Appendix B) to obtain

$$\frac{V^f(t)}{V^f_0} = \frac{\bar{P}}{\dfrac{\bar{\eta}^2}{12(1-\nu_f^2)} + \left(\dfrac{2B_2}{\bar{\eta}} + B_4\right)\bar{r}_{ve}(t) - \bar{P}}, \quad (15)$$

where

$$\bar{r}_{ve}(t) = (E_s/E_f)\Gamma(1-m)\gamma^m(t_s/t)^m + E_{eq}/E_f. \quad (16)$$

We note that $\bar{r}_{ve}(t)$ is not the LT of $r_{ve}(t)$. More details about the material property representation (i.e., for $r_{ve}(t)$) are given in Appendix C. Equation (15) gives a closed-form solution for the time-dependent response under constant load and is used for the computation of $\bar{\lambda}_{di}$.

For a perfectly slipping fiber under a constant load, the direct inverse of the CT of Eq. (8) yields time-dependent response as follows:

$$\frac{V^f(t)}{V^f_0} = \frac{\bar{P}}{\dfrac{\bar{\eta}^2}{12(1-\nu_f^2)} + \dfrac{\bar{r}_{ve}(t)}{\bar{\eta}(1-\nu_m^2)} - \bar{P}}. \quad (17)$$

This time-dependent response under constant load is used for the computation of $\bar{\lambda}_{di}$ (see Section 3.2). In case of time-dependent load, full numerical approach need to be adopted to obtain the $\bar{\lambda}_{di}$ using Eq. (6) and Eq. (8).

3.6 Analytical Observations on Imperfection-Sensitive Dominant Wavelength. To obtain $\bar{\lambda}_{di}$ as a function of applied load and material properties, we approach it from its physical interpretation. The origin of the concept of $\bar{\lambda}_{di}$, is based on the observation that any arbitrary imperfection may be expressed as its Fourier spectrum. Within this spectrum, the particular wavelength which grows the fastest is referred to as the imperfection-sensitive dominant wavelength. Hence, by plotting the growth of amplitudes of various wavelengths, it is possible to identify $\bar{\lambda}_{di}$, a global extremum over all the wavelengths.

Two *L*oading *H*istories (LH) are considered: a constant load (LH = 1) and a linearly varying load followed by a constant load (LH = 2, 3). The constant load case simulates the "long-time" in-service loading conditions while LH = 2, 3 simulate gradual loading to a steady state, i.e., ignoring any dynamic loading effects. For case 2 the ramp is applied twice as fast as that for case 3. In all the loading histories, the maximum load is the same; for comparison purposes, different levels of maximum loads are considered. The highest load ($\bar{P} = 0.005$) is chosen below the elastic buckling load for a single fiber with perfect

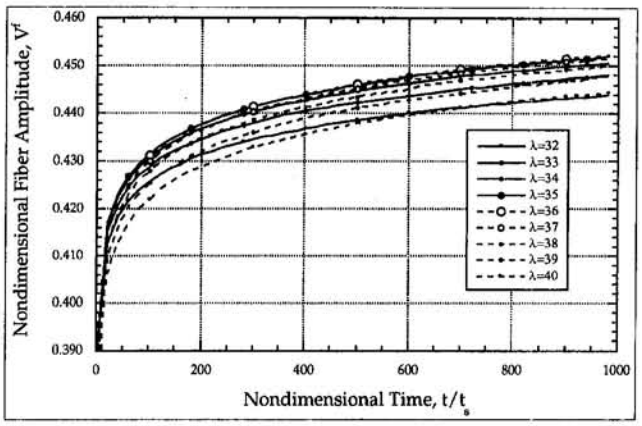


Fig. 3 Typical result for growth of imperfection amplitude and identification of $\bar{\lambda}_{di}$ (perfect slip condition, *LH* = 1, $\bar{P}$ = 0.0025, $E_s = E_{eq}$ = 0.005, m = 0.05, ν_f = 0.2, ν_m = 0.3)

Downloaded 04 May 2010 to 171.66.16.33. Redistribution subject to ASME license or copyright; see http://www.asme.org/terms/Terms_Use.cfm

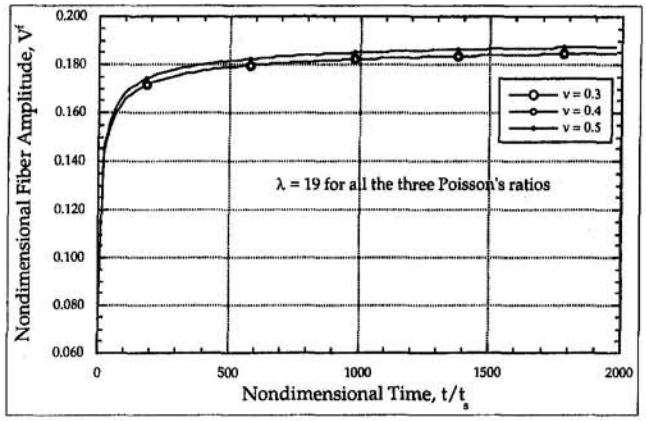


Fig. 4 Typical result for verification of nonviscoelastic behavior of matrix Poisson's ratio, ν_m = 0.3, 0.4, 0.5. (growth of amplitude for $\bar{\lambda}_{di}$ for dominant wavelength, LH = 1, $E_s = E_{eq}$ = 0.005, m = 0.5, ν_f = 0.2)

slip conditions, thereby forestalling any instantaneous buckling of the fiber, as well as the introduction of physically unrealistic parameters.

Before discussing the results, we provide verification for the essential assumptions built into the formulation. Figure 3 is a typical plot of growth of fiber amplitude versus time, with varying wavelength as a parameter. The load on the fiber in this particular case is a constant step (LH = 1); other material parameters and interfacial conditions are shown on the figure. The fiber amplitude is observed to grow monotonically with time. Of all wavelengths, that which possesses the fastest growing amplitude is defined to be the "imperfection-sensitivity dominant wavelength." To obtain the time domain response of the fiber amplitude under constant load, we use the direct inversion technique. We replot the fiber amplitude response on the log(time) scale to verify the validity of the inversion technique. It is observed that (not shown here) the inverted function in the time domain is "slowly varying" and the inversion is valid since the graph is approximately a straight line satisfying the enclosed area condition for direct inversion. For the sake of thoroughness, we have made a similar confirmation for all other cases presented here.

Obtaining a closed-form inverse is difficult when the applied load varies with time; a numerical procedure is required. Hence, a numerical procedure is employed even for the constant load case and the results are confirmed with the closed-form solution. We found that the numerical procedure is sensitive enough to capture the variation of dominant wavelength within a reasonable accuracy.

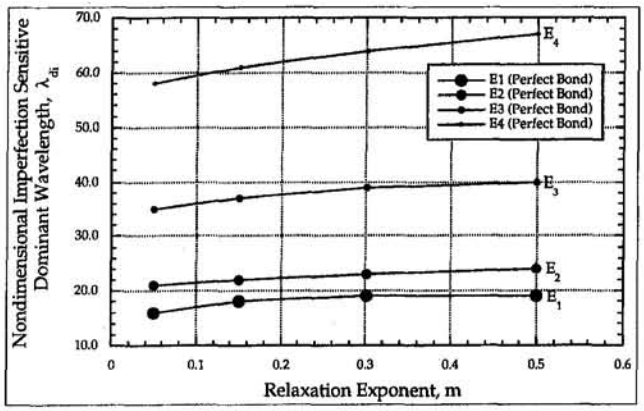


Fig. 5 Effect of matrix relaxation exponent and modulus on $\bar{\lambda}_{di}$: LH = 3, P = 0.005, ν_f = 0.2, ν_m = 0.3, $E_f = E_s = E_{eq}$, E_1 = 0.005, E_2 = 0.0025, E_3 = 0.0005, E_4 = 0.0001

Table 1 Effect of relaxation exponent m on $\bar{\lambda}_{di}$: LH = 3, ν_f = 0.2, ν_m = 0.3, P = 0.005

	Perfect Bond Condition			
E_s, E_{eq}	$m = 0.05$	$m = 0.15$	$m = 0.30$	$m = 0.50$
0.0050	16	18	19	19
0.0025	21	22	23	24
0.0005	35	37	39	40
0.0001	58	61	64	67
	Perfect Slip Condition			
E_s, E_{eq}	$m = 0.05$	$m = 0.15$	$m = 0.30$	$m = 0.50$
0.0050	16	18	19	19
0.0025	21	22	24	24
0.0005	35	38	40	41
0.0001	60	63	66	69

To verify the weak viscoelastic behavior of Poisson's ratio, we plot $\bar{\lambda}_{di}$ as a function of ν_m. Figure 4 shows the growth of amplitude with time. Based upon this and many similar observations, we note that $\bar{\lambda}_{di}$ is independent of ν_m for all practical purposes.

To further investigate the behavior of $\bar{\lambda}_{di}$, we now present the results of the parametric study investigating the variation of $\bar{\lambda}_{di}$ as a function of (1) typical values of the material parameters m, E_s, E_{eq}, ν_m; (2) the applied load, $\bar{P}$; and (3) the two interfacial conditions, perfect bond and perfect slip.

The exponent m is a measure of strength of the time dependence of the modulus E_m. Thermodynamic theory sets extremum limits on m (Flory, 1953). Typically, 0.05 and 0.50 are taken to be the limiting values. In addition, we study the growth behavior at intermediate values of m, such as 0.15 and 0.30. From the plots of growth of amplitude (similar to Fig. 3) for different values of m, we can extract $\bar{\lambda}_{di}$ as a function of m. This is illustrated in Fig. 5 and Table 1. For increasing time-dependence, i.e., increasing m, $\bar{\lambda}_{di}$ is observed to increase for all values of relaxation modulus—independent of the interfacial conditions.

In typical composites, e.g., AS4/3501-6, APC2, or T300/P1700, the ratio of elastic moduli ($r_e = E_m/E_f$) is on the order of 0.01. This estimate is used to select the ratio of viscoelastic moduli. Figure 5 also shows a plot of $\bar{\lambda}_{di}$ as a function of E_s (and E_{eq}); this is also illustrated in Table 1. We observe that for compliant materials, i.e., lower values of E_s (and E_{eq}), $\bar{\lambda}_{di}$ increases. Additionally, the material may be viewed as compliant for higher values of m, i.e., stiffness decaying at a faster rate. The numerical results for both lower E_s (and E_{eq}) and higher m are observed to be consistent with each other. As the matrix material becomes more and more compliant, it ceases to provide foundation support to the fiber and the fiber then starts resembling a very long, simply supported elastic beam. For such a beam, the most sensitive imperfection is the one which has the longest wavelength; the results presented here reaffirm this long wavelength sensitivity.

Table 2[1] reveals the effect of varying load level on $\bar{\lambda}_{di}$. In the range of applied loads, this effect is seen to be negligible, even though the loads are varied more than one decade of magnitude. Moreover, conclusion may be drawn for all the matrix relaxation moduli and both the interfacial conditions.

Consistent with the previous theoretical development, we present our results of the aforementioned parametric study for two types of interfacial conditions, namely, perfect bond and perfect slip. Table 3 compares the typical results corresponding

[1] No calculations were done for cells containing '–' due to numerical instability, which yields physically meaningless values. The numerical instabilities result from the physically unrealistic combinations of values of various parameters. A closer observation of Table 2 reveals that the numerical instabilities occur in the relatively high load and low matrix stiffness combinations. The low matrix stiffness values are the result of either initial low matrix stiffness values or relatively faster time-dependent decay of matrix stiffness, which is embedded in the higher values of m.

Downloaded 04 May 2010 to 171.66.16.33. Redistribution subject to ASME license or copyright; see http://www.asme.org/terms/Terms_Use.cfm

Table 2 Effect of load P on $\bar{\lambda}_{di}$ for perfect bond and perfect slip cases: $LH = 1$, $\nu_f = 0.2$, $\nu_m = 0.3$, $E_1 = E_s = E_{eq}$, $E_1 = 0.005$, $E_2 = 0.0025$, $E_3 = 0.0005$, $E_4 = 0.0001$

P	Perfect Bond Condition							
	$m = 0.05$				$m = 0.50$			
	E_1	E_2	E_3	E_4	E_1	E_2	E_3	E_4
0.0050	17	21	35	–	19	24	41	–
0.0025	17	21	35	60	19	24	41	–
0.0010	17	21	35	60	19	24	41	70
0.0001	17	21	35	60	19	24	41	70
P	Perfect Slip Condition							
	$m = 0.05$				$m = 0.50$			
	E_1	E_2	E_3	E_4	E_1	E_2	E_3	E_4
0.0050	17	21	–	–	–	–	–	–
0.0025	16	21	36	61	19	25	42	–
0.0010	17	21	36	61	20	25	42	72
0.0001	17	21	36	61	20	24	42	72

to the perfect bond condition with that of perfect slip condition for limiting values of m. It can be seen that values of $\bar{\lambda}_{di}$ are slightly, but consistently, lower for perfect bond case than the perfect slip case. The perfect bond case provides constraints for further deformation and thus is reflected in the shorter wavelengths.

4 Comparison of Results on $\bar{\lambda}_{db}$ and $\bar{\lambda}_{di}$ and Concluding Remarks

The two sets of results described in Section 3.4 ($\bar{\lambda}_{db}$) and Section 3.6 ($\bar{\lambda}_{di}$) deal with the phenomenon of growth-of-waviness for a viscoelastic matrix/elastic fiber in the context of bifurcation and imperfection sensitivity, respectively. Although bifurcation and imperfection sensitivity are two similar perspectives on instability of the fiber, their respective responses, i.e., computed dominant wavelengths, differ quite significantly. Here we summarize the two sets of results, illustrate the contrast between the two, make comparisons of our results with the similar results by Biot (1965), and finally, provide the significance of our results for processing and in-service behavior of composites. Again, the effect of material properties, load, and interface are compared mirroring the development in the earlier sections. In order to realistically study the processing or in-service problems, the thermo-viscoelastic effects for matrix and the thermal effect for fiber must be accounted for. Nevertheless, the contribution of the present study for the analysis of these problems is the identification of two clearly different results for two, apparently similar, physical phenomena that may take place under the compressive load on the fibers.

In the viscoelastic bifurcation problem[2] for a perfectly bonded fiber, the dominant wavelength is independent of all the matrix properties, i.e., E_s, E_{eq}, and m, except for the matrix Poisson's ratio, ν_m (Eq. (12)) and even that is negligible (Fig. 2). Meanwhile, for the analogous perfectly slipping fiber problem, the dominant wavelength is completely independent of the matrix properties (Eq. (13)). The only material property that is significant in bifurcation—for either bonding case—is the fiber Poisson's ratio, ν_f. Moreover, the dependence of $\bar{\lambda}_{db}$ on ν_f is identical for perfectly bonded and slipping fibers. The observations for a perfectly slipping fiber are analogous to those made by Biot (1965).

In the case of both the bifurcation and imperfection-sensitivity problem, ν_m plays an insignificant role in the determination of dominant wavelengths. On the other hand, the rest of the matrix properties, i.e., E_s, E_{eq}, and m, have a very strong effect on the dominant wavelength (Table 1). Thus, we conclude that imperfection sensitivity is a highly matrix-controlled phenomenon, and therefore, very susceptible to the thermoviscoelastic behavior of the matrix, either during processing or in-service.

Since the conditions used during the processing of laminated composites are moderate, the carbon or glass fibers may be considered to be thermoelastic. However, the treatment presented here is sufficiently general that bifurcation of a viscoelastic layer (i.e., a fiber or beam) embedded in a viscoelastic medium (i.e., matrix) may also be analyzed. The dependence of $\bar{\lambda}_{di}$ on matrix material properties is similar to that for bifurcation of a perfectly slipping viscoelastic fiber in a viscoelastic matrix (Biot, 1965). Furthermore, similar conclusions can be made for the bifurcation of a perfectly bonded viscoelastic fiber in a viscoelastic matrix.

The interface plays an important role in the case of bifurcation (Fig. 2). Similarly, for imperfection sensitivity, the interface does play a role, but a less significant one as compared to that in bifurcation (Table 3). Again, the fiber deformation is controlled by the matrix. The effect of interface is less significant due to the presence of shear-lag effects in the fiber deformation (Holister and Thomas, 1967) implying that the load transfer between the fiber and matrix is mainly due to the normal tractions rather than shear tractions. During processing, the formation of the interface is significant above glass transition temperature, while the load transfer is significant in the glassy stage; nevertheless, development of waviness may be viewed as an ongoing process from the stage where the fiber starts experiencing loads.

In this research, two extreme conditions for fiber-matrix interface are assumed—although the real conditions lie somewhere in between these two extremes. A wealth of research literature can be found in this context which describes the mechanics issues (Dundurs, 1990). An up-to-date review on the interface (or interphase) modeling can be found in Jayaraman et al. (1993).

In the viscoelastic bifurcation analysis, $\bar{\lambda}_{db}$ is observed to be highly sensitive to the applied load (Fig. 2) while, in the extreme contrast, the load has a negligible effect on $\bar{\lambda}_{di}$ (Table 2). The closed-form expression for a fiber under constant load (Eq. (15) and Eq. (17)) indicates the load-independence of $\bar{\lambda}_{di}$. The parametric study presented in Table 2 is conducted without any reference to the origin of load on the fibers. However, to obtain estimates for in-process loads, calculations using the large thermal expansion coefficient mismatch between fiber and matrix may be done. Such calculations tend to imply that the observed fiber deformation during processing is difficult to predict using the thermally induced bifurcation of the fibers. Nevertheless, imperfection sensitivity analysis provides evidence that growth-of-waviness is possible even under the relatively small thermal loads and this single most important analytical observation, as illustrated in this research, may be a useful tool to explain the observed fiber waviness in practice.

Acknowledgments

Support from Dr. Yapa Rajapakse of the ONR under contract ONR-N00014-92-J-1470 is gratefully acknowledged. Additional support is provided by Dr. Bruce Kramer of the NSF under grant DDM-9258413. Authors would like to express their thanks to Prof. Richard A. Schapery, Aerospace Engineering and Engineering Mechanics Department, The University of

Table 3 Effect of interface on $\bar{\lambda}_{di}$: $LH = 2$, $\nu_f = 0.2$, $\nu_m = 0.3$, $P = 0.005$

E_s, E_{eq}	$m = 0.05$		$m = 0.50$	
	Perfect Bond	Perfect Slip	Perfect Bond	Perfect Slip
0.0050	16	17	19	19
0.0025	20	21	24	25
0.0005	34	35	40	42
0.0001	58	60	66	68

[2] If the fiber is viscoelastic and matrix is elastic, analogous—albeit different—results are obtained. The interested reader is referred to Schapery (1991) for more details. Moreover, for elastic fiber and elastic matrix problem, the reader is referred to Minahen and Knauss (1989).

Downloaded 04 May 2010 to 171.66.16.33. Redistribution subject to ASME license or copyright; see http://www.asme.org/terms/Terms_Use.cfm

Texas at Austin, for many discussions. Data collection and graphical work was done by undergraduate research assistants Mr. Mahan H. Mirza and Mr. Timothy D. Wootan.

References

Bhalerao, M., and Moon, T., 1995, "Micromechanics of Local Viscoelastic Buckling of Multilayered Media," *Journal of Composites Engineering*, to appear.

Biot, M., 1958, "Linear Thermodynamics and the Mechanics of Solids," *Proceedings of the Third U.S. National Congress of Applied Mechanics*, ASME, New York, pp. 1–18.

Biot, M., 1965, *Mechanics of Incremental Deformations*, John Wiley and Sons, New York.

Biot, M., Odé, H., and Roever, W., 1961, "Experimental Verification of the Theory of Folding of Stratified Viscoelastic Media," *Geological Society of America Bulletin*, Vol. 72, pp. 1621–1632.

Daniel, I., Hsiao, H.-M., Wooh, S., and Vittoser, J., 1993, "Processing and Compressive Behavior of Thick Composites," *Mechanics of Thick Composites*, AMD-Vol. 162 ASME, New York, pp. 107–126.

Dundurs, J., 1990, "Boundary Conditions at Interfaces," *Micromechanics and Inhomogeneity: The Toshio Mura 65th Anniversary Volume*, Springer-Verlag, New York, pp. 109–114.

Ferry, J., 1960, *Viscoelastic Properties of Polymers*, John Wiley and Sons, New York.

Flory, P., 1953, *Principles of Polymer Chemistry*, Cornell University Press, Ithaca, NY.

Guynn, E., 1990, "Experimental Observations and Finite Element Analysis of the Initiation of Fiber Microbuckling in Notched Composite Laminates," Ph.D. dissertation, Texas A & M University, College Station, TX.

Holister, G., and Thomas, C., 1967, *Fibre Reinforced Materials*, Elsevier, New York.

Jayaraman, K., Reifsnider, K. L., and Swain, R. E., 1993, "Elastic and Thermal Effects in the Interphase: Part I; II," *Journal of Composites Technology and Research*, Vol. 15, pp. 3–13; 14–45.

Kyriakides, S., Arseculeratne, R., Perry, E., and Liechti, K., 1993, "On the Compressive Failure of Fiber Reinforced Composites," Tech. Rpt., EMRL Report No. 93/11, Department of Aerospace Engineering and Engineering Mechanics, The University of Texas at Austin, Austin, TX.

Lessard, L., and Chang, F., 1991, "Effect of Load Distribution on the Fiber Buckling Strength of Unidirectional Composites," *Journal of Composite Materials*, Vol. 25, pp. 65–87.

Minahen, T., and Knauss, W., 1989, "A Note on Microbuckling in Unidirectional Fibrous Composites," ASME JOURNAL OF APPLIED MECHANICS, Vol. 56, pp. 983–985.

Morland, L., and Lee, E., 1960, "Stress Analysis for Linear Viscoelastic Materials with Temperature Variation," *Transactions of the Society of Rheology*, Vol. IV, pp. 233–263.

Schapery, R., 1962, "Approximate Methods of Transform Inversion for Viscoelastic Stress Analysis," *Proceedings of 4th U.S. National Congress of Applied Mechanics*, ASME, New York, pp. 1075–1084.

Schapery, R., 1967, "Stress Analysis of Viscoelastic Composite Materials," *Journal of Composite Materials*, Vol. 1, pp. 228–267.

Schapery, R., 1975, "A Theory of Crack Initiation and Growth in Viscoelastic Media: Part I; II; III," *International Journal of Fracture*, Vol. 11, pp. 141–159; 369–388; 549–562.

Schapery, R., 1991, "Analysis of Local Buckling in Viscoelastic Composites," *IUTAM Symposium on Mechanics Concepts for Composite Material Systems*, Virginia Polytechnic Institute and State University, Blacksburg, VA.

Shuart, M., 1985, "Short Wavelength Buckling and Shear Failures for Compression-Loaded Laminates," Tech. Report NASA TM 87640.

Slaughter, W. S., and Fleck, N. A., 1993, "Viscoelastic Microbuckling of Fiber Composites," ASME JOURNAL OF APPLIED MECHANICS, Vol. 60, pp. 1–5.

Timoshenko, S., 1934, *Theory of Elasticity*, Engineering Societies Monographs, McGraw-Hill, New York.

Ting, E., and Chen, W., 1982, "Creep and Viscoelastic Buckling of Beams on Foundations," Tech. Report, School of Civil Engineering, Purdue University, West Lafayette, Indiana, Report No. CE-STR-83-16.

Vinogradov, A., 1987, "Buckling of Viscoelastic Beam Columns," *AIAA Journal*, Vol. 25, pp. 479–483.

Waas, A., 1988, "Compression Failure of Fibrous Laminated Composites in the Presence of Stress Gradients: Experiment and Analysis," Ph.D. dissertation, California Institute of Technology, Pasadena, CA.

APPENDIX A

Definitions of Integral Transforms

The Carson transform (CT) of a function $f(t)$, typically denoted by an over tilde, may be expressed as

$$CT\{f(t)\} \equiv \tilde{f}(s) = s \times LT\{f(t)\} = s\int_{0^-}^{\infty} e^{-st} f(t)dt.$$

APPENDIX B

Direct Inversion Technique for Laplace Transform (LT)

Schapery (1962) has derived a substitute for analytical inversion of LT called a direct inversion technique. He demonstrated that

$$f(t) \approx \tilde{f}(s)|_{s=\gamma/t},$$

where $\gamma = e^{-C} \approx 0.56$ (C is the Euler constant), provided that the solution $f(t)$ has a small curvature over two decades of time when plotted against $\log t$.

APPENDIX C

Representation of Viscoelastic Material Properties

Frequently, an exponential series representation with a distribution of relaxation times is used for the matrix modulus involving exponentials is used for viscoelastic moduli. Typically, the distribution of relaxation times is widely spread on the time scale and the condition of "slow variation" of viscoelastic moduli is generally honored (Ferry, 1960). Moreover, this representation yields an instantaneous zero-time response which requires a special technique for integration. Another form that is used for relaxation moduli is a power-law in time. It is observed that many viscoelastic materials obey the power-law to great degree of accuracy. Thus for the convenience of analysis, a power-law representation is used for the relaxation modulus of matrix material as (Schapery, 1991)

$$E_m(t) = E_s(t/t_s)^{-m} + E_{eq}. \tag{18}$$

The quantity t_s is a scaling time, so that E_s has dimensions of stiffness. It is observed that chemically cross-linked materials, i.e., thermosets, exhibit an elastic behavior as they reach equilibrium at long times, i.e., $E_{eq} > 0$. On the other hand, in thermoplastic materials, which lack any cross-linking among the polymer chains, E_{eq} is typically negligible (Ferry, 1960).

During processing, the polymer is in a liquid or rubbery phase immediately preceding curing or glass transition where it may be assumed to be incompressible with Poisson's ratio, ν_m, is taken close to 0.5. However, as the matrix cools down to a solid state where ν_m may typically assumed to be of the order 0.3. Moreover, the viscoelastic behavior of ν_m may be ignored (Schapery, 1967) since the bulk modulus is a relatively weak viscoelastic function (generally taken to be constant). In our analysis, the effect of ν_m, is investigated by considering several constant values, i.e., 0.3, 0.4, and 0.5.

Downloaded 04 May 2010 to 171.66.16.33. Redistribution subject to ASME license or copyright; see http://www.asme.org/terms/Terms_Use.cfm

Derivation of a Thin Film Equation by a Direct Approach

F. Y. Huang[1]
Research Assistant,
Assoc. Mem. ASME.

C. D. Mote, Jr.
FANUC Chair of Mechanical Systems,
Vice Chancellor and ASME Fellow.

Department of Mechanical Engineering,
University of California,
Berkeley, CA 94720

A new model of the thin viscous fluid film, constrained between two translating, flexible surfaces, is presented in this paper. The unsteady inertia of the film is included in the model. The derivation starts with the reduced three-dimensional Navier-Stokes equations for an incompressible viscous fluid with a small Reynolds number. By introduction of an approximate velocity field, which satisfies the continuity equation and the no-slip boundary conditions exactly, into weighted integrals of the three-dimensional equations over the film thickness, a two-dimensional thin film equation *is obtained explicitly in a closed form. The lth thin film equation is obtained when the velocity field is approximated by 2lth order polynominals, and the three-dimensional viscous film is described with increasing accuracy by thin film equations of increasing order. Two cases are used to illustrate the coupling of the film to the vibration of the structure and to show that the second thin film equation can be applied successfully to the prediction of a coupled film-structure response in the range of most applications. A* reduced thin film equation *is derived through approximation of the second thin film equation that relates the film pressure to transverse accelerations and velocities, and to slopes and slope rates of the two translating surfaces.*

1 Introduction

The continuum mechanics of a viscous fluid film constrained between two surfaces has been studied since the time of Reynolds (1886). When fluid inertial forces in the film are negligible compared to the viscous forces, the pressure distribution in the film is described by the Reynolds equation. However, with higher machine speeds and lower viscosity lubricants, inclusion of inertia effects in lubrication studies, and especially the inclusion of the unsteady inertia effects of film unsteadiness, are necessary (Tichy and Winer, 1970).

Viscous films exist in many mechanical systems (e.g., saw guides, journal bearings, and squeeze film dampers) and structures (e.g., riveted panels). The coupling of the viscous film to the continuous structure can significantly affect the system response. The response of the coupled film-structural systems has been studied in the frequency domain by Maidanik (1966), Ingard and Akay (1987), Tan and Mote (1990), and others. The pressure generated in the film due to transverse oscillation of one surface has been studied by Tichy and Modest (1978), Murray and Mote (1983), San Andres and Vance (1986), Chen and Mote (1994), and others. A good understanding of the contribution of film inertia on bearing load has been achieved, but these analyses are restricted to squeeze films under prescribed sinusoidal motion only. Also, three-dimensional films have received less attention. To predict the general response of the coupled film-structural system, a three-dimensional time domain formulation relating film pressure to general response of the coupled system is needed.

Cosserat (or *Directed*) *continua* are deformable bodies wherein each material point of the body manifold is endowed with additional kinematical structure (in addition to displacement) that is characterized by kinematical vector fields, called *directors* (Ericksen and Truesdell, 1958). The theory of Cosserat continua was first systematically developed by Cosserat and Cosserat (1909). Shells and fluid films (rods and fluid jets) can be modeled as two-dimensional (one-dimensional) directed continua, though they are three-dimensional bodies, because of their special features (Green et al., 1965; Green and Naghdi, 1974; Naghdi, 1979). One technology for construction of directors is through introduction of an approximate velocity field for fluids, or displacement field for solids, into the weighted integrals of the exact three-dimensional equations describing the continuum (Green and Naghdi, 1984; and Caulk and Naghdi, 1987). Results obtained earlier from these models have been shown to agree well with experiments (Naghdi and Rubin, 1981; and Green et al. 1993).

The purpose of this paper is to derive a two-dimensional thin film equation governing linear dynamic motion of a three-dimensional incompressible, viscous fluid film constrained between two translating, flexible surfaces. The derivation starts with the reduced three-dimensional Navier-Stokes equations for low Reynolds number flows in thin films. The fluid unsteady inertia is modeled to account for film unsteadiness. The form of the velocity field, which satisfies exactly both the incompressibility condition and the no-slip boundary conditions, is assumed a priori. The weighted integrals of the reduced three-dimensional Navier-Stokes equations are satisfied over the film thickness. The lth thin film equations are obtained in a closed form when the velocity field is approximated by $2l$th order polynominals in the coordinate direction across the film thickness. The results obtained from the lth thin film equation are expected to converge to those obtained from the three-dimensional formulation as $l \to \infty$.

Two coupled film-structural systems are studied to illustrate the film coupling, and to evaluate convergence of the thin film equations of different orders. It should be noted that the thin film equation can be applied to the general linear response of thin films and is not restricted to the cases studied here. The derivation in this paper is not identical to that used in the theory of Directed continua, because the starting point is not the exact three-dimensional Navier-Stokes equations, and the directors are neither defined nor expressed explicitly. However, the derivation is motivated by the direct approach.

2 Formulation

Consider the configuration depicted in Fig. 1 of a viscous fluid film constrained between two transversely vibrating sur-

[1] Currently at IBM, 5600 Cottle Road, San Jose, CA 95193.

Contributed by the Applied Mechanics Division of THE AMERICAN SOCIETY OF MECHANICAL ENGINEERS for publication in the ASME JOURNAL OF APPLIED MECHANICS.

Discussion on this paper should be addressed to the Technical Editor, Professor Lewis T. Wheeler, Department of Mechanical Engineering, University of Houston, Houston, TX 77204-4792, and will be accepted until four months after final publication of the paper itself in the ASME JOURNAL OF APPLIED MECHANICS.

Manuscript received by the ASME Applied Mechanics Division, Aug. 15, 1994; final revision, June 27, 1995. Associate Technical Editor: R. Abeyaratne.

Copyright © 1996 by ASME

Downloaded 04 May 2010 to 171.66.16.33. Redistribution subject to ASME license or copyright; see http://www.asme.org/terms/Terms_Use.cfm

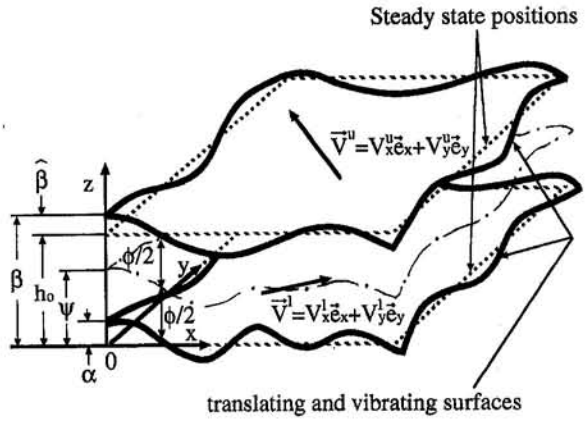


Fig. 1 Schematic of a thin viscous fluid film constrained between two vibrating surfaces that translate at speeds $\vec{V}^u$ and $\vec{V}^l$, respectively. Steady-state positions describe the surfaces when they are not vibrating. $\psi = (\beta + \alpha)/2$ and $\phi = \beta - \alpha$.

faces that translate at constant velocities $\vec{V}^u$ and $\vec{V}^l$, respectively. The film thickness is uniform, h_0, when the surfaces do not vibrate. $\alpha(x, y, t)$ and $\beta(x, y, t) = h_0 + \hat{\beta}(x, y, t)$ describe the transverse locations of the lower and upper surfaces with $|\alpha|$ and $|\hat{\beta}|$ much smaller than h_0. $\phi = \beta - \alpha$ is the dynamic film thickness, and $\psi = (\alpha + \beta)/2$ represents the transverse location of the middle surface of the film. From the relative orders of magnitude of terms in the Navier-Stokes equations when the Reynolds number (Re)† is much smaller than one, the fluid film response is governed by the reduced Navier-Stokes equations (Walowit and Anno, 1975)

$$\rho \frac{\partial u_x}{\partial t} = -\frac{\partial p}{\partial x} + \mu \frac{\partial^2 u_x}{\partial z^2} \tag{1a}$$

$$\rho \frac{\partial u_y}{\partial t} = -\frac{\partial p}{\partial y} + \mu \frac{\partial^2 u_y}{\partial z^2} \tag{1b}$$

$$0 = \frac{\partial p}{\partial z} \tag{1c}$$

and the continuity equation

$$\frac{\partial u_x}{\partial x} + \frac{\partial u_y}{\partial y} + \frac{\partial u_z}{\partial z} = 0 \tag{2}$$

where p is fluid pressure in the film, and u_x, u_y, and u_z are velocity components in the x, y, and z directions, respectively. Equation (1c) specifies that pressure is constant across the film thickness. The no-slip boundary conditions require

$$u_x = V^u_x, \quad u_y = V^u_y, \quad u_z = \frac{\partial \beta}{\partial t} + \vec{V}^u \cdot \nabla \beta, \quad \text{at} \quad z = \beta \tag{3a}$$

$$u_x = V^l_x, \quad u_y = V^l_y, \quad u_z = \frac{\partial \alpha}{\partial t} + \vec{V}^l \cdot \nabla \alpha, \quad \text{at} \quad z = \alpha \tag{3b}$$

where V^l_x, V^u_x and V^l_y, V^u_y are the x-y components of $\vec{V}^l$ and $\vec{V}^u$, and ∇ is gradient in x-y space. Application of the coordinate transformation

$$\xi = \frac{z - \psi}{\phi} \tag{4}$$

to (1)–(3) leads to

$$\rho\left[\frac{\partial u_x}{\partial t} - \left(\frac{1}{\phi}\frac{\partial \psi}{\partial t} + \frac{\xi}{\phi}\frac{\partial \phi}{\partial t}\right)\frac{\partial u_x}{\partial \xi}\right] = -\frac{\partial p}{\partial x} + \frac{\mu}{\phi^2}\frac{\partial^2 u_x}{\partial \xi^2} \tag{5a}$$

$$\rho\left[\frac{\partial u_y}{\partial t} - \left(\frac{1}{\phi}\frac{\partial \psi}{\partial t} + \frac{\xi}{\phi}\frac{\partial \phi}{\partial t}\right)\frac{\partial u_y}{\partial \xi}\right] = -\frac{\partial p}{\partial y} + \frac{\mu}{\phi^2}\frac{\partial^2 u_y}{\partial \xi^2} \tag{5b}$$

$$0 = \frac{\partial p}{\partial \xi} \tag{5c}$$

$$\frac{\partial u_x}{\partial x} - \left(\frac{1}{\phi}\frac{\partial \psi}{\partial x} + \frac{\xi}{\phi}\frac{\partial \phi}{\partial x}\right)\frac{\partial u_x}{\partial \xi} + \frac{\partial u_y}{\partial y} - \left(\frac{1}{\phi}\frac{\partial \psi}{\partial y} + \frac{\xi}{\phi}\frac{\partial \phi}{\partial y}\right)\frac{\partial u_y}{\partial \xi} + \frac{1}{\phi}\frac{\partial u_z}{\partial \xi} = 0 \tag{6}$$

$$u_x = V^u_x, \; u_y = V^u_y, \; u_z = \frac{\partial \beta}{\partial t} + \vec{V}^u \cdot \nabla \beta, \text{ at } \xi = \frac{1}{2} \tag{7a}$$

$$u_x = V^l_x, \; u_y = V^l_y, \; u_z = \frac{\partial \alpha}{\partial t} + \vec{V}^l \cdot \nabla \alpha, \text{ at } \xi = -\frac{1}{2}. \tag{7b}$$

2.1 Steady State. When the translating surfaces do not vibrate, $\alpha = 0$, $\beta = h_0$, and $2\psi = \phi = h_0$. The steady-state flow components (u_{xe}, u_{ye}, u_{ze}) and pressure (p_e) are time independent, and can be obtained by substituting these time-independent variables into (5)–(7) and by following the procedure used in lubrication theory (Walowit and Anno, 1975). Then

$$\nabla^2 p_e = 0 \tag{8}$$

$$u_{xe} = \frac{1}{2}\frac{h_0^2}{\mu}\frac{\partial p_e}{\partial x}\left(\xi^2 - \frac{1}{4}\right) + (V^u_x - V^l_x)\left(\xi + \frac{1}{2}\right) + V^l_x \tag{9a}$$

$$u_{ye} = \frac{1}{2}\frac{h_0^2}{\mu}\frac{\partial p_e}{\partial y}\left(\xi^2 - \frac{1}{4}\right) + (V^u_y - V^l_y)\left(\xi + \frac{1}{2}\right) + V^l_y \tag{9b}$$

$$u_{ze} = 0. \tag{9c}$$

p_e, governed by (8) in the domain of the film, can be nontrivial if the boundary conditions of the film are not homogeneous.

2.2 Dynamic State. When the surfaces vibrate,

$$u_x = u_{xe} + \hat{u}_x, \quad u_y = u_{ye} + \hat{u}_y, \quad u_z = \hat{u}_z,$$
$$p = p_e + \hat{p}, \quad \phi = \phi_e + \hat{\phi}, \quad \psi = \psi_e + \hat{\psi}, \tag{10}$$

where $|(\hat{\ })| \ll |(\ )_e|$, and $2\psi_e = \phi_e = h_0$. Substitution of (10) into (5)–(7) and neglect of higher order terms in the perturbation leads to

$$\rho\left[\frac{\partial \hat{u}_x}{\partial t} - \frac{1}{h_0}\frac{\partial u_{xe}}{\partial \xi}\left(\frac{\partial \hat{\psi}}{\partial t} + \xi\frac{\partial \hat{\phi}}{\partial t}\right)\right] = -\frac{\partial \hat{p}}{\partial x} + \frac{\mu}{h_0^2}\left(\frac{\partial^2 \hat{u}_x}{\partial \xi^2} - 2\frac{\hat{\phi}}{h_0}\frac{\partial^2 u_{xe}}{\partial \xi^2}\right) \tag{11a}$$

$$\rho\left[\frac{\partial \hat{u}_y}{\partial t} - \frac{1}{h_0}\frac{\partial u_{ye}}{\partial \xi}\left(\frac{\partial \hat{\psi}}{\partial t} + \xi\frac{\partial \hat{\phi}}{\partial t}\right)\right] = -\frac{\partial \hat{p}}{\partial y} + \frac{\mu}{h_0^2}\left(\frac{\partial^2 \hat{u}_y}{\partial \xi^2} - 2\frac{\hat{\phi}}{h_0}\frac{\partial^2 u_{ye}}{\partial \xi^2}\right) \tag{11b}$$

$$0 = \frac{\partial \hat{p}}{\partial \xi} \tag{11c}$$

$$\frac{\partial \hat{u}_x}{\partial x} - \frac{1}{h_0}\frac{\partial u_{xe}}{\partial \xi}\left(\frac{\partial \hat{\psi}}{\partial x} + \xi\frac{\partial \hat{\phi}}{\partial x}\right) + \frac{\partial \hat{u}_y}{\partial y} - \frac{1}{h_0}\frac{\partial u_{ye}}{\partial \xi}\left(\frac{\partial \hat{\psi}}{\partial y} + \xi\frac{\partial \hat{\phi}}{\partial y}\right) + \frac{1}{h_0}\frac{\partial \hat{u}_z}{\partial \xi} = 0 \tag{12}$$

† $\mathrm{Re} = \rho h_0^2 V/\mu L_{xy}$, where ρ and μ are density and viscosity of the fluid, $V = \max(|\vec{V}^u|, |\vec{V}^l|)$, and L_{xy} is the characteristic length in the xy-plane.

Downloaded 04 May 2010 to 171.66.16.33. Redistribution subject to ASME license or copyright; see http://www.asme.org/terms/Terms_Use.cfm

$$\hat{u}_x = 0, \quad \hat{u}_y = 0, \quad \hat{u}_z = \frac{\partial \beta}{\partial t} + \vec{V}^u \cdot \nabla \beta, \quad \text{at} \quad \xi = \frac{1}{2} \tag{13a}$$

$$\hat{u}_x = 0, \quad \hat{u}_y = 0, \quad \hat{u}_z = \frac{\partial \alpha}{\partial t} + \vec{V}^l \cdot \nabla \alpha, \quad \text{at} \quad \xi = -\frac{1}{2}. \tag{13b}$$

The time and spatial derivatives of ϕ and ψ equal those of $\dot{\phi}$ and $\dot{\psi}$. Summing the x derivative of (11a) and the y derivative of (11b) with the use of (8) and (9a, b) gives

$$-\rho \frac{\partial g}{\partial t} + \frac{\mu}{h_0^2} \frac{\partial^2 g}{\partial \xi^2} = \nabla^2 \hat{p} - \frac{\rho h_0}{\mu} \xi \nabla p_e \cdot (\nabla \dot{\psi} + \xi \nabla \dot{\phi}) - \frac{\rho}{h_0} (\vec{V}^u - \vec{V}^l) \cdot (\nabla \dot{\psi} + \xi \nabla \dot{\phi}) \tag{14}$$

where

$$(\dot{}) = \frac{\partial (\quad)}{\partial t} \quad \text{and} \quad g = \frac{\partial \hat{u}_x}{\partial x} + \frac{\partial \hat{u}_y}{\partial y}.$$

To this point the derivation describes a three-dimensional continuum model. A two-dimensional film model will be derived by approximation of the velocity field across the film thickness. We now specify that the dynamic components of flow velocity in the film can be expressed by polynominals in ξ

$$\hat{u}_x = \sum_{i=0}^{2(l-1)} a_{xi}(x, y, t) \xi^i (\xi^2 - \tfrac{1}{4}), \tag{15a}$$

$$\hat{u}_y = \sum_{i=0}^{2(l-1)} a_{yi}(x, y, t) \xi^i (\xi^2 - \tfrac{1}{4}) \tag{15b}$$

satisfying the boundary conditions on $\hat{u}_x$ and $\hat{u}_y$ described in (13a, b). By requiring that the continuity Eq. (12) be satisfied exactly, $\hat{u}_z$ can be obtained by integration of (12) subject to the boundary conditions on $\hat{u}_z$ in (13a, b) and the representations of $\hat{u}_x$ and $\hat{u}_y$ in (15a, b):

$$\sum_{j=0}^{l-1} \frac{b_{2j}}{2^{2j+1}(2j+3)(2j+1)} - \frac{1}{h_0} \left(\frac{\partial \phi}{\partial t} + \frac{1}{2} (\vec{V}^l + \vec{V}^u) \cdot \nabla \phi \right) + \frac{h_0}{12\mu} \nabla p_e \cdot \nabla \phi = 0 \tag{16}$$

where (9a, b) have been used, and

$$b_i = \frac{\partial a_{xi}}{\partial x} + \frac{\partial a_{yi}}{\partial y}. \tag{17}$$

It should be noted that the balances (16) do not involve b_{2j+1} because $\int_{-1/2}^{1/2} \xi^{2j+1} (\xi^2 - \frac{1}{4}) d\xi = 0$. Substitution of (15$a$, b) into (14), and integration of (14) multiplied by $\xi^{2k\dagger}$ ($k = 0, 1, \ldots, l-1$) with respect to ξ from $-\frac{1}{2}$ to $\frac{1}{2}$ leads to

$$\sum_{j=0}^{l-1} \frac{\rho}{2^{2j+1}(2k+2j+3)(2k+2j+1)} \dot{b}_{2j} + \frac{\mu}{h_0^2} \frac{8jk + 4j^2 + 2k - 1}{2^{2j-1}(2k+2j+1)(2k+2j-1)} b_{2j} = \frac{1}{2k+1} \nabla^2 \hat{p} - \frac{\rho h_0}{\mu} \frac{1}{4(2k+3)} \nabla p_e \cdot \nabla \dot{\phi} - \frac{\rho}{h_0} \frac{1}{2k+1} (\vec{V}^u - \vec{V}^l) \cdot \nabla \dot{\psi}. \tag{18}$$

† Integration of (14) multiplied by ξ^{2k+1} with respect to ξ from $-\frac{1}{2}$ to $\frac{1}{2}$ leads to equations involving b_{2j+1} and their time derivatives only, and independent of $\hat{p}$. Equations (16) and (18) and the above statement indicate that b_{2j} and b_{2j+1} are uncoupled and $\hat{p}$ is independent of b_{2j+1}. Therefore, the b_{2j+1} are not relevant to the film model.

Again, b_{2j+1} are not involved in (18) because $\int_{-1/2}^{1/2} \xi^{2k} \cdot \xi^{2j+1} (\xi^2 - \frac{1}{4}) d\xi = 0$. The $(l+1)$ Eqs. (16) and (18) are used to determine the $(l+1)\hat{p}$ and b_{2j} with ϕ, ψ, and their derivatives specified.

Equations (16) and (18) can be written in matrix form:

$$\boldsymbol{\gamma}^T \cdot \mathbf{v} - \Phi + \Pi = 0 \tag{19}$$

$$\dot{\mathbf{v}} = \mathbf{A}^{-1}\mathbf{B}\mathbf{v} + \nabla^2 \hat{p} \mathbf{A}^{-1} \bar{\mathbf{c}} + \dot{\Pi} \mathbf{A}^{-1} \bar{\mathbf{d}} + \dot{\Psi} \mathbf{A}^{-1} \bar{\mathbf{e}} \tag{20}$$

where

$$\Phi = \frac{1}{h_0} \left(\dot{\phi} + \frac{\mathbf{V}^u + \mathbf{V}^l}{2} \cdot \nabla \phi \right),$$

$$\Pi = \frac{h_0}{12\mu} \nabla p_e \cdot \nabla \phi, \quad \Psi = \frac{1}{h_0} (\vec{V}^u - \vec{V}^l) \cdot \nabla \psi \tag{21}$$

are scalar functions, $\mathbf{A}$ and $\mathbf{B}$ are $l \times l$ constant matrices, $\mathbf{v}$ is an $l \times 1$ vector of b_{2j}, $\boldsymbol{\gamma}$, $\bar{\mathbf{c}}$, $\bar{\mathbf{d}}$, and $\bar{\mathbf{e}}$ are $l \times 1$ constant vectors. The elements are

$$A_{mn} = \frac{1}{2^{2n-1}(2m+2n-1)(2m+2n-3)},$$

$$B_{mn} = -\frac{\mu}{\rho h_0^2} \frac{8mn + 4n^2 - 16n - 6m + 9}{2^{2n-3}(2m+2n-3)(2m+2n-5)}$$

$$\nu_n = b_{2(n-1)}, \quad \gamma_n = \frac{2^{-2n+1}}{(2n+1)(2n-1)},$$

$$\bar{c}_m = \frac{1}{\rho(2m-1)}, \quad \bar{d}_m = \frac{-3}{2m+1}, \quad \bar{e}_m = \frac{-1}{2m-1}$$

where $1 \le m, n \le l$. The time derivative of (20), and use of (20) to eliminate the $\dot{\mathbf{v}}$ dependence in the resulting equation, gives an expression for $\ddot{\mathbf{v}}$ involving $\mathbf{v}$. Repetition of the above time derivative procedure on the expression of $\mathbf{v}^{(n-1)}$ and use of (20) to eliminate $\dot{\mathbf{v}}$ dependence leads to

$$\mathbf{v}^{(n)} = \mathbf{D}^n \mathbf{v} + \sum_{i=1}^{n} \nabla^2 \hat{p}^{(n-i)} \mathbf{D}^{i-1} \mathbf{c} + \Pi^{(n-i+1)} \mathbf{D}^{i-1} \mathbf{d} + \Psi^{(n-i+1)} \mathbf{D}^{i-1} \mathbf{e} \tag{22}$$

where $(\quad)^{(n)} = (\partial^n (\quad))/\partial t^n$, $\mathbf{D} = \mathbf{A}^{-1}\mathbf{B}$, $\mathbf{c} = \mathbf{A}^{-1}\bar{\mathbf{c}}$, $\mathbf{d} = \mathbf{A}^{-1}\bar{\mathbf{d}}$, and $\mathbf{e} = \mathbf{A}^{-1}\bar{\mathbf{e}}$. Substitution of (22) into the nth time derivative of (19) for $n = 1, 2, \ldots, l$ leads to

$$\mathbf{E}\mathbf{v} + \mathbf{F}\tilde{\mathbf{p}} + \mathbf{G}\tilde{\Pi} + \mathbf{H}\tilde{\Psi} - \tilde{\Phi} = 0 \tag{23}$$

where $\mathbf{E}$, $\mathbf{F}$, $\mathbf{G}$, and $\mathbf{H}$ are $l \times l$ constant matrices, $\tilde{\mathbf{p}}$, $\tilde{\Pi}$, $\tilde{\Psi}$, and $\tilde{\Phi}$ are $l \times 1$ vector functions, and their components are

$$\begin{cases} F_{mn} = \boldsymbol{\gamma} \cdot \mathbf{D}^{m-n} \mathbf{c}, \\ G_{mn} = \boldsymbol{\gamma} \cdot \mathbf{D}^{m-n} \mathbf{d} + \delta_{mn}, \\ H_{mn} = \boldsymbol{\gamma} \cdot \mathbf{D}^{m-n} \mathbf{e}, \end{cases} \quad \text{for} \quad m \ge n$$

$$F_{mn} = 0, \quad G_{mn} = 0, \quad H_{mn} = 0, \quad \text{for} \quad m < n$$

$$E_{mn} = [(\mathbf{D}^m)^T \boldsymbol{\gamma}]_n, \quad \tilde{p}_n = \nabla^2 \hat{p}^{(n-1)},$$

$$\tilde{\Pi}_n = \Pi^{(n)}, \quad \tilde{\Psi}_n = \Psi^{(n)}, \quad \tilde{\Phi}_n = \Phi^{(n)}$$

where δ_{mn} is the Kroneker delta, and $[(D^m)^T \boldsymbol{\gamma}]_n$ is the nth component of vector $(D^m)^T \boldsymbol{\gamma}$. The explicit expression for $\mathbf{v}$ from (23) is substituted into (19) to give the expression governing $\hat{p}$ in ϕ, ψ and their derivatives

$$\tilde{\mathbf{p}}^T \cdot (\mathbf{E}^{-1}\mathbf{F})^T \boldsymbol{\gamma} = \Pi - \Phi - \tilde{\Pi}^T \cdot (\mathbf{E}^{-1}\mathbf{G})^T \boldsymbol{\gamma} - \tilde{\Psi}^T \cdot (\mathbf{E}^{-1}\mathbf{H})^T \boldsymbol{\gamma} + \tilde{\Phi}^T \cdot (\mathbf{E}^{-1})^T \boldsymbol{\gamma}. \tag{24}$$

Downloaded 04 May 2010 to 171.66.16.33. Redistribution subject to ASME license or copyright; see http://www.asme.org/terms/Terms_Use.cfm

Table 1 Coefficients in the thin film Eq. (25)

l	1	2	3	4	5
f_1^p	1	1	1	1	1
f_2^p	-	$\frac{1}{140}$	$\frac{3}{220}$	$\frac{1}{60}$	$\frac{7}{380}$
f_3^p	-	-	$\frac{1}{55440}$	$\frac{1}{18200}$	$\frac{3}{36176}$
f_4^p	-	-	-	$\frac{1}{43243200}$	$\frac{49}{478608460}$
f_5^p	-	-	-	-	1.78986×10^{-11}
f_1^Φ	1	$\frac{9}{7}$	$\frac{15}{11}$	$\frac{7}{5}$	$\frac{27}{19}$
f_2^Φ	-	$\frac{1}{140}$	$\frac{1}{66}$	$\frac{1}{52}$	$\frac{7}{323}$
f_3^Φ	-	-	$\frac{1}{55440}$	$\frac{1}{17160}$	$\frac{7}{77520}$
f_4^Φ	-	-	-	$\frac{1}{43243200}$	$\frac{8}{75246077}$
f_5^Φ	-	-	-	-	1.78986×10^{-11}
f_1^Π	0	$-\frac{24}{35}$	$-\frac{42}{55}$	$-\frac{4}{5}$	$-\frac{78}{95}$
f_2^Π	-	0	$-\frac{19}{4620}$	$-\frac{29}{4550}$	$-\frac{232}{29889}$
f_3^Π	-	-	0	$-\frac{17}{1801800}$	$-\frac{552}{28081619}$
f_4^Π	-	-	-	0	-1.13835×10^{-8}
f_5^Π	-	-	-	-	0
f_1^Ψ	1	1	1	1	1
f_2^Ψ	-	$\frac{1}{140}$	$\frac{3}{220}$	$\frac{1}{60}$	$\frac{7}{380}$
f_3^Ψ	-	-	$\frac{1}{55440}$	$\frac{1}{18200}$	$\frac{3}{36176}$
f_4^Ψ	-	-	-	$\frac{1}{43243200}$	$\frac{49}{478608460}$
f_5^Ψ	-	-	-	-	1.78986×10^{-11}

When expanded, (24) becomes

$$\sum_{j=1}^{j=l} T^{j-1} f_j^p \nabla^2 \hat{p}^{(j-1)} = 12\,\frac{\mu}{h_0^2}\,(\Phi - \Pi) + \frac{\mu}{h_0^2}\sum_{j=1}^{j=l} T^j (f_j^\Phi \Phi^{(j)} + f_j^\Pi \Pi^{(j)} + f_j^\Psi \Psi^{(j)}) \quad (25)$$

where $T = (\rho h_0^2)/\mu$ is a scaling of time, and f_j^p, f_j^Φ, f_j^Π, and f_j^Ψ are constants given in Table 1 for $l = 1$ to 5. In the sequel, (25) is called the "lth thin film equation."

3 Reduced Thin Film Equation

Time derivatives of $\nabla^2\hat{p}$ and of ϕ and ψ of orders higher than second appear in (25) for $l \geq 2$. In this section, we approximate the lth thin film equation for $l \geq 2$ by the *reduced thin film equation*

$$\nabla^2\hat{p} = \frac{\mu}{h_0^2}\,(s_1\Phi + s_2 T\dot{\Phi} + s_3 T\dot{\Psi} + s_4\Pi + s_5 T\dot{\Pi}). \quad (26)$$

Let $\hat{p}_2$ be the film pressure obtained from (25) with $l = 2$, and $\hat{p}_r$ be the solution to (26). Then subtraction of (26) plus $T/140$ times the time derivative of (26) from (25) with $l = 2$, and equation of the resulting coefficients of Φ, $\dot{\Phi}$, $\dot{\Psi}$, Π, and $\dot{\Pi}$ to zero to impose satisfaction, yields

$$s_1 = 12, \quad s_2 = \tfrac{6}{5}, \quad s_3 = 1, \quad s_4 = -12, \quad s_5 = -\tfrac{3}{5} \quad (27)$$

and

$$\frac{T}{140}\nabla^2\dot{\Delta}_2 + \nabla^2\Delta_2 = \frac{T^2}{700}\frac{\mu}{h_0^2}\left(-\ddot{\Phi} + \frac{1}{4}\ddot{\Pi}\right) \quad (28a)$$

where $\Delta_2 = \hat{p}_2 - \hat{p}_r$. Let $\bar{t} = t\bar{\omega}$, where $\bar{\omega}$ is a characteristic frequency of the coupled film-structure systems (e.g., the absolute values of dimensional eigenvalues of the film/plate system in Section 4.1, or the oscillation frequency of the film thickness in the bearing in Section 4.2) such that the magnitudes of $(\partial^n(\ )/\partial\bar{t}^n)$ $(\equiv (1/\bar{\omega}^n)(\partial^n(\ )/\partial t^n))$ are of the same order for all n. Then (28a) can be written as

$$\frac{\overline{\mathrm{Re}}_s}{140}\nabla^2\Delta_2' + \nabla^2\Delta_2 = \frac{\overline{\mathrm{Re}}_s^2}{700}\frac{\mu}{h_0^2}\left(-\Phi'' + \frac{1}{4}\Pi''\right) \quad (28b)$$

where $(\ )' = (\partial(\ )/\partial\bar{t})$ and

$$\overline{\mathrm{Re}}_s = T\bar{\omega} = \frac{\rho h_0^2\bar{\omega}}{\mu} \quad (29)$$

is a squeeze Reynolds number that is a measure of the magnitude of the unsteady fluid inertia forces relative to fluid viscous forces. Equation (28b) predicts the error between the second thin film equation and the reduced thin film equation at specified $\overline{\mathrm{Re}}_s$. When the form (26) is used to approximate the third thin film equation, the procedure above leads to s_k identical to those given in (27) and an error

$$\frac{\overline{\mathrm{Re}}_s^2}{55440}\nabla^2\Delta_3'' + \frac{3\overline{\mathrm{Re}}_s}{220}\nabla^2\Delta_3' + \nabla^2\Delta_3 = \frac{\overline{\mathrm{Re}}_s^3}{277200}\frac{\mu}{h_0^2}\left(-\Phi''' + \frac{1}{4}\Pi'''\right) + \frac{\overline{\mathrm{Re}}_s^2}{700}\frac{\mu}{h_0^2}\left(-\Phi'' + \frac{1}{4}\Pi''\right) \quad (30)$$

where $\Delta_3 = \hat{p}_3 - \hat{p}_r$. $\hat{p}_3$ is the film pressure obtained from the third thin film equation.

4 Case Study

Two cases are studied to demonstrate convergence of the thin film equations of different orders, and to illustrate the coupling of the viscous film to structural response. The first case is a flexible rectangular plate coupled over its entire surface to an adjacent rigid surface through a viscous film. The plate is simply supported along four edges, and film pressure is ambient at the boundary. The second case is a pair of infinitely wide, pressure-regulated, fluid lubricated hybrid thrust bearings (shown in Fig. 2(a)). Lubricant is supplied at the leading edge with a constant inlet pressure (p_0). Lubricant outlet pressure at the trailing end is ambient. Geometric symmetry of the bearing setup requires the translating surface to remain flat at one equilibrium state, so the dynamic load in a pair of opposing bearings is twice the

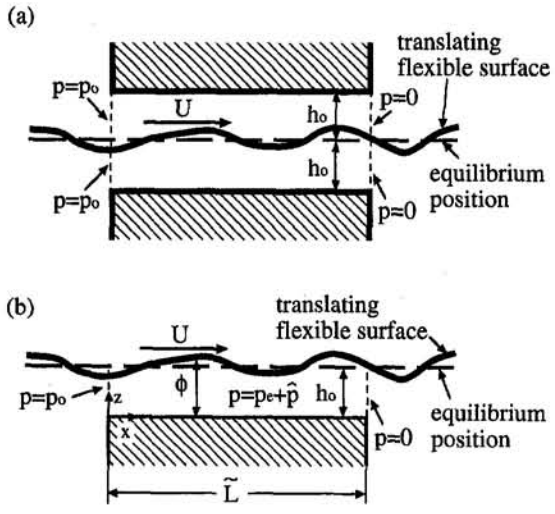


Fig. 2 (a) Schematic of a pair of infinitely wide, pressure-regulated hybrid bearings. The flexible surface remains flat at one equilibrium position. (b) Schematic of one infinitely wide, pressure-regulated hybrid bearing. The dynamic load in a pair of bearings is twice the dynamic load in one bearing.

Downloaded 04 May 2010 to 171.66.16.33. Redistribution subject to ASME license or copyright; see http://www.asme.org/terms/Terms_Use.cfm

dynamic load in one bearing. Therefore, it is necessary to consider the dynamic pressure, $\hat{p}$, generated in one bearing only (as shown in Fig. 2(*b*)).

4.1 Flexible Rectangular Plate Coupled to a Viscous Film. The equation of transverse motion of a classical rectangular plate is

$$D\nabla^4\phi + \rho_d\ddot{\phi} = \hat{p} \tag{31}$$

where D and ρ_d are flexural rigidity and mass per unit area of the plate, and the simple support boundary conditions are

$$\phi = \frac{\partial^2\phi}{\partial x^2} = 0 \quad \text{at} \quad x = 0, L \tag{32a}$$

$$\phi = \frac{\partial^2\phi}{\partial y^2} = 0 \quad \text{at} \quad y = 0, \kappa L \tag{32b}$$

where L and κ are the length and aspect ratio of the plate. Film pressure is modeled through (25) or (26) with $\psi = \frac{1}{2}\phi$ and $\hat{V}^u = \hat{V}^l = p_e = 0$. Boundary conditions on film pressure are

$$\hat{p} = 0 \quad \text{at} \quad x = 0, L \quad \text{and} \quad y = 0, \kappa L. \tag{33}$$

Introduction of dimensionless variables

$$\bar{x} = \frac{x}{L}, \quad \bar{y} = \frac{y}{\kappa L}, \quad \tau = t\omega_{mn}, \quad \bar{\phi} = \frac{\phi}{h_0}, \quad q = \frac{\hat{p}}{\rho_d\omega_{mn}^2 h_0}$$

into (25), (26), and (31)–(33), and assumption of an (m, n) plate displacement $\bar{\phi} = \bar{\phi}_{mn}(\tau)\sin(m\pi\bar{x})\sin(n\pi\bar{y})$ and film pressure $q = q_{mn}(\tau)\sin(m\pi\bar{x})\sin(n\pi\bar{y})$, reduces (31), (25), and (26) to

$$\bar{\phi}_{mn} + \bar{\phi}^{[2]}_{mn} = q_{mn} \tag{34}$$

$$\sum_{j=1}^{j=l} f_j^p \,\mathrm{Re}_0^{j-1} q_{mn}^{[j-1]} = -\sigma\left(\frac{12}{\mathrm{Re}_0}\bar{\phi}^{[1]}_{mn} + \sum_{j=1}^{j=l} f_j^{\Phi}\,\mathrm{Re}_0^{j-1}\bar{\phi}^{[j+1]}_{mn}\right) \tag{35}$$

$$q_{mn} = -\sigma\left(\frac{12}{\mathrm{Re}_0}\bar{\phi}^{[1]}_{mn} + \frac{6}{5}\bar{\phi}^{[2]}_{mn}\right) \tag{36}$$

where $(\ )^{[k]} = (\partial^k(\ ))/\partial\tau^k$, ω_{mn} is the natural frequency of the (m, n) mode of the plate before coupling to the viscous film, Re_0 is a modified squeeze Reynolds number, σ is mass ratio, and

$$\omega_{mn} = \sqrt{\frac{D}{\rho_d}}\frac{1}{L^2}M, \quad \mathrm{Re}_0 = \frac{\rho h_0^2\omega_{mn}}{\mu}, \quad \sigma = \frac{\rho L^2}{\rho_d h_0}\frac{1}{M}. \tag{37}$$

$M = m^2\pi^2 + (n^2\pi^2/\kappa^2)$ is a mode number. Substitutions of (34) into (35), and also into (36), and assumption of $\bar{\phi}_{mn}(\tau) = e^{\lambda\tau}$ leads to characteristic equations for λ. The eigenvalue λ is obtained from the roots of the characteristic equations, and they are shown in Fig. 3.

4.2 Fluid Lubricated Hybrid Thrust Bearing. The dynamic pressure in the bearing is modeled through y-independent (25) and (26) with $\psi = \frac{1}{2}\phi$, $\vec{V}^u = U\vec{e}_x$, $\vec{V}^l = 0$ and $p_e = p_0(\tilde{L} - x)/\tilde{L}$,

$$\sum_{i=1}^{i=l} f_i^p T^{i-1}\frac{\partial^2\hat{p}^{(i-1)}}{\partial x^2} = 12\frac{\mu}{h_0^3}\left[\dot{\phi} + \left(\frac{U}{2} + U_p\right)\frac{\partial\phi}{\partial x}\right] + \frac{\mu}{h_0^3}\sum_{j=1}^{j=l} T^j\left\{f_j^{\Phi}\phi^{(j+1)} + \left[(f_j^{\Phi} + f_j^{\Psi})\frac{U}{2} - f_j^{\Pi}U_p\right]\frac{\partial\phi^{(j)}}{\partial x}\right\} \tag{38}$$

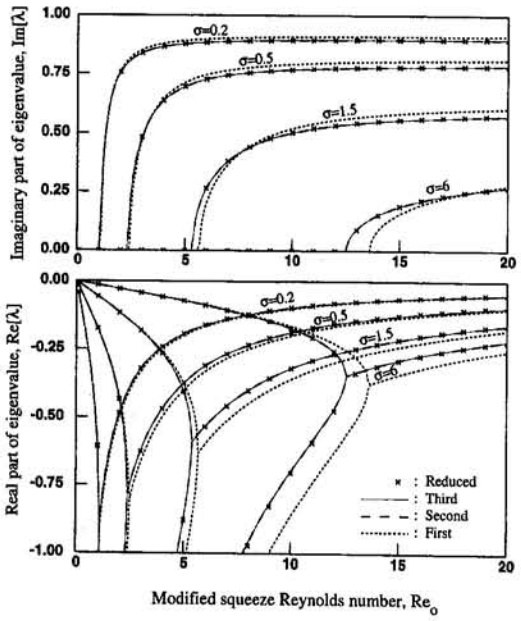


Fig. 3 Prediction of the dimensionless eigenvalue λ of a plate coupled to a viscous film through the thin film equations of different orders and the reduced thin film equation

$$\frac{\partial^2\hat{p}}{\partial x^2} = 12\frac{\mu}{h_0^3}\left[\dot{\phi} + \left(\frac{U}{2} + U_p\right)\frac{\partial\phi}{\partial x}\right] + T\frac{\mu}{h_0^3}\left[\frac{6}{5}\ddot{\phi} + \left(\frac{11}{10}U + \frac{3}{5}U_p\right)\frac{\partial\dot{\phi}}{\partial x}\right] \tag{39}$$

where $U_p = h_0 p_0/12\mu\tilde{L}$ is a velocity unit, $\tilde{L}$ is bearing length, and boundary conditions on the dynamic pressure are

$$\hat{p} = 0 \quad \text{at} \quad x = 0, \tilde{L}. \tag{40}$$

When $U = p_0 = 0$, and the flexible surface undergoes a transverse, uniform, and sinusoidal oscillation at a frequency ω, this model reduces to one studied by Tichy and Modest (1978). Substitution of $\tilde{\tau} = \omega t$ and $\partial\phi/\partial x = 0$ into (38) and (39) leads to

$$\sum_{j=1}^{j=l}\mathrm{Re}_s^{j-1} f_j^p\frac{\partial^2\hat{p}^{\langle j-1\rangle}}{\partial x^2} = \frac{\mu}{h_0^3}\left(12\phi^{\langle 1\rangle} + \sum_{j=1}^{j=l}\mathrm{Re}_s^j f_j^{\Phi}\phi^{\langle j+1\rangle}\right) \tag{41}$$

$$\frac{\partial^2\hat{p}}{\partial x^2} = \frac{\mu}{h_0^3}\left(12\phi^{\langle 1\rangle} + \frac{6}{5}\mathrm{Re}_s\phi^{\langle 2\rangle}\right) \tag{42}$$

where $(\ )^{\langle k\rangle} = (\partial^k(\ )/\partial\tilde{\tau}^k)$, $\mathrm{Re}_s = (\rho h_0^2\omega/\mu)$ is the squeeze Reynolds number. Assume $\phi = h_0 + \epsilon e^{i\tilde{\tau}}$ ($|\epsilon| \ll h_0$ is constant). Then $\hat{p}$ can be obtained through integration of (41), and/or (42), subject to (40), and the dynamic load in the bearing is

$$W(\tilde{\tau}) = \int_0^{\tilde{L}}\hat{p}dx = \epsilon\frac{\mu\tilde{L}^3}{h_0^3}\chi e^{i(\tilde{\tau}+\theta)} \tag{43}$$

where $\chi = \chi(\mathrm{Re}_s)$ is the load ratio, and $\theta = \theta(\mathrm{Re}_s)$ is the phase angle. They both depend on the squeeze Reynolds number Re_s only; $\chi(0) = 1$ and $\theta(0) = 270$ deg as shown in Fig. 4.

5 Results and Discussion

The derivation in this paper is based on the approximation of flow velocities in (15). When fluid inertia vanishes in (5), the film is described exactly by lubrication theory, and the ve-

Downloaded 04 May 2010 to 171.66.16.33. Redistribution subject to ASME license or copyright; see http://www.asme.org/terms/Terms_Use.cfm

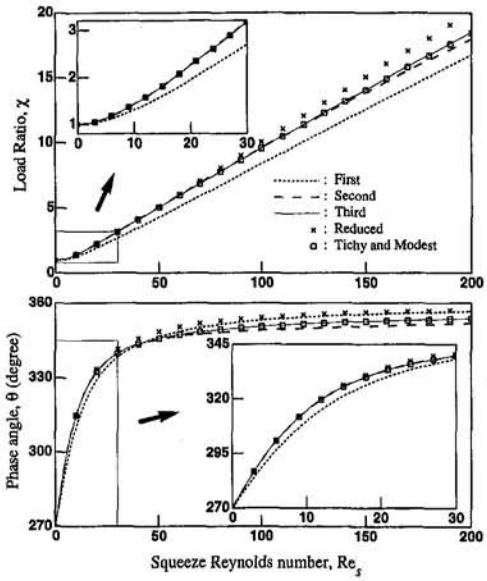


Fig. 4 Prediction of load ratio and phase angle of dynamic load in a hydrodynamic bearing ($p_o = 0$) when the flexible surface is not translating ($U = 0$) and it oscillates uniformly and sinusoidally ($\phi = h_o + \epsilon e^{i\omega t}$)

locities u_x and u_y are quadratic polynominals in ξ (Walowit and Anno, 1975). When fluid inertia is modeled, the velocity profiles are no longer parabolic in ξ. By assuming that fluid velocity profiles remain parabolic in ξ, which is used in the method of average inertia (Pinkus and Sternlicht, 1961) and is the case in the first thin film equation, the inertia forces are first included in the model. However, the error in this representation increases with inertia effects as will be shown later. By allowing the fluid velocities to be represented by higher order polynominals in (15), the velocity field under inertia forces can be modeled more accurately, and consequently the higher order thin film equations can be applied successfully to prediction of the mechanics of the film over wider range of inertia.

The thin film equations of all orders reduce to Reynolds equation as $T \to 0$; see (25). The first thin film equation adds two terms, $T(\dot{\Phi} + \dot{\Psi})$, to Reynolds equation to account for fluid inertia effects. The dynamic pressure modeled by the first thin film equation can be expressed as a functional of $\ddot{\phi}$, $\dot{\phi}$, $\nabla\dot{\phi}$, $\nabla\dot{\psi}$, and $\nabla\phi$. The pressure can be interpreted as generated by a combination of mass, damping, gyroscopic, and circulatory forces. When $l \geq 2$, (25) involves time derivatives of $\hat{p}$ and higher order time derivatives of ϕ and ψ. Therefore, it is no longer possible to classify the film coupling by the classical types of forces. However, the higher order thin film equations can also be modeled by the reduced thin film Eq. (26). The coefficients in the reduced thin film equation are given in (27) where the second and the third thin film equations are approximated. Equations (28*b*) and (30) predict the error of the approximation, and show that the error is small when $\overline{\mathrm{Re}}_s$ is not large. Through further calculation not shown here, approximation of the fourth and the fifth thin film equations by (26) lead to s_k coefficients that are identical to those given in (27). Equation (26) has the same structure as the first thin film equation with only the coefficients of $\dot{\Phi}$ changed from 1 to 6/5 and of $\dot{\Pi}$ changed from 0 to $-(3/5)$.

The eigenvalues of a classical rectangular plate coupled to a thin viscous film are shown in Fig. 3. $\lambda = \pm i$ when the plate is not coupled to the film. σ is a measure of film coupling, and Re_0 is a measure of the ratio of unsteady inertia force to viscous force in the film. The error between the predictions obtained from the second and the third thin film equations is much less than 0.5 percent over the region tested. The results from the second thin film equation have essentially converged in this range and describe successfully the coupled system. The reduced thin film equation predicts eigenvalues with error less than one percent, while use of the first thin film equation may lead to significant error in some region. Therefore, the reduced thin film Eq. (36) is shown to characterize the film-plate coupling for many problems. The form of (36) also shows that the film coupling can be modeled as distributed damping and inertia. As σ increases, the contribution of film pressure to the system response increases. Because σ is small for large M, higher modes (M is larger) are less affected by the film coupling. As Re_0 decreases, the damping force component in the film coupling increases. This is consistent with the overdamped response at small Re_0.

Comparisons of the load predicted in the thrust bearing to the exact solutions obtained in Tichy and Modest (1978) are shown in Fig. 4. The flexible surface is not translating and it oscillates transversely, uniformly and sinusoidally with an inlet film pressure of zero (hydrodynamic bearings). When $\mathrm{Re}_s < 30$, the error in the load ratio χ obtained from the second thin film equation is less than 0.5 percent, and 0.05 deg for the phase angle θ. Even when $\mathrm{Re}_s = 200$, the error in χ is about 2.5 percent, and 2 deg for θ. For the third thin film equation, the error in χ is less than 0.5 percent, and 0.03 deg for θ at $\mathrm{Re}_s = 200$. The bearing is characterized well by the reduced thin film equation (39). The first term on the right-hand side of (39) displays a bearing pressure component equivalent to damping translating at speed $U/2 + U_p$. Moving damping has been shown to significantly stabilize moving continua, like translating strings and rotating disks (Huang and Mote, 1995, 1996a, b). The second term, induced by the fluid inertia, contributes an inertial force and a gyroscopic force to the bearing pressure. They can be significant when fluid inertia forces are comparable or greater than viscous forces. It is also seen by comparing (42) and (39) that modeling the flexible surface as undergoing a uniform transverse oscillation without tilting may be inappropriate when studying coupled system dynamics because the circulatory and gyroscopic forces vanish in that special model.

6 Conclusions

1 The two-dimensional thin film Eq. (25), modeling a thin viscous film between two translating, flexible surfaces with unsteady fluid inertia considered, is derived explicitly in a closed form. The thin film equation relates the motion of the two surfaces to the film pressure, and can be applied to the dynamics of structures coupled to thin films, to transient and steady-state responses, to eigenvalue problems and to other models.

2 The derivation is based on an approximate representation of fluid velocity field (15) in the film. The lth thin film Eq. (25) results when the fluid velocities is approximated by $2l$th order polynominals in ξ. Higher order thin film equation can predict the response of coupled systems more precisely as the application range widens. In the two cases studied here the second thin film equation predicts the system response with error less than 0.5 percent.

3 The thin film equations of order higher than first contain time derivatives of $\hat{p}$ and time derivatives of ϕ and ψ of order higher than second. The fluid film coupling, when modeled by these equations, cannot be classified exactly into classical force types. When $T \to 0$, the thin film equations of all orders reduce to Reynolds equation.

4 The reduced thin film Eq. (26) approximates the second thin film equation with a simple form that relates the film pressure to transverse accelerations and velocities, slopes, and rate of change of slope of the two surfaces. The error of the approximation, predicted by (28*b*), is small when the squeeze Reynolds number $\overline{\mathrm{Re}}_s$ is not large. In the two cases analyzed the reduced thin film equation agrees well with the second thin film equation.

5 When modeled by the reduced thin film equation, the film between a flexible plate and a rigid wall creates forces that are

Downloaded 04 May 2010 to 171.66.16.33. Redistribution subject to ASME license or copyright; see http://www.asme.org/terms/Terms_Use.cfm

energetically equivalent to distributed mass and damping (see (36)). The dynamic pressure in a hybrid bearing is equivalent to translating damping, inertial, and gyroscopic forces (see (39)). The vibration of higher modes in the plate-film system are less dissipated by the viscous film than the lower ones.

Acknowledgment

The authors would like to thank the National Science Foundation, IBM, California Cedar Products Co., and the authors' industrial sponsors for their support and interest in this work.

References

Andres, L. A. San, and Vance, J. M., 1986, "Effects of Fluid Inertia and Turbulence on the Force Coefficients for Squeeze Film Dampers," ASME *Journal of Engineering for Gas Turbine and Power,* Vol. 108, pp. 332–339.

Caulk, D. A., and Naghdi, P. M., 1987, "Axisymmetric Motion of a Viscous Fluid Inside a Slender Surface of Revolution," ASME JOURNAL OF APPLIED MECHANICS, Vol. 109, pp. 190–196.

Chen, S. H., and Mote, C. D., Jr., 1994, "On the Parallel Hybrid Guide Bearings under Combined Sliding and Small Amplitude Vibration," ASME *Journal of Tribology,* Vol. 116, pp. 127–132.

Cosserat, E., and Cosserat, F., 1909, *Théorie des Corps Déformables,* A. Hermann et Fils, Paris.

Ericksen, J. L., and Truesdell, C., 1958, "Exact Theory of Stress and Strain in Rods and Shells," *Archive for Rational Mechanics and Analysis,* Vol. 1, pp. 295–323.

Green, A. E., and Naghdi, P. M., 1974, "On the Derivation of Shell Theories by Direct Approach," ASME JOURNAL OF APPLIED MECHANICS, Vol. 41, pp. 173–176.

Green, A. E., and Naghdi, P. M., 1984, "A Direct Theory of Viscous Fluid Flow in Channels," *Archive for Rational Mechanics and Analysis,* Vol. 86, pp. 39–63.

Green, A. E., Naghdi, P. M., and Stallard, M. J., 1993, "A Direct Theory of Viscous Fluid Flow in Pipes. II. Flow of Incompressible Viscous Fluid in Curved Pipes," *Proceeding of the Royal Society of London,* Vol. A342, pp. 543–572.

Green, A. E., Naghdi, P. M., and Wainwright, W. L., 1965, "A General Theory of Cosserat Surface," *Archive for Rational Mechanics and Analysis,* Vol. 20, pp. 287–308.

Huang, F. Y., and Mote, C. D., Jr., 1995, "On the Translating Damping Caused by a Thin Viscous Fluid Layer Between a Translating String and a Translating Rigid Surface," *Journal of Sound and Vibration,* Vol. 181, No. 2, pp. 251–260.

Huang, F. Y., and Mote, C. D., Jr., 1996a, "Mathematical Prediction of Stability of a Spinning Disk Under a Rotating, Arbitrarily Large Damping Force," ASME *Journal of Vibration and Acoustics,* in press.

Huang, F. Y., and Mote, C. D., Jr., 1996b, "Controlling Rotating Disk Vibration at All Speeds with a Fixed-Rotating-Dashpot," ASME JOURNAL OF APPLIED MECHANICS, submitted for publication.

Ingard, K. U., and Akay, A., 1987, "On the Vibration Damping of a Plate by Means of a Viscous Fluid Layer," ASME *Journal of Vibration, Acoustics, Stress, and Reliability in Design,* Vol. 109, pp. 178–184.

Maidanik, G., 1966, "Energy Dissipation Associated with Gas-Pumping in Structure Joints," *Journal of the Acoustic Society of America,* Vol. 40, No. 5, pp. 1064–1072.

Murray, Y. D., and Mote, C. D., Jr., 1983, "Analysis of a Plane Inclined Guide Bearing Under Transverse Vibration and Translation of a Plate," ASME *Journal of Lubrication Technology,* Vol. 105, pp. 335–341.

Naghdi, P. M., 1979, "Fluid Jets and Fluid Sheets: A Direct Formulation," *Proceeding of 12th Symposium on Naval Hydrodynamics,* pp. 500–515.

Naghdi, P. M., and Rubin, M. B., 1981, "On Inviscid Flow in a Waterfall," *Journal of Fluid Mechanics,* Vol. 103, pp. 375–387.

Pinkus, O., and Sternlicht, B., 1961, *Theory of Hydrodynamic Lubrication,* McGraw-Hill, New York, pp. 360–365.

Reynolds, O., 1886, "On the Theory of Lubrication and Its Application to Mr. Beauchamp Tower's Experiments, Including an Experimental Determination of the Viscosity of Olive Oil," *Proceeding of the Royal Society of London,* Vol. A177, pp. 157–234.

Tan, C. A., and Mote, C. D., Jr., 1990, "Analysis of a Hydrodynamic Bearing Under Transverse Vibration of an Axially Moving Band," ASME *Journal of Tribology,* Vol. 112, pp. 514–523.

Tichy, J. A., and Modest, M. F., 1978, "Squeeze Film Flow Between Arbitrary Two-Dimensional Surfaces Subject to Normal Oscillations," ASME *Journal of Lubrication Technology,* Vol. 100, pp. 316–322.

Tichy, J. A., and Winer, W. O., 1970, "Inertial Considerations in Parallel Circular Squeeze Film Bearings," ASME *Journal of Lubrication Technology,* Vol. 92, pp. 588–592.

Walowit, J. A., and Anno, J. N., 1975, *Modern Developments in Lubrication Mechanics,* John Wiley and Sons, New York, pp. 12–59.

Downloaded 04 May 2010 to 171.66.16.33. Redistribution subject to ASME license or copyright; see http://www.asme.org/terms/Terms_Use.cfm

Sen Yung Lee[1]
Professor,
Mechanical Engineering Department,
National Cheng Kung University,
Tainan, Taiwan 701, Republic of China

Shueei Muh Lin
Associate Professor,
Mechanical Engineering Department,
Kung Shan Institute of Technology,
Tainan, Taiwan 710, Republic of China

Dynamic Analysis of Nonuniform Beams With Time-Dependent Elastic Boundary Conditions

The dynamic response of a nonuniform beam with time-dependent elastic boundary conditions is studied by generalizing the method of Mindlin-Goodman and utilizing the exact solutions of general elastically restrained nonuniform beams given by Lee and Kuo. The time-dependent elastic boundary conditions for the beam are formulated. A general form of change of dependent variable is introduced and the shifting polynomials of the third-order degree, instead of the fifth-order degree polynomials taken by Mindlin-Goodman, are selected. The physical meaning of these shifting polynomial functions are explored. Finally, the limiting cases are discussed and several examples are given to illustrate the analysis.

1. Introduction

The transverse vibration of a uniform beam subjected to time-dependent boundary conditions happens in many structural fields and has been studied by many authors (Nothmann, 1948; Mindlin and Goodman, 1950; Herrmann, 1955; Berry and Nagdhi, 1956; Yen and Kao, 1959; Edstrom, 1981; Grant, 1983; Gou and Karim-Panahi, 1988). However, in many structural applications, nonuniform beams are widely used in order to optimize the distribution of weight and strength and sometimes to satisfy special architectural and functional requirements. Therefore, the analysis of nonuniform beams with time-dependent boundary conditions is important to many engineers.

The vibration of a uniform Bernoulli-Euler beam with classical time-dependent boundary conditions can be solved by using the method of Laplace transform (Nothmann, 1948; Yen and Kao, 1959) and the method of Mindlin-Goodman (Mindlin and Goodman, 1950; Grant, 1988). In the Mindlin-Goodman method, a procedure of change of dependent variable together with four shifting polynomials of fifth degree are introduced. By properly selecting these shifting polynomial functions, the nonhomogeneous boundary conditions are transformed into homogeneous ones. Consequently, the method of separation of variables was used to solve the problem. Edstrom (1981) pointed out that if a properly chosen change of dependent variable is made, a homogeneous linear partial differential equation will remain homogeneous as well as have homogeneous boundary conditions and nonhomogeneous initial conditions. However, Edstrom's method is not suitable for the system subjected to transverse forces. For the uniform Timoshenko beams, the vibration of beams with classical time-dependent boundary conditions was solved by the integral solution method (Herrmann, 1955).

From the existing literature, it can be found that all the previous investigations are restricted to the uniform beams with classical time-dependent boundary conditions. There still is no study on the vibrational analysis of nonuniform beams with time-dependent boundary conditions, especially with time-dependent elastic boundary conditions.

In this paper, we study the transverse vibration of a nonuniform Bernoulli-Euler beam with time-dependent general elastic boundary conditions. The time-dependent elastic boundary conditions for the nonuniform beam are formulated. We generalize the method of Mindlin-Goodman (1950) and utilize the exact solutions of general elastically restrained nonuniform beams given by Lee and Kuo (1992) to study the dynamic response of a nonuniform beam. A general form of change of dependent variable is introduced and the shifting polynomial functions of third degree, instead of polynomial functions of fifth degree taken by Mindlin-Goodman (1950), are selected. These shifting polynomial functions can be used to cover the very general cases and are shown to take physical meanings. Finally, the limiting cases of the general system are examined and several examples are given to illustrate the analysis.

2 System With Time-Dependent Elastic Boundary Conditions

Consider a nonuniform Bernoulli-Euler beam with time-dependent elastic boundary conditions, as shown in Fig. 1. In terms of the following nondimensional quantities,

$$\tau = \frac{t}{L^2}\sqrt{\frac{E(0)I(0)}{\rho(0)A(0)}}, \quad \xi = \frac{x}{L}, \quad m(\xi) = \frac{\rho(x)A(x)}{\rho(0)A(0)},$$

$$w(\xi, \tau) = \frac{W(x, t)}{L}, \quad p(\xi, \tau) = \frac{P(x, t)L^3}{E(0)I(0)},$$

$$b(\xi) = \frac{E(x)I(x)}{E(0)I(0)}, \quad f_1(\tau) = F_1(t), \quad f_2(\tau) = \frac{F_2(t)}{L},$$

$$f_3(\tau) = F_3(t), \quad f_4(\tau) = \frac{F_4(t)}{L}, \quad f_1^*(\tau) = \frac{F_1^*(t)L}{E(0)I(0)},$$

$$f_2^*(\tau) = \frac{F_2^*(t)L^2}{E(0)I(0)}, \quad f_3^*(\tau) = \frac{F_3^*(t)L}{E(0)I(0)},$$

$$f_4^*(\tau) = \frac{F_4^*(t)L^2}{E(0)I(0)}, \quad \beta_1 = \frac{K_{\theta L}L}{E(0)I(0)}, \quad \beta_2 = \frac{K_{TL}L^3}{E(0)I(0)},$$

$$\beta_3 = \frac{K_{\theta R}L}{E(0)I(0)}, \quad \beta_4 = \frac{K_{TR}L^3}{E(0)I(0)}, \tag{1}$$

[1] To whom all correspondence should be addressed.

Contributed by the Applied Mechanics Division of THE AMERICAN SOCIETY OF MECHANICAL ENGINEERS for publication in the ASME JOURNAL OF APPLIED MECHANICS.

Discussion on this paper should be addressed to the Technical Editor, Professor Lewis T. Wheeler, Department of Mechanical Engineering, University of Houston, Houston, TX 77204-4792, and will be accepted until four months after final publication of the paper itself in the ASME JOURNAL OF APPLIED MECHANICS.

Manuscript received by the ASME Applied Mechanics Division, Sept. 12, 1994; final revision, Mar. 22, 1995. Associate Technical Editor: J. N. Reddy.

Copyright © 1996 by ASME

Downloaded 04 May 2010 to 171.66.16.33. Redistribution subject to ASME license or copyright; see http://www.asme.org/terms/Terms_Use.cfm

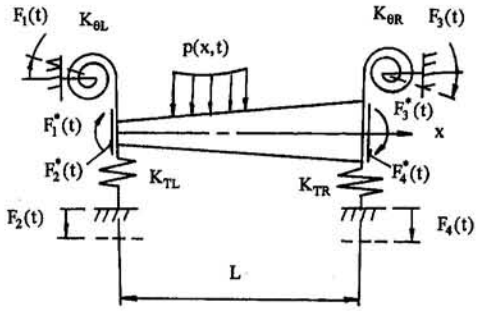


Fig. 1 Geometry and coordinate system of a nonuniform beam with time-dependent elastic boundary conditions, subjected to transverse forces

the governing differential equation of the system is

$$\frac{\partial^2}{\partial \xi^2}\left[b(\xi)\frac{\partial^2 w(\xi,\tau)}{\partial \xi^2}\right] + m(\xi)\frac{\partial^2 w(\xi,\tau)}{\partial \tau^2} = p(\xi,\tau), \quad (2)$$

the associated boundary conditions are
at $\xi = 0$:

$$\frac{\partial^2 w(\xi,\tau)}{\partial \xi^2} - \beta_1 \frac{\partial w(\xi,\tau)}{\partial \xi} = -\beta_1 f_1(\tau) - f_1^*(\tau), \quad (3)$$

$$\frac{\partial}{\partial \xi}\left(b(\xi)\frac{\partial^2 w(\xi,\tau)}{\partial \xi^2}\right) + \beta_2 w(\xi,\tau) = \beta_2 f_2(\tau) + f_2^*(\tau), \quad (4)$$

at $\xi = 1$:

$$b(\xi)\frac{\partial^2 w(\xi,\tau)}{\partial \xi^2} + \beta_3 \frac{\partial w(\xi,\tau)}{\partial \xi} = \beta_3 f_3(\tau) + f_3^*(\tau), \quad (5)$$

$$\frac{\partial}{\partial \xi}\left(b(\xi)\frac{\partial^2 w(\xi,\tau)}{\partial \xi^2}\right) - \beta_4 w(\xi,\tau) = -\beta_4 f_4(\tau) - f_4^*(\tau), \quad (6)$$

and the nondimensional initial conditions of the motions are specified by two arbitrary functions

$$w(\xi, 0) = w_0(\xi), \quad (7)$$

$$\partial w(\xi, 0)/\partial \tau = \dot{w}_0(\xi). \quad (8)$$

Here $W(x, t)$ is the flexural displacement, x is the coordinate along the beam, t is time, and L is the beam length. $E(x)$, $I(x)$, and $A(x)$ denote the Young's modulus, the area moment of inertia, and the cross-sectional area, respectively. $\rho(x)$ is the mass density per unit volume and $P(x, t)$ is the applied transverse force per unit length. $F_1(t)$, $F_2(t)$, $F_1^*(t)$, and $F_2^*(t)$ and $F_3(t)$, $F_4(t)$, $F_3^*(t)$, and $F_4^*(t)$ are the slope of the base, the displacement of the base, the external moment, and the shear force excitations at the left end and the right end of the beam, respectively. K_{TL} and $K_{\theta L}$ and K_{TR} and $K_{\theta R}$ are the translational spring constants and the rotational spring constants at the left end and the right end of the beam, respectively.

When the translational spring constant is infinity or zero, the time-dependent displacement or the time-dependent shear force is prescribed. If the rotational spring constant is infinity or zero, then the time-dependent slope or the time dependent moment is prescribed.

3 Solution Method

3.1 Change of Variable. To find the solution for this nonhomogeneous fourth-order differential equation with variable coefficients and nonhomogeneous elastic boundary conditions, one generalizes the method developed by Mindlin and Goodman (1950) by taking

$$w(\xi, \tau) = v(\xi, \tau) + \sum_{i=1}^{4} \bar{f}_i(\tau) g_i(\xi), \quad (9)$$

where

$$\bar{f}_i(\tau) = \frac{\beta_i}{1+\beta_i} f_i(\tau) + \frac{1}{1+\beta_i} f_i^*(\tau), \quad i = 1, 2, 3, 4, \quad (10)$$

and g_i, $i = 1, 2, 3, 4$ are the shifting functions and chosen to satisfy the following conditions:

$$\left(\frac{\beta_1}{1+\beta_1}\frac{dg_i}{d\xi} - \frac{1}{1+\beta_1}\frac{d^2 g_i}{d\xi^2}\right)\Bigg|_{\xi=0} = \delta_{ij}, \quad j = 1 \quad (11)$$

$$\left(\frac{\beta_2}{1+\beta_2} g_i + \frac{1}{1+\beta_2}\frac{d}{d\xi}\left[b(\xi)\frac{d^2 g_i}{d\xi^2}\right]\right)\Bigg|_{\xi=0} = \delta_{ij}, \quad j = 2 \quad (12)$$

$$\left(\frac{\beta_3}{1+\beta_3}\frac{dg_i}{d\xi} + \frac{b(\xi)}{1+\beta_3}\frac{d^2 g_i}{d\xi^2}\right)\Bigg|_{\xi=1} = \delta_{ij}, \quad j = 3 \quad (13)$$

$$\left(\frac{\beta_4}{1+\beta_4} g_i - \frac{1}{1+\beta_4}\frac{d}{d\xi}\left[b(\xi)\frac{d^2 g_i}{d\xi^2}\right]\right)\Bigg|_{\xi=1} = \delta_{ij}, \quad j = 4 \quad (14)$$

where δ_{ij} is a Kronecker symbol. After substituting Eqs. (9)–(14) into the Eqs. (2)–(8), one has a differential equation for $v(\xi, \tau)$

$$\frac{\partial^2}{\partial \xi^2}\left[b(\xi)\frac{\partial^2 v(\xi,\tau)}{\partial \xi^2}\right] + m(\xi)\frac{\partial^2 v(\xi,\tau)}{\partial \tau^2} = p(\xi,\tau) - \sum_{i=1}^{4}\left\{\bar{f}_i(\tau)\left[\frac{d^2}{d\xi^2}\left(b(\xi)\frac{d^2 g_i(\xi)}{d\xi^2}\right)\right] + m(\xi) g_i(\xi)\frac{d^2 \bar{f}_i(\tau)}{d\tau^2}\right\} \quad (15)$$

and the associated homogeneous boundary conditions:
at $\xi = 0$:

$$\frac{\partial^2 v(\xi,\tau)}{\partial \xi^2} - \beta_1 \frac{\partial v(\xi,\tau)}{\partial \xi} = 0, \quad (16)$$

$$\frac{\partial}{\partial \xi}\left(b(\xi)\frac{\partial^2 v(\xi,\tau)}{\partial \xi^2}\right) + \beta_2 v(\xi,\tau) = 0, \quad (17)$$

at $\xi = 1$:

$$b(\xi)\frac{\partial^2 v(\xi,\tau)}{\partial \xi^2} + \beta_3 \frac{\partial v(\xi,\tau)}{\partial \xi} = 0, \quad (18)$$

$$\frac{\partial}{\partial \xi}\left(b(\xi)\frac{\partial^2 v(\xi,\tau)}{\partial \xi^2}\right) - \beta_4 v(\xi,\tau) = 0. \quad (19)$$

The initial conditions, Eqs. (7)–(8), become

$$v(\xi, 0) = w_0(\xi) - \sum_{i=1}^{4} \bar{f}_i(0) g_i(\xi) \quad (20)$$

$$\frac{\partial v(\xi, 0)}{\partial \tau} = \dot{w}_0(\xi) - \sum_{i=1}^{4} \frac{d\bar{f}_i(0)}{d\tau} g_i(\xi). \quad (21)$$

Downloaded 04 May 2010 to 171.66.16.33. Redistribution subject to ASME license or copyright; see http://www.asme.org/terms/Terms_Use.cfm

As a result, function $v(\xi, \tau)$ is governed by a fourth-order differential equation in space (15) and satisfies the homogeneous elastic boundary conditions Eqs. (16)–(19) and the initial conditions (20)–(21). It takes the meaning of the forced dynamic response of an elastically restrained nonuniform beam and can be obtained through utilizing the results given by Lee and Kuo (1992) and Lee, Ke, and Kuo (1990). They developed a solution theory for the static and dynamic response of a nonuniform beam and expressed the solution in term of the fundamental solutions of the governing characteristic differential equation. It was shown that if the coefficients of the differential equation are in polynomial forms, then the closed-form fundamental solutions can be obtained. Consequently, the closed-form solution for the system is obtained (Lee and Kuo, 1992). If the closed-form fundamental solutions are not available, then approximate fundamental solutions can be obtained through a simple and efficient numerical method (Lee, Ke and Kuo, 1990).

It should be mentioned that if β_1 and β_2 are set to be infinity, $\beta_3 = 0$ and $\beta_4 = 0$, then Eqs. (9)–(21) yield to those given by Mindlin and Goodman (1950).

3.2 Shifting Functions and Their Physical Meanings. To find the shifting functions g_i, $i = 1, 2, 3, 4$ that satisfy the Eqs. (11)–(14), one lets the shifting functions be polynomials of the third degree in ξ

$$g_i = \alpha_{i,0} + \alpha_{i,1}\xi + \alpha_{i,2}\xi^2 + \alpha_{i,3}\xi^3, \quad i = 1, 2, 3, 4 \quad (22)$$

where $\alpha_{i,0}$, $\alpha_{i,1}$, $\alpha_{i,2}$ and $\alpha_{i,3}$ are constants to be determined. After substituting each of the g_i into the appropriate equations of Eqs. (11)–(14), the constants $\alpha_{i,0}$, $\alpha_{i,1}$, $\alpha_{i,2}$, and $\alpha_{i,3}$ for the general case are obtained:

$$\alpha_{1,0} = \gamma_{22}\{\gamma_{31}[6A_3 - 2b'(0)A_4] + \gamma_{41}[2b'(0)A_2 - 6A_1]\}/G,$$

$$\alpha_{1,1} = \{\gamma_{21}(A_2A_3 - A_1A_4) - \gamma_{41}\gamma_{22}[2b'(0)A_2 - 6A_1]\}/G,$$

$$\alpha_{1,2} = [\gamma_{21}(\gamma_{31}A_4 - \gamma_{41}A_2) - 6\gamma_{41}\gamma_{22}\gamma_{31}]/G,$$

$$\alpha_{1,3} = [2\gamma_{41}\gamma_{22}\gamma_{31}b'(0) - \gamma_{21}(\gamma_{31}A_3 - \gamma_{41}A_1)]/G; \quad (23)$$

$$\alpha_{2,0} = [\gamma_{11}(A_2A_3 - A_1A_4) + 2\gamma_{12}(\gamma_{41}A_2 - \gamma_{31}A_4)]/G,$$

$$\alpha_{2,1} = -2\gamma_{41}\gamma_{12}A_2/G, \quad \alpha_{2,2} = -\gamma_{41}\gamma_{11}A_2/G$$

$$\alpha_{2,3} = \gamma_{41}(\gamma_{11}A_1 + 2\gamma_{12}\gamma_{31})/G; \quad (24)$$

$$\alpha_{3,0} = \gamma_{22}\{\gamma_{11}[2b'(0)A_4 - 6A_3] - 12\gamma_{41}\gamma_{12}\}/G,$$

$$\alpha_{3,1} = \gamma_{12}[12\gamma_{41}\gamma_{22} - 2A_4\gamma_{21}]/G,$$

$$\alpha_{3,2} = \gamma_{11}(6\gamma_{41}\gamma_{22} - \gamma_{21}A_4)/G,$$

$$\alpha_{3,3} = [\gamma_{21}(\gamma_{11}A_3 + 2\gamma_{12}\gamma_{41}) - 2\gamma_{41}\gamma_{11}\gamma_{22}b'(0)]/G; \quad (25)$$

$$\alpha_{4,0} = \gamma_{22}\{12\gamma_{31}\gamma_{12} - \gamma_{11}[2b'(0)A_2 - 6A_1]\}/G,$$

$$\alpha_{4,1} = 2\gamma_{21}\gamma_{12}A_2/G, \quad \alpha_{4,2} = \gamma_{21}\gamma_{11}A_2/G,$$

$$\alpha_{4,3} = -\gamma_{21}(\gamma_{11}A_1 + 2\gamma_{12}\gamma_{31})/G, \quad (26)$$

where

$$G = -\gamma_{41}[2\gamma_{11}\gamma_{22}b'(0)A_2 - 12\gamma_{12}\gamma_{22}\gamma_{31} - 6\gamma_{11}\gamma_{22}A_1] - \gamma_{21}[\gamma_{11}A_1A_4 - 2\gamma_{12}\gamma_{41}A_2 - \gamma_{11}A_2A_3 + 2\gamma_{12}\gamma_{31}A_4],$$

$$A_1 = 2[\gamma_{31} + \gamma_{32}b(1)], \quad A_2 = 3\gamma_{31} + 6\gamma_{32}b(1),$$

$$A_3 = \gamma_{41} - 2\gamma_{42}b'(1), \quad A_4 = \gamma_{41} - 6\gamma_{42}[b(1) + b'(1)],$$

$$\gamma_{i1} = \frac{\beta_i}{1 + \beta_i}, \quad \gamma_{i2} = \frac{1}{1 + \beta_i}. \quad i = 1, 2, 3, 4. \quad (27)$$

The shifting functions g_i for the limiting cases can be obtained from Eqs. (22)–(27) by taking the appropriate limiting procedures and those for the four typical limiting cases of the general system are listed in the Appendix.

Since the shifting functions g_i in the form of Eq. (22) are the general solution of the differential equation

$$\frac{d^4 g_i}{d\xi^4} = 0, \quad (28)$$

and satisfy the appropriate boundary conditions (11)–(14), hence the shifting functions g_i, $i = 1, 2, 3, 4$ can be interpreted as the nondimensional static deflection of a generally elastically restrained uniform beam subjected to a unit nondimensional moment and a unit nondimensional slope of the base at the left end, a unit nondimensional shear force and a unit nondimensional displacement of the base at the left end, a unit nondimensional moment and a unit nondimensional slope of the base at the right end and a unit shear force and a unit nondimensional displacement of the base at the right end of the beam, respectively.

When the nondimensional translational and rotational spring constants β_i, $i = 1, 2, 3, 4$ are infinity, the uniform beam is clamped at both ends. Under this case, the shifting functions g_i, $i = 1, 2, 3, 4$ represent the nondimensional static deflection of a clamped-clamped uniform beam due to a unit nondimensional slope of the base at the left end, a unit nondimensional displacement of the base at the left end, a unit nondimensional slope of the base at the right end and a unit nondimensional displacement of the base at the right end of the beam, respectively. These shifting functions g_i are given in case 3 of the Appendix and are the same as the static deflection curves given by Paz (1980).

It should be mentioned that the shifting functions g_i in the form of Eq. (22) are simpler than the shifting polynomial functions of fifth degree given by Mindlin and Goodman (1950). They can be used to cover the very general cases. In addition, these shifting functions take physical meanings.

4 Verification and Examples

To verify the previous analysis, two examples are illustrated.

Example 1: Consider the vibration of a clamped-hinged uniform beam subjected to a displacement time-dependent excitation $f_4 = 0.01\,\tau^2$ at the right end of the beam. For convenience, one takes the initial conditions as $w_0(\xi) = \dot{w}_0(\xi) = 0$ and the transverse force $p(\xi, \tau) = 0$. Therefore, $f_1 = f_2 = f_3 = f_1^* = f_2^* = f_3^* = f_4^* = \bar{f}_1 = \bar{f}_2 = \bar{f}_3 = 0$ *and* $\bar{f}_4 = f_4$. After following the solution methods given in Section 3 and the paper by Lee and Kuo (1992), the results are listed in Table 1. The numerical results in the rows with mark "*" are given by the

Table 1 The dynamic response of clamped-hinged uniform beam subjected to a displacement excitation at the right end $[f_1 = f_2 = f_3 = f_1^* = f_2^* = f_3^* = f_4^* = p(\xi,\tau) = 0, \bar{f}_4 = f_4 = 0.01\tau^2, w_0(\xi) = \dot{w}_0(\xi) = 0]$

τ		$\xi = 0.2$	$\xi = 0.4$	$\xi = 0.6$	$\xi = 0.8$	$\xi = 1.0$
1	*	0.0006	0.0020	0.0043	0.0070	0.0100
	**	0.0005	0.0020	0.0042	0.0070	0.0100
2	*	0.0022	0.0083	0.0173	0.0282	0.0400
	**	0.0022	0.0083	0.0173	0.0282	0.0400
3	*	0.0050	0.0187	0.0389	0.0634	0.0900
	**	0.0050	0.0187	0.0389	0.0633	0.0900
4	*	0.0090	0.0333	0.0691	0.1126	0.1600
	**	0.0090	0.0333	0.0691	0.1126	0.1600
5	*	0.0140	0.0520	0.1080	0.1760	0.2500
	**	0.0140	0.0520	0.1080	0.1760	0.2500

* present study
** by Grant (1983)

Downloaded 04 May 2010 to 171.66.16.33. Redistribution subject to ASME license or copyright; see http://www.asme.org/terms/Terms_Use.cfm

present analysis and those in the rows with mark "*" are given by Grant (1983). It can be found that both results are very consistent.

Example 2: Consider the vibration of a cantilever beam with constant width and linearly varied depth, subjected to a harmonic shear excitation at the right end of beam. The nondimensional material properties and applied transverse force are given as

$$b(\xi) = (1 + \lambda\xi)^3, \quad m(\xi) = 1 + \lambda\xi, \quad p(\xi, \tau) = 0. \quad (29)$$

The excitation functions are

$$f_1 = f_2 = f_3 = f_4 = f_1^* = f_2^* = f_3^* = \bar{f}_1 = \bar{f}_2 = \bar{f}_3 = 0,$$

$$\bar{f}_4 = f_4^* = \gamma_0 \sin(\omega\tau). \quad (30)$$

The associated shifting functions g_i, $i = 1, 2, 3, 4$ are those listed on case 4 of the Appendix.

Since the time-dependent boundary excitations on the beam are in harmonic forms, it is not necessary to use the Laplace transform and inverse Laplace transform while solving the steady-state solution of the transfer-dependent variable $v(\xi, \tau)$ in Eq. (15) and the homogeneous boundary conditions Eqs. (16)–(19). The transfer-dependent variable $v(\xi, \tau)$ can be assumed to take the form

$$v(\xi, \tau) = b^*(\xi) \sin(\omega\tau), \quad (31)$$

where the coefficient $b^*(\xi)$ is to be specified. Substituting $v(\xi, \tau)$ into Eq. (15) and the boundary conditions Eqs. (16)–(19), one requires $b^*(\xi)$ to satisfy the following nonhomogeneous differential equation and the boundary homogeneous conditions:

$$\frac{d^2}{d\xi^2}\left[b(\xi)\frac{d^2b^*(\xi)}{d\xi^2}\right] - \omega^2 m(\xi) b^*(\xi)$$

$$= \gamma_0\left\{\omega^2 m(\xi) g_4(\xi) - \frac{d^2}{d\xi^2}\left[b(\xi)\frac{d^2 g_4(\xi)}{d\xi^2}\right]\right\}, \quad (32)$$

at $\xi = 0$:

$$\frac{db^*(\xi)}{d\xi} = 0, \quad (33)$$

$$b^*(\xi) = 0, \quad (34)$$

at $\xi = 1$:

$$\frac{d^2b^*(\xi)}{d\xi^2} = 0, \quad (35)$$

$$\frac{d}{d\xi}\left(b(\xi)\frac{d^2b^*(\xi)}{d\xi^2}\right) = 0. \quad (36)$$

Having found this $b^*(\xi)$ by utilizing the results given by Lee and Kuo (1992), one has

$$w(\xi, \tau) = [b^*(\xi) + \gamma_0 g_4(\xi)] \sin \omega\tau. \quad (37)$$

In Figure 2, the vibrational response curve at the tip of the beam is illustrated. It shows that when the shear excitation frequencies approach the natural frequencies of the beam, the response increases rapidly and becomes infinite as the shear excitation frequencies coincide with the natural frequencies.

Finally, it should be mentioned here that the present analysis can also be applied to study the static deflection of a nonuniform beam subjected to nonhomogeneous boundary conditions. Especially for the static deflection of a uniform beam with nonhomogeneous boundary conditions and subjected to no transverse force, instead of assuming the nondimensional displacement in the form of Eq. (9), it can be simply assumed as

$$w(\xi) = \sum_{i=1}^{4} f_i g_i(\xi) \quad (38)$$

where functions g_i, $i = 1, 2, 3, 4$ are the same as the shifting functions studied before. It is due to the fact that the transfer-dependent variable $v(\xi)$ will satisfy a homogeneous differential equation with homogeneous boundary conditions and is identically equal to zero.

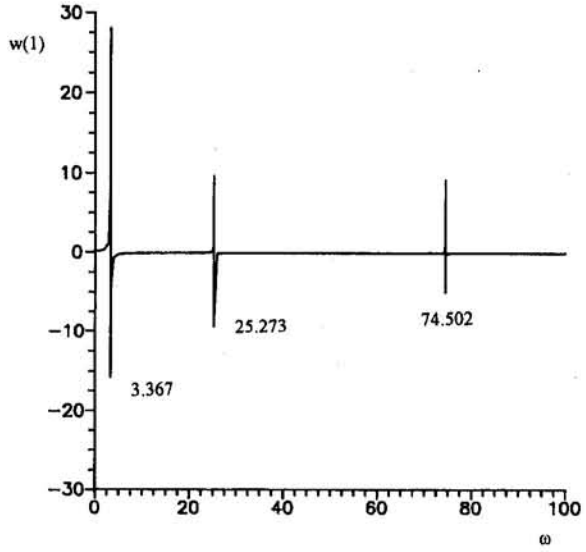


Fig. 2 The amplitudes of steady response at the right end of the cantilever nonuniform beam subjected to a harmonic shear excitation. [$p(\xi, \tau) = 0$, $b = (1 + 0.5\xi)^3$, $m = (1 + 0.5\xi)$, $\gamma_0 = 1$]

5 Conclusion

In this paper, a systematic development for the analysis of the dynamic response of a nonuniform Bernoulli-Euler beam with time-dependent elastic boundary conditions, subjected to arbitrary transverse forces is presented. The time-dependent elastic boundary conditions for the beam is formulated. By generalizing the method of Mindlin-Goodman and utilizing the exact solutions of general elastically restrained nonuniform beams given by Lee and Kuo, the dynamic response of the beam is obtained. A general form of change of dependent variable is introduced and the physical meanings of the selected shifting polynomial functions of the third order degree are explored. These shifting polynomial functions can be used to cover the very general cases. The present analysis can also be applied to study the static deflection of a nonuniform beam subjected to nonhomogeneous boundary conditions.

Acknowledgment

The support of the National Science Council of Taiwan, R. O. C., is gratefully acknowledged (Grant number: NSC82-0401-E006-059).

References

Berry, J. G., and Nagdhi, P. M., 1956, "On the vibration of elastic bodies having time-dependent boundary conditions," *Quarterly of Applied Mathematics*, Vol. 14, pp. 43–50.

Edstrom, C. R., 1981, "The Vibrating Beam with Non-homogeneous Boundary Conditions," ASME JOURNAL OF APPLIED MECHANICS, Vol. 48, pp. 669–670.

Gou, P. F., and Karim-Panahi, K., 1988, "Beam with time dependent boundary conditions, closed form (series) solution versus response spectrum method," *Dynamics and Seismic Issues in Primary and Secondary Systems*, Presented at the ASME Pressure Vessels and Piping Conference, PVP V137, pp. 33–44.

Downloaded 04 May 2010 to 171.66.16.33. Redistribution subject to ASME license or copyright; see http://www.asme.org/terms/Terms_Use.cfm

Grant, D. A., 1983, "Beam vibrations with time-dependent boundary conditions," *Journal of Sound and Vibration,* Vol. 89, No. 4, pp. 519–522.

Herrmann, G., 1955, "Forced Motions of Timoshenko Beams," ASME JOURNAL OF APPLIED MECHANICS, Vol. 22, pp. 53–56.

Honig, G., and Hirdes, U., 1984, "A method for the numerical inversion of Laplace transforms," *Journal of Computational and Applied Mathematics,* Vol. 10, pp. 113–132.

Lee, S. Y., Ke, H. Y., and Kuo, Y. H., 1990, "Analysis of non-uniform beam vibration," *Journal of Sound and Vibration,* Vol. 142, No. 1, pp. 15–29.

Lee, S. Y., and Kuo, Y. H., 1992, "Exact Solutions for the Analysis of General Elastically Restrained Nonuniform Beams," ASME JOURNAL OF APPLIED MECHANICS, Vol. 59, pp. S205–S212.

Meirovitch, L., 1967, *Analytical Methods in Vibrations,* Macmillan, New York.

Mindlin, R. D., and Goodman, L. E., 1950, "Beam Vibrations With Time-Dependent Boundary Conditions," ASME JOURNAL OF APPLIED MECHANICS, Vol. 17, pp. 377–380.

Nothmann, G. A., 1948, "Vibration of a cantilever beam with prescribed end motion," ASME JOURNAL OF APPLIED MECHANICS, Vol. 15, pp. 327–334.

Paz, M., 1980, *Structural Dynamics: Theory and Computation.* V. Nostrand Co., pp. 232–234.

Yen, T. C., and Kao, S., 1959, "Vibration of Beam-Mass System With Time-Dependent Boundary Conditions," ASME JOURNAL OF APPLIED MECHANICS, Vol. 26, pp. 353–356.

APPENDIX

Shifting Functions For The Limiting Cases

Case 1: Hinged-Hinged. In this case, β_2 and β_4 are infinite and $\beta_1 = \beta_3 = 0$, the boundary excitations become

$$\bar{f}_1(\tau) = f_1^*(\tau), \quad \bar{f}_2(\tau) = f_2(\tau),$$

$$\bar{f}_3(\tau) = f_3^*(\tau), \quad \bar{f}_4(\tau) = f_4(\tau).$$

The shifting functions are

$$g_1 = \frac{1}{6}(2\xi - 3\xi^2 + \xi^3), \; g_2 = 1 - \xi,$$

$$g_3 = \frac{-1}{6b(1)}(\xi - \xi^3), \; g_4 = \xi.$$

Case 2: Clamped-Hinged. In this case, β_1, β_2, and β_4 are infinite and $\beta_3 = 0$, the boundary excitations become

$$\bar{f}_1(\tau) = f_1(\tau), \quad \bar{f}_2(\tau) = f_2(\tau),$$

$$\bar{f}_3(\tau) = f_3^*(\tau), \quad \bar{f}_4(\tau) = f_4(\tau).$$

The shifting functions are

$$g_1 = \xi - \frac{3}{2}\xi^2 + \frac{1}{2}\xi^3, \quad g_2 = 1 - \frac{3}{2}\xi^2 + \frac{1}{2}\xi^3,$$

$$g_3 = \frac{-1}{4b(1)}(\xi^2 - \xi^3), \quad g_4 = \frac{3}{2}\xi^2 - \frac{1}{2}\xi^3.$$

Case 3: Clamped-Clamped. In this case, β_1, β_2, β_3, and β_4 are infinite, the boundary excitations become

$$\bar{f}_1(\tau) = f_1(\tau), \quad \bar{f}_2(\tau) = f_2(\tau),$$

$$\bar{f}_3(\tau) = f_3(\tau), \quad \bar{f}_4(\tau) = f_4(\tau).$$

The shifting functions are

$$g_1 = \xi - 2\xi^2 + \xi^3, \quad g_2 = 1 - 3\xi^2 + 2\xi^3,$$

$$g_3 = -\xi^2 + \xi^3, \quad g_4 = 3\xi^2 - 2\xi^3.$$

Case 4: Clamped-Free. In this case, β_1 and β_2 are infinite and $\beta_3 = \beta_4 = 0$, the boundary excitations become

$$\bar{f}_1(\tau) = f_1(\tau), \quad \bar{f}_2(\tau) = f_2(\tau),$$

$$\bar{f}_3(\tau) = f_3^*(\tau), \quad \bar{f}_4(\tau) = f_4^*(\tau).$$

The shifting functions are

$$g_1 = \xi, \quad g_2 = 1,$$

$$g_3 = \frac{1}{6b^2(1)}\{3[b'(1) + b(1)]\xi^2 - b'(1)\xi^3\},$$

$$g_4 = \frac{1}{6b(1)}(3\xi^2 - \xi^3).$$

Downloaded 04 May 2010 to 171.66.16.33. Redistribution subject to ASME license or copyright; see http://www.asme.org/terms/Terms_Use.cfm

An Analysis of Cracking in a Layered Medium With a Functionally Graded Nonhomogeneous Interface

Hyung Jip Choi
Power Engineering Research Institute,
Korea Power Engineering Company, Inc.,
P. O. Box 631, Young-Dong,
Seoul 135-606, Korea

The plane elasticity solution is presented in this paper for the crack problem of a layered medium. A functionally graded interfacial region is assumed to exist as a distinct nonhomogeneous transitional layer with the exponentially varying elastic property between the dissimilar homogeneous surface layer and the substrate. The substrate is considered to be semi-infinite containing a crack perpendicular to the nominal interface. The stiffness matrix approach is employed as an efficient method of formulating the proposed crack problem. A Cauchy-type singular integral equation is then derived. The main results presented are the variations of stress intensity factors as functions of geometric and material parameters of the layered medium. Specifically, the influences of the crack size and location and the layer thickness are addressed for various material combinations.

1 Introduction

The idea of utilizing bonded materials or structures is in recent years gaining fundamental interest and technical importance from a wide range of modern engineering practices. One of the major advantages of such a layered medium can be attributed to the role of shielding the base material from the adverse thermal and chemical environments. Additional potential benefits possibly arise from the enhanced resistance to crack initiation or growth in the base material. The layered assembly, however, acts as one unit and transmits load through its constituents in a complicated manner, making the stress and failure analyses of such a multiphase composite medium rather involved.

Earlier works on this subject are commonly based on the discrete nature of piecewise homogeneous structures with ideally bonded interfaces across which the elastic moduli are discontinuous. As a result, for a crack located along the interface, the crack-tip behavior exhibits the complex power singularity, leading to the physical anomalies of crack surface interpenetration (England, 1965). On the other hand, when the crack is aligned perpendicular to the interface, the corresponding singular stress field is characterized by the nonsquare-root type as the crack edge intersects the interface (Zak and Williams, 1963). A consequence of this unusual behavior is that the standard techniques in linear elastic fracture mechanics are not applicable. The solutions to crack problems obtained on the basis of this ideal interface model are well documented, to name a few, by Hilton and Sih (1971), Cook and Erdogan (1972), Gupta (1973), and Noda et al. (1992). The interface models other than the above are those of distributed tensile and shear springs and a homogeneous continuum reported by Gecit and Erdogan (1978) and Kaw and Goree (1990).

An observation of the interdifussion character of the bonding process, however, indicated the existence of a distinct transitional phase with functionally graded properties in the close vicinity of the materials junction. The ideal interface was thus improved by replacing it with a thin nonhomogeneous layer having continuously varying properties (Atkinson, 1977). The related plane elasticity problem for a crack lying in the nonhomogeneous layer bounded by dissimilar homogeneous half-planes was considered by Delale and Erdogan (1988a). Further results for an interface crack located along the kink line of the elastic property distribution between homogeneous and nonhomogeneous half-planes were also given by Delale and Erdogan (1988b). In both cases, the crack-tip singularity was maintained to be the standard square-root type, provided the spatial variation of elastic moduli is continuous near and at the crack tips. More recently, a solution to the problem of an antiplane shear interface crack for a nonhomogeneous medium bonded to a rigid half-space was given by Erdogan and Ozturk (1992) and that for homogeneous half-spaces bonded through a nonhomogeneous interfacial zone was considered by Ozturk and Erdogan (1993).

For a crack perpendicular to and intersecting the interface of two bonded nonhomogeneous half-spaces, Erdogan (1985) examined the singular behavior of the crack-tip stress field under antiplane shear loading. A plane-strain problem where a cracked homogeneous half-plane is bonded to a nonhomogeneous half-plane was studied by Erdogan et al. (1991a) and Martin (1992), while the bonded dissimilar nonhomogeneous half-planes having the same crack geometry are due to Gao and Kuang (1992). Considered by Kaw et al. (1992) is an extension of a symmetric problem of a cracked strip bonded to half-planes previously solved by Gupta (1973), by incorporating the effect of a nonhomogeneous interface. In addition, the problem of mode III collinear cracks in bonded homogeneous half-planes with a nonhomogeneous interfacial zone was formulated by Erdogan et al. (1991b). These recent contributions and Schovanec and Walton (1988) have demonstrated in a rigorous fashion that, similar to the crack along the material interface, the square-root behavior of the stress singularity remains to be unaffected when the crack tip terminates at the kink line of the continuous shear modulus distribution, despite the discontinuity in the derivative of shear moduli.

The crack problems are very often not amenable to comprehensive analytical treatments, apart from a few idealized cases,

Contributed by the Applied Mechanics Division of THE AMERICAN SOCIETY OF MECHANICAL ENGINEERS for publication in the ASME JOURNAL OF APPLIED MECHANICS.

Discussion on this paper should be addressed to the Technical Editor, Professor Lewis T. Wheeler, Department of Mechanical Engineering, University of Houston, Houston, TX 77204-4792, and will be accepted until four months after final publication of the paper itself in the ASME JOURNAL OF APPLIED MECHANICS.

Manuscript received by the ASME Applied Mechanics Division, Oct. 20, 1994; final revision, June 26, 1995. Associate Technical Editor: G. J. Dvorak.

Copyright © 1996 by ASME

Downloaded 04 May 2010 to 171.66.16.33. Redistribution subject to ASME license or copyright; see http://www.asme.org/terms/Terms_Use.cfm

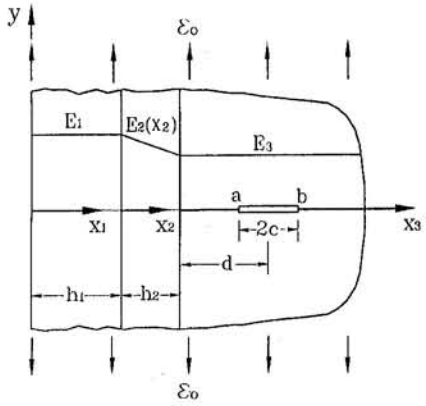


Fig. 1 Definition of the geometry, material properties, and loading condition for a layered medium containing a crack perpendicular to the interface

mainly due to the complexities and difficulties involved. This is especially true if interest is focused on examining the response of cracked media with bounded geometries, where the specific boundary conditions must be satisfied. In resolving the various crack problems with nonhomogeneous material interfaces, most of the previous studies in this category also appear to have apparently been limited to such simple configurations as having an infinite extent.

The objective of this paper is to investigate the fracture problem of a layered medium, composed of a surface layer and a semi-infinite substrate containing a crack normal to the boundary under the mode I loading. A distinct transitional phase is assumed to exist as the functionally graded interfacial region between the two dissimilar homogeneous constituents. Such a region is modeled as a nonhomogeneous layer with the elastic modulus varying continuously across its thickness. The stiffness matrix approach is employed as a viable alternative to efficiently overcome the algebraic difficulties involved in the analysis of a multiphase medium. This matrix approach was previously utilized for the static (Kausel and Seale, 1987; Choi and Thangjitham, 1991) and dynamic analyses (Wang and Rajapakse, 1994) of multilayered isotropic and anisotropic media. In particular, its versatility was demonstrated when dealing with more elaborate mixed boundary value problems of an interlaminar crack (Choi and Thangjitham, 1993, 1994) and a frictionless indentation (Urquhart and Pindera, 1994) for the multilayered anisotropic structures. The formulation of the current crack problem then results in having to solve a singular integral equation of the first kind with a Cauchy kernel. Particular attention is paid to the determination of stress intensity factors as important physical quantities in fracture mechanics. The effects of geometric and material parameters of the layered medium on the values of the stress intensity factors are addressed in conjunction with the nonhomogeneity in the interfacial layer.

2 Problem Statement and Formulation

The problem configuration considered in this paper is shown in Fig. 1, where a surface layer is bonded to a substrate through a functionally graded, nonhomogeneous interfacial layer. The surface and interfacial layers have the thicknesses h_1 and h_2, respectively, whereas the substrate is approximated to be semi-infinite containing a crack of length $2c = b - a$ perpendicular to its nominal interface. The surface layer, the interfacial layer, and the substrate are distinguished as constituent materials 1, 2, and 3, respectively. A far-field, uniform tensile strain ϵ_o is assumed to be applied in the direction normal to the crack surface.

The variable Young's modulus of the interfacial layer is represented as an exponential function such that (Erdogan et al., 1991a)

$$E_2(x) = E_o e^{\beta x} \tag{1}$$

where the continuous transition of elastic moduli throughout the medium via the interfacial layer, in the local coordinates $(x, y) = (x_k, y)$, $k = 1, 2, 3$, allows the constant E_o and the nonhomogeneity parameter β to be obtained as

$$E_o = E_1, \quad \beta = \frac{1}{h_2} \ln\left(\frac{E_3}{E_1}\right) \tag{2}$$

in which E_1 and E_3 are the Young's moduli of the materials 1 and 3, respectively. In addition, as a simplifying assumption, the Poisson's ratios are regarded to be constant as $\nu = \nu_k$, $k = 1, 2, 3$, which can be justified by the previous finding that neglecting the possible variation of the Poisson's ratios within a practical range is not a restrictive assumption (Delale and Erdogan, 1983).

2.1 Basic Equations and General Solutions. With $u_k(x, y)$ and $v_k(x, y)$, $k = 1, 2, 3$, denoting the displacement components in the x- and y-directions, respectively, the governing equations corresponding to (1) are written as

$$\nabla^2 u_k + \frac{2}{\kappa - 1}\left(\frac{\partial^2 u_k}{\partial x^2} + \frac{\partial^2 v_k}{\partial x \partial y}\right) + \frac{\beta}{\kappa - 1}\left[(1 + \kappa)\frac{\partial u_k}{\partial x} + (3 - \kappa)\frac{\partial v_k}{\partial y}\right] = 0 \tag{3a}$$

$$\nabla^2 v_k + \frac{2}{\kappa - 1}\left(\frac{\partial^2 u_k}{\partial x \partial y} + \frac{\partial^2 v_k}{\partial y^2}\right) + \beta\left(\frac{\partial u_k}{\partial y} + \frac{\partial v_k}{\partial x}\right) = 0; \quad k = 1, 2, 3 \tag{3b}$$

where the subscript k is the number referred to the constituent materials, $\kappa = (3 - 4\nu)$ for plane strain and $\kappa = (3 - \nu)/(1 + \nu)$ for plane stress, and $\beta \neq 0$ for $k = 2$ and $\beta = 0$ for $k = 1, 3$.

By the geometric and loading symmetry with respect to the cracked plane as well as by superposition, it suffices to consider the upper half of the medium $y \geq 0$ subjected to the equivalent crack surface traction $p_o = E_3\epsilon_o/(1 - \nu^2)$ for plane strain and $p_o = E_3\epsilon_o$ for plane stress, acting as the only nonzero external load, but opposite in sign. As a result, a set of homogeneous boundary and interface conditions relevant to the given problem is prescribed as

$$\sigma^-_{1xx} = 0, \quad \tau^-_{1xy} = 0; \quad 0 \leq y < \infty \tag{4a}$$

$$u_k^+ = u^-_{k+1}, \quad v_k^+ = v^-_{k+1}; \quad k = 1, 2, \quad 0 \leq y < \infty \tag{4b}$$

$$\sigma^+_{kxx} = \sigma^-_{(k+1)xx}, \quad \tau^+_{kxy} = \tau^-_{(k+1)xy}; \quad k = 1, 2, \quad 0 \leq y < \infty \tag{4c}$$

$$\tau_{kxy}(x_k, 0) = 0; \quad 0 \leq x_k \leq h_k, \quad k = 1, 2$$

$$\tau_{3xy}(x_3, 0) = 0; \quad 0 \leq x_3 < \infty \tag{4d}$$

$$u_3^+ = 0, \quad v_3^+ = 0; \quad \sqrt{x_3^2 + y_3^2} \to \infty \tag{4e}$$

where the superscripts $-$ and $+$ refer to the left and right-hand side surfaces of constituent materials and the mixed conditions by the presence of a crack along $y = 0$ can be written as

$$v_k(x_k, 0) = 0; \quad 0 \leq x_k \leq h_k, \quad k = 1, 2 \tag{5a}$$

$$v_3(x_3, 0) = 0; \quad 0 \leq x_3 \leq a, \quad b \leq x_3 < \infty \tag{5b}$$

$$\sigma_{3yy}(x_3, 0) = \sigma_o(x_3); \quad a \leq x_3 \leq b \tag{5c}$$

Downloaded 04 May 2010 to 171.66.16.33. Redistribution subject to ASME license or copyright; see http://www.asme.org/terms/Terms_Use.cfm

in which $\sigma_o(x_3)$ is an arbitrary function describing the crack surface traction.

Upon introducing an auxiliary function defined as

$$\phi(x_3) = \frac{\partial}{\partial x_3} v_3(x_3, 0); \quad 0 \le x_3 < \infty, \tag{6}$$

the conditions in (5) can now be replaced by a single homogeneous condition expressed in terms of the auxiliary function, under the single-valuedness of the displacement along the cracked plane

$$\phi(x_3) = 0; \quad 0 \le x_3 \le a, \quad b \le x_3 < \infty$$

$$\text{and} \quad \int_a^b \phi(x_3) dx_3 = 0. \tag{7a, b}$$

The general solutions of displacement components for the surface layer with $\beta = 0$ and $(x, y) = (x_1, y)$ are obtained by solving the governing equations in (3) using the Fourier integral transform technique

$$u_1 = -\frac{2}{\pi}\int_0^\infty \left[\left(A_1 + xB_1 - \frac{\kappa}{s}B_2\right)\sinh sx + \left(A_2 + xB_2 - \frac{\kappa}{s}B_1\right)\cosh sx\right]\cos syds \tag{8a}$$

$$v_1 = \frac{2}{\pi}\int_0^\infty [(A_1 + xB_1)\cosh sx + (A_2 + xB_2)\sinh sx]\sin syds;$$

$$0 \le x \le h_1, \quad y \ge 0 \tag{8b}$$

and those of stress components are obtained as

$$\sigma_{1xx} = -\frac{4\mu_1}{\pi}\int_0^\infty \left\{\left[s(A_1 + xB_1) - \left(\frac{1+\kappa}{2}\right)B_2\right]\cosh sx + \left[s(A_2 + xB_2) - \left(\frac{1+\kappa}{2}\right)B_1\right]\sinh sx\right\}\cos syds \tag{9a}$$

$$\sigma_{1yy} = \frac{4\mu_1}{\pi}\int_0^\infty \left\{\left[s(A_1 + xB_1) + \left(\frac{3-\kappa}{2}\right)B_2\right]\cosh sx + \left[s(A_2 + xB_2) + \left(\frac{3-\kappa}{2}\right)B_1\right]\sinh sx\right\}\cos syds \tag{9b}$$

$$\tau_{1xy} = \frac{4\mu_1}{\pi}\int_0^\infty \left\{\left[s(A_2 + xB_2) + \left(\frac{1-\kappa}{2}\right)B_1\right]\cosh sx + \left[s(A_1 + xB_1) + \left(\frac{1-\kappa}{2}\right)B_2\right]\sinh sx\right\}\sin syds;$$

$$0 \le x \le h_1, \quad y \ge 0 \tag{9c}$$

where $\mu_1 = E_1/2(1 + \nu)$, s is the transform variable, and $A_j(s)$, $B_j(s)$, $j = 1, 2$, are arbitrary unknowns to be evaluated.

For the interfacial layer which is nonhomogeneous with $\beta \neq 0$ and $(x, y) = (x_2, y)$, the general solutions of displacement and stress components are obtained as

$$u_2 = \frac{2}{\pi}\int_0^\infty \sum_{j=1}^4 m_j F_j e^{n_j x}\cos syds \tag{10a}$$

$$v_2 = \frac{2}{\pi}\int_0^\infty \sum_{j=1}^4 F_j e^{n_j x}\sin syds \tag{10b}$$

$$\sigma_{2xx} = \frac{2\mu_o e^{\beta x}}{\pi(\kappa - 1)}\int_0^\infty \sum_{j=1}^4 [(1 + \kappa)m_j n_j + s(3 - \kappa)]F_j e^{n_j x}\cos syds \tag{10c}$$

$$\sigma_{2yy} = \frac{2\mu_o e^{\beta x}}{\pi(\kappa - 1)}\int_0^\infty \sum_{j=1}^4 [s(1 + \kappa) + (3 - \kappa)m_j n_j]F_j e^{n_j x}\cos syds \tag{10d}$$

$$\tau_{2xy} = \frac{2\mu_o e^{\beta x}}{\pi}\int_0^\infty \sum_{j=1}^4 (n_j - sm_j)F_j e^{n_j x}\sin syds;$$

$$0 \le x \le h_2, \quad y \ge 0 \tag{10e}$$

where $\mu_o = E_o/2(1 + \nu)$, $F_j(s)$, $j = 1, \ldots, 4$, are arbitrary unknowns, $n_j(s)$, $j = 1, \ldots, 4$, are the roots of the characteristic equation

$$(n^2 + \beta n - s^2)^2 + \left(\frac{3-\kappa}{1+\kappa}\right)\beta^2 s^2 = 0 \tag{11}$$

from which the roots are obtained as

$$n_j = -\frac{1}{2}(\beta + \gamma\cos\theta) + (-1)^{j+1}\frac{i}{2}\gamma\sin\theta;$$

$$\mathrm{Re}(n_j) < 0, \quad j = 1, 2 \tag{12a}$$

$$n_j = -\frac{1}{2}(\beta - \gamma\cos\theta) + (-1)^{j+1}\frac{i}{2}\gamma\sin\theta;$$

$$\mathrm{Re}(n_j) > 0, \quad j = 3, 4 \tag{12b}$$

and $m_j(s)$, $j = 1, \ldots, 4$, are given as

$$m_j = \frac{(\kappa - 1)(n_j^2 + \beta n_j) - (\kappa + 1)s^2}{[2n_j + (\kappa - 1)\beta]s}; \quad j = 1, \ldots, 4 \tag{13}$$

in which $i = (-1)^{1/2}$ and $\theta(s)$, $\gamma(s)$ are expressed as

$$\theta = \frac{1}{2}\tan^{-1}\left(\frac{4\beta s}{\beta^2 + 4s^2}\sqrt{\frac{3-\kappa}{1+\kappa}}\right) \tag{14}$$

$$\gamma = \left[(\beta^2 + 4s^2)^2 + 16\beta^2 s^2\left(\frac{3-\kappa}{1+\kappa}\right)\right]^{1/4}. \tag{15}$$

For the substrate containing the crack with $\beta = 0$ and $(x, y) = (x_3, y)$, the general solutions of displacement and stress components satisfying the regularity conditions (4e) to provide the constraint against rigid-body displacements at infinity are obtained as

$$u_3 = \frac{2}{\pi}\int_0^\infty \left[H_1 + \left(x + \frac{\kappa}{s}\right)H_2\right]e^{-sx}\cos syds + \frac{1}{2\pi}\int_{-\infty}^\infty \left(\frac{1-\kappa}{2|s|} + y\right)H_3 e^{-|s|y - isx}ds \tag{16a}$$

$$v_3 = \frac{2}{\pi}\int_0^\infty (H_1 + xH_2)e^{-sx}\sin syds - \frac{i}{2\pi}\int_{-\infty}^\infty \frac{s}{|s|}\left(\frac{1+\kappa}{2|s|} + y\right)H_3 e^{-|s|y - isx}ds \tag{16b}$$

Downloaded 04 May 2010 to 171.66.16.33. Redistribution subject to ASME license or copyright; see http://www.asme.org/terms/Terms_Use.cfm

$$\sigma_{3xx} = -\frac{4\mu_3}{\pi}\int_0^\infty \left[s(H_1 + xH_2) + \left(\frac{1+\kappa}{2}\right)H_2 \right] e^{-sx} \times \cos syds - \frac{\mu_3 i}{\pi}\int_{-\infty}^{\infty} \left(sy - \frac{s}{|s|} \right) H_3 e^{-|s|y-isx} ds \quad (16c)$$

$$\sigma_{3yy} = \frac{4\mu_3}{\pi}\int_0^\infty \left[s(H_1 + xH_2) - \left(\frac{3-\kappa}{2}\right)H_2 \right] e^{-sx} \cos syds + \frac{\mu_3 i}{\pi}\int_{-\infty}^{\infty} \left(sy + \frac{s}{|s|} \right) H_3 e^{-|s|y-isx} ds \quad (16d)$$

$$\tau_{3xy} = \frac{4\mu_3}{\pi}\int_0^\infty \left[-s(H_1 + xH_2) + \left(\frac{1-\kappa}{2}\right)H_2 \right] e^{-sx} \sin syds - \frac{\mu_3}{\pi}\int_{-\infty}^{\infty} |s| yH_3 e^{-|s|y-isx} ds; \quad 0 \le x < \infty, \quad y \ge 0 \quad (16e)$$

where $\mu_3 = E_3/2(1+\nu)$, $H_j(s)$, $j = 1, 2$, are arbitrary unknowns and from (6), (7*a*), and (16*b*), the expression for $H_3(s)$ can be written as

$$H_3(s) = -\frac{2}{1+\kappa}\int_a^b \phi(r)e^{isr}dr. \quad (17)$$

It can be observed that the conditions (4*d*) and (5*a*) are identically satisfied by the general solutions as given above. Subsequent applications of the homogeneous boundary and interface conditions (4*a*)–(4*c*) result in a set of linear simultaneous equations to be solved for a total of ten unknowns, A_j, B_j, $j = 1, 2$, F_j, $j = 1, \ldots, 4$, and H_j, $j = 1, 2$. To circumvent the difficulties that may arise from directly applying such a complicated and lengthy algebraic manipulation, the stiffness matrix method is employed as an alternative procedure in efficiently formulating the current crack problem of a layered medium.

2.2 Application of the Stiffness Matrix Method. To utilize the stiffness matrix formulation for the layered medium, the following quantities are defined

$$\bar{\mathbf{d}}_k(x, s) = \{\bar{u}_k\ \bar{v}_k\}, \quad \bar{\boldsymbol{\sigma}}_k(x, s) = \{\bar{\sigma}_{kxx}\ \bar{\tau}_{kxy}\}; \quad k = 1, 2, 3 \quad (18a, b)$$

as vectors for the displacements and tractions, respectively, of the constituent materials in the Fourier transformed domain (x_k, s).

In terms of the arbitrary unknowns, the vectors containing the displacements $\bar{\mathbf{d}}_k^{\mp}(s)$ and tractions $\bar{\boldsymbol{\sigma}}_k^{\mp}(s)$ evaluated at the left- (−) and right-hand side (+) surfaces of each material can be written in matrix form. Upon eliminating the unknowns from these two matrix equations, the local stiffness matrix equations describing the relationship between the surface displacements and tractions in the Fourier domain can be established as

$$\left[\begin{array}{c|c} \mathbf{K}_{11}^{(k)} & \mathbf{K}_{12}^{(k)} \\ \hline \mathbf{K}_{21}^{(k)} & \mathbf{K}_{22}^{(k)} \end{array}\right] \left\{\begin{array}{c} \bar{\mathbf{d}}_k^- \\ \hline \bar{\mathbf{d}}_k^+ \end{array}\right\} = \left\{\begin{array}{c} \bar{\boldsymbol{\sigma}}_k^- \\ \hline -\bar{\boldsymbol{\sigma}}_k^+ \end{array}\right\}; \quad k = 1, 2 \quad (19a)$$

$$\mathbf{K}_{11}^{(3)}\,\bar{\mathbf{d}}_3^- - \mathbf{f}_o = \bar{\boldsymbol{\sigma}}_3^- \quad (19b)$$

where $\mathbf{K}_{lm}^{(k)}(s)$, $k, l, m = 1, 2$, are 2×2 submatrices of the 4×4 symmetric local stiffness matrices for the materials 1 and 2 and $\mathbf{K}_{11}^{(3)}(s)$ is a 2×2 symmetric local stiffness matrix for the material 3, which are functions of the Fourier transform variable, the elastic constants, and the geometry of the constituent materials.

In addition, the vector $\mathbf{f}_o(s) = \{f_{o1}\ f_{o2}\}$ in (19*b*) is written as

$$\left\{\begin{array}{c} f_{o1}(s) \\ f_{o2}(s) \end{array}\right\} = -\frac{\mu_3 s}{\kappa}\left[\begin{array}{cc} \kappa+1 & \kappa-1 \\ \kappa-1 & \kappa+1 \end{array}\right]\left\{\begin{array}{c} g_1 \\ g_2 \end{array}\right\} - 2\mu_3\left\{\begin{array}{c} g_3 \\ g_4 \end{array}\right\} \quad (20)$$

where $g_j(s)$, $j = 1, \ldots, 4$, are given by

$$g_1(s) = \frac{1}{\kappa+1}\int_a^b \left(\frac{\kappa-1}{2s} + r\right) e^{-sr}\phi(r)dr \quad (21a)$$

$$g_2(s) = \frac{1}{\kappa+1}\int_a^b \left(\frac{\kappa+1}{2s} - r\right) e^{-sr}\phi(r)dr - \frac{1}{2s}\int_a^b \phi(r)dr \quad (21b)$$

$$g_3(s) = \frac{1}{\kappa+1}\int_a^b sre^{-sr}\phi(r)dr \quad (21c)$$

$$g_4(s) = \frac{1}{\kappa+1}\int_a^b (1-sr)e^{-sr}\phi(r)dr \quad (21d)$$

in which the second term in $g_2(s)$ vanishes by the single-valuedness condition in (7*b*).

To be noted is that the imaginary part of the local stiffness matrix for the nonhomogeneous layer is a null matrix

$$\text{Im}\ \mathbf{K}_{lm}^{(2)}(s) = \mathbf{0} \quad (22)$$

and the following asymptotic behavior exists for the constituent materials as

$$\lim_{s\to\infty}\frac{1}{s}\mathbf{K}_{lm}^{(k)}(s) = \begin{cases} \mathbf{K}_{l\infty}^{(k)}; & l = m, \quad k = 1, 2, 3 \\ \mathbf{0}; & l \ne m, \quad k = 1, 2, 3 \end{cases} \quad (23)$$

where $\mathbf{K}_{l\infty}^{(k)}$, $k = 1, 2, 3$, are 2×2 symmetric submatrices containing limiting nonzero, real values.

By defining $\bar{\boldsymbol{\delta}}_1(s) \equiv \bar{\mathbf{d}}_1^-(s)$ and $\bar{\boldsymbol{\delta}}_{k+1}(s) \equiv \bar{\mathbf{d}}_k^+(s) = \bar{\mathbf{d}}_{k+1}^-(s)$, $k = 1, 2$, as vectors for the interfacial displacements common to the adjacent materials, a set of global stiffness matrix equations with the interfacial displacements as the basic unknown variables can be constructed by the assembly of local matrix equations in (19) through the successive applications of (4*a*)–(4*c*) such that

$$\mathbf{K}_{11}^{(1)}\bar{\boldsymbol{\delta}}_1 + \mathbf{K}_{12}^{(1)}\bar{\boldsymbol{\delta}}_2 = \mathbf{0} \quad (24a)$$

$$\mathbf{K}_{21}^{(1)}\bar{\boldsymbol{\delta}}_1 + (\mathbf{K}_{22}^{(1)} + \mathbf{K}_{11}^{(2)})\bar{\boldsymbol{\delta}}_2 + \mathbf{K}_{12}^{(2)}\bar{\boldsymbol{\delta}}_3 = \mathbf{0} \quad (24b)$$

$$\mathbf{K}_{21}^{(2)}\bar{\boldsymbol{\delta}}_2 + (\mathbf{K}_{22}^{(2)} + \mathbf{K}_{11}^{(3)})\bar{\boldsymbol{\delta}}_3 = \mathbf{f}_o. \quad (24c)$$

In matrix form, the above system of algebraic equations is expressed as

$$\mathbf{K}\bar{\boldsymbol{\delta}} = \mathbf{f} \quad (25)$$

where $\mathbf{K}(s)$ is a 6×6 symmetric global stiffness matrix, $\bar{\boldsymbol{\delta}}(s)$ is a global vector for the unknown interfacial displacements, i.e., $\{\bar{\boldsymbol{\delta}}_1\ \bar{\boldsymbol{\delta}}_2\ \bar{\boldsymbol{\delta}}_3\}$, and $\mathbf{f}(s)$ is a vector containing the auxiliary function ϕ and zero elements as $\{\mathbf{0}\ \mathbf{0}\ \mathbf{f}_o\}$. These vectors possess six units in length.

After solving the global matrix equations for the global interfacial displacement vector $\bar{\boldsymbol{\delta}}$, the expressions of the required unknowns A_j, B_j, $j = 1, 2$, F_j, $j = 1, \ldots, 4$, and H_j, $j = 1, 2$, for the general solutions of the elasticity problem can readily be obtained in terms of the resulting values of the local interfacial displacements $\bar{\boldsymbol{\delta}}_k = \bar{\mathbf{d}}_k^- = \{\bar{u}_k^-\ \bar{v}_k^-\}$, $k = 1, 2, 3$. The auxiliary function then becomes the only unknown that remains to be determined from the mixed boundary condition (5*c*).

Downloaded 04 May 2010 to 171.66.16.33. Redistribution subject to ASME license or copyright; see http://www.asme.org/terms/Terms_Use.cfm

2.3 Derivation of the Integral Equation. From Eqs. (16*d*) and (17), the traction component σ_{3yy} acting normal to $y = 0$ plane can be expressed as

$$\sigma_{3yy}(x, 0) = -\frac{2\mu_3 i}{\pi(1+\kappa)}\int_a^b \phi(r)dr\int_{-\infty}^{\infty}\text{sgn}\,(s)e^{is(r-x)}ds + \frac{4\mu_3}{\pi}\int_0^{\infty}\left[s(H_1 + xH_2) - \left(\frac{3-\kappa}{2}\right)H_2\right]e^{-sx}ds; \quad 0 \le x = x_3 < \infty \quad (26)$$

where sgn $(s) = 1$ for $s > 0$ and sgn $(s) = -1$ for $s < 0$.

The improper integral of the first term in the right-hand side of (26) can be evaluated by employing the Fourier representation of a generalized function (Friedman, 1969)

$$\int_{-\infty}^{\infty}\text{sgn}\,(s)e^{is(r-x)}ds = \frac{2i}{r-x} \quad (27)$$

and the expressions for the unknowns $H_j, j = 1, 2$, are obtained from the relationship between these unknowns and the local interfacial displacements $\bar{\boldsymbol{\delta}}_3 = \bar{\mathbf{d}}_3^- = \{\bar{u}_3^-\ \bar{v}_3^-\}$ such that

$$H_1(s) = \frac{\mu_3 s}{\kappa}\sum_{j=1}^{2}L_j g_j - 2\mu_3\sum_{j=3}^{4}F_{(j+2)6}g_j \quad (28a)$$

$$H_2(s) = \frac{\mu_3 s^2}{\kappa^2}\sum_{j=1}^{2}L_{j+2}g_j - \frac{2\mu_3 s}{\kappa}\sum_{j=3}^{4}(F_{5(j+2)} - F_{(j+2)6})g_j \quad (28b)$$

where $L_j(s), j = 1, \ldots, 4$, are written as

$$L_1(s) = -(1+\kappa)F_{56} + (1-\kappa)F_{66} \quad (29a)$$

$$L_2(s) = (1-\kappa)F_{56} - (1+\kappa)F_{66} - \frac{\kappa}{s\mu_3} \quad (29b)$$

$$L_3(s) = (1+\kappa)(F_{56} - F_{55}) + (1-\kappa)(F_{56} - F_{66}) - \frac{\kappa}{s\mu_3} \quad (29c)$$

$$L_4(s) = (1+\kappa)(F_{66} - F_{56}) + (1-\kappa)(F_{55} - F_{56}) + \frac{\kappa}{s\mu_3} \quad (29d)$$

and $F_{lm}(s), l, m = 1, \ldots, 6$, denote the elements of the global flexibility matrix, $\mathbf{F}(s) \equiv \mathbf{K}^{-1}(s)$.

The auxiliary function ϕ in (21) is the only unknown that is to be evaluated by applying the crack surface condition in (5*c*). Subsequently, substitution from (28) into (26) lends itself to a singular integral equation of the first kind for the auxiliary function:

$$\int_a^b \frac{\phi(r)}{r-x}dr + \int_a^b p(x, r)\phi(r)dr = \frac{\pi(1+\kappa)}{4\mu_3}\sigma_o(x); \quad a \le x \le b \quad (30)$$

where the kernel $p(x, r)$ is an improper integral such that

$$p(x, r) = -\mu_3\int_0^{\infty}\Lambda(s, x, r)e^{-s(r+x)}ds \quad (31)$$

in which $\Lambda(s, x, r)$ is written as

$$\Lambda(s, x, r) = \frac{1}{\kappa}\left(\frac{1-\kappa}{2s} - r\right)M_1(s, x) + \frac{1}{\kappa}\left(r - \frac{1+\kappa}{2s}\right)M_2(s, x) + 2srM_3(s, x) + 2(1-sr)M_4(s, x) \quad (32)$$

together with the expressions for $M_j(s, x), j = 1, \ldots, 4$, as

$$M_j(s, x) = s^2\left[L_j + \frac{1}{\kappa}\left(sx - \frac{3}{2} + \frac{\kappa}{2}\right)L_{j+2}\right]; \quad j = 1, 2 \quad (33a)$$

$$M_j(s, x) = s\left[F_{(j+2)6} + \frac{1}{\kappa}\left(sx - \frac{3}{2} + \frac{\kappa}{2}\right)(F_{5(j+2)} - F_{(j+2)6})\right]; \quad j = 3, 4. \quad (33b)$$

For the crack tips embedded within the material 3 such that $a > 0$, the integrand in (31) has the following asymptotic behavior as s approaches infinity;

$$\lim_{s\to\infty}\Lambda(s, x, r)e^{-s(r+x)} = 0; \quad a \le (x, r) \le b, \quad (34)$$

and the integral $p(x, r)$ is a Fredholm kernel which is bounded for all values of x and r in the closed interval $[a\ b]$. As a result, Eq. (30) is an ordinary singular integral equation having a simple Cauchy-type kernel $1/(r-x)$ as the dominant singular part (Muskhelishvili, 1953). When the crack tip extends up to the interface with the nonhomogeneous layer, i.e., $a = 0$, however, it can be shown that there occur logarithmic singularities in the kernel (31) which are square integrable and would have no influence on the singular behavior of the solution of the integral equation in (30). The dominant singular kernel in this limiting case is yet attributed to the same Cauchy type, with such additional unbounded terms being treated as a Fredholm kernel as demonstrated by Erdogan et al. (1991a).

With the Cauchy-type kernel in (30) thus being the sole contribution to the singular nature of the auxiliary function ϕ, the crack-tip behavior can be characterized by the standard square-root singularity for $a = 0$ as well as $a > 0$ such that (Muskhelishvili, 1953)

$$\phi(r) = \frac{h(r)}{\sqrt{(r-a)(b-r)}}; \quad a < r < b \quad (35)$$

where $h(r)$ is an unknown function which is bounded and nonzero at $r = a$ and $r = b$.

In the normalized interval given as

$$\begin{Bmatrix} r \\ x \end{Bmatrix} = \frac{b-a}{2}\begin{Bmatrix} \eta \\ \xi \end{Bmatrix} + \frac{b+a}{2}; \quad -1 < (\eta, \xi) < 1 \quad (36)$$

the integral equation in (30) is thus solved numerically by noting that its fundamental function corresponds to the weight function of the Chebyshev polynomial of the first kind $T_n(\eta)$. Upon defining the following quantities as

$$\phi(r) = \Phi(\eta) = \frac{H(\eta)}{\sqrt{1-\eta^2}}, \quad H(\eta) = \frac{2h(r)}{b-a}; \quad |\eta| < 1, \quad (37a, b)$$

the unknown function $H(\eta)$ can therefore be expressed as

$$H(\eta) = \sum_{n=1}^{\infty}c_n T_n(\eta); \quad |\eta| < 1, \quad (38)$$

where $c_n, n \ge 1$, are the unknown constants to be evaluated. It is observed that the compatibility condition (7*b*) is identically satisfied by the above series expansion.

After substituting (36)–(38), truncated with the first N terms in (38), into (30) and using the integral formulas (Abramowitz and Stegun, 1965)

Downloaded 04 May 2010 to 171.66.16.33. Redistribution subject to ASME license or copyright; see http://www.asme.org/terms/Terms_Use.cfm

$$\frac{1}{\pi}\int_{-1}^{1}\frac{T_n(\eta)d\eta}{\sqrt{1-\eta^2}(\eta-\xi)} = U_{n-1}(\xi);\quad n \geq 1,\quad |\xi| < 1 \tag{39a}$$

$$\frac{2}{\pi}\int_{-1}^{1} U_k(\eta)U_n(\eta)\sqrt{1-\eta^2}d\eta = \begin{cases} 0; & k \neq n \\ 1; & k = n \end{cases} \tag{39b}$$

where U_n is the Chebyshev polynomial of the second kind, the integral equation can be recast into a system of N linear algebraic equations to be solved for c_n, $1 \leq n \leq N$, such that

$$\frac{\pi^2}{2}c_k + \sum_{n=1}^{N} Y_{kn}c_n = f_k;\quad k = 1, 2, \ldots, N \tag{40}$$

where Y_{kn} and f_k are expressed as

$$Y_{kn} = \int_{-1}^{1} G_n(\xi)U_{k-1}(\xi)\sqrt{1-\xi^2}d\xi \tag{41a}$$

$$f_k = \frac{\pi(1+\kappa)}{4\mu_3}\int_{-1}^{1}\sigma_o(\xi)U_{k-1}(\xi)\sqrt{1-\xi^2}d\xi \tag{41b}$$

in which the function $G_n(\xi)$ is written as

$$G_n(\xi) = \frac{b-a}{2}\int_{-1}^{1}\frac{p(\xi,\eta)T_n(\eta)}{\sqrt{1-\eta^2}}d\eta. \tag{42}$$

Upon evaluating the constants c_n from (40), it can be seen that the left-hand side of the integral equation in (30) provides the expression for $\sigma_{3yy}(\xi, 0)$ outside $|\xi| > 1$ as well as inside $|\xi| < 1$ the crack. Thus, from (30) and (36)–(38), the dominant singular terms of the crack-tip traction can be obtained in the following form:

$$\begin{aligned}\frac{1+\kappa}{4\mu_3}\sigma_{3yy}(\xi, 0) &= \frac{1}{\pi}\sum_{n=1}^{N} c_n\int_{-1}^{1}\left[\frac{1}{\eta-\xi} + p_*(\xi,\eta)\right]\frac{T_n(\eta)}{\sqrt{1-\eta^2}}d\eta \\ &= -\sum_{n=1}^{N} c_n\frac{\text{sgn}(\xi)}{\sqrt{\xi^2-1}}[\xi - \text{sgn}(\xi)\sqrt{\xi^2-1}]^n \\ &\quad + \frac{1}{\pi}\sum_{n=1}^{N} c_nG_n(\xi);\quad |\xi| > 1\end{aligned} \tag{43}$$

where $p_*(\xi, \eta) = (b-a)p(\xi, \eta)/2$ and to be mentioned now is that due to the continuity of elastic moduli at the interfaces through the nonhomogeneous transitional interfacial layer, the cleavage stresses are also continuous at the location of the interface between the materials 2 and 3 such that $\sigma^{+}_{2yy}(y) = \sigma^{-}_{3yy}(y)$, $y \geq 0$.

As the local crack-tip characterizing parameters, the mode I stress intensity factors K_a and K_b at the left and right-hand side crack tips, respectively, can be defined as

$$K_a = \lim_{x\to a}\sqrt{2(a-x)}\,\sigma_{3yy}(x, 0);\quad x < a \tag{44a}$$

$$K_b = \lim_{x\to b}\sqrt{2(x-b)}\,\sigma_{3yy}(x, 0);\quad x > b \tag{44b}$$

and by substituting (43) into the above, in conjunction with (36), the stress intensity factors can be evaluated in terms of the solution to the integral equation such that

$$K_a = \frac{4\mu_3}{1+\kappa}\sqrt{\frac{b-a}{2}}\sum_{n=1}^{N}(-1)^n c_n \tag{45a}$$

$$K_b = -\frac{4\mu_3}{1+\kappa}\sqrt{\frac{b-a}{2}}\sum_{n=1}^{N} c_n \tag{45b}$$

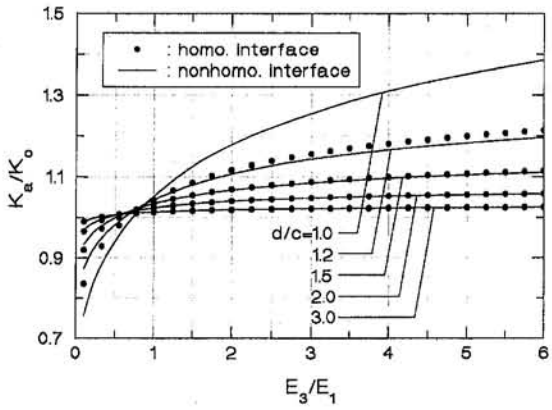


Fig. 2(a)

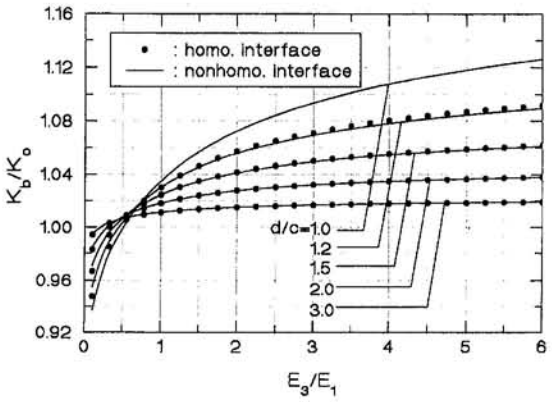


Fig. 2(b)

Fig. 2 Variations of stress intensity factors (a) at the left-hand side crack tip K_a/K_o; (b) at the right-hand side crack tip K_b/K_o with the elastic moduli ratio E_3/E_1 for different crack locations d/c ($K_o = p_o c^{1/2}$, $h_2/h_1 = 0.5$, $c/h_1 = 1.0$, $\nu = 0.3$)

where the continuity of the cleavage stresses at the interface validates the above definition of the stress intensity factors for $a = 0$ as well, which corresponds to the case of the crack-tip terminating at the interface.

3 Results and Discussion

For the purpose of numerical illustrations, the geometric properties of the layered medium are specified as $h_2/h_1 = 0.5$ and $c/h_1 = 1.0$, unless otherwise stated. Further assumed is a uniformly applied crack surface traction $\sigma_o(x_3) = -p_o = -E_3\epsilon_o/(1-\nu^2)$ in (5c) under the plane-strain state, with the Poisson's ratio being $\nu = 0.3$. Twelve-term expansion of the Chebyshev polynomial in (38) is then found to be large enough for obtaining the solutions to the defined problem with a required degree of accuracy. The related integrals are evaluated by using the Gauss-Chebyshev and Gauss-Legendre formulae (Abramowitz and Stegun, 1965).

Figures 2(a) and 2(b) show the variations of normalized stress intensity factors K_a and K_b at the left and right-hand side crack tips, respectively, as a function of the elastic moduli ratio E_3/E_1 for different crack locations d/c. The magnitude of K_a is, as expected, greater than that of K_b when $E_3/E_1 > 1$ and, in general, the reverse is true when $E_3/E_1 < 1$ offsetting the adjacent free-surface effect. Nevertheless, the stress intensity factors at both the crack tips increase as the ratio E_3/E_1 increases. The above behavior can be accounted for in terms of the relative stiffness reduction in the materials 1 and 2 for enlarged values of E_3/E_1, also implying that the crack tip can be shielded by decreasing E_3/E_1. The effect of such nonhomogeneity tends to

Downloaded 04 May 2010 to 171.66.16.33. Redistribution subject to ASME license or copyright; see http://www.asme.org/terms/Terms_Use.cfm

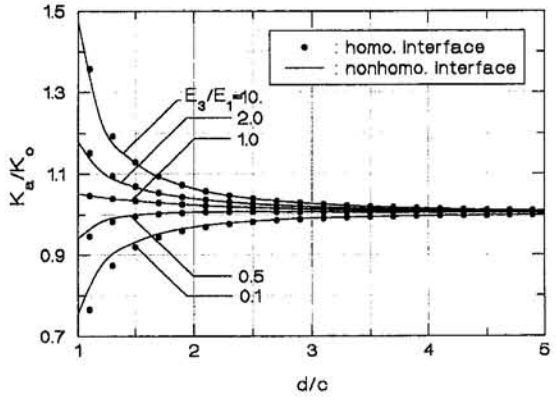


Fig. 3(*a*)

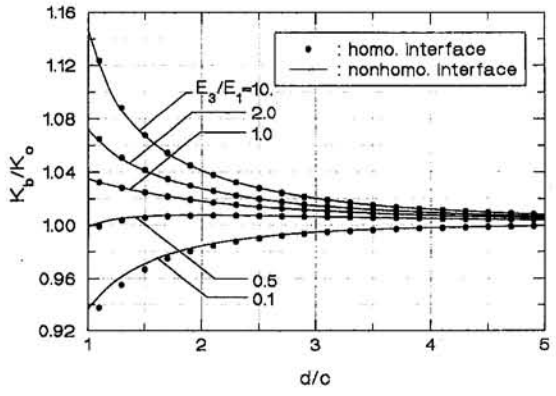


Fig. 3(*b*)

Fig. 3 Effects of crack location d/c on the values of stress intensity factors (a) at the left-hand side crack tip K_a/K_o; (b) at the right-hand side crack tip K_b/K_o for different elastic moduli ratios E_3/E_1 ($K_o = p_o c^{1/2}$, $h_2/h_1 = 0.5$, $c/h_1 = 1.0$, $\nu = 0.3$)

diminish as d/c increases, as can be seen from the slight variation of the stress intensity factors with respect to E_3/E_1 for $d/c = 3$.

To provide some insight into the degree of correspondence with the current nonhomogeneous interface model, the stress intensity factors for the homogeneous interface model are also evaluated based on the functionally averaged elastic modulus of the nonhomogeneous interfacial layer:

$$E_{\text{avg}} = \frac{1}{h_2}\int_0^{h_2} E_o e^{\beta x} dx = \frac{E_o}{\beta h_2}(e^{\beta h_2} - 1) \qquad (46)$$

and the resulting values are plotted and compared in Figs. 2(a) and 2(b) by circles. For relatively smaller geometric ratio of d/c, notable discrepancies of the stress intensity factors from the nonhomogeneous interface model are shown to exist. When the crack is located away from the interface, however, the solutions to both the homogeneous and nonhomogeneous interface models are in good agreement. To be remarked is that for the homogenized interface with $d/c = 1$ such that the crack tip touches the ideal nominal interface, the crack-tip singularity other than the square-root type is obtained (Cook and Erdogan, 1972). In this regard, the results corresponding to this case are not given herein.

The influence of d/c is more explicitly exhibited in Figs. 3(a) and 3(b) for different E_3/E_1. It is shown that for the stiffer surface layer with $E_3/E_1 < 1$, the normalized stress intensity factors increase with d/c, while the opposite trend is encountered for $E_3/E_1 \geq 1$. Also shown in these figures is that the discrepancies between the solutions of homogeneous and nonhomogeneous interface models become more noteworthy, especially when $E_3/E_1 = 0.1$, with the crack being brought closer to the location of the material interface. On the other hand, as d/c increases, the stress intensity factors at both the crack tips approach those of the unbounded homogeneous plane and are seemingly insignificantly affected by the material nonhomogeneity E_3/E_1 as well.

With the crack located directly beneath the nonhomogeneous interfacial layer such that $d/c = 1$ and $c/h_1 = 1$, the variations of stress intensity factors K_a and K_b with the thickness ratio h_2/h_1 are plotted in Figs. 4(a) and 4(b), respectively, for different E_3/E_1. These figures show that, similar to the effect of d/c as in Figs. 3(a) and 3(b), an increase in the thickness of the nonhomogeneous layer leads to an increase in the magnitude of normalized stress intensity factors for $E_3/E_1 < 1$, while the reverse response prevails for $E_3/E_1 \geq 1$. It is noted that as the ratio h_2/h_1 further increases, the present results tend to those obtained for a cracked half-plane bonded to a nonhomogeneous half-plane given by Erdogan et al. (1991a).

For the fixed crack location $d/c = 1$ and the thickness ratio $h_2/h_1 = 0.5$, Figs. 5(a) and 5(b) next illustrate the effects of varying crack size relative to the surface layer thickness, i.e., c/h_1. Of particular interest in Fig. 5(a) is that for the case of $E_3/E_1 < 1$, the values of K_a decrease monotonically even when c/h_1 increases (except for $E_3/E_1 = 0.5$ where a slight increase in K_a is observed). This may be indicative of stabilized crack growth in the substrate by stiffening its bounding surface. Another interesting feature predicted from Fig. 5(b) is that, however, under the same material condition of $E_3/E_1 < 1$, the corresponding values of K_b go through minima before increasing with respect to the increasing crack size c/h_1. It is further ob-

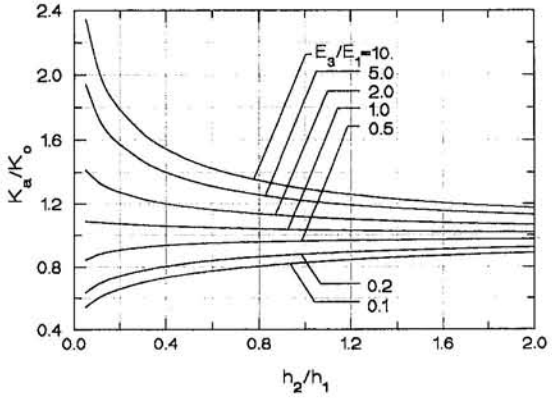


Fig. 4(*a*)

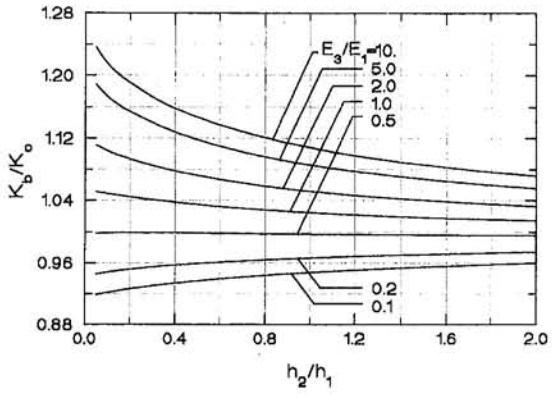


Fig. 4(*b*)

Fig. 4 Effects of layer thickness h_2/h_1 on the values of stress intensity factors (a) at the left-hand side crack tip K_a/K_o; (b) at the right-hand side crack tip K_b/K_o for different elastic moduli ratios E_3/E_1 ($K_o = p_o c^{1/2}$, $d/c = 1.0$, $c/h_1 = 1.0$, $\nu = 0.3$)

Downloaded 04 May 2010 to 171.66.16.33. Redistribution subject to ASME license or copyright; see http://www.asme.org/terms/Terms_Use.cfm

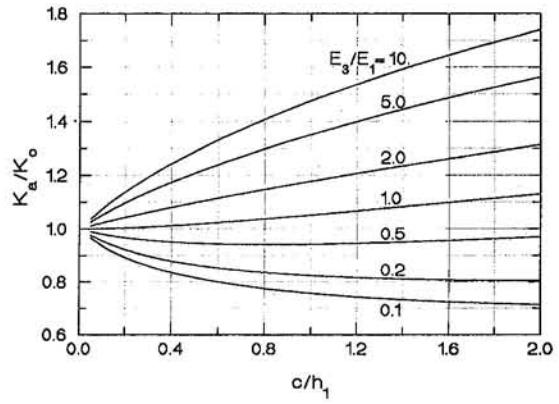


Fig. 5(*a*)

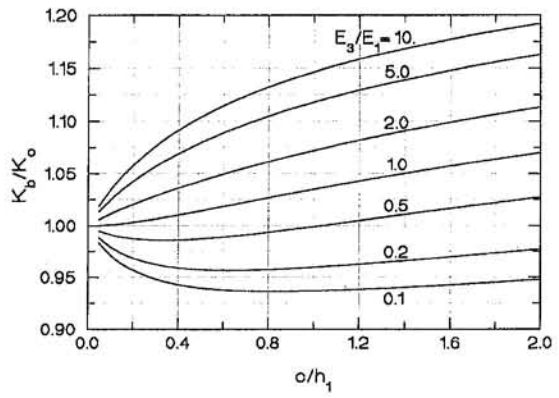


Fig. 5(*b*)

Fig. 5 Effects of crack size c/h_1 on the values of stress intensity factors (*a*) at the left-hand side crack tip K_a/K_o; (*b*) at the right-hand side crack tip K_b/K_o for different elastic moduli ratios E_3/E_1 ($K_o = p_o c^{1/2}$, $d/c = 1.0$, $h_2/h_1 = 0.5$, $\nu = 0.3$)

served that as the ratio c/h_1 tends to zero, the normalized stress intensity factors at both the crack tips appear to approach unity regardless of the given values of E_3/E_1.

4 Closure

The mode I crack problem for a layered medium with a functionally graded interface has been studied, by modeling that a surface layer is bonded to a cracked semi-infinite substrate through a nonhomogeneous interfacial layer. Together with the aid of the stiffness matrix approach in a straightforward manner, a singular integral equation was readily derived. The selected numerical results then illustrated the crack-tip behavior that is strongly affected by the geometric parameters of the crack size and location and the layer thickness, in conjunction with the material nonhomogeneity in the interfacial layer. In addition, the present results of stress intensity factors involving the effects of such graded interfacial properties indicated that, depending on the crack location, a quite different behavior may prevail from that which is obtained based on the use of the ideally bonded interface.

References

Abramowitz, M., and Stegun, I., 1965, *Handbook of Mathematical Functions,* Dover, New York.

Atkinson, C., 1977, "On Stress Singularities and Interfaces in Linear Elastic Fracture Mechanics," *International Journal of Fracture,* Vol. 13, pp. 807–820.

Choi, H. J., and Thangjitham, S., 1991, "Stress Analysis of Multilayered Anisotropic Elastic Media," ASME JOURNAL OF APPLIED MECHANICS, Vol. 58, pp. 382–387.

Choi, H. J., and Thangjitham, S., 1993, "Thermally Induced Interlaminar Crack-Tip Singularities in Laminated Anisotropic Composites," *International Journal of Fracture,* Vol. 60, pp. 327–347.

Choi, H. J., and Thangjitham, S., 1994, "The Interlaminar Crack-Tip Response in a Fiber-Reinforced Composite Laminate," *International Journal of Fracture,* Vol. 66, pp. 121–138.

Cook, T. S., and Erdogan, F., 1972, "Stresses in Bonded Materials with a Crack Perpendicular to the Interface," *International Journal of Engineering Science,* Vol. 10, pp. 677–697.

Delale, F., and Erdogan, F., 1983, "The Crack Problem for a Nonhomogeneous Plane," ASME JOURNAL OF APPLIED MECHANICS, Vol. 50, pp. 609–614.

Delale, F., and Erdogan, F., 1988a, "On the Mechanical Modeling of the Interfacial Region in Bonded Half-Planes," ASME JOURNAL OF APPLIED MECHANICS, Vol. 55, pp. 317–324.

Delale, F., and Erdogan, F., 1988b, "Interface Crack in a Nonhomogeneous Elastic Medium," *International Journal of Engineering Science,* Vol. 26, pp. 559–568.

England, A. H., 1965, "A Crack Between Dissimilar Media," ASME JOURNAL OF APPLIED MECHANICS, Vol. 32, pp. 400–402.

Erdogan, F., 1985, "The Crack Problem for Bonded Nonhomogeneous Materials under Antiplane Shear Loading," ASME JOURNAL OF APPLIED MECHANICS, Vol. 52, pp. 823–828.

Erdogan, F., Kaya, A. C., and Joseph, P. F., 1991a, "The Crack Problem in Bonded Nonhomogeneous Materials," ASME JOURNAL OF APPLIED MECHANICS, Vol. 58, pp. 410–418.

Erdogan, F., Kaya, A. C., and Joseph, P. F., 1991b, "The Mode III Crack Problem in Bonded Materials With a Nonhomogeneous Interfacial Zone," ASME JOURNAL OF APPLIED MECHANICS, Vol. 58, pp. 419–427.

Erdogan, F., and Ozturk, M., 1992, "Diffusion Problems in Bonded Nonhomogeneous Materials With an Interface Cut," *International Journal of Engineering Science,* Vol. 30, pp. 1507–1523.

Friedman, B., 1969, *Lectures on Application-Oriented Mathematics,* Holden-Day, San Francisco.

Gao, X., and Kuang, Z.-B., 1992, "Mode I Fracture in Two Dissimilar Functional Nonhomogeneous Planes," *Engineering Fracture Mechanics,* Vol. 42, pp. 33–44.

Gecit, M. R., and Erdogan, F., 1978, "The Effect of Adhesive Layers on the Fracture of Laminated Structures," ASME *Journal of Engineering Materials and Technology,* Vol. 100, pp. 2–9.

Gupta, G. D., 1973, "A Layered Composite With a Broken Laminate," *International Journal of Solids and Structures,* Vol. 9, pp. 1141–1154.

Hilton, P. D., and Sih, G. C., 1971, "A Laminate Composite With a Crack Normal to the Interfaces," *International Journal of Solids and Structures,* Vol. 7, pp. 913–930.

Kausel, E., and Seale, S. H., 1987, "Static Loads in Layered Halfspaces," ASME JOURNAL OF APPLIED MECHANICS, Vol. 54, pp. 403–408.

Kaw, A. K., and Goree, J. G., 1990, "Effect of Interleaves on Fracture of Laminated Composites: Part I Analysis," ASME JOURNAL OF APPLIED MECHANICS, Vol. 57, pp. 168–174.

Kaw, A. K., Selvarathinam, A. S., and Besterfield, G. H., 1992, "Comparison of Interphase Models for a Crack in Fiber Reinforced Composite," *Theoretical and Applied Fracture Mechanics,* Vol. 17, pp. 133–147.

Martin, P. A., 1992, "Tip Behaviour for Cracks in Bonded Inhomogeneous Materials," *Journal of Engineering Mathematics,* Vol. 26, pp. 467–480.

Muskhelishvili, N. I., 1953, *Singular Integral Equations,* Noordhoff, Groningen, The Netherlands.

Noda, N., Akari, K., and Erdogan, F., 1992, "Stress Intensity Factors in Two Bonded Elastic Layers with a Single Edge Crack under Various Loading Conditions," *International Journal of Fracture,* Vol. 57, pp. 101–126.

Ozturk, M., and Erdogan, F., 1993, "Antiplane Shear Crack Problem in Bonded Materials with a Graded Interfacial Zone," *International Journal of Engineering Science,* Vol. 31, pp. 1641–1657.

Schovanec, L., and Walton, J. R., 1988, "On the Order of Stress Singularity for an Antiplane Shear Crack at the Interface of Two Bonded Inhomogeneous Elastic Materials," ASME JOURNAL OF APPLIED MECHANICS, Vol. 55, pp. 234–236.

Urquhart, E. E., and Pindera, M.-J., 1994, "Incipient Separation Between a Frictionless Flat Punch and an Anisotropic Multilayered Half Plane," *International Journal of Solids and Structures,* Vol. 31, pp. 2445–2461.

Wang, Y., and Rajapakse, R. K. N. D., 1994, "An Exact Stiffness Method for Elastodynamics of a Layered Orthotropic Half-Plane," ASME JOURNAL OF APPLIED MECHANICS, Vol. 61, pp. 339–348.

Zak, A. R., and Williams, M. L., 1963, "Crack Point Stress Singularities at a Bimaterial Interface," ASME JOURNAL OF APPLIED MECHANICS, Vol. 30, pp. 142–143.

Downloaded 04 May 2010 to 171.66.16.33. Redistribution subject to ASME license or copyright; see http://www.asme.org/terms/Terms_Use.cfm

Chaotic Vibration in Fluid-Stiffness-Controlled Instability of a Tube Row in Crossflow[1]

S. H. Chen[2]
Mem. ASME.

S. S. Chen
Fellow ASME.

Energy Technology Division,
Argonne National Laboratory,
Argonne, IL 60439

The fluid-elastic instability of tube arrays in heat exchangers may become chaotic, especially when clearances exist between tubes and supports. When chaotic motion appears in tube arrays, significant sliding between the tubes and supports may be induced. An analytical model, consisting of a row of rigid tubes with three tubes supported by springs, is presented. Bifurcation diagrams, Poincaré maps, power spectral densities, and tube orbits are used to investigate the conditions under which the unpredictable motion can arise. The emphasis is on fluid-stiffness-controlled instability.

1 Introduction

An array of tubes in crossflow (commonly seen in heat exchangers) may undergo large-amplitude vibrations when flow speed exceeds a threshold value. This phenomenon is known as fluid-elastic instability and has been investigated extensively since the 1970s. Motion of the unstable tubes is often limited by the clearances between the tubes and supports; these clearances are usually intended to facilitate manufacturing and accommodate thermal expansion. The wear caused by the tube/support interaction is dictated by the contact forces and the amount of sliding (Ko and Basista, 1984). The wear rate may be higher if greater sliding is produced.

Numerical and experimental studies of chaos in fluid/structure systems have been reported by a number of researchers (Antunes et al., 1992; Axisa et al., 1988; Cai and Chen, 1993a, 1993b; Fricker, 1992; de Langre et al., 1992; Munteau and Moon, 1992; Paidoussis and Li, 1992; Vento et al., 1992). However, all previous studies were limited to quasistatic and quasi-steady flow theories or damping-controlled instability. The objective of this paper is to extend the investigation to fluid-stiffness-controlled instability on the basis of unsteady flow (Chen, 1987) incorporating all motion-dependent fluid forces.

The analytical model consists of a row of rigid tubes with three tubes supported by springs. Each of the three elastically supported tubes has two degrees-of-freedom, one each in the lift and the drag directions. Bifurcation diagrams were plotted to overview the effect of changing some system parameters. Poincaré maps, tube orbits, phase planes, and power spectral densities (PSDs) are plotted for cases selected from the bifurcation diagrams. Effects of chaos on wear are also investigated. The main purpose of this study is to gain an understanding of the possible causes of chaotic motion in a tube bank for fluid-stiffness-controlled instability. Analytical and experimental studies of fluid-damping-controlled instability have also been considered separately (Cai and Chen, 1993a, 1993b; Chen, Zhu, and Cai, 1994).

2 Mathematical Model

2.1 Equations of Motions. Consider a tube row vibrating in a flow with fluid density ρ, as shown in Fig. 1. The axes of the tubes are parallel to one another and perpendicular to the x-y plane. Each tube has the same radius R ($D = 2R$) and the fluid is flowing with a constant velocity U. All tubes are assumed to be rigid; Tubes 1, 2, and 3 are supported by springs in the x and y-directions, and Tubes 4 and 5 are rigidly supported. The displacement components of tube j in the x and y-directions are u_j and v_j, respectively.

Based on the unsteady-flow theory, which assumes that fluid forces are functions of tube motions, Chen (1987, 1989) presented a general theory for the motion of tubes oscillating in fluid flow. For the jth tube among a group of N tubes, the equations of motion are

$$\ddot{u}_j + 2\zeta_v\omega_v\dot{u}_j + \omega_v^2 u_j + \gamma\sum_{k=1}^{N}(\alpha_{jk}\ddot{u}_k + \sigma_{jk}\ddot{v}_k) - \frac{\gamma U_v^2\omega_v^2}{\pi^3\omega}\sum_{k=1}^{N}(\alpha'_{jk}\dot{u}_k + \sigma'_{jk}\dot{v}_k) - \frac{\gamma U_v^2\omega_v^2}{\pi^3}\sum_{k=1}^{N}(\alpha''_{jk}u_k + \sigma''_{jk}v_k) = 0, \quad (1)$$

and

$$\ddot{v}_j + 2\zeta_v\omega_v\dot{v}_j + \omega_v^2 v_j + \gamma\sum_{k=1}^{N}(\tau_{jk}\ddot{u}_k + \beta_{jk}\ddot{v}_k) - \frac{\gamma U_v^2\omega_v^2}{\pi^3\omega}\sum_{k=1}^{N}(\tau'_{jk}\dot{u}_k + \beta'_{jk}\dot{v}_k) - \frac{\gamma U_v^2\omega_v^2}{\pi^3}\sum_{k=1}^{N}(\tau''_{jk}u_k + \beta''_{jk}v_k) = 0, \quad (2)$$

where $j = 1$, 2, and 3, $\gamma = \rho\pi R^2/m$, and $U_v = U/f_vD$.

In Eqs. (1) and (2), α_{jk}, β_{jk}, σ_{jk}, and τ_{jk} are the added-mass coefficients, α'_{jk}, β'_{jk}, σ'_{jk}, and τ'_{jk} are the fluid-damping coefficients, α''_{jk}, β''_{jk}, σ''_{jk}, and τ''_{jk} are the fluid-stiffness coefficients, m is tube mass per unit length, ω is circular frequency of oscillations, and f_v ($\omega_v = 2\pi f_v$) and ζ_v are natural frequency and modal damping ratio of the tube in vacuum. The added-mass coefficients can be determined from the potential flow theory, while the fluid-damping coefficients and the fluid-stiffness coefficients

[1] Work supported by the U.S. Department of Energy, Office of Basic Energy Science, Division of Engineering and Geosciences, under Contract W-31-109-ENG-38.

[2] Currently at the Kuen-Xhan Institute of Technology and Commerce, Tainan, Taiwan.

Contributed by the Applied Mechanics Division of THE AMERICAN SOCIETY OF MECHANICAL ENGINEERS for publication in the ASME JOURNAL OF APPLIED MECHANICS.

Discussion on this paper should be addressed to the Technical Editor, Professor Lewis T. Wheeler, Department of Mechanical Engineering, University of Houston, Houston, TX 77204-4792, and will be accepted until four months after final publication of the paper itself in the ASME JOURNAL OF APPLIED MECHANICS.

Manuscript received by the ASME Applied Mechanics Division, Aug. 19, 1994; final revision, Jan. 3, 1995. Associate Technical Editor: W. K. Liu.

Copyright © 1996 by ASME

Downloaded 04 May 2010 to 171.66.16.33. Redistribution subject to ASME license or copyright; see http://www.asme.org/terms/Terms_Use.cfm

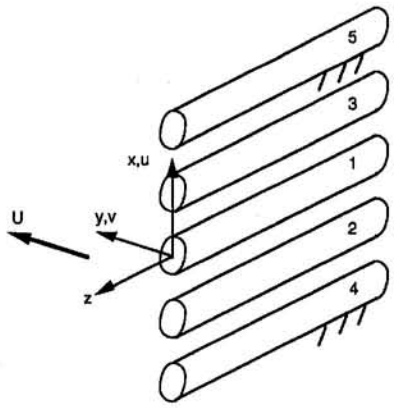


Fig. 1 Configuration of tube system

can be determined by experiment. Chen and Chandra (1991) have published these coefficients based on experimental data by Tanaka (1980).

It is noted that these coefficients were obtained for relatively small motions in which the oscillation amplitudes were about ten percent of the tube diameter (Tanaka, 1980). A question may be asked whether they can be applied to the post-instability region. Similar tests were performed by Chen, Zhu, and Jendrzejczyk (1994) for larger amplitudes with the peak amplitude of tube oscillations up to 70 percent of the tube gap. The effect of oscillation amplitudes on fluid force coefficients was still insignificant. In this study, because of the constraint provided by the stop, the tube motion is limited to the stop clearance. Therefore, the fluid force coefficients obtained for relatively small amplitudes will be applicable.

2.2 Tube/Support Interaction. The interaction between tubes and supports is modeled by a spring of stiffness K, viscous damping between tubes and supports C, and Coulomb friction against sliding with coefficient of friction μ. The viscous damping accounts for the dissipation of energy gained from the fluid force. Contact deflection δ is determined in terms of

$$\delta = \sqrt{(u + \epsilon_x)^2 + (v + \epsilon_y)^2} - (D_{\text{opening}} - D)/2, \quad (3)$$

where u and v are displacements in the x and y-directions and ϵ_x and ϵ_y are the distance in the x and y-directions between the equilibrium position of tube relative to the opening center. The force components in the x and y-directions acting on the tubes and caused by contact are

$$f_x = -(K\delta + C\dot{v}_n) \cos\theta - \mu \text{ sign } (\dot{v}_s) K\delta \sin\theta,$$

and

$$f_y = -(K\delta + C\dot{v}_n) \sin\theta - \mu \text{ sign } (\dot{v}_s) K\delta \cos\theta, \quad (4)$$

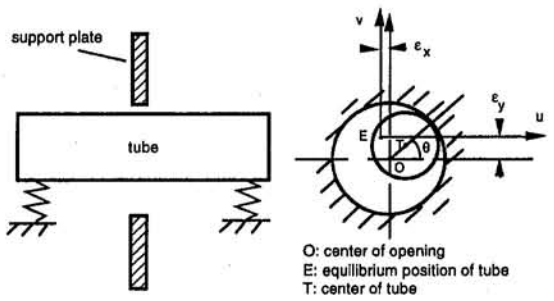


Fig. 2 Rigid tubes supported by springs, and gaps between tube and support plates

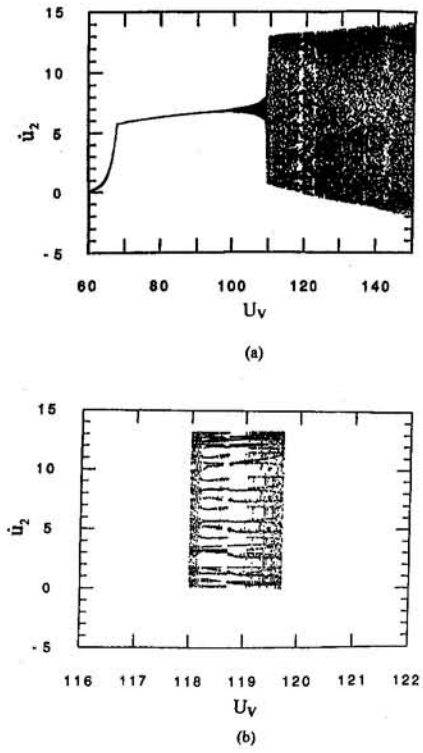


Fig. 3 (*a*) Bifurcation of dynamic behavior as U_v is varied; (*b*) the periodic window for $U_v = 118$ to $U_v = 119.8$

where θ is the azimuth angle of the contact point given by

$$\theta = \tan^{-1} [(v + \epsilon_y)/(u + \epsilon_x)],$$

and $\dot{v}_n$ and $\dot{v}_s$ given below are the velocity components of the tube in the normal and sliding directions to the contact, respectively.

$$\dot{v}_n = \dot{u} \cos\theta + \dot{v} \sin\theta \text{ and } \dot{v}_s = -\dot{u} \sin\theta + \dot{v} \cos\theta$$

3 Numerical Solutions

A number of chaos features can be applied to identify chaos from time-series data. The time-series data in this paper are obtained by integrating Eq. (1) with the Runge-Kutta method. The bifurcation diagram as well as Poincaré map are produced by sampling the trajectories with an imaginary plane in the phase space. Because no forcing frequency is present, the sampling time is position-triggered. Whenever Tube 1 passes through the equilibrium position in the direction under consideration, the tube motion is sampled. For the Poincaré map, the displacement and the velocity of Tube 2 are plotted. For the bifurcation diagram, the displacement of Tube 2 is plotted against the bifurcation parameter. Two bifurcation parameters are used, one is the reduced flow velocity, U_v, and the other is the equilibrium position of the tube in the y-direction, ϵ_y. In generating the bifurcation diagram, the first 30 cycles of time simulation data are discarded to allow a steady state is achieved. About 50 cycles of time-series data for each value of the bifurcation parameter are plotted.

For the classification of the types of tube motion, the Poincaré map is used. In the Poincaré map, periodic motion appears as a point; subharmonic motion, a finite number of points; quasi-periodic motion, a closed curve; and chaotic motion, a cloud of unorganized points. To generate a Poincaré map, about 1,000 cycles of time-series data are used. The tube orbits, phase planes, and power spectral density are also presented.

The system to be evaluated consists of a row of rigid tubes with three tubes supported by springs, as shown in Fig. 2. The middle three tubes are denoted as Tube 2, 1, and 3, respectively.

Downloaded 04 May 2010 to 171.66.16.33. Redistribution subject to ASME license or copyright; see http://www.asme.org/terms/Terms_Use.cfm

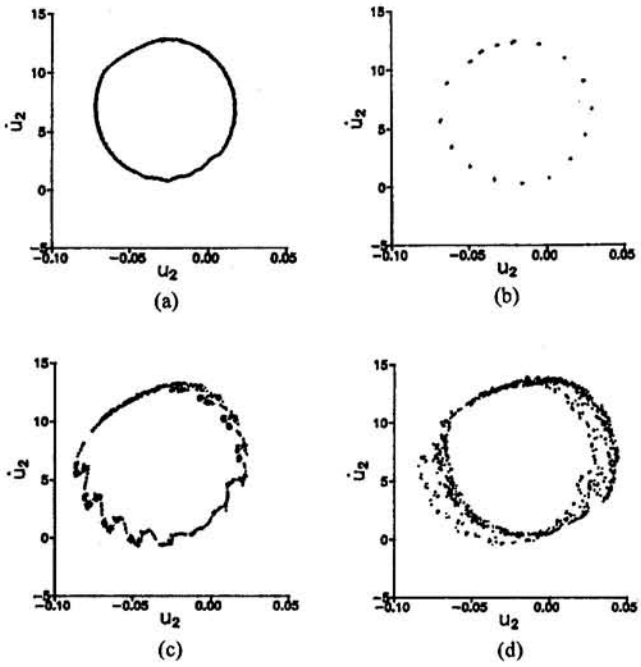


Fig. 4 Poincaré maps for (*a*) $U_v = 110$, (*b*) $U_v = 118.7$, (*c*) $U_v = 122$, and (*d*) $U_v = 130$

The parameters involved in the tube-supported system are shown as follows.

Constant parameters:

tube diameter, $D = 2.54$ cm
pitch/diameter ratio, $P/D = 1.33$
natural frequency of tubes, $f_v = 20$ Hz no contact
natural frequency of tubes, $f_v' = 250$ Hz at contact
structural damping of tubes, $\zeta_v = 0.02$
size of openings, $1.2D \times 1.2D$ for square openings
$1.2D$ for circular openings
Viscous damping of tube-support contact = 0.02

Variable parameters:

Reduced flow velocity, U_v
Mass-damping parameter, δ_s $(=2\pi m\zeta/\rho D^2)$
Equilibrium positions of tubes relative to opening centers, ϵ_x and ϵ_y
Coefficient of friction between tubes and support, μ

4 Results and Discussions

Numerical results are presented for two cases, the square support opening and the circular support opening. In the square opening, the coefficient of friction μ is assumed to be zero to make it simpler, while in the circular opening, μ is taken to be 0 and 0.1.

The fluid-elastic stability boundaries in terms of U_v and δ_s can be obtained by solving for the eigenvalues of the system. A more detailed discussion on the solution method has been presented by Chen (1983, 1989). There are two unstable regions: fluid-damping-controlled instability and fluid-stiffness-controlled instability. The fluid-damping-controlled instability has been reported elsewhere (Cai and Chen, 1993a, 1993b; Chen, Zhu, and Cai, 1995). In this study, only fluid-stiffness-controlled instability is presented. The two most unstable modes in the fluid-stiffness-controlled region are denoted as Mode 1 and Mode 2.

4.1 Square Opening. For this part of the study, the openings on the support plate are assumed to be square to preclude any possible effect by circular openings. Figure 3(*a*) shows

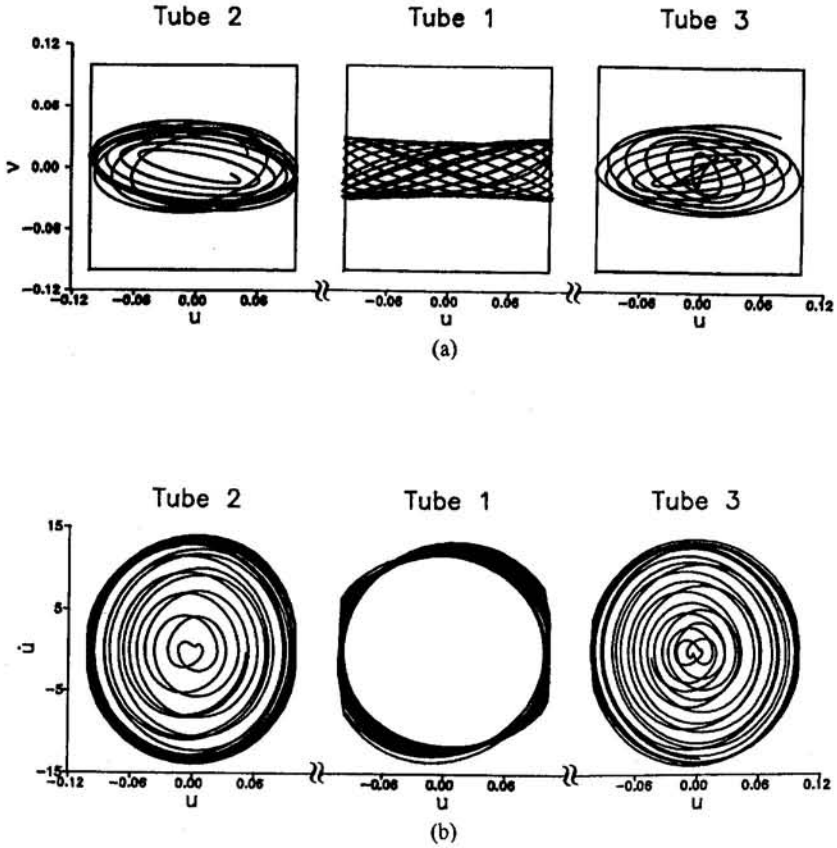


Fig. 5 (*a*) Tube orbits and (*b*) phase planes for $U_v = 130$

Downloaded 04 May 2010 to 171.66.16.33. Redistribution subject to ASME license or copyright; see http://www.asme.org/terms/Terms_Use.cfm

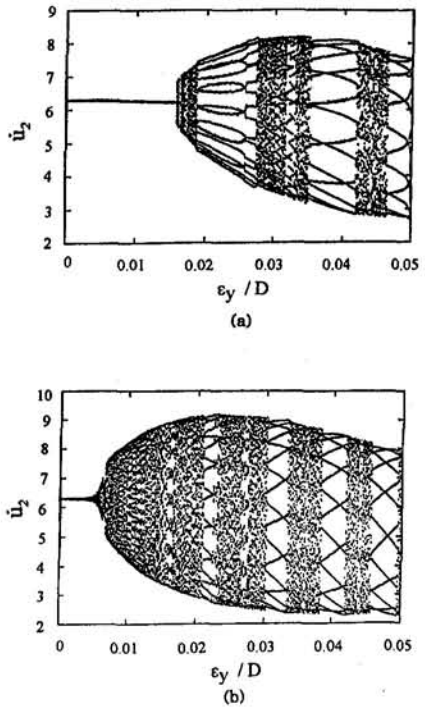


Fig. 6 Bifurcation diagrams with ϵ_y as the control parameter and ϵ_x = 0: (*a*) μ = 0.1, (*b*) μ = 0

the bifurcations of $\dot{u}_2$ (the velocity of Tube 2 in the x-direction) as U_v is varied (δ_s is fixed at 25). When U_v reaches 70, the first Hopf bifurcation occurs, and Mode 1 becomes unstable. When U_v is increased to 110, the second Hopf bifurcation occurs, and both Mode 1 and Mode 2 become unstable. As U_v is increased to 118, a periodic window caused by nonlinear effects appears. The periodic window from $U_v = 118$ to $U_v = 119.8$ is plotted again with a greater magnification in Fig. 3(b). After the periodic window, it is not possible to determine whether the motion is quasiperiodic or chaotic from the bifurcation diagram alone.

To better characterize the tube motion, Poincaré maps are plotted in Fig. 4 for four different values of U_v selected from the bifurcation diagram. When $U_v = 110$ (Fig. 4a), the motion is quasi-periodic. When $U_v = 118.7$ (Fig. 4(b)), the motion is subharmonic. When $U_v = 122$ (Fig. 4(c)), the Poincaré map is a broken curve with a fractal structure, which means that the motion approaches chaos. When $U_v = 130$ (Fig. 4(d)), a two-well potential situation is created due to the strong contacts between the tube and the support plate.

From the tube orbits in Fig. 5(a) for $U_v = 130$, it can be seen that the chaotic motion becomes more pronounced when all three tubes contact the supports. The tube motion is amplitude-modulated, due to the two vibration modes, and the variations of the amplitudes of Tubes 2 and 3 are 180 deg apart in phase. From the phase planes in Fig. 5(b), the two-well potential can be seen again. However, because the irregular motion is small compared to the regular motion, the PSD (for $U_v = 130$) shows two dominant peaks.

4.2 Circular Openings. If the tubes are at the centers of circular openings, circular and square openings have similar effects. However, if the tubes are displaced in the drag direction (may be caused by fluid drag force), Mode 2 will be excited even when only Mode 1 is unstable. To investigate this type of motion, U_v is set at 80 and δ_s at 25, and the equilibrium position of the tubes in the y (drag)-direction, ϵ_y, is chosen as the control parameter. Note that when $U_v = 80$ and $\delta_s = 25$, only Mode 1 is unstable.

Two bifurcation diagrams are plotted for two different values of coefficients of friction, 0.1 and 0, Fig. 6. For the higher

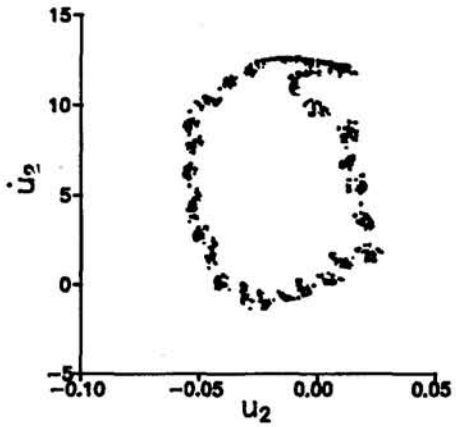


Fig. 7 The Poincaré map for U_v = 100, δ_s = 25, and ϵ_y = 0.15D

friction, the second Hopf bifurcation occurs at a higher value of ϵ_y, and the periodic window is larger. This shows that, for the current problem, friction has two effects: suppressing Mode 2 and increasing the nonlinear effects. For a higher value of U_v, the tube motion approaches chaos. Figure 7 shows a Poincaré map for the following condition: $U_v = 100$, $\delta_s = 25$, and $\epsilon_y = 0.015D$. All three tubes contact the support, and the motion approaches chaos.

The above bifurcations, however, only occur when the contact is two-sided. If the equilibrium position of the tube is also displaced in the x-direction, the contact becomes one-sided, and Mode 2 disappears. In Fig. 8, ϵ_x is varied while ϵ_y is fixed at $0.03D$ for $U_v = 80$ and $\delta_s = 25$. For small values of ϵ_x, the contact is two-sided and bifurcations occur. For large values of ϵ_x, the contact becomes one-sided, and the motion becomes a period 2.

4.3 Effects of Chaos on Wear Between Tubes and Support Plates. An important aspect of chaotic vibration is its effect on wear. Because chaotic motion for the system under consideration often requires two modes of vibration and strong interaction between the tube and the support, high wear rate can be induced. The time histories of contact forces and wear rates for different values of ϵ_y with $U_v = 80$ and $\delta_s = 25$ are studied; Fig. 9 shows the case of ϵ_y equal to $0.01D$, $0.0175D$, and $0.03D$. Wear rate is proportional to work rate, which is defined as

$$\text{work rate} = \text{contact force} \times \text{sliding speed}.$$

For small $\epsilon_y = 0.01D$, the motion is periodic, with tubes contacting the support regularly but with very little sliding. As ϵ_y is increased to $0.0175D$, quasi-periodic motion occurs, and wear rate increase dramatically. When ϵ_y is increased, wear rate increases as Mode 2 becomes stronger.

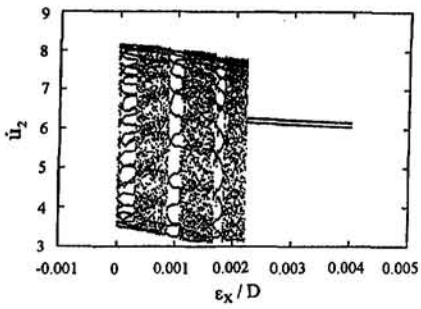


Fig. 8 Bifurcation diagram with ϵ_x as the control parameter and ϵ_y = 0.03D

Downloaded 04 May 2010 to 171.66.16.33. Redistribution subject to ASME license or copyright; see http://www.asme.org/terms/Terms_Use.cfm

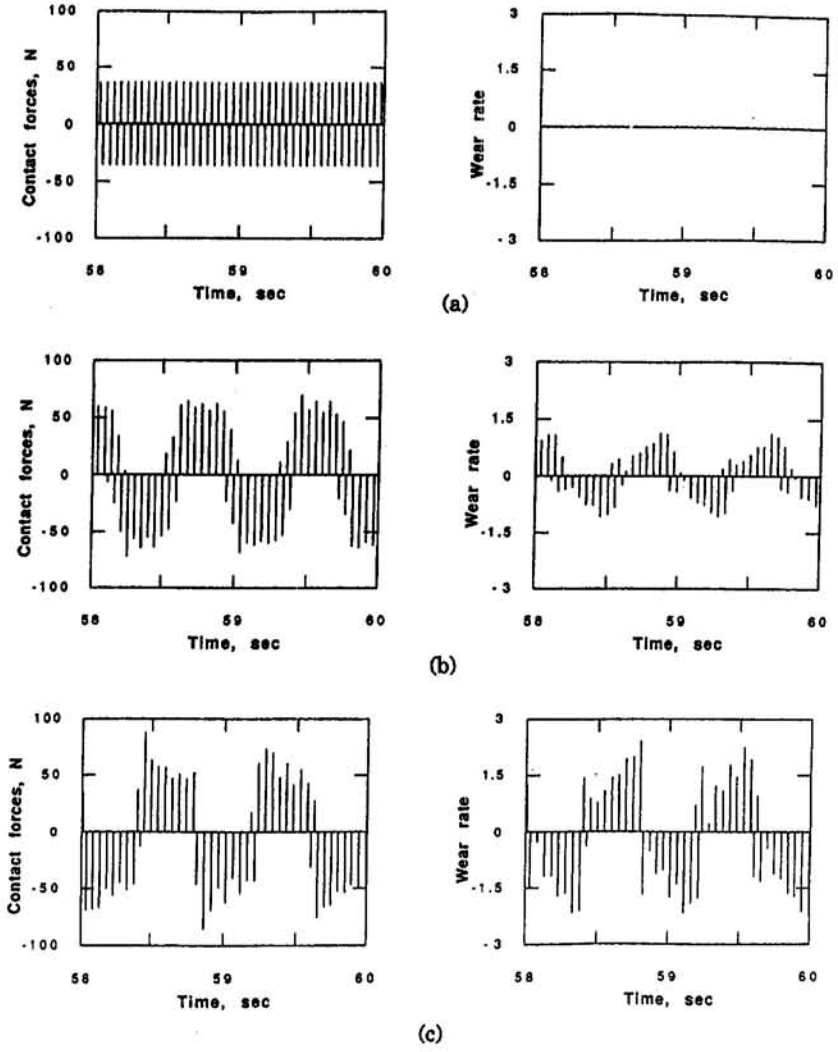


Fig. 9 Contact forces and wear rates for $U_r = 80$, $\mu = 0.1$ and (a) $\epsilon_y = 0.01D$; (b) $\epsilon_y = 0.175D$; (c) $\epsilon_y = 0.03D$

5 Closing Remarks

We have analyzed the motions of a row of loosely supported tubes in crossflow, with an emphasis on chaotic vibration associated with stiffness-controlled instability of loosely supported tubes on the basis of the unsteady flow theory. The purpose of this study is to gain an understanding of the possible cause of chaos and to estimate the effects of chaos on wear.

Based on the unsteady flow theory, the motions of a row of loosely supported tubes in crossflow has been analyzed with an emphasis on the bifurcation phenomenon and chaotic vibration. It was demonstrated that if the instability mechanisms are sufficiently strong, the tube motion can become chaotic after the system undergoes double Hopf bifurcations. If the openings are circular and the tubes are displaced in the drag direction, chaotic motion can occur more easily.

Currently, most mathematical models concentrate on the prediction of the first Hopf bifurcation. However, the prediction of the second Hopf bifurcation is also important because a quasi-periodic motion can produce significant sliding. It has been found that the onset of the quasi-periodic motion is dependent on the friction at the contacts, the equilibrium positions of the tubes, and even the stiffness of the contacts.

The type of motion discussed in this paper is generated by a strong-spring system. The possibility of creating multiple equilibrium points in the heat exchanger system should also be discussed. This is because the chaotic motion caused by successive period-doublings is much more pronounced.

In this study, the model considered consists of rigid tubes supported by springs. In practical cases, they are elastic tubes with multiple loose supports. The system considered in this paper is a simple model to illustrate the characteristics in the unstable region for fluid-stiffness-controlled instability. For fluid-damping-controlled instability, experimental data and analytical results for a tube row agree well (Chen, Zhu, and Cai, 1995). The distribution of chaotic region for fluid-damping-controlled instability of a loosely supported elastic tube in a tube row is different from fluid-stiffness-controlled instability of the simple model presented in this paper. It is expected that because they are nonlinear systems, detailed characteristics of the simple model of rigid tubes and practical models of elastic tubes with multiple supports are not necessarily the same. However, the general approach presented in this paper can be applied to practical cases based on the unsteady flow theory.

Another parameter in the practical cases is the turbulence excitation which always exists. In general, its effects are not significant in the subcritical region. However, the interaction of turbulence and fluid-elastic instability cannot be neglected in some cases. For example, the hysteresis effect of the critical flow velocity has been demonstrated in the experiment (Chen, Zhu, and Cai, 1995). Its effect on chaotic basins might be

Downloaded 04 May 2010 to 171.66.16.33. Redistribution subject to ASME license or copyright; see http://www.asme.org/terms/Terms_Use.cfm

significant. This problem has not yet been studied. It is expected that chaotic vibration of loosely supported tubes will be continue to receive attention because of its academic interest and practical applications in heat exchangers and steam generators.

Acknowledgments

This work was sponsored by the U.S. Department of Energy, Office of Basic Energy Science, Division of Engineering and Geosciences, under Contract W-31-109-Eng-38.

References

Antunes, J., de Langre, E., Vento, M. A., and Axisa, F. 1992, "A Theoretical Model for the Vibro-Impact Motions of Tube Bundles Under Fluidelastic Instability," ASME, PVP-Vol. 242, pp. 135–150.

Axisa, F., Antunes, J., and Villard, B., 1988, "Overview of Numerical Methods for Predicting Flow-Induced Vibration," ASME *J. Pressure Vessel Technol.*, Vol. 110, pp. 6–14.

Cai, Y., and Chen, S. S., 1993a, "Nonlinear Dynamics of Loosely Supported Tubes in Crossflow," *J. Sound Vib.*, Vol. 168, pp. 449–468.

Cai, Y., and Chen, S. S., 1993b, "Chaotic Vibrations of Nonlinearly Supported Tubes in Crossflow," ASME *J. Pressure Vessel Technol.*, Vol. 115, pp. 129–134.

Chen, S. S., 1983, "Instability Mechanisms and Stability Criteria of a Group of Circular Cylinders Subjected to Cross-Flow. Part 1: Theory; Part 2: Numerical Results and Discussions," ASME *J. Vibration, Acoustics, Stress, and Reliability in Design*, Vol. 105, pp. 51–58; 253–260.

Chen, S. S., 1987, "A General Theory for Dynamic Instability of Tube Arrays in Crossflow," *J. Fluids and Structures*, Vol. 1, pp. 35–53.

Chen, S. S., 1989, "Some Issues Concerning Fluid-Elastic Instability of a Group of Circular Cylinders in Cross-Flow," ASME *J. Pressure Vessel Technol.*, Vol. 111, pp. 507–518.

Chen, S. S., and Chandra, S., 1991, "Fluidelastic Instabilities in Tube Bundles Exposed to Nonuniform Cross-Flow," *J. Fluids and Structures*, Vol. 5, pp. 299–322.

Chen, S. S., Zhu, S., and Cai, Y., 1995, "Experiment of Chaotic Vibration of Loosely Supported Tube Arrays in Crossflow," ASME *J. Pressure Vessel Technol.*, Vol. 117, pp. 204–212.

Chen, S. S., Zhu, S., and Jendrzejczyk, J. A., 1994, "Fluid Damping and Fluid Stiffness of a Tube Row in Crossflow," ASME *J. Pressure Vessel Technol.*, Vol. 116, pp. 370–383.

Fricker, A. J., 1992, "Numerical Analysis of the Fluidelastic Vibration of a Steam Generator Tube with Loose Supports," *J. Fluids and Structures*, Vol. 6, pp. 85–107.

Ko, P. L., and Basista, H., 1984, "Correlation of Support Impact Force and Fretting-Wear for a Heat Exchanger Tube," ASME *J. Pressure Vessel Technol.*, Vol. 106, pp. 69–77.

de Langre, E., Hadj-Sadok, C., and Beaufils, B., 1992, "Non-Linear Vibrations Induced by Fluidelastic Forces in Tube Bundles," ASME, PVP-Vol. 242, pp. 107–134.

Munteau, G. C., and Moon, F. C., 1992, "Multifractals in Flow-Induced Vibrations," *Proc. 10th Symp. on Energy Engineering Sciences*, Argonne National Laboratory, pp. 226–232.

Paidoussis, M. P., and Li, G. X., 1992, "Cross-Flow-Induced Chaotic Vibrations of Heat-Exchanger Tubes Impacting on Loose Supports," *J. Sound and Vibration*, Vol. 152, No. 2, pp. 305–326.

Tanaka, M., 1980, "Study on Fluidelastic Vibrations of Tube Bundle," *Japan Society Mechanical Engineering, Trans.*, Section B, Vol. 46, No. 408, pp. 1398–1407.

Vento, M. A., Antunes, J., and Axisa, F., 1992, "Tube/support Interaction under Simulated Fluidelastic Instability: Two-Dimensional Experiments and Computations of the Nonlinear Response of a Straight Tube," ASME, PVP-Vol. 242, pp. 151–166.

Downloaded 04 May 2010 to 171.66.16.33. Redistribution subject to ASME license or copyright; see http://www.asme.org/terms/Terms_Use.cfm

Exact Stationary Solutions of Stochastically Excited and Dissipated Integrable Hamiltonian Systems

W. Q. Zhu
Professor.

Y. Q. Yang
Graduate Student.

Department of Mechanics,
Zhejiang University,
Hangzhou 310027,
P. R. China

It is shown that the structure and property of the exact stationary solution of a stochastically excited and dissipated n*-degree-of-freedom Hamiltonian system depend upon the integrability and resonant property of the Hamiltonian system modified by the Wong-Zakai correct terms. For a stochastically excited and dissipated nonintegrable Hamiltonian system, the exact stationary solution is a functional of the Hamiltonian and has the property of equipartition of energy. For a stochastically excited and dissipated integrable Hamiltonian system, the exact stationary solution is a functional of* n *independent integrals of motion or* n *action variables of the modified Hamiltonian system in nonresonant case, or a functional of both* n *action variables and* α *combinations of phase angles in resonant case with* α $(1 \leq \alpha \leq n - 1)$ *resonant relations, and has the property that the partition of the energy among* n *degrees-of-freedom can be adjusted by the magnitudes and distributions of dampings and stochastic excitations. All the exact stationary solutions obtained to date for nonlinear stochastic systems are those for stochastically excited and dissipated nonintegrable Hamiltonian systems, which are further generalized to account for the modification of the Hamiltonian by Wong-Zakai correct terms. Procedures to obtain the exact stationary solutions of stochastically excited and dissipated integrable Hamiltonian systems in both resonant and nonresonant cases are proposed and the conditions for such solutions to exist are deduced. The above procedures and results are further extended to a more general class of systems, which include the stochastically excited and dissipated Hamiltonian systems as special cases. Examples are given to illustrate the applications of the procedures.*

1 Introduction

It is well known that the response of a dynamic system to Gaussian white noise excitations is a diffusion process, and the transition probability density of the response process is governed by the Fokker-Planck-Kolmogorov (FPK) equation. Deriving and solving the FPK equation under appropriate boundary conditions and initial condition constitute the ideal way of obtaining exact solutions for such problems. This is the only way to obtain exact solutions for stochastically excited nonlinear dynamic systems.

Exact solutions are usually very difficult to obtain for nonlinear stochastic systems. Exact solutions for FPK equations are known only for very special first-order nonlinear systems (Caughey, 1971). For second and higher order nonlinear stochastic systems, solutions have been obtained only for the reduced FPK equations, namely, FPK equations without the time-derivative term. The solution of a reduced FPK equation is the stationary probability density of the response when the system reaches statistical stationarity after it is exposed to stationary excitations for a sufficiently long time. Much effort has been made to find the exact stationary solutions of various nonlinear stochastic systems. The early results can be found in a survey paper by Fuller (1969). In the last decade, a great progress has been achieved (Cai and Lin, 1988; Caughey and Ma, 1982a, b; Dimentberg, 1982; Lin and Cai, 1988; Soize, 1988, 1991; Zhu, 1990; Zhu, Cai and Lin, 1990, 1992). The most general results are those obtained by Zhu, Cai, and Lin (1990, 1992) for stochastically excited and dissipated Hamiltonian systems, i.e., for multi-degree-of-freedom nonlinear Hamiltonian systems subject to linear and (or) nonlinear damplings, and external (additive) and (or) parametric (multiplicative) excitations of Gaussian white noises.

All the exact stationary solutions obtained to date for multi-degree-of-freedom nonlinear stochastic systems are closely related to the Maxwell-Boltzmann distribution which belongs to classical statistical mechanics (Fuller, 1969). They have the property known as the equipartition of energy among various degrees of freedom. For a stochastically excited and dissipated Hamiltonian system, this property is manifested by that the stationary probability density is a functional of the Hamiltonian. For a multi-degree-of-freedom linear system subjected to external excitations of Gaussian white noises, on the other hand, the response has Gaussian distribution and the partition of the energy among various degrees-of-freedom can be adjusted by the magnitudes and distributions of the dampings and stochastic excitations (Wang and Ulenbeck, 1945). The inconsistency between these two kinds of solutions has been noted for many years and it has been a desire for a long time to find the reason for this inconsistency and to obtain the exact stationary solutions for multi-degree-of-freedom nonlinear stochastic systems which are consistent with those for multi-degree-of-freedom linear systems subject to external excitations of Gaussian white noises.

In the present paper the exact stationary solutions of stochastically excited and dissipated integrable Hamiltonian systems

Contributed by the Applied Mechanics Division of THE AMERICAN SOCIETY OF MECHANICAL ENGINEERS for publication in the ASME JOURNAL OF APPLIED MECHANICS.

Discussion on this paper should be addressed to the Technical Editor, Professor Lewis T. Wheeler, Department of Mechanical Engineering, University of Houston, Houston, TX 77204-4792, and will be accepted until four months after final publication of the paper itself in the ASME JOURNAL OF APPLIED MECHANICS.

Manuscript received by the ASME Applied Mechanics Division, Feb. 8, 1995; final revision, May 10, 1995. Associate Technical Editor: S. W. Shaw.

Copyright © 1996 by ASME

Downloaded 04 May 2010 to 171.66.16.33. Redistribution subject to ASME license or copyright; see http://www.asme.org/terms/Terms_Use.cfm

are investigated. First, the concepts of integrable Hamiltonian system and resonant and nonresonant systems are briefly reviewed and it is argued that for an n-degree-of-freedom integrable Hamiltonian system, if a function of state variables is in involution with the Hamiltonian, it is generally a functional of n independent integrals of motion or of n action variables in nonresonant case, or a functional of both n action variables and α combinations of phase angles in resonant case with α resonant relations. Based on this argument, it is shown that the exact stationary solution of a stochastically excited and dissipated integrable Hamiltonian system with n-degree-of-freedom is a functional of n-independent integrals of motion or of n action variables in nonresonant case, or a functional of both n action variables and α combinations of phase angles in resonant case with α resonant relations, which satisfies the conditions of vanishing probability potential flows in n directions. This solution has the property that the partition of energy among various degrees-of-freedom can be adjusted by the magnitudes and distributions of dampings and stochastic excitations and is consistent with those for linear systems subject to external excitations of Gaussian white noises. Procedures are then proposed to obtain the exact stationary solutions for stochastically excited and dissipated integrable Hamiltonian systems in both nonresonant and resonant cases and the conditions for such solutions to exist are deduced. The procedures are further extended to a more general class of systems, which include the stochastically excited and dissipated integrable Hamiltonian systems as special cases. Finally, three examples are given to illustrate the applications of the procedures, and the structure and existing conditions of the exact stationary solutions of stochastically excited and dissipated integrable Hamiltonian systems.

2 Integrable Hamiltonian Systems

Consider an n-degree-of-freedom Hamiltonian system governed by the following n pairs of Hamiltonian equations of motion

$$\dot{q}_i = \frac{\partial H}{\partial p_i} \tag{1a}$$

$$\dot{p}_i = -\frac{\partial H}{\partial q_i} \tag{1b}$$

$$i = 1, 2, \ldots, n$$

where q_i and p_i are generalized displacements and momenta, respectively; $H = H(\mathbf{q}, \mathbf{p})$ is a Hamiltonian with continuous first-order derivatives. A Hamiltonian system of n degree-of-freedom is said to be integrable or completely integrable if there exist n independent integrals of motion, $H_1, H_2, \ldots, H_n$, with say $H_1 = H$, which are in involution. This last term means that the H_i all commute with each other, i.e.,

$$[H_i, H_j] = 0 \tag{2}$$

$$i, j = 1, 2, \ldots, n$$

where

$$[H_i, H_j] = \frac{\partial H_i}{\partial p_k}\frac{\partial H_j}{\partial q_k} - \frac{\partial H_i}{\partial q_k}\frac{\partial H_j}{\partial p_k} \tag{3}$$

$$k = 1, 2, \ldots, n$$

is the Poisson bracket of H_i and H_j.

The integrability of a Hamiltonian system can also be stated as follows. A Hamiltonian system of n-degree-of-freedom governed by Eqs. (1a) and (1b) is said to be integrable or completely integrable if there exists a set of canonical transformations

$$I_i = I_i(\mathbf{q}, \mathbf{p}) \tag{4a}$$

$$\theta_i = \theta_i(\mathbf{q}, \mathbf{p}) \tag{4b}$$

$$i = 1, 2, \ldots, n$$

such that the new Hamiltonian equations of motion are of the following canonical form

$$\dot{I}_i = -\frac{\partial}{\partial \theta_i} H'(\mathbf{I}) = 0 \tag{5a}$$

$$\dot{\theta}_i = \frac{\partial}{\partial I_i} H'(\mathbf{I}) = \omega_i(\mathbf{I}) \tag{5b}$$

$$i = 1, 2, \ldots, n$$

where I_i and ω_i are action variables and frequencies associated with each degree-of-freedom, respectively; θ_i are the angle variables conjugate to I_i; $H' = H'(\mathbf{I})$ is the transformed Hamiltonian independent of θ_i. Equations (5a) and (5b) are then trivially integrated to yield

$$I_i = \text{const.} \tag{6a}$$

$$\theta_i = \omega_i(\mathbf{I})t + \delta_i \tag{6b}$$

$$i = 1, 2, \ldots, n$$

where δ_i are some arbitrary constants. Note that the set of $I_1, \ldots, I_n, \delta_1, \ldots, \delta_n$ constitute the set of $2n$ constants of integration. I_i are a set of such special constants that once they are known, the other set of constants δ_i can be obtained immediately. Thus, I_i can be regarded as n-independent integrals of motion which satisfy Eq. (2), i.e.,

$$[I_i, I_j] = 0 \tag{7}$$

$$i, j = 1, 2, \ldots, n.$$

The phase-space orbits of an n-degree-of-freedom integrable Hamiltonian system will lie on an n-dimensional torus. If the frequencies ω_i are not rationally related, the orbits on the torus with that set of frequencies are almost periodic and the system is termed nonresonant. The orbits on the torus will be periodic or closed and the system is called completely resonant if the frequencies ω_i are related by $n - 1$ equations of the following form

$$k_i^u \omega_i = 0 \tag{8}$$

$$u = 1, 2, \ldots, n-1; \quad i = 1, 2, \ldots, n$$

where k_i^u are integers and not all zeros for a fixed u. Obviously, the n frequencies ω_i of an integrable Hamiltonian system may satisfy α ($1 \le \alpha < n - 1$) resonant relations of the form of Eq. (8). In this case, the orbits are periodic on some subtorus and almost periodic on the complementary subtorus, and the system is termed partially resonant.

An integrable Hamiltonian system is termed nondegenerate if the condition

$$\det \left| \frac{\partial \omega_i(\mathbf{I})}{\partial I_j} \right| = \det \left| \frac{\partial^2 H(\mathbf{I})}{\partial I_i \partial I_j} \right| \neq 0 \tag{9}$$

is satisfied. This ensures that the frequencies vary from torus to torus and the system is nonlinear. On a given energy shell, some tori will be completely or partially covered by periodic orbits, whereas other tori will be covered by almost periodic orbits. For a nondegenerate system, the set of tori completely or partially covered by periodic orbits, although dense, will be infinitely outnumbered by the tori covered by almost periodic orbits. Thus, for a random vibration analysis purpose a nondegenerate system can be regarded as a nonresonant system.

Downloaded 04 May 2010 to 171.66.16.33. Redistribution subject to ASME license or copyright; see http://www.asme.org/terms/Terms_Use.cfm

Using the Poisson bracket, the following three conclusions can be drawn. They form the basis of constructing the exact stationary solutions of stochastically excited and dissipated integrable and nonintegrable Hamiltonian systems.

1 For an integrable Hamiltonian system of n degree-of-freedom, it can be readily shown that for a function F of state variables, if it is a functional of H_i, i.e., $F = F(H_1, H_2, \ldots, H_n)$, then it is in involution with the Hamiltonian, i.e.,

$$[F, H] = 0. \tag{10}$$

In fact,

$$\begin{aligned}[F, H] &= \frac{\partial F}{\partial p_k}\frac{\partial H}{\partial q_k} - \frac{\partial F}{\partial q_k}\frac{\partial H}{\partial p_k} \\ &= \frac{\partial F}{\partial H_l}\left(\frac{\partial H_l}{\partial p_k}\frac{\partial H}{\partial q_k} - \frac{\partial H_l}{\partial q_k}\frac{\partial H}{\partial p_k}\right) \\ &= 0.\end{aligned}$$

Conversely, for a functional F of state variables, if it satisfies Eq. (10), then it can be any functional of H_i, i.e., $F = F(H_1, H_2, \ldots, H_n)$.

2 For a functional G of action variables I_i and angle variables θ_i of an integrable Hamiltonian system with Hamiltonian H, the Poisson bracket of G and H is

$$\begin{aligned}[G, H] &= \frac{\partial G}{\partial I_i}\frac{\partial H}{\partial \theta_i} - \frac{\partial G}{\partial \theta_i}\frac{\partial H}{\partial I_i} \\ &= -\omega_i \frac{\partial G}{\partial \theta_i}.\end{aligned} \tag{11}$$

It can be shown in a similar way that for a nonresonant system, if G is in involution with H, i.e.,

$$[G, H] = 0 \tag{12}$$

then G can be any functional of I_i, i.e., $G = G(\mathbf{I})$. For a resonant system with α resonant relations of the form of Eq. (8), if Eq. (12) is satisfied, then G can be any functional of both I_i and $\psi_u = k_i^u \theta_i$ $(u = 1, 2, \ldots, \alpha)$, i.e., $G = G(\mathbf{I}_1, \ldots, \mathbf{I}_n; \psi_1, \ldots, \psi_\alpha)$.

3 For a nonintegrable or completely nonintegrable Hamiltonian system of n-degree-of-freedom, the Hamiltonian H is the only independent integral of motion. In this case, if Eq. (10) is satisfied, then F can be any functional of H.

It is believed that both (completely) integrable systems and (completely) nonintegrable systems are two extremely special cases among general dynamic systems. To date, there is no general procedure to judge whether a given Hamiltonian system is integrable or not. One way to find the canonical transformations in Eqs. (4a) and (4b) for a given Hamiltonian system is to solve the Hamilton-Jacobi equation associated with the system. This equation, however, is very difficult to solve except for a class of mechanical systems known as being separable. A rather simple subclass of the separable systems is one in which the Hamiltonian itself is the sum of n independent parts of the form

$$H(\mathbf{q}, \mathbf{p}) = \sum_{k=1}^{n} H_k(q_k, p_k). \tag{13}$$

In this case, action variables can be obtained in the same way as for single-degree-of-freedom Hamiltonian systems. For more information on the integrability of Hamiltonian systems see Arnold (1989) and Tabor (1989).

3 Reduced FPK Equation for Stochastically Excited and Dissipated Hamiltonian Systems

Consider a stochastically excited and dissipated Hamiltonian system of n-degree-of-freedom governed by the following equations of motion:

$$\dot{Q}_i = \frac{\partial H'}{\partial P_i} \tag{14a}$$

$$\dot{P}_i = -\frac{\partial H'}{\partial Q_i} - c_{ij}\frac{\partial H'}{\partial P_j} + f_{ik}W_k(t) \tag{14b}$$

$$i, j = 1, 2, \ldots, n; \quad k = 1, 2, \ldots, m$$

where Q_i and P_i are generalized displacements and generalized momenta, respectively; $H' = H'(\mathbf{Q}, \mathbf{P})$ is twice differentiable Hamiltonian; $c_{ij} = c_{ij}(\mathbf{Q}, \mathbf{P})$ are differentiable functions; $f_{ik} = f_{ik}(\mathbf{Q}, \mathbf{P})$ are twice differentiable functions; $W_k(t)$ are Gaussian white noises in the sense of Stratonovich with correlation functions

$$E[W_k(t)W_l(t + \tau)] = 2D_{kl}\delta(\tau) \tag{15}$$

$$k, l = 1, 2, \ldots, m.$$

The system governed by Eqs. (14a) and (14b) is generally nonlinear. The first summation terms on the right-hand side of Eq. (14b) may represent a set of linear and (or) nonlinear damping mechanisms, while the second summation terms may include external (additive) and (or) parametric (multiplicative) excitations of Gaussian white noises.

Equations (14a) and (14b) are equivalent to the following set of Itô stochastic differential equations

$$dQ_i = \frac{\partial H'}{\partial P_i}dt \tag{16a}$$

$$dP_i = \left(-\frac{\partial H'}{\partial Q_i} - c_{ij}\frac{\partial H'}{\partial P_j} + D_{kl}f_{jl}\frac{\partial f_{ik}}{\partial P_j}\right)dt + f_{ik}dB_k(t) \tag{16b}$$

$$i, j = 1, 2, \ldots, n; \quad k, l = 1, 2, \ldots, m$$

where $B_k(t)$ are the Wiener processes. The double summation terms on the right-hand side of Eq. (16b) are known as the Wong-Zakai correct terms (Wong and Zakai, 1965). These terms usually can be splitted into two parts: one has the effect of modifying the conservative forces and the other modifying the damping forces. The first part can be combined with $-\partial H'/\partial Q_i$ to form an overall effective conservative forces—$\partial H/\partial Q_i$ with a new Hamiltonian $H = H(\mathbf{Q}, \mathbf{P})$ and with $\partial H/\partial P_i = \partial H'/\partial P_i$. The second part may be combined with $-c_{ij}\partial H'/\partial P_j$ to constitute an effective damping forces—$m_{ij}\partial H/\partial P_j$ with $m_{ij} = m_{ij}(\mathbf{Q}, \mathbf{P})$. With these accomplished, Eqs. (16a) and (16b) can be rewritten as

$$dQ_i = \frac{\partial H}{\partial P_i}dt \tag{17a}$$

$$dP_i = -\left(\frac{\partial H}{\partial Q_i} + m_{ij}\frac{\partial H}{\partial P_j}\right)dt + f_{ik}dB_k(t) \tag{17b}$$

$$i, j = 1, 2, \ldots, n; \quad k = 1, 2, \ldots, m.$$

The reduced FPK equation governing the stationary probability density $p = p(\mathbf{q}, \mathbf{p})$ associated with Itô equations (17a) and (17b) is

$$-\frac{\partial}{\partial q_i}\left(\frac{\partial H}{\partial p_i}p\right) + \frac{\partial}{\partial p_i}\left(\frac{\partial H}{\partial q_i}p\right) + \frac{\partial}{\partial p_i}\left(m_{ij}\frac{\partial H}{\partial p_j}p\right) + \frac{1}{2}\frac{\partial^2}{\partial p_i \partial p_j}(b_{ij}p) = 0 \tag{18}$$

where $b_{ij} = 2(\mathbf{f}\mathbf{D}\mathbf{f}^{\mathrm{T}})_{ij}$ are diffusion coefficients with $\mathbf{f} = [f_{ik}]$ and $\mathbf{D} = [D_{kl}]$. The first two terms on the left-hand side of Eq. (18) are associated with circulatory probability flow with the remaining two terms with potential probability flow. Reduced

Downloaded 04 May 2010 to 171.66.16.33. Redistribution subject to ASME license or copyright; see http://www.asme.org/terms/Terms_Use.cfm

FPK Eq. (18) is solved subject to the following boundary conditions:

$$\frac{\partial H}{\partial p_i} p = 0 \tag{19a}$$

$$\left(\frac{\partial H}{\partial q_i} + m_{ij} \frac{\partial H}{\partial p_j}\right) p + \frac{1}{2} \frac{\partial}{\partial p_j} (b_{ij} p) = 0 \qquad (\mathbf{q}, \mathbf{p}) \in S \tag{19b}$$

$$i, j = 1, 2, \ldots, n$$

where S denotes boundaries. Usually the boundaries are at infinite, i.e., $|\mathbf{q}| + |\mathbf{p}| \to \infty$. Eqs. (19$a$) and (19$b$) imply vanishing probability flow at the boundaries.

Note that the first two terms on the left-hand side of Eq. (18) are the Poisson bracket of p and H, i.e.,

$$-\frac{\partial}{\partial q_i}\left(\frac{\partial H}{\partial p_i} p\right) + \frac{\partial}{\partial p_i}\left(\frac{\partial H}{\partial q_i} p\right) = -\frac{\partial p}{\partial q_i}\frac{\partial H}{\partial p_i} + \frac{\partial p}{\partial p_i}\frac{\partial H}{\partial q_i} = [p, H]. \tag{20}$$

Thus, Eq. (18) can be rewritten as

$$[p, H] + \frac{\partial}{\partial p_i}\left(m_{ij}\frac{\partial H}{\partial p_j} p\right) + \frac{1}{2}\frac{\partial^2}{\partial p_i \partial p_j}(b_{ij} p) = 0. \tag{21}$$

Let (Cai and Lin, 1988)

$$b_{ij} = b_{ij}^{(i)} + b_{ji}^{(j)}. \tag{22}$$

Then Eq. (21) can also be written as

$$[p, H] + \frac{\partial}{\partial p_i}\left(m_{ij}\frac{\partial H}{\partial p_j} p\right) + \frac{\partial^2}{\partial p_i \partial p_j}(b_{ij}^{(i)} p) = 0. \tag{23}$$

Note that the splitting of the diffusion coefficients in Eq. (22) retains the symmetry condition $b_{ij} = b_{ji}$.

4 Exact Stationary Solutions of Stochastically Excited and Dissipated Nonintegrable Hamiltonian Systems

Suppose that the Hamiltonian system with Hamiltonian H governed by Eqs. (17a) and (17b) without damping and stochastic excitation terms is nonintegrable. The terms in the square bracket (i.e., Poisson bracket) in Eq. (21) or (23) are the terms which would remain if the damping forces and stochastic excitations were removed from the system governed by Eqs. (17a) and (17b), i.e., the system was conservative. It has been shown in Section 2 that, for a nonintegrable Hamiltonian system, these terms cancel if p is a functional of H. Therefore, if we can find a particular such functional $p(H)$ which makes the remaining two terms in Eq. (21) or (23) vanish, we shall have found a solution of Eq. (21) or (23).

To ensure nonnegativeness of the stationary probability density p and to satisfy the natural boundary conditions in Eqs. (19a) and (19b), the solution of Eq. (21) or (23) is assumed of the form

$$p(\mathbf{q}, \mathbf{p}) = C \exp[-\varphi(H)]|_{H=H(\mathbf{q},\mathbf{p})} \tag{24}$$

where C is a normalization constant and φ is a functional to be determined. Substituting Eq. (24) into Eq. (23) and taking account of boundary conditions in Eqs. (19a) and (19b) lead to

$$m_{ij}\frac{\partial H}{\partial p_j} + \frac{\partial b_{ij}^{(i)}}{\partial p_j} - b_{ij}^{(i)}\frac{\partial H}{\partial p_j}\frac{d\varphi}{dH} = 0 \tag{25}$$

$$i = 1, 2, \ldots, n.$$

These are a set of n first-order linear ordinary differential equations for $\varphi = \varphi(H)$ and they represent vanishing potential probability flows in the n directions. To find a consistent functional $\varphi(H)$ satisfying all these n equations, certain restrictions must be imposed on the parameters of the damping and the stochastic excitations, as discussed below.

(i) If $c_{ij}(\mathbf{Q}, \mathbf{P}) = f(H)\bar{c}_{ij}(\mathbf{Q})$ and $f_{ik}(\mathbf{Q}, \mathbf{P}) = g(H)\bar{f}_{ik}(\mathbf{Q})$, then the Wong-Zakai correct terms are of the similar form as damping terms and contain no conservative force part. In this case, $H = H'$. Further, if the damping coefficients and stochastic excitation intensities satisfy the conditions $\bar{c}_{ij} = \bar{c}_{ji} = \eta\bar{b}_{ij}/2$, where $\bar{b}_{ij} = 2(\bar{f}\bar{D}\bar{f}^T)$, then the exact stationary solution to Eqs. (14a) and (14b) is

$$p(\mathbf{q}, \mathbf{p}) = Cg^{-1}(H)\exp\left[-\eta\int_0^H \frac{f(u)}{g^2(u)}\,du\right]\Bigg|_{H=H(\mathbf{q},\mathbf{p})} \tag{26}$$

which has been obtained previously by Zhu, Cai, and Lin (1990, 1992).

(ii) More generally, if damping coefficients c_{ij} and stochastic excitation intensities f_{ik} are functions of both $\mathbf{Q}$ and $\mathbf{P}$ and satisfy the following conditions

$$\frac{m_{ij}\dfrac{\partial H}{\partial p_j} + \dfrac{\partial b_{ij}^{(i)}}{\partial p_j}}{b_{ij}^{(i)}\dfrac{\partial H}{\partial p_j}} = h(H) \tag{27}$$

$$i = 1, 2, \ldots, n$$

then the exact stationary solution to Eqs. (14a) and (14b) is

$$p(\mathbf{q}, \mathbf{p}) = C\exp\left[-\int_0^H h(u)du\right]\Bigg|_{H=H(\mathbf{q},\mathbf{p})} \tag{28}$$

Note that in this case H is generally different from H'.

5 Exact Stationary Solutions of Stochastically Excited and Dissipated Integrable Hamiltonian Systems

Now suppose that the Hamiltonian system with Hamiltonian H governed by Eqs. (17a) and (17b) without damping and stochastic excitation terms is integrable and nonresonant and has n independent integrals of motion, $H_1, H_2, \ldots, H_n$. Based on the argument in Section 2, if p is a functional of $H_1, H_2, \ldots, H_n$, then the Poisson bracket in Eq. (21) or (23) vanishes. Thus, if we can find such a particular functional that makes the remaining two terms in Eq. (21) or (23) vanish, we shall have found a solution of Eq. (21) or (23).

Taking account of the non-negativeness of p and the boundary conditions in Eqs. (19a) and (19b), the solution of Eq. (21) or (23) in this case is assumed of the form

$$p(\mathbf{q}, \mathbf{p}) = C\exp[-\varphi(H_1, H_2, \ldots, H_n)]|_{H_k=H_k(\mathbf{q},\mathbf{p})} \tag{29}$$

where C is a normalization constant and φ is a functional to be determined. Substituting Eq. (29) into Eq. (23) and taking account of boundary conditions (19a) and (19b) lead to

$$m_{ij}\frac{\partial H}{\partial p_j} + \frac{\partial}{\partial p_j} b_{ij}^{(i)} - b_{ij}^{(i)}\frac{\partial H_l}{\partial p_j}\frac{\partial \varphi}{\partial H_l} = 0 \tag{30}$$

$$i = 1, 2, \ldots, n; \quad j, l = 1, 2, \ldots, n$$

Downloaded 04 May 2010 to 171.66.16.33. Redistribution subject to ASME license or copyright; see http://www.asme.org/terms/Terms_Use.cfm

which are a set of n first-order linear partial differential equations for φ and they represent vanishing potential probability flows in n directions. Equation (30) can be rewritten as

$$a_{il}\frac{\partial \varphi}{\partial H_l} = d_i \tag{31}$$

$$i = 1, 2, \ldots, n$$

where

$$a_{il} = b_{ij}^{(i)}\frac{\partial H_l}{\partial p_j} \tag{32a}$$

$$d_i = m_{ij}\frac{\partial H}{\partial p_j} + \frac{\partial}{\partial p_j}b_{ij}^{(i)}. \tag{32b}$$

If $\partial\varphi/\partial H_l\,(l = 1, 2, \ldots, n)$ can be obtained from Eq. (31) (this is the case when matrix $A = [a_{il}]$ is nonsingular) as functional of H_k $(k = 1, 2, \ldots, n)$ and satisfy the following compatibility conditions

$$\frac{\partial^2 \varphi}{\partial H_l \partial H_k} = \frac{\partial^2 \varphi}{\partial H_k \partial H_l} \tag{33}$$

$$k, l = 1, 2, \ldots, n,$$

then the solution of Eq. (31) is

$$\varphi = \varphi_0 + \int_0^{(H_1, H_2, \ldots, H_n)} \frac{\partial \varphi}{\partial H_1}\, dH_1 \tag{34}$$

where $\varphi_0 = \varphi(0, 0, \ldots, 0)$, the second term on the right-hand side is a line integral and the integrand is a summation over $l = 1, 2, \ldots, n$. The exact stationary probability density of the system governed by Eqs. (14a) and (14b) is obtained by substituting Eq. (34) into Eq. (29).

As another alternative, suppose that the action-angle variables I_k and θ_k for the modified Hamiltonian system with Hamiltonian H governed by Eqs. (17a) and (17b) without damping and stochastic excitation terms are obtainable. Then, following a similar procedure, we can obtain the exact stationary solution of the system governed by Eqs. (14a) and (14b) when the modified Hamiltonian system with Hamiltonian H is nonresonant. Instead of Eq. (29), the solution is of the form

$$p(\mathbf{q}, \mathbf{p}) = C \exp[-\lambda(I_1, I_2, \ldots, I_n)]_{I_k = I_k(\mathbf{q},\mathbf{p})} \tag{35}$$

where $\lambda(\mathbf{I})$ is the solution of the following set of n first-order linear partial differential equations

$$m_{ij}\frac{\partial H}{\partial p_j} + \frac{\partial}{\partial p_j}b_{ij}^{(i)} - b_{ij}^{(i)}\frac{\partial I_l}{\partial p_j}\frac{\partial \lambda}{\partial I_l} = 0 \tag{36}$$

$$i = 1, 2, \ldots, n; \quad j, l = 1, 2, \ldots, n.$$

Following the same procedure as that leading to Eq. (34), we can obtain

$$\lambda = \lambda_0 + \int_0^{(I_1, I_2, \ldots, I_n)} \frac{\partial \lambda}{\partial I_l}\, dI_l \tag{37}$$

in which $\lambda_0 = \lambda(0, 0, \ldots, 0)$, the second term on the right-hand side is a line integral and the integrand is a summation over $l = 1, 2, \ldots, n$.

If the modified Hamiltonian system with Hamiltonian H governed by Eqs. (17a) and (17b) without damping and stochastic excitation terms is resonant with $\alpha(1 \le \alpha \le n - 1)$ resonant relations of the form of Eq. (8), then, based on the argument in Section 2, the solution to Eq. (21) or (23) can be assumed of the form

$$p(\mathbf{q}, \mathbf{p}) = c \exp[-\rho(I_1, \ldots, I_n, \psi_1, \ldots, \psi_a)] \tag{38}$$

where $\psi_u = \psi_u(\mathbf{q}, \mathbf{p})$, $I_k = I_k(\mathbf{q}, \mathbf{p})$. Substituting Eq. (38) into Eq. (23) and taking into account of the boundary conditions in Eqs. (19a) and (19b) lead to

$$m_{ij}\frac{\partial H}{\partial p_j} + \frac{\partial b_{ij}^{(i)}}{\partial p_j} - b_{ij}^{(i)}\left(\frac{\partial I_l}{\partial p_j}\frac{\partial \rho}{\partial I_l} + \frac{\partial \psi_u}{\partial p_j}\frac{\partial \rho}{\partial \psi_u}\right) = 0 \tag{39}$$

$$i = 1, 2, \ldots, n \quad j, l = 1, 2, \ldots, n \quad u = 1, 2, \ldots, \alpha.$$

These are a set of n first-order linear partial differential equations for ρ as functional of I_k and ψ_u $(u = 1, 2, \ldots, \alpha)$, and they represent vanishing potential probability flows in the n directions. Obviously, ρ is a periodic function of ψ_u with period 2π. We can limit ψ_u to an interval of $[0, 2\pi)$. Let p be uniformly distributed in $[0, 2\pi)$ with respect to ψ_u, then Eq. (39) is reduced to Eq. (36).

Note that the solution in Eq. (24) and those in Eqs. (29), (35), and (38) have different physical implications. The solution in Eq. (24) has the property of equiparition of energy among various degrees of freedom and only the total energy of the system is controlled by the damping forces and stochastic excitations. The solution in Eq. (29), (35), or (38), on the other hand, implies that both the total energy of the system and its partitions among various degrees-of-freedom can be adjusted by the magnitudes and distributions of the damping forces and stochastic excitations. This property of the exact stationary solutions of stochastically excited and dissipated integrable Hamiltonian systems can be seen more clearly from the examples in Section 7.

It may be emphasized that the restrictions imposed on the system's parameters for the exact stationary solutions to exist for stochastically excited and dissipated integrable Hamiltonian systems are generally less severe than those for stochastically excited and dissipated nonintegrable Hamiltonian systems. The exact stationary solutions for stochastically excited and dissipated nonintegrable Hamiltonian systems, i.e., the solution of the form of Eq. (24), can be regarded as special case of those for stochastically excited and dissipated integrable Hamiltonian systems, i.e., the solutions of the form of Eqs. (29), (35), and (38), and the latter can be reduced to the former one if certain restrictions on the system's parameters are imposed. This may be seen clearly in the third example of Section 7.

Note also that all the exact stationary solutions obtained to date for nonlinear stochastic systems are of the form of Eq. (24). To the authors' knowledge, the exact stationary solutions of the form of Eqs. (29), (35), and (38) for nonlinear stochastic systems are obtained for the first time in the present paper.

6 Extension

The procedures described in Sections 4 and 5 can be further extended to a more general class of systems, which include the stochastically excited and dissipated Hamiltonian systems as special cases. Consider a system governed by the following Itô stochastic differential equations

$$dQ_i = D(\mathbf{Q})\frac{\partial H}{\partial p_i}\, dt \tag{40a}$$

$$dP_i = -\left[D(\mathbf{Q})\frac{\partial H}{\partial Q_i} + m_{ij}\frac{\partial H}{\partial P_j}\right]dt + f_{ik}\, dB_k(t) \tag{40b}$$

$$i, j = 1, 2, \ldots, n; \quad k = 1, 2, \ldots, m$$

where $D(\mathbf{Q})$ is an arbitrary function of $\mathbf{Q}$. The system governed by Eqs. (17a) and (17b) is a special case with $D(\mathbf{Q}) = 1$. Using the following property of Poisson bracket (Tabor, 1989)

$$[fg, h] = f[g, h] + g[f, h] \tag{41}$$

where f, g, and h are functions of state variables of a Hamiltonian system, it can be shown that the reduced FPK equation

Downloaded 04 May 2010 to 171.66.16.33. Redistribution subject to ASME license or copyright; see http://www.asme.org/terms/Terms_Use.cfm

for the stochastic system governed by Eqs. (40a) and (40b) can be written as follows:

$$[Dp^*, H] + \frac{\partial}{\partial p_i}\left(m_{ij}\frac{\partial H}{\partial p_j}p^*\right) + \frac{\partial^2}{\partial p_i \partial p_j}(b_{ij}^{(i)}p^*) = 0 \quad (42)$$

which is reduced to Eq. (23) when $D(\mathbf{Q}) = 1$. Comparison between Eqs. (42) and (23) shows that all the results obtained in Sections 4 and 5 for stochastically excited and dissipated Hamiltonian systems, including nonintegrable and integrable and nonresonant and resonant ones, still hold for the stochastic system governed by Eqs. (40a) and (40b) provided p in Eqs. (24), (29), (35), or (38) is replaced by $D(\mathbf{Q})p^*$. In other words, the structure and property of the exact stationary solution of the stochastic system governed by Eqs. (40a) and (40b) depend upon the integrability and resonant property of the Hamiltonian system with Hamiltonian H obtained from Eqs. (40a) and (40b) by letting $D(\mathbf{Q}) = 1$ and $c_{ij} = f_{ik} = 0$. A similar result has been obtained previously by Zhu, Cai, and Lin (1992) for stochastically excited and dissipated nonintegrable Hamiltonian systems. For example, if the Hamiltonian system is integrable and nonresonant, then the exact stationary solution of stochastic system (40a) and (40b) is of the form

$$p^*(\mathbf{q}, \mathbf{p}) = \frac{C}{D(\mathbf{q})}\exp[-\lambda(I_1, I_2, \ldots, I_n)]|_{I_k = I_k(\mathbf{q},\mathbf{p})} \quad (43)$$

where λ is defined by Eq. (37) for the case $D(\mathbf{Q}) = 1$.

7 Examples

Example 1. An important class of nonlinear stochastic systems consist of an n-degree-of-freedom coservative linear system, nonlinear dampings, and external and (or) parametric excitations of Gaussian white noises. An example of this class of systems is the one governed by the following equations of motion:

$$\ddot{X} + c_{11}\dot{X} + c_{12}\dot{Y} + k_{11}X + k_{12}Y = a_{11}XW_1(t) + a_{12}YW_2(t) + a_{13}W_3(t)$$

$$\ddot{Y} + c_{21}\dot{X} + c_{22}\dot{Y} + k_{21}X + k_{22}Y = a_{21}XW_1(t) + a_{22}YW_2(t) + a_{23}W_3(t) \quad (1\text{-}1)$$

where k_{ij} and a_{il} are constants with $k_{12} = k_{21}$; c_{ij} are functions of X, Y, $\dot{X}$, and $\dot{Y}$; $W_l(t)$ are Gaussian white noises with correlation functions $E[W_l(t)W_m(t+\tau)] = 2D_{lm}\delta(\tau)$.

Note that the Wong-Zakai correct terms vanish in this case. The Hamiltonian associated with the system governed by Eq. (1-1) is

$$H = \tfrac{1}{2}\dot{x}^2 + \tfrac{1}{2}\dot{y}^2 + \tfrac{1}{2}k_{11}x^2 + \tfrac{1}{2}k_{22}y^2 + k_{12}xy \quad (1\text{-}2)$$

which can be separated by using modal transformation and expressed in terms of action variables I_1 and I_2 and frequencies ω_1 and ω_2 as

$$H = \omega_1 I_1 + \omega_2 I_2 \quad (1\text{-}3)$$

where

$$I_1 = \frac{1+u_1^2}{2(u_1-u_2)^2\omega_1}[(\dot{y}-u_2\dot{x})^2 + \omega_1^2(y-u_2x)^2]$$

$$I_2 = \frac{1+u_2^2}{2(u_1-u_2)^2\omega_2}[(u_1\dot{x}-\dot{y})^2 + \omega_2^2(u_1x-y)^2]$$

$$\omega_{1,2}^2 = \frac{k_{11}+k_{22}}{2} \mp \frac{1}{2}\sqrt{(k_{11}-k_{22})^2 + 4k_{12}^2}$$

$$u_1 = \frac{\omega_1^2 - k_{11}}{k_{12}}$$

$$u_2 = \frac{\omega_2^2 - k_{11}}{k_{12}}. \quad (1\text{-}4)$$

Note that the $H = H(I_1, I_2)$ in Eq. (1-3) satisfies Eqs. (5a) and (5b). Thus, the system governed by Eq. (1-1) is a stochastically excited and dissipated integrable Hamiltonian system. Suppose that the Hamiltonian system is nonresonant, i.e., $\omega_1/\omega_2 \neq k_1/k_2$, where k_1 and k_2 are positive integers. Then the exact stationary solution is of the form of Eq. (35), where λ is the solution of the following two first-order linear partial differential equations

$$-\frac{u_2(1+u_1^2)}{(u_1-u_2)^2\omega_1}(\dot{y}-u_2\dot{x})\frac{\partial\lambda}{\partial I_1} + \frac{u_1(1+u_2^2)}{(u_1-u_2)^2\omega_2}(u_1\dot{x}-\dot{y})\frac{\partial\lambda}{\partial I_2} = d_{11}\dot{x} + d_{12}\dot{y}$$

$$\frac{1+u_1^2}{(u_1-u_2)^2\omega_1}(\dot{y}-u_2\dot{x})\frac{\partial\lambda}{\partial I_1} - \frac{1+u_2^2}{(u_1-u_2)^2\omega_2}(u_1\dot{x}-\dot{y})\frac{\partial\lambda}{\partial I_2} = d_{21}\dot{x} + d_{22}\dot{y} \quad (1\text{-}5)$$

where

$$d_{ij} = 2[[b_{ij}]^{-1}[C_{ij}]]_{ij} \quad i,j = 1,2 \quad (1\text{-}6)$$

and

$$b_{11} = 2[a_{11}^2D_{11}x^2 + 2a_{11}a_{12}D_{12}xy + a_{12}^2D_{22}y^2 + 2a_{11}a_{13}D_{13}x + 2a_{12}a_{13}D_{23}y + a_{13}^2D_{33}]$$

$$b_{12} = b_{21} = 2[a_{11}a_{21}D_{11}x^2 + (a_{11}a_{22} + a_{12}a_{21})D_{12}xy + a_{12}a_{22}D_{22}y^2 + (a_{12}a_{23} + a_{13}a_{22})D_{23}y + (a_{11}a_{23} + a_{13}a_{21})D_{13}x + a_{13}a_{23}D_{33}]$$

$$b_{22} = 2[a_{21}^2D_{11}x^2 + 2a_{21}a_{22}D_{12}xy + a_{22}^2D_{22}y^2 + 2a_{21}a_{23}D_{13}x + 2a_{22}a_{23}D_{23}y + a_{23}^2D_{33}]. \quad (1\text{-}7)$$

The conditions that $\partial\lambda/\partial I_1$ and $\partial\lambda/\partial I_2$ should be functionals of I_1 and I_2 and the compatibility condition similar to those in Eq. (33), i.e., $\partial^2\lambda/\partial I_2\partial I_1 = \partial^2\lambda/\partial I_1\partial I_2$, lead to

$$d_{21} = d_{12}$$

$$d_{11} = -[u_1u_2d_{22} + (u_1+u_2)d_{12}] \quad (1\text{-}8)$$

and

$$\frac{(u_1-u_2)^2\omega_1}{1+u_1^2}\frac{\partial d_{12}}{\partial I_2} - \frac{(u_1-u_2)^2\omega_2}{1+u_2^2}\frac{\partial d_{12}}{\partial I_1} = S(I_1, I_2)$$

$$\frac{u_1(u_1-u_2)^2\omega_1}{1+u_1^2}\frac{\partial d_{22}}{\partial I_2} - \frac{u_2(u_1-u_2)^2\omega_2}{1+u_2^2}\frac{\partial d_{22}}{\partial I_1} = S(I_1, I_2) \quad (1\text{-}9)$$

where $S(I_1, I_2)$ is an arbitrary functional of I_1 and I_2.

If d_{ij} $(i, j = 1, 2)$ are known and satisfy the conditions in Eqs. (1-8) and (1-9), then $\partial\lambda/\partial I_1$ and $\partial\lambda/\partial I_2$ can be obtained from Eq. (1-5) and the exact stationary solution of Eq. (1-1) is

$$p(x, y, \dot{x}, \dot{y}) = C\exp\left[-\int_0^{(I_1,I_2)}\left(\frac{\partial\lambda}{\partial I_1}dI_1 + \frac{\partial\lambda}{\partial I_2}dI_2\right)\right] \quad (1\text{-}10)$$

Equation (1-9) is a set of two first-order linear partial differential equations for d_{12} and d_{22} as functionals of I_1 and I_2. Given a functional $S(I_1, I_2)$, one can obtain a set of d_{12} and d_{22} as

Downloaded 04 May 2010 to 171.66.16.33. Redistribution subject to ASME license or copyright; see http://www.asme.org/terms/Terms_Use.cfm

functionals of I_1 and I_2 from Eq. (1-9). The exact stationary solution of the system governed by Eq. (1-1) is then

$$p(x, y, \dot{x}, \dot{y}) = C \exp\left\{ -\int_0^{(I_1, I_2)} \left[\frac{(u_1 - u_2)\omega_1}{1 + u_1^2} (d_{12} + u_1 d_{22}) dI_1 + \frac{(u_1 - u_2)\omega_2}{1 + u_1^2} (d_{12} + u_2 d_{22}) dI_2 \right] \right\}. \quad (1\text{-}11)$$

I_1 and I_2 in Eqs. (1-10) and (1-11) are functions of x, y, $\dot{x}$, and $\dot{y}$ defined by Eq. (1-4).

Example 2. To obtain more specific results, consider a simpler system governed by the following equations of motion

$$\ddot{X} + D_{11}\lambda_1 \dot{X} + D_{11}\lambda_2 \dot{Y} + k_{11}X + k_{12}Y = W_1(t)$$
$$\ddot{Y} + D_{22}\lambda_3 \dot{X} + D_{22}\lambda_4 \dot{Y} + k_{21}X + k_{22}Y = W_2(t) \quad (2\text{-}1)$$

where k_{ij} are constants with $k_{12} = k_{21}$; λ_1 are functions of X, Y, $\dot{X}$, and $\dot{Y}$; $W_1(t)$ and $W_2(t)$ are uncorrelated Gaussian white noises with correlation functions

$$E[W_i(t)W_i(t + \tau)] = 2D_{ii}\delta(\tau) \quad (2\text{-}2)$$
$$i = 1, 2.$$

Equation (2-1) describes a stochastically excited and dissipated integrable Hamiltonian system with the same Hamiltonian as in Example 1, i.e., that in Eqs. (1-2) and (1-3). In this case, similar derivation as that in example 1 leads to

$$\lambda_3 = \lambda_2$$
$$\lambda_1 = -[u_1 u_2 \lambda_4 + (u_1 + u_2)\lambda_2] \quad (2\text{-}3)$$

and

$$\frac{(u_1 - u_2)^2\omega_1}{1 + u_1^2} \frac{\partial \lambda_2}{\partial I_2} - \frac{(u_1 - u_2)^2\omega_2}{1 + u_2^2} \frac{\partial \lambda_2}{\partial I_1} = S(I_1, I_2)$$
$$\frac{u_1(u_1 - u_2)^2\omega_1}{1 + u_1^2} \frac{\partial \lambda_4}{\partial I_2} - \frac{u_2(u_1 - u_2)^2\omega_2}{1 + u_2^2} \frac{\partial \lambda_4}{\partial I_1} = S(I_1, I_2). \quad (2\text{-}4)$$

Let

$$S(I_1, I_2) = a \quad (2\text{-}5)$$

where a is a constant. The solution of Eq. (2-4) is

$$\lambda_2 = g_1\left[\frac{(u_1 - u_2)^2\omega_1}{1 + u_1^2} I_1 + \frac{(u_1 - u_2)^2\omega_2}{1 + u_2^2} I_2 \right] + a \frac{(1 + u_1^2)}{(u_1 - u_2)^2\omega_1} I_2 + C_1$$
$$\lambda_4 = g_2\left[\frac{u_1(u_1 - u_2)^2\omega_1}{1 + u_1^2} I_1 + \frac{u_2(u_1 - u_2)^2\omega_2}{1 + u_2^2} I_2 \right] + a \frac{u_1(u_1 - u_2)^2\omega_1}{1 + u_1^2} I_2 + C_2 \quad (2\text{-}6)$$

where g_1 and g_2 are arbitrary functions of the variables in brackets and C_1 and C_2 are constants. Further, let

$$a = 0$$
$$g_i(v) = v$$
$$C_i = -1$$
$$i = 1, 2. \quad (2\text{-}7)$$

Then

$$\lambda_2 = \frac{(u_1 - u_2)^2\omega_1}{1 + u_1^2} I_1 + \frac{(u_1 - u_2)^2\omega_2}{1 + u_2^2} I_2 - 1$$
$$\lambda_4 = \frac{u_1(u_1 - u_2)^2\omega_1}{1 + u_1^2} I_1 + \frac{u_2(u_1 - u_2)^2\omega_2}{1 + u_2^2} I_2 - 1 \quad (2\text{-}8)$$

and λ_1 and λ_3 are determined by Eq. (2-3). In this case, Eq. (2-1) governs two coupled van der Pol-Rayleigh oscillators subject to two uncorrelated external excitations of Gaussian white noises, and the exact stationary solution is

$$p(x, y, \dot{x}, \dot{y}) = C \exp\left\{ -\int_0^{(I_1, I_2)} \left[\frac{(u_1 - u_2)\omega_1}{1 + u_1^2} (\lambda_2 + u_1\lambda_4) dI_1 + \frac{(u_1 - u_2)\omega_2}{1 + u_2^2} (\lambda_2 + u_2\lambda_4) dI_2 \right] \right\} \quad (2\text{-}9)$$

where I_1 and I_2 are functions of x, y, $\dot{x}$, and $\dot{y}$ defined by Eq. (1-4).

Example 3. As an example having nonlinear restoring forces, consider two coupled quartic oscillators with linear or nonlinear dampings subject to external or parametric excitations of Gaussian white noises. The system is governed by the following equations of motion:

$$\ddot{X} + c_{11}\dot{X} + c_{12}\dot{Y} + AX + X^3 + 3XY^2 = \sigma_1 W_1(t)$$
$$\ddot{Y} + c_{21}\dot{X} + c_{22}\dot{Y} + BY + Y^3 + 3X^2Y = \sigma_2 W_2(t) \quad (3\text{-}1)$$

where c_{ij} are functions of X, Y, $\dot{X}$, and $\dot{Y}$; σ_i are functions of X and Y; A is a constant; $W_i(t)$ are Gaussian white noises with correlation functions

$$E[W_i(t)W_j(t + \tau)] = 2D_{ij}\delta(\tau) \quad (3\text{-}2)$$
$$i, j = 1, 2.$$

The Hamiltonian of the system governed by Eq. (3-1) is

$$H = \tfrac{1}{2}(\dot{x}^2 + \dot{y}^2 + Ax^2 + By^2) + \tfrac{1}{4}x^4 + \tfrac{1}{4}y^4 + \tfrac{3}{2}x^2y^2 \quad (3\text{-}3)$$

which can be separated in the case of $A = B$ as

$$H = H_1 + H_2 \quad (3\text{-}4)$$

where

$$H_1 = \frac{1}{4}(\dot{x} + \dot{y})^2 + \frac{A}{4}(x + y)^2 + \frac{1}{8}(x + y)^4$$
$$H_2 = \frac{1}{4}(\dot{x} - \dot{y})^2 + \frac{A}{4}(x - y)^2 + \frac{1}{8}(x - y)^4. \quad (3\text{-}5)$$

H_1 and H_2 are the two independent integrals of motion in involution. Thus, the system governed by Eq. (3-1) is a stochastically excited and dissipated integrable Hamiltonian system. Note that the corresponding Hamiltonian system is nondegenerate and can be regarded as a nonresonant one. The exact stationary solution is of the form (29), where φ is the solution of the following two first-order linear partial differential equations:

$$\begin{bmatrix} \sigma_1^2 D_{11} & \sigma_1\sigma_2 D_{12} \\ \sigma_1\sigma_2 D_{21} & \sigma_2^2 D_{22} \end{bmatrix} \begin{Bmatrix} \frac{\dot{x} + \dot{y}}{2} \frac{\partial \varphi}{\partial H_1} + \frac{\dot{x} - \dot{y}}{2} \frac{\partial \varphi}{\partial H_2} \\ \frac{\dot{x} + \dot{y}}{2} \frac{\partial \varphi}{\partial H_1} - \frac{\dot{x} - \dot{y}}{2} \frac{\partial \varphi}{\partial H_2} \end{Bmatrix} = \begin{bmatrix} C_{11} & C_{12} \\ C_{21} & C_{22} \end{bmatrix} \begin{Bmatrix} \dot{x} \\ \dot{y} \end{Bmatrix}. \quad (3\text{-}6)$$

Downloaded 04 May 2010 to 171.66.16.33. Redistribution subject to ASME license or copyright; see http://www.asme.org/terms/Terms_Use.cfm

The conditions that $\partial\varphi/\partial H_1$ and $\partial\varphi/\partial H_2$ should be functionals of H_1 and H_2 and the conditions in Eq. (33) lead to

$$a = d \quad b = c. \tag{3-7}$$

$(a + c)/\Delta_D$ and $(a - c)/\Delta_D$ are functionals of H_1 and H_2, and

$$\frac{\partial}{\partial H_2}\left(\frac{a+c}{\Delta_D}\right) = \frac{\partial}{\partial H_1}\left(\frac{a-c}{\Delta_D}\right) \tag{3-8}$$

where

$$\begin{aligned} a &= c_{11}\sigma_2^2 D_{22} - c_{21}\sigma_1\sigma_2 D_{12} \\ b &= c_{12}\sigma_2^2 D_{22} - c_{22}\sigma_1\sigma_2 D_{12} \\ c &= c_{21}\sigma_1^2 D_{11} - c_{11}\sigma_1\sigma_2 D_{21} \\ d &= c_{22}\sigma_1^2 D_{11} - c_{12}\sigma_1\sigma_2 D_{21} \\ \Delta_D &= \sigma_1^2\sigma_2^2(D_{11}D_{22} - D_{12}D_{21}). \end{aligned} \tag{3-9}$$

If Eqs. (3-7) and (3-8) are satisfied, the exact stationary solution of the system governed by Eq. (3-1) is

$$p(x, y, \dot{x}, \dot{y}) = C \exp\left\{-\int_0^{(H_1,H_2)}\left[\frac{(a+c)}{\Delta_D}\,dH_1 + \frac{(a-c)}{\Delta_D}\,dH_2\right]\right\} \tag{3-10}$$

In the case of linear dampings, i.e., c_{ij} are constants, and external excitations, e.g., $\sigma_1 = \sigma_2 = 1$, the solution in Eq. (3-10) is reduced to

$$p(x, y, \dot{x}, \dot{y}) = C \exp\left\{-\frac{1}{\Delta_D}\left[(a + c)H_1 + (a - c)H_2\right]\right\}. \tag{3-11}$$

It is noted that if $c_{21} = D_{21} = 0$, then $c = 0$, the solution in Eq. (3-11) is further reduced to

$$p(x, y, \dot{x}, \dot{y}) = C \exp\left[-\frac{a}{\Delta_D} H\right] \tag{3-12}$$

which is of the form of Eq. (24) for stochastically excited and dissipated nonintegrable Hamiltonian systems.

8 Concluding Remarks

In the present paper it has been shown for the first time that the structure and property of the exact stationary solution of a stochastically excited and dissipated n-degree-of-freedom Hamiltonian system depend upon the integrability and resonant property of the modified Hamiltonian system. For a stochastically excited and dissipated nonintegrable Hamiltonian system, the exact stationary probability density of the response, if it exists, is a functional of the Hamiltonian and the response has property of equipartition of energy. For a stochastically excited and dissipated integrable Hamiltonian system, the exact stationary probability density of the response, if it exists, is a functional of n-independent integrals of motion or n action variables in nonresonant case, or a functional of n action variables and α combinations of phase angles in resonant case with α ($1 \le \alpha \le n - 1$) resonant relations and the response has the property that the partition of the energy among n degree-of-freedom can be adjusted by the magnitudes and distributions of the damping forces and stochastic excitations. All the exact stationary solutions obtained to date for nonlinear stochastic systems are those for stochastically excited and dissipated nonintegrable Hamiltonian systems. The exact stationary solutions for stochastically excited and dissipated integrable Hamiltonian systems presented for the first time in this paper break the limitation of equipartition of energy of nonlinear stochastic systems and unify the exact stationary solutions for nonlinear stochastic systems and those for linear systems subject to external excitations of Gaussian white noises.

Although integrable Hamiltonian systems of finite degree-of-freedom found to date are few, stochastically excited and dissipated integrable Hamiltonian systems form an important class of nonlinear stochastic systems. For stochastically excited and dissipated integrable Hamiltonian systems, although the conditions for exact stationary solutions to exist are severe and may not satisfied by most real systems, the exact stationary solutions may serve as candidates of approximate solutions of really nonlinear stochastic systems and an equivalent nonlinear system method similar to that for stochastically excited and dissipated nonintegrable Hamiltonian systems (Zhu, Soong, and Lei, 1994) can be developed. This will be a subject of our future work.

Acknowledgment

The support from National Natural Science Foundation of China is acknowledged.

References

Arnold, V. I., 1989, *Mathematical Methods of Classical Mechanics,* Springer-Verlag, New York.

Cai, G. Q., and Lin, Y. K., 1988, "On Exact Stationary Solutions of Equivalent Non-Linear Stochastic Systems," *Int. J. Non-Linear Mech.*, Vol. 23, pp. 315–325.

Caughey, T. K., 1971, "Nonlinear Theory of Random Vibration," *Advances in Applied Mechanics,* Vol. 11, pp. 209–253.

Caughey, T. K., and Ma, F., 1982a, "The Steady-State Response of a Class of Dynamic Systems to Stochastic Excitations," ASME JOURNAL OF APPLIED MECHANICS, Vol. 49, pp. 629–632.

Caughey, T. K., and Ma, F., 1982b, "The Exact Steady-State Solution of a Class of Nonlinear Stochastic Systems," *Int. J. Non-Linear Mech.*, Vol. 17, pp. 137–142.

Dimentberg, M. F., 1982, "An Exact Solution to a Certain Nonlinear Random Vibration Problem," *Int. J. Non-Linear Mech.*, Vol. 17, pp. 231–236.

Fuller, A. T., 1969, "Analysis of Nonlinear Stochastic Systems by Means of the Fokker-Planck Equation," *Int. J. Control,* Vol. 9, pp. 603–655.

Lin, Y. K., and Cai, G. Q., 1988, "Exact Stationary Response Solution for Second-Order Nonlinear Systems Under Parametric and External White Noise Excitations: Part II," ASME JOURNAL OF APPLIED MECHANICS, Vol. 55, pp. 702–705.

Soize, C., 1988, "Steady-State Solution of Fokker-Planck Equation in High Dimension," *Probabilistic Engineering Mechanics,* Vol. 3, pp. 196–206.

Soize, C., 1991, "Exact Stationary Response of Multi-Dimensional Nonlinear Hamiltonian Dynamical Systems Under Parametric and External Stochastic Excitations," *Journal of Sound and Vibration,* Vol. 149, pp. 1–24.

Tabor, M., 1989, *Chaos and Integrability in Nonlinear Dynamics,* John Wiley and Sons, New York.

Wang, M. C., and Ulenbeck, G. E., 1945, "On the Theory of Brown Motion II," *Rev. Modern Phys.*, Vol. 17, pp. 323–342; reprinted in *Selected Papers on Noise and Stochastic Processes,* N. Wax, ed., Dover, New York, 1954.

Wong, E., and Zakai, M., 1965, "On the Relation Between Ordinary and Stochastic Equations," *Int. J. Engineering Science,* Vol. 3, pp. 213–229.

Zhu, W. Q., 1990, "The Exact Stationary Response Solutions of Several Classes of Nonlinear Systems to White Noise Parametric and/or External Excitations," *Applied Mathematics and Mechanics,* Vol. 11, pp. 165–175.

Zhu, W. Q., Cai, G. Q., and Lin, Y. K., 1990, "On Exact Stationary Solutions of Stochastically Perturbed Hamiltonian Systems," *Probabilistic Engineering Mechanics,* Vol. 5, pp. 84–87.

Zhu, W. Q., Cai, G. Q., and Lin, Y. K., 1992, "Stochastically Excited Hamiltonian Systems," *Nonlinear Stochastic Mechanics,* N. Bellomo and F. Casiati, eds., Springer-Verlag, Berlin, pp. 543–552.

Zhu, W. Q., Soong, T. T., and Lei, Y., 1994, "Equivalent Nonlinear System Method for Stochastically Excited Hamiltonian Systems," ASME JOURNAL OF APPLIED MECHANICS, Vol. 61, pp. 618–623.

Downloaded 04 May 2010 to 171.66.16.33. Redistribution subject to ASME license or copyright; see http://www.asme.org/terms/Terms_Use.cfm

G. L. Gray
Assistant Professor,
Department of Engineering Science and Mechanics,
The Pennsylvania State University,
University Park, PA 16802
Assoc. Mem. ASME.

I. Dobson
Associate Professor,
Department of Electrical and Computer Engineering.

D. C. Kammer
Associate Professor,
Assoc. Mem. ASME.
Department of Engineering Mechanics and Astronautics.

University of Wisconsin–Madison,
Madison, WI 53706

Chaos in a Spacecraft Attitude Maneuver Due to Time-Periodic Perturbations

We use Melnikov's method to study the chaotic dynamics of an attitude transition maneuver of a torque-free rigid body in going from minor axis spin to major axis spin under the influence of small damping. The chaotic motion is due to the formation of Smale horseshoes which are caused by the oscillation of small subbodies inside the satellite. The equations of motion are derived and then transformed into a form suitable for the application of Melnikov's method. An analytical criterion for chaotic motion is derived in terms of the system parameters. This criterion is evaluated for its significance to the design of artificial satellites.

1 Introduction

This paper deals with the dynamics of an attitude transition from minor to major axis spin[1] of a quasi-rigid, single-body spacecraft perturbed by small oscillating subbodies. A single-body satellite is directionally unstable in the presence of energy dissipation when perturbed from spinning about its minor axis (Hughes, 1986). In the absence of active stabilization, the body will eventually reorient itself and spin about the major axis. Oscillating subbodies can produce chaos in a region of the phase space traversed by the satellite during this attitude maneuver. This maneuver is of great practical interest since the initial rotation of many spacecraft is about their minor axis after launch vehicle separation. The addition of oscillating subbodies allows for simple modeling of perturbations within the carrier body. These perturbations might include: asymmetric rotors, reciprocating engines, and crew movement within the vehicle. It should be noted that we prove the existence of horseshoes, which imply the existence of chaotic transients (Greenspan and Holmes, 1983; Guckenheimer and Holmes, 1983). Therefore, throughout this work, when we refer to chaos or chaotic dynamics, we are generally referring to transient chaos and not the chaos associated with a strange attractor.

Certain aspects of the dynamics of attitude transition maneuvers have been studied for the special class of spacecraft called dual-spin satellites. These satellites are reoriented by spin-up of rotors relative to the main spacecraft body. Attitude resonances in this maneuver, occurring during the spin-up or spin-down, have been investigated using perturbation techniques and numerical simulation (Adams, 1980; Cochran and Holloway, 1980; Gebman and Mingori, 1976; Hall and Rand, 1991; Or, 1991). In the case of single-body satellites, the direction and control of the final major axis orientation have been studied by authors such as Barba et al. (1973), Cronin (1978), Kaplan and Cenker (1973), and Rahn and Barba (1991), but the dynamics of the maneuver itself have not been extensively investigated.

The non-Hamiltonian perturbations of rigid-body dynamics dealt with in this paper are due to time-periodic enforced motions of subbodies within a satellite possessing an energy dissipation mechanism. While the occurrence of chaos in this class of systems is not surprising, our application of Melnikov's method to detect the onset of chaos in this class of systems is new. We have overcome considerable difficulties in model formulation and in the application of Melnikov's method to obtain a criterion for chaos which can be used in satellite design. The most closely related work (Dovbysh, 1989; Holmes and Marsden, 1983; Koiller, 1984; Ziglin, 1982) is limited to

[1] In this work, the minor axis corresponds to the principal axis with the smallest mass moment of inertia, while the major axis denotes the principal axis with the largest inertia.

Contributed by the Applied Mechanics Division of THE AMERICAN SOCIETY OF MECHANICAL ENGINEERS for publication in the ASME JOURNAL OF APPLIED MECHANICS.

Discussion on this paper should be addressed to the Technical Editor, Professor Lewis T. Wheeler, Department of Mechanical Engineering, University of Houston, Houston, TX 77204-4792, and will be accepted until four months after final publication of the paper itself in the ASME JOURNAL OF APPLIED MECHANICS.

Manuscript received by the ASME Applied Mechanics Division, Dec. 4, 1992; final revision, Sept. 3, 1993. Associate Technical Editor: D. J. Inman.

Copyright © 1996 by ASME

Downloaded 04 May 2010 to 171.66.16.33. Redistribution subject to ASME license or copyright; see http://www.asme.org/terms/Terms_Use.cfm

chaos in satellite attitude dynamics when the perturbations are Hamiltonian. Some work has been done for non-Hamiltonian perturbations to spacecraft dynamics, but it has dealt almost exclusively with the stability of equilibria (Baillieul and Levi, 1987; Krishnaprasad, 1985; Krishnaprasad and Marsden, 1987; Rubanovskii, 1988). In particular, the non-Hamiltonian perturbations studied in this work are explicit functions of time, resulting in equations of motion with time-dependent coefficients. This type of perturbation is of considerable practical importance in satellite design. For example, the enforced time-dependent motion, modeled herein by harmonic functions of the form $A \cos \Omega t$, could be caused by reciprocating masses, unbalanced rotors with constant angular velocities, or rotor with time-dependent spin rates.

2 Satellite Model

The model used in this study is a torque-free, quasi-rigid body that is perturbed by time-dependent subbody motion. The quasi-rigid-body approximation is often used as a tool to study complex spacecraft systems and obtain analytical information about their global behavior. Understanding these rigid-body approximations is often the first step in a complete study of a complex spacecraft. The damping, which is implied by the term "quasi-rigid," is modeled by a quantitative energy sink technique recently derived by Kammer and Gray (1992).

The specific spacecraft model used in this investigation is shown in Fig. 1. The system's mass center c does not move relative to the carrier body since the two subbodies oscillate symmetrically with respect to c along the x-axis. The position of the subbodies relative to the carrier is a known periodic function of time and is denoted by $\eta(t)$. The $\eta = 0$ position is located a distance l from the mass center c. We let x, y, z denote a body-fixed orthogonal coordinate system aligned with the principal axes of the carrier body and centered at c. The principal moments of inertia of the carrier with respect to c are designated I_1, I_2, I_3. The moments of inertia are distinct and we assume $I_1 < I_2 < I_3$.

In order to apply Melnikov's method, it is assumed that the subbodies of mass m are "small" in comparison to the main body. In addition, the damping is assumed to be small. What we mean by small will be defined later with respect to a perturbation parameter ϵ. Therefore, both the subbodies and the damping mechanism are assumed to have an $\mathcal{O}(\epsilon)$ perturbing effect on the spacecraft.

3 Equations of Motion

Using standard methods such as Lagrange's equations or Newton-Euler techniques, the undamped equations of motion can be derived in terms of principal, body angular momentum components h_1, h_2, h_3 as

$$\dot{h}_1 = \left[\frac{B - C}{(B + \Delta)(C + \Delta)}\right] h_2 h_3 \tag{1}$$

$$\dot{h}_2 = \left(\frac{1}{A} - \frac{1}{C + \Delta}\right) h_1 h_3 \tag{2}$$

$$\dot{h}_3 = \left(\frac{1}{B + \Delta} - \frac{1}{A}\right) h_1 h_3 \tag{3}$$

where $A \triangleq I_1$, $B \triangleq I_2 + 2ml^2$, $C \triangleq I_3 + 2ml^2$, $\Delta = \Delta(t) \triangleq 2m\eta(t)[2l + \eta(t)]$, and the dot $(\dot{})$ denotes differentiation with respect to time, $d()/dt$.

The damping terms modeling the quasi-rigid body are readily added via the argument presented in Kammer and Gray (1992). The damping is implemented via a nonlinear control design that quantitatively simulates the effects of internal damping mechanisms which can be accurately modeled as energy sinks. The controller dissipates kinetic energy while maintaining the magnitude of the angular momentum vector. The control torques are nonlinear functions of the angular momentum components expressed in the body-fixed frame. Kammer and Gray (1992) specify a control law by identifying the conditions which must be met by the controller to simulate onboard energy dissipation. Assuming an asymmetric rigid-body representation for a spacecraft with principal mass moments of inertia $I_1 < I_2 < I_3$, Euler's equations for the attitude motion in momentum space are given by

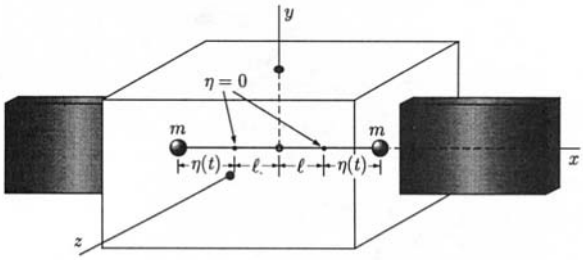


Fig. 1 The model spacecraft configuration

$$\dot{h}_1 = \frac{I_2 - I_3}{I_2 I_3} h_2 h_3 + u_1$$

$$\dot{h}_2 = \frac{I_3 - I_1}{I_1 I_3} h_1 h_3 + u_2$$

$$\dot{h}_3 = \frac{I_1 - I_2}{I_1 I_2} h_1 h_2 + u_3 \tag{4}$$

where the h_i are the components of the angular momentum vector $\mathbf{H}$ measured along the body-fixed principal axes and the u_i are the control torques which are nonlinear functions of the h_i to be determined.

The conditions that the controller must satisfy are that the magnitude of the angular momentum vector $\mathbf{H}$ must be conserved, the time derivative of the system kinetic energy must be negative semi-definite, and the controller must not dissipate energy for a pure spin about any of the principal axes. Although these conditions do not uniquely determine the form of the control law, for the purpose of energy sink simulation, we choose the control design given by

$$u_1 = -\beta h_1 h_2^2$$

$$u_2 = \beta h_2 \left(h_1^2 - h_3^2\right)$$

$$u_3 = \beta h_3 h_2^2 \tag{5}$$

where β is a positive valued control gain to be specified.

It can be shown that the control law given by Eq. (5) satisfies the above three conditions and that the closed loop equations of motion possess the same topological structure as the equations for a damped single-body spacecraft.

The equations of motion in Eqs. (1)–(3) become

$$\dot{h}_1 = \left[\frac{B - C}{(B + \Delta)(C + \Delta)}\right] h_2 h_3 - \beta h_1 h_2^2, \tag{6}$$

$$\dot{h}_2 = \left(\frac{1}{A} - \frac{1}{C + \Delta}\right) h_1 h_3 + \beta h_2 \left(h_1^2 - h_3^2\right), \tag{7}$$

$$\dot{h}_3 = \left(\frac{1}{B + \Delta} - \frac{1}{A}\right) h_1 h_2 + \beta h_2^2 h_3. \tag{8}$$

It is clear that Δ is the term that makes the system nonautonomous since $\Delta = \Delta(\eta)$ and η is a specified function of time.

Downloaded 04 May 2010 to 171.66.16.33. Redistribution subject to ASME license or copyright; see http://www.asme.org/terms/Terms_Use.cfm

We now nondimensionalize Eqs. (6)–(8). In order to perform the transformation, we define the following scaled quantities:

$$\epsilon \triangleq ml^2/B \qquad \tilde{h}_i \triangleq h_i/H \qquad \tilde{h}_i' \triangleq \frac{B}{H^2}\dot{h}_i$$

$$\tilde{\Delta} \triangleq \frac{\Delta}{\epsilon B} \qquad \tilde{\beta} \triangleq \beta\frac{HB^2}{ml^2} \qquad \tau \triangleq Ht/B$$

$$r_1 \triangleq C/B \qquad r_2 \triangleq A/B$$

where H is the total angular momentum and differentiation with respect to nondimensional time τ is denoted by a prime, $()' = d()/d\tau$. All quantities except ϵ are $\mathcal{O}(1)$. Notice that the number of moment of inertia parameters has been reduced to two, r_1 and r_2. The size of the parameter region involving the moments of inertia is now restricted to an easily determined domain due to the assumptions made on their relative size and the natural physical limitations restricting the choice of moments of inertia. We have assumed that $I_1 < I_2 < I_3$, therefore $A < B < C$. It immediately follows that $0 < r_2 < 1 < r_1$. In addition, since it can be shown that the individual moments of inertia are interrelated by $A + B > C$, it follows that $r_2 + 1 > r_1$ and therefore

$$0 < r_2 < 1 < r_1 < 1 + r_2. \tag{9}$$

These inequalities will restrict the size of the parameter space involving r_1 and r_2 that needs to be studied.

We do not use the usual Smelt (often called DeBra-Delp, see Rimrott, 1989) parameters since they were originally defined to simplify equations of motion when written in terms of angular velocity components, not angular momentum components. Our equations are much simpler when using the definitions for r_1 and r_2 given above. The final results will also be written in terms of the Smelt parameters so that the results can be shown in more familiar terms. Carrying out the above change of variables leads to an equivalent set of dimensionless equations:

$$\tilde{h}_1' = \frac{1 - r_1}{(1 + \epsilon\tilde{\Delta})(r_1 + \epsilon\tilde{\Delta})}\tilde{h}_2\tilde{h}_3 - \epsilon\tilde{\beta}\tilde{h}_1\tilde{h}_2^2, \tag{10}$$

$$\tilde{h}_2' = \left(\frac{1}{r_2} - \frac{1}{r_1 + \epsilon\tilde{\Delta}}\right)\tilde{h}_1\tilde{h}_3 + \epsilon\tilde{\beta}\tilde{h}_2\left(\tilde{h}_1^2 - \tilde{h}_3^2\right), \tag{11}$$

$$\tilde{h}_3' = \left(\frac{1}{1 + \epsilon\tilde{\Delta}} - \frac{1}{r_2}\right)\tilde{h}_1\tilde{h}_2 + \epsilon\tilde{\beta}\tilde{h}_2^2\tilde{h}_3. \tag{12}$$

Equations (10)–(12) are the full nondimensional equations of motion explicitly containing the perturbation parameter ϵ. No assumptions have yet been made about the size of any of the quantities in the development of the equations, although the definitions of the nondimensional quantities and ϵ are convenient for assumptions made later.

4 The Unperturbed Phase Space

In order to apply Melnikov's method to the system of Eqs. (10)–(12), there must be a heteroclinic cycle in the unperturbed phase space, and the unperturbed system must be integrable. The solution to the unperturbed system is needed since Melnikov's method makes use of the globally computable solutions of the unperturbed *integrable* system in computing the perturbed solutions. It can be shown that the attitude dynamics of a torque-free rigid body, when measured in body angular momentum components, occur on the surface of the angular momentum sphere (see Fig. 2). This sphere is also the reduced phase space for Euler's equations of motion for a torque-free rigid body. These equations are given by

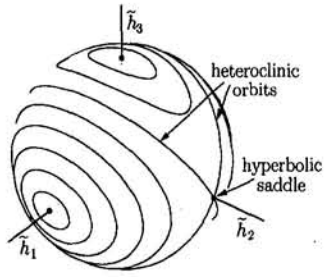


Fig. 2 The momentum sphere illustrating the heteroclinic orbits and the hyperbolic saddle points. The curves are orbits of constant energy.

$$\tilde{h}_1' = \frac{1 - r_1}{r_1}\tilde{h}_2\tilde{h}_3, \tag{13}$$

$$\tilde{h}_2' = \left(\frac{r_1 - r_2}{r_1 r_2}\right)\tilde{h}_1\tilde{h}_3, \tag{14}$$

$$\tilde{h}_3' = \left(\frac{r_2 - 1}{r_2}\right)\tilde{h}_1\tilde{h}_2. \tag{15}$$

Equations (13)–(15) are just the equations of motion, Eqs. (10)–(12), with $\epsilon = 0$, i.e., the unperturbed equations of motion. Euler's equations are integrable in terms of Jacobi elliptic functions or hyperbolic functions, depending on the angular momentum and energy. The phase space is a two-dimensional surface imbedded in $\mathbb{R}^3$. This phase space possesses six fixed points or equilibria corresponding to positive and negative spin about each of the three principal axes of the satellite. Two of the fixed points, corresponding to spin about the intermediate principal axis, are hyperbolic fixed points or saddles. In addition, there are four heteroclinic orbits linking the hyperbolic fixed points as shown in Fig. 2. During the transition of an energy dissipating satellite from spin near the minimum moment of inertia axis to spin about the maximum moment of inertia axis, the trajectory must cross the heteroclinic orbits in the phase space. More precisely, the trajectory of the damped system must cross a heteroclinic orbit of the undamped system. We study the chaotic motion in the perturbed system that may occur near the heteroclinic orbits.

5 Melnikov's Method and Equation Transformation

Melnikov's method is applied to detect chaos in the system of Eqs. (10)–(12). For a detailed exposition of Melnikov theory, see Guckenheimer and Holmes (1983) and Wiggins (1990). Briefly, Melnikov's method is a perturbation technique for proving the existence of transverse heteroclinic[2] orbits to hyperbolic periodic orbits in a class of time-periodic vector fields. Though it is perturbation method, Melnikov's method gives *global* information about the system's dynamics. The essential idea in Melnikov's method is to use the globally computable solutions to the unperturbed *integrable* system in studying the perturbed solution. The existence of transverse heteroclinic orbits implies the existence of horseshoes and chaos via the Smale-Birkhoff Theorem. These horseshoes appear near the unperturbed heteroclinic orbit in a "chaotic layer." A typical trajectory, when going from minor axis to major axis spin, must go through this chaotic layer, and possibly near the horseshoe. Although horseshoes are not attractors, their existence has profound consequences for physically realizable motions. The orbits in the horseshoes are saddle-type hyperbolic and a nearby orbit can first be

[2]The method applies equally well to systems with homoclinic orbits.

Downloaded 04 May 2010 to 171.66.16.33. Redistribution subject to ASME license or copyright; see http://www.asme.org/terms/Terms_Use.cfm

attracted to the chaotic horseshoe orbits and then be repelled from them. Therefore, when horseshoes are present, it is possible to see long chaotic transients before orbits settle down to equilibria or periodic orbits, see Greenspan and Holmes (1983), Guckenheimer and Holmes (1983), and Palis and Takens (1993).

However, the phase space, and in particular the chaotic layer, is very complex. Numerical and theoretical work on Duffing's equation suggests that stable subharmonic motions are possible, although the stable subharmonics of high period in the chaotic layer are thought to be unobservable. This is because the basins of attraction of the high period subharmonics are so small that numerical or physical noise dominates and perturbs the orbit out of a basin, making the orbit appear like transient chaos. Numerical work on Duffing's equations also shows "strange attractor" chaos for moderate values of damping and forcing, but the strange attractor does not coexist with stable T-periodic orbits. Since the stable T-periodic orbits correspond to slightly perturbed major axis spin in the satellite equations, this suggests that a chaotic attractor might not occur for parameter ranges of interest when studying the satellite attitude transition maneuver. Here we are assuming that it is reasonable to study the attitude transition to major axis spin only when the satellite design has already ensured that the final major axis spin dynamics are a simple periodic orbit. For a detailed discussion of all of these issues, see Greenspan and Holmes (1983) and Guckenheimer and Holmes (1983).

We are now left with the tasks of solving for the heteroclinic orbit $\mathbf{q}_0(t)$ of the unperturbed system, writing the perturbed equations of motion such that only terms through $\mathcal{O}(\epsilon)$ are kept, and then obtaining the two independent equations of motion (in convenient coordinates) describing the dynamics on the surface of the momentum sphere.

5.1 Solution for the Unperturbed Heteroclinic Orbit $q_0(t)$. For a torque-free rigid body with equations of motion given by Eqs. (13)–(15), there are two integrals of the motion—momentum and energy. In nondimensional coordinates, these integrals are given by

$$\tilde{h}_1^2 + \tilde{h}_2^2 + \tilde{h}_3^2 = 1 \qquad \text{(momentum)} \tag{16}$$

$$\frac{\tilde{h}_1^2}{r_2} + \tilde{h}_2^2 + \frac{\tilde{h}_3^2}{r_1} = \tilde{T} \quad \text{(energy)} \tag{17}$$

where $\tilde{T} \triangleq 2BT/H^2$ is the nondimensional total energy and T is the total energy. Any trajectory on the momentum sphere is determined by the intersection of the momentum sphere $\mathcal{S}$ defined by Eq. (16) and the energy ellipsoid $\mathcal{E}$ defined by Eq. (17). Recall that when viewed in body coordinates, the angular momentum vector appears to move such that its tip always remains on a particular intersection of $\mathcal{S}$ and $\mathcal{E}$. The radius of $\mathcal{S}$, which is $\tilde{H} = 1$, must lie between the smallest and largest semiaxes of the ellipsoid. Since $A < B < C$, or nondimensionally $0 < r_2 < 1 < r_1$, the condition on the radius of $\mathcal{S}$ is given by $r_2\tilde{T} < 1 < r_1\tilde{T}$. Since the heteroclinic orbits are formed when the $\mathcal{S}$ and $\mathcal{E}$ surfaces are tangent at the points $(0, \pm 1, 0)$, the energy level for the heteroclinic orbits must be given by $T = H^2/(2B)$, or $\tilde{T} = 1$ in terms of our nondimensional parameterization. The energy integral then becomes

$$\frac{\tilde{h}_1^2}{r_2} + \tilde{h}_2^2 + \frac{\tilde{h}_3^2}{r_1} = 1. \tag{18}$$

Using Eqs. (13), (14), (15), (16), and (18), it can be shown that the solutions for the $\tilde{h}_i$ along the heteroclinic orbits are given by (Hughes, 1986)

$$\tilde{h}_{1u} = \pm\left[\frac{r_2(1-r_1)}{r_2-r_1}\right]^{1/2} \operatorname{sech}\left\{\left[\frac{(r_2-1)(1-r_1)}{r_1 r_2}\right]^{1/2}\tau\right\} \tag{19}$$

$$\tilde{h}_{2u} = \pm\tanh\left\{\left[\frac{(r_2-1)(1-r_1)}{r_1 r_2}\right]^{1/2}\tau\right\} \tag{20}$$

$$\tilde{h}_{3u} = \pm\left[\frac{r_1(r_2-1)}{r_2-r_1}\right]^{1/2} \operatorname{sech}\left\{\left[\frac{(r_2-1)(1-r_1)}{r_1 r_2}\right]^{1/2}\tau\right\} \tag{21}$$

where the subscript u signifies an unperturbed quantity, $\tau = 0$ has been chosen to eliminate constants of integration, and the appropriate signs are chosen to give the four heteroclinic trajectories.

5.2 Equations of Motion to $\mathcal{O}(\epsilon)$. Using binomial expansions, the equations of motion given by Eqs. (10)–(12) can be expressed as

$$\tilde{h}_1' = \left(\frac{1-r_1}{r_1}\right)\tilde{h}_2\tilde{h}_3 - \epsilon\left[\left(\frac{1-r_1^2}{r_1^2}\right)\tilde{\Delta}\tilde{h}_2\tilde{h}_3 + \tilde{\beta}\tilde{h}_1\tilde{h}_2^2\right] \tag{22}$$

$$\tilde{h}_2' = \left(\frac{r_1-r_2}{r_1 r_2}\right)\tilde{h}_1\tilde{h}_3 + \epsilon\left[\frac{\tilde{\Delta}}{r_1^2}\tilde{h}_1\tilde{h}_3 + \tilde{\beta}\tilde{h}_2\left(\tilde{h}_1^2 - \tilde{h}_3^2\right)\right] \tag{23}$$

$$\tilde{h}_3' = \left(\frac{r_2-1}{r_2}\right)\tilde{h}_1\tilde{h}_2 + \epsilon\left(\tilde{\beta}\tilde{h}_2^2\tilde{h}_3 - \tilde{\Delta}\tilde{h}_1\tilde{h}_2\right) \tag{24}$$

where only terms through $\mathcal{O}(\epsilon)$ have been retained.

We now transform to spherical coordinates. It is convenient to choose the coordinate transformation so that one of the new coordinates is zero along the unperturbed trajectory. This can easily be done since the heteroclinic orbits are great circles on the momentum sphere. Consider the heteroclinic orbit that lies in the region $\tilde{h}_1 > 0$ and $\tilde{h}_3 > 0$. The angle ν between the $\tilde{h}_1$–$\tilde{h}_2$ plane and this heteroclinic orbit can be shown to be

$$\nu = \arctan\left[\frac{r_1(r_2-1)}{r_2(1-r_1)}\right]^{1/2}. \tag{25}$$

Starting with a set of coordinates ξ_1, ξ_2, ξ_3 aligned with the $\tilde{h}_1$, $\tilde{h}_2$, $\tilde{h}_3$ system, rotate the ξ coordinate system through the angle $-\nu$ about the $\tilde{h}_2$-axis so that the positive ξ_1-axis pierces the heteroclinic orbit in the region $\tilde{h}_1 > 0$, $\tilde{h}_3 > 0$. We can then transform from the ξ coordinates to the dimensionless spherical coordinates ϕ and θ to obtain the following equations relating the $\tilde{h}_i$, and ν, θ, and ϕ:

$$\tilde{h}_1 = \cos\nu\cos\theta\cos\phi - \sin\nu\sin\phi, \tag{26}$$

$$\tilde{h}_2 = \sin\theta\cos\phi, \tag{27}$$

$$\tilde{h}_3 = \sin\nu\cos\theta\cos\phi - \cos\nu\sin\phi. \tag{28}$$

Note that there is no radial dependence since the angular momentum sphere has a constant radius. The derivatives with respect to τ are also needed and they are given by

$$\tilde{h}_1' = \phi'(-\cos\nu\sin\phi\cos\theta - \sin\nu\cos\phi) - \theta'\cos\nu\sin\theta\cos\phi, \tag{29}$$

$$\tilde{h}_2' = \theta'\cos\theta\cos\phi - \phi'\sin\theta\sin\phi, \tag{30}$$

$$\tilde{h}_3' = \phi'(\cos\nu\cos\phi - \sin\nu\cos\theta\sin\phi) - \theta'\sin\nu\sin\theta\cos\phi. \tag{31}$$

Downloaded 04 May 2010 to 171.66.16.33. Redistribution subject to ASME license or copyright; see http://www.asme.org/terms/Terms_Use.cfm

Equations (26)–(31) are then substituted into Eqs. (22)–(24) and *any* two of the resulting three equations are then solved, using computer algebra (Wolfram, 1991), for θ' and ϕ'. Note that only two of the equations are independent due to the fact that our phase space lies on the surface of the sphere and is therefore two dimensional. This gives the final two first-order differential equations to which Melnikov's method is applied

$$\begin{aligned}\phi' = \{&[(r_2 - r_1)c\nu c2\nu + r_2(r_1 - 1)c\nu]c\phi c\theta s\phi s\theta \\ &+ [(r_2 - r_1)c^2\nu s\nu + r_2(r_1 - 1)s\nu]c^2\phi c^2\theta s\theta \\ &+ (r_1 - r_2)c^2\nu s\nu s^2\phi s\theta\}/r_1r_2(s\nu c\phi c\theta + c\nu s\phi) \\ &+ \epsilon\{\tilde{\Delta}[(2c\nu s^2\nu - r_1^2c\nu)c\phi c\theta s\phi s\theta \\ &+ (s^3\nu - r_1^2s\nu)c^2\phi c^2\theta s\theta + c^2\nu s\nu s^2\phi s\theta] \\ &+ \tilde{\beta}[r_1^2s\nu(4c^2\nu - 1)c^2\phi c\theta s\phi s^2\theta + 2r_1^2c\nu s^2\phi c^3\phi c^2\theta s^2\theta \\ &+ r_1^2c\nu c2\nu c\phi s^2\phi s^2\theta]\}/r_1^2(s\nu c\phi c\theta + c\nu s\phi). \quad (32)\end{aligned}$$

and

$$\begin{aligned}\theta' = \{&(r_1 - r_2)[c\nu s^2\nu c^3\phi c^2\theta + s\nu c2\nu c^2\phi c\theta s\phi \\ &+ c^2\nu s\nu c^2\phi c^3\theta s\phi - c\nu s^2\nu c\phi s^2\phi + c\nu c2\nu c\phi c^2\theta s^2\phi \\ &- c^2\nu s\nu c\theta c^3\phi] + r_2(r_1 - 1)[s\nu c^2\phi c\theta s\phi s^2\theta \\ &+ c\nu c\phi s^2\phi s^2\theta]\}/r_1r_2(s\nu c^2\phi c\theta + c\nu c\phi s\phi) \\ &+ \epsilon\{\tilde{\Delta}[c\nu s^2\nu c^3\phi c^2\theta + s\nu c2\nu c^2\phi c\theta s\phi + c^2\nu s\nu c^2\phi c^3\theta s\phi \\ &- c\nu s^2\nu c\phi s^2\phi + c\nu c2\nu c\phi c^2\theta s^2\phi - c^2\nu s\nu c\theta s^3 \\ &+ (1 - r_1^2)(s\nu c^2\phi c\theta s\phi s^2\theta + c\nu c\phi s^2\phi s^2\theta)] \\ &+ \tilde{\beta}[r_1^2s\nu c2\nu c^4\phi c^2\theta s\theta - 4r_1^2c\nu s^2\nu c^3\phi c\theta s\phi s\theta \\ &+ r_1^2c\nu c2\nu c^3\phi c^3\theta s\phi s\theta - r_1^2s\nu c2\nu c^2\phi s^2\phi s\theta \\ &- 4r_1^2c^2\nu s\nu c^2\phi c^2\theta s^2\phi s\theta \\ &- r_1^2c\nu c2\nu c\phi c\theta s^3\phi s\theta \\ &+ r_1^2c\nu c^3\phi c\theta s\phi s^3\theta - r_1^2s\nu c^2\phi s^2\phi s^3\theta]\} \\ &/r_1^2(s\nu c^2\phi c\theta + c\nu c\phi s\phi), \quad (33)\end{aligned}$$

where

$$s \triangleq \sin \text{ and } c \triangleq \cos. \quad (34)$$

Equations (32) and (33) are in the desired form, $\phi' = f_1 + \epsilon g_1$ and $\theta' = f_2 + \epsilon g_2$ (see the following section). Finally, the unperturbed solutions given by Eqs. (19)–(21) must be transformed to the same set of spherical coordinates. This transformation gives

$$\sin\theta_u = -\tanh\left\{\left[\frac{(r_2 - 1)(1 - r_1)}{r_1r_2}\right]^{1/2}\tau\right\} \quad (35)$$

$$\cos\theta_u = \operatorname{sech}\left\{\left[\frac{(r_2 - 1)(1 - r_1)}{r_1r_2}\right]^{1/2}\tau\right\} \quad (36)$$

$$\phi_u = 0 \quad (37)$$

along the selected unperturbed heteroclinic orbit, and time was chosen to move along the trajectory from positive to negative $\tilde{h}_2$.

6 The Melnikov Function

Melnikov's method considers systems of the form

$$\dot{\mathbf{x}} = \mathbf{f}(\mathbf{x}) + \epsilon\mathbf{g}(\mathbf{x},t), \quad \mathbf{x} = \begin{Bmatrix} u \\ v \end{Bmatrix} \in \mathbb{R}^2 \quad (38)$$

where $\mathbf{g}$ is of period T in t, $\mathbf{f}(\mathbf{x})$ is a Hamiltonian vector field defined on $\mathbb{R}^2$ and $\epsilon\mathbf{g}(\mathbf{x}, t)$ is a small perturbation which is not necessarily Hamiltonian.

We define the Melnikov function

$$M(t_0) = \int_{-\infty}^{\infty} \mathbf{f}(\mathbf{q}_0(t)) \wedge \mathbf{g}(\mathbf{q}_0(t), t + t_0)\,dt \quad (39)$$

where the symbol $\wedge$ is the wedge operator, defined by $\mathbf{a} \wedge \mathbf{b} = a_1b_2 - a_2b_1$.

Referring to Eqs. (38), (32), and (33), we can easily identify the components of the vector functions $\mathbf{f} = (f_1, f_2)$ and $\mathbf{g} = (g_1, g_2)$ for use in the Melnikov integral, Eq. (39). We must now prescribe the time-dependent form of η by letting $\tilde{\eta} \triangleq \eta/l$, $\tilde{\Omega} \triangleq \Omega B/H$, and $\eta \triangleq \eta_0\cos(\Omega t)$. This definition corresponds to a simple periodic oscillation of the masses, thus modeling phenomena such as reciprocating masses, unbalanced rotors with constant angular velocities, or rotors with time-dependent spin rates.

Any time-dependent form may be chosen for η, but it is clear that some are more tractable than others, and the periodic form we choose accurately models the phenomena we have discussed. It follows that the nondimensional form of Δ is then

$$\tilde{\Delta} = \tilde{\eta}^2 + 4\tilde{\eta}\cos(\tilde{\Omega}\tau) + \tilde{\eta}^2\cos(2\tilde{\Omega}\tau). \quad (40)$$

Substituting the unperturbed solutions $\mathbf{q}_0(\tau)$, given by Eqs. (35)–(37), into $\mathbf{f}(\mathbf{q}_0(\tau))$ and $\mathbf{g}(\mathbf{q}_0(\tau), \tau + \tau_0)$, carrying out the wedge product, and substituting the result into the Melnikov integral given by Eq. (39) yields

$$\begin{aligned}M(\tau_0) = \int_{-\infty}^{\infty} \big[&-C_1C_3\tilde{\eta}^2\operatorname{sech}^2(C_1\tau)\tanh(C_1\tau) \\ &-4C_1C_3\tilde{\eta}\cos\big(\tilde{\Omega}(\tau + \tau_0)\big)\operatorname{sech}^2(C_1\tau)\tanh(C_1\tau) \\ &-C_1C_3\tilde{\eta}^2\cos\big(2\tilde{\Omega}(\tau + \tau_0)\big)\operatorname{sech}^2(C_1\tau)\tanh(C_1\tau) \\ &+C_4\bar{\beta}\operatorname{sech}^2(C_1\tau)\tanh^2(C_1\tau)\big]d\tau. \quad (41)\end{aligned}$$

where the following new quantities have been defined:

$$C_1 \triangleq \left[\frac{(r_1 - 1)(1 - r_2)}{r_1r_2}\right]^{1/2} = C_1(r_1,r_2), \quad (42)$$

$$C_3 \triangleq \frac{(r_1 - 1)(r_2 - r_1 - 1)}{r_1(r_2 - r_1)} = C_3(r_1,r_2), \quad (43)$$

$$C_4 \triangleq \frac{2(r_1 - 1)(r_2 - 1)}{r_2 - r_1} = C_4(r_1,r_2). \quad (44)$$

The evaluation of the integrals in Eq. (41) can be accomplished via the residue theorem of complex variable theory. Upon carrying out the integration, we obtain the following Melnikov function:

$$\begin{aligned}M(\tau_0) = &\frac{2C_4\tilde{\beta}}{3C_1} + \frac{2\pi C_3\tilde{\eta}\tilde{\Omega}^2}{C_1^2} \\ &\times\left[\frac{\sin(\tilde{\Omega}\tau_0)}{\sinh\left[\pi\tilde{\Omega}/(2C_1)\right]} + \tilde{\eta}\frac{\sin(2\tilde{\Omega}\tau_0)}{\sinh(\pi\tilde{\Omega}/C_1)}\right]. \quad (45)\end{aligned}$$

Melnikov theory states that the condition for chaos is that $M(\tau_0)$ change sign for some τ_0. Inspection of the Melnikov function reveals that there are two harmonic terms, one with

Downloaded 04 May 2010 to 171.66.16.33. Redistribution subject to ASME license or copyright; see http://www.asme.org/terms/Terms_Use.cfm

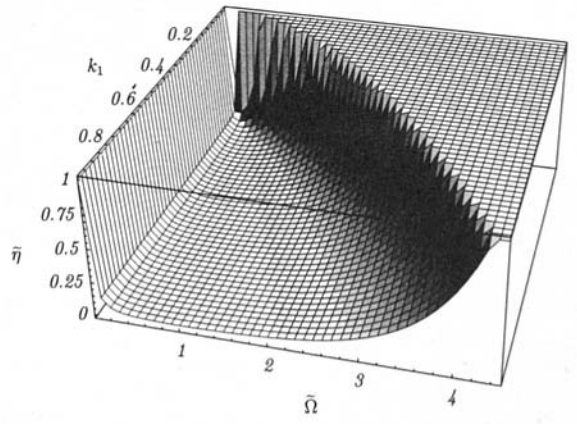


Fig. 3 The surface separating chaotic from nonchaotic motion for the parameter space $\tilde{\Omega}$-$\tilde{\eta}$-k_1 as given by the Melnikov criterion in Eq. (49). The parameters $\tilde{\beta}$ and k_3 were chosen to have the values 0.1 and 2/3, respectively.

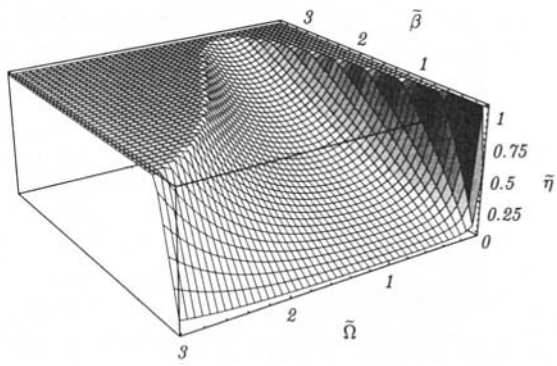


Fig. 4 The surface separating chaotic from nonchaotic motion for the parameter space $\tilde{\Omega}$-$\tilde{\eta}$-$\tilde{\beta}$ as given by the Melnikov criterion in Eq. (47). The parameters k_1 and k_3 were chosen to have the values 0.8 and 2/3, respectively.

twice the frequency of the other. Therefore, the maximum amplitude of the factor containing the harmonic terms is some function F_{max} of *both* of the harmonic amplitudes. It can be shown that F_{max} is given by

$$F_{max} = \frac{1}{4}\left(3\mathfrak{A} + \sqrt{\mathfrak{A}^2 + 32\,\mathfrak{B}^2}\right) \times \left[\frac{1}{2} + \frac{\mathfrak{A}}{32\,\mathfrak{B}^2}\left(\sqrt{\mathfrak{A}^2 + 32\,\mathfrak{B}^2} - \mathfrak{A}\right)\right]^{1/2}, \quad (46)$$

Given this relationship for F_{max}, the criterion for chaos becomes

$$\frac{3\pi(r_2 - r_1 - 1)\sqrt{r_2}\,\tilde{\eta}\tilde{\Omega}^2 F_{max}}{2(r_2 - 1)\sqrt{r_1(r_1 - 1)(1 - r_2)}} > \tilde{\beta}. \quad (47)$$

Equation (47) gives the analytical condition for chaos. This result divides the parameter space into regions where horseshoes and chaotic transients exist from regions where they do not. Close inspection reveals that Eq. (47) is a function of the five system parameters, r_1, r_2, $\tilde{\eta}$, $\tilde{\Omega}$, and $\tilde{\beta}$. If Eq. (47) is satisfied, then the system modeled by Eqs. (10)–(12) exhibits chaotic dynamics near the heteroclinic orbits for sufficiently small ϵ.

Before discussing the analytical Melnikov result, we first write Eq. (47) in terms of the Smelt (DeBra-Delp) parameters so that it can also be interpreted within that framework. Various authors define the Smelt parameters differently, but here we use the same definitions that DeBra and Delp (1961) used in their original paper

$$k_1 \triangleq \frac{C - B}{A}, \quad k_2 \triangleq \frac{A - C}{B}, \quad k_3 \triangleq \frac{B - A}{C}.$$

Then, choosing to use k_1 and k_3 as the two moment of inertia parameters, r_1 and r_2 become

$$r_1 = \frac{1 + k_1}{1 + k_1 k_3}, \quad r_2 = \frac{1 - k_3}{1 + k_1 k_3}. \quad (48)$$

Since $A < B < C$, it can be shown (Rimrott, 1989) that $0 < k_1 < 1$ and $0 < k_3 < 1$.

Using the relations in Eqs. (48), the definition for F_{max} remains unchanged, but the definition for C_1 becomes

$$C_1 = \sqrt{k_1 k_3}$$

and, the expression in Eq. (47) of the criterion for chaos becomes

$$\frac{3\pi(1 + k_3)(1 + k_1 k_3)\tilde{\eta}\tilde{\Omega}^2 F_{max}}{2k_3(1 + k_1)\sqrt{k_1 k_3}} > \tilde{\beta} \quad (49)$$

where F_{max} is given by Eq. (46).

7 Results

We have analytically proven the existence of transient chaos in the attitude motion of a quasi-rigid satellite with non-Hamiltonian, time-periodic perturbations. The derived criterion can be used to find chaotic and nonchaotic regions in parameter space and, if necessary, avoid chaotic motion in this class of satellite systems. The Melnikov criterion for chaos depends on five parameters: moment of inertia parameters r_1 and r_2 (or k_1 and k_3), forcing frequency $\tilde{\Omega}$, forcing amplitude $\tilde{\eta}$, and the damping $\tilde{\beta}$. By fixing two of the parameters, the others can be studied in a three-dimensional parameter space. Parametric studies of three-dimensional parameter subspaces for Eqs. (47) and (49) are shown in Figs. 3–6.

Figure 3 shows the dividing surface between chaotic and nonchaotic motion in $\tilde{\Omega}$-$\tilde{\eta}$-k_1 space as determined by Eq. (49). The moment of inertia parameter k_3 was chosen to be equal to 2/3 and the damping parameter $\tilde{\beta}$ was set equal to 0.1. By fixing $\tilde{\beta}$ at 0.1, we are not only fixing the amount of damping, but we are also fixing the size of the perturbing masses. Values of the parameters *above* the surface are chaotic. The surface "flattens" out at $\tilde{\eta} = 1$ since we impose $\tilde{\eta} < 1$ due to limits in the motion of the perturbing subbodies, i.e., we do not consider values of $\tilde{\eta} > 1$, corresponding to motion of the masses which pass through the spacecraft's mass center c. This is true for all figures where the surface flattens at $\tilde{\eta} = 1$. We can see that as k_1 increases it becomes easier to achieve chaotic motion. In addition we see what appears to be a resonance condition in the $\tilde{\Omega}$-$\tilde{\eta}$ plane. This resonance frequency changes slightly as k_1 changes and therefore depends on the shape of the satellite. The dependence of this resonance frequency upon the "natural" frequencies occurring in the motion of a torque-free rigid body, such as precessional and nutational frequencies, is being investigated. For small and large values of $\tilde{\Omega}$, it is impossible to obtain chaos for any value of $\tilde{\eta} < 1$. Whereas for intermediate values of $\tilde{\Omega}$ (e.g., $\tilde{\Omega} \approx 0.25$–$0.35$), chaos is much easier to attain and is virtually assured for large values of $k_1 \to 1$. We also see that for values of k_1 approaching zero, which corresponds to a nearly symmetric, prolate rigid body, no chaotic motion occurs for the constant values of k_3 and $\tilde{\beta}$ chosen and for $\tilde{\eta} < 1$ and *any* values of $\tilde{\Omega}$ and k_1.

Figure 4 illustrates the dividing surface between chaotic and nonchaotic regions in $\tilde{\Omega}$-$\tilde{\eta}$-$\tilde{\beta}$ space as determined by Eq.

Downloaded 04 May 2010 to 171.66.16.33. Redistribution subject to ASME license or copyright; see http://www.asme.org/terms/Terms_Use.cfm

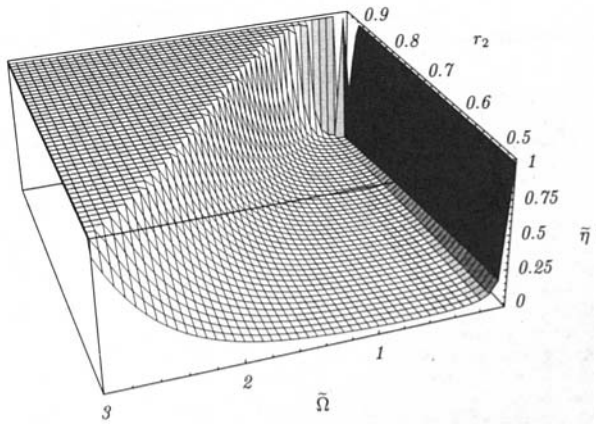


Fig. 5 The surface separating chaotic from nonchaotic motion for the parameter space $\tilde{\Omega}$-$\tilde{\eta}$-r_2 as given by the Melnikov criterion in Eq. (47). The parameters $\tilde{\beta}$ and r_1 were chosen to have the values 0.1 and 1.5, respectively.

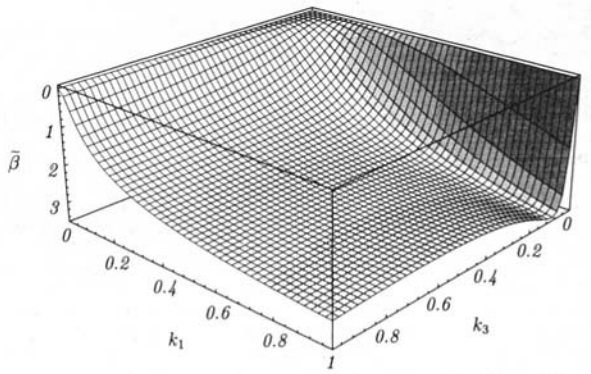


Fig. 6 The surface separating chaotic from nonchaotic motion for the parameter space $\tilde{\beta}$-k_1-k_3 as given by the Melnikov criterion in Eq. (49). The parameters $\tilde{\eta}$ and $\tilde{\Omega}$ were chosen to have the values 0.9 and 0.5, respectively.

(47). As in Fig. 3, the chaotic region is above the surface. We again see the resonance effect in the $\tilde{\Omega}$-$\tilde{\eta}$ plane, but now at $\tilde{\Omega} \approx 0.5$. The resonance frequency is constant in this figure since the moments of inertia of the satellite (k_1 and k_3) are fixed for all values of $\tilde{\eta}$, $\tilde{\Omega}$, and $\tilde{\beta}$ and therefore the shape of the satellite does not vary. As $\tilde{\beta} \to 0$, chaotic motion occurs for all values of $\tilde{\Omega}$ and $\tilde{\eta}$, which is what we expect from the theory of Hamiltonian systems: a generic perturbation of a Hamiltonian system yields chaotic motion in a layer surrounding a heteroclinic orbit (Lichtenberg and Lieberman, 1992). In addition, we see that if $\tilde{\beta}$ is increased to large enough values, it is impossible to attain chaotic motion for values of $\tilde{\eta} < 1$. This too is physically reasonable: sufficient damping suppresses the chaos. We should also note that $\tilde{\beta} \propto 1/m$, where m is the perturbing mass. Thus, as m is increased, $\tilde{\beta}$ decreases and we find that the chaotic surface is more easily reached. This too agrees with intuition. Larger perturbations (i.e., oscillating masses) are more likely to produce chaotic motion. If the masses are made small enough for a fixed amount of satellite damping, they will have a negligible effect on the satellite and chaotic motion will be impossible.

Figure 5 shows the dividing surface between chaotic and nonchaotic motion in $\tilde{\Omega}$-$\tilde{\eta}$-r_2 space for $\tilde{\beta} = 0.1$ and $r_1 = 3/2$. Motion is chaotic for values above the surface. The parameter r_2 ranges from 0.5 to 1 since r_1 was chosen to be 1.5 (see Eq. (9)). The behavior is very interesting in that chaotic motion is virtually assured for values of r_2 approaching unity and small values of $\tilde{\Omega}$. This corresponds to a nearly symmetric oblate spacecraft with small perturbing frequencies. This supplements the result described above for a nearly symmetric prolate spacecraft where chaos is impossible to attain. These results are not obvious and are a subject for further study.

In Fig. 6 the chaotic region is above the surface shown. It can be seen that for smaller values of k_3 and larger values of k_1, chaos can be achieved for a range of $\tilde{\beta}$. On the other hand, as $k_1 \to 0$ and $k_3 \to 1$, chaos cannot be achieved no matter how small $\tilde{\beta}$ is made. Again, $k_1 \to 0$ corresponds to a nearly symmetric and prolate body, and it is impossible to have chaos. As $k_3 \to 0$ the body becomes nearly symmetric and oblate and chaotic motion is assured for a large range of $\tilde{\beta}$.

It is important to note that the results correspond specifically to the case where the oscillating masses are aligned with the minor principal axis.

8 Conclusion

We have derived an analytical criterion for the occurrence of a chaotic region of phase space in terms of system parameters for an energy dissipating, quasi-rigid satellite with time-periodic perturbations. The analytical criterion for the occurrence of chaos is obtained by applying Melnikov's method to a quasi-rigid satellite model. This model is a Hamiltonian system perturbed by a non-Hamiltonian perturbation in the form of oscillations of subbodies and damping in the satellite. It is obvious from the modern theory of nonlinear dynamics that chaos can occur via the breakup of heteroclinic orbits in this class of systems. The contribution of this paper is the formulation of physically reasonable spacecraft models to which Melnikov's method can be applied and the performance of the difficult calculations required to obtain an uncomplicated criterion for chaos that can easily be used for satellite design.

The chaotic region occurs near heteroclinic orbits in the system's phase space and is traversed during a typical attitude maneuver. Since the chaotic region could introduce uncertainties into both the attitude maneuver and simulations checking the maneuver, it is prudent, at the present state of knowledge, to design the satellite so that the chaotic region does not exist. Chaos in the equations of motion for a satellite implies a sensitive dependence on initial conditions and a very complicated structure of the phase space. The sensitive dependence on initial conditions rules out the current practice of a straightforward check on the satellite attitude maneuver by a sample numerical integration. More extensive or elaborate simulations would have to be developed and applied to achieve confidence in a satellite design which maneuvered through a chaotic region. The specific effects of the chaotic region on the satellite mission are not well understood, but we suggest that the spacecraft could possibly be trapped in the chaotic layer for an unacceptably long time. The analytical criterion we have developed will be of great value in designing satellites such that chaotic motion is avoided.

In addition, subspaces of the full parameter space are readily studied to obtain a qualitative understanding of the interactions of the various parameters during chaotic motion. The complete Melnikov result is easily used to obtain the quantitative information needed when a satellite and its subsystems are being designed. Future work will further investigate this parameter space and extend our approach to better understand the onset of chaos in other classes of spacecraft.

Acknowledgments

The authors would like to thank Mark C. Stabb for his thoughtful discussions and assistance with the debugging of

Downloaded 04 May 2010 to 171.66.16.33. Redistribution subject to ASME license or copyright; see http://www.asme.org/terms/Terms_Use.cfm

Mathematica notebooks. The first author gratefully acknowledges the support of NASA through the National Space Grant College and Fellowship Program and the Wisconsin Space Grant Consortium. The second author gratefully acknowledges funding in part by NSF PYI grant ECS-9157192. In addition, the authors would like to acknowledge the work done by Junkins et al. (1973) as it was a major inspiration for our work.

References

Adams, G. J., 1980, "Dual-Spin Spacecraft Dynamics During Platform Spinup," *Journal of Guidance and Control*, Vol. 3, No. 1, pp. 29–36.

Baillieul, J., and Levi, M., 1987, "Rotational Elastic Dynamics," *Physica D.*, Vol. 27, pp. 43–62.

Barba, P. M., Furumoto, N., and Leliakov, I. P., 1973, "Techniques for Flat-Spin Recovery of Spinning Satellites," *AIAA Guidance and Control Conference*, Key Biscayne, FL, AIAA Paper 73-859.

Cochran, J. E., and Holloway, H. E., 1980, "Resonances in the Attitude Motions of Asymmetric Dual-Spin Spacecraft," *The Journal of the Astronautical Sciences*, Vol. 28, No. 3, pp. 231–254.

Cronin, D. L., 1978, "Flat Spin Recovery of a Rigid Asymmetric Spacecraft," *Journal of Guidance and Control*, Vol. 1, No. 4, pp. 281–282.

DeBra, D. B., and Delp, R. H., 1961, "Rigid Body Attitude Stability and Natural Frequencies in a Circular Orbit," *The Journal of the Astronautical Sciences*, Vol. 8, pp. 14–17.

Dovbysh, S. A., 1989, "Some New Dynamical Effects in the Perturbed Euler-Poinsot Problem Due to Splitting of Separatrices," *Journal of Applied Mathematics and Mechanics*, Vol. 53, No. 2, pp. 165–173.

Gebman, J. R., and Mingori, D. L., 1976, "Perturbation Solution for the Flat Spin Recovery of a Dual-Spin Spacecraft," *AIAA Journal*, Vol. 14, No. 7, pp. 859–867.

Greenspan, B. D., and Holmes, P. J., 1983, "Homoclinic Orbits, Subharmonics and Global Bifurcations in Forced Oscillations," *Nonlinear Dynamics and Turbulence*, G. I. Barenblatt, G. Iooss, and D. D. Joseph, eds., Pitman Publishing, Boston, MA, pp. 172–214.

Guckenheimer, J., and Holmes, P. J., 1983, *Nonlinear Oscillations, Dynamical Systems, and Bifurcations of Vector Fields*, Springer-Verlag, New York.

Hall, C. D., and Rand, R. H., 1991, "Spinup Dynamics of Axial Dual-Spin Spacecraft," *AAS/AIAA Astrodynamics Specialist Conference*, Durango, CO, Aug. 19–22, Paper AAS 91-403.

Holmes, P. J., and Marsden, J. E., 1983, "Horseshoes and Arnold Diffusion for Hamiltonian Systems on Lie Groups," *Indiana University Mathematics Journal*, Vol. 32, No. 2, pp. 273–309.

Hughes, P. C., 1986, *Spacecraft Attitude Dynamics*, John Wiley and Sons, New York.

Junkins, J. L., and Jacobson, I. D., and Blanton, J. N., 1973, "A Nonlinear Oscillator Analog of Rigid Body Dynamics," *Celestial Mechanics*, Vol. 7, pp. 398–407.

Kammer, D. C., and Gray, G. L., 1992, "A Nonlinear Control Design for Energy Sink Simulation in the Euler-Poinsot Problem," *The Journal of the Astronautical Sciences*, Vol. 41, No. 1, pp. 53–72.

Kaplan, M. H., and Cenker, R. J., 1973, "Control of Spin Ambiguity During Reorientation of an Energy Dissipating Body," *Journal of Spacecraft and Rockets*, Vol. 10, No. 12, pp. 757–760.

Koiller, J., 1984, "A Mechanical System with a 'Wild' Horseshoe," *Journal of Mathematical Physics*, Vol. 25, No. 5, pp. 1599–1604.

Krishnaprasad, P. S., 1985, "Lie-Poisson Structures, Dual-Spin Spacecraft and Asymptotic Stability," *Nonlinear Analysis, Theory, Methods & Applications*, Vol. 9, No. 10, pp. 1011–1035.

Krishnaprasad, P. S., and Marsden, J. E., 1987, "Hamiltonian Structures and Stability for Rigid Bodies with Flexible Attachments," *Archive for Rational Mechanics and Analysis*, Vol. 98, No. 1, pp. 71–93.

Lichtenberg, A. J., and Lieberman, M. A., 1992, *Regular and Chaotic Dynamics*, 2nd Ed., Springer-Verlag, New York.

Or, A. C., 1991, "Resonances in the Despin Dynamics of Dual-Spin Spacecraft," *Journal of Guidance, Control, and Dynamics*, Vol. 14, No. 2, pp. 321–329.

Palis, J., and Takens, F., 1993, *Hyperbolicity and Sensitive Chaotic Dynamics at Homoclinic Bifurcations*, Cambridge University Press, New York.

Rahn, C. D., and Barba, P. M., 1991, "Reorientation Maneuver for Spinning Spacecraft," *Journal of Guidance, Control, and Dynamics*, Vol. 14, No. 4, pp. 724–728.

Rimrott, F. P. J., 1989, *Introductory Attitude Dynamics*, Springer-Verlag, New York.

Rubanovskii, V. N., 1988, "On the Relative Equilibria of a Satellite-Gyrostat, Their Branchings and Stability," *Journal of Applied Mathematics and Mechanics*, Vol. 52, No. 6, pp. 710–714.

Wiggins, S., 1990, *Introduction to Applied Nonlinear Dynamical Systems and Chaos*, Springer-Verlag, New York.

Wolfram, S., 1991, *Mathematica: A System for Doing Mathematics by Computer*, 2nd Ed., Addison-Wesley, Redwood City, CA.

Ziglin, S. L., 1982, "Splitting of Separatrices, Branching of Solutions and Nonexistence of an Integral in the Dynamics of a Solid Body," *Transactions of the Moscow Mathematical Society*, Issue 1, pp. 283–298.

Downloaded 04 May 2010 to 171.66.16.33. Redistribution subject to ASME license or copyright; see http://www.asme.org/terms/Terms_Use.cfm

Analysis of a Nonlinear System Exhibiting Chaotic, Noisy Chaotic, and Random Behaviors

H. Lin
Research Associate.

S. C. S. Yim
Associate Professor,
Mem. ASME.

Department of Civil Engineering,
Oregon State University,
Corvallis, OR 97331-2303

This study presents a stochastic approach for the analysis of nonchaotic, chaotic, random and nonchaotic, random and chaotic, and random dynamics of a nonlinear system. The analysis utilizes a Markov process approximation, direct numerical simulations, and a generalized stochastic Melnikov process. The Fokker-Planck equation along with a path integral solution procedure are developed and implemented to illustrate the evolution of probability density functions. Numerical integration is employed to simulate the noise effects on nonlinear responses. In regard to the presence of additive ideal white noise, the generalized stochastic Melnikov process is developed to identify the boundary for noisy chaos. A mathematical representation encompassing all possible dynamical responses is provided. Numerical results indicate that noisy chaos is a possible intermediate state between deterministic and random dynamics. A global picture of the system behavior is demonstrated via the transition of probability density function over its entire evolution. It is observed that the presence of external noise has significant effects over the transition between different response states and between co-existing attractors.

Introduction

The effects of noise on nonlinear dynamical systems exhibiting chaotic behavior have been of interest to researchers in various fields in recent years. Frey and Simiu (1992) derived a generalized stochastic Melnikov function by considering the additive noise as a perturbation to the homoclinic orbit, and concluded that the presence of weak noise can not suppress chaotic motion. Probabilistic properties of noisy nonlinear responses have been demonstrated by probability density functions. By solving the Fokker-Planck equation for marginal probability density functions of nonlinear systems driven by periodic excitation and random noise, Kapitaniak (1988) observed that noisy chaotic response is nonstationary and can be characterized by a multi-maxima curve in marginal probability density functions. Examining the noise effect on the response behavior of nonlinear systems through the Lyapunov exponent and probability density function, Bulsara et al. (1990) numerically demonstrated the noise-induced chaos and smoothing effect. Employing a finite difference procedure to solve the Fokker-Planck equation, Kunert and Pfeiffer (1991) found that the resulting steady-state joint probability density function can portray the corresponding chaotic attractor on the Poincaré section.

This investigation systematically analyzes all the possible dynamical responses in a nonlinear system from a stochastic perspective. The links among distinct (in a classical sense) dynamical responses (i.e., nonchaotic, chaotic, random and nonchaotic, random and chaotic, and purely random) in a nonlinear system are examined. By introducing a modulation factor which governs the relative strengths of deterministic and stochastic forcings, all possible dynamics can be formulated under a single mathematical representation. By varying this factor, diverse dynamical phenomena are exhibited, and possible transition routes from deterministic responses to purely random responses can be demonstrated. Probabilistic representation of noisy responses is provided by the probability density function, which is obtained by solving the Fokker-Planck equation. The path integral solution is employed to numerically solve the Fokker-Planck equation to demonstrate the evolution of probability density function (not examined in previous works), which characterizes the global system behavior. Moreover, the steady-state probability density functions can reflect existing response attractors. The noise-induced transition between the co-existing attractors is also examined. A generalized stochastic Melnikov process is develop to identify a boundary for possible chaotic domain by extending the deterministic Melnikov function to include stochastic excitations. Contrasted to the work by Frey and Simiu (1992), ideal white noise instead of Shinozuka's band-limited noise is used in our formulation. Noise-induced transition from nonchaotic response to noisy chaotic response becomes analytically evident when a mean-square representation of generalized stochastic Melnikov criterion is derived. Although the proposed analysis approach is completely general, for convenience of demonstration, the well-studied Duffing system is employed.

System Considered

A periodically forced Duffing system with additive random perturbation is given by

$$\ddot{x} + c\dot{x} - x + x^3 = (1 - \gamma)B \cos \omega t + \gamma\xi(t) \qquad (1)$$

where $\xi(t)$ is a zero-mean and delta-correlated Gaussian white noise with noise intensity ν. In Eq. (1), γ is a modulation factor determining the relative strengths of deterministic and stochastic forcings. By varying γ, the full range from purely deterministic systems ($\gamma = 0$) to purely random systems ($\gamma = 1$) is represented. In the intermediate states ($0 < \gamma < 1$), the Duffing system is subjected to both periodic excitation and Gaussian white noise. The noise effect on the nonlinear response can be examined by fixing the deterministic excitation and varying the noise intensity. For this purpose, the modulated periodic forcing amplitude, $A = (1 - \gamma)B$, and noise intensity, $\kappa = \gamma^2\nu$, are introduced. Equation (1) becomes

$$\ddot{x} + c\dot{x} - x + x^3 = A \cos \omega t + \eta(t) \qquad (2)$$

Contributed by the Applied Mechanics Division of THE AMERICAN SOCIETY OF MECHANICAL ENGINEERS for publication in the ASME JOURNAL OF APPLIED MECHANICS.

Discussion on this paper should be addressed to the Technical Editor, Professor Lewis T. Wheeler, Department of Mechanical Engineering, University of Houston, Houston, TX 77204-4792, and will be accepted until four months after final publication of the paper itself in the ASME JOURNAL OF APPLIED MECHANICS.

Manuscript received by the ASME Applied Mechanics Division, Mar. 31, 1994; final revision, May 18, 1995. Associate Technical Editor: P. D. Spanos.

Copyright © 1996 by ASME

Downloaded 04 May 2010 to 171.66.16.33. Redistribution subject to ASME license or copyright; see http://www.asme.org/terms/Terms_Use.cfm

where $\eta(t)$ is a Gaussian white noise with modulated intensity κ. Depending on the purpose of illustration, Eqs. (1) and (2) are utilized alternatively. The corresponding Hamiltonian (unperturbed) system can be obtained by introducing two state variables, q and p:

$$\begin{Bmatrix} \dot{q} \\ \dot{p} \end{Bmatrix} = f(q, p) = \begin{Bmatrix} \dfrac{\partial H(q, p)}{\partial p} \\ -\dfrac{\partial H(q, p)}{\partial q} \end{Bmatrix} = \begin{Bmatrix} p \\ q - q^3 \end{Bmatrix} \quad (3)$$

where $[q, p]^T = [x, \dot{x}]^T$, and $H(q, p)$ represents the Hamiltonian (Guckenheimer and Holmes, 1983). Equation (2) can be expressed as follows:

$$\begin{Bmatrix} \dot{q} \\ \dot{p} \end{Bmatrix} = f(q, p) + g(q, p; t);$$

$$g(q, p; t) = \begin{Bmatrix} 0 \\ -cp + A \cos \omega t + \eta(t) \end{Bmatrix} \quad (4)$$

where $g(q, p; t)$ is the perturbation to the Hamiltonian system.

Methods of Analysis

To examine the (noisy) nonlinear behavior of the system in a stochastic sense, a Markov process approach is described in detail. Generalized stochastic Melnikov process is developed to analytically demonstrate noise-induced transition. Direct numerical simulations are employed to validate the analytical predictions.

Markov Process Approach. The behavior of a nonlinear system subjected to periodic excitation and white noise can be approximated as a Markov process (Kapitaniak, 1988), and the conditional probability density function of this process is determined by the knowledge of the most recent condition (Risken, 1984). Probability density functions of a Markov process obeys a statistically equivalent deterministic partial differential equation—the Fokker-Planck equation. The temporal solution to this equation can be obtained using a path integral solution procedure.

Fokker-Planck Equation. The Fokker-Planck equation associated to Eq. (3) is given by

$$\frac{\partial \mathbf{P}(q, p, t)}{\partial t} = -\frac{\partial}{\partial q}\{p\mathbf{P}(q, p, t)\} - \frac{\partial}{\partial p}\{(-cp + q - q^3 + A \cos \omega t)\, \mathbf{P}(q, p, t)\} + \frac{\kappa}{2}\frac{\partial^2}{\partial p^2}\mathbf{P}(q, p, t) \quad (5)$$

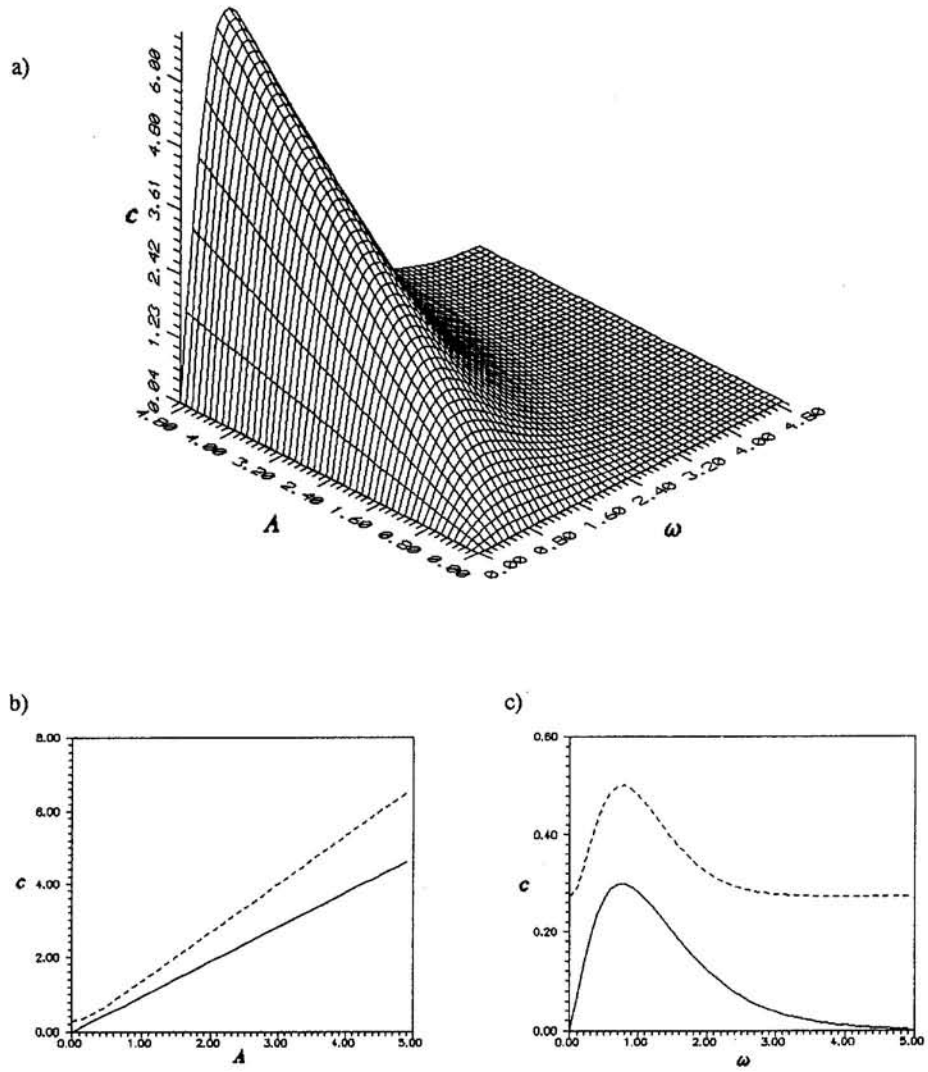


Fig. 1 Upper bound for possible chaotic domain based on generalized stochastic Melnikov process: (*a*) upper surface in *c*-*A*-ω space; (*b*) upper bound in *c*-*A* plane with $\omega = 1.0$; (*c*) upper bound in *c*-ω plane with $A = 0.3$; $\kappa = 0.0$ and 0.01 for solid and dashed lines, respectively.

Downloaded 04 May 2010 to 171.66.16.33. Redistribution subject to ASME license or copyright; see http://www.asme.org/terms/Terms_Use.cfm

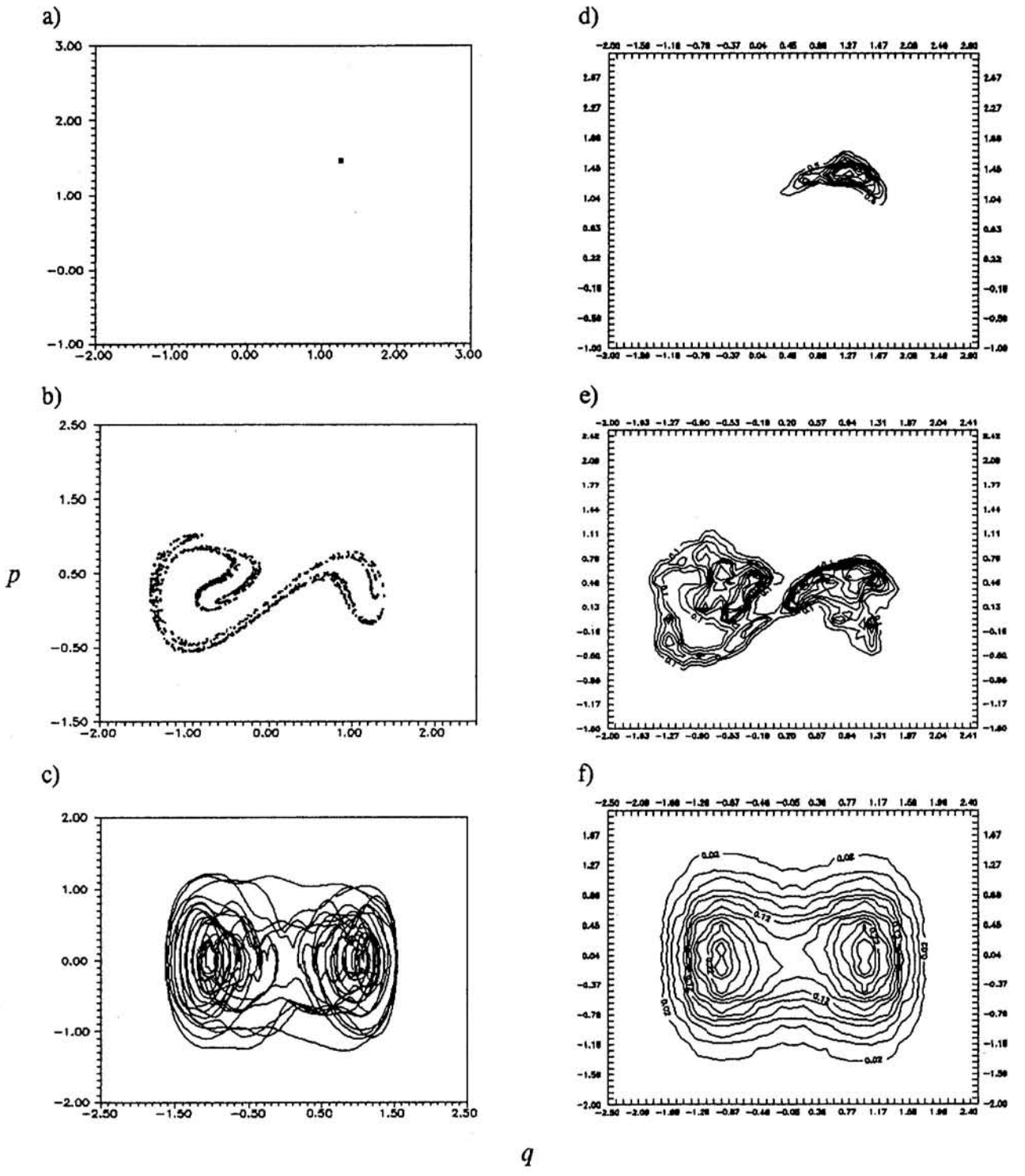


Fig. 2 Possible dynamical responses: (*a*) deterministic periodic attractor (Poincaré map); (*b*) deterministic chaotic attractor (Poincaré map); (*c*) sample realization of random response (phase plane); joint probability density functions of (*d*) random and periodic, (*e*) random and chaotic, and (*f*) random responses.

where $\mathbf{P}(q, p, t)$ denotes the probability density function, p and $-cp + q - q^3 + A \cos \omega t$ are the two components in the drift vector, and κ is the only nonzero entry in the diffusion matrix (Gardiner, 1985). The periodic excitation in the drift vector (Eq. (5)) implies that the probability density function is periodic with period $2\pi/\omega$ in time (Stratonovich, 1967). The periodicity in the joint probability density function can be suppressed by sampling the probability on the Poincaré section, $\mathbf{P}_p(q, p)$, and the steady state of which appears invariant (Kunert and Pfeiffer, 1991). This representation of probability density function will be used throughout the study.

Path Integral Solution. In the path integral solution procedure, the traveling path of the probability density function is discretized in terms of infinitesimal segments in probability space (Wissel, 1979). Each segment represents a short time propagation which is approximated by a time-dependent Gaussian distribution called the short time probability density

Downloaded 04 May 2010 to 171.66.16.33. Redistribution subject to ASME license or copyright; see http://www.asme.org/terms/Terms_Use.cfm

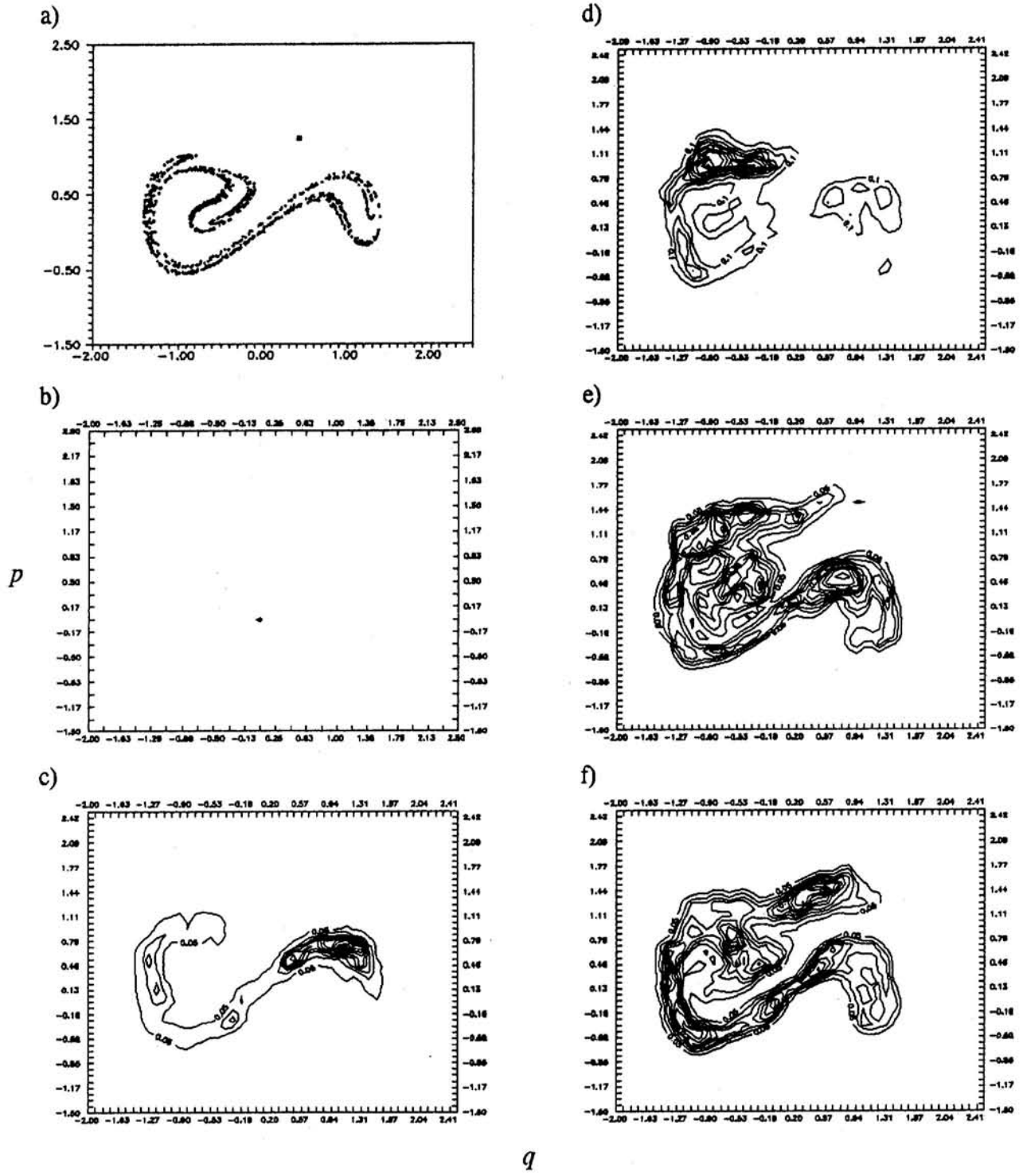


Fig. 3 Evolution of joint probability density function: (*a*) coexisting deterministic chaotic and periodic attractors in Poincaré map with $c = 0.163$, and initial conditions at (0, 0) and (1.0, 1.5), respectively; joint probability density function at (*b*) initiation, and at (*c*) the 2nd, (*d*) the 3rd, (*e*) the 5th, and (*f*) the 25th cycle of the forcing period, $c = 0.185$; $(A, \omega, \kappa) = (0.3, 1.0, 0.003)$.

function. The mean and variance of this probability density function are determined by the drift vector and the diffusion matrix, respectively. At the succeeding state, the probability density function can be obtained through a short time propagation and the probability density function at the desired state can be obtained by applying the propagation iteratively. For the system considered the short time probability density function, $\mathbf{G}(q', p', q, p, t; \tau)$, is given by

$$\mathbf{G}(q', p', q, p, t; \tau) = \frac{1}{\sqrt{2\pi\kappa\tau}} \exp\left[-\frac{\tau}{2\kappa} \left(-cp + q - q^3 + A \cos \omega t - \frac{p' - p}{\tau} \right)^2 \right] \delta\left(p - \frac{q' - q}{\tau} \right) \quad (6)$$

where vectors $[q', p']^T$ and $[q, p]^T$ represent the post-state and

Downloaded 04 May 2010 to 171.66.16.33. Redistribution subject to ASME license or copyright; see http://www.asme.org/terms/Terms_Use.cfm

pre-state, respectively, and the probability density function at the time t is given by

$$\mathbf{P}(q, p, t) = \lim_{\substack{\tau \to 0 \\ N \to \infty \\ N\tau \to t - t_o}} \prod_{i=0}^{N-1} \int \cdots \int \exp[-\tau \sum_{j=0}^{N-1} \mathbf{G}(q_{i+1}, p_{i+1}, q_i, p_i, t_j; \tau)] \mathbf{P}(q_o, p_o, t_o) dq_i dp_i \quad (7)$$

where $\mathbf{P}(q_o, p_o, t_o)$ is the probability density function of the initial conditions. The path integral solution procedure converges to the exact solution in the limit as $N \to \infty$ and $\tau \to 0$. It is noted that, as $\kappa \to 0$, the path integral solution converges to the path of the deterministic (single) response trajectory. The numerical approach of the path integral is based on a discrete lattice representation (Wehner and Wolfer, 1983). By discretizing the probability domains at the ends of the segments (i.e., pre-state and post-state), the short-time probability density function is converted to the transition tensor, and the probability density function at the post-state is obtained by accumulating all contributions from the pre-state. The desired probability density function can be achieved by iterating the above procedure. Numerical results obtained in this study indicate that the path integral solution procedure is quite computationally efficient.

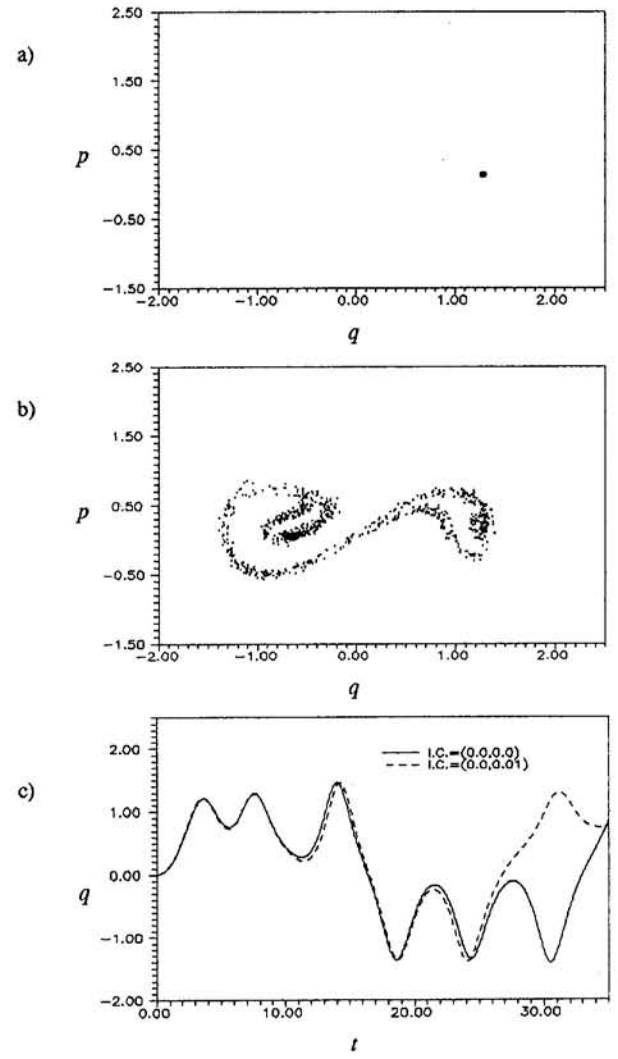


Fig. 4 Noise-induced chaos: (*a*) periodic response with $\gamma\sigma = 0.0$ (Poincaré map); (*b*) noise-induced chaotic response with $\gamma\sigma = 0.05$ (Poincaré map); (*c*) sensitivity to initial conditions (time history, corresponding to (*b*)); (A, ω, c) = (0.25, 1.0, 0.185).

Generalized Melnikov Method. A generalized version of the Melnikov function for a system subjected to an excitation with multiple frequencies was introduced by Wiggins (1988, 1990). The generalized stochastic Melnikov function (or more appropriately, the generalized stochastic Melnikov "process," due to its time dependency and random nature) for the Duffing system subjected to periodic and weak white noise is derived here. Unlike previous studies, a criterion based on the generalized Melnikov process is developed using a mean square representation to explicitly express the noise effects on possible occurrence of chaotic response.

The generalized stochastic Melnikov process is performed by treating the weak noise as a perturbation along with damping and periodic excitation. Assuming smallness of the perturbations, cp, $A \cos \omega t$, and $\eta(t)$, and expressing the pair of homoclinic orbits by explicit time functions, $(q^o(t), p^o(t)) = (\pm \sqrt{2} \operatorname{sech}(t), \mp\sqrt{2} \sinh(t) \operatorname{sech}^2(t))$ (Guckenheimer and Holmes, 1983), then the generalized stochastic Melnikov process is given by

$$\begin{aligned} M_g^+(t_{1o}, t_{2o}) &= \int_{-\infty}^{\infty} f[q_+^o(t), p_+^o(t)] \\ &\quad \wedge g[q_+^o(t), p_+^o(t); t_{1o}, t_{2o}] dt \\ &= -\sqrt{2} A \int_{-\infty}^{\infty} \frac{\tanh(t) \cos \omega(t + t_{1o})}{\cosh(t)} dt \\ &\quad + 2c \int_{-\infty}^{\infty} \frac{\tanh^2(t)}{\cosh^2(t)} dt \\ &\quad - \sqrt{2} \int_{-\infty}^{\infty} \frac{\tanh(t) \eta(t + t_{2o})}{\cosh(t)} dt \\ &= M_d^+(t_{1o}) + M_r^+(t_{2o}) \end{aligned} \quad (8)$$

where "+" (superscript or subscript) indicates the upper domain of phase plane. The first two integrals in Eq. (8), corresponding to $M_d^+(t_{1o})$, represent the mean of the stochastic Melnikov process due to the periodic excitation and damping force, and the last integral, corresponding to $M_r^+(t_{2o})$, represents the random portion due to white noise. $M_r^+(t_{2o})$, instead of directly integrated, is calculated by considering the convolution integral as a filtering process, i.e., a white noise process $\eta(t)$ passing through a linear filter given by the homoclinic orbits $p_+^o(t)$ (Frey and Simiu, 1992). Because of the linear filtering, the random process $M_r^+(t_{2o})$ is stationary and of zero mean

$$\langle M_r^+(t_{2o}) \rangle = \sqrt{2} \int_{-\infty}^{\infty} \frac{\tanh(t)}{\cosh(t)} \langle \eta(t_{2o}) \rangle = 0. \quad (9)$$

Its corresponding spectrum is obtained by directly multiplying white noise spectrum $S_\eta(\omega)$ and the transfer function $|F(\omega)|^2$ of the linear filter, $p_+^o(t)$. The variance of $M_r^+(t_{2o})$ can be calculated by integrating its spectrum over the entire frequency range

$$\sigma_{M_r}^2 = \int_{-\infty}^{\infty} |F(\omega)|^2 S_\eta(\omega) d\omega \simeq 13.15\kappa \quad (10)$$

The frequency response $F(\omega)$ is obtained through Fourier transform

$$F(\omega) = \int_{-\infty}^{+\infty} p_+^o(t) e^{-i\omega t} dt = \frac{-i\omega\pi}{\sqrt{2} \cosh \frac{\pi\omega}{2}} \quad (11)$$

The generalized stochastic Melnikov criterion is obtained by setting Eq. (8) equal to zero

$$M_g^+(t_{1o}, t_{2o}) = M_d^+(t_{1o}) + M_r^+(t_{2o}) = 0. \quad (12)$$

Note that the stochastic Melnikov process (Eq. (8)) is Gaussian

Downloaded 04 May 2010 to 171.66.16.33. Redistribution subject to ASME license or copyright; see http://www.asme.org/terms/Terms_Use.cfm

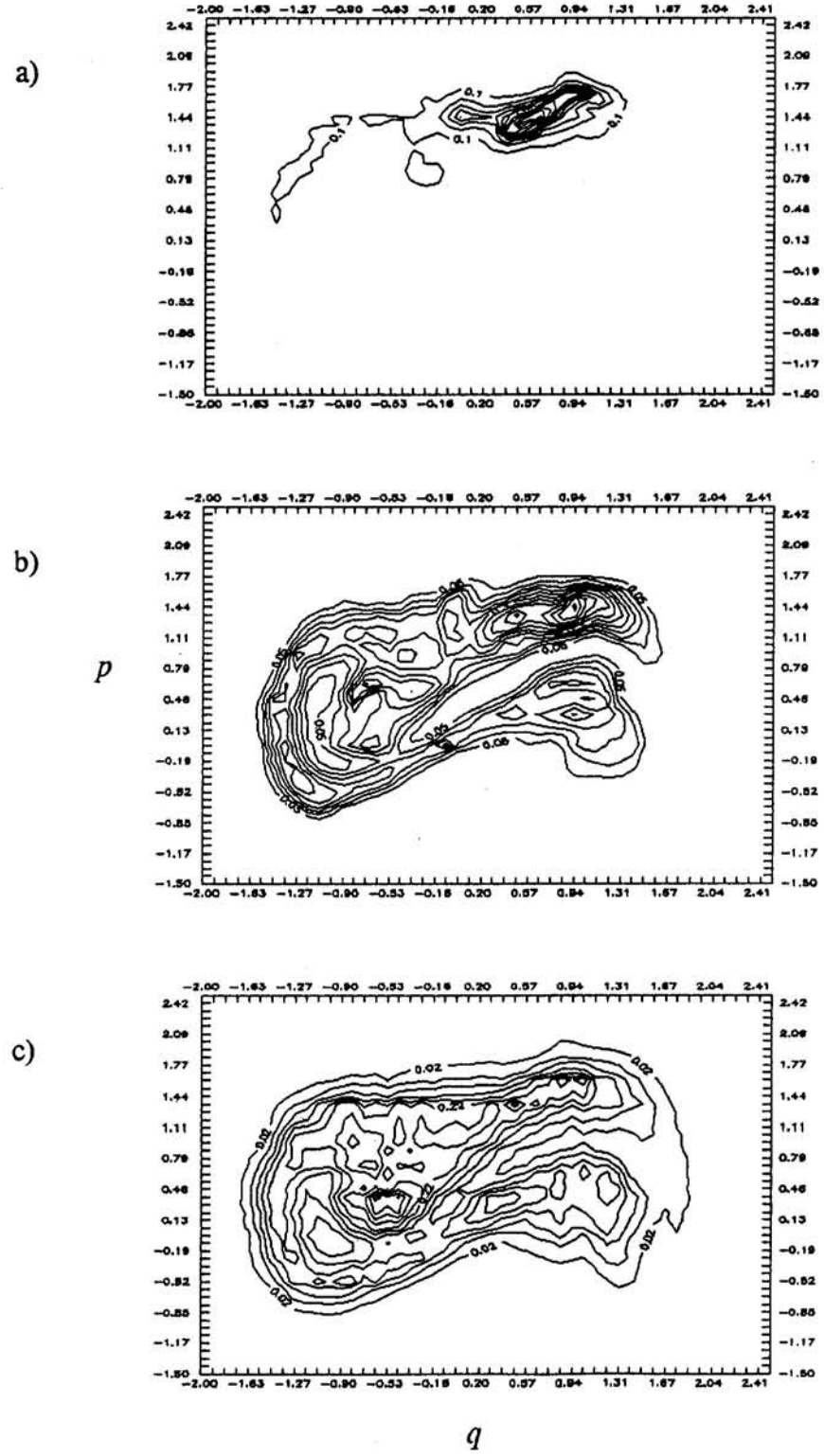


Fig. 5 Transition between coexisting attractors caused by various noise intensities: (*a*) κ = 0.001, (*b*) κ = 0.007, and (*c*) κ = 0.02, (A, ω, c, κ) = (0.3, 1.0, 0.185, 0.003).

with mean and variance equal to $M_d^+(t_{1o})$ and $\sigma_{M_r}^2$, respectively. In the limit as $\kappa \to 0$, the generalized stochastic and the standard deterministic Melnikov criteria coincide.

The standard Melnikov function renders a necessary condition for existence of chaos (Yim and Lin, 1991), and in this study the noise effects on the occurrence of possible chaotic response can be explicitly expressed by an energy interpretation. Thus, in regard to the presence of noise, the criterion for possible chaotic response based on generalized Melnikov process is performed in a mean-square representation

$$\left\langle \left(\frac{4c}{3}\right)^2 \right\rangle = \left\langle \left(\frac{\sqrt{2}\, A\pi\omega \cos\,(t_{1o})}{\cosh \dfrac{\pi\omega}{2}} \right)^2 \right\rangle + \langle M_r^2(t_{2o}) \rangle. \quad (13)$$

Then the mean-square criterion for possible chaotic response in terms of parameters (A, ω, c, κ) is given by

Downloaded 04 May 2010 to 171.66.16.33. Redistribution subject to ASME license or copyright; see http://www.asme.org/terms/Terms_Use.cfm

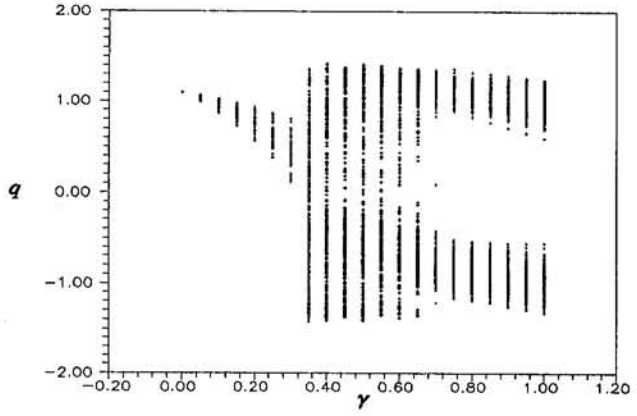


Fig. 6 Transition among nonchaotic, noisy chaotic, and random dynamics (Poincaré points versus γ with $(B, \omega, c, \sigma^2) = (0.5, 1.0, 0.185, 0.04)$).

$$\left(\frac{4c}{3}\right)^2 \leq \frac{2A^2\pi^2\omega^2}{\cosh^2\frac{\pi\omega}{2}} + \sigma_{M_r}^2. \tag{14}$$

The mean-square representation of the upper bound of possible chaotic domain is obtained by equating the expressions in Eq. (14) and portrayed in Fig. $1(a)$. It delineates the domain of possible occurrence of chaotic response in parameter space. The upper bounds for the cases with and without random perturbation in different parameter domains are also represented by the dashed and solid lines in Figs. $1(b)$ and (c), respectively. The positive correction term, $\sigma_{M_r}^2$ (Eq. (10)), elevates the upper bound for chaos (Figs. $1(b)$ and (c)). Thus, the presence of noise lowers the threshold and enlarges the possible chaotic domain in parameter space.

Direct Numerical Simulation. Numerical simulation is employed to validate the analytical predictions. Sample realizations of the system response are obtained by directly integrating Eq. (1), e.g., by a fourth-order Runge-Kutta integration algorithm. The numerical representation of the random noise selected here is based on Shinozuka's Gaussian noise (Shinozuka, 1977), the intensity of which is measured by its finite variance, σ^2. It is noted that Shinozuka's noise representation provides a good approximation to the ideal white noise (infinite variance with intensity scaled by the intensity parameter, κ), and it preserves the characteristics of the system response to ideal white noise excitation.

Probabilistic Representation of Possible Responses

By varying the excitation parameters, the Duffing system exhibits diverse and complex dynamical responses including nonchaotic, chaotic, random and nonchaotic, random and chaotic, and purely random behaviors. Links among these possible responses are examined via transient and steady-state probability density functions obtained from the Markov process approach.

Single Attractor. Figures $2(a)$ and (b) show sample periodic and chaotic responses in the Poincaré map. By adding a small amount of noise ($\kappa = 0.003$) to the deterministic excitation, the corresponding joint probability density functions ($\mathbf{P}_p$) is obtained and shown on the Poincaré section in Figs. $2(d)$ and (e). It is observed that, with weak noise intensity, joint probability density functions of random and periodic (Fig. $2(d)$), and random and chaotic responses can reflect the response attractors of their deterministic counterparts. It is noted that in Fig. $2(d)$ the fractal details in the chaotic attractor are clearly described by the joint probability density function.

Figure $2(c)$ demonstrates a sample realization of purely random response in the phase plane. It is observed that the phase trajectory drifts back and forth between the two basins in the potential. These two basins are reflected by the associated joint probability density function (Fig. $2(f)$).

The above numerical results indicate that probability density functions not only can delineate purely random response (Fig. $2(c)$) but also can reflect deterministic attractors, both nonchaotic and chaotic, in a probabilistic sense when the noise is weak. Thus, the probability density function may be a measure applicable to all possible dynamical responses (Lasota and Mackey, 1994). The asymptotic behaviors of the probability density functions as the noise intensity goes to zero will be the focus of future investigations.

Coexisting Attractors. An advantage of using probability density functions to demonstrate stochastic responses is further elaborated by examining coexisting attractors in this section. The coexistence of attractors is one of the characteristics of nonlinear systems. Figure $3(a)$ shows coexisting deterministic chaotic and periodic attractors in the Poincaré map (with initial conditions at (0, 0) and (1.5, 1.0), respectively). The joint probability density function, which describes the global behavior of the system, can be used to effectively portray these two coexisting attractors (Kunert and Pfeiffer, 1991) (Fig. $3(f)$).

This probabilistic representation of the coexistence of attractors is demonstrated by initiating the slightly randomly perturbed system with deterministic initial conditions in the domain of the chaotic attractor and sampling recurrently on the Poincaré section to demonstrate the evolution of the joint probability density function. Figures $3(b)$, (c), and (d) show the evolution of the probability density function from its deterministic initial conditions at (0, 0) to the domain of the chaotic attractor. The probability density function then drifts from the chaotic attractor to the periodic attractor after five cycles of the forcing period (Fig. $3(e)$). Finally, at about 20 cycles, steady state is achieved and the joint probability density function clearly reflects the two coexisting attractors (Fig. $3(f)$). The probability density function describes the trajectories and demonstrates the strengths of attractors in the mean sense. Under a detailed examination of the numerical results of Fig. $3(f)$, it is found that the probability density function is more concentrated in the domain of the periodic response, indicating that the periodic attractor is of the greater strength.

It is noted that the steady-state probability density function is independent of the initial conditions. In particular, although the coexisting attractors shown in Fig. $3(f)$ are obtained with initial conditions in the domain of the deterministic chaotic attractor, numerical results (not presented here due to space limitation) confirm that the same steady-state probability density function can be obtained by initiating the system within the domain of the deterministic periodic attractor. This is because the probability density function, although concentrated at the attractor, covers the entire phase space. Transitions between attractors are guaranteed by the presence of random perturbations. Hence, initial conditions become insignificant in describing the global behavior of stochastic systems, which is in contrast with the sensitivity to the initial conditions of a single deterministic chaotic trajectory. A slight difference in system parameters is noted in Figs. $3(a)$ and (f), which is due to a noise-induced shift of threshold of different response states (Just, 1989).

Noise-Induced Transition. The generalized Melnikov criterion analytically elaborates that the presence of noise enlarges the possible chaotic domain. The steady-state probability density functions in the previous section also indicate the noise-induced bridging effects on coexisting attractors. In this section noise-induced transitions between distinct response states and between coexisting attractors are numerically examined and in-

Downloaded 04 May 2010 to 171.66.16.33. Redistribution subject to ASME license or copyright; see http://www.asme.org/terms/Terms_Use.cfm

terpreted by fixing the deterministic excitation and varying the noise intensity.

Analytical prediction of the generalized Melnikov criterion is corroborated by the phenomenon called noise-induced chaos (Bulsara et al., 1990). This random and chaotic state is induced from the neighboring nonchaotic state due to the presence of weak noise perturbation. If the noise intensity increases, the system response exhibits more random-like behavior. The transition between nonchaotic response, and random and chaotic response caused by the presence of noise is demonstrated in Figs. 4(a) and (b). Figure 4(a) shows a sample deterministic periodic response (no random perturbation) with quiescent initial conditions. Figure 4(b) shows that, with the same initial conditions, a random and chaotic state is induced by a weak noise perturbation. Chaoticity of the response in Fig. 4(b) can be illustrated by examining the sensitivity of its trajectory to the initial conditions. Figure 4(c) shows that a slight variation in the initial conditions causes divergent response behavior and its chaoticity is demonstrated. As expected, with stronger noise intensity, the system response appears to become more random. Thus, with noise intensity as the control parameter in the vicinity of chaotic domain, random and chaotic response may be considered as an intermediate state between deterministic and random responses.

For coexisting periodic and chaotic attractors, numerical results indicate that the relative strength of the chaotic attractor is enhanced by the presence of a moderate amount of noise (Figs. 5(a)–(c)). Figure 5(a) shows, with very low noise intensity, the probability density function is mostly concentrated in the domain of periodic response, and system response mainly exhibits periodic behavior. When the noise intensity increases, the probability density function covers the domains of both periodic and chaotic responses, and the system behaves with characteristics of both responses. When the noise intensity is of relatively high strength, domains of periodic and chaotic responses are merged, and system behavior appears more random. Thus the noise intensity should be considered as an important parameter in search of chaotic response in practice.

Transition Between Deterministic and Random Dynamics. Diverse transition routes from deterministic responses to purely random results may result when the modulation factor γ in Eq. (1) varies from zero to one. Possible transition routes are 1. "non-chaotic" → "random and non-chaotic" → "random"; 2. "chaotic" → "random and chaotic" → "random"; 3. "non-chaotic" → "random and chaotic" → "random". Routes 1 and 2 are more easily understood, and route 3 is not as intuitively evident.

Route 3 is numerically demonstrated, with quiescent initial conditions, a possible transition from purely deterministic to purely random dynamics by varying γ in this section (Fig. 6). For each value of γ, the Poincaré points of ten random sample paths of the steady-state responses are combined and presented in the map in Fig. 5. The system response behaves in a deterministic periodic state at $\gamma = 0$. By examining the Poincaré map of each individual sample path, it is found that as γ increases, the system response behaves in a noisy periodic fashion up to $\gamma = 0.3$ (indicated by the closeness of the sample Poincaré points in Fig. 5). The typical sample response within the interval of γ between [0.35, 0.65] deviates to, and stays in, a noisy chaotic state, which is indicated by the large scattering of the Poincaré points in that region. When γ increases further to beyond 0.65, the typical response becomes more random and in the limit as γ approaches 1, the distribution of the Poincaré points approaches that of the steady-state response of a (pure) randomly excited double-well Duffing system (Lin, 1967).

As demonstrated above, "random and chaotic" response may be a possible intermediate state for system response drifting from the deterministic to the purely random. This highly nonlinear random response may be considered as a possible link between deterministic and random dynamics.

Concluding Remarks

This study presents a stochastic analysis of all currently known responses in a nonlinear system, and demonstrates the system behavior in a probabilistic sense. Several conclusions are summarized as follows:

1 "Random and chaotic" response has been demonstrated to be a possible intermediate state between deterministic and random responses using a simple, well-studied system. Stochastic characteristics of all possible dynamical behaviors have been demonstrated.

2 Based on generalized stochastic Melnikov process, an upper bound for possible chaotic domain has been identified. The presence of noise lowers the threshold and enlarges the possible chaotic domain.

3 The Fokker-Planck equation along with path integral solution provide a temporal solution of probability density function, which characterizes the global behavior of the system. The steady-state joint probability density function appears invariant on the Poincaré section, which reflects all the existing attractors.

4 The presence of noise decreases the order in the system response. It bridges domains of all the existing attractors and controls their relative stabilities. Sensitivity to initial conditions of the "random and chaotic response" is less significant in the representation by probability density function.

Acknowledgments

The authors gratefully acknowledge the financial support from the United States Office of Naval Research (Grant No. N00014-92-J-1221) and the valuable comments of the reviewers.

References

Bulsara, A. R., Jacobs, E. W., and Schieve, W. C., 1990, "Noise Effects in a Nonlinear Dynamic System: The rf Superconducting Quantum Interference Device," *Phys Rev A*, Vol. 42, pp. 4614–4621.

Frey, M., and Simiu, E., 1992, "Equivalence between Motions with Noise-Induced Jumps and Chaos with Smale Horseshoes," *Proc 9th Engrg Mech Conf, ASCE*, Texas A&M University, College Station, TX, May 24–27, pp. 660–663.

Gardiner, C. W., 1985, *Handbook of Stochastic Methods: for Physics, Chemistry and Natural Sciences*, Springer-Verlag, Berlin.

Guckenheimer, J., and Holmes, P., 1983, *Nonlinear Oscillations, Dynamical Systems, and Bifurcations of Vector Fields*, Springer-Verlag, New York.

Just, W., 1989, "Dynamics of the Stochastic Duffing Oscillator in Gaussian Approximation," *Physica D*, Vol. 40, pp. 311–330.

Kapitaniak, T., 1988, *Chaos in Systems with Noise*, World Scientific, Singapore.

Kunert, A., and Pfeiffer, F., 1991, "Description of Chaotic Motion by an Invariant Distribution at the Example of the Driven Duffing Oscillator," *Int Ser Numer Math*, Vol. 97, Birkhäuser Verlag Basel, pp. 225–230.

Lasota, A., and Mackey, M. C., 1994, *Chaos, Fractals, and Noise*, 2nd ed., Springer-Verlag, New York.

Lin, Y. K., 1967, *Probabilistic Theory of Structural Dynamics*, McGraw-Hill, New York.

Risken, H., 1984, *The Fokker-Planck Equation: Methods of Solution and Applications*, Springer-Verlag, Berlin.

Shinozuka, M., 1977, "Simulation of Multivariate and Multidimensional Random Processes," *J Acoustical Soc Amer*, Vol. 49, pp. 357–367.

Stratonovich, 1967, R. L., *Topics in the Theory of Random Noise*, Gordon and Breach.

Wehner, M. F., and Wolfer, W. G., 1983, "Numerical Evaluation of Path-Integral Solutions to Fokker-Planck Equations," *Phys Rev A*, Vol. 27, pp. 2663–2670.

Wiggins, S., 1988, *Global Bifurcations and Chaos: Analytical Methods*, Springer-Verlag, New York.

Wiggins, S., 1990, *Introduction to Applied Nonlinear Dynamical Systems and Chaos*, Springer-Verlag, New York.

Wissel, C., 1979, "Manifolds of Equivalent Path Integral Solutions of the Fokker-Planck Equation," *Zeit Physik B*, Vol. 35, pp. 185–191.

Yim, S. C. S., and Lin, H., 1991, "Nonlinear Impact and Chaotic Response of Slender Rocking Objects," *J Engrg Mech*, Vol. 117, pp. 2079–2100.

Downloaded 04 May 2010 to 171.66.16.33. Redistribution subject to ASME license or copyright; see http://www.asme.org/terms/Terms_Use.cfm

A Simple Model of a Stiffened Shell-Type Structure for an Investigation Into the Vibration-Buckling Correlation

V. M. Ryaboy[1]
Visiting Scientist.

T. Weller
Professor.

Faculty of Aerospace Engineering,
Technion—Israel Institute of Technology,
Haifa 32000, Israel

A nonlinear two-degree-of-freedom system is considered to simulate the peculiar behavior of stringer-stiffened cylindrical shells under nonuniform axial compression, which was observed in recent tests where the characteristic curves (eigenfrequency squared versus load) were nonmonotonic and decreasing steeply when approaching the critical load. Correlation is traced between the characteristic curves and equilibrium paths. It is shown that for particular nonzero values of load eccentricity, bifurcations are observed instead of the usual limit points. Nonunique stable post-buckling equilibrium paths are pointed out. The general properties of characteristic curves are discussed.

1 Introduction

Nondestructive vibration correlation techniques for estimating the critical buckling loads of real thin-walled structures have quite a long history (Singer, 1983). These methods are based on the analysis of the characteristic curves, which describe the relationship between the lower natural frequencies and the load parameter.

Two groups of vibration correlation procedures exist. The first group aims at determining the buckling load directly by extrapolation of the experimental "lowest natural frequency-load parameter" curve in order to find the intersection with the load axis ($\omega = 0$) and thus predict the buckling load. Several approaches were proposed to improve these estimates (Singer, 1983; Plaut and Virgin, 1990; Souza and Assaid, 1991). The second group employs advanced analytical models for predicting vibration and buckling, while the experimental vibration data are used to identify the exact values of the indefinite parameters included in the models. Extensive studies which were based on this approach and conducted at the Aircraft Structures Lab, Technion—I.I.T. (Rosen and Singer, 1976; Singer and Abramovich, 1979; Singer, 1983; Weller et al., 1986; Abramovich et al., 1988) resulted in improved predictions of buckling loads for stiffened cylindrical shells subjected to uniform axial loading and combined uniform axial loading and external pressure. In these studies, the experimental characteristic curves were qualitatively similar to the theoretical ones and the quantitative differences between the two allowed the identification of unknown factors like boundary stiffnesses and load eccentricities.

Further experimental investigations (Bornstein et al., 1991) aiming at extending these techniques to non-uniform loading of stringer-stiffened cylindrical shells (Fig. 1(a)) revealed some unusual features of the characteristic curves, which hampered the straightforward application of vibration correlation analysis. Local buckling, which is characteristic for buckling with unilateral constraints, like that described by Ryaboy (1975), and which emphasizes the importance of the asymmetric elastic characteristics of the shell, was observed. The formation of a single isolated buckle (Fig. 1(b)) instead of four is explained by the localization phenomenon due to small asymmetry of loading. Under this type of loading, the prebuckling bending deformations were considerably higher than in the case of uniform compression, which agrees with the results of the nonlinear numerical analysis by Andreyev et al. (1989). Buckling was nonviolent and "soft" in the sense that the drop in the axial force after the loss of stability was rather small (4 to 30 percent of the buckling load). This may imply that the shells were eccentrically loaded (Weller et al., 1974; Rosen and Singer, 1976; Singer and Abramovich, 1979). Typical experimental characteristic curves together with analytical results for two shells of different length over radius ratios, L/R, and two types of boundary conditions, which were reproduced from Bornstein et al., (1991), are presented in Fig. 2. Unlike the expectation, the experimental curves are not monotonically decreasing. Instead, the curve changes the sign of the slope from negative to positive in the course of loading as in Fig. 2(a), or it rises from the very beginning, reaches a shallow maximum and drops as in Fig. 2(b). In both cases, the natural frequency does not noticeably decrease prior to buckling, and the sudden occurrence of buckling seems to be uncorrelated with the behavior of the experimental characteristic curve. Somewhat analogous observations were reported by Galaka et al. (1975) for cylindrical shells reinforced by stringers of different sizes, and by Amiro et al. (1983) for reinforced cylindrical shells with rectangular cutouts.

This type of characteristic curve could be obtained by assuming that the actual boundary conditions change in course of loading, thus introducing a physical nonlinearity in addition to the geometric nonlinearity of the shell. Detailed analysis of this phenomenon was presented in recent papers by Souza (1988, 1993) using a single-degree-of-freedom model. Herein, an attempt is made to explain the nonmonotonic behavior of the characteristic curves without invoking any hypotheses about the explicit nonlinearity at the boundaries, but rather in terms of the inherent geometrical nonlinearity.

Since full-size finite element modeling of a nonuniformly loaded stiffened shell is extremely cumbersome and time-consuming, it is rational to compose a simplified model in order

[1] On leave from the Blagonravov Mechanical Engineering Research Institute, Moscow, Russia.

Contributed by the Applied Mechanics Division of THE AMERICAN SOCIETY OF MECHANICAL ENGINEERS for publication in the ASME JOURNAL OF APPLIED MECHANICS.

Discussion on this paper should be addressed to the Technical Editor, Professor Lewis T. Wheeler, Department of Mechanical Engineering, University of Houston, Houston, TX 77204-4792, and will be accepted until four months after final publication of the paper itself in the ASME JOURNAL OF APPLIED MECHANICS.

Manuscript received by the ASME Applied Mechanics Division, Apr. 28, 1994; final revision, Dec. 21, 1994. Associate Technical Editor: J. N. Reddy.

Copyright © 1996 by ASME

Downloaded 04 May 2010 to 171.66.16.33. Redistribution subject to ASME license or copyright; see http://www.asme.org/terms/Terms_Use.cfm

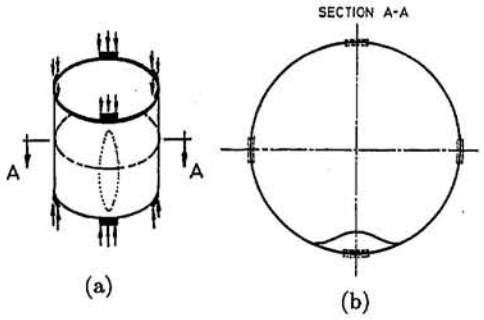


Fig. 1 The scheme of loading (*a*) and the shape of buckling (*b*) for the closely stringer-stiffened cylindrical shells subjected to nonuniform axial loading (reproduced from Bornstein et al., 1991)

to gain some qualitative understanding of the observed phenomena. Such an approach is undertaken in the present study, and in Section 2, a two-degree-of-freedom model, which seems to reflect some essential features of the stringer-stiffened shell behavior under nonuniform axial loading, is proposed. It should be noted that Budiansky et al. (1948) determined the buckling load corresponding to this model without load eccentricity. The model can be viewed as an augmented version of the single-degree-of-freedom models which were used by Thompson and Hunt (1973), Elishakoff et al. (1984), and Souza (1992) to clarify some principal aspects of buckling and vibration of elastic structures with asymmetric characteristics. It could be compared to the simplified model of the cylindrical shell mentioned by Souza and Assaid (1991). In Section 3, the characteristic curves and the equilibrium paths of the proposed model are presented. These results do mimic the behavior of nonuniformly loaded stringer-stiffened cylindrical shells. Furthermore, they seem to be instructive as a demonstration of the effects which are likely to be encountered in real imperfect and/or eccentrically loaded thin-walled structures.

It is worthwhile noting that the results obtained in this study provide an illustration of the general properties of characteristic curves which are proven in Appendix A.

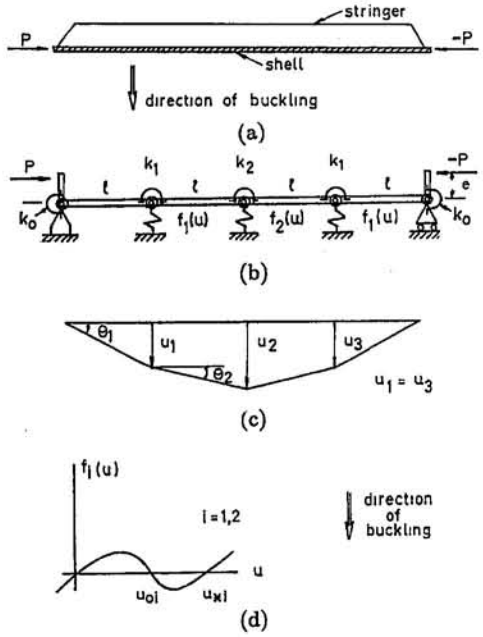


Fig. 3(*a*) The schematic of a single loaded strip of a stringer-stiffened cylindrical shell; (*b*) the mechanical model; (*c*) generalized coordinates; (*d*) force-displacement diagram of the nonlinear elastic supports

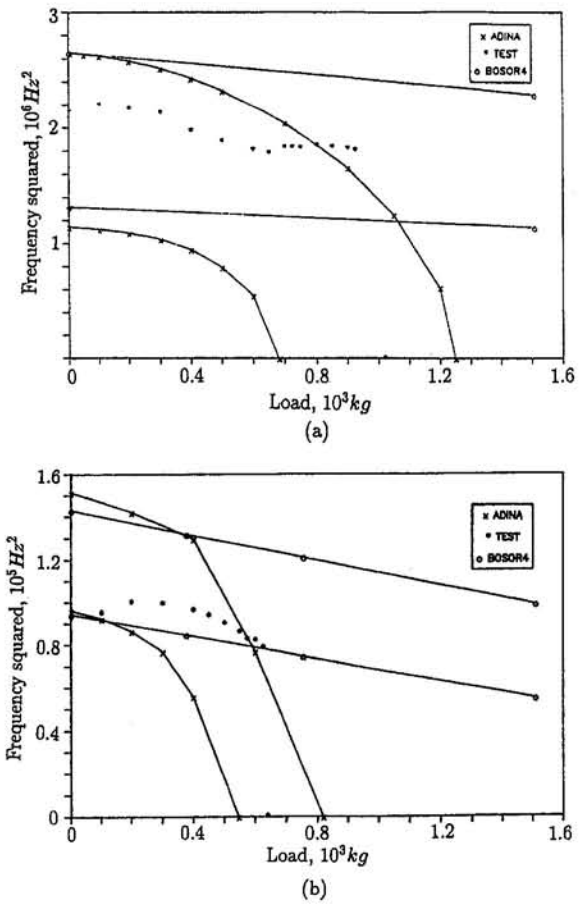


Fig. 2 Frequency squared versus axial load: (*a*) shell MR6, $L/R = 0.92$; (*b*) shell MR4, $L/R = 2.58$. Solid lines represent theoretical results by a finite element nonlinear model (ADINA) and a linearized finite difference model (BOSOR4) for two sets of boundary conditions *SS*3 ($w = w_{,xx} = N_x = v = 0$) with and without end rings, upper and lower curves, respectively (reproduced from Bornstein et al., 1991).

2 The Two-Degree-of-Freedom Model

The experimental evidence discussed above and preliminary estimates of the localization phenomenon lead to the conclusion that, starting from some level of load, the behavior of one loaded strip of the cylindrical shell dominates the response of the shell and is responsible for its lowest-frequency free vibration and buckling. This strip could be considered as being composed of a longitudinally loaded elastic beam (the stringers) resting on an elastic foundation (the rest of the shell). A few important points should be noted. First, if the load is applied through the mid-skin of the shell as shown in Fig. 3(*a*), then the strip experiences some eccentricity of loading relative to the section center of gravity. In practice some unknown amount of eccentricity may also exist due to uncertain conditions introduced by the loading device. Second, the elastic foundation should retain the properties of a circular shell or arch under transverse loading, i.e., the foundation itself must be elastically asymmetric and liable to buckling, with the preferred direction of buckling inward the shell. Third, in order to describe the buckling, in case the eccentricity is acting "against" the preferred buckling direction, at least two bending modes should be involved.

The mechanical model shown in Fig. 3(*b*) seems to be the simplest system which possesses all of the three properties mentioned above. It is assumed here that the nonlinear springs of the elastic foundation have force-displacement characteristics $f_i(u) = c_i u(1 - u/u_{0i})(1 - u/u_{*i})$, $i = 1, 2$, that model a structure liable to buckling. The system is assumed to be sym-

Downloaded 04 May 2010 to 171.66.16.33. Redistribution subject to ASME license or copyright; see http://www.asme.org/terms/Terms_Use.cfm

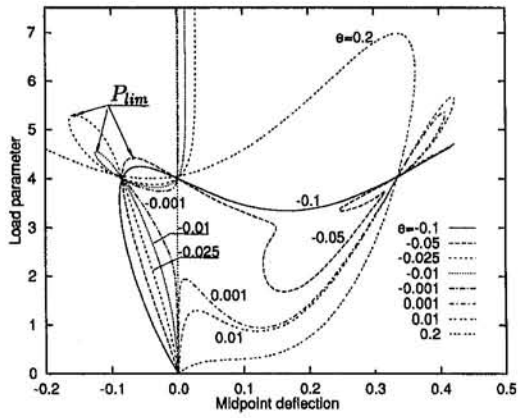


Fig. 4(*a*)

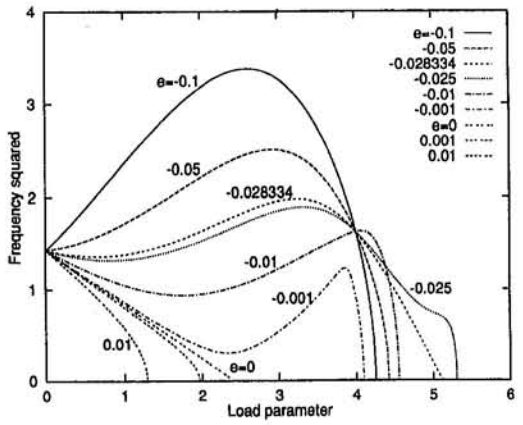


Fig. 4(*b*)

Fig. 4 P **versus** u_2 **(*a*) and** ω_1^2 **versus** P **(*b*) (**$k_0 = 0.5$, $k_1 = k_2 = 1$, $c_1 = 1$, $c_2 = 0.7$, $u_{01} = 0.07$, $u_{02} = 0.1$, $u_{*1} = 0.1$, $u_{*2} = 0.15$**)**

metric, and an additional requirement is imposed that $u_3 = u_1$. Thus, the system has two degrees-of-freedom.

The total potential energy of the system is $V = U - P\Delta$. Here, U is the elastic potential energy,

$$U = k_0\theta_1^2 + k_1(\theta_2 - \theta_1)^2 + 2k_2\theta_2^2 + 2V_1(u_1) + V_2(u_2),$$

where V_1 and V_2 are the potential energies of the nonlinear springs deformation such that $dV_i/du_i = f_i(u_i)$, $i = 1, 2$; $u_1 = \sin\theta_1$, $u_2 = \sin\theta_1 + \sin\theta_2$ and $P\Delta$ is the work of the external force, with P being the axial force and Δ the relative displacement of the loaded points. A unit length of each rod, $l = 1$, is assumed. So, $\Delta = 2[e\sin\theta_1 + (1 - \cos\theta_1) + (1 - \cos\theta_2)]$, where e is the load eccentricity. The nonlinear equilibrium equations $\partial U/\partial\theta_i - P\partial\Delta/\partial\theta_i = 0$, $i = 1, 2$, were solved by Newton's method. In the dynamic calculations it was assumed that the masses m_1 and m_2 are concentrated at the hinges. Natural frequencies were calculated from Lagrange's equations, with the kinetic energy $T = m_1(\dot{u}_1)^2 + \frac{1}{2}m_2(\dot{u}_2)^2$, linearized in the vicinity of the nonlinear equilibrium state.

The ideal system ($e = 0$) has two buckling loads $P_{cr1} \le P_{cr2}$, corresponding to the nonsymmetric bifurcation points. The trivial equilibrium state $\theta_1 = \theta_2 = 0$ is stable for $P < P_{cr1}$ and unstable for $P \ge P_{cr1}$. The first buckling mode shape depends on the sign of $(c_2/2 - k_1)$. It has a "half-wave" form, sign θ_1 = sign θ_2, if $(c_2/2 - k_1) < 0$, and a "zigzag" form, sign θ_1 = $-$sign θ_2, if $(c_2/2 - k_1) > 0$; for $c_2/2 - k_1 = 0$, $\theta_1 = 0$ or $\theta_2 = 0$. If $e \neq 0$, then the trivial state $\theta_1 = \theta_2 = 0$ is no longer an equilibrium state for $P > 0$, and the direction of the initial prebuckling deformation is defined by the signs of $(c_2/2 - k_1)$ and e. We call the eccentricity negative, $e < 0$, if the lever is placed on the side where the elastic foundation buckles (i.e., "inwards"). So, negative eccentricity tends to deform the system away from buckling. The eccentricity is positive if the lever is oriented opposite to the preferred buckling direction ("outwards"), and positive eccentricity assists buckling.

3 Results and Discussion

Typical results for a relatively soft foundation, $c_2/2 - k_1 < 0$, are presented in Figs. 4-8. Figure 4(a) shows the fundamental (i.e., starting from $\theta_1 = \theta_2 = 0$ for $P \ge 0$) equilibrium paths. All of these paths become unstable as P reaches the first maximum P_{lim}. The characteristic curves for $0 \le P \le P_{lim}$ are shown in Fig. 4(b). For small negative e (e.g., $e = -0.001$ and $e = -0.01$), these curves are nonmonotonic, with their slopes changing from negative to positive with increase in load parameter and an abrupt drop in frequency when approaching the critical point. This resembles the experimental data obtained in tests with the shorter stiffened shells (see Fig. 2(a)). On the other hand, the larger negative values of eccentricity ($e = -0.05$ and $e = -0.1$) lead to nonmonotonic characteristic curves with their slopes changing from positive to negative with increase in load, and a steep decrease in frequency when approaching the critical point. The apparent intersection points of the various curves, for different e values in Fig. 4, do not represent, of course, identical states of the system. Approximate formulas for these invariant points are presented in Appendix B.

Figure 5 represents the equilibrium states in the configuration plane (θ_1, θ_2). In Figs. 4 and 5, only the continuous equilibrium branches, starting from the origin, are shown. The picture would be much more complicated if all of the equilibrium branches were plotted. Figure 6 shows such plots for one value of eccentricity. It should be noted that the post-buckling behavior of the system is undefined because there exist several branches of stable equilibrium states with a level of potential energy (for the same level of load) lower than at the critical point.

The critical point of the system under consideration is associated with a limit point, except for two particular values of e. One is $e = 0$, and another is $e = -0.028334$ corresponding to a change in type of the ω_1^2 versus P and P versus u_2 curves, which is apparent in Figs. 4(a) and 5. These bifurcations are illustrated in Fig. 7. It appears that for $e = 0$ the nontrivial solutions form one curve passing through both bifurcation points. These two values of eccentricity correspond to the only two characteristic curves in Fig. 4(b) that do not have a vertical tangent at the intersection with the load axis. This is in accordance with the general fact proven in Appendix A that ω_1^2 behaves like $\sqrt{P_{cr} - P}$ as P approaches P_{cr} at the limit point, and like $(P - P_{cr})$ as P approaches P_{cr} at the bifurcation point. The bifurcations are usually associated with some kind of struc-

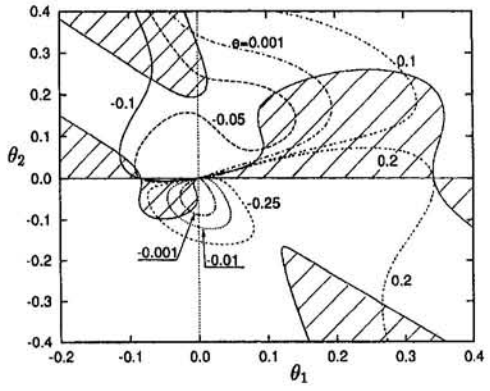


Fig. 5 Equilibrium states in the configuration plane (θ_1, θ_2)**. The domains of stability are hatched. (**$k_0 = 0.5$, $k_1 = k_2 = 1$, $c_1 = 1$, $c_2 = 0.7$, $u_{01} = 0.07$, $u_{02} = 0.1$, $u_{*1} = 0.1$, $u_{*2} = 0.15$**).**

Downloaded 04 May 2010 to 171.66.16.33. Redistribution subject to ASME license or copyright; see http://www.asme.org/terms/Terms_Use.cfm

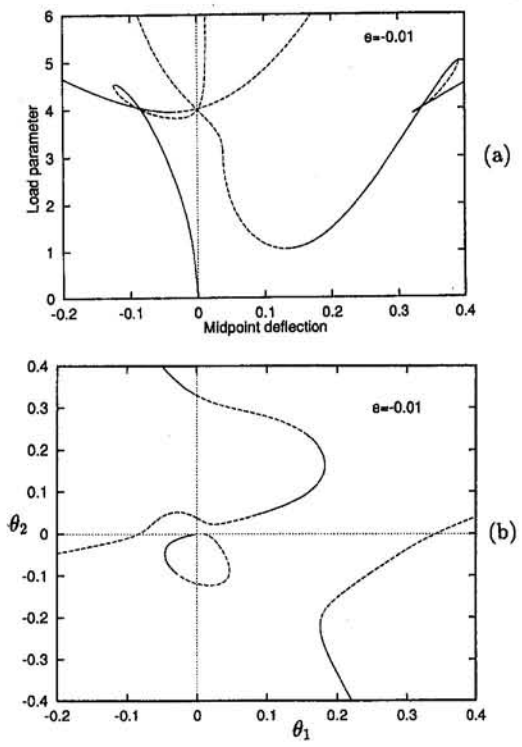


Fig. 6 A full set of the equilibrium paths for $P \geq 0$ in the (u_2, P) plane (a) and in the configuration plane (b). (Solid lines —— stable, broken lines – – – unstable. $e = -0.01$; $k_0 = 0.5$, $k_1 = k_2 = 1$, $c_1 = 1$, $c_2 = 0.7$, $u_{01} = 0.07$, $u_{02} = 0.1$, $u_{*1} = 0.1$, $u_{*2} = 0.15$).

tural symmetry (Thompson and Hunt, 1973). In our case, the system with $e = -0.028334$ exhibits a bifurcation which has no connection with any apparent symmetry. There are also bifurcations of the unstable path at $e = -0.05673$ (corresponding to a transition from the "deep" post-buckling curve to a "shallow" one) and in the large deflection domain for $e = 0.11291$, but they will not be considered in detail here.

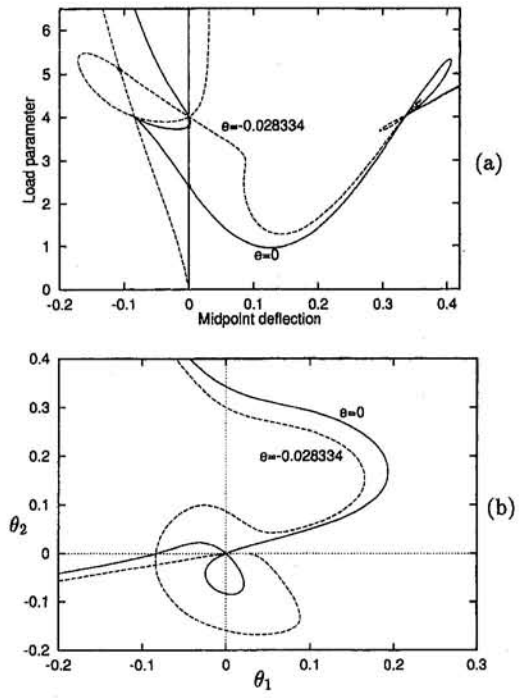


Fig. 7 Bifurcations in the load-deflection plane (a) and in the configuration plane (b) ($k_0 = 0.5$, $k_1 = k_2 = 1$, $c_1 = 1$, $c_2 = 0.7$, $u_{01} = 0.07$, $u_{02} = 0.1$, $u_{*1} = 0.1$, $u_{*2} = 0.15$)

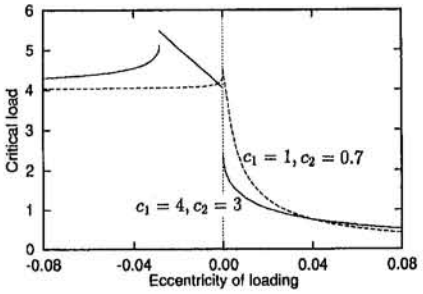


Fig. 8 The relationship between the critical load P and eccentricity e. (Solid lines: $k_0 = 0.5$, $k_1 = k_2 = 1$, $c_1 = 1$, $c_2 = 0.7$, $u_{01} = 0.07$, $u_{02} = 0.1$, $u_{*1} = 0.1$, $u_{*2} = 0.15$. Dashed lines: $k_0 = 0.5$, $k_1 = k_2 = 1$, $c_1 = 4$, $c_2 = 3$, $u_{01} = 0.02$, $u_{02} = 0.03$, $u_{*1} = 0.04$, $u_{*2} = 0.06$).

The relationship between the critical load and eccentricity for a relatively soft foundation is represented in Fig. 8 by the solid lines. The highest critical load occurs at negative eccentricity. This is in accordance with the analytical results for the heavily stiffened shells under uniform compression summarized by Weller et al. (1974).

Extrapolation of the characteristic curves depicted in Fig. 4(*b*) for $e < 0$ seems to be impossible. In the case of the curves changing the initial negative slope to a positive one in the course of deformation (e.g., $e = -0.001$ and $e = -0.01$), additional information can be gained from the higher eigenfrequency curves (see Fig. 9). The ω_2^2 versus P curves, corresponding to the above values of negative eccentricities, have substantial negative initial slopes, and the initial portions of these curves could be extrapolated to the correct critical loads. It is apparent from Figs. 4(*b*) and 9 that the problem is how to distinguish between small negative and small positive eccentricities, which have almost identical characteristic curves in the low-load domain for both first and second eigenfrequencies but yield drastically different values of critical loads. In this case, the fact that according to Fig. 5 the initial deformations have opposite signs for $e < 0$ and $e > 0$ can be used for the identification. The initial slope of a characteristic curve in Fig. 4(*b*) depends on e substantially. In fact, this slope is a linear function of the load eccentricity (see Appendix A). Thus, it can be used for identification of the eccentricity, provided a correct analytical model is available that contains the eccentricity as the indefinite parameter.

Figure 10 illustrates the properties of a system with a higher ratio of the elastic foundation stiffness to the beam model stiffness, for which the zigzag mode shape corresponds to the linear-

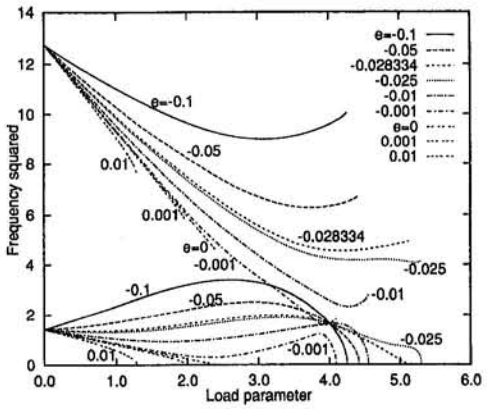


Fig. 9 ω_1^2 and ω_2^2 versus P ($k_0 = 0.5$, $k_1 = k_2 = 1$, $c_1 = 1$, $c_2 = 0.7$, $u_{01} = 0.07$, $u_{02} = 0.1$, $u_{*1} = 0.1$, $u_{*2} = 0.15$)

Downloaded 04 May 2010 to 171.66.16.33. Redistribution subject to ASME license or copyright; see http://www.asme.org/terms/Terms_Use.cfm

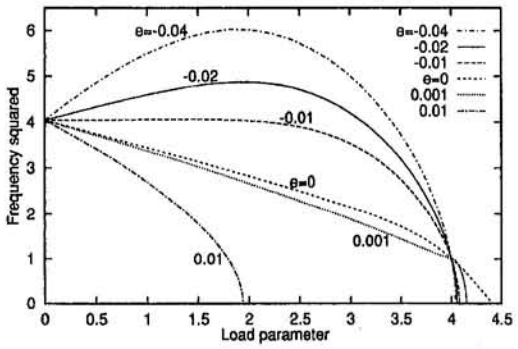


Fig. 10 ω_1^2 **versus** P ($k_0 = 0.5$, $k_1 = k_2 = 1$, $c_1 = 4$, $c_2 = 3$, $u_{01} = 0.02$, $u_{02} = 0.03$, $u_{*1} = 0.04$, $u_{*2} = 0.06$)

ized critical load. In this case the nonmonotonic characteristic curves are observed for $e < 0$. This qualitatively agrees with the experimental data for the longer shell in Fig. 2(b). The relationship between the eccentricity and critical load, corresponding to this case, is presented by the dashed line in Fig. 8. It is continuous for $e \leq 0$, whereas a discontinuity due to bifurcation exists at $e = 0$. The critical load approaches a maximum at $e = 0+$. This is in accordance with the numerical results of Weller et al. (1974) for uniformly loaded lightly stiffened shells. Similar calculations for an "intermediate" case, $c_2 = 2k_1$, show that the invariant point in the (P, ω_1^2) plane is on the load axis, and for $e \leq 0$ the critical load does not depend on e. More detailed data can be found in Ryaboy and Weller (1994). It should be noted that in all of the cases the appearance of the characteristic curve correlates with the type of load-deflection curve. Thus, the characteristic curves could be used for identification of systems liable to buckling.

4 Conclusions

A simple two-degree-of-freedom model, which imitates some properties of nonuniformly loaded ribbed cylindrical shells, was proposed.

The results of the model imply that nonmonotonic characteristic (eigenfrequency squared versus load) curves, which feature high negative slopes just prior to buckling, occur due to the influence of eccentric loading coupled with large pre-buckling deformations and nonsymmetric elastic properties. Hence, such a kind of complicated behavior of the natural frequencies in the course of loading can be expected for a wide class of realistic shell-type structures.

The results yielded by the model show that intimate correlation exists between characteristic curves (defined entirely in the subcritical domain) and load-deflection curves describing both pre- and post-buckling behavior. This correlation can form a basis for identification procedures aiming at predicting buckling characteristics from vibration tests.

The development of consistent nondestructive vibration techniques for the complicated cases, which experience nonmonotonic characteristic curves, is a challenging task for future research. Higher eigenfrequencies and the directions of initial equilibrium paths in the configuration space can be used as auxiliary data for predicting the critical loads.

Acknowledgments

This work was performed during V. M. Ryaboy's stay at the Faculty of Aerospace Engineering of the Technion—Israel Institute of Technology, sponsored by the Milton Petrie Chair for visiting lecturers. This support is gratefully acknowledged. The authors are also grateful to Profs. Joseph Singer, David Durban, Aviv Rosen, and Dr. Haim Abramovich for stimulating discussions.

References

Abramovich, H., Weller, T., and Singer, J., 1988, "Effect of sequence of combined loading on buckling of stiffened shells," *Experimental Mechanics*, Vol. 28, pp. 1–13.

Amiro, I. Ya., Zarutsky, V. A., and Palamarchuk, V. G., 1983, *Dynamics of Ribbed Shells*, Naukova Dumka, Kiev (in Russian).

Andreyev, L. V., Obodan, N. I., and Lebedev, A. G., 1989, *Stability of Nonsymmetric Shell Deformation*, Nauka, Moscow (in Russian).

Bornstein, A., Weller, T., and Singer, J., 1991, "Vibration and Buckling Tests of Stringer-Stiffened Cylindrical Shells Subjected to Non-Uniform Axial Loading," Technion—Israel Institute of Technology Report TAE 667, Haifa, Israel.

Budiansky, B., Seide, P., and Weinberger, R. A., 1948, "The buckling of a column on equally spaced deflectional and rotational springs," NACA Technical Note 1519, Washington, DC.

Elishakoff, I., Birman, V., and Singer, J., 1984, "Effect of imperfections on the vibrations of loaded structures," ASME JOURNAL OF APPLIED MECHANICS, Vol. 51, pp. 191–193.

Galaka, P. I., Zarutsky, V. A., Matsner, V. I., and Nosachenko, A. M., 1975, "Investigation of the effects of axial compressive forces on the frequency and form of vibrations of ribbed cylindrical shells," *Soviet Applied Mechanics*, Vol. 11, pp. 838–843.

Haftka, R. T., Cohen, G. A., and Mroz, Z., 1990, "Derivatives of buckling loads and vibration frequencies with respect to stiffness and initial strain parameters," ASME JOURNAL OF APPLIED MECHANICS, Vol. 57, pp. 18–24.

Johnson, E. R., Plaut, R. H., and Deel, C. C., 1980, "Load-frequency relationships for shallow elastic structures," *Recent Advances in Structural Dynamics*, M. Petyt, ed., University of Southampton, Southampton, U.K., pp. 611–620.

Plaut, R. H., and Johnson, E. R., 1981, "The effects of initial thrust and elastic foundation on the vibration frequencies of a shallow arch," *Journal of Sound and Vibration*, Vol. 78, No. 4, pp. 565–571.

Plaut, R. H., and Virgin, L. N., 1990, "Use of frequency data to predict buckling," *Journal of Engineering Mechanics*, Vol. 116, pp. 2330–2335.

Rosen, A., and Singer, J., 1976, "Vibration and buckling of eccentrically loaded stiffened cylindrical shells," *Experimental Mechanics*, Vol. 16, pp. 88–94.

Ryaboi, V. M., 1975, "The equilibrium problem for a cylindrical shell compressed in an elastic medium with omnidirectional coupling of the shell to the medium," *Mechanics of Solids*, Vol. 10, No. 6, pp. 74–82.

Ryaboy, V. M., and Weller, T., 1994, "A Simple Model of a Stiffened Shell Type Structure for an Investigation into the Vibration-Buckling Correlation," Technion—Israel Institute of Technology Report TAE 707, Haifa, Israel.

Singer, J., 1983, "Vibration and buckling of imperfect stiffened shells—Recent developments," *Collapse: The Buckling of Structures in Theory and Practice*, J. M. T. Thompson and G. W. Hunt, eds., Cambridge University Press, Cambridge, UK, pp. 443–479.

Singer, J., and Abramovich, H., 1979, "Vibration techniques for definition of practical boundary conditions in stiffened shells," *AIAA Journal*, Vol. 17, pp. 762–769.

Souza, M. A., 1989, "The influence of hardening of the supports on the response of structural elements liable to buckling," ASME *Applied Mechanics Reviews*, Vol. 42, No. 11, Part 2, pp. S245–S248.

Souza, M. A., 1992, "Vibration of thin-walled structures with asymmetric post-buckling characteristics," *Thin-Walled Structures*, Vol. 14, pp. 45–57.

Souza, M. A., 1993, "Dynamic post-buckling behavior of thin-walled structures with flexible knife-edge supports," ASME *Applied Mechanics Reviews*, Vol. 46, No. 11, Part 2, pp. S148–S155.

Souza, M. A., and Assaid, L. B. M., 1991, "A new technique for the prediction of buckling loads from nondestructive vibration tests," *Experimental Mechanics*, Vol. 31, pp. 93–97.

Thompson, J. M. T., and Hunt, G. W., 1973, *A General Theory of Elastic Stability*, Wiley, London.

Weller, T., Abramovich, H., and Singer, J., 1986, "Application of non-destructive vibration correlation technique to the buckling of spot-welded and riveted stringer-stiffened cylindrical shells," *Z FW—Zeitschrift fur Flugwissenschaften und Weltraumforschung*, Vol. 10, H. 3, pp. 183–189.

Weller, T., Singer, J., and Batterman, S. C., 1974, "Influence of eccentricity of loading on buckling of stringer-stiffened cylindrical shells," *Thin-Shell Structures: Theory, Experiment and Design*, Y. C. Fung, and E. E. Sechler, eds., Prentice-Hall, Englewood Cliffs, NJ, pp. 305–324.

APPENDIX A

General Properties of Characteristic Curves

Let us assume the total potential energy of the conservative multi-degree-of-freedom system in the particular form $V = U - \lambda\Delta$ (Thompson and Hunt, 1973), where λ is a load parameter, and U, Δ are analytical functions of the coordinate vector $\mathbf{x} = \{x_1, x_2, \ldots, x_n\}$. The system is in equilibrium at $\mathbf{x} = \mathbf{x}(\lambda)$ if

$$U_{,i} - \lambda\Delta_{,i} = 0 \quad (i = 1, 2, \ldots, n), \tag{A1}$$

where subscripts after commas denote differentiation with respect to the corresponding coordinates. The equilibrium is stable

Downloaded 04 May 2010 to 171.66.16.33. Redistribution subject to ASME license or copyright; see http://www.asme.org/terms/Terms_Use.cfm

if the stiffness matrix C, with the elements $c_{ij} = (V_{,ij})_{\mathbf{x}=\mathbf{x}(\lambda)}$, is positive definite. Small vibrations around the stable equilibrium are governed by an eigenvalue equation $(C - \omega^2 M)\phi = 0$ with a positive definite mass matrix $M = M(\mathbf{x})$.

The mass and stiffness matrices are reduced to a diagonal form by a single transformation $\Phi^T C \Phi = \Lambda$, $\Phi^T M \Phi = E$, where E is the identity matrix, the superscript T denotes transpose, $\Lambda = \text{diag}\,[\omega_1^2, \ldots, \omega_n^2]$ is a diagonal matrix composed of eigenvalues arranged in ascending order and Φ is a modal matrix whose columns $\phi_1, \phi_2, \ldots, \phi_n$ are eigenmodes. It is well known that

$$\omega_1^2 = \min_{\phi} \left(\frac{\phi^T C \phi}{\phi^T M \phi} \right) = \phi_1^T C \phi_1. \tag{A2}$$

Let us suppose that C is positive definite for $0 \le \lambda < \lambda_{cr}$ and positive semi-definite for $\lambda = \lambda_{cr}$. In this case, the unique fundamental equilibrium path $\mathbf{x} = \mathbf{x}(\lambda)$ exists for $0 \le \lambda \le \lambda_{cr}$, and it follows from (A2) that ω_1^2 is a continuous function of λ for $0 \le \lambda \le \lambda_{cr}$, vanishing at $\lambda = \lambda_{cr}$.

Let us derive an expression for the slope of the characteristic curve. From perturbation theory, $(\omega_1^2)' = \phi_1^T C' \phi_1$, where prime denotes derivative with respect to λ. Then, $c'_{ij} = c_{ij,l} x'_l - \Delta_{,ij}$ (repeated subscripts imply summation from 1 to n). From the equilibrium Eq. (A1), $V_{,ij} x'_j - \Delta_{,i} = 0$. Hence, $x'_l = b_{ij} \Delta_{,j}$, where b_{ij} are elements of a compliance matrix $B = C^{-1}$. It follows that

$$(\omega_1^2)' = \phi_{i1} \phi_{j1} c_{ij,l} b_{lr} \Delta_{,r} - \phi_{i1} \phi_{j1} \Delta_{,ij}, \tag{A3}$$

where ϕ_{ij} are elements of Φ. A formula of this type was derived by Haftka et al. (1990) for continuous structures.

In the initial state $\lambda = 0$ and c_{ij} are components of the stiffness matrix of an unloaded structure. Their first derivatives are associated with the elastic asymmetry of the structure. The first derivatives $\Delta_{,r}$ are usually due to geometric imperfections, and in the particular case of load eccentricity they are proportional to e. If both factors are present, the initial slope of the characteristic curve is a linear function of e. In the example above, $c_{ij,l}(0) = f''_2(0)$, except $c_{11,1}(0) = 2f''_1(0) + f''_2(0)$; $\Delta_{,1} = 2e$, $\Delta_{,2} = 0$, and the initial slopes of characteristic curves in Figs. 4(*b*), 9, and 10 depend linearly on e.

Since $C^{-1} = \Phi \Lambda^{-1} \Phi^T$, (A3) can be written as

$$(\omega_1^2)' = \sum_{k=1}^{n} \frac{\phi_{i1} \phi_{j1} c_{ij,l} \phi_{lk} \phi_{rk} \Delta_{,r}}{\omega_k^2} - \phi_{i1} \phi_{j1} \Delta_{,ij}. \tag{A4}$$

Transformation to the local normal coordinates $x_j - x_{j0} = \phi_{jl} q_l$ reduces formula (A4) to

$$(\omega_1^2)' = \sum_{k=1}^{n} \frac{\tilde{V}_{,11k} \tilde{\Delta}_{,k}}{\omega_k^2} - \tilde{\Delta}_{,11}, \tag{A5}$$

where the tilde denotes a function transformed to the local normal coordinates $q_1, q_2, \ldots, q_n$. As $\lambda \to \lambda_{cr}$, $\omega_1^2 \to 0$, and assuming a simple eigenvalue it follows from (A5) that

$$\frac{d(\omega_1^2)}{d\lambda} = \frac{\tilde{V}_{,111} \tilde{\Delta}_{,1}}{\omega_1^2} + O(1).$$

Multiplying by $\omega_1^2 d\lambda$ and integrating yields

$$\omega_1^2 = \sqrt{\alpha(\lambda_{cr} - \lambda)} + \text{higher order terms}, \tag{A6}$$

where $\alpha = -\frac{1}{2} \tilde{V}_{,111} \tilde{\Delta}_{,1} \ge 0$. As shown by Thompson and Hunt (1973), a limit point occurs at $\lambda = \lambda_{cr}$ if $\tilde{\Delta}_{,1} \ne 0$ and a bifurcation occurs if $\tilde{\Delta}_{,1} = 0$. So, in a generic limit point where $\tilde{V}_{,111} \ne 0$, $\alpha \ne 0$ and $\omega_1^2 = O(\sqrt{\lambda_{cr} - \lambda})$ according to (A6). If $\alpha = 0$, but λ_{cr} is still a maximum such that $q_1 = O((\lambda_{cr} - \lambda)^p)$, $0 < p < 1$, it is easy to show that $\omega_1^2 = O((\lambda_{cr} - \lambda)^{(p+1)/2})$. If λ has no smooth maximum approaching λ_{cr}, as in a typical bifurcation point, then $\omega_1^2 = O(\lambda_{cr} - \lambda)$. These properties are illustrated by Figs. 4(*b*) and 10. Johnson et al. (1980) and Plaut and Johnson (1981) reported similar observations for shallow arches.

APPENDIX B

Invariant Points

The analytical formulas for the approximate invariant points in Figs. 6–10 with respect to e are obtained from a simplified expression for V in terms of u_1, u_2 assuming that $\theta_1 = u_1$, $\theta_1 + \theta_2 = u_2$, $\Delta = 2eu_1 + u_1^2 + (u_2 - u_1)^2$. Then, for $P = 2(k_1 + k_2) = P_{\text{inv}}$, equilibrium equations are satisfied by three values of $u_2 = u_2^{inv}$, namely $(u_2^{inv})_1 = 0$, and

$$(u_2^{inv})_{2,3} = 0.5[(u_{02} + u_{*2}) \mp \sqrt{(u_{02} - u_{*2})^2 + (8k_1/c_2) u_{02} u_{*2}}], \tag{B1}$$

independently of e. Under the same assumptions, the frequency equation yields a constant value of ω^2 for all equilibrium curves which pass through the point (u_2^{inv}, P_{inv}):

$$\omega_{inv}^2 = \tfrac{1}{2}[f'_2(u_2^{inv}) - 2k_1]. \tag{B2}$$

Only $(u_2^{inv})_2$, which corresponds to the minus sign in formula (B1), belongs to a stable fundamental path. So, the invariant points of the characteristic curves in Figs. 4(*b*), 9, and 10 correspond to $P = P_{inv}$ and $\omega^2 = \omega_{inv}^2$ defined by Eq. (B2) with $u_2^{inv} = (u_2^{inv})_2$. Note that not necessarily $\omega_{inv}^2 = \omega_1^2$. In Fig. 9, it is ω_2^2 which passes through the invariant point for $e = -0.001$.

Downloaded 04 May 2010 to 171.66.16.33. Redistribution subject to ASME license or copyright; see http://www.asme.org/terms/Terms_Use.cfm

Transient Solutions of the Ring-Spinning Balloon Equations

D. M. Stump
Department of Civil Engineering,
The University of Queensland,
St. Lucia, QLD 4072, Australia

W. B. Fraser
School of Mathematics and Statistics,
The University of Sydney,
Sydney, NSW 2006, Australia

In the textile yarn manufacturing process of ring spinning, a loop of yarn rotates rapidly about a fixed axis. The surface generated by the rotating yarn loop is called a balloon. *The solutions of the time-independent, nonlinear, yarn-balloon equations have been extensively investigated for a reference frame that rotates with constant angular velocity and are termed* quasi-stationary *solutions. A linear perturbation stability analysis of these solutions has shown that while single-loop balloons are stable, multiple-loop balloons are typically unstable. In this paper a numerical method for the calculation of transient solutions of the nonlinear time-dependent PDEs is developed, and the stability of representative quasi-stationary balloons subjected to a model velocity impulse is studied. The results of the linearized analysis are confirmed: Single-loop balloons remain stable while multiple-loop balloons typically collapse within only a few spindle revolutions.*

1 Introduction

The ring spindle (Fig. 1) is widely used in the textile yarn manufacturing industry to insert twist in yarns made from staple fibers such as wool and cotton. Spinning is the final step in the manufacture of staple fiber yarns, and a detailed account of the process can be found in the books by de Barr and Catling (1965, Chapter 2) and Klein (1987).

Briefly, a strand of aligned fibers (called a *roving*) issues at a constant speed V from the *front-drafting rollers* D and passes through the guide eye O, which is coaxial with the spindle S. From here the yarn passes around the traveler T, which is free to rotate on the ring R, and thence to the *lay-point* L where it is wound onto the bobbin B which is driven at a constant angular speed ω_0. The traveler is dragged around the ring by the loop of yarn OTL. The amount of twist inserted in the yarn between D and T is determined by the difference between the delivery speed V and the lay point speed $\omega_0 b$ (where b is the bobbin radius at the lay point). If ω is the angular speed of the traveler then these three speeds are related by the equation

$$(\omega_0 - \omega)b = V. \tag{1}$$

In this equation the speed of the lay-point $\omega_0 b$ is very much greater than the yarn delivery speed V so that for all practical purposes the angular speed of the traveler can be taken to be the same as that of the spindle (de Barr and Catling, 1965, Eq. 2.1). This fact will be exploited in simplifying the equations that follow.

The imaginary surface swept out by the rotating yarn loop between O and T is called a *balloon,* and a knowledge of the yarn tension in, the shape of, and the stability of these balloons is crucial for the design and operation of ring-spinning machinery. Although the equations governing the dynamics of the yarn loop, and the boundary conditions appropriate to the ring-spinning balloon at O and T have been known for a long time, it is only recently that advances in large-scale computational power have allowed the initiation of a comprehensive investigation of the solutions of this highly nonlinear system of differential equations and boundary conditions. This was started with the papers by Batra et al. (1989a, b) and Fraser (1993a, b) where references to the earlier literature can be found. In these papers solutions of the equations corresponding to *quasi-stationary* balloons in which the shape of the yarn loop, viewed in a reference frame rotating with the angular velocity of the traveler, is stationary were investigated in some detail. More recently, Stump and Fraser (1995) have investigated the dynamic stability of these quasi-stationary balloon solutions to small perturbations in the yarn-loop shape and velocity profile. This linear perturbation analysis revealed a richness of behavior for the stability of the quasi-stationary balloons, including the existence of Hopf-like bifurcations that occur under certain operating conditions.

The present paper describes a method for the numerical solution of the time-dependent partial differential equations and boundary conditions for the ring-spinning balloon, which was undertaken in order to determine how adequately the linearized analysis approximates the full nonlinear results. Lisini et al. (1992) have also considered the integration of the time-dependent nonlinear equations, but their treatment of the traveler mass boundary conditions is different, and the intent of their paper was to study the effects of the feed velocity V.

In the next section the derivation of the ring-spinning equations is reviewed and in Section 3 these equations are transformed into a form more suited to the computational algorithm which is described in Section 4. In Section 5, the numerical results are discussed.

2 Mathematical Formulation

2.1 Yarn in the Balloon. A detailed development of the equations governing yarn in the balloon can be found in Batra et al. (1989a, b) and Fraser (1993a) as well as in the book by de Barr and Catling (1965).

The equation of motion is derived on the assumptions of a constant mass-linear-density $\bar{m}$, tension acting along the yarn tangent, and an air-drag force acting in the direction opposite to the normal velocity of the yarn. A final equation is provided by the condition of yarn inextensibility.

The dimensionless equation of motion for material points in the yarn balloon is

$$\frac{\partial^2 \mathbf{R}}{\partial t^2} + 2\mathbf{k} \wedge \frac{\partial \mathbf{R}}{\partial t} + \mathbf{k} \wedge (\mathbf{k} \wedge \mathbf{R}) = \frac{\partial}{\partial s}\left(T \frac{\partial \mathbf{R}}{\partial s}\right) + \mathbf{F} \tag{2}$$

Contributed by the Applied Mechanics Division of THE AMERICAN SOCIETY OF MECHANICAL ENGINEERS for publication in the ASME JOURNAL OF APPLIED MECHANICS.

Discussion on this paper should be addressed to the Technical Editor, Professor Lewis T. Wheeler, Department of Mechanical Engineering, University of Houston, Houston, TX 77204-4792, and will be accepted until four months after final publication of the paper itself in the ASME JOURNAL OF APPLIED MECHANICS.

Manuscript received by the ASME Applied Mechanics Division, June 6, 1994; final revision, Jan. 10, 1995. Associate Technical Editor: S. W. Shaw.

Copyright © 1996 by ASME

Downloaded 04 May 2010 to 171.66.16.33. Redistribution subject to ASME license or copyright; see http://www.asme.org/terms/Terms_Use.cfm

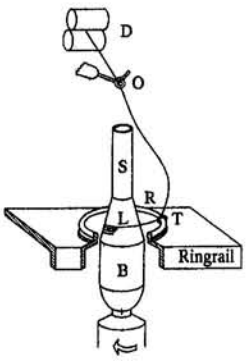


Fig. 1 General view of the ring spinner

where $\mathbf{R}(s, t)$ and $T(s, t)$ are the position and tension within a coordinate system that rotates with the angular speed of the traveler, ω, and oriented as shown in Fig. 2. The dimensionless path length $s = \bar{s}/a$, where $\bar{s}$ is measured from the guide eye, and a is the ring radius. The nondimensional time is defined by $t = \bar{t}\omega$. (Physical quantities other than a, ω, and V are distinguished by overbars.) The effects of the pull-through velocity V occur on a much longer time scale and have been neglected in accordance with Fraser (1993a). The air-drag force $\mathbf{F}$ is

$$\left.\begin{aligned} \mathbf{F} &= -\frac{p_0}{16}\,|\mathbf{v}_n|\mathbf{v}_n, \\ \mathbf{v}_n &= \mathbf{v} - \left(\mathbf{v}\cdot\frac{\partial \mathbf{R}}{\partial s}\right)\frac{\partial \mathbf{R}}{\partial s}, \\ \mathbf{v} &= \frac{\partial \mathbf{R}}{\partial t} + \mathbf{k}\wedge\mathbf{R}. \end{aligned}\right\} \tag{3}$$

The dimensionless air-drag coefficient

$$p_0 = \frac{16\bar{D}_n a}{\bar{m}}$$

was introduced by Padfield (1958) where $\bar{D}_n$ is the drag coefficient for a circular cylinder moving through a viscous fluid in turbulent flow. Other dimensionless variables used in these equations are related to the physical (barred) variables by the equations:

$$\left.\begin{aligned} \mathbf{R} &= \frac{\bar{\mathbf{R}}}{a} = \frac{\bar{x}}{a}\mathbf{i} + \frac{\bar{y}}{a}\mathbf{j} + \frac{\bar{z}}{a}\mathbf{k}, \\ \mathbf{v}_n &= \frac{\bar{\mathbf{v}}_n}{\omega a}, \quad \mathbf{v} = \frac{\bar{\mathbf{v}}}{\omega a}, \\ T &= \frac{\bar{T}}{\bar{m}\omega^2 a^2}, \quad \mathbf{F} = \frac{\bar{\mathbf{F}}}{\bar{m}\omega^2 a}. \end{aligned}\right\} \tag{4}$$

The inextensibility condition

$$\frac{\partial \mathbf{R}}{\partial s}\cdot\frac{\partial \mathbf{R}}{\partial s} = 1 \tag{5}$$

completes the equations.

Equations (2) and (5) constitute four equations for the three components of the position vector $\mathbf{R}(s, t)$ and the tension $T(s, t)$. An equation for T is derived by forming the dot product of $(\partial\mathbf{R}/\partial s)$ with Eq. (2) and then using (5) to obtain

$$\frac{\partial T}{\partial s} = \frac{\partial \mathbf{R}}{\partial s}\cdot\left\{\frac{\partial^2 \mathbf{R}}{\partial t^2} + 2\mathbf{k}\wedge\frac{\partial \mathbf{R}}{\partial t} + \mathbf{k}\wedge(\mathbf{k}\wedge\mathbf{R})\right\}. \tag{6}$$

2.2 The Boundary Conditions. Since the yarn at the guide eye remains fixed when the feed velocity V is neglected, the boundary condition at the guide eye is

$$\mathbf{R}(0, t) = \mathbf{O}, \tag{7}$$

and geometric boundary condition at the traveler is

$$\mathbf{R}[s_l(t), t)] = \mathbf{e}_r + h\mathbf{k}, \tag{8}$$

where $s = s_l(t)$ is the length of yarn in the balloon at time t, and the dimensionless balloon height $h = \bar{h}/a$.

At the bottom of the balloon, the yarn passes around a traveler and then wraps onto the bobbin. Following Stump and Fraser (1995), the dimensionless equation of motion for the dimensionless traveler mass $M_T = \bar{m}_T/(\bar{m}a)$ is

$$M_T\frac{d^2\theta_T}{dt^2}\mathbf{e}_\theta - M_T\left(1 + \frac{d\theta_T}{dt}\right)^2\mathbf{e}_r = -T\left.\frac{\partial \mathbf{R}}{\partial s}\right|_{s_l(t)} - T_b\cos\phi\mathbf{e}_r + T_b\sin\phi\mathbf{e}_\theta + \mathbf{N} - \mu_T|\mathbf{N}|\mathbf{e}_\theta, \tag{9}$$

where $\mathbf{N} = N_r\mathbf{e}_r + N_z\mathbf{k}$ is the normal force exerted by the ring rail on the traveler, $\mu_T|\mathbf{N}|\mathbf{e}_\theta$ is the friction force opposing the rotation of the traveler, and $\theta_T(t)$ is the angular displacement of the traveler relative to the polar-coordinate reference frame rotating at the steady velocity ω. T_b is the tension on the bobbin side of the traveler mass and is obtained from the Euler capstan equation:

$$T_b = T[s_l(t), t]e^{\mu_Y\alpha}, \tag{10}$$

where μ_Y is the friction coefficient of the yarn on the traveler, and α is the wrap angle obtained from the dot product between the yarn tangents at the traveler mass and the segment connecting the traveler and lay point:

$$\alpha = \cos^{-1}\left\{\left.\frac{\partial \mathbf{R}}{\partial s}\right|_{s_l(t)}\cdot(-\cos\phi\mathbf{e}_r + \sin\phi\mathbf{e}_\theta)\right\}, \tag{11}$$

where $\sin\phi = b = \bar{b}/a$ (Fig. 2).

The yarn velocity at the traveler end of the balloon must be equal to the velocity of the traveler and, following Stump and Fraser (1995), this leads to the yarn continuity condition

$$\frac{ds_l}{dt} = b\frac{d\theta_T}{dt} = b\frac{d}{dt}\{\theta[s_l(t), t]\}, \tag{12}$$

which is used to eliminate θ_T and its time derivatives from (9).

3 Transformation of Governing Equations

This section discusses a variable change that facilitates the numerical analysis of the above equations. The change is motivated by the boundary condition at the traveler mass which results in a balloon length $s_l(t)$ that is a function of time. The distance variable s is rescaled as $u = s/s_l(t)$ so that the domain

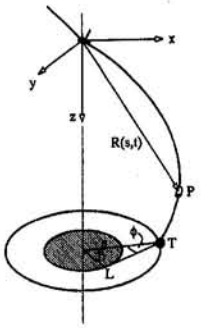


Fig. 2 Schematic representation of the spinner and reference frame

Downloaded 04 May 2010 to 171.66.16.33. Redistribution subject to ASME license or copyright; see http://www.asme.org/terms/Terms_Use.cfm

for integration is given by the open-ended rectangle $0 \le u \le 1$ and $t \ge 0$, which is preferable for numerical integration by finite difference operators. The coordinate transformation of the governing equations and boundary conditions is carried out below.

The partial derivatives with respect to s transform into

$$\frac{\partial}{\partial s} = \frac{1}{s_l(t)} \frac{\partial}{\partial u}, \tag{13}$$

while the partial derivative with respect to time becomes

$$\left.\frac{\partial}{\partial t}\right|_s = \left.\frac{\partial}{\partial t}\right|_u + \left.\frac{du}{dt}\right|_s \left.\frac{\partial}{\partial u}\right|_t = \frac{\partial}{\partial t} - \frac{u}{s_l}\frac{ds_l}{dt}\frac{\partial}{\partial u}, \tag{14}$$

where the explicit notation on the partial derivatives has been dropped in the last expression. Similarly,

$$\left.\frac{\partial^2}{\partial t^2}\right|_s = \frac{\partial^2}{\partial t^2} + \left\{2u\left(\frac{s_{l,t}}{s_l}\right)^2 - \frac{us_{l,tt}}{s_l}\right\}\frac{\partial}{\partial u} - \frac{2us_{l,t}}{s_l}\frac{\partial^2}{\partial t\partial u} + \left(\frac{us_{l,t}}{s_l}\right)^2\frac{\partial^2}{\partial u^2}, \tag{15}$$

with $s_{l,t} = ds_l/dt$. It is useful to introduce the notations $()' = \partial/\partial u$ and $()_{,t} = \partial/\partial t$, and to let

$$\left.\begin{aligned} P(u,t) &= 2u\left(\frac{s_{l,t}}{s_l}\right)^2 - \frac{us_{l,tt}}{s_l} \\ Q(u,t) &= \frac{us_{l,t}}{s_l}, \end{aligned}\right\} \tag{16}$$

so that

$$\left.\frac{\partial^2}{\partial t^2}\right|_s = \frac{\partial^2}{\partial t^2} + P\frac{\partial}{\partial u} - 2Q\frac{\partial^2}{\partial t\partial u} + Q^2\frac{\partial^2}{\partial u^2}. \tag{17}$$

The inextensibility condition (5) transforms into

$$\mathbf{R}' \cdot \mathbf{R}' = s_l^2(t), \tag{18}$$

from which it follows that

$$\left.\begin{aligned} \mathbf{R}' \cdot \mathbf{R}'' &= 0, \\ \mathbf{R}' \cdot \mathbf{R}'_{,t} &= s_l s_{l,t}. \end{aligned}\right\} \tag{19}$$

When the above change of coordinates is made in Eq. (2), cartesian components of the governing equations are given by

$$\left.\begin{aligned} x_{,tt} + Px' - 2Qx'_{,t} + Q^2x'' - 2y_{,t} + 2Qy' - x &= \frac{1}{s_l^2}\{T'x' + Tx''\} + F_x \\ y_{,tt} + Py' - 2Qy'_{,t} + Q^2y'' + 2x_{,t} - 2Qx' - y &= \frac{1}{s_l^2}\{T'y' + Ty''\} + F_y \\ z_{,tt} + Pz' - 2Qz'_{,t} + Q^2z'' &= \frac{1}{s_l^2}\{T'z' + Tz''\} + F_z. \end{aligned}\right\} \tag{20}$$

In terms of the new coordinates, the cartesian components of the normal velocity Eq. $(3)_2$ are

$$\left.\begin{aligned} (\mathbf{v}_n)_x &= x_{,t} - Qx' - y - \frac{qx'}{s_l^2} \\ (\mathbf{v}_n)_y &= y_{,t} - Qy' + x - \frac{qy'}{s_l^2} \\ (\mathbf{v}_n)_z &= z_{,t} - Qz' - \frac{qz'}{s_l^2} \end{aligned}\right\} \tag{21}$$

where

$$q = \mathbf{R}' \cdot \mathbf{v} = x_{,t}x' + y_{,t}y' + z_{,t}z' - Qs_l^2 - yx' + xy', \tag{22}$$

and the cartesian components of the air-drag force remain given by $(3)_1$. The tension Eq. (6) becomes

$$T' = x'x_{,tt} + y'y_{,tt} + z'z_{,tt} + Ps_l^2 - 2Qs_ls_{l,t} - 2x'y_{,t} + 2y'x_{,t} - xx' - yy'. \tag{23}$$

When the geometric boundary conditions (7) and (8) are transformed, they remain unchanged except that $s_l(t)$ is replaced by $u = 1$, and the yarn continuity condition (12) becomes

$$\frac{ds_l}{dt} = b\frac{d\theta_T}{dt} = b\theta_{,t}(1,t). \tag{24}$$

Finally, the polar coordinate components of the dynamic traveler mass Eq. (9) become

$$\left.\begin{aligned} N_r &= -M_T(1 + \theta_{,t})^2 + \frac{Tr'}{s_l} + T_b\cos\phi \\ N_z &= \frac{Tz'}{s_l} \\ M_T\theta_{,tt} &= -\frac{T\theta'}{s_l} + T_b\sin\phi - \mu_Y\sqrt{N_r^2 + N_z^2} \end{aligned}\right\} \tag{25}$$

where all yarn quantities are evaluated at $u = 1$, T_b is given by Eq. (10), and the wrap angle α transforms into

$$\alpha = \cos^{-1}\left\{\frac{-r'\cos\phi + \theta'\sin\phi}{s_l}\right\}. \tag{26}$$

The Eq. (25) provide only one boundary condition since Eq. $(25)_1$ and Eq. $(25)_2$ are used to eliminate N_r and N_z from Eq. $(25)_3$. It is straightforward to derive formulas connecting the polar coordinates (r, θ) and the cartesian coordinates (x, y).

4 Numerical Integration

The transformed PDEs must be integrated numerically over the domain $0 \le u \le 1$ and $t \ge 0$. Here, an implicit time integration strategy is employed by replacing the partial derivatives with respect to time by backward difference operators, in order to ensure stability, and then integrating the resulting system of spatial ODEs for successive time steps.

The time is discretized into $t_j = j(\Delta t)$, $(j = -1, 0, \ldots)$ and the time derivatives are written as backwards difference operators:

$$\left.\begin{aligned} x_{,t}(u,t_j) &= \frac{x_j - x_{j-1}}{\Delta t} \\ x_{,tt}(u,t_j) &= \frac{x_j + x_{j-2} - 2x_{j-1}}{\Delta t^2} \end{aligned}\right\} \tag{27}$$

and so on. This turns the four equations (20) and (23) into a set of nonlinear ODEs for $x(u, t_j)$, $y(u, t_j)$, $z(u, t_j)$ and $T(u, t_j)$, which are then integrated with the boundary conditions (7), (8), and $(25)_3$ by the relaxation method discussed by Press et al. (1986). This particular temporal discretization was moti-

Downloaded 04 May 2010 to 171.66.16.33. Redistribution subject to ASME license or copyright; see http://www.asme.org/terms/Terms_Use.cfm

vated by the lack of a spatial boundary condition involving the tension T.

Simulations were conducted in the following manner. First, a relaxation treatment of the quasi-stationary equations in u was used to compute the initial balloon shape $\mathbf{R}(u, t_0) = \mathbf{R}_0(u)$ and tension $T(u, t_0) = T_0(u)$. Next, the quasi-stationary balloon was subjected to the prescribed velocity impulse $\mathbf{R}_{,t}(u, 0) = \mathbf{g}(u)$. The method of false positions (Ames, 1977) was used to extrapolate the positions backwards in time to give the positions

$$\mathbf{R}(u, t_{-1}) = \mathbf{R}_0(u) - \mathbf{g}(u)\Delta t. \tag{28}$$

Since the partial derivatives of the tension with respect to time do not appear, it was unnecessary to calculate $T(u, t_{-1})$. The time incrementation began with t_1 and continued at uniform prescribed Δt. The relaxation method requires a guess for the solution at each time-step. For the first time-step, the quasi-stationary results together with the prescribed velocities were used to generate a guess. For subsequent time-steps, the results of the previous two time-steps were extrapolated to provide a starting guess.

As a check on the numerical stability of the code, shapes of stable single-loop balloons were used and the velocity impulse was turned off (i.e., $\mathbf{g}(u) = \mathbf{0}$). It was found that the algorithm was sensitive to the time-step size, due to the stiffness of the inextensibility constraint. For time-steps $\Delta t \leq 0.05$ the tension in the yarn loop jumped by about five percent during the first few time-steps before settling back down to the quasi-stationary value. For nonzero velocity impulses, time increments needed to be larger than $\Delta t \geq 0.1$ due to the lack of a good initial guess for the tension at the instant after the impulse was applied. It was found that $\Delta t = 0.2$ gave adequate results with moderate computation times, and this value has been used in all calculations unless otherwise stated. Several hundred spatial integration points were adequate for the relaxation procedure.

5 Simulation Results

5.1 Review of Quasi-Stationary and Stability Results. The quasi-stationary results have been discussed extensively in a number of recent articles (e.g., Fraser, 1993b; Fraser et al., 1994) and a detailed discourse is omitted here. Dimensional quantities without the bar notation are used here unless stated otherwise. The dimensionless guide-eye tension is a function in the six-dimensional parameter space,

$$\frac{T_{g_0}}{ma^2\omega^2} = \Phi\left(\frac{b}{a}, \frac{h}{a}, \frac{m_T}{ma}, \mu_T, \mu_Y, p_0\right). \tag{29}$$

Each solution corresponds to a specific balloon profile and guide-eye tension. It is impractical to explore all of parameter space and to make a connection with the previous linear perturbation stability study, the values

$$\frac{h}{a} = 10, \quad \mu_T = \mu_Y = 0.1, \quad p_0 = 4.0$$

are specified and serve to condense the solution surface to a three-dimensional space (Fig. 3).

The surface, Fig. 3, exhibits a hysteresis fold for values $m_T/ma \leq 70$. Two cross sections through the surface at the values $m_T/ma = 100$ and 40 are shown in Fig. 4 and these curves are referred to as *bifurcation diagrams* following Gray and Roberts (1988).

5.1.1 Heavy Traveler Mass: $m_T/ma = 100$. The results for the traveler $m_T/ma = 100$ show a unique guide-eye tension associated with only single-loop balloons. The linear stability analysis predicts a denumerable set of complex eigenvalues of increasing modulus. (Complex eigenvalues appear in complex conjugate pairs.) Studies of the three lowest modulus eigenvalue

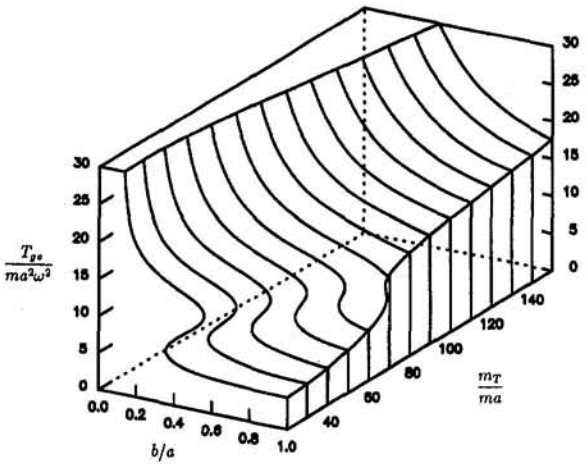


Fig. 3 Solution surface $T_{g_0}/m\omega^2a^2 = \Phi(b/a, m_T/ma)$ for the quasi-stationary balloon ($p_0 = 4.0$, $\mu_y = \mu_t = 0.1$, $h/a = 10$)

sets show that they remain in the negative real half-plane for all points along the bifurcation curves. Larger modulus eigenvalues presumably behave the same way so the entire diagram of Fig. 4 is stable, as is indicated by the solid line.

5.1.2 Medium Traveler Mass: $m_T/ma = 40$. The results for the $m_T/ma = 40$ traveler mass, which lies outside the range of commercial interest, are more interesting from a mathematical viewpoint since the bifurcation diagram contains one hysteresis fold (see Fig. 4). The top shelf of the diagram corresponds to single-loop balloons. The underside of the fold is bounded by two turning points B and C, where the tangent to the curve has an infinite slope. The balloon profiles on this section are one-and-a-half loop balloons. The lower shelf below the lower turning point is characterized by two-loop balloon profiles. Three different shape balloon profiles corresponding to $b/a = 0.65$, which lies approximately in the middle of the fold, are shown in Fig. 5, where the radial-axial coordinate system is centered on the bobbin axis at the ring rail. The balloons correspond to high (solid line), medium (long-dashed line) and low (short-dashed line) tensions in Fig. 4.

The perturbation analysis predicts that the single-loop balloons along the top surface of the bifurcation diagram are all stable (denoted by the solid line in Fig. 4). The one-and-a-half loop balloons along the underside of the fold and between the two turning points are all unstable due to the presence of a single positive *real* eigenvalue, and the instability is denoted by the dotted line segment for this portion of the curve.

Just below the lower turning point on the bottom shelf of solutions there is a small region of stable two-loop balloons between the points C and h_1. Between h_1 and h_2 a *complex* eigenvalue with a positive real part renders the intervening two-loop balloons unstable. This portion of the curve is bounded by two *Hopf-like* bifurcations which occur at undistinguished points along the bifurcation diagram. Beyond h_2 the two-loop balloons are predicted to be stable, so the curve is again drawn with a solid line.

5.2 Time-Dependent Simulation Results. The velocity impulse is somewhat arbitrary and, for the sake of convenience, the form

$$g_x(u) = A \sin(\pi u), \quad g_y(u) = g_z(u) = 0$$

was used. The constant A is an arbitrary amplitude that was varied to judge the effects of nonlinearity. This form has no real significance other than providing a smooth velocity impulse in the x-direction of the rotating axis system, but was found suitable for the major objective of the simulations: to study the

Downloaded 04 May 2010 to 171.66.16.33. Redistribution subject to ASME license or copyright; see http://www.asme.org/terms/Terms_Use.cfm

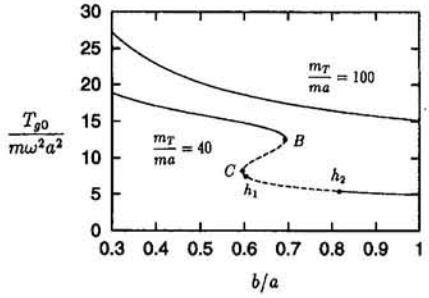


Fig. 4 Bifurcation diagram $T_{g_0}/m\omega^2a^2$ versus b/a for $m_T/ma = 100$ and $m_T/ma = 40$

response of stable and unstable quasi-stationary balloons to small velocity impulses. Some other impulse forms were tried, but the general conclusions reached below were not altered.

5.2.1 Heavy Traveler Mass: $m_T/ma = 100$. Three different stable single-loop balloons corresponding to the values of $b/a = (0.65, 0.85, 0.95)$ in Fig. 4 were each subjected to impulses with the magnitudes $A = (0.05, 0.25, 0.5)$. The greatest value of A represents a rather large velocity impulse and is unlikely to occur physically. In all cases, the transients induced by the impulses were seen to die way almost completely after $t\omega = 50$, which is about eight revolutions of the balloon.

Results for the particular example $b/a = 0.65$ and $A = 0.25$ are shown in Figs. 6(*a*) and 6(*b*), where the guide-eye tension $T_g/m\omega^2a^2$ and balloon length s_l/a are plotted versus time $t\omega$. Both sets of plots have been made for the three time-steps $\omega\Delta t = (0.1, 0.2, 0.4)$ and show the convergence of the results. (Because of the finite jump in tension and the stability difficulties associated with inextensibility, the tension at the very first time-step has been omitted.) The steady-state asymptotes, shown by the straight dotted lines, are $T_g/m\omega^2a^2 = 17.928$ and $s_l/a = 10.269$. The tension undergoes an instantaneous jump of about ten percent and then goes through a series of decaying oscillations about the quasi-stationary position. The balloon length shows a similar behavior, but the heavy traveler mass means that the total length of the loop varies only slightly (less than one percent from the quasi-stationary value). The inertia of the traveler also means that the balloon-length oscillations develop and decay away more slowly than those of the tension.

Two important features can be observed in Figs. 6(*a*) and 6(*b*). First, the initial tension and balloon length transients set up by the impulse have periods of 9 and 5, respectively, which are faster than values of around 18 predicted from the leading modes of the linear perturbation stability analysis. This may be due to the numerical dissipation introduced by the use of backwards difference operators Eq. (27). Second, transients die away very quickly, within about five rotations of the balloon. These results are not altogether unexpected since the single-loop balloons are predicted to be stable. The results for the other simulations were similar in character. Unfortunately, the difficulties of calculating the finite jump in tension just after the impulse was applied prevented an investigation of whether very large impulses would destabilize single-loop balloons.

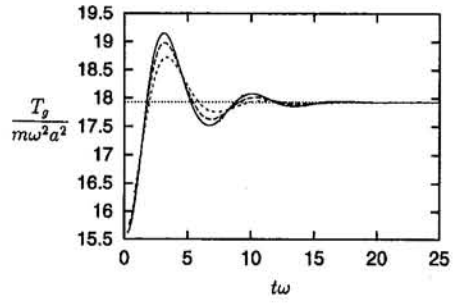


Fig. 6(*a*)

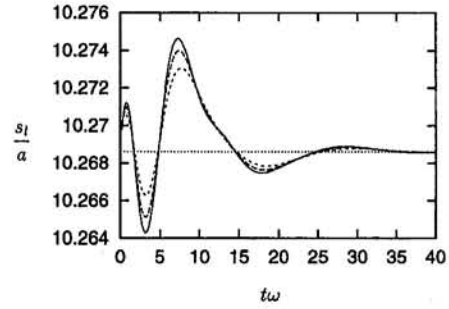


Fig. 6(*b*)

Fig. 6 (*a*) Guide-eye tension $T_g/m\omega^2a^2$ versus time $t\omega$ for $m_T/ma = 100$ ($b/a = 0.65$): $\omega\Delta t = 0.1$ (solid line), $\omega\Delta t = 0.2$ (long-dash line), $\omega\Delta t = 0.4$ (short-dash line); (*b*) balloon length s_l/t versus $t\omega$ for $m_T/ma = 100$ ($b/a = 0.65$)

5.2.2 Medium Traveler Mass: $m_T/ma = 40$. A set of simulations was performed for each of the three balloons corresponding to $b/a = 0.65$ shown in Fig. 5 and subjected to a small impulse of magnitude $A = 0.05$. (The lighter traveler mass created numerical difficulties that made it difficult to impose large values of A.)

A plot of the guide-eye tension versus the stable single-loop balloon is shown in Fig. 7, where the steady-state asymptote $T_{g_0}/m\omega^2a^2 = 14.06$ is shown by the horizontal short-dash line. The solid line corresponds to $A = 0.05$, while the long-dash line is for $A = -.05$. There are strong similarities with the results of the previous section for the $m_T/ma = 100$ balloon. The guide-eye tension exhibits transient oscillations which decay rapidly to the quasi-stationary values, although jump in tension in Fig. 7 is not as big as in Fig. 6(*a*) due to the smaller value of A. The balloon length as a function of time shows behavior

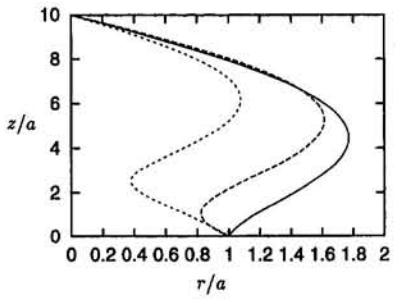


Fig. 5 Quasi-stationary balloons for $b/a = 0.65$ and $m_T/ma = 40$: single loop balloon (solid line), one-and-a-half-loop balloon (long-dash line), two-loop balloon (short-dash line)

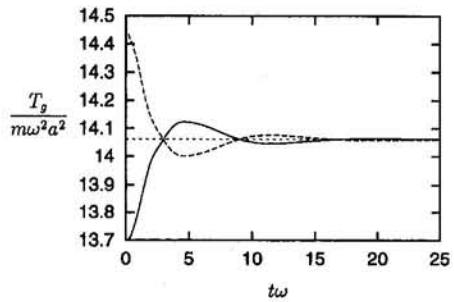


Fig. 7 Guide-eye tension $T_g/m\omega^2a^2$ versus time $t\omega$ for $m_T/ma = 40$ ($b/a = 0.65$, single-loop balloon)

Downloaded 04 May 2010 to 171.66.16.33. Redistribution subject to ASME license or copyright; see http://www.asme.org/terms/Terms_Use.cfm

similar to Fig. 6(b). Both guide-eye tension and balloon length transients have decayed away almost completely by $t\omega = 50$.

The one-and-a-half-loop balloon is predicted to be unstable due to a *real* positive eigenvalue controlling one of the linear perturbation modes. Guide-eye tension is plotted versus $t\omega$ in Fig. 8 for the values $A = -.05$, long-dashed line, and $A = 0.05$, solid line. The quasi-stationary tension for one-and-a-half-loop balloon, $T_{g_0}/m\omega^2a^2 = 10.537$ is indicated by short-dash line, while the value for the stable single-loop balloon is shown by the straight dotted line. The impulse $A = -.05$ is sufficient to knock the unstable one-and-a-half-loop balloon into the stable single-loop configuration. The curve for $A = 0.05$ terminates suddenly at a point where the tension in some portion of the balloon becomes negative and the calculation has been stopped. Physically, negative tension will cause balloon collapse and result in tangling with the bobbin, while mathematically, the leading terms of the governing PDE change from hyperbolic to elliptic, for which this solution scheme is numerically unstable. The transition to either the stable configuration or collapse occurs within about ten revolutions.

The curves of Fig. 8 do not show the oscillatory behavior found for the stable yarn loop studied in Fig. 7. This is consistent with the linear perturbation stability results which predicted a single unstable mode showing monotonic growth.

The guide-eye tension for the two-loop balloon, which lies on the region of the bifurcation diagram bounded by the two Hopf-like bifurcation points (Fig. 4), is plotted versus $t\omega$ in Fig. 9 for the two values $A = 0.05$, solid line, and $A = -.05$, long-dash line. The quasi-stationary value of $T_{g_0}/ma^2\omega^2 = 6.622$ is shown by the straight short-dash line. Guide-eye tension shows increasing oscillations that eventually result in collapse at $t\omega \geq 50$. Given the low level of tension in the two-loop balloon, it is not surprising that growing oscillations eventually produce a region of negative tension resulting in collapse. The time scale of the oscillations shown in Fig. 9 is on the same order as that associated with the unstable linear-perturbation mode. Based upon these and other results for two-loop balloons, it is difficult to determine whether the stable limit-cycle behavior exists for values of b/a between the Hopf-like bifurcation points.

6 Concluding Remarks

The linear perturbation stability analysis of quasi-stationary ring-spinning balloons predicts that single-loop balloons are stable while multiple-loop balloons are typically unstable. This study has further examined the issue of stability by integrating the time-dependent nonlinear PDEs for several quasi-stationary balloons subjected to a model velocity impulse. While it was possible to knock some unstable balloons into stable single-loop configurations, more often than not velocity impulses applied to multiple-loop balloons gave rise to eventual collapse when the tension at some point of the yarn loop became negative.

Technologically these results confirm that multiple-loop balloons are inherently unstable and should be avoided since they will almost certainly collapse. While the adequacy of the linear-perturbation method in describing all possible velocity impulses has not been resolved, the results of this study certainly confirm the validity of the perturbation analysis in assessing balloon stability.

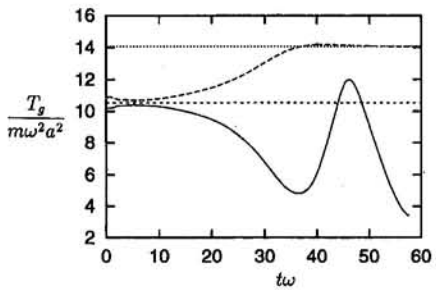


Fig. 8 Guide-eye tension $T_g/m\omega^2a^2$ versus time $t\omega$ for $m_T/ma = 40$ ($b/a = 0.65$, one-and-a-half-loop balloon)

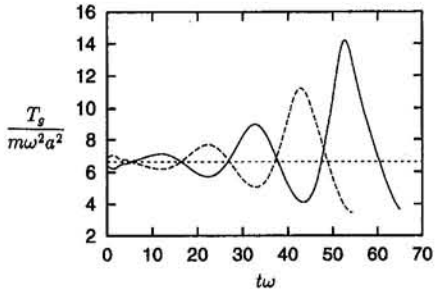


Fig. 9 Guide-eye tension $T_g/m\omega^2a^2$ versus time $t\omega$ for $m_T/ma = 40$ ($b/a = 0.65$, two-loop balloon)

Acknowledgments

DMS was supported by the Australian Research Council Post-Doctoral Fellowship Program. WBF was supported, in part, by the U.S. National Textile Center through a collaborative program with Professor S. K. Batra and Professor T. K. Ghosh at The College of Textiles, NCSU, Raleigh NC, and Professor B. Goswami at the School of Textiles, Clemson University, Clemson SC, and by an Australian Research Council grant. Discussions with Dr. C. Macaskill, Dr. A. M. Watts and Professor K. Burridge have been of help.

References

Ames, W. F., 1977, *Numerical Methods for Partial Differential Equations,* 2nd ed., Academic Press, New York.

Batra, S. K., Ghosh, T. K., and Zeidman, M. I., 1989a, "An Integrated Approach to Dynamic Analysis of the Ring Spinning Process, Part I: Without Air Drag and Coriolis Acceleration," *Textile Research Journal,* Vol. 59, pp. 309–317.

Batra, S. K., Ghosh, T. K., and Zeidman, M. I., 1989b, "An Integrated Approach to Dynamic Analysis of the Ring Spinning Process, Part II: Without Air Drag," *Textile Research Journal,* Vol. 59, pp. 416–424.

de Barr, A. E., and Catling, H., 1965, *The Principles and Theory of Ring Spinning,* Manual of cotton spinning, Vol. 5, F. Charnley and P. W. Harrison, eds.), Butterworths Press, Manchester, UK.

Fraser, W. B., 1993a, "On the Theory of Ring Spinning," *Philosophical Transactions of the Royal Society,* Vol. A342, pp. 439–468.

Fraser, W. B., 1993b, "The Dynamics of Ballooning Yarn in Ring Spinning and Two-for-one Twisting," *Proceedings of the IV-th Polish Conference on the Mechanics of Textile and Crane Machines,* Politechnika Lodzka Fila w Bielsko-Biala, pp. 61–78.

Fraser, W. B., Farnell, L. L., and Stump, D. M., 1994, "The Effects of Yarn Nonuniformity on the Stability of the Ring-Spinning Balloon," *Proceedings of the Royal Society,* in press.

Gray, B. F., and Roberts, M. J., 1988, "A Method for the Complete Qualitative Analysis of Two Coupled Ordinary Differential Equations Dependent on Three Parameters," *Proceedings of the Royal Society,* Vol. A416, pp. 361–389.

Klein, W., 1987, *A Practical Guide to Ring Spinning,* Manual of Textile Technology: Short-Staple Spinning Series, Vol. 4, ed. H. Sadler, ed., The Textile Institute, Manchester, U.K.

Lisini, G. G., Toni, P., Quilghini, D., and Campedelli, V. L. Di Gorgi, 1992, "A Comparison of Stationary and Non-Stationary Mathematical Models for the Ring-Spinning Process," *Journal of the Textile Institute,* Vol. 83, pp. 550–559.

Padfield, D. G., 1958, "The Motion and Tension in an Unwinding Balloon," *Proceedings of the Royal Society,* Vol. A245, pp. 382–407.

Press, W. H., Flannery, B. P., Teukolvsky, S. A., and Vetterling, W. T., 1986, *Numerical Recipes: The Art of Scientific Computing,* Cambridge University Press, Cambridge, U.K., pp. 588–600.

Stump, D. M., and Fraser, W. B., 1995, "Dynamic Bifurcations of the Ring-Spinning Balloons," *Mathematical Engineering for Industry,* Vol. 5, pp. 161–185.

Downloaded 04 May 2010 to 171.66.16.33. Redistribution subject to ASME license or copyright; see http://www.asme.org/terms/Terms_Use.cfm

Modeling of Interfacial Shear for Gas Liquid Flows in Annular Film Condensation

A. Narain
Department of Mechanical Engineering, and Engineering Mechanics, Michigan Technological University, Houghton, MI 49931-1295
Mem. ASME

Internal flow of pure vapor experiencing film condensation on the walls of a straight horizontal duct is studied. The commonly occurring annular *case of turbulent (or laminar) vapor flow in the core and laminar flow of the liquid condensate—with or without waves on the interface—is emphasized. We present a new methodology which models interfacial shear with the help of theory, computations, and reliable experimental data on heat transfer rates. The theory—at the point of onset of condensation—deals with issues of asymptotic form of interfacial shear, nonuniqueness of solutions, and selection of the physically admissible solution by a stability type criteria. Other details of the flow are predicted with the help of the proposed modeling approach. These predictions are shown to be in agreement with relevant experimental data. The trends for film thickness, heat transfer rates, and pressure drops are also made available in the form of power-law correlations.*

1 Introduction and Background

Typically both *shear* and *gravity* forces directly compete with each other to influence different regimes of condensing flows in horizontal or vertical pipes. To better understand flows driven by interfacial shear alone, and to model interfacial shear, we investigate film condensation flow between horizontal parallel plates (see Fig. 1).

We show that integral approaches must deal with issues of existence, uniqueness, stability, and the asymptotic form of interfacial shear at the point of onset of condensation. These issues are addressed here for the first time. As in the determination of friction factor in Moody chart (after Moody, 1944), the rest of the modeling is done with the help of first principles based theory, nondimensionalization, and reliable experimental data. This approach, again as in determination of wall shear through Moody chart, allows an estimate of interfacial shear without a detailed scientific understanding of the physical mechanisms and the flow fields near the interface.

The method and results given in this paper are of general value because they can also be adapted, if experimental data is available in a suitable form, for a study of annular film condensation flows in ducts of different cross-sections and orientation—orientation being irrelevant for microgravity environments.

There is a substantial body of scientific literature with regard to film condensation of vapors on surfaces. Here we briefly describe the background knowledge in the following categories (a)-(d):

(a) Studies of Relevant Film Condensation Problems. Classical results of Nusselt (1916) and Rohsenow (1956) dealt with film condensation of *stationary* vapor on vertical surfaces. Subsequently a significant amount of analytical and experimental studies dealt with external condensing flows (Sparrow and Gregg, 1959; Koh, 1962; Fujii and Uehara, 1972; etc.) and internal condensing flows (Carpenter and Colburn, 1951, etc). The flow between parallel plates is investigated here with the help of reliable experimental data of Lu (1992) and Lu and Suryanarayana (1992).

(b) First Principle and Model Equations. With regard to equations modeling film condensation, the knowledge base is rigorous and well established (see Delhaye, 1974; Narain and Kizilyalli, 1991; etc.). However, the simpler equations used here and in the literature remain valid approximate equations in the context of their respective problems.

(c) Relevant Interfacial Shear Models. An appropriate physical model for interfacial shear, in combination with the governing equations for the flow, can predict most of the details of *annular* condensing flows. For estimating interfacial shear on the condensate, some of the practices have been (i) to use friction factor models as if the gas was flowing over an impermeable wall (as in Soliman et al., 1986); (ii) to use Lockhart-Martinelli (1949) type correlations and to attempt to relate it to condensation (see Wang et al., 1990); (iii) to account for the significant effects of vapor-suction at the interface with the help of Shekriladze and Gomelauri (1966) model or film models proposed by Mickley (1954); (iv) to account for interfacial waves through Wallis-type correlation (see Carey, 1992) or Nikuradse-type equation in terms of an effective roughness (see Hewitt and Govan, 1990).

However, all of the above models, when used for prediction of a simple regime of annular flows considered here, yield results which are in poor quantitative agreement with reliable experimental measurements (e.g., see Fig. 4) on film thickness and heat transfer rates. The works of Blangetti (1979), Chen et al. (1987), Carey (1992), etc., also emphasize importance of interfacial shear models.

(d) Other Basic Issues. The following issues are relevant to understanding interfacial shear models:

(i) Flow regime maps of Bell et al. (1970), Palen et al. (1979), etc. for two phase duct flows are significant as various gas-liquid configurations are possible in the flow. Because vapor fraction is 100 percent at the inlet of the duct in Fig. 1—up to a certain inlet mass flux of dry vapor, temperature difference $\Delta\mathcal{T}$ between the vapor and the condensing surface, and sufficient lengths ($L \leq L_{crit}$) of the channel—stable *annular* film conden-

Contributed by the Applied Mechanics Division of THE AMERICAN SOCIETY OF MECHANICAL ENGINEERS for publication in the ASME JOURNAL OF APPLIED MECHANICS.

Discussion on this paper should be addressed to the Technical Editor, Professor Lewis T. Wheeler, Department of Mechanical Engineering, University of Houston, Houston, TX 77204-4792, and will be accepted until four months after final publication of the paper itself in the ASME JOURNAL OF APPLIED MECHANICS.

Manuscript received by the ASME Applied Mechanics Division, Aug. 4, 1994; final revision, June 23, 1995. Associate Technical Editor: S. A. Berger.

Copyright © 1996 by ASME

Downloaded 04 May 2010 to 171.66.16.33. Redistribution subject to ASME license or copyright; see http://www.asme.org/terms/Terms_Use.cfm

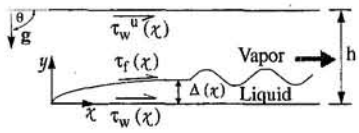


Fig. 1 The geometry of the flow is indicated above (θ = 90 deg). In the figure $\tau_w^u(x)$, $\tau_f(x)$, and $\tau_w(x)$, respectively denote shear stresses at the upper wall, the interface, and the bottom plate.

sation flows (with or without interfacial waves) are implied by the flow regime maps.

Large downstream distances ($L \geq L_{crit}$) are not considered here. However, it is well known that full condensation of vapor will occur for high heat removal flux; and for relatively low heat flux (associated with moderate $\Delta\mathcal{T}$ values considered here), two phase flow will continue with changing flow regimes until eventually a dry out occurs due to a substantial drop in pressure.

(ii) Annular condensing flows can have liquid film flows which are smooth *and* laminar, or wavy *and* laminar, or wavy *and* turbulent. For flows investigated in this paper, the condensate was always laminar. This is because the *condensate Reynolds number* (see Carey, 1992, p. 370) was mostly less than 1600 and also because a realistic estimate of critical Reynolds number is expected to be higher (e.g., see Mudawar and Houpt, 1993).

(iii) The interfacial shear for turbulent vapor is expected to be significantly affected by whether the interface is smooth or has an effective *oscillatory* roughness in the form of waves. When the waves pierce through the *laminar sublayer* of the vapor near the interface, they make the condensate experience additional pressure drag.

(iv) If noncondensible gaseous impurities are present, they tend to concentrate at the interface and set up diffusion processes and partial pressures which usually lead to significant reduction in heat transfer rates (Minkowycz and Sparrow, 1966, etc.). Here we focus exclusively on *pure* vapors.

(v) The current status (see Khoo et al., 1989) of a complete numerical solution of this type of nonlinear free boundary problem is inadequate because of problems with numerical convergence and handling of interface conditions. Also any meaningful use of popular turbulence models (k-ϵ, etc.) require (see Wilcox, 1993) an analogue of "law of the wall" velocity profile or "near wall" turbulence models—the development of neither of which is possible without development of reliable interfacial shear models which account for effects of *suction* and *oscillatory roughness elements* (the waves) at liquid vapor interface of condensing flows.

(vi) A significant amount of semi-empirical heat transfer correlations exist for condensing flows in pipes. Their relevance and role is described in Section 7.

2 Nondimensional Parameters and Model Equations for Flow Between Parallel Plates

After scaling approximations for the shear dominated pressure driven steady flow in Fig. 1, the general equations reduce to the commonly used forms given in this section.

We denote the liquid and vapor phases in the flow of Fig. 1 by a subscript I: $I = 1$ for liquid and $I = 2$ for vapor. The fluid properties (density ρ, viscosity μ, specific heat C_p, and thermal conductivity k) take their representative constant values for each phase ($I = 1$ or 2). Let $\mathcal{T}_I$ be the temperature fields, p_I be the pressure fields, $\mathcal{T}_s(p)$ be the saturation temperature of the vapor as a function of the pressure p, Δ be the film thickness, and $\mathbf{v}_I = u_I\mathbf{i} + v_I\mathbf{j}$ be the mean velocity fields (the distinction between mean and physical velocities vanish for smooth interface laminar flows). Let (x, y) be the length coordinates of a point with respect to the axes in Fig. 1. We nondimensionalize the variables as

$$\{x, y, \Delta, u_I\} \equiv \{hx, hy, h\delta, Uu_I\}$$

$$\{v_I, \mathcal{T}_I, p_I\} \equiv \{Uv_I, (\Delta\mathcal{T})T_I, p_o + \rho_l U^2\pi_I\}, \qquad (1)$$

where h is the gap between the plates, p_o is the inlet pressure, $\mathcal{T}_s(p_o)$ is the saturation temperature of the vapor at the inlet, $\mathcal{T}_w(<\mathcal{T}_s(p_o))$ is the average uniform temperature of the bottom plate, $\Delta\mathcal{T} \equiv (\mathcal{T}_s(p_o) - \mathcal{T}_w)$ is the controlling temperature difference between the vapor and the plate, and U is the *average* inlet vapor speed determined by the inlet mass flux.

The *scaled* differential forms of mass, momentum (x and y components), and energy equations for the interior of either of the phases, the interface conditions, the conditions at the upper ($y = 1$) and lower ($y = 0$) walls are well known (e.g., see, Narain, 1993). An inspection of these equations yield the fact that for thin films and fixed acceleration due to gravity, the flow is affected by the following minimal set of four independent nondimensional parameters:

$$\left\{\mathrm{Re}_{in}, \frac{\mathrm{Ja}}{\mathrm{Pr}_1}, \frac{\rho_2}{\rho_1}, \frac{\mu_2}{\mu_1}\right\}, \qquad (2)$$

where $\mathrm{Re}_{in} \equiv \rho_2 Uh/\mu_2$, $\mathrm{Pr}_1 \equiv \mu_1 C_{p1}/k_1$, $\mathrm{Ja} \equiv C_{p1}\Delta\mathcal{T}/\mathcal{H}_{fg}^0$, and $\mathcal{H}_{fg}^0 \equiv \mathcal{H}_g - \mathcal{H}_f$ is the latent heat of vaporization at the inlet temperature $\mathcal{T}_s(p_0)$. Here Re_{in} and $\mathrm{Ja}/\mathrm{Pr}_1$ are *control* parameters representing inlet speed U and temperature difference $\Delta\mathcal{T}$. The density ratio ρ_2/ρ_1 and viscosity ratio μ_2/μ_1 are *passive* fluid parameters. However, when the interface is *wavy*, the equations governing the evolution of superposed disturbances imply additional dependence on *gravity parameter* $U/\sqrt{gh}$ and *surface tension parameter* $\sigma/(\rho_1 U^2 h)$. For the flow under consideration, the gap width h is large compared to the film thickness, g is constant, surface tension σ is order 0.01 N/m; therefore wave effects, over flow speeds of interest, is entirely accounted for by the inlet Reynolds number Re_{in}.

For laminar or turbulent flows of vapor, the one-dimensional approach only needs the values of the vapor shear $(\tau_2)_{xy}$ at the interface ($y = \delta(x)$) and at the upper wall ($y = 1$). For these stresses, shown in Fig. 1, we define the friction factors f and f_u through the relations

$$\tau_f(x) \equiv (\tau_2)_{xy}|_{y=\delta(x)} \equiv \tfrac{1}{2}\rho_2(Uu_{av}(x))^2 f,$$

$$\tau_w^u(x) \equiv |(\tau_2)_{xy}|_{y=1}| \equiv \tfrac{1}{2}\rho_2(Uu_{av}(x))^2 f_u, \qquad (3)$$

where the nondimensional average speed $u_{av}(x)$ and the inlet speed U are given by

$$u_{av}(x) \equiv \frac{1}{1-\delta(x)}\int_{\delta(x)}^{1} u_2(x, y)dy$$

$$U \equiv \frac{1}{h}\int_0^h u_2(0, y)dy. \qquad (4)$$

Further Approximations for Thin Film Flows. The lengths of duct, inlet Reynolds numbers, and temperature differences considered here correspond to thin films of the liquid condensate which move sluggishly. Simple scaling of the governing equations suggest that inertia of the condensate can be ignored provided $\mathrm{Re}_1 u_f \delta^2 \ll 1$, where u_f is the speed $u_1(x, \delta(x)) = u_2(x, \delta(x))$ at the interface. Similarly convection in the film can be ignored compared to conduction provided $\mathrm{Re}_1 \mathrm{Pr}_1 u_f \delta^2 \ll 1$. However, the above estimates (see Koh, 1962) for ignoring inertia and convection are *conservative* and this approximation is commonly used (Koh, 1962; Chen and Kocamustafaogullari, 1987; etc.) for flow of non-metallic vapors over a larger range of flow parameters. Under this approximation, then, we find (see Narain, 1993) the well-known result that the liquid condensate velocity profile is given by

Downloaded 04 May 2010 to 171.66.16.33. Redistribution subject to ASME license or copyright; see http://www.asme.org/terms/Terms_Use.cfm

$u_1(x, y)$

$$= \frac{\mu_2}{\mu_1} \mathrm{Re}_{in} \left[\left(\frac{-d\pi}{dx} \right) y \left(\delta(x) - \frac{y}{2} \right) + \frac{y}{2} u_{av}^2(x) f \right], \quad (5)$$

where $\pi(x) \cong \pi_2(x, y)$ is the average uniform nondimensional vapor pressure across $\delta(x) \le y \le 1$. Similarly the liquid condensate temperature profile is given by the well-known expression

$$T_1(x, y) = (T_s(\pi(x)) - T_w) \left(\frac{y}{\delta(x)} \right) + T_w, \quad (6)$$

where $T_s (\equiv \mathcal{T}_s / \Delta\mathcal{T})$ and $T_w (\equiv \mathcal{T}_w / \Delta\mathcal{T})$ are, respectively, nondimensional saturation temperature and wall temperature.

The Non-Dimensional Governing Equations For The One-Dimensional Approach.

- The integrated form of vapor mass balance simply states that the sum of vapor mass flux and liquid mass flux at any x is a constant for steady flows. This is given as

$$\frac{\rho_2}{\rho_1} \int_{\delta(x)}^{1} u_2(x, y) dy + \int_0^{\delta(x)} u_1(x, y) dy = \frac{\rho_2}{\rho_1}. \quad (7)$$

- The heat conducted from the interface to the bottom wall is the sum of the latent heat released at the interface and the heat conducted by the vapor to the film. It is well known that even for superheated vapors (e.g., $0 \le \Delta\mathcal{T}_{sup} \le 15°C$), if the operating pressures are well below *critical* pressure, the value of latent heat released at the interface is significantly larger than any heat conducted from the vapor to the film. Under this approximation, interface energy equation, in conjunction with mass balance, becomes

$$\dot{m}(x) = \frac{\rho_2}{\rho_1} \frac{d}{dx} \left(\int_{\delta}^{1} - u_2 dy \right)$$

$$\cong \frac{\mathrm{Ja}}{\mathrm{Re}_1 \, \mathrm{Pr}_1 \phi_{fg}(x)} \left[\frac{\partial T_1}{\partial y} (x, \delta(x)) \right], \quad (8)$$

where ϕ_{fg}, close to unity (see Narain, 1993), is the ratio of the latent heat released at local interfacial pressure to the latent heat released at the inlet pressure.

Because of validity of (8), negligible contribution to heat transfer comes from vapor superheat, and hence one can ignore the vapor ($I = 2$) energy equation under the assumption that the vapor temperature is nearly constant.

- The integrated form of vapor momentum balance states that, at any location x, the algebraic sum of pressure force, frictional force, and "kick-back" force (associated with interface mass transfer) per unit length equals the cross-sectional rate of change of momentum-flux. This is given as

$$-\frac{d\pi}{dx}(1 - \delta(x)) - \frac{1}{2} u_{av}^2(x)(f + f_u) - \frac{\rho_1}{\rho_2} \dot{m}(x) u_f(x)$$

$$= \frac{d}{dx} \left[\int_{\delta(x)}^{1} u_2^2(x, y) dy \right]. \quad (9)$$

3 The Proposed Solution Scheme and its Differences From the Usual Approximate Techniques

We develop here a reliable solution scheme for local variations in the lower dimensional unknowns (film thickness $\delta(x)$, heat transfer rates, etc.) which will allow for different admissible models for interfacial shear. If we satisfy the total mass balance (7), the interface energy Eq. (8) for liquid velocity and temperature profiles respectively given by (5) and (6), and the vapor momentum balance (9), then we would have satisfied *all* the *differential* downstream evolution equations. This is because—loosely speaking—the underlying partial differential equations are parabolic in the downstream direction (significant derivatives are first order) and elliptic in the cross-stream direction (significant derivatives are second order).

There is a *difference* between the rationale of the proposed approach and many integral approaches (Narain and Kizilyalli, 1991; Soliman et al., 1986, etc.) which do not give accurate results. Our approach consists of not *assuming* a friction factor model, but *finding* a model which predicts the flow in accord with reliable experimental data.

The proposed method consists of the following three steps:

(i) Make a choice for vapor velocity profile. For example, consider uniform vapor velocity profile

$$u_2(x, y) = u_{av}(x) \quad (10)$$

for $\delta(x) \le y \le 1$. Alternatively consider a more realistic $u_2(x, y)$ for fully developed turbulent vapor flow at the inlet. This leads to $u_2(x, y)$ *close* to a fully developed turbulent vapor velocity profile for a single fluid flow in a channel (see experimentally measured velocity profile of Bouyer and Panday (1993) for condensing vapor in a vertical channel). Therefore we make the choice

$$u_2(x, y) = U_0(x)[1 - a\eta^2 - (1 - a)\eta^{2m}] + u_f(x) \left[\frac{1 - y}{1 - \delta(x)} \right], \quad (11)$$

where $\eta \equiv 2(y - \delta(x))/(1 - \delta(x)) - 1$, $a = 0.354$, $2m = 32$, interface speed $u_f(x)$ is obtained by setting $y = \delta(x)$ in (5), and $U_0(x)$ is to be determined. The first term on the right side of (11) models fully developed turbulent vapor velocity profile for a single fluid flowing in a channel (see White, 1974, p. 460) and has zero speed at the interface. The second term on the right side of (11) perturbs the first term *slightly* so as to make the vapor speed at the interface equal to its actual value $u_f(x)$. Computations for $u_2(x, y)$ given by (11) lead to an expected shape (see Fig. 2 in Narain, 1994) of the vapor velocity profile.

(ii) Solve the problem (Eqs. (7)–(9)) for either of the choices (10) or (11) and show, as in Fig. 2, that the solution for $\delta(x)$ and $u_{av}(x)$ is nearly independent of the choice of vapor velocity profile for any *given* friction factor model. This establishes that, in this one-dimensional approach, the two dimensionality of the vapor velocity profile does not significantly affect these two lower dimensional unknowns.

(iii) For any one choice of vapor velocity profile, find a friction factor model for f which yields mean film thickness in agreement (see Fig. 4) with reliable experimental data.

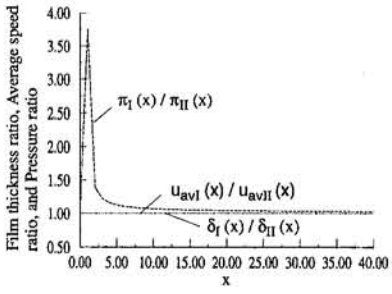


Fig. 2 The above *typical* values ($x > 3$) of computed ratios are for flow of R-113 at conditions specified by case #7 of Table 2. The subscripts *I* and *II* on flow variables respectively correspond to a uniform vapor velocity profile given by Eq. (10) and a more realistic vapor velocity profile given by Eq. (11). The friction f is given by the proposed model. The curves for $\delta_I(x)/\delta_{II}(x)$ and $u_{avI}(x)/u_{avII}(x)$ *coincide* as both the ratios remain close to unity.

Downloaded 04 May 2010 to 171.66.16.33. Redistribution subject to ASME license or copyright; see http://www.asme.org/terms/Terms_Use.cfm

Having stated the steps, for brevity, we *only* outline here the methodology for the choice in (10). The formulation for the profile in (11) can be similarly obtained.

Substituting (5) and (6) in (7)–(9), we can, respectively, rewrite these three equations, after some manipulations, as

$$\mathbf{A}(\mathbf{y})\frac{d\mathbf{y}}{dx} = \mathbf{b}(\mathbf{y}, f, f_u), \tag{12}$$

where

$$\mathbf{A} \equiv \begin{bmatrix} 1 & 0 & 0 \\ 0 & A_{22} & A_{23} \\ 0 & A_{32} & A_{33} \end{bmatrix}, \quad \mathbf{b} \equiv \begin{bmatrix} b_1 \\ b_2 \\ b_3 \end{bmatrix},$$

$\mathbf{y} \equiv [\pi(x), u_{av}(x), \delta(x)]^T$ and the scalar functions A_{22}, A_{23}, A_{32}, A_{33}, b_1, b_2, and b_3 are defined in Eqs. (A.1)–(A.8) of the Appendix. The function f for interfacial friction is to be *determined.*

The upper wall, which is dry, has a friction factor f_u and can be *estimated* because it is a nearly parallel single phase flow at the upper wall. The estimate depends on whether the flow is fully developed or nearly uniform at the inlet. For fully developed turbulent flow at the inlet, we can estimate (see p. 487 in White, 1985) f_u as

$$f_u \cong 0.0713(\mathrm{Re}_2 u_{av}(x))^{-0.25} \equiv f_0. \tag{13}$$

For uniform flow at the inlet, boundary layer development takes place over $0 \le x \le 40$, and we estimate (see Schlichting, 1968) f_u as

$$f_u \cong 0.6640(\mathrm{Re}_2 u_{av}(x)x)^{-0.5} \quad \text{for} \quad \mathrm{Re}_2 u_{av}(x)x \le 5 \times 10^5,$$

$$f_u \cong 0.0592(\mathrm{Re}_2 u_{av}(x)x)^{-0.2} \quad \text{for} \quad \mathrm{Re}_2 u_{av}(x)x > 5 \times 10^5. \tag{14}$$

A typical solution of (12) in Fig. 3 confirms that for a realistic (proposed model) f, the estimate of f_u, whether by (13) or (14), has an *insignificant* higher order effect on the significant flow variables of film thickness and average vapor speeds. Hence an *accurate* estimate of f_u is a *nonissue.* In what follows, unless otherwise stated, f_u is given by (13).

4 The Asymptotic Form of the Friction Factor at Onset of Condensation and Issues of Existence, Uniqueness, and Stability

First we rewrite (12) and the inlet conditions in the standard form

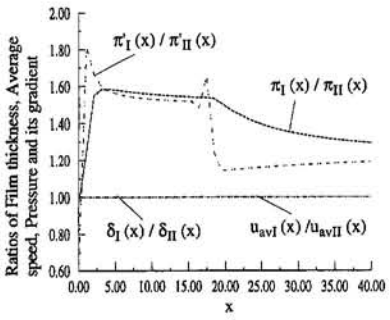


Fig. 3 The above *typical* values ($x > 3$) of computed ratios are for flow of R-113 at conditions specified by case #7 of Table 2. The subscripts *I* and *II* on flow variables respectively correspond to upper wall friction factor f_u given by Eq. (13) and upper wall friction factor f_u given by Eq. (14). The friction f is given by the proposed model. The curves for $\delta_I(x)/\delta_{II}(x)$ and $u_{avI}(x)/u_{avII}(x)$ *coincide* as both the ratios remain close to unity.

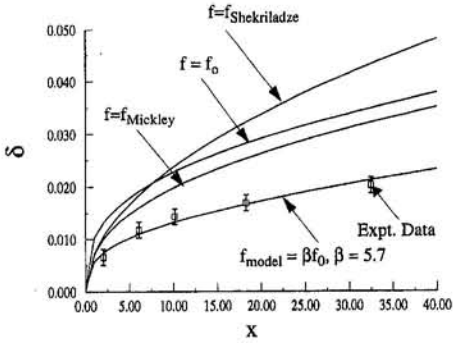


Fig. 4 The figure compares the film thickness variations predicted by some of the commonly used models and the proposed model (see Section 8) to experimental measurements (Lu, 1992). All the common models shown above are defined in Appendix A of Narain (1993). The comparisons above are for smooth interface flow of R-113 as specified by case #9 of Table 2.

$$\frac{d\mathbf{y}}{dx} = \mathbf{g}(\mathbf{y}, f),$$

$$f = f\left(x, \mathrm{Re}_{\mathrm{in}}, \frac{\mathrm{Ja}}{\mathrm{Pr}_1}, \frac{\rho_2}{\rho_1}, \frac{\mu_2}{\mu_1}\right),$$

$$\mathbf{y}(0) = [0, 1, 0]^T, \tag{15}$$

where $\mathbf{y} \equiv [\pi(x), u_{av}(x), \delta(x)]^T$, $\mathbf{g} \equiv [g_1, g_2, g_3]^T$, and components g_1, g_2, and g_3 of $\mathbf{g}$ are explicitly defined in equations (A9)–(A11) of the Appendix.

The requirement $\delta(0) = 0$ makes the function $\mathbf{g}$ in (15) singular at $x \sim 0$. Trial and error method of guessing an initial condition at small x (in the vicinity of $\mathbf{y}(0)$) and forward marching to obtain a numerical solution was found to have an extremely low success rate for any chosen model of f. The issue now is our ability to numerically solve (15) for *any* friction factor f. This is a significant challenge, not addressed in the literature, because (15) is not a *well-posed initial value problem.* This may lead to questions of existence and the problem may have multiple solutions (e.g., see Arnold, 1973, Fig. 69).

An inspection of the function $\mathbf{g}$, in combination with Taylor expansion by computer algebra, proves the following result:

Theorem: There exists a solution of (15) satisfying the initial condition if and only if the friction factor is of the form

$$f = 8\left(\frac{\mathrm{Ja}}{\mathrm{Pr}_1}\right)\left(\frac{\rho_2}{\rho_1}\right)\left(\frac{\mu_2}{\mu_1}\right)^{-2}(\mathrm{Re}_{\mathrm{in}})^{-2}\frac{1}{c_1^3}\frac{1}{x^{1/2}} + O(1)$$

$$= \left(8\mathrm{Re}_{\mathrm{in}}^{-1}\frac{\mu_1}{\mu_2}\right)\frac{1}{c_1^2}\dot{m}(x) + O(1), \tag{16}$$

where the constant c_1 is obtained as a convergent root of a sequence of well-defined non-linear functions $\Psi^{(N)}$ satisfying the equation

$$\Psi^{(N)}\left(c_1, \mathrm{Re}_{\mathrm{in}}, \frac{\mathrm{Ja}}{\mathrm{Pr}_1}, \frac{\rho_2}{\rho_1}, \frac{\mu_2}{\mu_1}\right) = 0, \tag{17}$$

where $N = 1, 2, 3, \ldots$ is a positive integer.

For a parameter range specified in (27) below, the numerically obtained convergent root of the sequence of functions in (17)—which leads to a *stable* solution—is put in the following approximate power-law form:

$$c_1 = 1.1884\left(\frac{\rho_2}{\rho_1}\right)^{0.1102}\left(\frac{\mu_2}{\mu_1}\right)^{-0.3689}\left(\frac{\mathrm{Ja}}{\mathrm{Pr}_1}\right)^{0.2509}\mathrm{Re}_{\mathrm{in}}^{-0.4005}. \tag{18}$$

Furthermore, for f as in (16), the solution of (15), over a small neighborhood $0 \le x \le \hat{\epsilon}$, is of the form

Downloaded 04 May 2010 to 171.66.16.33. Redistribution subject to ASME license or copyright; see http://www.asme.org/terms/Terms_Use.cfm

$$\mathbf{y}(x) = \mathbf{y}_0 + \mathbf{y}_1 x^{1/2} + \mathbf{y}_2 x + \mathbf{y}_3 x^{3/2} + o(x^{3/2}), \quad (19)$$

where $\mathbf{y}_0 \equiv \mathbf{y}(0) = [0, 1, 0]^T$, $\mathbf{y}_1 \equiv [k_1, -c_2, c_1]^T$, $\mathbf{y}_2$, and $\mathbf{y}_3$ are constant *vectors*.

The result in (16) is easily interpreted. At the onset of condensation ($x \sim 0$), the vapor suction rate $\dot{m}$ is very high, so the suction effect dominates and the friction factor is proportional to condensation rate. This proportionality is also seen in the models proposed by Shekriladze and Gomelauri (1966), Linehan et al. (1969), and Jensen and Yuen (1982). However, their proportionality constant, unlike the proportionality constant in (16), is based on a classical solution (Schlichting, 1968, p. 368) of the Navier-Stokes equation which does not allow integration—at onset of condensation—of the equations that govern condensing flows. At very small x, the first term on the right side of (16) dominates the $O(1)$ term. Therefore, for ease in preliminary modeling, the friction factor f in (16) is equivalently written as

$$f = \begin{cases} f_{\text{asy}} & \text{for} \quad x \le \epsilon \\ f_{\text{model}}(x, \text{Re}_{\text{in}}, \text{Ja}/\text{Pr}_1, \rho_2/\rho_1, \mu_2/\mu_1) & \text{for} \quad x \ge \epsilon, \end{cases} \quad (20)$$

where f_{asy} is given by the term proportional to $\dot{m}(x)$ in (16) and the value of f_{model} equals the value of f_{asy} at an $x = \epsilon(\text{Re}_{\text{in}}, \text{Ja}/\text{Pr}_1, \rho_2/\rho_1, \mu_2/\mu_1)$. Since f_{asy} drops rapidly from $+\infty$ to finite positive values (see Fig. 5), many of the commonly used models can be tested as f_{model} in (20) provided an appropriate choice of ϵ is made. However, the values of f near $x = \epsilon$, as circled in Fig. 5, is uncertain due to the matching there. The accuracy of this matching and the value of ϵ is not important because the solution of (15) at large $x (x \ge 0.5)$ remain almost unaltered because the equations *attract* initial conditions from a *neighborhood* of $\mathbf{y}(\epsilon)$ (but not from *any neighborhood* of $\mathbf{y}(0)$).

After an $x \sim 0$ solution described in (19) is obtained, a *numerical* solution of (15) for all admissible f over $x \ge \epsilon$ is readily implemented because the problem is well posed.

5 Proof of the Theorem in Section 4

The details of this section, though important, may be skipped in the first reading of this paper.

The vector equation in (15) is equivalent to the vector Eq. (12). The second row of the vector equation in (12), as $x \to 0$, implies

$$\lim_{x \to 0} \left[-(1 - \delta(x))\delta(x) \frac{du_{av}}{dx} + u_{av}(x)\delta(x) \frac{d\delta}{dx} \right] \equiv D_0, \quad (21)$$

where $D_0 \equiv (\rho_1/\rho_2)(\text{Ja}/(\text{Re}_1 \text{Pr}_1))$ is a nonzero constant. We assume[1] that the functions behave such that the limit of the sum on the left of (21) is equal to the sum of their limits. This means that the limit of each of the terms on the left of (21) exists because of the existence of

$$\lim_{x \to 0} \left(\delta \frac{d\delta}{dx} \right) \equiv \frac{c_1^2}{2} \quad \text{and} \quad \lim_{x \to 0} \left(\delta \frac{du_{av}}{dx} \right) \equiv -\frac{c_1 c_2}{2}. \quad (22)$$

Under the initial conditions specified in (15), (22) implies

$$\delta(x) = c_1 x^{1/2} + o(x^{1/2})$$

$$u_{av}(x) = 1 - c_2 x^{1/2} + o(x^{1/2}). \quad (23)$$

Using computer algebra, we now eliminate f from the first and third equations in (12) and solve the resulting equation for $d\pi/dx$. Substituting for δ and u_{av} from (23) and f_u from (13), an expansion of $d\pi/dx$ near $x = 0$ gives

$$\frac{d\pi}{dx} = \frac{k_1}{2} x^{-1/2} + O(1), \quad (24)$$

where k_1 in terms of c_1 and c_2 is given by Eq. (A12) of the Appendix. Because of $\pi(0) = 0$, (24) implies $\pi(x) \approx k_1 x^{1/2}$ for $x \sim 0$. Assuming sufficient differentiability with respect to $x^{1/2}$, (23) and (24) imply that the solution of (15) must be of the form given by (19).

Substitution of (19) in the first row of Eq. (12) implies that this equation is satisfied only if

$$f = \frac{4}{\text{Re}_1} \left(\frac{c_1 + c_2}{c_1^2} \right) \frac{1}{x^{1/2}} + O(1), \quad (25)$$

where the $O(1)$ term above is representable as $O(1) \equiv f_{00} + f_{01} x^{1/2} + \ldots$.

To find $\mathbf{y}(x)$ at $x \sim 0$, we substitute the right side of (19) for $\mathbf{y}$ on the left and right sides of the vector equation in (15). Then the leading term of (25) (i.e., choosing $f_{00} = f_{01} = \ldots = 0$ to make the $O(1)$ term zero) is substituted for f on the right side of the vector equation in (15). This gives

$$\tfrac{1}{2} \mathbf{y}_1 x^{-1/2} + \mathbf{y}_2 + \tfrac{3}{2} \mathbf{y}_3 x^{1/2} + \ldots = \mathbf{b}_1 x^{-1/2} + \mathbf{b}_2 + \mathbf{b}_3 x^{1/2} + \ldots, \quad (26)$$

where the constant vectors $\mathbf{b}_1$, $\mathbf{b}_2$, $\mathbf{b}_3$, etc., are found by expanding $\mathbf{g}$ with the help of computer algebra. Matching coefficients of similar powers of x in (26), we can—by careful use of somewhat lengthy computer algebra—solve the resulting equations which, with the exception of c_1, k_1 (Eq. (A12) of the Appendix) and c_2 (Eq. (A13) of the Appendix) equations, are *linear* in the scalar constants of $\mathbf{y}_2$, $\mathbf{y}_3$, etc. This allows the scalar constants (except c_1) appearing in the vectors $\mathbf{y}_1$, $\mathbf{y}_2$, $\mathbf{y}_3$, etc., to be given in terms of the constant c_1 while the constant c_1 itself is found to satisfy a nonlinear equation of the type given by (17). In (17), N is the number of terms matched. An example of computer generated $\Psi^{(3)}$ is given in Narain (1993). It can be established that regardless of the number of terms matched in (26) and regardless of the size (numbers f_{00}, f_{01}, etc.) of the $O(1)$ term in (25), c_2 and k_1 are determined by Eqs. (A12) and (A13) of the Appendix.

Existence. Substitution of (A13) in (25) gives the existence criterion (16) for solvability of (15).

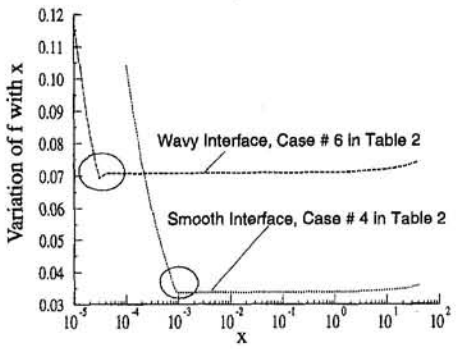


Fig. 5 The variations of interfacial friction factor f is shown for two *typical* flow situations specified on the curves

[1] Though it is not attempted here, mathematical solutions (without the regularities of (19)) for which none of the limits in (22) exist but the limit in (21) exists can be discarded on the basis of acceptability and regularity criteria given in this and the following section.

Downloaded 04 May 2010 to 171.66.16.33. Redistribution subject to ASME license or copyright; see http://www.asme.org/terms/Terms_Use.cfm

Nonuniqueness. As shown in Table 1, roots of $\Psi^{(N)}$—obtained by bisection method—give several values of c_1. As an example, for four terms on either side of (26), there are four verifiable accurate solutions of (16). The accuracy of the roots are good because, at small x, the solution given by (19) above does indeed satisfy the original (without expansions and truncations) equations in (15). Despite this non-uniqueness there is only one root which is robust (nearly independent of N) *and* stable.

Stability. Of the several good values of c_1, we expect only one of them to be physically realizable in the sense of corresponding solutions at $x \sim 0$ being stable to small disturbances. This stability, in the present context, is inferred from the criteria of a good root. Since the numbers c_2 and k_1 are completely determined (through Eqs. (A13) and (A12) of the Appendix) by c_1; a stable root in Table 1 is one for which *all* the values in the number triplet $\{c_1, c_2, k_1\}$ are nearly independent of the number of terms matched in (26). Only the bold roots (marked stable) in columns 2, 3, and 4 of Table 1 meet this stability type criteria.

The approximate power law curve fit given by (18) results from correlating (within ±7 percent) the stable root c_1 as parameters in (2) are varied within the range in (27). A different set of values of c_1 are similarly obtained if, instead of (13), f_u is given by (14). However, since f_{model} would typically remain the same, the solution at *large* x is not sensitive to the choice of f_u.

The proof of the theorem in the other direction simply consists of substituting (16) and (19) (with numerically obtained values of $\mathbf{y}_1, \mathbf{y}_2, \mathbf{y}_3$, etc.) into Eq. (15) and numerically verifying that this equation and its expanded form, Eq. (26), are indeed satisfied at $x \sim 0$.

6 Generality of the Proposed Asymptotic Model

The question remains as to whether the asymptotic form of f obtained in (16) has a more general applicability or is it merely true for this set of equations and this special geometry.

We find that for annular flow in a pipe (vertical configuration on earth or any configuration in zero gravity), the form of asymptotic friction in (16) remains the same. However, the characteristic length h appearing in the definition of Re_{in} following Eq. (2) has to be replaced by the pipe diameter D. The procedure for finding and correlating a stable root c_1 is similar to that given in Section 5 and will be given in a forthcoming paper.

7 Role and Availability of Reliable Experimental Data

In this and the next section, we outline use of experimental data for development of f_{model} in (20). No attempt is made here to come up with correlations covering the entire annular flow regime and most of the common nonmetallic vapors. On availability of more comprehensive and accurate experimental data, use of the proposed approach can lead to better and more comprehensive proposals of f_{model}.

Table 1 Typical c_1 satisfying $\Psi^{(N)} = 0$

Typical Flow situation	c_1 for $\psi^{(1)} = 0$	c_1 for $\psi^{(2)} = 0$	c_1 for $\psi^{(3)} = 0$	c_1 for $\psi^{(4)} = 0$
Case #4 of Table-2	0.01665[a]	0.00539[b]	0.004606[b]	0.004022[b]
Re_{in}=18089.59 Ja/Pr_1=.02529 ρ_2/ρ_1=.00491 μ_2/μ_1=.01747		**0.02283[b] (stable)**	0.011465[b]	0.005542[b]
			0.022748[b] (stable)	0.016959[b]
				0.022729[b] (stable)

a. root with unacceptable predictions
b. root with acceptable predictions

We use the data of Lu (1992). His experiments involve condensation on the bottom plate of a horizontal rectangular duct of length $a = 0.899$ m, height $h = 0.025$ m, and width $w = 0.04$ m. Though the ratio w/h is only 1.6, it is reasonable to use a one dimensional theory because the lower dimensional unknowns $\mathbf{y}(x)$ in Eq. (15) are not significantly affected by the two or three-dimensional nature of the vapor velocity profile. Also, in the experiments, the mean condensate thickness is observed to be essentially one dimensional ($\delta = \delta(x)$).

In the scientific literature, there is a significant amount of data available for horizontal and vertical pipes and some are also available for vertical channels. However, these flows are both *shear controlled* and *gravity controlled* and the correlations do not generally apply to the purely shear controlled flow under investigation. Despite this, in the shear dominant higher Reynolds number flow regimes, it is expected that average heat transfer coefficients are not likely to vary much with the geometry of the duct. Because of this, the data of Lu (1992) used here is in reasonable (given the experimental uncertainties) agreement (within ±25 percent) with correlations of Soliman et al. (1986) and Shah (1979). This agreement along with data of Traviss et al. (1973) are discussed in Lu (1992).

Furthermore, the method of modeling in this paper requires that experimental data acquisition cover the parameter set in (2) by varying only one parameter and keeping the remaining parameters fixed. To our knowledge, the data of Lu and Suryanarayana (1992) is the only one available in this form and is reliable because their estimates on heat transfer rates have been consistently obtained by two to three different and independent measurement approaches.

We consider approximately 150 experimental runs of Lu (1992) for flow of R-113 (Freon family) and FC-72 (Fluorinert Carbon) vapor. The available data limits us to consider x and the parameters in Eq. (2) in the restricted range

$$0 \le x \le 40, \quad 0.004 \le \rho_2/\rho_1 \le 0.009,$$

$$0.016 \le \mu_2/\mu_1 \le 0.026, \quad 0.009 \le \text{Ja}/\text{Pr}_1 \le 0.045,$$

$$9{,}500 \le \text{Re}_{\text{in}} \le 90{,}000. \tag{27}$$

In addition to heat transfer rates, Lu (1992) also provides an estimate on an inlet Reynolds number Re_L up to which ($\text{Re}_{\text{in}} \le \text{Re}_L(\text{Ja}/\text{Pr}_1, \rho_2/\rho_1, \mu_2/\mu_1, a/h)$) the interface is smooth and an estimate on inlet Reynolds number Re_U above which ($\text{Re}_{\text{in}} \ge \text{Re}_U(\text{Ja}/\text{Pr}_1, \rho_2/\rho_1, \mu_2/\mu_1, a/h)$) the interface is fully rough with steady three-dimensional wave patterns over the entire interface. Experimental data (see Tables 6.3 and 6.4 of Lu, 1992) in the parameter range (27) above provide the following estimate on Re_L and Re_U:

$$\text{Re}_L \cong a_1(\rho_2/\rho_1, \mu_2/\mu_1)\left(\frac{\text{Ja}}{\text{Pr}_1}\right)^{-0.2288},$$

$$\text{Re}_U \cong \hat{a}_1(\rho_2/\rho_1, \mu_2/\mu_1)\left(\frac{\text{Ja}}{\text{Pr}_1}\right)^{-0.2657}, \tag{28}$$

where a_1 and $\hat{a}_1$ are given in Table 3.

There is currently insufficient data for a *reliable* correlation with respect to density and viscosity ratios. However, if $(\mu_2/\mu_1)_{av}$ is considered approximately equal for both R-113 and FC-72, then (28), in the *limited* parameter range of (27), can be *tentatively* correlated as

Downloaded 04 May 2010 to 171.66.16.33. Redistribution subject to ASME license or copyright; see http://www.asme.org/terms/Terms_Use.cfm

$$a_1(\rho_2/\rho_1, \mu_2/\mu_1) \cong a_{10}(\mu_2/\mu_1)(\rho_2/\rho_1)^{0.449},$$

$$\hat{a}_1(\rho_2/\rho_1, \mu_2/\mu_1) \cong \hat{a}_{10}(\mu_2/\mu_1)(\rho_2/\rho_1)^{0.824}, \quad (29)$$

where a_{10} and $\hat{a}_{10}$ are given in Table 3.

8 The Modeling Principle and the Proposed Model for Friction Factor

Before proposing a new model for f, we tested, for a typical flow situation, some of the common models for f_{model} in (20). The resulting prediction of film thickness arising from a numerical solution of Eq. (15) is shown in Fig. 4. The common models did *poorly*. However, $f_{\text{model}} = \beta f_0$, $\beta \cong 5.7$, as shown in Fig. 4, did very well for the flow situation specified by case #9 in Table 2.

In fact, our modeling principle is that a suitable number β and function $f_0(x)$ in

$$f_{\text{model}}(x) = \beta f_0(x), \quad (30)$$

be chosen such that a solution of (15) would lead to predictions of mean film thickness—and therefore predictions of most one-dimensional flow variables of interest—in good agreement with their experimentally measured values. For the parameter range in (27), $f_0(x)$ in (30) was chosen to be the same as in (15). This is because this choice predicts the *qualitative* shape (see Fig. 4) of the condensate thickness to be in general agreement with the experimental thickness profiles. To achieve correct *quantitative* prediction, the number β in (30) was varied for a given flow situation until theoretical predictions of mean film thickness were also in quantitative agreement with experiments. For approximate models given in this paper, the above criteria of selecting β was relaxed to the criteria that theoretical predictions should agree with experimental film thickness measurements (when available) *or* experimental values of overall heat transfer rates. The above approach of finding $f_{\text{model}}(x)$ is similar, in principle, to the determination of friction factor f in Moody chart (after Moody, 1944) which requires that f be such that first-principle prediction of the pressure drops be in agreement with corresponding experimental measurements of pressure drops. Knowing that $\beta = \beta(\text{Re}_{\text{in}}, \text{Ja}/\text{Pr}_1, \rho_2/\rho_1, \mu_2/\mu_1)$, and knowing how it varies when one parameter is changed while the others are fixed, we correlate the β values in power-law form. Sample values of β are given as β (run) in Table 2 whereas a larger compilation of β (run) are given in Table 5 of Narain (1993). We remind the reader that different *forms* of power laws may closely fit the same data.

Furthermore, it is hoped, when this kind of semi-empirical interfacial shear models get established by a more thorough validation by experiments, they can serve as a guide for future turbulence modeling of "near interface" shears.

Note that (30) applies at locations of the interface where condensation rate $\dot{m}$ is small; therefore, this model may have something in common with interfacial shear models for air/water type internal flows where $\dot{m}$ is zero. Indeed, an extensive comparison of existing models by Spedding and Hand (1990) indicates (30) is one of the best models for annular and stratified regimes of such flows. However their work is in need of correlating β with "hold up" (i.e., ratio of liquid to duct cross-sectional areas), Reynolds numbers for each of the fluids, density ratio, and viscosity ratio.

The correlation for β for this paper was obtained by carefully selecting some 50 determination of β (runs) and the predictive capacity of the resulting models is tested against approximately 100 experimental runs which were not used in identifying β. We obtain good comparisons between theory and experiments (within ±20 percent for 96 percent of the data) and this can be seen, in a limited way, in Table 2. It suffices here to note that over the parameter range (27), we correlate β as

$$\beta = \begin{cases} \beta_0\left(\text{Re}_{\text{in}}, \dfrac{\text{Ja}}{\text{Pr}_1}, \dfrac{\rho_2}{\rho_1}, \dfrac{\mu_2}{\mu_1}\right) & \text{for} \quad \text{Re}_{\text{in}} \le \text{Re}_L \\ \beta_1\left(\text{Re}_{\text{in}}, \dfrac{\text{Ja}}{\text{Pr}_1}, \dfrac{\rho_2}{\rho_1}, \dfrac{\mu_2}{\mu_1}\right) & \text{for} \quad \text{Re}_{\text{in}} \ge \text{Re}_U, \end{cases} \quad (31)$$

and Re_L and Re_U are as defined in (28). The multiplier β_0 for *smooth* interface can be estimated from

$$\beta_0 = \begin{cases} \beta_{00}\left(\dfrac{\text{Ja}}{\text{Pr}_1}\right)^{1.6984} \text{Re}_{\text{in}}^{-1.4838} & \text{for} \quad 0.025 \le \dfrac{\text{Ja}}{\text{Pr}_1} \le 0.045 \\ \beta_{01}\left(\dfrac{\text{Ja}}{\text{Pr}_1}\right)^{0.4485} \text{Re}_{\text{in}}^{-1.4838} & \text{for} \quad 0.009 \le \dfrac{\text{Ja}}{\text{Pr}_1} < 0.025, \end{cases} \quad (32)$$

where the numbers $\beta_{00} = \beta_{00}(\rho_2/\rho_1, \mu_2/\mu_1)$, $\beta_{01} = \beta_{01}(\rho_2/\rho_1, \mu_2/\mu_1)$ are given in Table 3.

The multiplier β_1 for *wavy* interface can be estimated from

$$\beta_1 = \beta_{10}\left(\frac{\text{Ja}}{\text{Pr}_1}\right)^{1.7243} \text{Re}_{\text{in}}^{1.7845} \quad (33)$$

where the numbers $\beta_{10} = \beta_{10}(\rho_2/\rho_1, \mu_2/\mu_1)$ in (33) are given in Table 3.

Table 2 The table below specifies the flow conditions in the figures and compares the predictions for film thickness and average heat transfer coefficients with sample experimental measurements of Lu (1992). The fluid is R-113 and its properties are given in ASHRAE Handbook (1985). Liquid properties are evaluated at a *reference temperature* of $\mathcal{T}_w + \Delta\mathcal{T}/2$ and vapor properties at saturation temperature. Here $\Delta_3 = \Delta(x_3)$, where $x_3 = 0.457$ m; and $\bar{h}_2$ is $\bar{h}_2$ at $x = 0.5993$ m.

Case #	Expt. run # in Lu (1992)	Inlet Speed U (m/s)	Temp. $\mathcal{T}_s(p_o)$ (K)	Temp. $\mathcal{T}_w$ (K)	β (run)	β (fit)	Δ_3 Expt. (mm)	Δ_3 Model (mm)	% error in Δ_3	$\bar{h}_2$ Expt. (W/m²-K)	$\bar{h}_2$ Model (W/m²-K)	% error in $\bar{h}_2$
1	226	0.72	321.32	290.04	9.40	10.54				208.64	225.22	8
2	184	0.82	321.48	290.78	9.40	8.43				224.38	231.98	3
3	207	0.84	322.29	290.67	8.50	8.35	0.397	0.437	-10	217.37	231.82	7
4	196	1.03	321.22	290.67	5.50	6.00				220.00	243.16	10
5	247	2.20	320.55	290.30	4.80	6.01				346.95	400.83	15
6	234	3.92	320.56	291.38	16.00	15.97				707.75	798.63	13
7	279	1.59	321.01	310.26	1.90	2.04				303.95	331.00	9
8	---	0.82	300.78	290.78								
9	223	1.25	321.25	284.22	5.7	5.92	0.423	0.418	3	240.51	243.14	1
10	221	0.31	322.62	301.20	26.60	29.10	0.387	0.489	-26	203.78	204.07	0.1
11	185	0.84	321.25	300.79	5.70	6.83	0.370	0.397	-7	225.58	252.08	11
12	203	0.71	320.97	300.86		8.97	0.344	0.409	-18	235.06	244.53	4

Downloaded 04 May 2010 to 171.66.16.33. Redistribution subject to ASME license or copyright; see http://www.asme.org/terms/Terms_Use.cfm

Table 3 Values of coefficients defined in Sections 7-9

Coefficients dependent on ρ_2/ρ_1 and μ_2/μ_1	Fluid: R-113 $\rho_2/\rho_1 \cong 0.005$, and $\mu_2/\mu_1 \cong 0.0185$	Fluid: FC-72 $\rho_2/\rho_1 \cong 0.0082$, and $\mu_2/\mu_1 \cong 0.0218$
a_1	9864.78	12355.3
$\hat{a}_1$	11,154.30	16,822.30
β_{00}	6.4253×10^{9}	7.4270×10^{9}
β_{01}	6.3897×10^{7}	7.3858×10^{7}
β_{10}	2.3622×10^{-5}	2.3102×10^{-5}
δ_{00}	0.1178	0.1099
δ_{10}	1063.93	1131.66
ϵ_{00}	4.3638×10^{-18}	11.543×10^{-18}
ϵ_{01}	7.8831×10^{-14}	20.8523×10^{-14}
ϵ_{10}	4.2359×10^{13}	13.0428×10^{13}
f_{00}	1.3646×10^{9}	1.657×10^{9}
f_{01}	9.0447×10^{6}	10.9836×10^{6}
f_{10}	2.7349×10^{-7}	3.0552×10^{-7}
π_{00}	38004.33	6336.7
π_{01}	6.7706×10^{6}	11.2892×10^{6}
$\pi_1 = -\pi_{10}\,(\mathrm{Ja}/\mathrm{Pr}_1)^{1.6308}\mathrm{Re}^{1.9597}x^{1.1357}$, where		
π_{10}	2.1733×10^{-9}	2.4277×10^{-9}
Coefficients dependent on μ_2/μ_1 alone.	Fluids: R-113 and FC-72. It is assumed that for both the fluids $\mu_2/\mu_1 \cong 0.02$	
a_{10}	106,776.0	
$\hat{a}_{10}$	861,770.0	

In general, ϵ in (20) is of the form

$$\epsilon = \epsilon(\mathrm{Re}_{in}, \mathrm{Ja}/\mathrm{Pr}_1, \rho_2/\rho_1, \mu_2/\mu_1). \tag{34}$$

A correlation for ϵ is given in (79)–(81) of Narain (1993) with Table 3 of this paper replacing the correlation constants given in Table 4 of Narain (1993). However, as in discussions following (20), the correlation for ϵ is not important as the theory for $x \sim 0$ is primarily a tool for predicting results at downstream distances away from the origin. Furthermore, the present representation of f in the form of (20) can be used—though it is not done in this paper—to rewrite f in the original single expression form of Eqs. (16) and (25).

9 Predictions of Film Thickness, Heat Transfer Rates, Pressure Drops, and Average Vapor Speeds and the Representation of These Predictions in the Form of Correlations

Solution of (15), with the help of the friction factor model developed above, yields the film thickness $\delta(x)$, pressure $\pi(x)$, and the average speed $u_{av}(x)$. Figures 4 and 6 show some sample predictions of film thickness δ and pressure π. Knowing that these variables depend on the parameter set (2), we present a representative correlation of these predictions by the usual power law method (see Incropera and Dewitt, 1990) of varying one parameter while keeping the remaining fixed. The approximate correlations (average error within ±20 percent of experimental values) for δ, in the parameter range (27), is

$$\delta = \begin{cases} \delta_0\left(x, \mathrm{Re}_{in}, \dfrac{\mathrm{Ja}}{\mathrm{Pr}_1}, \dfrac{\rho_2}{\rho_1}, \dfrac{\mu_2}{\mu_1}\right) & \text{for } \mathrm{Re}_{in} \le \mathrm{Re}_L \\ \delta_1\left(x, \mathrm{Re}_{in}, \dfrac{\mathrm{Ja}}{\mathrm{Pr}_1}, \dfrac{\rho_2}{\rho_1}, \dfrac{\mu_2}{\mu_1}\right) & \text{for } \mathrm{Re}_{in} \ge \mathrm{Re}_U, \end{cases} \tag{35}$$

where δ_0 is the thickness for smooth interface, and δ_1 is the *mean* thickness for wavy interface. The Reynolds numbers Re_L and Re_U are as specified in (28)–(29). The correlation for δ_0, over $x \ge \epsilon$, is

$$\delta_0 = \delta_{00}(\rho_2/\rho_1, \mu_2/\mu_1)\left(\frac{\mathrm{Ja}}{\mathrm{Pr}_1}\right)^{0.2604} \mathrm{Re}_{in}^{-0.2023} x^{0.3393}, \tag{36}$$

and the correlation for δ_1, over $x \ge \epsilon$, is

$$\delta_1 = \delta_{10}(\rho_2/\rho_1, \mu_2/\mu_1)\left(\frac{\mathrm{Ja}}{\mathrm{Pr}_1}\right)^{0} \mathrm{Re}_{in}^{-1.1955} x^{0.3748}. \tag{37}$$

The numbers δ_{00} and δ_{10} in (36) and (37) are given in Table 3.

Representative correlations for pressure variations (for fully developed flow at the inlet) and variations in the average vapor speed are similarly obtained with the help of correlations given in Narain (1993) and revised constants in Table 3 of this paper.

The definition of local heat transfer coefficient $\mathscr{k}_x$, average heat transfer coefficient $\overline{\mathscr{k}}_x$, local Nusselt Number Nu_x, and the average Nusselt Number $\overline{\mathrm{Nu}}_x$ arise out of the following relations

$$q'' \equiv \mathscr{k}_x(\mathscr{T}_s(p_0) - \mathscr{T}_{w0}), \quad \mathrm{Nu}_x \equiv \frac{\mathscr{k}_x h}{k_1}$$

$$q \equiv \overline{\mathscr{k}}_x(x \times 1)(\mathscr{T}_s(p_0) - \mathscr{T}_{w0}), \quad \overline{\mathrm{Nu}}_x \equiv \frac{\overline{\mathscr{k}}_x x}{k_1}, \tag{38}$$

where q'' is the local heat flux per unit area and q is the total heat transfer rate through the bottom plate of length x. Using the fact that q'' and q can be directly computed from

$$q'' = k_1 \left.\frac{\partial \mathscr{T}_1}{\partial \mathscr{y}}\right|_{\mathscr{y}=0} \cong \frac{k_1 \Delta \mathscr{T}}{h\delta(x)}$$

$$q = \int_0^x q'' dx \cong k_1 \Delta \mathscr{T} \int_0^x \frac{1}{\delta(x)}\, dx, \tag{39}$$

we find (38)–(39) imply

$$\mathrm{Nu}_x = \frac{1}{\delta(x)} \quad \text{and} \quad \overline{\mathrm{Nu}}_x = \int_0^x \frac{1}{\delta(x)}\, dx. \tag{40}$$

Substitution of (35)–(37) in (40) easily yields the correlation for Nu_x and $\overline{\mathrm{Nu}}_x$.

10 Discussion of Results

The asymptotic form of friction factor model proposed in (16) holds near onset of condensation. This model is implied by the integral equations which in turn are implied by *scaled* differential equations of the type given in Sparrow and Gregg (1959) or Narain (1993). This scaling does not apply at very small $x \sim 0$ and the full unscaled equations will resolve the singularity, unlike the solution in this paper or in Sparrow and Gregg (1959), in a way so as to make $u_f(0^+) = 0$ and $f(0^+)$ finite. However, the proposed model is a valid and useful tool for effectively (e.g., by accurately insuring constant total mass

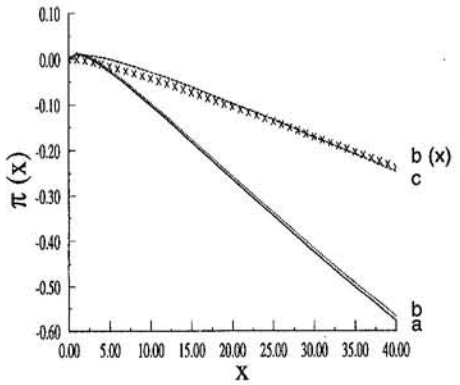


Fig. 6 Curves *b* and *c* above represent decreasing $\Delta\pi \equiv \pi(0) - \pi(x)$ due to increasing Re_{in} at a fixed $\Delta\mathscr{T}$. The curves *a*, *b*, *b*(*x*), and *c* correspond to case #s 1, 2, 8, and 5 specified in Table 2.

Downloaded 04 May 2010 to 171.66.16.33. Redistribution subject to ASME license or copyright; see http://www.asme.org/terms/Terms_Use.cfm

flux from $x = 0$ onwards) and rapidly (i.e., over a small distance) *connecting* the convenient inlet conditions to the true solutions of the appropriate equations at a length scale $x \equiv x / h$ of interest. Differences between the proposed asymptotic form of f and f based on full unscaled differential equations will only be apparent over a magnified length scale $\xi \equiv x/\epsilon$ (ϵ as in (20)). The proposed asymptotic form of f and associated results of existence, uniqueness, and stability are also likely to be useful in overcoming convergence problems associated with full two-dimensional numerical solution of the scaled partial differential equations for the underlying free boundary problem.

As shown in Fig. 2, the choice of vapor velocity profile, whether it varies realistically, or merely has an average uniform value, does not affect the predictions of condensate motion significantly. In this one-dimensional method, it is the interfacial shear which drives the liquid condensate and the requirement of continuity of tangential speeds has no noticeable impact.

The result in Fig. 3 shows that inlet conditions, affecting the model for f_u, leads to insignificant relative changes in the values of film thickness and average vapor speeds but more noticeable relative changes in pressure variations. This is consistent with the fact that changing the model for f_u primarily affects the vapor momentum balance and insignificantly affects the overall energy and mass balance. The overall energy balance is primarily a balance between heat removed by coolant under the bottom plate and rate of loss of stored energy due to phase change; there is a negligible contribution from pressure working and frictional heating. Therefore change in f_u does affect the pressure variations in vapor but these variations are not sufficient to change the condensate mass flux (driven primarily by interfacial shear) determining the heat removal rates. Accurate computations of pressure variations and assessment of sensitivity of different gradients in the governing equations are consistent with the above description. The results in Fig. 3 are good for $x > 3$. The kink in the pressure ratio curve is due to the fact that $\pi_{II}(x)$ has a kink at $x \cong 17$ because f_u, for the choice in (14), has changed from a laminar to a turbulent model near this transition point.

The comparisons in Fig. 4 establishes the value and need of the proposed modeling approach for interfacial shear as popular existing models give poor quantitative predictions for the annular (with zero or negligible entrainment) flow regime considered here.

In Fig. 5, we show the variation of the proposed friction factor f with distance x for two representative flow situations. However, a plot of the values of physical shear stress τ_f with distance shows that this value, unlike the nondimensional friction f itself, strongly decreases with x because of a decreasing average speed of the vapor.

Trends of film thickness, pressure, and the average vapor speeds can be inferred from their correlations given in Narain (1993) and Narain (1994).

Figure 6 shows some of the trends of computed pressure variations. Note that, in the smooth interface regime $\Delta\pi$ decreases with increasing Re_{in} (see case b and case c in Fig. 6); however, the physical pressure drop $\Delta p = \rho_2 U^2 \Delta\pi$ actually increases. Furthermore, if we use Shekriladze and Gomelauri (1966) model or any model other than the one developed here for interfacial shear, then we find an increase in pressure in the early part of the flow followed by a decrease in pressure in the subsequent downstream side of the flow. This phenomenon, believed to be factual by Shekriladze and Mestvirishvilli (1972) for flow in vertical tubes does not seem to occur for flow in horizontal channels.

The relative magnitude of forces (see Fig. 9 of Narain, 1994) in the vapor region show that friction, pressure, and inertia forces are comparable and the "kick-back" force associated with mass and momentum transfer is negligible. This means that the friction force, due to parity with inertia force, constrains vapor speed $u_{av}(x)$ as much as mass balance does.

Typical pressure drops in the duct are too small to affect either the saturation temperature at the interface or the latent heat released at the interface. This is true for the parameter range given in (27) and is shown in Fig. 12 of Narain (1993).

We also find significantly increased heat transfer rates in the wavy regime. The near proportionality of heat transfer coefficient (put (37) in (40)) to inlet Reynolds number Re_{in} is in agreement with known experimental correlations (Lu, 1992, etc.) for high-speed flows.

11 Conclusions

We showed the reliability of the proposed integral-differential scheme towards modeling of interfacial friction factor. Clearly this modeling approach leading to (30) is promising but the correlations in Sections 7-9 are very approximate and merely indicate what is possible if this approach is implemented with more and accurate experimental data covering a larger window of flow parameters. At large downstream distances, condensate will be thick and inertia and convective heat transfer in the condensate will become important. Full numerical simulation or iterative corrections to the present approach should be used for such cases.

We presented:

- a new and rigorous model for asymptotic friction factor at the point ($x \sim 0$) where condensation begins and condensation rate is high.
- results on existence, uniqueness, and stability issues with regard to integrability of the equations.
- interfacial shear models for flow regimes involving both smooth and wavy interface.
- a method for obtaining correlations, and some approximate correlations, for film thickness, pressure drops, heat transfer rates, etc., for both smooth and wavy interface annular flow regimes.

Acknowledgments

I thank Q. Lu and Prof. N. V. Suryanarayana for providing access to their experiments. My special thanks go to my former M. S. student R. Kamath and to my new students Qingyu Liu and Guang Yu for their assistance in checking and improving parts of this paper.

References

Arnold, V. I., 1973, *Ordinary Differential Equations,* MIT Press.

ASHRAE Handbook, 1985, Fundamentals SI Edition, American Society of Heating, Refrigeration and Air-Conditioning Engineers, Atlanta, GA.

Bell, K. J., Taborek, J., and Fenoglio, F., 1970, "Interpretation of Horizontal In-Tube Condensation Heat Transfer Correlations with a Two-Phase Flow Regime Map," *Chemical Engineering Progress Symposium Series,* Vol. 66, No. 102, pp. 150–163.

Blangetti, F., 1979, "Lokaler Wärmeübergang bei der Kondensation mit überlagerter Konvektion in vertikalen Rohr," Dissertation, Universität Karlsruhe.

Bouyer, T., and Panday, P. K., 1993, "Heat Transfer Coefficients for Condensation of Superheated and Saturated R12 Vapour Flowing Between Parallel Plates," *Condensation and Condenser Design,* J. Taborek, J. Rose, and I. Tanasawa, eds., United Engineering Trustees, pp. 431–442.

Carey, V. P., 1992, *Liquid-Vapor Phase-Change Phenomena* (Series in Chemical and Mechanical Engineering), Hemisphere.

Carpenter, F. G., and Colburn, A. P., 1951, (July), "The Effect of Vapor Velocity on Condensation Inside Tubes," *Proceedings of the General Discussion of Heat Transfer,* The Institute of Mechanical Engineers and the ASME, July, pp. 20–26.

Chen, S. L., Gerner, F. M., and Tien, C. L., 1987, "General Film Condensation Correlations," *Experimental Heat Transfer,* Vol. 1, pp. 93–107.

Chen, I. Y., and Kocamustafaogullari, G., 1987, "Condensation Heat Transfer Studies for Stratified, Cocurrent Two-Phase Flow in Horizontal Tubes," *International Journal of Heat and Mass Transfer,* Vol. 30, No. 6, pp. 1133–1148.

Delhaye, J. M., 1974, "Jump Conditions and Entropy Sources in Two-phase Systems; Local Instant Formulation," *International Journal of Multiphase Flow,* Vol. 1, pp. 395–409.

Fujii, T., and Uehara, H., 1972, "Laminar Filmwise Condensation on a Vertical Surface," *International Journal of Heat and Mass Transfer,* Vol. 15, pp. 217–233.

Downloaded 04 May 2010 to 171.66.16.33. Redistribution subject to ASME license or copyright; see http://www.asme.org/terms/Terms_Use.cfm

Hewitt, G. F., and Govan, A. H., 1990, "Phenomena and Prediction in Annular Two-Phase Flow," *Advances in Gas-Liquid Flows 1990,* J. H. Kim, V. S. Rohtagi, and A. Hashemi, eds., ASME FED-Vol. 99 and HTD-Vol. 155, pp. 41–55.

Incropera, F. P., and DeWitt, D. P., 1990, *Fundamentals of Heat and Mass Transfer,* 3rd ed., John Wiley and Sons, New York.

Jensen, R. J., and Yuen, M. C., 1982, "Local Heat and Mass Transfer Correlation in Horizontal Stratified Concurrent Flow," *Proceedings of the 7th International Heat Transfer Conference,* Munichen, pp. 95–100.

Khoo, B. C., Patera, A. T., and Sonin, A. A., 1989, "Direct Numerical Simulation of Pure Vapor Condensation At a Turbulent Liquid Interface: An Extracted-Subdomain Approach," *Heat Transfer With Phase Change,* I. S. Habib and R. J. Dallman, eds., ASME HTD-Vol. 114, pp. 39–50.

Koh, J. C. Y., 1962, "Film Condensation in a Forced-Convection Boundary-Layer Flow," *International Journal of Heat and Mass Transfer,* Vol. 5, pp. 941–954.

Linehan, J. H., Petrick, M., and El-Wakil, M. M., 1969, "On the Interface Shear Stress in Annular Film Condensation," ASME *Journal of Heat Transfer,* pp. 450–452.

Lockhart, R. W., and Martinelli, R. C., 1949, "Proposed Correlation of Data for Isothermal Two Phase, Two Component Flow in Pipes," *Chemical Engineering Progress,* Vol. 45, No. 1, pp. 39–48.

Lu, Q., 1992, "An Experimental Study of Condensing Heat Transfer with Film Condensation in a Horizontal Rectangular Duct," Ph.D. Thesis, Michigan Technological University, Houghton, MI.

Lu, Q., and Suryanarayana, N. V., 1992, "Condensation of a Vapor Flowing Inside a Horizontal Rectangular Duct," *Two Phase Flow in Energy Exchange Systems,* ASME-HTD Vol. 220, pp. 27–33; also ASME *Journal of Heat Transfer,* 1995, pp. 418–424.

Mickley, H. S., 1954, "Heat, Mass, and Momentum Transfer for Flow Over a Flat Plate With Blowing or Suction," NASA Report, NACA-TN-3208.

Minkowycz, W. J., and Sparrow, E. M., 1966, "Condensation Heat Transfer in the Presence of Non-condensables, Interfacial Resistance, Superheating, Variable Properties, and Diffusion," *International Journal of Heat and Mass Transfer,* Vol. 9, pp. 1125–1144.

Moody, L. F., 1944, "Friction Factors for Pipe Flow," *ASME Transactions,* Vol. 66, pp. 671–684.

Mudawar, I., and Houpt, R. A., 1993, "Mass and Momentum Transport in Smooth Falling Liquid Films Laminarized at Relatively High Reynolds Numbers," *International Journal of Heat and Mass Transfer,* Vol. 36, pp. 3437–3448.

Narain, A., and Kizilyalli, Y., 1991, "Pressure Driven Flow of Pure Vapor Undergoing Laminar Film Condensation Between Parallel Plates," *International Journal of Non-Linear Mechanics,* Vol. 26, No. 5, pp. 501–520.

Narain, A., 1993, "Interfacial Shear Modeling and Flow Predictions For Internal Flows of Pure Vapor Experiencing Film Condensation," IMA Preprint Series #1103, Institute for Mathematics and Its Applications, University of Minnesota, Minneapolis, MN.

Narain, A., 1994, "Modeling of Interfacial Shear and Heat Transfer Predictions for Internal Flows with Film Condensation," *Fundamentals of Phase Change-Boiling and Condensation,* S. G. Kandlikar and C. T. Avedisian, eds., ASME HTD-Vol. 273, pp. 29–40; also see *Fluid Mechanics Phenomena in Microgravity,* ASME AMD-Vol. 154 and FED-Vol. 142, pp. 23–38, (1992).

Nusselt, W., 1916, "Die Oberflächenkondesation des Wasserdampfes," *Zeitschrift des Vereines Deutschen Ingenieure,* Vol. 60, No. 27, pp. 541–546.

Palen, J. W., Breber, G., and Taborek, J., 1979, "Predictions of Flow Regimes in Horizontal Tube Condensation," *Heat Transfer Engineering,* Vol. 1, pp. 47–57.

Rohsenow, W. M., 1956, "Heat Transfer and Temperature Distribution in Laminar Film Condensation," *ASME Transactions,* Vol. 78, pp. 1645–1648.

Schlichting, H., 1968, *Boundary Layer Theory,* 6th ed., McGraw-Hill, New York.

Shah, M. M., 1979, "A General Correlation for Heat Transfer During Film Condensation Inside Pipes," *International Journal of Heat and Mass Transfer,* Vol. 22, pp. 547–556.

Shekriladze, I. G., and Gomelauri, V. I., 1966, "Theoretical Study of Laminar Film Condensation of Flowing Vapour," *International Journal of Heat and Mass Transfer,* Vol. 9, pp. 581–591.

Shekriladze, I. G., and Mestvirishvilli, S. A., 1972, "Study of The Process of Film Condensation of a Flowing Vapor within a Vertical Tube," *Heat Transfer—Soviet Research,* Vol. 4, No. 4, pp. 1–6.

Soliman, M., Schuster, J. R., and Berenson, P. J., 1986, "A General Heat Transfer Correlation For Annular Flow Condensation," ASME *Journal of Heat Transfer,* Vol. 90, pp. 267–276.

Sparrow, E. M., and Gregg, J. L., 1959, "A Boundary Layer Treatment of Laminar Film Condensation," ASME *Journal of Heat Transfer,* Vol. 81, pp. 13–18.

Spedding, P. L., and Hand, N. P., 1990, "Prediction of Holdup and Pressure Loss from the Two Phase Momentum Balance for Stratified Type Flows," *Advances in Gas-Liquid Flows 1990,* J. H. Kim, V. S. Rohtagi, and A. Hashemi, eds., ASME FED-Vol. 99 and HTD-Vol. 155, pp. 73–87.

Traviss, D. P., Rohsenow, W. M., and Baron, A. B., 1973, "Forced-Convection Condensation Inside Tubes: A Heat Transfer Equation for Condenser Design," *ASHRAE Transactions,* Vol. 79, Part 1, pp. 157–165.

Wang, L. P., Carey, V. P., Grief, R., and Abdollahian, D., 1990, "Experimental Simulation and Analytical Modeling of Two-Phase Flow Under Zero Gravity Conditions," *International Journal of Multiphase Flow,* Vol. 16, No. 3, pp. 407–419.

White, F. M., 1974, *Viscous Fluid Flow,* McGraw-Hill, New York.

Wilcox, D. C., 1993, *Turbulence Modeling for CFD,* DCW Industries.

APPENDIX

The functions appearing in (12) are defined as

$$A_{22} \equiv \frac{\rho_2}{\rho_1}(1 - \delta(x))\delta(x), \tag{A1}$$

$$A_{23} \equiv \frac{\rho_2}{\rho_1} u_{av}(x))\delta(x), \tag{A2}$$

$$A_{32} \equiv 2(1 - \delta(x))u_{av}(x), \tag{A3}$$

$$A_{33} \equiv -u_{av}^2(x), \tag{A4}$$

$$b \equiv \frac{\rho_2}{\rho_1}\{1 - u_{av}(x)(1 - \delta(x))\}, \tag{A5}$$

$$b_1 \equiv -\frac{3}{\delta^3(x)}\left[\frac{\mu_1}{\mu_2}\frac{1}{\mathrm{Re}_2} b - \frac{1}{4} u_{av}^2(x) f\delta^2(x)\right], \tag{A6}$$

$$b_2 \equiv \frac{\mathrm{Ja}}{\mathrm{Pr}_1}\frac{1}{\mathrm{Re}_1}\frac{[T_s(\pi(x)) - T_w]}{\phi_{fg}(\pi(x))}, \tag{A7}$$

$$b_3 \equiv -b_1(1 - \delta) - \frac{1}{2} u_{av}^2(x)(f + f_u) - \frac{\rho_1}{\rho_2}\frac{b_2}{\delta} u_f, \tag{A8}$$

where b_1 above is defined in terms of b; and b_3 is defined in terms of b_1 and b_2.

The components g_1, g_2, and g_3 appearing in (15) are defined below:

$$g_1 \equiv b_1, \tag{A9}$$

$$g_2 \equiv \frac{b_2 A_{33} - b_3 A_{23}}{A_{22}A_{33} - A_{23}A_{32}}, \tag{A10}$$

and

$$g_3 \equiv \frac{b_3 A_{22} - b_2 A_{32}}{A_{22}A_{33} - A_{23}A_{32}}. \tag{A11}$$

Note

$$k_1 = 2\left[c_2 - 2\left\{\frac{\mathrm{Ja}}{\mathrm{Pr}_1} + 1\right\}\left(\frac{1}{\mathrm{Re}_1}\right)\left\{\frac{c_2}{c_1^2} + \frac{1}{c_1}\right\} + \frac{c_1}{2}\right] \tag{A12}$$

$$c_2 = 2\left(\frac{\rho_1}{\rho_2}\right)\left(\frac{\mathrm{Ja}}{\mathrm{Pr}}\right)\left(\frac{1}{\mathrm{Re}_1}\right)\frac{1}{c_1} - c_1. \tag{A13}$$

Downloaded 04 May 2010 to 171.66.16.33. Redistribution subject to ASME license or copyright; see http://www.asme.org/terms/Terms_Use.cfm

A Simplified Displacement-Rotation Form for the Equations of Motion of Nonlinearly Elastic Shells of Revolution Undergoing Combined Bending and Torsion

J. G. Simmonds
Institute of Applied Mathematics and Mechanics,
University of Virginia,
Charlottesville, VA 22903
Fellow ASME.

By appropriately defining two displacements and a rotation, it is shown that the equations of motion of a shell of revolution undergoing combined axisymmetric bending and torsion, in which the extensional strains and the rotations may be arbitrarily large, can be given a form in which there are three effective extensional strains and two effective bending strains, each of which is only linear or quadratic in the displacements and rotation.

1 Introduction

Herein, we extend and combine the results of Simmonds (1985) on a simplified displacement form for the equations of motion of elastic shells of revolution undergoing *torsionless* axisymmetric motion and the results of England and Simmonds (1991) on a rotation-stress function form of the *static* equations of an elastic shell of revolution undergoing *combined* bending and torsion of arbitrary magnitude. We show, in terms of two translational displacements, u and w, and a rotation, ψ, that the six extensional and bending strains discussed by Simmonds and Danielson (1972) can be expressed in terms of *five, effective* extensional and bending strains. These, in turn, can be expressed as linear or quadratic functions of u, w, and ψ and their derivatives. Consequently, the associated equations of motion assume a relatively simple form. This is in contrast to the general theory of shells where the displacement form of the equations of motion are known to be exceedingly complicated (Budiansky, 1968; Libai and Simmonds, 1983). The key to the simplifications possible for the special case of combined axisymmetric bending and torsion of a shell of revolution is to introduce a set of *twisted* circular cylindrical base vectors, $\{\bar{\mathbf{e}}_r, \bar{\mathbf{e}}_\theta, \mathbf{e}_z\}$, in addition to the more conventional tangential and normal base vectors of standard shell theory, and to introduce certain modified stress resultants and couples as do many other authors in developing general shell theories.

2 The Exact Equations

Let $\{\mathbf{e}_x, \mathbf{e}_y, \mathbf{e}_z\}$ denote the standard orthonormal basis of a fixed, dextral Cartesian reference frame and let $\{\mathbf{e}_r, \mathbf{e}_\theta, \mathbf{e}_z\}$ denote the standard basis associated with a set of circular cylindrical coordinates (r, θ, z), where

$$\mathbf{e}_r = \cos\theta\mathbf{e}_x + \sin\theta\mathbf{e}_y, \quad \mathbf{e}_\theta = -\sin\theta\mathbf{e}_x + \cos\theta\mathbf{e}_y. \quad (1)$$

Then the reference surface $\mathcal{S}$ of an undeformed shell of revolution may be expressed as

$$\mathcal{S}: \mathbf{y} = r(s)\mathbf{e}_r(\theta) + z(s)\mathbf{e}_z, \quad 0 \le s \le L, \quad 0 \le \theta < 2\pi, \quad (2)$$

where s is arc length along a meridian. A unit tangent to such a meridian is given by

$$\mathbf{t} \equiv \mathbf{y}_{,s} = r'(s)\mathbf{e}_r(\theta) + z'(s)\mathbf{e}_z \equiv \cos\alpha(s)\mathbf{e}_r(\theta) + \sin\alpha(s)\mathbf{e}_z, \quad (3)$$

where here and elsewhere we denote (total or partial) derivatives of *scalars* with respect to s by a prime.

We assume that the external loads and material properties of the shell are such that the deformed reference surface $\bar{\mathcal{S}}$ has the representation

$$\bar{\mathcal{S}}: \bar{\mathbf{y}} = [r(s) + u(s,t)]\bar{\mathbf{e}}_r(\theta, s, t) + [z(s) + w(s,t)]\mathbf{e}_z, \quad (4)$$

where here and for future reference,

$$\bar{\mathbf{e}}_r \equiv \mathbf{e}_r(\theta + \psi(s,t)), \quad \bar{\mathbf{e}}_\theta \equiv \mathbf{e}_\theta(\theta + \psi(s,t)). \quad (5)$$

Thus,

$$\bar{\mathbf{y}}_{,s} = \Lambda_s(s,t)\bar{\mathbf{t}}(s,t,\theta) + \gamma(s,t)\bar{\mathbf{e}}_\theta(s,t,\theta),$$
$$\bar{\mathbf{y}}_{,\theta} = r(s)\Lambda_\theta(s,t)\bar{\mathbf{e}}_\theta(s,t,\theta). \quad (6)$$

Here,

$$\gamma = (r + u)\psi' \quad (7)$$

is an *effective* in-surface shear strain, bilinear in u and ψ', and

$$\Lambda_s = \sqrt{1 + 2\epsilon_s}, \quad \Lambda_\theta = 1 + \epsilon_\theta \quad (8)$$

are, respectively, meridional and hoop stretches, where

$$\epsilon_s = u'\cos\alpha + w'\sin\alpha + \tfrac{1}{2}(u'^2 + w'^2), \quad \epsilon_\theta = u/r \quad (9)$$

are, respectively, a Lagrange-like *effective meridional strain,* quadratic in u and w and their derivatives, and an engineering *effective hoop strain,* linear in u. Further,

$$\bar{\mathbf{t}} \equiv \Lambda_s^{-1}(s,t)\{[\cos\alpha(s) + u'(s,t)]\bar{\mathbf{e}}_r(s,t,\theta) + [\sin\alpha(s) + w'(s,t)]\mathbf{e}_z\} \equiv \cos\bar{\alpha}(s,t)\bar{\mathbf{e}}_r(s,t,\theta) + \sin\bar{\alpha}(s,t)\mathbf{e}_z \quad (10)$$

Contributed by the Applied Mechanics Division of THE AMERICAN SOCIETY OF MECHANICAL ENGINEERS for publication in the ASME JOURNAL OF APPLIED MECHANICS.

Discussion on this paper should be addressed to the Technical Editor, Professor Lewis T. Wheeler, Department of Mechanical Engineering, University of Houston, Houston, TX 77204-4792, and will be accepted until four months after final publication of the paper itself in the ASME JOURNAL OF APPLIED MECHANICS.

Manuscript received and accepted by the ASME Applied Mechanics Division, Aug. 12, 1994. Associate Technical Editor: W. K. Liu.

Copyright © 1996 by ASME

Downloaded 04 May 2010 to 171.66.16.33. Redistribution subject to ASME license or copyright; see http://www.asme.org/terms/Terms_Use.cfm

is a unit tangent to a meridian of $\bar{\mathcal{S}}$, where

$$\bar{\alpha} = \tan^{-1}\left[\frac{\sin\alpha(s) + w'(s,t)}{\cos\alpha(s) + u'(s,t)}\right] \equiv \alpha(s) + \beta(s,t). \quad (11)$$

The equations of motion (3.32) and (3.33) of Libai and Simmonds (1983), specialized to a shell of revolution, take the form

$$(r\mathbf{N}_s)_{,s} + \mathbf{N}_{\theta,\theta} + r\mathbf{p} = rm\ddot{\bar{\mathbf{y}}} \quad (12)$$

$$(r\mathbf{M}_s)_{,s} + \mathbf{M}_{\theta,\theta} + r\bar{\mathbf{y}}_{,s} \times \mathbf{N}_s + \bar{\mathbf{y}}_{,\theta} \times \mathbf{N}_\theta + r\mathbf{l} = r\mathbf{I}\cdot\dot{\boldsymbol{\omega}}. \quad (13)$$

Here, $r\mathbf{N}_s d\theta$ and $\mathbf{N}_\theta ds$ are, respectively, the forces acting across the deformed images of the differential coordinate elements $rd\theta$ and ds; $r\mathbf{M}_s d\theta$ and $\mathbf{M}_\theta ds$ are analogous couples. Further, $\mathbf{p}$ and $\mathbf{l}$ are, respectively, an external force and external couple per unit area of $\mathcal{S}$, m is the mass per unit area of $\mathcal{S}$, $\boldsymbol{I}$ is the moment of inertia tensor of the shell, and $\boldsymbol{\omega}$ is an angular velocity, yet to be related to the basic kinematic unknowns, u, w, and ψ. Simmonds (1979) shows that these equations of motion are *exact* consequences of the three-dimensional equations of motion of a continuum providing $\bar{\mathbf{y}}(s,t)$ is defined as a density-weighted average of the three-dimensional position vector.

To define our two effective bending strains and to properly incorporate these and the three effective extensional strains into the strain-energy density of the shell, we write down the virtual work principle by taking the dot product of (12) with $\delta\bar{\mathbf{y}}$, a virtual displacement, and the dot product of (13) with $\delta\boldsymbol{\phi}$, a virtual rotation. We then add the resulting equations and integrate over the reference surface. Integrating by parts to remove derivatives with respect to s and θ and dividing by 2π, we obtain

$$[r(\mathbf{N}_s\cdot\delta\bar{\mathbf{y}} + \mathbf{M}_s\cdot\delta\boldsymbol{\phi})]_0^L + \int_0^L [(\mathbf{p} - m\ddot{\bar{\mathbf{y}}})\cdot\delta\bar{\mathbf{y}} + (\mathbf{l} - \dot{\boldsymbol{\omega}}\cdot\boldsymbol{I})\cdot\delta\boldsymbol{\phi}]rds = \int_0^L [\mathbf{N}_s\cdot(\delta\bar{\mathbf{y}}_{,s} - \delta\boldsymbol{\phi}\times\bar{\mathbf{y}}_{,s}) + r^{-1}\mathbf{N}_\theta\cdot(\delta\bar{\mathbf{y}}_{,\theta} - \delta\boldsymbol{\phi}\times\bar{\mathbf{y}}_{,\theta}) + \mathbf{M}_s\cdot\delta\boldsymbol{\phi}_{,s} + r^{-1}\mathbf{M}_\theta\cdot\delta\boldsymbol{\phi}_{,\theta}]rds. \quad (14)$$

To reduce the right side of (14), let

$$\mathbf{n} = \mathbf{t}\times\mathbf{e}_\theta \quad (15)$$

be a unit normal to $\mathcal{S}$ at a point $\mathbf{y}$ and let the rigid triad $\{\mathbf{T}, \mathbf{E}_\theta, \mathbf{N}\}$ spin with angular velocity $\boldsymbol{\omega}$ relative to the triad $\{\mathbf{t}, \mathbf{e}_\theta, \mathbf{n}\}$ and coincide with it at $t = 0$. Then, there exists a proper orthogonal tensor, or *rotator*, $\boldsymbol{Q}$ such that

$$\{\mathbf{T}, \mathbf{E}_\theta, \mathbf{N}\} = \boldsymbol{Q}\cdot\{\mathbf{t}, \mathbf{e}_\theta, \mathbf{n}\}. \quad (16)$$

On the other hand, by the polar decomposition theorem, the deformed image of the triad $\{\mathbf{t}, \mathbf{e}_\theta, \mathbf{n}\}$ has the representation

$$\{\bar{\mathbf{y}}_{,s}, r^{-1}\bar{\mathbf{y}}_{,\theta}, \bar{\mathbf{n}}\} = \boldsymbol{V}\cdot\boldsymbol{R}\cdot\{\mathbf{t}, \mathbf{e}_\theta, \mathbf{n}\}, \quad (17)$$

where

$$\bar{\mathbf{n}} = \bar{\mathbf{t}}\times\bar{\mathbf{e}}_\theta = -\sin\bar{\alpha}\bar{\mathbf{e}}_r + \cos\bar{\alpha}\mathbf{e}_z \quad (18)$$

is a unit normal to $\bar{\mathcal{S}}$ at $\bar{\mathbf{y}}$, $\boldsymbol{V}$ is the (left symmetric positive-definite) stretch tensor, and $\boldsymbol{R}$ is another rotator. Under the Kirchhoff hypothesis, that we now adopt, $\boldsymbol{Q} = \boldsymbol{R}$, so that (16) and (17) imply that

$$\{\bar{\mathbf{y}}_{,s}, r^{-1}\bar{\mathbf{y}}_{,\theta}, \bar{\mathbf{n}}\} = \boldsymbol{V}\cdot\{\mathbf{T}, \mathbf{E}_\theta, \mathbf{N}\} = \boldsymbol{V}\cdot\boldsymbol{Q}\cdot\{\mathbf{t}, \mathbf{e}_\theta, \mathbf{n}\}. \quad (19)$$

Let the action of $\boldsymbol{Q}$ be represented by three successive rotations: first, a rotation $\psi\mathbf{e}_z$, that is, a rotation of ψ radians taken in a positive, right-handed sense about $\mathbf{e}_z$, then a rotation $-\beta\bar{\mathbf{e}}_\theta$, and, finally, a rotation $\eta\bar{\mathbf{n}}$. Then, recalling that $\bar{\alpha} = \alpha + \beta$,

$$\delta\boldsymbol{\phi} = \delta\psi\mathbf{e}_z - \delta\bar{\alpha}\bar{\mathbf{e}}_\theta + \delta\eta\bar{\mathbf{n}} = \sin\bar{\alpha}\delta\psi\bar{\mathbf{t}} - \delta\bar{\alpha}\bar{\mathbf{e}}_\theta + (\delta\eta + \cos\bar{\alpha}\delta\psi)\bar{\mathbf{n}}. \quad (20)$$

The angle ψ is one of our basic unknowns and $\bar{\alpha}$ is given in terms of u and w by (11). To express η in terms of u, w, and ψ, note from (19) that $\bar{\mathbf{y}}_{,s} = \boldsymbol{V}\cdot\boldsymbol{T}$ and $r^{-1}\bar{\mathbf{y}}_{,\theta} = \boldsymbol{V}\cdot\mathbf{E}_\theta$. Thus, $\mathbf{E}_\theta\cdot\bar{\mathbf{y}}_{,s} = r^{-1}\mathbf{T}\cdot\bar{\mathbf{y}}_{,\theta}$. Since,

$$\mathbf{T} = \cos\eta\bar{\mathbf{t}} + \sin\eta\bar{\mathbf{e}}_\theta, \quad \mathbf{E}_\theta = -\sin\eta\bar{\mathbf{t}} + \cos\eta\bar{\mathbf{e}}_\theta, \quad (21)$$

it follows from (6) that

$$\tan\eta = \frac{\gamma}{\Lambda_s + \Lambda_\theta}, \quad (22)$$

where γ, Λ_s, and Λ_θ are given in terms of u, w, and ψ by (7)–(9).

Following Simmonds and Danielson (1972), let us (temporarily) introduce alternative extensional strains by setting

$$\bar{\mathbf{y}}_{,s} = (1 + E_s)\mathbf{T} + E\mathbf{E}_\theta, \quad r^{-1}\bar{\mathbf{y}}_{,\theta} = E\mathbf{T} + (1 + E_\theta)\mathbf{E}_\theta. \quad (23)$$

Then, from (14) and (20),

$$\delta\bar{\mathbf{y}}_{,s} - \delta\boldsymbol{\phi}\times\bar{\mathbf{y}}_{,s} = \delta E_s\mathbf{T} + \delta E\mathbf{E}_\theta,$$
$$r^{-1}(\delta\bar{\mathbf{y}}_{,\theta} - \delta\boldsymbol{\phi}\times\bar{\mathbf{y}}_{,\theta}) = \delta E\mathbf{T} + \delta E_\theta\mathbf{E}_\theta. \quad (24)$$

To reduce $\delta\boldsymbol{\phi}_{,s}$ and $\delta\boldsymbol{\phi}_{,\theta}$ to component form (and thus to obtain scalar bending strains in terms of the three angles ψ, $\bar{\alpha}$, and η), we note from (5), (10), (18), and (20) that

$$\delta\boldsymbol{\phi}_{,s} = \delta\psi'\mathbf{e}_z - (\delta\bar{\alpha}' + \psi'\sin\bar{\alpha}\delta\eta)\bar{\mathbf{e}}_\theta + \psi'\delta\bar{\alpha}\bar{\mathbf{e}}_r + \delta\eta'\bar{\mathbf{n}} - \bar{\alpha}'\delta\eta\bar{\mathbf{t}} \quad (25)$$

and

$$\delta\boldsymbol{\phi}_{,\theta} = \delta\bar{\alpha}\bar{\mathbf{e}}_r - \sin\bar{\alpha}\delta\eta\bar{\mathbf{e}}_\theta. \quad (26)$$

Upon using (10), (18), and (21) to express all vectors in the basis $\{\mathbf{T}, \mathbf{E}_\theta, \mathbf{N} = \bar{\mathbf{n}}\}$, we may write

$$\delta\boldsymbol{\phi}_{,s} = \delta K_{s\theta}\mathbf{T} - \delta K_s\mathbf{E}_\theta + \delta L_s\bar{\mathbf{n}},$$
$$r^{-1}\delta\boldsymbol{\phi}_{,\theta} = -\delta K_{\theta s}\mathbf{E}_\theta + \delta K_\theta\mathbf{T} + \delta L_\theta\bar{\mathbf{n}}, \quad (27)$$

where

$$K_s = \bar{\alpha}'\cos\eta + \psi'\sin\bar{\alpha}\sin\eta - \alpha',$$
$$rK_\theta = \sin\bar{\alpha}\cos\eta - \sin\alpha \quad (28)$$

$$K_{s\theta} = \psi'\sin\bar{\alpha}\cos\eta - \bar{\alpha}'\sin\eta, \quad rK_{\theta s} = \sin\bar{\alpha}\sin\eta \quad (29)$$

and

$$L_s = \psi'\cos\bar{\alpha} + \eta', \quad rL_\theta = \cos\bar{\alpha} - \cos\alpha. \quad (30)$$

Let

$$K_{s\theta} \equiv T + B, \quad K_{\theta s} \equiv T - B. \quad (31)$$

Then, under the Kirchhoff hypothesis, it follows from the compatibility condition (34) of Simmonds and Danielson (1972) that

$$(2 + E_s + E_\theta)B = (r^{-1}\sin\alpha - \alpha' + K_\theta - K_s)E + (E_s - E_\theta)T. \quad (32)$$

This relation implies that δB can be written as a linear combination of the variations of E_s, E, E_θ, K_s, T, and K_θ, with coefficients depending on these six strains themselves. Moreover, Simmonds and Danielson (1972) show, in terms of certain *modified* stress resultants and couples,

$$\hat{\mathbf{N}}_s = \hat{N}_s\mathbf{T} + (\hat{S} + \hat{N})\mathbf{E}_\theta, \quad \hat{\mathbf{N}}_\theta = (\hat{S} - \hat{N})\mathbf{T} + \hat{N}_\theta\mathbf{E}_\theta \quad (33)$$

Downloaded 04 May 2010 to 171.66.16.33. Redistribution subject to ASME license or copyright; see http://www.asme.org/terms/Terms_Use.cfm

and

$$\hat{\mathbf{M}}_s = -\hat{M}_s\mathbf{E}_\theta + \hat{W}\mathbf{T}, \quad \hat{\mathbf{M}}_\theta = -\hat{W}\mathbf{E}_\theta + \hat{M}_\theta\mathbf{T}, \tag{34}$$

(see their Eqs. (40) and (41)) that, under the Kirchhoff hypothesis, the integrand on the right of (14)—the internal virtual work density—takes the following form for an *elastic shell:*

$$\hat{N}_s\delta E_s + 2\hat{S}\delta E + \hat{N}_\theta\delta E_\theta + \hat{M}_s\delta K_s + 2\hat{W}\delta T + \hat{M}_\theta\delta K_\theta = \delta\Phi(E_s, E, E_\theta, K_s, T, K_\theta), \tag{35}$$

where Φ is a strain energy density. As in classical shell theory and consistent with the Kirchhoff Hypothesis, we have set $\hat{\mathbf{M}}_s\cdot\mathbf{N} = \hat{\mathbf{M}}_\theta\cdot\mathbf{N} = 0$.

3 Effective Strain Measures

We now show that the six strains E_s, E, E_θ, K_s, T, and K_θ can be expressed in terms of the three basic kinematic variables, u, w, and ψ via the effective extensional strains ϵ_s, γ, and ϵ_θ and two new *effective* bending strains,

$$\kappa_s \equiv \Lambda_s^2\bar{\alpha}' - \alpha', \quad \kappa_\theta \equiv r^{-1}(\Lambda_s \sin\bar{\alpha} - \sin\alpha). \tag{36}$$

From (8)–(11),

$$\kappa_s = (\cos\alpha + u')w'' - (\sin\alpha + w')u'' + (u'\cos\alpha + w'\sin\alpha)\alpha', \quad \kappa_\theta = w'/r. \tag{37}$$

These are the same bending strains introduced by Simmonds (1985) for shells of revolution undergoing axisymmetric *torsionless* deformation.

Upon comparing (6) with (23), using (21), and noting (8), we find that

$$E_s = \Lambda_s\cos\eta - 1 + \gamma\sin\eta = E_s(\epsilon_s, \epsilon_\theta, \gamma)$$
$$E = -\Lambda_s\sin\eta + \gamma\cos\eta = \Lambda_\theta\sin\eta = E(\epsilon_s, \epsilon_\theta, \gamma)$$
$$E_\theta = \Lambda_\theta\cos\eta - 1 = E_\theta(\epsilon_s, \epsilon_\theta, \gamma). \tag{38}$$

To express the bending strains K_s, T, and K_θ in terms of κ_s, κ_θ, ϵ_s, γ, and ϵ_θ (and thus in terms of u, w, and ψ), note from (22) that

$$2\Lambda\cos\eta = \Lambda_s + \Lambda_\theta, \quad 2\Lambda\sin\eta = \gamma, \quad \text{where} \quad 2\Lambda \equiv \sqrt{(\Lambda_s + \Lambda_\theta)^2 + \gamma^2}, \tag{39}$$

and from (7) and $(36)_2$ that

$$\psi' = r^{-1}\Lambda_\theta^{-1}\gamma, \quad \bar{\alpha}' = \Lambda_s^{-2}(\alpha' + \kappa_s), \quad \sin\bar{\alpha} = \Lambda_s^{-1}(\sin\alpha + r\kappa_\theta). \tag{40}$$

Then, using (8) and (38)–(40) in (28), we find that

$$K_s = \frac{(\Lambda_s + \Lambda_\theta)\kappa_s}{2\Lambda\Lambda_s^2} + \frac{\gamma^2(\sin\alpha + r\kappa_\theta)}{2r\Lambda\Lambda_s\Lambda_\theta} + \left(\frac{\Lambda_s + \Lambda_\theta}{2\Lambda\Lambda_s^2} - 1\right)\alpha'$$
$$= K_s(\epsilon_s, \gamma, \epsilon_\theta, \kappa_s, \kappa_\theta)$$
$$K_\theta = \frac{(\Lambda_s + \Lambda_\theta)\kappa_\theta}{2\Lambda\Lambda_s} + \left(\frac{\Lambda_s + \Lambda_\theta}{2\Lambda\Lambda_s} - 1\right)\frac{\sin\alpha}{r}$$
$$= K_\theta(\epsilon_s, \gamma, \epsilon_\theta, \kappa_\theta). \tag{41}$$

Further, from (29) and (31),

$$T = \frac{1}{2}[(\psi'\cos\eta + r^{-1}\sin\eta)\sin\bar{\alpha} - \bar{\alpha}'\sin\eta]$$
$$= \frac{\gamma}{4\Lambda\Lambda_s}\left[\left(\frac{\Lambda_s + \Lambda_\theta}{\Lambda_\theta} + 1\right)\left(\frac{\sin\alpha}{r} + \kappa_\theta\right) - \frac{\alpha' + \kappa_s}{\Lambda_s}\right]$$
$$= T(\epsilon_s, \gamma, \epsilon_\theta, \kappa_s, \kappa_\theta). \tag{42}$$

Thus, the five strain measures ϵ_s, γ, ϵ_θ, κ_s, and κ_θ, each of which is, at most, quadratic in u, w, and ψ (and their derivatives), suffice to describe the arbitrary axisymmetric, coupled bending and torsion of a shell of revolution.

We now consider the strain-energy density Φ to be a function of the five effective strains, so that

$$\delta\Phi = \Phi_{,\epsilon_s}\delta\epsilon_s + \Phi_{,\gamma}\delta\gamma + \Phi_{,\epsilon_\theta}\delta\epsilon_\theta + \Phi_{,\kappa_s}\delta\kappa_s + \Phi_{,\kappa_\theta}\delta\kappa_\theta. \tag{43}$$

To express the right side of (43) in terms of variations of u, w, and ψ and their derivatives, first note that if we set

$$M_s \equiv \Lambda_s^2\Phi_{,\kappa_s}, \tag{44}$$

then by $(8)_1$ and $(36)_1$,

$$r\Phi_{,\kappa_s}\delta\kappa_s = (rM_s\delta\bar{\alpha})' + 2r\bar{\alpha}'\Phi_{,\kappa_s}\delta\epsilon_s - (rM_s)'\delta\bar{\alpha}. \tag{45}$$

Thus, with the aid of (7), (9), (11), and $(37)_2$, we may write

$$r\delta\Phi = rH\delta u' + rV\delta w' + r(r + u)S\delta\psi' + N_\theta\delta u + (rM_s\delta\bar{\alpha})', \tag{46}$$

where

$$H \equiv (\Phi_{,\epsilon_s} + 2\bar{\alpha}'\Phi_{,\kappa_s})(\cos\alpha + u') + r^{-1}\Lambda_s^{-2}(rM_s)'(\sin\alpha + w') \tag{47}$$

$$V \equiv (\Phi_{,\epsilon_s} + 2\bar{\alpha}'\Phi_{,\kappa_s})(\sin\alpha + w') + r^{-1}[\Phi_{,\kappa_\theta} - \Lambda_s^{-2}(rM_s)'(\cos\alpha + u')] \tag{48}$$

$$S \equiv \Phi_{,\gamma}, \quad N_\theta \equiv \Phi_{,\epsilon_\theta} + r\psi'\Phi_{,\gamma}. \tag{49}$$

Turning to the left side of (14), we set

$$\mathbf{N}_s = \bar{H}\bar{\mathbf{e}}_r + \bar{S}\bar{\mathbf{e}}_\theta + \bar{V}\mathbf{e}_z, \quad \mathbf{M}_s = -\bar{M}_s\bar{\mathbf{e}}_\theta + \bar{W}\mathbf{t}. \tag{50}$$

From (4),

$$\delta\bar{\mathbf{y}} = \delta u\bar{\mathbf{e}}_r + (r + u)\delta\psi\bar{\mathbf{e}}_\theta + \delta w\mathbf{e}_z. \tag{51}$$

With this relation, (20), and (50), we find that the integrated (boundary) term on the left of (14) takes the form

$$r\{\bar{H}\delta u + [(r + u)\bar{S} + \bar{W}\sin\bar{\alpha}]\delta\psi + \bar{V}\delta w + \bar{M}_s\delta\bar{\alpha}\}. \tag{52}$$

To express the virtual work of the external and inertial loads in component form, we set

$$\mathbf{p} = \bar{p}_r\bar{\mathbf{e}}_r + \bar{p}_\theta\bar{\mathbf{e}}_\theta + p_z\mathbf{e}_z \tag{53}$$

and note from (4) that

$$\ddot{\bar{\mathbf{y}}} = [\ddot{u} - (r + u)\dot{\psi}^2]\bar{\mathbf{e}}_r + [2\dot{u}\dot{\psi} + (r + u)\ddot{\psi}]\bar{\mathbf{e}}_\theta + \ddot{w}\mathbf{e}_z. \tag{54}$$

Finally, consistent with the Kirchhoff hypothesis, we neglect external surface couples and rotary inertia. Thus, inserting (46) and (51)–(54) into (14), integrating by parts to remove spatial derivatives on u, w, and ψ, and evoking the independence of the variations δu, δw, and $\delta\psi$ in the *interior* of the shell, we obtain the field equations

$$(rH)' - N_\theta + r\bar{p}_r = rm[\ddot{u} - (r + u)\dot{\psi}^2] \tag{55}$$

$$(rV)' + rp_z = rm\ddot{w} \tag{56}$$

$$[r(r + u)S]' + r(r + u)\bar{p}_\theta = r(r + u)m[2\dot{u}\dot{\psi} + (r + u)\ddot{\psi}]. \tag{57}$$

The simplest boundary conditions are *canonical.* That is, on an edge of a complete shell of revolution, we prescribe one or

Downloaded 04 May 2010 to 171.66.16.33. Redistribution subject to ASME license or copyright; see http://www.asme.org/terms/Terms_Use.cfm

the other of the pairs (u, H), (w, V), $(\psi, (r + u)S)$, or $(\bar{\alpha}, M_s)$. The virtual work principle, (14), then implies that

$$\begin{Bmatrix} u = u^* \\ w = w^* \\ \psi = \psi^* \\ \bar{\alpha} = \bar{\alpha}^* \end{Bmatrix} \text{ or } \begin{Bmatrix} H = \bar{H}^* \\ V = \bar{V}^* \\ (r + u)S = [(r + u)\bar{S} + \bar{W} \sin \bar{\alpha}]^* \\ M_s = \bar{M}_s^* \end{Bmatrix} \quad \text{at} \quad s = 0, L, \quad (58)$$

where an asterisk (*) denotes a prescribed quantity.

4 Approximations

Introducing the following norms of the curvature, extensional, and bending strains,

$$\|b\| = \sqrt{\alpha'^2 + r^{-2} \sin^2 \alpha}, \quad \|\epsilon\| = \sqrt{\epsilon_s^2 + \gamma^2 + \epsilon_\theta^2},$$
$$\|\kappa\| \equiv \sqrt{\kappa_s^2 + \kappa_\theta^2}, \quad (59)$$

we have from (41) and (42), with the aid of (8) and (39),

$$\begin{Bmatrix} K_s \\ T \\ K_\theta \end{Bmatrix} = \begin{Bmatrix} \kappa_s \\ 0 \\ \kappa_\theta \end{Bmatrix} + O(\|\epsilon\|\|b\|, \|\epsilon\|\|\kappa\|). \quad (60)$$

Thus, if we are willing to accept errors in the strain-energy density Φ of the type indicated in (60)—a type of approximation recently recommended by Schieck et al. (1992)—some of the strain-energy densities proposed in the literature for rubber-like shells can be considerably simplified. For example, that of Taber (1988) for a neo-Hookean shell reduces to

$$\Phi = \tfrac{1}{2}\mu h[\Lambda_s^2 + \Lambda_\theta^2 + \Lambda_s^{-2}\Lambda_\theta^{-2} - 3 + (1/3)h^2(\kappa_s^2 + \kappa_s\kappa_\theta + \kappa_\theta^2)], \quad (61)$$

where h is the undeformed thickness of the shell and μ is the shear modulus. This approximation ignores the effects of the torsional bending strain and the effects of a change of thickness on the bending stiffness of the shell. *In some situations,* where the stretches are large, this latter approximation seems justified intuitively because membrane effects then dominate everything. However, if there is significant unidirectional stretching, it might be necessary to use a more refined approximation to compute crosswise bending effects.

Acknowledgments

This research was supported by the National Science Foundation under grant MSS-91-02155 and by the U.S. Army Research Office under grant DAAH04-94-G-0189.

References

Budiansky, B., 1968, "Notes on Nonlinear Shell Theory," ASME JOURNAL OF APPLIED MECHANICS, Vol. 35, pp. 393–401.

England, R., and Simmonds, J. G., 1991, "Simplifications under the Kirchhoff Hypothesis of Taber's Nonlinear Theory for the Axisymmetric Bending and Torsion of Elastic Shells of Revolution," *Int. J. Solids Structures,* Vol. 28, pp. 507–515.

Libai, A., and Simmonds, J. G., 1983, "Nonlinear Elastic Shell Theory," *Advances in Applied Mechanics,* Vol. 23, J. W. Hutchinson and T. Y. Wu, eds., Academic Press, New York, pp. 271–371.

Schieck, B., Pietraszkiewicz, W., and Stumpf, H., 1992, "Theory and Numerical Analysis of Shells undergoing Large Elastic Strains," *Int. J. Solids Structures,* Vol. 29, pp. 689–709.

Simmonds, J. G., and Danielson, D. A., 1972, "Nonlinear Shell Theory with Finite Rotation and Stress-Function Vectors," ASME JOURNAL OF APPLIED MECHANICS, Vol. 39, pp. 1085–1090.

Simmonds, J. G., 1979, "Special Cases of the Nonlinear Shell Equations," *Trends in Solid Mechanics 1979* (the Koiter 65th Birthday Volume), J. F. Besseling and van der Heijden, eds., Delft University Press, Delft, pp. 211–223.

Simmonds, J. G., 1985, "A New Displacement Form for the Nonlinear Equations of Motion of Shells of Revolution," ASME JOURNAL OF APPLIED MECHANICS, Vol. 52, pp. 507–509.

Taber, L. A., 1988, "On a Theory for Large Elastic Deformation of Shells of Revolution including Torsion and Thick Shell Effects," *Int. J. Solids Structures,* Vol. 24, pp. 973–985.

Downloaded 04 May 2010 to 171.66.16.33. Redistribution subject to ASME license or copyright; see http://www.asme.org/terms/Terms_Use.cfm

Flow Past a Flat Plate With a Vortex/Sink Combination

N. J. Mourtos
Associate Professor.

M. Brooks
Graduate Student.

Department of Aerospace Engineering,
San Jose State University,
San Jose, CA 95192-0188

This paper presents a potential flow model for the leading edge vortex over a two-dimensional flat plate at an angle of attack. The paper is an extension of a model by Saffman and Sheffield (1977). A sink has been added in this model in an effort to satisfy the Kutta condition at both the leading edge and the trailing edge of the plate. The introduction of the sink was inspired by the fact that most steady vortices in nature appear in combination with a flow feature which can be interpreted as a sink at their cores when the flow is analyzed in a two-dimensional observation plane. As in the Saffman and Sheffield model, the presence of a vortex results in increased lift; however, in the current model a unique vortex/sink position is found at each angle of attack. A comparison has also been made between the lift and the drag of this model and the corresponding results for two classical solutions of flow over a flat plate: (a) the fully attached flow with the Kutta condition satisfied at the trailing edge only and (b) the Helmholtz solution of fully separated flow.

1 Introduction

It is well established that vortices resulting from separation at the sharp leading edge of a delta wing increase the lift (Hummel, 1978). Numerous investigators have studied vortical separation on slender delta wings. To mention a few, Brown and Michael (1954) studied the effect of the leading edge vortices on a flat delta wing using a "single line vortex" connected with a plane vortex sheet emanating from the leading edge on each side of the wing. Sacks, Lundberg, and Hanson (1967) introduced the "multiple line vortex" model which offered more flexibility while Mangler and Smith (1957) with their "rolled-up core" model offered even greater realism in describing the vortical separation on slender delta wings. The "single line vortex" model has also been used to study the possibility of controlling vortical separation by tangential blowing (Mourtos, 1990).

This paper is concerned with the possibility of maintaining a free vortex over a high aspect ratio wing for the purpose of increasing its lift, particularly at low speeds. Walton (1974) and Kruppa (1977) explored this concept experimentally using the so-called "Kasper Airfoil." Saffman and Sheffield (1977) considered the two-dimensional flow over a flat plate with a free vortex standing on the lee side. They found no solutions which satisfied the Kutta condition at both the leading edge and the trailing edge of the plate. Rossow (1978) used an airfoil in his model but added a flap to trap the vortex and also a sink at the vortex core. Finally, Huang and Chow (1982) extended Saffman's and Sheffield's work to include thickness and camber effects. In this paper, an attempt is made to improve the work of Saffman and Sheffield by including a sink together with a vortex on the lee side of a flat plate at an angle of attack. The idea of having a sink at the vortex core is consistent with the fact that most vortices in nature, especially those which occur at high Reynolds numbers and are in some sense steady with regard to their location, are coupled with a flow feature which can be interpreted as a sink in a two-dimensional observation plane perpendicular to the vortex axis. For example, to generate a vortex in a bathtub, in addition to steering the water, one must also pull the plug to generate an axial flow along the core of the vortex. Similarly, the very low pressure at the center of a tornado generates an upward axial flow along the core of the tornado. Even the leading edge vortices on delta wings at high angles of attack have been observed to break down when the sweep angle of the wing is decreased. This is because a large sweep angle provides the spanwise gradient necessary to evacuate the vortex core and helps to organize the angular momentum in the separation zones into two conically shaped, stable vortices. It is also interesting to note that as a remedy to this problem of vortex breakdown on delta wings, spanwise blowing along the cores of these vortices has been proposed (Campbell, 1975), which again could be interpreted as a sink in a two-dimensional observation plane perpendicular to the vortex axis.

Since the flow over a flat plate is a classic case which has been studied and recorded in many texts, it will be instructive to compare the results from the present model to the classic results of (i) fully attached flow with the Kutta condition satisfied at the trailing edge of the plate only (the classical potential flow solution, Fig. 1(a)) and (ii) fully separated flow on the upper surface of the plate (Helmholtz solution, Fig. 1(c)). The present model, considering partially separated flow, lies somewhere between the two (Fig. 1(b)).

2 Analysis of the Flow Field

Potential flow theory has been used to analyze the flow field of Fig. 1(b). The flow is assumed two-dimensional, inviscid, incompressible, and steady. First, the flow around a circular cylinder with circulation is considered, and then a conformal mapping sequence is used to transform the flow around the cylinder with circulation to the flow around a flat plate at an angle of attack (Fig. 2).

In the original circle plane (z-plane) the flow field consists of a uniform wind V_∞ coming from the negative x-axis, a doublet Λ_0 at the origin to simulate the circular cylinder $|z| = a$, and a bound vortex k_0 at the origin to account for the circulation Γ_0 around the plate. In addition, a point vortex is placed at $z_1(r_1, \theta_1)$ to simulate the leading edge vortex and a sink of strength m_1 ($m_1 < 0$) is also placed at the same point. However, the presence of the vortex and the sink outside the cylinder require additional singularities to be placed inside the cylinder if the cylinder is to remain a streamline of the flow. Thus, the images of the vortex and the sink are also placed at the inverse square point of z_1 and also at the origin (circle theorem, Milne-Thomson, 1958).

Contributed by the Applied Mechanics Division of THE AMERICAN SOCIETY OF MECHANICAL ENGINEERS for publication in the ASME JOURNAL OF APPLIED MECHANICS.

Discussion on this paper should be addressed to the Technical Editor, Professor Lewis T. Wheeler, Department of Mechanical Engineering, University of Houston, Houston, TX 77204-4792, and will be accepted until four months after final publication of the paper itself in the ASME JOURNAL OF APPLIED MECHANICS.

Manuscript received by the ASME Applied Mechanics Division, Aug. 1, 1994; final revision, Jan. 5. 1995. Associate Technical Editor: S. Lichter.

Copyright © 1996 by ASME

Downloaded 04 May 2010 to 171.66.16.33. Redistribution subject to ASME license or copyright; see http://www.asme.org/terms/Terms_Use.cfm

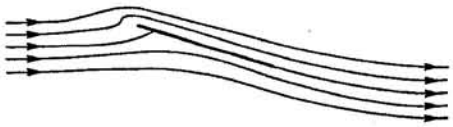


Fig. 1(a)

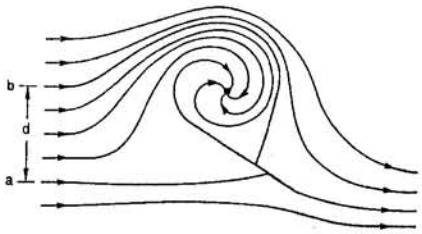


Fig. 1(b)

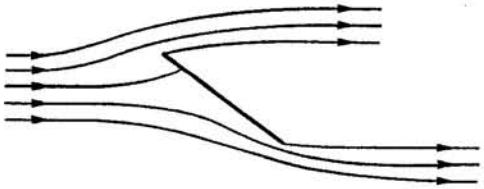


Fig. 1(c)

Fig. 1 Three possible streamline patterns for a flat plate at an angle of attack; (a) attached flow, (b) separated and reattached flow with detached vortex and sink, (c) separated flow

The complex potential for the flow field described above is given as follows:

$$w = V_\infty\left(z + \frac{a^2}{z}\right) + (-m_1 + \iota k)\ln z + (m_1 + \iota k_1)\ln(z - z_1) + (m_1 - \iota k_1)\ln\left(z - \frac{a^2}{\bar{z}_1}\right) \quad (1)$$

where

$$k = k_0 + k_1 \quad (2)$$

and $\bar{z}_1$ is the complex conjugate of z_1. Differentiation of the complex potential gives the velocity field in polar coordinates:

$$\frac{dw}{dz} = (u_r - \iota u_\theta)e^{-\iota\theta}. \quad (3)$$

From (1) and (3) the velocity components are found as follows:

$$u_r = V_\infty\left(1 - \frac{a^2}{r^2}\right)\cos\theta - \frac{m_1}{r} + \frac{m_1[r - r_1\cos(\theta - \theta_1)] + k_1 r_1 \sin(\theta - \theta_1)}{r^2 + r_1^2 - 2rr_1\cos(\theta - \theta_1)} + \frac{m_1 r_1[rr_1 - a^2\cos(\theta - \theta_1)] - k_1 r_1 a^2 \sin(\theta - \theta_1)}{r^2 r_1^2 + a^4 - 2rr_1 a^2\cos(\theta - \theta_1)} \quad (4)$$

$$u_\theta = -V_\infty\left(1 + \frac{a^2}{r^2}\right)\sin\theta - \frac{k}{r} + \frac{m_1 r_1 \sin(\theta - \theta_1) - k_1[r - r_1\cos(\theta - \theta_1)]}{r^2 + r_1^2 - 2rr_1\cos(\theta - \theta_1)} + \frac{m_1 r_1 a^2 \sin(\theta - \theta_1) + k_1 r_1[rr_1 - a^2\cos(\theta - \theta_1)]}{r^2 r_1^2 + a^4 - 2rr_1 a^2\cos(\theta - \theta_1)}. \quad (5)$$

At this point, a conformal mapping sequence is performed to transform the flow about the circle into the flow about a flat plate at an angle of attack. Combining the three steps shown in Fig. 2 we get

$$\zeta = z + \frac{a^2}{z}e^{-2\iota\alpha} \quad (6)$$

or

$$z = \frac{\zeta}{2} + \sqrt{(\zeta/2)^2 - (ae^{-\iota\alpha})^2}. \quad (7)$$

Setting

$$\zeta = \xi + \iota\eta \quad (8)$$

we get

$$\xi = r\cos\theta + \frac{a^2}{r}\cos(\theta + 2\alpha) \quad (9)$$

and

$$\eta = r\sin\theta - \frac{a^2}{r}\sin(\theta + 2\alpha). \quad (10)$$

On the surface of the cylinder (corresponding to the surface of the plate) $r = a$ so

$$\xi_{sp} = a[\cos\theta + \cos(\theta + 2\alpha)] \quad (11)$$

$$\eta_{sp} = a[\sin\theta - \sin(\theta + 2\alpha)]. \quad (12)$$

Now

$$\frac{dw}{d\zeta} = \frac{dw}{dz}\frac{dz}{d\zeta} \quad (13)$$

and

$$\frac{dz}{d\zeta} = \frac{1}{d\zeta/dz} = \frac{z^2 e^{2\iota\alpha}}{z^2 e^{2\iota\alpha} - a^2} = \frac{r^2 e^{\iota(2\alpha+2\theta)}}{r^2 e^{\iota(2\alpha+2\theta)} - a^2}. \quad (14)$$

The velocity components at the surface of the plate u_{rsp} and $u_{\theta sp}$ (calculated in the ζ-plane) may be derived by expanding the right-hand side of the above equation into sines and cosines while using (3)

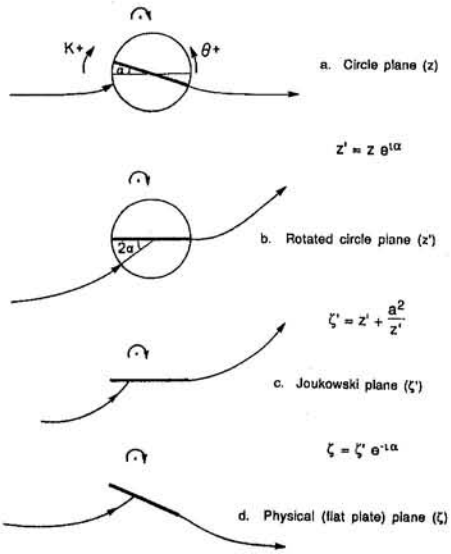


Fig. 2 Steps in mapping sequence from original circle plane to final flat plate plane (physical plane)

Downloaded 04 May 2010 to 171.66.16.33. Redistribution subject to ASME license or copyright; see http://www.asme.org/terms/Terms_Use.cfm

$$[u_{rsp}]_\zeta = \frac{\sin(4\theta + 4\alpha) - 2\sin(2\theta + 2\alpha) - 2\cos(2\theta + 2\alpha)}{2 + 2\cos(4\theta + 4\alpha) - 4\cos(2\theta + 2\alpha)}\,[u_{\theta sc}]_z \tag{15}$$

$$[u_{\theta sp}]_\zeta = \frac{1}{2\cos(2\theta + 2\alpha)}\,[u_{\theta sc}]_z \tag{16}$$

where $u_{\theta sc}$ is the velocity at the surface of the cylinder (calculated in the z-plane).

3 Boundary Conditions

The boundary conditions in the physical plane (of the plate) require that (a) the flow depart smoothly from the trailing edge, and (b) the flow depart smoothly from the leading edge. In other words, an attempt is made to satisfy the Kutta condition at both edges of the plate. In addition, the vortex/sink combination must be located at an equilibrium point in the flow field, that is, a point where the velocity induced by the remaining components of the flow field is zero. The last condition is that the total aerodynamic force on the plate must be normal to its plane because the flow is assumed to be inviscid. These conditions can be expressed as follows:

3.1 Kutta Condition at the Trailing Edge of the Plate. From (15) and (16) with $\theta = -\alpha$ we find the velocity components at the trailing edge of the plate:

$$[u_{rsp}]_\zeta^{TE} = -\frac{1}{0}\,[u_{\theta sc}]_z^{\theta=-\alpha} \tag{17}$$

$$[u_{\theta sp}]_\zeta^{TE} = -\frac{1}{0}\,[u_{\theta sc}]_z^{\theta=-\alpha}. \tag{18}$$

To satisfy the Kutta condition at the trailing edge (i.e., u_r finite and $u_\theta = 0$) we must require that

$$[u_{\theta sc}]_z^{\theta=-\alpha} = 0 \tag{19}$$

or, from (5) with $r = a$ and $\theta = -\alpha$

$$(2V_\infty a\sin\alpha - k)[r_1^2 + a^2 - 2r_1 a\cos(\theta_1 + \alpha)] - 2m_1 r_1 a\sin(\theta_1 + \alpha) + k_1(r_1^2 - a^2) = 0. \tag{20}$$

3.2 Kutta Condition at the Leading Edge of the Plate. In a similar fashion, to satisfy the Kutta condition at the leading edge we get

$$[u_{\theta sc}]_z^{\theta=\pi-\alpha} = 0 \tag{21}$$

which again, using (5) with $r = a$ and $\theta = -\alpha$ yields

$$(2V_\infty a\sin\alpha + k)[r_1^2 + a^2 + 2r_1 a\cos(\theta_1 + \alpha)] - 2m_1 r_1 a\sin(\theta_1 + \alpha) - k_1(r_1^2 - a^2) = 0. \tag{22}$$

3.3 Equilibrium Point Condition. Equation (3) cannot be used to find the conditions which make the velocity vanish at the location of the sink and vortex because the velocity given by (3) is singular there. Instead, the usual limiting process is used to find the velocity components at the center of the vortex/sink combination. The strengths of the singularities can then be adjusted so that they are stationary in the presence of the plate. Following this procedure the complex velocity function at the equilibrium point in the physical plane is found:

$$[u_p - \iota v_p]_{\zeta_1} = \left[(u_c - \iota v_c)\frac{dz}{d\zeta}\right]_{z_1} - \frac{1}{2}(m_1 + \iota k_1)\frac{[d^2z/d\zeta^2]_{\zeta_1}}{[dz/d\zeta]_{\zeta_1}} = 0. \tag{23}$$

The relationship between the cartesian velocity components employed in (23) and their polar counterparts is shown in Fig. 3. The derivative $dz/d\zeta$ is given by (14) from which we may also get

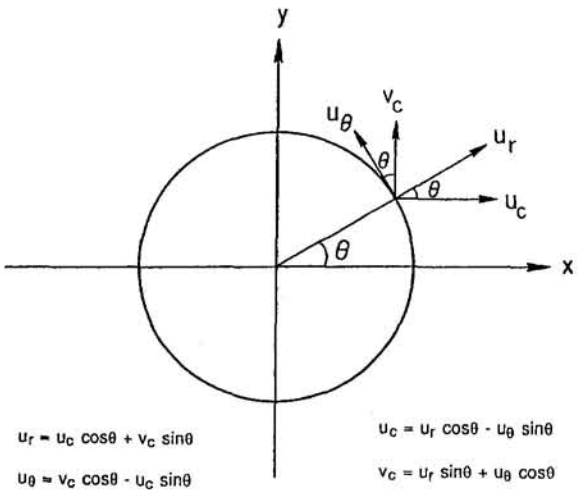


Fig. 3 Velocity components in cartesian and polar coordinate systems

$$\frac{d^2z}{d\zeta^2} = \frac{d}{d\zeta}\left(\frac{dz}{d\zeta}\right) = \frac{d}{d\zeta}\left[\frac{z^2e^{2\iota\alpha}}{z^2e^{2\iota\alpha} - a^2}\right]. \tag{24}$$

Now we may substitute z from (7) into (24), take the derivative and substitute back ζ from (6) to get

$$\frac{d^2z}{d\zeta^2} = \frac{a^2e^{2\iota\alpha}[4z^4 + 3(z^2 + a^2e^{-2\iota\alpha})^2]}{2z(a^2e^{-2\iota\alpha} - z^2)(z^2e^{2\iota\alpha} - a^2)^2}. \tag{25}$$

Using the transformations in Fig. 2 and substituting (7) and (25) into (23), we finally get

$$[u_{r1}\cos\theta_1 - u_{\theta 1}\sin\theta_1) - \iota(u_{r1}\sin\theta_1 + u_{\theta 1}\cos\theta_1)]z_1^2e^{2\iota\alpha} - (m_1 + \iota k_1)\frac{a^2[4z_1^4 + 3(z_1^2 + a^2e^{-2\iota\alpha})^2]}{2z_1(z_1^2 - a^2e^{-2\iota\alpha})^2} = 0 \tag{26}$$

where

$$z_1 = r_1e^{\iota\theta_1} = r_1(\cos\theta_1 + \iota\sin\theta_1). \tag{27}$$

Equation (26) is now split into real and imaginary parts while u_{r1} and $u_{\theta 1}$ are replaced with their equivalents from (4) and (5) setting $r = r_1$ and $\theta = \theta_1$:

$$\begin{aligned}
&2V_\infty r_1^5(r_1^2 - a^2)^2\cos\theta_1\cos(6\theta_1 + 2\alpha)\\
&- 4V_\infty r_1^3a^2(r_1^2 - a^2)^2\cos\theta_1\cos 4\theta_1\\
&+ 2V_\infty r_1a^4(r_1^2 - a^2)^2\cos\theta_1\cos(2\theta_1 - 2\alpha)\\
&- 2V_\infty r_1^5(r_1^4 - a^4)\sin\theta_1\sin(6\theta_1 + 2\alpha)\\
&+ 4V_\infty r_1^3a^2(r_1^4 - a^4)\sin\theta_1\sin 4\theta_1 - 2V_\infty r_1a^4(r_1^4 - a^4)\\
&\times\sin\theta_1\sin(2\theta_1 - 2\alpha) - 2k_0r_1^6(r_1^2 - a^2)\sin(6\theta_1 + 2\alpha)\\
&+ 4k_0r_1^4a^2(r_1^2 - a^2)\sin 4\theta_1 - 2k_0r_1^2a^4(r_1^2 - a^2)\\
&\times\sin(2\theta_1 - 2\alpha) + 2k_1r_1^6a^2\sin(6\theta_1 + 2\alpha)\\
&+ k_1r_1^4a^2(7r_1^2 - 11a^2)\sin 4\theta_1\\
&+ 7k_1r_1^4a^2(r_1^2 - a^2)\cos 4\theta_1 + 2k_1r_1^2a^4(3r_1^2 - 2a^2)\\
&\times\sin(2\theta_1 - 2\alpha) + 6k_1r_1^2a^4(r_1^2 - a^2)\cos(2\theta_1 - 2\alpha)\\
&+ 3(k_1 - m_1)(r_1^2 - a^2)a^6(\cos 4\alpha - \sin 4\alpha) + 2m_1r_1^6a^2\\
&\times\cos(6\theta_1 + 2\alpha) - m_1r_1^4a^2(7r_1^2 - 3a^2)\cos 4\theta_1\\
&- 7m_1r_1^4a^2(r_1^2 - a^2)\sin 4\theta_1 - 2m_1r_1^2a^4(3r_1^2 - 4a^2)\\
&\times\cos(2\theta_1 - 2\alpha) - 6m_1r_1^2a^4(r_1^2 - a^2)\\
&\times\sin(2\theta_1 - 2\alpha) = 0
\end{aligned} \tag{28}$$

Downloaded 04 May 2010 to 171.66.16.33. Redistribution subject to ASME license or copyright; see http://www.asme.org/terms/Terms_Use.cfm

$$
\begin{aligned}
&2V_\infty r_1^5(r_1^2 - a^2)^2 \cos\theta_1 \sin(6\theta_1 + 2\alpha) \\
&- 4V_\infty r_1^3 a^2(r_1^2 - a^2)^2 \cos\theta_1 \sin 4\theta_1 \\
&+ 2V_\infty r_1 a^4(r_1^2 - a^2)^2 \cos\theta_1 \sin(2\theta_1 - 2\alpha) \\
&+ 2V_\infty r_1^5(r_1^4 - a^4) \sin\theta_1 \cos(6\theta_1 + 2\alpha) \\
&- 4V_\infty r_1^3 a^2(r_1^4 - a^4) \sin\theta_1 \cos 4\theta_1 + 2V_\infty r_1 a^4(r_1^4 - a^4) \\
&\times \sin\theta_1 \cos(2\theta_1 - 2\alpha) + 2k_0 r_1^6(r_1^2 - a^2) \\
&\times \cos(6\theta_1 + 2\alpha) - 4k_0 r_1^4 a^2(r_1^2 - a^2) \cos 4\theta_1 \\
&+ 2k_0 r_1^2 a^4(r_1^2 - a^2) \cos(2\theta_1 - 2\alpha) - 2k_1 r_1^6 a^2 \\
&\times \cos(6\theta_1 + 2\alpha) - k_1 r_1^4 a^2(7r_1^2 - 11a^2) \cos 4\theta_1 \\
&- 7k_1 r_1^4 a^2(r_1^2 - a^2) \sin 4\theta_1 - 2k_1 r_1^2 a^4(3r_1^2 - 2a^2) \\
&\times \cos(2\theta_1 - 2\alpha) - 6k_1 r_1^2 a^4(r_1^2 - a^2) \sin(2\theta_1 - 2\alpha) \\
&- 3(k_1 + m_1)(r_1^2 - a^2)a^6(\cos 4\alpha - \sin 4\alpha) + 2m_1 r_1^6 a^2 \\
&\times \sin(6\theta_1 + 2\alpha) - m_1 r_1^4 a^2(7r_1^2 - 3a^2) \sin 4\theta_1 \\
&- 7m_1 r_1^4 a^2(r_1^2 - a^2) \cos 4\theta_1 - 2m_1 r_1^2 a^4(3r_1^2 - 4a^2) \\
&\times \sin(2\theta_1 - 2\alpha) - 6m_1 r_1^2 a^4(r_1^2 - a^2) \\
&\times \cos(2\theta_1 - 2\alpha) = 0. \quad (29)
\end{aligned}
$$

3.4 Normal Force Condition. The inclusion of two singularities (the vortex and the sink) at the equilibrium point of the flow requires one additional equation to get a unique solution for the strengths and the position of these singularities. Such a condition will be sought in relation with the physics of the flow. The flow has been assumed inviscid, therefore the total aerodynamic force on the flat plate must be perpendicular to the plane of the plate. This implies that

$$\tan\alpha = \frac{D}{L}. \quad (30)$$

The aerodynamic lift and drag forces (L and D) can be expressed in terms of the unknown (total) vortex and sink strengths (k and m_1). The drag force in this model comes from the sink. Figure 1(b) shows the streamline pattern for the flat plate at an angle of attack with a detached vortex and a sink at the equilibrium point. The mass flow rate between streamlines a and b (which are at a distance d apart) must be equal to the rate at which the mass flows into the sink, i.e.,

$$-\rho V_\infty db = m_1 \rho b 2\pi \quad (31)$$

where b is the span of the plate and ρ is the fluid density. Now the drag on the plate is equal to the rate of the fluid momentum loss,

$$D = (-\rho V_\infty db)V_\infty = (m_1 \rho b 2\pi)V_\infty, \quad (32)$$

while the lift on the plate can be evaluated from the Kutta-Joukowski law,

$$L = \rho V_\infty \Gamma b, \quad (33)$$

and since the total circulation around the plate is

$$\Gamma = 2\pi k,$$

(33) becomes

$$L = 2\pi\rho V_\infty bk. \quad (34)$$

Substitution of (32) and (34) into (30) yields

$$\tan\alpha = \frac{m_1}{k}. \quad (35)$$

3.5 Dimensionless Parameters. A system of five equations has been developed ((20), (22), (28), (29), and (35)) in five unknowns (the two vortex strengths k_0 and k_1, the sink strength m_1, and the equilibrium point coordinates r_1, θ_1). To facilitate the solution of this system the following dimensionless parameters are defined:

$$K_0 = \frac{k_0}{aV_\infty} \quad (36)$$

$$K_1 = \frac{k_1}{aV_\infty} \quad (37)$$

$$K = \frac{k}{aV_\infty} \quad (38)$$

$$M_1 = \frac{m_1}{aV_\infty} \quad (39)$$

$$R_1 = \frac{r_1}{a}. \quad (40)$$

A four-dimensional Newton-Raphson algorithm has been used to solve the aforementioned system of equations after nondimensionalization according to (36)–(40) and elimination of M_1 using (35). The solution gives the equilibrium point location, the strength of the bound and leading edge vortices as well as the sink strength. The results are presented in the following sections.

4 Results

4.1 Equilibrium Point Locus. Figure 4 shows the locus of the equilibrium point for $0 \le \alpha \le 90$ deg. The vortex/sink combination starts at the leading edge of the plate for zero angle of attack and follows almost a circular path. It moves initially up and forward from the leading edge as the angle of attack increases. It reaches its highest position, approximately 0.1 c above the plate (where c is the plate chord length), for $\alpha \approx$ 15 deg. Then it moves down and crosses the plane of the plate at roughly 0.2 c ahead of the leading edge for $\alpha \approx 35$ deg. As the angle of attack increases further, the equilibrium point moves below the chord line of the plate. At $\alpha \approx 73$ deg where the lower stagnation point reaches the trailing edge the equilibrium point is still ahead of the leading edge (0.12 c) and below the plate (0.3 c). Finally, the locus ends at a point approximately 0.2 c below the plate and 0.1 c behind the leading edge.

The same figure also shows the Saffman and Sheffield solution for three angles of attack. One of the common elements in both models is the fact that the equilibrium point, at least initially, moves forward as the angle of attack increases. One of the main differences, on the other hand, is the fact that the Saffman and Sheffield solution gives a vortex position always above the chord line of the plate while the present model gives a vortex position below the chord line of the plate for angles of attack greater than about 35 deg. However, Huang and Chow (1982) also found solutions on the lower surface of their Joukowski airfoil.

4.2 Vortex and Sink Strengths. The bound vortex strength increases almost linearly with angle of attack while the leading edge vortex strength grows non linearly reaching a maximum at $\alpha = 45$ deg and dropping to zero at $\alpha \approx 73$ deg when the lower stagnation point reaches the trailing edge and moves off the plate (Fig. 5). Thus, the total circulation is also nonlinear with angle of attack and has a maximum at $\alpha = 50$ deg (Fig. 5). The sink strength on the other hand, starts off with very small values and increases almost linearly with angle of attack up to $\alpha \approx 70$ deg. Then at $\alpha \approx 77$ deg it starts to decrease (Fig. 6).

Downloaded 04 May 2010 to 171.66.16.33. Redistribution subject to ASME license or copyright; see http://www.asme.org/terms/Terms_Use.cfm

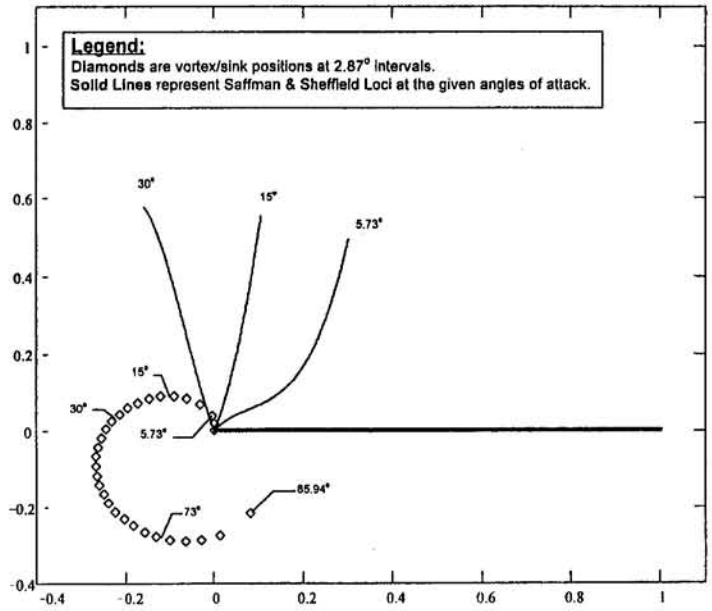


Fig. 4 Comparison of equilibrium point loci for the present and Saffman and Sheffield models

A direct comparison of the vortex strength with that of the Saffman and Sheffield model is not possible because of the multiplicity of their solutions for a given angle of attack. However, a general observation can be made by comparison of Figs. 5 in this paper, Fig. 3 in Saffman and Sheffield, and Figs. 3, 4, and 5 in Huang and Chow, that the vortex appears to be much weaker for a given angle of attack and/or given vortex distance from the plate when it is combined with a sink as in the present model. Also, regardless of the position of the vortex, its strength remains positive (clockwise, at least up to $\alpha \approx 73$ deg when the lower stagnation point reaches the trailing edge) while in the Huang and Chow (Fig. 5) the vortex strengths for the solutions on the lower surface are negative (counterclockwise).

4.3 Pressure Distribution on the Plate. The pressure distribution has been calculated on the ζ' plane (the most convenient one since the plate is horizontal and lies along the ζ'-axis). From the sequence of transformations shown in Fig. 2 the velocity components at the surface of the plate are

$$u_{rsp} = -\frac{1}{2}\frac{\cos\theta}{\sin(\theta+\alpha)}u_{\theta sc} \tag{41}$$

$$u_{\theta sp} = -\frac{1}{2}\frac{\sin\theta}{\sin(\theta+\alpha)}u_{\theta sc}. \tag{42}$$

From the last two equations the total velocity at the surface of the plate is

$$u_{sp} = \tfrac{1}{2}u_{\theta sc}\csc(\theta+\alpha). \tag{43}$$

From (5) we may calculate the velocity at the surface of the cylinder in terms of the dimensionless parameters defined in (36)–(40)

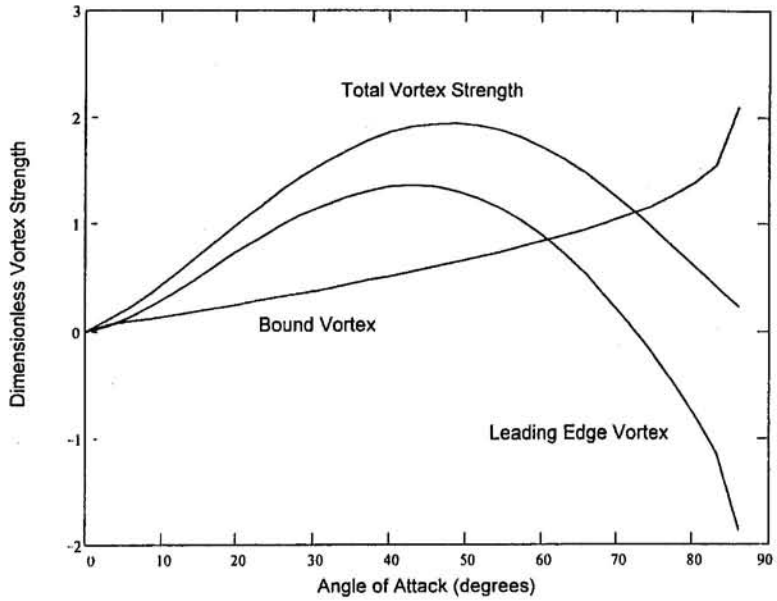


Fig. 5 Vortex strength versus angle of attack

Downloaded 04 May 2010 to 171.66.16.33. Redistribution subject to ASME license or copyright; see http://www.asme.org/terms/Terms_Use.cfm

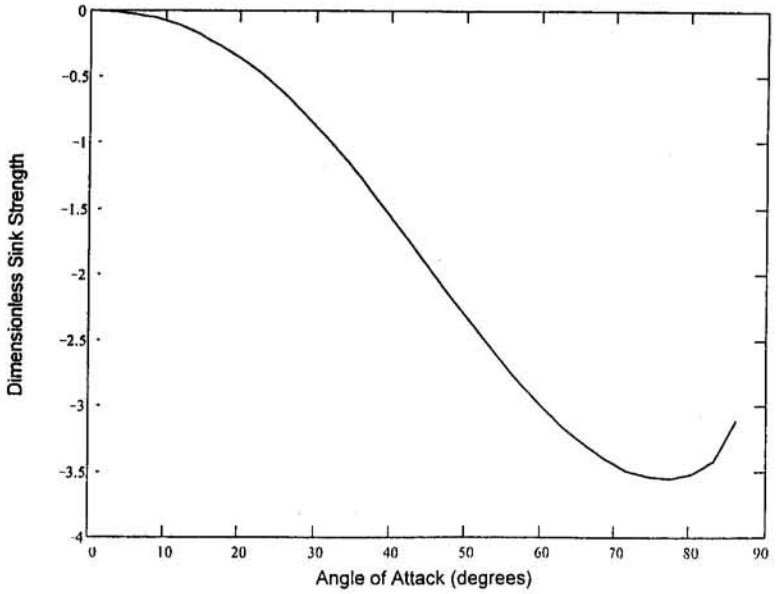


Fig. 6 Sink strength versus angle of attack

$$\frac{u_{\theta sc}}{V_\infty} = -2 \sin \theta - K + \frac{2M_1R_1 \sin (\theta - \theta_1) + K_1(R_1^2 - 1)}{1 + R_1^2 - 2R_1 \cos (\theta - \theta_1)}. \quad (44)$$

Substituting (44) as well as the corresponding solution sets (for K, K_1, M_1, R_1, and θ_1) for each angle of attack into (43) we find the pressure distribution on the surface of the plate from

$$C_{psp} = 1 - \frac{u_{sp}^2}{V_\infty^2} \quad (45)$$

where the pressure coefficient is defined as $C_p = (p - p_\infty)/[(1/2)\rho V_\infty^2]$. C_{psp} has been plotted for four angles of attack in Fig. 7 where the horizontal axis measures the non-dimensional parameter

$$n = \cos (\theta + \alpha) = \frac{\xi'_{sp}}{2a} \quad (46)$$

which varies from -1 at the leading edge to $+1$ at the trailing edge. As it may be seen from the pressure plots, both stagnation points ($C_p = 1$) move towards the trailing edge as the angle of attack increases but the one on the lower surface moves faster, being at about 70 percent of the chord from the leading edge at $\alpha = 60$ deg while the one on the upper surface is only at the midchord point. The pressure plots also show two suction peaks under the vortex locations as expected.

4.4 Lift and Drag. As an interesting part of this analysis one would like to see how the model discussed in this paper (Fig. 1(b)) compares in terms of lift and drag with the two classical solutions mentioned in the introduction, namely (i) attached flow over the plate with the Kutta condition satisfied at the trailing edge only and a singularity (infinite suction) at the leading edge (Fig. 1(a)), and (ii) the Helmholtz solution of separated flow over the plate (Fig. 1(c)).

The lift and the drag coefficients for the three models are given below. For the attached flow model,

$$C_{L1} = 2\pi \sin \alpha \quad C_{D1} = 0. \quad (47)$$

For the leading edge vortex model considered here

$$C_{L2} = \pi K \quad C_{D2} = -\pi M_1. \quad (48)$$

For the separated flow model,

$$C_{L3} = \frac{\pi \sin 2\alpha}{4 + \pi \sin \alpha} \quad C_{D3} = \frac{2\pi \sin^2 \alpha}{4 + \pi \sin \alpha}. \quad (49)$$

Figure 8 shows that the present model with the leading edge vortex exhibits the highest lift coefficient at least up to 60 deg angle of attack. At higher angles of attack it seems, again from Fig. 8 and (47)–(49) that the first model would give higher lift coefficients. From a practical point of view, however, this conclusion is misleading since even at moderate angles of attack attached flow is not possible over a flat plate with a sharp leading edge. Thus, one must keep in mind that the first model breaks down at some rather low angle of attack.

Figure 9 shows a comparison between the drag of the second and third models (since the first one gives zero drag for inviscid flow). As it may be seen, the leading edge vortex model gives much higher drag coefficients than the third model despite the fact that the flow is totally separated on the upper surface of the plate in the third model. This should not be surprising, however, the drag in the leading edge vortex model resulting from the large momentum loss associated with the sink (Fig. 1(b)). The fact that there is a large amount of drag associated with the presence of the vortex is also in agreement with results from previous investigations (Walton, 1974; Kruppa, 1977).

The lift-to-drag ratio for the second and third models is the same since $L/D = \cot \alpha$ in both cases. The second model yields a much higher lift than the third one but it also gives a much higher drag. This drag, can be thought of as induced drag (lift related drag). This is the only possible classification since the flow has been assumed inviscid.

4.5 Stability of the Vortex/Sink. Whether the vortex-lift benefits are realized in practice depends, to a large degree, upon the stability of the vortex/sink combination. Huang and Chow found that their vortex (which was considered without a sink) was always unstable for all loci emanating from the leading edge. Only for portions of some of the loci emanating from the trailing edge of their flat plate were their vortices stable. Adding thickness did not help the stability of their vortices near the leading edge, however, it offered more stable locations near the trailing edge. On the other hand, camber and angle of attack diminished the vortex-trapping ability of their airfoils.

Perhaps more relevant to the present study are the stability results of Rossow, since his model included also a sink. Rossow

Downloaded 04 May 2010 to 171.66.16.33. Redistribution subject to ASME license or copyright; see http://www.asme.org/terms/Terms_Use.cfm

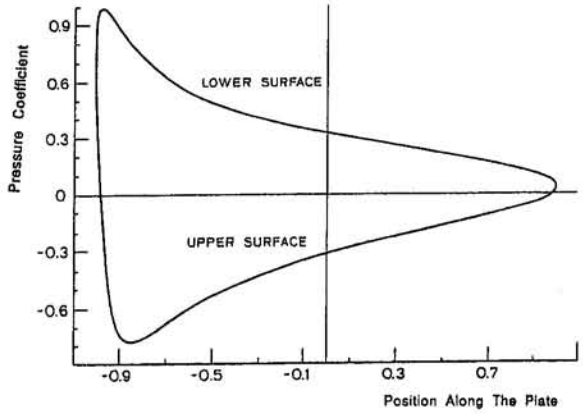


Fig. 7(a) for $\alpha = 10$ deg

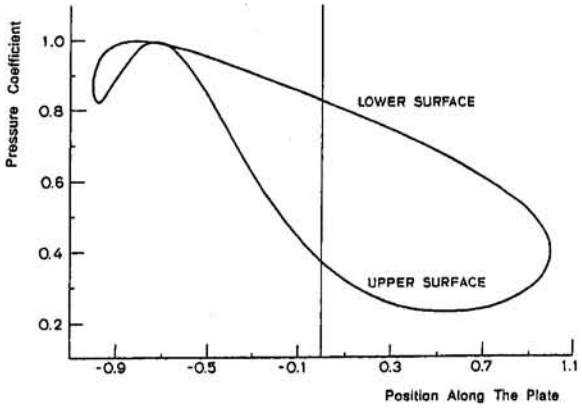


Fig. 7(b) for $\alpha = 30$ deg

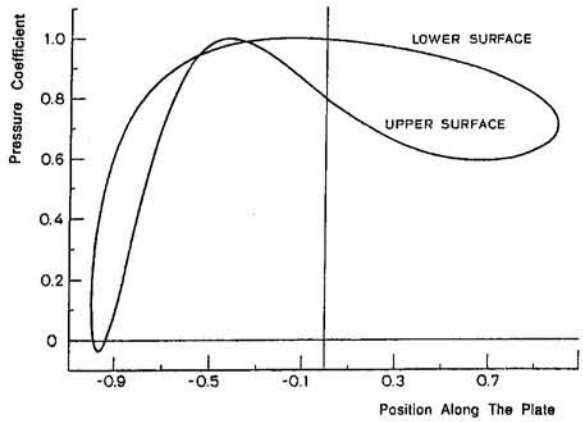


Fig. 7(c) for $\alpha = 45$ deg

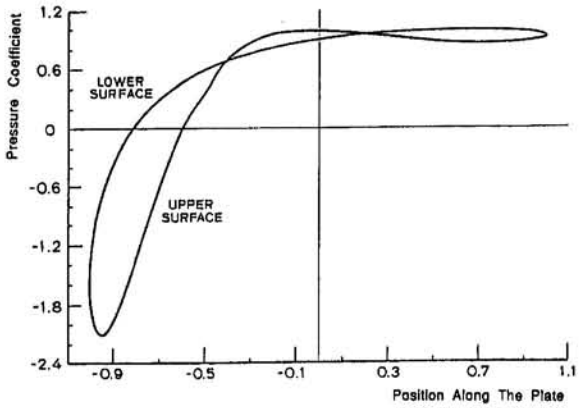


Fig. 7(d) for $\alpha = 60$ deg

Fig. 7 Pressure distribution on the plate

found that his vortex/sink pair would return to its equilibrium position when disturbed but only from a limited region of starting points. Thus, one may expect that the present model will at best exhibit a very delicate stability like in Rossow's case or at worse, no stability at all like in Huang and Chow's case. It is worth mentioning, however, Rossow's conclusion that a point vortex does not adequately represent the flow field as it rolls up around the leading edge. Rossow based his conclusion on observations during experiments that a rolled-up vortex sheet which spiraled inward toward the center of the cavity was present rather than a point vortex. Thus, one may argue that the instability observed with Huang and Chow's as well as with

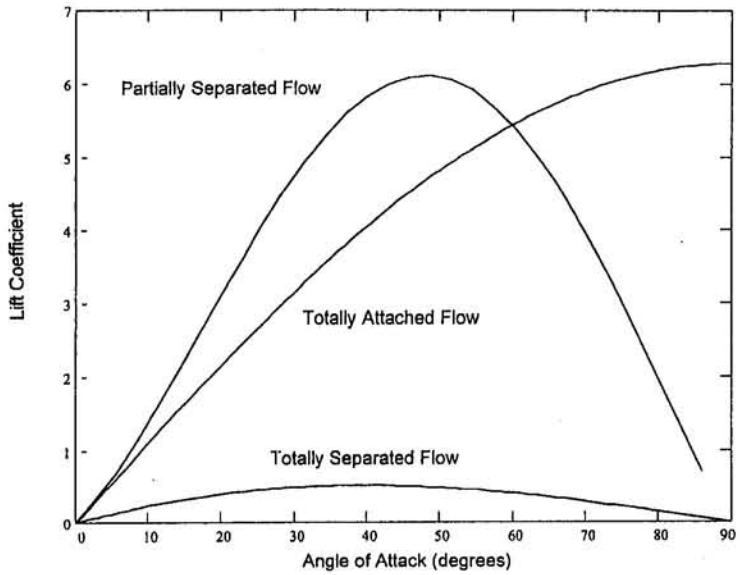


Fig. 8 Lift characteristics

Downloaded 04 May 2010 to 171.66.16.33. Redistribution subject to ASME license or copyright; see http://www.asme.org/terms/Terms_Use.cfm

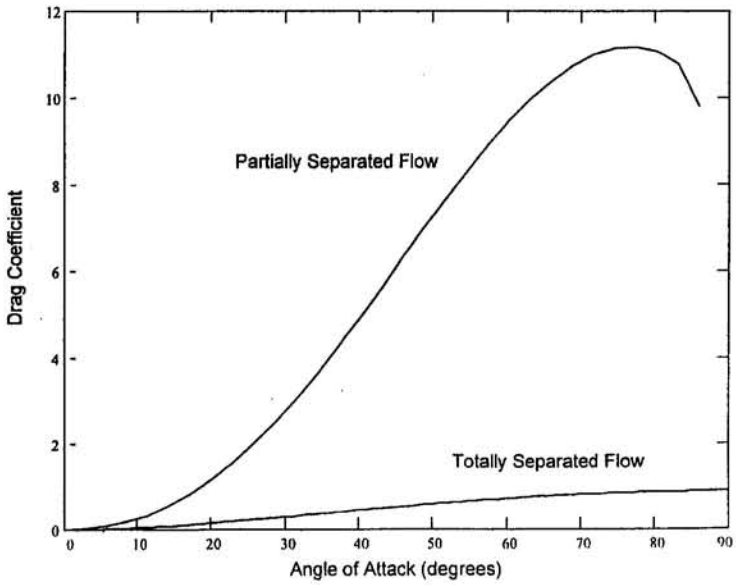


Fig. 9 Drag characteristics

Rossow's models and which should also be expected to extend to the present model, has to do more with the fact that the actual three-dimensional distribution of vorticity is not represented realistically with the point vortex model.

5 Conclusions

The possibility of maintaining a free vortex over a high aspect ratio wing for the purpose of increasing its lift at low speeds was explored using a simple, steady, two-dimensional, inviscid, incompressible flow model. A flat plate was considered at an angle of attack, with a stationary vortex detached on top like in the Saffman and Sheffield model, but a sink was also added following observations in nature where most vortices appear to be coupled with axial flow along their cores. Based on the simplified analysis presented in this paper, the following conclusions may be drawn:

(*i*) The present model of a flat plate with a detached vortex close to its leading edge indicates that lift coefficients up to around 6 are achievable. Higher values should also be possible if thickness and camber are added, i.e., considering an airfoil instead of a flat plate (Rossow, 1978; Huang and Chow, 1982).

(*ii*) To satisfy the Kutta condition at both the trailing edge and the leading edge, the presence of the sink is also necessary (see (20) and (22)). As was mentioned earlier, this seems to be in agreement with physical observations of steady vortices in nature which, excluding some low Reynolds number cases, tend to form only when there is a mechanism to evacuate their core.

(*iii*) For a given lift it was found that two possible solutions exist for the location of the equilibrium point and the corresponding strengths of the vortex and sink. One occurs at a lower angle of attack and gives a weaker sink and therefore less drag, while the other one occurs at a higher angle of attack and gives a stronger sink and the associated higher drag. The vortex strengths do not differ much for the two solutions since they are closely related to the lift (which is the same for the two solutions). This result is also in agreement with Rossow (1978).

References

Brown, C. E., and Michael, W. H., 1954, "On Slender Delta Wings with Leading Edge Separation," *Journal of the Aeronautical Sciences,* Vol. 21, Oct., pp. 690–694; also NACA TN-3430, Jan. 1955.

Campbell, J. F., 1975, "Effects of Spanwise Blowing on the Pressure Field and Vortex-Lift Characteristics of a 44° Swept Trapezoidal Wing," NACA TN D-7907, June.

Huang, M. K., and Chow, C. Y., 1982, "Trapping of a Free Vortex by Joukowski Airfoils," *AIAA Journal,* Vol. 20, No. 3, Mar., pp. 292–298.

Hummel, D., 1978, "On the Vortex Formation Over a Slender Wing at Large Angles of Incidence," AGARD CP-247, paper no. 15.

Kruppa, E. W., 1977, "A Wind Tunnel Investigation of the Kasper Vortex Concept," AIAA paper 77-310, Jan.

Mangler, K. W., and Smith, J. H. B., 1957, "A Theory of the Flow past a Slender Wing with Leading Edge Separation," RAE, Report Aero 2593.

Milne-Thomson, L. M., 1958, *Theoretical Aerodynamics,* Dover, New York.

Mourtos, N. J., 1990, "Control of Vortical Separation on a Circular Cone," *Aeronautical Journal,* Vol. 94, pp. 213–219.

Rossow, V. J., 1978, "Lift Enhancement by an Externally Trapped Vortex," *Journal of Aircraft,* Vol. 15, No. 9, pp. 618–625.

Sacks, A. H., Lundberg, R. E., and Hanson, C. W., 1967, "A Theoretical Investigation of the Aerodynamics of Slender Wing-Body Combinations Exhibiting Leading Edge Separation," NASA CR-719.

Saffman, P. G., and Sheffield, J. S., 1977, "Flow over a Wing with an Attached Free Vortex," *Studies in Applied Mathematics,* Vol. 57, pp. 107–117.

Walton, D., 1974, "A Brief Wind Tunnel Test of the Kasper Airfoil," *Soaring,* Vol. 38, No. 11, Nov., pp. 26–27.

Downloaded 04 May 2010 to 171.66.16.33. Redistribution subject to ASME license or copyright; see http://www.asme.org/terms/Terms_Use.cfm

Journal of Applied Mechanics

Brief Notes

A Brief Note is a short paper that presents a specific solution of technical interest in mechanics but which does not necessarily contain new general methods or results. A Brief Note should not exceed 1500 words *or equivalent* (a typical one-column figure or table is equivalent to 250 words; a one line equation to 30 words). Brief Notes will be subject to the usual review procedures prior to publication. After approval such Notes will be published as soon as possible. The Notes should be submitted to the Technical Editor of the JOURNAL OF APPLIED MECHANICS. Discussions on the Brief Notes should be addressed to the Editorial Department, ASME, United Engineering Center, 345 East 47th Street, New York, N. Y. 10017, or to the Technical Editor of the JOURNAL OF APPLIED MECHANICS. Discussions on Brief Notes appearing in this issue will be accepted until two months after publication. Readers who need more time to prepare a Discussion should request an extension of the deadline from the Editorial Department.

Viscoelastic Minimum Principles Revisited

S. Hazanov[1]

A problem of viscoelastic counterparts for the elastic minimum theorems is considered. A theorem is proved that gives a general algorithm for the construction of such viscoelastic minimum functionals. The established results are applied for the theoretical evaluation of the effective properties of inhomogeneous viscoelastic materials. As an example, simple bounds on the effective properties of viscoelastic composites are obtained.

1 Introduction

The problem under consideration is to construct for the theory of linear viscoelasticity some minimum variational principles analogous to the elastic ones, namely to the Lagrange and Castigliano theorems. The theoretical and practical importance of this problem cannot be overestimated, especially in view of the recent success in the production and application of viscoelastic composite materials. Numerous attempts to resolve this problem are known, but the question still remains open. The state of art can be briefly summarized as follows:

(a) In Gurtin (1963) certain variational theorems were proposed, based on the notion of the Stieltjes convolution of stress and deformation tensors $\boldsymbol{\sigma}$ and $\boldsymbol{\epsilon}$:

$$\boldsymbol{\sigma}\circ\boldsymbol{\epsilon} = \int_0^t \sigma(t-u)d\epsilon(u). \tag{1}$$

The main term in the basic functional for a variable kinematically admissible strain field $\tilde{\boldsymbol{\epsilon}}$ was taken in the biconvolution form $(\mathbf{r}\circ\tilde{\boldsymbol{\epsilon}}\circ\tilde{\boldsymbol{\epsilon}})$, with $\mathbf{r}$ the relaxation functions tensor. The theorems do work, but the biconvolution operator and hence the basic functional itself, do not have a physical sense. Moreover, the obtained variational principles give only the stationarity conditions and not the extremal ones.

(b) In Christensen (1971) another kind of minimum theorem was proposed, this time based on the classical Staverman-Schwarzl free energy presentation and on the work-type operator expressions:

$$W = \int_0^t \sigma d\epsilon. \tag{2}$$

These theorems also work pretty well, but they are valid only for the time factorizable solutions and only for isotropic materials with a constant Poisson's ratio.

(c) Among other important results in the mentioned domain one can recall Schapery (1964, 1974, 1984, 1990)—a profound study of viscoelastic variational principles with their application for evaluation of the bounds on composite viscoelastic properties; Breuer (1973)—theorems for an incompressible isotropic behaviour; Brilla (1975)—variational theorems in the Laplace space; Rabotnov (1980)—a detailed review with numerous original ideas and contributions; Huet (1992)—a pseudo-convolutive operator method for virtually symmetrizable problems; Tonti (1973), Reiss-Haug (1978), Kulejevska (1984), Giorgi and Marzocchi (1992), and Fabrizio and Morro (1992)—a general and powerful mathematical framework of the variational approach in physics that has not yet found wide engineering applications.

The key point in the general problem formulated above is the construction of such a functional (bilinear form) of virtual strain/stress fields that will have a physical sense and be at once symmetric and positive definite. In elasticity this is simply the potential energy, equal to the work done during the deformation cycle. But in linear viscoelasticity, even without ageing, no general expression is known yet for the free-energy functional. On the other hand, an automatical replacement of elastic constants by convolution operators (the classic Volterra principle) proves to be efficient only in linear relationships, but not in energetic ones, that are usually of a quadratic structure.

To illustrate this point, consider for example the Stieltjes convolution $\boldsymbol{\sigma}_1\circ\boldsymbol{\epsilon}_2 = \mathbf{r}\circ\boldsymbol{\epsilon}_1\circ\boldsymbol{\epsilon}_2$ basic for the Gurtin's method. Though being symmetric with respect to $\boldsymbol{\epsilon}_1$ and $\boldsymbol{\epsilon}_2$, this operator is not positive definite in the sense that we cannot guarantee its positivity for all real strain histories. But the positive definiteness is absolutely necessary for minimization procedures. Turning now to the Christensen's approach, we see that its basic

[1] Swiss Federal Institute of Technology, Department of Materials, MX-G, Ecublens, CH 1015, Lausanne, Switzerland.

Contributed by the Applied Mechanics Division of THE AMERICAN SOCIETY OF MECHANICAL ENGINEERS for publication in the ASME JOURNAL OF APPLIED MECHANICS. Manuscript received by the ASME Applied Mechanics Division, Oct. 21, 1994; final revision, May 15, 1995. Associate Technical Editor: C. F. Shih.

Copyright © 1996 by ASME

Downloaded 04 May 2010 to 171.66.16.33. Redistribution subject to ASME license or copyright; see http://www.asme.org/terms/Terms_Use.cfm

functional term, the work-type expression Eq. (2), is positive definite with respect to the strain histories (because of the work positivity) but is not symmetric.

The present communication shows that the traditional research direction in the formulated problem seems to lead to a dead end. A more general approach is proposed, leading in some particular cases to simple solutions that may be useful for applications.

2 Conditional Solution

For the sake of future analysis, we introduce several notations: D is a domain occupied in space by the body under study; ∂D its boundary; F^d, ∂D_σ, and ∂D_ξ parts of the boundary loaded correspondingly by prescribed mass forces; surface forces P^d, and surface displacements ξ^d. Then a theorem can be formulated:

Kinematic Theorem. Let functional H be

$$H(\tilde{\epsilon}) = \int_D U(\tilde{\epsilon})dV - \int_D F^d * \tilde{\xi} dV - \int_{\partial D_\sigma} P^d * \tilde{\xi} d\Sigma \quad (3)$$

where * is a linear operator on the space of kinematically admissible strain and displacement histories $\tilde{\epsilon}(t)$, $\tilde{\xi}(t)$, $-\infty \le t \le \infty$ and U is a differentiable functional (in the sense of Frechet).

Then functional H in the class of kinematically admissible fields reaches its minimum for the real strain and displacement fields only under the following conditions:

$$\begin{aligned} &\text{(a) } dU(\boldsymbol{\epsilon}) = \boldsymbol{\sigma} * \boldsymbol{\delta\epsilon}; \\ &\text{(b) } d^2U(\boldsymbol{\epsilon}) \text{ is a strongly positive quadratic functional.} \end{aligned} \quad (4)$$

Here dU and d^2U are correspondingly the first and the second Frechet differentials of the functional U and $\boldsymbol{\delta\epsilon}$ is a variation of $\boldsymbol{\epsilon}$.

Proof: Starting from the static equilibrium and the compatibility conditions,

$$\text{div } \boldsymbol{\sigma} = -F^d; \quad \boldsymbol{\epsilon} = \text{sym grad } \xi, \quad (5)$$

and recalling the divergence theorem,

$$\int_D \sigma * \tilde{\epsilon}\, dV = \int_D F^d * \tilde{\xi} dV + \int_{\partial D_\sigma} P^d * \tilde{\xi} d\Sigma + \int_{\partial D_\xi} P * \xi^d d\Sigma, \quad (6)$$

we see that the first Frechet differential of the functional H in the point $\boldsymbol{\epsilon}$ corresponding to the real strain field is

$$dH(\epsilon) = \int_D dU(\epsilon)dV - \int_D \sigma * \delta\epsilon\, dV. \quad (7)$$

The second Frechet differential will be expressed in the form

$$d^2H(\epsilon) = \int_D d^2U(\epsilon)dV. \quad (8)$$

Hence, the necessary and sufficient conditions of the minimum of the functional $H(\tilde{\epsilon})$ on the fields of real strain displacements $\boldsymbol{\epsilon}$, $\boldsymbol{\xi}$ lead (see, for example, Kolmogorov, 1989) to the conditions Eqs (4). This completes the proof.

3 Discussion and Particular Examples

1 Functionals of the form

$$H(\tilde{\epsilon}) = \frac{1}{2}\int_D (r \circ \tilde{\epsilon}) * \tilde{\epsilon} dV - \int_D F^d * \tilde{\xi} dV - \int_{\partial D_\sigma} P^d * \tilde{\xi} d\Sigma \quad (9)$$

where * is like in Eq. (3) a linear operator, can reach their minimum on real strain/displacement fields in the class of kinematically admissible strains/displacements only when operator * is symmetric with respect to the Stieltjes convolution operator $\circ$.

This follows from the calculation of the Frechet derivative for the functional of Eq. (9) and from its comparison with condition Eq. (4a). Clearly, this conclusion coincides with the aforementioned classical demand for the symmetricity of the bilinear form subjected to a minimization procedure. For instance, for a functional U taken in the work-type form Eq. (2) (see Christensen, 1971), the calculation of the term dU shows that condition (4b) is satisfied and condition (4a) is not.

2 A particular trivial example of a minimizing viscoelastic functional can be received from the proposed algorithm if we treat the functional U as the free energy and take it in a quadratic form proposed in (Rabotnov, 1980):

$$U = \frac{1}{2r_0}(\sigma^2 + p(\sigma - r_0\,\epsilon)^2) \quad (10)$$

where a positive coefficient p is a specific parameter of the model under study and r_0 its instantaneous modulus. Thus, for a standard linear solid composed of two springs with the moduli E_1 and E_2 and of a dashpot with the viscosity η, the value of p is

$$p = E_2/E_1. \quad (11)$$

Then for Eq. (10) one has

$$dU(\epsilon) = \frac{1}{r_0}(\sigma(r_o\delta\epsilon) + p(\sigma - r_0(f_o\sigma))(r_o\delta\epsilon - r_0\delta\epsilon))$$

$$d^2U(\epsilon) = \frac{1}{2r_0}((r_o\delta\epsilon)^2 + p(r_o\delta\epsilon - r_0\delta\epsilon)^2). \quad (12)$$

Here $\mathbf{f}$ is the creep function of the model. From the second of Eqs. (12), one can see that due to the positivity of the instantaneous modulus $\mathbf{r}_0$, condition (4b) always holds. Analysis of the first of Eqs. (12) shows that one can satisfy condition (4a) by choosing for example a class of materials with a space-independent operator in constitutive equations (in order to apply the divergence theorem, indispensable in the minimization procedure of the functionals like those in Eq. (3)). This holds for example for composites described by factorizable creep-relaxation tensors:

$$\mathbf{f}(\mathbf{t}, \mathbf{x}) = \mathbf{f}_1(\mathbf{x})\mathbf{f}_2(\mathbf{t}); \quad \mathbf{r}(\mathbf{t}, \mathbf{x}) = \mathbf{r}_1(\mathbf{x})\mathbf{r}_2(\mathbf{t}); \quad \mathbf{f}_1(\mathbf{x})\mathbf{r}_1(\mathbf{x}) = 1 \quad (13)$$

Then a functional constructed through expressions (3), (10), and (13) will be minimized if operator * is introduced as:

$$A * B = \left(\frac{r_2}{r_2(0)} \circ B\right)A + p(A - r_2(0)(f_2 \circ A)) \times \left(\frac{r_2}{r_2(0)} \circ B - B\right). \quad (14)$$

Thus, for the class of composites defined by Eqs. (13), one can use the viscoelastic minimum principle (3) combined with Eqs. (10) and (14).

For a homogeneous material, when $\mathbf{r}$ does not depend on the space variables, definition (14) becomes

$$A * B = \frac{1}{r_0}((r \circ B)A + p(A - r_0(0)(f \circ A))(r \circ B - B)). \quad (15)$$

These results correspond to those obtained in Schapery (1974, 1984, 1990) where the hypothesis Eq. (13) and its consequences were studied.

3 Another example of a minimizing functional following from the basic algorithm can be given if we will construct U in an alternative free-energy form, using for this the classical

Downloaded 04 May 2010 to 171.66.16.33. Redistribution subject to ASME license or copyright; see http://www.asme.org/terms/Terms_Use.cfm

Staverman-Schwarzl presentation (see, for example, Christensen, 1971):

$$U = \tfrac{1}{2}\int_0^t \int_0^t r(2t - u - v)d\epsilon(v)d\epsilon(u). \quad (16)$$

To use afterwards the divergence theorem, we rewrite (16) in terms of stresses and strains:

$$U = \tfrac{1}{2}\left(\int_0^t - \int_t^{2t}\right)\sigma(2t - u)d\epsilon(u). \quad (16a)$$

Now Eq. (16*a*) is suitable for a minimization procedure, except the fact that due to (16*a*), the free energy in the actual time moment t depends, among others, also on the deformations in the future moments $u > t$ that contradicts to the causality principle. To avoid this discrepancy let us define such forthcoming deformation values by means of an additional hypothesis, for example supposing that

$$d\epsilon(u) = 0,\ d\xi(u) = 0,\ d\xi^d(u) = 0;\ u > t. \quad (17)$$

Then one has

$$dU = \int_0^t \sigma(2t - u)\, d\delta\epsilon(u) = \sigma * \delta\epsilon \quad (18)$$

with operator * defined as

$$A*B = \int_0^t A(2t - u)dB(u). \quad (19)$$

This time, condition (4*b*) is automatically satisfied because of the positivity of the relaxation function. Then, defining in the respective manner the forthcoming values of the applied tractions we state that functional (20) can give real solutions of viscoelastic problems in the class of strain histories (17) and under the hypothesis of the free-energy representation (16).

$$H(\tilde{\epsilon}) = \frac{1}{2}\int_D \int_0^t \int_0^t r(2t - u - v)d\tilde{\epsilon}(v)d\tilde{\epsilon}(u)dV - \int_D F^d * \tilde{\xi}dV - \int_{\partial D_\sigma} P^d * \tilde{\xi}d\Sigma \quad (20)$$

4 For the case $\mathbf{r} = \mathbf{r}_o = \text{const}$, $U(\boldsymbol{\epsilon}) = \mathbf{r}_o - \boldsymbol{\epsilon}^2/2$, and * the multiplication operator, expression (3) turns into the classical Lagrange minimum theorem from the elasticity theory. Thus, the correspondence principle holds here, that again confirms the obtained results.

5 A corresponding *static* (complementary energy) *theorem* will operate with a functional:

$$H(\tilde{\sigma}) = \int_D Q(\tilde{\sigma})dV - \int_{\partial D_\xi} \xi^d * \tilde{P}d\Sigma. \quad (21)$$

Here the stress histories are to be varied. Conditions on the functional Q as well as all the consequences of the theorem are analogous to that of the kinematic case.

Conclusion: The construction of minimum theorems for linear viscoelasticity can be realized in the framework of the established kinematic and static theorems.

6 What is important and is contrary to the approaches discussed in the Introduction is that the presented algorithm imposes no conditions on the difference character of the relaxation function and is thus valid also for ageing viscoelastic materials (concrete, bitumen, numerous composites), widely used in engineering practice. Indeed, consider a constitutive law of an ageing viscoelastic material:

$$\sigma = \int_0^t r(t, u)d\epsilon(u). \quad (22)$$

Then, recalling for instance the Example 2 above, we see that its results remain valid if in formulae (10)–(15) one replaces r_0 by $r(t, t)$ and the Stieltjes convolution operator $\circ$ by a Stieltjes integral:

$$A \circ B \to \int_0^t A(t, u)dB(u) \quad (23)$$

4 Bounds on the Effective Properties of Inhomogeneous Viscoelastic Materials

An illustrative example of application of the presented results is in analytical evaluation of the effective properties of composite viscoelastic materials. Following the procedure exposed in Huet (1988) let us first consider an inhomogeneous viscoelastic specimen in uniform kinematic boundary conditions:

$$\boldsymbol{\xi}^d = \boldsymbol{\epsilon}_o(\mathbf{t})\mathbf{x} \quad \text{on} \quad \partial\mathbf{D}_\xi = \partial\mathbf{D};$$
$$\partial\mathbf{D}_\sigma = \boldsymbol{\phi};\ \mathbf{F}^d = \mathbf{0} \text{ in } \mathbf{D}. \quad (24)$$

A uniform strain field ϵ_o inside this specimen is an admissible virtual strain field. We apply the kinematic theorem established above to a functional (3) with any reasonable U:

$$H(\boldsymbol{\epsilon}_o) \geq H(\boldsymbol{\epsilon}) \quad (25)$$

If the chosen minimizing functional U has a physical sense, for example that of the free energy, and if the material effective properties can be defined through the spatial averages $\langle \ldots \rangle$ as

$$\langle U \rangle = 0.5\ \mathbf{r}_{\text{eff}} * \langle \epsilon \rangle * \langle \epsilon \rangle, \quad (26)$$

then taking into account Eq. (3) and definition (26), we will arrive to a following bound on the relaxation tensor of an inhomogeneous viscoelastic material:

$$\mathbf{r}_{\text{eff}} \leq \langle \mathbf{r} \rangle. \quad (27)$$

By analogy, for the case of uniform static boundary conditions one has

$$P^d = \sigma_o(t).n \quad \text{on} \quad \partial D;\ \partial D_\xi = \phi;\ F^d = 0 \text{ in } D. \quad (28)$$

Then our static (complementary energy) theorem gives

$$H(\boldsymbol{\sigma}_o) \geq H(\boldsymbol{\sigma}) \quad (29)$$

from where a bound on the effective creep functions tensor $\mathbf{f}$ follows:

$$\mathbf{f}_{\text{eff}} \leq \langle \mathbf{f} \rangle. \quad (30)$$

The first-order bounds (27) and (30) for the relaxation and creep tensor functions are quite reasonable and are similar to those proposed in Huet (1988). But now these bounds are obtained in a different manner.

It is necessary to emphasize that the main difficulty in the problem under study is to find an appropriate functional U that will lead to some physically nontrivial results. This task is not simple: for example, the work-type expressions mentioned in the Introduction can be minimized, but they give the bounds only on the instantaneous modulus $\mathbf{r}_o$, while we are certainly more interested in estimating the current values of the effective relaxation functions tensor $\mathbf{r}(t)$.

5 Conclusions

1 A brief review of the problem of the minimum principles in linear viscoelasticity is given. A theorem is proved that gives the general algorithm for the construction of viscoelastic minimizing functionals.

2 For several particular problems, the examples are given of physically reasonable extremum principles that can be treated in the first approximation as viscoelastic counterparts of the classical elastic extremum theorems.

Downloaded 04 May 2010 to 171.66.16.33. Redistribution subject to ASME license or copyright; see http://www.asme.org/terms/Terms_Use.cfm

3 The obtained results are valid also for the case of ageing materials that may be important for industrial applications (concrete, bitumen, composites).

4 The first-order bounds (27) and (30) on the effective properties of inhomogeneous viscoelastic materials are established that can be of interest for engineering science and practice, especially for the mechanics of composites.

Acknowledgments

The author is grateful to Prof. C. Huet for numerous fruitful discussions.

References

Breuer, S., 1973, "Minimum Principles for Incompressible Viscoelastic Solids," *Meccanica,* Vol. 8, pp. 102–104.

Brilla, J., 1975, "Generalized Variational Methods in Linear Viscoelasticity," *Mechanics of Viscoelastic Media and Bodies,* J. Hult, ed., Springer-Verlag, Berlin, pp. 215–228.

Christensen, R. M., 1971, *Theory of Viscoelasticity,* Academic Press, New York.

Fabrizio, M., and Morro, A., 1992, *Mathematical Problems in Linear Viscoelasticity,* SIAM, Philadelphia.

Frechet, M., 1910, "Sur les fonctionnelles continues," *Annales Science,* Paris, Vol. 27, pp. 193–216.

Giorgi, C., and Marzocchi, A., 1992, "A minimum principle for the quasi-static problem in linear viscoelasticity," *Bollettino U.M.I.(7),* Vol. 6–A, pp. 255–266.

Gurtin, M. E., 1963, "Variational Principles in the Linear Theory of Viscoelasticity," *Archives of Rational Mechanics and Analysis,* Vol. 13, pp. 179–191.

Huet, C., 1988, "Bounds for the Viscoelastic Properties of Heterogeneous Meterials through new Variational Theorems," *Proceedings of the Xth International Congress of Rheology,* Sydney, pp. 422–424.

Huet, C., 1992, "Minimum principles for viscoelasticity," *European Journal of Mechanics, A/Solids,* Vol. 11, No. 5, pp. 653–684.

Kolmogorov, A., and Fomin, S., 1989, *Elements of the Theory of Functions and of the Functional Analysis,* Nauka, Moscow, p. 623.

Kulejevska, E., 1984, "Functional Methods of Formulation of Rheological Constitutive Potentials," *Archives of Mechanics,* Vol. 36, pp. 67–76.

Rabotnov, Y., 1980, *Elements of Hereditary Solid Mechanics,* MIR, Moscow.

Reiss, R., and Haug, J., 1978, "Extremum Principles for Linear Initial-Value Problems of Mathematical Physics," *International Journal of Engineering Science,* Vol. 16, pp. 231–251.

Schapery, R. A., 1964, "On the Time Dependence of Viscoelastic Variational Solutions," *Quarterly of Applied Mathematics,* Vol. 22, pp. 207–215.

Schapery, R. A., 1974, "Viscoelastic Behaviour and Analysis of Composite Materials," *Composite Materials,* Vol. 2, G. P. Sendeckyj, ed., Academic Press, pp. 85–168.

Schapery, R. A., 1984, "Correspondence Principles and a Generalized *J* Integral for Large Deformation and Fracture Analysis of Viscoelastic Media," *International Journal of Fracture,* Vol. 25, pp. 195–223.

Schapery, R. A., 1990, "A Theory of Mechanical Behaviour of Elastic Media with Growing Damage and Other Changes in Structure," *Journal of the Mechanics and Physics of Solids,* Vol. 38, pp. 215–253.

Tonti, E., 1973, "On the Variational Formulation for Linear Initial Value Problems," *Annales Matematica Pura et Applicata,* Vol. 4, No. 95, pp. 331–359.

Some Faults in the Stress Analysis of Power-Hardening Materials With Pseudo-Stress Function Method

Peng Yafei,[2] Shen Yapeng,[2] and Chen Yiheng[2]

Introduction

The stress analysis of power hardening materials has received considerable attention in recent years. A new analytic method was suggested and described by Lee (1987), which is known as the pseudo-stress function method similar to the Airy stress function method in linear elasticity. Using this method, Lee and his co-workers have obtained the solutions of many practical problems, for example, the case that a plate made of power-hardening materials and containing a rigid inclusion or a hole is subjected to the simple tension (Lee, 1987; Lee and Gong, 1987; Lee and Smith, 1988; Lee and Batt, 1989). Since Lee's theory was considered as a better method for the stress analysis of power-law materials, it has been extensively applied by other researchers to the elastic-plastic problem, the crack problem, and so on (Gao et al., 1991; Wang et al., 1991; Wang and Zhang, 1992; Chen and Hahn, 1992). But, the authors recently have found some crucial and neglectful problems in Lee's theory. The exposure of these faults will show Lee's method to be unavailable and incorrect. Therefore, it is very necessary to present the serious errors of Lee's theory in detail.

Discussion

1 The original compatibility equation expressed by using Airy's stress function is

$$\frac{\partial^2}{\partial z^2}\left(\xi^n \frac{\partial^2 U}{\partial \bar{z}^2}\right) + \frac{\partial^2}{\partial \bar{z}^2}\left(\xi^n \frac{\partial^2 U}{\partial z^2}\right) = 0 \tag{1}$$

or

$$\begin{aligned}
&\frac{n}{2}\xi^{n-2}\left[\left(\frac{\partial^2 U}{\partial \bar{z}^2}\right)^2 \frac{\partial^4 U}{\partial z^4} + 2\left(\frac{n}{2}+1\right)\frac{\partial^2 U}{\partial \bar{z}^2}\frac{\partial^3 U}{\partial z^3}\frac{\partial^3 U}{\partial z \partial \bar{z}^2}\right.\\
&\left.\quad + \left(\frac{n}{2}+1\right)\frac{\partial^2 U}{\partial z^2}\left(\frac{\partial^3 U}{\partial z \partial \bar{z}^2}\right)^2\right]\\
&\quad + \frac{n}{2}\left(\frac{n}{2}-1\right)\xi^{n-4}\left(\frac{\partial^2 U}{\partial \bar{z}^2}\right)^3\left(\frac{\partial^3 U}{\partial z^3}\right)^2 + \left(\frac{n}{2}+1\right)\xi^n \frac{\partial^4 U}{\partial z^2 \partial \bar{z}^2}\\
&\quad + \frac{n}{2}\xi^{n-2}\left[\left(\frac{\partial^2 U}{\partial z^2}\right)^2 \frac{\partial^4 U}{\partial \bar{z}^4} + 2\left(\frac{n}{2}+1\right)\frac{\partial^2 U}{\partial z^2}\frac{\partial^3 U}{\partial \bar{z}^3}\frac{\partial^3 U}{\partial \bar{z} \partial z^2}\right.\\
&\left.\quad + \left(\frac{n}{2}+1\right)\frac{\partial^2 U}{\partial \bar{z}^2}\left(\frac{\partial^3 U}{\partial \bar{z} \partial z^2}\right)^2\right] + \frac{n}{2}\left(\frac{n}{2}-1\right)\xi^{n-4}\\
&\qquad \times \left(\frac{\partial^2 U}{\partial z^2}\right)^3\left(\frac{\partial^3 U}{\partial \bar{z}^3}\right)^2 + \left(\frac{n}{2}+1\right)\xi^n \frac{\partial^4 U}{\partial \bar{z}^2 \partial z^2} = 0
\end{aligned} \tag{2}$$

where

$$\xi^2 = \frac{\partial^2 U}{\partial z^2}\frac{\partial^2 U}{\partial \bar{z}^2}, \quad n = \frac{1-m}{m}.$$

2 The basic and key ideas of Lee's theory are based on the following assumptions (Lee, 1987; Lee and Gong, 1987):

$$\begin{cases} \dfrac{\partial^2 \Lambda}{\partial z^2} = \xi^n \dfrac{\partial^2 U}{\partial z^2} \\ \dfrac{\partial^2 \Lambda}{\partial \bar{z}^2} = \xi^n \dfrac{\partial^2 U}{\partial \bar{z}^2} \end{cases} \tag{3}$$

or

$$\begin{cases} \dfrac{\partial^2 U}{\partial z^2} = \eta^{m-1} \dfrac{\partial^2 \Lambda}{\partial z^2} \\ \dfrac{\partial^2 U}{\partial \bar{z}^2} = \eta^{m-1} \dfrac{\partial^2 \Lambda}{\partial \bar{z}^2} \end{cases} \tag{4}$$

where

$$\eta^2 = \frac{\partial^2 \Lambda}{\partial z^2}\frac{\partial^2 \Lambda}{\partial \bar{z}^2}.$$

[2] Department of Engineering Mechanics, Xian Jiao–Tong University, Xian Shaanxi 710049, P. R. China.

Contributed by the Applied Mechanics Division of THE AMERICAN SOCIETY OF MECHANICAL ENGINEERS for publication in the ASME JOURNAL OF APPLIED MECHANICS. Manuscript received by the ASME Applied Mechanics Division, Nov. 29, 1994; final revision, Apr. 19, 1995. Associate Technical Editor: C. F. Shih.

Downloaded 04 May 2010 to 171.66.16.33. Redistribution subject to ASME license or copyright; see http://www.asme.org/terms/Terms_Use.cfm

3 The obtained results are valid also for the case of ageing materials that may be important for industrial applications (concrete, bitumen, composites).

4 The first-order bounds (27) and (30) on the effective properties of inhomogeneous viscoelastic materials are established that can be of interest for engineering science and practice, especially for the mechanics of composites.

Acknowledgments

The author is grateful to Prof. C. Huet for numerous fruitful discussions.

References

Breuer, S., 1973, "Minimum Principles for Incompressible Viscoelastic Solids," *Meccanica,* Vol. 8, pp. 102–104.

Brilla, J., 1975, "Generalized Variational Methods in Linear Viscoelasticity," *Mechanics of Viscoelastic Media and Bodies,* J. Hult, ed., Springer-Verlag, Berlin, pp. 215–228.

Christensen, R. M., 1971, *Theory of Viscoelasticity,* Academic Press, New York.

Fabrizio, M., and Morro, A., 1992, *Mathematical Problems in Linear Viscoelasticity,* SIAM, Philadelphia.

Frechet, M., 1910, "Sur les fonctionnelles continues," *Annales Science,* Paris, Vol. 27, pp. 193–216.

Giorgi, C., and Marzocchi, A., 1992, "A minimum principle for the quasi-static problem in linear viscoelasticity," *Bollettino U.M.I.(7),* Vol. 6–A, pp. 255–266.

Gurtin, M. E., 1963, "Variational Principles in the Linear Theory of Viscoelasticity," *Archives of Rational Mechanics and Analysis,* Vol. 13, pp. 179–191.

Huet, C., 1988, "Bounds for the Viscoelastic Properties of Heterogeneous Meterials through new Variational Theorems," *Proceedings of the Xth International Congress of Rheology,* Sydney, pp. 422–424.

Huet, C., 1992, "Minimum principles for viscoelasticity," *European Journal of Mechanics, A/Solids,* Vol. 11, No. 5, pp. 653–684.

Kolmogorov, A., and Fomin, S., 1989, *Elements of the Theory of Functions and of the Functional Analysis,* Nauka, Moscow, p. 623.

Kulejevska, E., 1984, "Functional Methods of Formulation of Rheological Constitutive Potentials," *Archives of Mechanics,* Vol. 36, pp. 67–76.

Rabotnov, Y., 1980, *Elements of Hereditary Solid Mechanics,* MIR, Moscow.

Reiss, R., and Haug, J., 1978, "Extremum Principles for Linear Initial-Value Problems of Mathematical Physics," *International Journal of Engineering Science,* Vol. 16, pp. 231–251.

Schapery, R. A., 1964, "On the Time Dependence of Viscoelastic Variational Solutions," *Quarterly of Applied Mathematics,* Vol. 22, pp. 207–215.

Schapery, R. A., 1974, "Viscoelastic Behaviour and Analysis of Composite Materials," *Composite Materials,* Vol. 2, G. P. Sendeckyj, ed., Academic Press, pp. 85–168.

Schapery, R. A., 1984, "Correspondence Principles and a Generalized *J* Integral for Large Deformation and Fracture Analysis of Viscoelastic Media," *International Journal of Fracture,* Vol. 25, pp. 195–223.

Schapery, R. A., 1990, "A Theory of Mechanical Behaviour of Elastic Media with Growing Damage and Other Changes in Structure," *Journal of the Mechanics and Physics of Solids,* Vol. 38, pp. 215–253.

Tonti, E., 1973, "On the Variational Formulation for Linear Initial Value Problems," *Annales Matematica Pura et Applicata,* Vol. 4, No. 95, pp. 331–359.

Some Faults in the Stress Analysis of Power-Hardening Materials With Pseudo-Stress Function Method

Peng Yafei,[2] Shen Yapeng,[2] and Chen Yiheng[2]

Introduction

The stress analysis of power hardening materials has received considerable attention in recent years. A new analytic method was suggested and described by Lee (1987), which is known as the pseudo-stress function method similar to the Airy stress function method in linear elasticity. Using this method, Lee and his co-workers have obtained the solutions of many practical problems, for example, the case that a plate made of power-hardening materials and containing a rigid inclusion or a hole is subjected to the simple tension (Lee, 1987; Lee and Gong, 1987; Lee and Smith, 1988; Lee and Batt, 1989). Since Lee's theory was considered as a better method for the stress analysis of power-law materials, it has been extensively applied by other researchers to the elastic-plastic problem, the crack problem, and so on (Gao et al., 1991; Wang et al., 1991; Wang and Zhang, 1992; Chen and Hahn, 1992). But, the authors recently have found some crucial and neglectful problems in Lee's theory. The exposure of these faults will show Lee's method to be unavailable and incorrect. Therefore, it is very necessary to present the serious errors of Lee's theory in detail.

Discussion

1 The original compatibility equation expressed by using Airy's stress function is

$$\frac{\partial^2}{\partial z^2}\left(\xi^n \frac{\partial^2 U}{\partial \bar{z}^2}\right) + \frac{\partial^2}{\partial \bar{z}^2}\left(\xi^n \frac{\partial^2 U}{\partial z^2}\right) = 0 \tag{1}$$

or

$$\begin{aligned}
&\frac{n}{2}\xi^{n-2}\left[\left(\frac{\partial^2 U}{\partial \bar{z}^2}\right)^2 \frac{\partial^4 U}{\partial z^4} + 2\left(\frac{n}{2}+1\right)\frac{\partial^2 U}{\partial \bar{z}^2}\frac{\partial^3 U}{\partial z^3}\frac{\partial^3 U}{\partial z \partial \bar{z}^2}\right.\\
&\left.\quad + \left(\frac{n}{2}+1\right)\frac{\partial^2 U}{\partial z^2}\left(\frac{\partial^3 U}{\partial z \partial \bar{z}^2}\right)^2\right]\\
&\quad + \frac{n}{2}\left(\frac{n}{2}-1\right)\xi^{n-4}\left(\frac{\partial^2 U}{\partial \bar{z}^2}\right)^3\left(\frac{\partial^3 U}{\partial z^3}\right)^2 + \left(\frac{n}{2}+1\right)\xi^n \frac{\partial^4 U}{\partial z^2 \partial \bar{z}^2}\\
&\quad + \frac{n}{2}\xi^{n-2}\left[\left(\frac{\partial^2 U}{\partial z^2}\right)^2 \frac{\partial^4 U}{\partial \bar{z}^4} + 2\left(\frac{n}{2}+1\right)\frac{\partial^2 U}{\partial z^2}\frac{\partial^3 U}{\partial \bar{z}^3}\frac{\partial^3 U}{\partial \bar{z} \partial z^2}\right.\\
&\left.\quad + \left(\frac{n}{2}+1\right)\frac{\partial^2 U}{\partial \bar{z}^2}\left(\frac{\partial^3 U}{\partial \bar{z} \partial z^2}\right)^2\right] + \frac{n}{2}\left(\frac{n}{2}-1\right)\xi^{n-4}\\
&\qquad \times \left(\frac{\partial^2 U}{\partial z^2}\right)^3\left(\frac{\partial^3 U}{\partial \bar{z}^3}\right)^2 + \left(\frac{n}{2}+1\right)\xi^n \frac{\partial^4 U}{\partial \bar{z}^2 \partial z^2} = 0
\end{aligned} \tag{2}$$

where

$$\xi^2 = \frac{\partial^2 U}{\partial z^2}\frac{\partial^2 U}{\partial \bar{z}^2}, \quad n = \frac{1-m}{m}.$$

2 The basic and key ideas of Lee's theory are based on the following assumptions (Lee, 1987; Lee and Gong, 1987):

$$\begin{cases} \dfrac{\partial^2 \Lambda}{\partial z^2} = \xi^n \dfrac{\partial^2 U}{\partial z^2} \\ \dfrac{\partial^2 \Lambda}{\partial \bar{z}^2} = \xi^n \dfrac{\partial^2 U}{\partial \bar{z}^2} \end{cases} \tag{3}$$

or

$$\begin{cases} \dfrac{\partial^2 U}{\partial z^2} = \eta^{m-1} \dfrac{\partial^2 \Lambda}{\partial z^2} \\ \dfrac{\partial^2 U}{\partial \bar{z}^2} = \eta^{m-1} \dfrac{\partial^2 \Lambda}{\partial \bar{z}^2} \end{cases} \tag{4}$$

where

$$\eta^2 = \frac{\partial^2 \Lambda}{\partial z^2}\frac{\partial^2 \Lambda}{\partial \bar{z}^2}.$$

[2] Department of Engineering Mechanics, Xian Jiao–Tong University, Xian Shaanxi 710049, P. R. China.

Contributed by the Applied Mechanics Division of THE AMERICAN SOCIETY OF MECHANICAL ENGINEERS for publication in the ASME JOURNAL OF APPLIED MECHANICS. Manuscript received by the ASME Applied Mechanics Division, Nov. 29, 1994; final revision, Apr. 19, 1995. Associate Technical Editor: C. F. Shih.

Copyright © 1996 by ASME

Downloaded 04 May 2010 to 171.66.16.33. Redistribution subject to ASME license or copyright; see http://www.asme.org/terms/Terms_Use.cfm

According to Lee's above hypothesis, substituting Eq. (3) into (1), the compatibility equation will become

$$\frac{\partial^4 \Lambda}{\partial z^2 \partial \bar{z}^2} = 0. \tag{5}$$

From Eq. (5), the following equation can be obtained:

$$2\Lambda = \bar{z}\varphi(z) + \psi(z) + z\overline{\varphi(z)} + \overline{\psi(z)}. \tag{6}$$

Discussion about Lee's theory:

(1) Differentiating the second equation of Eq. (3) with respect to z, we can get

$$\frac{\partial^2}{\partial z^2}\left(\frac{\partial^2 \Lambda}{\partial \bar{z}^2}\right) = \frac{\partial^2}{\partial z^2}\left(\xi^n \frac{\partial^2 U}{\partial \bar{z}^2}\right) = \frac{n}{2}\xi^{n-2} \times \left[\left(\frac{\partial^2 U}{\partial \bar{z}^2}\right)^2 \frac{\partial^4 U}{\partial z^4} + 2\left(\frac{n}{2}+1\right)\frac{\partial^2 U}{\partial \bar{z}^2}\frac{\partial^3 U}{\partial z^3}\frac{\partial^3 U}{\partial z \partial \bar{z}^2} + \left(\frac{n}{2}+1\right)\frac{\partial^2 U}{\partial z^2}\left(\frac{\partial^3 U}{\partial z \partial \bar{z}^2}\right)^2\right] + \frac{n}{2}\left(\frac{n}{2}-1\right)\xi^{n-4} \times \left(\frac{\partial^2 U}{\partial \bar{z}^2}\right)^3\left(\frac{\partial^3 U}{\partial z^3}\right)^2 + \left(\frac{n}{2}+1\right)\xi^n \frac{\partial^4 U}{\partial z^2 \partial \bar{z}^2}. \tag{7}$$

Comparing Eq. (7) with Eq. (2), we can find that Lee's compatibility Eq. (5) is greatly different from the original compatibility Eq. (1).

(2) Differentiating the first equation of Eq. (3) with respect to $\bar{z}$, we can gain

$$\frac{\partial^2}{\partial \bar{z}^2}\left(\frac{\partial^2 \Lambda}{\partial z^2}\right) = \frac{\partial^2}{\partial \bar{z}^2}\left(\xi^n \frac{\partial^2 U}{\partial z^2}\right) = \frac{n}{2}\xi^{n-2} \times \left[\left(\frac{\partial^2 U}{\partial z^2}\right)^2 \frac{\partial^4 U}{\partial \bar{z}^4} + 2\left(\frac{n}{2}+1\right)\frac{\partial^2 U}{\partial z^2}\frac{\partial^3 U}{\partial \bar{z}^3}\frac{\partial^3 U}{\partial \bar{z} \partial z^2} + \left(\frac{n}{2}+1\right)\frac{\partial^2 U}{\partial \bar{z}^2}\left(\frac{\partial^3 U}{\partial \bar{z} \partial z^2}\right)^2\right] + \frac{n}{2}\left(\frac{n}{2}-1\right)\xi^{n-4} \times \left(\frac{\partial^2 U}{\partial z^2}\right)^3\left(\frac{\partial^3 U}{\partial \bar{z}^3}\right)^2 + \left(\frac{n}{2}+1\right)\xi^n \frac{\partial^4 U}{\partial \bar{z}^2 \partial z^2}. \tag{8}$$

From Eqs. (7) and (8), the following relation cannot be deduced:

$$\frac{\partial^2}{\partial z^2}\left(\frac{\partial^2 \Lambda}{\partial \bar{z}^2}\right) = \frac{\partial^2}{\partial \bar{z}^2}\left(\frac{\partial^2 \Lambda}{\partial z^2}\right). \tag{9}$$

In other words, substituting Eq. (3) into (1), the Lee's compatibility Eq. (5) cannot be found.

(3) Similarly, differentiating the first equation of Eq. (4) with respect to $\bar{z}$ and the second equation with respect to z, we cannot get

$$\frac{\partial^2}{\partial z^2}\left(\frac{\partial^2 U}{\partial \bar{z}^2}\right) = \frac{\partial^2}{\partial \bar{z}^2}\left(\frac{\partial^2 U}{\partial z^2}\right). \tag{10}$$

Therefore, the dilatational stress ($\partial^2 U/\partial z \partial \bar{z}$) cannot be given by using Lee's integrating equation (Lee, 1987; Lee and Gong, 1987).

(4) As for the example used by Lee (1987), from Lee's integrating equation and pseudo-stress function for the problem of the plate containing a rigid inclusion subjected to uniaxial tension (Lee and Gong, 1987)

$$\frac{\partial^2 \Lambda}{\partial z^2} = 0.5\left(\frac{P}{4}\right)^{1/m}\left(-\frac{4\bar{z}R^2}{z^3} - 2 + \frac{6R^4}{z^4}\right) \tag{11}$$

the correct dilataional stresses cannot be obtained, which will not depend on the integrating course. In the same way, Lee's other results (Lee, 1987; Lee and Gong, 1987; Lee and Smith, 1988; Lee and Batt, 1989) are also incorrect.

Conclusions

1 Lee's hypothesis shown in Eq. (3) or Eq. (4) cannot hold true.

2 The solutions and results obtained by Lee and his co-workers (Lee, 1987; Lee and Gong, 1987; Lee and Smith, 1988; Lee and Batt, 1989) with his own theory and by other researchers (Gao et al., 1991; Wang et al., 1991; Wang and Zhang, 1992; Chen and Hahn, 1992) with Lee's theory are incorrect.

References

Chen, Y. H., and Hahn, H. G., 1992, "Singular Behavior Near a Crack Tip In a Power Hardning Material Mixed Up With a Rigid Piece," *Chinese Journal of Applied Mechanics,* Vol. 9, No. 3, pp. 28–35.

Gao, X. L., Wei, X. X., and Wang, Z. K., 1991, "General Analytical Solution of a Strain-Hardnining Elasto-Plastic Plate Containing a Circular Hole Subjected To Biaxial Loading-With Applications In Pressure Vessels," *International Journal of Pressure Vessels and Piping,* Vol. 47, pp. 35–55.

Lee, Y. S., 1987, "Stress Analysis and Investigation of Void Formation Under External Stress of Power Law Creep Materials Using Complex Variables and the Pseudo-Stress Function." dissertation abstracts, University of Pittsburgh, Pittsburgh, PA.

Lee, Y. S., and Gong, H., 1987, "Application of Complex Variables and Pesudo-Stress Analysis of Single Rigid Inclusion in Power-Law Materials Subjected to Simple Tension and Pure Shear," *International Journal of Mechanical Sciences,* Vol. 29, pp. 669–694.

Lee, Y. S., and Smith, L. C., 1988, "Analysis of a Power-Law Material Containing a Single Hole Subjected to a Uniaxial Tensile Stress Using the Complex Pseudo-Stress Function." ASME JOURNAL OF APPLIED MECHANICS, Vol. 55, pp. 267–274.

Lee, Y. S., and Batt, T. J., 1989, "Investigation of Void Formation on a Bonded Interface of Power Law Creep Materials Containing a Cylindrical Particle," *ACTA Mechanica,* Vol. 79, pp. 183–205.

Wang, Z. K., Wei, X. X., and Gao, X. L., 1991, "Solution of the Plane Stress Problems of Strain-Hardening Materials Described by Power-Law Using the Complex Pseudo-Stress Function." *Chinese Journal of Applied Mathematics and Mechanics* (English Edition), Vol. 12, pp. 481–492.

Wang, Z. K., and Zhang, K., 1992, "Stress Concentration of a Power-Law Naterial Infinite Plate Containing an Elliptic Hole," *Journal of Xi'an Jiaotong University* (Chinese), Vol. 26, pp. 89–94.

Application of Normal Mode Expansion to Accoustic Emission Waves in Finite Plates[3]

M. R. Gorman[4] and W. H. Prosser[5]

Introduction

Breckenridge et al. (1975), Hsu (1985), and Pao (1978) adapted approaches from seismology to calculate the response at the surface of an infinite half-space and an infinite plate. These approaches have found use in calibrating acoustic emission (AE) transducers. However, it is difficult to extend this theoretical approach to AE testing of practical structures. Weaver and Pao (1982) considered a normal mode solution to the Lamb equations. Hutchinson (1983) pointed out the poten-

[3] Work supported by NASA Langley Research Center.

[4] Department of Physics, University of Denver, Denver, CO 80208-0177.

[5] Nondestructive Measurement Science Brance, NASA LaRC, Hampton, VA 23681-0001.

Contributed by the Applied Mechanics Division of THE AMERICAN SOCIETY OF MECHANICAL ENGINEERS for publication in the ASME JOURNAL OF APPLIED MECHANICS. Manuscript received and accepted by the ASME Applied Mechanics Division, May 1, 1995. Associate Technical Editor: I. M. Daniel.

Downloaded 04 May 2010 to 171.66.16.33. Redistribution subject to ASME license or copyright; see http://www.asme.org/terms/Terms_Use.cfm

According to Lee's above hypothesis, substituting Eq. (3) into (1), the compatibility equation will become

$$\frac{\partial^4 \Lambda}{\partial z^2 \partial \bar{z}^2} = 0. \tag{5}$$

From Eq. (5), the following equation can be obtained:

$$2\Lambda = \bar{z}\varphi(z) + \psi(z) + z\overline{\varphi(z)} + \overline{\psi(z)}. \tag{6}$$

Discussion about Lee's theory:

(1) Differentiating the second equation of Eq. (3) with respect to z, we can get

$$\frac{\partial^2}{\partial z^2}\left(\frac{\partial^2 \Lambda}{\partial \bar{z}^2}\right) = \frac{\partial^2}{\partial z^2}\left(\xi^n \frac{\partial^2 U}{\partial \bar{z}^2}\right) = \frac{n}{2}\xi^{n-2} \times \left[\left(\frac{\partial^2 U}{\partial \bar{z}^2}\right)^2 \frac{\partial^4 U}{\partial z^4} + 2\left(\frac{n}{2}+1\right)\frac{\partial^2 U}{\partial \bar{z}^2}\frac{\partial^3 U}{\partial z^3}\frac{\partial^3 U}{\partial z \partial \bar{z}^2} + \left(\frac{n}{2}+1\right)\frac{\partial^2 U}{\partial z^2}\left(\frac{\partial^3 U}{\partial z \partial \bar{z}^2}\right)^2\right] + \frac{n}{2}\left(\frac{n}{2}-1\right)\xi^{n-4} \times \left(\frac{\partial^2 U}{\partial \bar{z}^2}\right)^3\left(\frac{\partial^3 U}{\partial z^3}\right)^2 + \left(\frac{n}{2}+1\right)\xi^n \frac{\partial^4 U}{\partial z^2 \partial \bar{z}^2}. \tag{7}$$

Comparing Eq. (7) with Eq. (2), we can find that Lee's compatibility Eq. (5) is greatly different from the original compatibility Eq. (1).

(2) Differentiating the first equation of Eq. (3) with respect to $\bar{z}$, we can gain

$$\frac{\partial^2}{\partial \bar{z}^2}\left(\frac{\partial^2 \Lambda}{\partial z^2}\right) = \frac{\partial^2}{\partial \bar{z}^2}\left(\xi^n \frac{\partial^2 U}{\partial z^2}\right) = \frac{n}{2}\xi^{n-2} \times \left[\left(\frac{\partial^2 U}{\partial z^2}\right)^2 \frac{\partial^4 U}{\partial \bar{z}^4} + 2\left(\frac{n}{2}+1\right)\frac{\partial^2 U}{\partial z^2}\frac{\partial^3 U}{\partial \bar{z}^3}\frac{\partial^3 U}{\partial \bar{z} \partial z^2} + \left(\frac{n}{2}+1\right)\frac{\partial^2 U}{\partial \bar{z}^2}\left(\frac{\partial^3 U}{\partial \bar{z} \partial z^2}\right)^2\right] + \frac{n}{2}\left(\frac{n}{2}-1\right)\xi^{n-4} \times \left(\frac{\partial^2 U}{\partial z^2}\right)^3\left(\frac{\partial^3 U}{\partial \bar{z}^3}\right)^2 + \left(\frac{n}{2}+1\right)\xi^n \frac{\partial^4 U}{\partial \bar{z}^2 \partial z^2}. \tag{8}$$

From Eqs. (7) and (8), the following relation cannot be deduced:

$$\frac{\partial^2}{\partial z^2}\left(\frac{\partial^2 \Lambda}{\partial \bar{z}^2}\right) = \frac{\partial^2}{\partial \bar{z}^2}\left(\frac{\partial^2 \Lambda}{\partial z^2}\right). \tag{9}$$

In other words, substituting Eq. (3) into (1), the Lee's compatibility Eq. (5) cannot be found.

(3) Similarly, differentiating the first equation of Eq. (4) with respect to $\bar{z}$ and the second equation with respect to z, we cannot get

$$\frac{\partial^2}{\partial z^2}\left(\frac{\partial^2 U}{\partial \bar{z}^2}\right) = \frac{\partial^2}{\partial \bar{z}^2}\left(\frac{\partial^2 U}{\partial z^2}\right). \tag{10}$$

Therefore, the dilatational stress ($\partial^2 U/\partial z \partial \bar{z}$) cannot be given by using Lee's integrating equation (Lee, 1987; Lee and Gong, 1987).

(4) As for the example used by Lee (1987), from Lee's integrating equation and pseudo-stress function for the problem of the plate containing a rigid inclusion subjected to uniaxial tension (Lee and Gong, 1987)

$$\frac{\partial^2 \Lambda}{\partial z^2} = 0.5\left(\frac{P}{4}\right)^{1/m}\left(-\frac{4\bar{z}R^2}{z^3} - 2 + \frac{6R^4}{z^4}\right) \tag{11}$$

the correct dilataional stresses cannot be obtained, which will not depend on the integrating course. In the same way, Lee's other results (Lee, 1987; Lee and Gong, 1987; Lee and Smith, 1988; Lee and Batt, 1989) are also incorrect.

Conclusions

1 Lee's hypothesis shown in Eq. (3) or Eq. (4) cannot hold true.

2 The solutions and results obtained by Lee and his co-workers (Lee, 1987; Lee and Gong, 1987; Lee and Smith, 1988; Lee and Batt, 1989) with his own theory and by other researchers (Gao et al., 1991; Wang et al., 1991; Wang and Zhang, 1992; Chen and Hahn, 1992) with Lee's theory are incorrect.

References

Chen, Y. H., and Hahn, H. G., 1992, "Singular Behavior Near a Crack Tip In a Power Hardning Material Mixed Up With a Rigid Piece," *Chinese Journal of Applied Mechanics,* Vol. 9, No. 3, pp. 28–35.

Gao, X. L., Wei, X. X., and Wang, Z. K., 1991, "General Analytical Solution of a Strain-Hardnining Elasto-Plastic Plate Containing a Circular Hole Subjected To Biaxial Loading-With Applications In Pressure Vessels," *International Journal of Pressure Vessels and Piping,* Vol. 47, pp. 35–55.

Lee, Y. S., 1987, "Stress Analysis and Investigation of Void Formation Under External Stress of Power Law Creep Materials Using Complex Variables and the Pseudo-Stress Function." dissertation abstracts, University of Pittsburgh, Pittsburgh, PA.

Lee, Y. S., and Gong, H., 1987, "Application of Complex Variables and Pesudo-Stress Analysis of Single Rigid Inclusion in Power-Law Materials Subjected to Simple Tension and Pure Shear," *International Journal of Mechanical Sciences,* Vol. 29, pp. 669–694.

Lee, Y. S., and Smith, L. C., 1988, "Analysis of a Power-Law Material Containing a Single Hole Subjected to a Uniaxial Tensile Stress Using the Complex Pseudo-Stress Function." ASME JOURNAL OF APPLIED MECHANICS, Vol. 55, pp. 267–274.

Lee, Y. S., and Batt, T. J., 1989, "Investigation of Void Formation on a Bonded Interface of Power Law Creep Materials Containing a Cylindrical Particle," *ACTA Mechanica,* Vol. 79, pp. 183–205.

Wang, Z. K., Wei, X. X., and Gao, X. L., 1991, "Solution of the Plane Stress Problems of Strain-Hardening Materials Described by Power-Law Using the Complex Pseudo-Stress Function." *Chinese Journal of Applied Mathematics and Mechanics* (English Edition), Vol. 12, pp. 481–492.

Wang, Z. K., and Zhang, K., 1992, "Stress Concentration of a Power-Law Naterial Infinite Plate Containing an Elliptic Hole," *Journal of Xi'an Jiaotong University* (Chinese), Vol. 26, pp. 89–94.

Application of Normal Mode Expansion to Accoustic Emission Waves in Finite Plates[3]

M. R. Gorman[4] and W. H. Prosser[5]

Introduction

Breckenridge et al. (1975), Hsu (1985), and Pao (1978) adapted approaches from seismology to calculate the response at the surface of an infinite half-space and an infinite plate. These approaches have found use in calibrating acoustic emission (AE) transducers. However, it is difficult to extend this theoretical approach to AE testing of practical structures. Weaver and Pao (1982) considered a normal mode solution to the Lamb equations. Hutchinson (1983) pointed out the poten-

[3] Work supported by NASA Langley Research Center.

[4] Department of Physics, University of Denver, Denver, CO 80208-0177.

[5] Nondestructive Measurement Science Brance, NASA LaRC, Hampton, VA 23681-0001.

Contributed by the Applied Mechanics Division of THE AMERICAN SOCIETY OF MECHANICAL ENGINEERS for publication in the ASME JOURNAL OF APPLIED MECHANICS. Manuscript received and accepted by the ASME Applied Mechanics Division, May 1, 1995. Associate Technical Editor: I. M. Daniel.

Copyright © 1996 by ASME

Downloaded 04 May 2010 to 171.66.16.33. Redistribution subject to ASME license or copyright; see http://www.asme.org/terms/Terms_Use.cfm

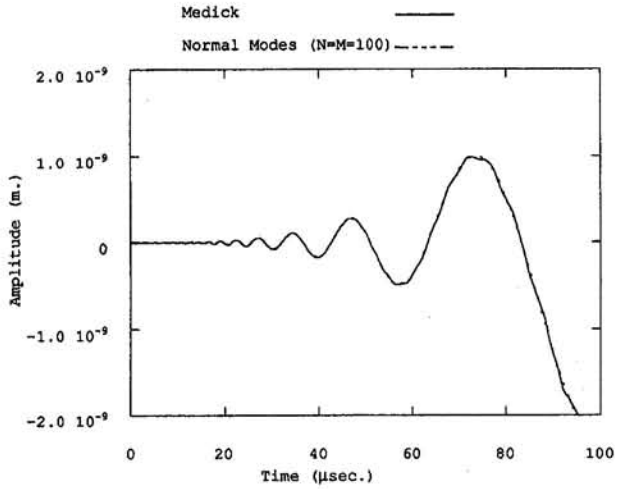


Fig. 1 Plate response to a step function for a source to receiver distance of 0.127 m

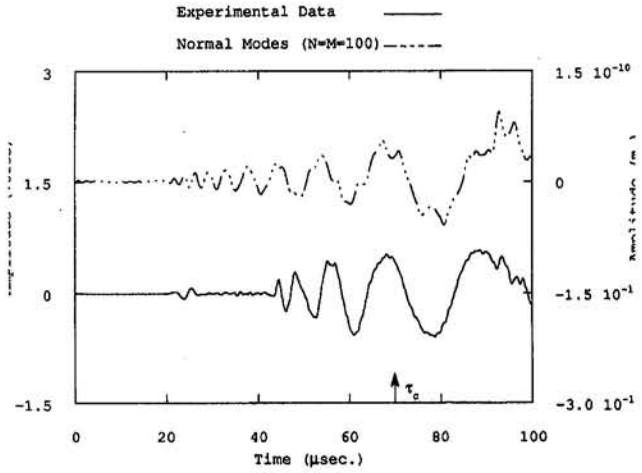


Fig. 3 Lead break at 0.1778 m from receiver

tial relevance of Mindlin's plate theory (1951) to AE. Pao (1982) reviewed Medick's (1961) classical plate theory for a point source, but rejected it as useful for AE and no one seems to have investigated its relevance to AE any further.

Herein, a normal mode solution to the classical plate bending equation was investigated for its applicability to AE. The same source-time function chosen by Weaver and Pao is considered. However, arbitrary source and receiver positions are chosen relative to the boundaries of the plate. This is another advantage of the plate theory treatment in addition to its simplicity. The source does not have to be at the center of the plate as in the axisymmetric treatment. The plate is allowed to remain finite and reflections are predicted. The importance of this theory to AE is that it can handle finite plates, realistic boundary conditions, and can be extended to composite materials.

Theoretical

The normal mode solution procedure has been widely applied to a number of elasticity problems including strings, beams, membranes, and plates. This solution technique is discussed in detail by Graff (1991). For a thin, homogeneous, isotropic plate, the governing equation of motion from classical plate theory is

$$D\nabla^4 w(x, y, t) + \rho h \partial^2 w(x, y, t)/\partial t^2 = f(x, y, t) \quad (1)$$

where the x and y-axes lie in the plane of the plate and the z-axis is perpendicular to the plane of the plate. Time is represented by t, $\nabla^4 = (\partial^2/\partial x^2 + \partial^2/\partial y^2)^2$ and $f(x, y, t)$ is the force (N/m^2) applied in the z direction. $w(x, y, t)$ is the transverse displacement, ρ the density, and h the plate thickness. D is the bending stiffness given by

$$D = Eh^3/12(1 - \nu^2) \quad (2)$$

where E is Young's modulus and ν is Poisson's ratio.

A step forcing function at $x = \xi$, $y = \zeta$, given by

$$f(x, y, t) = P\delta(x - \xi)\delta(y - \zeta)H(t) \quad (3)$$

where P is the amplitude of the step is used and the plate is assumed to be simply supported at its boundaries, $x = 0$, $x = l$, $y = 0$, and $y = w$. The resulting normal mode solution is given by

$$w(x, y, t) = \frac{4P}{\rho h l w} \times \sum_{n,m} \frac{\sin \alpha_n x \sin \gamma_m y \sin \alpha_n \xi \sin \gamma_m \zeta (1 - \cos \omega_{nm} t)}{\omega_{nm}^2} \quad (4)$$

where $\alpha_n = n\pi/l$ and $\gamma_m = m\pi/w$ for $n, m = 1, 2, \ldots,$

$$\omega_{nm} = \pi^2 \left[\frac{n^2}{l^2} + \frac{m^2}{w^2}\right] a \quad (5)$$

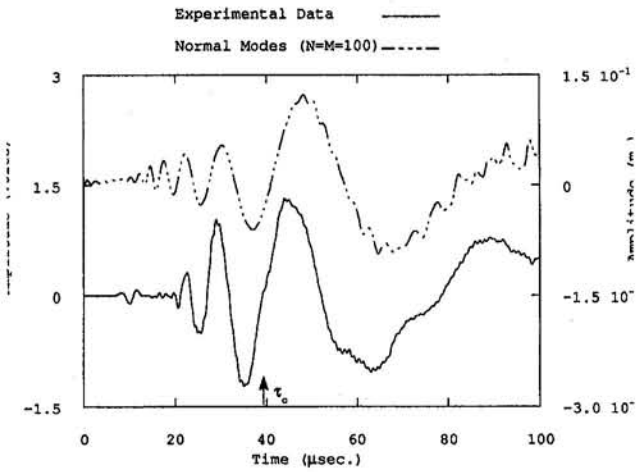


Fig. 2 Lead break at 0.1016 m from receiver

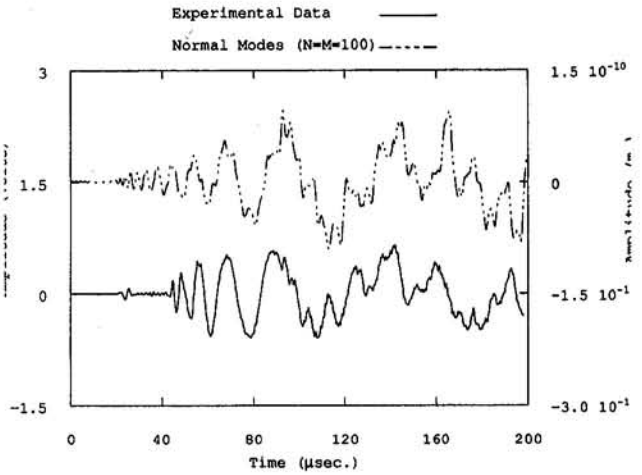


Fig. 4 Theory and experiment compared at longer time shows reflections

Downloaded 04 May 2010 to 171.66.16.33. Redistribution subject to ASME license or copyright; see http://www.asme.org/terms/Terms_Use.cfm

and

$$a^2 = D/\rho h.$$

This result is to be compared with Medick's (1961) result for an infinite plate subject to a step function in time at the origin

$$w(r, t) = \frac{P}{4\pi(\rho h D)^{1/2}} tH(4ar^2/t) \tag{6}$$

where

$$H(x) = \pi/2 - \text{Si}(x) + x\,\text{Ci}(x) - \sin(x) \tag{7}$$

with $\text{Si}(x)$ and $\text{Ci}(x)$ being the sine and cosine integrals, respectively. Equations (4) and (6) were programmed and evaluated for several source to receiver distances for an aluminum plate and compared with experimental data.

Experimental

A pencil lead break provided a source which approximates a vertical step function, but the magnitude of the force was not measured. The aluminum plate had dimensions $l = 0.381$ m, $w = 0.508$ m, and $h = 0.003175$ m. A 1.27 cm diameter, 2.5 MHz ultrasonic transducer (Panametrics) was used as the receiver because of its wideband behavior in the frequency range of interest (20–500 KHz). Papadakis (1980) pointed out that these transducers should provide flat frequency response from near zero frequency to just below their resonance frequency and thus make high-fidelity AE sensors. The large diameter of this sensor is not a concern in these measurements because of the long wavelengths of the flexural mode signals being measured. This sensor has been shown to be displacement sensitive in previous research by Prosser (1991). Although the frequency response of this sensor is much flatter and broader than conventional resonant AE sensors, its response does drop off at low frequencies. The frequency response of the transducer was determined and applied to the theoretical calculations. Because the frequency of each normal mode summed in the theoretical calculation is known, it was easier to apply the transducer filter response to the theoretical calculations than to the measured data.

Results and Discussion

Figure 1 shows a comparison between our normal mode solution and Medick's integral transform solution for the same source to receiver distance on the aluminum plate. This distance and the length of time shown in the plot in this figure were chosen such that there are no reflections from the plate boundaries included in the waveforms. Reflection signals are predicted in the normal mode solution but neglected by the Medick (1961) infinite plate solution. Also, since this is a comparison of theory with theory, the transducer response filtering was not applied. It can be seen that the agreement is quite good for $n = m = 100$. From Eq. (5), the highest frequency term in the normal mode solution is 834 KHz which is well above those seen in the experimental data. The 10,000 terms took less than five minutes to compute on a 68030 based microcomputer for 512 points.

Figures 2 and 3 show the measured waveforms and the theoretical waveforms at distances of 0.1016 m and 0.1778 m from the source. According to observations by Medick (1961), this theory should agree with experiment when the wavelength is greater than 16 times the thickness of the plate. This corresponds to a time greater than

$$\tau_c = 2\left(\frac{x}{c}\right) \tag{8}$$

where c is the characteristic velocity $(E/\rho)^{1/2}$. This implies that theory and experiment should begin to agree at the point indicated by the arrow in the figures. It can be seen that there is good agreement beyond this initial critical time. Note that the extensional mode can be seen in each of the experimental waveforms. Due to the higher wavespeeds of the extensional mode, it begins to separate from the flexural mode as the source to receiver distance increases. Figure 4 shows the response for longer times. It can be seen that there are reflections present in both theory and experiment which would not be predicted by theory for an infinite plate. It is interesting to note, as Medick (1961) does, that the quantitative predictions of the classical theory retain their accuracy even for points only several plate thicknesses removed from the loading area as illustrated for the response of the plate at a distance of 0.1016 m from the source.

Acknowledgment

We are grateful to NASA for supporting this work. E. I. Madaras, Langley Research Center, was the program monitor.

References

Breckenridge, F. R., Tschiegg, C. E., and Greenspan, M., 1975, "Acoustic Emission: Some Applications of Lamb's Problem," *J. Acoust. Soc. Am.*, Vol. 57, No. 3, pp. 626–631.

Graff, K. F., 1991, *Wave Motion in Elastic Solids*, Dover, New York.

Hsu, N. N., 1985, "Dynamic Green's Functions of an Infinite Plate—A Computer Program," NBSIR 85-3234.

Hutchinson, R., 1983, "Axisymmetric Elastic Waves Excited by a Point Source in a Plate," ASME JOURNAL OF APPLIED MECHANICS, Vol. 50, pp. 699–700.

Medick, M. A., 1961, "On Classical Plate Theory and Wave Propagation," ASME JOURNAL OF APPLIED MECHANICS, Vol. 28, pp. 223–228.

Mindlin, R. D., 1951, "Influence of Rotary Inertia and Shear on Flexural Motions of Isotropic, Elastic Plates," ASME JOURNAL OF APPLIED MECHANICS, Vol. 18, pp. 31–38.

Pao, Y. H., 1978, "Theory of Acoustic Emission," *Elastic Waves and Non-Destructive Testing of Materials*, AMD-Vol. 29, pp. 107–128.

Pao, Y. H., 1982, "Transient AE Waves in Elastic Plates," *6th International AE Symposium*, Japan, pp. 181–197.

Papadakis, E. P., 1980, "Broadband Flaw Detection Transducers: Application to Acoustic Emission Pulse Shape and Spectrum Recording Based on Pulse Echo Response Spectrum Corrected for Beam Spreading," *Acoustica*, Vol. 46, pp. 293–298.

Prosser, W. H., 1991, "The Propagation Characteristics of the Plate Modes of Acoustic Emission Waves in Thin Aluminum Plates and Thin Graphite/Epoxy Composite Plates and Tubes," NASA Technical Memorandum 104187.

Weaver, R. L., and Pao, Y. H., 1982, "Axisymmetric Elastic Waves Excited by a Point Source in a Plate," ASME JOURNAL OF APPLIED MECHANICS, Vol. 49, pp. 821–836.

Downloaded 04 May 2010 to 171.66.16.33. Redistribution subject to ASME license or copyright; see http://www.asme.org/terms/Terms_Use.cfm

Journal of Applied Mechanics

Discussion

Three-Dimensional Elasticity Solution for the Buckling of Transversely Isotropic Rods: The Euler Load Revisited[1]

K. T. Chau[2]. The author considered the interesting problem of the buckling of transversely isotropic rods using three-dimensional elasticity, and compared his result with the Euler's buckling formula and with two improved formulae including the effect of shearing force proposed by Timoshenko and Gere (1961). The simple formula proposed by the author for the buckling load of isotropic rods, I believe, provides an improvement over the existing formulae.

Actually, the use of three-dimensional elasticity to examine the buckling load for short columns is not a new idea. The author seems not aware of a couple of papers on nearly the same topic published in June 1993 and June 1995 (Chau, 1993, 1995). The omission of the first of these papers leads to the question of whether or not a literature search was done properly by the author. In fact, the author also published one paper (Kardomateas, 1993) in the June 1993 issue of the ASME JOURNAL OF APPLIED MECHANICS in which Chau's (1993) paper appeared. (Note that a complimentary issue is sent to all the contributing authors in the same issue by JAM.)

In the 1993 paper, Chau solved the antisymmetric modes of bifurcations in a compressible pressure-sensitive circular solid cylinder under both axisymmetric tension and compression. The material response of the cylinder is modeled by a physical model proposed by Rudnicki (1977). If the solid cylinder is not pressure-sensitive, the six material parameters proposed by Rudnicki (1977) reduces to five, and the conventional constitutive form of transversely isotropic elastic solids is recovered as a special case. The axisymmetric loading considered by Chau (1993) also incorporated the effect of confining stress on the buckling problem (i.e., when compression is considered). Thus, simple compression, which is studied by the author, can be considered as a special case of the more general problem investigated by Chau (1993), obtained by simply setting the confining stress zero and the material being pressure-insensitive. Recently, the results of Chau (1993) were further generalized to transversely isotropic solid cylinders governed by a constitutive law similar to Eq. (8) given by the author (Chau, 1995).

Therefore, the bifurcation analysis by Chau (1993, 1995) provides a more general solution compared to those obtained by the author. But, it also embraces the problem considered by the author as a special case. Although the main emphasis of Chau (1993) is to study the effect of geometric bifurcation modes, which is induced by the free boundary of the cylinders, on the localization of deformation in rock-like materials, Chau (1993) did consider the Euler's buckling as a special case.

In particular, after obtaining the general eigenvalue equations for the elliptic complex and elliptic imaginary sub-regimes (Eqs. (6.11) and (6.16) in Chau, 1993), Chau (1993) continued to consider the so-called long wavelength limit (i.e. $\gamma = m\pi a/L \rightarrow 0$, where m is an integer, a the radius of the solid cylinder, and L the length of the cylinder). It was shown analytically that the Euler's buckling formula corresponds to the first term in the series expansion of γ when the bifurcation stress is expanded in terms of γ (see Eq. (6.21) of Chau, 1993). More importantly, the conclusion applies even if the solid cylinders are pressure-sensitive and transversely isotropic; whereas the author is only able to show this for the isotropic limit. Although the full details in obtaining the Euler's formula were not reported by Chau (1993), the specialization involves a fairly delicate process of algebraic manipulation. Indeed, if one is interested in obtaining an approximate buckling formula for short columns, we can do so by simply retaining the higher order terms in the expansion shown in Eq. (6.18) of Chau (1993).

The main difference between the author's paper and Chau's (1993, 1995) papers is the method of solution. The author followed mainly the method of solution proposed by Elliott (1948) while the general theory proposed by Hu (1954) and used by Chen (1966) was modified and adopted by Chau (1993, 1995). The author also noted that "in general, the roots s_1 and s_2 (for Eq. (14b)) are either both real or complex conjugates." This classification on the nature of the roots of s is rather incomplete; the roots for s, actually, can also be partly real or purely imaginary. And the physical meaning for s being real or complex conjugates is not clear. On the contrary, by adopting Hu's (1956) approach Chau (1993) arrived at a parameter ν_α, which bears the same significance of s in the author's analysis, and the root-type of ν_α does carry a clear physical meaning (see Eq. (5.4) of Chau, 1993). That is, if a real root of ν_α exists, the shear band bifurcation or localization of deformation also becomes possible. For the case of no real root, ν_α can further be either complex conjugate pairs or purely imaginary. Chau (1993) showed analytically that the above conclusion on the validity of Euler's buckling formula as $\gamma \rightarrow 0$ applies for both cases. In particular, Euler's was recovered as the long wavelength limit for all the elliptic complex (all roots of ν_α are complex conjugates), elliptic imaginary (all roots of ν_α are purely imaginary), and hyperbolic (all roots of ν_α are real) regimes in the parameter space.

References

Chau, K. T., 1993, "Antisymmetric Bifurcations in a Compressible Pressure-Sensitive Circular Cylinder Under Axisymmetric Tension and Compression," ASME JOURNAL OF APPLIED MECHANICS, Vol. 60, pp. 282–289.

[1] By G. A. Kardomateas and published in the June 1995 issue of the ASME JOURNAL OF APPLIED MECHANICS, Vol. 62, pp. 346–355.

[2] Assistant Professor, Department of Civil and Structural Engineering, The Hong Kong Polytechnic University, Hung Hom, Kowloon, Hong Kong. Mem. ASME.

Copyright © 1996 by ASME

Downloaded 04 May 2010 to 171.66.16.33. Redistribution subject to ASME license or copyright; see http://www.asme.org/terms/Terms_Use.cfm

Chau, K. T., 1995, "Buckling, barrelling, and surface instabilities of a finite, transversely isotropic circular cylinder," *Quarterly of Applied Mathematics,* Vol. 53, pp. 225–244.

Chen, W. T., 1966, "On Some Problems in Transversely Isotropic Elastic Materials," ASME JOURNAL OF APPLIED MECHANICS, Vol. 33, pp. 539–546.

Elliott, H. A., 1948, "Three-Dimensional Stress Distributions in Hexagonal Aeolotropic Crystals," *Mathematical Proceedings of the Cambridge Philosophical Society,* Vol. 44, pp. 522–533.

Hu, H.-C., 1954, "On the Three-Dimensional Problems of the Theory of Elasticity of a Transversely Isotropic Body," *Acta Scientia Sinica,* Vol. 2, pp. 145–151.

Kardomateas, G. A., 1993, "Stability Loss in Thick Transversely Isotropic Cylindrical Shells Under Axial Compression," ASME JOURNAL OF APPLIED MECHANICS, Vol. 60, pp. 506–513.

Rudnicki, J. W., 1977, "The Effect of Stress-Induced Anisotropy on a Model of Brittle Rock Failure as Localization of Deformation," *Energy Resources and Excavation Technology, Proceeding of the 18th U.S. Symposium on Rock Mechanics,* Keystone, CO, June 22–24, pp. 3B4-1–3B4-8.

Timoshenko, S. P., and Gere, J. M., 1961, *Theory of Elastic Stability,* 2nd ed., McGraw-Hill, New York.

Author's Closure[3]

The author would like to thank Professor Chau for drawing his attention to his recent papers (Chau 1993, 1995) on the buckling of short columns. These papers were omitted from the reference list unintentionally since they are too recent and very close to the dates of preparation and submission of the present paper to be found in systematic literature searches at the time the manuscript was authored. Professor Chau's work, which follows a different method of solution, complements the present paper by including compressible pressure-sensitive material and providing an alternative formulation. The discussion on the roots s_1 and s_2 is also welcome.

In closing, the author would like to emphasize a few of the main objectives and unique contributions of the present paper such as the derivation of a new, simple, improved column buckling formula, which provides an additional term to the Euler buckling load, and the comparison of the three-dimensional elasticity results with the Timoshenko/Engesser/Haringx transverse shear correction column buckling formulas.

[3] Associate Professor, School of Aerospace Engineering, Georgia Institute of Technology, Atlanta, GA 30332-0150. Mem ASME.

Three-Dimensional Elasticity Solution for the Buckling of Transversely Isotropic Rods: The Euler Load Revisited[4]

C. W. Bert[5]. Professor Kardomateas' paper is a welcome addition to the literature of the subject. The two Timoshenko formulas cited in the paper by reference to Timoshenko and Gere (1961) are in fact the well-known Engesser formula (Engesser, 1891) and the Haringx formula (Haringx, 1948), referred to by Timoshenko and Gere as the "modified" formula.

For the case of isotropic materials, there has been extensive criticism of the Haringx formula; see Nanni (1971), Ziegler (1982), and Reissner (1982). In particular, in his extensive three-dimensional elasticity analysis, Nanni concluded that the Haringx analysis is less accurate than the Engesser one. This seems to be in direct contradiction to the conclusion of Kardomateas; an explanation for this apparent discrepancy would be welcomed.

The author has not provided any physical explanations as to why his Eq. (35) is more accurate than either the Engesser or the Haringx prediction. It is conjectured here that the difference is due to the inclusion of axial flexibility in the author's analysis, while it was tacitly omitted in Engesser's work and in the particular version of the Haringx work quoted by Timoshenko and Gere (1961).

[4] By G. A. Kardomateas and published in the June 1995 issue of the ASME JOURNAL OF APPLIED MECHANICS, Vol. 62, pp. 346–354.

[5] Perkinson Chair, School of Aerospace and Mechanical Engineering, The University of Oklahoma, Norman, OK 73019. Life Fellow ASME.

References

Engesser, F., 1891, "Die Knickfestigheit gerader Stabe," *Zentralblatt der Bauverwaltung,* Vol. 11, pp. 483–486.

Haringx, J. A., 1948, "On Highly Compressible Helical Springs and Rubber Rods, and Their Application for Vibration-Free Mountings," *Philips Research Reports,* Eindhoven, Holland, Vol. 3, pp. 401–449; Vol. 4, pp. 49–80.

Nanni, J., 1971, "Das Eulersche Knickproblem unter Berucksichtigung der Querkrafte," *Zeitschrift fur Angewandte Mathematik und Physik,* Vol. 22, pp. 156–185.

Reissner, E., 1982, "Some Remarks on the Problem of Column Buckling," *Ingenieur-Archiv,* Vol. 52, pp. 115–119.

Timoshenko, S. P., and Gere, J. M., 1961, *Theory of Elastic Stability,* 2nd. ed., McGraw-Hill, New York.

Ziegler, H., 1982, "Arguments For and Against Engesser's Buckling Formulas," *Ingenieur-Archiv,* Vol. 52, pp. 105–113.

Author's Closure[6]

The author would like to thank Professor Bert for his gracious comments regarding the paper under discussion. The formulas quoted in the paper as Timoshenko's (1961) first and second shear correction formulas are indeed the formulas of Engesser (1891) and Haringx (1948) as was pointed out correctly by Professor Bert (Haringx obtained the formula in connection with helical springs and Timoshenko applied Haringx's approach to bars).

Regarding Nanni's three-dimensional elasticity approach, a review of his paper (written in German) indicates that Nanni's (1971) treatment of the problem was based on a stress function approach and *an asymptotic scheme* with respect to the dimensions of the cross section (e.g., thickness); in this scheme, stresses were expanded in a polynomial series with coefficients that were subsequently determined through compatibility. Therefore, his conclusions (that Engesser's formula is more accurate than the Haringx analysis) may be influenced by the fact that a certain number of terms were retained (i.e., Nanni's results can be considered approximations); we may conjecture, therefore, that this conclusion may not hold if more terms in the asymptotic expansion were to be retained.

Instead, our three-dimensional elasticity results for the critical load are derived by numerically solving the determinant of the system of Eqs. (28) (and do not depend on an asymptotic scheme); therefore they can be considered exact. Our conclusion that the Haringx formula is more accurate than Engesser's was also the feeling of Timoshenko as expressed in Timoshenko and Gere (1961). Nevertheless, it should be noted that in most cases of practical interest, the difference between Engesser or Haringx formulas is small.

Regarding Professor Bert's conjecture as to why the author's Eq. (35) is more accurate than either the Engesser or the Haringx formulas, the author would like to thank Professor Bert for offering this reasoning, which seems, indeed, to be a plausible physical explanation.

[6] Associate Professor, School of Aerospace Engineering, Georgia Institute of Technology, Atlanta, GA 30332-0150. Mem. ASME.

Downloaded 04 May 2010 to 171.66.16.33. Redistribution subject to ASME license or copyright; see http://www.asme.org/terms/Terms_Use.cfm

Chau, K. T., 1995, "Buckling, barrelling, and surface instabilities of a finite, transversely isotropic circular cylinder," *Quarterly of Applied Mathematics,* Vol. 53, pp. 225–244.

Chen, W. T., 1966, "On Some Problems in Transversely Isotropic Elastic Materials," ASME JOURNAL OF APPLIED MECHANICS, Vol. 33, pp. 539–546.

Elliott, H. A., 1948, "Three-Dimensional Stress Distributions in Hexagonal Aeolotropic Crystals," *Mathematical Proceedings of the Cambridge Philosophical Society,* Vol. 44, pp. 522–533.

Hu, H.-C., 1954, "On the Three-Dimensional Problems of the Theory of Elasticity of a Transversely Isotropic Body," *Acta Scientia Sinica,* Vol. 2, pp. 145–151.

Kardomateas, G. A., 1993, "Stability Loss in Thick Transversely Isotropic Cylindrical Shells Under Axial Compression," ASME JOURNAL OF APPLIED MECHANICS, Vol. 60, pp. 506–513.

Rudnicki, J. W., 1977, "The Effect of Stress-Induced Anisotropy on a Model of Brittle Rock Failure as Localization of Deformation," *Energy Resources and Excavation Technology, Proceeding of the 18th U.S. Symposium on Rock Mechanics,* Keystone, CO, June 22–24, pp. 3B4-1–3B4-8.

Timoshenko, S. P., and Gere, J. M., 1961, *Theory of Elastic Stability,* 2nd ed., McGraw-Hill, New York.

Author's Closure[3]

The author would like to thank Professor Chau for drawing his attention to his recent papers (Chau 1993, 1995) on the buckling of short columns. These papers were omitted from the reference list unintentionally since they are too recent and very close to the dates of preparation and submission of the present paper to be found in systematic literature searches at the time the manuscript was authored. Professor Chau's work, which follows a different method of solution, complements the present paper by including compressible pressure-sensitive material and providing an alternative formulation. The discussion on the roots s_1 and s_2 is also welcome.

In closing, the author would like to emphasize a few of the main objectives and unique contributions of the present paper such as the derivation of a new, simple, improved column buckling formula, which provides an additional term to the Euler buckling load, and the comparison of the three-dimensional elasticity results with the Timoshenko/Engesser/Haringx transverse shear correction column buckling formulas.

[3] Associate Professor, School of Aerospace Engineering, Georgia Institute of Technology, Atlanta, GA 30332-0150. Mem ASME.

Three-Dimensional Elasticity Solution for the Buckling of Transversely Isotropic Rods: The Euler Load Revisited[4]

C. W. Bert[5]. Professor Kardomateas' paper is a welcome addition to the literature of the subject. The two Timoshenko formulas cited in the paper by reference to Timoshenko and Gere (1961) are in fact the well-known Engesser formula (Engesser, 1891) and the Haringx formula (Haringx, 1948), referred to by Timoshenko and Gere as the "modified" formula.

For the case of isotropic materials, there has been extensive criticism of the Haringx formula; see Nanni (1971), Ziegler (1982), and Reissner (1982). In particular, in his extensive three-dimensional elasticity analysis, Nanni concluded that the Haringx analysis is less accurate than the Engesser one. This seems to be in direct contradiction to the conclusion of Kardomateas; an explanation for this apparent discrepancy would be welcomed.

The author has not provided any physical explanations as to why his Eq. (35) is more accurate than either the Engesser or the Haringx prediction. It is conjectured here that the difference is due to the inclusion of axial flexibility in the author's analysis, while it was tacitly omitted in Engesser's work and in the particular version of the Haringx work quoted by Timoshenko and Gere (1961).

[4] By G. A. Kardomateas and published in the June 1995 issue of the ASME JOURNAL OF APPLIED MECHANICS, Vol. 62, pp. 346–354.

[5] Perkinson Chair, School of Aerospace and Mechanical Engineering, The University of Oklahoma, Norman, OK 73019. Life Fellow ASME.

References

Engesser, F., 1891, "Die Knickfestigheit gerader Stabe," *Zentralblatt der Bauverwaltung,* Vol. 11, pp. 483–486.

Haringx, J. A., 1948, "On Highly Compressible Helical Springs and Rubber Rods, and Their Application for Vibration-Free Mountings," *Philips Research Reports,* Eindhoven, Holland, Vol. 3, pp. 401–449; Vol. 4, pp. 49–80.

Nanni, J., 1971, "Das Eulersche Knickproblem unter Berucksichtigung der Querkrafte," *Zeitschrift fur Angewandte Mathematik und Physik,* Vol. 22, pp. 156–185.

Reissner, E., 1982, "Some Remarks on the Problem of Column Buckling," *Ingenieur-Archiv,* Vol. 52, pp. 115–119.

Timoshenko, S. P., and Gere, J. M., 1961, *Theory of Elastic Stability,* 2nd. ed., McGraw-Hill, New York.

Ziegler, H., 1982, "Arguments For and Against Engesser's Buckling Formulas," *Ingenieur-Archiv,* Vol. 52, pp. 105–113.

Author's Closure[6]

The author would like to thank Professor Bert for his gracious comments regarding the paper under discussion. The formulas quoted in the paper as Timoshenko's (1961) first and second shear correction formulas are indeed the formulas of Engesser (1891) and Haringx (1948) as was pointed out correctly by Professor Bert (Haringx obtained the formula in connection with helical springs and Timoshenko applied Haringx's approach to bars).

Regarding Nanni's three-dimensional elasticity approach, a review of his paper (written in German) indicates that Nanni's (1971) treatment of the problem was based on a stress function approach and *an asymptotic scheme* with respect to the dimensions of the cross section (e.g., thickness); in this scheme, stresses were expanded in a polynomial series with coefficients that were subsequently determined through compatibility. Therefore, his conclusions (that Engesser's formula is more accurate than the Haringx analysis) may be influenced by the fact that a certain number of terms were retained (i.e., Nanni's results can be considered approximations); we may conjecture, therefore, that this conclusion may not hold if more terms in the asymptotic expansion were to be retained.

Instead, our three-dimensional elasticity results for the critical load are derived by numerically solving the determinant of the system of Eqs. (28) (and do not depend on an asymptotic scheme); therefore they can be considered exact. Our conclusion that the Haringx formula is more accurate than Engesser's was also the feeling of Timoshenko as expressed in Timoshenko and Gere (1961). Nevertheless, it should be noted that in most cases of practical interest, the difference between Engesser or Haringx formulas is small.

Regarding Professor Bert's conjecture as to why the author's Eq. (35) is more accurate than either the Engesser or the Haringx formulas, the author would like to thank Professor Bert for offering this reasoning, which seems, indeed, to be a plausible physical explanation.

[6] Associate Professor, School of Aerospace Engineering, Georgia Institute of Technology, Atlanta, GA 30332-0150. Mem. ASME.

Downloaded 04 May 2010 to 171.66.16.33. Redistribution subject to ASME license or copyright; see http://www.asme.org/terms/Terms_Use.cfm

Initial Post-buckling Behavior of Thick Rings Under Uniform External Hydrostatic Pressure[7]

Robert Schmidt[8]. The third and sixth columns of Table 1 display values that seem unreasonable. After all, it is well known that consideration of the shear deformation in the analysis of thin structural elements does not appreciably alter the characteristic values obtained through purely flexural analysis. Moreover, the formula

$$q_{cr} = q_0 = (3EI/R^3)/[1 + 8(1 + \nu)kI/AR^2]$$

$$= (2Et^3/D^3)/[1 + 8(1 + \nu)kt^2/3D^2],$$

obtained by Schmidt and DaDeppo (1971), yields (for k = 1.2) the values q_{cr} = 39.037, 92.483, and 82803 for D/t = 80, 60, and 6, respectively. These values are noticeably greater than the authors' corresponding values 38.086, 90.239, and 82125 in column 3 of Table 1 (also see Smith and Simitses, 1969).

Furthermore, the authors' more precise 2-D analyses (columns 2 and 5 of Table 1) support the writer's contention stated in his first sentence.

The authors do not present a derivation of Eq. (7) in their paper, nor do they refer to a source. For that reason, it is difficult to verify its correctness. Nevertheless there is a reason or two to doubt its dependability. For instance, the pressure, q, is acting on the outer surface, while other quantities seem to be associated with the middle of the cross section. Moreover, this equation seems insufficiently similar to the corresponding equations presented by Budiansky (1974) and Chwalla and Kollbrunner (1938).

Since confidence in analyses is a necessary prerequisite for the use of the results, the writer would welcome the authors' comments on the matter discussed above. (Schmidt's 1979a and 1983 results confirm El Naschie's in columns 4 and 7 of Table 1.)

It is interesting to observe that Schmidt's (1979b) equations yield q_{cr} = 23.363, instead of 39.037, for D/t = 80, and also a negative eigenvalue, if the thin ring is fixed (clamped) at a point, i.e., if the two ends of hingeless arch coincide.

[7] By Lei Fu and A. M. Waas and published in the June 1995 issue of the ASME JOURNAL OF APPLIED MECHANICS, Vol. 62, pp. 338–345.

[8] Adjunct (retired) Professor of Engineering Mechanics, Department of Mechanical Engineering, University of Detroit Mercy, Detroit, MI 48219-0900. Mem. ASME.

References

Budiansky, B., 1974, "Theory of Buckling and Postbuckling Behavior of Elastic Structures," *Advances in Applied Mechanics,* Vol. 14, Chia-Shun Yih, ed., Academic Press, New York, pp. 1–65.

Chwalla, E., and Kollbrunner, C. F., 1938, "Beitraege zum Knickproblem des Bogentraegers und des Rahmens," *Der Stahlbau,* Vol. 11, No. 10, May, pp. 73–78.

Schmidt, R., 1979a, "A Critical Study of Postbuckling Analyses of Uniformly Compressed Rings," *Zeitschrift fuer angewandte Mathematik und Mechanik,* Vol. 59, No. 10, pp. 581–582.

Schmidt, R., 1979b, "Postbuckling Behavior of Uniformly Compressed Circular Arches with Clamped Ends," *Zeitschrift fuer angewandte Mathematik und Physik,* Vol. 30, pp. 553–556.

Schmidt, R., 1983, "Postbuckling State of a Ring Under Three Static Pressures," *Industrial Mathematics, Journal of the IMS,* Vol. 33, Part 1, pp. 51–55.

Schmidt, R., and DaDeppo, D. A., 1971, "Nonlinear Theory of Arches with Transverse Shear Deformation and Rotary Inertia," *Industrial Mathematics, Journal of the IMS,* Vol. 21, Part 1, pp. 33–49.

Smith, C. V., Jr., and Simitses, G. J., 1969, "Effect of Shear and Load Behavior on Ring Stability," ASCE *Journal of the Engineering Mechanics Division,* Vol. 95, No. EM3, pp. 559–569.

Author's Closure[9]

We are happy to note of Professor Schmidt's interest in our work, and would like to apologize for the oversight in our part of leaving out some key previous work by Professor Schmidt. Equation (7) of our paper was derived as given in the text (see reference below) by Brush and Almroth. Since this equation applies to the derivation corresponding to the development of a one-dimensional first-order shear deformation model, the location (with respect to the ring's thickness or radial direction) at which the external pressure acts is not significant just as in the case corresponding to Kirchoff-Love kinematics. Of course, this is not the case for the two-dimensional analysis as is shown in our paper. Our one-dimensional treatment is not "purely" flexural since it does not restrict the ring deformation to be inextensional. This is why our Eq. (7) is insufficiently similar to previous other work mentioned by Professor Schmidt. Also, note that we used a "shear-correction factor" of 1.0 when evaluating the shearing energy contribution in the process of deriving the governing equations. We have constructed the table below for critical buckling pressures, using the numbers provided by Professor Schmidt and our calculations. The last two columns provide the percentage deviation of the one-dimensional shear deformation theories against the two-dimensional elasticity solution.

D/t	Schmidt and DaDeppo (1971)	Fu and Waas (1D shear)	Fu and Waas (2D)	Relative Error of Schmidt and DaDeppo (1971)	Relative Error of Fu and Waas (1D shear)
80	39.037	38.086	39.035	0.005%	−2.43%
60	92.483	90.239	92.476	0.007%	−2.42%
6	82803	82125	81232	1.93%	−1.10%

From this table, the solution by Schmidt and DaDeppo (1971) is seen to diverge as the ring becomes thicker (D/t tending to zero), whereas the Fu and Waas (1995) solution is seen to approach the two-dimensional solution, albeit from below. For thicker rings, ring centerline extensionality is just as important as incorporating shear deformation.

[9] Lei Fu, Engineer/Scientist-Specialist, McDonnel Douglas Aerospace, Long Beach, CA 90810-1870, Mem. ASME; and A. M. Waas, Assoc. Prof., Department of Aerospace Engineering, University of Michigan, Ann Arbor, MI 48109-2118. Mem. ASME.

References

Brush, D. O., and Almroth, B. O., 1975, *Buckling of Bars, Plates and Shells,* McGraw-Hill, New York.

Copyright © 1996 by ASME

Downloaded 04 May 2010 to 171.66.16.33. Redistribution subject to ASME license or copyright; see http://www.asme.org/terms/Terms_Use.cfm

Journal of Applied Mechanics

Book Review

Micromechanics: Overall Properties of Heterogeneous Materials, by S. Nemat-Nasser and M. Lori. Elsevier Publishers B. V., Amsterdam, The Netherlands, 1993. 687 pages. Price: $120.00.

REVIEWED BY S. K. DATTA[1]

The book contains a careful exposition of the modeling of effective properties of an elastic solid having a dispersion of elastic inclusions, cavities, or cracks. It is assumed that the deformations are small and under this assumption the authors describe also some applications to elastoplastic or viscoelastoplastic materials. The basic idea of a representative volume element (RVE) with the associated boundary value problems is laid down in the beginning. Then the authors describe a systematic way to derive the macroscopic (overall) response from the variable microscopic response of the RVE. General results relating to bounds on the overall strain energy and complementary energy are established in the beginning and are used as a guiding element later for specific results.

The book is divided into two parts. Overall properties of the heterogeneous solids are dealt with in Part 1. Part 2 contains a basic introduction to the theory of elasticity. This way, it is self-contained and should prove to be useful as a graduate text in mechanics of materials with inhomogeneities.

[1]Department of Mechanical Engineering, CB427, University of Colorado, Boulder, CO 80309-0427.

Part 1 has four chapters. Chapter 1 lays down the foundation for modeling overall properties and averaging methods. Chapter 2 deals with elastic solids with cavities and cracks. Explicit results are derived for dilute volume fractions of cavities and cracks. Also, the self-consistent method is discussed for statistically homogeneous distributions. Finally, in this chapter, a brief review of microcrack-induced failure of brittle materials is presented. This section seems somewhat out of place in this book on overall properties. Even so, those interested in progressive failure due to microcracking could find the discussion and references useful. Elastic solids containing a distribution of elastic inclusions are treated in Chapter 3. Again, the dilute concentration limit and the self-consistent method are discussed in detail. Detailed treatment of bounds of overall properties can be found in this chapter as well as discussion of the differential scheme and some other averaging methods (the composite-spheres model due to Hashin and the three-phase model reported by Smith, Christensen, and Lo and others) are presented here. The final section of this chapter is devoted to properties of the Eshelby tensor and some related topics. Elastic solids with periodic distribution of inclusions are examined in details in Chapter 4, where a brief treatment of inelastic heterogeneous solids is given.

The authors are to be commended for presenting a fairly complete treatment of the static overall properties of elastic composite materials. It should prove to be useful to advanced graduate students in mechanics and materials as well as to researchers in these disciplines.

Copyright © 1996 by ASME

Downloaded 04 May 2010 to 171.66.16.33. Redistribution subject to ASME license or copyright; see http://www.asme.org/terms/Terms_Use.cfm